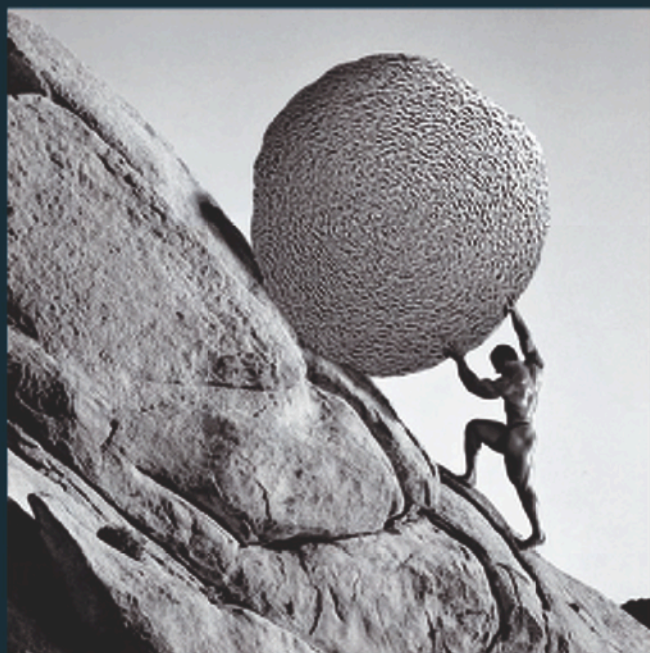


Edited by  
H. Bockhorn • A. D'Anna • A. F. Sarofim • H. Wang

# Combustion Generated Fine Carbonaceous Particles





H. Bockhorn, A. D'Anna, A. F. Sarofim, H. Wang (Eds.)

## **Combustion Generated Fine Carbonaceous Particles**

Cover picture by A. Ciajolo and A. Tregrossi „Sysiphus rolling a soot particle“  
Editorial coordination by DoppiaVoce, Napoli, Italy ([www.doppiaVoce.it](http://www.doppiaVoce.it))

# Combustion Generated Fine Carbonaceous Particles

Proceedings of an International Workshop  
held in Villa Orlandi, Anacapri,  
May 13-16, 2007

edited by  
H. Bockhorn  
A. D'Anna  
A. F. Sarofim  
H. Wang

## Impressum

Karlsruher Institut für Technologie (KIT)  
KIT Scientific Publishing  
Straße am Forum 2  
D-76131 Karlsruhe  
www.uvka.de

KIT - Universität des Landes Baden-Württemberg und nationales  
Forschungszentrum in der Helmholtz-Gemeinschaft



Dieses Buch ist im Internet unter folgender Creative Commons-Lizenz  
veröffentlicht: <http://creativecommons.org/licenses/by-nc-nd/3.0/de/>

KIT Scientific Publishing 2009  
Print on Demand

ISBN: 978-3-86644-441-6

We wish to dedicate this book to Klaus H. Homann, Jack B. Howard, and Heinz-Georg Wagner who, although they were not able to attend the workshop in person, were present through their ideas and seminal contributions that pervaded the presentations and discussions throughout the meeting.



# Editors

**Henning Bockhorn**

Universität Karlsruhe, Germany

**Andrea D'Anna**

Università di Napoli Federico II, Italy

**Adel F. Sarofim**

University of Utah, USA

**Hai Wang**

University of Southern California, USA

# Institutions of Workshop Organizers

Istituto di Ricerche sulla Combustione, CNR, Italy

Università degli Studi di Napoli Federico II, Italy

Universität Karlsruhe, Germany

University of Utah, USA

Sandia National Laboratories, USA

University of Southern California, USA

University of California, Berkeley, USA

Brandenburgische Technische Universität Cottbus, Germany

Imperial College London, UK

# International Workshop on Combustion Generated Fine Carbonaceous Particles

## INTERNATIONAL COMMITTEE

**Henning Bockhorn**

Universität Karlsruhe, Germany

**Andrea D'Anna**

Università di Napoli Federico II, Italy

**Michael Frenklach**

University of California, Berkeley, USA

**John Hewson**

Sandia National Laboratories, USA

**Peter R. Lindstedt**

Imperial College, UK

**Fabian Mauss**

Cottbus University, Germany

**Adel F. Sarofim**

University of Utah, USA (chair)

**Hai Wang**

University of Southern California, USA

## LOCAL ORGANIZING COMMITTEE

**Anna Ciajolo**

CNR Napoli, Italy

**Antonio Tregrossi**

CNR Napoli, Italy



# Preface

Discussion with a number of the leading researchers in the soot field indicated the desirability of holding a soot workshop as a sequel to that held in Heidelberg, September 30 to October 2 of 1991, leading to the publication “Soot Formation in Combustion”, edited by Henning Bockhorn and published in 1994. The arrangements for such a workshop were finalized by a self-appointed organizing committee of Henning Bockhorn, Andrea D’Anna, Michael Frenklach, John Hewson, Peter Lindstedt, Fabian Mauss, Adel Sarofim (Chair), and Hai Wang. The goals of the workshop were to:

- Review the current status of our understanding of soot formation mechanisms, new data and experimental methodology, and advances in the application of soot models to solve practical problems.
- Candid discussion of areas of discrepancies and the priorities for future research.
- The definition of a plan for collaboration between the soot community for the establishment of a web based data base and model comparison, using as a platform the initiative on process informatics (PrIME) that was initiated by Michael Frenklach, David Golden, and Michael Pilling and that is co-ordinated with the Collaborative on Multi-Scale Chemical Sciences (MSCS) headed up by Larry Rahn at Sandia and the initiative on kinetics for practical fuels headed up by Wing Tsang at NIST.

The products are summarized in this book that hopefully lays the groundwork for continued discussion and contributions by the community through PrIME.

The book reflects the structure and the results of the workshop. The single contributions have been grouped in five parts and an epilogue which summarizes the discussions recorded during the workshop. The articles from the different authors are mainly based on the contribution presented at the workshop.

The following Overview provides a brief guide to the different sections in the book. The cover picture of Sisyphus rolling a soot particle up a hill is to recognize that many of the ideas are old and are being revisited with the advantage of the continuing advances in theory and experimental measurement tools; that this long and sometimes frustrating process is a reflection of the complexity of the problem of measuring and modeling the growth of molecules consisting of a few carbon atoms into particles that may contain up to  $10^9$  carbons.



# List of participants

**Michael Balthasar**  
Volvo Technology Corporation, Sweden

**Henning Bockhorn**  
Universität Karlsruhe, Germany

**Kenneth Brezinsky**  
University of Illinois at Chicago,  
USA

**Helen Brocklehurst**  
Rolls Royce, UK

**Nabiha Chaumeix**  
CNRS, Orleans, France

**Anna Ciajolo**  
CNR, Napoli, Italy

**Meredith B. Colket III**  
United Technologies Research Center,  
USA

**Edwin Corporan**  
Wright Patterson Air Force Res. Lab.,  
USA

**Antonio D'Alessio**  
Università di Napoli Federico II, Italy

**Andrea D'Anna**  
Università di Napoli Federico II, Italy

**Pascale Desgroux**  
Université des Sciences et Technologies  
de Lille, France

**Richard A. Dobbins**  
Brown University, USA

**Ruud Eggel**  
Rolls Royce, Germany

**Michael Frenklach**  
University of California, Berkeley, USA

**Horst-Henning Grotheer**  
Institute of Combustion Technology,  
DLR, Germany

**Brian S. Haynes**  
University of Sydney, Australia

**John Hewson**  
Sandia National Laboratories, USA

**Ian M. Kennedy**  
University of California, Davis, USA

**John Kent**  
University of Sydney, Australia

**Stephen J. Klippenstein**  
Argonne National Laboratory, USA

**Katharina Kohse-Höinghaus**  
Bielefeld University, Germany

**Markus Kraft**  
Cambridge University, UK

**Shuichi Kubo**  
Toyota Central R&D Lab., Japan

**JoAnn Slama Lighty**  
University of Utah, USA

**R. Peter Lindstedt**  
Imperial College, UK

**M. Matti Maricq**  
Ford Motor Company, USA

**Fabian Mauss**  
Cottbus University, Germany

**Charles S. McEnally**  
Yale University, USA

**J. Houston Miller**  
The George Washington University,  
USA

**Patrizia Minutolo**  
CNR, Napoli, Italy

**Frederick Ossler**  
Lund University, Sweden

**Lisa D. Pfefferle**  
Yale University, USA

**Heinz Pitsch**  
Stanford University, USA

**Eliseo Ranzi**  
Politecnico di Milano, Italy

**Robert J. Santoro**  
Pennsylvania State University, USA

**Adel F. Sarofim**  
University of Utah, USA

**LeeAnn Sgrò**  
Università di Napoli Federico II, Italy

**Christopher R. Shaddix**  
Sandia National Laboratories, USA

**Mitchell D. Smooke**  
Yale University, USA

**Peter B. Sunderland**  
University of Maryland, USA

**Wing Tsang**  
National Institute of Standards and  
Technology, USA

**Angela Violi**  
University of Michigan, USA

**Pavel A. Vlasov**  
Semenov Institute of Chemical Physics,  
Russian Academy of Science, Russia

**Hai Wang**  
University of Southern California, USA

**Phillip R. Westmoreland**  
University of Massachusetts Amherst,  
USA

**Michael R. Zachariah**  
University of Maryland and National  
Institute of Standards and Technology,  
USA



Anacapri, Villa Orlandi, May 15, 2007.

# Contents

<i>Editors</i>	VII
<i>Institutions of Workshop Organizers</i>	VIII
<i>International Workshop on Combustion Generated Fine Carbonaceous Particles</i>	IX
<i>Preface</i>	XI
<i>List of participants</i>	XIII
<i>Overview</i>	XIX
<b>1. The role of soot in the health effects of inhaled airborne particles</b>	1
<i>B. Kumfer, I. Kennedy</i>	
<b>2. Soot structure and dimensionless extinction coefficient in diffusion flames: implications for index of refraction</b>	17
<i>C.R. Shaddix, T.C. Williams</i>	
<b>PART I</b>	
<b>Formation of soot precursors for real fuels</b>	35
<b>3. The prehistory of soot: small rings from small molecules</b>	37
<i>P.R. Westmoreland</i>	
<b>4. A priori kinetics for resonance stabilized hydrocarbon radicals</b>	49
<i>S.J. Klippenstein, L.B. Harding, Y. Georgievskii, J.A. Miller</i>	
<b>5. Soot precursors from real fuels: the unimolecular reactions of fuel radicals</b>	55
<i>W. Tsang, I.A. Avon, W.S. McGivern, J.A. Manion</i>	
<b>6. Role of diacetylene in soot formation</b>	75
<i>A. Raman, R. Sivaramakrishnan, K. Brezinsky</i>	
<b>7. Opportunities and issues in chemical analysis of premixed, fuel-rich low-pressure flames of hydrocarbon and oxygenate fuels using in situ mass spectrometry</b>	79
<i>K. Kohse-Höinghaus, T. Kasper, P. Oßwald, U. Struckmeier, N. Hansen, T.A. Cool, J. Wang, F. Qi, P.R. Westmoreland</i>	
<b>8. Detailed kinetics of real fuel combustion: main paths to benzene and PAH formation</b>	99
<i>E. Ranzi</i>	
<b>9. Aromatic hydrocarbon growth mechanisms in flames: insights from sooting tendency measurements</b>	125
<i>C.S. McEnally, L.D. Pfeifferle</i>	

<b>10. Selection of surrogates for jet fuels</b>	137
<i>H.R. Zhang, E.G. Eddings, A.F. Sarofim, C.L. Mayne, Z. Yang, R.J. Pugmire</i>	
<b>11. Pyrolysis and oxidation of n-decane, n-propylbenzene and kerosene surrogate behind reflected shock waves</b>	163
<i>D. Darius, N. Chaumeix, C. Paillard</i>	
<b>12. Ignition and emission characteristics of synthetic jet fuels</b>	173
<i>M. Kabandawala, M. DeWitt, E. Corporan, S. Sidhu</i>	
<b>PART II</b>	
<b>Particle inception and maturation</b>	187
<b>13. Precursor nanoparticles in flames and diesel engines: a review and status report</b>	189
<i>R.A. Dobbins</i>	
<b>14. Nanoparticles of Organic Carbon (NOC) formed in flames and their effects in urban atmospheres</b>	205
<i>A. D'Alessio, A. D'Anna, P. Minutolo, L.A. Sgro</i>	
<b>15. Characterization of particles collected from combustion systems by water-based sampling</b>	231
<i>P. Minutolo, L.A. Sgro, A. Bruno, A. D'Anna, A. D'Alessio</i>	
<b>16. Molecular dynamics simulations of PAH dimerization</b>	247
<i>D. Wong, R. Whitesides, C.A. Schuetz, M. Frenklach</i>	
<b>17. Computational and experimental evidence for polynuclear aromatic hydrocarbon aggregation in flames</b>	259
<i>J.H. Miller, J.D. Herdman</i>	
<b>18. Soot precursors consisting of stacked pericondensed PAHs</b>	277
<i>J. Happold, H.-H. Grotheer, M. Aigner</i>	
<b>19. Particle inception and growth: experimental evidences and a modelling attempt</b>	289
<i>A. D'Anna</i>	
<b>20. Insights on the formation and growth of carbonaceous nanoparticles in high temperature environments</b>	321
<i>S.H. Chung, A. Violi</i>	
<b>21. Condensed phases in soot formation process</b>	333
<i>A. Ciajolo</i>	

**PART III**

<b>Dynamic of mass and number growth</b>	345
<b>22. Electrical mobility based characterization of bimodal soot size distributions in rich premixed flames</b> <i>M.M. Maricq</i>	347
<b>23. Size distribution and chemical composition of nascent soot formed in premixed ethylene flames</b> <i>H. Wang, A. Abid</i>	367
<b>24. An experimental and modeling study of soot formation during shock-tube pyrolysis of toluene</b> <i>G.L. Agafonov, I. Naydenova, V.N. Smirnov, P.A. Vlasov, J. Warnatz</i>	385
<b>25. Soot formation simulation of shock tube experiments with the use of an empirical model</b> <i>I. Naydenova, J. Marquetand, J. Warnatz</i>	405
<b>26. Multivariate soot particle models</b> <i>M.S. Celnik, A. Raj, S. Mosbach, R.H. West, M. Kraft</i>	413
<b>27. A joint volume-surface-hydrogen multi-variate model for soot formation</b> <i>G. Blanquart, H. Pitsch</i>	437
<b>28. Modelling the soot particle size distribution functions using a detailed kinetic soot model and a sectional method</b> <i>F. Mauss, K. Netzell, C. Marchal, G. Moréac</i>	465
<b>29. Modeling particle formation and growth in a stirred reactor and its exhaust</b> <i>M.B. Colket</i>	483
<b>30. Laminar smoke points of condensed fuels</b> <i>P.B. Sunderland, J.L. de Ris</i>	489
<b>31. Oxidation of two-ringed aromatic species as models for soot surface reactions</b> <i>R.P. Lindstedt, V. Markaki, R.K. Robinson</i>	499
<b>32. Soot oxidation</b> <i>J.S. Lighty, V. Romano, A.F. Sarofim</i>	523
<b>33. Size resolved soot surface oxidation kinetics</b> <i>A.A. Lall, M.R. Zachariah</i>	537

**PART IV**

**Turbulent flames and practical applications** 569

**34. On the transport of soot relative to a flame: modeling differential diffusion for soot evolution in fire** 571

*J.C. Hewson, A.J. Ricks, S.R. Tieszen, A.R. Kerstein, R.O. Fox*

**35. Characterisation of the flame properties of moderately oscillating sooting methane-air diffusion flames** 589

*M. Charvath, J. Hentschel, R. Suntz, H. Bockhorn*

**36. Prediction of particulates in turbulent diffusion flames by conditional moment closure** 605

*J.H. Kent*

**37. Experimental comparison of soot formation in turbulent flames of kerosene and surrogate model fuels** 619

*R. Lemaire, E. Therssen, J.F. Pauwels, P. Desgroux*

**38. Computational and experimental investigation of soot and NO in coflow diffusion flames** 637

*B.C. Connelly, M.B. Long, M.D. Smooke, R.J. Hall, M.B. Colket*

**39. In-cylinder soot nanoparticle formation mechanism** 651

*S. Kubo*

**40. Soot modelling in heavy-duty diesel engines** 663

*M. Baltasar, J. Eismark, I. Magnusson*

**41. Challenges of soot modelling in gas turbine combustors** 689

*H. Brocklehurst*

**PART V**

**Establishment of an international soot collaborative** 695

**42. A study on the effect of experimental setup configuration on soot formation in a laminar premixed ethylene-air flame** 697

*G. Gothaniya, S.-Y. Lee, A.V. Menon, S. Iyer, M.J. Linevsky, R.J. Santoro, T.A. Litzinger*

*Epilogue* 713

*Author index* 719

*Sponsors* 721

# Overview

**Motivation:** Soot is of importance for its contribution to atmospheric particles with their adverse health impacts and for its contributions to heat transfer in furnaces and combustors, to luminosity from candles, and to smoke that hinders escape from buildings during fires and that impacts global warming or cooling. The first two chapters in the book address the questions of health impacts of soot and its optical constants. A review of epidemiological, *in-vitro*, and *in-vivo* is presented in Chapter 1. The characteristics of carbon, surface reactivity and adsorbed polycyclic aromatic hydrocarbons (PAH), that are relevant to soot toxicity, are discussed for carbon generated by a number of techniques, including spark-discharge carbon particles, carbon black, flame soot, and engine exhaust. Reactive oxide species (ROS), linked to inflammation and oxidative stress in human cells, were measured using a fluorescent probe and were found to have the highest concentrations for a diffusion-flame generated soot and lowest for carbon black, underlining the importance of using soots freshly generated by flames and engines for toxicological studies and of characterizing soot surface structure and the composition of adsorbed layers. Fuel type was also found to affect toxicity with biodiesels leading to an increased toxicity (attributed to carbonyls) but a lower mutagenicity (less PAH) than regular diesel fuels. Other toxicological findings in the book are those related to the formation of high concentrations of ultrafine particles (<10 nm) in emissions from wide range of laboratory and practical combustors that have been defined precursor nanoparticles (PNP in Chapter 13) and nano organic carbon (NOC in Chapter 14). Human cells studies of these particles as well as related PAH are provided in Chapter 13 and with bacterial cell assays and mouse cells in Chapter 14. Concern with fine particles has led the European Union to propose standards based on number concentration for diesel emissions starting in 2009 (EURO 5) and in 2014 (EURO 6) which emphasizes the importance of characterizing the emissions of fine particles in diesel combustion.

Soot optical properties are important for both determining the radiation from flames and for several in-situ diagnostic techniques. Potential errors in the measurement of the refractive index of soot are critically evaluated in Chapter 2. Experimental values are provided for soot produced by methane, ethylene, and kerosene laboratory diffusion flames and a pool fire to show that mature soots have a relatively constant refractive index (1.7 - 0.6i at 635nm). The sensitivity of the soot concentration to changes in refractive index measured by transmission in shock tube studies is illustrated in Chapter 11. Refractive index also impacts radiative heat transfer. An example is provided in Chapter 38 in which the major impact of including radiation in the calculations on the NO<sub>x</sub> distribution in a laboratory ethylene/air diffusion flame is demonstrated. Young soot (NOC) are non-absorbing; how the absorption coefficient increases with the dehydrogenation of the soot as it matures is provided in Chapter 21. Although the studies in Chapter 2 showed that mature soot dominated the extinction in practical flames, there is still a question if this transition is important in calculating the effective radiative temperature of diffusion flames where the transition in optical constants occurs in the presence of strong temperature gradients.

**Formation of Soot Precursors for Real Fuels:** Fundamental studies on soot formation have until recently focused on simple aliphatic compounds, olefins, acetylene, and simple aromatics. The studies have been extended to real fuels (e.g., gasoline, kerosene, jet fuels, diesel fuel), and most recently to bio-derived and synthetic fuels. In order to facilitate study of complex mixtures of real fuels that may consist of thousands of compounds, surrogates consisting of simple mixtures of compounds with well-defined thermodynamics and kinetics are used to mimic the behavior of real fuels for specific applications using both theoretical models and experiments. The components of petroleum distillates consist of n-paraffins, i-paraffins, cyclo-paraffins, and aromatics. Gasolines also contain highly branched i-paraffins and olefins that are produced during the refining of the petroleum. Fischer Tropsch fuels consist entirely of n-paraffins and i-paraffins. Lastly biodiesels contain significant amounts of oxygenated compounds. The challenge then is to obtain the kinetics for the components of the different surrogates.

The first step towards modeling soot formation from non aromatic fuels is the estimation of benzene formation. Progress has been made to the point that there is general agreement on the mechanisms and kinetics of formation of the first aromatic ring (Chapters 3 and 4). Under most combustion conditions, the dominant pathway to benzene/phenyl is  $C_3H_3 + C_3H_3$ , with added contributions from  $i-C_4H_3 + C_2H_2$  and  $i-C_4H_5 + C_2H_2$  and allyl. The understanding of the reactions of small molecules has benefited from theoretical developments, including ab initio quantum mechanical evaluation of thermodynamic and kinetic parameters, solution of master equation of collision energy transfer for reaction pathways and rate parameters (Chapters 3 and 4). The theoretical studies have shown the importance of resonantly stabilized intermediates in the major chemical pathways (Chapters 3 and 4). The improved theoretical tools have resulted in a move from qualitative to quantitative modeling of the reactions leading to the first aromatic ring from aliphatic precursors, including temperature and pressure dependence (Chapter 4). These developments are accompanied by the detailed characterization of chemical species in a flat flame (Chapter 7), shock tubes (Chapter 5, 6, 11, 12, and 25), and in a diffusion flame doped along the axis with minor amounts of the compound to be studied (Chapter 9). Measurements of chemical intermediates are made possible by molecular beam mass spectrometric techniques (MBMS) using three ionization techniques: resonance-enhanced multi-photon ionization (REMPI), electron ionization (EI), and a vacuum ultraviolet photoionization (VUV-PI) using tunable synchrotron radiation (Chapter 7).

Much of the attention traditionally have been applied to the development of detailed chemical kinetics for molecules of importance to gasoline, with much effort devoted to the reference fuels for gasoline i.e. n-heptane and i-octane. With the interest in modeling jet fuel (carbon numbers up to  $\sim 16$ ) and diesel fuel (carbon numbers up to  $\sim 19$ ), the number of elementary reactions increases to unmanageable sizes and lumping approaches have been developed drawing on the experience on modeling the thermal cracking of hydrocarbons to produce ethylene and propylene (Chapter 8); mechanisms have been developed for conversion of paraffins to benzene, PAH, and soot. An important part of modeling the pyrolysis of higher hydrocarbons is the isomerization of the radicals produced as intermediates. Improvements of the isomerization kinetics have been provided by the shock tube studies of the decomposition and

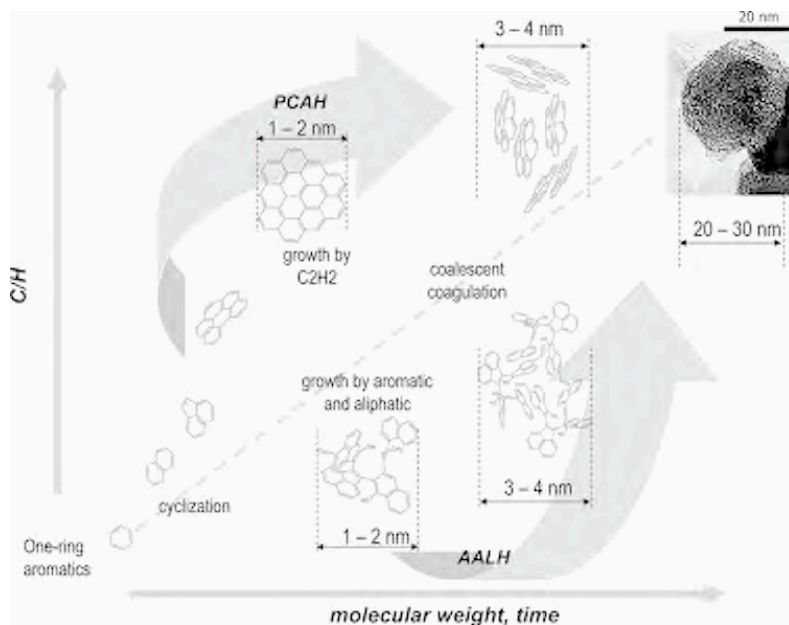
isomerization of all the heptyl radicals (Chapter 5); and reference is made to the additional compounds being studied including the *i*-paraffins that are a major component of diesel and jet fuels. Additional shock tube studies by several of the participants have provided data needed for model development and validation of mechanisms on ignition delay and soot formation for individual compounds and mixtures. These include studies of polymerization of diacetylene (Chapter 6), soot formation of *n*-propyl benzene, *n*-decane and their mixture (Chapter 11), ignition delay and soot formation studies of 2-methyl heptane, a heptane/toluene mixture, a Fischer-Tropsch jet fuel, and a conventional JP-8 (Chapter 12).

With the formation of the first ring relatively well understood, emphasis in the kinetic studies is shifting to the study of the formation of the second and larger rings. Relatively well studied pathways to naphthalene include the build up from benzene via the HACA mechanism and the combination of the cyclopentadienyl radicals. In addition, distillate petroleum products contain high concentrations of multi-substituted aromatics and cycloparaffins that are shown in Chapter 9 to dominate the formation of higher aromatics. In Chapter 9, the factors that control increased sooting tendencies are given as a function of aromatic carbon number for polybenzenoids, as a function of alkyl chain length and structure for primary alkyl benzenes, as a function of relative position, chain length, and degree of saturation for polyalkylated benzenes, and as a function of molecular structure for several biaryls. Mechanisms are proposed for the more than fivefold range of soot yield for the 130 compounds studied. The results show the importance of providing a realistic representation of the chemical structure of the aromatic compounds in calculating soot formation. Despite not including the details on substituents existing models show fair agreement in calculating soot yields from surrogate mixtures.

Although ideally one would like to calculate soot from a realistic chemical description of the fuel (Chapter 10), affordable mixtures of the multi-substituted aromatics and cycloparaffins in distillate fuels are not available. The interim solution is to select a surrogate mixture that matches the smoke point (Chapter 30) or, the Yield Sooting Index (YSI) of the real fuel (Chapter 9). A smoke point has the advantage of being easily measurable for real fuels using a standardized wick lamp (Chapter 30). The YSI, though more difficult to measure, could be calculated from model fuel representations that match the functional groups in the fuel (Chapter 9). It is expedient to use the minimum number of components in a surrogate mixture. Two compounds, an aromatic and an aliphatic, in a surrogate can be used to match the smoke point or YSI of the fuel (Chapters 30 and 9, respectively). Additional components will be needed to match combustion behavior and physical properties such as the boiling point distribution.

**Particle Inception and Maturation:** At the time of the Heidelberg meeting in 1991 Dobbins and D'Alessio provided preliminary reports of the existence of nanoparticles in the nanometer size range with liquid-like properties. The Anacapri meeting saw the great progress that has been made in the intervening years in the identification, characterization, and acceptance of the existence of these particles, designated Nano Organic Carbon (NOC) by the Naples research group and precursor nanoparticles (PNP) by Dobbins.

A review of the history of the formation of these nanoparticles is provided (Chapter 13). The particles are ubiquitous, found in a wide range of flames, combustors and the atmosphere (Chapters 13 and 14). In Chapter 13 the characteristics of PNP are given as sizes from 5 to 15 nm, a density of 1.2, and chemical analysis by laser desorption mass spectrometry (LAMMA) and by GC/MS showed PAH of mass 152 to 302 consisting mainly of stabilomers. The particles undergo dehydrogenation which is a function of temperature and time, which were used to determine a rate constant for the carbonization.



Oxidation and pyrolysis routes (D'Anna, Chapter 19).

In Chapter 15, several techniques were used to obtain the sizes of NOC in a pre-mixed flame, which were found to range from 1 to 10 nm. These were UV/Visible extinction and fluorescence, scattering, atomic force microscopy (AFM), and a nano-differential mobility analyzer. Satisfactory agreement between the results obtained by the different techniques provides confidence in the existence of NOC. NOC particles are non-absorbing in the visible in contrast to soot. Fourier Transform Infrared (FTIR) analysis showed the presence of C=O and C-O bands in addition to aliphatic and aromatic bonds showing a difference with the results on PNP. Further results on NOC particles collected in water to separate the hydrophilic particles are presented in Chapter 15. Additional methods of measuring size are introduced including Dynamic Light Scattering (DLS), Time Resolved Fluorescent Polarization Anisotropy (TRFPA),

Fluorescent Correlation Spectroscopy (FCS), and Differential Mobility Analyzers on particles produced in an electrospray (E-DMA). The mean size of NOC obtained by these techniques was between 2 and 3 nm. FTIR and Surface Enhanced Raman Spectroscopy (SERS) indicated that the particles collected in water consist of aromatic-aliphatic linked functionalities, with possibly some oxygen moieties.

In parallel, progress has been made in determining the mechanism of particle inception, following two approaches. The first is the stacking of PAH (Chapters 16, 17, and 18). Chapter 16 provides results for lifetimes of dimers of peri-condensed aromatics (PCAH) and aromatic molecules linked by aliphatic chains (AALH) calculated using molecular dynamic simulation with on-the-fly quantum forces. These show that the lifetimes of the PCAH dimers increase with size (up to 20 ps at 1600K for coronene). The AALH lifetimes with the exception of biphenyl were smaller than those for PCAH. The increase in binding energy between dimers with molecular size is supported by the calculations in Chapter 17 of intermolecular forces from atom-atom interactions, using force fields that had been developed for PAH. An interesting result is that an asymptote in the binding energy is approached at large sizes that corresponds to the experimental value of the exfoliation energy for graphite. Additional calculations were performed for stacks of up to 9 layers of PAH, showing a slight increase in binding with increased layer number but quickly approaching an asymptote. As supporting experimental evidence for the dimer formation, the authors propose the red shifting of fluorescence of PAH in flames, which they explain to be due to formation of aromatic excimer and provide experimental evidence for such shifts in the condensed phase. Additional support for the formation of stacks of particles is provided by mass spectra obtained by a time of flight mass spectrometer (TOFMS) on the exhaust from low pressure sooting flames that had been first passed through a flow reactor at 1 mbar for 1 ms (Chapter 18). The results on the mass spectra show a periodicity with a mass difference of about 450 mass units. These spectra were not obtained under all conditions and the authors conclude that alternative routes to the soot precursor might occur such as postulated by D'Anna and Violi and presented in Chapters 19 and 20. For some runs there are step changes in the H/C ratio associated with the stacking, perhaps due to aliphatic linkages between layers.

In Chapter 19, the particle inception is assumed to occur through the abstraction of H, initially from a PAH, followed by the addition of either an acetylene or a PAH molecule. Iteration of this sequence leads to the formation of high molecular mass particles. Growth can also occur by collision between these particles. The model is distinctive in assuming a low collision efficiency calculated from simple interaction energy considerations. This model of particle growth leading to soot predicts the measurements of UV and Visible light extinction and scattering profiles, and particle size distributions down to one nanometer in lightly sooting ethylene/air premixed flames as a function of height above burner. In the following chapter (Chapter 20), particle inception is modeled for two opposed diffusion flames that had been studied in the literature, one with the stagnation plane on the rich side of flame front (SF flame) and another with the stagnation plane on the lean side (SFO). For the SF flame the soot is convected away from the flame front and is at relatively low temperatures whereas for the SFO flame the soot is convected into the flame and is exposed to high temperatures and high radical concentrations. A chemical model (Atomistic Model for Particle

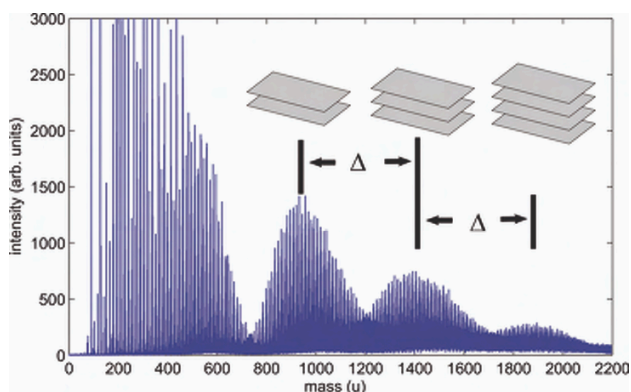
Inception or AMPI) of particle growth, calculated using alternating kinetic Monte Carlo (KMC) and Molecular Dynamics simulation, could adequately explain the experimental observed trends in particle loading for the SFO flame. However, for the SF flame where the soot was at lower temperature the AMPI model could not account for the entire particle inception but had to be supplemented by growth of clusters through collisions with the sticking between colliding species (assumed to be fullerenes) needing to have a mass greater than 2000 amu ( $C_{180}$ ). This suggests, again, that there may be different routes to soot inception, PAH stacking and polymerization, depending upon the conditions in the flame.

Complementary data is provided by the size exclusion chromatography (SEC) measurements of mass distribution on dichloromethane extracts and the insoluble fraction for soots formed in a premixed flame reported in Chapter 21. The extracts show a bimodal size distribution of PAH with mass ranges of 100-400 amu and 400-2000 amu. The insoluble fraction (soot) showed again a multimodal distribution over a molecular weight range of  $10^2$ - $10^{10}$  amu corresponding to spherical particle sizes of 1 to 100 nm. These results encompass the formation of nanoparticles and the growth of soot aggregates to be discussed next.

**Dynamics of Mass and Number Growth:** Instruments that have transformed our understanding of the particle dynamics are the Scanning Mobility Particle Sizer (SMPS) and thermophoretic particle samplers combined with atomic force microscopy (AFM) and transmission electron microscopy (TEM). These have provided data on the size evolution during soot formation and burnout that have been used to confirm hypotheses and critically test models on particle nucleation, coagulation and surface growth, soot burnout and fragmentation, although questions remain concerning possible artifacts in the data due to losses and coagulation in the sampling system. The size distribution is typically bimodal with sizes from 1 to about 10 nm in what is often called the nucleation model and particles from about 10 nm to over 100 nm in the so-called accumulation or agglomeration mode.

Data from premixed flames in Chapter 22 support a picture of a nucleation mode of nearly spherical uncharged particles under 10 nm in size, with a low contrast on electron grids relative to the accumulation mode. The particles in agglomeration mode consist of fractal aggregates with a high electron absorption, and with equal numbers of positively and negatively charged particles with Boltzmann charge distributions. Significant continuous decrease in particle diameter is observed when the particles in the nucleation mode are heated up to 600 °C. The agglomeration mode shows a relatively small mass loss by comparison.

The importance of jointly using multiple measurement techniques to characterize particles is emphasized in Chapter 23 which used a combination of small-angle neutron scatter (SANS), probe sampling/scanning mobility (SMPS), particle photo-ionization mass-spectrometry (PIAMS), and transmission electron microscopy (TEM) for characterizing particles in premixed flame covering a wide range of operating conditions. The results were used to map out the regimes of temperature and C/O ratio in which the particles exhibited only a nucleation mode or bimodal distribution with and without a 'tail' corresponding to persistent nucleation. This data base provides a resource for both providing insights on mechanisms and critically testing models.



TOFMS for Acetylene flame suggesting stacking of pericondensed PAH (Grotheer et al., Chapter 18).

Comprehensive models for soot were tested against data from flames and shock tubes in Chapters 24 to 29. In Chapter 24 data on soot volume fractions and H, OH, and CH<sub>3</sub> radicals were obtained under pyrolysis and oxidation conditions in a shock tube. The transient results for a wide range of temperatures and residence times were compared with soot models using two different surface growth rates, that given by the Appel-Bockhorn-Frenklach expression and one using Harris's rate. Although satisfactory agreement between model and experiment was obtained the need for refinement of the surface growth model was noted. Chapters 26 and 27 apply multi-variate models to develop more mechanistic surface growth models. In Chapter 26, site counting models are used to allow for different reactions at zig-zag, armchair, free edge, and bay sites. A stochastic approach is also used to provide information on aggregate structure allowing for the size distribution of the different primary particles in an aggregate. Chapter 27 provides an alternative multi-variate model which tracks volume, surface area, and number of hydrogenated sites on a surface. The model assumes nucleation occurs by the formation of dimers of selected PAH molecules (with a carbon number range of 10-18); allowance was made for both coalescent and aggregative coagulation; and different products for acetylene addition. The model was tested with data from a premixed ethylene, a premixed benzene, and an acetylene diffusion flame.

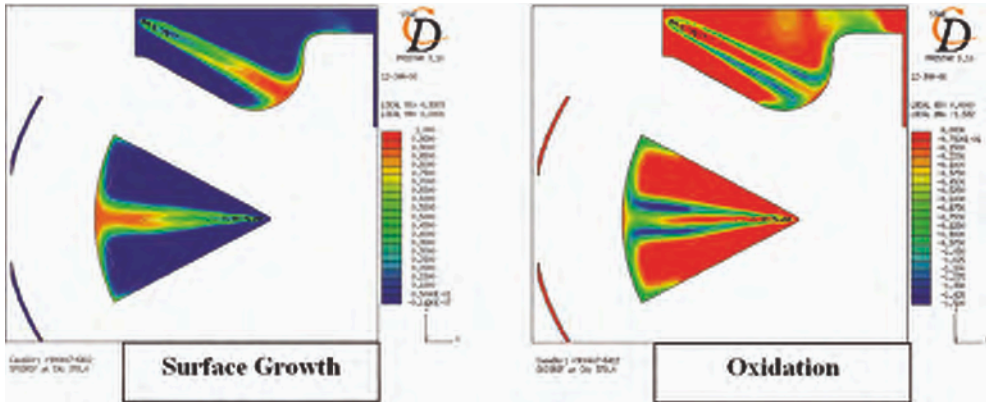
A newly developed sectional method is presented in Chapter 28. The model calculates particle size distribution functions in premixed flames by using a sectional method which uses first order polynomials within each section in order to reduce CPU time. Comparison of model results with experimental data shows that probe effects on the flame are very strong and a better understanding of flame perturbation by the sampling system is needed.

The modeling of a well-stirred reactor in Chapter 29 was tested with data on the particle size distributions over the range of 1-100 nm obtained with DMA. The preliminary results from the study showed the need to model reactions occurring in the exhaust of the well-stirred reactor.

Even if progress is being made on the development of fundamentally based models to predict soot formation, there is a continuing need for tools that are easy and fast to use. Chapter 30 addresses the use of laminar smoke points for determining the sooting tendency of condensed fuels, using wick lamps to determine the laminar smoke point for solid alkanes, alcohols, and acids using a candle-like flame. The paper examines the sensitivity of the results to the dimensions of the wick and compares the data with those in the literature for liquid fuels. Sooting indices, particularly for condensed fuels, will continue to be useful. Chapter 25 provides for ease of computation a simplified soot model consisting of four steps: nucleation, surface growth, coagulation and oxidation. The model was tested against shock tube data on soot yields obtained in a shock tube.

Oxidation kinetics receives surprisingly little attention considering that diesel and gas turbine engines have traditionally relied on post-combustion oxidation to control emissions. The principal soot oxidants are O, OH, and O<sub>2</sub>. In flames, premixed and diffusion, oxidation by OH dominates. The reaction efficiency of OH colliding with the surface seems to be well established, with values ranging around 0.13. For post-flame zones oxidation by O<sub>2</sub> becomes dominant and is believed to be the principal oxidant for soot in diesel and gas turbine engines. The rate for O<sub>2</sub> oxidation provided by Nagle and Strickland-Constable (NSC) continues to prevail after almost half a century. Although obtained on well-ordered pyrolytic graphite it appears to apply well to less ordered carbons, probably because at high rates of oxidation pitting of the graphitic surfaces makes available the more reactive edge carbons. Studies of soot oxidation in a two-stage burner (Chapter 32) showed the importance of fragmentation for conditions under which oxidation by O<sub>2</sub> is dominant, suggesting significant internal burning; additional evidence for internal burning are data in the literature showing a close to ten-fold increase in the surface area of a soot with increased extent of combustion. The reduction of soot emission from diesel engines by addition of ferrocene to the fuel was studied (Chapter 33) using Quantitative Single-Particle Mass Spectrometry (QSPMS) to determine both the composition and size distribution of the emissions from a diesel engine. In addition the reactivity of narrowly sized catalyst doped particle was studied by a tandem DMA to obtain the kinetics of the catalyzed soot oxidation. The activation energy for the oxidation of soot were found to decrease significantly from ~163 kJ/mol for a flame soot to around 110 kJ/mol for a diesel soot. Addition of an iron catalyst to the flame soot resulted in a similar reduction in the activation energy for oxidation. Fundamental studies of the oxidation of a soot precursor, 1-methyl naphthalene is reported in Chapter 31, calculating the major consumption paths using quantum mechanical calculations, providing results for intermediate oxidation products in good agreement with well-stirred reactor experiments reported in the literature. It is hoped that such fundamental studies will be extended to soot oxidation in the future.

**Turbulent Flames and Practical Applications:** Technically relevant systems are mostly turbulent and although concept of soot formation derived in laminar flames can be also applied to turbulent conditions, research in turbulent flames is necessary, particularly as related to the interaction of soot formation and turbulence taking into account thermophoresis and the low diffusivity of soot. To adequately describe soot in turbulent non-premixed flames, it is important to predict not only the chemical kine-



Rates of soot formation during injection in a HD diesel engine (Balthazar et al., Chapter 41).

tics and particle dynamics, but also the location of the soot relative to the near-stoichiometric flame regions and the interaction of the flame chemistry with particle formation under turbulent mixing.

Chapter 34 analyzes the role of transport phenomena on soot source terms in turbulent non-premixed flames by modelling soot formation with unsteady flamelet and conditional moment closure approaches showing the importance of differential diffusion in the prediction of soot.

To enhance the understanding of soot formation in turbulent conditions, Chapter 35 studies the properties of moderately oscillating diffusion flames by measuring and modelling soot formation, particle number density and size distributions. The non-stationary nature of the flame increases soot formation since trajectories of flame volume elements cross regions with conditions indispensable for rapid soot formation.

A full chemical kinetic and particle dynamics scheme is applied in Chapter 36 to predict particulate loading in turbulent non-premixed flames and compared with experimental results for both nanoparticles and soot. The kinetic scheme is tested in laminar flames in Chapter 19 and is used here with a Conditional Moment Closure approach. The model gives reasonable predictions of particle concentrations. Better results are obtained by using alternative flamelet template for conditional temperature showing the sensitivity of the model to the conditional temperature used.

Experimental data on soot and precursor concentrations in turbulent non-premixed flames are reported in Chapter 37 where formation of soot in turbulent kerosene and surrogate model fuels is reported. Two-dimensional LIF and LII measurements are used to follow precursor and soot particles. Optical and morphological properties of soot particles are also derived from LII signal analysis. They are not different for the different fuels.

Soot and NO<sub>x</sub> formation in a coflowing ethylene flame is studied both experimentally and numerically in Chapter 38. Results indicate that soot and accompanying radiation loss reduce the level of NO throughout the flame showing the strong interaction of thermal radiation with flame chemistry.

A study of particle formation in the cylinder of an homogeneous charged compression ignition engine burning n-heptane is reported in Chapter 39. Particles collected from the engine combustion chamber are analyzed using different diagnostics for particles. In the earlier stage of the engine combustion, nanoparticles with diameters less than 3nm are found which grow towards a bi-modal size distribution with the progress of the engine combustion. Results suggest that soot nanoparticles are formed by agglomerate of planar structured giant PAHs, in agreement with the hypotheses in Chapters 16, 17, and 18.

Soot modelling in diesel engines and gas turbine combustors is reported in Chapters 40 and 41. Results of the modelling of heavy-duty Diesel engines at Volvo show the capability of a detailed soot model combined with an interactive flamelet combustion model to reproduce sufficiently well soot emission for many engine applications. The implementation of the method of moments within the laminar flamelet framework for the modelling of gas turbine combustors at Rolls Royce gives better resolution of the soot size distribution. Nevertheless, a model with full predictive capability would need major improvements.

**Establishment of an International Soot Collaborative:** The papers in this volume show the large increase in the sophistication of computational and experimental methods. Results on mechanisms and kinetics for soot and its precursors are reported for a large number of fuels reacted in a large number of combustor configurations. However, it is often difficult to reconcile at present the differences between data and model predictions. There is a need for quantification of error in sampling and in species measurement (Chapter 7) as well as in the modeled results. Burners that are nominally the same and operating under the same flow conditions can give different results as a consequence of minor variations in boundary conditions. This was brought out in Chapter 42 where the impacts of slight changes in placement of a stabilizing plate or the flow rate of sheath gas were shown to have significant changes on the structure of a premixed flame. Can we accelerate developments through the study of reference flames using standardized burners and operating conditions?

A possible mechanism for the soot community to address these issues is through the resources made available through the PrIME ([www.primekinetics.org](http://www.primekinetics.org)) initiative to warehouse data, inter-compare model, develop recommended data and models, which was set up for this purpose. The abstracts and discussions of the International Soot Workshop will be archived at the PrIME site that can hopefully help the community interact and address the above issues on a continuing basis.





# The role of soot in the health effects of inhaled airborne particles

B. Kumfer, I. Kennedy

University of California

Department of Mechanical and Aeronautical Engineering

Davis, CA 95616

USA

*Abstract: After many years of study, the epidemiology of human exposures to ultra-fine ambient particulate matter (PM) has clearly established a statistically significant correlation between levels of fine particles and adverse health effects, which include increased incidence of respiratory and heart diseases and increased mortality. Soot particles from mobile and stationary combustion sources have been implicated as a source of these health effects, since elemental carbon makes up a large fraction of the ultra-fine particles in ambient PM. The various characteristics of soot particles that are potentially relevant to health effects are explored and discussed, including surface reactivity and the presence of adsorbed polycyclic aromatic hydrocarbons (PAH). To this end, a number of in vitro and in vivo studies of exposure to spark-discharge carbon particles, industrial carbon black, flame-generated soot, and engine exhaust particles are reviewed in detail. Inflammation is often observed upon exposure to particles, and it has been widely suggested that this is caused by oxidative stress on cells in response to reactive oxygen species (ROS). The generation ROS by carbonaceous particles in an aqueous solution was measured using the fluorescent probe (2'-7' dichloro-fluorescein, or DCFH), and the results for carbon black, diesel soot (NIST Standard Reference Material), and soot from a laboratory laminar diffusion flame are compared. All carbonaceous particles showed the capacity for generating ROS; diffusion flame soot was found to generate the highest concentrations of ROS on a mass basis while carbon black was the least reactive. The results suggest that carbon black and aged reference particles may not be good substitutes for freshly generated material produced from a flame or engine.*

## 1. INTRODUCTION

The potential impact on human health occasioned by the inhalation of soot from combustion sources has long been recognized. In general, epidemiological studies have demonstrated consistently significant associations between human exposures to ambient aerosols and adverse health effects. Effects include exacerbation of underlying pulmonary and cardiac problems that can lead to earlier death or increased morbidity [1-3]. Long-term effects may include cancer [4], lung disease and heart disease [5, 6].

Ambient particles consist in general of a variety of crustal material and carbonaceous materials, with organic and elemental carbon generally dominating the ambient aerosol in the ultrafine range (size less than 100 nm) [7]. Laden et al. [8] found that most of the increase in mortality in the Six Cities study in the USA was associated with fine particles (less than 2.5  $\mu\text{m}$ ) that derived from mobile combustion sources, with a

lesser impact ascribed to coal combustion sources. Fine crustal material (largely inorganic mineral matter) was not associated with an increase in mortality. Schwartz and Neas [9] also found that fine particles are more closely associated with respiratory effects in children than are coarse particles, and a study of adolescents exposed to traffic revealed that lung development is hampered and a decrease in lung function is found in children who live near freeways [10]. Cardiovascular effects are believed to be more associated with ultrafine particles [11], since particles of this size can more likely be translocated from the pulmonary system into the circulation. Studies of occupational exposures have shown similar effects with better-defined aerosol materials, including, for example, the association between cancer rates in locomotive drivers and diesel engine soot [12].

The biological mechanisms that lead to the observed impacts on health are not well-established. In fact, the primary characteristics of fine particles that lead to health problems are still the focus of much discussion and debate. As pointed out by Lighty et al. [13], there are a number of possible factors relevant to the uptake, translocation of particles from the lungs to other organs, and ultimately their toxicity. These may include particle size, number, mass, morphology, surface area, surface charge, and chemical composition. The fine particles emitted from combustion sources generally have a complex chemical composition, consisting of elemental carbon (in some contexts this could be referred to as soot), organic hydrocarbons, mostly in the form of polycyclic aromatic hydrocarbons (PAH) that are adsorbed onto the soot, and in some cases metals. Adding to the complexity of this problem, organic compounds on the particle surface may undergo chemical changes in the atmosphere, leading to more toxic oxygenated and nitrated PAH [14-16].

Laboratory-based studies have sought to unravel the fundamental interactions between particles and their impacts on living systems through the analysis of particle reactivity in nonliving systems, *in vitro* cell culture studies, and with animal or human exposure (*in vivo*) studies. These types of studies can make use of particles that are generated in the laboratory with well-controlled systems such as spark generators, flames, or engines, including spark ignition and diesel engines. In this work, we aim to provide a review of studies relating to the adverse health effects of soot, including laboratory-generated soot and internal combustion engine exhaust particles. While there are a number of studies specifically pertaining to the health effects of coal combustion emissions [17-19] and incinerator fly ash [20], we do not address in detail such issues since the complex composition of fine fly ash particles, which includes minerals and a wide variety of metals, is beyond the scope of research related to soot.

## 2. SURFACE REACTIVITY

Unpaired electrons in soot particles that could potentially react with cells or surrounding fluid can be measured using electron paramagnetic resonance spectroscopy (EPR). EPR can provide a determination of unpaired electron concentration; the characteristics of the EPR spectrum, i.e. the line width and the Lande  $g$ -factor, can provide information as to the molecular environment of the unpaired electron and the types of radical species that are present. Numerous EPR studies have been performed on soot par-

ticles generated from a wide variety of sources. Several groups have studied diesel exhaust particles [21-24]. Valavanidis et al. [22] compared the EPR spectra of diesel soot to gasoline soot, wood smoke, and cigarette tar. Soot generated from a variety of liquid fuels was studied in laboratory premixed [25, 26] and diffusion [27] flames. Catallo et al. [28] generated soot from 1,3-butadiene. In spite of the large variation in sources, there are properties of the EPR spectra common in nearly all of these studies. Unpaired electron spin concentrations of laboratory flame-generated soot have been reported in the range of  $10^{18}$ - $10^{20}$  spins/gram [25, 27, 28]. Chughtai et al. [25, 26] found that the spin-density of soot can be reduced by increasing the air/fuel ratio. This result was attributed to increased surface oxidation. Gasoline and diesel engine particulates have reported concentrations in the range of  $10^{15}$ - $10^{16}$  spins/gram, which is comparable to that associated with cigarette tar [22] and ambient PM [29].

The EPR spectra of soot particles can be broad, with Lande  $g$ -factors of in the range of 2.0025-2.0040, indicating that a variety of radical species may be present. Valavanidis et al. [22] reported a similar range of  $g$  factors for fresh diesel and gasoline exhaust particulates, but noted that the range in  $g$  factor was reduced to 2.0026-2.0028 after washing the particles with a solvent. A  $g$ -factor of 2.0028 is known to correspond to a highly-stable, carbon-centered radical that is associated with the solid carbonaceous material [22, 27, 28]. Catallo et al. found that this species remained stable over a period of 18 months and could not be extracted using reducing agents [28]. Measured EPR spectra of ambient PM [22, 29, 30] have characteristics similar to that of cigarette tar [31]. Pryor [31] identified the primary radical in cigarette tar to be associated with semi-quinones, which have  $g = 2.0035$ - $2.0038$ . Thus, Dellinger et al. have postulated that the semi-quinone-type radical is also a major cause of the observed health effects of combustion-generated PM [29, 30]. These species are relatively stable in the atmosphere and yet are more soluble and thus more bio-available. The semi-quinone radical is also capable of catalytic redox cycling, with the potential to continuously generate reactive species harmful to cells [29].

### 3. GENERATION OF REACTIVE OXYGEN SPECIES

There is ample evidence linking inflammation observed upon acute exposure to PM and oxidative stress experienced by cells [32-35]. This oxidative stress is believed to be the result of reactive oxygen species (ROS), such as hydrogen peroxide, superoxide anion, and/or the hydroxyl radical, that are either generated directly by the particle or generated by cells in response to particle exposure. Figure 1 summarizes the mechanism of continuous ROS generation via a semi-quinone-type species proposed by Squadrito et al. [29]. These species interact with biological reducing agents to reduce oxygen and form the superoxide radical and hydrogen peroxide. Oxidative stress may be enhanced in the presence of transition metals, such as iron or copper, which undergo Fenton-type reactions with hydrogen peroxide to continuously generate the hydroxyl radical.

Several researchers have sought to measure the capacity of soot particles to sustain redox reactions and generate ROS in non-living systems. The redox capability of gasoline and diesel engine exhaust particles was measured by Geller et al. [36] using a

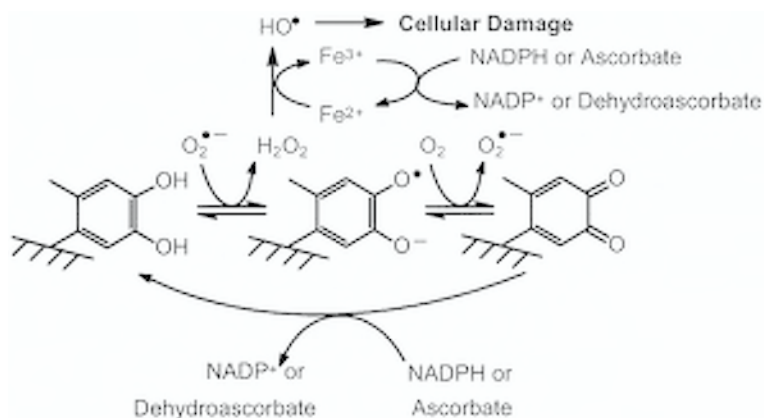


Figure 1. Mechanism of ROS generation by quinoid redox cycling. Reprinted with permission from Ref. [29].

dithiothreitol (DTT) assay [37]. This method is a measure of the reduction of oxygen by DDT, which is catalyzed by redox-active species. In this study, the particle composition was measured and a high degree of correlation between DDT consumption and several individual species and species classifications was found. This correlation was observed for elemental carbon, organic carbon, several lower molecular weight organic species, and some metals including Ni, Zn, Li, Be, but interestingly not Fe.

Hydroxyl radical generation by soot particles was measured quantitatively in a surrogate lung fluid by Jung et al. [38]. In this method, benzoic acid was employed to scavenge  $OH^\bullet$  generated in solution and the product of this reaction was determined by HPLC. Soot particles synthesized in an ethylene laminar diffusion flame were found to generate  $OH^\bullet$  in this solution, at a mass-normalized rate 10 times that of the generation by carbon black particles.

There are also a number of fluorescent probes which can be used to measure concentrations of ROS. One such probe is 2'-7' dichlorofluorescein (DCFH), which becomes fluorescent upon oxidation by many ROS, including  $OH^\bullet$ ,  $ONOO^\bullet$ ,  $NO_2^\bullet$ ,  $CO_3^\bullet$  and the peroxy and alkoxy radicals [39]. It is often used as a measure of cellular production of ROS [40, 41] and is considered to be a general measure of oxidative stress [39]. DCFH has also been utilized in non-biological systems as a measure of the capability of particles to generate ROS, and to measure the concentration of ROS that are bound to ambient particles [42]. Wilson et al. [43] utilized DCFH to measure ROS generated by carbon black particles both in a cell culture and in a cell-free system. The generation of ROS in both systems was found to be dependent on particle size – ultra-fine particles resulted in significant fluorescence while no significant fluorescence was found for larger (>100 nm) particles. Oxidation of DCFH was also detected in rat alveolar macrophages after exposure to carbon black particles [40].

In an experiment similar to the one described above, we have compared the relative abilities of carbonaceous particles from several different sources to oxidize DCFH. The DCFH solution was prepared by first cleaving 2'-7' dichlorofluorescein diacetate

(DCFH-DA) using 0.01N NaOH, according to the procedure described in [42]. No enzymes (e.g. horseradish peroxidase) were added to the probe solution to catalyze reactions with hydrogen peroxide. Particles were suspended in ethanol and sonicated in a water bath for 20 minutes to disperse the particles. A 0.5 mL aliquot of particle suspension was then added to 1.0 mL of DCFH probe solution in a microcentrifuge tube and the mixture was incubated in the dark for 10 minutes. After incubation, the suspension was centrifuged for 20 minutes to remove the particles. The solution was immediately transferred to a cuvette, wherein the fluorescence was measured. The excitation wavelength was 488 nm; the fluorescence at 530 nm was detected using a SpectraPro 300i spectrograph (Princeton Instruments, Inc.).

Carbon black particles (purchased from Cabot Corp.), standard reference particles from a forklift diesel engine obtained from the National Institute of Standards and Technology (NIST, SRM 2975), and soot particles generated from an ethene laminar co-flow diffusion flame were analyzed using the above procedure. The diffusion flame soot was found to consist of 96% elemental carbon, as measured by an EC/OC instrument (Sunset Laboratory Inc.). A linear dependence of DCFH oxidation on particle concentration (not shown) was found for each of the carbonaceous particles studied. Standard 33 nm polystyrene spheres (Duke Scientific) were also analyzed to test for interference from unexpected particle/DCFH interactions.

In Figure 2, ROS generation by the various particles is compared. The mass concentration of the particle suspension in this experiment was held constant (150  $\mu\text{g}/\text{mL}$ ). The carbon black particles showed a relatively small capacity to generate

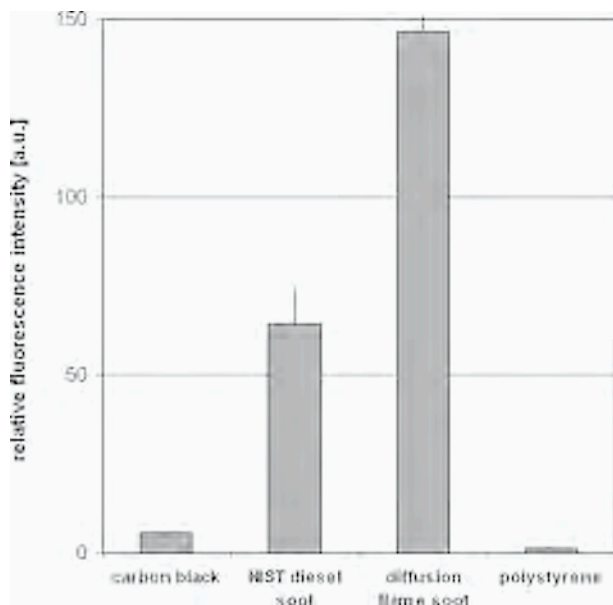


Figure 2. Comparison of ROS generation by various particles measured by the fluorescent probe DCFH. Mass concentration of particles is constant (150  $\mu\text{g}/\text{mL}$ ).

ROS, while the diffusion flame soot gave the largest response. TEM analysis of these particles indicated a mean primary particle size of the carbon black of approximately 100 nm, while the diffusion flame soot had a mean size of approximately 30 nm, which is similar to that of the standard NIST diesel soot. Since mass is held constant in this experiment, the total surface areas of the NIST reference soot and the diffusion flame soot are similar, but both are much larger than that of the carbon black, which may explain the lower response by carbon black. The difference between the older NIST diesel soot and the freshly-generated diffusion flame soot may be attributed to aging effects. The high reactivity of the diffusion flame soot, as indicated by the DCFH assay, suggests that reactive sites on the surface of carbon particles may be involved in the generation of ROS, even in the absence of significant amounts of quinones or transition metals.

The reactivity of the particle surface is dependent upon the nanostructure [44], and the nanostructure of soot particles has been shown to be dictated by combustion conditions, i.e. temperature and gas composition histories [44, 45]. Greater disorder on the surface results in a larger density of active sites, and it is reasoned that increased surface reactivity could enhance health effects. Lee et al [46] studied the impact of diesel engine operating conditions on the structure of the soot that the engine emitted. As expected, they found that the soot was formed of ultrafine carbonaceous particles that were linked in aggregates. The soot that was emitted at low load was largely amorphous with a significant component of organic carbon. On the other hand, high load operating conditions resulted in the emission of better-ordered graphitic material with smaller primary particle sizes and less organic carbon. The ordering of the material reflected the elevated temperatures at high load; the smaller primary particle size indicated that oxidation was significant under these conditions. The presence of organic carbon is certainly associated with health effects but the microstructure of the elemental carbon may also be important.

#### 4. ELEMENTAL CARBON EXPOSURE STUDIES

In order to elucidate the underlying causes of health effects of combustion-generated particles in the atmosphere, it is advantageous to break down the problem of complex composition and first measure the toxicity associated with pure elemental carbon particles, which can be generated in the laboratory. Taking into consideration the reactivity associated with a disordered carbon surface and the previously discussed ROS generation findings, one might expect that elemental carbon particles would induce inflammation – however, there is minimal direct evidence of inflammation caused by acute exposure to carbon. Frampton et al. [47] generated ultrafine carbon using the spark discharge method and exposed healthy and asthmatic human volunteers to these particles for 2 hours, while rested and while exercising. No airway inflammation was found, even for exercising asthmatic subjects exposed to particle concentrations 10-100 times that of urban environments. The acute toxicity of spark discharge carbon particles has also been investigated using animals as models [48]. Rats and mice were exposed to particles for 6 hours via inhalation in whole body exposure chambers, and as was the case in the human studies, no inflammatory response was observed in healthy animals.

Industrial carbon black is often used as a substitute for the elemental carbon content of combustion-generated soot in the study of toxicity. As previously discussed, industrial carbon black particles are generally larger than those emitted by mobile combustion sources – thus they are not an ideal substitute for soot, but such experiments are nonetheless informative. Jakab [49] found no indication of inflammation (nor any decrease in the lung resistance to viruses or bacteria) in mice exposed to carbon black via nose-only inhalation. Inflammation of human macrophages (cells that ingest foreign materials through a process of phagocytosis) exposed to carbon black was studied *in vitro* by Vogel et al. [50], and similarly, no increase in inflammatory markers was detected.

Zhou et al. [51] exposed rats (whole body) to 250  $\mu\text{g}/\text{m}^3$  of soot but utilized soot generated from a laminar diffusion flame burning ethylene, which more closely represents carbon generated from real combustion sources than does carbon generated via the spark discharge or carbon black. Soot generated by this method is expected to contain a very low concentration of organic compounds on the surface since the soot passes through a high-temperature oxidation zone prior to leaving the flame tip. As was the case with spark-discharge carbon particles, no respiratory effects were observed after exposure to diffusion flame soot. However, when iron was added to the flame in the form of iron pentacarbonyl, resulting in the co-formation of iron oxide nanoparticles, indications of oxidative stress were observed, and a synergistic interaction between the soot and the iron was reported. Reduced lung growth in neonatal rats was also observed after exposure to soot with iron added [52]. The results summarized thus far support the opinion that inflammation induced by engine exhaust particles or near-roadway PM is not mainly caused by elemental carbon particles, but rather by organic species or interactions between organics and included metals.

There is, however, evidence that *chronic* exposures to elemental carbon may lead to adverse health effects associated with tumor formation. Heinrich and Fuhst [63] dosed rats with carbon black,  $\text{TiO}_2$  particles, and diesel soot. At sufficiently high doses all types of particles induced the formation of pulmonary tumors in the animals. They claimed that the adsorbed PAH on the diesel was *not* responsible for tumor formation – they associated the formation of tumors with the carbon cores of the soot. A similar finding was reported by Nikula and Snipes [62] who found that the tumor-forming potential of carbon black and of diesel soot was about the same.

## 5. ROLE OF ADSORBED ORGANIC COMPOUNDS

Vogel et al. [50] examined the behavior of NIST diesel Standard Reference Material (referred to as DEP in Figure 3), urban dust (UDP, NIST Standard Reference Material 1649) and carbon black (CB) particles in human macrophages. The UDP is larger than the diesel or carbon black particles with a number mean diameter of 1.5  $\mu\text{m}$  and a volume mean diameter of 34.6  $\mu\text{m}$ . The authors examined the induction of 3 markers of chronic systemic inflammation that are associated with atherosclerosis:  $\text{TNF-}\alpha$ , COX-2 and IL-8. They removed the organic fraction of the aerosols so that they could test the organic fraction and so-called stripped particles separately.

To examine the effect of the stripped particles (sDEP) and the organic components (OE-DEP) of these particle samples, cells were treated with equivalent amounts of the

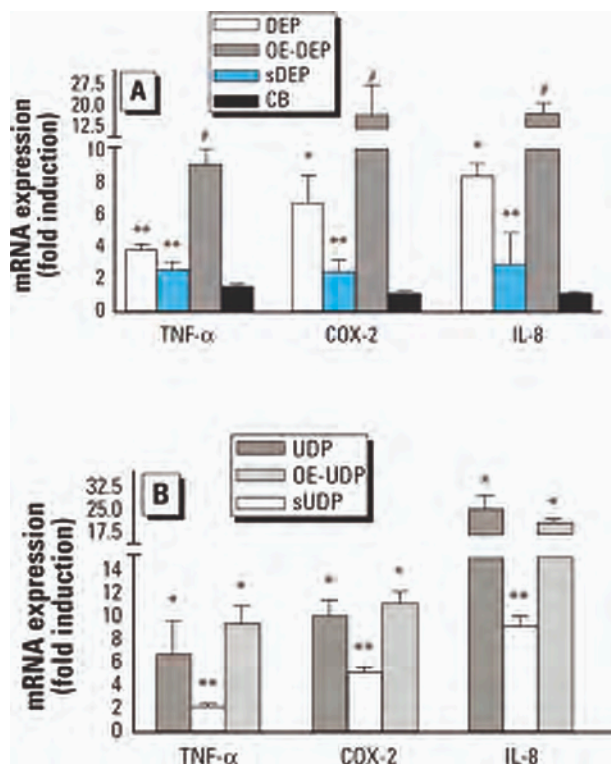


Figure 3. Effect of diesel exhaust particles (DEP) (A), urban dust particles (UDP) (B), and their corresponding stripped particles (sDEP, sUDP), or their organic extracts (OE) on the expression of inflammatory factors in U937 macrophages. \*Significantly increased compared to control cells ( $p < 0.05$ ). \*\*Significantly lower than in native particle-treated cells ( $p < 0.05$ ). #Significantly increased compared to native particles-treated cells ( $p < 0.05$ ) Reprinted from Ref. [50].

corresponding sDEP or OE-DEP. Figure 3 shows that DEP induced more inflammatory markers than the UDP. As mentioned earlier, carbon black appears not to be a significant agent for the induction of inflammation in these cells. When the extractable organic fraction was compared with the parent particles, it was found that the major contribution to the induction of inflammatory markers came from the soluble organic, not the elemental carbon particles.

The toxicity of laboratory flame-generated soot with adsorbed PAH has been studied *in vitro* using human bronchial epithelial cells in culture [28, 53]. This soot was generated by burning 1,3 butadiene in a Bunsen-type burner [53] and was well-characterized. These particles contained a variety of PAH on the surface. Utilizing the fluorescent properties of PAH, the researchers detected PAH within the cytoplasmic vesicles of cells. Uptake of whole particles was not observed, thus the conclusion is that cells are able to extract PAH from particles. This phenomenon was also observed by Gerde et al. [54], who studied the desorption of benzo(a)pyrene (BaP) from soot par-

ticles deposited in the alveolar lung region of dogs and subsequent absorption into the circulation. BaP is of particular concern since it is known to be mutagenic and highly carcinogenic, and is often found in significant quantities on fresh diesel exhaust particles [55]. These findings exemplify the role of soot particles as effective transporters of organic toxins and carcinogens that can be translocated into cells without requiring particle uptake.

## 6. DIESEL AND GASOLINE EXHAUST PARTICLES

A great deal of research over the past few decades has been directed towards understanding the toxicity that is caused by particles from diesel engines. More information on the health effects of diesel exhaust can be found in the Refs. [56-60]. Understandably, there are few studies that have been performed directly on humans. Salvi et al. [61] studied the acute response to diesel exhaust by exposing human volunteers for 1 hour, and found that while there was no measurable change in lung function after this short exposure, a number of markers indicating an inflammatory response were measured after 6 hours in airway lavages and bronchial biopsies. Early studies were concerned mostly with mutagenic effects and hence they focused on the formation of tumors, DNA adducts or DNA damage following exposure of rodents to diesel particulate matter [62-64]. Bond and Mauderly [64] found that lung DNA adduct levels in rats exposed to diesel soot accumulated slowly during a 12-week exposure, and were highest at the end of the exposure. However, they showed the tumor rate in the rats was not uniquely related to the production of DNA adducts, a result that indicated that the formation of DNA adducts was only one possible step along the tumor formation pathway.

A great deal of the research that has been carried out on the mutagenic activity of soot particles has focused on the use of a standard reference material from NIST [50, 65]. On the other hand, many of the studies of pulmonary toxicity have made use of engine-generated soot particles. DeMarini et al. [66] studied the relative toxicity of these two types of particles by using different soluble fractions that were extracted from the particles. The solvents ranged from non-polar hexane to polar methanol, which could extract alkane or alkene type materials in the first case to oxidized or nitrated-aromatic compounds in the latter case. They found that the NIST diesel reference material was generally less toxic compared to the automobile diesel engine particles. The latter type of particles generally had a much greater amount of soluble organic carbon material adsorbed to it. Singh et al. [67] examined the same materials, automobile diesel engine particulate matter and fork lift truck diesel particulate matter, and tested them and their extracts for a variety of end-points. On the basis of their results, they argued that there are significant differences in response to these two types of materials, and that more attention needs to be paid to the physical and chemical characteristics of particles that are used in human health effects studies. Engine characteristics, as well as the subsequent aging of particles, apparently play an important role in determining their impact on health.

The temperature and time in the combustion system will also have an impact on the amount and nature of organic carbon that is adsorbed to the surface of soot.

These characteristics are expected to have an impact on the health effects following inhalation of this material. Madden et al. [74] found that the response of human airway epithelial cells to soot depended on the operating load of a diesel engine; they related the effect to differences in the organic carbon composition that was adsorbed on the particles.

Liu et al. [68] compared the toxicity of particles emitted from gasoline and diesel engines. Particle emissions were collected from vehicles that were operated on the California driving cycle. Organic material from the particles was extracted, and tested for toxicity in terms of mutagenic activity and DNA damage; semi-volatile organic compounds were also collected during these tests. Differences were found between the potential for DNA damage caused by gasoline and by diesel engine exhausts, without any clear overall trend in terms of toxicity. Once again, the results highlighted the potential differences in the toxicity of particles derived from different sources.

In an effort to study the toxicity of diesel particles outside of the typical laboratory, Elder et al. [69] exposed rats to diesel emissions in a mobile laboratory housed in a tractor-trailer driven on a freeway. This study utilized older, compromised animals since it is believed that elderly humans, or those with pre-existing conditions, are particularly at risk of adverse effects from roadside PM. Lung inflammation combined with cardiovascular system effects were observed.

The potential for confusion in toxicology studies that use nominally the same material is illustrated by the apparently conflicting results that were reported by Iwai and Udagawa [70] and by McDonald et al. [71] in studies of rats and mice respectively that were exposed to diesel particulate matter with high and low sulfur fuels. Iwai and Udagawa found that low sulfur fuels reduced the acidity of the particulate matter – however, the tumor formation rate actually increased with the use of low sulfur fuel for the same mass concentration delivered to the animals. On the other hand, McDonald et al. reported that the use of low sulfur fuel significantly mitigated other effects such as inflammation, oxidative stress and resistance to viral infection. The difference in findings serves to demonstrate that different end-points i.e., different measures of toxicity, can lead to different conclusions about the potential health impact of diesel soot.

When considering the toxic behavior of diesel engine emissions, it is important to separate the effects of particles from those of exhaust gases. In an effort to separate these two potential sources of toxicity, Holder et al. [72] exposed human bronchial epithelial cells in culture to filtered, denuded, and whole diesel exhaust. By comparing cell viability and secretion of the inflammatory cytokine IL-8 by cells exposed to filtered exhaust with those exposed to the whole exhaust, it was determined that the exhaust gases alone contributed to half of the observed toxicity. Constituents of the exhaust that potentially elicited the toxic response included  $\text{NO}_2$ ,  $\text{SO}_2$ ,  $\text{O}_3$ , and volatile/semi-volatile organic compounds. Removal of the gas-phase organic species using a denuder also resulted in a reduction of IL-8, when compared to the whole exhaust. These results are potentially contradictory to the *inhalation* studies of Kleinman et al. [73], who compared the response due to diesel exhaust particles to that by a clean gaseous mixture containing  $\text{NO}_2$  &  $\text{O}_3$  only, with concentrations of  $\text{NO}_2$  &  $\text{O}_3$  equal to those measured in the diesel exhaust. In this study, it was concluded that the addition of diesel particles to an oxidant gas mixture resulted in no additional toxicity to rats, as measured by changes in lung histopathology, changes in mucosal permeability, and changes

in alveolar macrophage functions. We must emphasize, however, that caution needs to be exercised when making such comparisons since it is difficult to extrapolate *in vitro* results to whole animals.

Technology has had an impact on the toxicity of diesel engine soot. Seagrave et al. [75] investigated the emissions for three types of bus engines: a normal engine, a modern engine with oxidative catalyst, and a high-emitting older engine. A chemical analysis of the particulate matter showed that the high-emitting engine produced soot that had traces of lubricating oil components. This was not the case for the two cleaner engines. A variety of markers were assessed following intratracheal installation into rats. The effects from the normal and modern engines were modest; on the other hand, the high-emitting engine gave rise to significant effects. The soot from the high-emitting engine was also found to be more mutagenic.

The promotion of bio-diesel fuel, as an alternative to regular diesel fuel, has generated some interest in terms of its potential for health effects, as biofuel does not contain sulfur and contains less aromatic species. Bunker et al. [76] studied the emissions from a tractor that was fueled on both normal diesel and bio-diesel. The tractor was operated on a European standard test cycle. The total particle mass emissions were higher for the biofuel than for the normal diesel fuel, but the mass of insoluble PM was lower, thus the burning of this biofuel led to a large increase in the amount of soluble organic material. They examined the potential for mutagenicity as well as toxicity. They found that the bio-diesel fueled engine created particles that led to less mutagenicity. They attributed this finding to the reduction in formation of poly aromatic hydrocarbons (PAH) from the bio-diesel fuel. On the other hand, they found that the bio-diesel fueled engine emitted particles that exhibited greater toxicity with *in vitro* tests. This finding was attributed to the presence of carbonyls and other incompletely oxidized hydrocarbons on the surface of soot from the bio-diesel engine. The results serve to illustrate, once again, that the composition of materials adsorbed to soot particles is very important in determining environmental impacts and health effects.

Some modern diesel engines now incorporate a diesel particulate trap (DPF) on the exhaust system. The impact of fuel type and air pollution control equipment on the toxicity of engine exhaust was studied by McDonald et al. [71]. They examined a series of toxicological end points, including oxidative stress and inflammation, following exposure of mice to a base-line diesel engine exhaust and to exhaust from an engine operating on low-sulfur fuel and with a catalytic particle trap. Significant health effects were evident following exposure to the base-line exhaust. However, the use of a low-sulfur fuel and a particle trap eliminated essentially all the adverse health effects. Although this observation is specific to this engine, and cannot be generalized to other engines, other studies of emissions of diesel engines equipped with DPFs support this conclusion.

## 7. CONCLUDING REMARKS

Soot from combustion sources has been implicated as a contributor to respiratory and heart diseases and increased mortality. Understanding the underlying causes of these effects is necessary if effective regulations on soot emissions aimed at mitigating health

effects are to be developed. A number of studies have confirmed the harmful nature of particles emitted from internal combustion engines and of particles collected near traffic sources. However, the complex composition of such particles makes the determination of the root causes of toxicity a challenge. We have demonstrated that soot from the exhaust of a diffusion flame has a greater capacity for ROS generation than does carbon black or aged NIST standard diesel soot, suggesting that surface area and particle aging are important factors to consider. It is apparent that the addition of adsorbed organic compounds and the presence of metals enhance the toxicity of soot. Continued research focused on well-characterized, laboratory-generated particles with controlled chemical composition will provide valuable fundamental insight into the causation of health effects associated with airborne particles. This understanding will assist the combustion engineering community in avoiding new technologies that may exacerbate the impact of engine emissions on human health.

## ACKNOWLEDGMENTS

This publication was made possible by grant number 5 P42 ES004699 from the National Institute of Environmental Health Sciences (NIEHS), NIH and the contents are solely the responsibility of the authors and do not necessarily represent the official views of the NIEHS, NIH. Although the research described in the article has been funded wholly or in part by the United States Environmental Protection Agency through grant RD-83241401-0 to the University of California, Davis, it has not been subject to the Agency's required peer and policy review and therefore does not necessarily reflect the views of the Agency and no official endorsement should be inferred.

## REFERENCES

1. D. W. Dockery, C. A. Pope, X. Xu, J. D. Spengler, J. H. Ware, M. E. Fay, B. G. Ferris, F. E. Speizer, *N. Engl. J. Med.* 329:24 (1993) 1753-1759.
2. J. M. Samet, S. L. Zeger, F. Dominici, F. Curriero, I. Coursac, D. M. Dockery, J. Schwartz, A. Zanobetti, *The National Morbidity, Mortality, and Air Pollution Study. Part II: Morbidity and Mortality from Air Pollution in the United States*, Research Report no. 94, Health Effects Institute, 2000.
3. C. A. Pope, III, R. T. Burnett, G. D. Thurston, M. J. Thun, E. E. Calle, D. Krewski, J. J. Godleski, *Circulation* 109:1 (2004) 71-77.
4. C. A. Pope, R. T. Burnett, M. J. Thun, E. E. Calle, D. Krewski, K. Ito, G. D. Thurston, *J. Am. Med. Assoc.* 287:9 (2002) 1132-1141.
5. R. T. Burnett, S. Cakmak, J. R. Brook, D. Krewski, *Environ. Health Perspec.* 105:6 (1997) 61-620.
6. J. Schwartz, *Epidemiology* 10:1 (1999) 17-22.
7. S. B. Sardar, P. M. Fine, C. Sioutas, *J. Geophys. Res.* 110 (D7) (2005).
8. F. Laden, L. M. Neas, D. W. Dockery, J. Schwartz, *Environ. Health Perspec.* 108:10 (2000) 941-947.
9. J. Schwartz, L. M. Neas, *Epidemiology* 11:1 (2000) 6-10.

10. W. J. Gauderman, H. Vora, R. McConnell, K. Berhane, F. Gilliland, D. Thomas, F. Lurmann, E. Avoli, N. Kunzli, M. Jerrett, J. Peters, *Lancet* 369:9561 (2007) 571-577.
11. R. J. Delfino, C. Sioutas, S. Malik, *Environ. Health Perspec.* 113:8 (2005) 934-946.
12. W. Stober, U. R. Abel, *Int. Archives of Occupational and Environ. Health* 68 (1996) S3-S61.
13. J. S. Lighty, J. M. Veranth, A. F. Sarofim, *J. Air & Waste Management Assoc.* 50:9 (2000) 1565-1618.
14. J. L. Durant, W. F. Busby, A. L. Lafleur, B. W. Penman, C. L. Crespi, *Mutation Res. Genetic Toxicology* 371:3-4 (1996) 123-157.
15. Z. H. Fan, D. H. Chen, P. Birla, R. M. Kamens, *Atmosph. Environ.* 29:10 (1995) 1171-1181.
16. G. Perrini, M. Tomasello, V. Librando, Z. Minniti, *Annali di Chimica* 95:7-8 (2005) 567-577.
17. M. I. Gilmour, S. O'Connor, C. A. J. Dick, C. A. Miller, W. P. Linak, *J. Air & Waste Management Assoc.* 54:3 (2004) 286-295.
18. W. P. Linak, J.-I. Yoo, S. J. Wasson, W. Zhu, J. O. L. Wendt, F. E. Huggins, Y. Chen, N. Shah, G. P. Huffman, M. I. Gilmour, *Proc. Combust. Instit.* 31:Pt. 2 (2007) 1929-1937.
19. C. D. Okeson, M. R. Riley, A. Fernandez, J. O. L. Wendt, *Chemosphere* 51:10 (2003) 1121-1128.
20. S. Diabate, S. Mulhopt, H. R. Paur, R. Wottrich, H. F. Krug, *Int. J. Hygiene and Environ. Health* 204:5-6 (2002) 323-326.
21. E. Abi-Aad, R. Cousin, C. Pruvost, D. Courcot, R. Noirot, C. Rigaudeau, A. Aboukais, *Topics in Catalysis* 16:1-4 (2001) 263-268.
22. A. Valavanidis, K. Fiotakis, E. Bakeas, T. Vlahogianni, *Redox Report* 10:1 (2005) 37-51.
23. H. Saathoff, O. Moehler, U. Schurath, S. Kamm, B. Dippel, D. Mihelcic, *J. Aerosol Sci.* 34:10 (2003) 1277-1296.
24. C. Yamanaka, T. Matsuda, M. Ikeya, *App. Radiation and Isotopes* 62:2 (2005) 307-311.
25. A. R. Chughtai, J. M. Kim, D. M. Smith, *J. Atmosph. Chem.* 43:1 (2002) 21-43.
26. C. C. Jones, A. R. Chughtai, B. Murugaverl, D. M. Smith, *Carbon* 42:12-13 (2004) 2471-2484.
27. S. Yan, Y. J. Jiang, N. D. Marsh, E. G. Eddings, A. F. Sarofim, R. J. Pugmire, *Energy & Fuels* 19:5 (2005) 1804-1811.
28. W. J. Catallo, C. H. Kennedy, W. Henk, S. A. Barker, S. C. Grace, A. Penn, *Environ. Health Perspec.* 109:9 (2001) 965-971.
29. G. L. Squadrito, R. Cueto, B. Dellinger, W. A. Pryor, *Free Radical Biol. Med.* 31:9 (2001) 1132-1138.
30. B. Dellinger, W. A. Pryor, R. Cueto, G. Squadrito, W. A. Deutsch, *Proc. Combust. Instit.* 28 (2000) 2675-2681.
31. W. A. Pryor, *Free Radical Biol. Med.* 13:6 (1992) 659-676.
32. H. Schulz, V. Harder, A. Ibal-Mulli, A. Khandoga, W. Koenig, F. Krombach, R. Radykewicz, A. Stampfl, B. Thorand, A. Peters, *J. Aerosol Med.-Deposition Clearance and Effects in the Lung* 18:1 (2005) 1-22.
33. W. G. Kreyling, M. Semmler, W. Moller, *J. Aerosol Med.-Deposition Clearance and Effects in the Lung* 17:2 (2004) 140-152.
34. L. C. Renwick, D. Brown, A. Clouter, K. Donaldson, *Occupational Environ. Med.* 61:5 (2004) 442-447.
35. F. Tao, B. Gonzalez-Flecha, L. Kobzik, *Free Radical Biol. Med.* 35:4 (2003) 327-340.
36. M. D. Geller, L. Ntziachristos, A. Mamakos, Z. Samaras, D. A. Schmitz, J. R. Froines, C. Sioutas, *Atmosph. Environ.* 40:36 (2006) 6988-7004.

37. A. K. Cho, C. Sioutas, A. H. Miguel, Y. Kumagai, D. A. Schmitz, M. Singh, A. Eiguren-Fernandez, J. R. Froines, *Environ. Res.* 99:1 (2005) 40-47.
38. H. Jung, B. Guo, C. Anastasio, I. M. Kennedy, *Atmosph. Environ.* 40:6 (2006) 1043-1052.
39. B. Halliwell, M. Whiteman, *Br J Pharmacol* 142:2 (2004) 231-255.
40. B. B. Aam, F. Fonnum, *Archives of Toxicology* 81:6 (2007) 441-446.
41. S. Becker, L. A. Dailey, J. M. Soukup, S. C. Grambow, R. B. Devlin, Y.-C. T. Huang, *Environ. Health Perspec.* 113:8 (2005) 1032-1038.
42. P. Venkatchari, P. K. Hopke, W. H. Brune, X. Ren, R. Leshner, J. Mao, M. Mitchell, *Aerosol Sci. Tech.* 41:2 (2007) 97-111.
43. M. R. Wilson, J. H. Lightbody, K. Donaldson, J. Sales, V. Stone, *Toxicol. Appl. Pharmacol.* 184:3 (2002) 172-179.
44. M. D. Hays, R. L. Vander Wal, *Energy Fuels* 21:2 (2007) 801-811.
45. R. L. Vander Wal, A. J. Tomasek, *Combust. Flame* 136:1-2 (2004) 129-140.
46. K. O. Lee, R. Cole, R. Sekar, M. Y. Choi, J. S. Kang, C. S. Bae, H. D. Shin, *Proc. Combust. Instit.* 29 (2003) 647-653.
47. M. W. Frampton, M. J. Utell, W. Zareba, G. Oberdörster, C. Cox, L.-S. Huang, P. E. Morrow, F. E.-H. Lee, D. Chalupa, L. M. Frasier, D. M. Speers, J. Stewart, *Effects of Exposure to Ultrafine Carbon Particles in Healthy Subjects and Subjects with Asthma*, Research Report no.162, Health Effect Institute, 2004.
48. G. Oberdörster, J. N. Finkelstein, C. Johnston, R. Gelein, C. Cox, R. Baggs, A. C. P. Elder, *Acute Pulmonary Effects of Ultrafine Particles in Rats and Mice*, Research Report no. 96, Health Effects Institute, 2000.
49. G. J. Jakab, *Toxicol. Appl. Pharmacol.* 121:2 (1993) 167-175.
50. C. F. A. Vogel, E. Sciallo, P. Wong, P. Kuzmicky, N. Kado, F. Matsumura, *Environ. Health Perspec.* 113:11 (2005) 1536-1541.
51. Y. M. Zhou, C. Y. Zhong, I. M. Kennedy, V. J. Leppert, K. E. Pinkerton, *Toxicol. Appl. Pharmacol.* 190:2 (2003) 157-169.
52. K. E. Pinkerton, Y. M. Zhou, S. V. Teague, J. L. Peake, R. C. Walther, I. M. Kennedy, V. J. Leppert, A. E. Aust, *Inhalation Toxicol.* 16 (2004) 73-81.
53. A. Penn, G. Murphy, S. Barker, W. Henk, L. Penn, *Environ. Health Perspec.* 113:8 (2005) 956-963.
54. P. Gerde, B. A. Muggenburg, M. Lundborg, A. R. Dahl, *Carcinogenesis* 22:5 (2001) 741-749.
55. B. Zielinska, J. Sagebiel, J. D. McDonald, K. Whitney, D. R. Lawson, *J. Air Waste Management Assoc.* 54:9 (2004) 1138-1151.
56. J. L. Mauderly, *Environ. Health Perspec.* 102:Suppl. 4 (1994) 165-71.
57. J. L. Mauderly, *Toxicol. Environ. Chem.* 49:3 (1995) 167-80.
58. P. T. J. Scheepers, R. P. Bos, *Int. Arch. Occupational Environ. Health* 64:3 (1992) 163-177.
59. R. O. McClellan, A. L. Brooks, R. G. Cuddihy, R. K. Jones, J. L. Mauderly, R. K. Wolff, *Develop. Toxicol. Environ. Sci.* 10: (1982) 99-120.
60. J. L. Mauderly, R. K. Jones, R. O. McClellan, R. F. Henderson, W. C. Griffith, *Develop. Toxicol. Environ. Sci.* 13: (1986) 397-409.
61. S. Salvi, A. Blomberg, B. Rudell, F. Kelly, T. Sandstrom, S. T. Holgate, A. Frew, *Am. J. Respir. Critical Care Med.* 159:3 (1999) 702-709.
62. K. J. Nikula, M. B. Snipes, E. B. Barr, W. C. Griffith, R. F. Henderson, J. L. Mauderly, *Fund. Appl. Toxicol.* 25:1 (1995) 80-94.
63. U. Heinrich, R. Fuhst, S. Rittinghausen, O. Creutzenberg, B. Bellmann, W. Koch, Levens, *Inhalation Toxicol.* 7:4 (1995) 533-56.

64. J. A. Bond, J. L. Mauderly, R. K. Wolff, *Toxicology* 60:1-2 (1990) 127-135.
65. D. Cao, T. L. Tal, L. M. Graves, I. Gilmour, W. Linak, W. Reed, P. A. Bromberg, J. M. Samet, *AJP – Lung Cellular and Molecular Physiology* 292:2 (2007) L422-429.
66. D. M. DeMarini, L. R. Brooks, S. H. Warren, T. Kobayashi, M. I. Gilmour, P. Singh, *Environ. Health Perspec.* 112:8 (2004) 814-819.
67. P. Singh, D. M. DeMarini, C. A. J. Dick, D. G. Tabor, J. V. Ryan, W. P. Linak, T. Kobayashi, M. I. Gilmour, *Environ. Health Perspec.* 112:8 (2004) 820-825.
68. Y.-Q. Liu, M. Keane, M. Ensell, W. Miller, M. Kashon, T.-m. Ong, J. Mauderly, D. Lawson, M. Gautam, B. Zielinska, K. Whitney, J. Eberhardt, W. Wallace, *J. Environ. Monitoring*, 7:1 (2005) 60-66.
69. A. Elder, R. Gelein, J. Finkelstein, R. Phipps, M. Frampton, M. Utell, D. B. Kittelson, W. F. Watts, P. Hopke, C. H. Jeong, E. Kim, W. Liu, W. X. Zhao, L. M. Zhuo, R. Vincent, P. Kumarathasan, G. Oberdorster, *Inhalation Toxicol.* 16 (2004) 41-53.
70. K. Iwai, T. Udagawa, S. Mizuno, Y. Kawabata, I. Sugawara, S. Goto, H. Seto, S. Adachi, *Taiki Kankyo Gakkaishi* 37:3 (2002) 216-229.
71. J. D. McDonald, K. S. Harrod, J. Seagrave, S. K. Seilkop, J. L. Mauderly, *Environ. Health Perspec.* 112:13 (2004) 1307-1312.
72. A. L. Holder, D. Lucas, R. Goth-Goldstein, C. P. Koshland, *Chemosphere*, in press, corrected proof (2007).
73. M. T. Kleinman, D. K. Bhalla, B. Ziegler, S. Bucher-Evans, T. McClure, *Inhalation Toxicol.* 5:4 (1993) 371-88.
74. M. C. Madden, L. A. Dailey, J. G. Stonehuerner, D. B. Harris, *J. Toxicol. Environ. Health-Pt. A* 66 (2003) 2281-2297.
75. J. Seagrave, A. Gigliotti, J. D. McDonald, S. K. Seilkop, K. A. Whitney, B. Zielinska, J. L. Mauderly, *Toxicol. Sci.* 87:1 (2005) 232-241.
76. J. Bunger, J. Krahl, K. Baum, O. Schroder, M. Muller, G. Westphal, P. Ruhnau, T. G. Schulz, E. Hallier, *Arch. Toxicol.* 74:8 (2000) 490-498.
77. G. L. Finch, C. H. Hobbs, L. F. Blair, E. B. Barr, F. F. Hahn, R. J. Jaramillo, J. E. Kubatko, T. H. March, R. K. White, J. R. Krone, M. G. Menache, K. J. Nikula, J. L. Mauderly, J. Van Gerpen, M. D. Merceica, B. Zielinska, L. Stankowski, K. Burling, S. Howell, *Inhalation Toxicol.* 14:10 (2002) 1017-1048.



# Soot structure and dimensionless extinction coefficient in diffusion flames: implications for index of refraction

C.R. Shaddix, T.C. Williams

*Combustion Research Facility*

*Sandia National Laboratories*

*Livermore, California 94550*

*Abstract: Local soot populations have been examined within laminar diffusion flames fueled by methane, ethylene, and kerosene, and in the active flame zone of a large JP-8 fueled pool fire. Transmission electron microscopy (TEM) analysis, including high-resolution TEM, was applied to thermophoretically sampled soot to determine the characteristic soot primary particle and aggregate properties as well as the interlayer spacing ( $d_{002}$ ) of the graphitic crystalline layers of carbon. Little difference was found in the interlayer spacing for hard, graphitized soot particles as a function of residence time within a given flame or between different flames. The dimensionless extinction coefficient ( $K_e$ ) of extracted soot was measured at visible (635 nm) and near-infrared (1310 nm) wavelengths. Outside of the active soot inception zone,  $K_e$  was found to range from 9 to 10 for the ethylene and kerosene flames, consistent with previous studies by others of post-flame soot. Together with the measurements of interlayer spacing, this result implies that the soot nanostructure does not evolve significantly once the particles dehydrogenate from their initial liquid-like state and become hard, aggregating particles. The measured values of  $K_e$  are inconsistent with commonly referenced literature values of the soot refractive index. Rayleigh-Debye-Gans (RDG) fractal aggregate theory is applied to the measured soot structure properties and is combined with the  $K_e$  measurements to infer values of the soot index of refraction that are consistent with the measurements. At 635 nm, the deduced index of refraction is approximately 1.7 - 1.0i.*

## 1. INTRODUCTION

Accurate knowledge of the optical properties of soot particles is necessary for the proper interpretation of laser-based diagnostic measurements, for predicting radiant emission from sooty flames, and for predicting light extinction through smoke. Recently, considerable interest in soot optical properties has arisen in the atmospheric sciences because of the influence of elemental carbon on the scattering albedo (the ratio of scattering to total extinction) of atmospheric aerosol particles and hence on global climate change [1,2]. A wide variety of values for soot optical properties have been proposed over the years from researchers utilizing several different measurement techniques and many different flame sources [3], leading to considerable ambiguity in selecting appropriate values with which to interpret experimental measurements or to make predictions of radiant emission. Furthermore, it has been unclear whether soot opti-

cal properties change substantially for soot derived from different fuel sources, from different types of flames, and from different positions within a given flame.

Within the past 15 years, there has been significant clarification of the evolutionary process by which soot particles first form as discrete, liquid-like spherical nanoparticles and eventually become wispy aggregates of hardened primary particles. Dobbins and coworkers [4-7] have explored the presence and evolution of soot “precursor” particles in the soot inception region of diffusion flames. These nascent soot particles have a relatively high atomic H/C ratio of  $\sim 0.25 - 0.6$  and their generally spherical shape implies that they coalesce rather than aggregate upon colliding. These particles are only dimly apparent in transmission electron microscopy (TEM) micrographs, because of the disordered form of carbon in the particles. When these particles carbonize into hardened, aggregating soot, the H/C ratio decreases to approximately 0.2 [7]. D’Alessio and coworkers [8-12] and Wang and coworkers [13-15] have investigated soot precursor particles in premixed, flat flames, where the inception process is usually more protracted than in diffusion flames.

Concurrent with this improved understanding of the physico-chemical process of soot formation, careful measurements by Choi and Mulholland and coworkers [16-21] and Faeth and coworkers [22] have suggested that the fundamental optical properties of mature, carbonaceous soot may be more universal than previously believed. These researchers have focused on measuring the dimensionless extinction coefficient,  $K_e$ , or the closely related mass-specific extinction coefficient,  $\sigma_s$ , of soot emitted from a wide variety of flames. These extinction coefficients are derived from Bouguer’s law of light transmission, which can be expressed in the following two forms:

$$\frac{I}{I_0} = \exp\left(\frac{-K_e f_v l}{\lambda}\right) \quad (1)$$

$$\frac{I}{I_0} = \exp(-\sigma_s M_s l) \quad (2)$$

where  $I/I_0$  is the ratio of transmitted to incident monochromatic light intensity,  $f_v$  is the soot volume fraction,  $\lambda$  is the wavelength of light,  $l$  is the path length through the medium, and  $M_s$  is the mass concentration of soot. From these expressions one can see that  $K_e = \rho_s \lambda \sigma_s$ , where  $\rho_s$  is the soot mass density, approximately equal to  $1.8 \times 10^3$  kg/m<sup>3</sup> for mature soot. Physically, these extinction coefficients quantify the ability of soot to extinguish light, primarily through absorption, but with some contribution through scattering. The absorption of light by soot particles is generally believed to be independent of particle size and aggregate structure, because soot primary particles are almost always small enough relative to the wavelength of light to be in the Rayleigh limit (and thus are volume absorbers), and the commonly applied Rayleigh-Debye-Gans (RDG) fractal aggregate theory treats the absorption by an aggregate to be equal to the sum of the absorption by the primary particles.

The soot extinction coefficient is typically quantified by applying simultaneous gravimetric sampling and light extinction (GSL-E) [23]. The work of Choi, Mulholland, Faeth, and their coworkers has quantified  $K_e$  for soot emitted from laminar and turbulent diffusion flames and smoking laminar premixed flames for several fuels and over a range of visible and infrared wavelengths. For all but underventilated diffusion flames

[21], where complications arise from condensation of polycyclic aromatic hydrocarbons (PAH),  $K_e$  has been consistently measured to be between 8 and 10 over the wavelength range of 400 nm to 3  $\mu\text{m}$ . This is a much narrower range of variability than is suggested by previous measurements of the refractive index of soot, which yield derived values for the absorption coefficient of soot that vary by about a factor of two [3].

Despite the small range of values determined for post-flame  $K_e$ , it is clear that during soot inception the optical properties of the newly condensed material would be expected to be different from fully mature soot. In fact, Minutolo et al. [9] have presented an elegant analysis of the evolution of absorption spectra in a near-sooting premixed flame in which the extension of the absorption band from the ultraviolet to the visible (and ultimately into the infrared) of the large aromatic hydrocarbons and precursor particles is associated with the decreasing magnitude of the Tauc band gap (referring to the energy separation between valence electrons and conduction electrons) as the aromatic clusters grow in size within the particles. Indeed, the band gap energy appears to correlate linearly with the optical extinction dispersion coefficient and with the precursor material H/C ratio. Furthermore, Wersborg et al. [24] made an early measurement of the absorption coefficient of precursor particles in a low-pressure premixed flame and found the optical absorptivity to be over an order of magnitude lower than that of mature soot.

In this paper we discuss the results of our recent investigations into soot nanostructure and  $K_e$  values in a series of laminar diffusion flames and in a large JP-8 pool fire and focus on the implications of these measurements with respect to the universality of the optical properties of carbonaceous soot and the characteristic index of refraction of this material.

## 2. EXPERIMENTAL

### 2.1. Flame systems

A variety of laminar flame burners were employed to generate both steady and unsteady normal diffusion flames of gaseous jets emitted into coflowing air. For soot nanostructure determination using high-resolution transmission electron microscopy (HRTEM), samples were collected at several heights along the centerline for both steady and unsteady laminar ethylene diffusion flames. In addition, HRTEM was performed on soot collected from the flame zone of a fully turbulent 5 m diameter JP-8 pool fire. For soot microstructure determination via ordinary TEM and for GSLE measurements of the soot extinction coefficient, measurements were performed in the peak annular soot layer of steady and pulsed laminar diffusion flames of methane, ethylene, and nitrogen-diluted kerosene in both coannular and slot flame geometries. The slot flame geometry, combined with high fuel flow velocities, gave access to an extended region of soot particle inception. The slot geometry also facilitated soot sampling without penetration through the high temperature flame zone. A full description of the flames employed and the sampling heights used is given in refs. 25 and 26. Figure 1 shows photographs of the flames employed for the TEM and GSLE measurements.

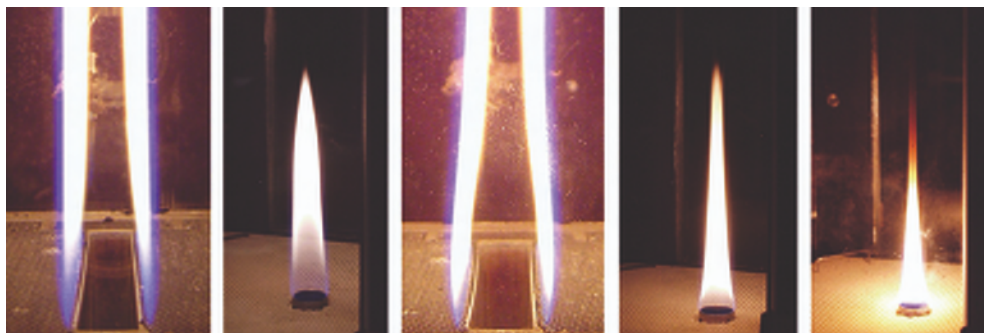


Figure 1. Photographs of the steady laminar diffusion flames employed in the analysis of soot microstructure and dimensionless extinction coefficient. The two leftmost flames are fueled by methane, the next two are fueled by ethylene, and the rightmost flame is fueled by a 3:1 mixture of nitrogen and kerosene. The image height for the slot burner flames is 65 mm whereas that for the coannular burner is 120 mm.

## 2.2. TEM grid sampling and analysis

For the laminar flames, TEM grid samples were collected using a rapid-injection, short-hold thermophoretic sampling technique with the grids oriented vertically in an ultraslim grid holder, to minimize flame disturbance [27]. The grid holder was mounted onto the end of a pneumatically driven piston. For the HRTEM analysis of the laminar flames, copper grids with a lacey carbon film were utilized, to avoid interference during the TEM analysis from the amorphous carbon film that is more typically used. For ordinary TEM analysis of the laminar flames, soot samples were collected using carbon-coated TEM grids (200 mesh, 3 mm diameter). Characteristic insertion and retraction times of the grids were 6 ms, with the hold times varied depending on the local soot loading within the flame. For sampling in the pool fire, carbon-coated grids were oriented horizontally and exposed for 0.3 s [28].

The collected soot samples were analyzed using a JEOL JEM 1200EX transmission electron microscope at magnifications of 10,000, 20,000, and 50,000. HRTEM was performed in lattice fringe mode on the collected soot samples using a Phillips CM30 microscope operating at 300 kV, with a point-to-point resolution of 0.18 nm. Photographic images were collected for representative soot particles and subsequently scanned into a computer for additional digital analysis. Five to seven HRTEM images were collected for each flame sampling position.

Digital analysis of the carbon ordering in the soot nanostructure was conducted using Semper<sup>TM</sup> image-processing software, with custom modifications previously reported by Palotás et al. [29]. A variety of parameters characterizing the turbostratic carbon may be statistically determined from the analyzed images, such as fringe length, fringe circularity/tortuosity, fringe pattern/orientation, fractional coverage, and the graphitic layer interplanar spacing,  $d_{002}$ . For the evaluation of the degree of graphitization of carbonaceous materials, the characteristic interplanar spacing has been most

commonly used [30] and has an advantage over the use of fringe length as a relative indicator of the degree of graphitization in that it is not constrained by the initial ordering of crystallites within the carbonaceous material.

From the ordinary TEM images, primary soot particle diameters and radius of gyration of the aggregates were determined, and the scattering albedo (i.e. the ratio of total scattering to extinction) was estimated using the Rayleigh-Debye-Gans theory of scattering and absorption by polydisperse fractal aggregates (RDG-PFA theory) [31,32]. Details of this procedure and the relevant equations from RDG-PFA are given in ref. 26.

### 2.3. GSLE measurements

Simultaneous measurements of gravimetric sampling and light extinction were performed using the apparatus shown in Figure 2. In this measurement, a sample of soot-laden gas is withdrawn from the flame through a probe, diluted with nitrogen, flows through a 1-m long transmission cell, and then is filtered for determination of the entrained soot mass. Through trial-and-error a sampling probe consisting of a stainless steel tube with a 3.2 mm outside diameter was chosen for use, because it allowed sampling in the sootier flames without excessive soot and tar buildup on the exterior of the probe. Further, by restricting the sample flow rate to 0.1 slpm, the probe had no noticeable effect on the local flame structure. From the entrance of the probe the sample traveled 0.3 m before being diluted with 5 slpm of nitrogen (50:1 dilution ratio). The dilution served to quench any reactions and minimize soot agglomeration within the GSLE system. A further two meters of tubing brought the sample to a wire mesh mixer and into the 1-m long transmission cell where light extinction measurements were performed simultaneously at 635 nm and 1310 nm with diode lasers directed down the center of the transmission cell. Approximately 60% of the flow exiting the transmission cell was sent through a Teflon filter for collection of the soot. The filter was weighed before and after the sample period to determine the soot mass, using a Mettler scale with a resolution of 0.01 mg. Collected soot masses varied from 0.4 mg to 4.3 mg. To verify the absence of any moisture condensation on the soot, several filters representing high and low derived  $K_e$  values were re-weighed after being placed in a dessicator for several days and showed no change of mass. At most sampling locations, at least two GSLE measurements were performed to verify the reproducibility of the measurement.

From the GSLE measurements,  $K_e$  was determined according to

$$K_e = \frac{-\lambda \rho_{soot} V \ln(I/I_0)}{m_{soot} l} \quad (3)$$

where  $\lambda$  is the wavelength of light,  $\rho_{soot}$  is the density of soot,  $V$  is the volume of gas drawn into the transmission tube over the sample period,  $m_{soot}$  is the total mass of soot pulled through the transmission tube, and  $l$  is the extinction pathlength. Because of occasional clogging and backflushing of the sampling tube (adding a significant dynamic to the soot loading in the extinction cell), mean values of the logarithm of the optical transmission ( $I/I_0$ ) had to be used in Eqn. 3, as discussed in ref. 26.

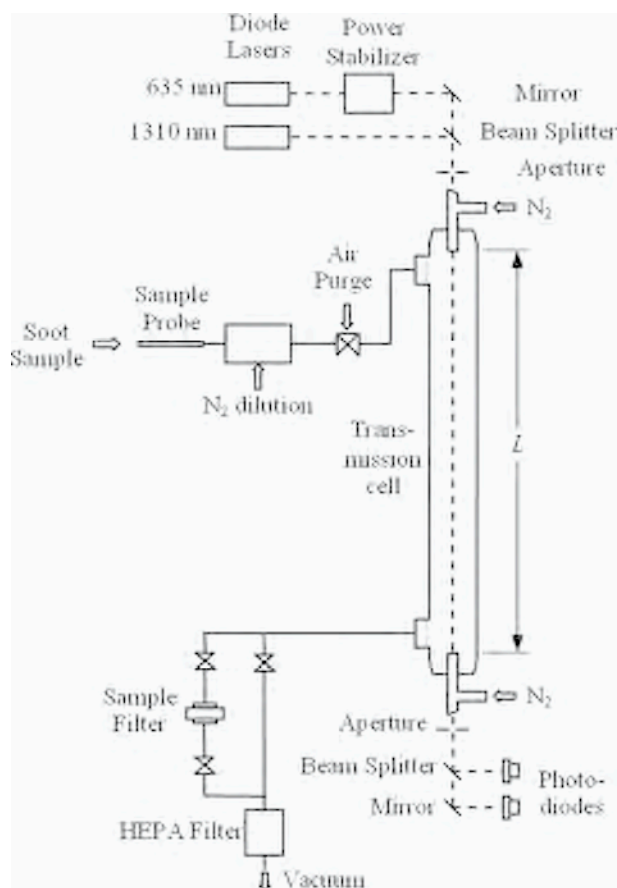


Figure 2. Schematic of gravimetric sampling and light extinction (GSLE) apparatus.

The mass density of the collected soot was not measured during this study. For ease of interpretation and consistency with most of the  $K_g$  literature, the soot density is assumed here to be equal to  $1.74 \text{ g/cm}^3$ , as previously determined by Choi and coworkers [33] using helium pycnometry on post-flame soot from a premixed acetylene/air flame.

Because of concerns over the contribution of condensed hydrocarbons (“tar-like material”) to the collected soot mass, vacuum extractions were performed on the filter samples using methylene chloride as the solvent. Approximately 20 ml of methylene chloride was pulled through each soot-containing filter, until subsequent extractions showed no evidence of additional mass loss. The filters were then allowed to dry and were reweighed, to determine the mass of material that went into solution in the methylene chloride.

### 3. RESULTS

#### 3.1. HRTEM analysis of soot nanostructure

Figure 3 shows a sample HRTEM image of neighboring primary particles. Table 1 shows the analyzed graphitic layer interplanar spacing in the soot samples from the different flames and at different flame heights along the centerline of the steady laminar flame. Both the mean values of the interplanar spacing and the standard deviations of the distribution of individual paracrystalline layer spacings are given. As previously shown by Palotás et al. [34,35], the standard deviation of the interplanar spacing of soot is relatively large, reflecting the inherently wide distribution of interplanar spacings in turbostratic carbons. Previous digital analysis of HRTEM images of a highly

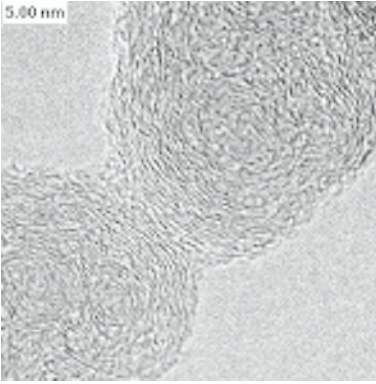


Figure 3. HRTEM micrograph of adjacent primary particles within a soot aggregate collected at a height of 210 mm in a steady (smoking) ethylene coannular flame.

Table 1. Graphitic layer interplanar spacing in collected soots.

Fuel	Flame characteristics/ Burner size	Sample height	$\overline{d_{002}}$ (Å)	$\sigma_{d_{002}}$ (Å)
ethylene	steady laminar 1.1 cm dia.	H = 50 mm	3.52	0.14
		H = 110 mm	3.48	0.15
		H = 210 mm	3.47	0.10
ethylene	unsteady laminar 6 cm dia.	postflame	3.57	0.12
JP-8	turbulent 5 m dia.	H = 1.2 m	3.55	0.14

graphitized carbon black yielded a standard deviation of the interlayer spacing of 0.07 Å [35], suggesting this is a practical lower limit of this quantity.

### 3.2. Soot microstructure and scattering albedo

Figure 4 shows typical TEM micrographs of soot aggregates as collected from the various laminar flames at a characteristic height (45 mm) where there are significant soot concentrations in all of the flames. Except for the methane slot flame, classic soot aggregates can be seen with more or less spherical soot primaries fused together to form chain structures. In the methane slot flame, the soot particles at this sampling height are still somewhat liquid-like, forming irregular shapes of partially coalesced aggregates, and the particles are semi-transparent to the electron beam. The results of the RDG-PFA analysis of the soot aggregate fields for all five flames are presented in Table 2, with scattering albedos calculated using several widely used or recently suggested values for the refractive index of soot [22,36-40]. Only the soot particles extracted from the kerosene and ethylene coannular flames have significant scattering albedos. At a wavelength of 635 nm the albedo ranges from 17% to 29% for the kerosene coannular flame, depending on the assumed refractive index, and it varies between 11% and 20% for the ethylene flame.

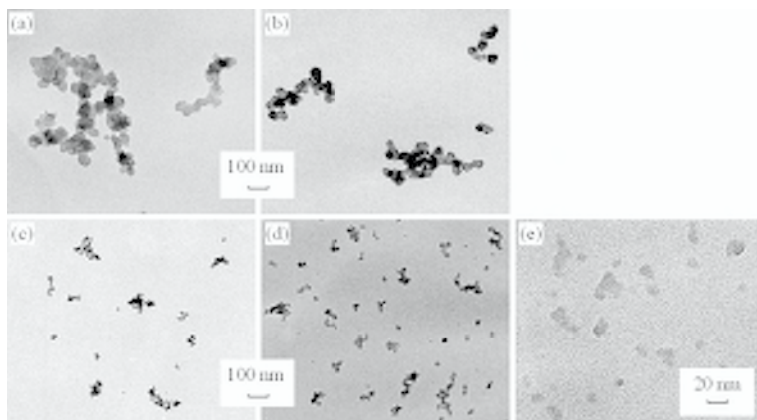


Figure 4. TEM micrographs of typical soot aggregates at a flame height of 45 mm from the following flames: (a) kerosene coannular, (b) ethylene coannular, (c) ethylene slot, (d) methane coannular and (e) methane slot.

### 3.3 Dimensionless Extinction Coefficient, $K_e$

Examination of the methylene chloride-soluble mass fractions reveals that significant organic content is present in the GSLE samples extracted from the two slot flames and

Table 2. Soot structure properties and Scattering albedos for presumed refractive index values.

Flame	$d_p \pm 1\sigma$	$\bar{N}$	$R_g$	Scattering albedo at 635 nm		Scattering albedo at 1310 nm			
				1.99-0.89j <sup>a</sup>	1.95-0.79j <sup>b</sup>	1.57-0.56i <sup>c</sup>	2.33-0.78i <sup>d</sup>	1.90-0.74i <sup>e</sup>	1.72-0.80i <sup>c</sup>
kerosene coannular	41 ± 11	30	74	0.29	0.27	0.17	0.09	0.05	0.04
C <sub>2</sub> H <sub>4</sub> coannular	36 ± 6	26	62	0.20	0.19	0.11	0.05	0.03	0.02
C <sub>2</sub> H <sub>4</sub> slot	25 ± 5	13	28	0.05	0.04	0.02	0.01	0.01	0.00
CH <sub>4</sub> coannular	20 ± 4	8	18	0.03	0.03	0.02	0.01	0.00	0.00
CH <sub>4</sub> slot	11 ± 3	3	6	0.00	0.00	0.00	0.00	0.00	0.00

<sup>a</sup> Krishnan et al [22].<sup>b</sup> Smith [36]; Bond and Bergstrom [37].<sup>c</sup> Dalzell and Sarofim [38].<sup>d</sup> Felske et al [39].<sup>e</sup> Lee and T'ien [40].

at the lowest sampling height (of 25 mm) in the methane coannular flame. The mean organic mass fractions are 35% and 28% for the methane and ethylene slot flame soot, respectively, and 37% for the soot at the lowest height in the methane coannular flame. Higher in the methane coannular flame the organic mass fraction is 6%. In contrast, no measurable amount of mass was removed by the solvent from either the kerosene or ethylene coannular flame soot samples.

Figure 5 shows the mean  $K_e$  values of the soot in the different flames. For those flames with organic content in the soot sample, two versions of  $K_e$  are shown: one that reflects the raw (tar-containing) soot mass (yielding a lower value of  $K_e$ ), and one that uses a corrected soot mass that excludes that portion of the soot sample that is soluble in methylene chloride, under the presumption that this soluble material was originally in the gas phase in the flame and is transparent to the extinction wavelengths used here. For the kerosene and ethylene coannular flames, the  $K_e$  results for both wave-

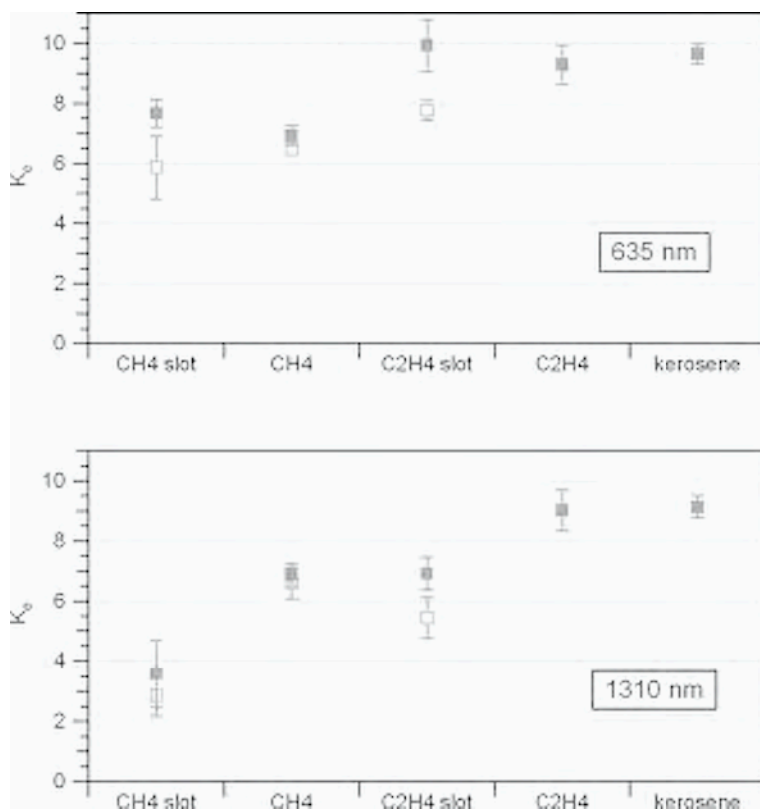


Figure 5. Mean dimensionless extinction coefficients measured in laminar diffusion flames. Unfilled symbols indicate “raw”  $K_e$  values, determined using the total mass of collected material, whereas the filled symbols indicate “corrected”  $K_e$  values determined using the mass of material that is insoluble in methylene chloride.

lengths fall into the 8 to 10 range, with a trend of slightly lower values in the near-infrared. The mean  $K_e$  value at 635 nm is 9.6 for the kerosene flame and 9.3 for the ethylene flame, as shown in Table 3. These compare to mean values of 9.1 and 9.0 for the kerosene and ethylene flames, respectively, at 1310 nm.

These measured in-flame  $K_e$  values are in good agreement with past measurements of postflame  $K_e$ . Zhu and coworkers [20] measured post-flame soot emitted from a laminar JP-8 diffusion flame, yielding a  $K_e$  value of 9.9 at 632.8 nm and 9.8 at 1314 nm (JP-8 is the U.S. military aviation fuel blend and is a form of kerosene). Measurements of soot extracted from the flame zone of a large JP-8 pool fire, where the soot sample is most likely a mixture of overfire and in-flame soot, with some condensed tar, yielded  $K_e$  values between 7 and 9 for both 635 nm and 1310 nm, with a slight trend towards higher values at 635 nm [41]. Measurements of the post-flame soot from an ethylene laminar diffusion flame yielded a  $K_e$  value of 9.7 at 632.8 nm and 9.2 at 1314 nm [18].

The  $K_e$  results for the methane coannular flame are substantially lower than the values obtained for the kerosene and ethylene coannular flames. The TEM micrographs (Figure 4) reveal small soot aggregates in the methane coannular flame and the calculated scattering albedo is only 3% at 635 nm (Table 2). Extinction of light by methane soot aggregates is therefore almost exclusively through absorption, producing a lower  $K_e$  value than seen with the larger soot aggregates of flames fueled with heavier hydrocarbons. The mean corrected  $K_e$  values are 6.9 at both 635 nm and 1310 nm.

The slot flame measurements exhibit some complex trends. At 635 nm, correction of the  $K_e$  values for the mass loss in methylene chloride yields higher values of  $K_e$  than measured for the corresponding coannular flames, despite the smaller primary particle sizes and lower degree of particle agglomeration (leading to less light scattering, as shown in Table 2). In contrast, at 1310 nm the corrected  $K_e$  values are substantially lower than for the corresponding coannular flames. As discussed in our earlier paper (ref. 26) we believe these apparent inconsistencies with the data from the coannular flames result from the sampling of soot precursor particles in the slot flames (because of continued soot inception at our sampling heights, as evidenced both by laser diagnostic techniques and the presence of substantial organic material in the soot mass samples). Soot precursor particles have a significantly lower mass density (of  $\sim 1.2 \text{ g/cm}^3$  [4]) than carbonaceous soot (affecting the derived  $K_e$  values) and also can exhibit a strong wavelength dependence of absorptivity that is consistent with the trends in slot flame  $K_e$ .

Table 3. Mean soot aggregate optical properties.

Flame	635 nm			1310 nm		
	$K_e$	$\omega_a^a$	$K_a^b$	$K_e$	$\omega_a$	$K_a$
kerosene coannular	9.6	0.28	6.9	9.1	0.07	8.5
$C_2H_4$ coannular	9.3	0.19	7.5	9.0	0.04	8.6
$CH_4$ coannular	6.9	0.03	6.7	6.9	0.01	6.8

<sup>a</sup> Mean from RDG analysis using first two refractive indices given in Table 2.

<sup>b</sup>  $K_a = K_e (1 - \omega_a)$ .

#### 4. DISCUSSION

Most measurements of mean interplanar spacing of graphitic layers in combustion-derived soot have yielded values of 3.4–3.6 Å [42,43], comparable to the range of interplanar spacing that has been measured from x-ray diffraction (XRD) for carbon black [44]. In comparison, the interlayer spacing is 3.35 Å in pure graphite. The values for mean  $d_{002}$  determined by HRTEM for the soot in the current investigation range from 3.47–3.57 Å and are therefore consistent with these previous findings. Similarly, the range of standard deviation in  $d_{002}$  found for the soot in the current investigation is similar to that found previously for carbon black and other partially ordered carbons when using the same analytical approach [35].

The similarity in both the mean values of the graphitic layer interplanar spacing and the width of the distribution of interplanar spacing for all of the analyzed soot samples implies that the optical absorptivity of the soot is more or less constant, once the soot inception process is complete and the soot has hardened into agglomerating primary particles. This interpretation is further bolstered by our  $K_e$  measurements, which show only a small increase with sampling height in laminar diffusion flames, once inception has ceased (and that increase is consistent with an increased scattering contribution from more highly agglomerated soot). The  $K_e$  values are also insensitive to whether the flame is steady or pulsed. Furthermore, at 635 nm the  $K_e$  measurements in the coannular flames, when combined with the soot microstructure measurements and RDG estimates of the soot scattering albedo,  $\omega_p$ , yield a common prediction for the dimensionless absorption coefficient,  $K_a$ , of  $\sim 7.0$  for all three investigated fuels, as shown in Table 3.

As is evident in Table 3, the corresponding analysis using the measured  $K_e$  values and RDG estimates at 1310 nm yields a consistent, large value of  $K_a$  for the ethylene and kerosene soot, but disagreement between the methane soot and those from the sootier fuels. The reason for this difference is not fully understood, but it suggests a problem either with application of the RDG-PFA theory to the soot in these flames or with the reported values for the refractive index of soot. Zhu and coworkers [45] highlighted an inconsistency between RDG-PFA predictions and scattering albedo by measuring the scattering and extinction of post-flame ethylene soot with a transmission cell reciprocal nephelometer. Contrary to the expected diminishment in the scattering contribution at longer wavelengths, they observed an increase in scattering albedo as the wavelength increased from 632.8 nm into the near infrared. Further work remains to resolve these inconsistencies.

#### 5. IMPLICATIONS FOR SOOT REFRACTIVE INDEX

From the discussion in Section 4, it appears that carbonaceous soot has a  $K_a \sim 7.0$  at 635 nm and the scattering albedo at 635 nm is in the range of 15–30% for soot aggregates at mid-height in the ethylene and kerosene coannular flames. These results have direct implications for the refractive index of soot, as shown in Figure 6. Here, solutions of the refractive index at 635 nm corresponding to specific values of  $K_a$  and  $\omega_a$  are shown.  $K_a$  has been calculated assuming Rayleigh-limit absorption of primary par-

ticles and a negligible effect of particle aggregation on absorption, as is commonly assumed and explicitly stipulated in RDG theory. In this case  $K_a = 6\pi E(m)$ , where  $E(m)$  is a function of the index of refraction. The scattering albedo is predicted as a function of the index of refraction using RDG theory for the soot aggregate population statistics determined at mid-height in the ethylene coannular flame.

As shown in Figure 6, the intersection of the ellipses for  $K_a = 7.0$  and  $\omega_a = 0.20$  (in the realistic domain of  $n > 1$ ) defines a unique value for the index of refraction of approximately  $1.87 - 1.25i$ . This value has a substantially larger imaginary component than has generally been proposed for soot, though values of  $k$  of this magnitude are often given for graphitic carbon [46]. In fact, several researchers [16,33,47,48] have pointed out that commonly quoted values for the refractive index of soot such as the Dalzell and Sarofim [38] value of  $1.57 - 0.56i$  and the Lee and Tien [40] value of  $1.90 - 0.55i$  yield  $K_a$  values that are far too low to be consistent with measured extinction coefficients ( $K_{aD\&S} = 4.9$  and  $K_{aL\&T} = 3.6$ ). Janzen [47] was the first to report this concern and derived an index of refraction of  $2.0 - 1.0i$  for carbon black particles suspended in water (giving a  $K_a$  of 5.5). More recently, Krishnan et al. [22] derived an index of refraction of  $1.99 - 0.89i$  from measurements of postflame soot aggregates (yielding a  $K_a$  of 5.1). Mulholland and Mountain [48] found that a refractive index of  $m = 1.55 - 0.8i$  gave good predictions of  $K_e$  when using a discrete dipole method to calcu-

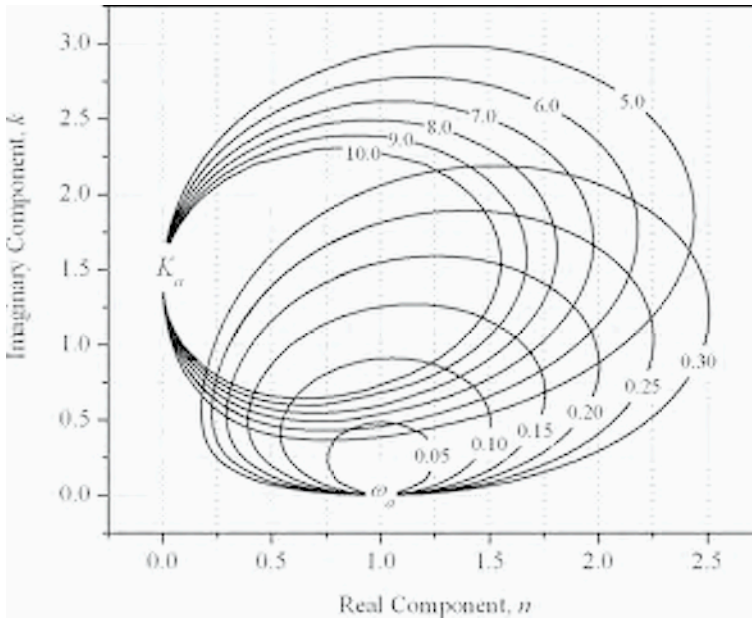


Figure 6. Solution map for Rayleigh-limit soot absorption coefficient and RDG scattering albedo (for the population of soot aggregates analyzed at  $H = 45$  mm in the ethylene coannular flame) as a function of the real and imaginary components of the soot index of refraction at 635 nm.

late soot aggregate absorption and scattering. This value of the refractive index yields a Rayleigh-limit  $K_a$  of 6.9, which is in good agreement with the current work.

Figure 7 overlays the values of  $K_e$  derived from the RDG analysis of the ethylene soot aggregates on top of the  $K_a$  and  $\omega_a$  curves shown in Figure 6. In addition, the locations of characteristic values of the soot refractive index suggested in the literature are shown. Clearly none of the suggested refractive index values shows good agreement with the measured  $K_e$  value of 9.3 for the ethylene soot, though the Mulholland and Mountain index comes closest. It is also clear that larger values of the real component of the refractive index tend to yield smaller values of  $K_e$ , whereas larger values of the imaginary component yield larger  $K_e$  values.

The discrepancy between the measured and predicted  $K_e$  values (for index of refraction values in the literature) may be due in part to inherent limitations of RDG theory itself or in the application of RDG theory to real soot aggregates in predicting  $K_a$  and/or  $\omega_a$ . Normally, predictions of the absorption coefficient according to Rayleigh-limit absorption are assumed to be accurate. However, the coupled dipole calculations of Mountain and Mulholland [48] showed that there is an inherent enhancement in the absorptivity of aggregated particles by  $\sim 10\%$ , for all primary

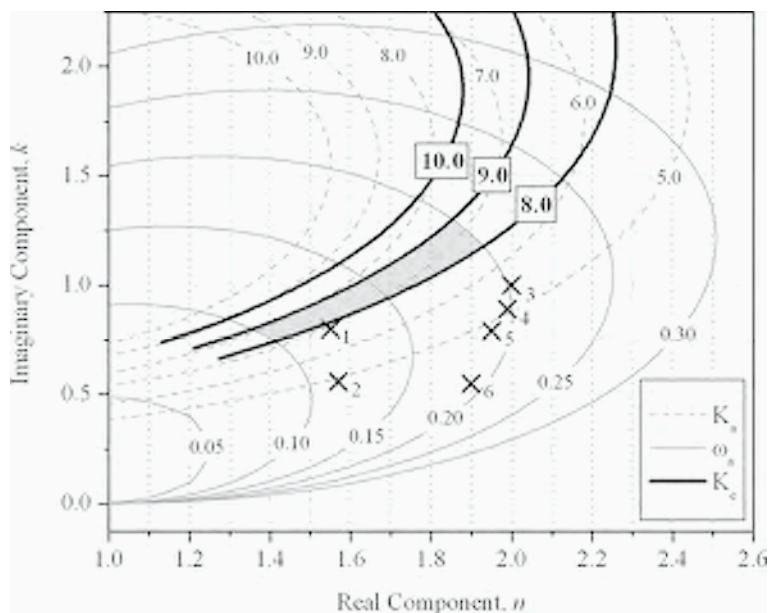


Figure 7. Solution map for the dimensionless extinction coefficient as a function of the real and imaginary components of the soot index of refraction at 635 nm. Solution ellipses corresponding to particular values of the absorption coefficient and the scattering albedo are shown in the background. Particular values of the refractive index are denoted by X's with the following identifying numbers: (1)  $1.55 - 0.8i$  [48], (2)  $1.57 - 0.56i$  [38], (3)  $2.0 - 1.0i$  [47], (4)  $1.99 - 0.89i$  [22], (5)  $1.95 - 0.79i$  [36,37], (6)  $1.90 - 0.55i$  [40]. Shading indicates the most probable solution set of index of refraction values consistent with the extinction and soot structure measurements.

particle sizes and aggregate sizes, because of the coupling of the electronic and magnetic dipoles in neighboring primary particles in aggregated soot. Therefore, the values of  $K_a$  predicted by Rayleigh-limit absorption are 10% low, meaning that the  $K_e$  values predicted by RDG theory for the ethylene soot are  $\sim 8\%$  low. Thus, to agree with the experimental data the RDG-derived value of  $K_e$  should be  $\sim 8.5$ , rather than the measured value of 9.3.

With respect to estimates of aggregate scattering, our numerical tests show that the RDG calculations are insensitive to minor variations in the measured aggregate radius of gyration and assumed fractal dimension but are sensitive to the measured mean primary particle size and statistical distribution of primary particles per aggregate (as also shown in ref. 49). For the soot particle aggregates observed in these flames, there is often a significant uncertainty associated with determining the characteristic diameter of any given primary particle within an aggregate, due to substantial necking between primaries, nonsphericity of primaries, and overlapping of primaries in the vertical plane of the TEM micrograph. The departures of practical aggregates from the RDG presumption of uniform, spherical primary particles touching at a point raises doubts about the accuracy of RDG scattering predictions, but previous analysis suggests the RDG theory is remarkably robust to variations in aggregate structure [49-51]. We estimate a typical uncertainty in the mean primary particle size from the TEM micrographs to be 10%, as supported by calculations of the standard deviation of the particle size, corresponding to an uncertainty in the scattering albedo of the ethylene soot of 8%. There is also uncertainty in the determination of the statistical distribution of primary particles per aggregate. A realistic assessment of this uncertainty shows that this factor has a similar 8% effect on the calculated scattering albedo. Overall, we estimate the total uncertainty in the scattering albedo to be on the order of 20%.

With evidence (from coupled dipole calculations) of the underestimation of the absorption coefficient by RDG and the uncertainty in the calculation of scattering albedo, a most-probable range of index of refraction values is defined by the shaded area in Figure 7. This region is defined by the intersecting ellipses corresponding to  $8.0 < K_e < 9.0$  and  $0.10 < \omega_a < 0.20$ . This region is bound by lower and upper values of index of refraction of  $1.4 - 0.77i$  and  $1.9 - 1.25i$ . A characteristic mid-point value for the refractive index within this region is  $1.7 - 1.0i$ . While the analysis presented in this paper cannot pinpoint a single best-fit value for the refractive index, the value of  $1.7 - 1.0i$  seems to be a good compromise of the various considerations.

## 6. CONCLUSIONS

HRTEM analysis of soot nanostructure as well as dimensionless extinction coefficient ( $K_e$ ) measurements of soot show minimal variation in the fundamental soot material properties for hard, graphitized soot particles, whether sampled from methane, ethylene, or kerosene laminar diffusion flames, or from the active flame zone of a large JP-8 fueled pool fire.  $K_e$  was found to range from 9 to 10 for ethylene or kerosene soot, whereas methane soot had a small scattering albedo and  $K_e \sim 7$ . Rayleigh-Debye-Gans (RDG) fractal aggregate theory calculations of soot scattering, when combined with the  $K_e$  measurements, imply a common  $K_a$  value of  $\sim 7$  at 635 nm, which is inconsi-

stent with commonly referenced literature values of the soot refractive index. However, RDG analysis probably underestimates absorption cross-sections by 10%. This fact, coupled with the measured soot aggregate structures and RDG calculations of soot scattering, is used to infer that the index of refraction of carbonaceous soot is approximately  $1.7 - 1.0i$ .

## ACKNOWLEDGMENTS

Funding for this work was provided by the Laboratory Directed Research and Development program of Sandia National Laboratories. Nancy Y.C. Yang of Sandia is gratefully acknowledged for her assistance in performing the TEM work. Árpád Palotás of the University of Miskolc is acknowledged for performing the digital analysis of the HRTEM micrographs. Kirk Jensen assisted in the implementation of the GSLE technique. Sandia is a multi-program laboratory operated by Sandia Corporation, a Lockheed Martin Company, for DOE's National Nuclear Security Administration under Contract DE-AC04-94AL85000.

## REFERENCES

1. M.O. Andreae, A. Gelencser, *Atmos. Chem. Phys.* 6 (2006) 3131-3148.
2. T.C. Bond, R.W. Bergstrom, *Aerosol Sci. Technol.* 40 (2006) 27-67.
3. K.C. Smyth, C.R. Shaddix, *Combust. Flame* 107 (1996) 314-320.
4. R.A. Dobbins, in *Physical and Chemical Aspects of Combustion: A Tribute to Irvin Glassman, F.L. Dryer, R.F. Sawyer* (Eds.) Gordon and Breach Science Publishers, The Netherlands, 1997, pp. 107-133.
5. R.A. Dobbins, R.A. Fletcher, W. Lu, *Combust. Flame* 100 (1995) 301-309.
6. R.A. Dobbins, R.A. Fletcher, H.-C. Chang, *Combust. Flame* 115 (1998) 285-298.
7. R.A. Dobbins, G.J. Govatzidakis, W. Lu, A.F. Swartzman, R.A. Fletcher, *Combust. Sci. Technol.* 121 (1996) 103-121.
8. A. D'Alessio, A. D'Anna, A. D'Orsi, P. Minutolo, R. Barbella, A. Ciajolo, *Proc. Combust. Inst.* 24 (1992) 973-980.
9. P. Minutolo, G. Gambi, A. D'Alessio, *Proc. Combust. Inst.* 26 (1997) 951-957.
10. A. D'Alessio, A. D'Anna, G. Gambi, P. Minutolo, *J. Aerosol Sci.* 29 (1998) 397-409.
11. A.C. Barone, A. D'Alessio, A. D'Anna, *Combust. Flame* 132 (2003) 181-187.
12. L.A. Sgro, A. De Filippo, G. Lanzaolo, A. D'Alessio, *Proc. Combust. Inst.* 31 (2007) 631-638.
13. B. Zhao, Z. Yang, M.V. Johnston, H. Wang, A.S. Wexler, M. Balthasar, M. Kraft, *Combust. Flame* 133 (2003) 173-188.
14. B. Oktem, M.P. Tolocka, B. Zhao, H. Wang, M.V. Johnston, *Combust. Flame* 142 (2005) 364-373.
15. B. Zhao, K. Uchikawa, H. Wang, *Proc. Combust. Inst.* 31 (2007) 851-860.
16. G.W. Mulholland, M.Y. Choi, *Proc. Combust. Inst.* 27 (1998) 1515-1522.
17. J. Zhu, M.Y. Choi, G.W. Mulholland, L.A. Gritzo, *Int. J. Heat Mass Transfer* 43 (2000) 3299-3303.
18. J. Zhu, M.Y. Choi, G.W. Mulholland, S.L. Manzello, L.A. Gritzo, J. Suo-Anttila, *Proc. Combust. Inst.* 29 (2002) 2367-2374.

19. J.F. Widmann, J.C. Yang, T.J. Smith, S.L. Manzello, G.W. Mulholland, *Combust. Flame* 134 (2003) 119-129.
20. J. Zhu, A. Irrera, M.Y. Choi, G.W. Mulholland, J. Suo-Anttila, L.A. Gritzso, *Int. J. Heat Mass Transfer* 47 (2004) 3643-3648.
21. J.F. Widmann, J. Duchez, J.C. Yang, J.M. Conny, G.W. Mulholland, *J. Aerosol Sci.* 36 (2005) 283-289.
22. S.S. Krishnan, K.-C. Lin, G.M. Faeth, *J. Heat Transfer* 122 (2000) 517-524.
23. Z.-Q. Zhou, T.U. Ahmed, M.Y. Choi, *Exp. Thermal Fluid Sci.* 18 (1998) 27-32.
24. B.L. Wersborg, L.K. Fox, J.B. Howard, *Combust. Flame* 24 (1975) 1-10.
25. C.R. Shaddix, Á.B. Palotás, C.M. Megaridis, M.Y. Choi, N.Y.C. Yang, *Int. J. Heat Mass Transfer* 48 (2005) 3604-3614.
26. T.C. Williams, C.R. Shaddix, K.A. Jensen, J.M. Suo-Anttila, *Int. J. Heat Mass Transfer* 50 (2007) 1616-1630.
27. R.A. Dobbins, C.M. Megaridis, *Langmuir* 3 (1987) 254-259.
28. J.M. Williams, L.A. Gritzso, *Proc. Combust. Inst.* 27 (1998) 2707-2714.
29. Á.B. Palotás, L.C. Rainey, C.J. Feldermann, A.F. Sarofim, J.B. Vander Sande, *Micros. Res. Technique* 33 (1996) 266-278.
30. K. Kinoshita, *Carbon: Electrochemical and Physicochemical Properties*, John Wiley & Sons, New York, 1988, p. 60.
31. R.A. Dobbins, C.M. Megaridis, *Appl. Optics* 30 (1991) 4747-4754.
32. C.M. Sorensen, *Aerosol Sci. Technol.* 35 (2001) 648-687.
33. M.Y. Choi, G.W. Mulholland, A. Hamins, T. Kashiwagi, *Combust. Flame* 102 (1995) 161-169.
34. Á.B. Palotás, L.C. Rainey, A.F. Sarofim, J.B. Vander Sande, R.C. Flagan, *Chemtech* 28 (1998) 24-30.
35. Á.B. Palotás, L.C. Rainey, A.F. Sarofim, J.B. Vander Sande, P. Ciambelli, *Energy & Fuels* 10 (1996) 254-259.
36. F.W. Smith, *J. Appl. Phys.* 55 (1984) 764-771.
37. T.C. Bond, R.W. Bergstrom, *Aerosol Sci. Technol.* 40 (2006) 27-67.
38. W.H. Dalzell, A.F. Sarofim, *J. Heat Transfer* 91 (1969) 100-104.
39. J.D. Felske, T.T. Charalampopoulos, H.S. Hura, *Combust. Sci. Technol.* 37 (1984) 263-284.
40. S.C. Lee, C.L. Tien, *Proc. Combust. Inst.* 18 (1981) 1159-1166.
41. K.A. Jensen, J.M. Suo-Anttila, L.G. Blevins, *Combust. Sci. Technol.* 179 (2007) 2453-2487.
42. H.X. Chen, R.A. Dobbins, *Combust. Sci. Technol.* 159 (2000) 109-128.
43. R.H. Munoz, T.T. Charalampopoulos, *Proc. Combust. Inst.* 27 (1998) 1471-1479.
44. A.E. Austin, in *Proceedings of the 3rd Conference on Carbon*, University of Buffalo, New York, 1958, pp. 389-394.
45. J. Zhu, M.Y. Choi, G.W. Mulholland, L.A. Gritzso, *Proc. Combust. Inst.* 28 (2000) 439-446.
46. R. Tsu, J.H. Gonzalez, I.C. Hernandez, *Solid State Comm.* 27 (1978) 507-510.
47. J. Janzen, *J. Coll. Interface Sci.* 69 (1979) 436-447.
48. G.W. Mulholland, R.D. Mountain, *Combust. Flame* 119 (1999) 56-68.
49. R.K. Chakrabarty, H. Moosmuller, W.P. Arnott, M.A. Garro, J.G. Slowik, E.S. Cross, J.-H. Han, P. Davidovits, T.B. Onasch, D.R. Worsnop, *Appl. Optics* 46 (2007) 6990-7006.
50. T.L. Farias, Ü.Ö. Köylü, M.G. Carvalho, *J. Quant. Spectrosc. Radiat. Transfer* 55 (1996) 357-371.
51. T.L. Farias, Ü.Ö. Köylü, M.G. Carvalho, *Appl. Optics* 35 (1996) 6560-6567.



**Part I**  
**Formation of soot precursors for real fuels**



# The prehistory of soot: small rings from small molecules

P.R. Westmoreland

*Department of Chemical Engineering, University of Massachusetts, Amherst, MA 01003, USA*

*Abstract: A chemically plausible picture of how soot forms has been a longtime scientific goal of combustion researchers because of soot's health impacts and crucial role in heat transfer. Through many contributions, we have achieved such a picture for the molecular stages leading to soot. That description is suitably quantitative for the step thought to be rate-limiting, formation of the first aromatic ring. Further growth and oxidation chemistry is more uncertain, yet there is growing insight into the small-molecule chemistry involving two- and three-ring polycyclics. The present review examines evolution of these insights, focusing on the formation of the first ring with an eye toward identifying crucial features of our present knowledge and crucial deficiencies to be addressed.*

## 1. INTRODUCTION

Clean air was one of the central concerns as the environmental movement grew through the 1960's, and sooty air has been one of the worst offenders throughout time. Percivall Pott observed in the 18th century that combustion-generated soot was linked to cancer [1], but this insight only led to better personal hygiene requirements for chimney sweeps, not to reduced amounts of soot. Coal use in the Industrial Revolution exacerbated the problem. Reduction began in the 20th century, spurred by an increased scale of industry and increased acceptance of individual rights relative to those industries, and aided by the use of natural gas and new environmental control technologies. Forming the US Environmental Protection Agency in 1970 was a landmark step.

Chemical understanding of soot origins has evolved over time as well. It is now conventional wisdom that nonaromatic species form aromatics, particularly the single-ring species benzene and phenyl, which eventually grow to environmentally undesirable polycyclic aromatic hydrocarbons (PAH or PCA) and soot. Propargyl ( $C_3H_3$ ) is now accepted as a principal growth species through self-reaction and chemically activated isomerizations, while contributions from cyclohexane dehydrogenation are more recently identified. Cyclopentadienyl ( $cy-C_5H_5$ ) may have a role in forming naphthalene, and allyl+allyl,  $i-C_4H_3+C_2H_2$ , and  $i-C_4H_5+C_2H_2$  may be involved. Growth to larger rings probably proceeds by side-chain growth.

Analyzing the origin and evolution of this thought reveals once-apparent insights that have now been discarded, as well as the evolution of our present standards for molecular-level understanding of the chemical physics of soot formation. This presentation will review the bases for mechanistic understanding, acknowledging the present limitations to understanding and pointing toward future advances.

## 2. STEPS IN UNDERSTANDING

The path to this present state of knowledge has evolved over time by successively accumulating key aspects of the chemistry and physics. Even before a modern concept of chemical elements had developed, soot was a recognized physical material, and its adverse effects on health had been established empirically by linking soot exposure in unwashed chimney sweeps to abnormally high rates of scrotal cancer.

The steps and stages that have occurred to advance this knowledge may be summarized as follows:

- (1) Simplified overall chemistry.
- (2) Conceptual routes based on:
  - (a) Molecule-molecule reactions.
  - (b) Radicals.
  - (c) Chemi-ions.
- (3) Mechanistic routes based on elementary reactions.
- (4) Recognizing the dominant role of chemical activation.
- (5) Application of computational quantum chemistry.
- (6) Acceptance of multiple routes.

In the earliest thoughts about how soot forms chemically, the general vision was of overall chemistry directly to soot. Soot was recognized early as being mostly carbon, so identifying the chemical source of this carbon was a reasonable first step. However, as the chemical natures of graphite and aromatics were recognized as related to soot, there was early acceptance that small aromatics were associated with soot, perhaps as precursors. Thus, finding the chemical origin of benzene and other small aromatics became the principal goal of studying soot inception.

This discussion then emphasizes the question of how the first aromatic ring forms, while acknowledging that other theories such as polyacetylene routes have been considered. By considering these steps in more detail, these stages and their transformative aspects will become clearer. The analysis also suggests the direction of future advances.

*(1) Simplified overall chemistry.* At the outset, the target was what carbon compounds could contribute to yield the carbon of soot. Berthelot was the first to study acetylene (ethyne) in detail, and in 1866 he proposed that soot might be formed by direct polymerization of  $C_2H_2$  [2]. This hypothesis was not mechanistic, but rather it was consistent with the high conversion of acetylene to soot at high temperatures. Similarly, Bone and Coward proposed in 1908 that aromatics might be formed by incorporating  $CH_2$  and  $CH$  fragments [3], and in 1919 Hurd and Spence proposed that alkenes might simply trimerize into a six-carbon ring [4].

*(2) Conceptual routes (a) based on molecule-molecule reactions.* The first attempts to propose specific reactions leading to single-ring aromatics were based on molecular reactions, specifically Diels-Alder reactions. Davidson had proposed in 1918 [5] that benzene might come from reaction of 1,3-butadiene and ethene. [These structures can be displayed typographically as  $=- =$  and  $=$ , illustrating the pi and sigma carbon-carbon bond

arrangements and implying maximum occupancy of H's, although not showing the bended nature of the butadiene skeleton.]

Hague and Wheeler echoed this proposal in 1929 [6], identifying it as a reaction of the recently named Diels-Alder type. Wheeler and Wood further surmised in 1930 that the Diels-Alder reaction of 1,3-butadiene with cyclohexene might form a double-ring species [6]. Such a species might reasonably proceed to naphthalene. Badger et al. further proposed in 1958 that Diels-Alder reaction of two 1,3-butadienes at high temperatures (forming 4-ethenylcyclohexene) could lead to styrene formation [7].

Another conceptual route is through "polyacetylenes" or polyynes. The species have long been detected in flames [8, 9], and recent measurements detect polyenes as large as  $C_{12}H_2$  [10]. Bonne et al. [8] observed that the polyynes were closely correlated to soot formation and concluded that they played a crucial role in soot formation. Until recent years, subsequent reflections on mechanism focused on side-by-side rearrangement, which would necessarily make straight, anthracene-like polycyclic aromatic hydrocarbons (PAH). This outcome is contrary to the observed high ratio of nonlinear to linear PAH [11], suggesting that polyynes are present in significant levels instead because they are relatively unreactive. Nevertheless, this possibility has continued to be the subject of thoughtful inquiry [12-13]. Homann and Pidoll suggested that  $C_4H_2$  biradicals might combine and cyclize, leading to tri-ethynyl aromatics [14]. Much later, the modeling of Vlasov and Warnatz suggests that polyynes may instead be significant in large-particle growth stages during pyrolysis [15].

(2b) *Conceptual routes based on radicals.* By the 1950's, free-radical chemistry had become accepted as a key aspect of combustion, thanks largely to the pioneering work of Semenov and of Hinshelwood, who shared the 1956 Nobel Prize in Chemistry [16]. Radical-based  $C_3+C_4$  or  $C_3+C_3$  reactions began to be proposed that might account for benzene formation. [Note: This common simplified manner of describing the reactions merely focuses on the backbone carbons; it does not imply that the actual species  $C_2$ ,  $C_3$ , and  $C_4$  are involved. It would more precise to write " $C_2H_x+C_4H_y$  or  $C_3H_x+C_3H_y$  reactions" but the shorter form is a useful and more compact generalization.)

Kinney and Crowley proposed several such routes conceptually in 1954 in the context of process chemistry for ethane production [17]. One route was the reaction of the buta-1,3-dienyl ( $1-C_4H_5$  or  $\cdot=$ ) to ethene, subsequently losing an H to form 1,3,5-hexatriene ( $=--=$ ), which in turn would cyclize and lose more H's to make benzene eventually. It is important to re-emphasize that this was a descriptive route, not a quantitative one. As will be discussed later, it was also implicitly a sequence from one set of thermalized products to another.

Kinney and Crowley also proposed benzene formation from allyl radical combination and from addition of vinyl (ethenyl,  $\cdot=$ ) to 1,3-butadiene, again proceeding by subsequent hydrogen loss to form 1,3,5-hexatriene, molecular cyclization, and hydrogen loss. The vinyl + butadiene hypothesis was revisited more quantitatively by Weissman and Benson 30 years later [18].

A similar hypothesis by Stehling et al. in 1956 was for  $C_4H_3$  addition to  $C_2H_2$  [19]. They proposed that 1-buten-3-ynyl ( $\cdot CC=$ ,  $1-C_4H_3$ , or  $n-C_4H_3$ ) could add to various alkynes, followed by cyclization of the adduct to phenyl or its analogues. This scheme was analyzed most notably by Frenklach et al. about 30 years later [20].

Likewise, Colket proposed in 1986 that  $C_2H_3 + 3\text{-butenyne}$  ( $C_4H_4$ , vinyl acetylene) might also be a route to benzene [21]. This hypothesis was based on his  $C_2H_2$  and 3-butenyne pyrolyses in a single-pulse shock tube, subsequently modeling the stable species with overall rate expressions. Depending on the conditions, the modeling predicted that benzene formation was dominated by  $C_4H_5 + C_2H_2$ ,  $C_4H_3 + C_2H_2$ , or  $C_2H_3 + C_4H_4$ .

In 1983 Bockhorn et al. proposed another conceptual route, this one based on  $C_1$  chemistry [22]. Methyl would add to pi bonds, abstract H's, and combine with resonantly stabilized radicals such as allyl ( $C_3H_5$ ), eventually forming aromatics.

(2c) *Conceptual routes based on chemi-ions.* Calcote established in 1949 that ions in flames were "chemi-ions" produced by the chemical reaction  $CH + O \rightarrow CHO^+ + e^-$  [23]. Ion-molecule chemistry is very fast. Their reactions with hydrocarbons at fuel-rich conditions have particularly inspired inquiries and careful consideration of possible roles in soot formation [e.g., 24-27]. They do not seem to be significant for forming the first rings, but ionic character of soot particles may be quite important in growth.

(3) *Mechanistic routes based on elementary reactions.* To go beyond conceptual and overall, empirical routes, it was necessary that attention turns to full mechanistic pathways involving elementary reactions to capture the full potential-energy surface. In the initial stages, these potential-energy surfaces used estimated thermochemistry and kinetics, most of them estimated by analogies.

In 1979 Glassman [28] proposed examining the reaction of 1,3-butadiene with acetylene, forming 1,4-hexadiene and proceeding via low-energy molecular elimination of  $H_2$  to form benzene. The first step was an example of the well-characterized set of Diels-Alder cyclization reactions, mentioned above. Kinetics of the second reaction had been measured directly.

Cole, Bittner, Howard, and Longwell then developed an hypothesis that  $1-C_4H_5 + C_2H_2$  would proceed through plausible elementary reactions to form benzene + H [29]. Intrigued by Glassman's suggestion and having access to flame-sampling molecular-beam mass spectrometry (MBMS) to measure concentrations, they examined a laminar, premixed flat flame burning fuel-rich 1,3-butadiene [29]. In it, they measured spatially resolved mole-fraction profiles of the pertinent species, including  $C_4H_5$ . However, the 1,3-butadiene with acetylene reaction did not prove fast enough. Instead, their conclusion was that benzene would be formed by the radical reaction  $1-C_4H_5 + C_2H_2$  through forming a linear adduct ( $\cdot C=C + HCCH \rightarrow C=C-C=C$ ), cyclization to cyclohexadienyl, and beta-scission to H + benzene. They could not experimentally determine the specific isomer of  $C_4H_5$ , basing their interpretation on relative abstraction kinetics estimated for forming the isomers. Callear and Smith provided support for this reaction when they invoked it to explain high benzene yields from  $H + C_2H_2$  experiments [30].

Independently, Frenklach et al. had begun re-examination of  $1-C_4H_3 + C_2H_2$  through modeling PAH formation in shock tubes with full sets of elementary reactions: 600 reactions with 180 species [20]. The dominant route they found to the first ring was a thermal sequence of  $1-C_4H_3$  ( $\cdot CC=C$ ) + HCCH, forming a linear adduct  $\cdot C=C-CCH$ , and finally isomerizing by head-to-tail addition to make phenyl.

This study effort was a landmark step requiring real boldness because at that time, some proponents of molecular, polyacetylene, and chemi-ion routes argued that radi-

cals could not be the explanation for aromatics formation because concentrations were too low or their rate constants were too low. A major technical challenge for the modeling approach was that many of the rate constants were unknown. Their approach was to apply upper-bound rate constants, arguing that if these values were not fast enough, then radicals would be ruled out as precursors. In fact, their modeling qualitatively predicted the soot-yield bell distribution over temperature. They had shown persuasively that radical-based growth reactions of PAH were indeed feasible for forming soot.

In other work, Harris et al. modeled aromatics in 1-atm  $\text{CH}_4$  flat flame using overall reactions for  $\text{C}_4\text{H}_5 + \text{C}_2\text{H}_2$  and  $\text{C}_4\text{H}_3 + \text{C}_2\text{H}_2$  [31]. Using his set and its thermochemistry, the latter route dominated.

The real breakthrough was a detailed  $\text{C}_3\text{H}_3 + \text{C}_3\text{H}_3$  hypothesis. This hypothesis has evolved over time to be the basis of much of our understanding of flame formation of aromatics.

In 1962, Hurd et al. had proposed a conceptual model that  $\text{C}_3\text{H}_3$  as trimethine ( $\text{CHCHCH}$ ) might dimerize to form benzene [32]. However, the dominant  $\text{C}_3\text{H}_3$  species is propargyl, the resonantly stabilized  $\text{CHCCH}_2$  radical that combines to form

1,5-hexadiynyl (, “head to head” combination), 1,2,4,5-hexatetraene (, “tail to tail”), or hexa-4,5-dienyne (, “head to tail”).

To test whether propargyl might form benzene, Kern and co-workers conducted shock-tube pyrolyses of propadiene and 1,2-butadiene [33-34]. They concluded that propargyl did make benzene, based in part of their observation of mass 78 ( $\text{C}_6\text{H}_6$ ) by mass spectrometry. Furthermore, they were able to model the effects of temperature and time on species in the experiments. Using overall reactions  $\text{C}_3\text{H}_3 + \text{C}_3\text{H}_3 \rightarrow \text{benzene}$  and  $1\text{-C}_4\text{H}_5 + \text{C}_2\text{H}_2 \rightarrow \text{benzene} + \text{H}$ , the former reaction dominated in the model.

They made clear their assumption that  $\text{C}_6\text{H}_6$  was benzene. They justified it based on pyrolysis data for the presumed intermediates, citing a conceptual scheme of Henry and Bergman [35] that proceeds from the combination product 1,2,4,5-hexatetraene to

dimethylenecyclobutene (, DMCB), benzene via 1,3-cyclohexadienyl, or fulvene () via a singlet allylic diradical of methylenecyclopentene.

There is additional, interesting circumstantial evidence for such routes. Isomerization between 1,5-hexadiyne and 1,2,4,5-hexatetraene may be recognized as a classical Cope rearrangement, linking these two combination products. Henry and Bergman had based their hypothesis on their own and others' thermal pyrolysis experiments on 1,5-hexadiyne, which yielded DMCB, fulvene, and benzene [36-39]. Pyrolysis of hexatetraene yields the same products [39]. Pyrolysis of DMCB forms fulvene and benzene, and pyrolysis of fulvene yields benzene [34, 40]. These data indicated that there might be a single potential-energy surface involving all these species, although involvement of bimolecular reactions could not be ruled out.

(4) *Recognizing the dominant role of chemical activation.* Chemical activation allows the most important aromatics-forming reactions to skip past any oxidative side-reactions and

go directly to aromatics. It had been neglected in all the above routes based on elementary reactions, but its impact on kinetics and the lifetime of reaction intermediates is profound. It can affect all gas kinetics involving association reactions; i.e., combination or addition reactions. Classical falloff behavior is observed for the thermalized adduct at low pressures (low densities  $P/RT$ ), yet the overall rate constant with respect to reactants can remain constant and additional product channels can occur with at low pressure with no pressure dependence, skipping past thermal intermediates.

Forming a new bond happens because the bonded state is energetically lower than the unbonded state. Then, until the nascent adduct can interact with its surroundings, energy released by bond formation is retained within it. Thus, as pressure decreases and bath-gas collisions are insufficient to remove this energy, the adduct may fly back apart to reactants, causing the apparent bimolecular rate constant to decrease. On the other hand, at sufficiently high pressures this energy is rapidly removed and all adducts will be thermalized. This is normal falloff behavior.

The key effect of chemical activation is that when pressure is low, new reaction channels for the adduct may be easier than reversion to reactants. The adduct may isomerize, perhaps by addition of a terminal radical to the opposite end of the species or by internal abstraction from one part of the species to another. It may decompose by scission of a bond beta to the radical (beta-scission). It is even possible that molecular reactions like reverse Diels-Alder reactions may occur if the excess of energy is sufficiently high.

Dean and Westmoreland had developed Bimolecular Quantum-RRK as a means of rapidly estimating the effects of chemical activation [41, 42], adapting the unimolecular Quantum-RRK model of Kassel that treats rovibrational energy storage most simply as having a single average quantum size  $h\langle \mathbf{v} \rangle$  [43]. This work had the additional effect of showing how all oxidation and growth reactions were chemically activated associations, even when disguised as for  $\text{H} + \text{O}_2 \rightarrow \text{O} + \text{OH}$  (via chemically activated  $\text{HO}_2$ ) or  $\text{CH}_3 + \text{O} \rightarrow \text{H} + \text{CH}_2\text{O}$  (via chemically activated  $\text{CH}_3\text{O}$ ).

In 1989, Westmoreland et al. used this approach to assess the impact of chemical activation on aromatics formation in a premixed fuel-rich  $\text{C}_2\text{H}_2$  flame [44]. First, mole fraction profiles of all the species were obtained using MBMS, and a profile of the net rate of benzene formation was extracted from these data. Second, the upper-bound rate of benzene formation was determined for all candidate reactions using the high-pressure-limit association rate constants and the concentration product of the reactants. Only  $\text{C}_3\text{H}_3 + \text{C}_3\text{H}_3$ ,  $\text{C}_4\text{H}_3 + \text{C}_2\text{H}_2$ , and  $\text{C}_4\text{H}_5 + \text{C}_2\text{H}_2$  met or exceeded the experimental net rate of benzene formation. Third, pressure-dependent rate constants were computed for product channels from  $\text{C}_4\text{H}_3 + \text{C}_2\text{H}_2$  and  $\text{C}_4\text{H}_5 + \text{C}_2\text{H}_2$  (no elementary-reaction scheme yet being available for  $\text{C}_3\text{H}_3 + \text{C}_3\text{H}_3$ ). For both these cases, a set of steps through the thermalized intermediates would be too slow. Only direct, chemically activated association/isomerization is fast enough to form the aromatic species. More subtly, because collisions are not fast enough to stabilize the intermediates, they also are too slow to oxidize the intermediates and prevent soot formation at this point.

Subsequently, we proposed and tested a Henry-Bergman-like chemically activated model of the  $\text{C}_3\text{H}_3 + \text{C}_3\text{H}_3$  reaction sequence from the initial association reaction via molecular reactions to DMCB, fulvene, and benzene in turn [45]. In that work and

later, more refined analysis of  $C_3H_3 + C_3H_3$  and  $C_3H_3 + C_3H_4$  kinetics [46], the crucial uncertainties were activation energies for  $DMCB \rightarrow$  fulvene  $\rightarrow$  benzene.

Independently and at about the same time, Stein [47] proposed a similar route for  $C_3H_3 + C_3H_3$ , and Alkemade and Homann proposed another, quite different route [48]. Stein pyrolyzed 1,5-hexadiyne at different temperatures in a VLPP reactor. At low temperatures, DMCB was formed, while at higher temperatures, fulvene and benzene were formed apparently from a DMCB intermediate; Stein proposed that parallel paths to the two products may occur. Alkemade and Homann made the first direct experimental studies of  $C_3H_3$  combination, finding a mixture of products including benzene. Their mechanism involved cyclopropenyl intermediates similar to those proposed as intermediates in propyne/propadiene isomerization.

(5) *Application of computational quantum chemistry.* Over the next decade,  $C_3H_3 + C_3H_3$  became accepted as the dominant reaction in flames to form the first aromatic ring. Two central reasons were insightful use of computational quantum chemistry for thermochemistry and kinetics and the acceptance of these calculations as having useful accuracy. A pivotal event in this evolution was at the Fall 1987 American Chemical Society National Meeting, where several estimates were advanced for enthalpy differences (relative stability) of  $n-C_4H_3$  vs.  $i-C_4H_3$  and  $n-C_4H_5$  vs.  $i-C_4H_5$ . Upon finding that BAC-MP4 calculations had been performed on these quantities by Miller and Melius, the participants quickly recognized that the preferred standard for estimating thermochemistry had changed from group additivity and other analogies to *ab initio* calculations.

The greatest advances were by Miller and co-workers. First, Miller et al. [49] analyzed the importance of benzene formation from propargyl relative to  $C_2+C_4$  routes, estimating from thermochemistry that  $1-C_4H_x$  radicals were sufficiently less stable than  $2-C_4H_x$  to rule them out as unimportant. They initially argued that singlet species would proceed through 1,2,4-cyclohexatriene to form benzene.

Miller and Melius [50] and Melius, Miller, and Evleth [51] then proposed routes requiring routes based on singlet carbene intermediates, in particular from DMCB to Henry and Bergman's singlet allylic diradical of methylenecyclopentene to fulvene [34]. Thermochemistry and the reaction stationary states were computed with BAC-MP4//MP4/6-31G(d,p)//UHF/6-31G(d), a high level of theory that had been amply tested and proven to be useful. None of the energy barriers proved to be as high as the initial combined energies of the two  $C_3H_3$  radicals. As a result, adiabatic RRKM calculations implied the end products were phenyl + H at high temperature because of chemical activation, as discussed in Miller's 1996 review [52].

Miller and co-workers have continued to probe, improve, and extend these calculations of  $C_3H_3 + C_3H_3$  kinetics by higher-level quantum-chemical calculations and consideration of additional channels, as reviewed in ref. [53]. The biggest advances were the work of Miller and Klippenstein [54], which used microcanonical RRKM rate constants in a master-equation solution to give higher-quality rate constants; Miller and Klippenstein [55], which significantly advanced the quality of the quantum-chemical calculations to the equivalent of QCISD(T,Full)/6-311++G(3df,2pd) and to an infinite-basis-set limit; and Miller and Klippenstein [56], which added a conversion reaction of 1,2,4,5-hexatetraene to 1,3-hexadien-5-yne ("head-to-tail"); combined the high-level quantum chemistry results with a master-equation solution.

(6) *Acceptance of multiple routes.* With these advances, formation of benzene and of small aromatic molecules began to settle into a picture that was usually dominated by  $C_3H_3 + C_3H_3$  but where other reactions could also contribute and occasionally dominate. The calculations of Frenklach et al. [20] and Harris et al. [31] in the 1980's had focused on the  $C_4H_3 + C_2H_2$  vs.  $C_4H_5 + C_2H_2$  product spectrum. Modeling in the 1986 Colket research [21] found  $C_4H_5 + C_2H_2$ ,  $C_4H_3 + C_2H_2$ , or  $C_2H_3 + C_4H_4$  playing lead roles. Richter and Howard examined a large number of the routes in a comprehensive 2000 review [57].

Including  $C_3H_3 + C_3H_3$  and more careful consideration of the above alternatives worked against the latter. Wang and Frenklach predicted flame compositions that implied that  $C_4H_3$  route might be more important than the  $C_3H_3$  route in some flames and at lower temperatures [58]; however, Miller et al. later argued that errors in kinetics and thermochemistry caused the  $C_4H_3$  route to be overpredicted [53]. Law et al. studied an allene-doped ethylene flame with the  $C_4$  and  $C_3$  reactions included, and they found the  $C_3H_3 + C_3H_3$  route to dominate [59].

Interestingly, it was the re-examination of the  $C_4H_5$  route by Senosiain and Miller that restored it to feasibility [60].  $C_4H_5$  isomers had finally been resolved by using precisely resolved vacuum-UV photons for photoionization MBMS in the experiments of Hansen et al. [61]. For a variety of fuels,  $C_4H_5$  was found to include  $i$ - $C_4H_5$  ( $=\cdot\cdot\cdot$  /  $\cdot\cdot\cdot$ ) and some combination of the  $CH_3-C=C=CH_2$  and  $CH_3-CH=C\cdot$ CH radicals. No  $n$ - $C_4H_5$  was detected. The Senosiain and Miller *ab initio* and reaction-theory calculations indicated that  $i$ - $C_4H_5 + C_2H_2$  does have a feasible route to benzene. When we used these rate constants to model our 1,3-butadiene flames (new PI-MBMS data and the earlier data of Cole et al. [29], re-interpreting his  $C_4H_5$  as  $i$ - $C_4H_5$ ), benzene was found to come in nearly equal proportion from  $C_3H_3 + C_3H_3$  and  $i$ - $C_4H_5 + C_2H_2$  with a small contribution predicted from  $C_3H_3 + C_3H_5$  [61]. The rate constant for making benzene from  $n$ - $C_4H_5 + C_2H_2$  is much higher than that for  $i$ - $C_4H_5 + C_2H_2$ , but the higher concentration of  $i$ - $C_4H_5$  was the deciding difference.

Other radical channels have also been proposed and tested. Pope and Miller proposed  $i$ - $C_5H_3 + CH_3$  in 2000 as a possible minor route to benzene [62] but later decided it was unlikely to contribute [53]. Kohse-Höinghaus et al. tested an empirical  $C_3H_6 + CH_3$  rate constant to  $C_6H_8$ , expecting rapid dehydrogenation to benzene, but this channel proved minor at best [63]. Marinov et al. proposed the interesting hypothesis that cyclopentadienyl combination might be a route to naphthalene, and they performed BAC-MP4 calculations to support of the hypothesis [64]. However, this channel proved inconsistent with experimental benzene yields when Lindstedt and Rizos examined cyclopentene and methylcyclopentadiene pyrolyses [65], and it has gradually fallen out of favor.

A completely different channel is stepwise radical dehydrogenation of cyclohexane, shown by Law et al. to be the dominant route to benzene in a stoichiometric, low-pressure, cyclohexane flat flame [67]. No evidence was found for this route in non-premixed cyclohexane flames [68], it appears significant at near-stoichiometric conditions in a rapid compression machine [69], a jet-stirred reactor [70], and a single-cylinder internal combustion engine [71]. When cyclohexyl is formed by radical H-abstraction, most of it is consumed by the ring-opening beta scission of a C-C bond, but some beta-scission of an H occurs, forming cyclohexene. The process is repeated twice to

form benzene, which was in reasonable agreement with model predictions. As the flame becomes richer, cyclohexane dehydrogenation and  $C_3H_3 + C_3H_3$  begin to co-exist, and  $C_3H_3$  route eventually dominates.

### 3. CLOSING REMARKS

The presence and growth of side chains, formation of two-ring and higher aromatics, and aromatics oxidation are other small-molecule topics relevant to soot formation, yet they are not discussed in any detail here:

- Miller et al. [52] contended that larger resonantly stabilized free radicals can combine with  $C_3H_3$  to form aromatics with side chains, but addition of phenyl to  $C_2H_2$  and other pi-bonded species are likely to contribute.
- Each of these schemes may contribute to PAH growth when cyclization occurs by the HACA mechanism [20, 58] and variations of it.
- Oxidation of the ring is apparently by O-atom, but extension of the CO elimination observed in benzene to PAH oxidation is uncertain.

These topics are fruitful, active areas of research. In large part, they are fruitful because of the evolution of methods and mechanistic insights in growing to understand formation of the first aromatic ring. As soot formation and destruction are understood more and more quantitatively, the researchers cited in this review will continue to deserve much of the credit for creating this foundation of understanding.

### ACKNOWLEDGEMENTS

I gratefully acknowledge the long-term support for our flame research from the US Department of Energy, Contract DE-FG02-91ER14192, presently coordinated through T. J. Mountziaris as substitute P.I.

### REFERENCES

1. J. Dobson, *Ann. Roy. Coll. Surg. Eng.* 50 (1972) 54.
2. M. Berthelot, *Ann. Chim. Phys.* 9 (1866) 469.
3. W. Bone, H. J. Coward, *Chem. Soc.* 93 (1908) 1201.
4. C. D. Hurd, L. U. Spence, *J. Am. Chem. Soc.* 51 (1929) 3561.
5. E. N. Hague, R. V. Wheeler, *J. Chem. Soc. (London)* (1929) 378.
6. R. V. Wheeler, W. Wood, *J. Chem. Soc. (London)* (1930) 1819.
7. G. M. Badger, R. G. Buttery, R. W. Kimber, G. E. Lewis, A. G. Moritz, I. M. Napier, *J. Chem. Soc. (London)* (1958) 2449.
8. U. Bonne, K.-H. Homann, H. Gg. Wagner, *Proc. Combust. Inst.* 10 (1965) 50.
9. P. R. Westmoreland, J. B. Howard, J. P. Longwell. *Proc. Combust. Inst.* 1986, 21 773; P. R. Westmoreland, "Experimental and Theoretical Analysis of Oxidation and Growth Chemistry in a Fuel-Rich Acetylene Flame," Ph.D. dissertation, Massachusetts Institute of Technology, 1986. <http://hdl.handle.net/1721.1/38573>.

10. N. Hansen, S.J. Klippenstein, P.R. Westmoreland, T. Kasper, K. Kohse-Höinghaus, J. Wang, T.A. Cool, *Phys. Chem. Chem. Phys.* 10 (2008) 366.
11. G. Prado, P.R. Westmoreland et al., in *Analytical Chemistry and Biological Fate*, M. Cooke, A. J. Dennis (Eds.) Columbus, Battelle Memorial Institute, 1981, p. 189.
12. A. V. Krestinin, *Proc. Combust. Inst.* 27 (1998) [series formerly listed as 27th Symposium (International) on Combustion, The Combustion Institute: Pittsburgh, PA], p. 1557.
13. A. V. Krestinin, *Chem. Phys. Rep.* 17 (2000) 1441.
14. K.-H. Homann, U. v. Pidoll, *Ber. Bunsen-Ges. Phys. Chem.* 90 (1986) 847.
15. P. A. Vlasov, J. Warnatz, *Proc. Combust. Inst.* 29 (2002) 2335.
16. N. Semenov, in *Nobel Lectures, Chemistry 1942-1962*, Elsevier Publishing Company, Amsterdam, 1964, [http://nobelprize.org/nobel\\_prizes/chemistry/laureates/1956/semenov-lecture.pdf](http://nobelprize.org/nobel_prizes/chemistry/laureates/1956/semenov-lecture.pdf).
17. R. E. Kinney, D. J. Crowley, *Ind. Eng. Chem.* 46 (1954) 258.
18. M. Weissman, S. W. Benson, *Int. J. Chem. Kin.* 16 (1984) 307.
19. F. C. Stehling, J. D. Frazee, R. C. Anderson, *Proc. Combust. Inst.* 6 (1956) 247.
20. M. Frenklach, D. W. Clary, W. C. Gardiner Jr., S. E. Stein, *Proc. Combust. Inst.* 20 (1984) 887.
21. M. B. Colket, *Proc. Combust. Inst.* 21 (1986) 851.
22. H. Bockhorn, F. Fetting, H. W. Wenz, *Ber. Bunsen-Ges. Phys. Chem.* 87 (1983) 1067.
23. H. F. Calcote, *Proc. Combust. Inst.* 3 (1949) 245.
24. H. F. Calcote, in *Soot in Combustion Systems and Its Toxic Properties*, J. Lahaye, G. Prado (Eds.) NATO Conference series, Series VI: Materials Science, Plenum Press, New York and London, 1981, p. 197.
25. A. N. Hayhurst, H. R. N. Jones, *J. Chem. Soc. Faraday Trans.* 83 (1987) 1.
26. H. F. Calcote, D. B. Olson and D. G. Keil, *Energy Fuels* 2 (1988) 494.
27. K. Schofield, *Prog. Energy Comb. Sci.* 34(3) (2008) 330.
28. I. Glassman, "Phenomenological Models of Soot Processes in Combustion Systems," Department of Mechanical and Aerospace Engineering, Princeton University, Report 1450, 1979.
29. J. A. Cole, J. D. Bittner, J. B. Howard, J. P. Longwell, *Combust. Flame* 56 (1984) 51.
30. A. B. Callear, G. B. Smith, *Chem. Phys. Lett.* 105 (1984) 119; A. B. Callear, G. B. Smith, *J. Phys. Chem.* 90 (1986) 3229.
31. S. J. Harris, A. M. Weiner, R. J. Blint, *Combust. Flame* 72 (1988) 91.
32. C. D. Hurd, A. R. Macon, J. I. Simon, R. V. Levetan, *J. Am. Chem. Soc.* 84 (1962) 4509.
33. C. H. Wu, R. D. Kern, *J. Phys. Chem.* 91 (1987) 6291.
34. R. D. Kern, H. J. Singh, C. H. Wu, *Intl. J. Chem. Kin.* 20 (1988) 731.
35. T. J. Henry, R. G. Bergman, *J. Am. Chem. Soc.* 91 (1972) 5103.
36. W. D. Huntsman, H. J. Wristers, *J. Am. Chem. Soc.* 89 (1967) 342; W. D. Huntsman, *Intra-Science Chem. Rept.* 6 (1972) 151.
37. M. L. Heffernan, A. J. Jones, *Chem. Commun.* 4 (1966) 120.
38. J. E. Kent, A. J. Jones, *Aust. J. Chem.* 23 (1970) 1059.
39. H. Hopf, *Angew. Chem. Int. Ed.* 9 (1970) 732.
40. B. J. Gaynor, R. G. Gilbert, K. D. King, P. J. Harman, *Aust. J. Chem.* 34 (1981) 449.
41. A. M. Dean, *J. Phys. Chem.* 89 (1985) 4600.
42. P. R. Westmoreland, J. B. Howard, J. P. Longwell, A. M. Dean, *AIChE J.* 32 (1986) 1971.
43. L. S. Kassel, *J. Phys. Chem.* 32 (1928) 1065.
44. P. R. Westmoreland, A. M. Dean, J. B. Howard, J. P. Longwell, *J. Phys. Chem.* 93 (1989) 8171.

45. S.D. Thomas, P.R. Westmoreland, AIChE Annual Meeting, San Francisco, November 5-10, 1989, Paper 130g.
46. S.D. Thomas, F. Communal, P.R. Westmoreland, Div. of Fuel Chemistry, American Chemical Society, 36:4 (1991) 1448.
47. S. E. Stein, J. A. Walker, M. M. Suryan, A. Fahr, Proc. Combust. Inst. 23 (1991) 85.
48. U. Alkemade, K.H. Homann, Z. Phys. Chem. N.F. 161 (1989) 19.
49. J.A. Miller, R.J. Kee, C.K. Westbrook, Ann. Rev. Phys. Chem. 41 (1990) 345.
50. J.A. Miller, C.F. Melius, Combust. Flame 91 (1992) 21.
51. C.F. Melius, J.A. Miller, E.M. Evleth, Proc. Combust. Inst. 24 (1992) 621.
52. J.A. Miller, Proc. Combust. Inst. 26 (1996) 461.
53. J.A. Miller, M. J. Pilling, J. Troe, Proc. Combust. Inst. 30 (2005) 43.
54. J.A. Miller, S. J. Klippenstein, J. Phys. Chem. A 105 (2001) 7254.
55. J.A. Miller, S. J. Klippenstein, J. Phys. Chem. A 107 (2003) 7783.
56. J.A. Miller, S. J. Klippenstein, J. Phys. Chem. A 107 (2003) 2680.
57. H. Richter, J. B. Howard, Prog. Energy Combust. Sci. 26 (2000) 565.
58. H. Wang, M. Frenklach, Combust. Flame 110 (1997) 173.
59. M. E. Law, T. Carrière, P. R. Westmoreland, Combust. Inst. 30 (2005) 1353.
60. J. P. Senosiain, J. A. Miller, J. Phys. Chem. A 111 (2007) 3740.
61. N. Hansen, S.J. Klippenstein, C. A. Taatjes, J.A. Miller, J. Wang, T.A. Cool, B. Yang, R. Yang, L. Wei, C. Huang, J. Wang, F. Qi, M.E. Law, P.R. Westmoreland, T. Kasper, K. Kohse-Höinghaus, J. Phys. Chem. A 110 (2006) 3670.
62. C.J. Pope and J.A. Miller, Proc. Combust. Inst. 28 (2000) 1519.
63. K. Kohse-Höinghaus, B. Atakan, A. Lamprecht, G. Gonzalez Alatorre, M. Kamphus, T. Kasper, N.-N. Liu, Phys. Chem. Chem. Phys. 4 (2002) 2056.
64. N. M. Marinov, W. J. Pitz, C. K. Westbrook, A. M. Vincitore, M. J. Castaldi, S.M. Senkan, C. F. Melius, Combust. Flame 114 (1998) 192.
65. R. P. Lindstedt, K.-R. Rizos, Proc. Combust. Inst. 29 (2000) 2291.
66. N. Hansen, J. A. Miller, T. Kasper, K. Kohse-Höinghaus, P. R. Westmoreland, J. Wang, T. A. Cool, Proc. Combust. Inst. 32 (2009) doi:10.1016/j.proci.2008.06.050.
67. M. E. Law, P. R. Westmoreland, T. A. Cool, J. Wang, N. Hansen, T. Kasper, Proc. Combust. Inst. 31 (2007) 565.
68. C. S. McEnally, L. D. Pfefferle, Combust. Flame 136 (2004) 155.
69. O. Lemaire, M. Ribaucour, M. Carlier, R. Minetti, Combust. Flame 127 (2001) 1971.
70. D. Voisin, A. Marchal, M. Reuillon, J.-C. Boettner, M. Cathonnet, Combust. Sci. Technol. 138 (1998) 137.
71. P. J. Bennett, D. Gregory, R. A. Jackson, Combust. Sci. Technol. 115 (1996) 83.



# A priori kinetics for resonance stabilized hydrocarbon radicals

S.J. Klippenstein<sup>1</sup>, L.B. Harding<sup>1</sup>, Y. Georgievskii<sup>2</sup>, J.A. Miller<sup>2</sup>

<sup>1</sup> *Chemistry Division, Argonne National Laboratory*

*Argonne, IL 60439*

<sup>2</sup> *Combustion Research Facility, Sandia National Laboratories*

*Livermore, CA 94551-0969*

Reactions between resonance stabilized hydrocarbon radicals play an important role in the formation of polycyclic aromatic compounds. A detailed understanding of their kinetics is central to the development of accurate soot formation models. We review some of our recent a priori calculations for the kinetics of resonance stabilized hydrocarbon radicals [1, 2, 3]. For the high-pressure limit addition kinetics we employ a direct CASPT2 variable reaction coordinate transition state theory approach [4, 5]. For the pressure dependent kinetics we implement our master equation based approach to deriving phenomenological rate models [6, 7].

Predictions are made for the kinetics of H atom association with a large set of resonance stabilized hydrocarbon radicals [2]. The calculations are based on direct CASPT2/cc-pvdz evaluations of the orientation dependent interaction energies within

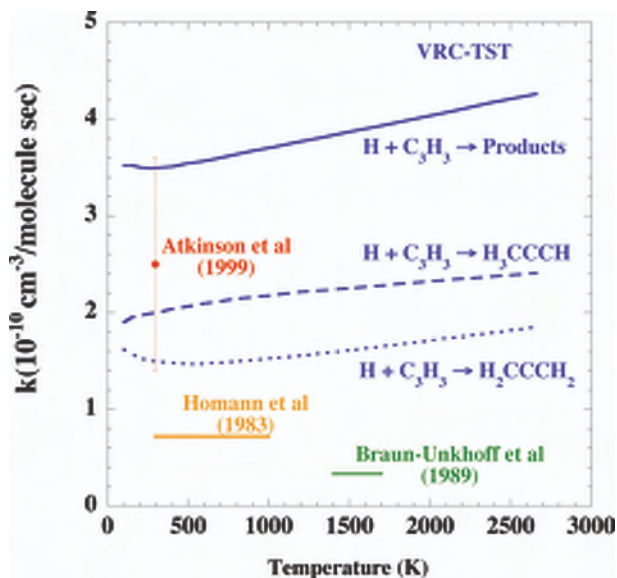


Figure 1. Plot of direct CASPT2 VRC-TST predictions and experimental measurements for the H plus propargyl addition rate constant.

variable reaction coordinate transition state theory. One-dimensional corrections to the interaction energies are estimated from a CASPT2/aug-cc-pvdz minimum energy path (MEP) for the specific reaction of interest and a CASPT2/aug-cc-pvtz MEP for the H + CH<sub>3</sub> reaction. For the H + propargyl [8, 9, 10], allyl [11], cyclopentadienyl [12, 13, 14], and benzyl [15, 16] reactions, where the experimental values appear to be the most well determined, theory and experiment agree to within their error bars. Predictions are also made for the combinations with triplet propargylene, CH<sub>2</sub>CCCH, CH<sub>3</sub>CCCH<sub>2</sub>, CH<sub>2</sub>CHCCH<sub>2</sub>, CH<sub>3</sub>CHCCH, cyclic-C<sub>4</sub>H<sub>5</sub>, CH<sub>2</sub>CCCCH, and CHCCHCCH.

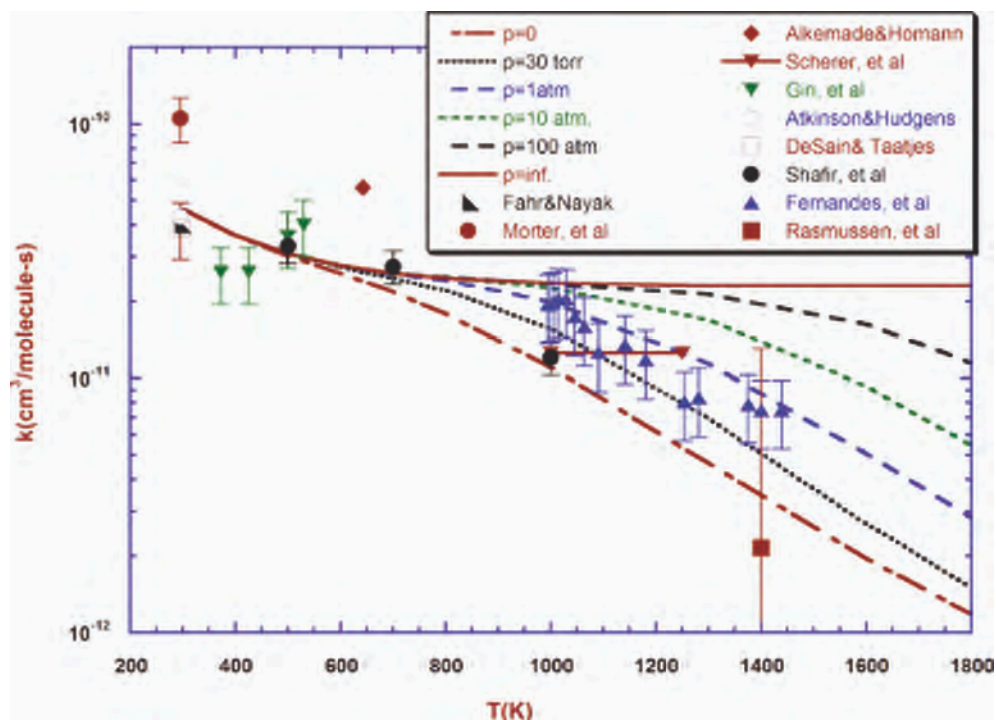


Figure 2. Plot of direct CASPT2 VRC-TST predictions and experimental measurements of the self-recombination rate coefficients for propargyl radicals.

Direct CASPT2 VRC-TST predictions for the association rate constants for the self and cross reactions of propargyl and allyl radicals are also made [3]. The prior studies of the H plus resonance stabilized radicals provide important background information for these studies. For each reaction, a set of multifaceted dividing surfaces is used to account for the multiple possible addition channels [17]. Because of their resonant nature, the geometric relaxation of the radicals is important. Here, the effect of this relaxation is explicitly calculated with the UB3LYP/cc-pvdz method for each mutual orientation encountered in the configurational integrals over the transition state divi-

ding surfaces. The final energies are obtained from CASPT2/cc-pvdz calculations with all pi orbitals in the active space. Evaluations along the minimum energy path suggest that basis set corrections are negligible. The rate constants for the  $C_3H_3 + C_3H_3$  [9, 18, 19, 20, 21, 22, 23, 24, 25, 26] and  $C_3H_5 + C_3H_5$  [27, 28, 29, 30, 31] self-reactions compare favorably with the available experimental data.

Such recombination reactions occur over complex potential energy surfaces. The time dependent master equation directly provides predictions for the time dependent populations in the various molecular complexes. We have described a procedure for

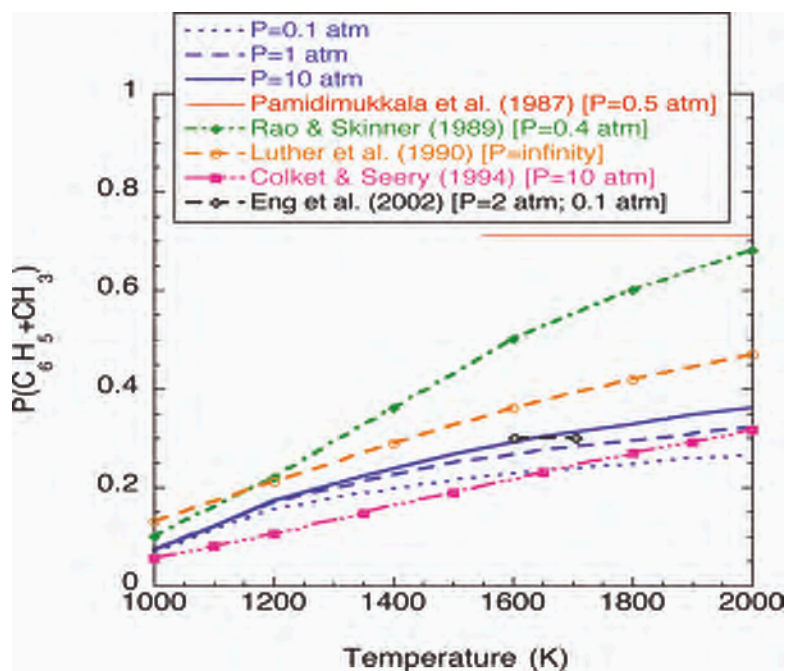


Figure 3. Plot of the predicted and observed branching ratios between  $C_6H_5 + CH_3$  and  $C_7H_7 + H$  in the dissociation of toluene.

deriving phenomenological rate coefficients from the eigensolutions to the master equation [6, 7]. This approach has been applied to the study of the full temperature and pressure dependent kinetics of the propargyl + propargyl reaction [32].

The master equation simulations for the kinetics on the  $C_7H_8$  potential energy surface yield predictions for the temperature and pressure dependence of each of the recombination and dissociation processes, as well as for the  $C_7H_7 + H \rightarrow C_6H_5 + CH_3$  bimolecular reaction [1]. The theoretical predictions are found to be in satisfactory agreement with the available experimental data for the photodissociation of toluene [33, 34, 35, 36, 37, 38, 39, 40, 41, 42, 43, 44], the temperature and pressure dependent dissociation of toluene [10, 45, 46, 47, 48, 49, 50, 51, 52, 53, 54], and the reaction of

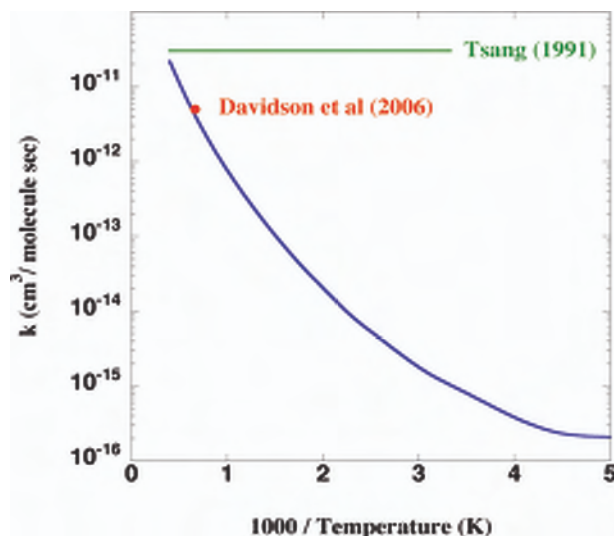


Figure 4. Plot of the predicted and observed rate coefficients for the  $\text{H} + \text{C}_3\text{H}_5 \rightarrow \text{C}_3\text{H}_5 + \text{H}_2$  abstraction reaction.

benzyl radical with H [15, 16]. For the  $\text{C}_6\text{H}_5 + \text{CH}_3$  recombination, the theoretical predictions exceed the experimental measurements of Lin and coworkers by a factor of 2 or more for all temperatures [55, 56, 57].

A final study examines the H atom abstraction reaction,  $\text{H} + \text{C}_3\text{H}_5 \rightarrow \text{C}_3\text{H}_4 + \text{H}_2$  [58]. As with other highly exothermic abstractions, this reaction had been assumed to be rapid [59]. Ab initio transition state theory calculations, employing multireference wavefunctions, demonstrate that, for electronic reasons, this reaction actually has a large barrier and a corresponding slow rate in agreement with the recent study of Davidson et al. [60].

## ACKNOWLEDGMENT

This work is supported by the Division of Chemical Sciences, Geosciences, and Biosciences, the Office of Basic Energy Sciences, the U. S. Department of Energy. The work at Argonne was supported under DOE Contract Number DE-AC02-06CH11357. Sandia is a multi-program laboratory operated by Sandia Corporation, a Lockheed Martin Company, for the United States Department of Energy under contract DE-AC04-94-AL85000.

## REFERENCES

1. S. J. Klippenstein, L. B. Harding, Y. Georgievskii, *Proc. Combust. Inst.* 31 (2007) 221-229.
2. L. B. Harding, S. J. Klippenstein, Y. Georgievskii, *J. Phys. Chem. A* 111 (2007) 3789-3801.

3. Y. Georgievskii, J. A. Miller, S. J. Klippenstein, *Phys. Chem. Chem. Phys.* 9 (2007) 4259-4268.
4. L. B. Harding, Y. Georgievskii, S. J. Klippenstein, *J. Phys. Chem. A* 109 (2005) 4646-4656.
5. S. J. Klippenstein, Y. Georgievskii, L. B. Harding, *Phys. Chem. Chem. Phys.* 8 (2006) 1113-1147.
6. S. J. Klippenstein, J. A. Miller, *J. Phys. Chem. A* 106 (2002) 9267-9277.
7. J. A. Miller, S. J. Klippenstein, *J. Phys. Chem. A* 110 (2006) 10528-10544.
8. K. H. Homann, C. Wellman, *Ber. Bunsen. Ges. Phys. Chem.* 87 (1983) 609-616.
9. D. B. Atkinson, J. W. Hudgens, *J. Phys. Chem. A* 103 (1999) 4242-4252.
10. M. Braun-Unkloff, P. Frank, T. Just, *Proc. Combust. Inst.* 22 (1989) 1053-1061.
11. M. A. Hanning-Lee, M. J. Pilling, *Int. J. Chem. Kinet.* 24 (1992) 271-278.
12. J. L. Emdee, K. Brezinsky, I. Glassman, *J. Phys. Chem.* 96 (1992) 2151-2161.
13. P. Frank, J. Herzler, T. Just, C. Wahl, *Proc. Combust. Inst.* 25 (1994) 833-840.
14. K. Roy, M. Braun-Unkloff, P. Frank, T. Just, *Int. J. Chem. Kinet.* 33 (2001) 821-833; 34 (2002) 209.
15. M. Bartels, J. Edelbuttel-Einhaus, K. Hoyermann, *Proc. Combust. Inst.* 22 (1989) 1041-1051.
16. L. Ackerman, H. Hippler, P. Pagsberg, C. Reihls, J. Troe, *J. Phys. Chem.* 94 (1990) 5247-5251.
17. Y. Georgievskii, S. J. Klippenstein, *J. Phys. Chem. A* 107 (2003) 9776-9781.
18. U. Alkemade, K. H. Homann, *Z. Phys. Chem., Neue Folge* 161 (1989) 19-34.
19. C. L. Morter, S. K. Farhat, J. D. Adamson, G. P. Glass, R. F. Curl, *J. Phys. Chem.* 98 (1994) 7029-7035.
20. A. Fahr, A. Nayak, *Int. J. Chem. Kinet.* 32 (2000) 118-124.
21. S. Scherer, T. Just, P. Frank, *Proc. Combust. Inst.* 28 (2000) 1511-1518.
22. B. R. Giri, H. Hippler, M. Olzmann, A. N. Unterreiner, *Phys. Chem. Chem. Phys.* 5 (2003) 4641-4646.
23. J. D. DeSain, C. A. Taatjes, *J. Phys. Chem. A* 107 (2003) 4843-4850.
24. E. V. Shafir, I. R. Slagle, V. D. Knyazev, *J. Phys. Chem. A* 107 (2003) 8893-8903.
25. C. L. Rasmussen, M. S. Skjoth-Rasmussen, A. D. Jensen, P. Glarborg, *Proc. Combust. Inst.* 30 (2005) 1023-1031.
26. R. X. Fernandes, H. Hippler, M. Olzmann, *Proc. Combust. Inst.* 30 (2005) 1033-1038.
27. D. M. Golden, N. A. Gac, S. W. Benson, *J. Am. Chem. Soc.* 91 (1969) 2136.
28. J. J. Throssell, *Int. J. Chem. Kinet.* 4 (1972) 273.
29. J. M. Tulloch, M. T. Macpherson, C. A. Morgan, M. J. Pilling, *J. Phys. Chem.* 86 (1982) 3812-3819.
30. M. E. Jenkin, T. P. Murrells, S. J. Shalliker, G. D. Hayman, *J. Chem. Soc. Faraday Trans.* 89 (1993) 433-446.
31. A. A. Boyd, B. Noziere, R. Lesclaux, *J. Phys. Chem.* 99 (1995) 10815-10823.
32. J. A. Miller, S. J. Klippenstein, *J. Phys. Chem. A* 107 (2003) 7783-7799.
33. H. Hippler, V. Schubert, J. Troe, H. J. Wendelken, *Chem. Phys. Lett.* 84 (1981) 253-256.
34. N. Ikeda, N. Nakashima, K. Yoshihara, *J. Chem. Phys.* 82 (1985) 5285-5286.
35. K. Tsukiyama, R. Bersohn, *J. Chem. Phys.* 86 (1987) 745-749.
36. Y. Kajii, K. Obi, I. Tanaka, N. Ikeda, N. Nakashima, K. Yoshihara, *J. Chem. Phys.* 86 (1987) 6115-6118.
37. H. Hippler, L. Lindemann, J. Troe, *Ber. Bunsen. Ges. Phys. Chem.* 92 (1988) 440-441.
38. J. Park, R. Bersohn, I. Oref, *J. Chem. Phys.* 93 (1990) 5700-5708.
39. U. Brand, H. Hippler, L. Lindemann, J. Troe, *J. Phys. Chem.* 94 (1990) 6305-6316.

40. K. Luther, J. Troe, K.-M. Weitzel, *J. Phys. Chem.* 94 (1990) 6316-6320.
41. H. Hippler, C. Riehn, J. Troe, K.-M. Weitzel, *J. Phys. Chem.* 94 (1990) 6321-6326.
42. T. Shimada, Y. Ojima, N. Nakashima, Y. Izawa, C. Yamanaka, *J. Phys. Chem.* 96 (1992) 6298-6302.
43. R. Frochtenicht, *J. Chem. Phys.* 102 (1995) 4850-4859.
44. R. Frochtenicht, M. Hartmann, *J. Phys. Chem.* 99 (1995) 16290-16295.
45. S. J. Price, *Can. J. Chem.* 40 (1962) 1310-1317.
46. C. T. Brooks, C. P. R. Cummins, S. J. Peacock, *Trans. Farad. Soc.* 67 (1971) 3265.
47. V. S. Rao, G. B. Skinner, *J. Phys. Chem.* 88 (1984) 4362-4365.
48. K. M. Pamidimukkala, R. D. Kern, M. R. Patel, H. C. Wei, J. H. Kiefer, *J. Phys. Chem.* 91 (1987) 2148-2154.
49. W. Muller-Markgraf, J. Troe, *Proc. Combust. Inst.* 21 (1986) 815-824.
50. L. D. Brouwer, W. Muller-Markgraf, J. Troe, *J. Phys. Chem.* 92 (1988) 4905-4914.
51. O. S. L. Bruinsma, R. S. Geertsman, P. Bank, J. A. Loulijn, *Fuel* 67 (1988) 327-333.
52. V. S. Rao, G. B. Skinner, *J. Phys. Chem.* 93 (1989) 1864-1869.
53. H. Hippler, C. Reihls, J. Troe, *Z. Phys. Chem. Neue Folge* 167 (1990) 1-16.
54. R. A. Eng, A. Gebert, E. Goos, H. Hippler, C. Kachiani, *Phys. Chem. Chem. Phys.* 4 (2002) 3989-3996.
55. J. Park, I. V. Dyakov, M. C. Lin, *J. Phys. Chem. A* 101 (1997) 8839-8843.
56. I. V. Tokmakov, J. Park, S. Gheyas, M. C. Lin, *J. Phys. Chem. A* 103 (1999) 3636-3645.
57. J. Park, S. I. Gheyas, M. C. Lin, *Int. J. Chem. Kinet.* 31 (1999) 645-653.
58. L. B. Harding, S. J. Klippenstein, personal communication, 2008.
59. W. Tsang, *J. Phys. Chem. Ref. Data* 20 (1991) 221-273.
60. D. F. Davidson, M. A. Oehlschlaeger, R. K. Hanson, *Proc. Combust. Inst.* 31 (2007) 321-328.

# Soot precursors from real fuels: the unimolecular reactions of fuel radicals

W. Tsang, I.A. Awan, W.S. McGivern, J.A. Manion  
*National Institute of Standards and Technology*

*Abstract: This paper describes studies aimed at defining in a quantitative fashion the cracking pattern of fuel radicals under combustion conditions. The experimental procedure involves studies using a single pulse shock tube and combining the observations with available literature data. This leads to the deduction of high pressure rate expressions for the decomposition and isomerization processes and the departure from such values as a result of energy transfer effects. The unique features of these processes are the low reaction thresholds, the relatively large size of the radicals of interest and the possibility of isomerization. The justification for this type of work is the need to connect fuel decomposition with the unsaturated precursors to polynuclear aromatic hydrocarbon and particle formation and to extend the stoichiometric range of existing combustion models. The unimolecular reactions of heptyl radicals is described in detail as an example of the procedure and results. A summary of related results and on going work on more complex and larger fuel radicals is given.*

## 1. INTRODUCTION

It is well known that combustion properties such as ignition behavior and soot formation are dependent on the nature of the fuel and how the combustion process is carried out. Quantitative definition of the relationships of the properties of the fuel, the operational variables and global effects has been a long term goal of combustion research. Recent progress in computational fluid dynamics has opened the possibility of establishing such relationship for real fuels in real devices on a fundamental basis with the help of simulations [1,2]. This paper describes work being carried at the National Institute of Standards and Technology aimed at supplying the requisite chemical kinetic information. Particular attention is focused on the breakdown products from real fuel molecules. The aim is to use this information to improve existing polynuclear aromatic hydrocarbon (PAH)/SOOT models. Such models generally use small unsaturated compounds as the starting point of their simulations. These simple compounds are however rarely used as fuels. This work attempts to provide a quantitative bridge between fuel structure and PAH/SOOT formation models. It is based on substantial evidence that pyrolysis rates and mechanisms have important impacts on the tendency of a fuel to soot [3].

Combustion is a free radical process. The initial step must therefore be the creation of these free radicals. They involve the breaking of C-C bonds and radical attack on the fuel molecule to form fuel radicals. Except at the highest temperatures, the former is not very important. In any case the rate constants for these processes can be estimated on the basis of existing data with good accuracy [4]. Rate constants for radical attack on organic radicals are also well known [5]. The focus of this work is the next step, the breakdown of the newly formed radical to form a smaller radical and a 1-olefin.

Radical decomposition and isomerization are unimolecular processes. The physical phenomenon is well understood [6]. It involves a molecule receiving energy from the bath until a reaction threshold is reached. Above this energy, decomposition or isomerization processes can occur. Ultimately small unsaturated compounds and various fragments, the precursors for Soot/PAH, are formed.

Within the framework of unimolecular processes, the special aspects of these reactions are the low reaction thresholds, a multiplicity of reaction channels, the possibility of isomerizations and the relatively large size of the radicals of interest [7]. This leads to unique situations that are not usually treated in standard texts. In this paper we will begin with a brief description of the background for the work. This will be concerned with the treatment of unimolecular reactions, the nature of the fuels of interest, the models that are used for simulations and related past work. We will then illustrate our approach using our studies of the unimolecular decomposition and isomerization of the normal heptyl radicals as an example. Heptyl radicals are directly derived from heptane, a reference fuel and also formed from the decomposition of larger hydrocarbon fuels. Its reactions must therefore be an integral part of any reaction models of a realistic fuel. We will conclude with a brief summary of work on related fuel molecules and describe future challenges.

The decomposition of the fuel radicals is competitive with their oxidation. Thus these processes should play key roles in many aspects of combustion models. Their absence in combustion models represents a significant defect and may well account for the limited range of predictive capability of current models.

## 2. BACKGROUND

**A. Unimolecular Reactions:** The alkyl radicals formed from fuel decomposition can undergo beta bond scission and isomerization processes. The former involves breaking a bond beta from the radical site leading to the formation of a smaller alkyl radical. Thus the complete description of the decomposition of any large alkyl radical must also include those for the small entities. Isomerization involves the transfer of H-atoms within a radical across two or more carbon atoms. It is known that the reaction across one carbon atoms has too high a reaction threshold

These reactions are all unimolecular processes. When a unimolecular reaction occurs with the molecular energy characterized by a Boltzmann distribution, the rate constants can be expressed as a single expression in the Arrhenius or modified Arrhenius form. Under higher temperature combustion conditions, the rapidity of reactions leads to the failure to maintain the Boltzmann distribution. The consequence is that a new steady state distribution is achieved. Since this will be dependent on the pressure, this will also be manifested in the rate constants. The proper treatment of such phenomenon is well understood. The energy space occupied by the molecular distribution function is divided into a number of slices. The population of each slice is then determined by taking into consideration reactions as well as augmentation and depletion by collisions. This leads to a new distribution function that is convoluted with the microcanonical rates derived from the RRKM formulation. The key parameters are the properties of the transition state as determined from the high pressure

rate expression. High pressure rate expressions for unimolecular reactions are fundamental properties of any molecule in that they contain all the experimentally derivable properties of the transition states.

For the reactions under consideration, the low reaction thresholds and large molecular sizes are features that are not usually encountered in descriptions of unimolecular reactions. In these cases the reaction threshold is lower in energy than the maximum of the molecular distribution function. If treated in the standard “closed system” [7] a steady state distribution is never attained. Instead it is necessary to treat the process as an open system where a continuous flux of molecules is introduced into the system, thus assuring a steady state distribution and hence the possibility of describing the reaction in terms of rate constants. This is of course the actual physical situation with regard to radical decomposition. Isomerizations are reversible. The practical consequence is to have extra components in the system. This has consequences with regard to increased calculational efforts.

**B. Fuels:** Real fuels are complex mixtures of hydrocarbons containing scores of intermediate to large compounds. They range from five carbon species found in gasoline to compounds with as many as twenty carbons in diesel fuel. Unless these are enumerated it is not possible to carry out the molecule based simulations that are the basis for the fundamental approach. The scores of compounds are however limited to much smaller classes of molecules. There is general agreement among combustion scientists that a selected small number of compounds in a mixture can in fact represent a real fuel. A typical surrogate mixture can be found in Table 1 [8]. A series of workshops have been held in recent months and surrogates for gasoline and diesels have been proposed. A similar listing for aviation fuels is in the process of development [9]. With such a listing it will be possible to build information bases for simulations. At the same time experiments can be carried out with well-specified systems. From Table 1 one notes the importance of normal alkanes. The present work will use a molecule in this class, heptane, as an example.

Table 1. Typical surrogate mixture [8].

Compound	Mole percent
methylcyclohexane	5%
cyclooctane	5%
butylbenzene	5%
Tetralin	5%
Meta-xylene	5%
1,2,4,5 tetramethylbenzene	5%
1-methylnaphthalene	5%
isooctane	5%
decane	15%
dodecane	20%
tetradecane	15%
hexadecane	10%

**C. Models:** The chemistry of combustion can conceptually be divided into four separate modules. These include (a) fuel cracking (b) fuel oxidation (c) combustion of light hydrocarbons and (d) PAH/Soot formation. Most existing fuel combustion models deal with category (b) [10-14]. This is because the emphasis in combustion research before the advent of concerns regarding pollution has always been on oxidative aspects. Thus models have usually been validated against experimental measurements on parameters such as ignition delays, flame speed, etc. Thus the oxidative models are limited to regions near stoichiometric. Our work will concentrate on category (a). It will permit the extension of models to more fuel rich regions. Category (c) is represented by GRIMECH [15] and concentrates on methane combustion. However for completeness, light hydrocarbons are necessarily included. This is the area where there are the most experimental data and the database of information is most fully developed. PAH/Soot models represent the research frontier [16-18] and are the most challenging conceptually. For the three other cases, reactions simplify the diversity of chemical species. In contrast, for PAH/Soot formation, a relatively small number of precursors leads to the formation of many diverse and not very well understood molecular entities. Thus the models are necessarily incomplete and they are very much tied to the system that they seek to replicate.

Most of the existing combustion models deal with fuels as a single component. Even within this limitation the models are very large and can contain hundreds of species and thousands of reactions. The basic process of model generation involves collecting as much as possible direct experimental rate data on the specific fuel and intermediates of interest. Since these models are very large, the set of direct measurements is never sufficient. Thus many of the rate constants are based on rules or essentially empirical correlations derived from limited measurements on smaller molecules. More recently, *ab initio* theory is used to provide the necessary data. However they are obtained, the base data are then typically adjusted in an attempt to fit a limited set of global experiment. Due to the complexity, it is difficult to make subsequent adjustments of the models as more information is obtained. The problem is exacerbated by the diversity of combustion applications. Experience has shown that although combustion models can be made to fit observations their capability for prediction is much less satisfactory.

The necessity of using mixtures for simulation purposes is a serious challenge. The methodology of constructing models described above means that it will not be possible to simply combine the database for single compounds. This is the rationale for approaching the problem at as fundamental a level as possible. Presumably if adjustments must be made, then they can all be made together. By fundamental, we mean the definition of the kinetic properties of the system in terms of transferable molecular parameters that is independent of the environment except for energy transfer effects. We also pay particular attention to the combustion environment that is always above 1 bar and ambient temperatures.

**D. Past work:** The molecular size of real fuels described above means that it is necessary to deal with radicals containing 5 carbon atoms and larger. There is very little direct information on such radicals. Thus most of the data must be indirect. There have been many studies on radical addition to olefins [19]. This is the reverse of the reactions of interest and the desired rate constants can be derived from detailed balance. For accurate results this requires knowledge of the molecular and thermodynamic

properties of all species involved. This is not a problem for stable molecules. For alkyl radicals, the prescription of Benson [20] has proved to be quite satisfactory. Data from detailed balance extends the information base to six or seven carbon structures. Further extension will involve making assumptions through extrapolation of existing data. For the present purposes we have shown that beta C-C bond cleavage reactions have rate constants that are equal regardless of the extent of the size of the departing normal alkyl group [21]. This is expected and this observation will be used for all primary radicals. In the course of the present work this can in fact be demonstrated directly. Obviously this will also hold for secondary radicals.

Aside from beta bond scission, the other type of reaction that alkyl radicals can undergo is isomerization via hydrogen atom transfer. It is known that transfers involving 3 member rings have very high barriers and are hence unimportant [22-23]. Six member transition states are very much favored over those involving 5 member transition states. Since the former has minimal strain energy the assumption is that rate constants involving larger ring transition state cannot be larger than those with 6 members. There are very few direct measurements on the rate-constants for these processes and, because the reactions are very fast, the determinations have been made not far from room temperature. A further problem with the existing data is that the rate expressions derived from the existing measurements have extraordinarily small A-factors. The consequence is that it is not possible to construct a reasonable transition state that will reproduce the A-factor. Yet the measurements do not seem to be in error. For example, there are two direct measurements on the isomerization of 1-hexyl radical that lead to the formation of the 2-hexyl [21,22]. Although they involve two completely different systems the results are in excellent agreement. Examination of the papers shows no obvious errors. There is no reason to reject the results.

The decomposition and isomerization of hexyl radicals have recently been studied using the same technique as that described here. On the basis of the rate constants for beta C-C bond scission described earlier, rate constants for isomerization have been determined. In combination with lower temperature results the Arrhenius plots show very strong positive curvature. The only way of rationalizing all the data is the assumption of tunneling influencing the low temperature measurements. This is reasonable. The process involves the transfer of a hydrogen atom across a significant barrier. The cyclic nature of the transition state means that the width of the barrier cannot be too large. Thus to fit all the results an unsymmetrical barrier of 1.15 Angstroms was used. The same barrier width also apparently can fit the data involving the five member transition states. In the course of this work this width was used for all H-transfer isomerization rate constants. Since the rate constants we have derived are determined relative to beta C-C bond scission, they are of course directly dependent on those rates.

### 3. EXPERIMENTAL AND TREATMENT OF DATA

The experimental procedure involves generating the radical of interest from a suitable precursor and determining the cracking pattern of the olefins that are formed. Recent work in this laboratory has focused on the use of a heated single pulse shock tube. This is a well established technique [24] and has produced a whole host of data on the quan-

titative aspects of classical unimolecular reactions. The present application is an extension of earlier work in the sense of studying more complex processes with low reaction thresholds and isomerizations. Figure 1 contains a schematic of the apparatus and the accompanying wave diagram that define the experimental variables. For the present purposes the shock tube can be considered to be a pulse reactor and within the constraints of its length has a heating time of approximately 500  $\mu$ s. The experimental pressures used in these experiments are in the range of 1.5 to 7 bars and the temperatures are in the 860 to 1050 K. When this is combined with an alkyl radical at concentrations below several hundreds ppm, their short lifetimes and the presence of an overwhelming excess of a radical scavenger, 1% (10000 ppm), the only reaction that the alkyl radicals can undergo is unimolecular decomposition and isomerization. Thus a true thermal cracking pattern is obtained in the same sense as the cracking pattern in a mass spectrometer.

The task is to rationalize these results in terms of high pressure rate constants. As noted earlier, these contain all the experimentally available properties of the transition state. Due to the large rate constants these reactions are in the fall-off region. Thus it is necessary to correct the results for this effect. Actually, these effects are masked in the cracking patterns due to the fact that all reactions are affected by fall-off effects to some degree. We have developed a program [25] to deal with such effects. Since potential energy surfaces for these large molecules do not exist, the procedure is semi-empirical in nature. It makes use of the high pressure rate expression and solves for the new non-Boltzmann

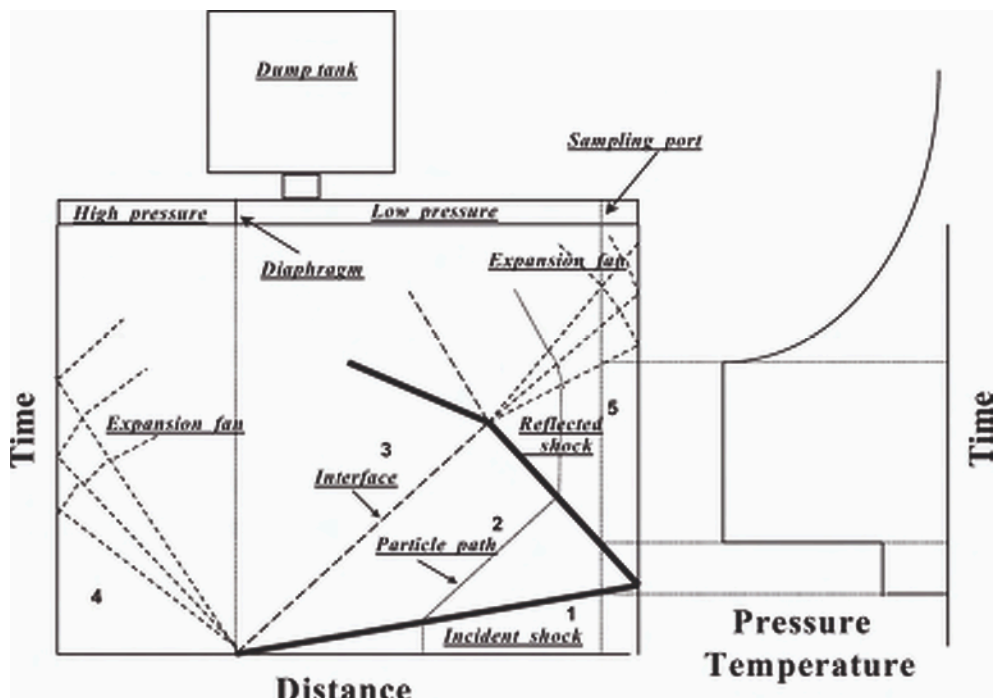


Figure 1. Schematics of single pulse shock tube and wave diagrams.

distribution function. It then calculates new rate constants on this basis. This is particularly useful for the present application because the reverse radical addition reactions upon which the radical decomposition rate constants are derived are from experiments at low temperature. They are therefore the high pressure values. For the present study the energy transfer parameter in terms of the step size down is of  $.3 \cdot T \text{ cm}^{-1}$  for collisions with argon with  $T$  in K. This is based on the determination of Slagle and Knyazev [26] for the decomposition of 1-butyl radical and has been used in all the calculations.

For most of the experiments that have been carried out, the primary iodides have been used as the precursor. The C-I bond is very weak. Hence it is readily cleaved and the appropriate primary alkyl radical is released into the system. There is also a molecular reaction that leads to the direct formation of HI and 1-heptene. Since the latter cannot be a decomposition product from C-C bond cleavage of the alkyl radical it can be ignored. The reaction temperature was determined by the internal standard method. The presence of the radical inhibitor assures that it can only decompose via a non-radical unimolecular process. The standard reaction from which the reaction temperature is derived is the HCl elimination from cyclopentyl chloride [27]. The rate expression for this process is

$$k(\text{c-C}_5\text{H}_9\text{Cl} = \text{c-C}_5\text{H}_8 + \text{HCl}) = 3 \times 10^{13} \exp(-24220/T) \text{ s}^{-1}.$$

This can then be converted to the reaction temperature through the relation

$$1/T = -24330 \times [\ln(\ln(1 - \text{fractional conversion}) / 3 \times 10^{13} \times t)]$$

where the fractional conversion is derived from the conversion to cyclopentene from cyclopentyl chloride,  $t$  is the residence time and has been found to be 500  $\mu\text{sec}$  for the present geometry. Cyclopentene is not a decomposition product of the  $n$ -alkyl radicals. Hence there is no possibility of interferences. Analysis was by gas chromatography with flame ionization detection. Olefins up to 1-heptene were separated with a 1 m x 1mm Hayesep S [28] and Hayesep Q columns operated in series. The heavier compounds were separated using a Restek 30m c 0.53 mm RTX-624 fused silica column (a cross bonded 6% cycamopropylphenyl/94% dimethylpolysiloxan). The  $n$ -heptyl iodide and cyclopentyl chloride used in these experiments were purchased from Aldrich Chemicals. Gas chromatography did not reveal the presence of any impurities that will effect the results.

#### 4. RESULTS

Figure 2 contains the cracking pattern for olefins from 1-heptyl radical from single pulse shock tube studies during 1-iodoheptane pyrolysis. It is important to note that all the possible products from beta bond scissions can be found. This implies the presence as intermediates of all the heptyl isomers. This is a clear demonstration of the importance of isomerization processes in the present environment since if these were not important ethylene would be the only product. The mechanism can be seen in Figure 3. Note that the process involves 4 isomers, 5 beta bond scission reactions and 4 reversible isomerizations.

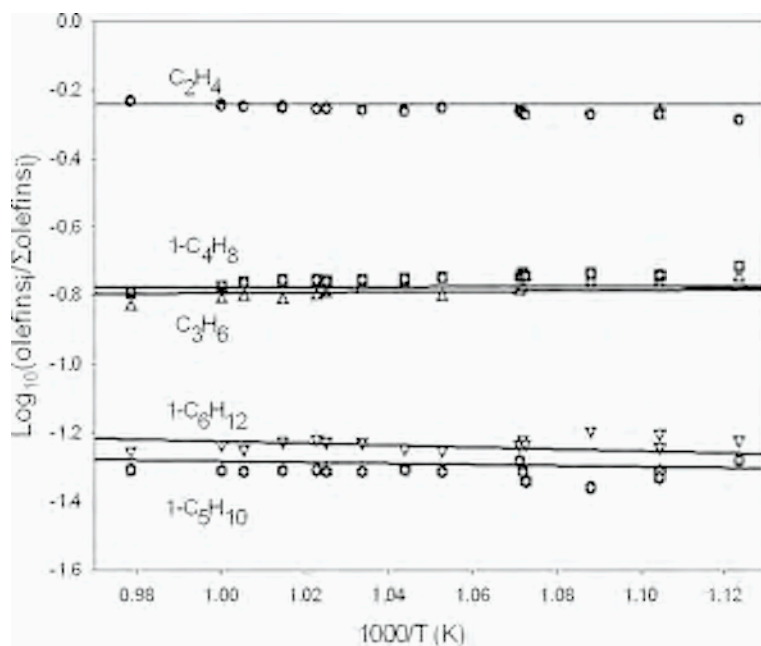


Figure 2. Branching ratio for olefins production for the decomposition of 1-heptyl radicals from 1-iodoheptane decomposition.

As in all the cases that have been studied ethylene is an important product and can originate from most of the reaction channels. Thus its presence does not yield much information regarding mechanisms. It is the heavier olefins that yield more interesting information. For example, 1-butene and 1-hexene can only originate from heptyl-3. The former is the result of the ejection of an n-propyl radical, while the latter is from methyl formation. The difference in rate constants is a factor of slightly more than a factor of 3. This is exactly the same factor for the formation of ethyl and methyl radicals from hexyl-3. This is completely consistent with the assumption that beta bond scission for alkyl radicals is a localized phenomena. It is interesting that this difference is the same in alkanes even though the values of the activation energies are different by over 200 kJ/mol. More important, the consistency provides a basis for estimation.

The yields of 1-olefins with four or more carbons are of particular importance. This is because they can lead to the formation of more highly unsaturated compounds such as butadiene which have greater propensity to form soot [3]. In addition, for 1-hexenyl-6, there is also a cyclization channel leading to the formation of cyclohexyl and ultimately cyclohexene. This provides a direct route for aromatization. There is thus a distinct difference between small and larger hydrocarbon fuels.

The lines in Figure 2 are the results of fitting data on the basis of a set of the reactions implied by Figure 3. The most interesting observation is that the rate expressions for 1-4 and 1-5 hydrogen transfer process are virtually the same as those for the hexyl radicals. This means that extending the adjacent alkyl groupings for H-transfer reac-



Table 2. High pressure rate expressions used in fitting data in Figure 3. Rate expressions are expressed as  $k=AT^n\exp(-E/RT)$ .

Reaction	Log A	N	Activation energy E/R
$1-C_7H_{15} = C_2H_4 + 1-C_5H_{11}$	11.90	.33	13694
$2-C_7H_{15} = C_3H_6 + 1-C_4H_9$	11.70	.56	14138
$3-C_7H_{15} = 1-C_4H_8 + 1-C_3H_7$	12.47	.31	14221
$3-C_7H_{15} = 1-C_6H_{12} + CH_3$	11.04	.75	14797
$4-C_7H_{15} = 1-C_5H_{10} + C_2H_5$	12.77	.31	14221
$3-C_7H_{15} = 1-C_7H_{15}$	2.87	2.43	6441
$4-C_7H_{15} = 1-C_7H_{15}$	2.10	2.88	9884
$2-C_7H_{15} = 1-C_7H_{15}$	1.52	2.81	7561
$3-C_7H_{15} = 2-C_7H_{15}$	2.30	2.83	9048
$1-C_7H_{15} = 3-C_7H_{15}$	2.83	2.39	5237
$1-C_7H_{15} = 4-C_7H_{15}$	2.07	2.85	8680
$1-C_7H_{15} = 2-C_7H_{15}$	2.39	2.51	6292
$2-C_7H_{15} = 3-C_7H_{15}$	1.39	3.09	9113

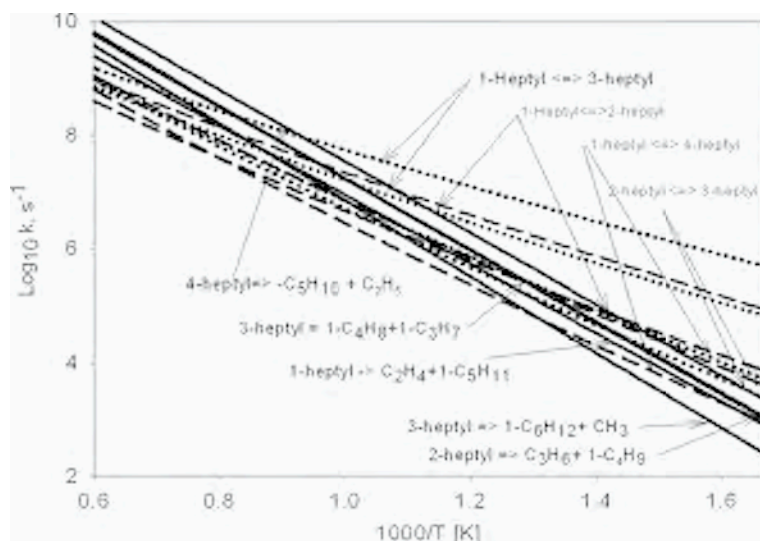


Figure 4. High pressure rate constants for heptyl radical decomposition and isomerization.

stant of formation of the four heptyl and other radicals can be found in Table 3 They are derived using the standard methods described in our earlier publication on hexyl radicals [21].

The departures for heptyl radical from high pressure behavior are summarized in Tables 4a-d. We present the data in this form since we have not been able to parameterize the results in standard analytical formats. Users can use the data to derive wha-

Table 3. Equilibrium constants of formation for radicals considered in this work.

Radical	Equilibrium constants of formation
1-C <sub>7</sub> H <sub>15</sub>	$\text{Log } K_p = -33.395 - 1.738 \times 10^3/T + 4.103 \times 10^6/T^2 - 2.199 \times 10^9/T^3 + 3.785 \times 10^{11}/T^4$
2-C <sub>7</sub> H <sub>15</sub>	$\text{Log } K_p = -33.621 - 8.987 \times 10^2/T + 4.027 \times 10^6/T^2 - 2.202 \times 10^9/T^3 + 3.812 \times 10^{11}/T^4$
3-C <sub>7</sub> H <sub>15</sub>	$\text{Log } K_p = -33.540 - 1.202 \times 10^3/T + 4.116 \times 10^6/T^2 - 2.210 \times 10^9/T^3 + 3.809 \times 10^{11}/T^4$
4-C <sub>7</sub> H <sub>15</sub>	$\text{Log } K_p = -33.537 - 1.215 \times 10^3/T + 4.137 \times 10^6/T^2 - 2.222 \times 10^9/T^3 + 3.834 \times 10^{11}/T^4$
1-C <sub>5</sub> H <sub>11</sub>	$\text{Log } K_p = -22.670 - 3.096 \times 10^3/T + 2.533 \times 10^6/T^2 - 1.422 \times 10^9/T^3 + 2.478 \times 10^{11}/T^4$
1-C <sub>4</sub> H <sub>9</sub>	$\text{Log } K_p = -17.270 - 3.767 \times 10^3/T + 1.803 \times 10^6/T^2 - 1.058 \times 10^9/T^3 + 1.866 \times 10^{11}/T^4$
1-C <sub>3</sub> H <sub>7</sub>	$\text{Log } K_p = -11.823 - 4.587 \times 10^3/T + 1.074 \times 10^6/T^2 - 6.971 \times 10^8/T^3 + 1.262 \times 10^{11}/T^4$
C <sub>2</sub> H <sub>5</sub>	$\text{Log } K_p = -6.296 - 5.197 \times 10^3/T + 3.363 \times 10^5/T^2 - 3.359 \times 10^8/T^3 + 6.606 \times 10^{10}/T^4$

tever form that is most suitable for their simulation program. Note that each reaction has different fall-off behavior depending on the nature of the initial isomer. There are some negative values for the isomerization reactions near the high pressure limit. This is due to the small values of the reaction thresholds for such processes. The user should probably simply adjust the values to zero under such conditions.

Figure 5 is a plot of the departures from high pressure behavior for the beta bond fission reactions involving heptyl radicals. Each reaction has its own fall-off behavior and depends on the nature of the starting reactant. Furthermore, the nature of the deviation from high pressure behavior is unique and is a direct outgrowth of the large size of the molecule being analyzed and the low reaction threshold. Such behavior has

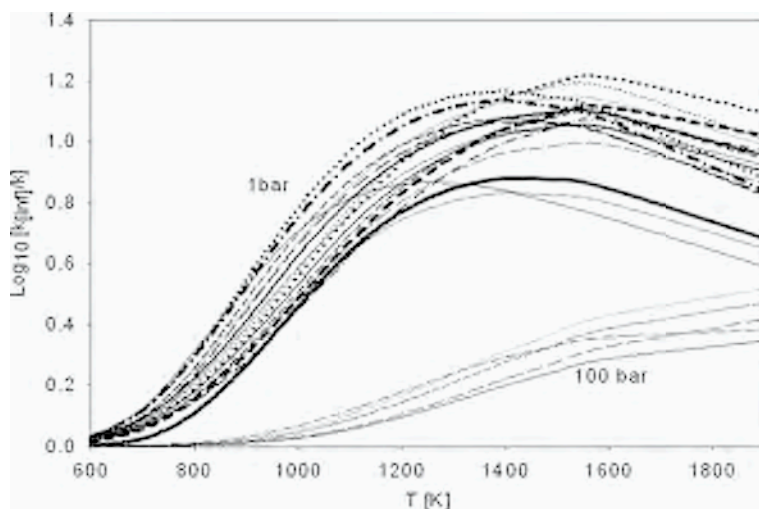


Figure 5. Departure from high pressure values at 1 and 100 bars for various beta bond scission reactions involving heptyl radicals. The light lines are for 1-heptyl and the increasingly darker lines for 2-heptyl, 3-heptyl and 4-heptyl.

Table 4a. Departures from high pressure behavior for reactions originating from 1-heptyl radical expressed as  $\log k_{\infty}/k$  at various pressures and temperatures.

	Log P	500	700	900	1100	1300	1500	1700	1900
1-C <sub>7</sub> H <sub>15</sub> =	-1	0.00	0.41	1.00	1.22	1.13	0.95	0.77	0.63
C <sub>2</sub> H <sub>4</sub> + 1-C <sub>5</sub> H <sub>11</sub>	0	0.03	0.13	0.52	0.81	0.86	0.80	0.69	0.59
	1	0.01	0.02	0.17	0.41	0.56	0.59	0.57	0.52
	2	0.00	0.01	0.03	0.12	0.24	0.33	0.38	0.38
2-C <sub>7</sub> H <sub>15</sub> =	-1	0.02	0.24	0.74	1.17	1.36	1.35	1.21	1.02
C <sub>3</sub> H <sub>6</sub> + 1-C <sub>4</sub> H <sub>9</sub>	0	0.01	0.06	0.31	0.66	0.90	0.99	0.96	0.87
	1	0.01	0.01	0.08	0.27	0.48	0.62	0.67	0.66
	2	0.01	0.01	0.02	0.06	0.16	0.28	0.37	0.42
3-C <sub>7</sub> H <sub>15</sub> =	-1	0.02	0.30	0.86	1.26	1.40	1.37	1.24	1.07
1-C <sub>4</sub> H <sub>8</sub> + 1-C <sub>3</sub> H <sub>7</sub>	0	0.00	0.08	0.39	0.76	0.98	1.05	1.02	0.92
	1	0.00	0.01	0.11	0.33	0.55	0.69	0.74	0.72
	2	0.00	0.00	0.02	0.09	0.21	0.34	0.43	0.47
3-C <sub>7</sub> H <sub>15</sub> =	-1	0.03	0.36	0.98	1.39	1.52	1.47	1.32	1.13
1-C <sub>4</sub> H <sub>8</sub> + 1-C <sub>3</sub> H <sub>7</sub>	0	0.01	0.10	0.46	0.85	1.08	1.14	1.10	0.99
	1	0.00	0.02	0.14	0.38	0.62	0.76	0.81	0.79
	2	0.00	0.00	0.02	0.10	0.24	0.38	0.47	0.52
4-C <sub>7</sub> H <sub>15</sub> =	-1	0.03	0.24	0.73	1.10	1.19	1.09	0.91	0.73
1-C <sub>5</sub> H <sub>10</sub> + C <sub>2</sub> H <sub>5</sub>	0	0.00	0.07	0.31	0.63	0.81	0.82	0.75	0.65
	1	0.00	0.01	0.08	0.26	0.44	0.54	0.56	0.53
	2	0.00	0.00	0.01	0.06	0.15	0.25	0.32	0.35
3-C <sub>7</sub> H <sub>15</sub> =	-1	0.01	0.07	0.34	0.63	0.82	0.90	0.88	0.80
1-C <sub>7</sub> H <sub>15</sub> =	0	0.01	0.02	0.15	0.37	0.55	0.66	0.70	0.67
	1	0.01	0.01	0.04	0.16	0.30	0.42	0.49	0.52
	2	0.01	0.01	0.01	0.04	0.11	0.20	0.28	0.33
4-C <sub>7</sub> H <sub>15</sub> =	-1	0.01	0.14	0.53	0.92	1.07	1.03	0.89	0.73
1-C <sub>7</sub> H <sub>15</sub> =	0	0.01	0.04	0.23	0.53	0.72	0.78	0.73	0.65
	1	0.01	0.01	0.06	0.22	0.40	0.51	0.54	0.53
	2	0.01	0.01	0.01	0.05	0.14	0.24	0.31	0.35
2-C <sub>7</sub> H <sub>15</sub> =	-1	0.01	0.07	0.35	0.70	0.92	1.01	0.97	0.86
1-C <sub>7</sub> H <sub>15</sub> =	0	0.01	0.02	0.14	0.38	0.60	0.72	0.75	0.71
	1	0.01	0.01	0.03	0.15	0.31	0.44	0.52	0.54
	2	0.01	0.00	0.01	0.03	0.10	0.19	0.28	0.33
3-C <sub>7</sub> H <sub>15</sub> =	-1	0.01	0.15	0.57	0.95	1.15	1.20	1.13	1.00
2-C <sub>7</sub> H <sub>15</sub>	0	0.01	0.04	0.25	0.57	0.80	0.91	0.92	0.86
	1	0.01	0.01	0.07	0.25	0.45	0.59	0.66	0.67
	2	0.01	0.01	0.02	0.07	0.17	0.29	0.38	0.44
1-C <sub>7</sub> H <sub>15</sub> =	-1	-0.02	0.08	0.42	0.62	0.64	0.59	0.50	0.45
3-C <sub>7</sub> H <sub>15</sub>	0	-0.02	0.01	0.23	0.40	0.46	0.46	0.43	0.41
	1	-0.02	-0.01	0.09	0.21	0.28	0.32	0.34	0.35
	2	-0.02	-0.02	0.04	0.07	0.11	0.17	0.21	0.25
1-C <sub>7</sub> H <sub>15</sub> =	-1	-0.02	0.21	0.73	1.00	0.97	0.84	0.70	0.60
4-C <sub>7</sub> H <sub>15</sub>	0	-0.02	0.05	0.40	0.66	0.72	0.69	0.62	0.57
	1	-0.02	0.00	0.15	0.34	0.45	0.50	0.50	0.50
	2	-0.02	-0.01	0.05	0.12	0.19	0.27	0.33	0.37
1-C <sub>7</sub> H <sub>15</sub> =	-1	-0.05	0.10	0.49	0.71	0.73	0.66	0.56	0.49
2-C <sub>7</sub> H <sub>15</sub>	0	-0.05	0.00	0.26	0.46	0.52	0.52	0.48	0.45
	1	-0.05	-0.03	0.09	0.23	0.32	0.37	0.38	0.39
	2	-0.05	-0.03	0.03	0.07	0.12	0.19	0.24	0.28
2-C <sub>7</sub> H <sub>15</sub> =	-1	0.04	0.13	0.50	0.90	1.14	1.20	1.12	0.98
3-C <sub>7</sub> H <sub>15</sub>	0	0.03	0.05	0.21	0.51	0.75	0.87	0.89	0.82
	1	0.03	0.03	0.07	0.21	0.40	0.55	0.62	0.63
	2	0.03	0.02	0.02	0.06	0.14	0.25	0.34	0.40

Table 4b. Departures from high pressure behavior for reactions originating from 2-heptyl radical expressed as  $\log k_{\infty}/k$  at various pressures and temperatures.

Reaction	Log P	500	700	900	1100	1300	1500	1700	1900
1-C <sub>7</sub> H <sub>15</sub> = C <sub>2</sub> H <sub>4</sub> + 1-C <sub>5</sub> H <sub>11</sub>	-1	0.03	0.29	0.83	1.28	1.46	1.42	1.27	1.07
	0	0.01	0.07	0.34	0.72	0.96	1.05	1.01	0.90
	1	0.00	0.01	0.08	0.28	0.50	0.65	0.71	0.69
	2	0.00	0.00	0.01	0.05	0.16	0.28	0.38	0.43
2-C <sub>7</sub> H <sub>15</sub> = C <sub>3</sub> H <sub>6</sub> + 1-C <sub>4</sub> H <sub>9</sub>	-1	0.02	0.31	0.92	1.33	1.44	1.35	1.16	0.94
	0	0.01	0.09	0.45	0.84	1.03	1.05	0.97	0.83
	1	0.01	0.02	0.14	0.41	0.63	0.74	0.74	0.69
	2	0.01	0.01	0.03	0.12	0.28	0.41	0.49	0.50
3-C <sub>7</sub> H <sub>15</sub> = 1-C <sub>4</sub> H <sub>8</sub> + 1-C <sub>3</sub> H <sub>7</sub>	-1	0.02	0.25	0.76	1.24	1.48	1.51	1.38	1.15
	0	0.00	0.06	0.32	0.69	0.97	1.08	1.06	0.94
	1	0.00	0.01	0.09	0.28	0.51	0.67	0.73	0.71
	2	0.00	0.00	0.01	0.07	0.18	0.31	0.41	0.46
3-C <sub>7</sub> H <sub>15</sub> = 1-C <sub>4</sub> H <sub>8</sub> + 1-C <sub>3</sub> H <sub>7</sub>	-1	0.03	0.30	0.88	1.38	1.62	1.63	1.47	1.22
	0	0.01	0.08	0.38	0.78	1.07	1.18	1.14	1.01
	1	0.00	0.02	0.11	0.32	0.57	0.74	0.80	0.77
	2	0.00	0.00	0.02	0.08	0.20	0.35	0.45	0.50
4-C <sub>7</sub> H <sub>15</sub> = 1-C <sub>5</sub> H <sub>10</sub> + C <sub>2</sub> H <sub>5</sub>	-1	0.03	0.23	0.70	1.18	1.46	1.52	1.42	1.22
	0	0.00	0.06	0.28	0.62	0.91	1.05	1.06	0.97
	1	0.00	0.01	0.07	0.23	0.43	0.60	0.69	0.70
	2	0.00	0.00	0.01	0.04	0.12	0.23	0.33	0.40
3-C <sub>7</sub> H <sub>15</sub> = 1-C <sub>7</sub> H <sub>15</sub> =	-1	0.01	0.05	0.28	0.59	0.83	0.95	0.96	0.87
	0	0.01	0.02	0.11	0.32	0.53	0.67	0.72	0.69
	1	0.01	0.01	0.03	0.13	0.27	0.40	0.48	0.51
	2	0.01	0.01	0.01	0.03	0.09	0.18	0.26	0.32
4-C <sub>7</sub> H <sub>15</sub> = 1-C <sub>7</sub> H <sub>15</sub> =	-1	0.01	0.13	0.51	0.96	1.27	1.40	1.36	1.20
	0	0.01	0.04	0.21	0.52	0.80	0.97	1.01	0.96
	1	0.01	0.01	0.05	0.19	0.39	0.56	0.67	0.69
	2	0.01	0.01	0.01	0.04	0.11	0.22	0.33	0.40
2-C <sub>7</sub> H <sub>15</sub> = 1-C <sub>7</sub> H <sub>15</sub> =	-1	0.01	0.10	0.48	0.82	1.01	1.04	0.95	0.79
	0	0.01	0.03	0.22	0.51	0.71	0.79	0.77	0.69
	1	0.01	0.01	0.07	0.24	0.42	0.54	0.58	0.57
	2	0.01	0.00	0.01	0.07	0.19	0.30	0.37	0.41
3-C <sub>7</sub> H <sub>15</sub> = 2-C <sub>7</sub> H <sub>15</sub>	-1	0.01	0.11	0.49	0.91	1.19	1.30	1.25	1.08
	0	0.01	0.03	0.20	0.51	0.78	0.93	0.95	0.88
	1	0.01	0.01	0.06	0.21	0.41	0.57	0.66	0.66
	2	0.01	0.01	0.01	0.05	0.14	0.27	0.37	0.43
1-C <sub>7</sub> H <sub>15</sub> = 3-C <sub>7</sub> H <sub>15</sub>	-1	-0.02	0.03	0.29	0.52	0.72	0.80	0.80	0.77
	0	-0.02	-0.01	0.13	0.28	0.46	0.56	0.61	0.63
	1	-0.02	-0.02	0.05	0.09	0.22	0.33	0.41	0.48
	2	-0.02	-0.02	0.03	0.01	0.06	0.13	0.21	0.30
1-C <sub>7</sub> H <sub>15</sub> = 4-C <sub>7</sub> H <sub>15</sub>	-1	-0.02	0.12	0.57	0.94	1.18	1.22	1.15	1.04
	0	-0.02	0.01	0.25	0.52	0.77	0.89	0.90	0.88
	1	-0.02	-0.01	0.08	0.19	0.40	0.54	0.63	0.68
	2	-0.02	-0.01	0.03	0.03	0.12	0.23	0.33	0.43
1-C <sub>7</sub> H <sub>15</sub> = 2-C <sub>7</sub> H <sub>15</sub>	-1	-0.05	0.03	0.35	0.62	0.84	0.92	0.90	0.85
	0	-0.05	-0.02	0.14	0.33	0.53	0.65	0.69	0.70
	1	-0.05	-0.03	0.04	0.11	0.26	0.38	0.47	0.53
	2	-0.05	-0.03	0.02	0.00	0.06	0.15	0.24	0.33
2-C <sub>7</sub> H <sub>15</sub> = 3-C <sub>7</sub> H <sub>15</sub>	-1	0.04	0.18	0.65	1.04	1.22	1.22	1.08	0.90
	0	0.03	0.06	0.32	0.66	0.87	0.94	0.90	0.79
	1	0.03	0.03	0.11	0.32	0.53	0.66	0.69	0.66
	2	0.03	0.02	0.03	0.11	0.24	0.37	0.45	0.48

Table 4c. Departures from high pressure behavior for reactions originating from 3-heptyl radical expressed as  $\log k_{\infty}/k$  at various pressures and temperatures.

Reaction	Log P	500	700	900	1100	1300	1500	1700	1900
1-C <sub>7</sub> H <sub>15</sub> =	-1	0.03	0.35	0.94	1.36	1.48	1.44	1.29	1.10
C <sub>2</sub> H <sub>4</sub> + 1-C <sub>5</sub> H <sub>11</sub>	0	0.01	0.09	0.41	0.81	1.03	1.10	1.06	0.95
	1	0.00	0.01	0.11	0.33	0.56	0.71	0.76	0.74
	2	0.00	0.00	0.01	0.07	0.19	0.32	0.42	0.47
2-C <sub>7</sub> H <sub>15</sub> =	-1	0.02	0.24	0.74	1.21	1.46	1.50	1.37	1.14
C <sub>3</sub> H <sub>6</sub> + 1-C <sub>4</sub> H <sub>9</sub>	0	0.01	0.06	0.30	0.67	0.95	1.07	1.05	0.94
	1	0.01	0.01	0.08	0.26	0.49	0.65	0.72	0.71
	2	0.01	0.01	0.01	0.06	0.16	0.29	0.40	0.45
3-C <sub>7</sub> H <sub>15</sub> =	-1	0.02	0.33	0.96	1.35	1.44	1.34	1.14	0.92
1-C <sub>4</sub> H <sub>8</sub> + 1-C <sub>3</sub> H <sub>7</sub>	0	0.00	0.10	0.48	0.87	1.05	1.06	0.97	0.82
	1	0.00	0.02	0.16	0.45	0.67	0.76	0.76	0.70
	2	0.00	0.00	0.03	0.15	0.31	0.45	0.51	0.52
3-C <sub>7</sub> H <sub>15</sub> =	-1	0.03	0.39	1.08	1.48	1.55	1.43	1.21	0.98
1-C <sub>4</sub> H <sub>8</sub> + 1-C <sub>3</sub> H <sub>7</sub>	0	0.01	0.12	0.55	0.97	1.15	1.14	1.03	0.88
	1	0.00	0.02	0.19	0.50	0.74	0.83	0.82	0.75
	2	0.00	0.00	0.04	0.17	0.35	0.50	0.56	0.57
4-C <sub>7</sub> H <sub>15</sub> =	-1	0.03	0.24	0.73	1.21	1.47	1.53	1.44	1.25
1-C <sub>5</sub> H <sub>10</sub> + C <sub>2</sub> H <sub>5</sub>	0	0.00	0.06	0.30	0.66	0.94	1.08	1.10	1.02
	1	0.00	0.01	0.07	0.25	0.46	0.64	0.73	0.74
	2	0.00	0.00	0.01	0.05	0.13	0.25	0.36	0.43
3-C <sub>7</sub> H <sub>15</sub> =	-1	0.01	0.09	0.41	0.70	0.86	0.90	0.83	0.71
1-C <sub>7</sub> H <sub>15</sub> =	0	0.01	0.03	0.20	0.44	0.61	0.69	0.68	0.62
	1	0.01	0.01	0.06	0.22	0.38	0.48	0.52	0.51
	2	0.01	0.01	0.02	0.07	0.18	0.28	0.34	0.37
4-C <sub>7</sub> H <sub>15</sub> =	-1	0.01	0.14	0.53	0.99	1.29	1.41	1.38	1.23
1-C <sub>7</sub> H <sub>15</sub> =	0	0.01	0.04	0.22	0.55	0.83	1.00	1.05	1.00
	1	0.01	0.01	0.06	0.21	0.42	0.60	0.70	0.74
	2	0.01	0.01	0.01	0.04	0.12	0.24	0.35	0.43
2-C <sub>7</sub> H <sub>15</sub> =	-1	0.01	0.07	0.35	0.71	0.97	1.10	1.09	0.96
1-C <sub>7</sub> H <sub>15</sub> =	0	0.01	0.02	0.13	0.38	0.62	0.77	0.82	0.77
	1	0.01	0.01	0.03	0.14	0.32	0.46	0.55	0.57
	2	0.01	0.00	0.01	0.03	0.10	0.21	0.30	0.36
3-C <sub>7</sub> H <sub>15</sub> =	-1	0.01	0.17	0.65	1.03	1.19	1.18	1.05	0.87
2-C <sub>7</sub> H <sub>15</sub>	0	0.01	0.05	0.32	0.66	0.87	0.93	0.88	0.77
	1	0.01	0.01	0.11	0.34	0.55	0.66	0.69	0.65
	2	0.01	0.01	0.02	0.11	0.26	0.39	0.46	0.49
1-C <sub>7</sub> H <sub>15</sub> =	-1	-0.02	0.05	0.36	0.56	0.75	0.82	0.82	0.79
3-C <sub>7</sub> H <sub>15</sub>	0	-0.02	0.00	0.17	0.31	0.50	0.59	0.64	0.67
	1	-0.02	-0.01	0.06	0.11	0.26	0.36	0.44	0.51
	2	-0.02	-0.02	0.04	0.00	0.08	0.15	0.23	0.32
1-C <sub>7</sub> H <sub>15</sub> =	-1	-0.02	0.15	0.67	1.00	1.21	1.24	1.17	1.07
4-C <sub>7</sub> H <sub>15</sub>	0	-0.02	0.02	0.31	0.58	0.83	0.93	0.95	0.93
	1	-0.02	-0.01	0.10	0.23	0.44	0.59	0.68	0.73
	2	-0.02	-0.01	0.04	0.03	0.14	0.26	0.37	0.47
1-C <sub>7</sub> H <sub>15</sub> =	-1	-0.05	0.05	0.42	0.67	0.87	0.93	0.92	0.87
2-C <sub>7</sub> H <sub>15</sub>	0	-0.05	-0.02	0.19	0.37	0.58	0.68	0.72	0.74
	1	-0.05	-0.03	0.06	0.13	0.30	0.42	0.50	0.57
	2	-0.05	-0.03	0.03	0.00	0.08	0.17	0.26	0.36
2-C <sub>7</sub> H <sub>15</sub> =	-1	0.04	0.13	0.50	0.92	1.21	1.32	1.26	1.09
3-C <sub>7</sub> H <sub>15</sub>	0	0.03	0.05	0.21	0.51	0.78	0.94	0.97	0.89
	1	0.03	0.03	0.06	0.21	0.41	0.58	0.66	0.67
	2	0.03	0.02	0.02	0.05	0.14	0.26	0.37	0.43

Table 4d. Departures from high pressure behavior for reactions originating from 3-heptyl radical expressed as  $\log k_{\infty}/k$ .

Reaction	Log P	500	700	900	1100	1300	1500	1700	1900
1-C <sub>7</sub> H <sub>15</sub> =	-1	0.02	0.22	0.72	1.16	1.26	1.15	0.96	0.77
C <sub>2</sub> H <sub>4</sub> + 1-C <sub>5</sub> H <sub>11</sub>	0	0.00	0.03	0.27	0.64	0.85	0.88	0.80	0.68
	1	0.00	-0.01	0.03	0.23	0.44	0.57	0.59	0.56
	2	0.00	0.00	-0.01	0.03	0.13	0.25	0.33	0.37
2-C <sub>7</sub> H <sub>15</sub> =	-1	0.02	0.20	0.66	1.15	1.44	1.51	1.41	1.22
C <sub>3</sub> H <sub>6</sub> + 1-C <sub>4</sub> H <sub>9</sub>	0	0.01	0.05	0.27	0.61	0.90	1.04	1.05	0.97
	1	0.01	0.01	0.07	0.23	0.44	0.61	0.69	0.70
	2	0.01	0.01	0.01	0.05	0.14	0.25	0.35	0.41
3-C <sub>7</sub> H <sub>15</sub> =	-1	0.02	0.21	0.71	1.20	1.46	1.53	1.44	1.25
1-C <sub>4</sub> H <sub>8</sub> + 1-C <sub>3</sub> H <sub>7</sub>	0	0.00	0.06	0.30	0.67	0.95	1.09	1.10	1.02
	1	0.00	0.01	0.09	0.28	0.50	0.67	0.75	0.75
	2	0.00	0.00	0.02	0.07	0.18	0.30	0.40	0.46
3-C <sub>7</sub> H <sub>15</sub> =	-1	0.03	0.26	0.82	1.34	1.61	1.65	1.54	1.33
1-C <sub>4</sub> H <sub>8</sub> + 1-C <sub>3</sub> H <sub>7</sub>	0	0.01	0.07	0.36	0.76	1.06	1.20	1.19	1.10
	1	0.00	0.02	0.11	0.32	0.56	0.74	0.82	0.82
	2	0.00	0.00	0.02	0.09	0.20	0.34	0.44	0.50
4-C <sub>7</sub> H <sub>15</sub> =	-1	0.03	0.39	1.03	1.44	1.53	1.42	1.20	0.95
1-C <sub>5</sub> H <sub>10</sub> + C <sub>2</sub> H <sub>5</sub>	0	0.01	0.12	0.53	0.93	1.11	1.11	1.00	0.84
	1	0.00	0.02	0.18	0.48	0.70	0.80	0.78	0.71
	2	0.00	0.00	0.04	0.16	0.34	0.47	0.53	0.53
3-C <sub>7</sub> H <sub>15</sub> =	-1	0.01	0.04	0.26	0.57	0.81	0.95	0.99	0.93
1-C <sub>7</sub> H <sub>15</sub> =	0	0.01	0.01	0.11	0.31	0.52	0.67	0.74	0.73
	1	0.01	0.01	0.03	0.13	0.27	0.40	0.49	0.53
	2	0.01	0.01	0.01	0.03	0.10	0.18	0.26	0.31
4-C <sub>7</sub> H <sub>15</sub> =	-1	0.02	0.23	0.78	1.20	1.38	1.34	1.16	0.94
1-C <sub>7</sub> H <sub>15</sub> =	0	0.01	0.07	0.40	0.78	1.00	1.04	0.97	0.83
	1	0.01	0.02	0.14	0.41	0.63	0.75	0.76	0.70
	2	0.01	0.01	0.03	0.14	0.31	0.44	0.52	0.53
2-C <sub>7</sub> H <sub>15</sub> =	-1	0.01	0.06	0.31	0.66	0.94	1.10	1.11	1.01
1-C <sub>7</sub> H <sub>15</sub> =	0	0.01	0.02	0.12	0.35	0.58	0.75	0.81	0.79
	1	0.01	0.01	0.03	0.13	0.28	0.43	0.52	0.56
	2	0.01	0.00	0.01	0.03	0.09	0.17	0.26	0.32
3-C <sub>7</sub> H <sub>15</sub> =	-1	0.01	0.10	0.45	0.87	1.17	1.31	1.29	1.17
2-C <sub>7</sub> H <sub>15</sub>	0	0.01	0.03	0.19	0.49	0.76	0.93	0.99	0.95
	1	0.01	0.01	0.06	0.21	0.40	0.57	0.67	0.70
	2	0.01	0.01	0.02	0.06	0.15	0.26	0.36	0.43
1-C <sub>7</sub> H <sub>15</sub> =	-1	-0.02	0.00	0.25	0.47	0.64	0.68	0.63	0.57
3-C <sub>7</sub> H <sub>15</sub>	0	-0.02	-0.02	0.10	0.24	0.40	0.48	0.50	0.50
	1	-0.02	-0.02	0.04	0.07	0.20	0.29	0.35	0.39
	2	-0.02	-0.02	0.03	0.00	0.05	0.11	0.18	0.26
1-C <sub>7</sub> H <sub>15</sub> =	-1	-0.02	0.07	0.50	0.85	1.04	1.01	0.88	0.76
4-C <sub>7</sub> H <sub>15</sub>	0	-0.02	-0.01	0.20	0.46	0.68	0.75	0.72	0.68
	1	-0.02	-0.02	0.05	0.15	0.35	0.47	0.53	0.55
	2	-0.02	-0.02	0.03	0.01	0.09	0.20	0.29	0.37
1-C <sub>7</sub> H <sub>15</sub> =	-1	-0.05	0.00	0.29	0.56	0.74	0.77	0.70	0.63
2-C <sub>7</sub> H <sub>15</sub>	0	-0.05	-0.04	0.11	0.28	0.47	0.55	0.56	0.55
	1	-0.05	-0.04	0.03	0.08	0.23	0.33	0.39	0.43
	2	-0.05	-0.03	0.02	-0.01	0.05	0.13	0.21	0.28
2-C <sub>7</sub> H <sub>15</sub> =	-1	0.04	0.11	0.44	0.87	1.18	1.32	1.30	1.16
3-C <sub>7</sub> H <sub>15</sub>	0	0.03	0.04	0.18	0.47	0.74	0.91	0.96	0.92
	1	0.03	0.03	0.06	0.18	0.37	0.54	0.64	0.66
	2	0.03	0.02	0.02	0.05	0.12	0.23	0.32	0.39

never been described in any discussion of unimolecular chemical processes. It can be seen that at 1 bar, departures from high pressure behavior may be as large as an order of magnitude and thus must be considered. At 100 bar effects are much smaller and are probably within estimated uncertainties. Similar curves could be drawn for the various processes. Note that for reversible isomerization processes detailed balance does not necessarily apply.

The rate constants presented here are based on the measured branching ratios. The latter should have accuracies of 5 to 10%. The rate constants are referenced to those of the beta bond scission processes. These should have uncertainties of about 50%. The 1,4 and 1,5 H-transfer isomerization processes will have relative uncertainties of 10 to 20%. On an absolute basis they may have errors as large as 60 to 70%. We have discussed the problems with the rate constants for 1,6 H-transfer and 2-3 H-transfer isomerizations and assign an uncertainty of a factor of 2. For the fall-off behavior summarized in Tables 4a-d, the uncertainties in the step size down parameter is estimated to be a factor of 2. However, the pressure dependence is not large and the spread of results from such uncertainties simply involves changing the pressure scale. The important factor to remember is that in estimating the effect of uncertainties it is necessary to propagate them for all the reactions in question.

A disappointing feature of the result for heptyl radical is the relatively small changes in the departure from high pressure behavior in comparison to the situation for hexyl radicals. The larger size of the molecule is apparently partly compensated for by more reaction channels being opened up with increasing molecular size. This suggests that the molecular size must be considerably larger before pressure effects can be completely ignored. Thus it is still not possible to use a single rate expression to describe a particular process. Figure 6 shows a plot of the magnitude of the fall-off effect of the beta bond cleavage reaction from the four alkyl radicals that have now been studied. For the three larger compounds the reaction refers to the initial isomer being the 1-

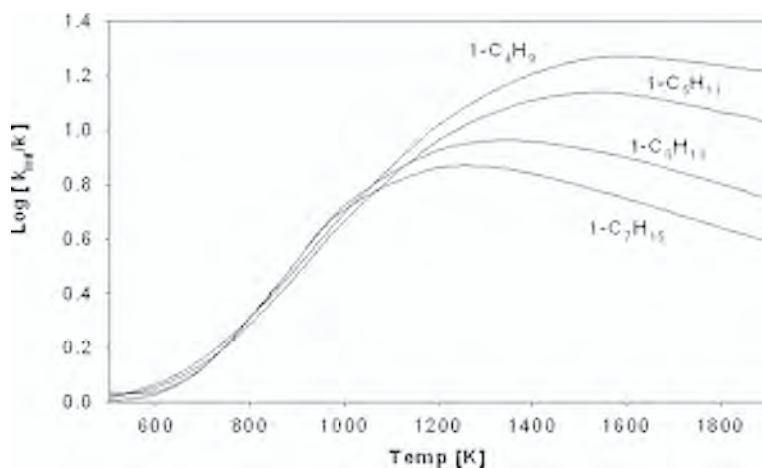


Figure 6. Departure from high pressure values for beta bond scission of 1-alkyl radicals. For  $C_5$  and higher the initial reactants are the 1-alkyl compounds.

alkyl radical. It is interesting that at the lower temperatures the fall-off behavior is equal to each other. The effect of molecular size only manifests itself at the higher temperatures. The former is due to the fact that as one approaches the high pressure limit the fall-off effects become less sensitive to molecular parameters in general. It also suggests that there are possibilities for simplifying the complex fall-off behavior that makes necessary the data in Table 4.

Finally, rate expressions are derived in order to provide a basis for applying results to related molecules. In addition it is necessary for the description of behavior at the lower temperatures where ignition phenomena are of importance. An important issue is the accuracy of the extrapolations. For higher temperatures, the lifetimes of the radicals become so short that oxidation reactions are no longer competitive. Thus for simulation processes under such conditions, the olefin yields can be used directly and indeed the radicals need not even be considered in the models. A very satisfactory feature of this study is the demonstration that the rate expressions from smaller linear alkyl radical can be directly carried over to the larger linear structures. Each addition of the chain length leads to new isomerization processes whose rate constants must be assigned. However as noted before it is highly likely that internal isomerization processes will become so dominant that larger ring structures for transition states can be ignored.

## 5. EXTENSIONS

The above discussion is indicative of the possibilities for deriving rate constants for the breakdown of components in complex fuel mixtures. The use of surrogates can provide some degree of simplification. It is clear that single pulse shock tube experiments will permit the determination of the cracking pattern for any type of fuel radical. For high temperature behavior this may be all that is needed for many applications. Within the model for any large fuel, many of the rate constants for the small radicals can apparently be carried over to larger structures. This forms the rationale for starting with small compounds and gradually building up to larger structures. The main scientific problems deal with the description of H-transfer isomerization processes. The number of such processes may however be limited and may not increase with molecular size.

Table 5 summarizes experimental results that have been obtained from single pulse shock tube experiments and for which rate constants have been derived. Referring to Table 1 it can be seen that the results now encompasses, linear hydrocarbons, branch hydrocarbons, olefins and cyclanes. Work on the former has largely been completed. Analysis of the data on larger radicals and those with branched structure is now underway. These are listed in Table 6. The olefins are not in Table 1. However, the 1-olefins are the immediate product from the decomposition of any alkyl radical. They are also the precursors for the dienes. The general trends in term of the olefinic products are discussed earlier. With methyl branching isobutene becomes an olefinic product. This brings branched structures such as in Fischer-Tropsch fuels into the picture. In all cases the analysis of the data reduces to the assignment of rate constants for the various isomerization processes. Special problems are posed by the possibility of parallel or serial isomerization processes. Under such circumstances the cracking patterns

Table 5. Radicals that have been studied using the single technique and results analyzed in terms of rate constants as discussed in text.

Source	Radicals created	Isomerization processes	Products (beta bond scission)
n-pentyl iodide	1-pentyl (a) 2-pentyl (b)	1-4 H-transfer (a)	Ethylene, n-propyl Propene, ethylene
n-hexyl iodide	1-hexyl (a) 2-hexyl, (b) 3-hexyl (c)	1-5 H-transfer (a) 1-4 H-transfer (a)	Ethylene, n-butyl Propene, N-propyl 1-butene ethyl 1-pentene methyl
n-heptyl iodide	1-heptyl (a) 2-heptyl, (b)  3-heptyl, (c)  4-heptyl (d)	1-6 H-transfer (a) 3-6 H-transfer (c) 1-5 H-transfer (a) 1-4 H-transfer (a)	Ethylene, n-pentyl Propene, n-butyl  1-butene, n-propyl 1-hexene,methyl 1-pentene, ethyl
1,7 octadiene	1-pentenyl-5 (a) Cyclopentyl (b)	Ring closing	Allyl + ethylene Cyclopentyl
1,8 nonadiene	1-hexenyl-6 Cyclohexyl 1-hexenyl-3 (c) Cyclopentyl-methyl (d)  2-hexenyl-1 (e) 3-methylcyclopentyl-1 5-hexenyl-2 2-methyl-4- pentenyl-1	Ring closing 1-4 H-transfer (b) Ring closing (b)  1-4 H-transfer (c) Ring closing (b) Ring opening (d) ring opening (d)	Ethylene, 1-butenyl-3 Cyclohexene 1,3-butadiene, ethyl Methylene cyclopentane 1,3-pentadiene,methyl  Propene, allyl Propene, allyl
t-butylcyclohexane	Cyclohexyl (a) 1-hexenyl-6 (b) 1-hexenyl-3 (c) Cyclopentyl-methyl (d)  2-hexenyl-1 (e) 3-methylcyclopentyl-1 5-hexenyl-2 2-methyl-4- pentenyl-1	Ring opening (a) 1-4 H-transfer (b) Ring closing (b)  1-4 H-transfer (c) Ring closing (b) Ring opening (d) ring opening (d)	Cyclohexene Ethylene, 1-butenyl-3 1,3butdiene, ethyl Methylene cyclopentane 1,3pentadiene, methyl  Propene, allyl Propene, allyl

from a single precursor do not yield unique results and recourse must be made to ancillary data or through studies using the initial reactant as a different isomer. It may well be that theory can play an important role for such situations. Finally, having defined the data for pyrolysis it is now possible to consider the oxidation processes through the addition of oxygen molecules into the reaction mixture and setting the conditions so that it will dominate the pyrolysis process. These are extremely important chemical activation reactions and have never been treated as such in combustion models.

Table 6. Radicals that have been studied using the single pulse shock tube technique and results being analyzed.

Source	Radicals created	Isomerization processes	Products (beta bond scission)
n-octyl iodide	1-octyl (a)		Ethylene, n-hexyl
	2-octyl, (b)	1-7 H-transfer (a)	Propene, n-pentyl
		3-7 H-transfer (c)	
	3-octyl, (c)	4-7 H-transfer (d)	1-butene, n-butyl
1-6 H-transfer (a)			
4-octyl (d)	2-6 H-transfer (b)	1-heptyl, methyl	
		1-4 H-transfer (a)	1-pentene, n-propyl
	1-5 H-transfer (b)	1-hexyl, ethyl	
1-iodo-3 methylbutane	3- methylbutyl-1 (a)		Ethylene, isopropyl
	2-imethylbutyl-1 (b)	1-4 H-transfer	Propene, ethyl 1-butene, methyl
1-iodo-4-methylpentane	4-methylpentyl-1 (a)		Ethylene, isobutyl
	2-methylpentyl-1 (b)	1-5 H-transfer (a)	Propene, n-propyl
			1-pentene, methyl
	2-methylpentyl-2 (c)	1-4 H-transfer (a)	isobutene, ethyl
4-methylpentyl-2 (d)	1-4 H-transfer (b)	propene isopropyl	
1-iodo-5-methylhexane	5-methylhexyl-1 (a)		Ethylene, 3-methylbutyl-1
	2-methylhexyl-1 (b)	1-6 H-transfer (a)	Propene, 1-butyl
			1-hexene, methyl
	2-methylhexyl-2 (c)	1-5 H-transfer (a)	isobutene, n-propyl
	2-methylhexyl-3 (d)	1-4 H-transfer (a)	hexene-2, methyl
			3-methylbutene-1, ethyl
2-methylhexyl-4 (e)	1,4 H-transfer (b)	2-methylpentyl-1, methyl	
2-methylhexyl-5 (f)	1,5 H-transfer (b) 2,5 H-transfer (c)	1-butene, isopropyl	
		propene, isobutyl	

## REFERENCES

1. J.T. Oden, T. Belytschko, J. Fish, T. J. R. Hughes, C. Johnson, D. Keyes, A. Laub, L. Petzold, D. Srolovitz, S. Yip, "Revolutionizing Engineering Science Through Simulations", A Report of the National Science Foundation Blue Ribbon Panel on Simulation-Based Engineering Science, May 2006, National Science Foundation.
2. R. J. Kee, M. E. Coltrin, P. Glarborg, Chemically Reacting Flow, Theory and Practice, Wiley, Interscience, New York, 2003.
3. I. Glassman, Combustion, 2nd ed. Academic Press, NY, 1987.
4. W. Tsang, J. H. Kiefer, Unimolecular Reactions of Large Polyatomic Molecules over Wide Ranges of Temperatures, World Scientific, Singapore, 1995.
5. R. W. Walker, in Reaction Kinetics, Vol 1, Chemical Society, London, 1974.
6. K. A. Holbrook, M. J. Pilling, S. H. Robertson, Unimolecular Reactions, John Wiley, 1996.

7. W. Tsang, V. Bedanov, M. R. Zachariah, *Berichte der Bunsen-Gesellschaft-Phys. Chem. Chem. Phys.* 101 (3) (1997) 491-499.
8. T. Edwards, W. E. Harrison III, L. Q. Maurice, AIAA 2001-0498, 39th AIAA Aerospace Sciences Meeting and Exhibit, January 8-11, 2001 Reno.
9. M. Colket, C. T. Edward, S. Williams, N. P. Cernansky, D. L. Miller, F. Egolfopoulos, P. Lindstedt, K. Seshadri, F. L. Dryer, C. K. Law, D. Friend, D. B. Lenhart, H. Pitsc, A. Sarofim, M. Smooke, W. Tsang, 45th AIAA Aerospace Sciences Meeting and Exhibit, Reno, Nevada, January 9, 2007.
10. H. J. Curran, P. Gaffuri, W. J. Pitz, C. K. Westbrook, *Combust. Flame* 114 (1998) 149.
11. R.P. Lindstedt, L.Q. Maurice, *Combust. Sci. Technol.* 107 (1995) 317-353.
12. A.E. Bakali, J-L. Delfau, C. Vovelle, *Combust. Flame* 118 (1999) 381-389.
13. G. Bikas, N. Peters, *Combust. Flame* 126 (2001) 1456-1475.
14. R. Fournet, V. Warth, P.A. Glaude, F. Battin-Leclerc, G. Scacchi, G.M. Come, *Int. J. Chem. Kinet.* 32 (2000) 36-51.
15. G. P. Smith, D. M. Golden, M. Frenklach, N. W. Moriarty, B. Eiteneer, M. Goldenberg, C. T. Bowman, R. K. Hanson, S. Song, W. C. Gardiner Jr., V. V. Lissianski, Z. Qin, [http://www.me.berkeley.edu/gri\\_mech/](http://www.me.berkeley.edu/gri_mech/).
16. J. Appel, H. Bockhorn, M. Frenklach, *Combust. Flame* 121 (2000) 122-136.
17. S. Kazakov, H. Wang, M. Frenklach, *Combust. Flame*, 100 (1995) 111-120.
18. H. Richter, J.B. Howard, *Prog. Energ. Combust.* 4 (2000) 565-608.
19. J.A. Kerr, M. J. Parsonage, *Evaluated Kinetic Data on Gas Phase Addition Reactions, Reactions of Atoms and Radicals with Alkenes, Alkynes and Aromatic Compounds*, CRC Press, 18901 Cranwood.
20. S. W. Benson, *Thermochemical Kinetics*, John Wiley and Sons, New York, 1974.
21. W. Tsang, J. A. Walker, J.A. Manion, 31st Symp. Comb. 158-166, 1006.
22. H. M. Frey, R. Walsh, *Chem. Rev.* 69 (1969) 103-124.
23. E. A. Hardwidge, C. W. Larson, B. S. Rabinovitch, *J. Amer. Chem. Soc.* 92 (1970) 3278-3283.
24. W. Tsang, A. Lifshitz, in *Part III Chemical Reactions in Shock Waves*, Academic Press, New York, 2001, p. 108-193.
25. W. Tsang, AIAA-2001-0359, 39th AIAA Aerospace Sciences Meeting and Exhibit, January 8-11, 2001, Reno.
26. V. D. Knyazev, I. R. Slagle, *J. Phys. Chem.* 100 (1996) 5318-5328.
27. E. S. Swinbourne, *J. Chem. Soc.* (1960) 4668-4671.
28. Certain commercial materials and equipment are identified in this paper in order to specify adequately the experimental procedure. In no case does such identification imply recommendation or endorsement by the National Institute of Standards and Technology, nor does it imply that the material or equipment is necessarily the best available for the purpose.

# Role of diacetylene in soot formation

A. Raman, R. Sivaramakrishnan, K. Brezinsky

*Departments of Chemical, Mechanical and Industrial engineering*

*University of Illinois at Chicago*

*Chicago, IL-60607*

*Kenbrez@uic.edu*

The initial step in the study of formation of soot involves examining the formation of the first and second aromatic ring, which represent the key rate limiting steps and building blocks that form soot. Hansen et al., [1] from results of their recent flame studies, state that the key proposed pathways to the formation of the first aromatic ring generally involve reactions of unsaturated hydrocarbon radicals (and/or resonance stabilized free radicals). Hansen et al. [1] also note that there is considerable uncertainty as to the relative importance of various pathways involving different radicals. The even numbered carbon addition mechanism ( $C_2+C_4$ ) has been overlooked in favor of the odd numbered carbon addition mechanism ( $C_3+C_3$ ) viz., the propargyl recombination which has received considerable attention from experimentalists and theoreticians alike over the past decade [2].

Richter and Howard [3] in their article have reviewed potentially important mechanistic steps involving even numbered carbon additions that lead to soot. These steps essentially involve the addition of linear acetylene, diacetylene and their radicals that eventually cyclize to aromatics. Many of these theorized pathways have not been explored experimentally, specifically under practical high pressure conditions wherein  $C_2$  and  $C_4$  radicals can be potentially long lived and subsequently react with other radicals and stable species. Recent flame studies [1] provide evidence for the presence of abundant concentrations of such  $C_4$  radicals, the  $i-C_4H_3$  and  $i-C_4H_5$  radicals. This information coupled with the revised thermodynamic properties (for these radicals) based on high level theoretical methods [4] that lead to lower addition barriers for these radicals with acetylene suggest the even carbon addition mechanism to be a potentially dominant route to cyclization and eventually soot formation.

Cyclization to form the first and second aromatic ring, though the most significant channel, is not the only theorized pathway for soot formation. Soot formation could also occur through formation of large carbon polymer chains, such as polyynes and the formation of fairly large aromatic clusters from large polyne chains through the mechanism proposed by Bockhorn [5]. In order to better evaluate the importance of these alternate pathways to soot, experimental data at high pressures on  $C_2$  and  $C_4$  species are essential. The absence of these data has motivated our current single pulse shock tube study on the pyrolysis of diacetylene at high pressures. Prior experimental work on the pyrolysis of diacetylene span a relatively low pressure range from 0.5 to 2.6 atm, with only two of the experimental studies, Kiefer et al. [7] and Hidaka et al. [8], resulting in a chemical kinetic model. These prior experiments and their modeling represent a good starting point to understand the relevance of the even carbon addi-

tion mechanism but it is clear that data at high pressures are essential to test the importance of radical stabilization.

To develop a chemical kinetic model for diacetylene which would accurately describe its role in high pressure soot formation, experimental data were obtained over a wide range of pressures, temperatures and initial diacetylene concentrations. The high pressure single pulse shock facility at UIC [9] was used to obtain experimental data for the pyrolysis of diacetylene at pressures ranging from 35 to 300 atm, temperatures ranging from 1050 -1800 K and initial diacetylene mole fractions ranging from 5-400 ppm. The shock tube was operated in two configurations, one with the shock tube heated to  $100\pm 2^\circ\text{C}$  and another without any external heating to the shock tube. Heating of the shock tube was carried out to avoid potential condensation of the fuel as well as the heavy polyne and aromatic intermediates that can potentially form. Diacetylene, a highly unstable molecule is not available commercially and an essential part of this work involved synthesizing diacetylene with a high purity. A synthesis [10] provided diacetylene of the required purity. The products and intermediates from shock heated diacetylene were analyzed using GC, GC/MS techniques. The primary intermediates observed in our analyses were  $\text{C}_2\text{H}_2$ ,  $\text{C}_6\text{H}_2$ ,  $\text{H}_2$  with trace quantities of  $\text{C}_4\text{H}_4$  (vinylacetylene),  $\text{C}_6\text{H}_6$  (benzene), *a*- $\text{C}_3\text{H}_4$  and *p*- $\text{C}_3\text{H}_4$ .

$\text{C}_2\text{H}_2$  was observed as the major intermediate along with  $\text{C}_6\text{H}_2$  at reflected shock pressures ranging from 35 atm to 100 atm. At 300 atm,  $\text{C}_2\text{H}_2$  remained the dominant species but only trace quantities of  $\text{C}_6\text{H}_2$  were observed. A carbon balance revealed that the carbon recovered in post shock sample decreased with an increase in temperature and this phenomenon was more pronounced for the 300 atm experiments. To account for the poor carbon recovery we examined the walls of the shock tube, which had a distinct coloration and odor consistent with the formation of potentially large aromatic species. The coloration became more prominent at high temperatures, high initial concentration and high pressures indicative of large molecule formation under these conditions. In the 300 atm experiments the amount of  $\text{C}_6\text{H}_2$  was close to 1 ppm at its maximum, while trace quantities of  $\text{C}_4\text{H}_4$  were detected in the post shock samples, indicating a potential shift in the chemistry away from these smaller addition products to larger ones.

The experimental data obtained over such a wide range of pressure and temperature conditions were then simulated using two comprehensive chemical kinetic models proposed by Kiefer et al. [6] and Hidaka et al. [7]. The Kiefer et al. and Hidaka et al. mechanisms were developed against experimental data obtained at much lower pressure conditions. These mechanisms when tested against our experimental data, did not predict experimentally observed  $\text{C}_4\text{H}_2$  decomposition, since these models lacked key chemical species (for example,  $\text{C}_6\text{H}_2$  and the *i*- $\text{C}_4\text{H}_3$  isomer) and their associated pathways of relevance to diacetylene pyrolysis. Even though both the Kiefer et al. and Hidaka et al. models failed to predict experimentally observed  $\text{C}_4\text{H}_2$  decomposition, the Kiefer et al. model contained essential polyne steps necessary to build a comprehensive mechanism. In addition to this Kiefer et al. previously examined benzene decomposition where routes involving diacetylene were hypothesized. Hence the Kiefer et al. mechanism was used a basis to develop a comprehensive kinetic model. We have added a series of steps summarized below that better reflect our and current understanding of essential chemical pathways relevant in the high pressure pyrolysis of diacetylene.

1. Pressure dependent rate coefficients for  $\text{H} + \text{C}_4\text{H}_2 \rightleftharpoons \text{n, i-C}_4\text{H}_3$ , reported by Miller and Klippenstein.
2. Reaction steps involving the addition of  $\text{C}_2\text{H}_2$  and  $\text{C}_2\text{H}_3$  to n, i- $\text{C}_4\text{H}_3$  and  $\text{C}_4\text{H}_5$  isomers [11], to form phenyl and benzene, as in the HACA mechanism.
3. Reaction steps involving  $\text{C}_4\text{H}_5$  leading to the formation of fulvene.
4. Reaction steps involving the addition of  $\text{C}_{2n}\text{H}$  and  $\text{C}_{2n}\text{H}_2$  to  $\text{C}_{2n}\text{H}_3$  leading to the formation of polyynes
5. Reaction pathways leading to the formation of  $\text{C}_{10}\text{H}_2$ .
6. Updated rate coefficients for reactions involving acetylene and some modifications to account for elevated pressure and temperature conditions in our experiments.

In addition to updating rate coefficients and adding new chemical pathways, the high pressure diacetylene (HPDA) model was also tuned with updated thermochemistry for several polyyne and radical species. The high pressure diacetylene model thus developed was able to accurately simulate data obtained at 50 atm and 100 atm. The salient feature of this model was the good polyyne predictions for the entire data set.

Sensitivity analysis was performed using the high pressure diacetylene mechanism to highlight the important routes involved in diacetylene pyrolysis. The reaction with the new rate coefficient determined by Miller and Klippenstein for the addition of H to  $\text{C}_4\text{H}_2$  to form i- $\text{C}_4\text{H}_3$  was shown to be a dominant pathway to  $\text{C}_4\text{H}_2$  decomposition. In addition,  $\text{C}_4\text{H}_2 + \text{i-C}_4\text{H}_3 \rightleftharpoons \text{C}_6\text{H}_2 + \text{C}_2\text{H}_3$ , also provided a significant pathway for  $\text{C}_4\text{H}_2$  disappearance. In the case of 300 atm experiments at  $T > 1550$  K, the high pressure, HPDA, model over predicted the  $\text{C}_2\text{H}_2$  concentration while under predicting the  $\text{C}_4\text{H}_2$  concentration in the same temperature region. This observation along with the poor carbon balance, suggested that in this temperature region the pathways for consumption of acetylene and  $\text{C}_4\text{H}_2$  needs to be better characterized.

To obtain a quantitative picture of the contribution of the different reactions steps included in the high pressure diacetylene mechanism, a rate of production analysis was performed. The rate of production analysis showed that polyyne routes leading to the formation of  $\text{C}_6\text{H}_2$ , the species that Bockhorn proposed to play a role in the formation of phenyl acetylene and its subsequent growth to larger hydrocarbons, contributed to 45% of  $\text{C}_4\text{H}_2$  decomposition. While the H addition to  $\text{C}_4\text{H}_2$  to form i- $\text{C}_4\text{H}_3$ , another species which has been recently postulated to be involved in the formation of the first aromatic ring, contributes to 45% of the diacetylene decay.

The HPDA mechanism developed in this work was able to accurately simulate experimental data obtained at 50 atm and 100 atm although the HPDA mechanism under predicted the decomposition of  $\text{C}_4\text{H}_2$  at the higher pressure of 300 atm and over predicted the formation of  $\text{C}_2\text{H}_2$  at high temperatures. A detailed chemical pathway which would involve reaction between i- $\text{C}_4\text{H}_3$  and  $\text{C}_2\text{H}_2$  would probably reconcile these discrepancies. The discrepancies are most likely due to the formation of heavy polyynes and aromatic species which were undetected because of condensation on the walls of the shock tube. A detailed examination of these reactions would also give credence to the role of diacetylene in forming the first aromatic ring, subsequently leading to the formation of soot.

**REFERENCES**

1. N. Hansen, S.J. Klippenstein, C.A. Taatjes, J.A. Miller, J. Wang, T.A. Cool, B. Yang, L. Wei, C. Huang, J. Wang, F. Qi, M.E. Law, P.R. Westmoreland, *J. Phys. Chem. A* (110) (2006) 3670-3678.
2. W. Tang, R. S. Tranter, K. Brezinsky, *J. Phys. Chem. A* 110 (2006) 2165.
3. H. Richter, J. B. Howard, *Prog. Ener. Comb. Sci.* 26 (2000) 565-608.
4. S.J. Klippenstein, J.A. Miller, *J. Phys. Chem* (109) (2005) 4285-4295.
5. H. Bockhorn (Ed.) *Soot formation in combustion: mechanisms and models*, Berlin, Springer, 1994.
6. M. Frenklach, *Phys. Chem. Chem. Phys.* 4 (2002) 2028-2037.
7. J.H. Kiefer, S.S. Sidhu, R.D. Kern, K. Xie, H. Chen, L.B. Harding, *Combust. Sci. Technol.* 82 (1992) 101-130.
8. Y. Hidaka, Y. Henmi, T. Ohonishi, T. Okuno, T. Koike, *Combust. Flame* 130 (2002) 62-82.
9. R.S. Tranter, D. Fulle, K. Brezinsky, *Rev. Sci. Inst.* 72 (2001) 3046.
10. H. Hopf, personal communication.
11. J. P. Senosiain, J. A. Miller, *J. Phys. Chem.* (2007).

# Opportunities and issues in chemical analysis of premixed, fuel-rich low-pressure flames of hydrocarbon and oxygenate fuels using in situ mass spectrometry

K. Kohse-Höinghaus<sup>1</sup>, T. Kasper<sup>1,2</sup>, P. Oßwald<sup>1</sup>, U. Struckmeier<sup>1</sup>,  
N. Hansen<sup>2</sup>, T.A. Cool<sup>3</sup>, J. Wang<sup>3</sup>, F. Qi<sup>4</sup>, P.R. Westmoreland<sup>5</sup>

<sup>1</sup> Department of Chemistry, Bielefeld University, Universitätsstraße 25, D-33615 Bielefeld, Germany

<sup>2</sup> Combustion Research Facility, Sandia National Laboratories, Livermore, CA 94551, USA

<sup>3</sup> School of Applied and Engineering Physics, Cornell University, Ithaca, NY 14853, USA

<sup>4</sup> National Synchrotron Radiation Laboratory, University of Science and Technology of China, Hefei, Anhui 230029, P. R. China

<sup>5</sup> Department of Chemical Engineering, University of Massachusetts, Amherst, MA 01003, USA

*Abstract: A rich pool of minor species, including radicals, is assumed to be important for the detailed chemical reaction network in the molecular phase which precedes the formation of polycyclic aromatic hydrocarbons (PAH) and soot. For a realistic simulation of fuel-rich chemistry in hydrocarbon- and oxygenate-fuelled flames, the development and validation of respective models requires interaction with reliable experiments. One useful environment to study fuel-rich chemistry is a premixed low-pressure flame, where major and intermediate species concentrations can be obtained experimentally with good spatial resolution. Here, we focus on molecular beam mass spectrometric (MBMS) techniques, which are applied in situ to measure the chemical composition in low-pressure flames of different neat fuels and fuel blends, including hydrocarbons, alcohols, ethers and esters. Three different ionization techniques are employed, including resonance-enhanced multi-photon ionization (REMPI), electron ionization (EI), and vacuum ultraviolet photoionization (VUV-PI) using tunable synchrotron radiation. We concentrate here on several aspects of these studies. A large part of this article is devoted to a discussion of quantitative measurements and typical error limits, especially regarding intermediate species. Further, we focus on concentration measurements of intermediates which are assumed to be involved in the formation of the first and second ring from aliphatic fuels. Strategies are now available to provide isomer-specific information from the study of flames burning hydrocarbon and oxygenate fuels and mixtures thereof – information which is only partially reflected in present flame models.*

## 1. INTRODUCTION

Because of their perceived potential to reduce undesired combustion emissions, bio-fuels are discussed as one alternative to conventional hydrocarbon fuels of fossil origin [1]. Fuels obtained from biological sources, e.g. plant matter or organic waste, are thought to have a beneficial impact on the emission of carbon dioxide from combu-

stion devices. They are also being used or discussed as oxygenated additives of neat fuels, since they may decrease the emission of particulate matter. To assess their emission potential, however, either as a neat fuel or as fuel additive, more detailed investigation of their combustion chemistry is highly desirable. A huge body of information on hydrocarbon combustion chemistry is available, including the results of decades of collaborative work of experimental and modelling groups. They have studied aliphatic and aromatic hydrocarbon fuel decomposition and oxidation and investigated the mechanism of soot formation in shock tubes, flow reactors, flames, rapid compression machines and other reactive combustion environments; important aspects of hydrocarbon combustion can now be reliably modelled and predicted. In contrast, similarly detailed studies of oxygenated fuels are comparatively rare. Many features in oxygenated fuel combustion chemistry should, of course, be quite similar – small hydrocarbon radicals will be formed in the decomposition process, and the build-up of larger hydrocarbon molecules including aromatic structures, polycyclic aromatic hydrocarbons (PAH) and soot may potentially proceed from the same hydrocarbon intermediates. The pool of active intermediate species will depend to a certain extent on the fuel structure, however, and the additional functional groups in the oxygen-containing fuel molecule will give rise to new sets of intermediates and reaction products that may not be formed or not be of similar importance in hydrocarbon combustion. In particular, the formation of aldehydes, including formaldehyde and acetaldehyde, needs further study since these are hazardous air pollutants.

In recent years, our groups have contributed to the investigation of several aspects of fuel-rich flame chemistry in hydrocarbon and oxygenate fuel flames and fuel blends as part of an ongoing collaboration. Detailed studies have been performed to measure quantitative concentrations of families of flame species, including main constituents as well as stable and radical intermediates. To facilitate comparison with chemical-kinetic modelling, premixed, one-dimensional flames have been studied, mostly at low pressures around 50 mbar. The emphasis in our experiments has been on the molecular phase preceding soot; thus, stoichiometries have been selected which permit formation of small aromatic compounds from aliphatic fuels, but do not produce soot. Flames of oxygenated fuels have been studied using similar stoichiometries. Since the development and optimization of chemical reaction mechanisms will depend on reliable experimental information, the emphasis is to determine quantitative species concentration profiles. The experimental strategies will thus be discussed in light of potential sources for measurement errors. The discussion will concentrate on the chemistry in the molecular phase that precedes PAH and soot formation with an additional focus on the role of isomer-specific information.

## 2. QUANTITATIVE SPECIES CONCENTRATION PROFILES

Quantitative measurements of intermediate species in flames have a long tradition, with laser spectroscopy as one of the major instruments for the detection of small radicals. Laser-induced fluorescence (LIF), cavity ringdown spectroscopy (CRDS), degenerate four-wave mixing (DFWM) and other sensitive laser spectroscopic techniques and their specific advantages and applications have been discussed in textbooks

and reviews [2-5]. Under low-pressure premixed fuel-rich flame conditions, these non-invasive spectroscopic techniques are very useful to measure the flame temperature and concentrations of some smaller radicals. As a more generally suited technique, molecular beam mass spectrometry (MBMS) has been developed [6-12], which probes the flame by means of an invasive sampling nozzle. The gas sample is introduced into a mass spectrometer with special care to quench further reaction and avoid fragmentation. Several strategies for ionization have been used in this work, including electron ionization (EI), resonance-enhanced multi-photon ionization (REMPI) and vacuum ultraviolet photoionization (VUV-PI).

Coupling laser diagnostics and mass spectrometry permits an extensive species pool analysis. In fuel-rich, non-sooting low-pressure flames, such strategies have been used to investigate the molecular precursor phase of larger PAH and soot [13,14]. The flame front under these conditions is especially rich in hydrocarbon radicals which may be involved in the build-up of higher molecular rich structures. The detection of a certain species, however, does not provide information about its importance in the process. The species profiles are thus typically compared with full simulations of the entire reaction network up to benzene and beyond. Many details about the formation of the first aromatic ring in flames have been obtained using this approach.

## 2.1. Temperature

If a model is to be developed, extended and validated on the basis of measured species profiles, the measurements are expected to provide optimum reliability. For such a comparison of experiment and model, the analysis typically includes measurement of an accurate temperature profile (from fresh to burnt gases): the temperature rise throughout the flame zone is particularly important, and flames stabilized on water-cooled disk-shaped burners as in this study will not attain fully the temperature calculated from adiabatic equilibrium. If a series of stoichiometries for the same fuel is studied without changing the mass flow, the stand-off distance of the flame front to the burner may be different, leading to different cooling effects; e.g. the flame front in a stoichiometric flame is closer to the burner surface than in a fuel-rich flame and is therefore subjected to larger cooling by the burner. Temperature measurement strategies and their implications have been discussed in the literature [2,15,16]. In the fuel-rich, premixed, laminar low-pressure flames discussed here, the temperature profile has mostly been obtained by LIF of OH or of seeded molecules such as NO following the approach described in [17] or, more sensitively, by CRDS of OH as detailed in [18]. The typical error is  $\leq 80$  K at a flame temperature of  $\geq 2000$  K. Especially high precision can be obtained in NO-LIF temperature measurements with fits to multiple spectral lines, using extended spectroscopic databases and appropriate fitting routines [19]; here, the procedure by Atakan et al. was adopted [19b]. In combination with species profiles from MBMS measurements, however, it may be problematic that a non-invasive optical temperature measurement is usually performed without the presence of a sampling nozzle [20,21]. To compare with modelling, it must thus be determined whether a shift of the measured species profiles will account quantitatively for such probe effects, a procedure which may be questioned [21]. Temperature is often also measured by thermocouples,

where care must be taken to avoid catalytic effects and to correct for radiative and other heat losses. Recently, it has been demonstrated that thermocouples coated with a thin alumina layer by chemical vapor deposition (CVD) can provide results in close agreement with optical methods in some of the flames studied here [22].

## 2.2. Species profiles

Similar care is required for the quantification of species concentrations, and protocols to achieve accurate data have been developed, often independently, in many laboratories. For LIF measurements, the data evaluation needs accurate, quantitative fluorescence quantum yields, and for CRDS and other absorption techniques, the respective absorption coefficient must be known quantitatively. The mass spectrometric measurement can rely on calibration gases for stable molecules, but such procedures are not feasible for radicals. The absolute calibration will need a cross section for the specific ionization process (i.e. for electrons or photons), and it must accommodate insufficient mass resolution/partial overlap, fragmentation, auto-ionization resonances, and other potentially problematic influences. Also, mass discrimination factors (due to different radial velocities of the species) and a temperature-dependent sampling function (considering changing gas density) may have to be taken into account. Often, it may be helpful to calibrate a radical with respect to a related stable species, using procedures given in the literature [6-12]. Despite all efforts devoted to calibration issues, results of different techniques may be in “excellent” agreement if they deviate by only 20-30%, and “quite good” agreement may still be claimed if the results agree within a factor of 3. This seems reasonable for the combined error regarding radicals that are quantified using estimated cross sections for both electron ionization and VUV photoionization. Uncertainties of this order should be kept in mind when comparing measured, potentially “shifted” profiles to simulation/modelling results with the aim to verify chemical-kinetic model assumptions.

## 2.3. “Standard” flame conditions and typical uncertainties

We have adopted several precautions in our strategy to provide quantitative results on fuel-rich combustion chemistry. One useful approach is to define “standard” flame conditions which are repeatedly re-investigated whenever changes in the experimental apparatus or procedures are performed, or when nominally identical flame conditions are studied in different set-ups or laboratories. A fuel-rich low-pressure propene-oxygen-argon flame with a C/O ratio of 0.77 [23] has been used for this purpose in our laboratory, and the resulting intermediate species concentrations have typically shown agreement of a factor of two or better. To investigate more than one stoichiometry for the same fuel extends the basis for a potential model comparison. As an example in a propene-oxygen-argon (25%) flame at 40 mbar with a C/O ratio of 0.5, Figure 1 presents a quantitative comparison of several species mole fraction profiles resulting from VUV-PI measurements at two different measurement cycles. Identical equipment was used in both measurement periods, and data acquisition and evaluation procedures were kept unchanged.

Figure 1 presents three important species which are involved in the build-up of hydrocarbon structures: acetylene ( $C_2H_2$ ), propargyl radical ( $C_3H_3$ ), and benzene ( $C_6H_6$ ); all can be calibrated using known ionization cross sections, fulvene concentration was below the detection limit. It is noted that acetylene persists beyond the flame front with a non-zero concentration in the burnt gas up to about 8-9 mm, and it may be involved in the reactions toward larger hydrocarbon structures in this broad range, while propargyl and benzene are exclusively found in the flame front with a maximum near 3.5 mm and negligible mole fractions above 5 mm. The shape of both sets of curves in Figure 1 agrees quite well, but there are differences on the absolute scale which need further explanation. The differences for acetylene are within less than 10%, for benzene, the agreement is within about 30%, and the agreement for propargyl is within about 50%. The error bars for the measurement are indicated, and in each case, the results agree considering combined errors. Several features in Figure 1 should be noted to appreciate this result. First, acetylene is present in the highest concentrations (in the percent level) of the three species, while maximum benzene mole fractions are a few tens of ppm in this not

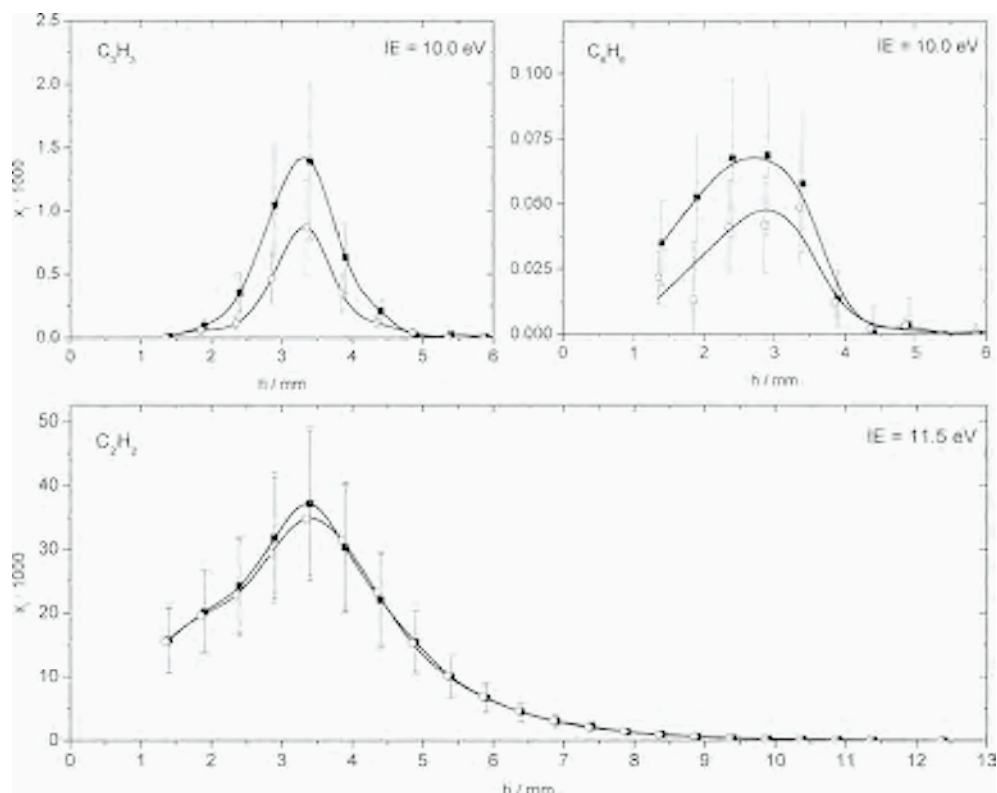


Figure 1. Quantitative species profiles in a C/O=0.5 propene-oxygen-argon (25%) flame at 40 mbar; measurements were obtained under nominally identical conditions during two different measurement cycles with VUV-PI-MBMS. Top left: propargyl radical, top right: benzene, bottom: acetylene.

overly rich flame, which is close to the typical detection limit. Propargyl radicals attain maximum mole fractions of about 100 ppm. Thus, signal-to-noise ratio is different and plays a significant role. The ionization energy must be chosen as a compromise regarding different ionization potentials, achievable signal strength and potential fragmentation.

Second, it is interesting to consider the nominal error in the experimental conditions and calibration procedures. Typical errors in the stoichiometry (flow controller settings with up to 5% stated accuracy per individual gas flow, if gas correction factors are used) may amount to about 10%, photodiode calibration was estimated with 5% error, mass discrimination factors were determined from the two different runs with 15% uncertainty, temperature-dependent sampling functions which reflect the changing gas density are within about 15% uncertainty, and ionization cross sections are assumed to be known within 20%. An error analysis for repeated, careful measurements with the same apparatus reveals that 30% deviation for “well-behaved” species is not unexpected. Errors may be larger for smaller signal-to-noise ratios (lower species concentrations or lower cross sections), or when fragmentation or poorer mass resolution have to be taken into account. The almost perfect agreement in the case of acetylene in Figure 1 may thus seem somewhat fortuitous and is linked to the fact that  $C_2H_2$  concentrations do not change dramatically with the flame parameters. Also, if a cross section must be estimated, or if isomers cannot be fully resolved, the measurements will exhibit accordingly larger error limits.

#### 2.4. Comparison of different MBMS techniques, role of mass and energy resolution

Knowledge of experimental accuracy, as demonstrated above for repeated measurements using a single set-up, can provide important guidance when comparing model calculations with experimental profiles, especially if kinetic parameters such as rate coefficients and their temperature dependences are varied to match the measured concentrations. It is similarly instructive to compare results for the same species under nominally identical flame conditions with different MBMS techniques. Such comparisons have been reported in [24], for example, where benzene concentrations in a C/O 0.77 propene-oxygen-argon flame are seen to agree within about 30% between EI-MBMS and VUV-PI-MBMS; the mole fraction has recently been confirmed also by REMPI-MBMS [25]. The different techniques and instruments exhibit complementary advantages and drawbacks, especially regarding energy and mass resolution. In the EI experiments, the mass resolution is  $m/\Delta m \approx 3000$ , enabled by a time-of-flight (TOF) instrument with reflectron, while it is  $\approx 400$ -600 for the linear instrument using VUV-PI. The energy distribution in the former experiment is quite broad, enabling detection of all species including Ar at a nominal ionization energy of 10.5 eV, while the energy resolution is  $\Delta E$  (*FWHM*)  $\approx 40$  meV in the latter. The requirements for unambiguous species identification and quantitative interpretation of the mass spectra are even more acute when studying oxygenate flames, since numerous oxygenated intermediates will lead to additional features and potential overlaps.

The effect of mass resolution is illustrated in Figure 2 where a spectrum near a mass-to-charge ratio  $m/z$  of 44 is displayed for EI (top row) and VUV-PI (bottom

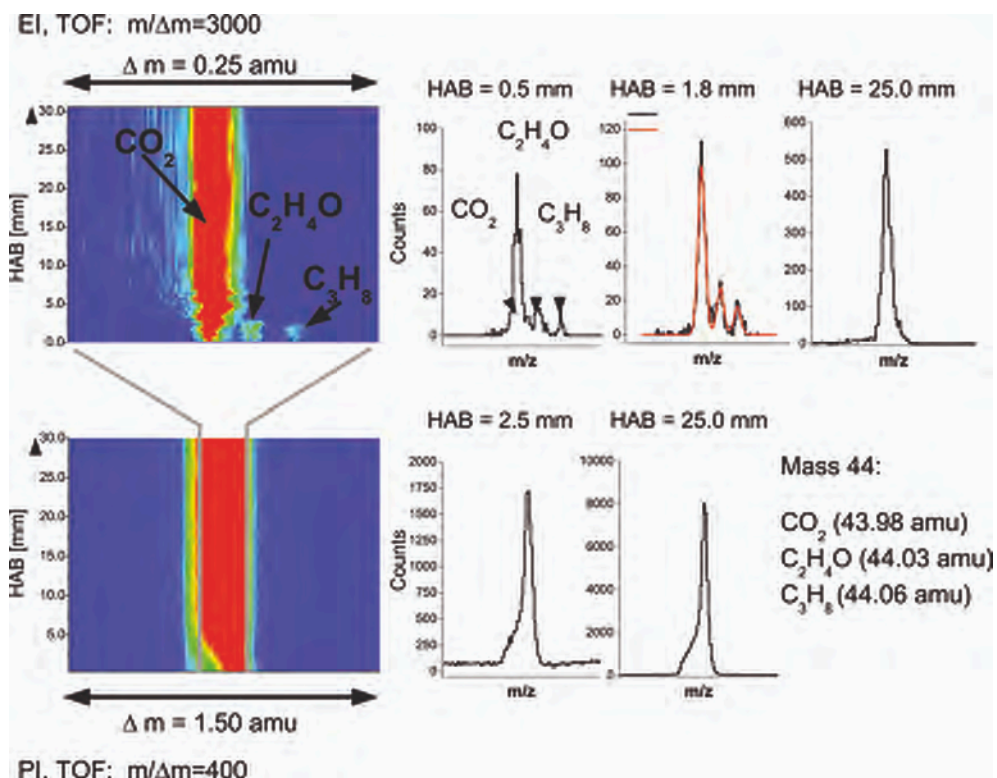


Figure 2. Comparison of energy and mass resolution in a fuel-rich ethanol-oxygen-argon (25%) flame at 50 mbar. Top: EI-MBMS, bottom: VUV-PI-MBMS; the two-dimensional images show the measured signal for  $m/z=44$  as a function of height above the burner (HAB), the diagrams on the right provide mass-resolved spectra at different HAB. Adapted from [26].

row) measurements [26]. The two-dimensional images on the left provide the signal intensity (for an increment of 0.25 amu) as a function of height above the burner (HAB). The EI data show the three individual peaks of  $\text{CO}_2$ ,  $\text{C}_2\text{H}_4\text{O}$  and  $\text{C}_3\text{H}_8$  at  $m/z=43.98$ , 44.03 and 44.06, respectively. These features are clearly resolved as shown in the mass spectra at heights of 0.5 and 1.8 mm. The signatures exhibit a Gaussian shape, and individual peak intensities can be determined from a fitting routine. The same signatures overlap and appear as a single broad peak in the VUV-PI experiment, but can be distinguished by their ionization energies. In addition, contributions of both acetaldehyde and ethenol to  $\text{C}_2\text{H}_4\text{O}$  can be separated using VUV-PI [27]. At 25 mm above the burner, the contribution of  $\text{CO}_2$  is dominant. Note also that the signals are much smaller in the EI-MBMS measurement.

Especially when species with weaker bond strengths are to be detected in the EI-MBMS experiment, fragmentation may occur already at nominal ionization energies near the ionization potential. The rather broad energy distribution does not permit to separate fragmentation products easily from the flame species with the same chemical

composition. This is illustrated in Figure 3 for a cold gas sample of ethanol. All traces are normalized to the signal intensity of the parent ion (mass 46) at 12 eV. In the EI measurements it is obvious that signals from fragmentation products at  $m/z=31$  ( $\text{CH}_3\text{O}$ ) and 45 ( $\text{C}_2\text{H}_5\text{O}$ ) produce higher signal intensities than the parent ion itself. Furthermore, strong signals of the parent and fragment ions can already be detected below the ionization potential of ethanol of 10.48 eV [28], which can be ascribed to the presence of electrons with a higher than the nominal ionization energy. In the PI experiment, ethanol ions can be produced separately from its fragment ions – which appear at higher ionization energy – as shown in the right panel of Figure 3.

A more detailed comparison of species profiles in a fuel-rich ethanol flame, measured with both EI-MBMS (symbols) and VUV-PI-MBMS (solid lines), is presented in Figure 4. Here, the results for major species, acetylene, ethylene, formaldehyde and the propargyl radical are given; profiles from the photoionization measurements have been shifted by 0.4 mm to larger distances from the burner to match the peak positions [26]. A shift of this order may have several reasons, including uncertainties in the stoichiometry, in determining the zero height position, different sampling orifice diameters and different cooling effects of the burner and the sampling probe. Temperature profiles in both configurations are indicated; they have been obtained without the presence of a sampling cone. Differences at smaller heights are attributed to different heat transfer to the burner in the two instruments. In general, the agreement between both sets of measurements is quite good. Major species mole fraction profiles agree well in the burnt gases, with the exception of  $\text{H}_2$  and  $\text{H}_2\text{O}$ , and deviate somewhat earlier in the flame, especially for  $\text{O}_2$  and fuel. The latter effect may be related to different heat transfer and diffusion. The discrepancy between  $\text{H}_2$  and  $\text{H}_2\text{O}$  profiles has been noted

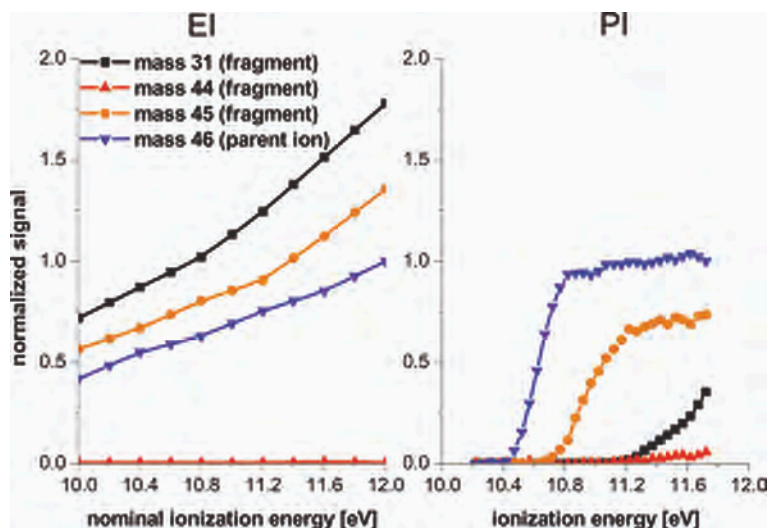


Figure 3. Fragmentation issues in EI-MBMS. Adapted from [26].

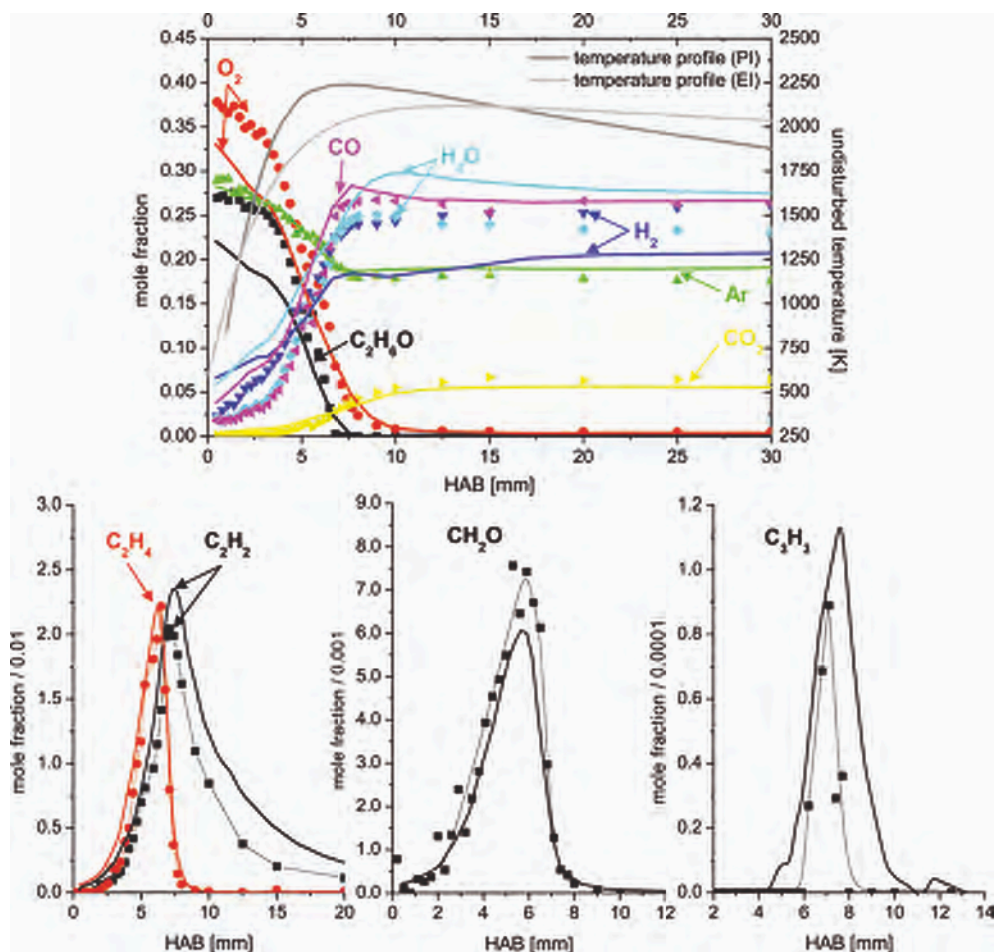


Figure 4. Selected species profiles in a fuel-rich ethanol flame measured by EI-MBMS (symbols) and VUV-PI-MBMS (lines). Adapted from [26].

before in these experiments; this suggests the influence of an instrumental parameter such as the accumulation of background gases [26]. The peak mole fractions of the stable intermediate products ( $C_2H_2$ ,  $C_2H_4$ ,  $CH_2O$ ) agree within 10-15%, and peak position and shape of the profiles are also in very reasonable agreement.

We thus conclude, in particular with respect to the rich pool of intermediates encountered in fuel-rich hydrocarbon- and oxygenate-fuelled flames, that species profiles of stable and radical intermediates can be provided with high confidence levels when experiments with high energy and mass resolution are combined, and when calibration samples and/or absolute cross sections for the ionization process in question are available. This does not resolve the issue of sampling probe effects; for this, comparison with optical measurements is highly desirable.

### 3. FORMATION OF BENZENE AND FURTHER SMALL AROMATICS

In the study of fuel-rich flames, we have mainly concentrated on the detection of species involved in the formation of the first aromatic ring as a function of the fuel structure. Flames of several  $C_2$ -,  $C_3$ - and  $C_5$ -fuels were studied in particular, including acetylene [29], propene [23,29], cyclopentene [30], 1-pentene [31], 1,3-pentadiene [32] and fuel blends [32]. Pressure and C/O ratio, C/H ratio or both were kept fixed when the fuel was changed in the same experimental environment. Temperature was typically measured with LIF, and species concentrations of the major species and many intermediates of the  $C_xH_y$  type with  $1 \leq x \leq 6$  and  $1 < y \leq 10$  were obtained from EI-MBMS [29,33] using direct calibration or cross section estimation procedures from the literature [6]. The results provided strong indications for fuel-dependent importance of the different pathways yielding benzene [32]. In a comparison of flames of propene and of several  $C_5$ -fuels,  $C_3H_3$  recombination was seen to be of importance in all flames studied, while contributions of other reactions depended on the specific decomposition pattern of the fuel and the corresponding intermediate pool [32]. It should be noted that the perceived relative importance of a specific reaction will depend on its temperature-dependent rate coefficient. Some of the key reactions continue to be investigated, hopefully eliminating remaining uncertainties in their rate coefficients, so that the relative importance of a specific pathway for a given flame condition may be ascertained [25,32]. Some of the results from these earlier studies have been modelled [34-38] with quite good agreement. Well-predicted features include the benzene concentration and some key intermediates like propargyl.

#### 3.1. Mole fraction ratios for small aromatic species beyond benzene

While the EI-MBMS method is well suited to provide an overview of the species pool, its sensitivity for larger aromatic species beyond benzene is limited. Here, REMPI-MBMS has been used to identify aromatic intermediates up to  $m/z \approx 200$  in fuel-rich propene and cyclopentene flames [25]. Since both flames have been investigated with the same instrument under identical conditions, it has been assumed that the ratios of the respective REMPI signals at a given  $m/z$  will reflect the concentration ratio of this species. The reliability of the REMPI method has been demonstrated for the example of benzene, where independent, quantitative MBMS measurements with EI and REMPI (and, most recently, VUV-PI-MBMS) resulted repeatedly in good agreement [24,25,39]. For several aromatic intermediates, including benzene, toluene, phenol, phenylacetylene, styrene, naphthalene and others, the ratios of their REMPI signals in both flames (i.e. of the respective species mole fractions) were thus determined: they are of the order of 3-10, with the cyclopentene flame generally providing higher concentration levels. These ratios have been measured in flames of both fuels with identical stoichiometry (C/O ratio), initial gas flow and pressure, and have been corroborated using VUV-PI-MBMS [40]. Such relative measurements can be particularly useful since the influences of insufficiently well known parameters will cancel. This was also a preferred approach in modelling the two flames, in addition to comparing selected individual profiles [25]. Effects of poorly known kinetic data might in fact cancel

in some cases, and predicted concentration ratios could still be reliable. If pathways are very different in the two flames, however, this might be revealed from the comparison of predicted and measured ratios, and key reaction sequences can be analyzed via reaction flow and sensitivity analysis.

In our investigation [25], many features of the reaction network leading to benzene were predicted quite reasonably, while intriguing differences of up to several orders of magnitude were observed between the measured and simulated mole fraction ratios for small aromatic compounds beyond benzene. Overprediction of the mole fraction ratio can occur when the respective species concentration is overestimated in the cyclopentene flame, or if it is underestimated in the propene flame, or both. The modelling attempt [25] has not revealed an easy explanation of the observed behavior, and many details deserve further study. It is highly plausible, however, that the particularly rich chemistry of the cyclopentene flame, which involves some reaction sequences for which the kinetics are still under debate, may need further investigation. Most recently, an independent data set for the same cyclopentene flame has been provided [38] using VUV-PI-MBMS, with many intermediate species in good agreement with the earlier measurements [30].

### 3.2. Oxygenated additives, trends in benzene and aromatics formation

Aromatics formation as well as soot emission is assumed to be reduced in flames of oxygenated fuels or flames doped with oxygenates. Thus, flame chemistries have been studied using the same combinations of methods, for example, for ethanol [39], dimethyl ether [41] and other oxygenated fuels. This demands identification of additional oxygenated intermediates not present in pure hydrocarbon flames. Experimental challenges include an increasing tendency of fragmentation of species with labile bonds and more overlaps of peaks in the mass spectra. Families of flames with different amounts of oxygenated additives were studied [24], with substantial increase in the number of profiles to be recorded, evaluated and, eventually, compared to models. As expected, preliminary analysis of the combustion chemistry of oxygenates and of hydrocarbon-oxygenate mixtures shows a tendency to decrease the concentrations of aromatic species, at the expense of an increase of some oxygenated compounds, however, including aldehydes [24,39].

As an example, Figure 5 shows the maximum signal intensities of aromatic molecules in ethanol-blended propene flames ( $C/O=0.6$ ) with varying ethanol fraction from 0-60% in the fuel mixture, normalized to those in the unblended propene flame. An almost linear decrease is evident for most detected compounds, including benzene at  $m/z = 78$ , toluene at  $m/z = 92$ , phenol at  $m/z = 94$ , indene at  $m/z = 116$  and naphthalene at  $m/z = 128$  [39]. An even more pronounced decrease was observed for a propene-ethanol-oxygen-argon flame series at  $C/O=0.773$  [39], where the ethanol fraction in the fuel could be varied from 0-15%. The complete replacement of propene by ethanol was recently studied in a series at  $C/O=0.5$  [24,42], and a similar analysis was performed for hydrocarbon and oxygenated intermediates.

Figure 6 shows trends in the maximum mole fractions for selected hydrocarbon species in these ethanol-blended propene flames with changing ethanol fraction in the fuel

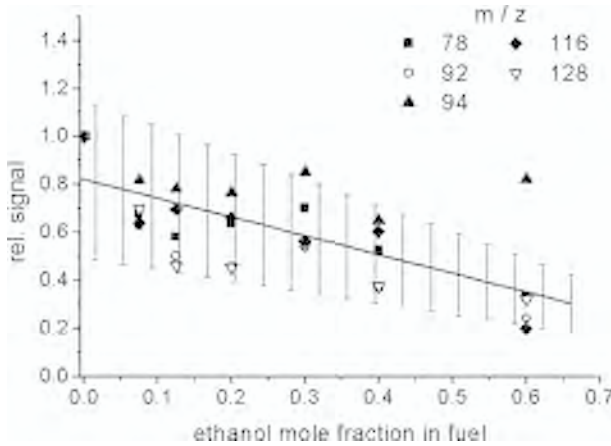


Figure 5. Maximum signal intensities of aromatic molecules in ethanol-blended propene flames ( $C/O=0.6$ ) with varying ethanol fraction in the fuel mixture. Signals are normalized to those in the unblended propene flame. Benzene:  $m/z = 78$ , toluene:  $m/z = 92$ , phenol:  $m/z = 94$ , indene:  $m/z = 116$ , naphthalene:  $m/z = 128$ . From [39] with permission.

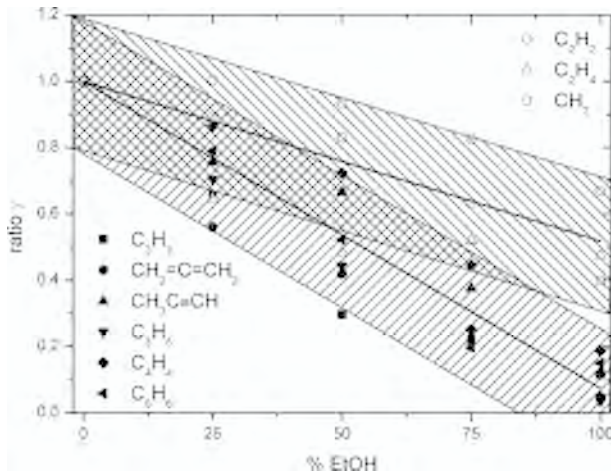


Figure 6. Trends in the maximum mole fraction for different hydrocarbon species in ethanol-blended propene flames ( $C/O=0.5$ ) with varying ethanol fraction in the fuel mixture. Ratios  $\gamma$  are defined as maximum mole fraction in the blended flame normalized by that in the pure propene flame.

mixture. The effect of changing fuel composition is shown in a ratio  $\gamma$ , depicted on the ordinate, which is defined as maximum mole fraction of the individual species in the blended flame normalized by that in the pure propene flame. The behavior of many hydrocarbon intermediates is seen to fall into two categories, which are illustrated by the

shaded areas in Figure 6: those which show a pronounced decrease of more than a factor of 3, and those which show a less substantial decrease of about a factor of 2 or less. In the first category,  $C_3$  intermediates common to the propene flame are found such as  $C_3H_3$ , allene, propyne and  $C_3H_5$ , together with vinyl acetylene and benzene itself. Methyl, ethylene and acetylene show a less pronounced effect. Many of these small intermediates are involved in aromatic hydrocarbon growth, and details of the influence of ethanol on this chemistry are under study. Trends in the maximum mole fractions of some oxygenated intermediates are shown in Figure 7 for the same set of flames. The ratios given here have been normalized to the pure ethanol flame, to avoid division by a small number, since the acetaldehyde and ethenol concentrations in the pure propene flame are rather low. A preliminary analysis shows that the formaldehyde mole fraction changes by about a factor of two or less, while both acetaldehyde and ethenol are lower in the pure propene flame by about an order of magnitude.

A quantitative analysis of the impact of these findings with regard to emission regulations must consider, however, that temperature and composition will be changed by replacement of one fuel with the other. Effects of the interaction of hydrocarbon and oxygenate chemistries [41,42] will be resolved only by analyzing the species pool in accurate, quantitative detail and by eventually modelling the specific conditions.

#### 4. ISOMER-SELECTIVE CHEMISTRY

Since the availability of tunable synchrotron radiation with high photon flux and energy resolution, the chemistry of fuel-rich flames can be studied in unprecedented detail, with the main advantage that isomeric species can be unambiguously identified. While REMPI-MBMS can specifically detect isomers whenever suitable radiative transitions are known, synchrotron-based flame mass spectrometers can employ energy-selective detection more generally [43,44]. Typically, a flame study can now be performed routinely with respect to several dimensions in an “imaging” analysis [45]. Flame species are detected according to their mass in the range up to about  $m/z \approx 200$  either in “burner scans” at a given energy, where the distance from the burner is varied to provide species profiles, and they can also be recorded at a given distance from the burner in “energy scans”, where different ionization thresholds permit identification of several isomers at a given mass when the ionization energy is scanned. Two-dimensional color-coded intensity matrices of photon energy or height above the burner versus mass-to-charge ratio, as seen in Figure 2, may be viewed as representation of key features of the combustion chemistry at a given flame condition.

##### 4.1. Identification of “new” species

The technique has been instrumental in the identification of species never detected in a flame before, such as enols [27], an example for which was also shown in Figure 7. Another example is the quantitative measurement of the two isomers of  $C_3H_4$ , allene and propyne [24,43], which are involved in different pathways in aromatics formation [46]. With respect to the cyclopentene flame mentioned above, the analysis using this

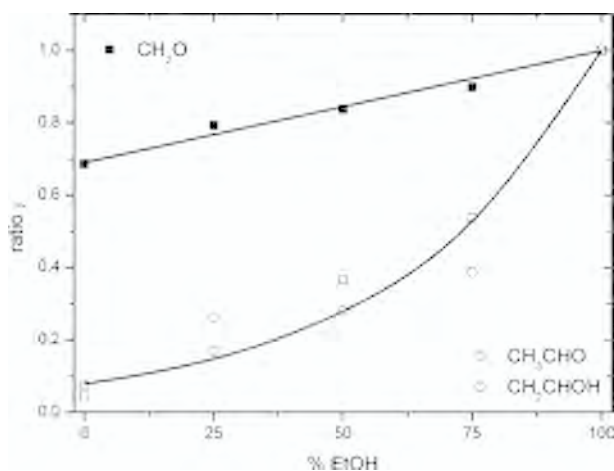


Figure 7. Trends in the maximum mole fraction for key oxygenated species in ethanol-blended propene flames ( $C/O=0.5$ ) with varying ethanol fraction in the fuel mixture. Ratios  $\gamma$  are defined as maximum mole fraction in the blended flame normalized by that in the pure ethanol flame.

method has tentatively identified at least two cyclic species of chemical composition  $C_7H_6$  ( $m/z=90$ ) and two or more cyclic species of formula  $C_7H_8$  ( $m/z=92$ ) [38]. Some of them are not included in present mechanisms for aromatics and soot formation, and their role in this process – if any – is yet unknown. Further details in the analysis of many flames using this method may reveal “new” species, the combustion reactions of which (and their respective kinetic, thermodynamic and transport data) will not – or not precisely – be known under such conditions. While the “discovery” of such new species may be a satisfactory result in itself, it may eventually slow down the process of flame model development, because some information may turn out to be unimportant after all.

#### 4.2. Study of isomeric fuels

Another approach in isomer-selective flame chemistry makes use of the advanced measurement capabilities of synchrotron flame instruments in the investigation of isomeric fuel combustion under identical conditions. The two isomers of propanol have been studied [47] and the respective species mix is found to be quite different, in particular with respect to aldehyde formation. The four butanol isomers [48,49] show a distinctly different species pool in all four flames – not unexpectedly regarding the fuel decomposition reactions to different radical species. Similarly, the combustion of isomeric esters [50,51] is being investigated. Again, the results show the importance of fuel-specific decomposition pathways which result in different concentrations of intermediates, although temperature and main species concentration profiles are almost indistinguishable.

As an example, results from flames of the four isomers of butanol are shown in Figures 8 and 9 [48] to illustrate the potential of the technique. Figure 8 shows the isomers of mass 72 determined in the four flames. Butanal is detected in the 1-butanol flame, 2-methyl-propanal in the *iso*-butanol flame, 2-butanone in both the 2-butanol and *tert*-butanol flames, indicating that the carbonyl function is detected at the position of the OH group in the fuel, except in the *tert*-butanol flame, where formation of 2-butanone is possible upon C-C bond fission. Also, butenols are seen to be present. Similarly, differences are seen with respect to further decomposition products from the fuel, for example at  $m/z = 58$  ( $C_3H_6O$ ), where acetone is seen in the *tert*- and 2-butanol flames and propanal in the *iso*- and *tert*-butanol flames. Also, for  $m/z = 56$  ( $C_4H_8 + C_3H_4O$ ), 1-butene is formed in the *tert*- and 1-butanol flames, 2-butene in the 2-butanol flame, and further species including methylketene and 2-methylpropene are also identified. The decomposition products generally show good agreement with the expected breakdown of the molecules, with a noticeable dependence of oxygenated intermediates on fuel structure, and a less pronounced dependence of the hydrocarbon intermediates on fuel structure. As shown in Figure 9, the build-up of benzene as the first aromatic ring is seen in all four flames, with fulvene also being detected as a further  $C_6H_6$  isomer.

The exploration of isomer-selective combustion chemistry in this level of detail has only recently begun, and opportunities to resolve previously unobserved details in combustion chemistry are expanding. The wealth of experimental results, of which

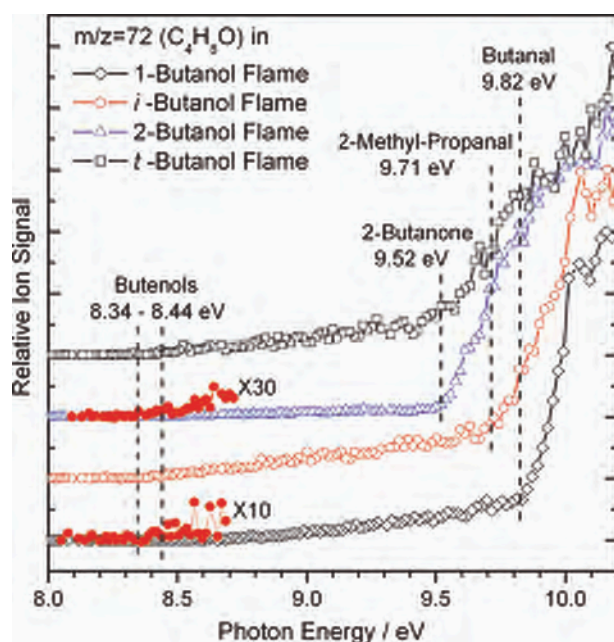


Figure 8. Isomers of  $m/z = 72$ , identified in flames of the four isomers of butanol by their ionization energies. From [48] with permission.

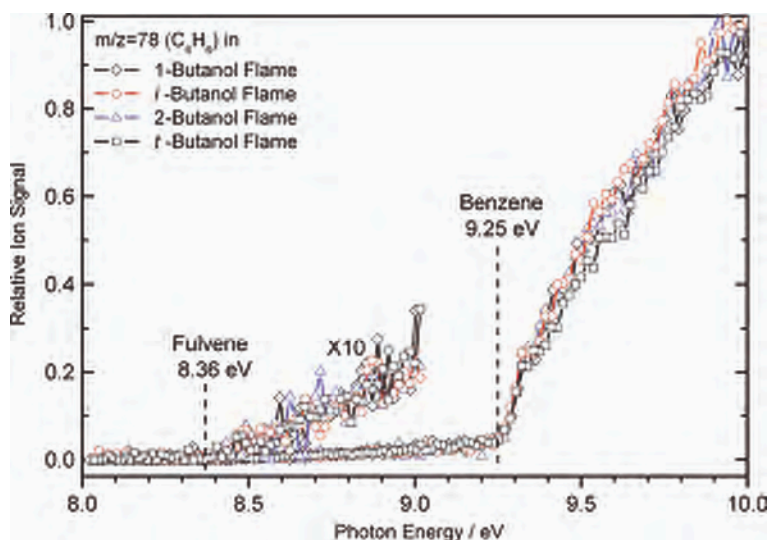


Figure 9. Isomers of  $m/z = 78$ , identified in flames of the four isomers of butanol by their ionization energies. From [48] with permission.

only a few examples could be illustrated here, and which could only be achieved through close multi-national collaboration, must now be considered as an important source of information in the development of hydrocarbon and oxygenate combustion models.

## 5. CONCLUSIONS

Detailed analysis of fuel-rich flame chemistry was discussed focussing on combinations of different mass spectrometric techniques. Examples were demonstrated from laminar, premixed low-pressure flames, using molecular beam mass spectrometry with electron ionization, resonance-enhanced multi-photon ionization, and photoionization with tunable vacuum UV radiation from synchrotron sources. Some attention was given to the discussion of typical uncertainty levels for stable and radical species, and to the comparison of the results obtained with a combination of techniques in several laboratories. The attainable accuracy depends largely on the availability of absolute ionization cross sections of the species in question and/or of sample gases of known concentrations; also, energy and mass resolution as well as fragmentation problems must be considered. The MBMS instruments were used to study fuel-rich hydrocarbon combustion in propene and cyclopentene flames, and have revealed remarkably large differences between predicted and measured concentration ratios for some aromatic species beyond benzene. The understanding of how the second and third aromatic rings are formed in premixed flames of aliphatic fuels from molecular precursors needs further investigation. Also, the effect of oxygenated additives such as ethanol

has been studied in families of propene flames. As a first tendency, benzene and its precursors are seen to decrease in concentration, while some oxygenated species are formed in larger concentrations when propene is replaced by ethanol. Quantification and interpretation of these effects will be forthcoming and will eventually need modeling to resolve the influence of temperature on the observed changes. As a major breakthrough in mass spectrometric analysis of combustion chemistry, the potential of isomer-selective detection and of the study of isomeric fuels has been demonstrated. Clearly, “new” species which had not been detected with conventional instruments must be investigated further with respect to their roles. Also, the discussion of bio-derived fuels with respect to cleaner and potentially CO<sub>2</sub>-efficient or CO<sub>2</sub>-neutral combustion may encourage study of flames with fuels that exhibit even further functional groups. It may be a challenge to select the experiments which will provide reliable, quantitative and useful data for advancing soot models regarding such fuels and fuel-blends, and which will address remaining open questions in fuel-rich hydrocarbon combustion.

## REFERENCES

1. Basic Research Needs for Clean and Efficient Combustion of 21st Century Transportation Fuels, Office of Science, US Department of Energy, BES Workshop November 2006, available also at [www.sc.doe.gov/bes/reports/list.html](http://www.sc.doe.gov/bes/reports/list.html).
2. A. C. Eckbreth, *Laser Diagnostics for Combustion Temperature and Species*, 2nd edition, Gordon and Breach, UK, 1996.
3. K. Kohse-Höinghaus, *Prog. Energy Combust. Sci.* 20 (1994) 203-279.
4. K. Kohse-Höinghaus, R. S. Barlow, M. Aldén, J. Wolfrum, *Proc. Combust. Inst.* 30 (2005) 89-123.
5. K. Kohse-Höinghaus, J. B. Jeffries (Eds.) *Applied Combustion Diagnostics*, Taylor and Francis, New York, 2002.
6. J. C. Biondi, C. P. Lazzara, J. F. Papp, *Prog. Energy Combust. Sci.* 3 (1977) 151-173.
7. K. Bonne, K. H. Homann, H. G. Wagner, *Proc. Combust. Inst.* 10 (1965) 503-512.
8. J. Peeters, G. Mahnen, *Proc. Combust. Inst.* 14 (1973) 133-146.
9. A. Bhargava, P. R. Westmoreland, *Combust. Flame* 115 (1998) 456-467.
10. J. Vandooren, M. C. Branch, P. J. van Tiggelen, *Combust. Flame* 90 (3-4) (1992) 247-258.
11. K. H. Homann, *Angew. Chem. Int. Ed.* 37 (18) (1998) 2434-2451.
12. J. H. Werner, T. A. Cool, *Combust. Flame* 117 (1998) 78-98.
13. H. Bockhorn (Ed.) *Soot Formation in Combustion*, Springer-Verlag, Berlin, 1994.
14. C. S. McEnally, L. D. Pfefferle, B. Atakan, K. Kohse-Höinghaus, *Prog. Energy Combust. Sci.* 32 (3) (2006) 247-294.
15. W. P. Stricker, in: K. Kohse-Höinghaus, J. B. Jeffries (Eds.) *Applied Combustion Diagnostics*, Taylor and Francis, New York, 2002, p. 155-193.
16. N. M. Laurendeau, *Prog. Energy Combust. Sci.* 14 (1988) 147-170.
17. A. T. Hartlieb, B. Atakan, K. Kohse-Höinghaus, *Appl. Phys. B* 70 (2000) 435-445.
18. a) K. Kohse-Höinghaus, A. Schocker, T. Kasper, M. Kamphus, A. Brockhinke, *Z. Phys. Chem.* 219 (2005) 583-599, and b) A. Schocker, K. Kohse-Höinghaus, A. Brockhinke, *Appl. Optics* 44 (31) (2005) 6660-6672.
19. a) W. G. Bessler, C. Schulz, V. Sick, J. W. Daily, A versatile modeling tool for nitric oxide LIF spectra, Proceedings of the Third Joint Meeting of the U.S. Sections of The Com-

- bustion Institute (Chicago, March 16-19, 2003, paper PI05), <http://www.lifsim.com>.
- and b) B. Atakan, J. Heinze, U. E. Meier, *Appl. Phys. B* 64 (1997) 585-591.
20. P. Desgroux, L. Gasnot, J. F. Pauwels, L. R. Sochet, *Combust. Sci. Technol.* 100 (1994) 379-384.
  21. A. T. Hartlieb, B. Atakan, K. Kohse-Höinghaus, *Combust. Flame* 121 (2000) 610-624.
  22. N. Bahlawane, U. Struckmeier, T. S. Kasper, P. Oßwald, *Rev. Sci. Instrum.* 78 (2007) 013905.
  23. B. Atakan, A.T. Hartlieb, J. Brand, K. Kohse-Höinghaus, *Proc. Combust. Inst.* 27 (1998) 435-444.
  24. K. Kohse-Höinghaus, P. Oßwald, U. Struckmeier, T. Kasper, N. Hansen, C. A. Taatjes, J. Wang, T. A. Cool, S. Gon, P. R. Westmoreland, *Proc. Combust. Inst.* 31 (2007) 1119-1127.
  25. M. Kamphus, M. Braun-Unkhoff, K. Kohse-Höinghaus, *Combust. Flame* 152 (2008) 28-59.
  26. T. Kasper, K. Kohse-Höinghaus, N. Hansen, C. A. Taatjes, M. E. Law, A. Morel, P. R. Westmoreland, J. Wang, T. A. Cool, 5th US Combustion Meeting, San Diego, USA, March 2007, paper A24.
  27. C. A. Taatjes, N. Hansen, A. McIlroy, J. A. Miller, J. P. Senosiain, S. J. Klippenstein, F. Qi, L. Sheng, Y. Zhang, T. A. Cool, J. Wang, P. R. Westmoreland, M. E. Law, T. Kasper, K. Kohse-Höinghaus, *Science* 308 (2005) 1887-1889.
  28. S. G. Lias, J. E. Bartmess, J. F. Liebman, J. L. Holmes, R. D. Levin, W. G. Mallard, Ion energetics data, NIST Chemistry WebBook, NIST Standard Reference Database Number 69, P. J. Linstrom, W. G. Mallard, S. A. Kafafi (Eds.) June 2005, National Institute of Standards and Technology, Gaithersburg, MD, 20899, available at <http://webbook.nist.gov>.
  29. A. Lamprecht, B. Atakan, K. Kohse-Höinghaus, *Combust. Flame* 122 (4) (2000) 483-491.
  30. A. Lamprecht, B. Atakan, K. Kohse-Höinghaus, *Proc. Combust. Inst.* 28 (2000) 1817-1824.
  31. G. González Alatorre, H. Böhm, B. Atakan, K. Kohse-Höinghaus, *Z. Phys. Chem.* 215 (2001) 981-995.
  32. B. Atakan, A. Lamprecht, K. Kohse-Höinghaus, *Combust. Flame* 133 (2003) 431-440.
  33. K. Kohse-Höinghaus, B. Atakan, A. Lamprecht, G. González Alatorre, M. Kamphus, T. Kasper, N.-N. Liu, *Phys. Chem. Chem. Phys.* 4 (2002) 2056-2062.
  34. C. J. Pope, J. A. Miller, *Proc. Combust. Inst.* 28 (2000) 1519-1527.
  35. H. Böhm, A. Lamprecht, B. Atakan, K. Kohse-Höinghaus, *Phys. Chem. Chem. Phys.* 2 (2000) 4956-4961.
  36. K. Hoyermann, F. Mauß, T. Zeuch, *Phys. Chem. Chem. Phys.* 6 (14) (2004) 3824-3835.
  37. R. P. Lindstedt, K.-A. Rizos, *Proc. Combust. Inst.* 29 (2002) 2291-2298.
  38. N. Hansen, T. Kasper, S. J. Klippenstein, P. R. Westmoreland, M. E. Law, C. A. Taatjes, K. Kohse-Höinghaus, J. Wang, T. A. Cool, *J. Phys. Chem. A* 111 (19) (2007) 4081-4092.
  39. T. S. Kasper, P. Oßwald, M. Kamphus, K. Kohse-Höinghaus, *Combust. Flame* 150 (3) (2007) 220-231.
  40. N. Hansen, T. Kasper, P. Oßwald, T. A. Cool, K. Kohse-Höinghaus, personal communication, 2006.
  41. T. A. Cool, J. Wang, N. Hansen, P. R. Westmoreland, F. L. Dryer, Z. Zhao, A. Kazakov, T. Kasper, K. Kohse-Höinghaus, *Proc. Combust. Inst.* 31 (2007) 285-293.

42. P. Oßwald, U. Struckmeier, T. Kasper, K. Kohse-Höinghaus, N. Hansen, C. A. Taatjes, J. Wang, T. A. Cool, S. Gon, P. R. Westmoreland, Experimental study of premixed propene/ethanol fuel blends, WIP Poster, 31st Int. Symp. on Combustion, August 6-11, 2006, University of Heidelberg, Germany.
43. T. A. Cool, K. Nakajima, T. A. Mostefaoui, F. Qi, A. McIlroy, P. R. Westmoreland, M. E. Law, L. Poisson, D. S. Peterka, M. Ahmed, *J. Chem. Phys.* 119 (2003) 8356.
44. T. A. Cool, A. McIlroy, F. Qi, P. R. Westmoreland, L. Poisson, D. S. Peterka, M. Ahmed, *Rev. Sci. Instrum.* 76 (2005) Art. No. 094102.
45. C. A. Taatjes, N. Hansen, D. L. Osborn, K. Kohse-Höinghaus, T. A. Cool, P. R. Westmoreland, *Phys. Chem. Chem. Phys.* 10 (1) (2008) 20-34.
46. N. Hansen, J. A. Miller, C. A. Taatjes, J. Wang, T. A. Cool, M. E. Law, P. R. Westmoreland, *Proc. Combust. Inst.* 31 (2007) 1157-1164.
47. a) Tina Kasper, Molekularstrahlmassenspektrometrie zur Analytik in Flammen oxygenierter Brennstoffe, PhD thesis, Cuvillier-Verlag, Bielefeld, 2007, ISBN-10: 3867273073, ISBN-13: 9783867273077, and b) T. Kasper, P. Oßwald, K. Kohse-Höinghaus, C.A. Taatjes, J. Wang, T. A. Cool, M. E. Law, A. Morel, P. R. Westmoreland, Isomeric propanol flames investigated by mass spectrometry, WIP Poster, 31st Int. Symp. on Combustion, August 6-11, 2006, University of Heidelberg, Germany.
48. B. Yang, P. Oßwald, Y. Li, J. Wang, L. Wei, Z. Tian, F. Qi, K. Kohse-Höinghaus, *Combust. Flame* 148 (4) (2007) 198-209.
49. C. S. McEnally, L. D. Pfefferle, *Proc. Combust. Inst.* 30 (2005) 1363-1370.
50. P. Oßwald, U. Struckmeier, T. Kasper, K. Kohse-Höinghaus, J. Wang, T. A. Cool, N. Hansen, P. R. Westmoreland, *J. Phys. Chem. A* 111 (19) (2007) 4093-4101.
51. W. R. Schwartz, C. S. McEnally, L. D. Pfefferle, *J. Phys. Chem. A* 110 (2006) 6643-6648.



# Detailed kinetics of real fuel combustion: main paths to benzene and PAH formation

E. Ranzi

CMIC Department, Politecnico di Milano (Italy)  
Piazza Leonardo da Vinci 32 20133 Milano (Italy)

*Abstract: The aim of this paper is to discuss the potential and limitations of detailed chemistry when it comes to handling large hydrocarbon molecules and describing the combustion behavior of real transportation fuels, such as gasolines and jet propulsion fuels. The complexity of hydrocarbon fuel mixtures not only makes simplification of the reaction mechanisms essential but demands properly designed surrogate mixtures, both for modeling and experimental testing. One of the key points in this process is understanding the effect of the different simplifications on the formation of benzene and poly-cyclic-aromatic hydrocarbons (PAH), well recognized precursors of nano-sized organic carbon particles (NOC) and soot. After the detailed and semi-detailed kinetic modeling of pyrolysis and combustion of large reference molecules, the role of adopted simplifications is the next focal point. The definition of surrogate mixtures of gasolines and jet propulsion fuels are then discussed to verify the effect of different selections of reference components. The main focus is on the formation of unsaturated species, such as acetylene, methyl-acetylene and propargyl radicals, as relevant precursors of benzene and PAH species. A very distinct difference between the timescales of odd and even mechanisms towards benzene and PAH formation emerges in the model predictions and seems to support different experimental results.*

## 1. INTRODUCTION

Combustion processes are characterized by gas-phase, high temperature radical reactions. One relevant aspect of these complex and detailed reaction schemes is their modular and hierarchical structure [1]. This feature allows combustion or pyrolysis reactions to be studied starting from the simpler systems and then progressively extending the simulation capability of the model to new and more complex situations. The  $\text{H}_2\text{-O}_2$  system is the simplest combustion sub-model and is always active in all the combustion environments. High temperature combustion and large hydrocarbon pyrolysis rely strictly on the successive reactions of small radicals and intermediate species.  $\text{H}_2$ ,  $\text{CH}_4$ , and  $\text{C}_2$  hydrocarbons reactions together with their parent radicals are the core of and the first hierarchical step in the pyrolysis model. Furthermore the combustion of any fuel at high temperatures involves the initial breaking down of the fuel to smaller radicals before the ultimate products are formed. With the exception of several resonance-stabilized radicals, their decomposition rates are so fast that they form smaller unsaturated compounds. These compounds can then be oxidized to their final products or they can react to form poly aromatic hydrocarbons. Pyrolysis reactions are thus vital to extending the available databases to encompass the combustion of liquid fuels. The relative weight of these radical reactions depends on the operating

conditions of the reacting system and the competitive nature of the pyrolysis and combustion process is of key importance. Thus, the pyrolysis reactions of heavy and light hydrocarbon species hierarchically precede the combustion models of heavy fuels [2].

The complexity of the combustion chemistry of real liquid fuels depends not only on the large and complex molecules of the fuel mixture but also on the huge number of hydrocarbon isomers. Large molecules undergo a sequential reduction in size during combustion and therefore simulations of real fuels then move from the detailed kinetics of small hydrocarbons. This chemistry of small species must be extended to include the relevant reactions of the heavy species of liquid fuels [3].

The first section of this paper is devoted to the discussion of the automatic generation of complex oxidation mechanisms, the value of lumping procedures and finally the need for surrogate formulation. Once pyrolysis and oxidation reactions convert the large fuel molecules to smaller species, the kinetic model must be extended to include all the different classes of condensation reactions governing the growth of polycyclic aromatic hydrocarbons (PAHs) and soot. Several kinetic studies have investigated different aspects of the complex growing of PAHs, soot inception as well as the successive condensation steps. Very recently, Blanquart and Pitsch [4] presented a new database of thermodynamic properties for PAHs from G3MP2B3 calculations. This database includes all the relevant species present in detailed mechanisms of soot formation, ranging from benzene to coronene.

In this case, however, the focus is only on the very first steps of PAH formation through the analysis of the reliability of model predictions in describing acetylene, methyl-acetylene, propadiene and first aromatic ring formation. Successive PAH growth always relies on the HACA mechanism as well as on the recombination and condensation reactions of resonantly stabilized radicals.

## **2. KINETIC MODELING OF PYROLYSIS AND OXIDATION REACTIONS OF LARGE MOLECULES**

Pyrolysis and oxidation reactions of n-decane are discussed as a useful example of the analysis of primary pyrolysis and oxidation reactions of large molecules.

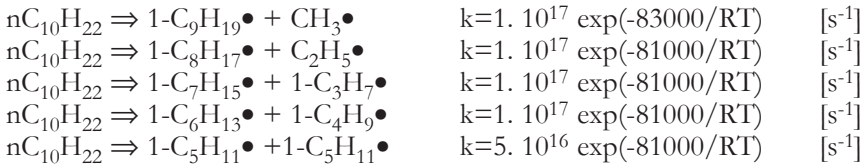
### **2.1. Pyrolysis reactions and high temperature mechanism**

The most common initiation or homolysis reaction is the breaking of a covalent C-C bond with the formation of two radicals. This initiation process is highly sensitive to the stability of the radicals formed. The activation energy equals the bond dissociation enthalpy because the reverse radical-radical recombination reaction is so exothermic that it does not require activation energy. C-C bonds are usually weaker than the C-H bonds and therefore the initial formation of H radicals is negligible. The total radical concentration in the reacting system is controlled both by radical initiation and by radical recombination reactions. In accordance with Curran et al. [5], the rate constant expressions of these decomposition reactions are calculated from the reverse recombination of the two radical species, and from microscopic reversibility. The reference

kinetic parameters of the unimolecular decomposition reactions of n-alkanes for each single fission of a C-C bond between secondary C atoms, is:

$$k_{ref} = 5.0 \cdot 10^{16} \exp(-81000/RT) \quad [s^{-1}]$$

About 2000 kcal/kmol of extra energy is required to split off a terminal methyl group. Taking into account fuel symmetry, it is thus possible to summarize the initiation reactions of n-decane with the following five elementary steps:



Once radicals are formed in the system, propagation reactions are the main grounds of the initial feed decomposition. Figure 1 shows the complete reaction path of H-abstraction reactions on n-decane and is in itself an example of the complexity of the pyrolysis mechanism. All the different H-abtracting radicals (R•) can produce the five dif-

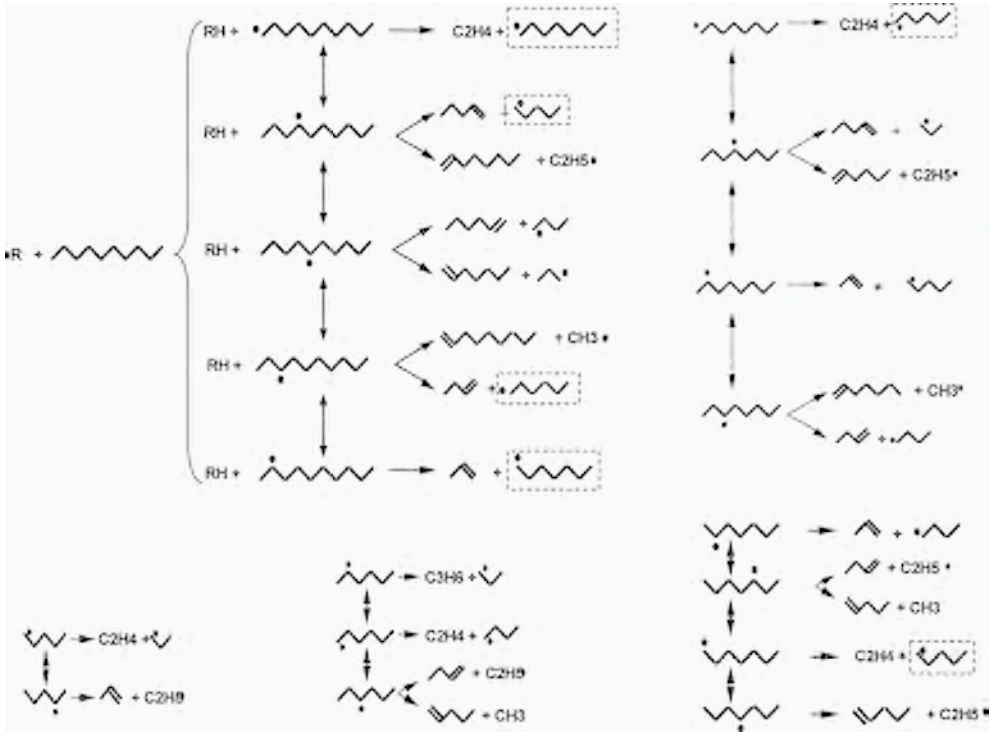
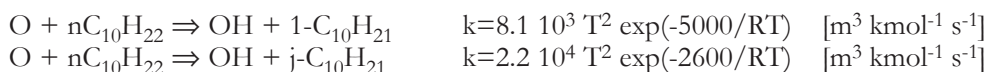
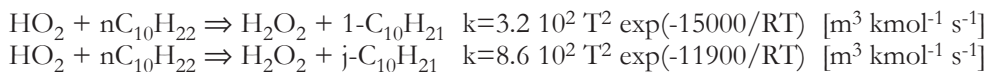
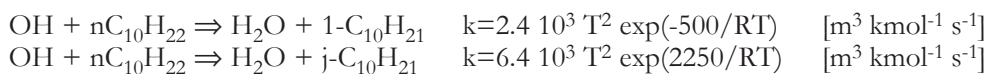
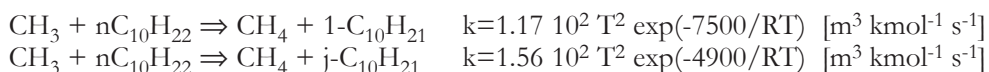
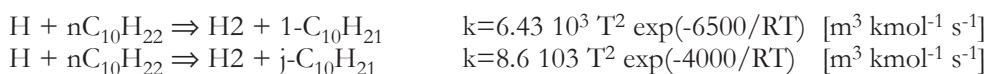


Figure 1. H abstraction reactions of n-decane. Successive isomerization and decomposition reactions of alkyl radicals larger than C4 are also reported.

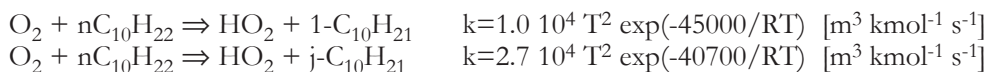
ferent isomers of n-decyl radical. These radicals can then isomerize and/or decompose. The H-abstraction or metathesis reactions are systematically described in their general form:



R and RH stand for all the possible H abstracting radicals and for the corresponding saturated species. Details regarding the direct derivation of the kinetic parameters can be found elsewhere [6]. Thus, the H-abstraction reactions on n-decane are estimated by considering the presence of 6 primary H-atoms, with the formation of the primary 1-decyl radical, and the presence of 16 secondary H-atoms, with the corresponding formation of the four different secondary radicals ( $j$ -C<sub>10</sub>H<sub>21</sub>,  $j=2,5$ ). Depending on the different attacking radicals, the estimated rate constants for each n-decyl isomer are:

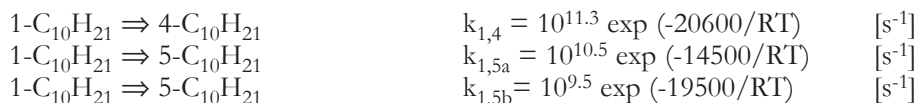


Similar H-abstraction reactions are easily evaluated for all the H-abtracting radicals. H-abstraction reactions of O<sub>2</sub> contribute to the chain initiation reactions, forming HO<sub>2</sub> and n-decyl radicals:



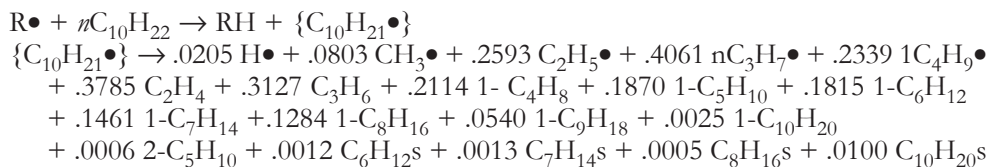
As clearly shown in Figure 1,  $\beta$ -decomposition reactions represent an important fate of alkyl radicals. Kinetic parameters of this reaction class are well known [7,8,9]. Dehydrogenation reactions are less favored than the side  $\beta$ -decomposition reactions due to their higher activation energy. At temperatures larger than 1000 K, rate constants of decomposition reactions are higher than 10<sup>6</sup> s<sup>-1</sup>. Due to these very short lifetimes, Rice and Herzfeld [10] suggested a decomposition mechanism where all the intermediate alkyl radicals directly decompose to form smaller alkenes and CH<sub>3</sub> and H radicals. As already observed by Kossiakoff and Rice [11], radical decomposition reactions compete with isomerization reactions, explained on the basis of internal H-abstraction reactions, via 5-, 6- and 7-membered ring intermediates. The rate constants

of these isomerization reactions are described in terms of the number of atoms in the transition state ring structure and the sites involved in the H transfer [5,12,13]. For instance, 1-decyl radicals can undergo the following isomerization reactions:



The two different (1,5) isomerization reactions are the result of a 6- and a 7-membered ring intermediate, due to the symmetry of position 5 and 6 of n-decane. Decomposition reactions prevail only at temperatures higher than 1100 K while the 1-5 isomerization reaction dominates at temperatures lower than 900 K.

At high temperatures, the insignificance of the interactions between large radicals and the reacting mixture allows the direct substitution of n-decyl radicals with their primary isomerization and decomposition products. In principle, heavy radicals could also undergo H-abstraction, addition on unsaturated bonds and recombination reactions. Due to the limited weight of these reactions compared to the isomerization and decomposition ones, it is possible to drastically reduce the total number of radicals and reactions to be considered. All of the intermediate alkyl radicals higher than  $\text{C}_4$  are supposed to be instantaneously transformed into their final and more stable products. Large sections of the kinetic scheme can be reduced to a few equivalent or lumped reactions while still maintaining a high level of accuracy. The complex kinetic scheme of Figure 1, which accounts for all the decomposition, dehydrogenation and isomerization reactions, can be reduced quite simply to a couple of equivalent or lumped reactions:



The equivalent or lumped species  $\{\text{C}_{10}\text{H}_{21}\bullet\}$  is an average mixture of all the decyl radicals, as obtained by the elementary H-abstraction reactions on n-decane. This lumped stoichiometry was directly evaluated by the MAMA Program at 1040 K [2,14], and is only slightly temperature dependent. Note that H radical formation, not reported in Figure 1, is due to the dehydrogenation reactions of all the intermediate radicals.

Table 1 reports the small set of reference kinetic parameters used by MAMA program to analyze the high temperature pyrolysis reactions of normal and branched alkanes. It is worth pointing out at this stage that the MAMA program is somewhat more than a simple automatic generator of elementary reactions. It not only generates the isomerization and decomposition reactions of the intermediate species but, importantly, also solves the continuity equations of intermediate radicals and evaluates the primary distribution products in accordance with the simplifying hypothesis of the autonomous fate of the large intermediate radical species. The net result is the final generation of the equivalent or lumped reactions with a drastic reduction of the overall dimension of the reacting system, in terms of both species and reactions.

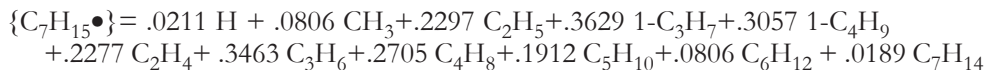
Table 1. Reference kinetic parameters for pyrolysis reactions [2] (units are kmol, m, s and kcal).

<b>Initiation Reactions: Unimolecular decomposition of C-C bonds</b>			
<b>CH3-Csec</b>	<b>Csec-Csec</b>	<b>Csec-Cter</b>	<b>Csec-Cquat</b>
$10^{16.7} \exp(-84500/RT)$	$10^{16.7} \exp(-82000/RT)$	$10^{16.7} \exp(-81000/RT)$	$10^{16.7} \exp(-78500/RT)$
<b>H-Abstraction Reactions of Alkyl Radicals</b>			
	Primary H atom	Secondary H atom	Tertiary H atom
<b>Primary radical</b>	$10^{8.0} \exp(-13500/RT)$	$10^{8.0} \exp(-11200/RT)$	$10^{8.0} \exp(-9000/RT)$
<b>Secondary radical</b>	$10^{8.0} \exp(-14500/RT)$	$10^{8.0} \exp(-12200/RT)$	$10^{8.0} \exp(-10000/RT)$
<b>Tertiary radical</b>	$10^{8.0} \exp(-15000/RT)$	$10^{8.0} \exp(-12700/RT)$	$10^{8.0} \exp(-10500/RT)$
<b>Isomerization Reactions (Transfer of a Primary H-atom<sup>a</sup>)</b>			
	<b>1-4 H Transfer</b>	<b>1-5 H Transfer</b>	<b>1-6 H Transfer</b>
<b>Primary radical</b>	$10^{11.0} \exp(-20600/RT)$	$10^{10.2} \exp(-14500/RT)$	$10^{9.5} \exp(-19500/RT)$
<b>Secondary radical</b>	$10^{11.0} \exp(-21600/RT)$	$10^{10.2} \exp(-15500/RT)$	$10^{9.5} \exp(-20500/RT)$
<b>Tertiary radical</b>	$10^{11.0} \exp(-22100/RT)$	$10^{10.2} \exp(-16000/RT)$	$10^{9.5} \exp(-21000/RT)$
<b>Alkyl Radical Decomposition Reactions (to form Primary Radicals)</b>			
Primary radical	Secondary radical	Tertiary radical	
$10^{14.0} \exp(-30000/RT)$	$10^{14.0} \exp(-31000/RT)$	$10^{14.0} \exp(-31500/RT)$	
<b>Corrections of decomposition rates to form:</b>			
<b>Methyl radical</b>	<b>Secondary radical</b>	<b>Tertiary radical</b>	<b>Allyl radical</b>
$\exp(-2500/RT)$	$\exp(1500/RT)$	$\exp(2500/RT)$	$10^{-5} \exp(8000/RT)$

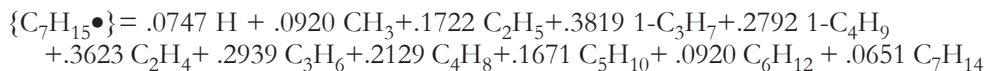
<sup>a</sup> Corrections for secondary and tertiary H-atoms are the same as for H-abstractions.

## 2.2. Consistency of lumped approach and lumped reactions

The following simple example further supports the lumped approach already used in modeling steam cracking reactions, for several years now [14]. n-heptane is a typical reference fuel and is used here mainly to verify the effect of the lumping temperature, i.e. the temperature used to evaluate rate parameters of decomposition and isomerization reactions. At 1040 K, the equivalent lumped decomposition reaction of the n-heptyl radical mixture  $\{C_7H_{15}\bullet\}$  is:



The same lumped reaction evaluated by the MAMA program at 1500 K becomes:



Ethylene formation increases significantly (from .2277 to .3623), mainly at expenses of propylene, butene and pentene formation. Similarly, the radical distribution is different as H and CH<sub>3</sub> radical formation increases, due to the greater importance of

decomposition reactions. Despite these differences in primary product distribution, the practical effect during high temperature *n*-heptane decomposition is quite limited. Figure 2 compares the yields of major species and relevant radicals as predicted by the kinetic model at 1300 K by using the two different reaction sets, lumped respectively at 1040 K and 1500 K.

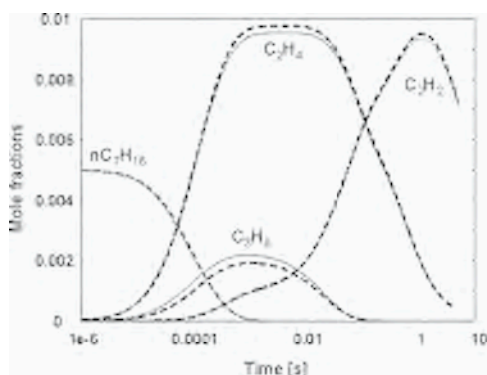


Figure 2a. Pyrolysis of *n*-heptane at 1300 K. Mole fractions of relevant species as predicted with kinetics lumped at 1040 K (lines) and 1500 K (dashed lines).

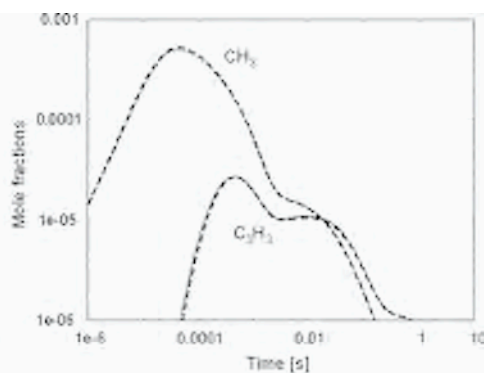


Figure 2b. Pyrolysis of *n*-heptane at 1300 K. Mole fractions of relevant radicals as predicted with kinetics lumped at 1040 K (lines) and 1500 K (dashed lines).

The reactivity of the fuel is very similar in both cases, the small discrepancy in ethylene and propylene reproduces the different stoichiometry but deviations completely vanish when observing acetylene, methyl and propargyl radical formation. These results further support the reliability and significance of the lumped approach that allows a drastic reduction in the overall dimension of the reacting system both in terms of intermediate species and elementary reactions. Only a very limited set of lumped reactions is needed to include new heavy and large molecules in detailed kinetic schemes capable of handling the chemistry of small hydrocarbon species.

### 2.3. Low temperature oxidation mechanism

Lumped decyl {C<sub>10</sub>H<sub>21</sub>•} and heptyl {C<sub>7</sub>H<sub>15</sub>•} radicals can also undergo low temperature oxidation reactions, as already discussed elsewhere [15]. Large *n*-alkanes (heavier than *n*-heptane) display the same kinetic behavior in both the high- and the low-temperature regions and allow a direct extension of the overall kinetic model to species up *n*-hexadecane. There are 362 primary propagation reactions of *n*-hexadecane, involving 100 different radicals (R, ROO, QOOH and OOQOOH) and 80 primary parent molecules always retaining 16 C atoms (alkenes, ethers, hydroperoxides and carbonyl-hydroperoxides). The detailed description of successive reactions of all these new interme-

diates species rapidly makes the overall mechanism unmanageable. Consequently, the kinetic modeling of large molecules benefits great from simplifications and semi-detailed approaches. The limitations and advantages of the lumped approach as compared to detailed kinetic schemes are discussed in the aforementioned paper.

### 3. GASOLINES AND JET PROPULSION FUELS. FUEL SURROGATES

Liquid fuels consist of complex mixtures of thousands of hydrocarbons that vary from refinery to refinery (and day to day in a given refinery depending on the crude source). This makes simplifications in the modeling and simulation of liquid fuels inevitable. A common approach is the use of fuel surrogates, where a limited set of model components is used to simulate the real fuel, either in modeling or experimental testing. The surrogate selection depends on the property being simulated. For modeling simple flame behavior, a one- or two-component surrogate may be adequate but a more complex surrogate may often be required. [16,17]. The very real need for extreme simplifications in modeling and testing pyrolysis and combustion behavior of real liquid fuels containing large hydrocarbon molecules is made even clearer by Table 2 where the number of paraffin isomer versus the carbon number of different petroleum fractions are reported [18].

Table 2. Carbon number, boiling temperatures and number of alkane isomers of different petroleum fractions. Adapted from [18].

Carbon no.	Boiling temperature [°C]	# of paraffin isomers	Petroleum fraction
8	126	18	Gasoline and Naphthas
10	174	75	Kerosene
12	216	355	Jet Fuels
15	271	4347	Diesel Fuels
20-30	344-449	$3.7 \cdot 10^5$ - $4.1 \cdot 10^9$	Light-Heavy Gasoil
35	489	$4.93 \cdot 10^{11}$	Atmospheric Residue

#### 3.1. Gasolines

Two primary reference fuels (PRF) – n-heptane and iso-octane (2,2,4-trimethyl pentane) – are commonly used to mimic gasoline reactivity and these define the octane reference scale (ON=0 for n-heptane and ON=100 for iso-octane). The octane number is a measure of the anti-knock characteristics of gasoline. Low speed and low load knock characteristics are determined by the RON test method (600 rpm) while the MON method tests high speed (900 rpm), higher load and conditions of higher power output. The sensitivity of a gasoline, i.e. the difference in octane number between RON and MON, is a clear early indication that the simple mixture of the two PRF is unable to characterize the real gasolines even across a limited range of operating conditions.

For this reason, it was suggested that alkenes and aromatics should also be included in surrogate mixtures. Gauthier et al. [19] measured ignition delay times of surrogate fuel mixtures containing n-heptane, iso-octane and toluene. Similarly, in the kinetic modeling of surrogate gasoline in HCCI, Naik et al [20] used n-heptane and iso-octane to represent n- and iso-alkanes, methyl-cyclohexane to represent cycloalkanes and finally toluene and 1-pentene to represent aromatics and alkenes.

The reliability of detailed and semi-detailed kinetic models of gasoline surrogate in analyzing knock-related combustion behavior with particular focus on octane numbers and octane sensitivity has been discussed recently in the literature [21]. Detailed chemistry explains the different reactivities of various hydrocarbon mixtures and explains the effect of various components on the knocking behavior of the fuel under different operating conditions. It is also a reliable and useful tool in formulating new fuels and designing new engines.

The interest here is in confirming the reliability of the detailed kinetic models at high flame temperatures too, where PAH and soot formation can become relevant. Roesler et al. [22] observed the existence of synergistic chemical effects when adding methane to ethylene in the production of aromatics, despite reduced acetylene concentrations. They attributed this effect to the ability of methane to enhance the production of methyl radicals which will then promote production channels of aromatics reliant on odd-carbon numbered species. They also observed that the total mass of PAH rose, while the soot concentration stayed constant, due to a compensating reduction in surface growth from acetylene. The ability of the detailed kinetic model to properly predict not only ethylene and small species but also methyl radical concentration is critical in the successive prediction of benzene as a first step toward PAH and soot formation.  $\text{CH}_3$  radical concentration time-histories were recently measured during the oxidation and pyrolysis of iso-octane and n-heptane behind reflected shock waves by Davidson et al. [23]. Species time-histories for OH and  $\text{CH}_3$  during iso-octane and n-heptane oxidation were reported with kinetic analysis of key decomposition reactions of normal and branched alkanes at high temperatures.

The oxidation and thermal degradation mechanism of the PRF suggest a rapid conversion of the initial fuel to form  $\text{CH}_3$ , small radicals and intermediates with a successive oxidation to formaldehyde, HCO and CO. Once formed, the  $\text{CH}_3$  radicals are quite stable and remain in relatively large concentrations with long pre-ignition plateaus during the oxidation for both fuels. At high temperatures ( $T > 1200\text{K}$ ) the decomposition of iso-octane and n-heptane is dominated by simple pyrolysis, and iso-octane is more reactive than n-heptane due to the presence of tertiary and quaternary carbon atoms. The kinetic models can follow this experimental behavior. Figure 3a shows that iso-octane is more reactive than n-heptane and predicted conversions agree quite well with the first order decomposition rates proposed by Davidson on the basis of the best fit of experimental data for the high temperature range:

$$\begin{array}{lll} \text{n-heptane:} & k = 9. \cdot 10^{14} \exp (-67300/RT) & [\text{s}^{-1}] \\ \text{iso-octane:} & k = 5.2. \cdot 10^{15} \exp (-67800/RT) & [\text{s}^{-1}] \end{array}$$

Figures 3c and 3d show the reliable comparisons between model predictions and experimental measurements of  $\text{CH}_3$  radical concentrations, from n-heptane and iso-

octane respectively. Finally, Figure 3b shows that  $\text{CH}_3$  radical concentration from iso-octane is always more abundant than  $\text{CH}_3$  radical from n-heptane. As will be discussed later, this fact is of interest when it comes to explaining the greater soot propensity of branched fuels.

The model predictions and kinetic analysis presented in this work are always based on TOT0703, a semi-detailed kinetic model of hydrocarbon pyrolysis and oxidation (from  $\text{CH}_4$  up to jet fuels) [<http://www.chem.polimi.it/CRECKModeling/>].

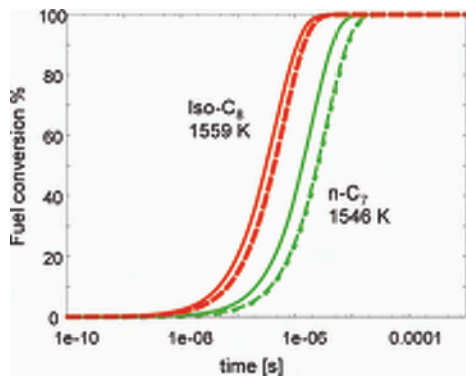


Figure 3a. n-heptane and iso-octane conversion. Model predictions (solid lines) vs. best fitting of experimental data (dashed lines) [23].

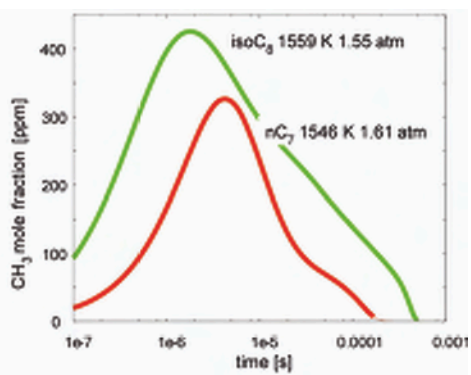


Figure 3b.  $\text{CH}_3$  radical formation from high temperature decomposition of iso-octane and n-heptane.

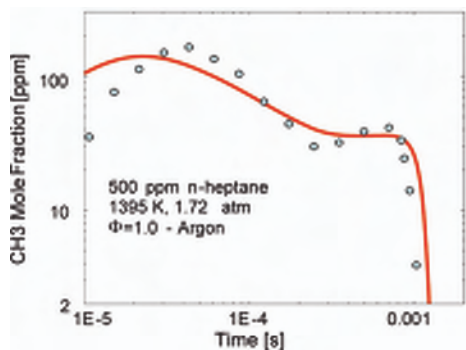


Figure 3c.  $\text{CH}_3$  radical formation from n-heptane conversion. Model predictions (solid line) vs. experimental measurements (points) [23].

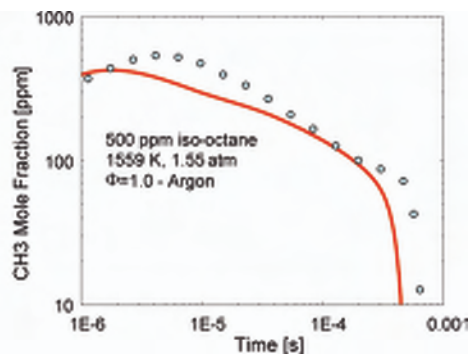


Figure 3d.  $\text{CH}_3$  radical formation from iso-octane conversion. Model predictions (solid line) vs. experimental measurements (points) [23].

### 3.2. Kerosenes and jet propellant fuels

Kerosenes are complex mixtures containing C<sub>9</sub> to C<sub>16</sub> hydrocarbons, their composition depends on the crude source and the refinery process. Kerosene-type jet fuels are relatively non-volatile with respect to wide-cut jet fuels (140-300°C). The major components of kerosenes are linear and branched alkanes (35-50%) and cyclo-alkanes or naphthenes (30-35%). One- and two-ring aromatic hydrocarbons are normally below 20-25% by volume.

Jet fuels are made by refining crude petroleum and are blends of kerosene streams, sometimes supplemented with naphthas and low concentrations of additives to improve stability and performance. Stringent standards and specifications are applied to such fuels, for both civil and military aircraft. Common aviation fuels, mostly used for commercial and military aircraft, are Jet A, Jet A-1 and JP-8. The United States Air Force military fuel, JP-8, is manufactured according to military specifications.

Reference and model components usually selected to define surrogate fuels include [3]:

Normal-alkanes	: Heptane, Decane, Dodecane, Tetradecane and Hexadecane,
Branched-alkanes	: Iso-octane and iso-cetane
Cyclo-alkanes	: Methylcyclohexane
Aromatics	: Toluene, Xylenes and Methylnaphthalene
Multi-ring compounds	: Tetralin and Decalin
Alkenes	: 1-Pentene

Table 3 reports different surrogate mixtures proposed for JP-8 fuels by different researchers.

Table 3. Surrogate mixtures for JP-8 fuels (mol %).

	Surrogate components	[24] Agosta (2004)	[25] Montgomery (2002)	[26] Violi (2002)	[27] Eddings (2005)	[28] Humer (2007)	[28] Humer2 (2007)
<b>Normal Alkanes</b>	normal-octane				3.5		
	normal decane		32.6				
	normal dodecane	26	34.7	30	40	60	60
	normal tetradecane			20			
	normal hexadecane				5		
<b>Branched-Alkanes</b>	Iso-octane			10			
	Iso-cetane	36					
<b>Cyclo-Alkanes</b>	methyl-cyclo-hexane	14	16.7	20		20	20
	Decaline	6			35		
<b>Aromatics</b>	Toluene						20
	Xylene			15	8.5	20	
	butyl-benzene		16.				
	α-methylnaphthalene	18					
	Tetralin			5	8		

Different surrogates are designed to reproduce different chemico-physical properties; thus the Utah surrogate [26] was selected to reproduce the volatility of the fuel, while the Drexel [24] and San Diego surrogates [28] were respectively designed to mimic fuel autoignition property and flame extinction limits. Recently, Eddings et al. [27] analyzed a series of six-component surrogates for the simulation of JP-8 burning rate in pool fires. With particular focus on the sooting tendency of jet fuel under steady-state pool fire conditions, this study highlighted the difficulties associated with formulating an appropriate surrogate to mimic jet fuel behavior over the lifetime of a batch pool fire.

Zhang and Sarofim [29] are studying the average composition of JP fuels, including the distribution of methyl and alkyl substitutions, on the basis of literature information and NMR statistics.

The reliability of a semidetained kinetic model of pyrolysis and oxidation of JP-8 in reproducing different targets, such as auto-ignition delay times, extinction and ignition

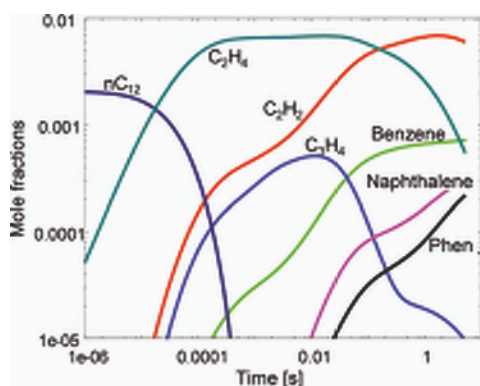


Figure 4a. Pyrolysis of San Diego surrogate at 1300K. Mole fractions vs. time [s].

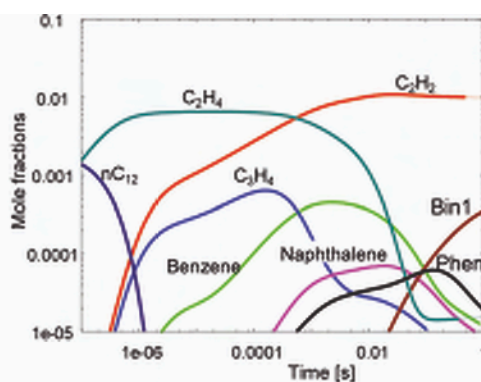


Figure 4b. Pyrolysis of San Diego surrogate at 1600K. Mole fractions vs. time [s].

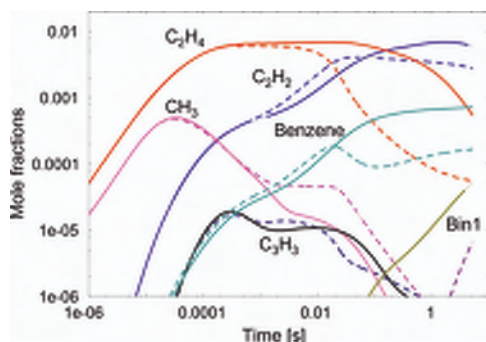


Figure 4c. Pyrolysis (solid lines) and combustion (C/O=1 dashed lines) of San Diego surrogate at 1300K. Mole fractions vs. time [s].

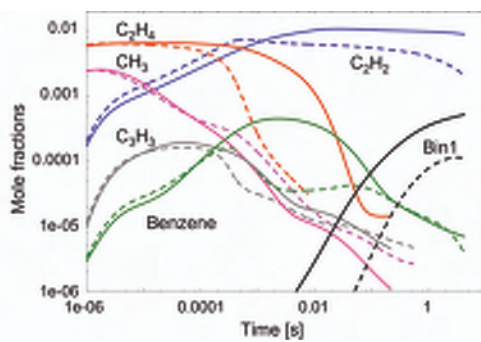


Figure 4d. Pyrolysis (solid lines) and combustion (C/O=1 dashed lines) of San Diego surrogate at 1600K. Mole fractions vs. time [s].

limits in diffusion flames, has been already discussed [30]. Here the focus is mainly on the high temperature pyrolysis conditions and the differing behavior of different surrogates mainly with respect to  $C_2H_2$ ,  $C_3H_4$ , and benzene formation. Figures 4a and 4b provide some detail regarding the pyrolysis of San Diego surrogate in terms of intermediates and final products as predicted by the model, at 1300 K and 1600 K respectively. These data refer to a carbon content in the whole mixture of 3.5%, with  $N_2$  dilution at 1 atm. These figures show the primary fuel decomposition with ethylene formation, the successive formation of acetylene and  $C_3H_4$  (propadiene and allene) and the progressive formation of PAHs, moving from benzene, through naphthalene and phenanthrene up to the Bin1, used as the first pseudocomponent of the successive and sequential growth of PAH and soot [31]. The lifetime of  $C_3H_4$  is rather shorter when compared to the corresponding stability of  $C_2H_2$ . The log scale for the contact times allows clearer characterization of the different behaviors of the different species and their differing roles in the successive PAH formation and growth phase. Figures 4c and 4d compare pyrolysis and combustion conditions (at  $C/O=1$ ) at the same temperatures. The  $O_2$  effect in the reacting mixture only becomes significant after the initial decomposition of the fuel. To enhance this discussion of the overall mechanism, it is better to start with a simpler example, however.

#### 4. PYROLYSIS AND COMBUSTION OF $C_2H_4$ AND $CH_4$ MIXTURES IN A LAMINAR FLOW REACTOR

As recently summarized by McEnally et al. [32], optical techniques can not measure crucial intermediates to PAH formation, such as propargyl and benzene. The species detected by laser diagnostics, such as OH and CH, can only be used to characterize the overall flame structure but are not directly involved in aromatics and carbon particle formation. Probe sampling methods can properly measure most of the hydrocarbon species but the insertion of the probe disturbs the flame structure, causing significant changes of the flow field, the temperature and the concentration profiles.

For these reasons, it seems useful to analyze the combustion of  $C_2H_4$  and  $C_2H_4$ - $CH_4$  mixtures in a flow reactor. Recently, Roesler et al. [22] studied the effect of methane addition on the formation of soot precursors in the rich oxidation of ethylene in a laminar flow reactor at 1430K. The fuel was initially  $C_2H_4$ , and  $CH_4$  was gradually added to the system, maintaining the total carbon content (3% mole) and a C/O ratio equal 0.67. The mixture parameter  $\beta$  characterizes the fuel composition:

$$\beta = \frac{X_{C_2H_4}}{X_{C_2H_4} + 2X_{CH_4}}$$

and represents the fraction of fuel carbon injected as methane. The equivalence ratio slightly varies between 6, when  $\beta=0$ , up to 7 due to the higher H content of  $CH_4$ .

Roesler [33] already studied the rich combustion of pure methane ( $\Phi = 4.5$ ) in a laminar flow reactor and verified that model predictions from a one-dimensional plug flow reactor closely correspond to the ones of a two-dimensional model accounting for radial inhomogeneities. Predicted conversions in the plug flow reactor are slightly higher than the corresponding ones of a two-dimensional model.

Figure 5 shows a comparison between the model prediction and experimental measurements in the laminar flow reactor of Roesler et al. [22]. The model correctly predicts the increase in benzene and PAH when  $\beta$  increases.  $\text{CH}_4$  addition to the fuel mixture is responsible for the benzene increase.

Large discrepancies are present mostly in  $\text{H}_2$  and  $\text{H}_2\text{O}$  predictions. A sensitivity analysis shows that both species are mainly controlled by H abstraction reactions. It seems very difficult to improve this comparison because the large  $\text{H}_2\text{O}$  overprediction agrees with the total oxygen balance. Experimental measurements at  $\beta = 0$  indicate a 10% lack in the oxygen balance. (3% of C fuel with  $\Phi = 6$  corresponds to 1.5 % O, total O in the product is about 1.35 %). The underprediction of  $\text{CO}_2$  can not balance  $\text{H}_2\text{O}$  overprediction, because  $\text{CO}_2$  fraction is one order of magnitude lower.

Figure 6 show the time evolution of different species on a log scale. As expected, the acetylene peak decreases from .008 to about .006 when methane is added to the mixture. Methyl radical peak is a good indicator of the overall reactivity of the system and it is about double when ethylene alone is present in the initial fuel. It is also worthwhi-

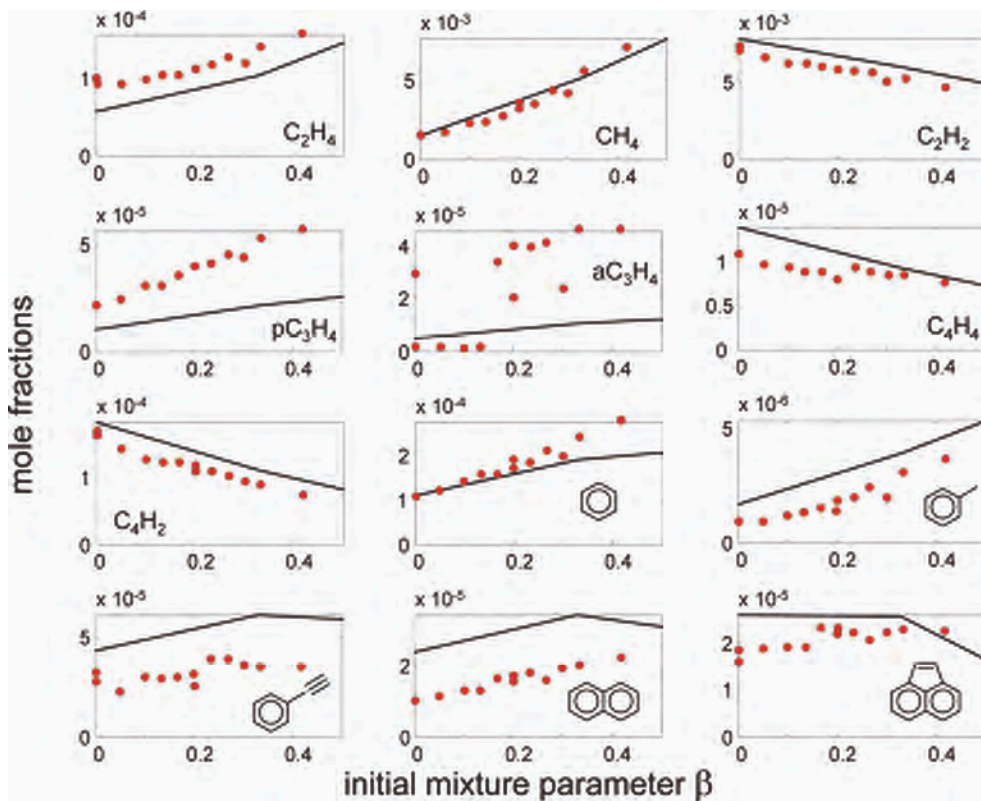


Figure 5. Combustion of  $\text{C}_2\text{H}_4$  and  $\text{C}_2\text{H}_4$ - $\text{CH}_4$  mixtures in a laminar flow reactor ( $T = 1425$  K,  $\text{C}/\text{O} = 0.67$ ). Mole fractions vs. the initial mixture parameter  $\beta$ . Comparison between model predictions (lines) and experimental measurements (points) [Roesler et al., 2003].

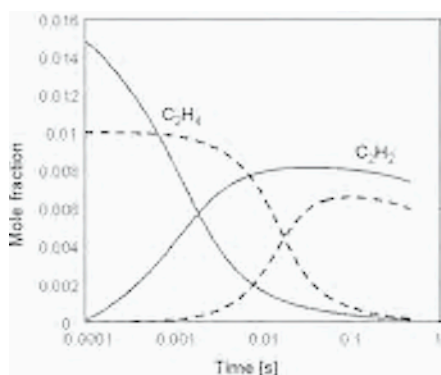


Figure 6a. Mole fractions of Ethylene and acetylene vs. contact time [s].

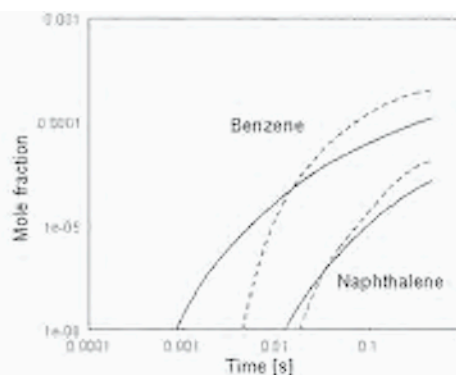


Figure 6b. Mole fractions of benzene and naphthalene vs. contact time [s].

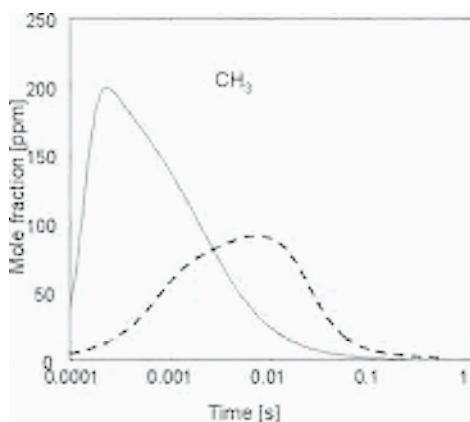


Figure 6c. Mole fractions of methyl radicals vs. contact time [s].

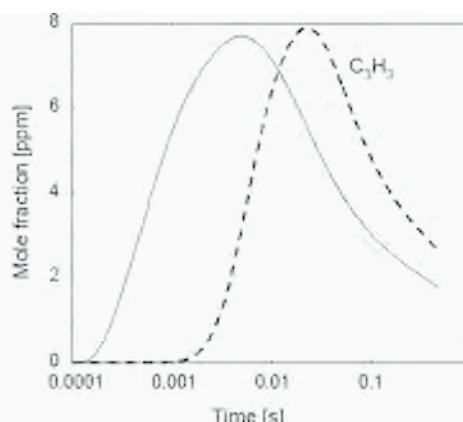


Figure 6d. Mole fractions of propargyl radicals vs. contact time [s].

Figure 6. Combustion of ethylene (solid lines) and ethylene-methane mixtures (dashed lines). Mole fractions of relevant species vs. contact time [s].

le noting that the maximum concentration of propargyl radical does not change too much and remains practically constant at 7.5-8 ppm. The lower reactivity of the ethylene-methane mixture, which is evident in Figure 6a, justifies the more stable presence of  $C_3H_3$  radicals in the reacting system and therefore its role in benzene formation. Thus, the benzene and PAH increase due to the odd mechanism of propargyl radicals has to be attributed more to the extended life of  $C_3H_3$  radicals than to larger concentrations of  $C_3H_3$  radicals in the reacting system when methane is added to the mixture.

Benzene and naphthalene formation is initially due to the odd mechanism of  $C_3H_3$  radicals, then the HACA and the even mechanisms supported by  $C_2H_2$  become the prevailing or the exclusive ones. This fact agrees quite well with the experimental

observation of Roesler et al. [22]: the total mass of PAH rose due to  $\text{CH}_4$  addition while the soot concentration stayed constant due to a compensating reduction in surface growth from acetylene.

#### 4.1. Pyrolysis of n-heptane and branched $\text{C}_7$ alkanes

This situation is even clearer when analyzing the pyrolysis of n-heptane and different  $\text{C}_7$  alkane isomers. Peaks of  $\text{C}_3\text{H}_4$  and  $\text{C}_2\text{H}_2$  reflect their stability and show that  $\text{C}_3$  species and radicals are responsible for benzene and PAHs at low contact times or severity, while the even  $\text{C}_2$  species mechanism seems to become more important in the post-flame regions, as per Figure 7a where the pyrolysis of n-heptane is reported. Figure 7b compares benzene and naphthalene formation from the pyrolysis of n-heptane and 2,2,3tri-methyl-butane at 1300 K. PAH formation is faster when branched fuel is decomposed, due to the larger amount of  $\text{C}_3$  species. These data indicate that the different behavior observed in soot and benzene formation must also be related to other intermediates, for instance isobutene via methyl-ally and methyl-propargyl radicals. According to the conclusions of McEnally et al. [34], kinetic models need to include detailed chemistry that describes alkane decomposition to alkenes, such as propene and butenes, including mechanisms that start with both unimolecular dissociation and H-atom abstraction, and the successive decomposition of alkenes to benzene precursors, such as propargyl radical. Once again, the successive HACA and acetylene mechanisms tend to have equal PAH formation.

#### 4.2. Reliability of kinetic mechanisms of pyrolysis and combustion of naphthenes

Cyclo-alkanes in gasoline and jet fuel are made up of both alkyl cyclo-hexanes and cyclo-pentanes. A 60:40 ratio indicates that significant levels of cyclo-pentanes are present too [2].

Detailed kinetic schemes of low and high temperature oxidation of naphthenes are mainly limited to cyclo-hexane and methyl-cyclohexane [20,35,36] and agree quite satisfactorily with the experimental data. A couple of examples relating to cyclo-hexane flames confirm this reliability. Law et al. [37] studied a low pressure (30. Torr), stoichiometric flat flame of cyclohexane/ $\text{O}_2$  with 32.5% Ar, at 35.0 cm/s feed velocity. Benzene formation was dominated by a stepwise dehydrogenation of cyclohexane through cyclohexene and cyclohexadiene intermediates. The higher rate of benzene production via dehydrogenation relative to the possible small-molecule addition routes helps explain the larger amount of PAH and soot from fuels that contain cyclohexane. Model predictions are reported in Figure 8 and indicate an overestimation of cyclohexene and cyclohexadiene, but a reasonable agreement with benzene experimental measurements.

A better agreement with experimental measurements is shown in Figure 9, where the comparisons refer to a premixed laminar sooting flame of cyclohexane in air, at atmospheric pressure [38].

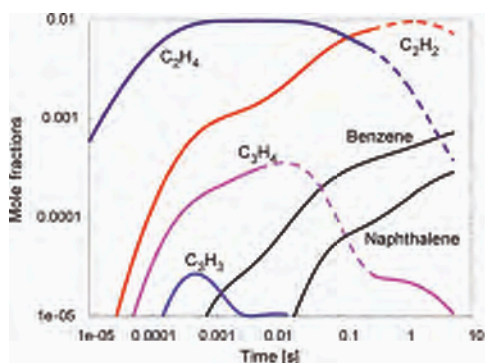


Figure 7a. Pyrolysis of n-heptane at 1300 K. Mole fractions of relevant species vs. contact time [s].

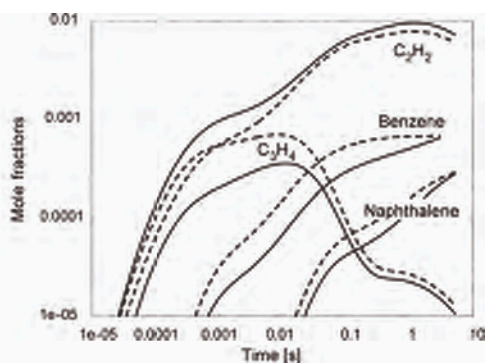


Figure 7b. Pyrolysis of n-heptane (solid line) and 2,2,3tri-methyl-butane (dashed lines) at 1300 K. Mole fractions of relevant species vs. contact time [s].

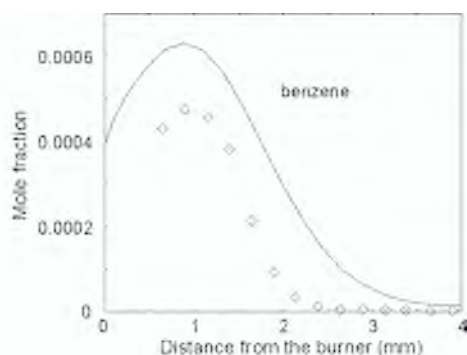
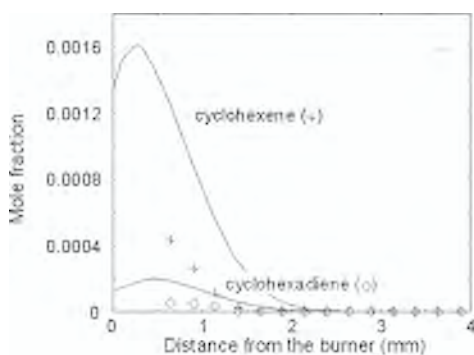


Figure 8. Low pressure stoichiometric flame of cyclohexane [37]. Comparisons of experimental measurements (points) and model predictions (lines).

Recently, Hansen et al. [39] performed a detailed analysis of the combustion chemistry of a fuel-rich, nonsooting, premixed laminar cyclopentene flame ( $\Phi = 2.0$ ) at 50 mbar, employing flame-sampling molecular beam mass spectrometry. Mole fraction profiles of 49 intermediates were presented and critically discussed with regard to the initial steps in fuel consumption and aromatic ring formation. These experimental data are very useful in verifying and validating the model predictions, reported in Figure 10.  $C_3$  and  $C_4$  species are properly predicted while the model indicates a presence of methane and acetylene in the postflame region, something that is not observed experimentally. The role of cyclopentadiene and  $C_5H_5$  radical (overestimated) is clear. Benzene is underestimated and the predicted maximum naphthalene fraction is higher than  $1 \cdot 10^{-3}$ . As already observed by Lindstedt and Rizos [40], a two-step recombination of cyclohexadienyl radicals seems more consistent.

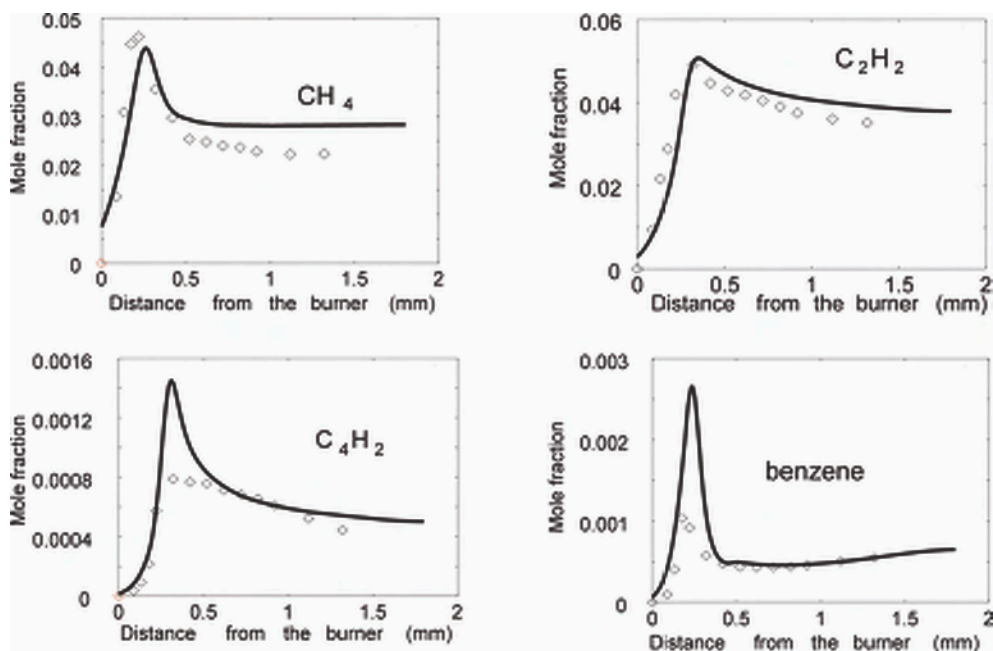


Figure 9. Atmospheric pressure, sooting flame of cyclohexane [38]. Comparisons of experimental measurements (points) and model predictions (lines).

Aimed at discussing the reliability of detailed kinetics in the area of naphthenes, the examples reported give an idea of the limitations and the potential of the models. The kinetic parameters of the direct dehydrogenation of cyclohexane, a significant source of benzene, are properly defined. It is more difficult to describe benzene formation from cyclopentadiene and C<sub>5</sub> radicals. All the interactions between C<sub>5</sub> and C<sub>2</sub> species require further analysis.

Under mild pyrolysis conditions (900-1100 K), it is known that cyclopentadiene is an important precursor of the first aromatic ring. The experimental measurements of Kunugi et al. [41] on ethylene pyrolysis clearly support this fact. Pyrolysis of ethylene at 1000 K shows that a relevant path to benzene formation is the Diels-Alder cycloaddition reaction of ethylene to cyclopentadiene, via norbornene and/or norbornadiene intermediates:

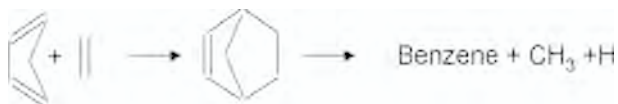


Figure 11 shows that cyclopentadiene, formed via butadiene and vinyl radical, is a precursor of benzene and naphthalene via cyclopentadienyl radical recombination.

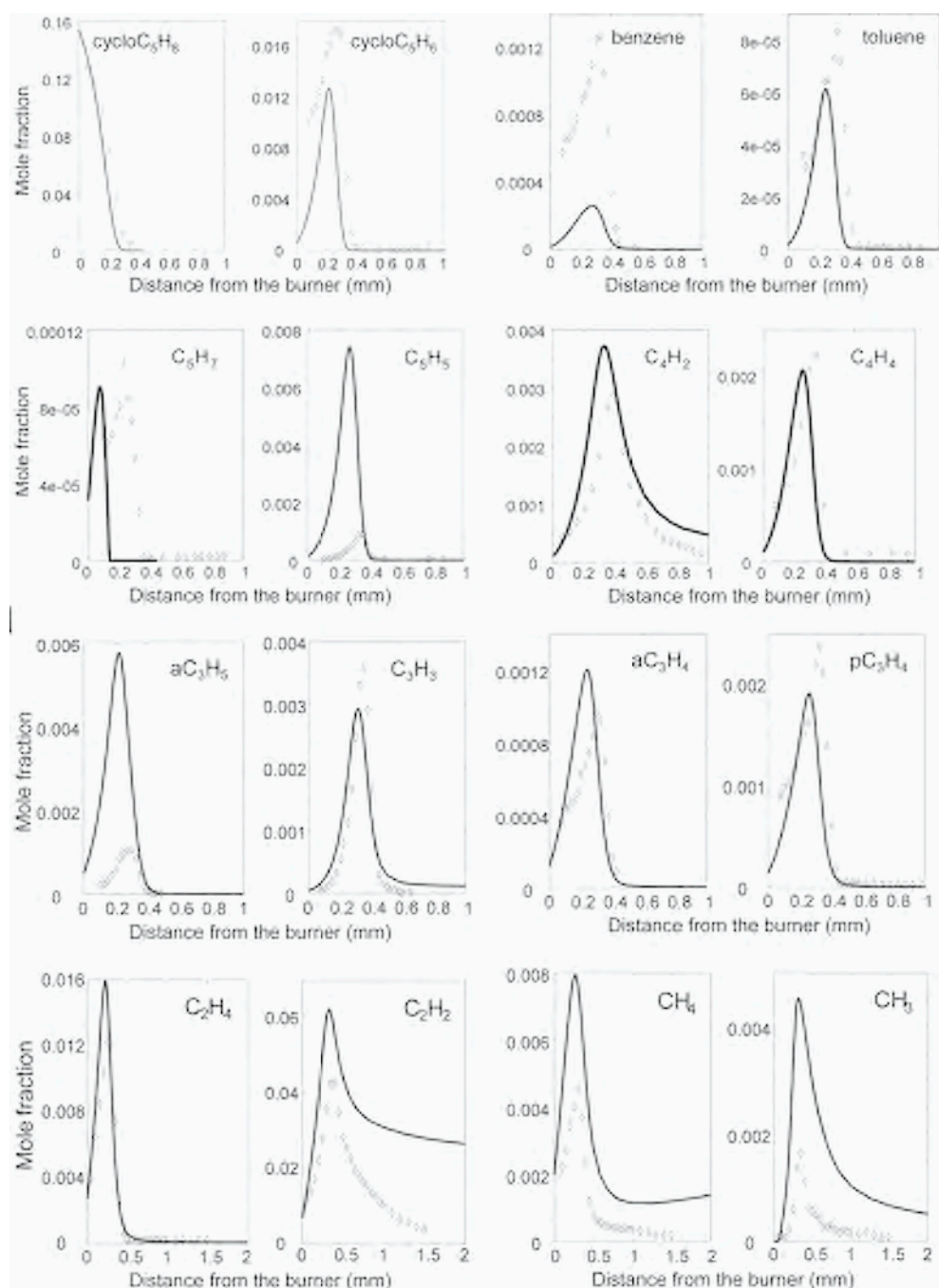


Figure 10. Premixed laminar cyclopentene flame ( $\Phi = 2.0$ ) at 50 mbar [39]. Comparisons of experimental measurements (points) and model predictions (lines).

Cyclopentadiene is a precursor of benzene only at intermediate temperatures. At temperatures higher than 1200 K, the even  $C_4 + C_2$  mechanism becomes the dominant one.

Detailed pyrolysis of cycloalkanes, as well alkenes, can give rise to all the skeletal isomers as a result of successive cyclization and decomposition reactions. This is very clearly shown in Figure 12, in which the isomerization and decomposition reactions of cyclohexyl radical are considered. Starting from cyclo-hexane and cyclo-hexyl radical, it is possible to obtain all the hexenyl radicals, the methyl- pentenyl and cyclopentyl

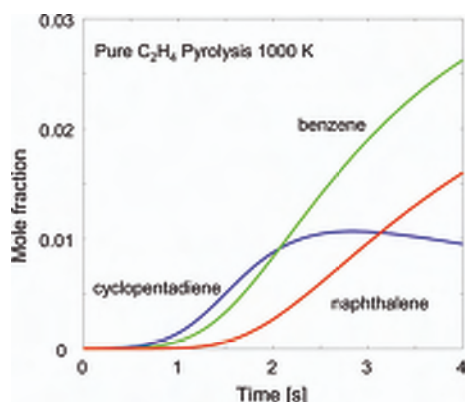


Figure 11. Ethylene pyrolysis (1000 K and 1 bar). Predicted mole fractions vs. contact time.

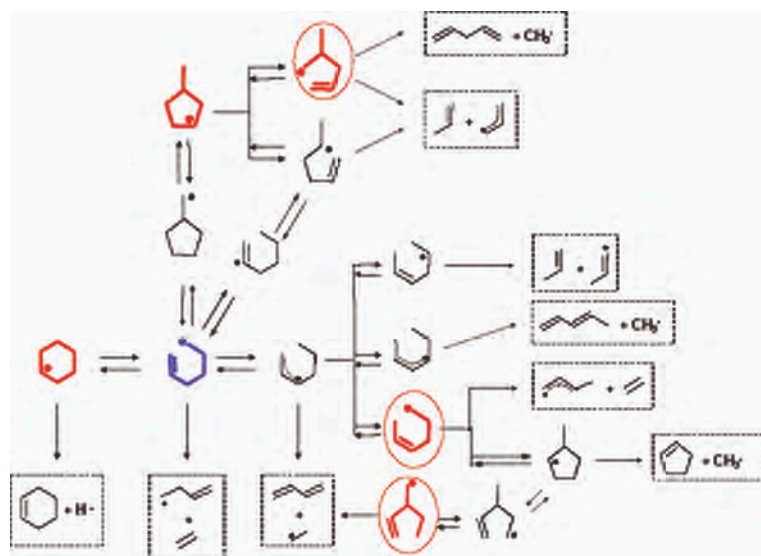


Figure 12. Isomerization and decomposition reactions of cyclohexyl radical. Almost all the skeletal isomers can be formed.

radicals. Several unsaturated radicals, such as  $C_5H_7$  and  $C_6H_9$  radicals, are resonantly stabilized and can, through cyclization reactions, form cyclopentadiene or benzene and toluene or can add on unsaturated species or recombine. Thus all these reactions need to be accounted for in the model. Similar considerations are also reported in Tsang's paper [42] in which he stresses the need to define rate parameters for new reaction classes, i.e. cyclization of alkenyl radicals and H transfer in cyclic molecules.

The overall system is partially simplified because of the great number of possible isomerization reactions and the propensity of the reacting system to move following the faster and easier reaction paths. Similar difficulties in characterizing the behavior of hexadiene isomers, added as a doped agent in a methane flame, are referred to by Pfefferle and McEnally [43]. They report the relative reactivity of the 9 different hexadienes with the parameter  $T_{g,1\%}$ , which is the centerline temperature at the height where the centerline dopant concentration has decreased to 1% of its value in the fuel. Figure 13 simply shows the primary decomposition reactions of all the isomers and explains this relative reactivity. 3methyl-1,4pentadiene, together with 1,3 and 1,5-hexadiene are the more reactive isomers due to the formation of allyl type radicals with direct breaking of C-C bonds. 1,3 and 2,4-hexadiene isomerizes quickly through a 6 center molecular path. 2,3dimethyl-1,3butadiene and 2methyl-1,3pentadiene are the less reactive due to the formation of resonantly stabilized radicals, the ultimate fate of which is either recombination or addition reactions. The remaining isomers of hexadienes, after the initial dehydrogenation of allyl sites, can only move through cyclization and dehydrogenation reactions. The successive demethylation reactions are not straightforward for hexadiene isomers with methyl substitutions in vinyl positions and this fact reduces their reactivity. Larger alkenyl and cycloalkyl radicals can always decompose simply and once again the kinetic difficulties are in the area of the smaller species where decomposition, isomerization or cyclization reactions are not possible, and radicals can only add on unsaturated species or recombine, contributing in this way to aromatic and PAH formation.

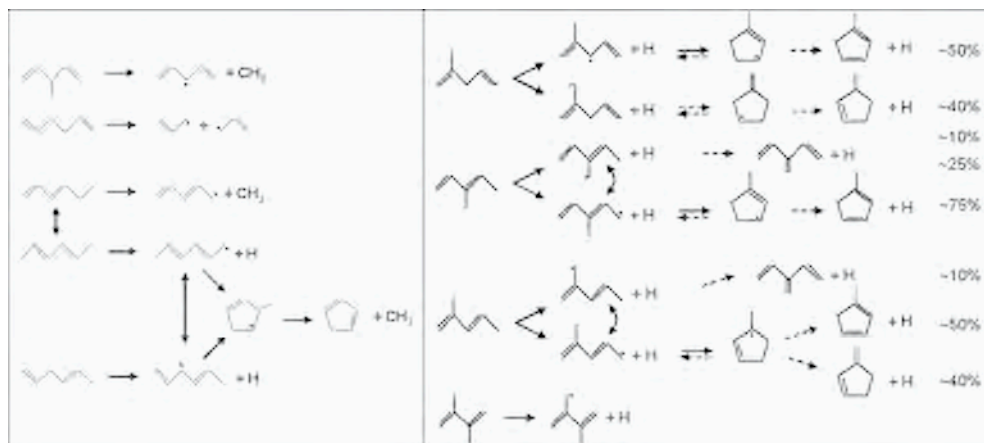


Figure 13. Primary decomposition reactions of the nine isomers of hexadiene.

### 4.3. Reliability of the kinetic mechanisms of pyrolysis and combustion of aromatics

As recently observed by Farrell et al. [44], even though benzene and toluene has been the focus of much attention in terms of kinetic modeling and detailed mechanisms do exist for pyrolysis and combustion [45,46,47], there is still a lack of high-quality rate coefficient data for many of the reactions of importance. As clearly discussed by Tsang [48], once alkyl side chains of large aromatic molecules have been reduced to one or two carbon atoms, end primary products include significant amounts of resonantly stabilized radicals, principally benzyl and  $C_8H_9\bullet$  radicals together with methyl- and dimethyl-styrene. Once again, the key point is the kinetic modeling of benzene, toluene and xylene decomposition. Vanhove et al. [49] studied the effect of aromatic addition to PRF in the Lille rapid compression machine, and these data are very useful in validating the low temperature mechanisms, mostly in terms of total and cool flame ignition delay times. Figure 14 shows a sample of comparisons between experimental data and model predictions. Delay times predicted with the LLL06 model [20] show that detailed and semi-detailed schemes give equivalent predictions.

Recent efforts to revise the toluene mechanism at high temperatures were discussed by Sivaramakrishnan et al. [50]. A detailed kinetic model was developed to predict the oxidation of toluene in the high temperature regime (1200-1500 K) over wide pressure ranges based on experimental data obtained in the high pressure single pulse shock tube. This model, which was derived from a previous reaction scheme, is a further step towards the development of a more comprehensive kinetic model for aromatic pyrolysis and combustion.

Sooting tendencies for several aromatic hydrocarbons have been determined by McEnally and Pfefferle [43]. They observed that soot propensity depends strongly on molecular structure and also discuss the chemical mechanisms responsible for fuel decomposition and hydrocarbon growth. Important naphthalene formation pathways,

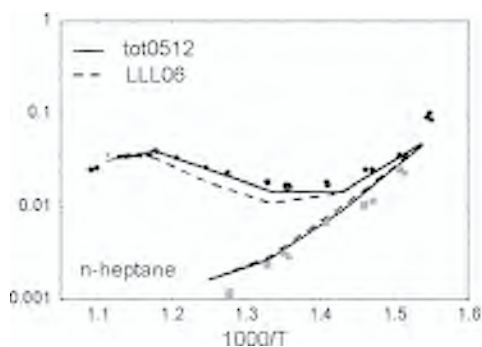


Figure 14a. n-heptane oxidation in RCM. Total and cool flame delay times[s] vs.  $1000/T$ . Experimental data (points) and model predictions (lines) [49].

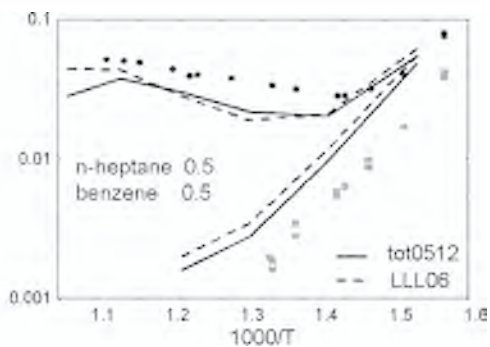


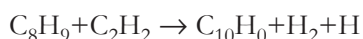
Figure 14b. n-heptane-benzene oxidation in RCM. Total and cool flame delay times[s] vs.  $1000/T$ . Experimental data (points) and model predictions (lines) [49].

including methyl addition to indenyl, were analyzed. This pathway is particularly significant for the conversion of indene to naphthalene. Finally, the oxidation reactions of two ring aromatics were discussed in a paper by Lindstedt et al. [51] in which particular attention was also devoted to the successive reactions of indene and to the different paths to naphthalene formation.

## 5. MODEL PREDICTIONS FROM PYROLYSIS OF DIFFERENT SURROGATES OF JET FUELS

Figure 15 shows model prediction of different species from pyrolysis of different surrogates, always at 1300 K. The effect of the different reference components is quite clear. For instance, the significant presence of methyl-naphthalene in the Drexel surrogate makes two ring aromatic compounds directly available in the reacting system thus favoring the formation of soot precursors and the successive soot inception. A more similar behavior, in terms of intermediate PAH, is observed when comparing San Diego and Utah surrogates.

As a final example, Figure 16 compares two different formulations of San Diego surrogate, substituting the 20% of xylene with toluene. The different yields of intermediate PAHs obtained from the pyrolysis of the two different formulations, respectively referred as surrogates X and T, indicate the importance of the proper characterization of all the successive steps of PAH growth. The larger content of benzene obtained from surrogate T is clearly the result of the initial presence of toluene in the fuel due to the demethylation reaction. The expected larger amount of naphthalene from surrogate X, as a result of acetylene addition on xylene radical:



is balanced by the larger amount and activity of phenyl radical in surrogate X. The predicted coronene from surrogate X is significantly higher. To properly predict large PAHs becomes increasingly difficult and the works of McEnally and Pfefferle [43] and Lindstedt et al. [51] are good examples of the need for further modeling and experimental work in this area of research.

## 6. CONCLUSIONS

The following features can be outlined quite simply using this kinetic analysis:

- ‘ab initio’ calculations and a systematic classification of elementary reactions of small molecules already allows the characterization of the formation of precursors and first PAH species.
- Lumping procedures easily allow large hydrocarbon molecules to be handled and to the extension of the simulation capability of semi-detailed kinetic models. Large alkyl radicals can be directly transformed into their decomposition products.
- Selection of proper candidates of fuel surrogates depends more on the target to be reproduced than on the availability of kinetic information.

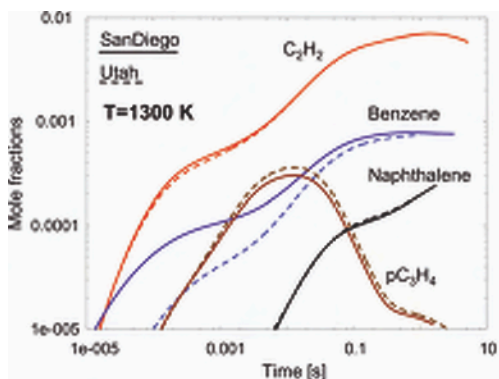


Figure 15a. Pyrolysis of San Diego (solid lines) and Utah surrogate (dashed lines) at 1300K. Mole fractions vs. time [s].

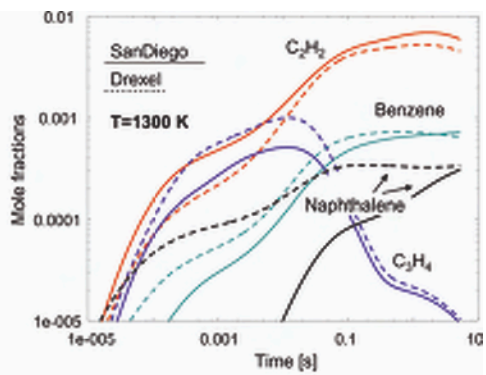


Figure 15b. Pyrolysis of San Diego (solid lines) and Utah surrogate (dashed lines) at 1300K. Mole fractions vs. time [s].

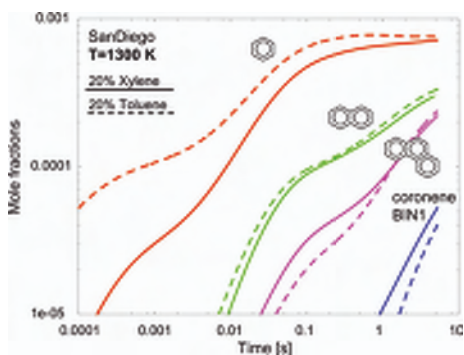


Figure 16. Pyrolysis of San Diego surrogates, with 20% xylene (solid lines) and 20% toluene (dashed lines) at 1300K. Mole fractions vs. time [s].

- Naphthene and aromatic components require further kinetic efforts, both in modeling and experimental testing. Once again, large radical species promptly decompose and the very good paper by McEnally et al [32] provides useful information on the key stable radicals to be included in detailed kinetic models.

Finally, as Frenklach [52] quite correctly stated the critical point remains the organization of the scientific data, the availability of the tools for the analysis and processing of the data, and the engagement of the entire combustion community in the collection of data.

## ACKNOWLEDGEMENTS

I wish to acknowledge and state my appreciation for the suggestions of my colleagues Mario Dente, Tiziano Faravelli, Guido Buzzi Ferraris and Sauro Pierucci at the Politecnico di Milano, as well as all the work and activity of my young coworkers Silvia Granata and Alessio Frassoldati.

## REFERENCES

1. C. K. Westbrook, F. C. Dryer, *Prog. Energy Combust. Sci.* 10(1) (1984) 1-57.
2. M. Dente, G. Bozzano, T. Faravelli, A. Marongiu, S. Pierucci, E. Ranzi, in *Advances in Chemical Engineering*, G.B. Marin (Ed.) 32 (2007) 51-168.
3. J. W. Hudgens, *Workshop on combustion simulation databases for real transportation fuels* NIST Gaithersburg, MD, (2003).
4. G. Blanquart, H. Pitsch, 5th US Combustion Meeting. San Diego, March 25-28, 2007.
5. H. J. Curran, P. Gaffuri et al. *Combust. Flame* 114 (1-2) (1998) 149-177; *Combust. Flame* 129 (3) (2002) 253-280.
6. E. Ranzi, M. Dente, T. Faravelli, G. Pennati, *Combust. Sci. Technol.* 95 (1994) 1-50.
7. J. Warnatz, in *Combustion Chemistry*, W. C. Gardiner. (Ed.) New York, Springer-Verlag, 1984.
8. A. M. Dean, *J. Phys. Chem.* 89 (1985) 4600.
9. W. Tsang, *J. Phys. Chem. Ref. Data* 17 (1988) 887.
10. F. O. Rice, K. F. Herzfeld, *J. Am. Chem. Soc.* 55 (1933) 3035-3040.
11. A. Kossiakoff, F. O. Rice, *J. Am. Chem. Soc.* 65: (1943) 590-595.
12. S. W. Benson, *Thermochemical Kinetics*, New York, John Wiley & Sons, 1976, 2nd ed.
13. D. M. Matheu, W. H. Green et al., *Int. J. Chem. Kinet.* 35 (2003) 95-119.
14. M. Dente, E. Ranzi, in *Pyrolysis: Theory and Industrial Practice*, L. F. Albright, B. L. Crines, W. H. Corcoran (Eds.) Academic Press, San Diego, 1983, chap. 7.
15. E. Ranzi, T. Faravelli, A. Frassoldati, S. Granata, *Ind. Eng. Chem.* 44 (2005) 5170-5183.
16. C. P. Wood, V. McDonell, R. Smith, G. Samuelson, *J. Propul. Power* 5 (4) (1989) 399-405.
17. T. Edwards, L. Q. Maurice, *J. Propul. Power* 17 (2) (2001) 461-466.
18. K. H. Altgelt, M. M. Boduszynski, *Composition and Analysis of Heavy Petroleum Fractions*, New York, Marcel Dekker, 1994.
19. B. M. Gauthier, D. F. Davidson, R. K. Hanson, *Combust. Flame* 139 (2004) 300-311.
20. C. V. Naik, W. J. Pitz, M. Sjöberg, J. E. Dec, J. Orme, H. J. Curran, J. M. Simmie, C. K. Westbrook, SAE paper 2005-01-3741.
21. M. Mehl, T. Faravelli, F. Giavazzi, E. Ranzi, P. Scorletti, A. Tardani, D. Terna, *Energy & Fuels* 20 (2006) 2391-2398.
22. J. F. Roesler, S. Martinot, C.S. McEnally, L.D. Pfefferle, J.-L. Delfau, C. Vovelle, *Combust. Flame* 134 (2003) 249-260.
23. D.F. Davidson, M.A. Oehlschlaeger, R.K. Hanson, *Proc. Combust. Inst.* 31 (2007) 321-328.
24. A. Agosta, N. P. Cernansky, D. L. Miller, T. Faravelli, E. Ranzi, *Exp. Therm Fluid Sci.* 28 (7) (2004) 701-708.
25. C.J. Montgomery, S.M. Cannon, M.A. Mawid, B. Sekar, 40th AIAA Aerospace Sciences Meeting, Reno, Nevada, January 2002, Paper 2002-0336.

26. A. Violi, S. Yan, E.G. Eddings, F. Sarofim, S. Granata, T. Faravelli, E. Ranzi, *Combustion Sci. Technol.* 174 (2002) 399-417.
27. E. G. Eddings, S. Yan, W. Ciro, A. F. Sarofim, *Combust. Sci. Technol.* 177 (2005) 715-739.
28. S. Humer, A. Frassoldati, S. Granata, T. Faravelli, E. Ranzi, R. Seiser, K. Seshadri, *Proc. Combust. Inst.* 31 (1) (2007) 393-400.
29. H. Zhang, E. G. Eddings, A. F. Sarofim, C. L. Mayne, Z. Yang, R. J. Pugmire, in *Combustion Generated Fine Carbonaceous Particles*, H. Bockhorn, A. D'Anna, A.F. Sarofim, H. Wang (Eds.) Karlsruhe University Press, 2009, pp. 137-162.
30. E. Ranzi, *Energy & Fuels* 20 (2006) 1024-1032.
31. S. Granata, F. Cambianica, S. Zinesi, T. Faravelli, E. Ranzi, *European Combustion Meeting Louvain-la-Neuve Belgium April 3-6, 2005*.
32. C.S. McEnally, L.D. Pfefferle, B. Atakan, K. Kohse-Höinghaus, *Prog. Energy Combust. Sci.*, 32 (2006) 247-294.
33. J. F. Roesler, *Proc. Combust. Inst.* 27 (1998) 287-293.
34. C. S. McEnally, D. M. Ciuparu, L. D. Pfefferle, *Combust. Flame* 134 (2003) 339-353.
35. S. Granata, T. Faravelli, E. Ranzi, *Combust. Flame* 132 (2003) 533-544.
36. C. Cavallotti, R. Rota, T. Faravelli, E. Ranzi, *Proc. Combust. Inst.* 31 (1) (2007) 201-209.
37. M. E. Law, P. R. Westmoreland, T. A. Cool, J. Wang, N. Hansen, C. A. Taatjes, T. Kasper, *Proc. Combust. Inst.* 31 (2007) 565-573.
38. A. Ciajolo, A. Tregrossi, personal communication, 2007.
39. N. Hansen, T. Kasper, S. J. Klippenstein, P. R. Westmoreland, M. E. Law, C. A. Taatjes, K. Kohse-Höinghaus, J. Wang, T. A. Cool, *J. Phys. Chem. A* 111 (19) (2007) 4081-4092.
40. R. P. Lindstedt, K.-A. Rizos, *Proc. Combust. Inst.* 29 (2002) 2291-2298.
41. T. Kunugi, T. Sakai, K. Soma, Y. Sasaki, *Ind. Eng. Chem. Fund.* 8 (1969) 374.
42. W. Tsang, I.A. Awan, W.S. McGivern, J.A. Manion, in *Combustion Generated Fine Carbonaceous Particles*, H. Bockhorn, A. D'Anna, A.F. Sarofim, H. Wang (Eds.) Karlsruhe University Press, 2009, pp. 55-74.
43. C. S. McEnally, L. D. Pfefferle, *Combust. Flame* 148 (2007) 210-222.
44. J. T. Farrell, N. P. Cernansky, F. L. Dryer, D. Friend, C-A. Hergart, C. K. Law, R. M. McDavid, C. J. Mueller, A. Patel, H. Pitsch, *SAE Pap. 2007-01-0201 World Congress, April 2007, Detroit*.
45. R.P. Lindstedt, L.Q. Maurice, M. Meyer, *Faraday Discuss.* 119 (2001) 409-432.
46. S.D. Klotz, K. Brezinsky, I. Glassman, *Proc. Combust. Inst.* 27 (1998) 337-344.
47. H. Richter, J. B. Howard, *Phys. Chem. Chem. Phys.* 4 (2002) 2038-2055.
48. W. Tsang, *Data Science Journal* 3 (2004) 1-9.
49. G. Vanhove, G. Petit, R. Minetti, *Combust. Flame* 145 (3) (2006) 521-532.
50. R. Sivaramakrishnan, R.S. Tranter, K. Brezinsky, *Proc. Combust. Inst.* 30 (2005) 1165-1173.
51. R.P. Lindstedt, V. Markaki, R.K. Robinson, in *Combustion Generated Fine Carbonaceous Particles*, H. Bockhorn, A. D'Anna, A.F. Sarofim, H. Wang (Eds.) Karlsruhe University Press, 2009, pp. 499-522.
52. M. Frenklach, *Proc. Combust. Inst.* 31 (2007) 125-140.

# Aromatic hydrocarbon growth mechanisms in flames: insights from sooting tendency measurements

C.S. McEnally, L.D. Pfefferle

Department of Chemical Engineering and Center for Combustion Studies,  
Yale University, New Haven CT 06520-8286

*Abstract: Over the last two years we have measured sooting tendencies for 130 aromatic hydrocarbons. The dependence of these sooting tendencies on fuel structure has several implications about the chemical processes that grow aromatic hydrocarbons into soot particles in flames. First, cyclohexadienyl and cyclopentadienyl rings readily convert into benzenoid rings. Second, addition of the first additional benzenoid ring to the fuel is a rate-limiting step for one, two, and three ring aromatics. Third, aromatic growth rates correlate more strongly with degree of unsaturation and cyclization than they do with molecular size. However, the correlations are not particularly strong in either case, such that the specific details of fuel structure strongly affect aromatics growth. Finally, chemical condensation pathways are an important growth process for many biaryls.*

## 1. INTRODUCTION

One of the most striking phenomenological aspect of soot formation is that different fuels often produce very different amounts of soot under the same combustion conditions [1]. Over the last two years we have systematically studied these differences for aromatic fuels by measuring the sooting tendencies of over 130 one-, two-, and three-ring hydrocarbons [2, 3]. These measurements have revealed several important elements of the chemical mechanisms that grow aromatic hydrocarbons into soot particles. This paper summarizes these observations.

Sooting tendency was defined as the maximum soot volume fraction  $f_{v,max}$  measured on the centerline of a methane/air nonpremixed flame whose fuel was doped with small concentrations (5 to 400 ppm) of the test compound. The dopants were added to the methane with a syringe pump and soot volume fraction was measured with laser-induced incandescence. Solid dopants were dissolved in 2-heptanone and then the liquid solutions were injected. In order to compare measurements from flames with different dopant concentrations, the results were converted into apparatus-independent Yield Sooting Indices (YSI's) by the relation  $YSI = C * f_{v,max} + D$ , where C and D are apparatus-dependent constants chosen so that YSI-benzene = 30 and YSI-naphthalene = 100. The uncertainties range from  $\pm 3\%$  for volatile liquid aromatics to  $\pm 10\%$  for solid aromatics, such as anthracene, that have very low solubilities in heptanone.

For aromatics this definition of sooting tendency is superior to the conventional definition based on the heights or fuel flowrates of smoke point flames [4, 5]. First,

the smoke point flames for aromatics are typically less than 10 mm tall, so their heights or flowrates cannot be measured accurately. In contrast, with our definition the dopant concentration can be tuned to produce an easily measured range of  $f_{v,max}$  for any group of test compounds. Second, very little sample is required to dope a flame to 400 ppm ( $\sim 100 \mu\text{L}$ ), which greatly expands the range of compounds that can be tested. The net result of these advantages is that our YSI database includes more than five times as many aromatic sooting tendencies as were previously available in the literature, and with much smaller uncertainties.

To illustrate this point, Figure 1 compares the YSI's we have measured for n-alkylbenzenes with literature sooting tendencies for some of the same species based on smoke point flames. These literature values are Threshold Sooting Indices (TSI's) that use the same scale as the YSI's; i.e.,  $\text{YSI-benzene} = \text{TSI-benzene} = 30$  and  $\text{YSI-naphthalene} = \text{TSI-naphthalene} = 100$  [4, 5]. The literature TSI's vary erratically as the side-chain expands from ethylbenzene to pentylbenzene, whereas our YSI's follow a more believable trend of a slow and steady increase. Furthermore, while TSI's have not been measured for any n-alkylbenzenes larger than pentylbenzene, our YSI's extend to tetradecylbenzene ( $\text{C}_{20}\text{H}_{34}$ ).

## 2. CYCLOPENTADIENYL AND CYCLOHEXADIENYL RINGS CONVERT RAPIDLY TO BENZENOID RINGS

The first observation about aromatic growth mechanisms concerns the fate of cyclopentadienyl and cyclohexadienyl rings in the fuel. The first four rows in Figure 2 compare the sooting tendencies of several hydrocarbons that contain cyclohexadienyl rings

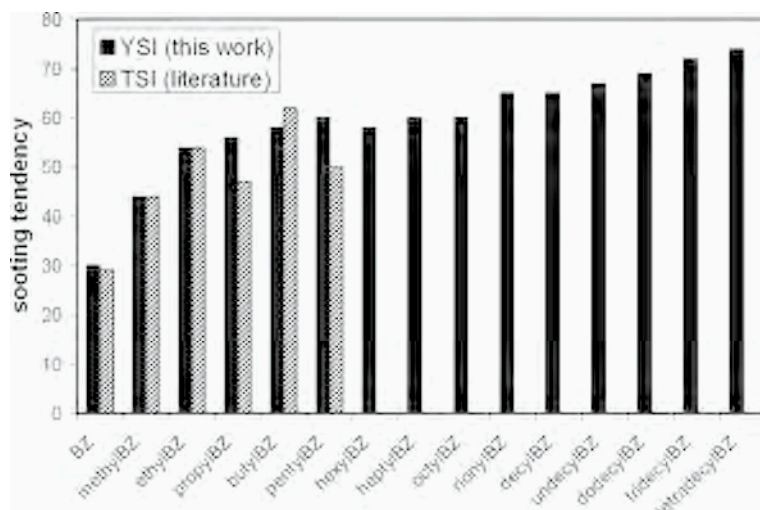
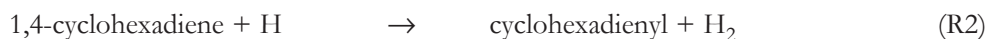


Figure 1. Sooting tendencies of n-alkylbenzenes. YSI = yield sooting index measured in our work and based on maximum soot volume fractions in fuel-doped flames [2, 3]; TSI = threshold sooting index from the literature based on smoke point flames [5].

(left) with the analogous hydrocarbons that contain only benzenoid rings (right). In each case the sooting tendencies agree to within experimental error, which indicates that cyclohexadienyl rings readily convert to benzenoid rings in nonpremixed flames. Possible reaction mechanisms include unimolecular  $H_2$  elimination, e.g.,



and abstraction of a hydrogen atom to produce a resonantly-stabilized cyclohexadienyl-type radical that then dissociates by C-H fission, e.g.,

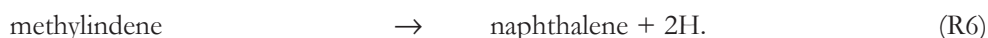
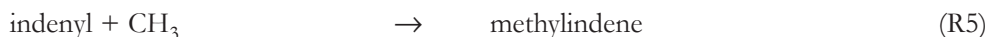
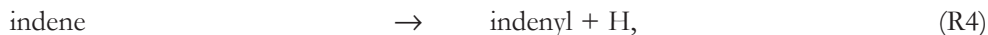


In some cases, such as 1,4-cyclohexadiene, unimolecular  $H_2$  elimination is symmetry-allowed and is known to have a very high rate [6]. In other cases, such as 1,3-cyclohexadiene,  $H_2$  elimination is symmetry-forbidden; however, measurements in very-low-pressure-pyrolysis experiments have determined that it nonetheless has a substantial rate as a unimolecular process, possibly due to initial isomerization to the 1,4 isomer [7]. We have made species measurements in flames doped with benzene, 1,3-, and 1,4-cyclohexadiene [8]; they show that both cyclohexadienes convert to benzene at rates consistent with the Arrhenius parameters measured for unimolecular  $H_2$  elimination in References 6 and 7.



Figure 2. Sooting tendencies and molecular structures of several aromatic hydrocarbons containing cyclohexadienyl, cyclopentadienyl, and benzenoid rings.

The last two rows in Figure 2 compare the sooting tendencies of two hydrocarbons that contain cyclopentadienyl rings (left) with the analogous hydrocarbons that contain only benzenoid rings (right). Again, the sooting tendencies agree to within experimental error, which indicates that cyclopentadienyl rings readily enlarge to benzenoid rings in nonpremixed flames. A possible reaction mechanism for this process is decomposition of the reactant to a resonantly-stabilized cyclopentadienyl-type radical by C-H fission or abstraction of an H-atom, methyl radical addition, and then a series of isomerizations and C-H fissions, e.g.,



This process has been observed experimentally during indene pyrolysis in a shock tube and a flow reactor [9, 10]; the naphthalene yields were  $\sim 10\%$ , even though the only source of methyl radical was indene decomposition. In our flames methyl is much more plentiful, so this mechanism should have a much higher rate and a naphthalene yield near  $100\%$  is reasonable. Virtually all practical combustion fuels contain large alkanes that decompose to methyl radical, so ring enlargement will be similarly rapid in most combustion devices.

### 3. ADDITION OF THE FIRST BENZENOID RING TO THE FUEL IS A RATE-LIMITING SOOT FORMATION STEP

Figure 3 shows how the sooting tendencies of benzene and polycyclic aromatics depend on the number of benzenoid rings. The sooting tendency increases significantly with each additional ring. These results indicate that formation of the first additional ring beyond the number of rings in the fuel is a rate-limiting soot formation step for aromatics with one, two, or three rings. This size range includes virtually all of the aromatic hydrocarbons in practical combustion fuels.

As additional evidence regarding which growth steps are rate limiting, Figure 4 shows the change in the sooting tendency of several aromatics when a methyl group replaces one of their hydrogen atoms. (I.e., the first column is the ratio of YSI-methylbenzene to YSI-benzene, the second is YSI-2-methylindene to YSI-indene, etc.) Four of the aromatics contain only benzenoid rings (solid bars), whereas two also contain cyclopentadienyl rings (striped bars). For all of the species that contain only benzenoid rings, methyl substitution increases the sooting tendency by at least  $20\%$ . This observation suggests that methyl substitution opens up pathways that form the next benzenoid ring more quickly than the pathways from unsubstituted aromatics. A likely candidate for the faster pathways is that the methyl-substituted species are converted to resonantly-stabilized benzyl-type radicals by C-H fission or abstraction of an H-atom, and then propargyl addition leads to the additional ring via a series of isomerizations and C-H fissions, e.g.,

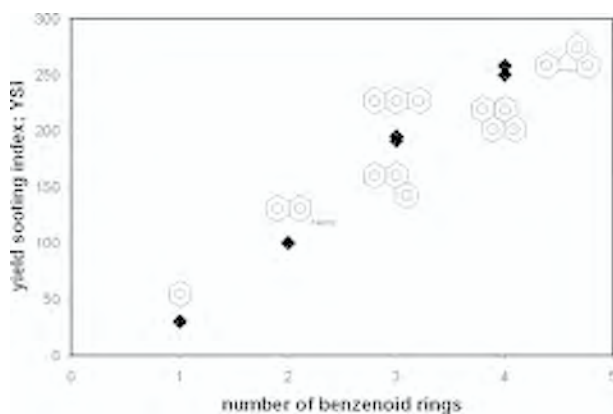


Figure 3. Sooting tendencies of benzene and several polycyclic aromatics.

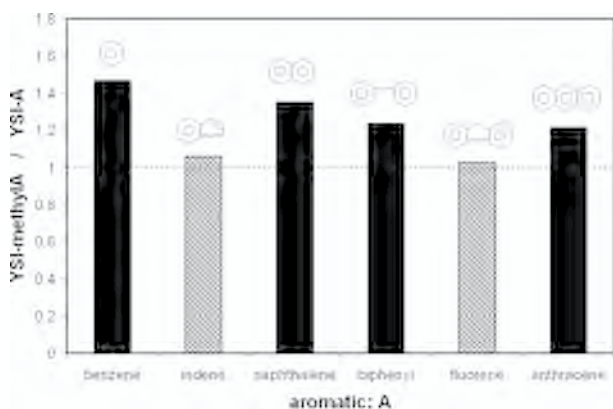
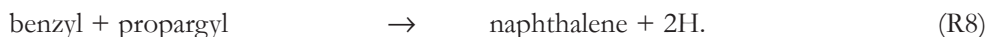
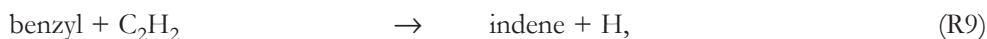


Figure 4. Ratios between sooting tendencies of methyl-substituted and unsubstituted isomers of several aromatic species. The specific isomers for methylA are methylbenzene, 2-methylindene, 1-methylnaphthalene, 4-methylbiphenyl, 1-methylfluorene, and 9-methylantracene.



This mechanism has been proposed to explain naphthalene formation in shock-tube pyrolysis of methylbenzene [11]. As an alternative to (R8), the benzyl-type radicals may also grow by reacting with acetylene to produce species that contain cyclopentadienyl rings, e.g.,



followed by enlargement of the cyclopentadienyl rings to benzenoid rings via sequences such as (R4) to (R6) [12]. In either case, the fact that methyl substitution increases the sooting tendency provides further evidence that formation of the next benzenoid ring is a rate-limiting step.

In contrast, for the species that contain cyclopentadienyl rings, methyl substitution only enhances the sooting tendency by about 5 %. The likely effect of methyl substitution in these cases is to provide an “internal” source of the extra carbon atom required for ring-enlargement; i.e., to replace (R4) and (R5) in the reaction sequence discussed in Section 2.0. Therefore the fact that methyl substitution barely increases the sooting tendency of indene and fluorene suggests that the rate-limiting soot formation step for them is not enlargement to naphthalene and anthracene, but growth of the next aromatic ring onto the naphthalene and phenanthrene.

#### 4. AROMATIC GROWTH RATES ARE MORE SENSITIVE TO UNSATURATION THAN TO MOLECULAR SIZE

Figures 5 and 6 show the sooting tendencies measured for all of the aromatics that contain only carbon and hydrogen atoms. The data are plotted against two molecular descriptors: the carbon number  $N_C$ , which is a measure of molecular size, and the hydrogen deficiency HD, which is a measure of unsaturation and cyclization. For the arbitrary hydrocarbon  $C_xH_y$ ,  $N_C = x$  and  $HD = x + 1 - y/2$ . HD is used instead of the carbon to hydrogen ratio because the latter has a size dependence.  $HD = 0$  for alkanes and increases by one each time a double bond or ring is added to the molecule.

Figure 5 shows that the upper limit to YSI increases linearly with  $N_C$ . However, the lower limit depends weakly on  $N_C$ , so the range of possible sooting tendencies for a given  $N_C$  quickly becomes very large. For example, the YSI's vary by a factor of 4 for  $N_C = 15$  (from 65 for nonylbenzene to 262 for cyclopenta[def]phenanthrene).

In contrast, Figure 6 shows that both the upper and lower limits of YSI scale linearly with HD, such that the range of possible sooting tendencies stays roughly

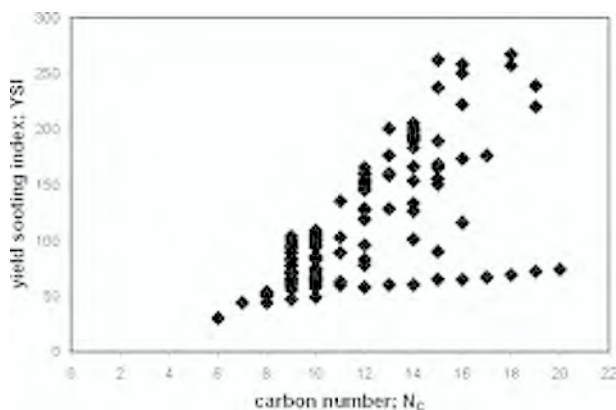


Figure 5. Sooting tendencies of aromatic hydrocarbons.  $N_C = x$  for the hydrocarbon  $C_xH_y$ .

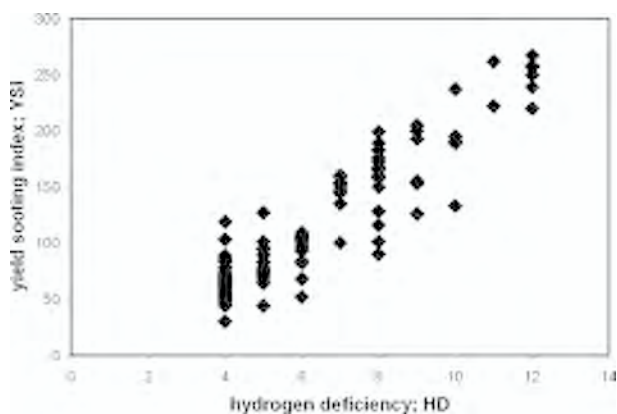


Figure 6. Sooting tendencies of aromatic hydrocarbons.  $HD = x + 1 - y/2$  for the hydrocarbon  $C_xH_y$ .

fixed. Thus the sooting tendencies correlate much better with HD than with  $N_C$ , which indicates that aromatic growth rates are more strongly affected by degree of unsaturation/cyclization than by molecular size.

## 5. AROMATIC GROWTH RATES ARE HIGHLY SENSITIVE TO FUEL STRUCTURE

In many cases hydrocarbons with very similar structures have very different sooting tendencies. Usually these differences can be readily explained in terms of the likely decomposition and aromatic growth reactions. Figure 7 presents three examples. The first row shows that propylbenzene (left) soots more heavily than isopropylbenzene (right). Propylbenzene likely decomposes by C-C fission between the  $\alpha$  and  $\beta$  carbon atoms to produce a resonantly-stabilized benzyl radical and an ethyl radical. Thus propylbenzene has a sooting tendency similar to other species that dissociate to benzyl (e.g., ethylbenzene with  $YSI = 54$ ). In contrast, isopropylbenzene likely decomposes by C-C fission between the  $\alpha$  carbon atom and either of the two  $\beta$  carbon atoms to produce a resonantly-stabilized  $\alpha$ -methyl-benzyl radical and a methyl radical. The  $\alpha$ -ethylbenzyl radical likely then dissociates by C-H fission to styrene. Thus isopropylbenzene has a sooting tendency similar to styrene ( $YSI = 44$ ).

The second row of Figure 7 shows that (1-butynyl)-benzene (left) soots much more heavily than (3-butynyl)-benzene (right) even though the only difference between these species is the location of the triple bond relative to the aromatic ring. (1-butynyl)-benzene likely dissociates by C-C fission between the  $\gamma$  and  $\delta$  carbon atoms since this produces a resonantly-stabilized phenyl-propargyl radical. This radical can then cyclize to form a five-membered ring, which in turn can grow to a benzenoid ring. Thus the sooting tendency of (1-butynyl)-benzene is comparable to indene ( $YSI = 100$ ). In contrast, (3-butynyl)-benzene likely dissociates by C-C fission between the  $\alpha$  and  $\beta$  carbon atoms since this produces resonantly-stabilized benzyl and propargyl radicals. Thus (3-

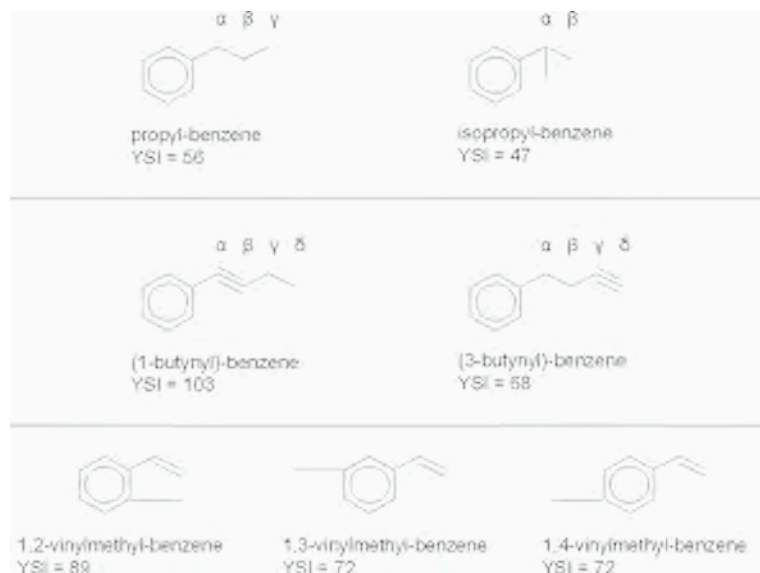


Figure 7. Sooting tendencies and molecular structures of several groups of hydrocarbons.

butynyl)-benzene has a sooting tendency similar to other species that dissociate to benzyl (e.g., pentylbenzene with YSI = 60).

Finally the last row of Figure 7 shows the three geometric isomers of vinylmethylbenzene. The sooting tendency is relatively large for the 1,2 isomer (left), where the side-chains are attached to adjacent carbon atoms, and is smaller for the 1,3 and 1,4 isomers (middle and right), where at least one carbon atom is between the two side-chains. All three isomers likely decompose to resonantly-stabilized vinylbenzyl radicals by C-H fission in the methyl group or by abstraction of a hydrogen atom from the methyl group. The 1,3 and 1,4 isomers likely then grow by propargyl addition reactions analogous to (R8) with the vinyl groups not directly participating. In contrast, in the vinylbenzyl radical produced from the 1,2 isomer the side-chains can link together to form indenyl and then grow to naphthalene by the sequence (R5) to (R6).

## 6. CHEMICAL CONDENSATION PATHWAYS ARE IMPORTANT FOR SOME BIARYLS

Biaryls are stable hydrocarbons that consist of two aromatic radicals held together by aliphatic bonds. Figure 8 shows nine examples. Biaryls can potentially grow to larger aromatics by two mechanisms: *fragmentation* of their aliphatic bonds to produce aromatic radicals which then grow separately, and chemical *condensation* where the aliphatic bonds serve as the basis for new rings. Figure 9 shows three examples of condensation pathways.



Figure 8. Sooting tendencies and molecular structures of several biaryls.

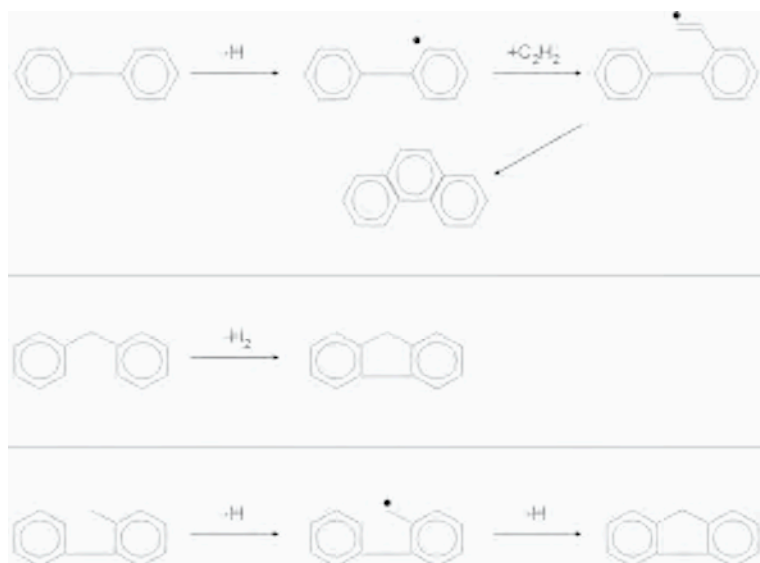


Figure 9. Several possible chemical condensation pathways for biaryls.

The sooting tendencies for the biaryls suggest that condensation is important in some cases. Figure 8 shows three series of biaryls that illustrate this observation. The first row compares the sooting tendencies of three biaryls that contain varying numbers of carbon atoms between their rings. Fragmentation of biphenyl (left) produces two phenyl radicals, fragmentation of diphenylmethane (middle) produces one phenyl radical and one benzyl radical, and fragmentation of dibenzyl (right) produces two benzyl radicals. Since benzyl is a better nucleus for growth to naphthalene as discussed in Section 3.0, this implies that if fragmentation were the dominant decomposition process then the sooting tendencies would follow the order biphenyl < diphenylmethane < dibenzyl. However, the observed order is biphenyl = diphenylmethane > dibenzyl, which suggests that condensation reactions are important for biphenyl and diphenylmethane. Furthermore, the sooting tendency of dibenzyl (YSI = 101) is roughly twice that of species that decompose readily to benzyl radical (e.g., ethylbenzene with YSI = 54), whereas the sooting tendencies of biphenyl (YSI = 128) is much more than twice the sooting tendency of species that decompose readily to phenyl radical (e.g., bromobenzene with YSI = 37).

The top row of Figure 9 shows a possible condensation process for biphenyl: a hydrogen atom is abstracted from or dissociates from one of the four carbon atoms adjacent to the aliphatic bond, an acetylene fills the radical site, and finally the radical site at the end of the C2 side-chain links with the other benzenoid ring to produce a new ring. This reaction was proposed at least twenty years ago [13]; more recently it has been studied with high level calculations [14], and it has been shown to be important for modeling soot formation in shock tube pyrolysis of acetylene and benzene [15].

The middle row of Figure 9 shows a possible condensation reaction for diphenylmethane. It consists of unimolecular H<sub>2</sub> elimination to produce fluorene, which would then be expected to grow rapidly to phenanthrene as discussed in Section 2.0. This reaction has been proposed to produce fluorene production during shock tube pyrolysis of toluene [11].

The middle row of Figure 8 provides additional evidence that this type of pathway is important. It compares the sooting tendencies of three isomers of diphenylpropane. The 1,3 isomer (left), where the benzenoid rings are separated by three carbon atoms, has a relatively sooting tendency. On the other hand, the 1,1 and 2,2 isomers (middle and right), where the benzenoid rings are separated by only one carbon atom, have much higher sooting tendencies. The latter isomers are equivalent to substituted diphenylmethanes, so they can condense by pathways analogous to the middle pathway in Figure 9, which explains their high sooting tendencies.

The bottom row of Figure 8 provides evidence for another type of condensation pathway. It compares the sooting tendencies of the three geometric isomers of methylbiphenyl. The 1,2 isomer (left), where the methyl group is adjacent to the aliphatic bond linking the benzenoid rings, has a relatively large sooting tendency. The 1,3 and 1,4 isomers (middle and right), where the methyl group is separated from the aliphatic bond by at least one carbon atom, have similar and lower sooting tendencies.

The bottom row of Figure 9 shows a condensation pathway that can explain the high sooting tendency for the 1,2 isomer. First a hydrogen atom dissociates from or is abstracted from the methyl group to produce a benzyl-type radical, and then the radi-

cal site links with the other benzenoid ring to form fluorene. Again, the fluorene would then grow rapidly to phenanthrene.

## ACKNOWLEDGMENTS

We thank Wenjing Zeng for assistance with the experiments and the National Science Foundation (CTS-0121765) for financial support.

## REFERENCES

1. I. Glassman, *Proc. Combust. Inst.* 22 (1988) 295-311.
2. C.S. McEnally, L.D. Pfefferle, *Combust. Flame* 148 (2007) 210-222.
3. C.S. McEnally, L.D. Pfefferle, *Proc. Combust. Inst.*, in press.
4. H.F. Calcote, D.M. Manos, *Combust. Flame* 49 (1983) 289-304.
5. D.B. Olson, J.C. Pickens, R.J. Gill, *Combust. Flame* 62 (1985) 43-60.
6. S.W. Benson, R. Shaw, *Trans. Faraday Soc.* 63 (1967) 985-992.
7. Z.B. Alfassi, S.W. Benson, D.M. Golden, *J. Am. Chem. Soc.* 95 (1973) 4784-4788.
8. C.S. McEnally, L.D. Pfefferle, *Combust. Flame* 136 (2004) 155-167.
9. A. Laskin, A. Lifshitz, *Proc. Combust. Inst.* 27 (1998) 313-320.
10. M. Lu, J.A. Mulholland, *Chemosphere* 42 (2001) 625-633.
11. M.B. Colket, D.J. Seery, *Proc. Combust. Inst.* 25 (1994) 883-891.
12. P. Lindstedt, L. Maurice, M. Meyer, *Faraday Discuss.* 119 (2001) 409-432.
13. M. Frenklach, D.W. Clary, W.C. Gardiner, S.E. Stein, *Proc. Combust. Inst.* 21 (1986) 1067-1076.
14. V.V. Kislov, A.M. Mebel, S.H. Lin, *J. Phys. Chem. A* 106 (2002) 6171-6182.
15. H. Böhm, H. Jander, D. Tanke, *Proc. Combust. Inst.* 27 (1998) 1605-1612.



# Selection of surrogates for jet fuels

H.R. Zhang<sup>1</sup>, E.G. Eddings<sup>1</sup>, A.F. Sarofim<sup>1</sup>, C.L. Mayne<sup>2</sup>,

Z. Yang<sup>1</sup>, R.J. Pugmire<sup>1,2</sup>

<sup>1</sup> Department of Chemical Engineering

<sup>2</sup> Department of Chemistry

University of Utah

Salt Lake City, UT 84112

*Abstract: A detailed characterization of JP fuels is provided based on literature data for the average of 55 worldwide and 4 US Jet-A fuels. These are complemented by NMR analysis of a JP-8 that provides the fractions of the carbon in the fuel that are present as protonated, bridgehead, and non-substituted aromatic carbons and the fractions of aliphatic carbons present methyl, methylene, methine, and quaternary structures. A JP-8 fuel for the study was proposed that satisfied the Jet-A average composition as well as the NMR data. The composite results were used to obtain model representations of chemical compositions of a JP-8 that satisfied the constraints imposed by the classes of chemicals, carbon chain lengths, and average number of substituents for the US average and the breakdown of carbons determined by NMR experiments. The results provide a complete characterization of the n-paraffins, iso-paraffins, cyclo-paraffins, benzenes, tetralins, indans, and naphthalenes. The model representations have been used to show how the class distribution of compounds and the side chain substituents on both aromatic and aliphatic fractions influence soot formation.*

## 1. INTRODUCTION

Surrogate formulations are now commonly used to represent practical fuels in computer simulations and to provide reference fuels for use in characterizing the combustion behavior of fuels without the variations inherent in the composition of real fuels because of differences in crude source, refinery conditions, and aging. Furthermore, the complexity of real fuels makes it impossible to follow, in detail, the physical and chemical processes involved in combustion. Surrogate formulations in current use vary widely depending upon the properties, physical or chemical, of the real fuel that needs to be reproduced. The present paper describes the characterization of jet fuels and the development of methods for defining surrogates for selected applications. In this study, we will complement the excellent review on surrogate jet fuels provided by Colket et al. [1], providing additional information on the use of NMR for functional group analysis and on selecting surrogates that accurately match the sooting characteristics of jet fuels.

### 1.1. Origin of jet fuels

Jet fuels are derived from crude petroleum as a distillate cut of about 140 to 300 C, as shown schematically in Figure 1 (adapted from Speight [2]). This figure also provides

the distillate ranges for other common transportation fuels for comparison. The components of petroleum are determined by its biogenic origin, modified by the molecular scrambling that occurs during geological time spans. From Figure 1 it can be seen that the major classes of compounds contained in petroleum are normal and branched (iso-) paraffins, mono- and polycyclic cycloparaffins (also known as cycloalkanes and naphthenes) and mono- and polynuclear aromatics. Within the distillate cut for jet fuels it can be seen that the relative amounts of the different classes change with boiling temperature with the concentrations of polycyclic paraffins and polynuclear aromatics increase with boiling point while the total paraffin content decreases. The aromatic and polycyclic paraffins are usually substituted, several substituents per ring. The iso-paraffins often reflect their biogenic origin, i.e., they have structures clearly derived from those of saturated polyisoprenes (methyl substituted n-paraffins with three methylene substituted groups between successive methyl substituents). The composition of jet fuel will vary with the composition of the parent crude, the refining conditions, and small amounts of additives used (e.g., U.S. domestic airlines often use Jet-A fuels with a higher freezing point, called Jet-A1, to reduce cost; JP-8 will typically include a military additive package; see page 29 of reference [3] from Chevron). An important measure of the variability in sooting tendency of jet fuels is the aromatic content, which ranges from

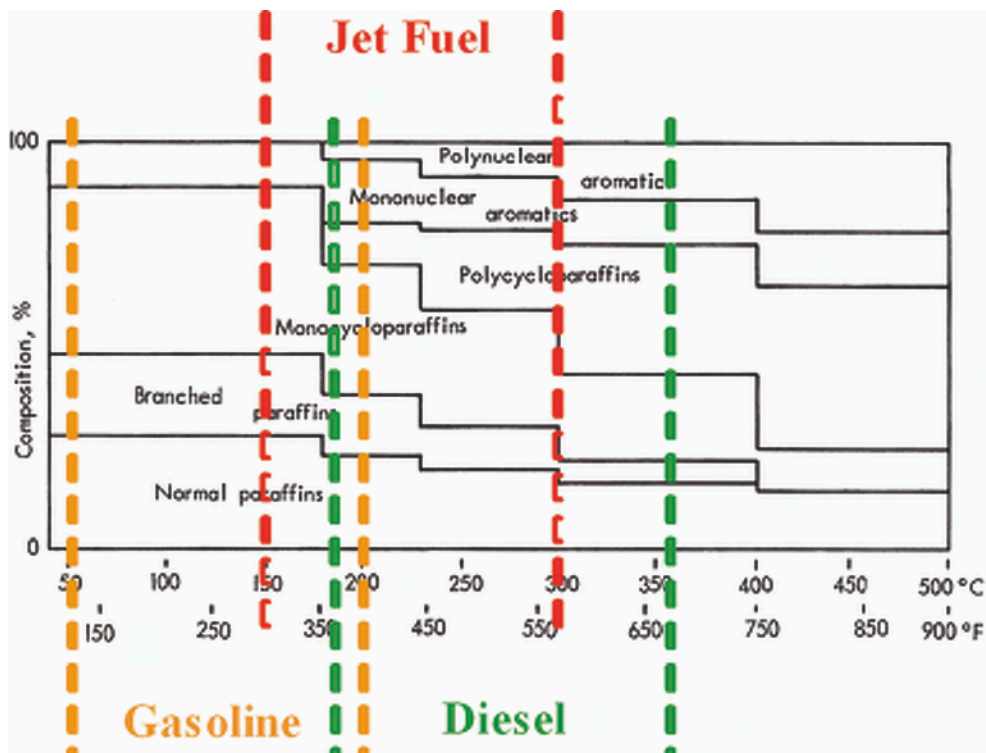


Figure 1. Composition distribution for distillate cuts of petroleum used for different fuels (adapted from Speight [2]).

11.5 to 25% by volume in JP-8 deliveries during 2004 (see Figure 1 in Colket et al. [1]). Additional measures of variability are provided by the percentage range of chemical classes in jet fuels from four US refiners specified by Edwards [4] for aviation fuels. The aromatic content ranges from 8% to 26% by volume with a mean of 19.1% ( $\sigma = 3.1\%$ ). Monocyclic paraffin content ranges from 0 to 26% (estimated mean 13.4%,  $\sigma = 4.8\%$ ) and iso- plus normal paraffin content ranges from 34 to 78% (mean 55.1%,  $\sigma = 7.6\%$ , with 17.6% normal paraffin).

## 1.2. Characterization of fuels

Jet fuels are composed of thousands of compounds, present in widely varying amounts that fall into the classes shown in Figure 1. A gas chromatographic (GC/MS) analysis of a Jet-A fuel is shown in Figure 2. The peaks for normal paraffins, present in relatively high concentrations, stand out clearly (the odd ones only are marked) but many (in the thousands) peaks represent compounds in low concentration and form an unresolved hump that can only be analyzed by additional fractionation to separate

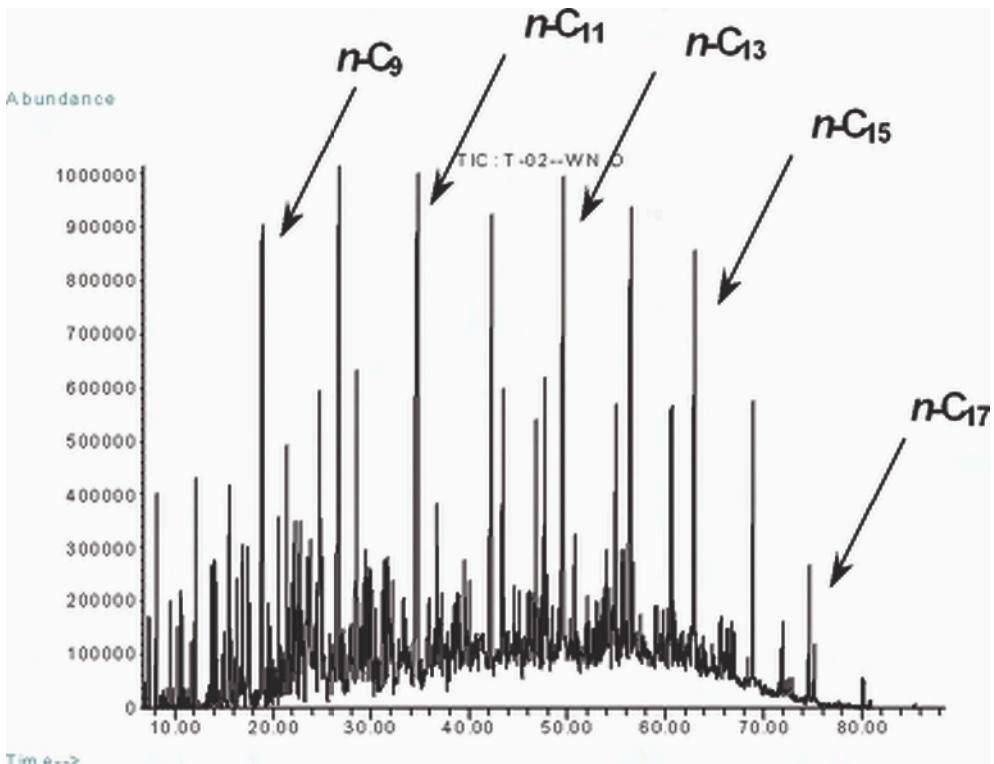


Figure 2. Gas chromatogram of a Jet-A fuel with prominent peaks labeled for n-paraffins having an odd number of carbons.

the compounds. As a first approximation, the boiling point of a compound increases by about 20 C per carbon number, but the boiling point varies with compound class for molecules of the same carbon number being, for example, higher for more compact molecules (smaller specific molar volumes) such as aromatic compounds. Note that the normal paraffins identified here run from C<sub>9</sub> to C<sub>17</sub>, consistent with a boiling point range of 160 C. The boiling point range determines the range of carbon numbers in the different classes. For a typical jet fuel, the average carbon number may vary from 9 to 16 for paraffins (normal and iso-), 8 to 15 for cyclo-paraffins, and 7 to 14 for aromatics.

## 2. CHEMICAL CHARACTERIZATION OF A TYPICAL JP FUEL

The average composition, by chemical class, reported [1], for 55 international (world) jet fuels are summarized in column 1, 4 US jet fuels [9] in column 2, and a specific JP8 fuel selected for the present study in column 3 of Table 1. The rows provide the average volume percent of the different chemical classes for each fuel category. The cyclo-paraffins are further subdivided into mono-, di-, and tri-cyclo; the substituted benzenes are classified under benzenes; the tetralins, indans and naphthalenes also include substituted compounds. The compositions for the JP-8 are also reported on a mole percent and a weight percent basis in columns 4 and 5. The conversions from volume to mole and weight percent were made using average properties for each class of hydrocarbons. Average carbon numbers are listed in column 6 for each class, based on the measurements by Hodgson and Kremmer [10] for a Jet-A fuel; average densities (column 7) and molecular weights (column 8) of each chemical class were calculated using several representative compounds for each class of compounds as shown in the footnotes to Table 1.

The data in Table 1 are average numbers over the boiling point distribution. From the range of boiling points in Figure 1, as mentioned previously, one can expect a variation in the composition of the different distillate cuts of the JP fuels, with the lower boiling point compounds having carbon numbers typically between 7 and 9, composed of lighter paraffins and monocyclic aromatics and cycloparaffins. The higher boiling point compounds will typically have carbon numbers of 14 to 16 with significant concentrations of bicyclic aromatics and cycloparaffins and lower concentrations of tricyclic compounds. Complementary information on the composition of JP fuels is provided by NMR data.

### 2.1. NMR analysis of jet fuels

NMR spectroscopy, in conjunction with other spectrometric information, has been used extensively in identifying organic compounds. The present account is intended to be sufficient for our limited objective, i.e., to differentiate the structural features in jet fuels at the sub-molecular level. NMR spectroscopy is extremely sensitive to the nature of the bonds connecting the atoms of a molecule as well as the molecular dynamics of the structure. Each atom has a unique chemical signature called a chemical shift

Table 1. The composition of world average, US average, and JP8 used in this study.

Species class	world avg vol %	US avg vol %	JP-8 fuel vol %	mol %	Weight %	Avg C No.	Density (g/ml)	Mol weight
n-paraffins	18	17.6	20.6	18.12	16.34	12	0.749 <sup>a</sup>	170.3 <sup>a</sup>
iso-paraffins	41	37.5	37.9	35.05	27.35	12	0.759 <sup>b</sup>	164.3 <sup>b</sup>
cyclo-paraffins	21.1	25.8	26.05			12		
mono-cyclo	11	13.45	13.65	14.37	13.49		0.81 <sup>c</sup>	154 <sup>c</sup>
di-cyclo	9	11.0	11.1	11.78	12.00		0.88 <sup>d</sup>	166 <sup>d</sup>
tri-cyclo	1.1	1.35	1.3	1.28	1.61		0.944 <sup>e</sup>	192.3 <sup>e</sup>
benzenes	13.3	12.8	9.4	11.50	13.99	10.7	0.88 <sup>f</sup>	144 <sup>f</sup>
tetralins/indans	5	4.8	5.05	6.58	5.69	11	0.95 <sup>g</sup>	146 <sup>g</sup>
naphthalenes	1.6	1.5	1	1.34	1.86	11.5	1 <sup>h</sup>	149 <sup>h</sup>
Total	100	100	100	100	100		0.803 <sup>i</sup>	

<sup>a</sup> The average normal paraffin is C<sub>12</sub> [4]; therefore the physical properties of normal paraffins were assumed to be the averages of normal undecane, dodecane, and tridecane. All density data were obtained from the CRC handbook [5].

<sup>b</sup> Represented by the narrow distillate cut of Isopar H, the analytical composition of which indicates 38% C<sub>11</sub> and 60% C<sub>12</sub> species, with an average of 3.25 branches [6], equivalent to an average chemical formula of C<sub>11.6</sub>H<sub>25.2</sub>. Density of Isopar H was obtained from ExxonMobil [7].

<sup>c</sup> Assume the average chemical formula for monocyclo-paraffins to be C<sub>11</sub>H<sub>22</sub> [1, 4]. Pentyl cyclohexane was used for the average density as the reference species.

<sup>d</sup> Assume the average chemical formula for dicyclo-paraffins to be C<sub>12</sub>H<sub>22</sub> [1, 4]. Density was taken to be the average of cis and trans decalins.

<sup>e</sup> Reference species is tetradecahydro phenanthrene.

<sup>f</sup> Assume the average chemical formula of alkylated benzenes to be C<sub>10.7</sub>H<sub>15.4</sub> [4]. Tert-butyl methyl benzene and 2-ethyl cumene were used as reference species for the average density.

<sup>g</sup> Assume the average chemical formula of tetralins/indans to be C<sub>11</sub>H<sub>14</sub> [4]. Methyl and dimethyl tetralins and indans were used as reference species for the average density.

<sup>h</sup> Assume the average chemical formula of naphthalenes to be C<sub>11.5</sub>H<sub>11</sub> [4]. Reference species are methyl and 1- and 2- ethyl naphthalenes.

<sup>i</sup> Calculated using the volume % of the JP8 fuel. The reported range of densities for JP8 at 15 C is between 0.775 and 0.840 g/ml [4, 8].

relative to a standard reference compound. For hydrocarbon fuels, the carbon-13 chemical shifts can be used to identify the classes of compounds discussed above.

NMR spectra used for this study were recorded on a Varian Inova 500 spectrometer operating at 125.64MHz for <sup>13</sup>C. Deuterated Chloroform (CDCl<sub>3</sub>) was the solvent, and tetramethylsilane (TMS) was added to provide a chemical shift reference. Broadband proton decoupling was used in all cases.

Although the principles are quite well understood, prediction of chemical shifts from molecular structure is quite complex. For alkanes, both normal and iso-, chemical shifts can be predicted quite accurately using simple additivity rules explained in many elementary NMR texts. (See, for example, reference [11].) Chemical shifts depend most strongly on neighboring atoms one or two bonds removed from the

atom in question but are influenced to a lesser extent by neighbors connected through three or more bonds. Orbital hybridization and electronegativity of substituents are prime factors in determining chemical shift, but steric crowding, solvent, concentration, and temperature may also be important. In the case of hydrocarbon fuels, the “solvent” may consist mainly of the other thousands of compounds in the fuel; and, thus, natural variations in the composition of samples of the same fuel type from different sources may slightly alter the chemical shifts of a given component.

Probably the most accurate way to predict the chemical shifts of an unknown compound is to compare its chemical shifts to a library of known compounds. Spectra of hundreds of thousands of compounds have been catalogued and computer programs have been devised to predict structure from a list of chemical shifts or to predict chemical shifts of a given structure.

In Figure 3, the chemical shifts of the aliphatic carbon atoms in the various components of a surrogate fuel, Hex12, are given. Primary carbons (methyl groups,  $\text{CH}_3$ ) in normal paraffins appear upfield at 14.2 ppm on the standard reference scale. The C2 and C3 carbons ( $\text{CH}_2$ , methylene) show a progressive deshielding (downfield) trend. Of course, for a chain of length  $n$ ,  $C_m$  carbons have the same chemical shift as  $C_{n-m+1}$  carbons, i.e., carbons at the same distance from the ends of the normal hydrocarbon chain exhibit identical chemical shifts, since they experience identical bonding

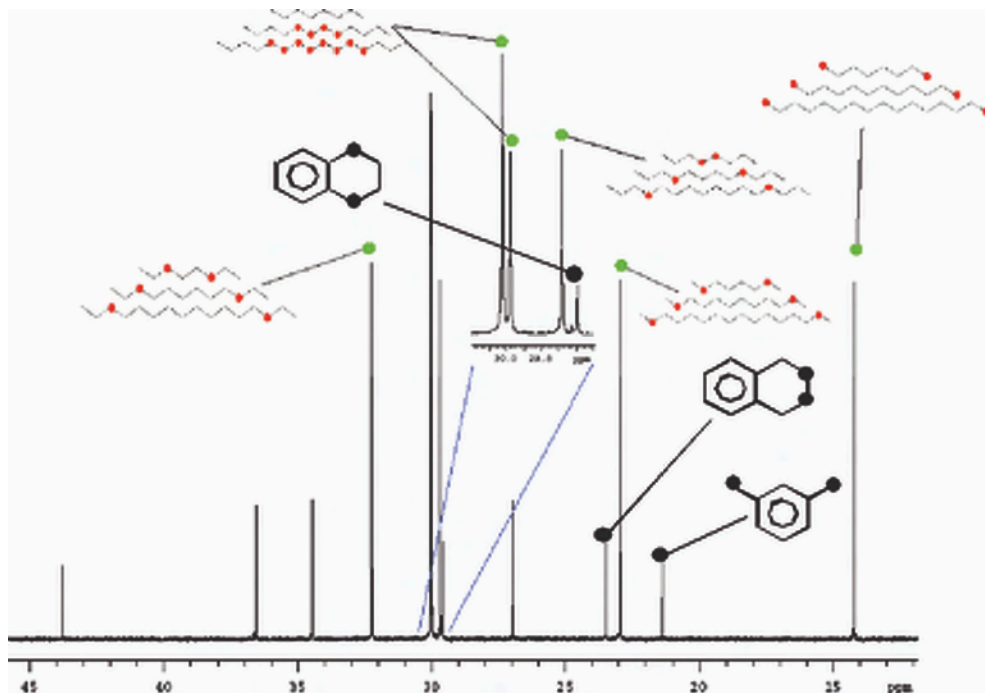


Figure 3. The aliphatic region of the carbon-13 spectrum of the Hex12 surrogate fuel showing the assignment of resonances to carbons in the fuel components.

environments. Interestingly, the C4 carbons break the trend to appear 2.5 ppm upfield from the C3 carbons because of steric congestion or gauche shielding from the C3 carbons. This effect is discussed in detail in reference [11]. The shift of the C5 carbons in normal paraffin's again adopt the downfield trend. For chains of length greater than nine, carbons removed from the chain ends by more than five carbons exhibit shifts differing very little from that of C5, since their bonding environments differ very little from that of C5. Note that attachment to a phenyl ring moves the shift of the alkyl carbons near the attachment point downfield because the phenyl ring has a large electronegativity compared to the alkyl groups, and the phenyl carbons are  $sp^2$  rather than  $sp^3$  hybridized

Chemical shifts of aromatic carbons in surrogate model compounds, i.e., m-xylene and tetralin, are shown in Figure 4. In general, protonated aromatic carbons appear between 120-130 ppm while non-protonated (substituted) aromatics appear downfield from 130-139 ppm. Bridgehead (ring junction) carbons of polynuclear aromatics can also appear upfield from 130 ppm.

There are numerous practical issues associated with obtaining accurate NMR data. These are discussed in many standard NMR texts. Several of particular importance in the context of jet fuels will be briefly mentioned here.

The high precision with which chemical shifts can be measured in jet fuels and surrogates yields a wealth of information about the types of chemical structures contained in any given sample. This high precision can be maintained only with careful attention to magnet shimming and adequate digitization of the NMR signal. Of equal importance, however, is knowledge of the amount of each type of structure present

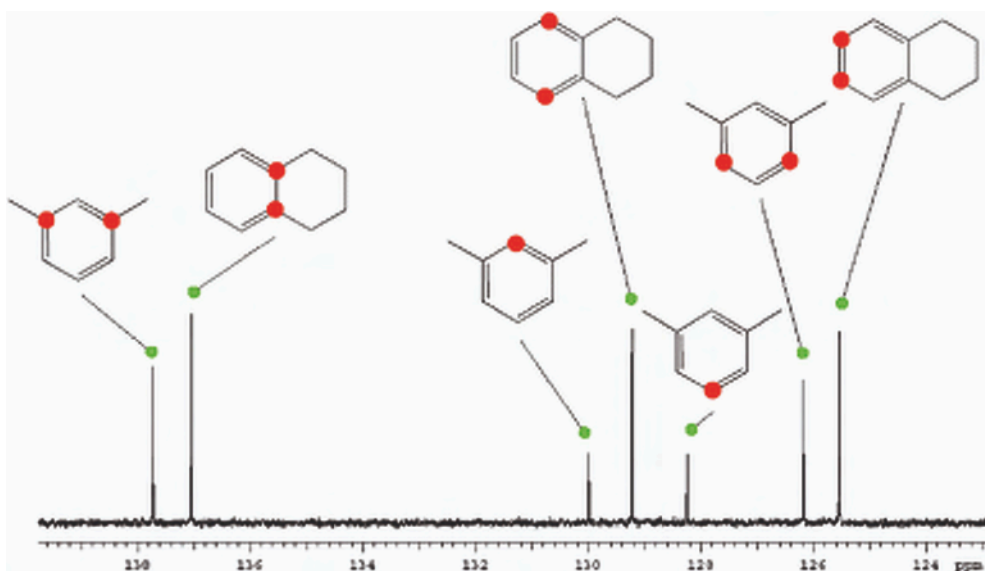


Figure 4. The aromatic region of the carbon-13 spectrum of the Hex12 surrogate fuel showing the assignment of resonances to carbons in the fuel components.

in the material being studied. Obtaining accurate quantitative data from carbon-13 NMR spectra requires that careful attention be paid to several practical issues associated with obtaining the spectra.

The intensity of a carbon resonance is proportional to the number of carbons at thermal equilibrium in the sample that contribute to that particular resonance. However, the proportionality constant is not necessarily the same for all the carbons in a sample due to a combination of the Nuclear Overhauser Effect (NOE) and the thermal equilibrium of the carbon atoms. Thus, the relative intensities of various resonances do not necessarily represent the relative number of carbons contributing to each resonance. The NOE arises from broadband decoupling of protons according to Equation (2),

$$I = (1 + \eta) I_0 \quad (2)$$

where  $I$  is the observed intensity of the resonance,  $I_0$  is the thermal equilibrium intensity of the resonance with no NOE, and  $\eta$  is the enhancement factor that can take on values between 0 and 1.988. Using gated decoupling, the NOE can be suppressed [11] so that  $\eta = 0$ , and  $I = I_0$ . By suppressing the NOE, the intensities of various resonances can be normalized and do represent the relative number of carbons at thermal equilibrium contributing to each resonance. The spectra shown in Figure 3 and Figure 4 were acquired with the NOE suppressed.

The longitudinal relaxation time ( $T_1$ ) is a measure of the time necessary for the magnetization of a sample to assume its thermal equilibrium value when disturbed from thermal equilibrium. Obtaining an NMR spectrum involves disturbing the sample from thermal equilibrium by means of a radio frequency (rf) pulse and usually requires time averaging by multiple repetitions of the rf pulse. Since different carbons have different  $T_1$ 's it is necessary to wait five times the longest  $T_1$  before initialing the next rf pulse so that thermal equilibrium can be re-established. Otherwise, the carbons with longer  $T_1$ 's will exhibit lower intensities relative to those with shorter  $T_1$ 's resulting in non quantitative results.

The structural details derived from NMR data for the JP-8 modeled in this study are presented in Table 2. The first row provides NMR measurements of the concen-

Table 2. Structure parameters for JP8 and four model jet fuels

	$f_a$	$f_a^H$	$f_a^N$	$f_a^S$	$f_a^B$	$f_{al}$	$f_{al}^C$	$f_{al}^{CH}$	$f_{al}^{CH2}$	$f_{al}^{CH3}$
JP8	0.11	0.06	0.05			0.89	<0.01	0.16	0.47	0.26
Mod_1	0.109	0.060	0.049	0.035	0.014	0.891	0.004	0.157	0.460	0.270
Mod_2	0.111	0.061	0.05	0.038	0.012	0.889	0	0.160	0.469	0.260
Mod_3	0.112	0.061	0.051	0.038	0.012	0.888	0	0.160	0.463	0.265
Hex12	0.153	0.102	0.051	0.051	0	0.846	0	0.049	0.688	0.109

$f_a$ , fraction of aromatic carbon;  $f_{al}$ , fraction of aliphatic carbon;  $f_a^H$ , protonated;  $f_a^N$ , not protonated;  $f_a^S$ , substituted;  $f_a^B$ , bridgehead;  $f_a + f_a^I = 1$ ;  $f_a^H + f_a^N = f_a^I f_a^C + f_a^I f_a^{CH} + f_a^I f_a^{CH2} + f_a^I f_a^{CH3} = f_a^I (f_a^C + f_a^{CH} + f_a^{CH2} + f_a^{CH3}) = f_a^I f_a^N$ .

tration of different aliphatic and aromatic carbons. The information on aliphatic carbon is the fraction of total carbon that is aliphatic  $f_{al}$  and the subfractions  $f_{al}^C$ ,  $f_{al}^{CH}$ ,  $f_{al}^{CH_2}$ , and  $f_{al}^{CH_3}$  that have 0, 1, 2, and 3 (e.g., quaternary, methyne, methylene, and methyl) hydrogen atoms attached to them. For the aromatic carbons,  $f_a$  represents the fraction of the total carbon that is aromatic and  $f_a^H$ ,  $f_a^N$ ,  $f_a^S$ , and  $f_a^B$  are the subfractions of the aromatic carbons that are protonated, non-protonated, substituted, and bridgehead (examples of bridgehead carbons are the carbons at the junction of the aromatic rings in compounds such as naphthalene or the inner carbons in pyrene). For the JP fuel the ratio between the aromatic and aliphatic carbons is 11/89. Of the 11% of the carbons that are aromatic, the protonated/non-protonated ratio is 6/5 with the non-protonated carbons consisting of either bridgehead carbons or carbons with substituent attachments. Of the 89% of the total carbons that are aliphatic, only trace amounts are quaternary (non-protonated), and 16%, 47% and 26% of the total carbons are tertiary, secondary and primary aliphatic carbons, respectively. In addition, NMR data indicates that the average length of the n-paraffins is  $C_{12}$ . The table also includes the characterizations of three surrogate fuels that come close to matching the NMR characteristics of the J8 and that of Hex 12 to be discussed in Section 4. The following section describes how these relatively simple (compared to the thousands of compounds in real fuels) model fuels were selected.

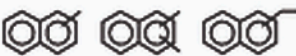
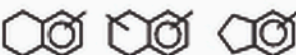
### 3. SELECTION OF MODEL REPRESENTATION OF JET FUELS

The interest here is to obtain model representations of jet fuels that capture much of the detail provided by the GC/MS and NMR characterization of fuels with a limited number of compounds. Since the GC/MS and NMR data were obtained on different fuels a jet fuel composition was selected that was close to the average of the composition of the US average for jet fuels (column 2 in Table 1) and the NMR analysis. In the current study, we assume the JP-8 fuel has a composition very close to the US average of aviation fuels surveyed by Edwards [4, 8], which translates into a 23.6 mole % aromatic fraction. However, the 11% aromatic carbon derived from NMR analysis (Table 2) indicates that the aromatic fraction in the current fuel is near 19.1 mole % by assuming: 1) the average carbon number of jet fuel is 11 [4] and, 2) the average number of aromatic carbons in the aromatic species is 6.3 [9] which was obtained by considering the mole percentages and carbon numbers of benzenes, indans/tetralins, and naphthalenes. Therefore, we slightly reduced the aromatic contents from the average suggested by Edwards and increased the normal paraffin content. We assume in this study a composition of 20.6% (by volume) normal paraffins, 37.9% iso-paraffins, 13.6% mono-cyclo, 11.1% di-cyclo, and 1.3% tri-cyclo paraffins, 9.4% benzenes, 5.1% tetralins/indans, and 1% naphthalenes, which corresponds to a 19.4 mol % aromatic content.

The methodology for arriving at the model representation of jet fuels is that they should meet the distribution between chemical classes, the average number of carbons in each class, and, where available, the number of side chain substituents obtained from GC/MS analyses such as those provided by Edwards [4, 8]. The analysis selects possible combinations that satisfy both these constraints and the additional constraints

imposed by the NMR analysis. The NMR data provides constraints, for example, on the number of side chain substitution on aromatics from the fraction of aromatic carbons that are available for substitution and the length and branching of the substituents from balances on primary, secondary, tertiary, and quaternary carbons. The surrogate fuel formulation methodology is presented in Table 3. The details of the analysis are provided in the Appendix leading to the following constraints on the selection of model representations of our JP-8 (Table 4) and suggested surrogate components (Table 5).

Table 3. Fuel structure characterization steps

Chemical Class	Derivation Steps	Rationale																		
<table border="1"> <thead> <tr> <th>Class</th> <th>avg mol%</th> </tr> </thead> <tbody> <tr> <td><i>n</i>-paraffin</td> <td>18.1 %</td> </tr> <tr> <td>iso-paraffin</td> <td>35.1 %</td> </tr> <tr> <td></td> <td>14.4 %</td> </tr> <tr> <td></td> <td>11.8 %</td> </tr> <tr> <td></td> <td>1.3 %</td> </tr> <tr> <td></td> <td>11.5 %</td> </tr> <tr> <td></td> <td>6.6 %</td> </tr> <tr> <td></td> <td>1.4 %</td> </tr> </tbody> </table>	Class	avg mol%	<i>n</i> -paraffin	18.1 %	iso-paraffin	35.1 %		14.4 %		11.8 %		1.3 %		11.5 %		6.6 %		1.4 %	     Balance check of aliphatic CH <sub>3</sub> Length of substituents on cyclics	Average carbon number is 12 Average carbon number is 11.5 Average carbon number is 11 Decide the number of substituents using aromatic C/CH functionalities because there are three aromatic chemical class only Only iso-paraffin and naphthene fractions contribute to the aliphatic CH functionality; constrained by availability of species chemistry Contributions from all chemical classes are known; Balance check of aliphatic CH <sub>3</sub>
Class	avg mol%																			
<i>n</i> -paraffin	18.1 %																			
iso-paraffin	35.1 %																			
	14.4 %																			
	11.8 %																			
	1.3 %																			
	11.5 %																			
	6.6 %																			
	1.4 %																			

*Normal paraffins* include species with an average carbon number of  $C_{12}$ . Considerable freedom is available in selecting the paraffin mix as long as the mixture satisfies the average carbon number constraint.

*Iso-paraffins* include, on average,  $\approx 5$  primary,  $> 2.5$  tertiary and  $< 0.3$  quaternary carbons with an average carbon number of 12. We used an estimated functional distribution for iso-paraffins, which includes 5.2 primary, 3.6 secondary, 3 tertiary and 0.1 quaternary carbons with an equivalent chemical formula of  $C_{12}H_{26}$ . One likely composition of  $C_{12}$  iso-paraffins is given in Table 6. About 12.5% of iso-paraffins have a quaternary carbon. We assume that a candidate species with a quaternary carbon also contributes 6 primary carbons (4 substituents) because the average number of substituents in the narrow distillate cut of Isopar H ( $C_{11.6}H_{25.2}$ ) is 3.2 [6]. Qualified candidates include 2,4,6,6-tetramethyl octane. The other candidates (87.5%) have no qua-

Table 4. Selection criteria and structural functionalities of various surrogates

Chemical Functionality	C # <sup>a</sup>	Mod 1			Mod 2			Mod 3	
		Selection Criteria <sup>b</sup>	mol% proposed structure		Selection Criteria <sup>b</sup>	mol% proposed structure		mol% proposed structure	
Fuel	C <sub>11</sub>	C <sub>11</sub>		C <sub>11.1</sub>	C <sub>11.0</sub>	100	C <sub>11.0</sub>	100	C <sub>11.2</sub>
n-paraffins	C <sub>12</sub>	C <sub>12</sub>	18.1	C <sub>12</sub>	C <sub>12</sub>	15.9	C <sub>12</sub>	15.9	C <sub>12</sub>
iso-paraffins	C <sub>12</sub>	C <sub>12</sub>	35.0	C <sub>12</sub>	C <sub>12</sub>	35.6	C <sub>12</sub>	35.6	C <sub>11.6</sub>
Primary		≈ 4.9 C		5.2 <sup>c</sup>	≈ 5.2		5.2 <sup>d</sup>		5.2 <sup>e</sup>
Tertiary		> 2.5 C		3 <sup>f</sup>	≈ 3.2		3.2 <sup>d</sup>		3.2 <sup>g</sup>
Quaternary		< 0.3 C		0.1 <sup>f</sup>	≈ 0		0 <sup>d</sup>		0 <sup>g</sup>
naphthenes	C <sub>12</sub>	C <sub>12</sub>		C <sub>10.1</sub>	C <sub>12</sub>		C <sub>12.0</sub>		C <sub>12.1</sub>
			14.4			14.5		15.3	
		Methyl	11.8	Methyl	Methyl	12	Methyl	12.6	Methyl
		Dimethyl	1.3	Dimethyl	Dimethyl	1.3	Dimethyl	0	
# of sub		1.5 <sub>±0.1</sub>		1.5	1.5 <sub>±0.0</sub>		1.5		1.5
# C in sub		2.2 <sub>±0.1</sub>		2.2	5.6 <sub>±0.1</sub>		5.6		6
	C <sub>10.7</sub>	C <sub>10.7</sub>	11.5	C <sub>9.9</sub>	C <sub>10.7</sub>	13.5	C <sub>11.0</sub>	13.5	C <sub>10.2</sub>
# of sub		2.7		2.7	2.8		2.8		2.8
# C in sub		2.2 <sub>±0.1</sub>		2.2	3.2 <sub>±0.1</sub>		3.2		3.1
	C <sub>11</sub>	Methyl, C <sub>11</sub>	6.6	mono- & dimethyl, C <sub>11</sub>	Methyl, C <sub>11</sub>	5.4	mono- & dimethyl, C <sub>11</sub>	5.4	Methyl, C <sub>11</sub>
# of sub. (al)		0.2 <sub>±0.2</sub>		0.2	0.2 <sub>±0.2</sub>		0.2		0
# of sub. (ar)		1		1	1		1		1
	C <sub>11.5</sub>	Methyl & Ethyl C <sub>11.5</sub>	1.3	Methyl & Ethyl C <sub>11.5</sub>	Methyl & Ethyl C <sub>11.5</sub>	1.7	Methyl & Ethyl C <sub>11.5</sub>	1.7	Methyl & Ethyl C <sub>11.5</sub>
# of sub		1.2 <sub>±0.2</sub>		1.2	1.2 <sub>±0.2</sub>		1.2		1

<sup>a</sup> references 4 and 10.

<sup>b</sup> derived from experimental data, see the text for detailed derivation.

<sup>c</sup> 12.5% 2,4,6,6-tetramethyl octane, 75% 3,5,7-trimethyl nonane and 12.5% 2,3,5,7-tetramethyl octane.

<sup>d</sup> 75% 3,5,7-trimethyl nonane and 25% 2,3,5,7-tetramethyl octane.

<sup>e</sup> estimated value for Isopar H with average 3.25 substituents and carbon number of 11.6 [6]

ternary carbons and will contribute 2.7 tertiary carbons. If only two species are considered, then the set is likely a mixture of 75% trimethyl nonane and 12.5% tetramethyl octane to match the tertiary carbons. Fortunately, the structures of the two generic species also match the values of other carbon functionalities. Qualified candidates include 3,5,7-trimethyl nonane and 2,3,5,7-tetramethyl octane.

*Naphthenes (cycloparaffins)* have an average number of substituents of about 1.5. All substituents except one are methyl, and the average length of the other substituent is

Table 5. Model representations of JP8 fuel. Mod\_1 is for a JP fuel with an average carbon number of 11, Mod\_2 (and Mod\_3) is with an average carbon number of 11.8.

<b>Mod_1</b>		<b>Mod_2</b>		<b>Mod_3 (Simplified Mod_2)</b>	
<b>Components</b>	<b>Mol%</b>	<b>Components</b>	<b>Mol%</b>	<b>Components</b>	<b>Mol%</b>
Normal-C <sub>12</sub>	18.1	Normal-C <sub>12</sub>	15.9	Normal-C <sub>12</sub>	15.9
Isoparaffins	35.0	Isoparaffins	35.6	Isopar H	35.6
Cyclohexanes	14.4	Cyclohexanes	14.5	Cyclohexanes	15.3
ethyl	(2.1)	pentyl	(0.5)	pentyl	(0)
propyl	(0.5)	hexyl	(0.9)	hexyl	(0)
ethyl methyl	(9.4)	pentyl methyl	(4.6)	pentyl methyl	(0)
propyl methyl	(2.4)	hexyl methyl	(8.5)	hexyl methyl	(15.3)
Methyl Decalin	11.8	Methyl Decalin	12	Methyl Decalin	12.6
Higher Naphthene	1.3	Higher Naphthene	1.3	Higher Naphthene	0
Benzenes	11.5	Benzenes	13.5	Benzenes	13.5
ethyl methyl	(2.9)	propyl methyl	(2.5)	p-isopropyl methyl	(2.8)
propyl methyl	(0.7)	butyl methyl	(0.8)	butyl methyl	(0)
ethyl dimethyl	(6.3)	propyl dimethyl	(7.8)	propyl dimethyl	(9.3)
propyl dimethyl	(1.6)	butyl dimethyl	(2.4)	butyl dimethyl	(1.4)
Tetralins/Indans	6.6	Tetralins/Indans	5.4	Tetralins/Indans	5.4
methyl tetralin	(3.3)	methyl tetralin	(2.7)	methyl tetralin	(5.4)
dimethyl tetralin	(1.6)	dimethyl tetralin	(1.3)	dimethyl tetralin	(0)
methyl indan	(1.6)	methyl indan	(1.3)	methyl indan	(0)
Naphthalenes	1.3	Naphthalenes	1.7	Naphthalenes	1.7
methyl	(0.7)	methyl	(0.9)	methyl	(0.9)
dimethyl	(0.3)	dimethyl	(0.4)	dimethyl	(0)
ethyl	(0.3)	ethyl	(0.4)	ethyl	(0.9)

Table 6. Model Representation of Components in iso-paraffins.

<b>Mole %</b>	<b>Species</b>	<b>Primary</b>	<b>Secondary</b>	<b>Tertiary</b>	<b>Quaternary</b>
12.5%	2,4,6,6-tetramethyl octane	0.7	0.4	0.2	0.1
12.5%	2,3,5,7-tetramethyl octane	0.7	0.2	0.5	0
75%	3,5,7-trimethyl nonane	3.7	3	2.2	0

about 2.2 carbons. The selection criteria for naphthenes include an average number of substituents of approximately 1.5 and the average length of substituents of 2.2 carbons. In order to estimate a distribution among cyclo-paraffins, we assume that multi-ring compounds are di-substituted and decalins are mono-substituted only to reduce the number of degrees of freedom. The mono-substituted decalins are selected also for simplification of the reaction mechanism because there are only simple lumping

models available in the literature for methyl cyclohexane. Mono-substitution will also ease the generation of chemical mechanisms for these species by reducing the number of possible isomers of fused cyclo-paraffins. With these assumptions and a preference of hexagonal species that is evident in the GC/MS data, the distribution of naphthenes can be represented as follows (Scheme 1), in which R is 80% ethyl and 20% propyl.

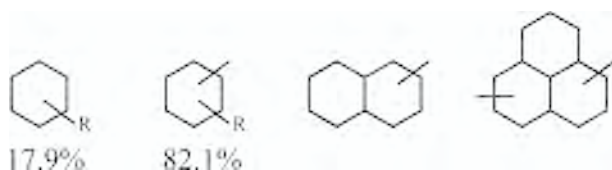
*Naphthalenes* have an average number of substituents of  $1.2 \pm 0.2$ . Methyl substitution is dominant. This can be met by a mixture 50% methyl, 25% dimethyl, and 25% ethyl naphthalenes

*Benzonaphthenes* have an average number of substituents on the aromatic ring of 1 and on the aliphatic ring of  $0.2 \pm 0.2$ . Methyl substitution is dominant. A possible compound distribution that satisfies these constraints is 50% methyl tetralin with the methyl on the benzene ring, 25% dimethyl tetralin with a methyl on each ring, and 25% methyl indan with the methyl on the benzene ring.

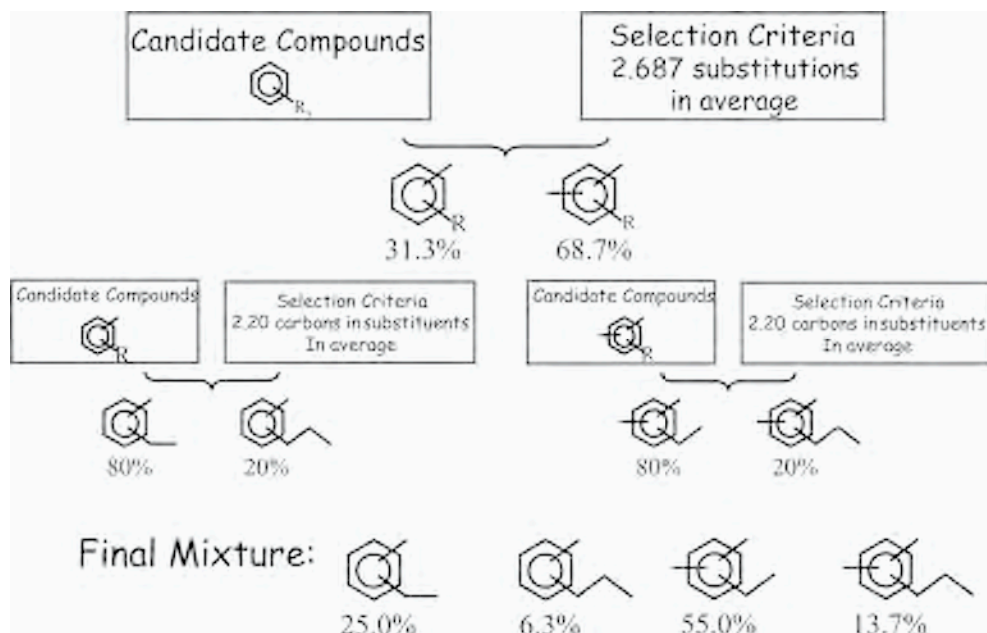
*Benzenes* have 2.7 substituents on average. All substituents except one are methyl, and the average length of the other substituent is 2.2 carbons. The estimated values of the number and the length of the substituents on the benzene rings provide two selection criteria to obtain a set of proper surrogate components for the benzene chemical class as shown in the Scheme 2. In the first selection criterion, an average of 2.7 substituents on rings, will divide the generic substituted benzenes  $\text{Ph-R}_x$  into a substituted toluene (31.3 mol %) and a substituted xylene (68.7 %). In the second selection criterion, with an average of 2.2 carbons per substituent, each candidate sub-class divides into ethyl (80%) and propyl (20%) sub-groups. In reality, the presence of non-, mono- and higher-substituted benzenes, and methyl-only and longer alkyl benzenes cannot be ruled out, but the content of these sub-classes are likely to be small since they are farther removed from the average structures. For the simplicity of the surrogate set, these species are not included in the formulation. The final set of surrogate compounds (Scheme 2) includes 25.0% ethyl toluene, 6.3% propyl toluene, 55.0% ethyl xylene, and 13.7% propyl xylene.

The chemical composition of the model representation of JP-8 derived above (Mod\_1) is summarized in Table 5. The carbon functionalities are calculated and summarized in Table 2. The proposed surrogate composition closely matches the NMR experimental data. The structural features of each chemical class are found to compare favorably with the measured values and the selection criteria except the proposed surrogate composition leading to a lower carbon numbers for cyclics (see Table 4). For example, the proposed composition has a  $\text{C}_{10.1}$  equivalent formula in comparison with  $\text{C}_{12}$  from the GC /MS data [4, 10].

Scheme 1.



Scheme 2.



Two additional model representations of JP-8 have been derived. Mod\_2, the second column in Tables 4 and 6, adjusts the average carbon number of the JP-8 from a value close to 11 to one closer to 12, to reflect the variability of the reported value of carbon number. Edwards [4] and Duvall et al. [12] reported values corresponding to a chemical formula of  $C_{11}H_{21}$  or lower while the data of Hogson and coworkers [10, 13] correspond to an average carbon value of around 11.8, which would correspond to a formula closer to  $C_{11.8}H_{22.6}$ , using an elemental H/C ratio of  $1.9 \pm 0.4$  based on the Edwards [14] correlation of the US military database on JP-8. Since the carbon length for each chemical class was kept constant, the aromatic content (mol %) for this higher average carbon number needed to be adjusted to 20.6% (in comparison with 26.3% for the US average and 19.4% for Mod\_1), so that the aromatic carbon percentage is 11% which is close to that determined by NMR data. Therefore the US average composition for aromatic fractions is reduced proportionally and the reduced percentage is also proportionally distributed to other fractions as shown in Table 5. The proposed surrogate composition (Mod\_2) matches the selection criteria very well except for a small deviation of the average carbon number for the benzene fraction. The proposed composition leads to a value of  $C_{11.0}$  in comparison with the measured data of  $C_{10.7}$  for benzenes and a match of the carbon number of 12 for the naphthenes. The third column in Tables 4 and 5 is for a formulation (Mod\_3) which takes into consideration the availability of chemicals at reasonable costs. The iso-paraffins are replaced by Isopar H and the naphthenes and substituted aromatics, and cyclo-aromatics by compounds that are available at modest cost.

## 4. SURROGATE FORMULATION USING SOOTING INDEX

The formulations in the above section try to provide mixtures that satisfy both the information on chemical classes, average carbon length, and the carbon types obtained from GC/MS and NMR data in the JP-8 fuels. In principle these should also match combustion behavior. However, the mixtures are complex and are provided to help guide the selection of simpler surrogates, based on considerations of fuel analyses. In the interim, surrogates are selected that match experimental measurements of interest for a specific application. Two illustrations will be provided.

### 4.1. Surrogates for pool fire simulations

In pool fires the radiation from the soot is of great importance both because it governs the radiation from the flames, the burning rates (determined by the heat flux to the pool and the vapor pressure of the fuel), and smoke emitted by the fires. A surrogate formulation for jet fuels that takes sooting as well as vapor pressure into account is that by Eddings et al. [15]. The mixture was selected to match both the boiling point distribution and the Threshold Sooting Index (TSI). The boiling point distribution of the Jet-A used in the study and that of several surrogates is shown in Figure 5. The surrogate of interest is Hex-12, the composition of which is 3% n-octane, 30% n-dodecane, 12% n-hexadecane, 15% xylenes, 13% tetralin, and 27% decalin. The TSI for Hex-12 was 22.1 compared with 26.7 for the Jet-A. Other physical properties and the heat of combustion of the Jet-A were well matched by the Hex-12 [15]. The success

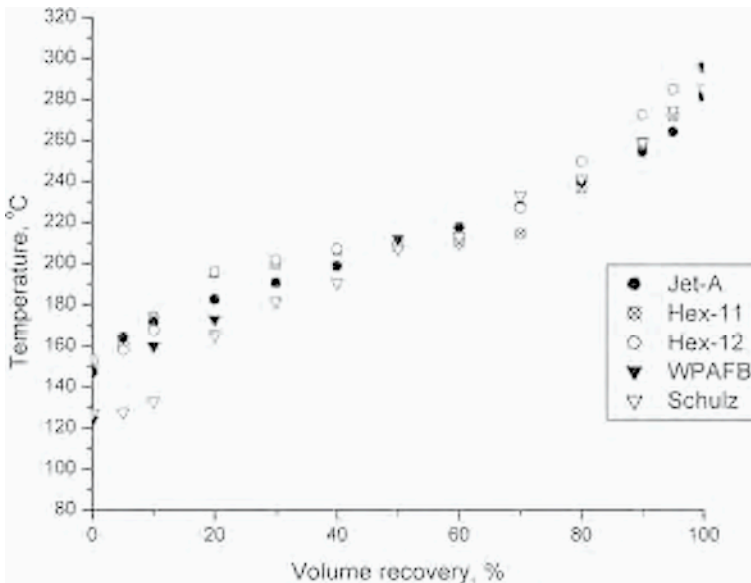


Figure 5. Boiling point distributions for a Jet A fuel and those of various surrogates in the literature.

of the matching of the heat flux and vapor pressure of the Jet-A is determined by the ability of the surrogate to reproduce the rate of burning in a pool fire. Figure 6 provides a comparison of the rate of regression of the burning surface of a 0.3 m diameter pool fire with a pool depth of 0.1 m showing a satisfactory agreement between the regression rates vs. burning time for Jet-A and the Hex-12 surrogate. Analysis of the burning liquid versus time showed that the sooting index for the Jet-A increased with time due to the accumulation of heavier hydrocarbons whereas that of the Hex-12 decreased with time due to the depletion of the relatively light aromatic compounds. If this transient behavior of the soot is to be reproduced then aromatic compounds, which dominate the sooting behavior, should be selected with a range of boiling points to simulate the boiling point distribution of the aromatics in the Jet-A. Despite its ability to match various properties, Hex-12 has quite different carbon functionalities from those obtained from the NMR measurements of the JP-8 fuel as seen in Table 2 as do those of other JP surrogates as described in the literature [1].

#### 4.2. Surrogate for gas turbine combustors

The major priorities in a jet turbine combustor are ignition and blowout, although there are many other considerations [1]. Surrogates for gas turbines are often selected to match experimental data on ignition and extinction. Figures 9 in Colket et al. [1] provide a comparison of the ignition temperature for a fixed fuel mass fraction versus strain rate for a number of surrogates with that of JP fuel. Of the surrogates tested all but two, the

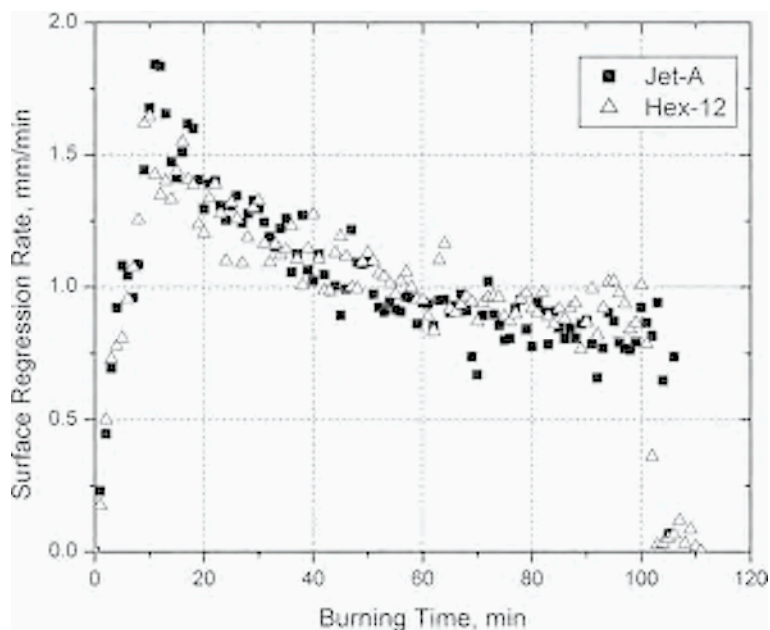


Figure 6. Rate of burning of Jet-A and Hex-12 for a 0.3m diameter pool fire, 0.1m deep.

Aachen surrogates, had a lower ignition temperature at a given strain rate than that for the JP fuel indicating that most of the surrogates were more reactive than the JP fuel. The Aachen surrogates consisted of a mixture of n-decane (or n-dodecane) and 20% by weight 1,2,4-trimethyl benzene. Their ignition temperatures were greater than that of the JP fuel. However the reactivity could clearly be controlled by increasing the amount of TMB, and this provides an attractive two-component surrogate. Similar results were can be seen in Figure 8 of Colket et. al. [1] on a comparison of the fuel/N<sub>2</sub> mass ratio versus strain rate at extinction for a number of surrogates with that of JP fuel. The two-components of an Aachen surrogate are a normal paraffin which has a low sooting tendency and an aromatic compound that has a high sooting tendency. The two-component surrogate can be made to work by using the additional degree of freedom of changing the number, position, length, and branching of the alkyl substituents which have a major influence (*vide infra*) on the sooting tendency of substituted benzenes.

### 4.3. Use of YSI in place of TSI

The TSI is the standard method of measuring the sooting tendency of fuels by determining the length of the wick that will just soot using a standard ASTM lamp. The sooting tendency of a JP fuel is currently matched by adjusting the surrogate composition to give a TSI that matches that of a JP fuel. This methodology cannot be expected to simulate the sooting index under a wide range of combustion conditions. Wick lamps provide a stop gap measure used while mechanistic models for soot prediction are being developed. The recently developed YSI by McEnally and Pfefferle [16, 17] provides a far superior measure of sooting tendency based on the conversion of a wide range of compounds injected into a diffusion flame in small enough amounts not to perturb the flame (see chapter in this book), although involving a more elaborate experimental set up. YSI results not only provide relative sooting potential for a large number of compounds but also provide mechanistic insights. For example, McEnally and Pfefferle have provided an understanding of sooting potential from substituted benzenes showing that compounds that form benzyl structures are rate limited by the formation of benzyl radical, that compounds that go quickly to a C<sub>5</sub> second ring have a YSI similar to naphthalene, and compounds that form styrene/phenyl acetylene also are highly sooting. The work of McEnally and Pfefferle is particularly relevant to the multiply substituted benzenes that are prevalent in jet fuels, showing that the 1,2 substituted compounds are highly sooting because of their potential of forming naphthalene. Given the prevalence of substituted benzenes in JP fuels the application of the YSI can be used to modify the sooting propensity of a substituted benzene to be used, for example, in a two-component surrogate such as the Aachen surrogate.

## 5. PROSPECTS FOR SURROGATE FORMULATION BASED ON KINETIC MODELS

The compositions in Table 4 provide representations of the composition of JP fuels that match the major features (chemical classes, average carbon number, NMR analysis)

of an average JP fuel. In the long run, such compositions could be used to define JP surrogates. In the short term, the composition can be used to define simpler surrogates that match simpler surrogate mixtures that capture the more important aspects of the chemistry of the JP fuel. For example, the compositions in Table 4 could be used to obtain the YSI of a JP fuel in place of having to run an experiment. The YSI could then be used to define the composition of simple, two or three component, mixtures that should provide a good match of the sooting tendency of the real fuel. This presumes the availability of kinetic mechanisms for the components that can predict soot formation. Other chapters in this book describe the progress that has been made in modeling soot formation, usually for simple fuels. This section will provide selected vignettes on the ability of current mechanisms on gas phase kinetics that can be used to predict the trends in soot precursor formation (e.g., benzene and naphthalene) as a function of classes of fuel constituents, of the size and branching of paraffins, and of the side chain substituents for benzene in order to underline those aspects of the details of the chemical composition that are important for soot formation.

The Utah Surrogate Mechanisms developed for modeling composite fuel combustion provides a tool for studying benzene formation in flames based on the structural functionality of the fuel. The mechanism was validated for an atmospheric premixed kerosene flame with an equivalence ratio of 1.7 [18] using a surrogate of five components (n-dodecane, isooctane, methyl cyclohexane, benzene and toluene), and then used to model flames burning each surrogate component under the same experimental conditions. The relative importance in benzene formation of each component in the kerosene surrogate was found, as expected, to follow the trend: aromatics > cycloparaffins > iso-paraffins > normal-paraffins. The fractions of the benzene formation contributed by each component are summarized in Figure 7. Although n-dodecane constitutes approximately three quarters of the fuel used, its contribution to the ben-

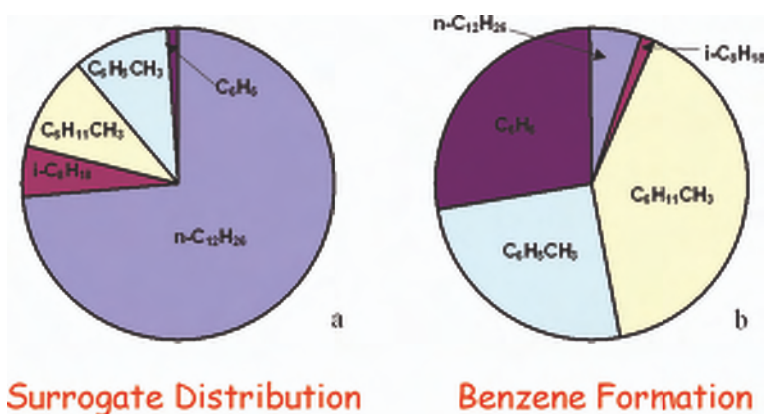


Figure 7. Benzene sources in the kerosene flame (right) from the surrogate components in the fuel (left). Data are re-interpreted from ref 17. The contribution to benzene formation of an individual component is estimated to be the benzene concentration in the modeled flame of that individual component multiplied by its mole fraction in the fuel.

zene formation is minor. The major contributors to benzene formation are methyl cyclohexane and toluene. Cyclohexanes form benzene via dehydrogenation [19, 20], and toluene generates benzene via dealkylation; the entire subject was reviewed recently [21].

The following application of the Utah Surrogate Mechanisms is to demonstrate the impact of changes in size and branching of paraffins on benzene formation for a premixed stoichiometric flame at atmospheric pressure with a European gasoline using a surrogate formulation of 22 compounds that closely approximates the real fuel [22]. Flames were modeled burning individual components at the same experimental conditions. The importance of molecular weight and branching factor on the benzene formation in the gasoline flame is evident in the results in Figure 8. Soot increases with increasing chain length and increased branching, consistent with the experimental results of McEnally and Pfefferle [17].

The third set of simulations, summarized in Figure 9 is related to the role of benzene substituents on the formation of PAHs with two (naphthalenes + indenes) or more rings. The aromatics larger than naphthalene and indene are widely believed to be the major soot precursor species. The formation, shown in Figure 9, of  $C_{10}+$  aromatics increases with carbon number in the order of propyl benzene > ethyl benzene > toluene as well as with increases in the number of substituents on the benzene rings. Xylene produces more aromatics than ethyl benzene, and ethyl toluene produces more than propyl benzene although each pair has a same carbon number. The patterns of the aromatic formation potential summarized from the modeled flames were suppor-

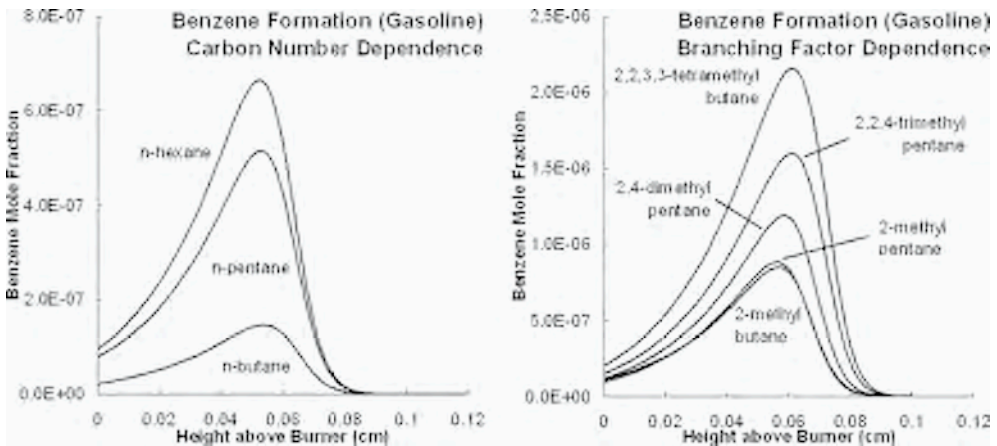


Figure 8. Predicted benzene concentrations in modeled flames burning paraffinic surrogate components (n-butane, n-pentane, n-hexane, 2-methyl butane, 2-methyl pentane, 2,4-dimethyl pentane, 2,2,4-trimethyl pentane, 2,2,3,3-tetramethyl butane) using experimental conditions of a validated atmospheric premixed flame of a European gasoline. The benzene formation potential following the order of carbon number: n-butane < n-pentane < n-hexane and 2-methyl butane < 2-methyl pentane; and the order of branching: 2,4-dimethyl pentane < 2,2,4-trimethyl pentane < 2,2,3,3-tertramethyl butane.

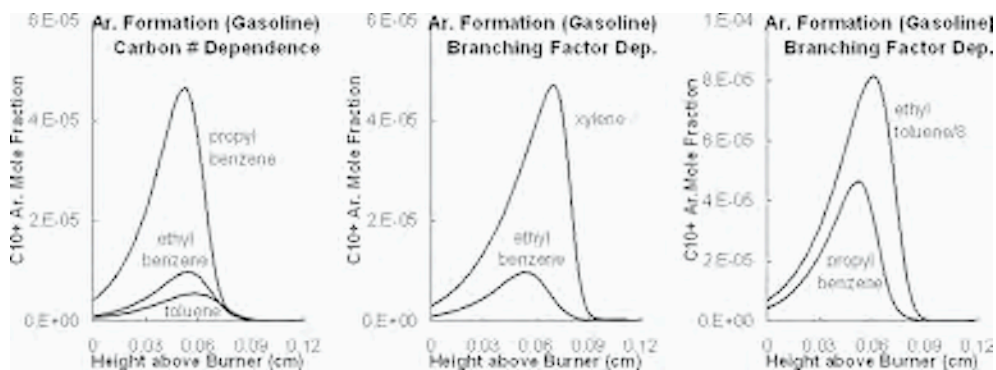


Figure 9. Predicted benzene concentrations in modeled flames burning aromatic surrogate components (toluene, ethyl benzene, xylene, propyl benzene, ethyl toluene) using experimental conditions of a validated atmospheric premixed flame of a European gasoline. The C10+ aromatic formation potential following the order of carbon number: toluene < ethyl benzene < propyl benzene and xylene < ethyl toluene; and the order of branching: ethyl benzene < xylene and propyl benzene < ethyl toluene.

ted by experimental evidence as published by McEnally and Pfefferli [16,17, 23, 24]. The yield sooting indices (YSI) measured in their co-flow methane flame doped with 400 ppm aromatics include toluene (YSI is 43.5) < xylene (*o, m, p* = 50.0, 53.2, 51.2) < ethyl benzene (53.6) < propyl benzene (55.9) < ethyl toluene (*o, m, p* = 61.9, 64.0, 60.0). These trends show the problems that exist with the following rules of thumb: “Soot decreases with increases in H/C ratio;” or “Soot increases with increasing fraction of aromatic carbon”. Both rules give the inverse trends to the data on which the YSI is based.

## 6. CONCLUDING COMMENTS

The information provided by NMR and GC/MS data provide a representation of JP fuels that are much more complicated than the current surrogate fuels, particularly those having constituents with a much larger number of side chain substituents than are normally used in surrogate formulations. The substituents on both paraffins and aromatic compounds have been shown by the Yale and Utah researchers [16, 17, 21-23] to increase sooting tendency. The impact of these substituents depends on their structure and ring position and need to be taken into account in formulating JP surrogates that correctly reproduce the sooting potential of the parent fuel, e.g., by matching the YSI. The data on YSI provide a measure of sooting tendency on, among others, the average molecular weight, the branching factor, the number of substituents of cyclo-paraffins and aromatics, the length of substituent chains, and the number of rings. Given the difficulty of matching the composition of JP fuels with affordable components, sensitivity studies, experimental and computational, are needed to determine the extent to which the substituents must be matched. The detailed knowledge

of the structural properties of JP fuels is probably best used to guide the selection of simple mixtures of affordable components rather than serve as a surrogate composition, until kinetic models become available for the more complicated compounds present in real fuels.

## ACKNOWLEDGMENTS

The authors are grateful to the DOE/ASC Academic Alliance Program, DOE contract LLL B341493 for financial support and Tim Edwards of the WPAFRL for his insights on the composition of JP fuels and for providing samples of JP fuels representative of current US consumption.

## APPENDIX

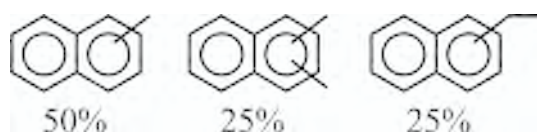
Detailed structural composition, e.g., number of substituents and length of carbon chains, will be derived from NMR spectral data and chemical class distribution information. Some of the structural features are easier to determine than others. For example, the carbon number of the normal paraffin class has been determined in experiments to be 12. The average number of substituent carbons on naphthalenes is 1.5 because the average carbon number for this class is 11.5 and there are 10 carbon atoms in the naphthalene base frame. Because the average carbon number of tetralin/indan is 11, dominant species in this class are mono or di-methyl rings, although the difference between 9-carbon indan and 10-carbon tetralin provides more degrees of freedom in choosing candidate compounds. For each chemical class, the derivation is described in detail here.

The average carbon number of normal paraffinic species is 12 reported by Hodgson and Kemmer [10], which is confirmed in the current study from results of GC-FI-TOFMS. Although most chemical properties depend on carbon number of normal paraffins, it is highly likely that the lower and the higher ends of the normal paraffin compound distribution will compensate each other in terms of average properties. Therefore, a few normal paraffin species averaged at dodecane should be adequate for most applications. In Table 1, the average physical properties of normal undecane, dodecane, and tridecane were used to derive the molar distribution of chemical classes. However, the candidate species for the normal paraffin class are not necessarily limited to a consecutive homologous series. For example, decane, dodecane, and tetradecane could have equally been selected. The inclusion of a wider range of paraffins is especially attractive if matching a continuous spectrum of physical properties is necessary. For example, smaller and larger paraffins might be included in the surrogate to reproduce the boiling range curve that is between 140 C and 280 C, corresponding to  $C_7$  to  $C_{14}$  aromatics,  $C_8$  to  $C_{15}$  naphthenes, and  $C_9$  to  $C_{16}$  paraffins. Considerable freedom is available in choosing candidate species for the normal paraffin class. It is noteworthy that the number of candidate compounds will not alter the average calculated values for carbon atom characterization listed in Table 1 as long as the average carbon number of those compounds is 12.

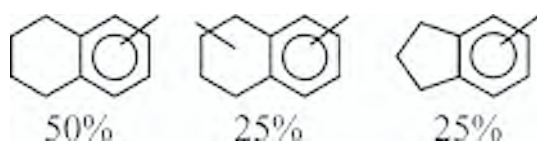
The average carbon number of naphthalenes is 11.5 [10], which indicates the dominant species in the jet fuel are methyl-, dimethyl- and ethyl-naphthalenes. The fraction of naphthalenes higher than  $C_{13}$  must be small, because their existence should be balanced by the naphthalene fraction, which accounts for only 0.13 vol % in the world survey of 55 jet fuels, in comparison with 1.55 % for substituted naphthalenes. If the surrogate set includes only methyl-, dimethyl- and ethyl-naphthalenes, it is concluded that 50% of the class is methyl naphthalene, in order to match the average carbon number of 11.5. For a first approximation, dimethyl- and ethyl-naphthalenes are selected with equal importance in this work. Therefore, the selected compounds for the naphthalene class include 50% methyl, 25% dimethyl and 25% ethyl naphthalenes as shown in Scheme 3. The average number of substituents is  $50\% \times 1 + 25\% \times 1 + 25\% \times 2 = 1.2$ . It is noted that the distribution between dimethyl and ethyl naphthalenes can provide an additional degree of freedom that results in a range of the average number of substituents from 1 to 1.5.

The average carbon number for the indan/tetralin chemical class is 11 [10] and the dominant species have one or two substituents. The evidence of substituents on the aromatic rings is found in the NMR spectrum for the fuel as the peaks at 125.0, 126.2, 129.0 and 129.7 ppm are indicative of the substituent bearing aromatic carbons. It is very difficult to quantify the amount of substituents on the aliphatic ring of benzo-naphthenes since these NMR peaks are superimposed with aliphatic carbons from paraffins. In GC/MS data, substituents on the aromatic ring of benzo-naphthenes were found to be more abundant than those on the aliphatic ring. Therefore, we assumed in this work that mono-substituents of benzo-naphthenes are dominantly on aromatic rings. For di-substituted species, we assume only one substituent on each of the rings. Because there is a very small fraction of non-substituted naphthalenes identified in jet fuels [4], we assume that for the benzo-naphthenes substituted compounds also dominate. Therefore, the inclusion of dimethyl or ethyl tetralins ( $C_{12}$ ) should be balanced by methyl indan ( $C_{10}$ ) in order to match the average carbon number of 11. Therefore, a combination, as in Scheme 4, is formulated with a small indan content of 25%. The exclusion of ethyl tetralin is to favor multi-substituted species. The average

Scheme 3.



Scheme 4.



substituents on the aromatic ring is 1 as seen in Scheme 4. The number on the aliphatic ring is 0.2 and the total number of substituents, on average, is 1.2. A range of the average number of substituents on the aliphatic ring from 0 to 0.5 can be assigned due to the freedom concerning methyl tetralin.

The average carbon number of jet A-type fuels is approximately 11 [4], and NMR data in Table 2 indicates that 5% of the total carbon in the fuel is non-protonated aromatic carbon. Therefore  $11 \times 5\% = 0.5$  atoms out of the equivalent chemical formula  $C_{11}$  are non-protonated aromatic carbons. The contribution to this carbon functionality from the selected naphthalene surrogate species is  $(2 + 1.2) \times 1.34\% = 0.04$ , and that from the selected benzo-naphthene species is  $(2 + 1) \times 6.58\% = 0.2$ , where 1.2 and 1 are the average numbers of substituents on the aromatic rings selected in this paper for these two classes. Therefore, the contribution from benzenes to the non-protonated aromatic carbons is  $0.5 - 0.04 - 0.2 = 0.3$ , which translates into  $0.3/11.50\% = 2.7$  substituents, on average, for benzenes.

The NMR data in Table 2 indicates that 16% of the total carbon in the fuel is aliphatic methine carbon. Therefore  $11 \times 16\% = 1.8$  atoms among the 11 carbons in the equivalent chemical formula  $C_{11}$  are methine carbons. Only naphthenes, benzo naphthenes, and iso-paraffins have tertiary carbons. Because only mono- and di-substituted cyclohexane and mono-substituted decalins were identifiable for jet fuels in GC/MS data, we assume the average methine carbon number of naphthenes is less than 2. The contribution from naphthenes to the methine carbon functionality is  $14.4\% \times 2 + 11.8\% \times (2 + 2) + 1.3\% \times (4 + 2) = 0.8$ . The contribution from benzo naphthenes is 0.02. The average number of methine carbons in iso-paraffins is at least  $(1.8 - 0.8 - 0.03)/35\% = 2.8$  carbons. Therefore, we estimate the average number of methine carbons in the iso-paraffin chemical class is approximately 3 because the average number of branches is 3.2 in the narrow distillate of Isopar H [6]. Isopar H has an equivalent chemical formula of  $C_{11.6}H_{25.2}$ , which is the closest isopar cut to the average carbon number ( $C_{12}$ ) of iso-paraffins in jet fuels [14]. If the average number of branches in iso-paraffins is 3, then the contribution of this class to methine carbons is  $35\% \times 3 = 1$ , which translates into a contribution of  $1.8 - 1 - 0.02 = 0.8$  methine carbons from naphthenes. The average number of substituents on naphthenes is  $(0.7 - 11.78\% \times 2 - 1.28\% \times 4) / (27.43\%) = 1.5$ , where the 2 ring-fused carbons in decalin and 4 others in multi-ring compounds are accounted for.

The average number of aliphatic quaternary C in iso-paraffinic species is at most 0.3, which corresponds to 1% of the total carbons in the assumed formula  $C_{11}H_x$  for JP fuel with the assumption that the iso-paraffin content in the current fuel is 35 vol %, i.e., near the average of US JP-8 fuels.

These estimates provide enough detail to derive the average number of methyl carbons in iso-paraffins. With an average carbon number of Jet-A type fuels of approximately 11 [4]. The NMR data in Table 2 shows 26% of the total carbon in the fuel consists of methyl groups. Therefore  $11 \times 26\% = 2.9$  atoms among the 11 carbons in the assumed formula for JP fuel are methyl carbons. The contribution from normal paraffins is  $18.12\% \times 2 = 0.4$  atoms; that from naphthenes is  $(14.37\% + 11.78\% + 1.28\%) \times 1.477 = 0.4$ ; that from benzenes is  $11.5\% \times 2.687 = 0.3$ ; that from naphthalenes and benzo naphthenes is  $(1.34\% + 6.58\%) \times 1.25 = 0.1$ . Therefore the contribution to this carbon functionality from iso-paraffins is 1.2 methyl carbons of the 11 in the assumed

formula for JP fuel, which corresponding to  $1.6845/35.05\% = 3.4$  methyl carbons per iso-paraffin molecule on average. This value is in the vicinity of the average number of methyl carbons (5.2) in Isopar H.

The length of substituents on the mono-cyclic compounds, i.e., cyclohexanes and benzenes, can be derived by counting the contribution from chemical classes toward the aliphatic methylene carbons. It is noted that we assume methyl-substitution only on naphthalenes, benzo naphthenes, and higher naphthenes. The average carbon number of jet A-type fuels is close to 11 [4], and NMR data in Table 2 indicates that 47% of the total carbon in the fuel is methylene carbon. Therefore  $11 \times 47\% = 5.2$  atoms among the 11 carbons in the assumed formula for JP fuel are methylene carbons. The contribution from normal paraffins to this carbon functionality is  $18.12\% \times 10 = 1.8$  (Only 10 of the 12 carbons in n-dodecane are methylene). We use the structural details of the narrow distillate cut Isopar H to estimate the functionalities in iso-paraffins. We assume 0.2 methyl substituents out of the 3.2 total substituents are on quaternary carbons, which leads to, on average, 3.0 methine carbons and 0.1 quaternary carbons (constrained to  $< 0.3$  as discussed earlier). Therefore, we assume there are 3.6 methylene carbons on average per iso-paraffin molecule since the average carbon number of iso-paraffins is 12 (Table 1) for jet A-type fuels. The contribution of methylene carbons from iso-paraffins is 1.3; that from the ring portion of naphthenes is  $14.37\% \times 6 + 11.78\% \times 8 + 1.28\% \times 10 - (14.37\% + 11.78\% + 1.28\%) \times 1.477 = 1.5$ ; that from benzo naphthenes is 0.2. Therefore, the contribution from the substituent chains on the mono-cyclic compounds is about 0.3, which corresponds to  $0.3131/(14.37\% + 11.50\%) = 1.2$  secondary carbons. Therefore, the average length of the substituents on benzenes and cyclohexanes is 2.2 carbons.

Our results above are supported by some of the detailed compositions of petroleum, other than proprietary industry data, available in the literature on the fingerprinting of hydrocarbons for purposes of forensics on oil spills or determining the origin of petroleum. Evidence of the biogenic source of petroleum is provided by the detection of isoprenoid alkanes ( $C_{15}$ ,  $C_{16}$ ,  $C_{18}$ ,  $C_{19}$ ,  $C_{20}$ ) in a 200 million year old Australian oil [24]. Identification of the alkylated benzenes in Paleozoic petroleum [25] showed an unusual abundance of 1,2,3,4-tetramethyl benzene as well as significant peaks for trimethyl benzenes (1,2,3 and 1,2,4), xylenes; toluene had the largest peak followed by the tetramethyl benzene then benzene.

## REFERENCES

1. M. Colket, T. Edwards, S. Williams, N.P. Cernansky, D. L. Miller, F. Egolfopoulos, P. Lindstedt, K. Seshadri, F. L. Dryer, C. K. Law, D. Friend, D. B. Lenhart, H. Pitsch, A. Sarofim, M. Smooke, W. Tsang, AIAA 2007-770, 45th AIAA Aerospace Sciences Meeting and Exhibit, Reno, January 2007.
2. J. Speight, *The Chemistry and Technology of Petroleum*, 2nd ed., Dekker, 1991, p. 218.
3. [http://www.chevronglobalaviation.com/docs/aviation\\_tech\\_review.pdf](http://www.chevronglobalaviation.com/docs/aviation_tech_review.pdf).
4. T. Edwards, AIAA 2002-3874 (2002).
5. D. R. Lide, *CRC Handbook of Chemistry and Physics*, 81st ed., CRC Press, Boca Raton, (2000-2001).

6. Advisory Committee on Hazardous Substances, Twenty-third meeting, European Chemicals Bureau, 5 December 2006.
7. [http://www.exxonmobilchemical.com/Public\\_Files/Fluids/Aliphatics/AsiaPacific/Data\\_Sheet\\_Isopar\\_Fluid\\_H\\_ap.pdf](http://www.exxonmobilchemical.com/Public_Files/Fluids/Aliphatics/AsiaPacific/Data_Sheet_Isopar_Fluid_H_ap.pdf).
8. T. Edwards, *J. Eng. Gas Turbines Power* 129 (2007) 13-20.
9. T. Edwards, Workshop on "Combustion Simulation Databases for Real Transportation Fuels, NIST, March (2005).
10. F. N. Hodgson, A.M. Kremmer, AFAPL-TR-76-26, March (1976).
11. E. Breitmaier, W. Voelter, *Carbon-13 NMR Spectroscopy*, 3rd ed., VCH Publishers, New York.
12. D.S. Duvall, A. D. Snyder, J. Henry, D. J. Lewis, F. N. Hodgson, A. K. Behme, S. Chatteraj, AFWAL-TR-85-2049, August 1985.
13. F. N. Hodgson, J. D. Tobias, AFWAL-TR-79-2016, March 1979.
14. T. Edwards, Analysis of 8000 data in (<http://www.desc.dla.mil/DCM/DCMPage.asp?pageid=99>), reported in email to Jet Fuel Working Group, May 17, 2006.
15. E. G. Eddings, S. Yan, W. Ciro, A. F. Sarofim, *Combust. Sci. Technol.* 177 (2005) 715-739.
16. C. S. McEnally, L. D. Pfefferle, *Combust. Flame* 148 (2007) 210-222.
17. C. S. McEnally, D. M. Ciuparu, L. D. Pfefferle, *Combust. Flame* 134 (2003) 339-353.
18. H. R. Zhang, E. G. Eddings, A. F. Sarofim, *Proc. Combust. Inst.* 31 (2007) 410-409.
19. P. E. Law, P. R. Westmoreland, T. A. Cool, J. Wang, N. Hansen, C. A. Taatjes, T. Kasper, *Proc. Combust. Inst.* 31 (2007) 565-573.
20. H. R. Zhang, L. K. Huynh, N. Kungwan, Z. Yang, S. Zhang, *J. Phys. Chem. A* 111 (2007) 4102-4115.
21. H. R. Zhang, E. G. Eddings, A. F. Sarofim, *Proc. Combust. Inst.* 32 (2009) 10.1016/j.proci.2008.06.011.
22. H. R. Zhang, E. G. Eddings, A. F. Sarofim, *Preprints of Symposia, American Chemical Society, Division of Environmental Chemistry*, 47 (2007) 629-643.
23. L. Pfefferle, C. S. McEnally, Invited Lecture, 5th US Combustion Meeting, San Diego, March 23-25, 2007.
24. C. S. McEnally, L. Pfefferele, in *Combustion Generated Fine Carbonaceous Particles*, H. Bockhorn, A. D'Anna, A.F. Sarofim, H. Wang (Eds.) Karlsruhe University Press, 2009, pp. 125-136.
25. W. Van Hoven, P. Haug, A. L. Burlingame, K. Calvin, Lawrence Berkeley National Laboratory, Paper UCRL 17015, 1966.
26. Y. Sun, S. Xu, H. Lu, P. Cuai, *Org. Geochem.* 34 (2003) 629-634.



# Pyrolysis and oxidation of n-decane, n-propylbenzene and kerosene surrogate behind reflected shock waves

D. Darius, N. Chaumeix, C. Paillard

*Institut de Combustion, Aérothermique, Réactivité et Environnement C.N.R.S.*

*Abstract: The aim of this study is to build and provide an experimental database on soot formation from kerosene-model fuel (80% n-decane + 20% n-propylbenzene). The early soot formation study is carried out, using a stainless steel shock tube coupled to a laser extinction setup. Soot formation parameters were determined (induction delay time, yield and mean particle diameter) for the pyrolysis and the oxidation ( $\Phi=5$ ) of n-decane, n-propylbenzene and the binary mixture. The highly diluted mixtures were heated between 1450 and 2360 K, the pressure ranged from 11 to 17.9 bar. The addition of n-propylbenzene to n-decane had a weak effect on induction delay times and soot yield. Nevertheless, soot from kerosene surrogate appear in a temperature range which is larger than the n-decane one. The oxygen addition (equivalence ratio of 5) also had a weak effect on the induction delay time whereas the soot yield decreased strongly. In our pyrolysis conditions, the mean particle diameter for n-decane and n-propylbenzene was found to decrease from 20 to 16 nm as the temperature is raised from 1660 to 2060 K.*

## 1. INTRODUCTION

For the last decade, jet engine development has led to an increase in the pressure and temperature levels of the thermodynamic process in order to improve the engine efficiency. The high pressure reached in the engine is responsible for a significant increase in pollutant emissions. In order to meet the incoming regulations for jet engines and consequently to optimise new design, it is necessary to couple experiments with 3D CFD calculations in order to shorten the development delay as well as their cost. To predict soot level at the exhaust of jet engines it is mandatory to construct and validate a chemical kinetic mechanism that can be used to simulate the soot formation process. The reaction kinetics, the fuel preparation process, the turbulent fluid flow and the radiative heat transfer to the combustor walls, is essentially due to soot, are needed for the combustion process simulation. Although soot formation conditions have been widely studied essentially with flame and shock tube methods, the mechanism is not fully understood in engines. Moreover few studies on soot formation from kerosene combustion were carried out and the results concern essentially the soot texture [1, 2, 3, 4] which was observed by transmission electron microscopy (TEM) or scanning electron microscopy (SEM). For any soot sample source (laboratory experiments or atmospheric sampling), the soot texture was similar and has composed of primary particles aggregating. Recently, Aksit and Moss [5] focused their research on the soot formation from kerosene turbulent flame. They measured soot volume fraction of kerosene, n-decane and representa-

tive kerosene binary mixture (80% n-decane and 20% n-propylbenzene), however there experimental conditions are far from those encountered in engines (pressure, equivalence ratio). In order to improve the kerosene soot formation model, some experiments in engine condition are necessary. The shock tube is a homogeneous reactor which allows the characterization of the early soot formation process. For this study a stainless steel shock tube was used coupled to a laser extinction method. Following the soot formation behind reflected shock waves allows to built and provide an experimental database on soot formation from kerosene-model fuels. The aim of the paper is to study the soot formation tendency of different hydrocarbons mixtures representative of kerosene by measuring the soot induction delay time ( $\tau_{\text{ind}}$ ), volume fraction ( $f_v$ ), soot yield ( $Y_{\text{soot}}$ ), and mean diameter ( $d_{\text{mean}}$ ) for a large temperature range and at high pressure.

## 2. EXPERIMENTAL APPARATUS

### 2.1. Apparatus

This experimental apparatus has been used in previous studies [6, 7]. Experimental Soot formation was studied in a heated stainless steel shock tube (7.15 m total length). The driven section was blackened in order to suppress multiple reflections of light near the measurement section. The last part of the driven section (0.7 m long) is equipped with four piezoelectric pressure transducers (equally spaced by 150 mm) mounted flush with the internal surface of the shock tube. In the same plane as the last transducer, 10 mm before the shock tube end wall, two fused silica windows are mounted. In this work, the observation time was around 2 ms for a driven section 5.15 m long (52 mm i.d.). Reflected shock parameters ( $P_5$  and  $T_5$ ), at which soot formation is studied, were calculated using the classical procedure from the shock speed and the initial conditions [8].

### 2.2. Instrumentation

High frequency digitizing oscilloscopes recorded the He-Ne laser (632.8 nm) light attenuation detected by the photomultiplier equipped with an interferential filter (633 nm width  $\pm 2$  nm). At 633 nm, the PAH absorption is neglected: the attenuation is assumed to be only due to soot [9]. Since kerosene is constituted of hundreds of different compounds, a kerosene model fuel was chosen. This model fuel was chosen to be constituted of 80% n-decane/20% n-propylbenzene. The present work focuses then on the soot formation tendency of these pure fuels and of the binary mixture. The hydrocarbon/oxygen mixtures were highly diluted in argon. The high pressure gas used for the experiments was helium. The liquid hydrocarbons were vaporized in a heated bulb and introduced into the 30 l mixing tank through heated pipe. The magnetic fan was then switched on for at least 30 min to get a homogeneous mixture. The tank and the shock tube were kept at an initial temperature of 90°C. The shock tube end-wall had to be carefully taken off since the soot particles deposited on its surface. The support was plunged in a glass of anhydrous ethanol and underwent a 5 min cycle of ultrasonic waves. A droplet of the mixture of soot and anhydrous ethanol was deposited on a 3 mm dia-

meter carbon grid (30  $\mu\text{m}$  thick, 400 meshes per inch). The grids were coated with a very thin amorphous carbon supporting film which provided very low contrast and did not interfere with the soot structure. Several micrographs were taken at a magnification of  $5 \times 10^4$  using the bright field technique, which revealed the soot aggregates and texture.

### 2.3. Test conditions

The conditions for which highly diluted mixtures (more than 98.2% of argon) were studied are summarized in the Table 1. The experiments were performed for the pyrolysis and an equivalence ratio of 5. The initial molar fractions were adjusted in order to keep an initial carbon concentration equal to  $2 \pm 0.07 \times 10^{18}$  atoms/ $\text{cm}^3$ .

Table 1. Experimental conditions behind reflected shock waves for pyrolysis and oxidation conditions ( $\phi=5$ ).

Mixtures	80% $\text{C}_{10}\text{H}_{22}$ + 20% $\text{C}_9\text{H}_{12}$	$\text{C}_{10}\text{H}_{22}$	$\text{C}_9\text{H}_{12}$	
Temperature (K)	1595 - 2205	1605 - 2020	1850 - 2350	1450 - 2360
Pressure (bar)	11 - 15.8	11 - 17.9	13 - 16.6	11.5 - 17.5
$[\text{C}] \times 10^{-18}$ (C atoms/ $\text{cm}^3$ )	1.96 - 2.06	1.96 - 2.09	5.98 - 7.56	1.94 - 2.04
Ar(%)	98.5-99.6	98.2-99.7	98.75	98.6-99.6
$\text{O}_2$ (%)	0-1.0	0-1.4	0	0-1.0

## 3. RESULTS

### 3.1. Soot volume fraction

Using the laser light extinction technique in the detection of soot formation needs some hypothesis. Among others, the soot particle size is supposed much smaller than the wavelength of the laser and the soot distribution size is supposed monodispersed. Figure 1a shows the signal recorded by the oscilloscope linked to the photomultiplier and to the last piezoelectric pressure transducer. Before the experiment begins, the light is fully transmitted. After the shock wave passages in the gas, the transmitted laser light intensity decreases after a certain laps of time named soot induction delay time (Figure 1a). From  $\tau_{\text{ind}}$ , the declining of the transmitted light increases quickly then it slows down to reach a minimum value. The soot volume fraction evolution versus time is deduced from the transmitted signal using the Beer-Lambert law (Figure 1b) using the following expression:

$$f_v = \frac{\lambda}{6\pi d_{\text{soot}} \ln \left( \frac{m^2 - 1}{m^2 + 2} \right)} \ln \frac{I}{I_0} \quad (1)$$

where  $f_v$  is the soot volume fraction,  $\lambda$  laser wavelength,  $I_0$  and  $I$  the initial and transmitted intensity,  $d_{\text{tube}}$  optical path and  $m$  the complex soot refractive index.

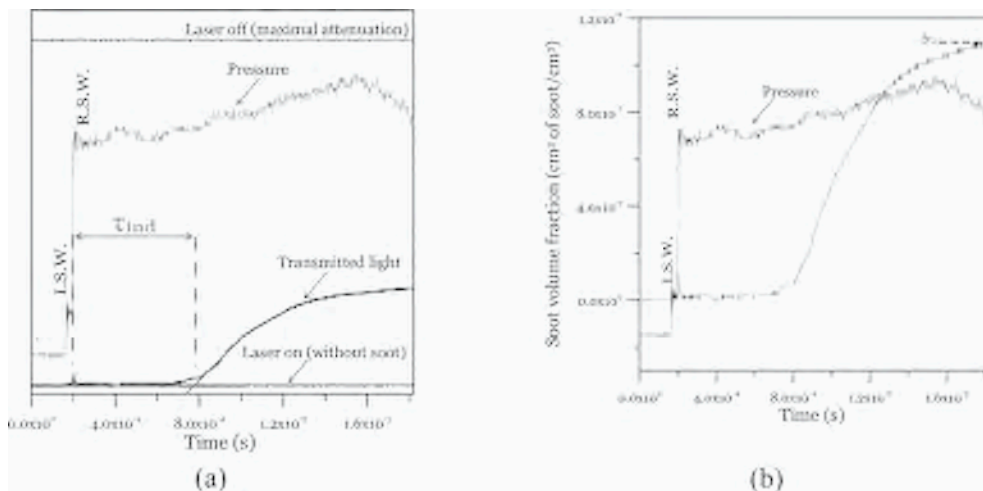


Figure 1. Transmission signal (a) and soot volume fraction (b) and the last pressure transducer signal as a function of time for a 0.44% n-decane/99.56% argon mixture (1934 K, 12.24 bar).

### 3.2. Soot induction delay time

One of the most important parameter to characterize a fuel tendency to form soot is the induction delay time. This delay is defined as the interval time between the moment at which the fuel mixture is heated to a given temperature and the moment where soot particles appear. This delay (labeled  $\tau_{\text{ind}}$ ) depends on the fuel nature, the mixture equivalence ratio and, finally, at a lower extent, on the pressure. This parameter is graphically determined as the period between the passage of the reflected shock and the intersection of the inflectional tangent with the time axis [6, 10, 11]. The maximum error on this soot formation parameter depends on the the soot volume fraction profile, the highest error is obtained for short induction delay times and it is below 25%. As it is shown in Figure 2, the soot induction delay time decreases exponentially as the temperature is increased. As it is expected, aromatic fuel exhibits lower  $\tau_{\text{ind}}$  than alkanes as it was observed in the literature [6, 10]. n-Propylbenzene addition to n-decane in order to form the kerosene surrogate mixture induces a weak decrease of  $\tau_{\text{ind}}$  (Figure 2). The effect of initial carbon concentration on  $\tau_{\text{ind}}$  was investigated in the case of n-decane. This concentration increase had a weak influence on the  $\tau_{\text{ind}}$  but soot appeared at higher temperatures (Figure 3). Oxygen addition had different influence on  $\tau_{\text{ind}}$  depending on the hydrocarbon nature. For n-decane and the binary mixture,  $\tau_{\text{ind}}$  decreases as oxygen is added whereas no strong difference for the n-propylbenzene was observed (Figure 2).

$\tau_{ind}$  depends on fuel nature, temperature, pressure and equivalence ratio. An Arrhenius type equation was investigated to express the variation of the induction delay time,  $\tau_{ind}$ , versus inverse of temperature. Table 2 summarizes the different values of the apparent activation energy,  $E_{ind}$ , and pre-exponential factor,  $A_{ind}$ , obtained in this study.  $E_{ind}$  is around 200kJ/mol in the pyrolysis condition, the oxygen addition decreases this parameter except for n-propylbenzene for which  $E_{ind}$  increases when equivalence ratio decreases.

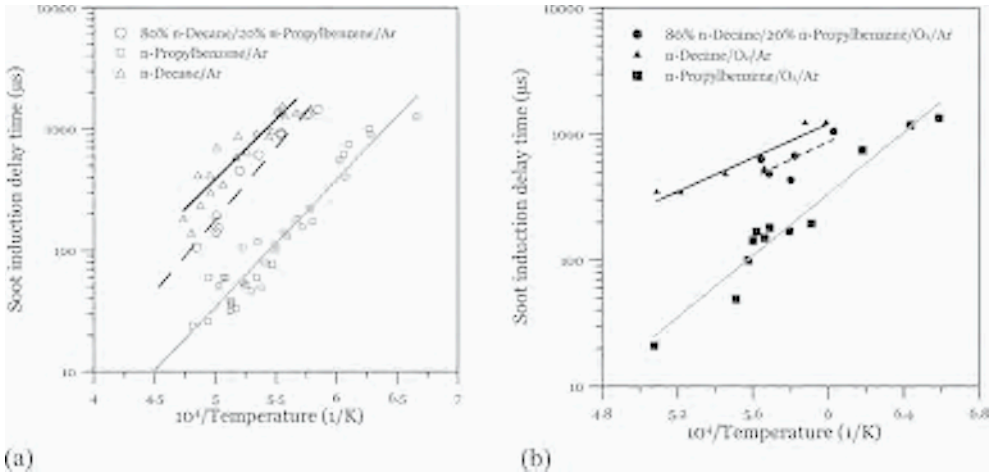


Figure 2. Soot induction delay time versus shock temperature for pyrolysis (a) and oxidation,  $\phi=5$  (b).  $11 < P_5 \text{ (bar)} < 17.9$  and  $1.94 \times 10^{18} < [C] \text{ (C atoms/cm}^3) < 2.09 \times 10^{18}$ .

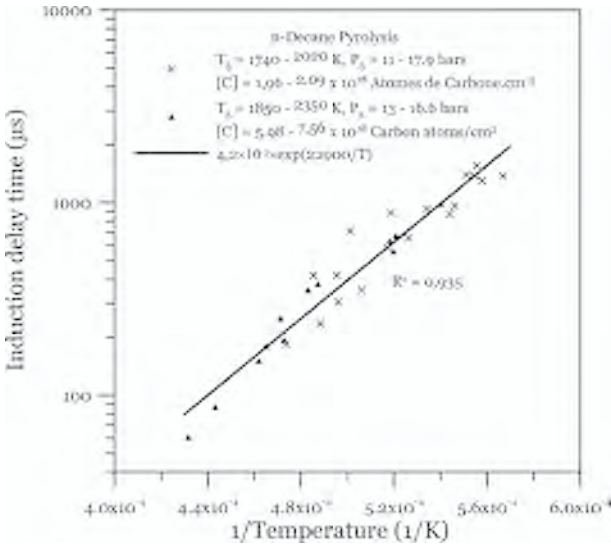


Figure 3. Soot induction delay time evolution versus inverse of temperature for n-decane concentration from  $1.96 \times 10^{18}$  to  $7.56 \times 10^{18}$  carbon atoms/cm<sup>3</sup>.

### 3.3. Soot yield

Soot yield is defined as a ratio of total carbon number accumulated in soot particles over available initial total carbon number in fuel behind the reflected shock wave. The soot yield is deduced from the initial condition and  $t$  from the absorption signal using Graham’s model [12] using:

$$Y = [C]_{\text{soot}} / [C]_{\text{initial}} = N_{\text{av}} \rho f_v / 12 [C]_{\text{initial}} \tag{2}$$

where  $\rho$  is soot density equal to 1.86g/cm<sup>3</sup>,  $f_v$  soot volume fraction,  $N_{\text{av}}$  : Avogadro’s number.

The error on the soot yield does not exceed 15% for a given soot complex refractive. For n-decane, below 1765 K, no soot was formed. As the temperature increases above 1765 K, the soot yield increases first and reaches the maximum value of 5.75% at an optimal temperature of 1920 K ( $T_{\text{opt}}$ ). Beyond this  $T_{\text{opt}}$  the soot yield decreases. However, no maximum limit was observed for soot inception in the high temperature range.

For n-propylbenzene, the minimum temperature necessary for soot to be formed was shifted to a lower value (1500 K),  $T_{\text{opt}}$  for which the maximum soot yield was around 5.75%, was found around 1790 K. The decrease of  $Y_{\text{soot}}$  as the temperature was raised beyond the optimal one was much slower than in the case of n-decane. Although, the maximum soot yield was comparable between n-decane and n-propylbenzene, the existence domain was much wider in the case of n-propylbenzene than in the case of n-decane. For the binary mixture, the minimum temperature limit was lower than the n-decane one: around 1710 K. First, the soot yield is raised and reaches

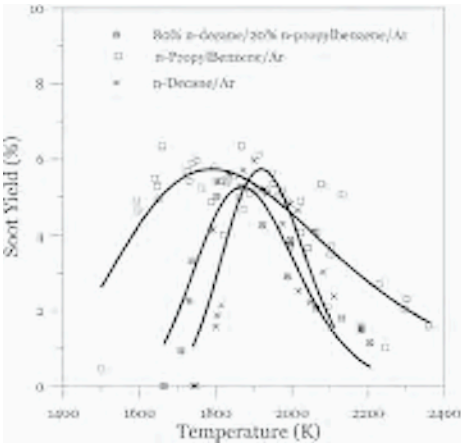


Figure 4. Soot yield versus reflected shock temperature for pyrolysis  $11 < P5 \text{ (bar)} < 17.5$  and  $1.94 \times 10^{18} < [C] \text{ (carbon atoms/cm}^3) < 2.05 \times 10^{18}$ .

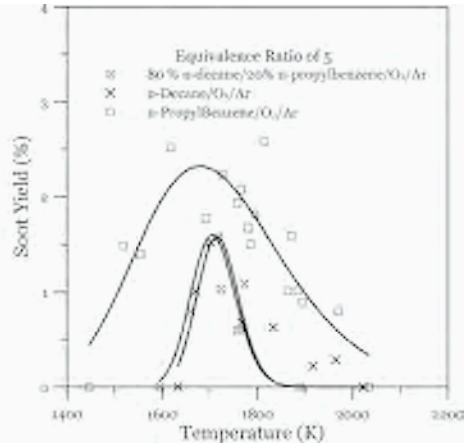


Figure 5. Soot yield versus reflected shock temperature for oxidation. Equivalence ratio 5;  $11 < P5 \text{ (bar)} < 17.9$   $1.96 \times 10^{18} < [C] \text{ (C atoms/cm}^3) < 2.09 \times 10^{18}$ .

its maximum around 5.25% at 1870 K before decreasing. For oxidation conditions, the evolution of soot yield for each mixture also describes a bell-shape curve but the maximum soot yield and  $T_{opt}$  decreased. In the case of the n-decane, the maximum soot yield was divided by a factor of 3.60 and the  $T_{opt}$  down to 1715 K. For the n-propylbenzene oxidation,  $T_{opt}$  for which the maximum soot yield was around 2.30%, was 1680 K. Concerning the kerosene surrogate, the oxygen addition decrease the  $T_{opt}$  down to 1705 K and the maximum soot yield down to 1.60%. The soot yield evolution versus the temperature was expressed by a modified Gaussian's equation:

$$Y = Y_{max} \cdot \exp\left(A \times \left(\frac{(T_{opt} - T)}{T}\right)^2\right) \quad (3)$$

The different values of these equation parameters are summarized in Table 2.

Table 2. Parameters deduced from  $\tau_{ind}$  and  $Y$  correlations ( $A_{ind}$  and  $E_{ind}$ ) according to the equations  $\tau_{ind} = A_{ind} \exp(E_{ind}/RT)$  and  $Y = Y_{max} \cdot \exp(A \times ((T_{opt} - T)/T)^2)$ .

Mixtures	$A_{ind}$	$E_{ind}$ (kJ/mol)	$T_{opt}$ (K)	$Y_{max}$ (%)
$(0.8C_{10}H_{22} + 0.2C_9H_{12}) + Ar$	$2 \times 10^{-4}$	230	1870	5.25
$C_{10}H_{22} + Ar$	$4.50 \times 10^{-3}$	190	1920	5.73
$C_9H_{12} + Ar$	$2.05 \times 10^{-5}$	200	1790	5.73
$0.8C_{10}H_{22} + 0.2C_9H_{12} + O_2 + Ar$	$5 \times 10^{-2}$	135	1705	1.60
$C_{10}H_{22} + O_2 + Ar$	0.11	130	1715	1.58
$C_9H_{12} + O_2 + Ar$	$1.56 \times 10^{-5}$	235	1680	2.32

### 3.4. Importance of the refractive index

Several values of soot complex refractive index ( $m$ ) are available (Table 3). Two works were particularly used [13, 14] because they present the results of experiments and provide dispersion models that extend their observations over a significant range of wave-

Table 3. Effect of different soot complex refractive index,  $E(m)$ , on  $f_{\infty}$ .

Authors	$E(m)$	$((f_{\infty})^{14} - (f_{\infty})^{litt}) / (f_{\infty})^{14}$
Lee and Tien [14]	0.1927	/
Dalzell and Sarofim [13]	0.2595	25 %
Felske et al. [15]	0.1607	20 %
Chippet et al. [16]	0.1763	10 %
Bockhorn et al. [17]	0.2416	20 %
Erickson et al. [18]	0.5060	60 %

lengths. The complex refractive index of Lee and Tien [14] was chosen for this study. As one can see in Figure 6, the maximum soot volume fraction achieved for a given temperature varies according to the adopted refractive index.

For a given profile, one can derive the values of induction delay time,  $\tau_{\text{ind}}$ , soot yield and surface growth constant rate based on different values of  $m$ . The induction delay time is not sensitive to the adopted value since the maximum variation is about 0.6 %. For the soot yield, the difference between the soot volume fraction derived using Lee and Tien [14] refractive index and the different soot volume fraction using the different values of the literature varies from 10 to 60 %.

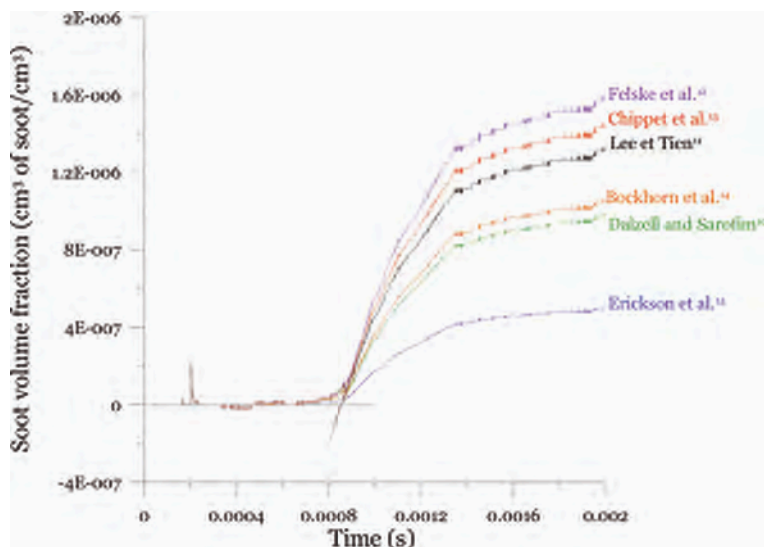


Figure 6. Soot volume fraction evolution versus time and  $E(m)$  for n-decane (1900 K, 12 bars).

### 3.5. Soot texture

Soot texture was observed from samples which are obtained in pyrolysis conditions, with a TEM at a magnification of  $5 \times 10^4$ . Soot were composed of primary particles which aggregated in order to form some chains as it is shown on the picture of Figure 7. Primary particle mean diameters were determined at different temperatures. As it can be seen in Figure 8, the mean particle diameter decreases as the temperature is increased. In the case of n-decane,  $d_{\text{mean}}$  ranges from 19.7 to 16.2 nm as the temperature is raised from 1750 to 2060 K. In the case of n-propylbenzene,  $d_{\text{mean}}$  ranges from 19.7 to 15.7 nm for a temperature range from 1660 K to 1915 K. These values were lower than those of literature [6] for the same pressure domain. The order of magnitude of the soot mean diameter shows that the hypothesis used for the calculation of the soot volume fraction ( $d_{\text{mean}} \ll \lambda$ ) was valid.  $d_{\text{mean}}$  of n-decane and n-propylben-

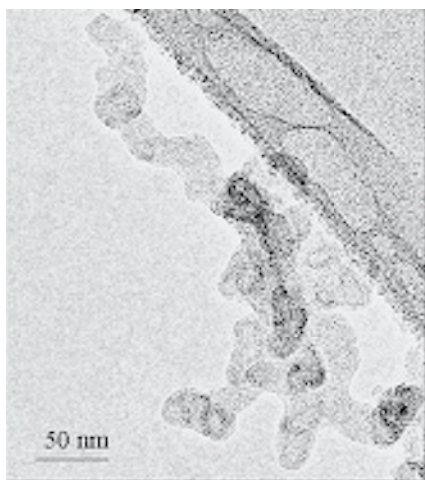


Figure 7. Soot of n-decane at 1750 K in pyrolysis case.

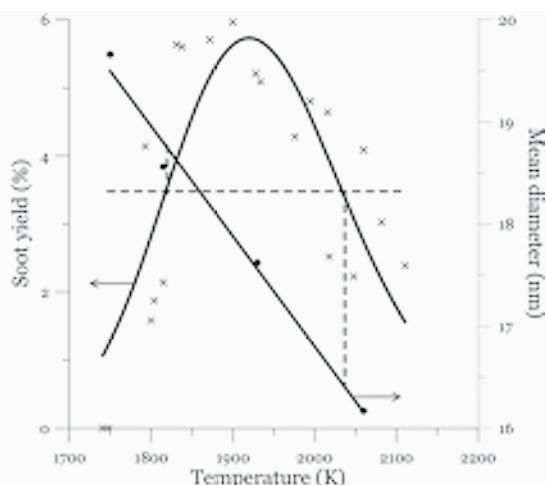


Figure 8.  $d_{\text{mean}}$  and  $Y_{\text{soot}}$  evolution versus temperature in the case of n-decane pyrolysis.

zene are smaller than those of toluene [6]. Moreover, the cloud of soot which is formed behind the reflected shock wave is characterized by its soot volume fraction, its soot mean diameter (supposed monodispersed) and its density. These three parameters are linked by the following expression:  $N = 6f_v / \pi d_{\text{mean}}^3$ . Figure 8 shows the evolution of  $Y_{\text{soot}}$  which is linked to  $f_v$  and the evolution of  $d_{\text{mean}}$  versus the temperature. In the case of n-decane,  $d_{\text{mean}}$  is around 18.7 nm at 1815 K and 16.4 nm at 2035 K,  $f_v$  is around  $4.70 \times 10^{-7} \text{ cm}^3$  of soot/ $\text{cm}^3$  at this both temperatures. This observation means that  $N$  (soot nuclei number) increases with the temperature.

#### 4. CONCLUSION

In this work, new data were obtained concerning soot formation behind reflected shock wave for different mixture of n-decane, n-propylbenzene and kerosene surrogate (80% n-decane + 20% n-propylbenzene) in pyrolysis and oxidation conditions. The following parameters were studied: the soot induction delay time, soot yield, surface growth constant rate, maximum soot growth rate, soot yield and soot mean diameter.  $\tau_{\text{ind}}$  of n-decane is longer than this of n-propylbenzene as it is expected. The addition of n-propylbenzene to the n-decane in order to form the surrogate kerosene decreases the soot induction delay time. In the condition of this study,  $Y_{\text{soot}}$  of each mixture is expressed by the modified Gaussian equation. In the oxidation condition, the aromatic hydrocarbon forms more soot than the alkane. On the contrary in pyrolysis conditions, the both hydrocarbons form similar quantity of soot. Nevertheless, n-propylbenzene temperature range in which the soot is formed is larger than this of n-decane in all conditions of this study. The addition of n-propylbenzene to n-decane

only raised weakly the soot existence domain in low temperature. The mean diameter of soot from pyrolysis of the n-decane and n-propylbenzene were smaller than the literature. The mean diameter and soot yield evolutions versus temperature indicate the number of soot nuclei increases with the temperature.

## ACKNOWLEDGEMENT

This work has been financially supported by the European Community in the framework of FP4 under contract n° G4RD-CT-2002-00670.

## REFERENCES

1. T.C. Fang, C.M. Megaridis, W.A. Sowa, G.S. Samuelsen, *Combust. Flame* 112 (1998) 312-328.
2. W. Choi, M.T. Leu, *J. Phy. Chem. A* 102 (1998) 7618-7630.
3. D.F. Blake, K. Kato, *J. Geophys. Res* 100, D4 (1995) 7195-7202.
4. R.F. Pueschel, D.F. Blake, K.G. Snetsinger, A.D.A. Hansen, S. Verma, K. Kato, *Geophys. Res. Letters* 19, 16 (1992) 1659-1662.
5. I. M. Aksit, J. B. Moss, *Fuel* 84 (2005) 239-24.
6. F. Douce, N. Djebaili-Chaumeix, C.-E. Paillard, C. Clinard, J.-N. Rouzaud, *Proc. Combust. Inst.* 28 (2000) 2523-2529.
7. F. Douce, N. Djebaili-Chaumeix, C.-E. Paillard, C. Clinard, J.-N. Rouzaud, *Proc. of the Intern. Conf. on Internal Combustion Engine: Experiments and Modeling, ICE 99*, Vol. 4, G. Peritore (Ed.) Pozzuoli, Italy, 1999, pp. 251-258.
8. W. C. Gardiner Jr., B. F. Walker, C. B. Wakefield, *Narcel Dekker*, New York, 1981, pp. 319-374.
9. B. S. Haynes, H. Jander, H. Gg. Wagner, *Ber. Bunsen-Ges. Phys. Chem.* 84 (1980) 585-592.
10. St. Bauerle, Y. Karasevich, St. Slavov, D. Tanke, M. Tappe, Th. Thienel, H.Gg. Wagner, *Proc. Combust. Inst.* 25 (1994) 627-634.
11. V.G. Knorre, D. Tanke, Th. Thienel, H.Gg. Wagner, *Proc. Combust. Inst.* 26 (1996) 2303-2310.
12. S.C. Graham, J.B. Homer, J.L.J. Rosenfeld, *Proc. Royal Society London A*344 (1975) 259-285.
13. W.H. Dalzel, A.F. Sarofim, *J. Heat Transfer-Transactions of the ASME* (1969) 100-104.
14. S.C. Lee, C.L. Tien, *Proc. Combust. Inst.* 18 (1981) 1159-1166.
15. J.D. Felske, T.T. Charalampopoulos, H.S. Hura, *Combust. Sci. Technol.* 37 (1984) 263.
16. S. Chipplet, A. Gray, *Combust. Flame* 31 (1978) 149-159.
17. H. Bockhorn, F. Fetting, U. Meyer, R. Reck, G. Wannemacher, *Proc. Combust. Inst.* 18 (1981) 1137-1147.
18. W.D. Erickson, G.C. Williams, H.C. Hottel, *Combust. Flame*, 8 (1964) 127-132.

# Ignition and emission characteristics of synthetic jet fuels

M. Kahandawala<sup>1</sup>, M. DeWitt<sup>1</sup>, E. Corporan<sup>2</sup>, S. Sidhu<sup>1</sup>

<sup>1</sup>Energy and Environmental Engineering, University of Dayton Research Institute  
300 College Park, Dayton, OH 45469

<sup>2</sup>AFRL/RZTG, 1790 Loop Road North, Bldg 490  
Wright-Patterson AFB, OH 45433

*Abstract: Aircraft have been identified as a significant source of particulate matter (PM) emissions, which have been associated with adverse health effects and decreased ambient air quality. Recent published studies have shown that synthetic fuels, such as iso-paraffinic Fischer-Tropsch (F-T) fuels, can significantly reduce PM emissions compared to operation with petroleum-derived fuels. It is believed that the absence of aromatics in synthetic fuels slows the molecular growth to higher ringed polycyclic aromatic hydrocarbons (PAHs), which ultimately leads to lower soot emissions. However, it is not known if differences in chemical composition between synthetic and conventional (JP-8) fuel also change the ignition and combustion characteristics, which likely impact high altitude relight and combustor lean blowout (LBO) limits. This study was conducted to investigate how differences in fuel composition can impact the chemical ignition and emissions characteristics of a fuel and to help deconvolute the effect of physical and chemical processes on combustion efficiency. Only the chemical ignition delay was considered as the fuels were prevaporized and premixed prior to ignition. The fuels investigated in this study were a F-T processed synthetic jet fuel (synjet), a conventional JP-8, 2-methylheptane (surrogate synjet fuel), and a mixture of 80% heptane and 20% toluene (surrogate JP-8). The experiments were conducted using a modified single-pulse reflected shock tube instrumented to measure fuel ignition delay times and PAH and soot yields. The shock tube results show that both the actual and surrogate synjet fuels produced lower soot and PAH emissions than the actual and surrogate JP-8 fuels at temperatures of interest. These results are consistent with previous turbine engine test results with the actual fuels. It was observed, however, that, for the conditions tested, both surrogate and actual synjet and JP-8 fuels evaluated had similar ignition delays, which may imply that there is no correlation between soot emissions and chemical ignition delay. However, these results may be controlled by the test conditions, and accordingly, future tests at different conditions (e.g. higher equivalence ratios, pressures, lower pre-ignition temperatures) are warranted.*

## 1. INTRODUCTION

The aviation industry consumes 2% of all fossil fuels burned in the world. This is approximately 12% of the total fuel consumed by the entire transportation sector (80% is consumed by road transport). In 2005, a total of 55 billion U.S. gallons of Jet A-1 fuel were consumed by the aviation sector. The aviation fleet average emission index for soot has been estimated to be approximately 0.04 g/kg of fuel burned

[International Civil Aviation Organization (ICAO) Data Base] [1,2]. This means that 8000 tons per year of particulate are generated by aviation fuels worldwide. Although there is a large uncertainty (factor of 2) in these estimates, they are consistent with the magnitude being used to estimate global emissions from aircraft [3]. With aviation fuel consumption increasing at a rate of  $\sim 4\%$  a year, the adverse impact of aviation on the environment and human health is also increasing.

Recent developments in combustion fuel studies have cited benefits from paraffinic Fisher-Tropsch (F-T) fuels and its blends as an alternative to reduce particulate matter (PM) emissions [4-14]. The characteristics of F-T fuels make them attractive as alternate diesel fuels, and has prompted the U.S. Department of Energy (DOE) to initiate a rule to determine if F-T fuels should be designated as alternative fuels under the Energy Policy Act of 1992, which requires that the fuels provide "substantial environmental benefits" [14]. All published studies on F-T fuels have been based on engine and in-use vehicle tests. However, studies were conducted using different engines, which make it difficult to compare results because fuels were combusted under different combustion conditions.

Recently, blends of an *iso*-paraffinic F-T fuel with conventional JP-8 fuels have been evaluated for aviation applications [15,16]. The results of a study conducted using a T63 turboshaft engine and atmospheric research combustor fueled with blends of a JP-8 and a natural-gas-derived F-T synthetic jet fuel showed dramatic reductions in particle concentrations and mean size with the neat F-T and synjet fuel blends relative to operation with JP-8 [15]. Reductions of over 90% in particle number and 80% in smoke number were observed with neat F-T fuel. The results of this study provided information about the relationship between turbine engine soot emissions and fuel chemical composition; however, it was not possible to readily determine whether these effects were solely due to either physical or chemical aspects of the combustion process. To understand the relationship between fuel kinetics and emissions, a study is needed to determine the effects of fuel composition on ignition delay times, polycyclic aromatic hydrocarbon (PAH) products, and soot yields. Therefore, the main objective of the current study is to evaluate the ignition characteristics of surrogate component fuels to compare these to a standard JP-8 and synjet fuel and to correlate ignition data with the soot and PAH emissions generated. These data can be compared to those from the T63 turboshaft engine studies to determine if quantitative trends can be identified. The current study was performed using a single-pulse reflected shock tube to decouple the complex physical and chemical phenomena during combustion. Previous research has shown that *iso*-alkanes and aromatics have higher ignition delays than *n*-alkanes; however, their behavior in mixtures is not well-understood [17].

## 2. EXPERIMENTAL APPARATUS

### 2.1. Shock tube

A single pulse reflected shock tube was used to conduct all experiments (see Figure 1). The shock tube is comprised of a 7.6 cm I.D. x 274 cm long driver section, a 5.08 cm I.D. x 275 cm long driven section, and a 5.08 cm I.D. x 90 cm long test section. It also

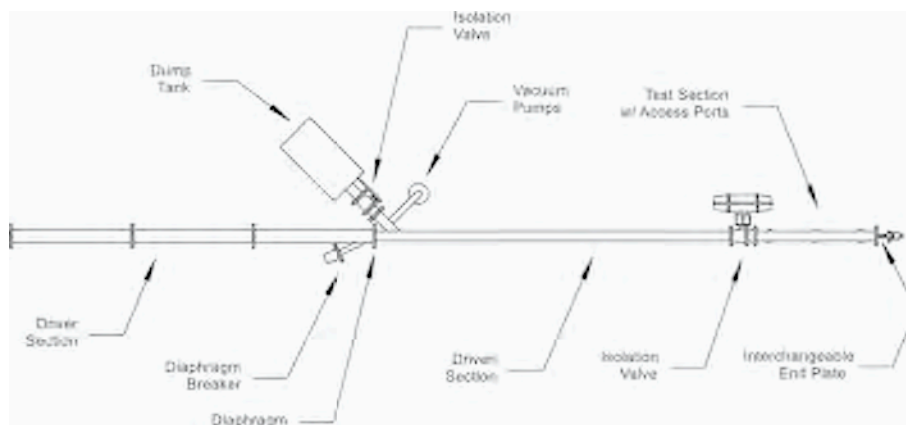


Figure 1. General schematic of the UDRI shock tube.

includes a 30.5 cm I.D. x 61 cm long dump tank and an evacuation subsystem. For this study, the test section was fitted with high-speed pressure transducers (PCB Piezotronics, Model 113A21), a fuel injection port connected to a sample preparation unit, optical sensor, helium purge, particle sampler, and a 25 L gas sample bag (Tedlar) that is used to capture the volatile and semivolatile products. The gas used in the driver section was predominantly helium with some argon added to help achieve the longer dwell times required to generate sufficient amounts of soot. The dwell time for this study was on the order of  $\sim 7.5$  ms.

Since the objective of the current studies was to investigate the effect of chemical composition on ignition and soot formation, the fuels were completely prevaporized and premixed in a separate sample preparation unit (SPU) to ensure that a homogeneous gaseous mixture was introduced into the test section. The SPU includes an injection port, a custom-made glass sample receiver, a 15 L silico-steel chemically inert gas handling canister (TO-Can, Restek), a pressure gauge, and a stainless-steel manifold for gas/sample inlet into the canister/test section connected to a vacuum pump. A detailed schematic of the test section and SPU is shown in Figure 2 [18].

The fuel mixture composition was verified by gas chromatography/mass spectrometry (GC/MS) analysis by filling the test section with the fuel/argon mixture and sampling it after  $\sim 10$  minutes (the approximate time it takes to complete the shock run after filling the test section during normal shock tube operation). From previous studies, it has been determined that the relative error in the fuel mixture composition is  $\ll 0.5\%$  [18]. For the synjet and JP-8 experiments, the shock tube and the SPU were wrapped in a custom designed heating jacket and the system was maintained at  $145^\circ\text{C}$ . The heating jacket contains 2.5 cm thick insulation, heating elements, and control and measuring thermocouples. The control thermocouples are linked to a temperature control system that includes a thermal cutoff option.

The reflected and incident shock velocities were measured to calculate post-shock temperature and pressure conditions in the test section using the shock solution model of CHEMKIN 4.0 [19]. The kinetic mechanism and thermodynamic data for the reac-

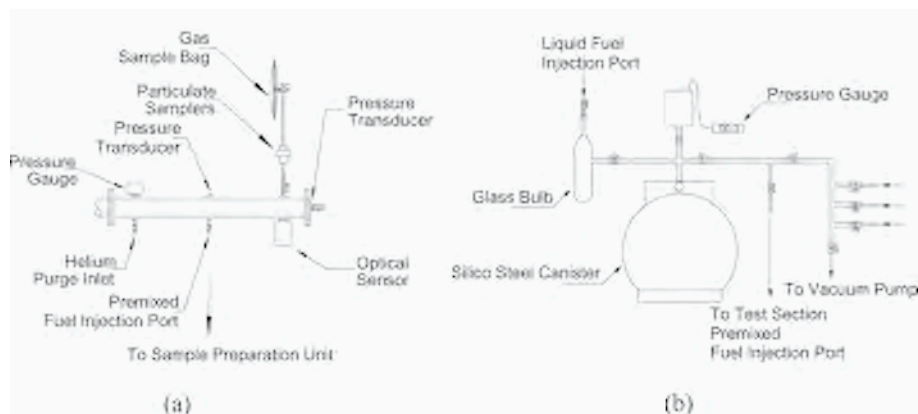


Figure 2. Schematic of the (a) test section and the (b) sample preparation unit.

ting species needed for this calculation were obtained from the National Institute of Standards (NIST) database. The ignition delay times were determined using the optical sensor in the test section (response of 190-1100 nm) and the end plate pressure transducer data. The fire control system closes the test section isolation valve approximately 0.5 s after the diaphragm burst, sealing the combustion products in the test section. For each test, the exhaust valve to the sampler is opened and the test section is purged with ~25 L (~10 change volumes) of dry helium immediately after the isolation valve closes. As the gas is swept from the system, the particulate fraction from the combustion products is captured on pretreated quartz filters using a high volume particulate sampler, and the gas is captured in a 25 L Tedlar sample bag to identify and quantify the volatile and semivolatile products. The filters are pretreated by baking at 420°C to remove any organics that could contribute to soot yields. Previous studies have shown that >98% of the combustion products are captured using this sampling method [18].

The mass of the collected particle (soot) samples was determined via the temperature-programmed oxidation (TPO) or carbon burnoff method with a LECO Model RC 412 multiphase carbon determinator. In this method, the mass of the collected PM is inferred via measurement of the CO<sub>2</sub> generated during oxidation of the soot. The gases captured in the sample bag were analyzed for volatile compounds by direct on-column injection (DB-5MS column) in HP5890GC-5970 MSD. The gas sample bag was evacuated through a trap containing sodium sulfate to remove water vapor formed during combustion and an XAD-2 polymeric sorbent trap to collect the semivolatile compounds. The sorbent traps were then extracted, and the semivolatile products were analyzed using HP5890GC-5970 MSD.

### 3. FUELS

JP-8 is Jet A-1 fuel with a military additive package that includes an icing inhibitor (~1000-1500 ppm), corrosion inhibitor/lubricity enhancer (~20 ppm) and a static dis-

sipater additive ( $\sim 5$  ppm). JP-8 contains hundreds of different types of hydrocarbons. In a typical JP-8 fuel, branched (*iso*-) and normal (*n*-) paraffins account for approximately 60% of the total hydrocarbons. The *n*-paraffins ( $\sim 20$ -25%) typically range from *n*-octane (*n*-C<sub>8</sub>) to *n*-hexadecane (*n*-C<sub>16</sub>), with maximum concentrations from *n*-decane (*n*-C<sub>10</sub>) to *n*-dodecane (*n*-C<sub>12</sub>). JP-8 also contains approximately 20% mono-, di- and tri-cycloparaffins. Aromatics are the other significant fraction ( $\sim 15$ -20%) of JP-8 fuel. However, the exact fuel composition can vary (within a predetermined acceptable range) from one batch of JP-8 to another. In these experiments, JP-8 POSF-3773 (AFRL/RZTG designation) was used. The synjet fuel used in this study (also referred to as S-8) was produced from natural gas via the F-T process by the Syntroleum Corporation. The fuel is comprised solely of *iso*- (82%) and normal (18%) paraffins with a distillation (e.g. molecular weight) range consistent with that typically observed for an aviation fuel. The *iso*-paraffins in this fuel are mainly monomethyl-substituted alkanes. The chemical composition of the fuels was determined using a variety of chromatographic techniques, including GC/MS and high-performance liquid chromatography (HPLC). The chromatograms of JP-8 and synjet are shown in Figures 3 and 4, respectively. Detailed information on the chemical and physical properties of this F-T fuel have been provided elsewhere [15,16].

The first set of shock tube experiments were conducted using surrogates for synjet and aviation fuels to verify proper operation of the fuel vaporizer and SPU and to investigate the effects of molecular structure on ignition delay. A mixture of *n*-heptane (80 vol %) and toluene (20 vol %) was chosen as the surrogate JP-8 fuel and 2-methylheptane as the surrogate synjet fuel because of the high concentration of methyl alkanes in the F-T fuels of interest. In the second phase, shock tube experiments were conducted using a fully formulated petroleum aviation fuel (JP-8) and synjet fuel. The T63 engine study also used the same fuels [15].

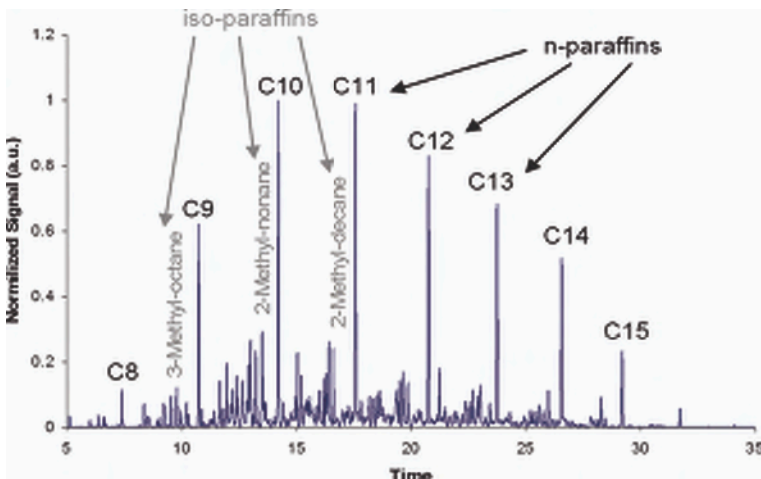


Figure 3. Gas chromatogram of JP-8 fuel.

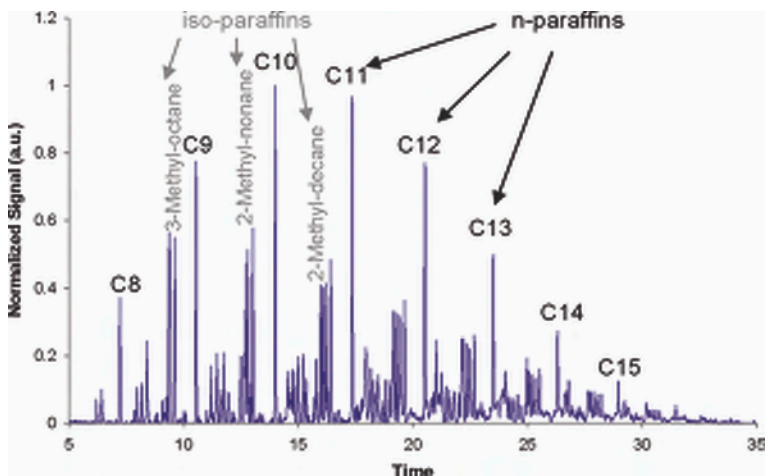


Figure 4. Gas chromatogram of synthetic jet fuel.

## 4. EXPERIMENTAL CONDITIONS

The experimental conditions for the shock tube are listed in Table 1. All shock tube experiments were conducted at a pressure of approximately 21 atm over a precombustion temperature range of 1100-1600 K (postcombustion temperature range of 1650-1950 K). These conditions were selected to mimic typical conditions found in turbine engine combustors.

## 5. RESULTS AND DISCUSSION

### 5.1. Emissions results

Combustion products from the shock tube studies with the surrogates were quantified to investigate the effects of fuel chemical composition on emissions and

Table 1. Experimental conditions for shock tube studies.

Shock tube	
Equivalence ratio ( $\Phi$ )	0.5, 3.0
Pressure (atm)	21
Temp (K)	1100 - 1600
Dwell Time (ms)	7.5
Test section composition	93v/v% Argon, Fuel, O <sub>2</sub>

assess potential similarities with actual engine emission trends with the fully formulated fuels. Both gaseous products (PAH) and soot yields were measured and normalized with respect to the mass of carbon in the fuel. The amount of fuel used in each experiment was very small (60 to 120 mg) and was combusted under premixed/prevaporized conditions. The experiments were conducted under fuel rich conditions ( $\Phi = 3.0$ ) to generate quantifiable yields of PAH and soot. This equivalence ratio was chosen because, at lower equivalence ratios ( $\Phi = 0.5-2.0$ ), the soot and PAH yields were insufficient and, at higher equivalence ratios ( $\Phi \geq 4.0$ ) the soot yields were excessive and caused sampling difficulties. Results from the LECO carbon analysis of soot mass yields for the surrogate fuels are shown in Figure 5. The solid/dashed lines indicate polynomial trend lines used to fit the experimental soot yields.

The results show that surrogate synjet fuel (2-methylheptane) generated less soot mass than surrogate JP-8 at the lower pre-ignition temperatures. At these lower temperatures, the slower rates of ring formation and molecular growth combined with the absence of aromatics in surrogate synjet led to lower soot yields. As the system temperature increases, the molecular growth reactions accelerate and soot formation reactions are initiated, leading to an increase in soot production and a maxima in the soot yield. Near the soot maxima, a small difference in temperature and reaction time is observed to cause a significant change in soot yield. This explains the higher data scatter observed near the maxima. A further increase in temperature improves the soot oxidation efficiency thus leading to reduced yields and the anticipated classic bell-shaped curve [21-27]. As such, at higher temperatures (near the soot peak), the system has sufficient energy and the rates of ring formation and molecular growth are high enough that initial fuel structure has a smaller effect on soot yield. These soot yield

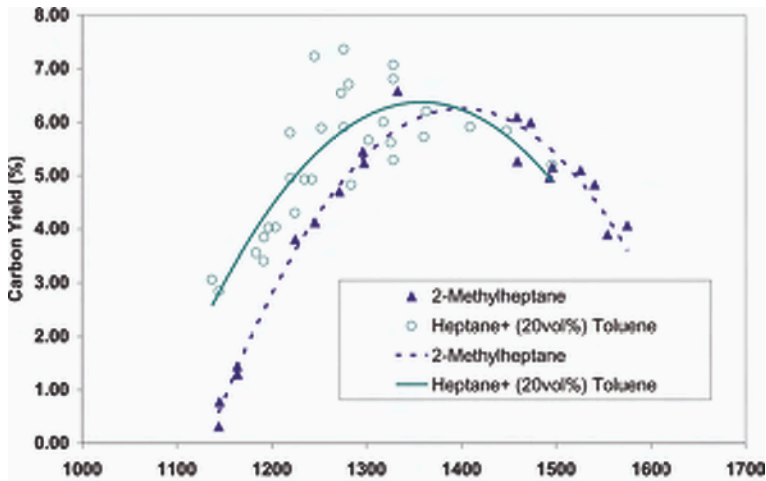


Figure 5. Carbon yield from combustion of 2-methylheptane and the heptane/toluene mixture at  $\Phi = 3.0$ . The solid/dashed lines indicate polynomial trend lines that were used to fit the experimental carbon yields.

trends agree with those observed in the T63 engine tests [15]. Although the system temperatures in each device were controlled differently, i.e., by changing the power setting (equivalence ratio) in the engine and precombustion conditions in the shock tube, the trends of fuel soot yield relative to system temperature were similar. In the T63 engine, operation at lower temperature (i.e., idle) showed significantly higher impact (i.e., reductions) in PM yield with the synjet fuel compared to JP-8 than operation at higher temperature (cruise). These findings support that the initial fuel composition has a smaller effect on soot production at higher combustion temperatures and suggest that the increase in kinetic reaction rates at higher temperatures overcome the differences in fuel molecular type. These results were consistent for all synjet/JP-8 fuel blends tested in the engine.

The results of the shock tube and T63 studies are also in agreement with heavy duty and passenger vehicle diesel engine studies, which found that particulate emissions decreased with the addition of an F-T fuel [20]. The diesel engine studies attributed the decrease in particle emissions to a decrease in particle nucleation because of the absence of sulfur. However, nucleation of sulfur-based particles does not play an important role in this study because mostly nonvolatile particles were sampled in both the shock tube and T63 experiments. It is believed that most of the PM emissions measured in this study are carbonaceous in nature, and the observed decrease is primarily because of the absence of aromatics in synjet fuel and a higher fuel hydrogen/carbon (H/C) ratio. Aromatics are known precursors of soot, and studies performed on a variety of combustors from shock tubes, premixed flames, diffusion flames, to engines have shown that aromatics lead to increases in soot yields [21-27]. To form soot, paraffins have to go through dissociation, addition, and cyclization reactions, which are significantly slower than aromatic condensation and molecular growth reactions [27]. Emission reduction during synjet combustion can also be attributed to their higher H/C ratio compared to conventional JP-8 fuel. Earlier studies have shown that, especially for the cases where fuel multi-ring aromatic content is less than 5%, the H/C ratio can serve as a better indicator for soot yields [28,29].

The yields of PAH were also measured as indicators of fuel soot formation tendencies. These were collected in Tedlar bags, concentrated on adsorbent traps, and analyzed by GC/MS. Figures 6 and 7 show the yields of selected PAH (naphthalene and acenaphthalene) from the shock tube experiments for the surrogates at  $\Phi = 3.0$ . The observed PAH yield trends are consistent with the soot yield trends, but their shape is exactly opposite because the PAH yields decrease as the soot yields approach the maxima ( $T = 1200\text{-}1400\text{K}$ ). This occurs because the PAH are being converted to soot. The naphthalene and acenaphthalene yields are observed to be significantly lower for surrogate synjet fuel at lower temperatures. As discussed above, the rates of cyclization reactions for paraffins are considerably slower than the aromatic condensation reactions at these reduced temperatures, thus resulting in lower yields in comparison to the JP-8 surrogate. In a previous combustion study with F-T and JP-8 fuel blends on a swirl-stabilized research combustor, soot analysis showed that the addition of synjet fuel decreased the amount of fluoranthene, pyrene and benz[a]anthracene in the soot [15]. These findings are consistent with PAH trends observed in the present study.

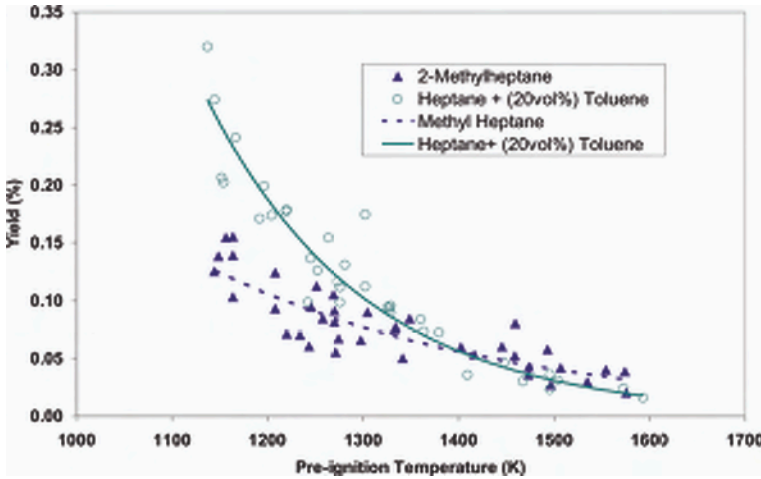


Figure 6. Naphthalene yields (wt %) from combustion of 2-methylheptane and the heptane/toluene mix at  $\Phi = 3.0$ . The solid/dashed lines indicate polynomial trend lines that were used to fit the experimental yields.

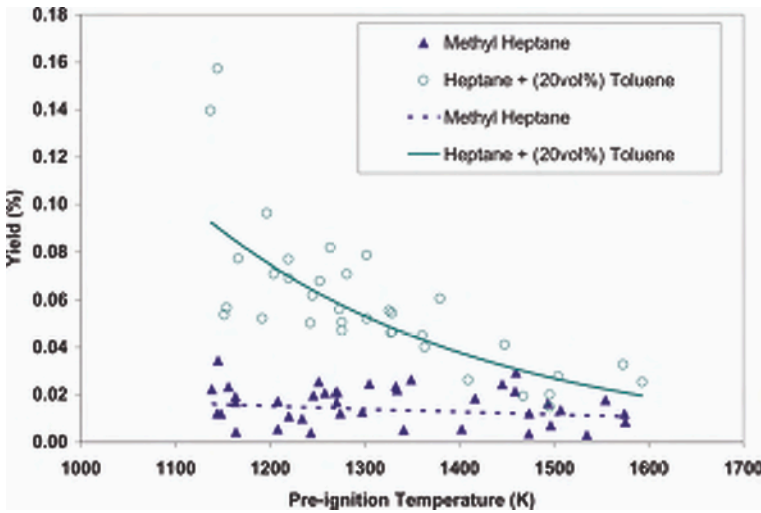


Figure 7. Acenaphthalene yields (wt %) from combustion of 2-methylheptane and the heptane/toluene mix at  $\Phi = 3.0$ . The solid/dashed lines indicate polynomial trend lines that were used to fit the experimental yields.

### 5.2. Ignition delay results

One of the primary objectives of this study was to determine if the chemical ignition delay of the fuel can be correlated with its emission characteristics; therefore, ignition

delay times were measured in all shock tube experiments. Ignition delay times for the surrogate fuels ranged from 0.40-2.50 ms for pre-ignition temperatures of 1100-1600 K (see Figure 8). As expected, the ignition delay times for both fuels decreased as the pre-ignition temperature increased mainly because of the increased kinetic reaction rates. However, no significant differences in ignition delays were observed between the surrogate fuels. These results were unexpected because the differences in fuel composition were anticipated to yield measurable changes in ignition delay times. Changes in ignition delays with fuel composition have been observed in earlier experimental studies [30]. These showed that, for the same carbon chain length, an increase in chain branching typically increases ignition delay times. For example, trimethylbutane ( $C_7$ ) has much higher ignition delay times than *n*-heptane ( $C_7$ ). However, further examination reveals that single methylated paraffins have similar ignition delays as *n*-paraffins with the same carbon chain length [17,30]. Under similar conditions ( $T = 1445$  K,  $P = 1.2$ - $1.4$  atm., and  $\Phi = 1.0$ ), the ignition delay of *iso*-butane was observed to be only 0.135 ms longer than that of *n*-butane [17]. Therefore, the present results indicate that the concentration of toluene in the JP-8 surrogate was insufficient to change the ignition delay of *n*-heptane to values significantly different than those for 2-methylheptane. However, the differences in chemical structure between the two fuels were sufficient to cause dramatic changes in soot and PAH yields, which indicates that the fuel chemical structure has a significantly higher impact on emissions than on chemical ignition delay.

Shock tube experiments with fully formulated JP-8 and synjet fuels were also conducted to investigate if they exhibit similar ignition behavior as the surrogate fuels. Experiments were conducted under fuel-lean conditions ( $\Phi = 0.5$ ) to verify effective operation of the SPU and provide initial ignition delay data. Figure 9 shows that, at

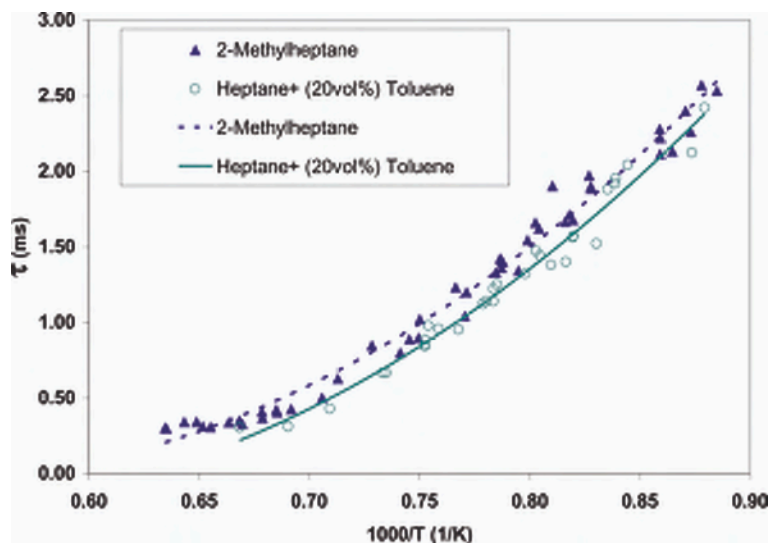


Figure 8. Ignition delay times for combustion of 2-methylheptane and the heptane/toluene mixture at  $\Phi=3.0$ .

$\Phi = 0.5$ , fully formulated synjet and JP-8 have similar ignition delays for the temperature range evaluated, and the results are consistent with those observed for the fuel surrogates.

The primary differences in the hydrocarbon composition between the synjet and JP-8 fuels used in this study are that the synjet contains no aromatics or cycloparaffins and a much higher (2 times) concentration of *iso*-paraffins (mostly monomethyl species) [15]. Both fuels contain approximately 18% normal paraffins. Similar to increased branching, aromatics and cycloparaffins are known to have higher ignition delays compared to normal paraffins [31]. Therefore, experimental results suggest that the combination of aromatics and cycloparaffins in JP-8 had a similar effect on ignition delay as the methyl alkanes in the synjet fuel, thus resulting in comparable ignition delays for both fuels. However, the influence of fuel molecular structure on ignition delay in mixtures has proven to be complex and difficult to predict and has shown that the change in ignition delays is not typically proportional to changes in composition. A study by Fieweger et al. showed that, at temperatures between 1000 and 1200 K, addition of up to 40% *n*-heptane to *iso*-octane caused negligible change in ignition delay times; however, significant differences were observed for temperatures below 1000 K [32]. To address the impact of aromatics and mixtures on ignition delay times, a CHEMKIN shock module was used to calculate delay times for *n*-heptane and *n*-heptane (80%)/toluene (20%) mixtures at equivalence ratios of 0.5, 1.0 and 3.0 over a temperature range of 1000-1700 K at a pressure of 20 atm. The modeling results showed that there is a slight reduction in *n*-heptane/toluene ignition delays ( $\sim 90 \mu\text{sec}$ ) only at lower temperature ( $\sim 1100\text{K}$ ); otherwise, the addition of 20% aromatic has minimal impact on ignition. These modeling results are consistent with results of a recent study that showed that dilution of *n*-decane with 20% benzene only caused a slight decrease in ignition delay [33]. These

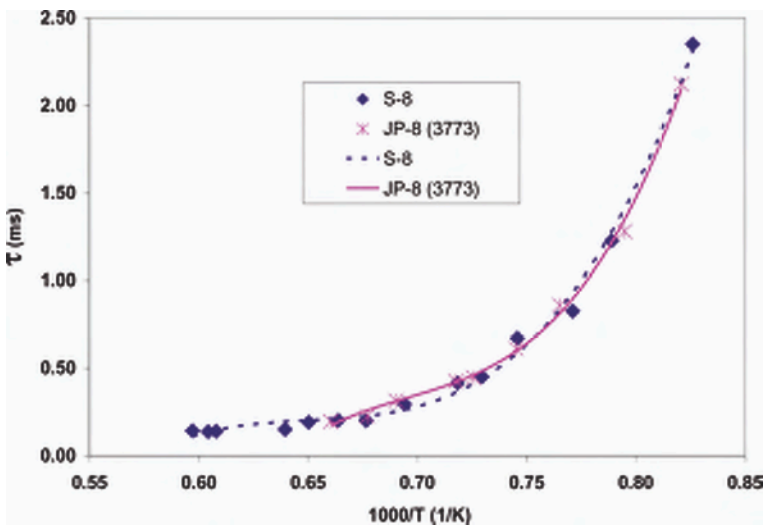


Figure 9. Ignition delay times for combustion of S-8 and JP-8 fuels at  $\Phi = 0.5$ .

modeling and experimental results agree with the negligible differences in ignition delay between the synjet and JP-8 observed in this effort. Future shock tube studies with JP-8 and synjet fuels will be conducted under a wider set of operating conditions to verify the trends observed in this study. These include JP-8 and synjet fuel studies at the higher equivalence ratio for direct comparison to the surrogate fuels.

## 6. SUMMARY AND FUTURE WORK

Combustion studies of synthetic and conventional fuel surrogates and actual fuels were conducted in a shock tube to investigate differences in fuel chemical ignition delay and to study potential correlations between fuel ignition delay and soot yields. The shock tube results show that the synjet and surrogate synjet (2-methylheptane) fuels produced lower soot and PAH than actual and surrogate JP-8 (80% heptane and 20% toluene) fuels at temperatures of interest, which is in agreement with previous engine test results. Test results suggest that, as combustion temperatures increase, the initial fuel composition has a reduced effect on soot production, which is also consistent with turbine engine results. Similar chemical ignition delay times were observed for both synjet and JP-8 fuels and their surrogates, and therefore, no correlation was observed between chemical ignition delay and soot yield for the conditions evaluated. However, these results may be controlled by the test conditions, and therefore, future shock tube studies with JP-8 and synjet fuels will be conducted under a wider set of operating conditions to verify the trends observed in this study. In addition, studies with alternative jet fuels from unconventional sources, such as coal and crop oils, will be conducted to evaluate their ignition and emission characteristics.

## ACKNOWLEDGEMENT

The efforts of UDRI were supported by the Air Force Research Laboratory under the cooperative research agreement number F33615-03-2-2347.

## REFERENCES

1. M. Landau et al., Jet aircraft engine exhaust emissions database development-Year 1990 and 2015 scenarios. NASA Contractor Report 4613, July 1994.
2. A. M. Thompson, Atmospheric effects of aviation: First report on the subsonic. NASA Reference Publication 1385, 1996.
3. J. S. Lewis, R. W. Niedzwiecki, Aircraft Technology and Its Relation to Emissions, Oxford University Press, Oxford, U.K., 1999, chapt. 7.
4. R. H. Clark, J. F. Unsworth, Proc. of the 2nd International Colloquium on Fuels, Tech. Akad. Esslingen, Ostfildern, Germany, 1999.
5. T. P. Gardner, S. S. Low, T. E. Kenney, SAE Tech. 2001-01-0149, 2001.
6. J. W. Johnson, P. J. Berlowitz, D. F. Ryan, R. J. Wittenbrink, W. B. Genetti, L. L. Ansell, Y. Kwon, D. J. Rickeard, SAE Tech. 2001-01-3518, 2001.
7. S. J. Korn, SAE Tech. 2001-01-0150, 2001.

8. N. N. Clark, C. M. Atkinson, G. J. Thompson, R. D. Nine, SAE Tech. 1999-01-1117, 1999.
9. M. P. May, K. Vertin, S. Ren, X. Gui, I. Myburgh, P. Schaberg, SAE Tech. 2001-01-3520, 2001.
10. P. Norton, K. Vertin, B. Bailey, N. Clark, D. Lyons, S. Goguen, J. Eberhardt, SAE Tech. 982526, 1998.
11. P. Norton, K. Vertin, N. Clark, D. Lyons, M. Gautam, S. Goguen, J. Eberhardt, SAE Tech. 1999-01-1512, 1999.
12. C. Bertoli, M. Migliaccio, C. Beatrice, N. Del Giacomo, SAE Tech. 982492, 1998.
13. D. Schmidt, V. W. Wong, W. H. Green, M. A. Weiss, J. B. Heywood, ASME 36 (1) (2001) 23-37.
14. T. L. Alleman, R. L. McCormick, K. Vertin, Assessment of criteria pollutant emissions from liquid fuels derived from natural gas. Report NREL/TP-540-31873, National Renewable Energy Laboratories, Golden, CO, 2002.
15. E. Corporan, M. J. DeWitt, V. Belovich, R. Pawlik, A. C. Lynch, J. R. Gord, T. R. Meyer, Energy Fuels 21 (5) (2007) 2615-2626.
16. M. J. DeWitt, R. Striebich, L. Shafer, S. Zabarnick, W. E. Harrison, III, D. E. Minus, T. Edwards, Proc. of AIChE Spring National Meeting, 58b, 2007.
17. D. F. Davidson, R. K. Hanson, Fundamental kinetic database utilizing shock tube measurements. <http://hanson.stanford.edu/>, 2006.
18. M. S. Kahandawala, Fuel composition effects on particle and PAH emissions. Ph.D. Dissertation, University of Dayton, Dayton, 2004.
19. R. J. Kee, F. M. Rupley, J. A. Miller, M. E. Coltrin, J. F. Grcar, E. Meeks, H. K. Moffat, A. E. Lutz, G. Dixon-Lewis, M. D. Smooke, J. Warnatz, G. H. Evans, R. S. Larson, R. E. Mitchell, L. R. Petzold, W. C. Reynolds, M. Caracotsios, W. E. Stewart, P. Glarborg, C. Wang, O. Adigun, W. G. Houf, C. P. Chou, S. F. Miller, Chemkin Collection, Release 3.7, Reaction Design, Inc., San Diego, CA, 2002.
20. P. W. Schaberg, D. D. Zarling, R. W. Waytulonis, D. B. Kittleson, SAE SP-1724, (2002) 55-67.
21. H. Bockhorn (Ed.) Soot Formation in Combustion: Mechanisms and Models, Springer, Berlin, 1994.
22. H. Richter, J. B. Howard, Prog. Energy Combust. Sci. 26 (2000) 565-608.
23. I. Glassman, Proc. Combust. Inst. 22 (1988) 295-311.
24. R. J. Santoro, Soot formation: A review of our current understanding, Invited Lecture Fall Technical Meeting, The Eastern States Section of the Combustion Institute, 1995.
25. M. Frenklach, D. W. Clary, S. E. Stein, Proc. Combust. Inst. 20 (1985) 887.
26. M. Frenklach, J. Warnatz, Combust. Sci. Technol. 51 (1987) 265.
27. M. Frenklach, H. Wang, Soot Formation in Combustion, H. Bockhorn (Ed.) Springer-Verlag, Heidelberg, 1994, p. 165.
28. S. A. Mosier, Combustion Problems in Turbine Engineering, AGARD-CP-353, 1984, pp. 5.1-5.15.
29. C. Moses, Combustion Problems in Turbine Engineering, AGARD-CP-353, 1984, pp. 7.1-7.10.
30. J. B. Heywood, Internal Combustion Engine Fundamentals, McGraw-Hill, New York, 1988, pp. 550-552.
31. W. Lovell, Ind. Eng. Chem. 40 (1948) 2388-2438.
32. K. Fieweger, R. Blumenthal, G. Adomeit, Combust. Flame 109 (1997) 599-619.
33. A. J. Dean, O. G. Penyazkov, K. L. Sevruck, B. Varatharajan, Proc. Combust. Inst. 31 (2007) 2481-2488.



**Part II**  
**Particle inception and maturation**



# Precursor nanoparticles in flames and diesel engines: a review and status report

R.A. Dobbins

*Division of Engineering*

*Brown University*

*Providence, R. I. 02912, USA*

*Fax 401-863-9107 – richard\_dobbins@brown.edu*

*Abstract: The discovery of small, 3 to 15 nm, particles in diverse hydrocarbon flames burning a variety of gaseous, liquid, and solid fuels is reviewed and leads to the conclusion that they represent a universal, early stage, condensed particulate form. These polydisperse particles are distinguished by their nanometer size range, their single-particle spheroidal morphology, and their transparency to the electron beam in TEM. They are called precursor nanoparticles (PNP) to emphasize their role in the formation of the more mature soot aggregates, and they are closely related to the particles referred to as nanoparticles of organic carbon (NOC). Chemical analyses by gas chromatography-mass spectrometry (GCMS) of PNP from an inverse diffusion flame reveal high concentrations of polycyclic aromatic hydrocarbons (PAHs) in the 200 to 302 amu mass range that prominently include the benzenoid stabilomer species and their isomers. Engine samples are found to contain both the PAHs of purely combustion origin, pyrogenic PAHs, and also the unburned fuel components of petrogenic origin. Recent studies of human cell mutagenicity of atmospheric samples from northeastern US reveal that many of the dominant mutagens are the intermediate size stabilomer PAHs. These results are found in the data from a rural and two urban northeastern sites. It is concluded that the mutagenic species found in the several geographic regions originate from local sources but may also be subject to transport by the atmospheric circulation. The northeastern US mutagenicity studies are also consistent with studies conducted at the distant urban locations of Los Angeles and Washington, D.C. Control of the nanoparticle emissions is clearly an important priority in engine design.*

Since September 1991 many investigators have found young particles as small as about 3 nanometers in the lower regions of many hydrocarbon flames. These particles are herein designated as precursor nanoparticles (PNPs), and they compose the nucleation mode of the particle size distribution function (PSDF). They are defined by their small polydisperse, spheroidal single-particle geometry, their transparency to the electron beam in the TEM, and their early presence in flames. Some PNPs show signs of crystallinity in the form of dark edges or dark interior structures in TEM. The PNP particles were independently reported by D'Anna et al. [1] using scattering/extinction observations and by Dobbins et al. [2] using thermophoretic sampling, both at the September 1991 Heidelberg meeting. This article is a broad survey of the formation and properties of PNP and quotes extensively from the results of the numerous investigations cited below.

## 1. UBIQUITY, MORPHOLOGY AND PHYSICAL PROPERTIES

The diverse flame types wherein PNP have been observed by TEM include (1) laminar diffusion flames, (2) inverse diffusion flames, (3) premixed flames, (4) turbulent diffusion flames, (5) opposed flow flames, (6) microgravity flames, (7) unsteady flickering flames, (8) pool fire flames, (9) well-stirred reactor, (10) bituminous coal flame, and tentatively in recent diesel engine tests. The results of some of these works will be included in this discussion. (See [3] and references cited in Appendix A therein). The above flames have burned diverse fuels including the pure gases  $\text{CH}_4$ ,  $\text{C}_2\text{H}_2$ ,  $\text{C}_2\text{H}_4$ ,  $\text{C}_3\text{H}_8$ , the highly heterogeneous JP-8 and diesel fuels, and bituminous coal. Thus PNP appear to be a universal early-stage particulate matter in the burning of diverse flame types supplied by a wide variety of hydrocarbon fuels. When formed by the flame processes as in the case of formation from pure gaseous fuels, they are of pyrogenic origin. On the other hand, PNP containing chemical species originally present as components of a heterogeneous fuel are said to be of petrogenic origin.

Examination of the upper regions of various flames burning a diversity of fuels show the fractal-like aggregates to display a relatively narrow range of fractal dimension  $D_f$  viz., 1.80 to 1.85. This range applies to both laminar and turbulent flames and to the recent diesel engine tests as well. These results are consistent with the theoretical studies demonstrating aggregate growth by diffusion-limited cluster aggregation. This range of  $D_f$  has been found to apply to aggregates produced by some  $\text{C}_2\text{H}_2$  flames wherein the primary particles per aggregate ranged from about 10 to over  $10^{+8}$  [4]. These clustered particles were widely detected, photographed and presented as representative soot particles in the earlier literature [5] although the details of their formation were never elucidated. Figure 1b shows a population of clustered aggregates captured on a lacey carbon grid from the upper region,  $Z=50$  mm, of the diluted ethene diffusion flame.

Low in this same flame there are very high concentrations of single isolated spherule particles. Micrographs on lacey carbon grids of PNP undergoing transformation into the aggregate form, Figure 1a  $Z=20$  mm, show many particles clinging by surface tension to the edges of the holes in the lacey carbon substrate. The micrographs shown in Figures 1a and 1b were obtained from the  $\text{C}_2\text{H}_4$  flame diluted 4/1 with  $\text{N}_2$ , and they reinforce the previous results with pure  $\text{C}_2\text{H}_4$  that also show surface tension effects [3]. No clinging particles appear in the upper panel Figure 1b at  $Z=50$  mm where the morphological transformation from PNP to carbonaceous aggregates has occurred. These clinging particles shown in Figure 1a constitute a demonstration of surface tension effects associated with a liquid-like state. The lack of surface tension in the aggregate stage implies the primary particles that constitute the aggregates are solid particles that are not subject to coalescent collisions while the presence of surface tension in the PNPs is consistent with their apparent display of coalescent collisions.

These polydisperse particles show only early evidence of agglomeration suggesting they undergo coalescent collisions while in a liquid-like state.

Recent experiments [6] have demonstrated development of a dynamic bimodal particle size distribution found in the premixed  $\text{C}_2\text{H}_4/\text{O}_2/\text{Ar}$  flame. Bimodal size distributions can be accounted for by the coexistence of PNP and carbonaceous aggrega-

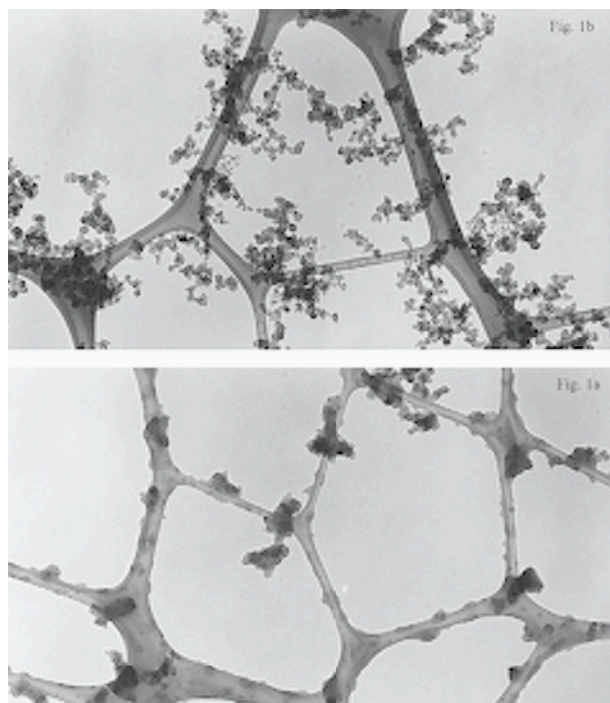


Figure 1. Micrographs of particles captured on lacey carbon grids at (a)  $Z=20$  and (b)  $Z=50$  mm in the diluted  $C_2H_4$  diffusion flame. The dilution ratio is 4/1 of  $N_2$  to  $C_2H_4$ . Evidence of surface tension effects is present only at height  $Z=20$  mm.

tes. Coexisting PNP and aggregate particles have also been demonstrated in recent studies of samples from turbulent flames [7]. A bimodal distribution of particle sizes then results wherein the PNP form the nucleation mode and aggregates comprise the accumulation mode. Scavenging of nanoparticles by aggregates, as described by Friedlander et al. [8], would also contribute their surface growth of an outer layer of PAHs. Further discussions of bimodal size distributions are given in the present volume. The material density of the PNP is estimated to be 1.2 gm/ml [9] and contrasts with the widely quoted density of the aggregate material of about 1.8 gm/ml.

## 2. CHEMICAL ANALYSES OF PRECURSOR NANOPARTICLES (PNP)

The small samples of particles captured by the momentary immersion of the electron microscope grid in the diffusion flame can be employed to derive limited information on the chemical composition of the PNP. Laser desorption with mass spectrometry by the LAMMA-500 provides a broad mass analysis on ex-situ samples as small as  $10^{-11}$  gm. This instrument was used to explore the chemical development of the particles in both the ethene and deuterated ethene diffusion flames [10, 11]. Figure 2 presents the results of mass spectrographic results for ethene flame and for a diesel soot sample

from a truck tunnel [12]. Although the mass spectroscopy results contain no information on isotopic makeup and give only limited quantitative analysis, its ability to provide a wide range mass analysis proves to be invaluable. The 202, 252, 276, 300 amu mass sequence that is present in both samples suggests the presence of benzenoid PAHs as was confirmed by the substitution of a deuterated ethene fuel [11]. The 202 to 302 amu species are prominent in the PNP from pure gaseous ethene are formed by the flame combustion processes and are said to be of pyrogenic origin. The near absence of these higher PAHs in diesel fuel suggests the above cited mass sequence is also of pyrogenic origin in the case of the diesel particulates shown in Figure 2. (The 200 amu and larger mass sequence are essentially absent in US and UK diesel fuels [13] and their abundant presence in the effluent attests to pyrogenic PAH formation in the engine as well as in the flame fueled by a pure gaseous hydrocarbon.)

It is noteworthy that Palmer and Cullis [14] in 1965 observed that "...properties of carbons formed in flames are remarkably little affected by the type of flame, the nature of the fuels being burnt and other conditions under which they are produced... a striking experimental finding." The results of studies of fused polycyclic aromatics [15] and their high temperature stability [16] both reported in 1985 are consistent with this contention. The PAHs detected earlier in 1984 from an underground shale oil retort [17] show near perfect agreement with the grid of stabilomer species presented of Stein and Fahr [16]. The shale oil soot sample is obtained after an elapsed time of the order of minutes that allows ample time for thermodynamic stability to be achieved and strongly favored the benzenoid unsubstituted PAH members of the stabilomer grid (See Figure 1 of [13] where near perfect agreement is displayed between the ben-

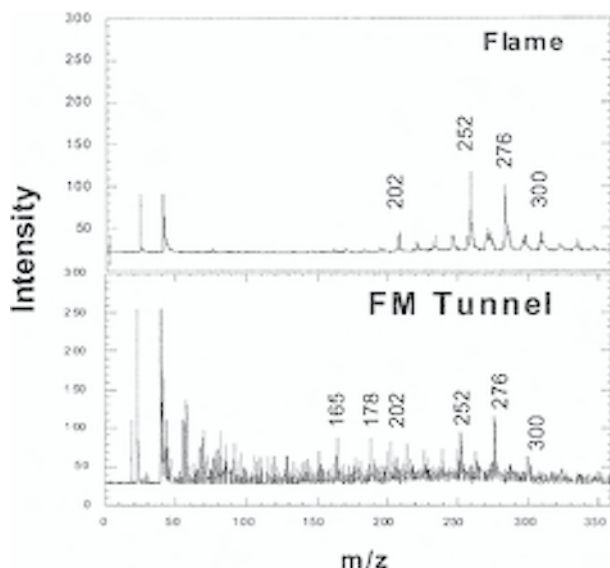


Figure 2. Mass spectra of flame soot and soot collected from the Fort McHenry (Truck) Tunnel. From Fletcher et al. [12].

zenoid species in the shale oil sample and the staircase curve.) Laboratory flames burning  $C_2H_4$  [10] showed mass spectroscopic results in general agreement with these thermodynamic predictions [16]. Finally, the recent flame results from [18] wherein PAHs were detected by advanced sampling techniques were well predicted by the stabilomer grid of Stein and Fahr and ranged in mass from  $C_8H_6$ , 102 amu to  $C_{34}H_{16}$ , 424 amu. The PAH growth depicted in the above studies can be explained by HACA mechanism described at the 1991 meeting [19]. In summary, the Palmer and Cullis statement is consistent with the high temperature stability issues of PAHs formed in flames and still applies after 40 years of additional intensive research.

The PAH masses of interest in flames and engines is predominately in the 202 u to 302 u range. Some articles have suggested that growth through the large PAHs provides the route to the soot aggregates in the accumulation mode. Our MS data suggests the latter aggregates result from the carbonization process of intermediate mass PAHs contained mainly in the nucleation mode PNP.

More detailed chemical analyses were the object of the later research using GCMS that required a larger particle sample. The inverse diffusion flame (IDF) allows for the collection of a 10 mg sample for analysis by GCMS which identifies the chemical species including the PAH isomers. The GCMS analysis [20] of PNP from an ethene inverse diffusion flame provides the most detailed composition of the PNP including the identification of many isomers, and reinforces the prominence of the intermediate size PAHs (see Table 1). These data reinforce and extend the MS data found earlier and is essential in the evaluation of the toxicity of PNP by providing positive identifications and quantitative data on the various PAH isomers. For example, both benzo(a)pyrene and its isomer benzo(e)pyrene were detected in the IDF flame (see Table 1) but the relative mutagenicity of the former is some 600 times greater.

Also shown in Table 1 are the results of GCMS analyses of diesel engines samples [21, 22] that are shown for comparison with the IDF data. Although the targeted PAHs are more limited, there is some correspondence in all three samples.

### 3. DEVELOPMENT OF CRYSTALLINITY AND THE CARBONIZATION PROCESS

Bragg diffraction verifies the development of crystallinity weakly in the PNP in the nucleation mode and strongly in the accumulation mode composed of chained aggregates. The polyaromatic ring structures of the PAH molecules were proposed by Oberlin [23] as the origin of the bright domains produced in DFTEM of immature carbonaceous materials. The development of crystallinity was displayed by dark field TEM [24, 25], and by both DFTEM and X-ray diffraction (XRD) [26]. The  $d_{100}/d_{110}$  ratio [26] is the square root of 3 from the hexagonal unit cell geometry and is at least a mild test of the existence of the hexagonal ring structure. This ratio was found to be 1.85 by XRD [26] for soot from the  $C_2H_4$  flame, while the value 1.73 was reported for diesel soot in the literature [27]. The interlayer spacing  $d_{002}$  of the lattice planes is measured by XRD and was reported to be 0.35 nm in the case of soot formed from diesel fuel [27]. The conversion of PNP to aggregates is accompanied by the loss of hydrogen, the development of crystallinity, and the increase in material density descri-

Table 1. PAHs, mutagenicities, and GCMS yields for diesel and IDF particulates.

Mass (u)	Formula	PAH Compound	% Mnty Boston Air Samples <sup>a</sup>	PAH Yields		IDF <sup>d</sup>
				Diesel Exht <sup>b</sup>	Diesel Part. <sup>c</sup>	
152	C <sub>12</sub> H <sub>8</sub>	Acenaphthylene				2295
154	C <sub>12</sub> H <sub>10</sub>	Biphenyl				97
154	C <sub>12</sub> H <sub>10</sub>	Acenaphthene				163
166	C <sub>13</sub> H <sub>10</sub>	Fluorene				2710
178	C <sub>14</sub> H <sub>10</sub>	Anthracene			1.5	2285
178	C <sub>14</sub> H <sub>10</sub>	Phenanthrene			68.4	5775
190	C <sub>15</sub> H <sub>10</sub>	4,5-Methylenephenanthrene				5635
192	C <sub>15</sub> H <sub>12</sub>	Methylphenanthrenes			194	1083
202	C <sub>16</sub> H <sub>10</sub>	Fluoranthene		1426	49.9	7000
202	C <sub>16</sub> H <sub>10</sub>	Acphenanthrene				5870
202	C <sub>16</sub> H <sub>10</sub>	Acenanthrylene				1880
202	C <sub>16</sub> H <sub>10</sub>	Pyrene		2220	47.5	8990
226	C <sub>18</sub> H <sub>10</sub>	Benzo[ghi]fluoranthene			12.1	3040
226	C <sub>18</sub> H <sub>10</sub>	Cyclopenta[cd]pyrene	2.2			8550
228	C <sub>18</sub> H <sub>12</sub>	Benzo[a]anthracene		3640	6.3	880
228	C <sub>18</sub> H <sub>12</sub>	Chrysene & Triphenylene		4800	26	1102
252	C <sub>20</sub> H <sub>12</sub>	Benzo[x]fluoranthene x=b+j+k	2.0	1896	14.9	2585
252	C <sub>20</sub> H <sub>12</sub>	Benzo[e]pyrene			7.44	815
252	C <sub>20</sub> H <sub>12</sub>	Benzo[a]pyrene	2.5	540	1.33	2760
252	C <sub>20</sub> H <sub>12</sub>	Perylene			0.16	235
276	C <sub>22</sub> H <sub>12</sub>	Indeno[1,2,3cd]pyrene	1.8		5.62	2300
276	C <sub>22</sub> H <sub>12</sub>	Benzo[ghi]perylene	1.1		6.50	3150
300	C <sub>24</sub> H <sub>12</sub>	Coronene & isomers			2.0	4731
302	C <sub>24</sub> H <sub>14</sub>	17 Isomers	1.5			1000

<sup>a</sup> Pedersen et al. 2005 [41].

<sup>b</sup> Units (μg/g). Sum of particulate and vapor PAH, 50% engine load, without aftertreatment, Table 35, Bagley et al., 1996 [21].

<sup>c</sup> Units (μg/g). Certificate of Analysis SRM1650a, NIST 2000 [22].

<sup>d</sup> Units (ng/m<sup>3</sup>). Average of two samples from the IDF, Blevins et al., 2002 [20].

bed above. The faint Bragg diffraction detected in PNP indicate the initial formation of crystallinity. The stronger diffraction displayed in DFTEM show the progressive development of crystallinity and the densification of the particle material. Excellent DFTEM micrographs of the formation of Bragg diffraction in soot forming materials have been given by Vander Wal [24, 25].

From the carbon black literature [28] of the carbonization process is described as a pyrolytic, first order reaction that obeys an Arrhenius reaction rate. The elementary formulation [29] is recapitulated here to account for the depletion of the precursor nanoparticle material by the carbonization process. This formulation can be used to test the measured soot inception temperatures that appear in the literature from four

different investigative teams using eleven fuels. From the above description the disappearance of the PNP mass fraction  $m(t)$  is given by

$$dm/dt = -k_{ca}(T)m(t) \quad (1)$$

where the carbonization reaction rate  $k_{ca}$  in Arrhenius form is given by

$$k_{ca} = A \exp\{-E/[RT(t)]\} \quad (2)$$

in terms of the frequency factor  $A$  (s<sup>-1</sup>) and the activation energy  $E$  (kJ/mole), the relevant rate constants. For this analysis the temperature profile taken to be simple linear function of time,

$$T = T_o + \beta t \quad (3)$$

where  $T_o$  is an arbitrary low temperature and  $\beta$  is the temporal gradient (K/s).

While this linear profile is restrictive, it is adequate to describe the thermal history during the brief interval during which the conversion of the precursor material is transformed from the liquid-like material to the carbonaceous aggregates. The above equations lead to a formulation of  $m(t)$  which will reach a prescribed fraction of its initial value  $m_o$ . The fraction of precursor material consumed,

$$f_c = 1 - m/m_o \quad (4)$$

is introduced to characterize the sensitivity of the several experimental protocols as discussed below. These equations lead to an implicit expression for predicted soot inception temperature  $T(\beta, f_c)$  [29].

The rate constants used in the above equations were  $A = 1.78 \times 10^{+6}$  s<sup>-1</sup> and  $E = 113$  kJ/mole that are based on observations of the development of the aggregate phase in an ethene diffusion flame diluted with various amounts of nitrogen to achieve a range of soot inception temperatures [30]. The above rate constants are in reasonable agreement with those obtained from observations of the conversion of tar to “primary soot” using an optimization code in a study of the burning of bituminous coals [31].

A moderate body of observed soot inception temperatures by four investigative teams exists in the literature [32-36]. Each group of investigators employed a different definition and method of observation of the soot inception temperature  $T_{si}$  although all observations were based flame temperature measurements by fine thermocouples. The value of  $f_c = 0.20$  was chosen as applicable for three teams whose methods of detection of the onset was considered to be of “high sensitivity”. The fourth team employed the curvature of the measured temperature profile to detect  $T_{si}$  which was considered less sensitive and suggested a higher value of  $f_c = 0.80$ . These two values were preselected and were not adjusted during the data reduction process. The soot inception temperature graph (see Figure 3 of [29]) a plot of the normalized temperature difference of the observed soot inception temperatures  $T_{si}$  from the predicted temperature  $T(\beta, f_c)$  vs. fuel molecular mass; i.e.,  $[T_{si} - T(\beta, f_c)]/T_{si}$  (%) vs. fuel mass, using the observational data from the literature [32-36].

Although the scatter shown in the soot inception graph is moderate, the agreement is fair considering the mass variation and structural diversity of fuels ranging from methane to benzene that were tested in the several cited experimental studies [32-36]. The scatter of the data points may relate to the approximations in the model, to the difficulty in defining the soot inception temperatures in the several experimental protocols, and to the difficulty in measuring flame temperatures in soot bearing flames.

The independence of the values of the soot inception temperature  $T_{si}$  from the fuel molecular mass is an interesting outcome that is supported by the results of the several teams of investigators. Chemical analyses of the particulates produced in other investigations provide a tentative answer to this unanticipated result. Gaseous PAHs sampled from a ethene diffusion flame [37] using two-photon ionization mass spectroscopy found the most prominent species as large as 600 amu to be the benzenoid PAHs, which correspond to the stabilomer species. Gaseous species analyzed by photoionization single photon mass spectroscopy for six diverse hydrocarbon fuels in diffusion flames [36] revealed the prominence of the benzenoid stabilomer PAHs in the flames of all six fuels. In yet another series of tests, the "condensed material" from a premixed benzene/air flame was collected by a suction probe and analyzed by direct injection into a mass spectrometer, and showed close agreement with an analysis of precursor particles from a  $C_2H_4$  flame (See Figure 4 in [29]). The prominence of the stabilomer PAHs as the principal components of PNP is strongly supported for these various flame types and fuels.

Thus a series of experiments suggests that the product gaseous or condensed PAHs formed in hydrocarbon flames are the benzenoid species that correspond to the stabilomer PAHs. In view of this outcome, it is not surprising that the soot inception temperatures  $T_{si}$  from diverse hydrocarbon flames show mutual agreement with the theoretical description. We suggest that the likely universal presence of stabilomer PAHs in the PNP accounts for the agreement of the  $T_{si}$  data that is displayed among the eleven different fuels.

#### **4. HEALTH IMPACT OF PARTICLES AND PAHS IN OF URBAN AIR SAMPLES**

The health impact of combustion sources in general has been recently surveyed [39]; here a more limited discussion relating to the potential impact of engine-generated PNP is presented. Our knowledge of the properties of fine particles and of certain PAHs in this matter is making important progress through studies on the pulmonary effects of ultrafine particles [40]. Singlet ultrafine particles were found to have a very high size-specific deposition as compared to aggregate particles. Singlet 20 nm particles had the highest deposition rate and could result in very high human lung deposition even in spite of low mass concentrations. Low doses of ultrafine carbonaceous particles can cause mild pulmonary inflammation in rodents. These results have potential implications in regard to the impact of the nanometer size range of PNP particles. This size property becomes more serious when the chemical makeup of these materials is taken into consideration.

Human cell mutagenicity has been studied at three locations in the northeastern United States – in urban Boston, in rural Massachusetts and in Rochester, New York [41]. These locations possess a near common latitude in a region where the prevailing winds are from the west. This study is particularly relevant to the potential impact of PNP to human health, and only their results for Kenmore Square in urban Boston are here described in more detail. The atmospheric samples were collected on quartz fiber filters using high volume impactors in year 1995 from which annual composite samples were prepared. GCMS was used to quantify some 150 organic compounds including 31 known human cell mutagens. The samples were found to contain relatively high levels of unalkylated PAHs and lower levels of alkylated PAHs which suggested pyrogenic sources to be significant contributors. High abundances of certain highly reactive PAHs as well as nitro-PAHs also suggested fresh diesel emissions to be the important contributors at this urban location. Also at the urban Boston site the higher ratios of lower molecular weight alkylated species, which are commonly found in diesel exhaust gases, suggested contributions from local petrogenic sources.

An abbreviated summary of the results of this study is given in Table 2 where the relative contributions of the most prominent contributors to the sample mutagenicity are listed. These prominent mutagens include certain PAH isomers at 226, 252, 276, 266, and 302 amu, as well as a ketone at 254 amu. These compounds total ten in number two of which are among the stabilomers [16] that were found to be present in the IDF flame [20] and six others are isomers of stabilomers [16]. The oxygenated 254 amu  $C_{19}H_{10}O$  compound is attributed to noncatalyst gasoline-powered motor vehicles. Only 16% to 26% of the sample mutagenicity could be attributed to the known mutagens. The possibility of synergistic interactions among the constituent mutagens was not included in this analysis. The results of these tests were consistent with similar studies reported at the two other locales in northeastern US, and also with other investigations conducted in Los Angeles, and in Washington, DC. It was concluded that combustion emissions, either formed locally or carried by long-distance atmospheric transport, are common factors that affect the three localities examined in this study [41] and also the cities cited above.

Comparison of the results Pedersen et al. [41] with chemical analysis of PNP reported found in the inverse diffusion flame [20] is particularly revealing. Seven of PAHs cited in the urban study were found to be present in the sample of PNP recovered from the inverse diffusion flame (IDF). Seventeen unnamed isomers of the  $C_{24}H_{14}$  PAHs were found in the analysis of the species detected in the PNP sampled from the inverse diffusion flame [20], see Table 1, and suggests this class of compounds, which belong to a  $C_{24}H_{14}$  class of over 80 isomers that vary strongly in mutagenicity [42], warrants further consideration. Nitro-PAHs were not found at high levels in the northeast US study and were considered to be weakly mutagenic to the particular human cell line used in these tests.

Structural formulae of selected mutagenic PAHs found in the 1995 Boston air sample are shown in Figure 3. The formation and release of the 226 to 302 u PAH species will have widespread applicability and constitute a strong incentive for progress in controlling these mutagens. Inhalation of PNPs could result in their retention in the lungs and possible interorgan translocation as discussed elsewhere [39, 40].

Table 2. Prominent mutagens in urban Boston, 1995. From Pedersen et al. [41], *Envir. Sci. and Tech.* 39, 9547-9560 (2005).

Compound	Chem. Frmla	Mol. Wt.	Concen. <sup>a</sup>	% Mutgnty <sup>b</sup>
Cyclopenta[cd]pyrene	C <sub>18</sub> H <sub>10</sub>	226	3.5	2.2
Benzo[x]fluoranthenes x=b+j+k	C <sub>20</sub> H <sub>12</sub>	252	130	2.0
Benzo[a]pyrene	C <sub>20</sub> H <sub>12</sub>	252	37	2.5
Indo[123-cd]pyrene	C <sub>22</sub> H <sub>12</sub>	276	86.3	1.8
Benzo[ghi]perylene	C <sub>22</sub> H <sub>12</sub>	276	85.5	1.1
Dibenzo[a,e]pyrene	C <sub>24</sub> H <sub>14</sub>	302	5.8	1.5
1-Methylbenzo[cd]pyrene	C <sub>21</sub> H <sub>14</sub>	266	15.0	1.5
6H-Benzo[cd]pyren-6-one	C <sub>19</sub> H <sub>10</sub> O	254	220	3.7

<sup>a</sup> Concn is expressed in ng/mg of equivalent organic carbon.

<sup>b</sup> % Mtgnty is concentration times the specific mutagenicity of the compound.

<sup>c</sup> These compounds comprise 16.3% of the total mutagenicity at this location.

<sup>d</sup> The first eight unsubstituted PAHs were also found in PNP by Blevins et al. [20] in the IDF burning pure C<sub>2</sub>H<sub>4</sub>.

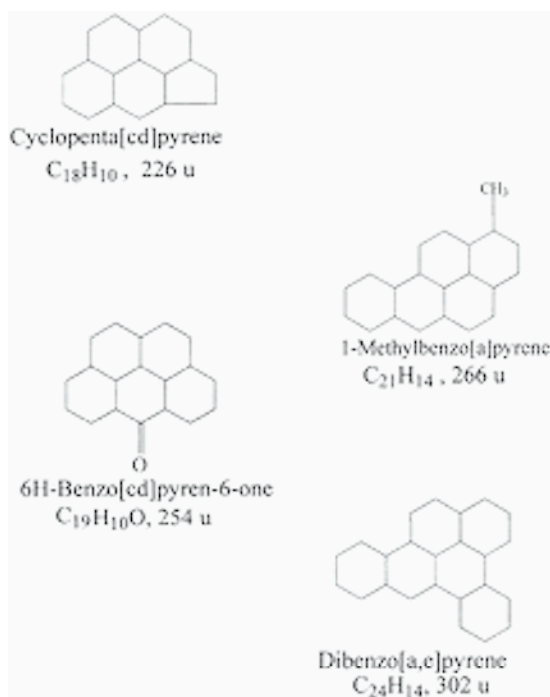


Figure 3. Structural formulae of selected mutagenic PAHs found in the 1995 Boston air sample. [41].

## 5. DIESEL ENGINE TESTS

Sampling PNP from engines is clearly much more challenging than is extracting these particles from the steady laboratory flames cited above. Table 3 summarizes the results of five studies of fine particles observed in diesel engine emissions and reveals some of the challenges in obtaining reliable engines tests of fine particle properties.

A study of the physical and chemical properties of particles released by a heavy duty engine burning fuel with 427 ppm of sulfur [43] found very fine single particles of uncertain origin. Some 23 PAH compounds were identified in the particulate phase but their identities were not provided. Liquid fractions were found to be sensitive to the high vacuum of the TEM. Very fine single particles smaller than 10 nm attributed to sulfuric acid were found at the first dilution stage.

A single cylinder engine was used as the basis for morphological studies with No. 2 diesel fuel employed [44]. Direct particle sampling was employed without the use of a dilution stream. Micrographs samples at low loads showed many agglomerated primary particles with nebulous boundaries between adjacent particles. Fractal dimensions ranged from 1.80 to 1.88 over a moderate range of engine load and rpm, slightly higher than the values found for laminar and turbulent flames. Diffusion-limited cluster-cluster growth was considered to be the dominant particle growth mechanism.

In another study the particles were sampled from a four cylinder, 75 kW diesel engine burning 360 ppm sulfur [45]. Dilution by a differential mobility analyzer augmented with a aerosol mass analyzer was employed. Small, single particle “fragments” of unspecified origin were found and considered to be artifacts. The fractal dimensions were determined from TEM images was 1.75 while a higher value was found by a mass-mobility method. Particle density was observed to increase from 1.27 to 1.78 gm/ml as particle size increased.

The effect of engine operating conditions on the particulate emissions of a light duty engine operating on low sulfur 110 ppm sulfur fuel was studied using direct sam-

Table 3. Nanoparticles observed from diesel engines.

Citation	Engine and S Content	Method	Comment
Shi et al., 2000 [43]	1995 Vehicle 1 L Turbocharged 427 ppm S	Therm. Precip.	Fine Singles, <10 nm shown Figure 5
Lee et al., 2002 [44]	One cylinder DI 75 HP, S=?	70 ms Smpng at engn exhst	Agglutination Shown
Park et al., 2004 [45]	Four Cyl., 75 kw 360 ppm S	Diff. Mobil. Analyzer	TEM show Sngls?, in Figure 6
Zhu et al., 2005 [46]	Light duty 1.7 L 110 ppm S	Sampling Chamber	Mixed Morphology
Neer et al., 2006 [47]	Medium duty 5.9 L, 500 ppm S	Therm. Sampling	Singles, shown in Figures 2 and 3

pling and TEM observations [46]. At low load the TEM images showed nebulous particles with unclear boundaries and suspected liquid phase content. Higher engine loads resulted in particles of distinctive aggregate formation. Smaller fractal dimensions, 1.46 to 1.70, were found for this engine. Graphitic structures of samples captured at high engine load were measured by Raman scattering spectroscopy and were found to be close to the values typical of graphite.

Particle properties produced by a medium duty 5.9 L engine operating on fuel of 500 ppm sulfur content using direct sampling at the engine exhaust pipe [47] without dilution. The fractal dimension was found to be 1.77 in agreement with flame measurements of this quantity. Many small particles, consisting of one or a few primary particles, were emitted at all engine loads. An improved method of measuring the low particle volumes that may be of future interest was also an outcome of this study. The diesel particulates were said to be comparable to the soot found in many laboratory studies in spite of the substantial differences in the combustion environments.

From the above studies one is obliged to conclude that sampling particles from diesel engines is not unexpectedly fraught with difficulties that are not encountered with laboratory flames. The extensive literature from studies of particle formation in hydrocarbon flames, nevertheless, does provide a basis exploring the techniques that may have applicability in engine research and also provides a data base for comparison between flame and engine results. Clearly there is a need for much more work along these lines.

## 6. CONTROL OF PNP FROM DIESEL ENGINES

Control of engine generated PNP is clearly a high priority in view of their small sizes, single particle morphology, and their likely genotoxic chemical composition. Engine designers have developed a panoply of features to improve engine combustion. These include high pressure fuel injection to minimize fuel droplet particle size, positive control of fuel pulse shape and timing possibly with piezo-electric valve programming, cooled exhaust gas recirculation (EGR) to control combustion temperature, the use of low sulfur fuels that are now becoming more widely available to reduce sulfate particle formation, and finally the adoption of catalytic diesel particle filters.

Several of the above engine modifications have a more direct impact on the completeness of combustion and thus the elimination of the petrogenic fuel components. The elimination of the pyrogenically formed species that includes many of the mutagenic components appears more difficult to address because of their formation in the engine cylinder and their chemical stability. The use of cooled EGR to lower the combustion temperature and provide nitrogen dilution can be favorable if increased particulate formation does not result. The use of the diesel particle filter, which involves a penalty in cost, total weight, and engine power, appears to be the ultimate solution for the capture of the particles in all size ranges and unburned gaseous PAHs as well.

Emission standards are being reconsidered to be specified in terms of a limitation of the number of particles emitted per unit distance traveled as a preferred surrogate for the particulate reactive surface effects [39]. This limit is being explored and in Europe has been proposed as  $10^{+11}$  particles per km. Particle coagulation which can reduce particle number concentration may cast an uncertainty on this proposed stan-

dard. The ability of diesel particle filters (DPFs) to meet this standard has been demonstrated [48] for a passenger car operating on two different low sulfur fuels. In this case 95 to 99.5% mass efficiencies in particle removal were achieved. A cautionary note is that ultrafine PNP contribute negligibly to the particle mass and could be present in the unfiltered particle component. The catalytic diesel particle filter appears to have excellent prospects to capture both the gaseous PAHs and the fine particle component of engine emissions.

## 7. SUMMARY

Precursor nanoparticles (PNP) are formed in a wide diversity of flame types burning diverse fuels and are a likely universal antecedent of carbonaceous soot. A study of their chemical composition has been performed [20] using GCMS of PNP extracted by a suction probe from an inverse diffusion flame. Over two dozen PAHs were identified ranging in molecular masses from 152 to 302 amu. Many of these species are stabilomer PAHs that have been widely found in hydrocarbon flames by various investigators.

Human cell mutagenicity of air samples in several urban areas were measured along with the mutagenicity of the component pollutant species [41]. These tests were conducted on samples from three sites in northeastern US and produced similar results to those found in Los Angeles and Washington, D. C. Dominant mutagenic PAHs include many of the benzenoid stabilomer species that were found to be present in the PNP particles sampled from the inverse diffusion flame. Thus PNP are of particularly concern to human health because of their single-particle morphology, their small ca 10 nm sizes, and their likely mutagenic chemical content. Control of PNP emissions is a high priority in the design of diesel engines.

## ACKNOWLEDGEMENTS

This work is based on earlier research funded by the Center for Fire Research of the NIST and later by the US Army Research Office whose financial support is acknowledged with gratitude. The particle sampling and electron microscopy methods were developed in collaboration with Prof. C. M. Megaridis now of the University of Illinois at Chicago. Later electron microscopy was conducted by Drs. H.-C. Chang and H. X. Chen. Mass spectroscopy of the PNP were conducted by Mr. R. A. Fletcher on the LAMMA-500 instrument located at the NIST on particle samples secured at Brown University. The capable assistance of Mr. Jeffrey S. Brown in the preparation of this manuscript is deeply appreciated.

## REFERENCES

1. A. D'Anna, A. D'Alessio, P. Minutolo, in *Soot Formation in Combustion*, H. Bockhorn (Ed.) Springer-Verlag 1994, p. 83.

2. R. A. Dobbins, H. Subramaniasivam, in *Soot Formation in Combustion*, H. Bockhorn (Ed.) Springer-Verlag, 1994, p. 290.
3. R. A. Dobbins, *Aerosol Sci. Technol.* 41 (2007) 485-496.
4. C. M. Sorensen, G. D. Feke, *Aerosol Sci. Technol.* 25 (1996) 328-337.
5. C. A. Amann, D. C. Sieglä, *Aerosol Sci. Technol.* 1 (1982) 73-101.
6. B. Oktem, M. P. Tolocka, B. Zhao, H. Wang, M.V. Johnson, *Combust. Flame* 142 (2005) 364-373.
7. B. Hu, B. Yang, U. O. Koylu, *Combust. Flame* 134 (2003) 93-106.
8. S. K. Friedlander, W. Koch, H. H. Main, *J. Aerosol Sci.* (1991) 22, 1-8.
9. A. D'Alessio, A. D'Anna, A. Dorsi, P. Minutolo, R. Barbella, A. Ciajolo, *Proc. Combust. Inst.* 24 (1992) 973-980.
10. R. A. Dobbins, R. A. Fletcher, H.-C. Chang, *Combust. Flame* (1998) 115, 285-298.
11. R. A. Fletcher, R. A. Dobbins, H.-C. Chang, *Anal. Chem.* (1998) 70, 2745-2749.
12. R. A. Fletcher, R. A. Dobbins, B. A. Benner Jr., S. Hoeft, *Proc. of the Carbon Society 2004*, the American Carbon Society, Providence, 2004.
13. R. A. Dobbins, R. A. Fletcher, B. A. Benner Jr., S. Hoeft, *Combust. Flame* (2006) 144, 773-781.
14. H. B. Palmer, C. F. Cullis, in *Chemistry and Physics of Carbon Vol I*, P.L. Walker, P. A. Thrower (Eds.) Marcel Dekker, 1965, pp. 265-325.
15. M. Frenklach, D. W. Clary, W. C. Gardener, Jr., S. E. Stein, *Proc. Combust. Inst.* 20 (1984) 887-901.
16. S. E. Stein, A. Fahr, *J. Phys. Chem.* 89 (1985) 3714-3725.
17. T. Mauney, F. Adams, M. R. Sine, *Sci. Total Environ.* 36 (1984) 215-224.
18. Y. Bouvier, C. Mihean, M. Ziskind, E. Therssen, C. Focsa, J. F. Pauwels, P. Desgroux, *Proc. Combust. Inst.* 31 (2006) 841-849.
19. M. Frenklach, H. Wang, in *Soot Formation in Combustion*, H. Bockhorn (Ed.) Springer-Verlag, 1994, p. 162.
20. L. G. Blevins, R. A. Fletcher, B. A. Benner Jr., E. B. Steele, G. W. Mulholland. *Proc. Combust. Inst.* 29 (2002) 2325-2333.
21. S. T. Bagley, K. J. Baumgard, L.D. Gratz, J. H. Johnson, D. G. Leddy, *Research Report 76*, Health Effects Institute, Cambridge, Mass.
22. *Certificate of Analysis, Standard Reference Material 1650a* (2000), National Institute of Standards and Technology, Gaithersburg, MD.
23. A. Oberlin, *Carbon* (1984) 22, 521-541.
24. R. L. Vander Wal, *Combust. Flame* 112 (1998) 607-616.
25. R. L. Vander Wal, *Combust. Sci. Technol.* 126 (1998) 333-357.
26. H. X. Chen, R. A. Dobbins, *Combust. Sci. Technol.* 159 (2000) 109-128.
27. L. B. Ebert, J. C. Scanlon, C. A. Clausen, *Energy & Fuels* 2 (1988) 438-445.
28. L.S. Singer, I.C. Lewis, *Carbon* 16 (1978) 417-423.
29. R. A. Dobbins, *Combust. Flame* 130 (2002) 204-214.
30. R. A. Dobbins, G. J. Govatzidakis, W. Lu, A. F. Schwartzman, R. A. Fletcher, *Combust. Sci. Technol.* 121 (1996) 103-121.
31. J. Ma, *Doctoral Thesis* (1996) Department of Chemical Engineering, Brigham Young University, Salt Lake City.
32. A. Gomez, M. G. Littman, I. Glassman, *Combust. Flame* 70 (1987) 225-241.
33. K. Saito, A. S. Gordon, F. A. Williams, W. F. Stickler, *Comb. Sci. Technol.* 80 (1991) 103-119.
34. I. Glassman, O. Nishida, G. Sidebotham, in *Soot Formation in Combustion*, H. Bockhorn (Ed.) Springer-Verlag, 1994, p. 316.
35. C. S. McEnally, L. D. Pfeifferle, *Proc. Comb. Inst.* 27 (1998) 1539-1547.

36. C. S. McEnally, L. D. Pfefferle, *Combust. Flame* 117 (1999) 362-372.
37. K. Siegmann, H. Hepp, K. Sattler, *Combust. Sci. Technol.* 109 (1995) 165-181.
38. A. Tregrossi, A. Ciajolo, R. Barbella, *Combust. Flame* 117 (1999) 553-561.
39. I. M. Kennedy, *Proc. Comb. Inst.* 31 (2007) 2757-2770.
40. G. Oberdorster, *Int. Arch. Occup. Env. Health* 74 (2001) 1-8.
41. D. U. Pedersen, J. L. Durant, K. Taghizadeh, H. F. Hemond, A. L. Lafleur, G. R. Cass, *Env. Sci. Technol.* 39 (2005) 9547-9560.
42. J. L. Durant, A. L. Lafleur, W. F. Busby Jr., L. L. Donhoffner, B. W. Penman, C. L. Crespi, *Mutation Res.* 446 (1999) 1-14.
43. J. Shi, D. Mark, R. M. Harrison, *Environ. Sci. Technol.* 34 (2000) 748-756.
44. K.O. Lee, R. Cole, R. Sekar, M. Y. Choi, J. S. Kang, C. S. Bae, H. D. Shin, *Proc. Combust. Inst.* 29 (2002) 647-653.
45. K. Park, D. B. Kittelson, P. H. McMurry, *Aerosol Sci. Technol.* 38 (2004) 881-889.
46. J. Zhu, K. O. Lee, A. Yozgatligil, M. Y. Chio, *Proc. Combust. Inst.* 30 (2005) 2781-2789.
47. A. Neer, U. O. Koylu, *Combust. Flame* 146 (2006) 142-154.
48. L. Ntziachristos, Z. Samaras, E. Zervas, P. Dorlhene, *Atmospheric Environ.* 39 (2005) 4925-4936.



# Nanoparticles of Organic Carbon (NOC) formed in flames and their effects in urban atmospheres

A. D'Alessio<sup>1</sup>, A. D'Anna<sup>1</sup>, P. Minutolo<sup>2</sup>, L.A. Sgro<sup>1</sup>

<sup>1</sup> *Dipartimento di Ingegneria Chimica, Università degli Studi di Napoli Federico II,*

*P. Tecchio 80, Napoli 80125, Italy*

<sup>2</sup> *Istituto Ricerche sulla Combustione, CNR, Naples, Italy*

*Abstract: The process by which carbonaceous nanoparticles are produced in premixed flames is reviewed. The focus of the paper is on the formation and properties of nanoparticles in laboratory laminar, premixed and diffusion flames and on the methods of sampling and detection of these particles. Particle chemical nature is analyzed from data obtained by several measurement techniques. Measurements characterizing nanoparticles in the exhausts of practical combustion systems such as engines and commercial burners are also reported. Two classes of carbonaceous material are mainly formed in combustion: nanoparticles with sizes in the range 1-5nm, and soot particles, with sizes from 10nm to 100nm. Nanoparticles show unique chemical composition and morphology; they maintain molecular characteristics in terms of chemical reactivity, but at the same time exhibit transport and surface related properties typical of particles. The emission of these particles contributes to atmospheric pollution and constitutes a serious health concern.*

## 1. INTRODUCTION

Fine particles in urban atmospheres constitute a serious concern for public health and affect the radiation balance of the atmosphere mainly by serving as condensation nuclei for cloud formation. Fine Particulate Matter (PM) smaller than 2.5  $\mu\text{m}$  (PM<sub>2.5</sub>) is composed mainly of nitrates, sulphates, Organic Carbon (OC) and Elemental Carbon (EC). The fraction of OC increases as particle size decreases, and ultrafine PM (smaller than 100 nm) is mostly comprised of OC [1, 2]. The smallest fraction of atmospheric PM plays a particularly important role in health effects since it dominates size distributions in terms of number concentration and translocates more than larger particles throughout the body beyond the respiratory system [3-5]. There is also mounting toxicological evidence showing well defined mechanistic pathways explaining how the ultrafine OC fraction of atmospheric PM may cause noted health effects related to PM exposure [6-12]. Ultrafine OC PM is mostly produced by combustion sources, and is of central interest in the field of atmospheric chemistry, where there is much debate on the relative role of primary OC PM (particle phase in combustion exhausts) and secondary OC PM (formed from combustion products through atmospheric reactions) [13].

Therefore, the combustion community has a specific role to provide a detailed characterization of primary organic aerosol and their precursors and furnish an accurate picture of the initial conditions at the exhausts of vehicles/stationary sources for stu-

dies examining atmospheric chemistry related to PM and for epidemiological studies. Nanoparticles of Organic Carbon (NOC) with similar size and optical properties as those formed in fuel rich premixed flames are measured in the exhausts of diesel and gasoline engines [14-16], industrial burners [16], near cook stoves [17] and are detected in urban atmospheres [18, 19]. Therefore, the systematic study of the formation and properties of NOC in simple laboratory flames is needed in order to interpret their formation in more complex systems such as engines and practical burners and to identify successful control strategies.

This paper addresses mainly formation and properties of NOC in laminar premixed flames, underlining methods of sampling and detection for particles (or macromolecules) that have shown to be particularly useful in the size range of interest for NOC (1-10 nm). On this basis, coagulation and surface growth rates of NOC are considered as well as their solubility and behaviour in water suspensions. Further, we speculate on their chemical nature based on the combination of information gained from several measurement techniques. Formation of NOC starting from diffusion and turbulent flames is briefly addressed, and some measurements characterizing the ultrafine PM emissions in the exhausts of vehicles and cook stoves are illustrated. Finally, we outline the status of knowledge on the toxicological properties of combustion-generated NOC.

## 2. GAS PHASE OC, NOC, AND SOOT: DEFINITIONS

Before discussing current knowledge on particle formation and the production of NOC and soot in atmospheric pressure combustion processes, we briefly discuss the reason for the need to define a separate class of flame generated particulate material, named Nanoparticles Organic Carbon (NOC). The name NOC distinguishes a class of PM from the class of combustion-generated PM typically called soot, which is larger, has different properties/behaviours, and has a graphitic structure that is roughly associated with Elemental Carbon (EC). In past publications and in this work we use the word "particle" in reference to both NOC and soot, even though the size of the smallest NOC is approaching molecular dimensions. In fact, a 1-3 nm NOC is on the order of some thousand amu, assuming unit density, which is notably larger than what is usually thought of as gas phase precursors to particles, mostly identified as PAHs and substituted PAHs, with molecular weights lower than 300-500 amu. Since there is little doubt that larger NOC is in the particulate phase, and the size of NOC ranges depending on the combustion conditions, we will refer to this class of combustion generated material using the word "particle".

The definitions of soot and the combustion conditions considered to mark the onset of soot are operational, and they depend on the measurement technique used and its detection limits, similar to the problem of exactly defining OC and EC in atmospheric PM measurements [20]. Here, we use *in situ* extinction in the visible (at a wavelength,  $\lambda=532$  nm) to define the presence/absence of soot. It is worth noting the behaviors or measured properties of soot that are different from NOC, as identified by different diagnostic methods (Table 1). The loss of hydrogen, increase in aromatic structure or graphitic nature, shifting of fluorescence toward longer wavelengths, increase in coagulation rate, particle emissivity, and sphericity in AFM measurements all occur at the same com-

Table 1. Selected observations describing the difference between two main classes of carbonaceous PM formed in atmospheric pressure hydrocarbon flames.

<b>NOC</b>	<b>Soot</b>	<b>Diagnostic method</b>
Extinction in the far UV	Extinction in the entire UV-visible wavelength range	Optical [21]
UV fluorescence	UV-visible fluorescence	Optical [22]
$d_{6.3}=3$ nm	$d_{6.3}>3$ nm	Optical [23], DMA [24], AFM [25, 26]
Soluble in dichloromethane	Not soluble in dichloromethane	Batch sampling compared with optical methods [27, 28]
At least partially soluble in water	Not soluble in water	Batch sampling [21, 29]
Coagulation rate < collision rate	Coagulation rate = collision rate	Optical [23, 26], DMA [24]
Extended/flattened on mica substrates – low sphericity	Less extended/flattened on mica substrates – higher sphericity approaching 1	AFM [25]
Fuzzy or blurry Electron Microscope images	Clear Electron Microscope images	TEM [30, 31]
H/C = 0.5-1	H/C = 0.1-0.05	Elemental analysis on sampled material
Density = 1.2 g/cm <sup>3</sup>	Density = 1.8 g/cm <sup>3</sup>	Batch sampling gravimetric measurements
Produced in fuel rich blue flames	Not produced in fuel rich blue flames	Optical, AFM, DMA
Emissivity = 0.5	Emissivity = 1	Transient thermocouple measurements [32]
High mutagenic potency (on the order of those reported for OC extracts from filter samples)	Non-mutagenic in Ames and other mutagenicity assays – or has a relatively low potencies compared to organic extracts	Ames testing on fractions of filter collected PM separated by solvent extraction or collected by water sampling to isolate NOC [33]

bustion conditions, in concert with the appearance of a significant extinction signal at  $\lambda=532$  nm. Therefore, the operational definition of the onset of soot based on extinction/fluorescence in the visible agrees well with the onset of a strongly changing particle behaviour/characteristic determined by several other measurement methods.

### 3. EXPERIMENTAL CHARACTERIZATION OF NOC

The formation of nanoparticles in laboratory flames and diesel engines was recently reviewed by Dobbins who illustrated mainly the results obtained through Transmission Electron Microscopy (TEM) and GC-MS chemical analysis [34]. Here, we provide a

concentrated review on the experimental characterization of NOC using methods developed and used in our group in Naples: mainly *in situ* optical spectroscopy, Differential Mobility Analysis (DMA) and Atomic Force Microscopy (AFM). We also present some results on the analysis of batch sampled NOC collected from flames and the exhausts of vehicles by bubbling combustion products through water and/or condensing combustion-generated water to analyze off-line combustion products with an affinity for water; details on the use of water sampling to isolate NOC from gas phase OC and soot particles and the sampling procedure can be found in [14, see also the chapter by Minutolo et al. in this volume]. We also discuss some first results of two new optical methods: Fluorescence Time Resolved Polarization Anisotropy (FTRPA), which is promising for measuring particle size independently from extinction and scattering measurements [35-37] and Surface Enhanced Raman (SERS) [38], which has the potential to determine chemical structure on low mass samples.

### 3.1. In situ optical methods

The optical methods for characterizing the average size and the volume fraction of nanoparticles formed in combustion have been reviewed several times previously [39-42], and only a short discussion will be given in this paper. Measurement of the extinction coefficient,  $K_{\text{ext}}$ , gives the total volume fraction of absorbing species present. The total particle volume fraction can be determined from  $K_{\text{ext}}$  when the contribution of gas phase species ( $\text{CO}_2$  at high temperature and PAHs),  $K_{\text{ext, gas phase}}$ , is known and subtracted from the total signal. The following equations may be used to determine particle size, number concentration and volume fraction from optical measurements in the Rayleigh limit:

$$Q_{\text{sc}} = \frac{\pi^4}{4\lambda^4} \sum \left| \frac{m_i^2 - 1}{m_i^2 + 2} \right|^2 N_i d_i^6 \quad (1)$$

$$K_{\text{ext}} = \frac{\pi^2}{\lambda} \sum \text{Im} \left( \frac{m_i^2 - 1}{m_i^2 + 2} \right) N_i d_i^3 \quad (2)$$

$$f_v = N \frac{\pi d^3}{6} \quad (3)$$

where  $m_i$  is the refractive index for a certain type of scatter/absorber,  $i$ , and  $\lambda$  is wavelength. Larger particles require Mie theory. This work focuses on gas-to-particle combustion reactions and the conditions are chosen to be mostly near particle inception onsets, which for the most part contain only particles within the Rayleigh criteria. The refractive indexes used for soot and NOC are:  $m_{\text{soot}}(\lambda=266 \text{ nm})=1.4-i0.75$ ,  $m_{\text{soot}}(\lambda=532 \text{ nm})=1.6-i0.6$ , and  $m_{\text{NOC}}(\lambda=266 \text{ nm})=1.4-i0.08$  [23]. Combining extinction and scattering measurements determines the mean diameter,  $d_{6-3}$ , calculated as the ratio of the sixth-to-third moment of the size distribution function:

$$d_{6-3} = \left( \frac{\left( \sum N_i d_i^6 \right)^{1/3}}{\left( \sum N_i d_i^3 \right)} \right) \quad (4)$$

When both NOC and soot particles are simultaneously present measurements at different wavelengths give the average size and volume fractions for both classes of particles. When spatial resolution is needed, as is the case for non-premixed flames and turbulent combustion conditions, equivalent information can be obtained from Laser Induced Fluorescence (LIF) and Laser Induced Incandescence (LII) measurements employing pulsed laser sources [22, 43]. UV excited fluorescence exhibits a much shorter time delay with respect to the laser pulse compared to that due to LII, so that a single shot measurement can be applied. LII is proportional to the soot volume fraction. Fluorescence is a linear function of NOC extinction so that its intensity can be used to determine NOC volume fraction. Optical methods have the advantage of being *in situ* so that the effect of sampling systems on particles smaller than 3-5 nm can be avoided. On the other hand, spectral fluorescence and extinction due to gas phase compounds, such as PAHs and CO<sub>2</sub> at high temperature can confound the measurement [44, 45].

### 3.2. Off-line AFM measurements

The first application of Atomic Force Microscopy (AFM) to diagnostics of nanometric particles in combustion was reported by Barone, et al. [25, 26], and we summarized and re-analyze some of those results here. The advantage of AFM over TEM is that it furnishes a 3-D topological mapping of particles deposited on atomically flat substrates, with Angstrom resolution in height and nanometer resolution in the x-y plane parallel to the surface. TEM gives only a 2-D characterization of the particles. Operating AFM in tapping mode allows the analysis of particles generated in the flame and deposited on substrates without having to further coat the sample. Since AFM directly counts single particles distinct from the substrate, the deposition density must allow unambiguous measurement of the substrate, and the technique can be used in rather dilute aerosol concentrations. Particles from flames can be deposited on cool substrates by thermophoresis. We find a good deposition density inserting room temperature mica substrates in hydrocarbon flames with a sampling time of 30-40 ms. Preliminary experiments, which tested different material substrates, including gold, Highly Ordered Pyrolytic Graphite (HOPG), and mica, found that mica gives the best atomically flat background surface and good resistance to flame conditions. A wide range of flames both below and above the onset of soot can be well characterized with this technique since the number concentration of agglomerates is relatively low in slightly sooting flames.

### 3.3. On-line DMA measurements

DMA measurements require a high dilution sampling system to reduce the sample temperature and concentration and to avoid further reaction or particle coagulation in the sampling lines and DMA instrumentation [46-48]. Particles are charged and separated in an electrostatic classifier based on their electrical mobility. A mobility or size distribution is determined by counting the charged particles that exit the classifier while varying the applied voltage. When state of the art instrumentation is used, the complete size distribution from 1-100 nm can be measured. The accuracy of the measure-

ment relies on knowing the dilution ratio ( $DR = 10^4$ - $10^5$  in slightly fuel rich premixed ethylene air flames) required to suppress particle coagulation in the sampling line, charging efficiency and particle losses through the sampling lines/instrument. The charging efficiency and particle losses are mainly diffusional processes resulting from collisions of particles with ions or the instrument walls, and as such, they are strong functions of particle size [49-51]. To reduce the problems related to Brownian motion (significant particle losses in the DMA, loss of instrument resolution [52] and even errors in size determination [53]), we operate our sheath flow rate at 50 lpm (or higher), which is considerably higher than typical sheath flow rates (10-25 lpm).

The DMA measures the electrical mobility distribution of the particles,  $Z$ , which is a function of the particle free carrier gas sheath flow rate,  $Q_{sh}$ , through the cylindrical electrostatic classifier, with inner radius,  $R_1$ , and outer radius,  $R_2$ , at a given applied voltage,  $V$ . The size distribution is calculated from the distribution of  $Z(V)$ , while varying applied voltage or the electric field in the classifier, in terms of mobility diameter,  $d_{mobility}$ , by the Millikan-Fuchs' equation, which is valid for spherical particles:

$$Z = \frac{Q_{sh} b}{\pi(R_2^2 - R_1^2)V} = \frac{qeC_c}{3\pi\mu d_{mobility}} \quad (5)$$

where  $q$  is the number of charges on the particle,  $e$  is the unit charge, and  $\mu$  is the viscosity of the carrier gas. The Cunningham correction factor,  $C_c$ , is a function of the Knudsen number ( $Kn = 2\lambda_m/d$ ), where  $\lambda_m$  is the mean free path and  $d$  is the particle diameter. For small particles,  $C_c$  becomes nearly equal to  $Kn$  so that  $Z$  is inversely proportional to  $d^2$  in eqn.5. When comparing DMA measurements with measurements from other diagnostic techniques, the actual diameter must be used, which is slightly smaller than the mobility diameter. De la Mora, et al. [54] created spherical particles of known actual diameters,  $d_{actual}$  by electrospray drying solutions of known concentrations of Ag, polymers, and protein solutions and found that the relationship between actual and mobility diameter can be well predicted considering a non-zero diameter as the effective diameter,  $d_o$ , of the gas in which the aerosol is immersed for the measurement ( $d_o, \text{air}(273 \text{ K}) = 0.5 \text{ nm}$ ):

$$Z = 0.441 \frac{q \left( \frac{kT}{m} \right)^{1/2}}{p(d_{actual} + d_o)^2} \quad (6)$$

For the same  $Z$ ,  $d_{actual}$  calculated by eqn. (6) is equal to  $d_{mobility}$  calculated by eqn. (5) when  $d_o = 0$ , and it is in good agreement for particles as small as  $d_{mobility} = 1 \text{ nm}$  with a more general relationship derived by Li and Wang [55], who considered the potential energy of interactions between particles and gas molecules in terms of the reduced collision integral.

#### 4. RESULTS

Results of optical measurements show that small particles with  $d_{6.3} = 2$ - $3 \text{ nm}$ , which exhibit UV extinction and LIF spectra, are formed at the end of the reaction zone just

after the flame front in significant quantities in atmospheric pressure fuel rich flames of aliphatic hydrocarbons. Figures 1-3 show results obtained by optical measurements in a soot forming flame (ethylene-air,  $C/O=0.77$ ,  $v_{\text{cold gas}}=10$  cm/s). Figure 1 shows extinction and fluorescence spectra early (Figure 1a,b) and late (Figure 1c,d) in the post-flame zone [21]. Figure 2 shows the measured scattering ( $Q_{\text{vv}}$ ) and extinction ( $K_{\text{ext}}$ ) coefficients as a function of Height above the burner,  $H$ , or flame residence time, and Figure 3 shows the volume fraction, mean diameter and number concentration calculated from  $Q_{\text{vv}}$  and  $K_{\text{ext}}$  and eqns. 1-4, assuming optical properties for NOC and soot, listed earlier in the experimental section [23]. Figure 2 shows the gas phase contribution to scattering. The gas phase contribution to scattering is significant (Figure 2a), whereas the amount of extinction estimated for high temperature  $\text{CO}_2$  and the main PAHs in the flame is low compared to the total measured extinction, so that the total extinction and that after subtracting the gas phase contribution practically overlap.

Both the form and intensity of the optical spectra change as a function of  $H$  in this flame (Figure 1). Early in the post-flame zone, just after the main reaction zone of the flame front a large number concentration of  $d_{6-3}=2-3$  nm particles are observed (Figure 3). The extinction and fluorescence spectra of these  $d_{6-3}=2-3$  nm particles are limited to UV wavelengths (Figures 1a,b and 2), which suggests that their structure is likely a composite of aliphatic and aromatic bonding, but with a maximum of 2-3 ring

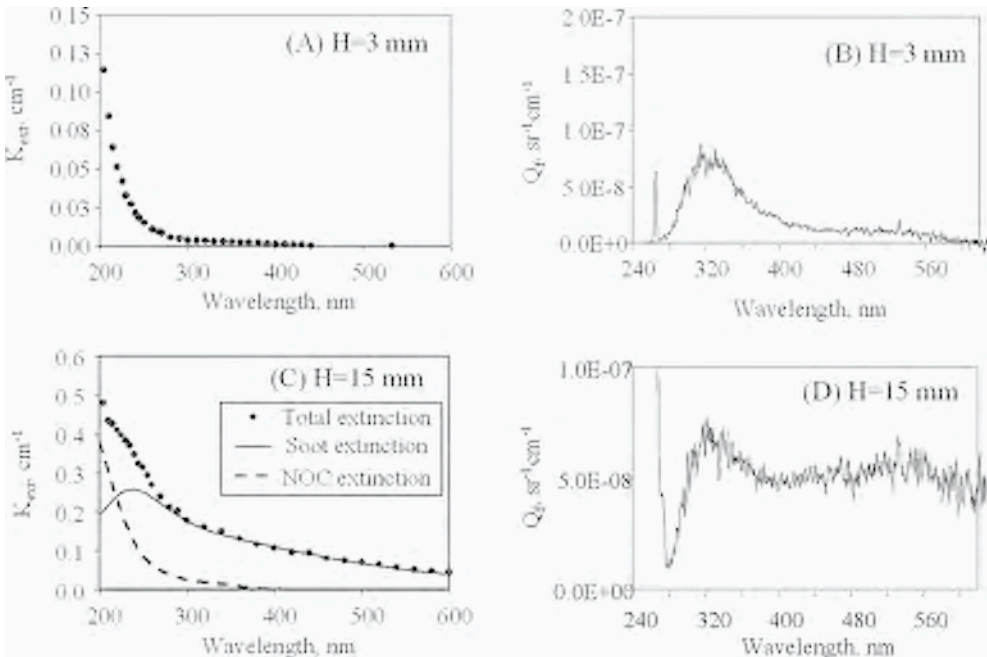


Figure 1. Extinction ( $K_{\text{ext}}$ ) and fluorescence ( $Q_f$ ) spectra in the UV-visible wavelength range early in an ethylene-air premixed  $C/O=0.77$ ,  $v_{\text{cold gas}}=10\text{cm/s}$  flame (A and B), prior to the onset of soot, and later in the post flame zone (C and D), where more soot-like material that absorbs and fluoresces in the visible is clearly present.

chromophores [21]. In fuel rich non-sooting flames, extinction and fluorescence spectra with the same form as Figure 1a,b are measured throughout the entire post-flame region, and scattering and extinction measurements indicate that these  $d_{6,3}=2-3$  nm do not grow larger, even at long post-flame residence times.

On the contrary, in soot-forming flames the extinction and fluorescence spectra change notably with H. Significant extinction and fluorescence at visible wavelengths is measured later in the post-flame zone (Figure 1c,d), indicating the presence of aromatic chromophores with many rings typical of soot [21]. The onset of particles with a higher degree of aromaticity or more graphitic, soot-like structure is clearly observed (at  $H>5.5$  mm) with an increase in the extinction signal at 532 nm, and contemporaneously, the marked increase in the intensity of the scattering signal (Figure 2) indicates that particle size is increasing (Figure 3). These changes (rapid particle growth and significant extinction and fluorescence in the visible) mark the onset of soot particles.

The rapid particle growth after the onset of soot ( $H>5.5$  mm Figures 2 and 3) is accompanied by a strong decrease in particle number concentration, resulting in a relatively unchanging volume fraction, which indicates that the main growth mechanism is coagulation. Contrary to soot particles, the  $d_{6,3}=2-3$  nm particles have a coagulation rate that is orders of magnitude lower than that predicted by the collision rate (the gas kinetic limit). The low coagulation rate the  $d_{6,3}=2-3$  nm particles is deemed the cause

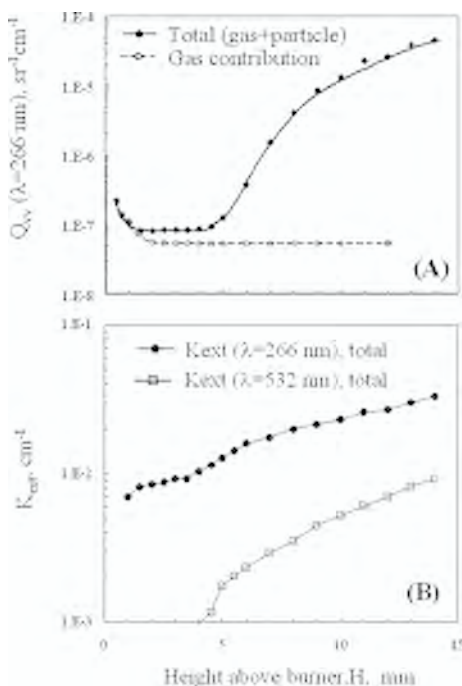


Figure 2. Scattering ( $Q_{vv}(\lambda_o=266 \text{ nm})$ ) (A) and extinction coefficients (at  $\lambda=266$  and  $532 \text{ nm}$ ) (B) for an ethylene-air premixed  $C/O=0.77$ ,  $v_{\text{cold gas}}=10 \text{ cm/s}$  flame as a function of height above the burner, H, or flame residence time.

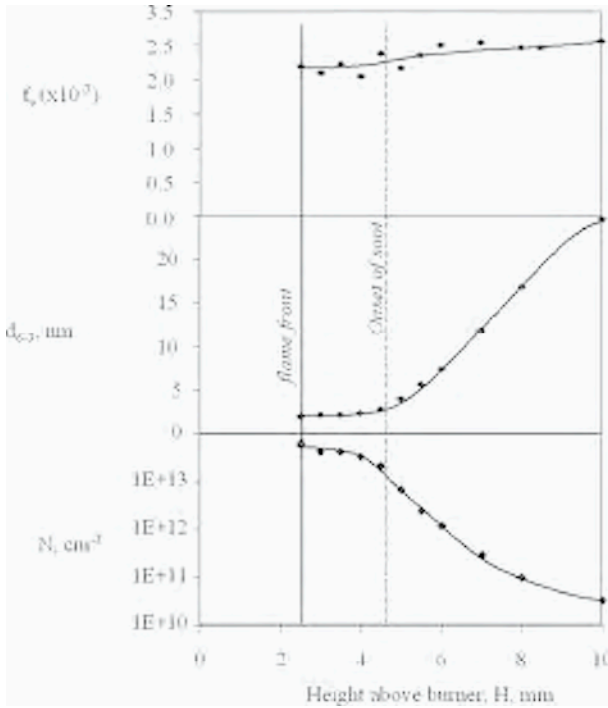


Figure 3. Volume fraction,  $d_{6-3}$ , and number concentration elaborated from the measurements in Figure 2 for an ethylene-air premixed  $C/O=0.77$ ,  $v_{\text{cold gas}}=10\text{cm/s}$  flame as a function of height above the burner. The solid vertical line shows the flame front, while the dotted vertical line denotes the post-flame region where marked particle growth by coagulation and visible extinction and fluorescence is observed.

of the plateau of unchanging  $d_{6-3}$ ,  $N$  and  $f_v$  for  $H < 5.5$  after the flame front (in Figure 3) and throughout the entire post-flame zone in rich non-sooting flames [23, 26]. Instead, soot particles, with primary particle diameters that are an order of magnitude larger,  $d_{6-3}=10\text{-}30\text{ nm}$ , have a coagulation rate that is well-predicted by the collision rate, even at high flame temperatures [26].

Optical measurements made in other hydrocarbon premixed flames (burning methane and benzene) consistently find that the total measured extinction is a linear combination of gas phase species and two types of particles: NOC with an extinction spectra limited to the far UV and soot with a continuous extinction spectra throughout the UV-visible. Even without assuming optical properties for NOC and soot, a plot of the measured extinction and scattering coefficients in the UV ( $\lambda=266\text{ nm}$ ) shows two separate behaviors (Figure 4). When  $Q_{\text{vv}}$  is low, there is a constant linear relationship between  $K_{\text{ext}}$  and  $Q_{\text{vv}}$ , indicating that also the particle size is constant (with a  $d_{6-3}=2\text{-}4\text{ nm}$  – see the lines in Figure 4). These are the flame conditions where only NOC particles are present. In soot forming flame conditions, the scattering signal increases more rapidly with an increase in extinction signal, indicating a growing particle diameter ( $K_{\text{ext}} > 0.01\text{ cm}^{-1}$  in Figure 4).

In summary, optical measurements in atmospheric pressure laminar premixed flames show that mainly two types of carbonaceous material are present in the particle phase, namely NOC and soot. The onset of the smallest ( $d_{6,3}=2-3$  nm) particles occurs at a significantly lower C/O ratio than the onset of soot, and these onset values depend on the cold gas velocity or flame temperature. Increasing C/O from stoichiometric flame conditions, one observes first flames that produce no measurable particles, then flames that produce only NOC, and finally, flames that produce NOC (just after the flame front) and also soot later in the post flame region. The spectral form of the extinction and fluorescence measurements give some indication of the chemical nature of the particles, and they show that the larger particles are composed of many-ring aromatics and have lower H/C ratio than the 2-3 nm particles; 2-3 nm NOC particles are thought to be polymer-like structures containing sub-structures with aliphatic and aromatic (limited to 2-3 rings) bonds and possibly oxygen [21]. The process of soot formation seems to be that of coagulation of the 2-3 nm particles, which at the same time lose H and gain a higher-ringed aromatic or graphitic structure [21, 23, 26, 32].

In-situ optical measurements have been used to identify particulate matter formed in both laminar and turbulent non-premixed flames. These methods identified NOC and soot particles also in diffusion controlled or non-premixed flame conditions. The mean size of nano-organic carbon particles was estimated through light scattering/extinction measurements. The concurrent presence of NOC and soot particles did not allow the measurement of the bimodal size-distribution function of the combustion formed aerosol (NOC and soot particles) since the scattering measurements are biased to the largest particles. It was, however, possible to estimate the mean size of NOC particles in soot-free regions of non-premixed flames. Their size is of the

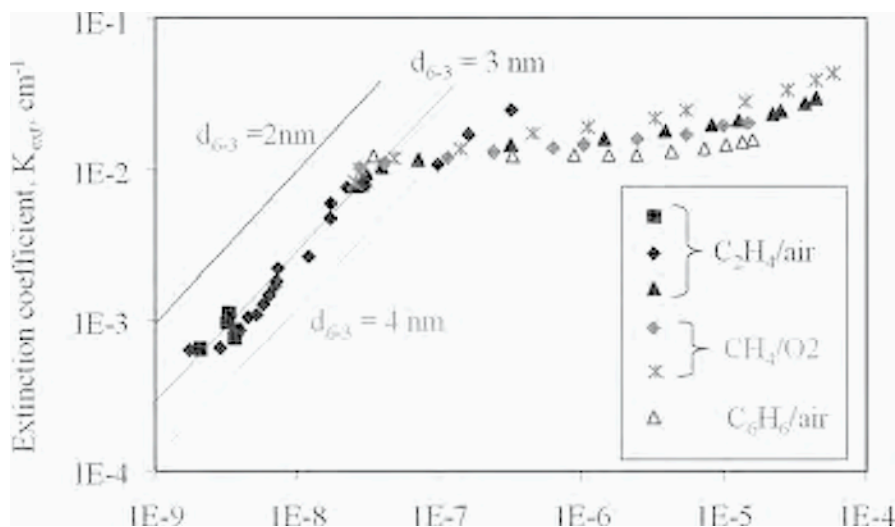


Figure 4. Light extinction vs scattering coefficient in various conditions in atmospheric pressure premixed flames burning different hydrocarbon-air mixtures. Lines report the theoretical  $K_{\text{ext}}(Q_{\text{vv}}, d)$  for  $m=1.4-i$  0.008 and  $\lambda=266$  nm.

order of 3-4 nm in agreement with previous results obtained in rich premixed flames with equivalence ratios crossing the soot formation threshold. The experimental results indicate that NOC particles are formed in large amounts in the central part and at the beginning of the flame reaching a concentration level comparable to that of soot particles. Soot prevails in the final flame plume where the concentration of NOC particles is very low. The intermediate spatial location of these particles between the fuel and soot-containing regions, and their high concentration in the flame suggest that soot formation is just the consequence of coagulation of NOC particles without a major role of surface growth in the soot loading process.

Spectral UV-laser-induced emission and laser light scattering measurements have been used in turbulent non-premixed ethylene flames to measure different classes of combustion-formed compounds with a single-shot, point measurement. Broad-band emissions in the wavelength range of 270-450 nm, synchronized with the excitation light is attributed to fluorescence of aromatic compounds whereas the broad emission signal in the visible detected after a longer delay time is attributed to incandescence of soot particles. Aromatic compounds are immediately formed in the central part of the flame and they reach a maximum concentration in a narrow annular region close to the flame centerline. Excess scattering with respect to gas-phase compounds measured in that region indicates that these compounds have a mean size of the order of 2-3 nm. As in laminar conditions, soot prevails in the final flame plume where the concentration of aromatics is very low. Soot is located in a narrow annular region closer to the maximum flame temperature zone, and its maximum is measured just after the decrease of the concentration of high molecular mass aromatic compounds. The correlation of the fluorescence signals with mixture fraction in each of the flames is an important result for modelers. Soot modelling usually involves an inception stage. If it can be assumed that the early large molecule concentrations are simply related to mixture fraction or to some gas phase species which correlate with mixture fraction then at least one uncertainty has been reduced.

Atomic Force Microscopy measurements confirms that particles as small as 2 nm are present in fuel rich non sooting flames with C/O as low as 0.56 for ethylene-air flames with cold gas velocity=10 cm/s, and the method finds no particles (blank mica substrate) in stoichiometric flames. Figure 5 shows the 3-D topographical map obtained by AFM measurements in combustion conditions that produce NOC but not soot (Figure 5a) and in a sooting flame condition (Figure 5b). Also shown in the figure are the size distributions calculated from the measured particle volumes in terms of spherical equivalent diameters, ED, including both the size distribution counted by AFM (raw data) as well as that corrected for the size-dependent adhesion efficiency ( $\gamma_{SD}$ ). An earlier work comparing AFM and optical measurements found that the rate at which particles adhere to the mica substrate when sampled at flame temperatures is less than the rate of particle collisions with the surface for particles smaller than about 5 nm, and the adhesion efficiency ( $\gamma_{SD}$ ) decreases with particle size similar to the measured coagulation efficiency [26]. The flame condition of Figure 5a has an extinction and fluorescence spectra with the same form as that attributed to NOC (Figure 1a,b) with no measurable extinction detected at wavelengths in the near UV or visible. Similar images to that in Figure 5a are also measured throughout non-sooting flames where the optical measurements show no significant visible absorption and find a  $d_{6-3}=2-3$

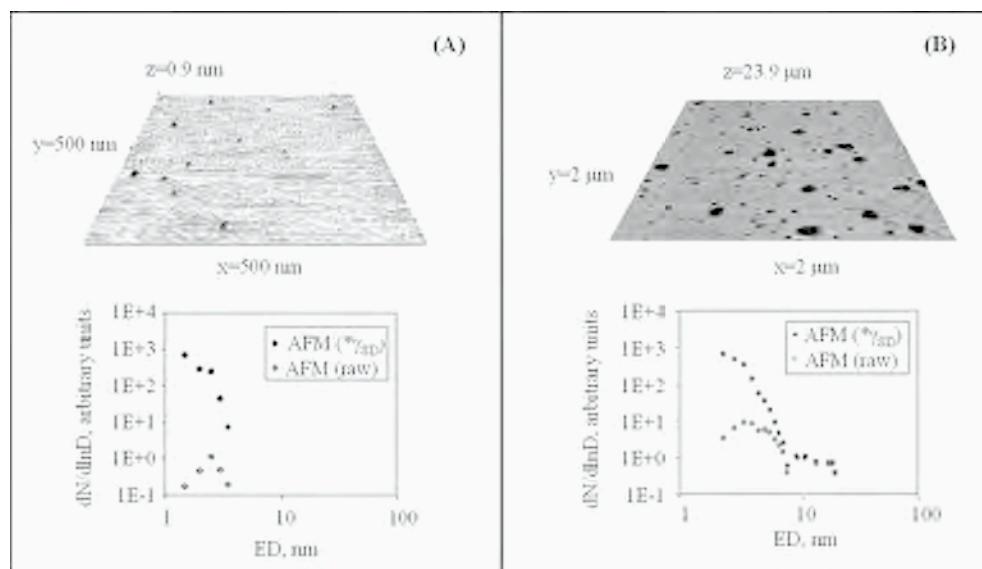


Figure 5. Topographical maps and size distributions of equivalent spherical diameters (ED) obtained from AFM measurements in ethylene-air premixed flames  $V_{\text{cold gas}}=10$  cm/s that produces no measurable particles  $C/O=0.56$  (A), and late in the post-flame zone after the onset of soot in a sooting flame  $C/O=0.77$  (B).

nm. Also, images like Figure 5a are obtained from AFM measurements in sooting flames at early residence times (after the flame front but prior to the onset of soot), where only  $d_{6,3}=2-3$  nm particles are observed by optical measurements. Figure 5b shows a size distribution measured by AFM in a flame condition where both NOC and soot are observed (similar to the conditions of Figure 1c,d or after the onset of soot in the same flame conditions as Figures 2 and 3).

Another interesting aspect of AFM measurements is that they give the three dimensional structure of particles deposited on the substrate. All single particles measured by AFM in non-sooting and sooting flames have shown a non-spherical shape on the mica substrate. The shape on the x-y plane is almost always circular, and the aspect ratio (maximum height/base diameter) is always less than one. This result suggests that the measured particles are probably spherical in the aerosol being sampled and they spread out on the mica substrate upon impaction or over time. If, instead, the flatness of the particles were due to stacked graphene layers, they should not always have a circular base, and their height should increment in discrete amounts equal to the stacking layer of graphene, which is within the resolution of AFM and which we do not see. The degree to which the particles spread over the surface may be related to their affinity for water since polar substances are reported to spread out on the hydrophilic mica substrate [56]. Figure 6 plots of the sphericity ratio (maximum height/base diameter) measured for all particles sampled in a sooting flame ( $C/O=0.77$ ) vs. their ED. Early in the flame, where optical measurements find only  $d_{6,3}=2-3$  nm particles, the AFM

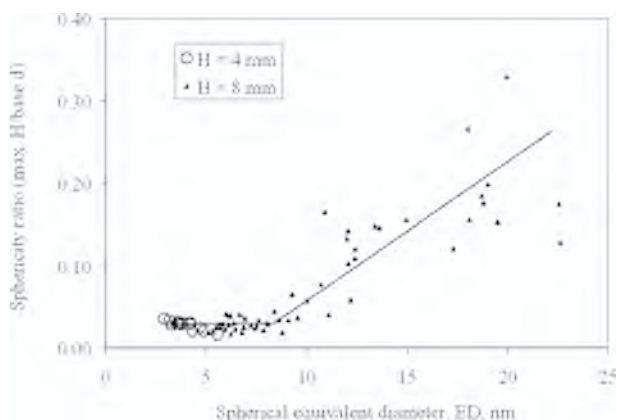


Figure 6. Aspect ratio determined by AFM of particles sampled from an ethylene-air premixed  $C/O=0.77$ ,  $v_{\text{cold gas}}=10\text{cm/s}$  flame before ( $H=4\text{ mm}$ ) and after ( $H=8\text{ mm}$ ) the onset of soot.

measurements find particles with very low aspect ratios (less than 0.05). Higher in the flame, a wider bimodal distribution of sizes are measured both by AFM and optical measurements, and the sphericity ratio of particles larger than about 10 nm increases toward the spherical limit (1) with increasing particle size. AFM measurements over a wide range of operating conditions (varying  $C/O$ , flame residence times, temperatures, and hydrocarbon fuel burned) find a relationship of aspect ratio and equivalent diameter that is similar to the one reported in Figure 6 [25]. The result that the smaller particles spread out more than larger particles indicates that they have a different structure; they may be more liquid like and/or more polar. TEM images of NOC are reported to be fuzzy compared to the clearer images seen by soot particles, and the fuzzy TEM images are thought to be due to a more liquid like structure [30].

Figure 7 shows the main peaks of particle size distributions that have been measured by on-line DMA in hydrocarbon-air flames: a rather mono-disperse peak with a modal mobility diameter of about 2 nm and a standard deviation of about 0.8 (mode I), a second broader mode (mode II) with a modal diameter that ranges from 3-4 nm, depending on the combustion conditions, and a third larger mode with diameters larger than 10 nm that is only present in flames above the sooting threshold (mode III) [24]. The smallest two modes (I and II) are measured in conditions where the optical measurements find extinction and fluorescence spectra that are limited to the far UV (shown in Figure 1a,b), and only the  $d_{6.3}=2\text{-}3\text{ nm}$  NOC particles are present. Therefore, the DMA measurements seem to show that NOC particles have (at least) a bimodal size distribution. Flame conditions that produce material that has significant extinction and fluorescence signals in the visible wavelength range ( $C/O>0.7$ ,  $v_{\text{cold gas}}=10\text{ cm/s}$ ) show a size distribution that includes also mode III with mobility diameters larger than 10 nm, in addition to the two smaller peaks associated with NOC. It is worth noting that it is experimentally impossible to accurately measure all three modes (I, II and III) with the same dilution ratio and the DMA system employed. The dilution ratio required to avoid particle coagulation of mode I in the sampling lines at

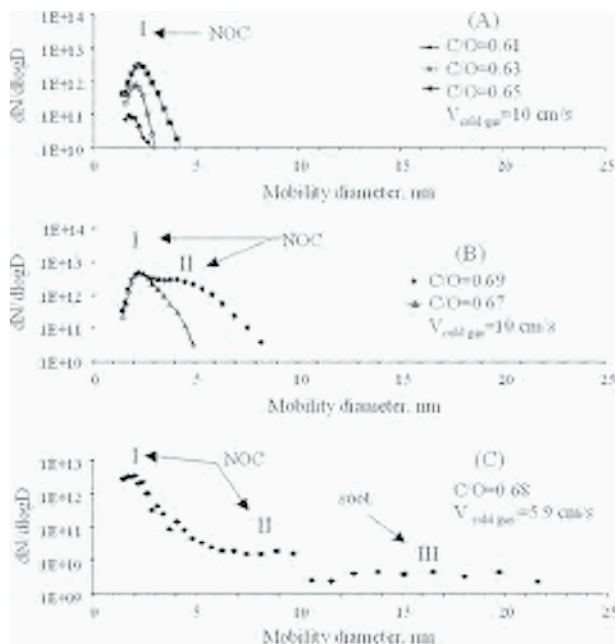


Figure 7. On-line DMA measurements in hydrocarbon premixed flames operating at different combustion conditions, which produce unimodal (A) and bimodal (B) size distributions, both of which show no measurable visible extinction or fluorescence, indicating that these flames are non-sooting. Trimodal distributions (C) are measured in richer sooting flames. A sub-nanometer flame-generated peak is also detected, but cannot be accurately quantified due to the confounding signal measured for ion-induced molecular clusters formed by the excess ions and trace gas molecules in the particle charger.

room temperature causes the concentration of mode III particles to be lower than or right at the detection limit of the electrometer, giving noisy data. Also, in moderately sooting flames the amount of ion-pairs in the charger is not enough to fully charge the aerosol to the so-called steady state charge distribution predicted by Fuchs' theory, rendering the measurement quantitatively inaccurate. A larger source of error/noise in soot-forming flames is that the sample orifice closes much faster (within 20 seconds) than the scan time of the DMA measurement (2 minutes). Interestingly, in flames that produce only NOC (and no soot), we do not observe any loss in the DMA signals over time associated with the closing of the sample orifice, even though in some conditions the amount of sampled material is high enough to close the hole entirely in a matter of minutes. This observation may indicate thermal rebound between the particle and metal surface of the orifice, similar to the size dependent adhesion efficiency observed for NOC at 1700 K on flat mica AFM substrates [26].

DMA measurements also detect a sub-nanometer flame-generated peak, slightly smaller than mode I, which we removed from the size distributions in Figure 7 but can be seen in Figure 8a. Unlike the peaks with  $d_{\text{mobility}} > 1$  nm, this sub-nanometer peak

cannot be accurately quantified due to interferences in the size range of 0.6-1.4 nm from molecular clusters formed by ion-induced nucleation in the bipolar charger. The presence of the sub-nanometer ion-induced molecular cluster peak is an indicator that the charger is producing enough ion pairs to fully charge the incoming aerosol, and excess ions are available to produce molecular clusters by ion-induced nucleation reactions with trace gases (probably mostly water molecules). Since the amount of clusters formed in the ionizer depends on the concentration of excess ions and trace gas molecules in the particle charger, it cannot be simply quantitatively estimated and subtracted. The dimensions of the subnanometer peak are too small to be considered a ‘particle’ mode, and this material would certainly be better characterized with higher resolution instrumentation like high resolution DMA [52] or Time of Flight Mass Spectrometry [57, 58] employing a different particle charging mechanism.

We observe two main differences between mode I NOC and mode II NOC. First, the particle size distribution does not change in time as fast as it should if all collisions resulted in particle coagulation in conditions where only mode I NOC is formed. DMA measurements find that the coagulation rate is significantly lower than the collision rate for NOC at flame temperatures [24], in agreement with earlier observa-

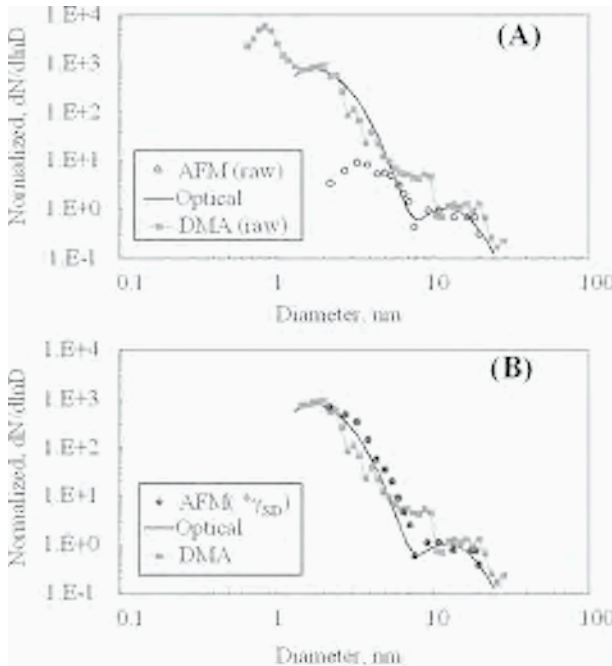


Figure 8. Size distributions obtained by *in situ* extinction and scattering measurements, on-line DMA measurements and off-line AFM measurements on particles deposited on substrates sampled from an ethylene-air premixed C/O=0.77,  $v_{\text{cold gas}}=10\text{cm/s}$  flame (A). The sub-nanometer peak from the DMA measurements has been removed and the AFM measurements are corrected for the size-dependent adhesion efficiency in (B).

tions from optical measurements [23, 26]. Second, water samples collected from flame conditions which present only mode I NOC, both modes I and II NOC, and all three modes (mode I and II NOC as well as mode III soot particles) contain only particles with the size of mode I dispersed within the sample [14]. Also, a significant amount of volatile OC in addition to NOC is captured in the water samples, but can be removed by evaporation. Several particle sizing diagnostics find that water samples from flames contain material in mode I but no particles with sizes similar to modes II or III, including Dynamic Light Scattering, FTRPA, Fluorescence Correlation Spectroscopy, and Electrospray-DMA [14]. This result suggests that mode I NOC remains dispersed in the water samples while mode II NOC and mode III soot particles do not, probably because mode I NOC has a higher affinity for water than the other two modes.

Figure 8 compares the size distribution of NOC and soot determined by *in situ* optical measurements, on-line DMA measurements and AFM measurements for the same soot-forming flame as the one discussed earlier in Figures 1-3. The size distribution calculated from optical measurements assuming that the particle size distribution is the superposition of 2 lognormal distribution functions, one for soot and one for NOC; more details on this calculation can be found in [26]. The DMA size distribution averaged over three scans is still noisy, mostly because of the fast closing of the orifice due to soot deposits. Figure 8a shows the original DMA and AFM measurements. In Figure 8b, the sub-nanometer peak was removed from the DMA measurement since that peak includes both flame-generated material as well as ion-induced clusters formed in the particle charger from smaller gas molecules and excess ions, and the AFM measurements are corrected for the size dependent adhesion efficiency,  $\gamma_{SD}$  [26]. There is excellent agreement between all three techniques when the adhesion efficiency is taken into account. The relative volume fractions of NOC (integrating over modes I and II) and soot (integrating mode III) determined by on-line DMA measurements agrees well with the values of volume fraction determined from optical measurements for NOC and soot. Also, the agreement between the  $d_{6,3}$  values determined by DMA, optical, and AFM is good for this soot-forming flame.

On the contrary, there is considerable disagreement between on-line DMA and optical measurements in flame conditions that produce only mode I NOC. Figure 9 plots the total particle volume fraction obtained from on-line DMA, AFM and optical measurements as a function of C/O for ethylene-air flames at a fixed height above the McKenna burner. A measure of total particle volume fraction was obtained from AFM measurements:  $fv_{AFM} = \pi/6 \sum (ED)^3 n_i \gamma_i$ , where  $n_i$  and  $\gamma_i$  are the counts and size dependent adhesion efficiency per size bins. Note that the units of  $fv_{AFM}$  are not the same as the DMA and optical measurements, which are in units of particle volume/sampled gas volume; here, we are interested in examining the trend of  $fv_{AFM}$  in C/O in Figure 9 and not its absolute value. The particle volume fraction measured by on-line DMA drastically decreases at low C/O and no particles are measured for  $C/O < 0.6$ . Instead, AFM and optical measurements measure a much less dramatic decrease in particle volume fraction and a significant amount of NOC particles at C/O as low as 0.5 nm.

If it is assumed that the DMA measurements are correctly measuring the onset of NOC and the volume fraction in conditions near its onset (as was done in a recent arti-

cle by Theirley, et al. [59]), then both the optical and AFM measurements must be overestimating NOC in these conditions. However, it is quite unlikely that AFM measurements cause homogeneous condensation of semi-volatile gas phase species during thermophoretic sampling at high temperature. A related study examining thermophoresis, condensation and thermal rebound for PM<sub>2.5</sub> deposition on cooled impactor plates, reports that water condensation did not occur when the aerosol temperature was raised from ambient to 50°C [60]. Further evidence that the volume fraction does not change appreciably in the C/O=0.56-0.63 range comes from off-line analysis of flame generated (mode I) NOC captured in water samples. As discussed earlier, water samples selectively collect (or isolate) mode I particles even when the mass and/or number concentration of mode II particles are on the same order of magnitude. Assuming that the collection efficiency is not a strong function of C/O, if the DMA measurements in Figure 11 were correctly measuring what occurs in the flame, we would expect to see at least two orders of magnitude less material in the water samples at 0.56 compared to those collected from a C/O=0.63 flame, which we do not see.

If the volume fraction is unchanging, as it seems to be from AFM, optical, and batch sampling measurements, then the loss in signal by DMA probably indicates that the on-line DMA measurements is losing more particles when the size distribution contains only mode I particles. Particles could be ‘lost’ in these measurements because they either do not enter into the probe, they are not charged in the bipolar diffusion charger, or they are lost to the walls of the probe or the DMA instrumentation. It is unlikely that mode I NOC in the sample volume near the probe does not enter the probe since the dilution ratio is calibrated by measuring CO<sub>2</sub>, which has a higher mobility than mode I NOC. The possibility that mode I NOC has a lower charging probability than mode II NOC and mode III soot is contrary to current thinking regarding particle charging mechanisms since diffusion charging is thought to be independent of

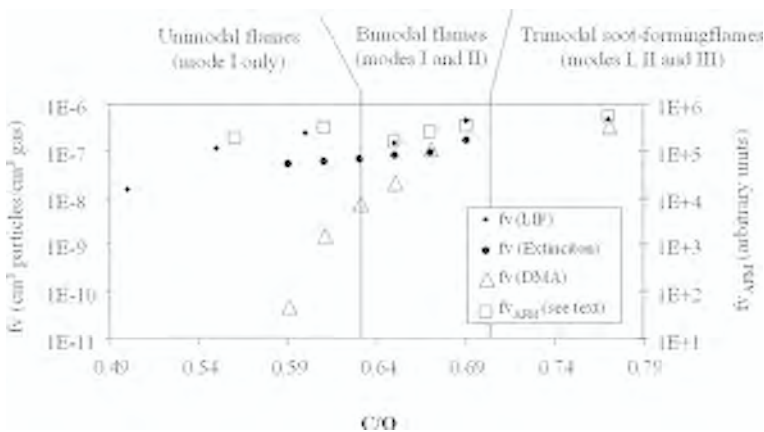


Figure 9. Total particle volume fraction determined by: *in situ* optical measurements (LIF and extinction), on-line DMA measurements, and AFM measurements on particles deposited on substrates from C<sub>2</sub>H<sub>4</sub>/air premixed flames. The optical and DMA measurements were taken at H=10 mm. The AFM samples were taken at H=5 mm.

chemical structure [61]. Experimentally measured charging efficiencies by diffusion charging depend on particle diameter, in excellent agreement with Fuchs' theory for nanoparticles as small as  $d_{\text{mobility}}=2.5$  nm made from evaporation-condensation of silver [62], tungsten [49] and NaCl [63-65]. The drop off in particle volume fraction at low C/O was found to change as a function of probe geometry/operating conditions and DMA system (results not shown), presumably because of diffusional losses. However, preliminary loss calculations (assuming no thermal rebound) only seem to increase the volume fraction measured by on-line DMA at C/O=0.6 by one order of magnitude. The difference between DMA (uncorrected for losses) and optical measurements in volume fraction is about 3 orders of magnitude at C/O=0.6 and within experimental error at C/O larger than about 0.65.

The lower concentrations of NOC measured by on-line DMA compared to optical, AFM, and off-line batch sampling in conditions near the onset of NOC is not yet fully understood. Since the optical measurements do not suffer from sampling errors and agree well with the trend in particle volume fraction in C/O for off-line AFM and batch sampling measurements, we currently have more confidence in these measurements (the odds are three independent measurement methods to one). Certainly, studies that validate chemical kinetic mechanisms describing particle inception using exclusively on-line DMA measurements [66] are premature, especially if they employ the TSI nano-DMA system (SMPS model 3936) and its analysis software, which excludes the measurement of mode I NOC that may play an important role in the inception processes in combustion systems [67]. Also, although it is recognized that the probe extensively cools flame products near its surface [46], the effect of the probe on particle concentrations is not well understood. Future work should systematically study how the probe affects local particle concentrations.

On the other hand, further elements for the interpretation of the optical data are given by Time Resolved Fluorescence Polarization Anisotropy (TRFPA), which determines particle size *in situ*. This technique excites fluorescence with a femtosecond laser source and determines the rotational diffusion coefficient of species present from the measured polarization decay, thus furnishing an optical (*in situ*) measure of average particle size. Earlier studies using TRFPA to measure the size of particles collected in water samples from flames showed only mode I particles [35] with a mean size smaller than 3 nm, in good agreement with other sizing techniques applied to the same samples, thus validating the sizing capability of the measurement [14]. Recently, the technique has been successfully applied *in situ* in soot-forming flames [37]. These flames show both a short and a longer decay time, indicating the presence of particles with a mean size of 2.5-3.4 nm in addition to larger particles with a mean diameter of 4-8 nm. Future work will aim to provide additional information for validating the reliability of extinction, fluorescence and scattering measurements by measuring particle size using *in situ* TRFPA measurements as a function of C/O and flame height in pre-mixed flames, especially in conditions near the onset of NOC.

It is worth noting that the size and extinction spectra associated with flame-generated NOC is similar to that measured in the exhausts of vehicles operated on a dynamometer [14, 15], in emissions of cook stoves [17] and industrial burners [16], and in atmospheric fog samples [18]. Figure 10 compares the size distributions of particles collected by thermophoretic sampling from the emissions of a 2004 model gasoline

and diesel powered vehicle with the volume fraction of soot and NOC determined by *in situ* extinction measurements in the same operating conditions [14]. The same three particle modes observed in premixed flames are also seen in diesel vehicle exhausts, which contain significant amounts of soot particles and extinction in the visible. Instead, the gasoline vehicle exhaust shows only the first two NOC peaks, and the extinction spectra of these emissions has the form attributed to NOC (dashed line in Figure 1c). Also, there is rather good agreement between the relative amounts of NOC and soot determined by UV extinction and AFM measurements corrected for the size dependent sticking efficiency (Figure 10b). By the similarity in size and extinction spectra, one may conclude that the NOC measured in vehicle exhaust is generated in the combustion chamber, and both NOC and soot modes survive the exhaust without significant growth. Dobbins also recently concluded that flame generated particulate accounts for most of the smallest mode nanoparticles emitted from diesel powered vehicles based on Transmission Electron Microscopy (TEM) measurements of particulate and the detailed speciation of PAHs adhered on particulate matter formed in flames and diesel exhausts [34].

Figure 11 shows size distributions measured by two different DMA systems of aerosols formed near by a typical cook stove fueled with methane gas operating with blue flames. While the size distribution calculated by the TSI software cuts off at a lower detection limit of  $d_{\text{mobility}}=3$  nm, the TapCon DMA utilizing an electrometer

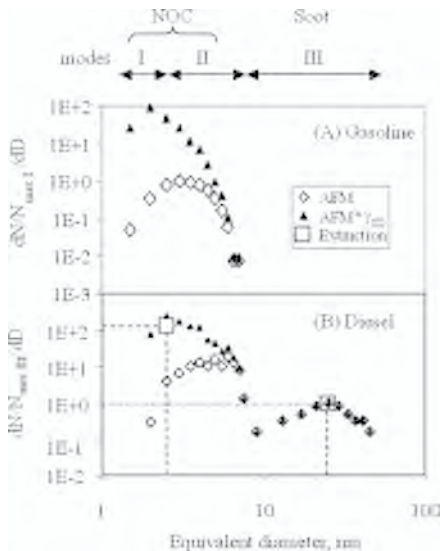


Figure 10. Size distribution measurements of particles deposited on substrates and measured by AFM off-line measurements in emissions of a gasoline (A) and diesel (B) powered vehicle operated at constant speed=50 km/hr on a dynamometer. Also plotted are the volume fractions of NOC and soot determined by *in situ* extinction measurements assuming a size of 2.5 nm for NOC and 25 nm for soot. The measurements are normalized for the maximum value of mode I (max I) in (A) and the maximum value of the largest size particle mode (max II) in (B).

measures smaller particles. The size distribution has a similar form and modal diameter at  $d_{\text{mobility}}=2$  nm to those measured in rich but non-sooting methane/oxygen premixed flames. Similarly, the extinction and fluorescence spectra and size of NOC captured in water samples from the same cook stove were similar to those measured in water samples from premixed laboratory flames [17]. Merola, et al. found that UV extinction spectra measured in water samples collected from the exhausts of applied combustion systems and rain samples in a polluted urban air shed were similar to that of flame-generated NOC [16]. Similarly, atmospheric fog samples were found to contain material with the same UV extinction and size of flame-generated NOC [18]. The observation that PM in combustion emissions have the same size and optical properties of flame generated NOC implies that NOC emissions may affect the atmosphere and human exposure to NOC is likely.

An interesting behavior of NOC that may explain why it escapes exhaust systems without significantly growing to larger sizes is that its coagulation rate is lower than the collision rate at high temperature [19, 23, 26]. The measured coagulation rate of NOC depends on particle size, and it is currently explained with a simple model, which predicts that collisions result in particle coagulation only if the potential energy during interaction is less than the thermal kinetic energy of the particles, which is mainly a function of size and the polarizability of the chemical structure of the particle (embedded in the Hamaker constant) [26]. A better understanding of the coagulation rate of NOC may be useful for pollution reduction strategies or industrial processes designed to produce nanoparticles of controllable size with combustion sources. We are currently working on the hypothesis that the lower coagulation rate for mode I NOC may be related to functional groups that contain oxygen within the chemical structure of NOC. If oxygen containing functionalities are indeed a notable characteristic of combustion-generated NOC, this may also explain why 1-3 nm NOC remains dispersed in water samples, while larger NOC and more graphitic soot particles do not. The hypothesis that functional groups containing oxygen cause the observed lower coagulation

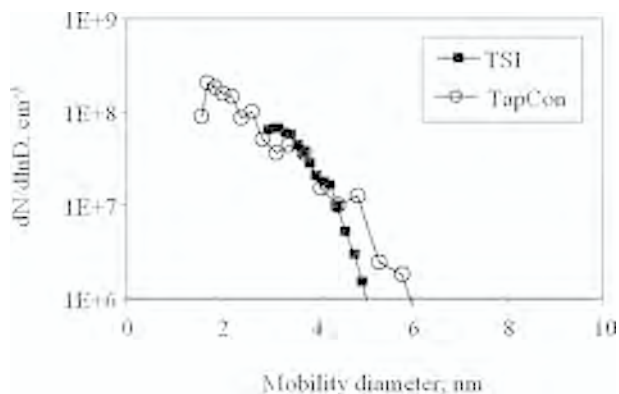


Figure 11. Size distribution measurements of aerosols formed with a typical cook stove operating with a blue flame burning methane using either the TSI SMPS Model 3936 (filled symbols) or the TapCon (open symbols) DMA systems.

rate for smaller NOC (mainly in mode I) is based on two measurements that show oxygen bonding in NOC samples collected from flames, one using Fourier Transform Infrared (FTIR) spectroscopy and one using Surface-Enhanced Raman Spectroscopy (SERS). Both the SERS and FTIR measurements were performed on samples collected by batch sampling of combustion-generated material from premixed ethylene-air flames and deposited on a substrate. Also, the inclusion of oxygen was shown by Stankovich, et al. [68] to hinder coagulation of graphite oxide (GO) in aqueous suspensions, and the removal of oxygen in reduction reactions that occur with the addition of hydrazine resulted in growth of GO to graphene sheets. Analogously, we added hydrazine to our NOC samples, and we noted a significant growth in particle size in these hydrosols compared to those without hydrazine addition, which are otherwise stable suspensions that contain only mode I NOC smaller than 3 nm.

Figure 12 shows the infrared spectra of samples of soot, which is broad and resembles the absorption curve of a black body and NOC, which shows complex molecular structure [69-73]. Both samples show evidence of aromatic structure, including the sharp peaks at  $703\text{ cm}^{-1}$  and  $740\text{ cm}^{-1}$  (and overtones in the wavenumber range  $1800\text{--}2000\text{ cm}^{-1}$ ), which indicate phenyl ring substitutions and sharp weak peaks at  $1500\text{ cm}^{-1}$  and  $1600\text{ cm}^{-1}$  due to the C=C bond of an aromatic nucleus. The IR spectrum of the NOC sample also shows considerable evidence of functionalities containing oxygen and aliphatic bond structure. More recent measurements using surface-enhanced-

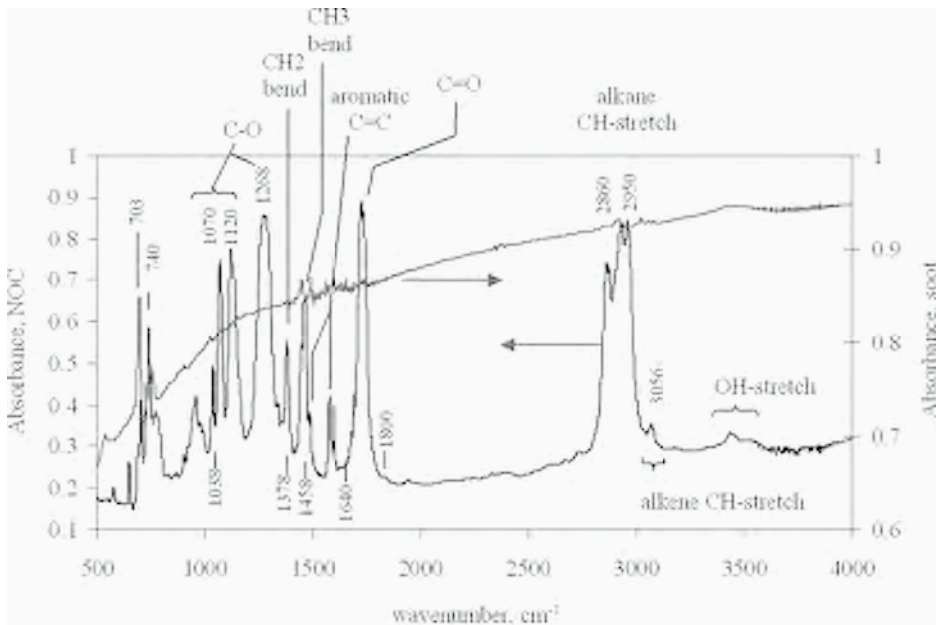


Figure 12. FTIR spectra of a soot and NOC sample collected from fuel rich ethylene-air flames in sooting and non-sooting conditions. The absorbance is plotted on a linear scale in units of wavenumber.

ced Raman spectroscopy on NOC samples collected from rich but non-sooting flames deposited on substrates with a layer of silver coated glass microparticles also found evidence of carbon oxygen bonding and oxygen-containing functionalities [38]. The SERS measurements are exciting since they may be able to give information on chemical structure from a very small sample size. Further work is needed to discern whether oxygen containing functionalities are a result of high temperature combustion reactions or off-line oxidation of the sample at ambient temperature.

If oxygen is present in the structure of NOC, it may also play a role in how NOC affects biological systems. Further investigation may find that NOC plays a significant role in the observed health effects related to pollution from combustion sources. While several studies have examined the OC fraction of atmospheric PM [11, 74, 75] or the extractable organic fraction of PM collected on filters [76-79], very few studies have directly examined the toxicological properties of combustion-generated NOC. We recently collaborated with toxicologists and medical researchers to collect and characterize samples of NOC from flames and vehicle exhausts and discern the toxicological properties of NOC in different biological assays [33, 80]. Ames testing revealed that NOC induces mutations in the Salmonella bacteria with a potency on the order of those reported in the literature for the extracted organic fraction of PM samples collected on filters [33, 80]. While NOC also showed high reactivity with peptides, the highly complex chromatographic-mass spectra prevented the identification of specific adducts [33]. NOC induced dose-dependent cell death in mouse embryo fibroblast NIH3T3 cells, which were swelled and more fluorescent than control cells, possibly indicating cellular uptake of NOC. Arenz, et al. [81] used a genetic engineering approach to investigate the toxicological nature of NOC collected in water samples from fuel rich propane flames prior to the onset of soot. They found a dose-dependent cell death associated with NOC on a created cell line derived from human bronchus alveolar carcinoma. Further, the authors conclude that the specific gene expressions observed indicate that cell death is mediated by activation of NF- $\kappa$ B.

In summary, the first screening tests on combustion-generated NOC all seem to show high reactivity with biological samples and toxicological potential for NOC.

Aside from the human health concerns, NOC may also play a significant role in atmospheric nucleation, cloud formation, and indirect climate forcing. In a recent review of proposed mechanisms for atmospheric nucleation processes, Holmes states, "*Since observations of particle formation only occur following growth to observable sizes, it is possible that a pool of undetectable particles exist at all times but are only observed following significant condensational growth*" [82]. Since flame generated NOC are detected in the emissions of practical combustion systems and are smaller than the lower size detection limits of most currently available particle instrumentation, future work should evaluate the possible role of NOC in atmospheric 'nucleation bursts'. Studies that try to give a detailed speciation of atmospheric PM only describe about 20 % of the total material because of the complexity of chromatographic and mass spectra of OC PM [1, 83], and a similar limitation exists for OC PM in vehicle emissions [84] and flames [27]. NOC accounted for a significant portion of the unchromatographable fraction of flame products in a study that compared the quantity of NOC determined by optical methods and the quantity of unchromatographable OC in batch samples washed with dichloromethane [28]. Future work should be aimed at determining the degree to

which NOC may account for the unchromatographable fraction (~80%) of OC in urban atmospheres and in vehicle emissions.

## 5. CONCLUSIONS

Combustion of fossil fuels produces carbonaceous nanoparticles both in premixed and non-premixed flame conditions. Two classes of carbonaceous material are mainly formed in combustion: nanoparticles with sizes in the range 1-5nm, and soot particles, with sizes from 10nm to 100nm. Chemical and spectroscopic analysis give an indication of the chemical nature of the particles and show that the smaller particles can be thought of as polymer-like structures containing sub-units with aliphatic and aromatic bonds and occasionally oxygen.

The process of soot formation is the coagulation of the 1-5 nm particles, which at the same time adds compounds from the gas-phase and loses H, gaining a higher condensed-ring aromatic or graphitic structure.

Nanoparticles are also found in the exhaust of practical combustion systems. This has been mainly attributed to condensation of low volatility hydrocarbons during dilution and cooling of the exhausts. However, the similarity of the chemical properties and the size distribution functions of the emitted particles with those found in laboratory flames suggests that combustion-formed nanoparticles can escape the combustion process and be emitted into the atmosphere. Thus combustion, as well as the fuel, may have a dominant role in determining the type and amount of particles emitted.

Nanoparticles are present in low mass concentration, but surprisingly high number concentrations due to their very low sizes. The emission of these particles into the atmosphere constitutes a serious concern for health and for their contribution to photochemical smog. The smallest particles play a particularly important role in health since they are able to penetrate deeper than larger particles into the respiratory system. They may also affect the radiation balance of the atmosphere by serving as condensation nuclei for cloud formation and for contrails in the upper atmosphere. For these reasons, the role of combustion-formed nanoparticles is of central interest in the field of atmospheric chemistry. These particles may account for a large part of the organic carbon in urban atmospheres and they might also explain the phenomenon of "nucleation burst" after agglomeration in rain.

Nanoparticles have low coagulation rates at flame temperatures. This interesting behavior may explain why they escape exhaust systems without significant growth at high temperature. The low coagulation rate is due to the weak van der Waals-interactions between particles relative to their thermal energy and it may also be related to the chemical nature of the particles. If oxygen containing functionalities are present in combustion-generated nanoparticles, it is also possible to explain why nanoparticles with sizes below 3nm remain dispersed in water samples in contrast to larger and more graphitic soot particles. The presence of oxygen in nanoparticles is of great importance, and it may also play a role in how these particles affect biological systems.

The low coagulation rate of nanoparticles means that some of them survive for a long time. They undergo atmospheric reactions, and they can also spread to areas

without particle emissions making nanoparticles emitted from combustion systems a global problem.

## ACKNOWLEDGEMENTS

This paper reviews several years of work, and we thank the many graduate students and post-graduate collaborators who contributed through their thesis work. The authors acknowledge particularly the work of A.C. Barone, A. Bruno, M. Commodo and A. De Filippo.

## REFERENCES

1. C.S. Christoforou, L.G. Salmon, M.P. Hannigan, B. Solomon, G.R. Cass, J. Air and Waste Manag. Assoc. 50 (2000) 43-53.
2. EPA, 2004, The Particle Pollution Report: Current Understanding of Air Quality and Emissions through 2003, U.S. Environmental Protection Agency Office of Air Quality Planning and Standards Emissions, Monitoring, and Analysis Division, EPA 454-R-04-002.
3. K.S. Woo, D.Y.H. Chen, D.Y.H. Pui, P.H. McMurry, Aerosol Sci. Technol. 34 (2001) 75-87.
4. G. Oberdörster, E. Oberdörster, J. Oberdörster, Environ. Health Perspect. 113:823-839 (2005), 113 (2005) 823-839.
5. T. Osunsanya, G. Prescott, A. Seaton, Occup. Environ. Med. 58 (2000) 154-159.
6. V. Stone, K. Donaldson, Nature Nanotoxicology, 1 (2006) 23-26.
7. J. Xuejun, X.J. Yin, J.Y.C. Ma, J.M. Antonini, V.A. Castranova, J.K.H. Ma, Toxicol. Sci. 82 (2004) 143-153.
8. V. Castranova, J.Y.C. Ma, H.-M. Yang, J.M. Antonini, L. Butterworth, M.W. Barger, J. Roberts, J.K.H. Ma, Environ. Health Perspect. 109 (2001) 609-612.
9. T. Xia et al., Nano Lett. 6 (2006).
10. A.K. Cho et al., Aerosol Sci. Technol. 38 (2004) 68-81.
11. N. Li et al., Environ. Health Perspect. 111 (2003) 455-460.
12. A. Nel, Science, 308 (2005) 804-806.
13. A.L. Robinson et al., Science, 315 (2007) 1259-1262.
14. L.A. Sgro, L. Speranza, A. Borghese, A. Barone, P. Minutolo, A. Bruno, A. D'Anna, A. D'Alessio, Env. Sci. Technol., in press (2007) ASAP Article, doi: 10.1021/es070485s.
15. A. Borghese, S.S. Merola, Proc. Combust. Inst. 27 (1998) 2101-2109.
16. S.S. Merola, G. Gambi, C. Allouis, F. Beretta, A. Borghese, A. D'Alessio, Chemosphere 42 (2001) 827-834.
17. P. Minutolo, A. Bruno, D. Galla, A. D'Anna, A. D'Alessio. Characterization of nanoparticles formed in gas fuelled burners, in AAA Symposium, 2006, Milan, Italy.
18. A. Bruno, A. D'Alessio, S. Decesari, S. Fuzzi, Chem. Eng. Trans. 10 (2006) 291-302.
19. G. Lanzuolo, A. De Filippo, L.A. Sgro, A.C. Barone, A. Borghese, A. D'Alessio, Environmental Engineering Science, in press (2007) doi:10.1089/ees.2007.0189.
20. B.J. Turpin, P. Saxena, E. Andrews, Atmos. Environ. 34 (2000) 2983-3013.
21. A. D'Alessio, A. D'Anna, G. Gambi, P. Minutolo, J. Aerosol Sci. 29 (1998) 397-409.
22. M. Commodo, S. Violi, A. D'Anna, A. D'Alessio, C. Allouis, F. Beretta, P. Minutolo, Comb. Sci. Technol. 179 (2007) 387-400.

23. P. Minutolo, G. Gambi, A. D'Alessio, S. Carlucci, *Atmos. Environ.* 33 (1999) 2725-2732.
24. L.A. Sgro, A. De Filippo, G. Lanzuolo, A. D'Alessio, *Proc. Comb. Inst.* 31 (2007) 631-638.
25. A.C. Barone, A. D'Alessio, A. D'Anna, *Combust. Flame* 132 (2003) 181-187.
26. A. D'Alessio, A.C. Barone, R. Cau, A. D'Anna, *Proc. Combust. Inst.* 30 (2005) 2595-2603.
27. A. Ciajolo, A. D'Anna, R. Barbella, *Combust. Sci. Technol.* 100 (1994) 271-281.
28. A. D'Alessio, A. D'Anna, A. D'Orsi, P. Minutolo, R. Barbella, A. Ciajolo, *Proc. Combust. Inst.* 24 (1992) 973-980.
29. L.A. Sgro, G. Basile, A.C. Barone, A. D'Anna, P. Minutolo, A. Borghese, A. D'Alessio, *Chemosphere* 51/10 (2003) 1079-1090.
30. R.A. Dobbins, H. Subramaniasivam, in *Soot Formation in Combustion*, H. Bockhorn, (Ed.) 1994, Springer-Verlag, Heidelberg, p. 290-301.
31. R.L. Vander Wal, *Proc. Combust. Inst.* 26 (1996).
32. G. Basile, A. Rolando, A. D'Alessio, A. D'Anna, P. Minutolo, *Proc. Combust. Inst.* 29 (2002).
33. A. D'Alessio, A. Acampora, A. Borghese, I. Borrelli, A. D'Anna, N. Miraglia, P. Minutolo, N. Sannolo, A. Simonelli, L.A. Sgro, Available on request-Final report of an expedited Pilot Study "Toxicological Examination of Combustion-Generated Nanoparticles Smaller than 5 Nanometers", Contract #4702-RFPA03-4/03-14 1.
34. R.A. Dobbins, *Aerosol Sci. Technol.* 41 (2007) 485-496.
35. A. Bruno, C. de Lisio, P. Minutolo, A. D'Alessio, *J. Opt. A: Pure Appl. Opt.* 8 (2006) S578-S584.
36. A. Bruno, C. de Lisio, P. Minutolo, *Opt. Express* 13 (2005) 5393-5408.
37. A. Bruno, F. Ossler, C. de Lisio, P. Minutolo, N. Spinelli, A. D'Alessio, *Opt. Express* 16(8) (2008) 5623.
38. G. Rusciano, A.C. De Luca, A. D'Alessio, P. Minutolo, G. Pesce, A. Sasso, *Carbon*, 46 (2008), 335-341.
39. A. D'Alessio, in *Particulate Carbon Formation During Combustion*, D.C. Siegla, G.W. Smith (Eds.) 1981, Plenum Press, New York.
40. A. D'Alessio, A. D'Anna, P. Minutolo, L.A. Sgro, in *Chemical Engineering Greetings to Prof. Mario Dente*, 1999, AIDIC, ERIS C.T. S.r.l., Milano.
41. A. D'Anna, A. D'Alessio, P. Minutolo, in *Soot formation in combustion: mechanisms and models*, H. Bockhorn (Ed.) 1994, Springer-Verlag, Berlin, p. 83-103.
42. A. D'Alessio, G. Gambi, P. Minutolo, S. Russo, A. D'Anna, *Proc. Combust. Inst.* 25 (1994) 645-651.
43. A. D'Anna, M. Commodo, S. Violi, C. Allouis, J. Kent, *Proc. Combust. Inst.* 31 (2007) 621-629.
44. A. Nakajima, *Bulletin of Chemical Society of Japan* 45 (1972) 1687-1695.
45. T. Joutsenoja, A. D'Anna, A. D'Alessio, M.I. Nazzaro, *Appl. Spect.* 55 (2001) 130-135.
46. B. Zhao, Z. Yang, J. Wang, M.V. Johnston, H. Wang, *Aerosol Sci. Technol.* 37 (2003) 611-620.
47. M.M. Maricq, *Combust. Flame* 137 (2004) 340-350.
48. M. Kasper, K. Siegmann, K. Sattler, *J. Aerosol Sci.* 28 (1997) 1569-1578.
49. G.P. Reischl, J.M. Makela, R. Karch, J. Neid, *J. Aerosol Sci.* 27 (1996) 931-949.
50. W.C. Hinds, *Aerosol Technology*, 2nd ed. 1999, New York, John Wiley & Sons.
51. R.C. Flagan, in *Aerosol Measurement: Principles, Techniques, and Applications*, P.A. Baron, K. Willeke (Eds). 2001, John Wiley & Sons, New York.
52. J. Fernández de la Mora, L. de Juan, T. Eichler, J. Rosell, *Trends in Anal. Chem.* 17 (1998) 328-339.

53. M. Alonso, Y. Kousaka, T. Hashimoto, N. Hashimoto, *J. Aerosol Sci.* 29 (1998) 985-994.
54. J. Fernández de la Mora, L. de Juan, K. Liedtke, A. Schmidt-Ott, *J. Aerosol Sci.* 34 (2003) 79-98.
55. Z. Li, H. Wang, *Phys. Rev. E*, 68 (2003) 061206:1-9.
56. M.J. Sherratt, D.F. Holmes, C.A. Shuttleworth, C.M. Kieley, *Biophys. J.* 86 (2004) 3211-3222.
57. H.-H. Grotheer, H. Pokorny, K.-L. Barth, M. Thierley, M. Aigner, *Chemosphere* 57 (2004) 1335-1342.
58. K.H. Homann, in *Soot Formation in Combustion*, H. Bockhorn (Ed.) 1994, Berlin, Springer-Verlag, 300-301.
59. M. Thierley, H.-H. Grotheer, M. Aigner, Z. Yang, A. Abid, B. Zhao, H. Wang, *Proc. Combust. Inst.* 31 (2007) 639-647.
60. B.U. Lee, S.S. Kim, *J. Aerosol Sci.* 34 (2003) 957-962.
61. J. Jiang, M.-H. Lee, P. Biswas, *J. Electrostatics* 65 (2007) 209-220.
62. F.J. Romay, D.Y.H. Pui, *Aerosol Sci. Technol.* 17 (1992) 134-147.
63. M. Alonso, Y. Kousaka, T. Nomura, N. Hashimoto, T. Hashimoto, *J. Aerosol Sci.* 28 (1997) 1479-1490.
64. F.J. Romay, B.Y.H. Liu, D.Y.H. Pui, *Aerosol Sci. Technol.* 20 (1994) 31-41.
65. F.J. Romay, D.Y.H. Pui, M. Adachi, *Aerosol Sci. Technol.* 15 (1991) 60-68.
66. J. Singh, R.I.A. Patterson, M. Kraft, H. Wang, *Combust. Flame* 145 (2006) 117-127.
67. P. Minutolo, A. D'Anna, A. D'Alessio, *Combust. Flame* 152 (2007) 287-292.
68. S. Stankovich et al., *Nature* 442 (2006) 282-286.
69. D. Lin-Vien, N.B. Colthup, *The Handbook of Infrared and Raman Characteristic Frequencies of Organic Molecules*, 1991, Boston, Academic Press.
70. B.H. Stuart, *Infrared Spectroscopy: Fundamentals and Applications*, 2004, New York, John Wiley & Sons.
71. J.R. Dyer, *Applications of absorption spectroscopy of organic compounds*. 1965, Englewood Cliffs, Prentice Hall.
72. L.D.S. Yadav, *Organic Spectroscopy*, 2005, New Delhi, Anamaya Publishers.
73. J.B. Lambert, H.F. Shurvell, L. Berbit, R.G. Cooks, G.H. Stout, *Organic structural analysis*, 1976, New York, Macmillan Publishing Co.
74. T. Kameda, K. Inazu, H. Bandow, S. Sanukida, Y. Maeda, *Atmos. Environ.* 38 (2004) 1903-1912.
75. D.M. DeMarini, M.L. Shelton, D.A. Bell, *Environ. Mol. Mutagen.* 24 (1994) 262-275.
76. M. Lippmann et al., *Environ. Health Perspect.* 111 (2003) 1074-1092.
77. J.C. Seagrave, J.D. McDonald, A.P. Gigliotti, K.J. Nikula, S.K. Seilkop, M. Gurevich, J.L. Mauderly, *Toxicol. Sci.* 70 (2002) 212-226.
78. D.M. DeMarini, L.R. Brooks, S.H. Warren, T. Kobayashi, M.I. Gilmour, P. Singh, *Environ. Health Persp.* 112 (2004) 814-819.
79. D.U. Pedersen, J.L. Durant, K. Taghizadeh, H.F. Hemond, A.L. Lafleur, G.R. Cass, *Environ. Sci. Technol.* 39 (2005) 9547-9560.
80. N. Miraglia, A. Simonelli, A. Acampora, L. Pascarella, A. D'Alessio, L.A. Sgro, N. Sannolo, *G. Ital. Med. Lav. Ergon.* 27 (2005) 326-328.
81. A. Arenz, C.E. Hellweg, N. Stojicic, C. Baumstark-Khan, H.-H. Grotheer, *Ann. N.Y. Acad. Sci.* 1091 (2006) 170-183.
82. X.Y. Li, K. Donaldson, W. MacNee, *J. Immunology* 169 (2002) 4531-4541.
83. L.S. Hughes, G.R. Cass, J. Jones, M. Ames, L. Olmec, *Environ. Sci. Technol.* 32 (1998) 1153-1161.
84. M.J. Kleeman, J.J. Schauer, G.R. Cass, *Env. Sci. Technol.* 34 (2000) 1132-1142.

# Characterization of particles collected from combustion systems by water-based sampling

P. Minutolo<sup>1</sup>, L.A. Sgro<sup>2</sup>, A. Bruno<sup>3</sup>, A. D'Anna<sup>2</sup>, A. D'Alessio<sup>2</sup>

<sup>1</sup> *Istituto Ricerche sulla Combustione – CNR P.le Tecchio, 80 – 80125 Naples, Italy*

<sup>2</sup> *Dip. di Ing. Chimica, Università di Napoli Federico II, P.le Tecchio, 80 – 80125 Naples, Italy*

<sup>3</sup> *Dip. di Scienze Fisiche, Università di Napoli Federico II, Complesso di Monte S. Angelo, Via Cinzia – 80126 Naples, Italy*

*Abstract: In this paper, sampling of carbon particles based on water interaction is described. The water-sampling allows to selectively collect the fraction of carbonaceous particles having the highest affinity with water.*

*Chemico-physical characterization of the material collected from premixed hydrocarbon flames as water suspension has been performed by optical methods, like light absorption and Laser Induced Fluorescence (LIF), together with Fourier Transform Infrared (FTIR), and Surface Enhanced Raman Spectroscopy (SERS). From these analysis methods the material collected in water samples results to be composed of aromatic-aliphatic linked functionalities and possibly also oxygen atoms. Particle sizes have been investigated by using various techniques, each one gives a relevant piece of information even suffering for some limitations due to the very small size of the species to analyze. Dynamic Light Scattering and electrospray-Differential Mobility Analyser furnished the particle size distribution from the measurement of particle diffusivity in water and mobility in an electric field. Time Resolved Fluorescence Polarization Anisotropy, TRFPA, and Fluorescence Correlation Spectroscopy, FCS, have confirmed the size determination by E-DMA and DLS and they have further demonstrated that the laser induced fluorescence detected in water-sample and in flames by in-situ measurements is emitted by particles with mean sizes of about 2 nm.*

## 1. INTRODUCTION

Several studies, using a variety of techniques, report that particles formed in slightly sooting premixed flames have a bimodal size distribution function [1-6]. The first mode has a mean diameter of about 2-3 nm, while the second one is composed of larger particles with mean diameter on the order of tens of nanometers. It is widely accepted that soot particles constitute the larger mode of flame-generated particles. However, although there is relatively good agreement on the size of incipient particles determined by various measurement strategies, there is not yet a consensus on the origin and chemical nature of the smaller mode, and different interpretations of experimental data have been proposed [1,3]. One interpretation is that the smaller mode derive from continuous soot nucleation [3]. Alternatively, the smaller mode is considered to be composed of a class of particles formed earlier than soot, named Nanoparticles of Organic Carbon, NOC, with chemico-physical properties substantially different from soot [1]. NOC concentration and size do not change sensibly with flame residence time because of a very low coagulation propensity at flame temperature [7].

An exhaustive chemico physical characterization of the particles belonging to the smaller mode (1-3 nm) of the particle distribution function is necessary to shed light on the nature and fate of incipient nanoparticles formed in combustion.

The interest in understanding better the formation mechanisms and chemical nature of particles smaller than 100 nm formed by hydrocarbon combustion is also driven by possible adverse environmental and human health effects of very small carbon particles if emitted in the atmosphere. Even if their total mass is lower respect to the mass of larger particles, their number concentration is large enough to be of concern for possible effects in climate and public health. Moreover these smaller particles might show a water-affinity due their small sizes and their chemical nature hence influencing many important atmospheric processes, like the growth of aerosol particles in presence of water, and the formation of cloud droplets [8-9]. Water affinity is relevant also for possible role in biological effects since it influences particle absorption in human tissues, fluids, and organs as well as translocation throughout the body [10].

Water condensation is a method generally used to grow, capture and concentrate ultrafine atmospheric aerosols [11-13]. We have used for the first time water-based sampling technique to collect combustion formed materials in rich non-sooting ethylene/air flames with C/O equal to 0.61 and 0.71 [14]. The sampling line consisted of a stainless steel water-cooled suction probe followed by a cold trap containing distilled water. Condensable material and substances with a certain affinity for water remain in the water trap while the more hydrophobic compounds pass through to the exhaust. In conditions where large amounts of hydrophobic soot are present, a portion of these particles may also remain in the water trap, but they quickly migrate to the bottom or top of the sample and can be removed. Therefore, sampling through water offers a way to preferentially capture very small particles and organic compounds, which remain suspended in water. The water sampling first developed and tested in hydrocarbon fuel premixed flames, was then also applied to collect organic carbon from practical combustion systems like engines [15, 16] or stationary burners [17-19]. Toxicological analysis of water samples collected from flame and vehicle exhausts has been also performed [16, 20].

The object of this paper is to review the chemico-physical characterization performed on material sampled from premixed hydrocarbon flames as water suspensions.

## 2. EXPERIMENTAL PROCEDURE

Water-based sampling was developed in order to collect the fraction of carbonaceous material with organic functionalities without the interference of the soot particles or PAH species with low solubility in water [14]. The key point of this sampling method is to exploit the effect of water in collecting a particular class, specifically the fraction of the total carbonaceous particulate showing higher water affinity. A suction probe is employed to extract material from the flame or from the exhaust manifold. Extracted material is forced to interact with water, and a sample is eventually collected in the form of a water suspension.

Two mechanisms can be considered for trapping particles in water samples. The first one is based on absorption: a gas sample is bubbled through water, which acts as

an absorbing liquid for small particles and compounds with high solubility in water. The second mechanism is based on condensation: the gas sample is caused to flow through a cold trap, creating a supersaturated environment, and water condensation on cold walls or on hygroscopic and water soluble nuclei enables the scavenging and collection of particles/macromolecules, which remain trapped in the water reservoir. As we will show later, water sampling enables the capture of very small nanoparticles/macromolecules, which would require supersonic flow and extremely high pressure drops to be collected/concentrated by impactors [21] and which seem to escape filters [22, 23].

Various experimental set ups, with slight differences, have been used to perform the water-based sampling. A vacuum pump is used to draw the combustion products through a water cooled stainless steel vertical probe [14] or an horizontal quartz probe [16]. The material extracted from the flame then interacts with combustion-formed water in a condenser cooled with a water based heat-exchanger or by submersion in an ice bath. Alternatively, the sampled exhausts interact with water by bubbling through a reservoir of laboratory grade bi-distilled water. This last set up is preferentially used for isokinetic sampling performed in premixed laboratory flames where the condensation procedure requires very long sampling times compared to the bubbling technique, which collects enough material for off-line analysis in time intervals on the order of one hour. In the last experimental set up, the geometry of the bubblers and the amount of water were chosen so that the residence time of the bubbles in the water is sufficient for particles with sizes of a few nanometers to diffuse to the interface between the gas and sampling water. Figure 1 reports a typical experimental set up.

In order to remove volatile compounds dissolved in water, the samples are partially evaporated under low pressure. During evaporation, performed by continuously reducing pressure from the atmospheric one to few millibar, we observe that the pressure reduces down to about 200-100 mbar, where it remains constant while a boiling stage is observed. The boiling stage is rapid, and the amount of liquid before and after the bubbling is observed is relatively constant. This boiling stage is particularly evident for the samples obtained by bubbling in water instead of condensing the exhausts and can be attributed to the removal of gaseous species like  $\text{CO}_2$  and semivolatile organic species. After the boiling stage, the pressure continues to decrease down to a value on the order of tens of mbar, where it remains almost constant and the volume of liquid decreases at a rate of about 50 cc/hour.

### 3. COLLECTION EFFICIENCY

In previous papers the efficiency of water sampling was estimated to be of the order of few percent [24]. This estimate was given by comparing the amount of material present in the flame and the amount of material collected in water, which were determined from the measurements of light absorption in the UV. The estimated efficiency was given by the product of two efficiencies: the first one is the efficiency in capturing particles by means of the interaction between the aerosol flow and water; the second one is the particle collection efficiency by the probe and sampling

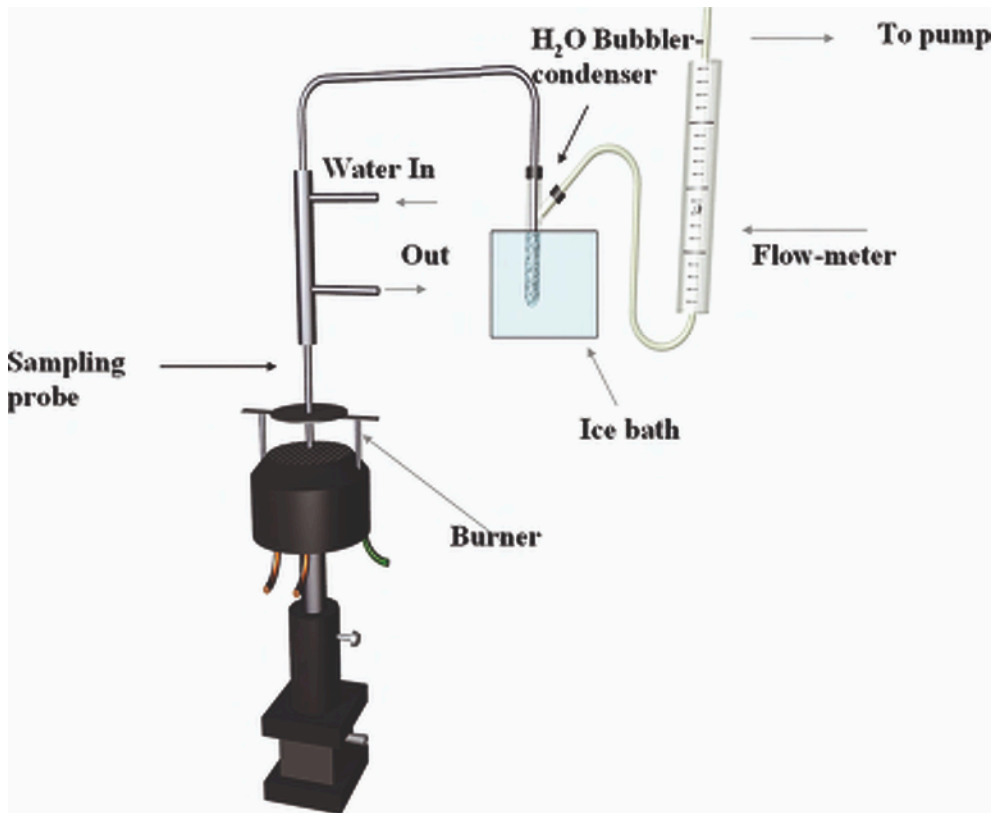


Figure 1. Typical experimental set-up for water-sampling.

line. It is, in fact, expected from aerosol dynamics that a significant amount of nanoparticles is lost to the walls in the water cooled probe and throughout the entire sampling line.

In order to estimate only the effect of water interaction on collecting particles with mean sizes smaller than 10nm, we inserted a DMA (Tapcon) downstream of the bubbling reservoir in the experimental set-up reported in Figure 1 and measured the size distribution of particles present in the sampled gases, in three conditions: without the condenser/bubbler in the sampling line, with the empty condenser/bubbler in the ice bath, and with the condenser/bubbler filled with 8 ml of deionized water and positioned in the ice bath. The three size distributions are reported in Figure 2, as a function of the diameter evaluated from the measured electrical mobility as reported in ref. [4]. In the same figure, the curve obtained measuring ambient air through the sample line with the empty bubbler when the flame was off is also reported for comparison.

The size distribution of the particles in the sampled gases which arrive to the DMA, when the cooled condenser is not inserted into the line, present a peak between

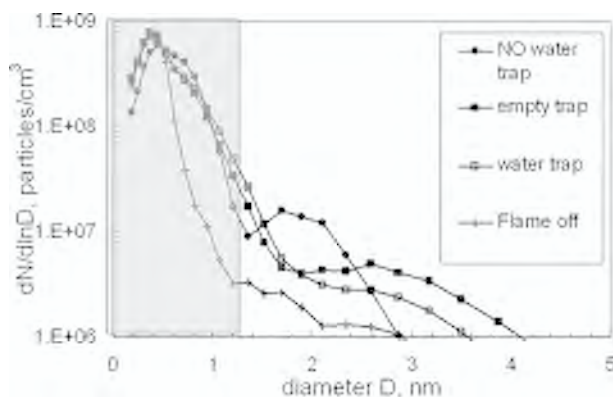


Figure 2. Number distribution of particles sampled from an ethylene/air flame,  $C/O=0.58$ , as function of particles diameter. Full circles:  $dN/d\ln D$  measured without inserting the trap into the line; full squares  $dN/d\ln D$  measured with the empty trap into the line; empty squares:  $dN/d\ln D$  measured with the water trap into the line; crosses:  $dN/d\ln D$  measured with the flame off as a background.

2-4nm. When the empty condenser placed in an ice bath is inserted into the line, the mean particle size become larger than 3 nm, the number concentration decreases, and the total mass of particles decrease by about 20%. The additional time spent in the condenser/bubbler, and the lower temperature experienced within the condenser may enhance particle coagulation, causing the increase in particle size and reduction in number concentration, and also heterogeneous condensation of low vapor pressure gases on already existing particles which causes the increase in particle size. The reduction in the total mass of particles, however, cannot be due to these effects, and instead indicates losses that occur in the condenser/bubbler.

The size distribution measured after adding 8 ml of deionized water into the condenser does not shift notably in size, but its amplitude considerably reduces.

The efficiency of particle collection due to the interaction with water can be estimated from the size distribution function of the particles in the gas flow entering the DMA with and without the water in the reservoir by measuring the reduction in the total number,  $\Delta N/N$ , or volume fraction,  $\Delta f_v/f_v$  of the particles produced by the presence of water. Comparable results are obtained for both efficiencies so defined, of the order of 40%.

#### 4. LIGHT ABSORPTION AND FLUORESCENCE SPECTROSCOPY

Light absorption and fluorescence have been employed to investigate the chemical structure of the material sampled by water-sampling.

The spectroscopic characteristics of the sampled material suspended in water, determined by UV-visible light absorption and Laser Induced Fluorescence techniques are quite similar to those measured “in situ” in non-sooting laminar premixed hydro-

carbon flames [14, 24]. In particular, UV absorption spectrum of water-sampled material has a maximum around 200 nm and decreases very fast in the near UV. It is completely different from the typical absorption spectrum due to soot, which exhibits a broad maximum at 250 nm and decreases toward the visible with an inverse power law [25]. In the as-collected samples, i.e. water-samples not subjected to any evaporation procedure or thermal treatment, a few absorption bands are generally measured superimposed to the continuous absorption curve. These peaks have been attributed to light aromatic molecules suspended in water, like benzene and naphthalene, which are quite abundant in flame and, among the PAH class, have the highest solubility in water [14]. The intensity of these bands decreases when the water-sample is subjected to the degassing process by means of a rotary evaporator as can be observed in Figure 3 where the absorption curve measured in the as-collected sample and in the same sample after evaporating are reported.

The presence of small PAH is even more evident in fluorescence spectra, as can be observed in Figure 4. Using an UV excitation source, the fluorescence emission of as-collected samples is composed of a broad band in the UV, and a smaller one in the visible spectral range. This last band is also emitted when excitation wavelength in the visible ( $\lambda > 400\text{nm}$ ) is used. In the UV, the as-collected samples present structured bands typical of PAH-like molecules [24]. The intensity of the peaks with respect to the broadband backgrounds is dependent on the flame conditions and the details in the sampling set up, like temperature of the collecting water or the use of a bubbler or condenser for sampling. The molecular species responsible for the structured peaks in absorption and fluorescence spectra can be removed from the sample by using a rotary evaporator under low pressure. In fact, the absorption and fluorescence spectra of the water-sample subjected to evaporation do not present structures

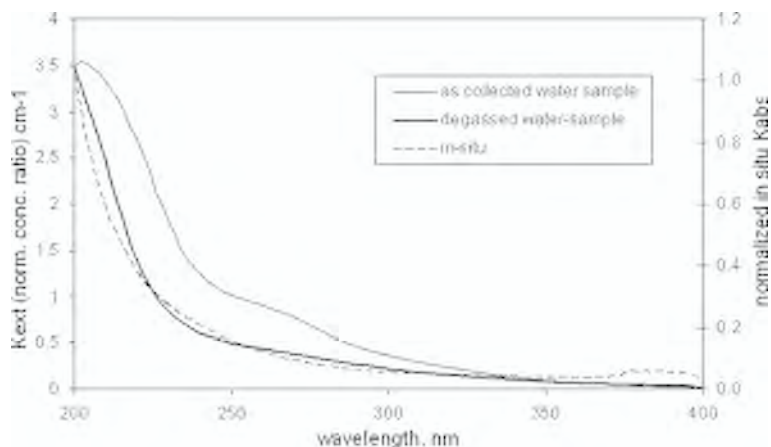


Figure 3. Light absorption spectra of the water-sampled material from the ethylene/air flame,  $C/O=0.65$   $z=5\text{mm}$ , measured in diluted samples and normalized for dilution. Thin line: spectrum of the as collected sample; thick: spectrum of the degassed sample; dashed line: Light absorption spectrum measured in-situ [16].

anymore while the broad profile remains substantially unchanged as can be observed in Figures 3 and 4. This is a proof of the attribution of peaks in the absorption and fluorescence spectra to molecular species instead of particles and of the attribution of the broad background to compounds which are not removed by evaporation under low pressure.

The broadband spectrum in the degassed sample is very similar to the fluorescence spectra measured “in situ” in hydrocarbon flames also reported in Figure 4.

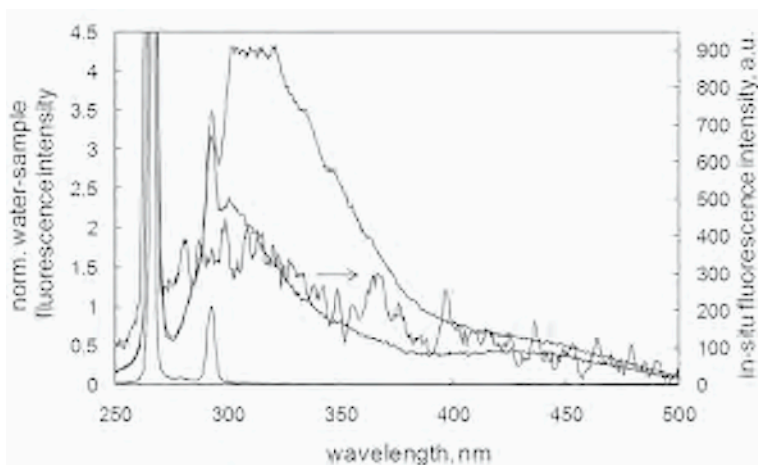


Figure 4. Laser Induced fluorescence spectra of the water-sampled material from the ethylene/air flame, C/O=0.65  $z=5\text{mm}$ , normalized by the intensity of the Raman band of water at 292nm.  $\lambda_{\text{exc}}=266\text{ nm}$ . a: spectrum of the as collected sample; b: spectrum of the degassed sample; c: LIF spectrum measured in situ in the same flame; d: LIF spectrum of pure water.

## 5. TOTAL ORGANIC CARBON MEASUREMENT

The amount of organic carbon contained in the water-sample was measured with a Shimadzu TOC-5000A analyzer. Measurements performed in samples taken from ethylene/air flames with various C/O ratios ranging from C/O=0.56 to C/O=0.92 have shown that the as-collected samples have a total organic carbon, TOC, content much higher than the evaporated samples, and in the evaporated samples, the TOC amount is roughly proportional to the absorption coefficient. At the wavelength of 266 nm the proportionality factor, measured from the sample taken in the flame with C/O=0.65, is about  $K_{\text{abs}}/M_{\text{TOC}}=4.3 \times 10^4\text{ cm}^2/\text{g}$ . Considering particle density of  $1\text{ g}/\text{cm}^3$ , from this ratio, the  $E(m)$  factor in the Rayleigh expression of light extinction is estimated to be  $E(m_p)=K_{\text{abs}}/f_v \cdot (\lambda/6\pi)=0.044$  where  $m_p$  is the imaginary refractive index of particles relative to water and  $\lambda$  is the light wavelength in the water. This value for  $E(m_p)$  is consistent with the value of refractive index usually employed for nanoparticles in non sooting in flame  $m=1.35-i0.09$  [26].

## 6. PARTICLE SIZE DISTRIBUTION

The presence of nanometer size particles in aqueous samples collected from flames was demonstrated for the first time by means of Dynamic Light Scattering, DLS, and electrospray-Differential Mobility Analyser, e-DMA [26]. DLS furnishes the distribution function of translational diffusivity of particles in a medium by measuring fluctuations in the intensity of scattered light, which are caused by the Brownian motion of particles in the scattering probe volume. Under the assumption that the scattering particles behave as hard spheres in a dilute solution, the particle radius distribution function is then calculated from the diffusivity distribution function using the well-known Stokes-Einstein equation. The size distribution function of the particles collected in water from the center of an ethylene/air (C/O=0.65) flame 5 mm above the burner surface was found to be approximately lognormal ranging from 2 to 4 nm with  $\sigma=1.2$ , and median diameter of about 2.5 nm [26].

A in-house-built electrospray source was used to dry and positively charge the solute material in the water sample which was then transported to a DMA, which measures the electrical mobility distribution of the sample as an aerosol immersed in a gas rather than a suspension in water. The semi-empirical equation reported by Fernández de la Mora, et al. [27] has been used to calculate the size distribution of the particles in terms of actual diameter. The electrospray was operated in cone-jet mode producing very small droplets, of the order of tens of nanometers, so that unwanted effects of agglomeration during spray were reduced. Furthermore, a drawback of electrospray process is to produce dimers of the analyte particles during the drying of the droplets. To reduce this effect, we operated with very dilute concentrations, so that most of the spray droplets contained a single analyte particle and the dried electrospray products were prevalently monomers.

We used a corona ionizer, which produce negative ions in a nitrogen flow with a variable concentration as a function of the applied voltage. The operative conditions were optimized for reducing the charge of the particles to one.

The DMA was run with a high carrier gas flow rate (50 l/min) in order to reduce diffusional effects, and a condensation nuclei counter, CNC, which grows positively charged nanometer and subnanometer particles to a detectable size ( $>0.3 \mu\text{m}$ ) was used as detector [28]. A typical size distribution function measured by e-DMA is reported in Figure 5. The size distribution measured by charge-neutralized E-DMA unambiguously gives the size of the particles contained in the sample, and from the peak area, the concentration of particles in the spray solution can be determined.

Unlike standard solutions of pure polymers with a single molecular weight, we observed that the size of the combustion products shifts slightly toward larger sizes with increasing concentration. This effect could be because of a slightly increase of the electrospray droplet size brought about because of changing fluid properties or due to the polydispersity of the sample, which contains both large particles and smaller molecules (on the order of 100 amu), the latter of which are likely responsible for the slight shifting at higher concentrations.

The modal diameter measured by E-DMA was in the same range of that measured for macromolecules with a molecular weights on the order of 1000-2000 amu. We calibrated the signal using a pure standard with a singular molecular weight of 1400 amu,

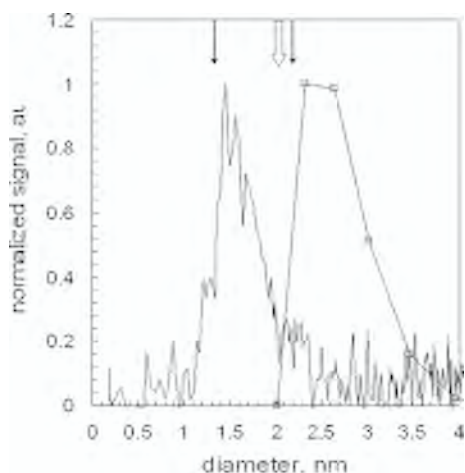


Figure 5. Normalized distribution function of the water-sampled material from the ethylene/air flame,  $C/O=0.65$   $z=5\text{mm}$ , measured by e-DMA (line), DLS (empty squares) as function of particles diameters. Mean sizes of the fluorescing particles measured by TRFPA (black arrows) and FCS (white arrow) are also reported.

measured with the same spray and DMA, to determine the quantity of particles measured by E-DMA from the combustion samples. The concentration of non volatile species determined by E-DMA, and of total organic carbon in the sample determined by TOC-analysis, were in agreement within a factor of two with the particles concentration determined by  $K_{\text{abs}}$ . This is a reasonable agreement considering the differences in concentration and related errors for each of these techniques [16].

The size distribution of particles sampled in the flame with  $C/O=0.65$  measured with e-DMA is reported in Figure 5 in comparison with the DLS result. The distribution function measured by e-DMA shows a single mode ranging from 1 to 3nm, which seems significantly smaller than that one measured by DLS, ranging from 2 to 4 nm. Nevertheless, none of these measurements gives the geometric diameter of the particles and the two size determinations should be compared with caution. DLS measures diffusion properties of an ensemble of particles and, following a sophisticated inversion procedure, provides an estimate of the distribution function of the hydrodynamic radius of the particles, which is the radius of a hypothetical hard sphere that diffuses in the medium with the same rate as the particle under examination. DLS is based on light scattering which depends on the sixth power of particle diameter, so that larger particles are detected more efficiently than smaller one, and a diameter of 1 nm was approximately the detection limit of the employed DLS set up so that it is possible that the smaller part of the particles distribution function was not detected by the instrument. Furthermore, for particles measured in a liquid medium, the possible solvation shells that can form around the particles, which depend on the surface functional groups also can influence the measured diffusion coefficients furnishing an overestimate of particle size. On the other side, DMA measures the electrical mobility of the particles from which mobility diameter, and finally actual particle diameter can be

derived under a series of approximations [3, 27]. Electro spray-DMA can erroneously measure a larger diameter because of residual water molecules or impurities which can agglomerate on particles during drying process or because of incomplete evaporation, but it does not measure a diameter that is smaller than that expected and it does not break chemical bonds [29]. The comparison with DLS result allows us to exclude that significant agglomeration occurred in the E-DMA measurement. Nevertheless, during the drying process particles are subjected to strong forces, which likely influence the shape of the dried particles. Proteins and polymers, which may be non-spherical in the liquid phase are forced into a spherical shape when they are dried by electro spray at atmospheric conditions [30]. The larger diameter measured in DLS compared to E-DMA may indicate that the particles are more expanded or non-spherical or have a layer of water molecules attached to them in solution. We can further consider that we had to use highly diluted samples in order to obtain single particles per droplet in the E-DMA measurements. As a consequence, the sensitivity of the measurements was quite poor and it was impossible to detect the presence of particles when their concentration was less than 20% lower than the maximum. It is, therefore, possible that the larger particles measured by DLS are in lower concentration than the smaller particles measured by E-DMA, and below the detection limit of E-DMA. In fact a small hump is noted at 2-2.5 nm, which is practically within the noise of the measurement while the smaller particles detected by E-DMA are below the lower size detection limit of DLS, and are therefore not detected by DLS.

Two other optical methods, Time Resolved Fluorescence Polarization Anisotropy, TRFPA, and Fluorescence Correlation Spectroscopy, FCS, were also used to measure the size of species collected in water samples from flames [16, 31]. Both TRFPA and FCS selectively investigate only particles that can absorb light and emit fluorescence at a fixed wavelength. Similar to DLS, these measurements were performed in the water medium. FCS and TRFPA determined the size of fluorescing particles from the measured translational or rotational diffusion coefficient, respectively.

TRFPA technique consists in irradiating an ensemble of particles in a medium with ultrafast, linearly polarized, laser pulses and measuring the time evolution of the two polarization components (parallel and orthogonal to the excitation field) of the fluorescence emission. Fluorescence emission is initially polarized as the laser beam, since the particles with transition moment parallel to the polarization vector of the incident light are preferentially excited. Afterwards, rotations of the molecules due to their Brownian motion give rise to a component of fluorescence light orthogonal to the excitation field and, finally, fluorescence emission becomes depolarised. The characteristic time of the process is dependent on the rotational diffusivity of the fluorescing species, from which the volume of the fluorescent structure is determined applying the well-known Stokes-Einstein-Debye equation. A detailed description of this technique is reported in the book of Lakowicz [32].

TRFPA analysis performed on water-samples collected in rich flames with C/O above and below the soot threshold, demonstrated that fluorescence bands emitted by the samples are due to particles with mean size of the order of 2nm [31].

Excitation wavelengths at 266 nm and 400 nm have been employed to selectively measure the sizes of species fluorescing prevalently in the UV or in the visible band. In all samples, particles with average diameter of about 1.5 nm that emit a fluorescen-

ce band in the UV at 330 nm, when excited at 266 nm, are present. The anisotropy of the fluorescence excited and emitted in the visible exhibits a longer decay time compared to that emitted in the ultraviolet, thus indicating that larger nanoparticles are responsible for this emission. Their volume is more than twice that of the UV-emitting species and the mean diameter is about 2-2.5 nm [31]. The two classes of particles detected in the water-sample collected in the ethylene/air flame with C/O=0.65 are reported in Figure 5 as black arrows. The red shift of the fluorescence emitted by the larger particles respect to the fluorescence emitted by the smaller ones, may be due to the presence of larger aromatic chromophores, with more than three condensed rings, inside the particles, as was previously hypothesized by the analysis of in situ- LIF spectra [33]. However, we cannot rule out that this class of particles is formed from the aggregation of about 3-4 of the smaller UV fluorescing particles, which gives rise to a delocalisation of  $\pi$ -electrons over a larger area and consequently produces a red-shifts of the fluorescence emission. It is well known that particles with sizes of 1-3 nm are present in ethylene/air rich flames and have been measured by on-line DMA employing high dilution of the sample to avoid condensation and particle coagulation [3, 4]. Similar sizes have also been measured within the sampling line used for water-sampling downstream the probe, as can be seen from the full circle curve in Figure 2. Nevertheless, we cannot asses with certainty if the visible fluorescing, larger particles, measured in the water are produced in flame or in the sampling line.

Fluorescence Correlation Spectroscopy, FCS, determines particle translational diffusivity by measuring the fluctuations in fluorescence intensity emitted by the molecules contained within a probe volume of the order of fl. Such fluctuations are caused by the Brownian motion of the particles, which determine molecules entering and leaving the excitation volume during the measurements, and provide information on diffusional properties of the fluorescent molecules. From translational diffusivity, the diameter of the particles is eventually derived by the Stokes-Einstein equation. FCS measurements have been performed on water-sample collected from various ethylene/air flame using a Zeiss-EVOTEC ConfoCor inverted confocal microscope with the excitation wavelength of 488 nm. The value of the particle size determined for the sample collected in the flame with C/O=0.65 is reported in Figure 5 as a white arrow. The result is comparable to that one measured by TRFPA with the excitation wavelength in the visible.

It is interesting to note that although the water-sampling-system induces condensation and particle coagulation forming also particles larger then 3nm (see Figure 2), those particles were not observed from the sizing methods employed for water-sample analysis. One possible explanation is that water condensation on particles in the gas stream is the prevailing effect for the shift in PDF operated by the sampling line, and this effect does not influence the real particle size when suspended in water.

## 7. FTIR AND SURFACE ENHANCED RAMAN SPECTROSCOPY

In situ optical measurements performed in non-sooting rich hydrocarbon flames suggested for the first time that nanoparticles are composed by 1-, 3-ring aromatic groups connected by aliphatic groups and oxygen functionalities [1, 33]. The aliphatic matrix in the

particles is consistent with the light absorption band measured in the far UV with the maximum below 200 nm. The aromatic functionalities are responsible for the shape of the fluorescence spectra while the aliphatic component justifies the low quantum efficiency measured in flame and in water sampled material [1, 24, 33]. In fact, aromatic-aliphatic linked particles have a less rigid structure than pericondensed PAHs, with a consequent lower quantum efficiency having a higher number of non radiative energy dissipation channels.

The presence of aliphatic bondings in the particles collected by water sampling has been recently demonstrated by Fourier transform infrared spectra, FTIR, measured after deposition of these particles on KBr pellets [34] (see also Figure 12 in the paper by D'Alessio, et al in this book [35]). FTIR spectra of water-sampled particles present significant features in the range between 600 and 1600  $\text{cm}^{-1}$  and between 2800 and 3100  $\text{cm}^{-1}$ . It is quite interesting to note the relative sharpness of the observed absorption peaks with respect to that obtained in the investigation of soot and other amorphous carbon materials, whose spectra are characterized by broad absorption bands [36]. It seems to suggest the molecular character of the carbonaceous structures in the water samples collected from flames, which are in the transition region between large molecules and particles. Several peaks evidence the presence of aliphatic  $\text{CH}_n$  groups. The analysis of various samples collected in flames with different C/O ratio evidenced the reduction in the  $\text{sp}^2$  aliphatic component with respect to the  $\text{sp}^3$  one with increasing C/O ratios. It was interpreted as due to a reduction in the length of aliphatic chain in particles sampled from richer flames.

Further information on particle composition was derived from Surface Enhanced Raman Spectroscopy, SERS, performed on the water-sample collected in an ethylene/air flame with C/O=0.6 which was deposited on SERS substrates made of Ag coated glass microspheres [37]. Raman bands usually detected in amorphous carbon have been detected, the first one is denominated the G band and indicates the presence of graphitic areas in the particles, the second band is denominated as Disorder band, is composed by various peaks, and indicate the presence of structural disorder in the material. The analysis of the band shapes, which are well described by Gaussian instead of Lorentzian line-shape functions, was interpreted as indicative of a sample heterogeneity due to a statistical distribution in the particles compositions. Another valuable piece of information obtained by SERS was the detection of various peaks due to oxygen bondings present in the sample. This evidence is in agreement with the FTIR spectrum of a water-sample reported by D'Alessio et al. [35].

## 8. MUTAGENICITY AND REACTIVITY TESTS

Various water-samples collected from ethylene/air non sooting flames and at the exhausts of diesel and gasoline engines have been object of mutagenicity and the reactivity tests [20]. These experiments are discussed in the contribution to this book by D'Alessio et al. [35], and are here briefly repeated to give a complete view on the analysis of water-sampled material from combustion sources.

Mutagenicity was tested following the Ames Test, with and without metabolic activation. Reactivity was investigated by using a new approach aimed to identify electro-

philic agents present in the sample material, which, if introduced into the organism, could interact with nucleophilic sites of biological macromolecules (DNA and proteins), forming adducts. Given the large number of nucleophilic sites within biological macromolecules, the complexity and partial knowledge of the chemical structure of water-sampled species, this approach was simplified by examining *in vitro* interactions between water-sampled particles and model peptides through Liquid Chromatography/Mass Spectrometry analyses of incubation mixtures.

The results indicated a high reactivity and, in several cases, the mutagenicity of water-samples, thus calling for suitable biomarkers to assess nanoparticle exposure associated with combustion emissions.

Further biological analysis have been also performed to test cell vitality using mouse embryo fibroblasts NIH3T3 by a colorimetric assay (AlamarBlue, BioSource).

After incubation at 37°C for 1-3 hours of a suspension of water-samples, dramatic cell morphology changes were observed. In fact, cells treated with particles were rounded with great vacuoles inside, compared to well-spread control cells. By confocal microscopy analysis, treated cells appeared more fluorescent than control ones indicating possible cellular uptake. In addition, a dose/response test using the Alamar blue assay showed cytotoxicity of the material water-sampled from the engine exhausts.

## 9. CONCLUSIONS

In this paper, sampling of the fraction of carbonaceous particles produced in flame which have the highest affinity with water has been described as well as the chemico-physical analysis performed for its characterization.

Water assisted particulate sampling has been developed with the aim to collect the organic fraction of particulate carbon, which has a higher affinity with water compared to larger more graphitic and hydrophobic particles. Although the sampling procedure has not been optimized yet, the basic principles have been here discussed and a first estimate for the efficiency of water effect in capturing nano-size particles have been reported. Further work is needed to better understand the water sampling efficiency and how condensation of low vapour pressure species on particles and particle coagulation affect the efficiency of the sampling procedure.

Sampling in water has enabled to use various advanced *ex situ* methods for particle characterization. Beside Light Absorption and Laser Induced Fluorescence, FTIR and SERS have given valuable information on the chemico-physical composition of the sampled material. All of these methods indicate that the material collected in water samples is composed of aromatic-aliphatic linked functionalities and possibly also oxygen atoms. Various techniques have been used to measure the size of the material collected in water samples from flames. Each method gives a relevant piece of information even suffering for some limitations due to the very small size of the species to analyze. DLS and e-DMA allowed to measure the particle size distribution function giving complementary results in reasonable agreement, they have shown for the first time the presence of nanometric particles in these samples. Advanced Optical sizing methods like TRFPA and FCS have also confirmed the size determination by E-DMA and DLS and they have further demonstrated that the same particles present in water

are the species responsible for in-situ laser induced fluorescence. Those species which can be excited in the visible and emit fluorescence above 400nm are sensibly larger than the UV fluorescing species. Even though the fluorescence band in the visible is usually detected in flame, it is more evident in the water-samples collected from flames. Enhancement of the fluorescence band in the visible could be a consequence of the lower temperature or the presence of the water medium, but we can not completely exclude that it may be due to particle transformations that occur in the sample line by condensation or coagulation. Further analysis is needed to investigate the fate of particles following sampling procedure. Relevant information will be obtained with the use of spectrally resolved TRFPA technique in situ to measure the size and spectroscopic properties of the particles produced in premixed flames and their evolution with residence time during the soot inception process. The developing of this in situ technique is only at its beginning and preliminary measurements have been performed in Bunsen-type propane diffusion flames [38].

The affinity with water of combustion produced nanoparticles are relevant for the possible climate and biological adverse effects they can produce if emitted in the atmosphere. A first study for biological effects of water-samples have shown that particles captured by water are reactive with various biological assays. Further analysis are needed to quantify their possible role in human health effects or climate change.

## REFERENCES

1. A. D'Alessio, A. D'Anna, A. D'Orsi, P. Minutolo, R. Barbella, A. Ciajolo, *Proc. Combust. Inst.* 24 (1992) 973-980.
2. A. D'Alessio, A.C. Barone, R. Cau, A. D'Anna, P. Minutolo, *Proc. Combust. Inst.* 30 (2005) 2595-2603.
3. B. Zhao, Z. Yang, M.V. Johnston, H. Wang, A.S. Wexler, M. Balthasar, M. Kraft, *Combust. Flame* 133 (2003) 173.
4. L.A. Sgro, A. De Filippo, G. Lanzaolo, A. D'Alessio, *Proc. Combust. Inst.* 31 (2007) 631-638.
5. J.P. Hessler, S. Seifert, R.E. Winans, *Proc. Combust. Inst.* 29 (2002) 2743-2748.
6. M.M. Maricq, *Combust. Flame* 137 (2004) 340-350.
7. P. Minutolo, G. Gambi, A. D'Alessio, S. Carlucci, *Atmos. Environ.* 33 (1999) 2725-2732.
8. T. Novakov, J.E. Penner, *Nature* 365 (1993) 823-826.
9. C.A. Rivera-Carpio, C.E. Corrigan, T. Novakov, J.E. Penner, C.F. Rogers, J.C. Chow, *J. Geophys. Res.* 101 (1996) 19483-19493.
10. G. Oberdorster, Z. Sharp, V. Atudorei, A. Elder, R. Gelein, W. Kreyling, C. Cox, *Inhalation Toxicology* 16 (2004) 437-445.
11. P. Demokritou, T. Gupta, S. Ferguson, Koutrakis, *P. Inhal. Toxicol.* 15 (2) (2003) 111-129.
12. S. J. Kim, P. A. Jaques, M. Chang, T. Barone, C. Xiong, S. K. Friedlander, C. Sioutas, *J. Aerosol Sci.* 32 (11) (2001) 1299-1314.
13. C. Sioutas, P. Koutrakis, J. J. Godleski, S. T. Ferguson, C. S. Kim, R. M. Burton, *J. Aerosol Sci.* 28 (6) (1997) 1057-1071.
14. A. D'Alessio, A. D'Anna, G. Gambi, P. Minutolo, *J. Aerosol Sci.* 29 (1998) 397-409.

15. A. Borghese, S.S. Merola, *Proc. Combust. Inst.* 27 (1998) 2101-2109.
16. L.A. Sgro, A. Borghese, L. Speranza, A.C. Barone, P. Minutolo, A. Bruno, A. D'Anna, A. D'Alessio, *Environ. Sci. Technol.* 42 (2008) 859-863.
17. P. Minutolo, A. D'Anna, M. Commodo, R. Pagliata, G. Toniato, C. Accordini, *Environ. Eng. Sci.*, in press (2008).
18. P. Minutolo, A. Bruno, D. Galla, A. D'Anna, A. D'Alessio, *Chemical Engineering Transactions* 10 (2006) E. Ranzi (Ed.).
19. S.S. Merola, G. Gambi, C. Allouis, F. Beretta, A. Borghese, A. D'Alessio, *Chemosphere* 42/3-4 (2000) 375-382.
20. A. D'Alessio, A. Acampora, A. Borghese, I. Borrelli, A. D'Anna, N. Miraglia, P. Minutolo, N. Sannolo, A. Simonelli, L.A. Sgro, Available on request-Final report of an expedited Pilot Study "Toxicological Examination of Combustion-Generated Nanoparticles Smaller than 5 Nanometers", Contract #4702-RFPA03-4/03-14 1.
21. J. F. Fernández de la Mora, S. V. Hering, N. Rao, P. H. McMurry, *J. Aerosol Sci.* 21(2) (1990) 169-187.
22. C. S. Kim, L. Bao, K. Okuyama, M. Shimada, H. Niinuma, *J. Nanopart. Res.* (2006) 8: 215-221.
23. H.C. Wang, G. Kasper, *J. Aerosol Sci.* 22 (1991) 31-41.
24. L.A. Sgro, P. Minutolo, G. Basile, A. D'Alessio, *Chemosphere* 42 (2001) 671-680.
25. A. D'Alessio, F. Beretta, C. Venitozzi, *Combust. Sci. Technol.* 5 (1972) 263-272.
26. D. Cerere, L.A. Sgro, G. Basile, A. D'Alessio, A. D'Anna, P. Minutolo, *Combust. Sci. Technol.* 174 (2002) 377-398.
27. J. Fernández de la Mora, L. de Juan, K. Liedtke, A. Schmidt-Ott, *J. Aerosol Sci.* (2003) 34:79-98.
28. L.A. Sgro, J. Fernandez de la Mora, *Aerosol Sci. Technol.* 38 (2004) 1-11.
29. J.B. Fenn et al., *Science* 246 (1989) 64-71.
30. J. Fernandez de la Mora, *Anal. Chim. Acta* 406 (2000) 93-104.
31. A. Bruno, C. de Lisio, P. Minutolo, A. D'Alessio, *Combust. Flame* 151(3) (2007) 472-481.
32. J.R. Lakowicz, *Principles of Fluorescence Spectroscopy*, Kluewer Academic/Plenum Publisher, New York, 2002, p. 291.
33. P. Minutolo, G. Gambi, A. D'Alessio, A. D'Anna, *Combust. Sci. Technol.* (1994) 101:311-325.
34. G. Rusciano, G. Cerrone, A. Sasso, A. Bruno, P. Minutolo, *Appl. Phys. B* 82 (2006) 155-160.
35. A. D'Alessio, A. D'Anna, P. Minutolo, L.A. Sgro, in *Combustion Generated Fine Carbonaceous Particles*, H. Bockhorn, A. D'Anna, A.F. Sarofim, H. Wang (Eds.) Karlsruhe University Press, 2009, pp. 205-230.
36. J.F. Widmann, J.C. Yang, T.J. Smith, S.L. Manzello, G.W. Mulholland, *Combust. Flame* 134 (2003) 119.
37. G. Rusciano, A.C. De Luca, A. D'Alessio, P. Minutolo, G. Pesce, A. Sasso, *Carbon* 46 (2) (2008) 335-341.
38. A. Bruno, F. Ossler, C. de Lisio, P. Minutolo, A. D'Alessio, *Opt. Express* 16 (8) (2008).



# Molecular dynamics simulations of PAH dimerization

D. Wong, R. Whitesides, C.A. Schuetz, M. Frenklach

*Department of Mechanical Engineering, University of California, and Environmental Energy Technologies  
Division, Lawrence Berkeley National Laboratory, Berkeley, CA 94720, USA*

*Abstract: In pursuit of mechanistic understanding of soot nucleation, collisions between aromatic molecules were investigated using molecular dynamics (MD) simulations with on-the-fly quantum forces. Simulations were conducted at a temperature of 1600 K, with vibrationally and rotationally equilibrated colliders, investigating the formation of dimers for a series of aromatic hydrocarbons. Colliders of aromatic molecules linked by aliphatic chains (AALH) were examined and compared to those of peri-condensed aromatics (PCAH). Numerical results indicated that molecules as small as biphenyl can produce dimers with lifetimes comparable to larger-size PCAH molecules. The dominant trend is an increase in the dimer lifetime with an increase in molecular mass. However, while the smaller AALH dimers seem to follow the same trend with the dimer mass as seen for the PCAH dimers, the larger AALH dimers appear to have substantially lower lifetimes than the PCAH ones of comparable mass. The obtained trends appear to be in accord with past and recent experimental observations and associated interpretations given by the corresponding authors.*

## 1. INTRODUCTION

Polycyclic aromatic hydrocarbons (PAH) are widely accepted to be the chemical precursor to soot [1-6]. Numerous experimental studies confirm that soot is composed of PAHs with weights ranging from hundreds to thousands of amu. However, the exact nucleation mechanism by which gas-phase PAHs are transformed into solid soot particles is not well understood.

One of the possibilities advanced in the literature is PAH clustering: formation of dimers, trimers, and so on, of PAH moieties [6-8]. In the previous study [9], the feasibility of PAH to form van der Waals dimers was investigated by performing molecular dynamics (MD) simulations of collisions between pyrene molecules. At temperatures around 1600 K, it was found that collisions between pyrene molecules form dimers of significant lifetimes. The MD runs in that initial study [9] were performed with the molecules prepared rotationally cold, to emphasize the key mechanistic feature identified – trapping energy in internal rotations developed upon collision.

In the present study, the numerical simulations were performed with monomer molecules rotationally equilibrated. We simulated collisions between PAH molecules by explicitly considering the molecular structure and internal molecular motions using a technique of molecular dynamics with quantum forces that are computed “on-the-fly” [10]. This method allows us to examine, in a physically realistic way, the dynamics of energy transfer between external and internal degrees of freedom.

The initial study [9] focused on dimerization of pyrene because of the species exceptional stability and suggested role in initiating particle nucleation [6]. In the present study, we investigate the effects of monomer size on the dynamics of PAH collisions to further explore the phenomena of PAH dimerization and the role it may play in soot nucleation. With this in mind, collisions were extended to include PAH as small as naphthalene and as large as coronene. Additionally, we explored the effect of radicals on PAH dimerization with collisions between pyrene and its radical.

One of the principal conclusions of the previous study [9] was that the mechanism of PAH dimerization is in large part due to the trapping of energy in internal rotors. This conclusion suggests that collision of PAH molecules with a larger number of internal rotors could be stickier. There is a class of PAH molecules with a large number of internal rotors – aromatic-aliphatic-linked hydrocarbons (AALH). Past theoretical [11] and recent experimental [12] results have implicated such molecular moieties in the nucleation process based on different reasoning. From the theoretical point of view, it was noticed [11] that while it was “hard” to grow PAHs in some flame simulations and outflow of red giant stars, the same model had no problem to produce enormously large PAHs at solar nebular conditions. The latter results were interpreted [11] as forming AALH (kerogen-like) rather than peri-condensed aromatic hydrocarbons (PCAH). Experimental observations of soot precursors by D’Alessio and co-workers [13] and Dobbins and co-workers [14] were interpreted by those authors as liquid-like particles, with D’Anna et al. [13] suggesting for their structure two-three-ring aromatics connected by aliphatic and oxygen bonds (i.e., AALH). More recent observations of Wang and co-workers [12] reported a large aliphatic signal in forming soot. Considering the possibility of such compounds participating in the nucleation process, we extended the MD simulation to collisions of aromatic-aliphatic-linked hydrocarbons.

## 2. COMPUTATIONAL PROCEDURE

The computer simulations of colliding molecules employed the molecular dynamics method with on-the-fly quantum forces [10]. The MD method calculates the trajectories of the molecular system over time by solving Newton’s equations of motion for each of the atoms. As in the previous study [9], the PM3 potential energy function, a member of the MNDO family of semiempirical quantum mechanical methods, was used to calculate the forces on each atom at each time step. As discussed in the previous study, PM3 is well suited to model PAH interactions. For example, PM3 reproduces the enthalpies of formation of naphthalene and biphenyl within 4 kcal/mol of their respective experimental values [15], and the heat of association of the benzene dimer within 2 kcal/mol [16] of *ab initio* calculations [17]. The resulting set of ordinary differential equations of positions and velocities was solved numerically by using the predictor in Beeman’s third-order predictor-corrector method [18]. Use of this numerical technique was able to maintain the total energy loss to less than 1 kcal/mol per 10 ps of simulation time.

To regulate the temperature of the collision simulations, a series of equilibration and relaxation runs were performed on each molecule. The molecule’s initial geometry

was determined by minimizing the PM3 potential energy of the molecule at 0 K. Then, the equilibration runs used the Berendsen velocity rescaling algorithm to increase the rotational and vibrational kinetic temperatures of the molecule by simulating the coupling of a heat bath to the molecular system [19]. After the kinetic temperature of the molecule reached 1600 K, the molecule was allowed to undergo a 3 to 12 ps relaxation run without rescaling atomic velocities to reach a state of equilibrium. Sometimes, the equilibration and relaxation runs were repeated as necessary until an equilibrium temperature of 1600 K was achieved.

Starting with initially equilibrated molecules, the collision simulation runs were conducted adiabatically. The collision runs were initialized by specifying the relative position, the relative orientation, and the relative velocity of two candidate molecules. The initial relative distance between the centers of mass of the two molecules ranged from 15 to 25 Å and the relative velocity ranged between 70 to 100 % of the most probable relative velocity, assuming a Maxwell-Boltzmann distribution.

A total of 1782 production runs were performed during the course of the present study. The number of runs and the length of each run were limited by the computational requirements of calculating the PM3 energy at each time step. The high computational demand of the technique, especially for such large molecules, prohibited collecting sufficient statistics for the collision efficiency. Instead, the approach was aimed at exploring the phenomena of PAH collisions at high temperatures and the obtained results allowed drawing conclusions on the underlying mechanism.

For each type of dimer, an effort was made to sample the phase space of collision configurations that are favorable to dimerization. Our own experience suggests that edge-to-edge collisions are more conducive to forming dimers than other configurations. Based on this experience, a series of collision runs were conducted for each type of dimer, where in each series, an impact parameter such as relative position and orientation was varied. For example, the relative position of one molecule could be varied in 0.25 Å increments up to 4 Å, and the orientation of a molecule could be rotated in 10 degree increments up to 180 degrees about 3 different axes.

### 3. NUMERICAL RESULTS

#### 3.1. Rotational equilibration

First, collisions between rotationally-equilibrated pyrene molecules were compared to collisions between initially rotationally cold pyrene molecules. The previous analysis of the latter case showed that out of 200 pyrene-pyrene runs, approximately 15 % produced dimers [9]. The majority of the dimers had lifetimes between 2 and 8 ps, with two dimers having lifetimes greater than 17 ps. In comparison to these figures, out of 339 collision runs performed in the present study with rotationally-equilibrated pyrene molecules, approximately 20 % produced dimers, the majority of which had lifetimes between 2 and 10 ps, and the longest lived pyrene dimer observed had a lifetime of 10.5 ps. Despite the difference in the longest lifetimes, most of the lifetimes fell in essentially the same time range in both cases. These and the following results confirm the earlier assessment made based on simple considerations (see authors reply in [9])

that rotational equilibration of incoming molecules does not alter the principal mechanistic picture identified in Ref. [9].

The analysis of the new simulation runs, with prior rotational equilibration of the colliding molecules, indicated a pattern of energy transfer similar to that discussed in [9]. The excess energy is effectively trapped in the internal modes of the molecules. When the molecules collide, the intermolecular translational kinetic energy drops in magnitude while one or more of the molecules' rotational or vibrational modes increase in energy. The dynamics of energy transfer is highly sensitive to the collision geometry between the molecules. For instance, a 0.25 Å variation in position along one axis can completely change the pattern of energy redistribution during the collision event.

We illustrate the redistribution of energy pattern with the following example of pyrene dimerization. Before the run, a pyrene molecule was equilibrated at 1600 K, which corresponds to a rotational kinetic energy (RKE) of 5 kcal/mol and a vibrational kinetic energy (VKE) of 112 kcal/mol, respectively. In the beginning of this run, two such equilibrated pyrene molecules were set 15.6 Å apart with the relative velocity set to 70 % of the most probable one, corresponding to an intermolecular translational kinetic energy (TKE) of 1.5 kcal/mol. The initial orientation of the two molecules was set so that they roughly collide in an edge-to-edge geometry.

The energy changes computed for dimer formation are presented in Figure 1 and the simulations snapshots in Figure 2. As can be seen in Figure 1, the TKE of the dimer stays relatively constant as the two pyrene molecules initially move toward each other. As the attractive forces become stronger between the two molecules, the TKE starts to increase until the two pyrene molecules collide edge-to-edge at 1.8 ps, as seen in Figure 2. Upon colliding, the TKE of the dimer experiences a sudden drop in energy. At the same time, the RKE of the first pyrene molecule experiences a sudden drop while the RKE and VKE of the second pyrene molecule experience sudden increases. After the initial collision, the molecules continue to repeatedly collide, rebound, and rotate in place about multiple axes. Every time a collision occurs, energy gets redistributed among the different RKE and VKE modes of the molecules, but the TKE of the dimer does not increase enough to overcome the intermolecular bond energy until 12 ps. At this time, the two molecules collide one last time, causing the TKE of the dimer to rise enough to exceed the intermolecular bond energy and break the dimer apart.

It is clear that both the rotational and vibrational modes of the two molecules act to absorb the energy from the intermolecular modes when the molecules collide. As mentioned earlier, the pattern of energy redistribution is very sensitive to collision geometry and hence not every collision transfers substantial amounts of energy in or out of the intermolecular modes. As a result, the excess energy is effectively trapped in the internal modes of the molecules. The absorbing and trapping dynamics of energy redistribution seen in this run are typical for all simulations that formed dimers.

### 3.2. Dimerization of larger PAH molecules

The effect of colliding-molecule masses on dimerization was examined by considering PAH as small as naphthalene and as large as coronene. The results obtained in the performed runs are summarized in Table 1. Inspection of these results indicates that the

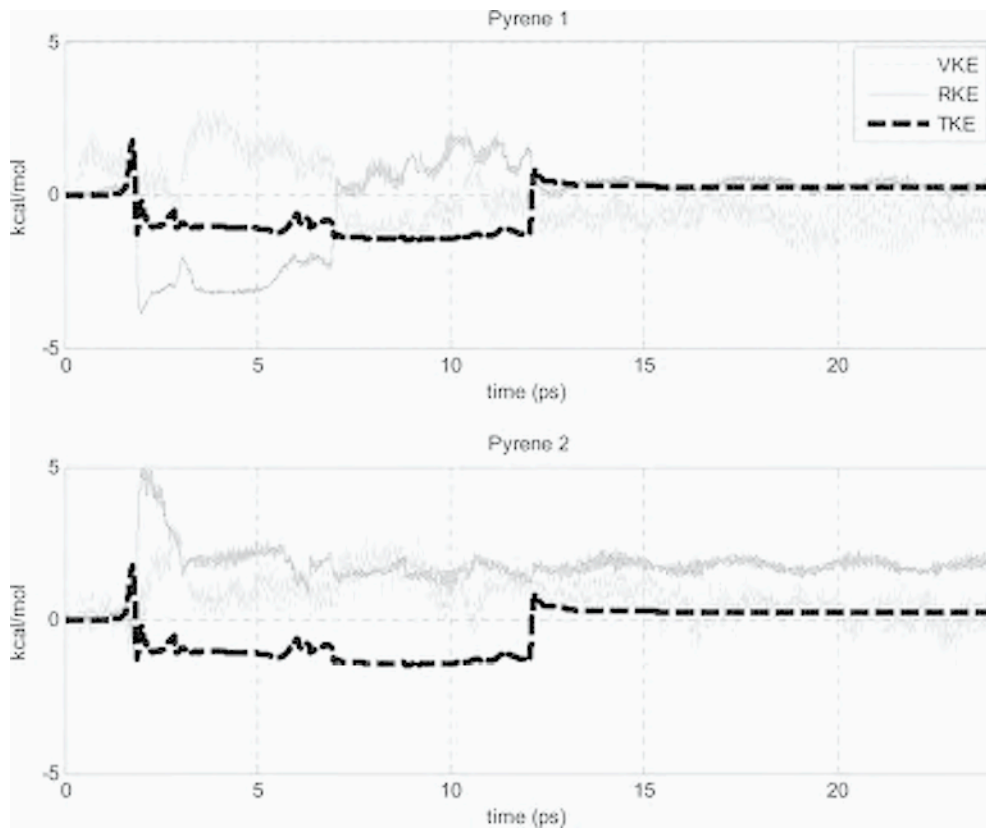


Figure 1. Net change in components of intermolecular (TKE), rotational (RKE), and vibrational (VRE) kinetic energy for each of the colliding pyrene molecules at 1600 K.

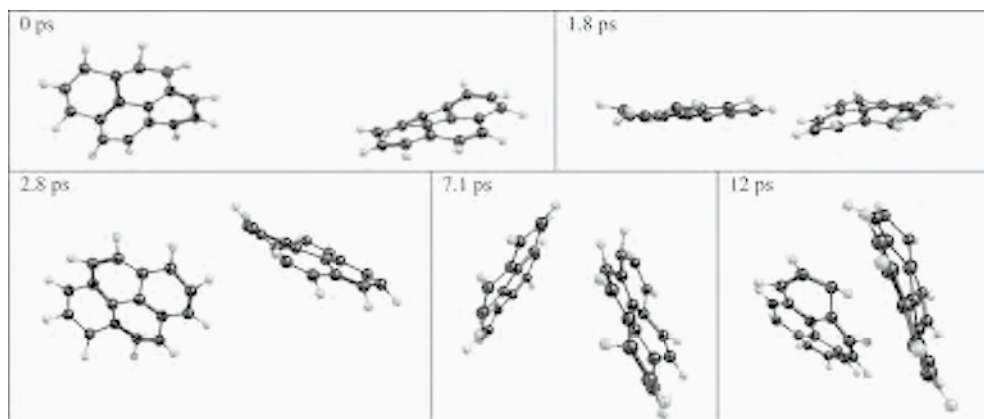


Figure 2. Snapshots of pyrene-pyrene run.

Table 1. Summary of PCAH simulation results.

Dimer	Designation in Figure 5	Mass (amu)	Number of runs	% runs with lifetime > 2 ps	Longest lifetime (ps)
(naphthalene) <sub>2</sub>	<i>a</i>	256	57	7	3.75
(anthracene) <sub>2</sub>	<i>b</i>	356	67	21	6.25
(phenanthrene) <sub>2</sub>	<i>c</i>	356	83	30	11.62
perylene-naphthalene	<i>d</i>	380	18	0	1.3
(pyrene) <sub>2</sub>	<i>e</i>	404	339	20	10.5
pyrene-coronene	<i>f</i>	502	112	40	15.6
(perylene) <sub>2</sub>	<i>g</i>	504	90	21	12.1
(benzo[ <i>c</i> ]pyrene) <sub>2</sub>	<i>h</i>	504	37	16	6.5
(benzopyrene) <sub>2</sub>	<i>i</i>	504	18	28	6.3
(coronene) <sub>2</sub>	<i>j</i>	600	120	38	20.0

percentage of runs that form dimers and the maximum observed lifetimes for each dimer type both increase as the mass of the dimer increases. This is not surprising since the predicted PM3 intermolecular bonding energy increases with the mass of the constituent molecules.

For instance, let us consider the coronene-coronene dimer, which is 50 % more massive than the pyrene-pyrene dimer. Out of a total of 120 coronene-coronene collision runs, 38 % of the runs produced dimers with lifetimes greater than 2 ps, and the longest-lived coronene-coronene dimer had a lifetime of 20 ps. Both the percentage of runs that produced dimers and the maximum observed lifetime are approximately twice the corresponding values obtained in the pyrene-pyrene simulations.

Despite the difference in size and bonding energy, the dynamics of coronene dimer formation exhibit many similarities to the one previously described with the pyrene dimer. Like pyrene, edge-to-edge collisions between coronene molecules are more conducive to producing dimers, and the rotational and vibrational modes of the molecules both act to absorb and trap energy from the intermolecular modes of the dimer. A series of snapshots for a coronene-coronene run is shown in the Figure 3.

### 3.3. Collision of pyrene with its radical

Over 300 collisions were conducted to explore the dimerization of pyrene and its radical. It was thought that collisions between a molecule and a radical would be more favorable to dimerization, because the radical site would be “sticky”. Surprisingly, no strong effect was observed; e.g., the longest dimer lifetime was only ~15 ps. The numerical results showed that the radical site is indeed sticky, and it exerts an attractive force that pulls sharply on the other molecule. In spite of this strong attraction, when a dimer is formed the monomers begin to rotate and the radical site turns away from the molecule, at which point the dimers tend to break apart. In other words, the intermolecular bond is excited by the strong radical-molecule interaction, yet once the radical

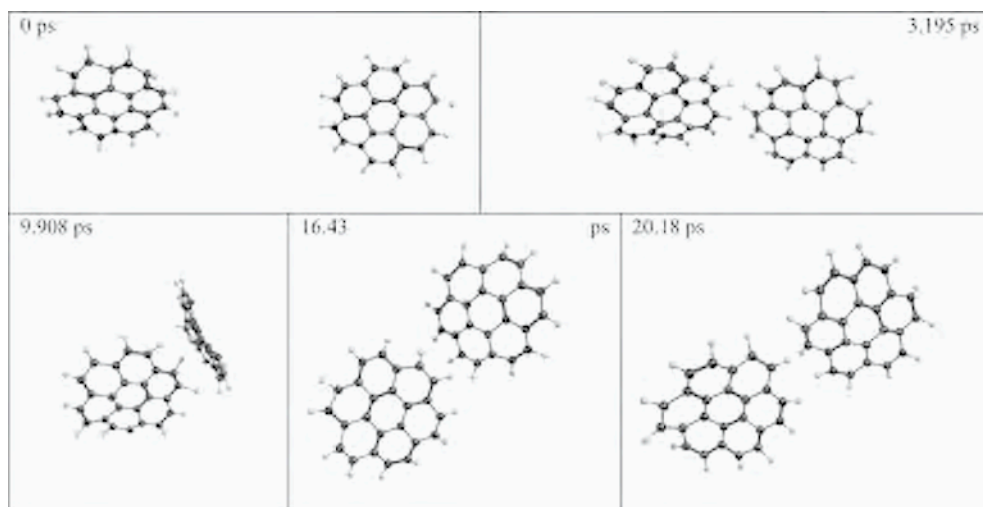


Figure 3. Snapshots of coronene-coronene run. Initially, the two coronene molecules were equilibrated at 1600 K, which corresponds to 5 kcal/mol RKE and 162 kcal/mol VKE. The two molecules were placed 20 Å apart and set with the relative velocity of 70 % of the most probable one, corresponding to TKE of 1.6 kcal/mol.

site rotates away from the molecule there is no longer an increased attractive force, causing the dimer to break.

### 3.4. Dimerization of AALH

As discussed above, one of the principal conclusions of the previous [9] and the present studies is that the mechanism of PAH dimerization is in large part due to the trapping of energy in internal rotors. This conclusion suggests that collision of PAH molecules with a larger number of internal rotors should be stickier. Motivated by these considerations, we investigated collisions of PAH molecules with a larger number of internal rotors – aromatic-aliphatic-linked hydrocarbons (AALH).

The investigated AALH dimers have masses ranging from 308 amu, such as (biphenyl)<sub>2</sub>, to 508 amu, such as (1,2-binaphthyl)<sub>2</sub>. The results obtained in the performed runs are summarized in Table 2. Out of 71 biphenyl-biphenyl runs, 13 % produced dimers having lifetimes greater than 2 ps, with the longest lived biphenyl-biphenyl dimer having a lifetime of 8.25 ps. Contrasting these results with those of two-ring peri-condensed aromatics, we note that collisions of naphthalene molecules form fewer dimers on average with a longest lifetime of only 3.75 ps. Instead, the lifetimes of biphenyl dimers are comparable to those of larger PCAH, such as anthracene and pyrene, whose longest lifetimes were 6.25 and 10.5 ps, respectively.

In terms of mechanistic features, collision of AALH molecules continues to follow the previously described pattern of trapping energy within the vibrational and rotational modes of the molecules. A typical series of snapshots is shown in the Figure 4.

Table 2. Summary of AALH simulation results.

Dimer	Designation in Figure 5	Mass (amu)	Number of runs	% runs with lifetime > 2 ps	Longest lifetime (ps)
(biphenyl) <sub>2</sub>	<i>k</i>	308	71	13	8.25
(biphenylmethane) <sub>2</sub>	<i>l</i>	336	68	3	4.25
(biphenylethane) <sub>2</sub>	<i>m</i>	364	106	16	8.81
(biphenylethylene) <sub>2</sub>	<i>n</i>	360	130	13	5.55
(biphenylacetylene) <sub>2</sub>	<i>o</i>	356	128	11	5.88
(1-phenylnaphthalene) <sub>2</sub>	<i>p</i>	408	19	16	3.25
(2-phenylnaphthalene) <sub>2</sub>	<i>q</i>	408	80	6	7.00
(triphenylmethane) <sub>2</sub>	<i>r</i>	488	80	45	7.67
(1,1-binaphthyl) <sub>2</sub>	<i>s</i>	508	36	17	6.26
(1,2-binaphthyl) <sub>2</sub>	<i>t</i>	508	87	20	7.25
(1,2-bipyrene) <sub>2</sub>	<i>u</i>	804	36	17	12.57

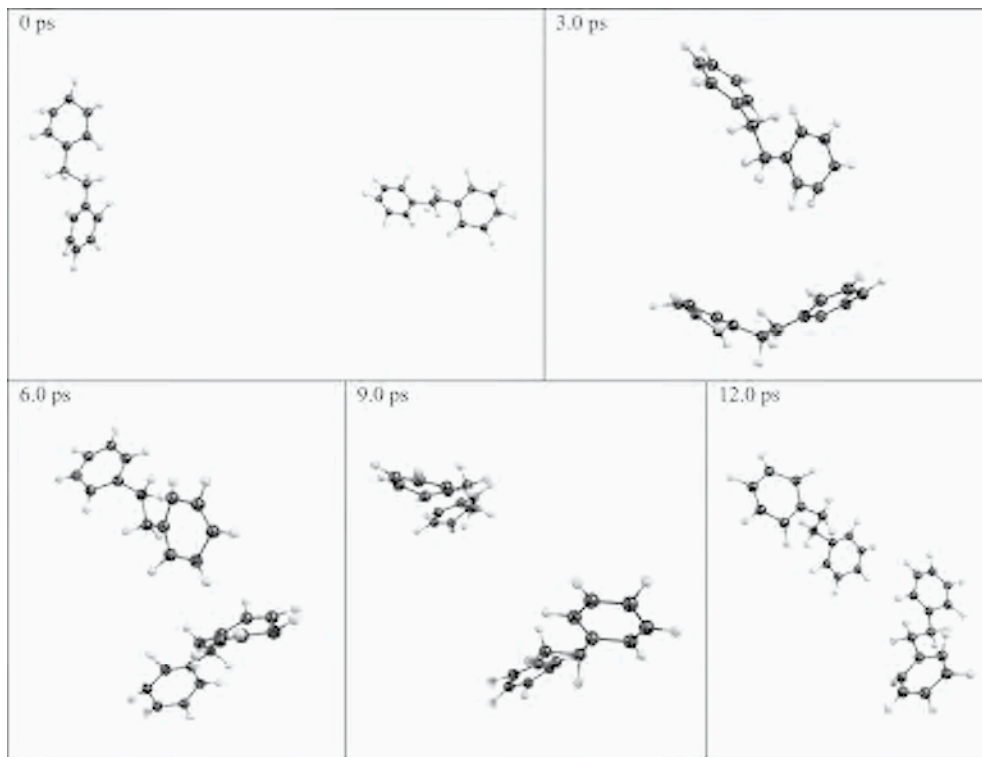


Figure 4. Snapshots of biphenylethane-biphenylethane run at 1600 K.

#### 4. DISCUSSION: AALH VS PCAH

Figure 5 summarizes the present MD results, displaying the maximum lifetimes of PCAH dimers with open diamonds and those of AALH dimers with solid circles. For PCAH dimers, we see a clear trend of increasing lifetimes with the dimer mass. For AALH this trend is less evident.

Comparing the results for smaller masses, we observe that collisions of *two*-ring AALH (e.g., biphenyl molecules, Point *k*, and biphenylethane molecules, Point *m*, in Figure 5) produced dimers with lifetimes comparable to those produced in collisions of larger, *four*-ring PCAH (e.g., pyrene molecules, Point *e*) and significantly larger than those from *two*-ring PCAH (naphthalene molecules, Point *a*). While this observation could be interpreted as an increased stickiness of AALH as compared to PCAH, the effect, perhaps surprisingly, is not as dramatic as one would expect. Indeed, based on the mechanism of PAH dimerization identified as being energy trapping in internal rotors, the expectation, and hence motivation for the present study, was that a substantial increase in the number of internal rotors in the colliding molecules should substantially increase the dimer lifetimes. Yet, the numerical effect is not an order-of-magnitude but a relatively small factor.

Still, it could be that even these relatively small differences in the stickiness of the smaller, incepting particles have a profound influence on the overall rate of nucleation.

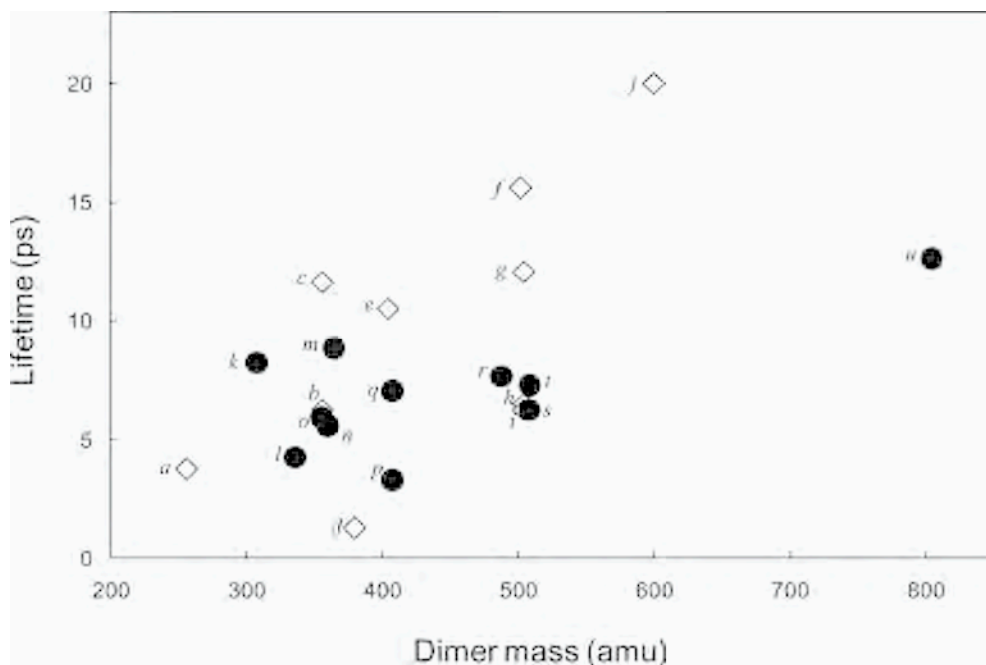


Figure 5. Maximum dimer lifetimes vs. dimer mass for PCAH (open diamonds) and AALH (solid circles) dimers. The letter labels refer to designation in Tables 1 and 2.

The two types of precursor molecules should produce different precursor particles: collisions of PCAHs resulting in graphitic-like turbostratic stacks of graphene sheets and collisions of AALHs producing kerogen-like material. The numerical results [11], those mentioned in the Introduction as suggesting formation of AALH, also led to consider [6] that soot particle nucleation can proceed through two regimes, via AALH at conditions of high propensity to chemical growth (e.g., low temperatures, fuel-rich composition) and via most stable intermediates, PCAH, at harsh growth condition (e.g., high temperatures, near-stoichiometric mixtures). Following the present MD results, the initial, small-ring-size AALH molecules will dimerize faster than equivalent-ring-size PCAH molecules, consistent with the high- and low-propensity to growth, and hence soot formation, regimes.

At the same time, and perhaps more importantly, the results obtained for the smaller AALH dimers seem to follow the same trend with the dimer *mass* as seen for the PCAH dimers, perhaps implying that the aliphatic linking is not really a dominating factor.

With the increase in mass there is a clear difference between the two groups: AALH dimers appear to have substantially lower lifetimes than the PCAH ones of comparable mass. This result could be consistent with the interpretation given to recent experimental observations by D'Alessio et al. [20] on lower stickiness of emergent carbon nanoparticles.

## 5. CONCLUSIONS

The molecular dynamics simulations performed in this work confirm the feasibility of dimerization of peri-condensed aromatic hydrocarbons (PCAH) ranging from phenanthrene to coronene at flame conditions, similar to the results reported for pyrene in the previous study [9]. The dynamics of the dimerization process consist of the absorption and trapping of the energy from the intermolecular modes into the rotational and vibrational modes of the molecules.

The previous study [9] emphasized the development of rotations to stabilize the pyrene-pyrene dimer by starting the simulations with rotationally cold molecules. The present study extended the simulations to rotationally equilibrated colliders, and no significant effect on the results was observed.

Numerical simulations between aromatic-aliphatic-linked hydrocarbons (AALH) indicated that molecules as small as biphenyl can produce dimers with lifetimes comparable to larger-size PCAH molecules.

The dominant trend observed in the present MD simulations is an increase in the dimer lifetime with an increase in molecular mass. However, while the smaller AALH dimers seem to follow the same trend with the dimer mass as seen for the PCAH dimers, the larger AALH dimers appear to have substantially lower lifetimes than those for PCAH of comparable mass.

The obtained trends appear to be in accord with past and recent experimental observations and associated interpretations given by the corresponding authors.

## ACKNOWLEDGMENTS

The work was supported by the Director, Office of Energy Research, Office of Basic Energy Sciences, Chemical Sciences, Geosciences and Biosciences Division of the U.S. Department of Energy, under Contract No. DE-AC03-76F00098.

## REFERENCES

1. B.S. Haynes, H.G. Wagner, *Prog. Energy Combust. Sci.* 7 (1981) 229-273.
2. K.H. Homann, *Proc. Combust. Inst.* 20 (1985) 857-870.
3. J.B. Howard, *Proc. Combust. Inst.* 23 (1991) 1107-1127.
4. H. Bockhorn (Ed.) *Soot Formation in Combustion: Mechanisms and Models*. Springer-Verlag, Berlin, 1994.
5. I. Glassman, *Combustion*, Academic, San Diego, 1996.
6. M. Frenklach, *Phys. Chem. Chem. Phys.* 4 (2002) 2028-2037.
7. M. Frenklach, H. Wang, *Proc. Combust. Inst.* 23 (1991) 1559-1566.
8. J.H. Miller, *Proc. Combust. Inst.* 23 (1991) 91-98.
9. C.A. Schuetz, M. Frenklach, *Proc. Combust. Inst.* 29 (2003) 2307-2314.
10. M. Frenklach, C.S. Carmer, in *Molecular Dynamics of Clusters, Liquids, and Interfaces*, W.L. Hase (Ed.) JAI, Stamford, 1999, pp. 27-63.
11. W.A. Morgan, E.D. Feigelson, H. Wang, M. Frenklach, *Science* 252 (1991) 109-112.
12. B. Oktem, M.P. Tolocka, B. Zhao, H. Wang, M.V. Johnston, *Combust. Flame* 142 (2005) 364-373.
13. A. D'Anna, A. D'Alessio, P. Minutolo, in *Soot Formation in Combustion: Mechanisms and Models*, H. Bockhorn (Ed.) Springer-Verlag, Heidelberg, 1994, pp. 83-101.
14. R.A. Dobbins, H. Subramaniasivam, in *Soot Formation in Combustion: Mechanisms and Models*, H. Bockhorn (Ed.) Springer-Verlag, Heidelberg, 1994, pp. 290-299.
15. P.J. Linstrom, W.G. Mallard (Eds.), *NIST Chemistry WebBook*, NIST Standard Reference Database Number 69. National Institute of Standards and Technology, Gaithersburg MD, 2005.
16. J.J.P. Stewart, *J. Comput. Chem.* 10 (1989) 221-264.
17. S. Tsuzuki, K. Honda, T. Uchimaru, M. Mikami, K. Tanabe, *J. Am. Chem. Soc.* 124 (2001)
18. D. Beeman, *J. Comput. Phys.* 20 (1976) 130-139.
19. H.J.C. Berendsen, J.P.M. Postma, W.F. van Gunsteren, A. DiNola, J.R. Haak, *J. Phys. Chem.* 81 (1984) 3684-3690.
20. A. D'Alessio, A.C. Barone, R. Cau, A. D'Anna, P. Minutolo, *Proc. Combust. Inst.* 30 (2005) 2595-2603.



# Computational and experimental evidence for polynuclear aromatic hydrocarbon aggregation in flames

J.H. Miller, J.D. Herdman

Department of Chemistry  
The George Washington University  
Washington, DC 20052, USA

*In the combustion of fossil or bio-derived fuels under rich conditions, some fraction of the fuel carbon is converted into fine particulate carbon. This carbonization process usually leads to “soot”, a form of amorphous carbon characterized by small primary particles aggregated into fractal structures. It is our hypothesis that the most critical step in soot inception is the transition from 2-dimensional to 3-dimensional structures and that, for soot formation, this transition is the agglomeration of polynuclear aromatic hydrocarbons of modest molecular size. In the current paper, a review of available literature on experimental observation of PAH in flames as well as computational work that assesses the role of PAH condensation in soot inception is presented. Results of recent atom-pair calculations of intermolecular interactions of homo-molecular and hetero-molecular clusters for many peri-condensed PAH spanning monomer masses ranging from 78-1830 Da are presented. Binding energies of homo-molecular dimers rise rapidly with molecular size and asymptotically approach the experimentally established exfoliation energy for graphite of  $5.0 \pm 0.5 \text{ kJ}(\text{mol})^{-1}(\text{carbon atom})^{-1}$ . Binding energies of hetero-molecular dimers correlate well with the reduced mass of the pair. From calculations of homo-molecular stacks, binding energies were observed to increase with each added molecule and rise asymptotically, approaching a limit which scales linearly with monomer molecular mass.*

## 1. INTRODUCTION

Non-bonded interactions between small molecules such as gas-phase fuels and their oxidation products produce attractive wells that are shallow ( $<2 \text{ kJ/mol}$ ) compared to the average kinetic energy available in molecular collisions ( $k_B T \approx 10\text{-}12 \text{ kJ/mol}$  in the hydrocarbon growth regions of flames) and chemical bonds ( $\approx 400 \text{ kJ/mol}$ ) and are thus thermally inconsequential in flames. However, the attractive interactions between  $\pi$  electrons in aromatic systems are among the strongest non-covalent interactions in nature and govern binding in systems ranging from biomolecular recognition in DNA and proteins to macrocyclic molecular wires. In graphite, adjacent sheets are bound by a well of  $5.0 \pm 0.5 \text{ kJ}(\text{mol})^{-1}(\text{carbon atom})^{-1}$  [1]. Thus, two graphene sheets of 100 carbon atoms each would be bound more tightly than a typical, covalent chemical bond. The purpose of this contribution is to review more than two decades of work on the subject of the non-bonded interactions of polynuclear aromatic hydrocarbons in the context of the formation of fine carbon particulate in flames. The review will be infor-

med by contributions from combustion researchers (some of whom are contributors to this volume) as well as literature from other disciplines, notably the astrophysics community.

Soot formation in hydrocarbon flames is kinetically controlled and occurs in short times (1-10 msec to reach particle diameters of 500 Å) [2]. This constraint of rapid particle formation limits the possible chemical processes that may form soot. Polynuclear aromatic hydrocarbons (PAH) have often been invoked as important intermediates in this chemistry. These species, which are found in all sooting, hydrocarbon flames, have structures similar to the soot's graphic morphology and possess C/H ratios between most starting fuels (<1) and soot particles (>5).

This ubiquitous class of molecules has emerged as centrally important in astrophysics. In the 1970s a spectral feature near 11.3 μm was identified in interstellar dust clouds [3]. Subsequently, several additional bands, known collectively as the diffuse interstellar bands (DIB), have been observed at 3.3, 6.2, 7.7, 8.6 μm. Astrophysicists have also investigated a broad luminescence known as the extended red emission (ERE). Circumstantial evidence put forward over the last several years suggests that the source of these features is vapor phase PAH. Experiments aimed at validation of this hypothesis have produced a great deal of recent literature in which low temperature PAH spectroscopy (either through jet-cooling or matrix isolation techniques) has been studied in the context of the astrophysical observations. Spectra for both neutral and ionic species [4] have been collected as well as those for PAH containing nitrogen [5], for very large PAH species (up to 600 Dalton), and for those with 5-membered rings [6].

A recent paper in PNAS may reignite the debate about the role of ions in soot formation [7]. In this manuscript, the authors performed HF/MP2 calculations of the electronics structure of closed shell, cationic PAH dimers and showed that they possess large emission oscillator strengths in the red region of the spectrum. Circumstantial evidence lends credence to the theory that charged clusters play a roll in soot formation as well:

- Charged PAH clusters are known to be more tightly bound than their neutral counterparts.
- PAH and ionic species are known to be spatially correlated in rich flames [8, 9].
- PAH have proton affinities in excess of those for prevalent flame ions, providing a possible mechanism for accumulation of charge [10].

Thus, ionization of clusters as a mechanism for incipient particle stabilization may be relevant to particle growth in flames. However, it is our hypothesis that the most critical step in “carbonization” is the transition from 2-dimensional to 3-dimensional structures, and, for soot formation, this transition is the agglomeration of *neutral* polynuclear aromatic hydrocarbons of modest molecular size.

## 2. THE FORMATION AND GROWTH OF PAH IN FLAMES

In a landmark paper in the mid-1980s Stein and Fahr evaluated the thermodynamic stabilities of hydrocarbons with the empirical formula  $C_{2n}H_{2m}$  with n ranging from 1-

21 and  $m$  between 1 and 8 [11]. As noted by these authors, at or near 300 K, large hydrocarbons favor  $sp^3$  bonding (such as that found in diamond). At very high temperatures ( $>3000$  K) polyacetylenes are the most stable bonding geometry. In the intermediate range, polynuclear aromatic hydrocarbons become the thermodynamically stable HC form. Within this class, the number of isomers grows rapidly with molecular mass. Stein and Fahr found that near temperatures typical of molecular growth in flames, the most stable isomers were those with a central core of condensed, 6-membered aromatic rings. Molecules along this path of stability have become known collectively as the “stabilomer” grid (Figure 1). Perhaps as a direct consequence of their paper, most kinetic models for soot inception begin with the assumption that early chemistry results in the formation of highly condensed aromatic structures.

Kinetic mechanisms have been developed for the formation of the first several aromatic rings that successfully predict measured profiles in reactors, premixed, and non-premixed flames. For non-aromatic fuels, the initial chemistry forms unsaturated hydrocarbon radicals that undergo cyclization to form benzene. Historically, it was thought that this process proceeded through a sequential addition of  $C_2$  species (i.e. acetylene) [12]. More recently, a consensus has developed that much of the benzene formation rate is carried through combination of two resonantly stabilized propargyl radicals [13-15]. The ensuing formation of PAH rings from benzene is thought to occur as a hydrogen abstraction reaction followed by acetylene addition to the radical aromatic core [12].

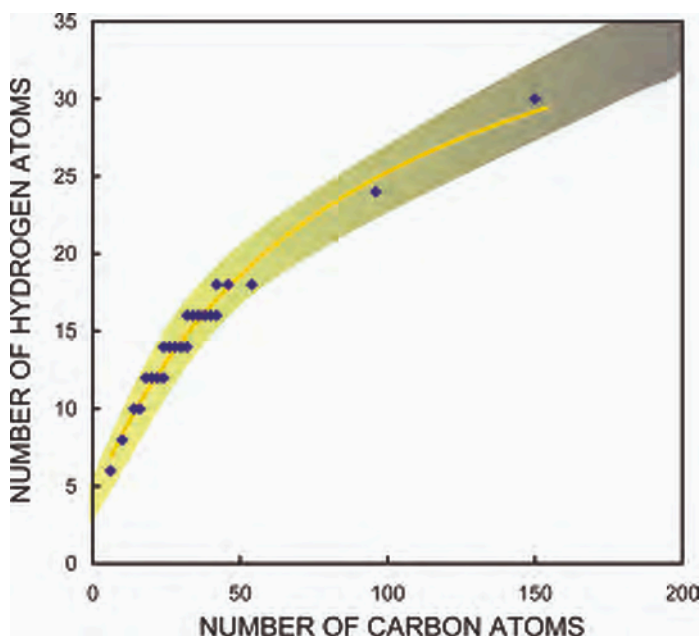


Figure 1. Representative species along the Stein and Fahr stabilomer grid illustrating carbonization accompanying molecular growth.

At some point in the growth of large species, a chemical reaction between two colliding particles of similar size is no longer a necessary condition for “sticking”, i.e. the magnitude of the attractive interaction potentials will be sufficiently large relative to the kinetic energy of the other molecules in the bath that an aggregate will be formed and will survive. For many decades, researchers in the soot community have explored this transition beginning with the application of homogeneous nucleation theory [16], an approach that has largely been supplanted by sectional modeling approaches [17, 18]. In the latter, soot particles are typically treated as coalescing spheres whose size is divided into several size ranges. The smallest is seeded with an inception process. In most computations, these inception species are PAH species as small as two rings in size, but more typically four-ring species, i.e., pyrene.

In several recent papers, other researchers and we have hypothesized that PAH agglomeration in flames occurs at modest molecular size [19-21]. In the Twentieth (International) Symposium on Combustion, our group calculated equilibrium concentrations for PAH dimers in flames estimated from monomer concentrations [22]. Our calculations at the time suggested that because dimer concentrations fell short of the number densities of the earliest soot particles, homogeneous nucleation of PAH was less important than chemical growth in particle inception. A potential flaw in this analysis may be the assumption of equilibrium of the dimerization steps. Several years later, we revisited the problem from a kinetic perspective. In this later analysis, the lifetimes of dimers under flame conditions were calculated assuming that either energy of the initial collision could be accommodated by the PAH molecules themselves or could be removed by molecules in the bath. Our hypothesis was that PAH agglomeration would contribute to particle growth if the dimer lifetime was long with respect to the characteristic time for chemical growth. Our conclusion at the time was that this process could occur, but only for relatively large PAH species ( $> 800$  Da). However, our calculation of energy accommodation during collision neglected conversion of the collision kinetic energy into internal molecular degrees of freedom. Further, several simplifying assumptions were made in the characterization of PAH structure during the calculation of the intermolecular potentials, integrating the second virial coefficient from these potentials, and calculating the equilibrium constant of the association reaction. With modern computational resources, a more rigorous treatment in all of these calculations is accessible, as is described below.

In the Twenty-ninth Combustion Symposium, Schuetz and Frenklach used a semi-empirical molecular dynamics approach to calculate dimer lifetimes for pyrene under flame conditions [23]. They found that deposition of energy into internal rotations in the colliding pair greatly extended dimer lifetimes. Scheutz and Frenklach’s finding is an extremely important result not just because it dramatically shifts the onset of PAH condensation to much smaller size, but also because this result is *required* for many models to accurately predict measured soot profiles [12].

Given the important role that PAH aggregates might play in the conceptual framework of soot formation theory, it is surprising that no direct experimental evidence has yet been proffered for their existence. In fact, as reviewed below, until recently scant data existed for substantial concentrations of PAH larger than a handful of aromatic rings.

### 3. DIAGNOSTICS FOR PAH IN FLAMES

#### 3.1. Extractive sampling

Prior to the mid 1980s, there were relatively few studies in which the concentrations of individual PAH species were measured in hydrocarbon flames. The most extensive data sets available at that time were those of Crittenden and Long [13] and Prado et al., [24] which reported concentration profiles for many 2-, 3-, 4-, and 5-ring compounds and a few 6- and 7-ring molecules. Crittenden and Long [13] used quartz microprobes to sample fuel rich premixed acetylene/oxygen and ethylene/oxygen flames at 40 torr. Samples of stable gaseous products and the dichloromethane extract from the collected soot were analyzed by mass spectrometry, gas chromatography, and UV absorption spectroscopy. Prado et al. [24] collected gas samples containing soot with a stainless steel water-cooled probe from turbulent, diffusion benzene/air and kerosene/air flames at atmospheric pressure. The methylene chloride extract was then analyzed for dissolved PAH by gas chromatography and mass spectrometry. In addition to these investigations, Di Lorenzo et al. [25] sampled PAH from rich, premixed methane/oxygen flames at atmospheric pressure using a stainless steel probe cooled to 470 K by nitrogen. Individual PAH were identified by gas chromatography and mass spectrometry. Prado et al. [26] also studied premixed flames of toluene and heptane with oxygen enriched air. Both gaseous samples and the methylene chloride extract from collected soot were analyzed by gas chromatography and mass spectrometry. Finally, Bittner and Howard [27] used a molecular beam mass spectrometer to characterize the flame structure of benzene-oxygen-argon flames at 20 torr. Profiles of nine PAH with 2, 3, and 4 rings were measured. For all of these early flame studies the concentration of PAH generally decreased as the number of rings increased, and the concentrations of the heavier PAH were found to grow relative to the lighter PAH as a function of time. In these early studies, it was found that typical values for 3- and 4- ring PAH concentrations were in the range of 1-10 parts per million (ppm). No evidence existed for individual PAH with molecular weights larger than 300 Da. The total concentration of PAH in a hydrocarbon flame certainly is a strong function of the fuel structure and the flame conditions, such as stoichiometry, premixed vs. diffusion mixing, and laminar vs. turbulent flow [28]. However, the distribution of PAH has been found to be relatively insensitive to the fuel structure or to the combustion conditions.

Within the last decade, the combination of molecular beam sampling from low-pressure flames with laser ionization techniques has extended the upper size limit of sampled flame species. Like the early studies, it has been observed that the concentration of PAH drops exponentially with molecular size up to species with 20-30 carbon atoms [29]. In agreement with the early work, the concentrations of molecules in this size range are on the order of 1-10 ppm. However, it has been found the concentrations of species larger than  $\approx 30$  carbon atoms do not continue to decrease and, in fact, may increase with molecular mass leading to a bimodal distribution. For example, Grothreer has observed a series of peaks at molecular masses  $>650$  Da when performing photoionization mass spectrometry on material sampled from a low-pressure ethylene/oxygen flame [30]. A reasonable explanation for their results is that the species responsible for these peaks are dimers (or larger aggregates) of smaller PAH.

### 3.2. Optical diagnostics

Almost as soon as rare gas plasma lasers became available in the 1970s, combustion researchers noted a visible, broadband laser induced fluorescence that was observed in fuel-rich premixed flames or on the rich side of the stoichiometric surface in non-premixed hydrocarbon flames [31-33]. In the ensuing years, scores of papers have been written that report both visible (Figure 2) and ultraviolet emissions, and have attempted to unambiguously assign the fluorescing species [31, 34-41]. This rich literature has been reviewed in two recent contributions and will only be summarized briefly below [42, 43]. As noted by Smyth et al. [42], there are numerous species that might contribute to an unstructured emission in flames. In general, these candidates must be large enough that their density of states obscures the vibrational and rotational band structure, and they must have accessible single photon transitions at the appropriate wavelengths. Polynuclear aromatic hydrocarbon species meet this size criterion, have well known ultraviolet transitions, and combined probe and optical measurements put them in the correct regions of the flames studied.

In general, the wavelength of fluorescence from PAH species increases to longer wavelengths with increasing molecular size [43]. Fluorescence signals have been observed with both ultraviolet and visible excitation. For ultraviolet excitation, two emission maxima can be observed. Although both maxima are attributed to PAH, their profiles are different. In methane/air non-premixed flames supported on a Wolfhard Parker slot burner, excitation at 282 nm produced two maxima in the profile of broadband ultraviolet fluorescence. [44]. One of these profiles, whose emission maximum occurs  $\approx 310$  nm, follows a temperature contour with increasing height above the burner surface and closely follows the peak profile for soot particles. The other feature that peaks at  $\approx 340$  nm follows a convective streamline into cooler, richer flame regions.

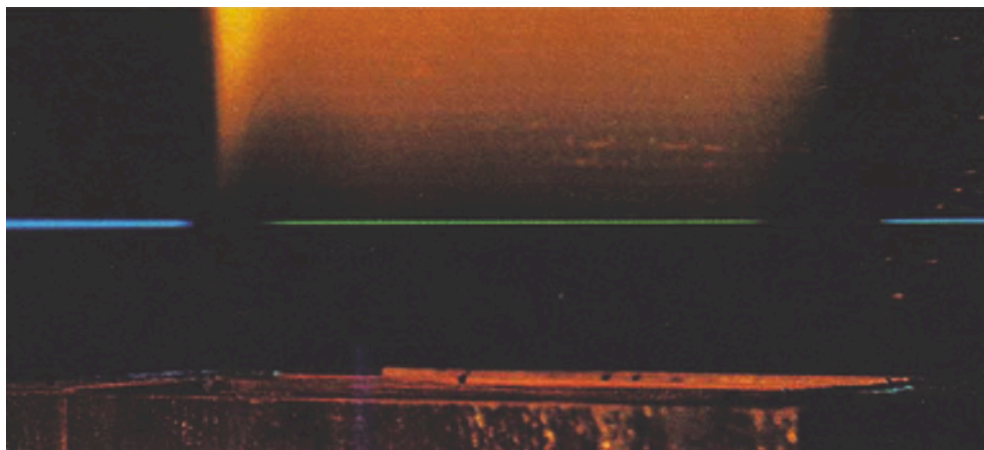


Figure 2. Broadband laser induced fluorescence observed in a hydrocarbon, non-premixed flame. The excitation source was the 488 nm line of an Ar<sup>+</sup> laser [36, 41].

In premixed flames, UV excitation has been found to excite both a UV and a visible emission depending on flame location and stoichiometry [45-48]. In the recent work of Cajolo et al. [47], the visible emission is seen only with high PAH loading in the flame, but these researchers argue that small aromatic molecules (<4 rings) are unlikely to be its source. Rather, their work suggests that an unidentified constituent of the “condensed species” collected in their flames is responsible for visible fluorescence. Several groups in the soot community have postulated that early particulate matter is composed of aromatic ring systems joined by aliphatic linkages [47, 49, 50]. It has been proposed that initially these species form from reactions between small aromatic radicals and parent compounds or from aromatic radical recombinations. Dynamic simulations of the growth of these structures predicts organic structures with 1-10 nanometer extents, but with seemingly lower density than graphitic carbon [51] and low sticking probabilities with each other at flame temperatures [52]. How these molecules might be expected to contribute to visible fluorescence is not well defined.

#### 4. AROMATIC EXCIMERS

In a laser induced fluorescence experiment for an isolated molecule, an electron is excited by absorption of one or more photons generally from the electronic ground state to an excited state. The electron may return to the ground state by emitting a photon or through one or more non-radiative steps (e.g., quenching.) In a molecular condensed phase, there is a possibility that the excited state has the excitation energy delocalized across the entire aggregate structure leading to weak bonding between adjacent molecules, an excimer (originally shorthand for “excited dimer”). In the quantum mechanical view, bonding may be dominated by charge resonance interaction, exciton (electron-hole) resonance, or mixing of the two [53]. The spectra of aromatic excimer states have been studied extensively for several decades for aggregates in solutions [54-58], adsorbed onto surfaces, and in microcrystals [58-63]. The fluorescence from an aromatic excimer is observed substantially red-shifted from that of the isolated molecules (Figure 3). In addition to the shift to lower transition energies, emissions from aromatic excimers are generally broad, featureless and, in solutions, highly dependent on concentration [64].

##### 4.1. Calculations of PAH aggregate electronic structure and binding energies

For the past several years we have explored the use of semi-empirical and density functional theory calculations of electronic transitions for small aromatic aggregates in support of this theory (Figure 4). Unfortunately, none of the quantum chemistry calculations can reliably calculate intermolecular binding energies [65]. In fact, because the semi-empirical basis sets are not parameterized for these intermolecular electronic interactions, they often predict repulsive interactions for all electronic levels for molecular separations on the order of 3.5 Å (known to be the approximate plane separation distance in most parallel packed aromatic systems) [65].

For more exact predictions of electronic structure, *ab initio* methods, specifically density functional theory calculations for many atom systems, are required. DFT tech-

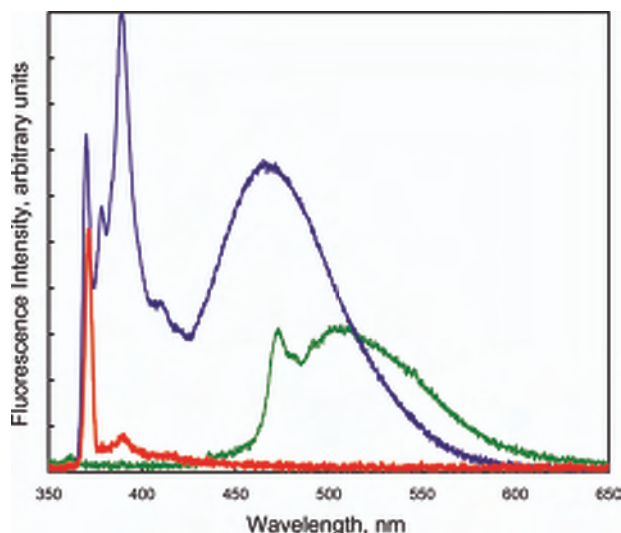


Figure 3. Fluorescence observed for aromatic condensed phase systems. Red:  $5 \times 10^{-5}$  M pyrene in cyclohexane. Blue:  $5 \times 10^{-3}$  M pyrene in cyclohexane showing excimer emission. Excitation wavelength for both spectra was 370 nm. Green: coronene crystal emissions observed with excitation from a 337 nm  $N_2$  laser.

niques using different levels of theory will result in different predicted energetics. For example, recent calculations of the benzene excimer using the BPW91/6-31+G\* level of theory failed to converge to the required monomer energies for parallel pairs of monomers moved to large separations [66]. Further, it is now clear that DFT methods alone do not accurately predict aggregate binding energies [67, 68].

Although not quantitatively accurate in their prediction of binding energies, the quantum calculations reveal the complex interplay between intermolecular orientation and electronic excitation. The most stable dimers of aromatic molecules with one or two rings are those with the molecular planes anti-parallel to one another attributable to quadrupole repulsion between the two ring systems in fully eclipsed geometries [69]. However, excited states in the same systems rearrange themselves into plane parallel conformation attributable to excimer formation [70].

Several computational groups are now pursuing two distinct approaches to correcting binding energies by either including a damped-dispersive correction to the Hamiltonian solved by the DFT routine [71, 72] or by simply using the partial atomic charges resulting from the DFT calculations in a classical atom-pair calculation [73].

The interaction of two molecules at medium and long-range separation is a difficult problem that increases dramatically in complexity with molecular size. The construction of a complete potential energy surface and integration of a function which includes this surface over all space (as is required in the calculation of the equilibrium constant for dimerization from the second virial coefficient [22]) can be an overwhelming task for small PAH such as benzene molecules, and prohibitively time-consuming for larger aromatic systems. Less rigorous approaches such as atom-pair models for

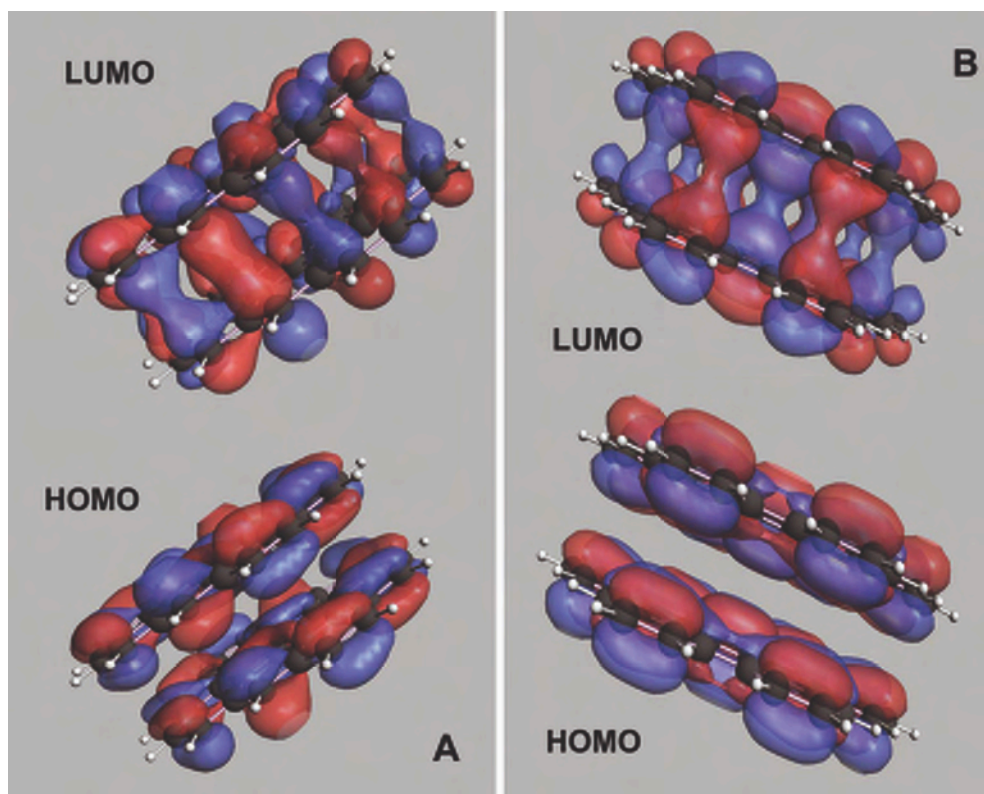


Figure 4. Electron density contours calculated using the Amsterdam Density Functional program (DFT) for ovalene (A) and hexabenzocoronene (B) revealing shared electron density in the lowest occupied molecular orbital (LUMO) of each and none in the highest occupied molecular orbital (HOMO). Radiative transitions from the bound excited state to the unbound ground state produce broad and featureless emission spectra.

intermolecular potentials and Monte Carlo integration in the evaluation of virial coefficients have been applied to the calculation of intermolecular interactions of large systems.

## 5. ATOM-PAIR POTENTIAL CALCULATIONS FOR PAH

The interaction potential for molecules is the sum of dispersive and electrostatic contributions. Generally, each contribution is taken as the sum of the individual interaction potential of each atom in one molecule with every atom in the other molecule. The magnitude of the atom-atom interactions is dependent on the atoms involved; is usually derived from experimental data such as heat of sublimation, crystal packing distances, etc.; and is evaluated from a “basis set” of analogous molecular species. Our group pioneered the calculation of intermolecular potentials based on atom-pair inte-

reactions for large PAH aggregates more than 20 years ago [69]. Below, we evaluate atom pair parameters proposed by us in this historic context [73-76] and compare resulting interaction potentials for homo-molecular dimers of several PAH along the Stein-Fahr stabilomer grid [77].

For non-polar PAH monomers, the long-range attractive dispersive potential is dominated by instantaneous dipole-induced dipole interactions which have a  $r^{-6}$  dependence, where  $r$  is the separation between the molecules. The entire dispersive potential, including short-range repulsive contributions, has been parameterized by both Lennard-Jones potentials, such as the LJ 6-12 potentials [69, 75, 78-87] of the form:

$$V_{ij}^{\text{disp}} = 4\epsilon_{ij} \left[ \left( \frac{\sigma_{ij}}{r_{ij}} \right)^{12} - \left( \frac{\sigma_{ij}}{r_{ij}} \right)^6 \right] \quad (1)$$

or, as was done in our earlier work, with an exp-6 potential [69, 85-89]:

$$V_{ij}^{\text{disp}} = -\frac{A_{ij}}{r_{ij}^6} + B_{ij} \exp(-C_{ij} \cdot r_{ij}) \quad (2)$$

The electrostatic potential between pairs of atoms on adjacent molecules is calculated from [75]

$$V_{ij}^{\text{elec}} = \left( 1389.963 \frac{\text{kJ } \text{\AA}}{\text{mol } e^2} \right) \frac{q_i q_j}{r_{ij}} \quad (3)$$

Because the computation time at each point on the potential surface increases as the square of the number of atoms in the molecules, a challenge in this approach is that the calculation may be prohibitively time-consuming for large polyatomic molecules. For that reason, in our earlier work, we introduced a modeling approach in which the atom pair potentials were calculated for a limited set of nearly circular PAH (benzene, coronene, circumcoronene) for a small number of relative geometries. From these data, effective Lennard-Jones 6-n potentials were derived for interacting disks. Because the molecules were assumed to be axially symmetric, details of the interaction potential were missed. For example, two ‘‘Tee’’ shaped orientations of benzene were calculated, one with a single hydrogen closest to the plane of the second molecule and another calculated for a geometry in which two hydrogens were equally close. Although these calculations result in different binding energies, a single number, the average of the two, characterized them.

Assumptions made in establishing the effective charge on individual atoms in large PAH also have a major impact on the resulting total interaction potential. Although atom charges are available in the results of both semi-empirical and *ab initio* calculations, these can be highly dependent on the basis set used and even the methodology in calculating the atomic charge. The charge set we developed in our earlier work was based on group additivity, which considered the local environment for each atom. For PAH, we define 5 types of  $sp^2$  carbon atoms; Type A: an edge carbon bound to a hydrogen as well as two other edge carbons, Type B: an edge carbon bound to two Type A carbons (e.g., the central carbons in naphthalene), Type C: an edge carbon bound to one Type A and one Type C (e.g., the ‘‘bay’’ carbons in phenanthrene), Type D: an interior carbon bound to one of the edge carbon types

described above, and Type E: a “buried” interior carbon bound to only Type D or Type E carbons [69, 90].

In our recent calculations, coordinates of planar PAH were calculated through geometry optimization using the MM+ force field in HyperChem [91]. The resultant coordinate files were modified to include the assigned atom type and charge. For dimers, binding energy minimization was accomplished using a Simplex algorithm coded into a Delphi (PASCAL) [92] computer program. In this procedure, one of the monomers was centered at the origin and constrained to the  $xy$  plane. The second molecule was placed in space by random rotational orientation around three internal axes (pitch, roll, and yaw) and translation of the molecule’s center of mass. (The latter is conveniently done in spherical polar coordinates so as to constrain the minimization search using symmetry considerations.) It is important to note that the internal molecular structure was fixed and only the relative molecular orientation was optimized. The geometry of minimum energy, as well as the resultant binding energy, were both found to be largely invariant of the initial geometry guess.

Calculations for clusters containing 3 or more molecules were performed using an analogous Simplex algorithm. The first molecule was centered at the origin and in the  $xy$  plane. Subsequently added molecules were quasi-randomly distributed by slightly varying relative orientation angles but distributing the molecules at 4 1 Å steps along the  $z$ -axis.

## 6. RESULTS AND DISCUSSION

### 6.1. Homo-molecular dimers

Calculations were performed for several permutations of dispersive potentials (using both Eqs. 1 and 2) and electrostatic potentials using Eq. 3 and several published sets of charges for different atom types. Relatively minor differences were observed in the dispersive potential calculated using the LJ 6-12 potential of van de Waal and that calculated using our earlier exp-6 potential. Electrostatic potentials calculated using the Miller et al. charge set [69] agreed well with those using charges suggested by Obolensky et al. [93]. However, substantial differences in the electrostatic potential and consequently the total intermolecular potential were found using the charge set of Rubio et al. [94]. This is likely due to the latter’s assumption of higher charges for internal carbons.

For coronene pairs, the intermolecular potentials were calculated (using both Miller et al. dispersive and electrostatic functions and employing the charge set from the same source [69]) for translation along a slip parallel plane, with plane separation of 3.5 Å. The highest binding energy was observed for a nearly, but not completely, eclipsed formation. Further, substantial binding energy between the two molecules was observed even when a fairly large distance displaced them. Specifically, when the first carbon atoms on opposite molecules begin to overlap, with a center of mass (COM) separation of 7.4 Å, there is already binding energy of 25.8 kJ/mol. At a COM separation of 4.9 Å (which corresponds to the first complete ring overlap), the binding energy exceeds 50 kJ/mol.

We also investigated energy barriers to rotation around the axis of symmetry in the fully eclipsed coronene dimer. At a fixed intermolecular separation of 3.5 Å, the rotation barrier was found to be slightly less than 2 kJ/mol, less than 1% of the total binding energy, and less than  $k_B T$  at flame temperatures. These calculations illustrate how thermal energy can be accommodated in the aggregate's internal degrees of freedom.

Minimum binding energies were calculated for a series of homo-molecular dimers along the Stein-Fahr stabilomer grid (Figure 5) [77]. For these results, the van de Waal LJ 6-12 dispersive potential was summed with an electrostatic potential using the Miller et al. [69] charge set. For the vast majority of dimer pairs, the most stable configuration was the plane-parallel, displaced geometry with relatively small displacements for larger monomers. Further, the calculations show that binding energies rise rapidly with molecular size and asymptotically approach the experimentally established exfoliation energy for graphite of  $5.0 \pm 0.5$  kJ (mol)<sup>-1</sup>(carbon atom)<sup>-1</sup> [68, 95]. For smaller PAH species, the difference between the calculated binding energy and this limit is a reflection of electrostatic repulsion, driven by interactions of atoms near the molecules' edges.

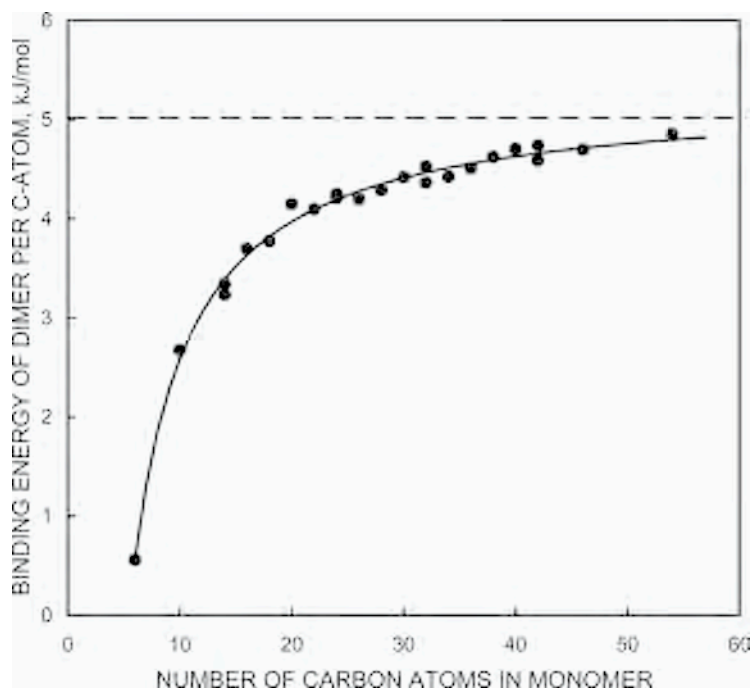


Figure 5. Computed binding energy for homo-molecular pairs of PAH along the Stein-Fahr stabilomer grid. Energy is expressed as binding energy per carbon atom in monomer for comparison with the experimental exfoliation energy of graphite ( $5.0$  kJ (mol)<sup>-1</sup> (C-atom)<sup>-1</sup>), shown as the dashed line.

## 6.2. Hetero-molecular dimers

As noted above, as both the computational models and experimental data suggest, a given aromatic molecule is unlikely to encounter species during a flame encounter. We have used the same computational approach to calculate binding energies of mixed (hetero-molecular) dimers. Twenty-five PAH ranging from benzene to circum-circum-circumcoronene ( $C_{150}H_{30}$ ) in size were used to run 321 unique energy minimizations, including the 23 homo-molecular dimers discussed above. The binding energies for this grid of dimers are shown in Figure 6. Finally, it was observed that this binding energy correlated well with the reduced mass of the colliding pair (Figure 7); an observation result that may be of value to the modeling community.

Soot inception generally occurs in flames in a temperature window of 1300 to 1600 K. At a temperature of 1500 K, 99% of dimers with a binding energy of 57 kJ/mol are bound. From our calculations, this is equivalent to a reduced mass greater or equal to 83 Da. The vast majority of the dimer calculations performed fall above this limit.

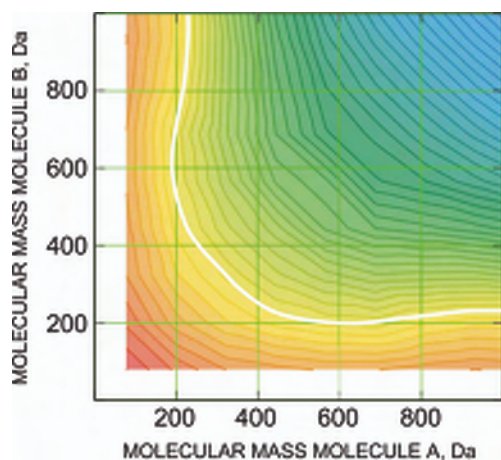


Figure 6. Contour map of computed binding energy for PAH dimers. The white line shows the approximate location of the 100 kJ/mol binding energy contour. Other contour lines are separated by 10 kJ (mol)<sup>-1</sup>.

## 6.3. Homo-molecular stacks

Calculations were performed for eight molecules ranging from 128 to 666 Da and stacks from two up to nine molecules. For each molecule, as the number of molecules in the stack increases, the binding energy *per added molecule* asymptotically approaches a limit (Figure 8) that was found to depend linearly on the size of the molecule. The geometries of clusters of PAH have been evaluated in the context of their role in

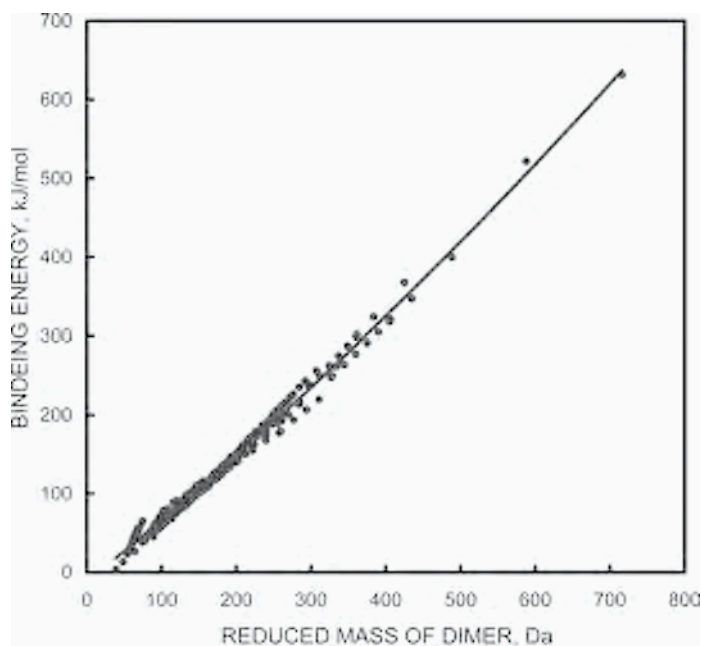


Figure 7. Binding energy for PAH dimers as a function of reduced mass. The equation of the polynomial fit is  $BE \text{ (kJ (mol)}^{-1}\text{)} = -11.93 + 0.7622 \times \mu \text{ (Da)} - 2.006 \times 10^{-4} \times (\mu \text{ (Da)})^2$ .

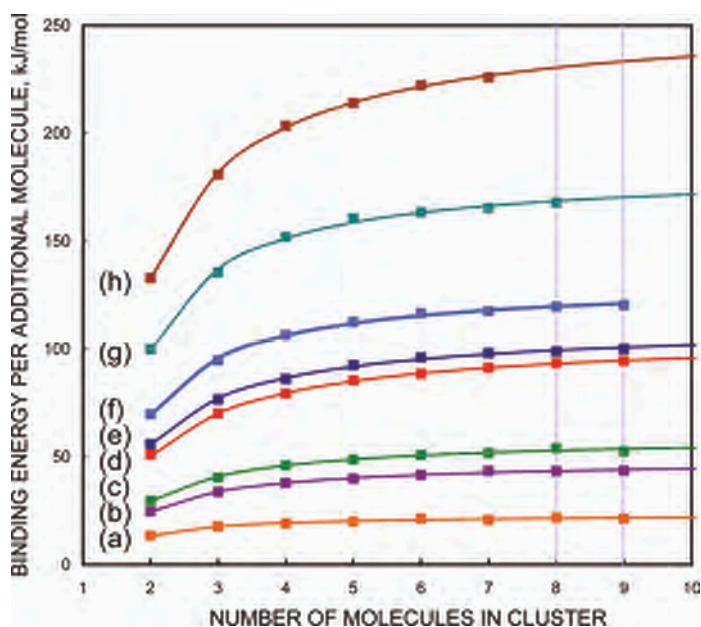


Figure 8. Binding energy per molecule added for stacked PAH aggregates. The asymptotic limit for each curve was found to scale linearly with molecular mass.

astrophysics. In 1983, van de Waal studied the geometry and stability of 13-molecule clusters of carbon dioxide, methane, benzene, cyclohexane and naphthalene. The favorable geometry of both benzene and naphthalene were calculated to be an icosahedral (regular in the case of benzene and slightly distorted for naphthalene) structure with a single molecule in the center [75]. Rapacioli et al. studied pyrene, coronene, and circumcoronene cluster structures. For each of these, a stability threshold in the size of a single stack of molecules was observed. Their calculations suggest that clusters of pyrene arrange into multiple stacks for clusters of more than seven molecules. For coronene and circumcoronene the transition point occurs for more than eight or seventeen molecules, respectively [73].

## 7. CONCLUSIONS

As noted earlier, the most critical step in the carbonization that accompanies soot inception may be the transition from 2-dimensional to 3-dimensional structures. In the present paper we evaluated atom pair parameters for intermolecular interactions and compared the resulting potentials for homo-molecular dimers of several PAH along the Stein-Fahr stabilomer grid. We found that binding energies rise rapidly with molecular size and asymptotically approach the experimentally established exfoliation energy for graphite of  $5.0 \pm 0.5 \text{ kJ (mol)}^{-1}(\text{carbon atom})^{-1}$ . For smaller PAH species, the difference between the calculated binding energy and this limit is a reflection of electrostatic repulsion, driven by interactions of atoms near the molecule's edge. Several important empirical results have emerged from our recent calculations:

- The binding interaction for mixed PAH dimers correlates directly with the reduced mass of the pair.
- The total binding energy of PAH clusters rises with each additional molecule, but approaches an asymptotic limit that depends on the molecular size.

These calculations are more rigorous than those our group has published in the past in that more realistic potentials have been used covering more configuration space. We now find that binding energies for PAH are high enough that binding is thermally likely at flame temperatures for the vast majority of PAH along the Stein-Fahr stabilomer grid. Future work will include use of these new results in an evaluation of the second virial coefficient and the resulting equilibrium constant for the condensation process.

*Note added in proof.* The results of our atom-pair potential calculations outlined above have now been published [96].

## ACKNOWLEDGMENTS

The authors acknowledge support for this work from the US National Science Foundation (NSF-CTS 0330230) with Drs. Farley Fisher, Linda Blevins, and Philip Westmoreland serving as technical monitors.

## REFERENCES

1. A. G. Donchev, *Phys. Rev. B* 74 (2006) 235401-235406.
2. H. G. Wagner, *Proc. Combust. Inst.* 17 (1979) 3-19.
3. F. Salama, G. A. Galazutdinov, J. Krelowski, L. J. Allamandola, F. A. Musaev, *Astrophys. J.* 526 (1, Pt. 1) (1999) 265-273.
4. L. Biennier, F. Salama, L. J. Allamandola, J. J. Scherer, A. O'Keefe, NASA Conference Publication 2002-211863 (*Proc. of the NASA Laboratory Astrophysics Workshop, 2002*) (2002) 113-116.
5. D. M. Hudgins, C. W. Bauschlicher, Jr., L. J. Allamandola, *Astrophys. J.* 632 (1, Pt. 1) (2005) 316-332.
6. R. Ruiterkamp, T. Halasinski, F. Salama, B. H. Foing, L. J. Allamandola, W. Schmidt, P. Ehrenfreund, *Astronom. and Astrophys.* 390 (3) (2002) 1153-1170.
7. Y. M. Rhee, T. J. Lee, M. S. Gudipati, L. J. Allamandola, M. Head-Gordon, *Proceedings of the National Academy of Sciences* 104 (13) (2007) 5274-5278.
8. H. F. Calcote, D. B. Olson, D. G. Keil, *Energy & Fuels* 2 (1988) 494-504.
9. P. Weilmunster, A. Keller, K. H. Homann, *Combust. Flame* 116 (1/2) (1998) 62-83.
10. D. K. Bohme, *Chemical Review* 92 (1992) 1487-1508.
11. S. E. Stein, A. Fahr, *J. Phys. Chem.* 89 (1985) 3714-3725.
12. M. Frenklach, *Phys. Chem. Chem. Phys.* 4 (2002) 2028-2037.
13. B. D. Crittenden, R. Long, *Combust. Flame* 20 (359) (1973)
14. M. J. Castaldi, N. M. Marinov, C. F. Melius, J. Huang, S. M. Senkan, W. J. Pitz, C. K. Westbrook, *Symposium (International) on Combustion, [Proceedings] 26th (Vol. 1)* (1996) 693-702.
15. C. S. McEnally, L. D. Pfefferle, *Combust. Flame* 115 (1/2) (1998) 81-92.
16. D. E. Jensen, *Proc. R. Soc. London, Ser. A, Mathematical and Physical Sciences* 338 (1974) 375-396.
17. M. D. Smooke, M. B. Long, B. C. Connelly, M. B. Colket, R. J. Hall, *Combust. Flame* 143 (4) (2005) 613-628.
18. K. Netzell, H. Lehtiniemi, F. Mauss, *Proc. Combust. Inst.* 31 (Part 1) (2007) 667-674.
19. C. A. Schuetz, M. Frenklach, *Proc. Combust. Inst.* 29 (2002) 2307-2314.
20. J. H. Miller, *Proc. Combust. Inst.* 23 (1991) 91-98.
21. J. H. Miller, *Proc. Combust. Inst.* 30 (2005) 1381-1388.
22. J. H. Miller, K. C. Smyth, W. G. Mallard, *Proc. Combust. Inst.* 20 (1985) 1139.
23. C. A. Schuetz, M. Frenklach, *Proc. Combust. Inst.* 29 (2002) 2307-2314.
24. G. P. Prado, M. L. Lee, R. A. Hites, D. P. Hoult, J. B. Howard, *Proc. Combust. Inst.* 16 (1977) 649-661.
25. A. Di Lorenzo, A. D'Alessio, V. Cincotti, S. Masi, P. Menna, C. Venitozzi, *Symp. (Int.) Combust., [Proc.] FIELD Full Journal Title: Symposium (International) on Combustion, [Proceedings] 18th* (1981) 485-491.
26. G. Prado, P. R. Westmoreland, B. M. Andon, J. A. Leary, K. Biemann, W. G. Thilly, J. P. Longwell, J. B. Howard, *Formation of Polycyclic Aromatic Hydrocarbons in Premixed Flames. Chemical Analysis and Mutagenicity* (1981).
27. J. D. Bittner, J. B. Howard, *Proc. Combust. Inst.* 18 (1981) 1105-1116.
28. J. P. Longwell, *Proc. Combust. Inst.* 19 (1982) 1339.
29. A. Keller, R. Kovacs, K.-H. Homann, *Phys. Chem. Chem. Phys.* (2000) 1667-1675.
30. J. Happold, H.-H. Grotheer, M. Aigner, *Rapid. Commun. Mass Spectrom.* 21 (7) (2007) 1247-1254.
31. A. Di Lorenzo, A. D'Alessio, V. Cincotti, S. Masi, P. Menna, C. Venitozzi, *Symposium (International) on Combustion, [Proceedings] 18th* (1981) 485-491.

32. B. S. Haynes, H. Jander, H. G. Wagner, *Berichte der Bunsen-Gesellschaft* 84 (1980) 585.
33. D. S. Coe, J. I. Steinfeld, *Chem. Phys. Lett.* 76 (3) (1980) 485-489.
34. D. S. Coe, B. S. Haynes, J. I. Steinfeld, *Combust. Flame* 43 (2) (1981) 211-214.
35. R. Barbella, F. Beretta, A. Ciajolo, A. D'Alessio, *Polynucl. Aromat. Hydrocarbons: Phys. Biol. Chem., Int. Symp.*, 6th (1982) 83-92.
36. J. H. Miller, W. G. Mallard, K. C. Smyth, *Combust. Flame* 47 (2) (1982) 205-214.
37. F. Beretta, V. Cincotti, A. D'Alessio, P. Menna, *Combust. Flame* 61 (3) (1985) 211-218.
38. F. Beretta, A. D'Alessio, A. D'Orsi, P. Minutolo, *Combust. Sci. Technol.* 85 (1-6) (1992) 455-470.
39. A. D'Alessio, A. Ciajolo, A. D'Anna, P. Minutolo, *From Mol. Dyn. Combust. Chem., Workshop Int. Inst. Pure Appl. Chem.* (1992) 309-331.
40. A. Ciajolo, R. Barbella, A. Tregrossi, L. Bonfanti, *Symposium (International) on Combustion, [Proceedings]* 27th (Vol. 1) (1998) 1481-1487.
41. W. C. Gardiner, *The Chemistry of Flames* (1982).
42. K. C. Smyth, C. R. Shaddix, S. A. Everest, *Combust. Flame* 111 (1997) 185-207.
43. A. Leipertz, F. Ossler, M. Alden, *Polycyclic Aromatic Hydrocarbons and Soot Diagnostics by Optical Techniques* (2002).
44. K. C. Smyth, J. H. Miller, R. C. Dorfman, W. G. Mallard, R. J. Santoro, *Combust. Flame* 62 (2) (1985) 157-181.
45. A. D'Alessio, G. Gambi, P. Minutolo, S. Russo, *Symposium (International) on Combustion, [Proceedings]* 25 (1994) 645-651.
46. A. Ciajolo, R. Ragucci, B. Apicella, R. Barbella, M. De Joannon, A. Tregrossi, *Chemosphere* 42 (5-7) (2001) 835-841.
47. A. Ciajolo, A. Tregrossi, R. Barbella, R. Ragucci, B. Apicella, M. de Joannon, *Combust. Flame* 125 (4) (2001) 1225-1229.
48. P. Minutolo, G. Gambi, A. D'Alessio, A. D'Anna, *Combust. Sci. Technol.* 101 (1-6) (1994) 311-325.
49. C. Allouis, B. Apicella, R. Barbella, F. Beretta, A. Ciajolo, A. Tregrossi, *Chemosphere* 51 (10) (2003) 1097-1102.
50. H. Richter, T. G. Benish, O. A. Mazyar, W. H. Green, J. B. Howard, *Proc. Combust. Inst.* 28 (2000) 2609-2618.
51. A. Violi, *Combust. Flame* 139 (4) (2004) 279-287.
52. S. L. Fiedler, S. Izvekov, A. Violi, *Carbon* 45 (2007) 1786-1794.
53. J. B. Birks, *Photophysics of Aromatic Molecules*. Wiley-Interscience, London, 1970.
54. B. Stevens, E. Hutton, *Nature (London, United Kingdom)* 186 (1960) 1045-1046.
55. J. B. Birks, D. J. Dyson, I. H. Munro, *Proc. R. Soc. London, Ser. A* 275 (1363) (1963) 575-588.
56. M. A. Slifkin, *Nature (London, United Kingdom)* 200 (4908) (1963) 766-767.
57. C. R. Goldschmidt, Y. Tomkiewicz, A. Weinreb, *Spectrochim. Acta, Part A* 25 (8) (1969) 1471-1477.
58. T. Seko, K. Ogura, Y. Kawakami, H. Sugino, H. Toyotama, J. Tanaka, *Chem. Phys. Lett.* 291 (3,4) (1998) 438-444.
59. T. Fujii, E. Shimizu, *Chem. Phys. Lett.* 137 (5) (1987) 448-452.
60. H. Auweter, D. Ramer, B. Kunze, H. C. Wolf, *Chem. Phys. Lett.* 85 (3) (1982) 325-329.
61. H. Daeubler, V. I. Yudson, P. Reineker, *J. Luminol.* 60-61 (1994) 454-457.
62. A. Matsui, K. Mizuno, M. Kobayashi, *J. Phys., Colloque (C7)* (1985) 19-23.
63. K. A. Nelson, D. D. Dlott, M. D. Fayer, *Chem. Phys. Lett.* 64 (1) (1979) 88-93.
64. Straughton and Walter (Eds.), *Spectroscopy*, V. 3 Chapman and Hall, London, 1976.
65. A. L. L. East, E. C. Lim, *J. Chem. Phys.* 113 (20) (2000) 8981-8994.

66. J. C. Amicangelo, *J. Phys. Chem. A* 109 (2005) 9174-9182.
67. S. Grimme, *J Comput Chem* 25 (2004) 1463-1473.
68. A. G. Donchev, *Phys. Rev. B* 74 (2006) 235401/235401-235401/235406.
69. J. H. Miller, W. G. Mallard, K. C. Smyth, *J. Phys. Chem.* 88 (21) (1984) 4963-4970.
70. H. Saigusa, M. Morohoshi, S. Tsuchiya, *J. Phys. Chem. A* 105 (2001) 7334-7340.
71. Q. Wu, W. Yang, *J. Chem. Phys.* 116 (2002) 515-524.
72. S. Grimme, *J. Comput. Chem.* 27 (15) (2006) 1787-1799.
73. M. Rapacioli, F. Calvo, F. Spiegelman, C. Joblin, D. J. Wales, *J. Phys. Chem. A* 109 (11) (2005) 2487-2497.
74. O. I. Obolensky, V. V. Semenikhina, A. V. Solov'yov, W. Greiner, *Int. J. Quant. Chem.* 107 (2007) 1335-1343.
75. B. W. van de Waal, *J. Phys. Chem.* 79 (8) (1983) 3948-3961.
76. B. W. van de Waal, *Chem. Phys. Lett.* 123 (1,2) (1986) 69-72.
77. S. E. Stein, A. Fahr, *J. Phys. Chem.* 89 (1985) 3714-3725.
78. D. Mainwaring, T. Jakubov, L. Calvitto, *J. Nanopart. Res.* 7 (59) (2005)
79. M. Rapacioli, F. Calvo, C. Joblin, P. Parneix, F. Spiegelman, *J. Phys. Chem. A* 111 (2007) 2999.
80. L. L. Lohr, C. H. Huben, *J. Chem. Phys.* 99 (6369) (1993)
81. Y. Paterson, G. Nemethy, H. A. Scheraga, *J. Solution Chem.* 11 (1982) 831.
82. R. L. Ornstein, R. Rein, D. L. Breen, R. D. Macelroy, *Biopolymers* 17 (2004) 2341.
83. H. B. Levin, D. A. McQuarrie, *J. Chem. Phys.* 44 (1966) 3500.
84. J. R. Olsen, S. Legvold, *J. Chem. Phys.* 39 (11) (1963) 2902-2908.
85. C. L. Kong, *J. Chem. Phys.* 59 (2) (1973) 968-967.
86. J. Han, A. Globus, R. Jaffe, G. Deardorff, *Nanotechnology* 8 (1997) 95-102.
87. S. Chalmet, M. F. Ruiz-Lopez, *Chem. Phys. Lett.* (329) (2000) 154.
88. A. Gavezotti, *Chem. Phys. Lett.* 161 (1) (1989) 67-72.
89. M. A. Spackman, *J. Chem. Phys.* 85 (1986) 6579.
90. R. Hoffmann, *J. Chem. Phys.* 39 (1963) 1397-1412.
91. I. HyperCube, program: HyperChem, 2003.
92. Borland, program: Delphi 7 Professional, 2002.
93. O. I. Obolensky, V. V. Semenikhina, A. V. Solov'yov, W. Greiner, Los Alamos National Laboratory, Preprint Archive, Physics (2005) 1-13, arXiv:physics/0511027.
94. M. Rubio, E. Orti, J. Sanchez-Marin, *Int. J. Quant. Chem.* 57 (1996) 567-573.
95. R. Zacharia, H. Ulbricht, T. Hertel, *Phys. Rev. B* 69 (2004) 155406-155406-155407.
96. J. D. Herdman, J. H. Miller, *J. Phys. Chem. A* 112 (2008) 6249-6256.

# Soot precursors consisting of stacked pericondensed PAHs

J. Happold, H.-H. Grotheer, M. Aigner

*DLR Institute of Combustion Technology, Pfaffenwaldring 38-40, 70569 Stuttgart, Germany*

*Abstract: As a consequence of electronic interaction between layers soot precursors consisting of stacked PAHs exhibit a reduced ionization potential (work function) in comparison to PAH monolayers. This enables ionization via a single photon step when 193 nm radiation (ArF excimer laser) is used in a photoionization mass spectrometer. Furthermore it enables a clear distinction between these particles and gas phase molecules. Consequently the smallest masses (sizes) of these particles can be taken directly from the mass spectra. An analysis in terms of H numbers as a function of C numbers reveals that these particles are composed of pericondensed PAHs. Other particles that show up as giant molecules presumably exhibit an ionization behaviour like normal molecules and escape detection under the conditions of this work.*

## 1. INTRODUCTION

In a previous paper [1] we have shown that it is possible to distinguish mass spectrometric signals of gaseous PAHs and those of soot precursor particles through their photo ionization schemes. Aim of the current paper is to exploit this capability to trace the formation and further fate of soot precursor particles as a function of burning conditions and for several fuels. Such a study is insofar of interest as current soot models are only similar with regard to the gas phase submechanism, i. e. formation of the first aromatic rings and their growth through the well-known HACA mechanism [2] or reactive dimerisation [3]. Major differences, however, are found with regard to particle formation mechanisms. Two extremes are considered here.

- (i) Frenklach and several other authors (see [4] and references therein) characterize soot particle formation as sticking of PAHs to form stacks of dimers, then trimers and so on while individual PAH species keep increasing in size via molecular chemical growth reactions. The sticking in turn is a merely physical process as it is caused by van der Waals forces without involving any chemical reactions. The emergence of the “solid” particle phase, i. e. inception, is marked through the formation of dimers, which are mostly assumed to consist of pyrene molecules (202 u).
- (ii) In other mechanisms aromatics are assumed to grow to much larger sizes through radical molecule reactions. An example is the mechanism advanced by Violi and coworkers [5-8]. Characteristic is the addition of an aryl radical (e.g. naphthyl) to the double bond of a cyclo penta- (CP) PAH such as acenaphthylene followed by an H abstraction from the site where the addition took place. This restores a resonant structure that is particularly stable. When the process is repeated high molecular species are formed (called: nanoparticles) consisting of smaller aromatic substructures of up to 3 rings that are tied together through aliphatic bonds [6].

Inception occurs in this scenario when bays are closed upon H abstraction leading to an extension of the “aromatic islands” [7].

When using mass spectrometry to monitor the process of soot formation, for primary soot particles with lowest masses around several  $10^5$  u it is hardly conceivable that useful information other than the total mass can be obtained through non-fragmenting mass spectrometry. For soot precursor particles in the mass range between 600 u and several 1000 u [1], however, the situation is more promising. Here unity resolution may be achieved and this potentially allows to deduce structural information. Goal of this study is therefore to learn more about inception and subsequent growth of soot precursor particles. As has been pointed out only recently [9] an important and sensitive feature in this regard is the size of incipient soot particles which should be an easy target of mass spectrometry.

## 2. EXPERIMENTAL

The apparatus has been described in some detail in our previous paper [1]. Soot, soot precursor particles and other flame species were generated in a movable low pressure burner (diameter 40 mm, 130 mbar). The fuels  $C_2H_2$ ,  $C_2H_4$  and  $CH_4$ ,  $C_2H_6$ ,  $C_3H_6$  were burnt with  $O_2$ . The burner discharged via a nozzle into a fast flow reactor which in

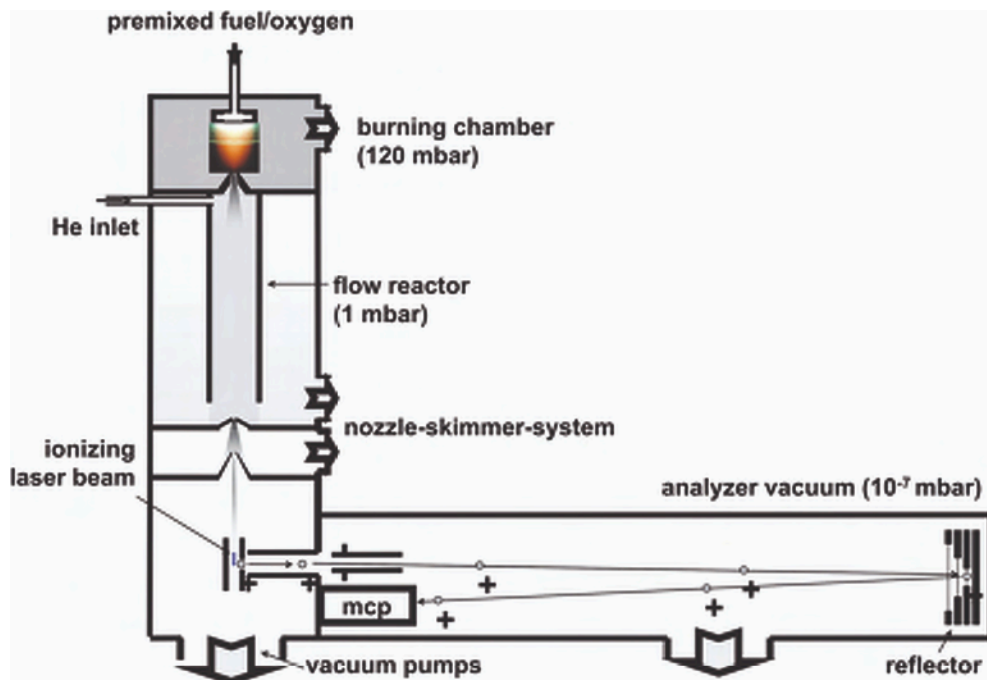


Figure 1. Experimental set-up of the photo ionization time-of-flight mass spectrometer.

turn was connected via a molecular beam inlet to the MS. The reactor used in the current experiments was only 110 mm long and 15 mm wide resulting under our operating conditions in residence times on the order of 1.5 ms. Thus reactions taking place in the reactor were minimised. Only under these conditions spectra as clearly structured as those of the subsequent figures could be obtained. The 60 cm reactor used in an earlier version [10] had a tendency to blur these structures. All experiments were conducted under rich sooting conditions ( $C/O \geq 1.0$ ), in a height above burner (HaB) of 30 mm and at pressures of 120 mbar in the combustion chamber and 1.4 mbar in the flow reactor section. The total gas flow in the burner (fuel and oxygen, no nitrogen used) was 1.2 standard liters / min.

A commercial reflectron time-of-flight MS was modified to enable detection of heavier ions (up to 2.000.000 u). It was equipped with a photoionization source consisting of an excimer laser (10 ns pulse length, laser gas ArF or KrF). The beam was collimated by rectangular apertures and no focussing lens was used in order to avoid fragmentation. By means of a set of attenuators fluences for photo ionization of 0.01 up to 0.1 MW/cm<sup>2</sup> could be obtained. The mass scale of our mass spectrometers is known through frequent calibrations. The sensitivity of our ion signals, however, could not yet be determined.

Mass spectra were obtained as averages over 20.000 laser shots.

### 3. RESULTS

Using an ArF laser for photo ionization (193 nm, 6.4 eV) spectra exhibiting hilly structures were observed extending well into the region of several 1000 u (Figure 2).

By contrast, using KrF (248 nm, 5.0 eV) only gas phase spectra as those described in the previous literature [11] were found (inset of Figure 2). They are mainly comprised of the well-known PAH series with strong signals around pyrene (202 u) and decreasing signal intensity towards PAHs of higher masses.

The investigations with an ionization laser wavelength of 193 nm revealed that the same PAH series can be detected. The maximum signal intensity is, as well, around pyrene. The decrease in signal intensity, however, is much less pronounced and the spectra extend to significantly higher masses.

The hilly structure of those spectra above 800 u has never been described in the literature and is of particular interest. Under certain flame conditions the hilly structure could be enhanced to yield spectra that are typical for polymers (Figure 3). From the mass difference of the equidistant hills it is concluded that the mass of the monomer is about 450 u. Consequently, Figure 3 shows dimers, trimers and tetramers.

A closer examination of the reactants and products helps to characterize the polymerization process.

#### 3.1. Analysis of the spectra

The gas phase portions of the spectra (lower masses) always show the typical pattern of the PAH series. At certain flame conditions and only visible under 193 nm ioniza-

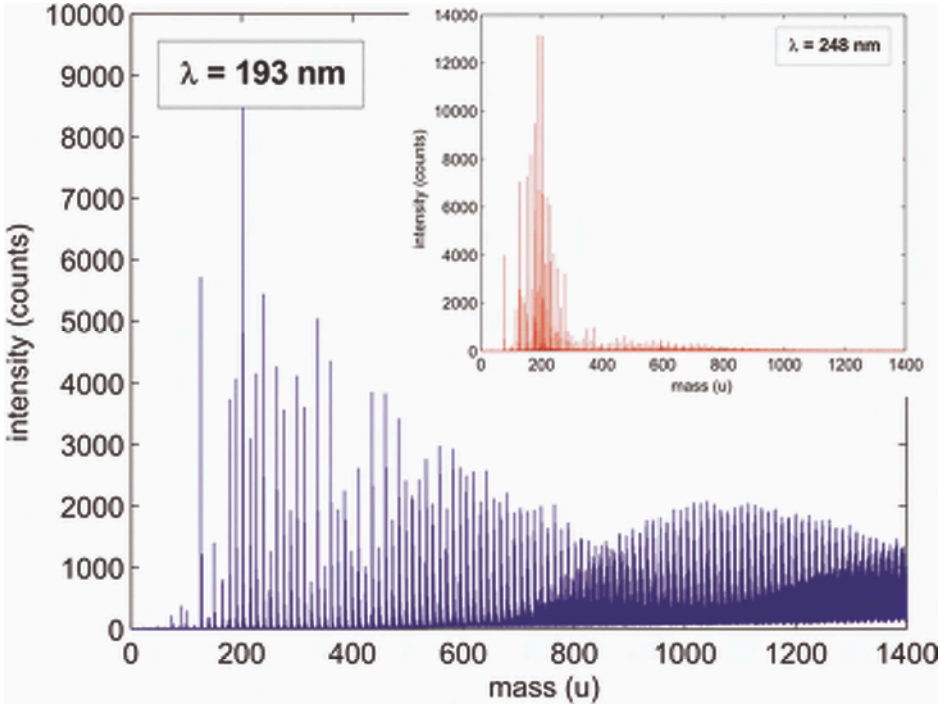


Figure 2. Mass spectra of an ethylene/oxygen flame with ionization laser wavelengths of 193 nm and 248 nm (inset).

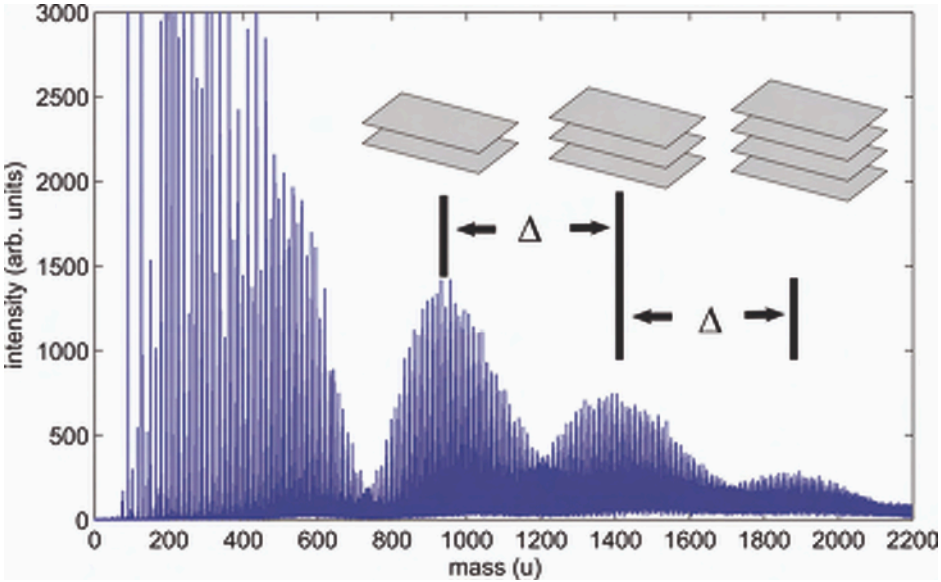


Figure 3. Spectrum of ethine/oxygen flame (193 nm ionization laser wavelength, C/O = 1.3).

tion, a second series emerges (“overlaid” series, corresponding to the dimer in Figure 3) which is shifted relative to the first series (Figure 4). Obviously the start of this “dimer” series is around 680 u, i.e. considerably above 404 u which corresponds to a pyrene double layer.

After correction for  $^{13}\text{C}$  isotopes the spectra were analyzed for H and C numbers assuming that these atoms are the only product constituents. For flames exhibiting no hilly structure in the spectra, an H vs. C distribution was found (Figure 5) as is typical for pericondensed PAHs [11], curves in Figures 5 and 6.

It was found that ethane and propane do not show hilly structures and here the mass spectra only consist of an extended PAH series (up to 120 carbon atoms). Fuels that we found to exhibit the hilly structures are ethylene, acetylene, propylene. Note that the flames with the different fuels were compared using a ratio of  $\text{C}/\text{O} = 1.0$ , a height above burner of 30 mm and a pressure in the combustion chamber of 120 mbar.

When using different fuels under these conditions temperatures and pressures in the flame vary greatly. At first sight, the main difference between fuels that lead to spectra with a hilly structure and those that do not is the flame temperature. Ethane and propane in our case lead to calculated adiabatic flame temperatures of about 1200-1400 K whereas ethylene, acetylene and propene burn at temperatures above 2000 K. Preliminary studies attempting a variation of flame temperatures by addition of helium or nitrogen to ethylene/oxygen flames show that temperature is indeed the domina-

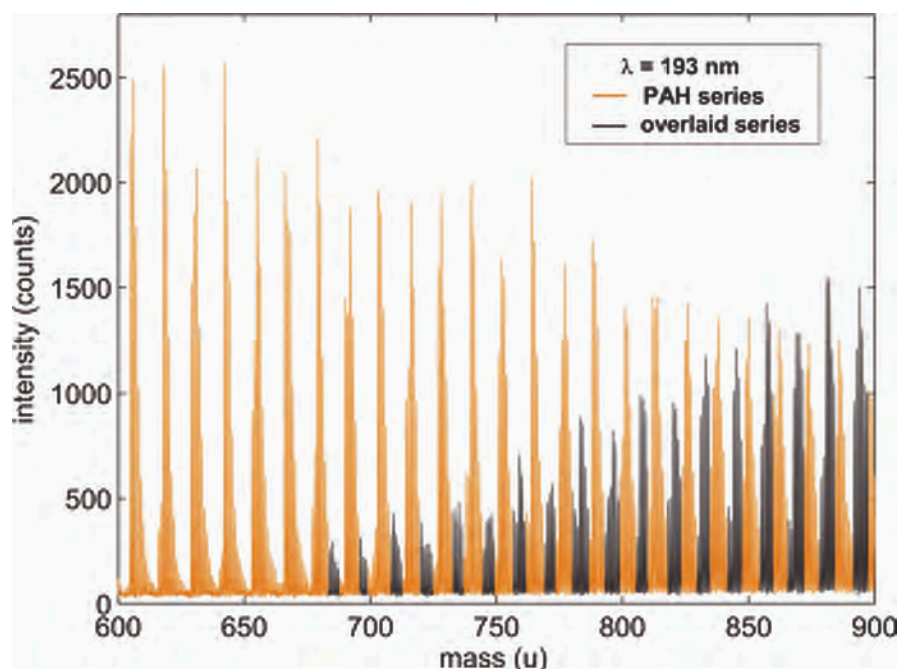


Figure 4. Mass spectrum of an ethylene/oxygen flame between 600 and 900 u.

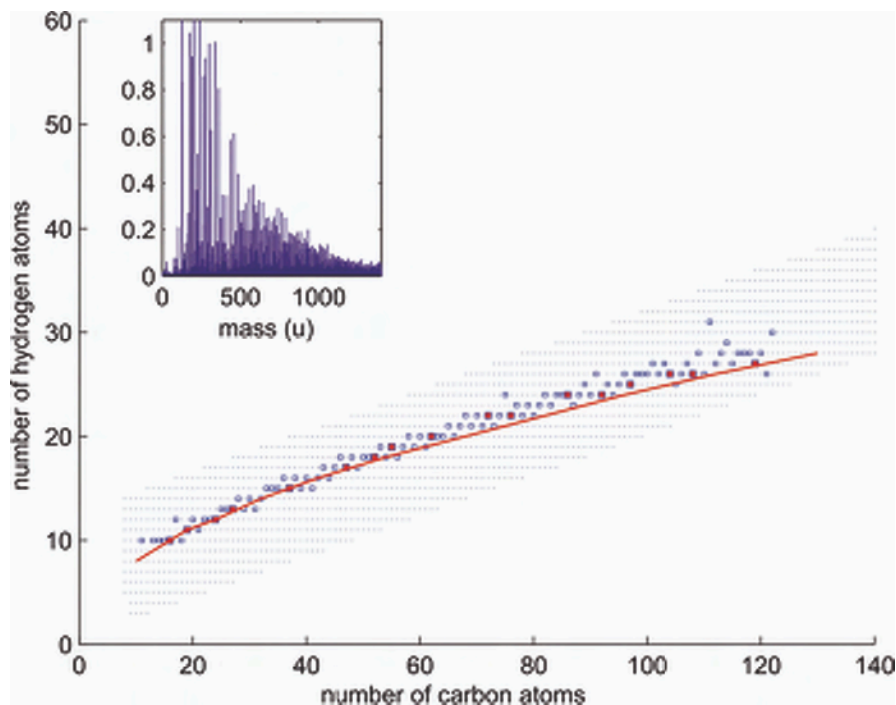


Figure 5. H/C-diagram and mass spectrum of an ethane/oxygen flame ( $C/O = 1.0$ ). Red dots denote strong signals.

ting variable in the formation of the hilly structures in the spectra. Still further research in this area is required.

For spectra showing hill-structures the first portion of the H vs. C curves was indistinguishable from Figure 5. Dimer formation shows up as a break in the H vs. C curve which continues with the same slope, yet a higher H number (Figure 6). The same behavior is found for the next hill (trimer) and it is interpreted again through structures consisting of pericondensed PAH polymers.

The exact position of the dimers and trimers in the H/C-diagrams, i.e. the size and shape of the constituents, depends not solely on fuel and temperature. A very sensitive dependency on pressure has also been found. The present set-up only allowed for pressures in the burner chamber of up to 250 mbar. It has been found that with increasing pressure the size of the monomers also increases. A new set-up for the investigation of flame exhaust at pressures up to 1 bar is under construction.

### 3.2. Polymer chains or stacks?

When comparing the mass spectra of 193 nm and 248 nm laser ionization wavelength it is obvious that the hilly structures show up in addition to the PAH series. This fact

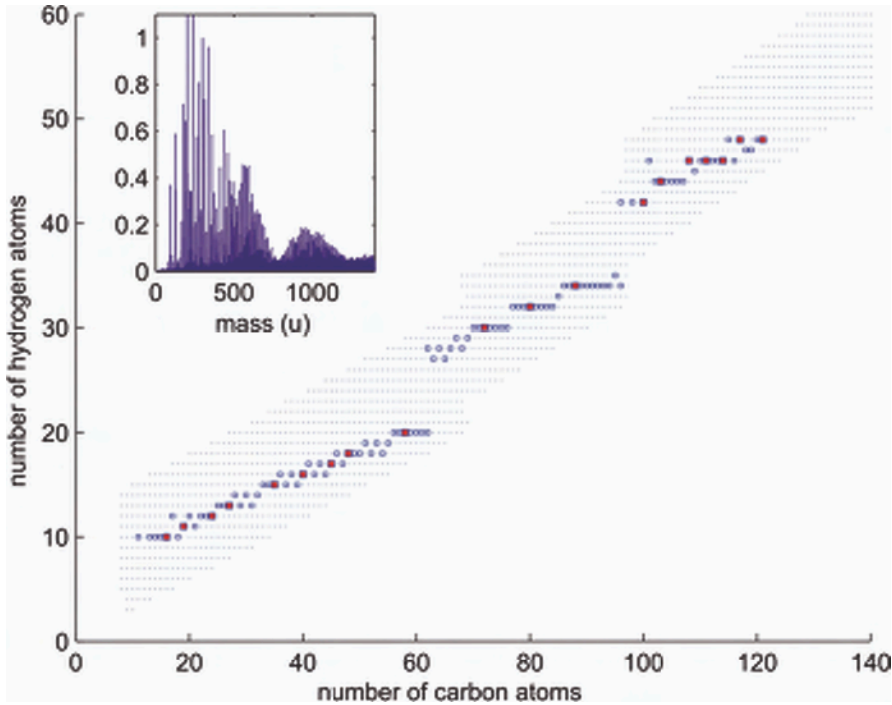


Figure 6. H/C-diagram and mass spectrum of an ethylene/oxygen flame ( $C/O = 1.0$ ).

reveals that not a series of similar chemical composition and a more or less unchanged ionization potential is detected. Instead, a completely different type of molecules or particles is measured. Nevertheless the new series most probably consists of the molecules that can also be detected when using the 248 nm as ionization wavelength. So the question is: Can the hilly structure really resemble conventional polymer chains?

To answer that one needs to know more about the kind of bonds that exists between the monomers. Usually one refers to polymers if there are covalent chemical bonds between the monomers. For instance, in the case of two PAHs connected by a covalent chemical bond (biaryls) one would not expect a different ionization behavior. Thus a closer look at the ionization itself is necessary.

The determination of the ionization order (IO) is a good method to find out about the interaction of the laser beam with the molecules and particles. The ionization order  $n$  is defined as

$$I_m^+ = \text{const} \cdot (P_L)^n,$$

where  $I_m^+$  denotes the intensity of the ion signal at mass  $m$  (which ideally should contain only one constituent),  $P_L$  denotes the power density of the laser pulse.  $n$  is determined as slope in an  $\lg(I_m^+)$  vs.  $\lg(P_L)$  plot (see for example Figure 7). In the absence

of saturation effects the IO represents the number of photons required for the ionization process in question. Results are shown in Figures 8 and 9.

For 248 nm (KrF) we observe an IO of 2 for all detected ions (Figure 8). For 193 nm (ArF) two branches are found, one branch starting from IO = 2 in the limiting case, the other one starting from IO = 1.4 and rapidly reaching IO = 1. This means that the energy needed to ionize the overlaid series (second branch in Figure 9) decreases relative to that necessary for the ionization of PAHs. This effect can be explained through the mutual influence of stacked layers. Quantum mechanical calculations confirm that the ionization energy is reduced when two PAHs form stacks [12]. Experimentally the hypothesis of a stacked structure is supported by Bragg reflexions as reported in the literature [13].

Given that the stacked PAHs behave similar to solid state matter (such as in the case of carbon graphite) one can assume, that the reason why they cannot be detected with 248 nm laser wavelength lies in the fast internal energy dissipation which is typical for solid state matter.

The mutual interaction leads to a reduced work function [12] and thus enables single photon ionization (IO = 1) with 193 nm wavelength.

#### 4. DISCUSSION

It has already been pointed out that through the change in ionization order of the first overlaid series, i.e. the dimer in Figure 4, an assignment of these species as double

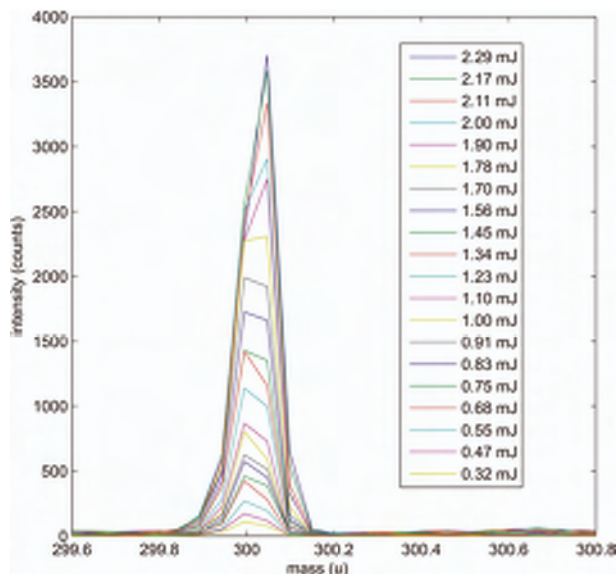


Figure 7. Signal of coronene as an exemplary PAH molecule for different laser pulse energies (248 nm).

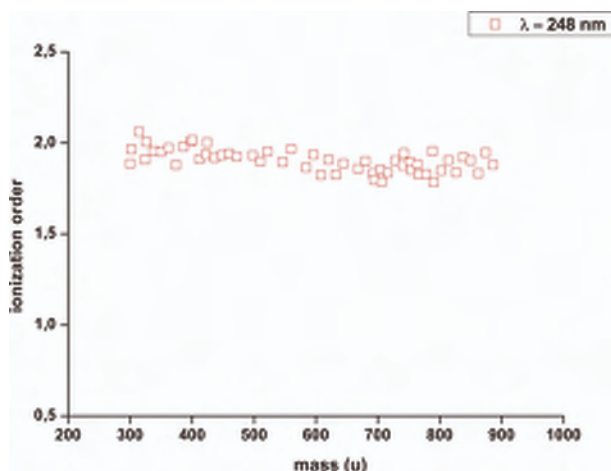


Figure 8. Ionization order for PAH molecules (248 nm laser wavelength).

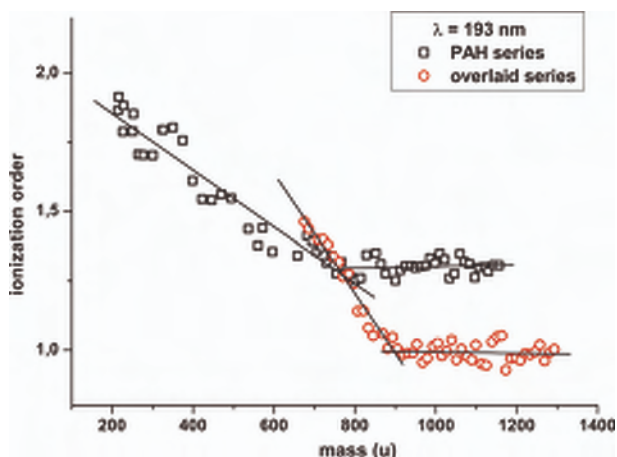


Figure 9. Ionization orders for PAH molecules and the additional overlaid series (193 nm).

layers becomes possible and that they can easily be distinguished from gas phase molecules. Their lowest mass is about 680 u, i.e. considerably above a pyrene double-layer (404 u).

Further implications of this single photon ionization (SPI) are

- (i) SPI indicates stacks instead of chains (solid state matter instead of molecular polymers)
- (ii) these particles are well distinguishable from molecules

- (iii) it explains the high sensitivity observed for the signals of the particles
- (iv) other workers have not been able to measure those particles as mainly longer wavelengths have been used for ionization.

A shift of ionization energy (work function) as described above is not expected for molecular clusters. Precursors of this type (as advanced by Violi et al. [5-8], Figure 10) would not be detectable under the ionization conditions described above. Consequently, the existence of this type of particles in the flame cannot be ruled out.

In fact, we could recently show behind an atmospheric ethylene air flame [14] that in a narrow window in terms of C/O and under certain ionization conditions two types of soot precursor particles with diameters below 4 nm can be detected simultaneously. The heavier species shows an IO of 1 and is obviously identical to the type of particles described in the present study. The lighter species, by contrast, follows an IO of 2, i.e. a behavior as expected for molecules. This suggests to tentatively assign them as molecular clusters of the type proposed by Violi [8].

The roles of these different structures in soot formation are discussed by Warnatz and coworkers [15] to be governed by different temperature regimes in the flame. At higher temperatures chemical growth is limited due to a high degree of reaction reversibility, i.e. high mass structures decompose. Only relatively small PAHs survive and form physically bound clusters. At lower temperatures there is no thermodynamic limitation of the structural form, and networks of aromatic-aliphatic-linked structures may form.

These workers [15] also note that under high resolution transmission electron microscopy (TEM) a primary soot particle shows up as an inner core surrounded by

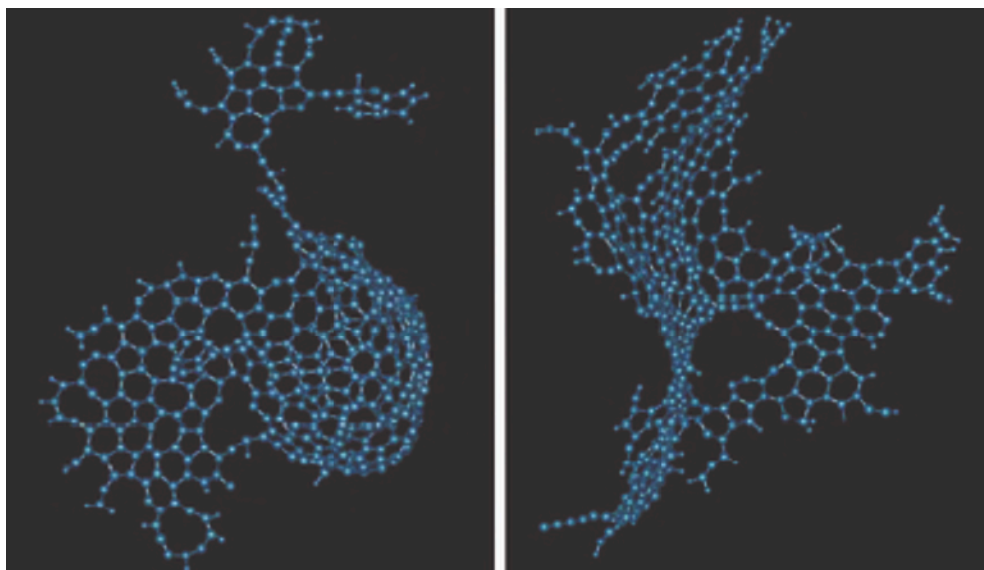


Figure 10. Visualization of soot precursors in the soot model of Violi et al. [8].

an outer shell. Only the outer shell is rigidly composed by graphitic structures whereas the inner core contains fine particles surrounded by carbon networks and is relatively unstable (see Figure 11).

It is a plausible assumption that these different structures originate from the two types of nanoparticles described above although the exact formation mechanism is still unclear.

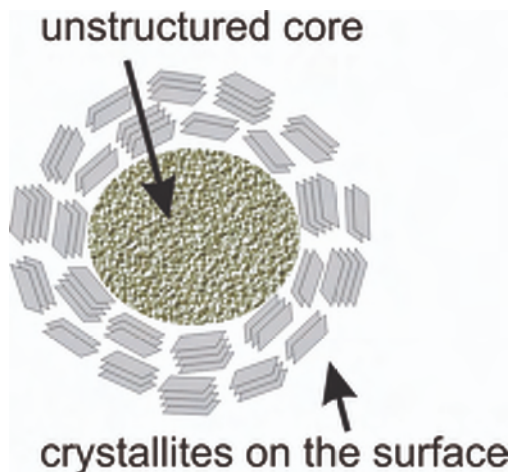


Figure 11. Visualization of primary soot as described by Naydenova et al. [15].

## 5. CONCLUSION

- Using 193 nm photo ionization spectra of soot precursors were found consisting of stacks of pericondensed PAHs.
- Under certain conditions and with certain fuels even rich sooting flames do not lead to the formation of stacked PAHs.
- Consequently this stacking of PAHs is not the only process in soot precursor formation.
- Therefore the results presented here add a further piece to current soot models.
- Especially in view of the soot formation mechanism put forth by Violi et al. [4,5] we do not see a contradiction but instead one more possible route to soot.

## ACKNOWLEDGEMENT

We thank H. Pokorny for his help in designing the apparatus and for carrying out some of the measurements.

**REFERENCES**

1. J. Happold, H.H. Grotheer, M. Aigner, *Rapid Commun. Mass Spectrom.* 21 (2007) 1247-1254.
2. H. Wang, M. Frenklach, *Combust. Flame* 110 (1997) 173-221.
3. K. Siegmann, H. Hepp, K. Sattler, *Combust. Sci. Technol.* 109 (1995) 165-181.
4. M. Frenklach, *Phys. Chem. Chem. Phys.* 4 (2002) 2028-2037.
5. A. Violi, A.F. Sarofim, T.N. Truong, *Combust. Flame* 126 (2001) 1506-1515.
6. A. D'Anna, A. Violi, A. D'Alessio, A. F. Sarofim, *Combust. Flame* 127 (2001) 1995-2003.
7. A. Violi, A.F. Sarofim, T.N. Truong, *Combust. Sci. Technol.* 174 (2002) 205-222.
8. A. Violi, *Combust. Flame* 139 (2004) 279-287.
9. J. Singh, R.I.A. Patterson, M. Kraft, H. Wang, *Combust. Flame* 145 (2006) 117-127.
10. H.H. Grotheer, H. Pokorny, K.L. Barth, M. Aigner, M., *Chemosphere* 57 (2004) 1335-1342.
11. A. Keller, R. Kovacs, K.H. Homann, *Phys. Chem. Chem. Phys.* 2 (2000) 1667-1675.
12. H. Miller, *Proc. Combust. Inst.* 30 (2005) 1381-1388.
13. H.X. Chen, R.A. Dobbins, *Combust. Sci. Technol.* 159 (2000) 109-128.
14. T. Gonzalez Baquet, H.H. Grotheer, M. Aigner, *Rapid Commun. Mass Spectrom.* 21 (2007) 4060-4064.
15. X.I. Naydenova, M. Nullmeier, J. Warnatz, P.A. Vlasov, *Combust. Sci. Technol.* 176 (2002) 1667-1703.

# Particle inception and growth: experimental evidences and a modelling attempt

A. D'Anna

Dipartimento di Ingegneria Chimica – Università di Napoli Federico II  
Piazzale V. Tecchio, 80 – 80125 Napoli, Italy

*Abstract: A detailed kinetic mechanism of aromatic growth and particle formation is presented and it is tested over a range of different operating conditions in rich premixed laminar flames and non-premixed flames of various hydrocarbons. Model development is refined in strictly connection with new experimental data on the formation of molecular particles, i.e. compounds of high molecular mass. Reaction pathways leading to the formation of molecular particles and their coagulation to soot have been included by using a discrete-sectional approach for the gas-to-particle process. Good predictions of major oxidation and pyrolysis products are obtained, as well as of trace species and particulate concentrations and particle size distributions. The model predicts particle size distribution functions with a single mode centered at about 2nm in premixed flames below the soot formation threshold and in the fuel side of non-premixed flames, in good agreement with experimental data. In premixed sooting flames and in the external zones of non-premixed flames the particle size distribution functions develop towards a bimodal shape with a first mode due to nanoparticles and a second mode due to primary soot particles. The kinetic model has been used to predict particle formation by using different hydrocarbons including methane, ethylene, n-heptane, benzene and mixtures of n-heptane with toluene, benzene and iso-octane. Sensitivity of the predictions to the particulate-phase reaction rates is performed. Model analysis shows the importance of the mechanism of aromatic-molecule addition to aromatic radicals in the formation of nanoparticles in premixed flames and the physical coagulation of PAHs in the formation of nanoparticles in non-premixed flame. The importance of acetylene addition in soot loading is also discussed.*

## 1. INTRODUCTION

Particle inception at high-temperature remains one of the less understood step in the process of soot formation. The development of new and sophisticated diagnostic tools in the last years has increased our knowledge about the transformation of gaseous precursors in the molecular particles. However, there are still many controversial and stimulating debates on the physical and chemical nature of nascent particles and on their number and sizes which strongly affect the amount and the size distribution of the final emitted particulate matter [1,2].

The aim of this paper is to present a detailed kinetic model of particle inception and growth able to describe the current picture of particulate matter formation in both premixed and diffusion flames through the prediction of the concentration profiles of trace pyrolysis products involved in the process of particle formation and the details of particle size distributions (PSDs). Comparison of model predictions with experi-

mental data on the formation of molecular particles, i.e. compounds of high molecular mass, mainly obtained in recent years by the research groups in Napoli at CNR and at the University, have assisted the model development.

The model includes fuel oxidation and pyrolysis, molecular weight grow of pyrolysis products up to particle nucleation, i.e. the transition from gas-phase species to nascent particles, and particle coagulation to larger soot particles [3,4]. A discrete-sectional approach [5] is used for the modeling of the gas-to-particle process; the ensemble of aromatic compounds with molecular mass higher than the largest aromatic compounds in the gas-phase is divided into classes of different molecular mass and all reactions are treated in the form of gas-phase chemistry by using compound properties such as mass, numbers of carbon and hydrogen atoms averaged within each section.

The model has been tested in different flame conditions in order to verify its capability to reproduce the main experimental evidences and to identify reaction pathways responsible for particle formation and PSD evolution with respect to changes in flame structure.

The paper is divided into five sections. The first section reports a summary of the experimental evidences on high-molecular-mass nascent particles. The second section deals with the development of the kinetic model. In the third section model predictions in various flame conditions burning different hydrocarbons are reported and compared with experimental data. Hydrocarbons include methane, ethylene, n-heptane, benzene and mixtures of n-heptane with benzene, toluene and *iso*-octane. The fourth section reports on the analysis of reaction pathways leading to particle formation for different flame structures. Finally, the main outcomes of the model are summarized in the Final Discussion section.

## 2. EXPERIMENTAL EVIDENCES

The first evidence of high-molecular-mass nascent particles in flames came out from the mass spectrometric studies of Homann and Wagner in the early sixties [6]. They had evidence in premixed flames of reactive Polycyclic Aromatic Hydrocarbons (PAHs), probably with side chains, containing more hydrogen than aromatics (mass range between 150 to 500). Some years later Howard and co-workers detected nascent particles in premixed flames first by molecular beam-sampling and electron microscopic analysis [7] and then by time-of-flight mass spectrometric analysis [8].

At the beginning of the nineties two research groups independently reported evidence of nano-sized precursor particles in flames. Dobbins and co-workers [9,10] found young particles as small as about 3 nanometers transparent to the electron beam of the TEM in the fuel-side of diffusion flames. D'Alessio and co-workers, using both in situ scattering/extinction measurements [11-15] and probe sampling and off-line chemical characterization [16-18], observed high-molecular-mass compounds with equivalent spherical sizes of 2-3 nm just downstream of the flame front of laminar premixed flames of methane and ethylene. Carbonaceous nanoparticles were observed later by in-situ optical measurements also in non-premixed laminar and turbulent flames [19-21]. In co-flowing diffusion flames they were detected in the lower tempera-

ture flame regions and closer to the flame axis, in agreement with Dobbins results [10], whereas in counter-flow configurations they were detected both in the fuel side and closer to the maximum flame temperature zones [21].

The main characteristic that allowed in-situ distinction of nanoparticles from typical soot particles was the light absorption property. Soot particles absorb strongly in a large spectral region from the UV to the visible, whereas precursor nanoparticles are transparent to visible light [11,22-23]. In addition, laser induced fluorescence measurements have shown that visible-transparent particles are also UV-fluorescing [14,23]. They show a typical broadband fluorescence peaked in the UV in premixed flames and some fluorescence also shifting in the visible in non-premixed flames [21].

The spectral behaviors suggest that, depending on the flame environment, nanoparticles can be thought as polymer-like structures containing aromatic sub-units with aliphatic bonds and occasionally oxygen or staked PAH with few condensed aromatic rings [24]. Aromatic-aliphatic linked hydrocarbon (AALH) structures are formed when a chemical-growth mechanism is activated by the oxidative flame environment. Staked PAH structures are formed if coalescent coagulation occurs. Oxidative-pyrolytic conditions, typical of fuel-rich premixed flames, favor the AALH formation mechanism while purely-pyrolytic conditions, typical of the fuel side of diffusion flames, favor PAH cluster formation [24].

The extensive use of in-situ spectral absorption, UV laser induced fluorescence and light scattering measurements have shown that:

#### **in premixed flames**

- particles with typical sizes of 1-3nm are formed at a high rate just downstream of the flame front of rich premixed flames of aliphatic hydrocarbons and in the main oxidation region of aromatic flames [11-13,15,25-27];
- premixed-flame nanoparticles are polymer-like structures containing aromatic sub-units with few condensed rings with aliphatic bonds and occasionally oxygen [11,28-29];
- the formation of nanoparticles occurs either in rich premixed flames below the soot threshold, where the flames exhibit a blue luminosity, and above the soot limit (yellow-orange coloured flames), where nanoparticles coexist with larger soot particles [12-13,15,30-32];
- the average size of nanoparticles remains quite constant up to the inception of soot showing a very low coagulation rate [12,15,33];
- the continuous growth and chemical transformation of nanoparticles causes the increase of their coagulation rate and the formation of larger soot particles [33-34];
- the mass concentration of nanoparticles decreases in correspondence of soot particle formation [11-12,18,25-26]
- nanoparticle concentration accounts for the total amount of soot formed in slightly-sooting conditions with a minor contribution from the addition of gas-phase compound. Acetylene addition from the gas-phase contributes to soot loading only in very fuel-rich conditions [35].

#### **in non-premixed flames**

- nanoparticles and soot particles are measured in comparable concentrations but in different flame regions [19];

- nanoparticles are preferentially formed in the lower temperature flame regions and closer to the flame axis [19];
- soot particles are present in a narrow annular region closer to the maximum flame temperature zone and their maximum volume fraction is measured just in correspondence of the decrease of nanoparticle concentration [19,36-39];
- different spectroscopic characteristics detected in different locations of the same flame suggest that two types of nanoparticles having sizes of the order of few nanometers are formed in diffusion flames: PAH clusters held together by weak van der Waals-forces and polymer-like nanoparticles [21,24];
- stacked PAH clusters are preferentially formed in the low-temperature fuel-side regions whereas polymer-like nanoparticles, similar to those found in premixed flames, are formed in the region closer to the flame front [21,24].

The in-situ spectroscopic characterization have been confirmed by characterization of the samples withdrawn from the flames.

Thermophoretic probing conducted by Dobbins and co-workers [9-10] along the radial direction of co-flowing diffusion flames has revealed the existence of nanoparticles on the fuel side of the reaction zone. TEM and mass spectrometric measurements have shown that:

- nanoparticles appear transparent on the fuel side, more opaque near the luminosity front and highly opaque near the reaction zone [10];
- the smallest observable nanoparticles by TEM are estimated to be 3nm diameter in excellent agreement with the optical results [10];
- mass spectrometric analyses of nanoparticle samples in the fuel-side of diffusion flames show the prominence of the benzenoid PAH in the mass range of 202u to 300u supporting the aromatic, cluster-like, nature of nanoparticles [40].

Ciajolo and co-workers [16-18] analyzed the process of particle growth in premixed flames by measuring the axial concentration profiles of the main combustion products, light hydrocarbons, PAH up to 300u and total particulate matter (dry soot and soot extract). Total particulate matter was subject to a variety of chemical and analytical procedures in order to assess its chemical nature: high pressure liquid chromatography, mass spectrometry, absorption from UV to IR and fluorescence. The chemical and spectroscopic characterization of the soot extracts from premixed flames have shown that:

- nanoparticles are constituted of aromatic compounds, not fully condensed, having spectroscopic characteristics similar to those of 2-, 3-ring PAHs [11,16-18];
- the H/C ratios for these species in the soot pre-inception region is of the order of 1 showing the presence of aliphatic connections between aromatics and/or side-chains [41];
- small amounts of oxygen might be present as shown by FTIR and SERS analysis [16,29];
- nanoparticles represent a large fraction (70-80%) of the aromatic compounds present in flames and their concentration is much higher than that of gas-phase PAHs [18,42-43].

In recent years, the extensive use of advanced diagnostics able to measure the size distributions [30,32,43-46,48-50] and the morphology [33,41,47] of the particles, such as differential mobility analysis (DMA), atomic force (AFM) and transmission electron microscopy (TEM), and size exclusion chromatography (SEC), together with in-situ optical measurements has increased our knowledge of nascent particle formation in flames. The main outcomes are:

- nascent particles formed in blue flames have a unimodal size distribution function with a maximum around 1-3nm [30,33];
- the molecular masses of nascent particles are between 1000 u and 100,000u as shown by SEC measurements on particulate extracts [43,48-50];
- nanoparticles show an elongated shape which might be due to their intrinsic flat form, confirmed also by the high depolarization ratio of the scattered light measured in these flames, or they are deformed by the impact on the surface during sampling showing viscoelastic properties [11,47];
- when the flame becomes yellow-orange a bimodal size distribution function of the particles is measured: a first mode at about 1-3nm is due to nascent particles whereas a second mode at 20-30nm is due to primary soot particles [22];
- soot can be considered as the coagulation and carbonization of molecular particles with gaseous species added from the gas-phase, mainly PAHs in slightly-sooting conditions and acetylene in very-rich conditions [18,34-35].

### 3. MODEL DEVELOPMENT

Experimental data have assisted the development of a detailed kinetic model of particle formation. The aim of the model is to predict the concentration profiles of trace pyrolysis products involved in the process of particle formation and the details of the particle size distributions. Generally models which focus on PSD predictions neglect to simultaneously verify gas-phase flame products, which define the particle nucleation and surface growth rates. On the other hand, the particle dynamics submodel affects the correctness of species profiles of intermediates compounds, particularly benzene and PAHs.

The model used is a development of a previous oxidation and pyrolysis model including aromatic formation and growth [3,4] which now is extended to include reaction pathways responsible for nano-sized particle nucleation, i.e. the transition from gas-phase species to nascent molecular particles, their coagulation to larger soot particles, gas-phase species addition through surface reactions and carbon removal by O<sub>2</sub> and OH oxidation.

A discrete-sectional approach is used for the modelling of the gas-to-particle process; the ensemble of aromatic compounds with molecular mass higher than the largest aromatic compounds in the gas-phase (coronene) is divided into classes of different molecular mass and all reactions are treated in the form of gas-phase chemistry using compound properties such as mass, numbers of carbon and hydrogen atoms averaged within each section. In the sectional method approach, the molecular mass distribution of the species is obtained from the calculation and not hypothesized *a priori*.

In the following a description of the most important reaction pathways forming particles is presented whereas the detailed reaction mechanism is available elsewhere [4].

Figure 1 reports a schematic representation of the process.

### 3.1. Formation of pyrolysis products and cyclization

During oxidation and pyrolysis hydrocarbon fuel generates small fragments which react to form oxidation and pyrolysis products depending on oxygen availability. A small fraction of the hydrocarbon fragments can also cycle forming the first aromatic ring.

The gas-phase kinetic mechanism used to model hydrocarbon oxidation and pyrolysis is built on the GRI mechanism for C1 and C2 species [51]. Reactions are added to extend the mechanism to higher hydrocarbons. *n*-Heptane decomposition has been adapted from ref.[52], benzene and toluene decomposition from ref.[53] whereas *iso*-octane decomposition from ref.[54].

Two reaction pathways are considered for the formation of phenyl radical and benzene: the addition of  $n\text{-C}_4\text{H}_3$  and  $n\text{-C}_4\text{H}_5$  to  $\text{C}_2\text{H}_2$ , leading to phenyl and benzene + H, respectively, and the self-combination of propargyl radicals. Details of the reaction pathways leading to the first aromatic ring and the reaction constants used is reported elsewhere [55-56].

The formation of naphthalene, the first compound in the PAH series, is modeled through two routes: the first is the sequential addition of  $\text{C}_2\text{H}_2$  to phenyl radical; the second is the combination of resonantly stabilized radicals. The first route is known as the HACA mechanism (H-abstraction- $\text{C}_2\text{H}_2$ -addition) [57]. It occurs by way of a two-step process involving hydrogen abstraction to activate aromatics, followed by subsequent acetylene addition. This process is also used here to model the formation of multi-ring structures such as phenanthrene and coronene (the largest compounds modelled explicitly). By-products of the HACA process are alkyl-substituted PAH and five-membered aromatics such as acenaphthylene.

Two different reaction sequences of resonantly-stabilized radicals are included for the formation of naphthalene: the combination of two cyclopentadienyl radicals [58-59] and the combination of benzyl and propargyl radicals [60]. Reaction rates for the resonantly-stabilized radical combination pathways are evaluated by assuming activation energy equal to the heat of reaction [56]. The pathway involving the combination of resonantly-stabilized radicals is also used for the modeling of phenanthrene through the cyclopentadienyl and indenyl radical combination. These two reaction pathways are the dominant ones when aromatic fuels are used since both cyclopentadienyl and benzyl radicals can be intermediates in the process of fuel fragmentation and oxidation.

### 3.2. Growth of aromatics and particle inception

Aromatics and acetylene are the building blocks for the growth process which lead to the formation of high-molecular-mass, molecular particles. The mechanism consists in

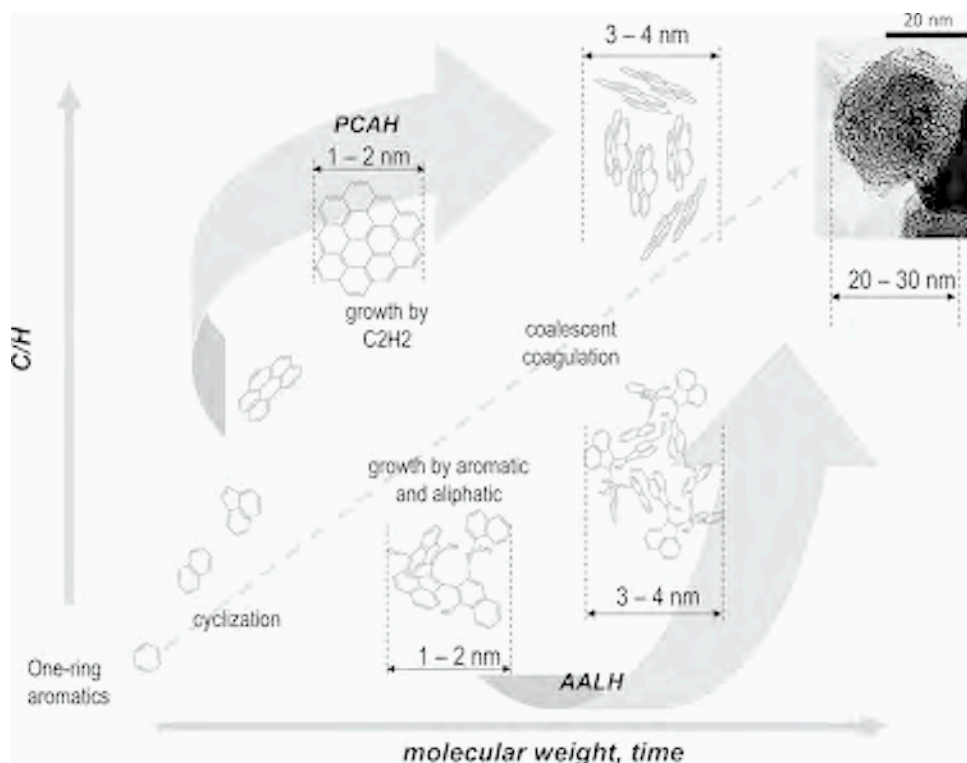


Figure 1. Schematic representation of oxidation and pyrolysis routes.

the sequential addition of acetylene and aromatic molecules to aromatic radicals and the formation of aromatic clusters after collision.

Acetylene addition is the extension of the HACA mechanism to larger compounds with the assumption that, due to the high number of sites where acetylene can be attached, it is possible to hypothesize that each acetylene addition sequence forms a closed aromatic ring and hence it leads to the formation of peri-condensed aromatic hydrocarbons (PCAH). This is possible in view of the fast migration of radical sites on aromatic molecules as molecular mass increases [61].

Aromatic molecule addition to aromatic radicals leads to the formation of aromatic-linked, biphenyl-like, compounds which occasionally might also contain aliphatic and oxygen inclusions. This reaction sequence is favored by the presence of a non negligible concentration of five-member ring PAHs in the PAH inventory. These aromatic-aliphatic-linked hydrocarbons (AALH) grow rapidly forming resonantly-stabilized radical intermediates [3].

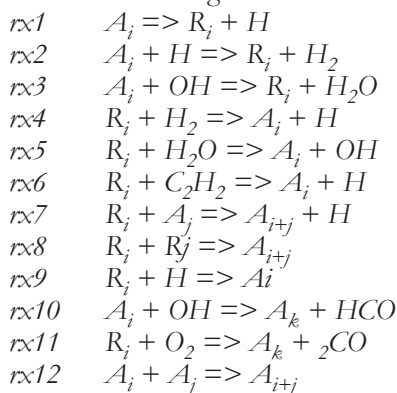
Both acetylene and the aromatic addition sequences begin with the H-loss of an aromatic compound to produce the corresponding PAH radical either through decomposition reactions of aromatics or H-abstraction by H and OH radicals. Aromatic radi-

cals can react with other aromatic radicals or with H atoms ending the growth sequence. Iteration of these pathways leads to the formation of a large number of high-molecular-mass compounds and of its structural isomers.

PCAHs and AALHs grow up to form agglomerates of the molecules forming compounds a few nanometers in diameter held together by the weak van der Waals-interactions. As the molecular mass of the molecular compounds increases van der Waals-interactions become stronger leading to the formation of stable clusters. Colliding molecular particles coalesce completely yielding nanoparticles.

The increasing number of species formed with increasing molecular mass makes impossible to follow the evolution of single compounds. Instead, starting from coronene, classes of compounds, each covering a mass range, have been utilised. Classes are characterized by their average molecular mass and by the number of carbon and hydrogen atoms. Reactions are treated in the same way as for gas-phase chemistry.

The aromatic growth and oxidation mechanism is schematized as follows:



Here  $A_i$  is an aromatic compound having a molecular mass corresponding to the  $i^{\text{th}}$  class of compounds and  $R_i$  is its radical.

The first lumped species ( $A_i$  and  $R_i$  with  $i=1$ ) have 24 C-atoms and are formed by reactions between acetylene and gas-phase aromatic radicals with gas-phase aromatic molecules, by the self-combination of gas-phase aromatic radicals and by dimerization of planar PAHs, similar to reactions rx6, rx7, rx8 and rx12 in the growth and oxidation mechanism.

The sectional size dependence in reactions rx1 and rx6 are obtained by interpolating the kinetic data of the MIT kinetic scheme [62]. For all other reactions size dependence is obtained from gas-kinetic theory with an exponent of 2/3 for a gaseous species colliding with a particle (surface area to volume ratio) and with 1/6 for a particle to particle collision based on the average size of the two particles [5].

Rate constants for the aromatic growth and oxidation mechanism are evaluated on the basis of structural similarities with the reaction rates of PAHs. The rate of hydrogen loss via the unimolecular reaction (rx1) is evaluated using as reference the rate of benzene decomposition. Initiation reactions (rx2 and rx3) are reversible, and the forward reaction rates are assumed to be equal to H atom abstraction from naphthalene molecules. Reaction rate is scaled by the variation in collision efficiencies to take into account the increase of reactivity.

Equilibrium of the initiation reactions (rx4 and 5) is strongly affected by the number of C atoms in the molecule. Radical compounds composed of a large number of C atoms are stable enough to survive in their radical form, because of the delocalization of the unpaired electron resulting in a lower rate of the reverse reactions [63]. At present, reverse reaction rates (rx4 and 5) for the lumped species belonging to the first three classes of compounds (300-1200u) are here evaluated from equilibrium constant of coronene. For larger molecular masses thermodynamic properties are not known; in these case, reactions rx4 and rx5 are considered irreversible.

The rate constant for acetylene addition to aromatic radicals (rx6) is based on the reaction rate of naphthyl + acetylene scaled by increasing collision efficiencies.

On the basis of structural similarity, the rate constant for phenyl + benzene is used as the reference for the corresponding aromatic radical + aromatic molecule reaction (rx7) which is scaled for variation in collision efficiencies. Termination reactions of aromatic radicals with other aromatic radicals (rx8) or with H atoms (rx9) ending the growth sequence have rate constants evaluated from the collision efficiencies of the reacting species.

Oxidation by OH (rx10) is estimated from similar reactions for benzene and PAH's and the collision frequency accounts for the size of the oxidized particles. Oxidation by O<sub>2</sub> molecules (rx11) uses the rate constant of naphthyl + O<sub>2</sub> accounting for the increase of the collision efficiency of large species [64-65].

The agglomeration rate (rx12) is considered to depend on two phenomena: the collision rate, determined from gas-kinetic theory applied to large molecules, and the pairwise interaction between particles according to a Lennard-Jones attractive and repulsive potential. The energy of interaction between two particles is given by the sum of all the interactions between molecules which constitute the particles. Thus the energy of interaction is a function of both the geometry of the interacting particles and of their physico-chemical characteristics through the Hamaker constant [66]. In this formulation, energy redistribution inside the forming clusters is neglected. Although this is an approximation the simple model reproduces the experimentally observed low coagulation efficiency of small particles in premixed flames well [33]. The low coagulation efficiency is in agreement with the results obtained by Wong et al. [67] on the lifetimes of clusters of aromatics having aromatic-aliphatic-linked structures. These compounds show a lower lifetime, i.e. lower coagulation efficiency, with respect to peri-condensed aromatics having the same molecular weight. Particle collision efficiency is evaluated for a Hamaker constant  $5 \times 10^{-20}$  J. This value of the Hamaker constant is typical of benzenic rings ( $3 \times 10^{-20}$  J) more than of graphite ( $5 \times 10^{-19}$  J). A variation of the Hamaker constant as a function of the change of the chemical structure of the particles towards mature soot is not considered here. During flame computations the coagulation efficiency  $\gamma$  is calculated at the local flame temperature as a function of particle size. An increase in temperature by 500K reduces  $\gamma$  by approximately half.

### 3.3. Coagulation and surface growth

Colliding molecular particles coalesce completely yielding new spherical structures, whereas larger particles may aggregate into chainlike structures. The rate of coagula-

tion is evaluated as a function of the size of the colliding particles. Small particles, characterized by a large Knudsen number ( $Kn \gg 1$ ), evolve in the free molecular regime, while large aggregates, characterized by a small Knudsen number, evolve in the continuum regime ( $Kn < 1$ ) [68]. Actually, the model considers the coagulation of particles as large as 20nm as coalescent whereas larger particles are considered to form chainlike clusters, whose size is assigned based on the volume-equivalent spherical diameter.

Several chemical reactions could take place on the surface of a particle. In the present model, we use the same mechanism used for the aromatic growth also for the surface reactions. In this mechanism, the addition of mass on the surface of a particle proceeds by addition of acetylene and aromatics whereas hydroxyl radical and  $O_2$  remove mass from the particles through the formation of CO and HCO.

Rate constant for surface reactions are estimated on the basis of structural similarity with gas-phase reactions accounting for the increase of the collision efficiency for particles.

### 3.4. Computations

The kinetic mechanism is used to simulate different flame configurations by solving enthalpy and species mass balance. In the present work, species include the gas-phase molecules and the particle size classes, as described by Pope and Howard [69] and Richter et al.[62]. Particle size distribution is defined by a range of sections, each containing a nominal hydrocarbon species in order of increasing atomic mass. The carbon number of each section ranges from 24 to  $4 \times 10^8$ , a particle size range of 1-250nm if a density varying from 1.2 to 1.8 is considered. Twenty six sections are used in a geometric series with a carbon number ratio of two between sections. This distribution is considered to give adequate resolution of particle size distribution and the range is large enough not to constrict the scheme. The decrease of the H/C ratio with increasing particle size is fixed by definition of the number of carbon and hydrogen atoms in each section; it ranges from 0.5 in the first section down to 0.08 in the last section. Characteristics of the sections are given elsewhere [4].

Transport and thermodynamic properties for the gas-phase species are from Chemkin [57] data base. Diffusivities of the large sectional species are obtained from Stokes friction with Cunningham correction factors based on the Knudsen number [68]. Thermophoretic flux is applied to sections.

Premixed flame modeling was performed by using a modified version of the PREMIX code of the CHEMKIN package. In premixed flame modeling experimental temperature profiles are used as input to the model in order to reduce the uncertainties in the heat loss through the cooling system of the burner. An accurate temperature profile is needed since temperature strongly affects the concentration profiles particularly of trace compounds.

In co-flow flames, the transport equations for axial and radial momentum, species mass fraction and enthalpy are solved in elliptic form for axisymmetric flow. Radiative transfer is modelled by the discrete transfer method [5]. Radiation heat loss is strongly influenced by the absorption coefficient of soot whose concentration is a dependent variable here. The soot absorption constant is therefore set to a value in each flame to

bring the predicted temperatures into approximate agreement with the measured temperatures. Computations are generally carried out in a domain 100mm axial by 50mm radial. The polar, axisymmetric grid expands, a typical grid size in the flame region being 0.1mm radial by 1-2mm axial. Finer grids do not appreciably change the results. All the species equations are solved simultaneously at each spatial location in turn by a modified Newton-Raphson scheme. Velocity and enthalpy employ a tri-diagonal matrix form of solution. For a converged solution, the mean absolute residual for a species, normalized by the species maximum value is typically of order  $10^{-8}$  and overall carbon element mass balance error is less than 0.1%.

Nanoparticle formation has also been modeled in turbulent non-premixed flames by using Large Eddy Simulation (LES) coupled with an unsteady flamelet approach and Conditional Moment Closure. Details on turbulent flame modelling are reported elsewhere [70-71].

## 4. MODELLING RESULTS

The kinetic mechanism is used to model particle inception and growth in various atmospheric pressure flames, both premixed and diffusion controlled.

The flames have been characterized by using different experimental approaches and techniques obtaining experimental data which cover the main flame structures, the aromatic formation and growth and the particle dynamic.

In the following, modelling of flames of various hydrocarbons are presented. Probe data are used to verify the model capability in predicting the main flame structure and the aromatic formation and growth in gas-phase. Both probe data and in-situ optical and spectroscopic measurements are used to follow the transition from gas-phase compounds to incipient particles and to final soot formation.

### 4.1. Methane

The first set of experimental data used is a sooting premixed flame of methane/oxygen at C/O=0.50 with a cold gas velocity of 4.74cm/s [16]. Figure 2 reports comparison between model predictions and experimental concentration profiles of methane and oxygen, CO and CO<sub>2</sub> and acetylene and ethylene. The model well reproduces the main flame structure: maximum reactant consumption occurs at about 3mm above the burner in correspondence to the maximum flame temperature, thereafter oxidation products, CO and CO<sub>2</sub>, and pyrolysis products, ethylene and acetylene are the dominant species in the post-oxidation zone of this flame. Ethylene shows typical rise-decay profile of intermediate species whereas acetylene slightly decreases in the post-oxidation zone of the flame. PAHs are minor pyrolytic products also reasonably well reproduced by the model which shows a rise-decay profile and a gently re-increase at higher flame heights.

In-situ spectroscopic measurements and probe sampling have been performed in the same flame [72]. Figure 3 (top) reports the concentrations of nanoparticles and soot obtained by laser induced fluorescence (LIF) and incandescence (LII) measurements along the flame axis.

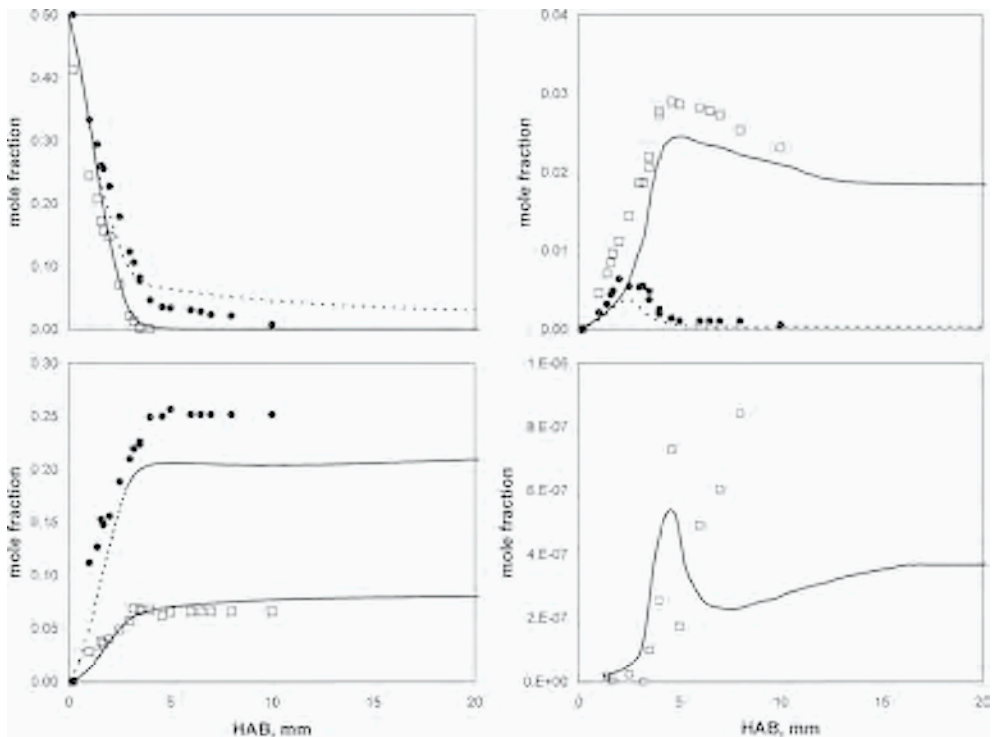


Figure 2. Mole fraction profiles along the flame axis of the  $\text{CH}_4/\text{O}_2$  flame with  $\text{C}/\text{O}=0.50$ . Left side: (top)  $\text{CH}_4$  (●) and  $\text{O}_2$  (□), and (bottom)  $\text{CO}$  (●) and  $\text{CO}_2$  (□). Right side: (top)  $\text{C}_2\text{H}_4$  (●) and  $\text{C}_2\text{H}_2$  (□), and (bottom) sum of PAH (□). Experimental data from ref.[14]; lines are model predictions.

The fluorescence signal due to particles starts at larger heights with respect to gas-phase PAHs and reaches a quite constant value at the end of the flame. It precedes the incandescence signal due to soot.

The concentration profiles of condensed species and soot, determined by probe sampling and solvent extraction [16], are reported in the same figure. The concentration profile of condensed species is in excellent agreement with the concentration profile of nanoparticles determined by laser induced fluorescence measurements. Soot concentration determined by sampling is of the same order of magnitude of that measured by laser induced incandescence but it is detected at higher heights above the burner.

Experimental concentration profiles are compared in the top of Figure 3 with the results of the numerical modeling. The use of the sectional method allows to distinguish two fundamental types of particles by size: molecular particles with masses between 500 and 100,000 u, defined nanoparticles (sizes from 1 to 7 nm) and soot particles with masses higher than 100,000 u (particles with sizes larger than 7 nm) [4]. Model predictions agree well with the concentration profiles of both nanopar-

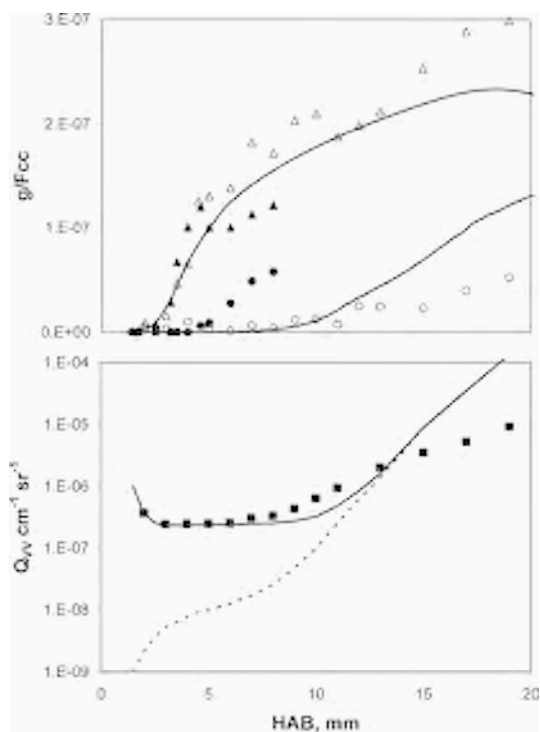


Figure 3. Top: concentration profiles of nanoparticles detected by laser induced fluorescence ( $\Delta$ ) and soot detected by laser induced incandescence ( $\circ$ ), and condensed species ( $\blacktriangle$ ) and soot ( $\bullet$ ) measured by probe sampling along the flame axis of the  $\text{CH}_4/\text{O}_2$  flame with  $\text{C}/\text{O}=0.50$ . Bottom: scattering coefficient. Experimental data from refs. [16,72]. Lines are model predictions (dashed line in the lower part is the modeled scattering in excess to gaseous species).

ticle/condensed species and soot being able to reproduce both the absolute concentration values and the concentration profiles.

From the modeled distribution function the light scattering cross section has been evaluated using Rayleigh theory. The results are able to reproduce the light scattering measured along the axis of the flames as shown in the bottom of Figure 3. The light scattered by an aerosol strongly depends on both concentration and size of the scattering entities and hence the comparison of the model predictions with the scattering measured in the flame is a good test of the validity of the aromatic growth mechanism.

The good agreement of model predictions with the experimental results, at least at soot inception, indicates that the proposed kinetic model for aromatic formation and growth is able to predict not only the total amount of particulate matter but also the mean sizes of the particles along the flame axis.

Measurements of nanoparticles and soot have also been performed at a fixed height (10mm) above the burner by LIF and LII. Figure 4 reports the comparison of model results with experimental data obtained by changing the equivalence ratio from

1.6 to 2.8. Nanoparticles are already detectable just above the stoichiometric value and their concentration increases with the equivalent ratio. Soot particles, instead, are practically absent in flames with equivalence ratios ranging from 1.6 to 2; for these flames the incandescence signal of soot particles was not detectable. Thereafter, soot volume fraction quickly increases.

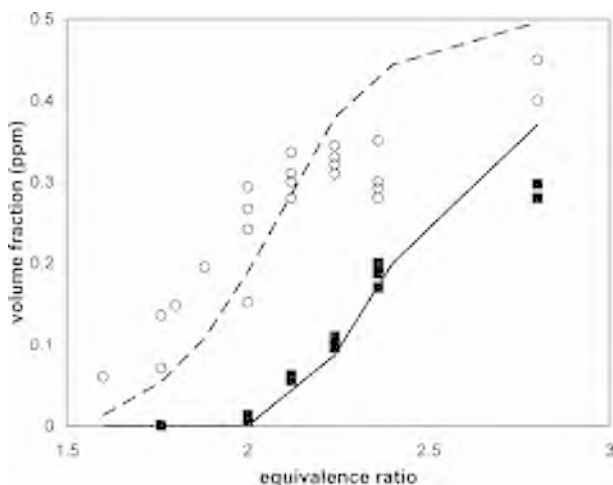


Figure 4. Volume fractions of nanoparticles (o) and soot (■) determined by laser induced fluorescence and incandescence measurements at 10mm above the burner outlet of  $\text{CH}_4/\text{O}_2$  premixed flames with C/O ratios ranging from 1.6 to 2.8. Experimental data [72]. Lines are model predictions.

The above reported results clearly show that methane combustion in laminar premixed condition needs very fuel-rich condition in order to produce and therefore to emit soot particles while nanoparticles are formed also in less rich conditions. In the premixed flames investigated nanoparticles are also formed in higher concentration with respect to soot particles.

Modelling of methane combustion has also been performed in diffusion flames. Figure 5 reports predicted temperature and concentration profiles of methane, acetylene and benzene against experimental data from Smooke et al. [73] at 10mm and 25mm above the nozzle in a co-flowing methane/air flame.

Predicted temperatures are reasonably good over the whole data range by adjusting the radiation soot absorption coefficient to match temperature only at the location of peak temperature. The fuel concentration, methane, is well reproduced showing the capability of the model to predict the general shape and structure also of non-premixed flames. Predictions of acetylene and benzene are also shown in Figure 5. These are important pyrolysis species in the processes of soot inception and growth. The model slightly under-predicts their concentrations on the flame axis whereas off-axis (where soot is formed) the predictions are better.

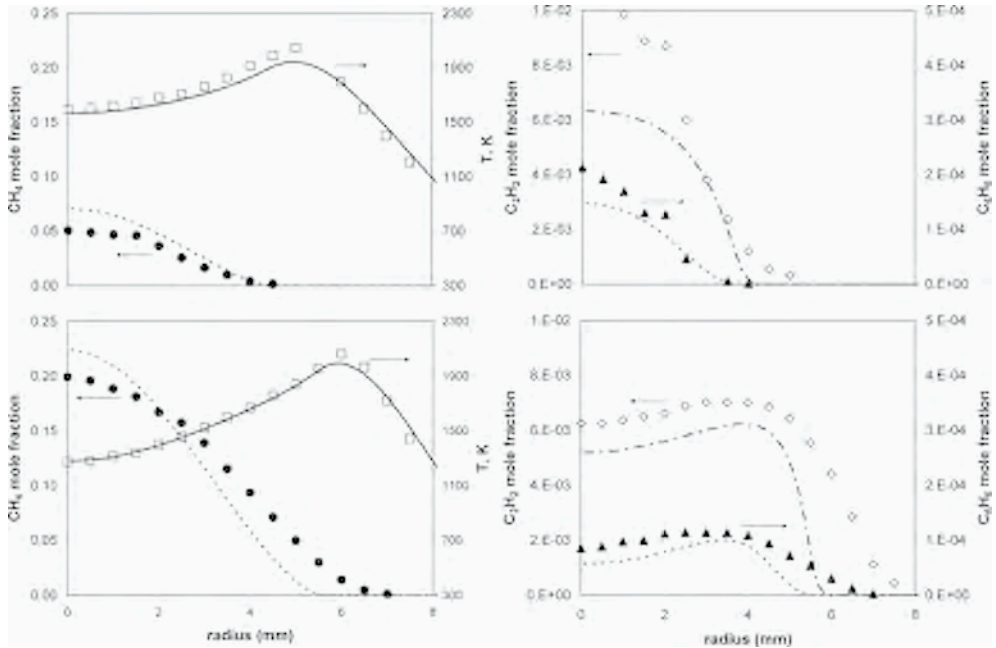


Figure 5. Temperature and species radial profiles in a methane/air co-flowing flame. Bottom, 10mm height; top, 25mm height. — □ temperature, - - - ● methane, - - - ◇ acetylene, ---- ▲ benzene. Data [73].

Radial profiles of predicted and measured particulate volume fraction are reported at three heights in Figure 6. The particulate data shown were obtained by differing techniques. Total particulates were measured by thermophoretic deposition [73]. Soot particle volume fraction was measured by LII [74] and small precursor particle volume fraction was measured by LIF [74]. As for the premixed flame calculations, small precursor particles comprise nanoparticles with sizes from 1 to 7 nm whereas soot particles include particles with sizes larger than 7 nm.

The distinguishing features of the CH<sub>4</sub> flame measurements are that total particulate volume fraction is low, approximately 0.5ppm maximum, and the small, particle size range dominates the whole field. These characteristics are represented well by the predictions. The predicted small concentration of soot shows good correspondence with the LII measurements at all measured heights. The total particulates predictions show good agreement at 30mm height with LIF and also with the deposition measurements. At lower heights the predictions are low; they do not exhibit the observed early rise in total particulate volume fractions.

Particulate growth processes are indicated by particle mean size  $D_{03}$ ,  $\{\Sigma(N_i D_i^6) / \Sigma(N_i D_i^3)\}^{1/3}$ . The predictions, not presented here, show the correct trends but are higher than measured at all locations by a factor of about two. The disagreement might be in the error of the measured scattering values which are very low and comparable to the scattering of gaseous compounds in the methane flame [74].

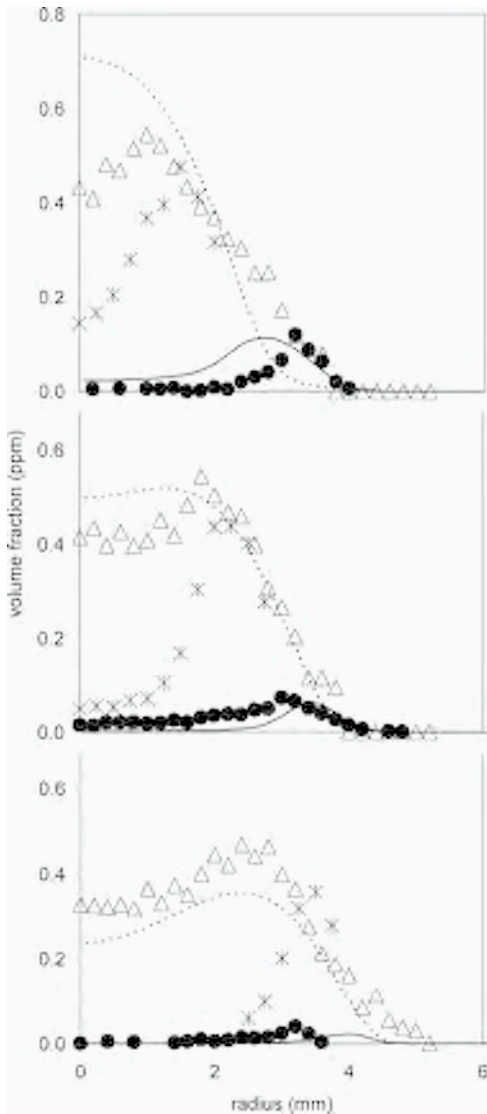


Figure 6. Particulate volume fraction radial profiles in the methane co-flowing flame. Bottom to top: 20mm; 25mm; 30mm height. Predictions: — soot; ----- precursor nanoparticles. Measurements: \* total particulates [73]; • soot particles [74];  $\Delta$  Precursor particles [74].

The actual kinetic model has also been applied to a turbulent flame of methane using conditional moment closure. The predictions show that the use of a conditional temperature gives predicted particulate concentrations which are about a fifth to a half of the measured values. Details on the simulations of turbulent flames is reported in the contribution to this book by Kent [70].

## 4.2. Ethylene

A sooting premixed flame of ethylene/oxygen at  $C/O=0.80$  with a cold gas velocity of  $4\text{cm/s}$  [18] is used for the analysis of model capability to predict also ethylene combustion. The model well reproduces the main flame structure and the concentration profiles of oxidation and pyrolysis products, not shown here.

Modeled concentration profiles of benzene and gas-phase PAHs are reported in Figure 7 compared with experimental data [18]. Benzene shows a rise-decay profile and a slight increase in the post-flame region in this flame condition. The decrease of benzene concentration at the flame front is due both to the high temperature which causes benzene decomposition and to molecular growth leading to higher molecular mass aromatics. The increase of benzene in the post-flame regions is due to the decrease of the temperature which favors a new formation of benzene. Model predictions are in good agreement with experimental data for both absolute concentration values and concentration profiles.

Naphthalene and acenaphthylene are the most abundant PAHs. They are formed just downstream of the maximum concentration of benzene. The model well reproduces both the concentration profiles of single PAHs (comparison is made on a linear scale) and also the decrease of PAH concentration moving from naphthalene to pyrene. It is

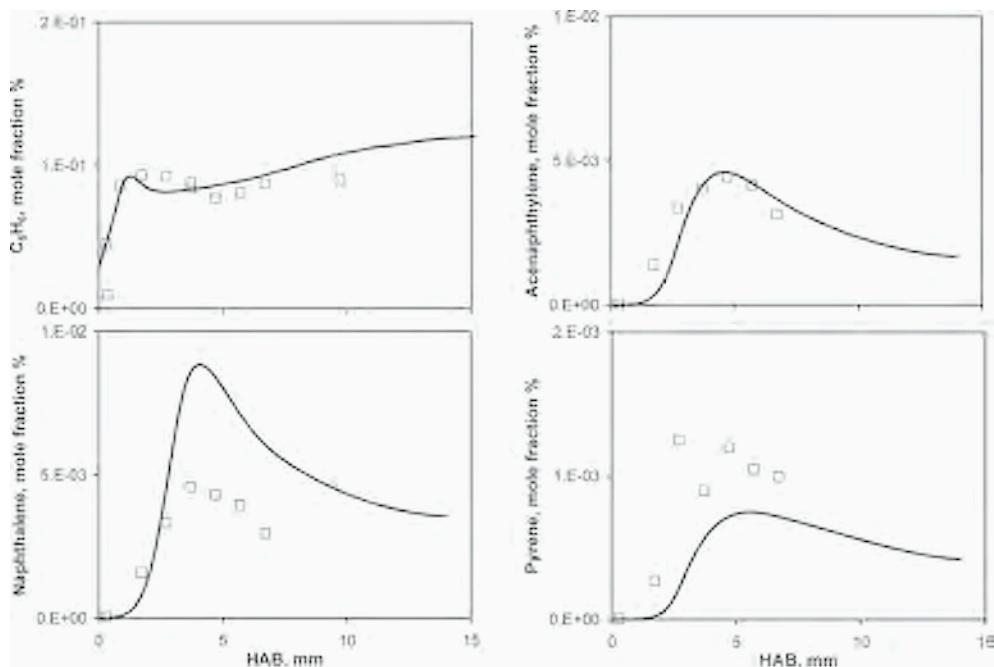


Figure 7. Modelled concentration profiles compared with experimental data in an ethylene/ $O_2$  flame with  $C/O=0.80$  and cold gas velocity of  $4\text{cm/s}$ . Left: (top) benzene and (bottom) naphthalene. Right: (top) acenaphthylene and (bottom) pyrene. Data from [18].

interesting to note that the amount of PAHs is reasonably well reproduced if the gas-phase sub-mechanism is coupled with the particulate sub-mechanism. Indeed, aromatics are building bricks of particulate and hence are continuously consumed by particle nucleation and surface reactions. If the particulate sub-mechanism is removed from the kinetic scheme the amount of aromatics predicted by the model is much higher [4].

Figure 8 reports the comparison between model prediction and experimental concentration values of condensed species (CS) and soot. CS are reasonably well predicted by the model whereas the concentration of soot is underestimated by 30%.

Benzene and particle concentration profiles are strongly affected by flame temperature. Figure 9 (top) reports the comparison of the model results with benzene concentration profiles measured keeping constant the C/O ratio at 0.80 and changing the cold gas flow velocity from 2 to 6 cm/s, which correspond to different maximum temperatures.

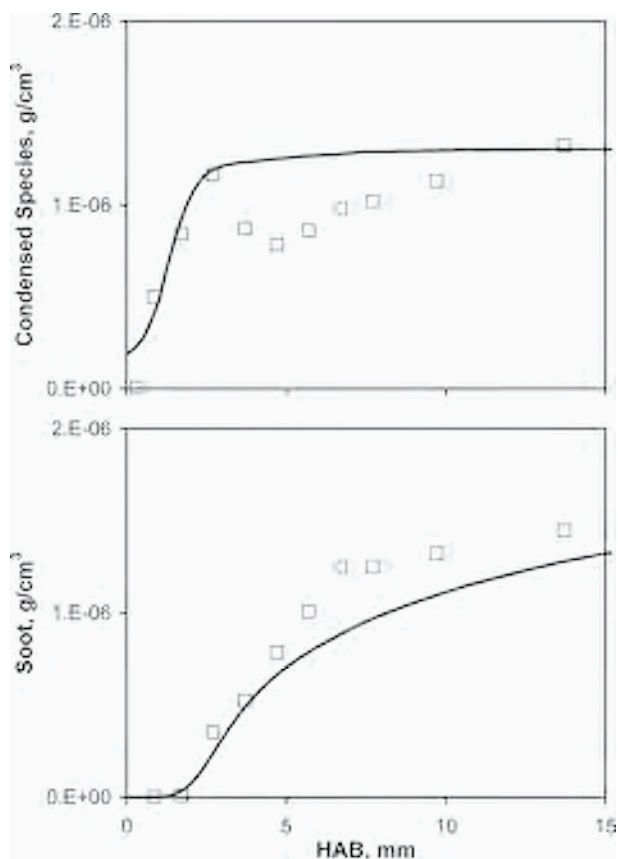


Figure 8. Comparison of experimental (top) Condensed Species and (bottom) soot concentration profiles with modelled data in an ethylene/O<sub>2</sub> flame with C/O=0.80 and cold gas velocity of 4cm/s. Experimental data from [18].

Benzene shows a rise-decay profile and a gentle increase in the post-flame region in the intermediate temperature flame (cold gas flow velocity  $v=4$  cm/s,  $T_{max}=1650$ K), whereas in the highest temperature flame (cold gas flow velocity  $v=6$  cm/s), about 1750K at the peak value, benzene concentration increases to a maximum value downstream of the flame front and decreases to very low values in the post-oxidation zone of the flame (dashed-point line), due to decomposition more than to oxidation or molecular growth. In the lowest temperature flame (cold gas flow velocity  $v=2$  cm/s), about 1550K at the peak value, benzene profile shows a continuous rise downstream of the flame front and a level-off in the post-flame region (dashed line). The model reproduces reasonably well the three concentration profiles of benzene in the ethylene flames showing the importance of flame temperature in determining the behavior of benzene concentration profiles.

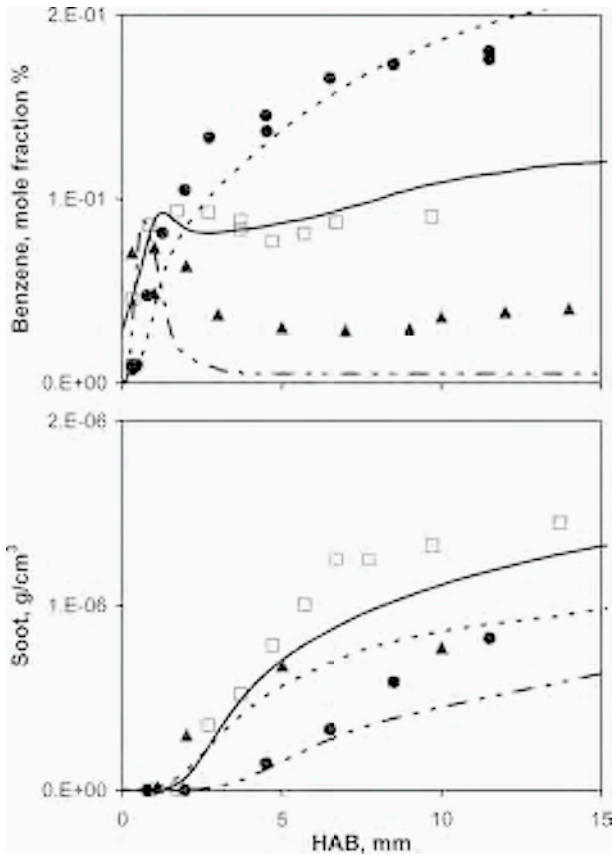


Figure 9. Concentration profiles of (top) benzene, and (bottom) soot along the axes of three ethylene flames with  $C/O = 0.80$  and different cold gas velocities. ●,-----  $v=2$  cm/s ( $T_{max}=1550$  K); □ ———  $v=4$  cm/s ( $T_{max}=1650$  K); ▲ - - -  $v=6$  cm/s ( $T_{max}=1750$  K). Experimental data from [18].

The model is able to reproduce the bell-shaped behavior of soot concentration by changing the maximum flame temperatures from 1550K and 1750K as shown in Figure 9 (bottom) where experimental and modeled soot concentration profiles in the three flames are reported. The increase of the temperature in the range examined determines a first increase of the soot concentration and a decrease in the highest temperature flame.

Model predictions indicate that temperature affects also the size distribution functions of the particulate. Figure 10 reports the predicted size distribution functions along the axis of the three ethylene flames.

The lowest temperature flame is characterized by the formation of particles with fully-developed bimodal size distribution functions with the first mode in the 1-2nm range and a second mode with particles between 10 and 250nm (Figure 10a). As temperature is increased from 1550K to 1650K the first mode remains unchanged whereas particles belonging to the second mode have lower sizes (from 10 to 200nm Figure 10b). In the higher temperature conditions (1750K) the second mode is less evident than before (Figure 10c). These results can be explained with a continuous nucleation of nano-sized particles in the lower temperature flames due to the formation of benzene and gas-phase aromatics also in the post-oxidation region of the flames. Newly-nucleated particles react with already-formed soot particles increasing their sizes. In the highest temperature flame, either benzene and gas-phase aromatics are almost completely decomposed downstream of the flame front and cannot contribute to the growth of aromatics and nucleation of new particles. As a consequence the increase of soot particle size is reduced.

Comparison of model results with the probe data has allowed us to show that the developed kinetic mechanism is able to reproduce the main flame structure and the formation of soot, PAHs and condensed species quite well but do not allow us to verify the aromatic growth model, due to the lack of experimental data on the details of particle dynamic in these flames.

In the last years, a series of experimental data on the dynamic of the particles formed in slightly-sooting ethylene flames have been reported [30,33,47]. Particle size distributions were obtained by using Atomic Force Microscopy (AFM) and Differential Mobility Analyzers (DMA).

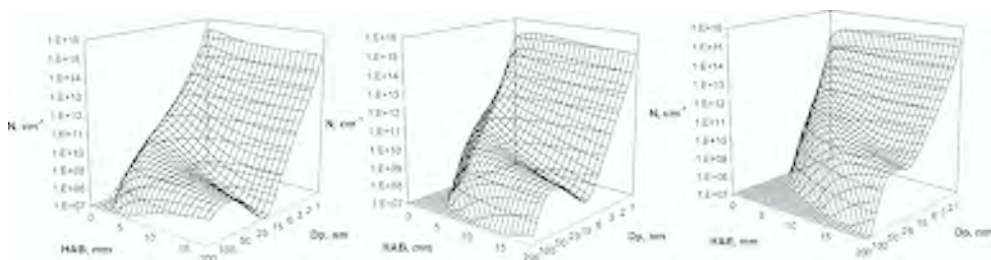


Figure 10. Predicted size distribution functions in the particle range between 1 and 200nm along the flame axes of three ethylene flames with C/O = 0.80 and different cold gas velocities. From left to right:  $v=2$  cm/s ( $T_{max}=1550$  K);  $v=4$  cm/s ( $T_{max}=1650$  K);  $v=6$  cm/s ( $T_{max}=1750$  K).

AFM is an intrusive technique and AFM data need to be corrected for the adhesion efficiency on the mica disk in order to retrieve the true distribution in the flame. Figure 11 shows the comparison of modelled PSDs with the particle size distribution measured by AFM at 5 and 8 mm from the burner exit in a  $C/O=0.77$  ethylene/air flame, corrected by the size-dependent adhesion efficiency of the particle. At 5mm above the burner, the size distribution function predicted by the model shows only particles with sizes below 10nm in good agreement with the experimental results. Moving downstream from the flame zone, namely at 8mm above the burner, the modeled PSD function shows a bi-modal distribution. The modeled PSD function is still in close agreement with the experimental data although the modeled data do not show a clear dip crossing from the first to the second mode of the PSD function.

A co-flowing non-premixed ethylene/air flame of Santoro and co-workers [36-39] has also been modelled. Figure 12 shows the comparison between predicted and measured temperature and species for this flame. Ethylene, acetylene and benzene species are shown at 10mm and 40mm above the nozzle. The temperatures are a little lower than the radiation-corrected thermocouple measurements. The fuel concentration is

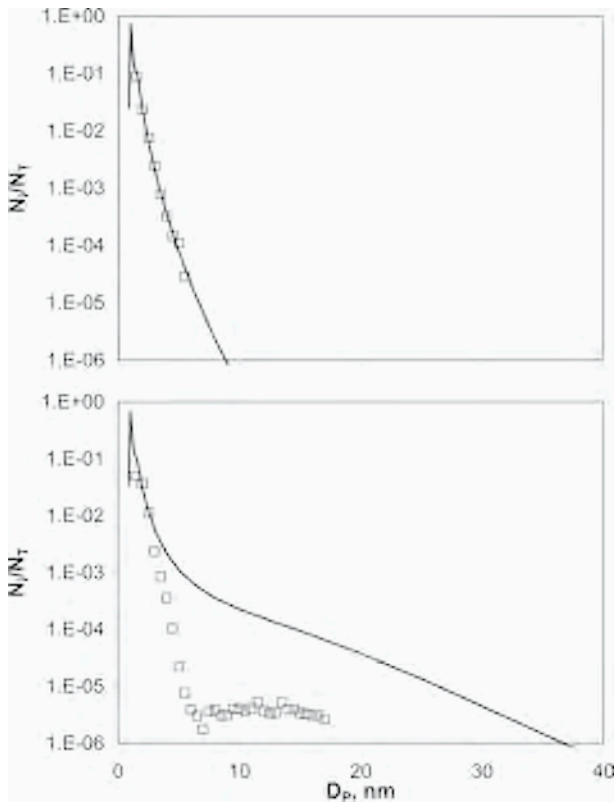


Figure 11. Size distribution functions of the particles at (top) 5mm, and (bottom) 10mm along the axis of a  $C/O=0.77$  ethylene/air flame. Experimental data from [33].

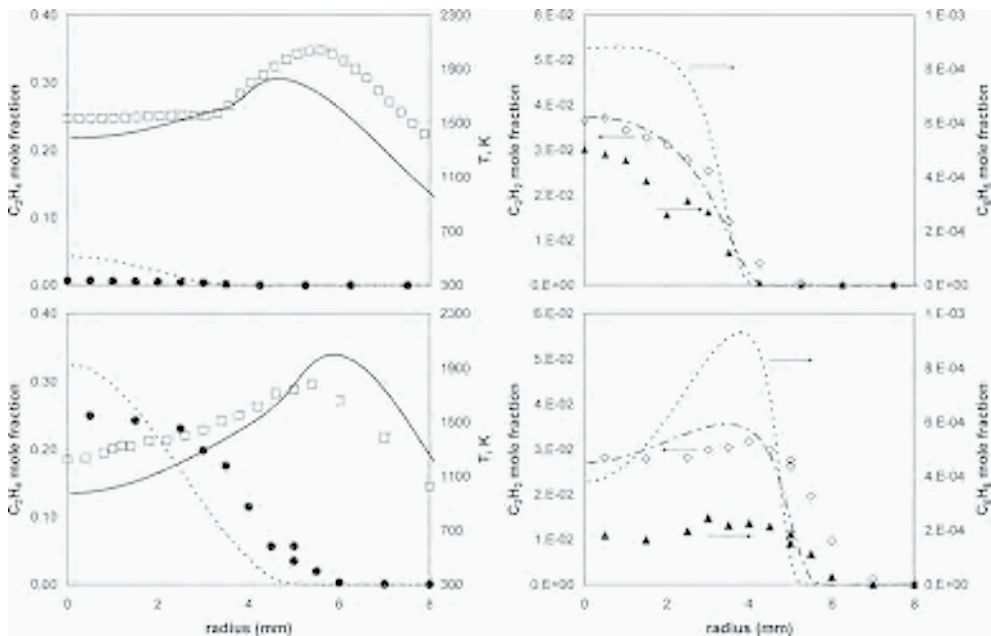


Figure 12. Temperature and species radial profiles in ethylene co-flowing flame. From bottom to top at: 10mm, and 40mm height, predictions against data [36-39]. — □ temperature; --- ● ethylene; - - - ◇ acetylene; ---- ▲ benzene.

well represented by the model at all heights. Benzene and acetylene predictions are somewhat high in the lower part of the flame and do not show the measured decay of these species at 40mm height.

Radial profiles of particulate volume fractions are shown in Figure 13 at measurement heights 10mm and 40mm above the nozzle. Attention is first drawn to soot volume fractions measured by LII [36] which are an order of magnitude higher than in the methane flame (Figure 6) with maximum values of 8ppm. The model gives good predictions of soot volume fractions. Measurements of precursor particle volume fraction are also shown in Figure 13.

Generally, measured precursor volume fraction as a proportion of soot volume fraction is much lower than for the methane flame. The predictions of nanoparticles are however lower than the measurements at 10mm but satisfactory at 40mm. Particle size  $D_{63}$  is also shown in Figure 13. In contrast to the methane flame large particles are formed in this flame with sizes of the order of 100-200nm. The model responds well to the more heavily sooting fuel by generally representing the measured sizes well.

The kinetic model has been also applied to a turbulent flame of ethylene by applying both Large Eddy Simulation (LES) and Conditional Moment Closure approaches. The predictions show that the use of a CMC model gives predicted

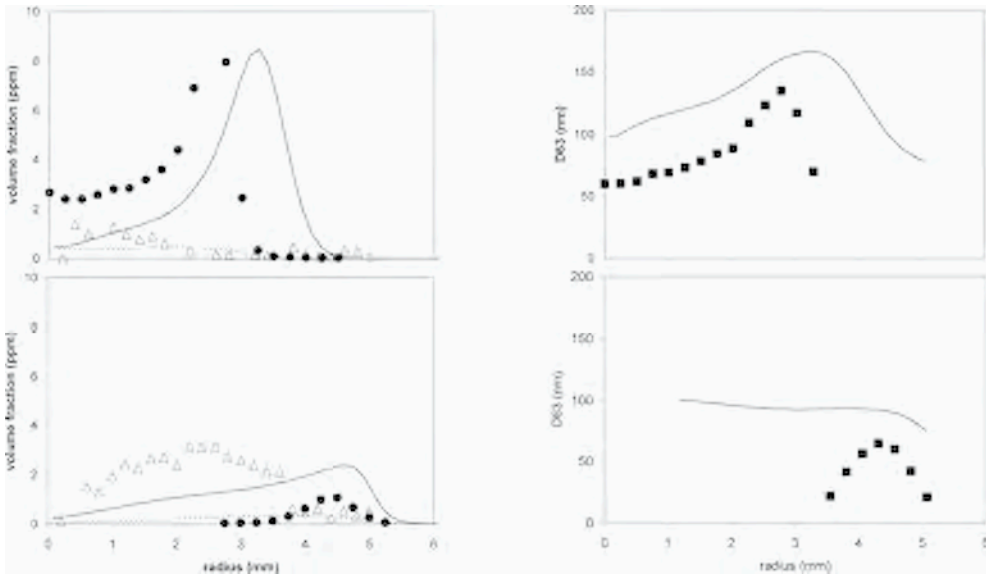


Figure 13. Particulate volume fraction and mean diameter in ethylene co-flowing flame. From bottom to top radial profiles at 10mm and 40mm height. — ● predicted and measured [36] soot; - - Δ predicted and measured [19] precursor particles — ■ predicted and measured [36] soot mean diameter ( $D_{63}$ ).

particle concentrations of the same order of magnitude of the experimental data (see the contribution to this book by Kent [70]). Also LES modelling gives a quantitative good prediction of nanoparticles at different heights above the nozzle, confirming the hypothesis of a fast formation rate of nanoparticles which is related to turbulence mixing more than to kinetics [71]. The results obtained open a new perspective in the possibility of predicting nanoparticles in turbulent combustion.

### 4.3. n-Heptane

The kinetic model is able to reproduce quite well also the main structure of a premixed n-heptane/ $O_2/N_2$  (6.9/30.3/62.1) flame with  $C/O=0.80$  and maximum flame temperature of about 1750K [75]. Figure 14 (top of the left side) reports comparison between model predictions and experimental concentration profiles of the most abundant light hydrocarbons deriving from fuel pyrolysis/oxidation: methane, acetylene and ethylene. In the main oxidation zone ethylene exhibits the rise-decay profile typical of reaction intermediates, being both a fuel oxidation product and a source of acetylene through dehydrogenation reactions. Methane and acetylene are formed just above the maximum flame temperature, rise to a maximum and then decrease in the post-oxida-

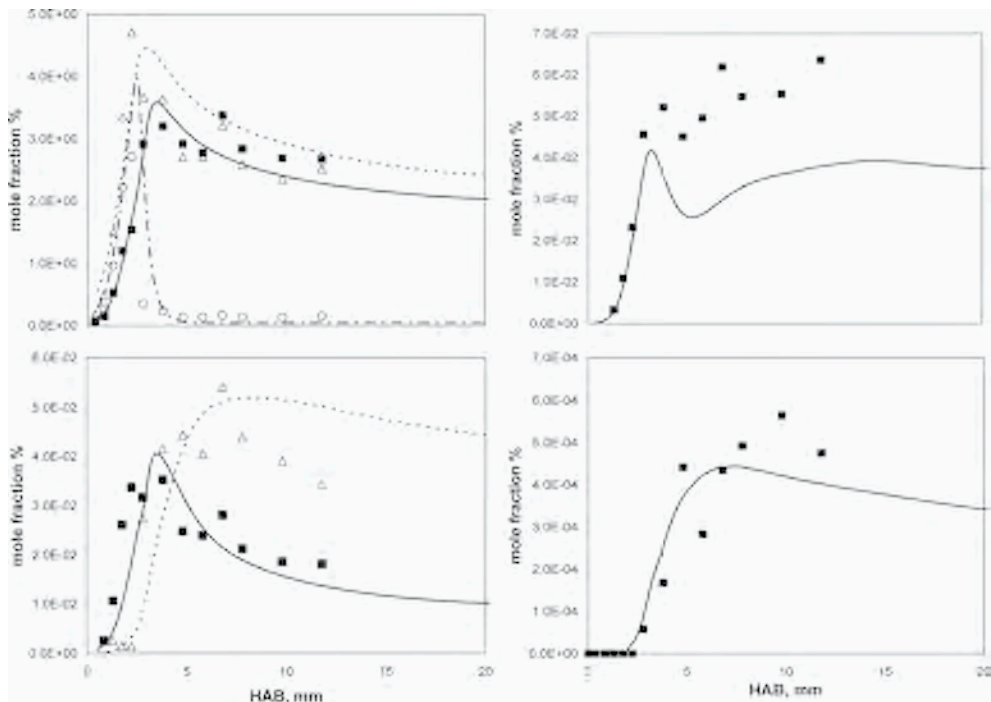


Figure 14. Concentration profiles along the flame axis of a n-heptane/ $O_2/N_2$  (6.9/30.3/62.1) premixed flame with  $C/O=0.80$ . Left: (top) methane ( $\Delta$ ), ethylene (o) and acetylene ( $\blacksquare$ ) and (bottom) propyne ( $\blacksquare$ ) and diacetylene ( $\Delta$ ). Right: (top) benzene and (bottom) sum of gas-phase PAH. Experimental data [75].

tion zone of the flame. Minor gas components, C3-C4 hydrocarbons and benzene are also well reproduced by the model. Unsaturated C3-C4 hydrocarbons, propyne and diacetylene (Figure 14 bottom of left side) are also reasonably well reproduced.

Benzene and the sum of gas-phase PAH concentrations are reported in the right side of Figure 14. Benzene concentration (Figure 14 top) rises in the main oxidation zone and decreases at the beginning of the post-oxidation flame region with a slight tendency to increase again at the end of the flame. PAH concentration (Figure 14 bottom) shows a fast increase in correspondence of benzene concentration decrease and a level-off in the post flame region. The model underestimates benzene concentration by a factor of two and well reproduce PAH concentration. But the trends are well reproduced for both.

The concentration profiles of Condensed Species and soot are reported in Figure 15 and compared with model predictions. CS concentration increases just after PAH formation, reaches a maximum value and gently decreases moving downstream of the flame. Soot is formed in correspondence of CS maximum formation then it increases at increasing flame heights. The concentration of CS is about one third of the final soot concentration of soot showing the importance of CS transformation in soot inception and carbon addition from the gas-phase on particle surfaces in the soot loa-

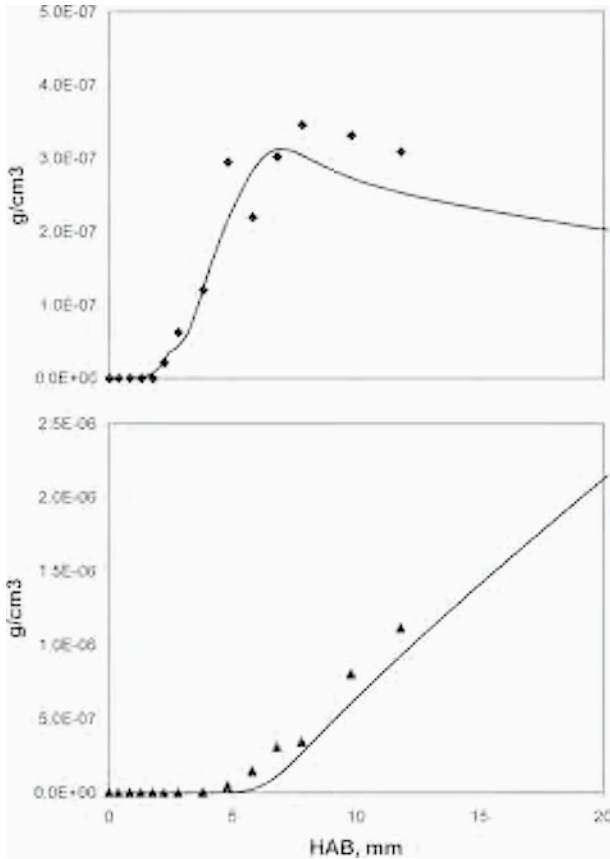


Figure 15. Concentration profiles of (top) Condensed Species and (bottom) soot along the flame axis of a n-heptane/ $O_2/N_2$  (6.9/30.3/62.1) premixed flame with  $C/O=0.80$ .

ding region. Model predictions agree well with experimental data showing the capability of the kinetic mechanism in reproducing the oxidation of n-heptane and the formation of particulate matter.

#### 4.4. Benzene

Benzene flame modelling is reported in Figure 16 and compared with experimental data obtained in a premixed benzene/air flame with  $C/O=0.78$  and maximum flame temperature of about 1750K [25]. Again the model reproduces the concentration profiles of light hydrocarbons well as shown by the comparison of ethylene, methane and acetylene reported in the top of Figure 16 and propyne and diacetylene in the bottom of the same figure. Light hydrocarbon formation occurs after 4mm in correspondence of the end of the flame zone.

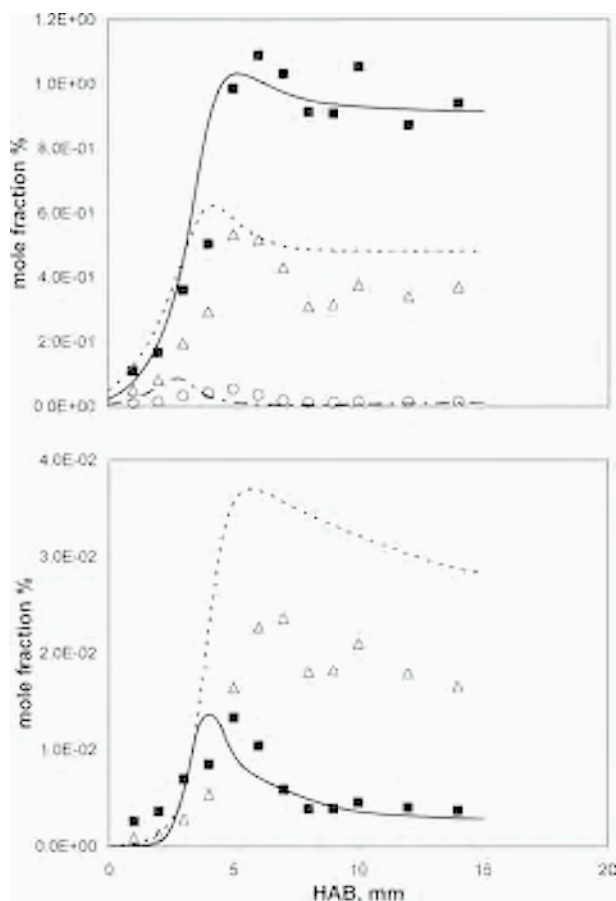


Figure 16. Concentration profiles of (top) methane ( $\Delta$ ), ethylene (o) and acetylene ( $\blacksquare$ ) and (bottom) propyne ( $\blacksquare$ ) and diacetylene ( $\Delta$ ) along the flame axis of a benzene/air premixed flame with C/O=0.78.

In the oxidation of benzene fuel, aromatic rings are already present in the main oxidation zone, and they are mainly oxidized to *c*-C<sub>5</sub>H<sub>5</sub> radicals and CO. As a consequence, a large amount of intact aromatic rings and cyclopentadienyl radicals are available for recombination reactions in the main oxidation process, leading to multi-ring aromatic formation already below the flame front. At the flame front the first soot particles appear and their concentration increases with a very fast inception rate in correspondence of the decrease of the concentration of condensed species. These compounds finally reach an almost constant concentration downstream of the flame zone in correspondence to the level-off of soot concentration. Model predictions correctly reproduce the experimental data and showing the fast formation rate of soot in benzene flame in correspondence of the decay of CS concentration as shown in Figure 17 where the comparison between modelled and experimental concentration profiles of CS and soot are reported.

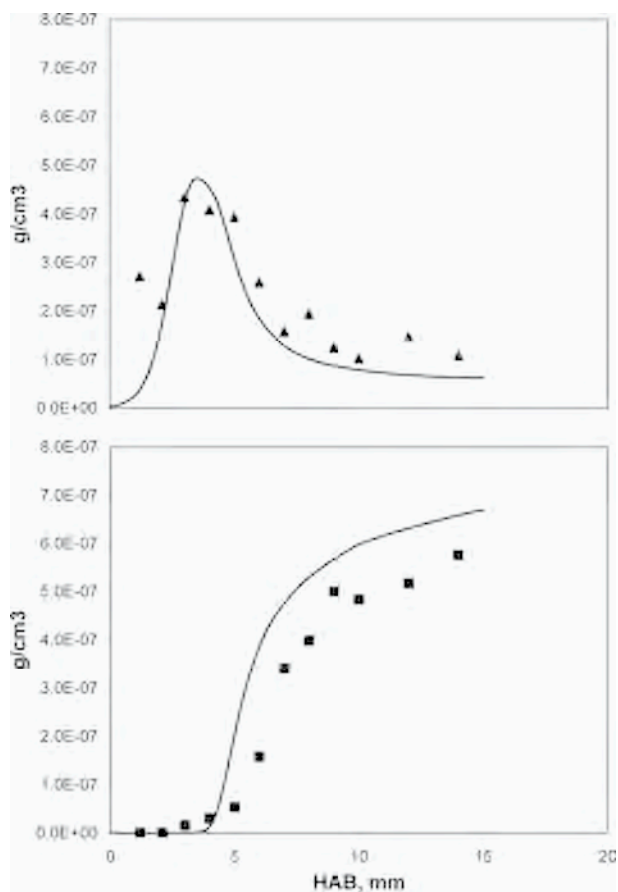


Figure 17. Concentration profiles of (top) Condensed Species and (bottom) soot along the flame axis of a benzene/air premixed flame with  $C/O=0.80$ .

By comparing benzene flame with n-heptane flame in comparable conditions of  $C/O$  ratio and temperature, two main differences clearly appear: the upward shift of particle nucleation and the decrease of CS in the post-flame zone. In the benzene flame, benzene shows high concentrations near the burner which is consistent with the observed fast formation of CS which rapidly evolve towards soot particles. Because the aromatics are consumed in the oxidation zone, the nucleation peak in the upper regions of the flame is depressed. By contrast, in the n-heptane flame, acetylene and benzene are formed downstream of the flame front and their concentrations persist at even high heights above the burner causing the observed delayed and persistent formation of CS at larger heights. Although the clear difference in the inception process, ultimate soot loading remains quite constant in the two flames [75].

#### 4.5. Larger hydrocarbons

The kinetic model has been used to study the effect of fuel molecule structure interaction on the formation of CS and soot. Four flames of different hydrocarbons have been studied experimentally keeping constant the C/O ratio ( $C/O=0.70$ ) and temperature profiles. The flames have been stabilized burning n-heptane and adding 10% by vol. of benzene, toluene and iso-octane to n-heptane.

Figure 18 reports the comparison of predicted concentration profiles of condensed species and soot in the four flames with experimental concentration profiles obtained by LIF and LII measurements.

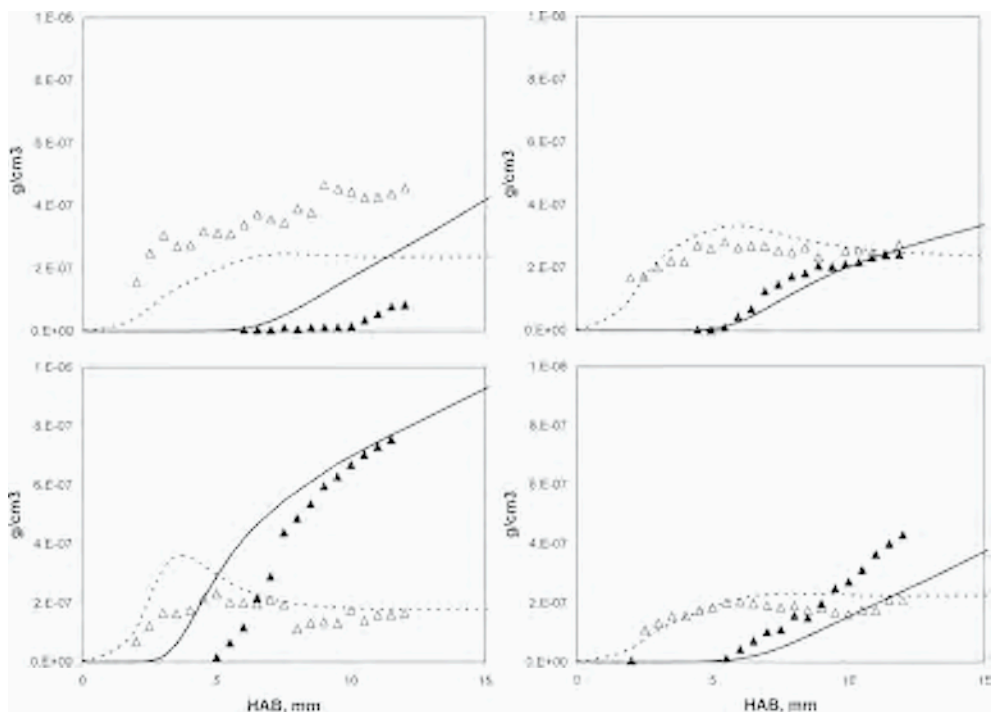


Figure 18. Concentration profiles of CS and soot along flames burning mixtures of n-heptane with toluene, benzene and iso-octane at  $C/O=0.70$ . Left: (top) n-heptane and (bottom) toluene. Right: (top) benzene and (bottom) iso-octane.

The model reproduces satisfactorily the concentration values and profiles of CS and soot and the increase of soot concentration for effect of hydrocarbon addition to n-heptane. Toluene has the maximum effect on soot inception followed by iso-octane and benzene. The addition of aromatic rings in the fuel also causes the earlier soot inception, well reproduced by the model.

## 5. SENSITIVITY ANALYSIS

A sensitivity analysis of the growth pathways in different flame structures has been performed. Figure 19 reports the relative contribution to particle formation of three main reaction paths: the acetylene addition, the formation of aromatic-linked compounds (chemical growth) and the coagulation of aromatics (physical growth). The formation of nanoparticle downstream of the flame front of premixed flames (top of left side of Figure 19) is mainly due to a chemical growth mechanism of aromatics. Coagulation of nanoparticles becomes the controlling route only at higher heights. Acetylene addition is also important but it follows the chemical growth process. Larger particles (i.e. primary soot particles of 20nm size) are instead formed mainly by coagulation of the smaller ones and by acetylene addition. The chemical growth process still contributes to larger particle formation but at lesser extent (top of the right side of Figure 19).

In non-premixed flames, coagulation is the dominant pathways for particle formation, both nanoparticles and primary soot particles (Figure 19 bottom). The chemical growth process has a minor effect and closer to the flame front. Acetylene addition dominates in the high temperature flame region.

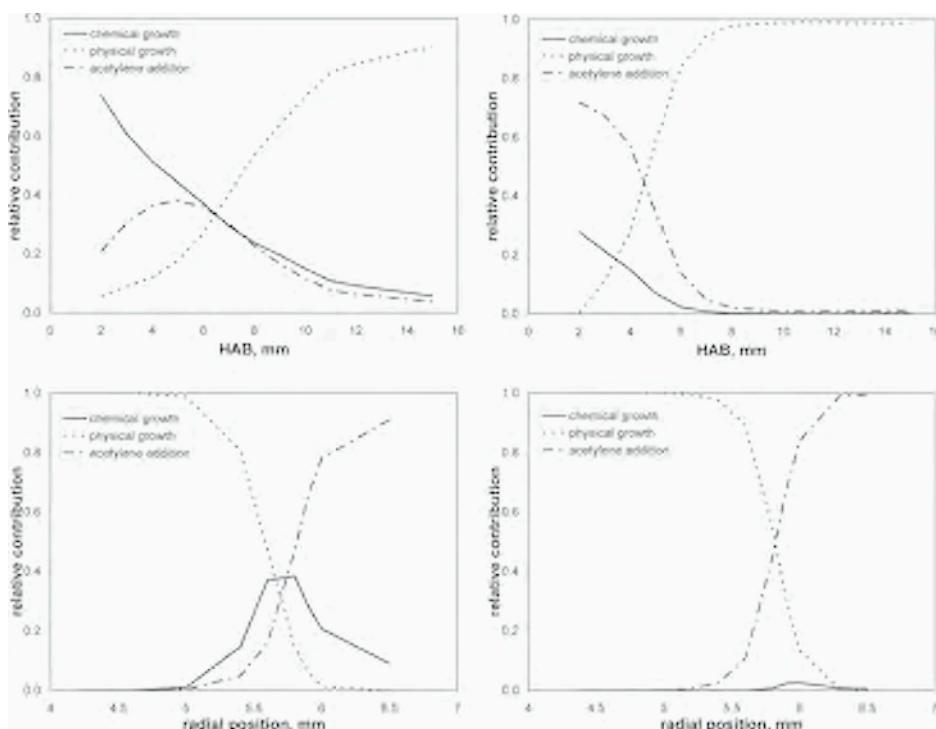


Figure 19. Relative contribution to (left) nanoparticle and (right) soot particle formation of the acetylene addition, the chemical growth and the physical growth pathways in (top) premixed and (bottom) non-premixed flames.

The relative importance of the chemical growth mechanism respect to the physical one in different flame conditions confirms that staked PAH structures are formed in the low temperatures and low radical concentrations typical of the fuel-side of non-premixed flames and in the post-flame zones of rich premixed flames. Aromatic-aliphatic linked structures are instead formed in the higher temperatures and higher radical concentrations typical of fuel-rich, premixed flames.

## 6. CONCLUDING REMARKS

A detailed kinetic mechanism of aromatic growth and particulate formation is presented and it is tested over a range of different operating conditions in rich premixed and non-premixed flames of various hydrocarbons. The kinetic model has been built-up and refined by comparing model predictions with experimental data on the formation of molecular particles.

Good predictions are obtained of major oxidation and pyrolysis products, as well as of trace species and particle concentrations and size distributions. The model predicts particle size distribution functions with a single mode centered at about 2nm in premixed flames below the soot formation threshold and in the fuel side of non-premixed flames, in good agreement with experimental data. In premixed sooting flames and in the external zones of non-premixed flames the particle size distribution functions develop towards a bimodal shape with a first mode due to nanoparticles and a second mode due to primary soot particles.

The kinetic model has been used to predict particle formation by using different hydrocarbons including methane, ethylene, n-heptane, benzene and mixtures of n-heptane with toluene, benzene and iso-octane.

Sensitivity of the predictions to the particulate-phase reaction rates has been performed showing the importance of the mechanism of aromatic-molecule addition to aromatic radicals in the formation of nanoparticles in premixed flames and the physical coagulation of PAHs in the formation of nanoparticles in non-premixed flame. Acetylene addition is important in both flame conditions for soot loading but doesn't contribute to particle inception.

## REFERENCES

1. M. Frenklach, *Phys. Chem. Chem. Phys.* 4 (2002) 2028.
2. I. M. Kennedy, *Prog. Energy Combust. Sci.* 23 (1997) 95.
3. A. D'Anna, A. Violi, A. D'Alessio, A.F. Sarofim, *Combust. Flame* 127(1/2) (2001) 1995.
4. A. D'Anna, *Energy Fuels* 22(3) (2008) 1610.
5. A. D'Anna, J. Kent, *Combust. Flame* 152 (2008) 573.
6. K.-H. Homann, H.Gg. Wagner, *Proc. Combust. Inst.* 11 (1967) 371.
7. B.L. Wersborg, J.B. Howard, G.C. Williams, *Proc. Combust. Inst.* 14 (1973) 929.
8. J.D. Bittner, J.B. Howard, *Proc. Combust. Inst.* 18 (1981) 1105.
9. R.A. Dobbins, C.M. Megaridis, *Langmuir* 3 (1987) 254.
10. R.A. Dobbins, H. Subramaniasivam, in *Soot Formation in Combustion*, H. Bockhorn (Ed.), 1994, Springer-Verlag, Heidelberg, 290.

11. A. D'Alessio, A. D'Anna, A. D'Orsi, P. Minutolo, R. Barbella, A. Ciajolo, *Proc. Combust. Inst.* 24 (1992) 973.
12. A. D'Alessio, A. D'Anna, G. Gambi, P. Minutolo, *J. Aerosol Sci.* 29 (1998) 397.
13. A. D'Anna, A. D'Alessio, P. Minutolo, in *Soot formation in combustion: mechanisms and models*, H. Bockhorn (Ed.) 1994, Springer-Verlag, Berlin 83-103.
14. P. Minutolo, G. Gambi, A. D'Alessio, A. D'Anna, *Combust. Sci. Technol.* 101(1-6) (1994) 309.
15. P. Minutolo, G. Gambi, A. D'Alessio, S. Carlucci, *Atmos. Environ.* 33 (1999) 2725.
16. A. Ciajolo, A. D'Anna, R. Barbella, *Combust. Sci. Technol.* 100 (1994) 271.
17. A. Ciajolo, R. Barbella, A. Tregrossi, L. Bonfanti, *Proc. Combust. Inst.* 27 (1998) 1481.
18. A. Ciajolo, A. D'Anna, R. Barbella, A. Tregrossi, A. Violi, *Proc. Combust. Inst.* 26(2) (1996) 2327.
19. A. D'Anna, A. Rolando, C. Allouis, P. Minutolo, A. D'Alessio, *Proc. Combust. Inst.* 30 (2005) 1449.
20. A. D'Anna, M. Commodo, S. Violi, C. Allouis, J. Kent, *Proc. Comb. Inst.* 31 (2007) 621.
21. A. D'Anna, M. Commodo, M. Sirignano, P. Minutolo, R. Pagliara, *Proc. Combust. Inst.* 32 (2009) doi:10.1016/j.proci.2008.06.172.
22. L.A. Sgro, G. Basile, A.C. Barone, A. D'Anna, P. Minutolo, A. Borghese, A. D'Alessio, *Chemosphere* 51/10 (2003) 1079.
23. L.A. Sgro, A. Borghese, L. Speranza, A.C. Barone, P. Minutolo, A. Bruno, A. D'Anna, A. D'Alessio, *Environ. Sci. Technol.* 42(3) (2008) 859.
24. A. D'Anna, *Proc. Combust. Inst.* 32 (2009) doi:10.1016/j.proci.2008.09.005.
25. A. Tregrossi, A. Ciajolo, R. Barbella, *Combust. Flame* 117(3) (1999) 553.
26. M. Alfè, B. Apicella, R. Barella, A. Tregrossi, A. Ciajolo, *Proc. Combust. Inst.* 31(1) (2007) 585.
27. C.A. Echavarria, A.F. Sarofim, J. Lighty, A. D'Anna *Proc. Combust. Inst.* 32 (2008) doi:10.1016/j.proci.2008.06.172.
28. B. Apicella, R. Barella, A. Ciajolo, A. Tregrossi, *Chemosphere* 51 (2003) 1063.
29. G. Rusciano, A.C. De Luca, A. D'Alessio, P. Minutolo, G. Pesce, A. Sasso, *Carbon* 46 (2008) 335.
30. L.A. Sgro, A. De Filippo, G. Lanzuolo, A. D'Alessio, *Proc. Comb. Inst.* 31 (2007) 631.
31. P. Minutolo, A. D'Anna, A. D'Alessio, *Combust. Flame* 152(1-2) (2008) 287.
32. L.A. Sgro, P. Minutolo, A. De Filippo, A.C. Barone, M. Commodo, G. Lanzuolo, A. D'Alessio, *Proc. Combust. Inst.* 32 (2008) doi:10.1016/j.proci.2008.06.216.
33. A. D'Alessio, A.C. Barone, R. Cau, A. D'Anna, P. Minutolo, *Proc. Comb. Inst.* 30 (2005) 2595.
34. G. Basile, A. Rolando, A. D'Alessio, A. D'Anna, P. Minutolo, *Proc. Combust. Inst.* 29(2) (2002) 2391.
35. A. D'Alessio, A. D'Anna, P. Minutolo, L.A. Sgro, A. Violi, *Proc. Combust. Inst.* 28(2) (2000) 2547.
36. R.J. Santoro, H.G. Semerjian, R.A. Dobbins, *Combust. Flame* 51 (1983) 203.
37. R.J. Santoro, H.G. Semerjian, *Proc. Combust. Inst.* 20 (1984) 997.
38. R.J. Santoro, T.T. Yeh, J.J. Horvath, H.G. Semerjian, *Combust. Science Technol.* 53 (1987) 89.
39. K.C. Smyth, J.H. Miller, R.C. Dorfman, W.G. Mallard, R.J. Santoro, *Combust. Flame* 62 (1985) 157.
40. R.A. Dobbins, R.A. Fletcher, H.-C. Chang, *Combust. Flame* 115 (1998) 285.
41. M. Alfè, B. Apicella, R. Barbella, J.-N. Rouzaud, A. Tregrossi, A. Ciajolo, *Proc. Combust. Inst.* 32 (2009) doi:10.1016/j.proci.2008.06.193.
42. R. Barbella, A. Ciajolo, A. D'Anna, *Fuel* 68(6) (1989) 690.

43. B. Apicella, A. Ciajolo, A. Tregrossi, *Anal. Chem.* 76(7) (2004) 2138.
44. B. Zhao, Z. Yang, Z. Li, M.V. Johnston, H. Wang, *Proc. Combust. Inst.* 30 (2005) 1441.
45. B. Zhao, Z. Yang, J. Wang, M.V. Johnston, H. Wang, *Aerosol Sci. Technol.* 37 (2003) 611.
46. M.M. Maricq, *Combust. Flame* 137 (2004) 340.
47. A.C. Barone, A. D'Alessio, A. D'Anna, *Combust. Flame* 132 (2003) 181.
48. B. Apicella, A. Ciajolo, R. Barella, A. Tregrossi, T.J. Morgan, A.A. Herod, R. Kandiyoti, *Energy Fuels* 17 (2003) 565.
49. B. Apicella, A. Ciajolo, I. Suelves, T.J. Morgan, A.A. Herod, R. Kandiyoti, *Combust. Sci. Technol.* 174 (2002) 403.
50. M. Alfè, B. Apicella, R. Barbella, A. Tregrossi, A. Ciajolo, *Energy Fuels* 21 (2007) 136.
51. R.J. Kee, F.M. Rupley, J.A. Miller, M.E. Coltrin, J.F. Grcar, E. Meeks, H.K. Moffat, A.E. Lutz, G. Dixon-Lewis, M.D. Smooke, J. Warnatz, G.H. Evans, R.S. Larson, R.E. Mitchell, L.R. Petzold, W.C. Reynolds, M. Caracotsios, W.E. Stewart, P. Glarborg, CHEMKIN Collection, Release 3.5, Reaction Design, Inc., San Diego, CA (1999).
52. A. El Bakalia, J.-L. Delfau, C. Vovelle, *Combust. Flame* 118(3) (1999) 381.
53. H.Y. Zhang, J.T. McKinnon, *Combust. Sci. Technol.* 107(4-6) (1995) 261.
54. E. Ranzi, T. Faravelli, P. Gaffuri, A. Sogaro, A. D'Anna, A. Ciajolo, *Combust. Flame* 108(1/2) (1997) 24.
55. J.A. Miller, C.F. Melius, *Combust. Flame* 91 (1992) 21.
56. A. D'Anna, A. Violi, *Energy Fuels* 19(1) (2004) 79.
57. M. Frenklach, H. Wang, H., *Proc. Combust. Inst.* 23 (1990) 1559.
58. N.M. Marinov, W.J. Pitz, C.K. Westbrook, M.J. Castaldi, S.M. Senkan, *Combust. Sci. Technol.* 1996, 116-117, 211-226.
59. M.J. Castaldi, N.M. Marinov, C.F. Melius, J. Huang, S.M. Senkan, W.J. Pitz, C.K. Westbrook, *Proc. Combust. Inst.*, 1996, 26, 693.
60. M.B. Colket, D.J. Seery, *Proc. Combust. Inst.* 25 (1994) 883.
61. N.W. Moriarty, M. Frenklach, *Proc. Combust. Inst.* 28 (2000) 2563.
62. H. Richter, S. Granata, W.H. Green, J.B. Howard, *Proc. Combust. Inst.* 30 (2005) 1397.
63. J.B. Howard, *Proc. Combust. Inst.* 23 (1990) 1107.
64. K.G. Neoh, J.B. Howard, A.F. Sarofim, *Proc. Combust. Inst.* 20 (1985) 951-957.
65. F. Xu, A.M. El-Leathy, C.H. Kim, G.M. Faeth, *Combust. Flame* 132 (2003) 43-57.
66. J. Israelachvili, *Intermolecular and Surface Forces*, Academic Press, London (UK), 1991.
67. D. Wong, R. Whitesides, C.A. Schuetz, M. Frenklach, in *Combustion Generated Fine Carbonaceous Particles*, H. Bockhorn, A. D'Anna, A.F. Sarofim, H. Wang (Eds.) Karlsruhe University Press, 2009, pp. 247-258.
68. S.K. Friedlander, *Smoke, dust and haze: fundamentals of aerosol behaviour*, John Wiley & Sons, New York (USA), 1977.
69. C. J. Pope, J. B. Howard, *Aerosol Sci. Technol.* 27 (1997) 73.
70. J. Kent, in *Combustion Generated Fine Carbonaceous Particles*, H. Bockhorn, A. D'Anna, A.F. Sarofim, H. Wang (Eds.) Karlsruhe University Press, 2009, pp. 605-618.
71. D. Cecere, G. Gaudioso, A. D'Anna, R. Verzicco, in *Complex Effects in Lecture Notes in Computational Science A "Large Eddy Simulations"*, S.C. Kassinos, C.A. Langer, G. Iaccarino, P. Moinz (Eds.), Springer-Verlag, New York, 2007.
72. A. D'Anna, M. Sirignano, M. Commodo, R. Pagliara, P. Minutolo, *Combust. Sci. Technol.* 180(5) (2008) 950.
73. M.D. Smooke, C.S. McEnally, L.D. Pfefferle, *Combust. Flame* 117 (1999) 117
74. M. Commodo, S. Violi, A. D'Anna, C. Allouis, P. Minutolo, 29th Meeting of the Italian Section of the Combustion Institute, Pisa, June 14-17, 2006.
75. A. D'Anna, M. Alfe, B. Apicella, A. Tregrossi, A. Ciajolo, *Energy & Fuels*, 21(5) (2007) 2655.

# Insights on the formation and growth of carbonaceous nanoparticles in high temperature environments

S.H. Chung, A. Violi

Department of Mechanical Engineering, University of Michigan, Ann Arbor, MI 48109-2125, United States

*Abstract: In this paper we report a detailed analysis of the particle inception region in counterflow diffusion flames using computational approaches. The rate of nanoparticle mass growth is modeled in two different flame configurations to address the influence of combustion environments on the inception process. The results suggest that particle inception can be considered as result of a chemical growth and a physical process. The contribution of these pathways to the particle inception varies according to the combustion conditions. In the case of high temperature and polycyclic aromatic hydrocarbon (PAH) concentrations relatively low, the Atomistic Model for Particle Inception (AMPI) code successfully predicts the nanoparticle formation based on chemical reactions between gas-phase species and growing particle. In these conditions, the particle loading is mainly associated with the formation of high-molecular structures through chemical reactions. At relatively low temperatures (~1400K) and high PAH concentrations, the combined mechanism of chemical reactions described by the AMPI code and physical coagulation may contribute to particle growth. Molecular Dynamics simulations of nanoparticles of different masses at various temperatures are carried out to identify combustion regimes where the physical coagulation is significant.*

## 1. INTRODUCTION

In flame conditions, the growth mechanism that bridges the transition from small polycyclic aromatic hydrocarbons (PAH), which are widely regarded as soot precursors, to nano-sized organic particle is still the least known step of soot formation. Currently, experimental data in this transition zone are very limited due to the nature of the processes characterized by small size and short time scales. Recently, Violi et al. have reported results for the evolution of nanoparticle formed from small hydrocarbons using a combination of Molecular Dynamics (MD) and kinetic Monte-Carlo (KMC) methods (Atomistic Model for Particle Inception – AMPI code) to describe the formation of particles in a chemically specific way [1, 2]. The transition process is defined as chemical growth between gas-phase species and the growing particle. The capability of the AMPI code has been validated in different combustion conditions. Nanoparticles have been characterized in terms of chemical structure/components and relationships between structure and pathways, structure and properties, and structure and reactivity population of active sites have been addressed. In particular, computed properties of nanoparticles have been compared with experimental data in

terms of H/C trends, particle morphology and depolarization ratio, and free radical concentration for premixed flames [1, 3, 4].

In this paper we extend the range of combustion conditions investigated to include counterflow diffusion flames and we apply computational methods, including the AMPI code and Molecular Dynamics simulations to study the region of particle formation and growth. The goal of this study is to gain insights on the effect of combustion conditions such as temperature and species concentrations on nanoparticle formation and their further growth. At the same time we are interested in understanding whether particle inception defined as a chemical process is enough to describe the formation and growth of nanoparticles in different environments or additional processes, such as physical coagulation, need to be taken into account.

The systems chosen for this computational study are two counterflow diffusion flames experimentally studied by Kang et al. [5]. The availability of experimental data will help to guide and validate the numerical approach. Particle formation in counterflow diffusion flames has been extensively investigated for their ability to represent turbulent flames within the laminar flamelet model. One of the most appealing features of these systems is the influence of flow characteristics on the formation, growth, and oxidation of particles [6, 7].

When a diffusion flame is located on the fuel side, the gas velocity is directed toward the flame and particles follow the gas-phase streamlines. On the other hand, when the flame is located on the oxidizer side, the gas velocity is directed to the stagnation plane and particles move away from the flame [5]. As a consequence particle growth will be significantly different and this makes the counter-flow diffusion flames very appealing to study the processes that contribute to the formation of particles.

After describing the methodologies used to study the formation of particles from gasphase hydrocarbons and their subsequent coagulation, we present results in two counterflow configurations of propane. The results suggest that particle formation can be considered as combination of a chemical and a physical process and the relative importance of the two steps is highly dependent on the combustion conditions.

## 2. METHODOLOGY

### 2.1. From gas-phase to particle formation: the AMPI algorithm

Particle growth occurs on a time scale that is generally not accessible to fully atomistic models such as MD with reactive potentials, whereas an atomically resolved Monte Carlo method parameterized by accurate chemical kinetic data is capable of exploring growth over long times and large length scales. The AMPI code proposes a new approach to study the transition from gas-phase to nanoparticles, involving the coupling of kinetic Monte Carlo and MD. This coupling provides a key to the multiple time-scales involved in the formation of nanoparticles, spanning from pico- or nanoseconds for intramolecular processes to microseconds for intermolecular reactions.

As inputs, the AMPI code requires a detailed description of the gas-phase environment that for this work is provided by the OPPDIF code [9] of the CHEMKIN

suite of programs, with a chemical model that includes 172 species and 4890 reactions steps up to the C16 mechanism<sup>1</sup>.

After reading a set of inputs, including temperature, species concentrations in the gasphase and reaction rates, the AMPI code determines the number of sites available for reactions on the growing structure by identifying each atom as a radical, neutral, aliphatic and aromatic site. A check for steric hindrance is then performed and the reactions available at that time are classified as either accepted or rejected. Once a list of possible reactions is created, along with possible sites and reaction rates, the code randomly selects a reaction based on the reaction probability, and it then modifies the structure of the growing particle according to the selected reaction. Finally the code performs a MD simulation run that allows the newly formed structure to reach thermal equilibrium. The NVT ensemble is used for the simulation and the temperature is set equal to the flame temperature at the location analyzed. The AMPI code alternates between a kMC step and a MD step. Details have been described elsewhere [1, 3, 4, 8].

## 2.2. Flame conditions

Figure 1 reports the schematics for the two flame configurations used in this study. Counterflow diffusion flames are frequently located on the oxidizer side when pure hydrocarbon is supplied from the fuel side. Upon appropriate dilution of the fuel and oxidizer streams, however, the flame can be moved to the fuel side [10, 11]. A soot formation (SF) flame is obtained when the flame is located on the oxidizer side of a stagnation plane, such that particles once formed are convected away from the flame toward the stagnation plane. In this way particles do not undergo oxidation. In the configuration

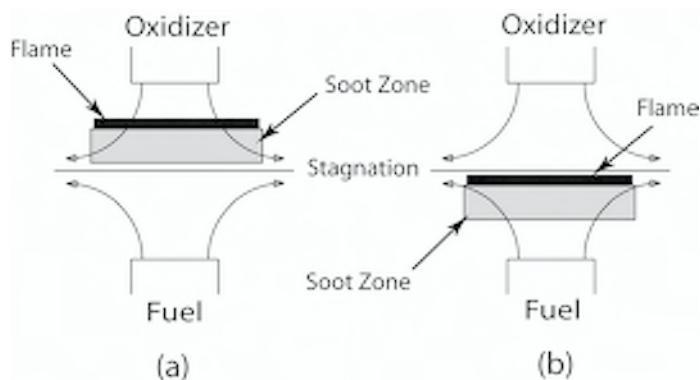


Figure 1. Schematics of the (a) soot formation (SF) and (b) soot oxidation (SFO) counter flow diffusion flames [5].

<sup>1</sup> <http://www.chem.polimi.it/CRECKModeling/>.

depicted on the right, particles are transported toward the high temperature oxidizer side. This occurs when the flame is located on the fuel side such that soot particles are transported toward the high temperature oxidizer side. Due to oxidation, this soot formation/oxidation (SFO) flame shows a behavior similar to sooting premixed flames.

Below we report a detailed analysis of a SFO flame ( $X_{C_3H_8}, X_{O_2}$ ) = (0.25, 0.7) and a SF flame ( $X_{C_3H_8}, X_{O_2}$ ) = (1.0, 0.3). In both cases the diluent is nitrogen. The separation distance between two nozzles is 14.2 mm and the volume-averaged nozzle exit velocity for both nozzles are 0.2 m/s. These flames have been experimentally investigated by Kang et al. [5] who employed soot extinction-scattering, PAH fluorescence, and laser Doppler velocimetry measurements to determine the characteristics of the particle zone structures.

### 3. RESULTS

#### 3.1. From gas-phase to nanoparticles

##### 3.1.1. Soot Formation Oxidation (SFO) flame

Figure 2 shows the computed results obtained with OPPDIF for the concentrations of acetylene and hydroxyl radical together with the temperature profile for the SFO flame ( $X_{C_3H_8}, X_{O_2}$ ) = (0.25, 0.7) along with a schematic diagram corresponding to the flame structure [12]. These conditions correspond to a flame location close to the gas-phase stagnation plane. In such case, the soot zone is located on the fuel side and particles are transported toward the particle stagnation plane, that is, toward the high temperature region, where they are finally get oxidized.

The computed temperature values agree well with the measured temperature profile from coherent anti-Stokes Raman spectroscopic measurements reported by Kang et al. [5]. Propane is pyrolyzed to form hydrocarbons such as  $C_2H_2$  that exists in the range  $z = 3-6$  mm where  $z$  is the distance from the fuel nozzle. The concentration profile of OH identifies the position of the flame front. The particle stagnation plane is located around  $z = 6.77$  mm and the luminous zone has been experimentally identified between  $z = 6.21$  mm and  $z = 7.36$  mm.

To determine the characteristics of the sooting zone, we analyzed several locations in the flame covering eight points from the fuel to the oxidizer side. The circles in Figure 2 show the locations sampled with the AMPI code. Upon inclusion of the gas-phase species concentrations and temperature into the AMPI code, five runs were carried out at each point to study particle formation at these eight locations with the distance  $z$  ranging from 5.19 to 6.15 mm. Figure 3 shows the number of carbon atoms present on the nanoparticles as a function of time for locations 1 through 3. For distances smaller than  $z = 5.19$  mm (point 1) the rate of growth of particles was very slow. The rate of growth of nanoparticles dramatically changes between locations 1 and 2. At location 2, particle growth occurs on the order of  $10^{-4}$  sec and since the gas velocity at this point is  $\sim 10$  cm/s, particles can proceed  $O(10^{-4} \text{ sec}) * O(10 \text{ cm/s}) = O(0.01 \text{ mm})$ . Since the distance between locations 2 and 3 is around 0.43 mm, the particle has enough time to grow before it is convected away from Point 2.

Following these results, we can conclude that for the SFO flame analyzed in this study, particle inception occurs between locations 1 and 2 where the concentration of acetylene reaches its peak. The computational results are in very good agreement with the data measured by Kang et al. [5]. Figure 4 reports examples of particle configurations obtained at Points 2 and 3. In this region, a detailed analysis of the results obtained with the AMPI code shows that ring closure reactions, in which nascent rings are formed through dehydrogenation mechanisms [13], acetylene addition and hydrogen eliminations and additions are the most frequent reactions that contribute to the particle formation. The importance of acetylene indicates that the particle inception occurs from PAH through  $C_2H_2$ .

At around  $z = 6$  mm oxidation reactions start to play an important role and we did not observe particle growth beyond this location. Figure 5 shows the number of carbon atoms present on the growing species as a function of time at locations 5-8. The curves are representative of different runs. Around  $z = 6.21$  mm, location 5, the mole fractions of OH and  $C_2H_2$  become almost equal and the burnout is significant. The contributions of OH and O to the particle growth are twofold: they remove carbon

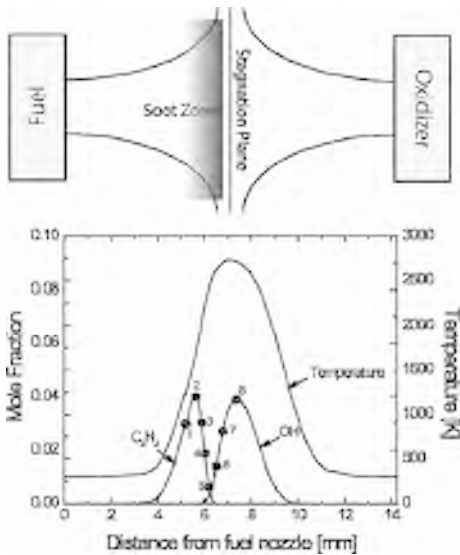


Figure 2. Numerical results of the temperature profile and  $C_2H_2$  and OH concentrations in the SFO flame together with the corresponding schematic of the flame structure. (●) represents the locations sampled by the AMPI code.

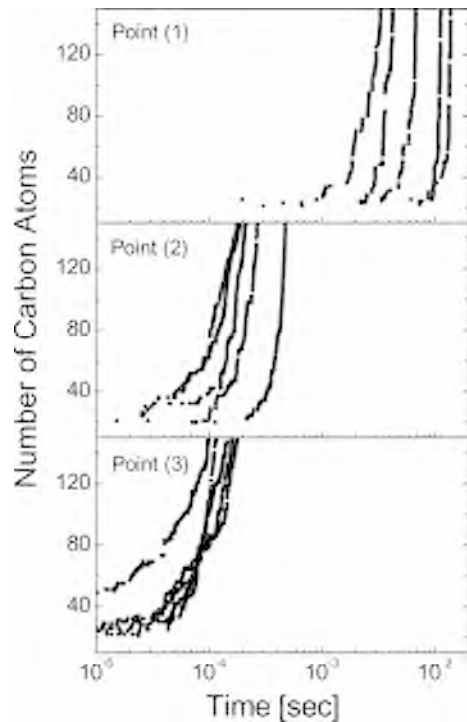


Figure 3. Number of carbon atoms on the particle as a function of time for  $z=5.19$ mm (Point 1),  $z=5.62$ mm (Point 2),  $z=5.88$ mm (Point 3).

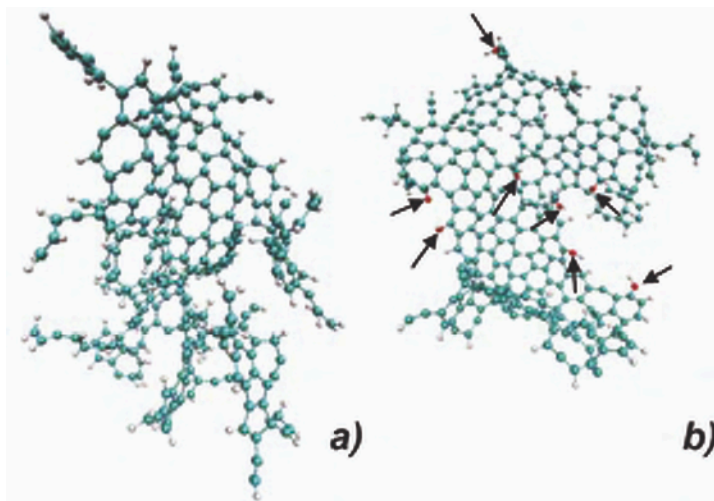


Figure 4. Carbonaceous nanoparticles produced by the AMPI code at points 2 (a), and 3 (b). Carbon atoms are shown in gray, hydrogen atoms in white and oxygen atoms are indicated by arrows.

from the nanoparticle producing CO and CO<sub>2</sub> and they react with radicals on the particle, preventing further addition of hydrocarbons.

From Point 5 toward the oxidizer stream, OH radicals oxidize the particles causing a decrease of the particle sizes. This result agrees well with the experimental data [5] showing after  $\bar{x} = 6$  mm a decrease in the particle size and volume fraction. This counterflow flame located near the stagnation plane can be classified as a soot formation-oxidation flame as the particle mechanism is dominated by oxidation.

#### H/C ratio

H/C ratios of the particles generated at locations 2, 3 and 4 are reported in Figure 6 as function of time. We carried out the simulations until particles of similar sizes were produced by the AMPI code. Low values of the H/C ratios at  $\bar{x} = 5.88$  mm (Point 3) and 6.03 mm (Point 4) are indicative of more aromatic structures as compared to higher values of H/C ratios obtained at  $\bar{x} = 5.62$  mm, location 2. This is due to the high concentration of hydrocarbons that can react with the particle and to the frequent cyclodehydrogenation reactions in which hydrogen atoms are lost, and a new ring is created by the formation of a new transannular C-C bond [13].

#### 3.1.2. Soot-formation (SF) flame

Figure 7 illustrates the computed profiles of temperature and species concentrations for the SF flame ( $X_{C_3H_8}, X_{O_2} = (1.0, 0.3)$ ) with the corresponding schematic the flame structure. In this case, the soot zone is located on the oxidizer side in the region of  $5 \text{ mm} < \bar{x} < 7 \text{ mm}$ , next to the flame zone of  $7.5 \text{ mm} < \bar{x} < 8.5 \text{ mm}$  and particles are

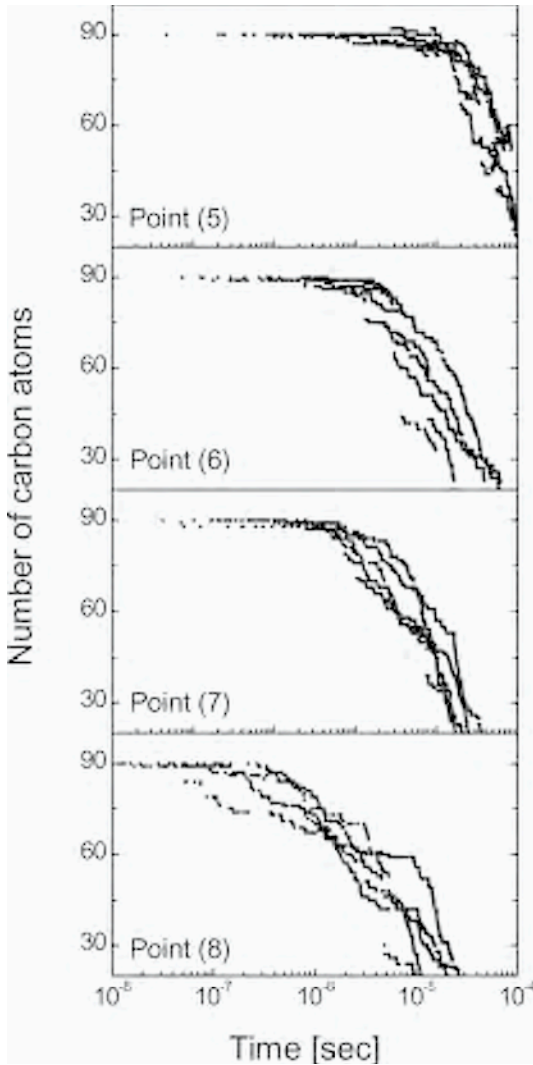


Figure 5. Number of carbon atoms on the growing particle as a function of time for  $z=6.21\text{mm}$ (Point 5),  $z=6.50\text{mm}$  (Point 6),  $z=6.77\text{mm}$  (Point 7), and  $z=7.36\text{mm}$  (Point 8).

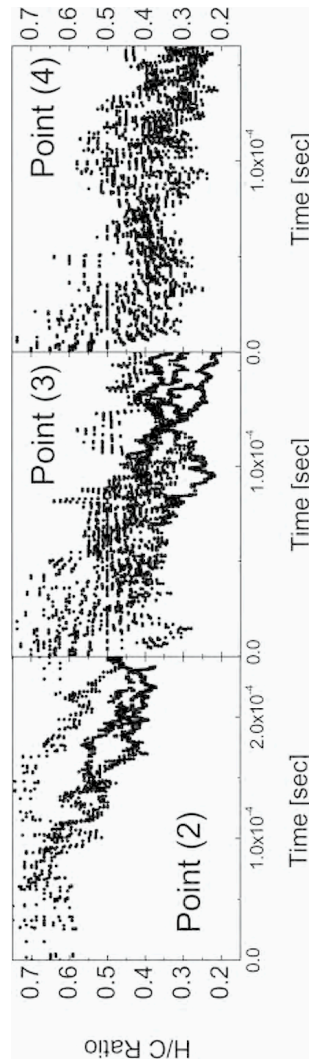


Figure 6. H/C ratios of nanoparticles at points 2, 3 and 4 as a function of time.

transported away from the flame toward the fuel side. We analyzed four points in the inception zone and they are reported in Figure 7.

Figure 8 shows the change in number of carbon atoms on the growing particle as function of time for Points 1 through 4. No significant particle growth was computed at larger distances. At Point 1,  $z = 7.7 \text{ mm}$ , particle growth suddenly increases. The computational results are in agreement with the experimental measurements by Kang et al. [5]

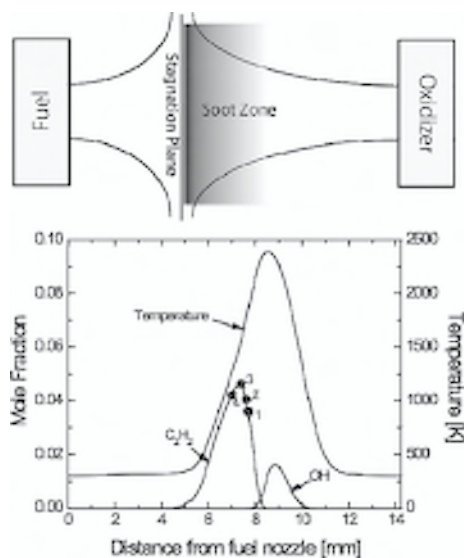


Figure 7. Numerical results for the temperature profile and  $C_2H_2$  and OH concentrations in the SF flame together with the corresponding schematic of the flame structure. (●) represents the locations sampled by the AMPI code.

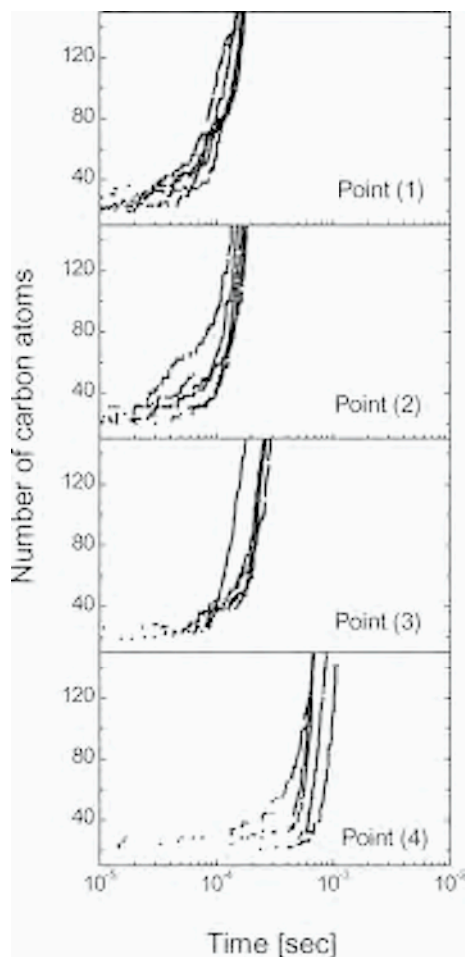


Figure 8. Number of carbon atoms on the growing particles as function of time in the SF flame at  $z=7.7$  mm (Point 3),  $z=7.6$  mm (Point 4),  $z=7.4$  mm (Point 5),  $z=7.2$  mm (Point 6) and  $z=7.0$  mm (Point 7).

showing that the soot inception is located around  $z \sim 7$  mm, having almost the same temperature as in the case of the SFO flame. Nanoparticles are formed in the region between the flame front and the maximum aromatic concentration since the presence of hydrogen atoms initiates the growth process. The fastest growth rates were computed at  $z = 7.7$  mm (Point 1) and  $z = 7.6$  mm (Point 2) and no significant growth was obtained beyond 7 mm due to the low temperature and rapid decrease of hydrocarbon concentrations.

Figure 9 shows examples of particle configurations formed at various locations in the flame. Differently from the SFO flame, at the beginning of particle inception

(Point 1) we observed oxygen atoms on the particle. We identified a maximum concentration of 15% of oxygen atoms on the particles. The number of oxygen atoms on the particle decreases moving further from the flame front. In this flame, acetylene additions still play an important role and PAH contribution to particle growth is not significant in this region.

Going from  $z = 7.7$  mm to  $z = 7.0$  mm, the contribution of hydrogen abstraction by hydrogen and OH radicals to particle growth decreases while hydrogen abstractions by hydrocarbon radicals becomes more frequent.

As mentioned above, when the stagnation plane is approached (around at  $z = 5$  mm) with the decrease in temperature, the inception rate due to the chemical growth decreases (Points 3 and 4 in Figure 8). When comparing this result with the experimental data by Kang et al., the particle inception based solely on the chemical growth does not seem to adequately describe the particle growth in the SF configuration. The particle nucleation zone in the SF flame is characterized by low concentrations of hydrogen radicals and relatively low temperature, while the PAH concentrations are much higher than in the SFO flame. Hence, soot inception via physical interaction with PAH and nanoparticles instead of a solely chemical growth can be a viable particle growth process for this environment.

Figure 10 reports the total concentrations of PAH in the SF and SFO flames. PAH concentration is defined as the sum of aromatic species obtained from the Chemkin results and include as main species  $C_5H_5$ ,  $C_5H_6$ ,  $C_6H_5$ ,  $C_6H_6$ ,  $C_6H_8$ ,  $C_6H_{10}$ ,  $C_6H_5C_2H$ ,  $C_6H_5C_2H_2$ ,  $C_6H_5C_2H_3$ , indenyl, naphthalene, naphthyl, acenaphthalene and acenaphthyl. The concentration of PAH in the particle inception region of the SF flame (grey area) is almost twice that of the inception zone of the SFO flame ( $2.8 \times 10^{-8}$  vs  $1.5 \times 10^{-8}$ ). These results together with the much lower temperature of the SF flame ( $T \sim 1400$ K) compared with the SFO flame might be indicative of the importance of PAH or nanoparticle coagulation process.

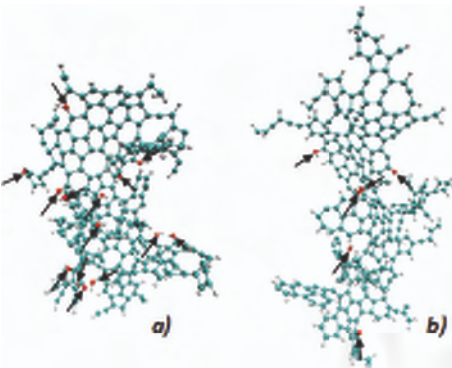


Figure 9. Carbonaceous nanoparticles produced by the AMPI code at points 1 (a) and 2 (b). Carbon atoms are shown in gray, hydrogen atoms are in white and oxygen atoms are indicated by arrows.

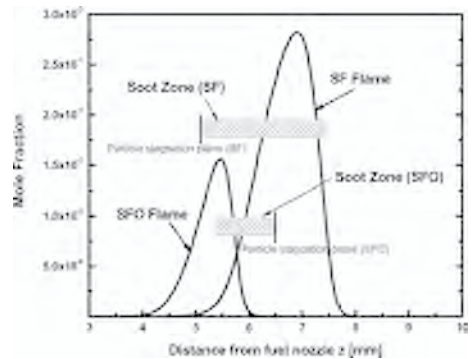


Figure 10. Sum of PAH concentrations for SF and SFO flames. Soot zones for the two flames are indicated as gray boxes.

### 3.2. Nanoparticle coagulation: molecular dynamics simulations

The results reported in the previous section indicate that nanoparticle growth from PAH, described with the AMPI code as pure chemical growth, can adequately predict the experimental evidences in the SFO flames, but underestimate the particle formation rate in the SF flame. These results lead to the possibility that, at least for some flame conditions, chemical growth can be a viable process to describe the transition from small PAH species to nanoparticles.

In this section, we examine the clustering behaviors of nanoparticles as function of mass and flame temperature to identify the combustion regimes where the physical process can play a significant role. Specifically, we carried out MD simulations of  $C_{80}$  and  $C_{180}$  fullerene molecules at different temperatures. These structures were chosen as representatives of the carbonaceous materials produced in flames. Specifically,  $C_{180}$  fullerene has mass and size similar to the nanoparticles of 2-3 nm detected in flames. The second system composed of  $C_{80}$  fullerene molecules is studied to address the influence of mass on clustering behavior. Both systems,  $C_{80}$  and  $C_{180}$ , are studied in the same temperature ranges. Simulations are carried out using the canonical ensemble with the Berendsen thermostat with relaxation constant of 20 ps and the Velocity Verlet integration is used with a time step of 0.05 ps. The Lennard-Jones (LJ) potential is employed to describe the atomistic van der Waals interactions and the parameters are obtained from discrete carbon-carbon potential for  $C_{60}$  by Girifalco et al. [14, 15]. Each cubic box has a number concentration of  $8 \times 10^{18}$  ( $\text{cm}^{-3}$ ) with 343 rigid molecules in the cases of  $C_{80}$  and 125 rigid molecules in the cases of  $C_{180}$  with periodic boundary conditions.

Figure 11 shows the results for both systems. The graphs report the percentage of molecules in the state of cluster and non-cluster as function of time and temperatures. Obviously, as a general trend, low temperatures and large fullerene molecules present a significant clustering rate. For the  $C_{80}$  (960 amu), we do not detect significant clustering of the molecules for temperatures above 1200K. Differently, the system composed of  $C_{180}$  fullerenes (2160 amu) shows significant transient clustering behavior even at 1700K. At a temperature of 1400K, that is similar to the conditions of points 2, 3, and 4 in the SF flame, the binding of fullerene molecules is very fast.

The results from these simulations suggest that physical interactions of 2-3 nm nanoparticles may be the main growth pathway in low temperature regions of the SF flame.

## 4. CONCLUSIONS

In this paper, we reported a detailed study of the particle formation and growth in counterflow diffusion flames using various computational tools. The results suggest that particle inception can be considered as the result of a chemical growth and a physical coagulation. The contribution of these two pathways to the particle inception rate varies according to the combustion conditions. In situations where the temperature and H concentration are relatively high (SFO flame) the inception rate is well described by the AMPI code (chemical growth). At lower temperatures ( $T \sim 1400\text{K}$ ) with a relatively high PAH concentration and low H atoms available, particle inception can be mainly due to physical coagulation.

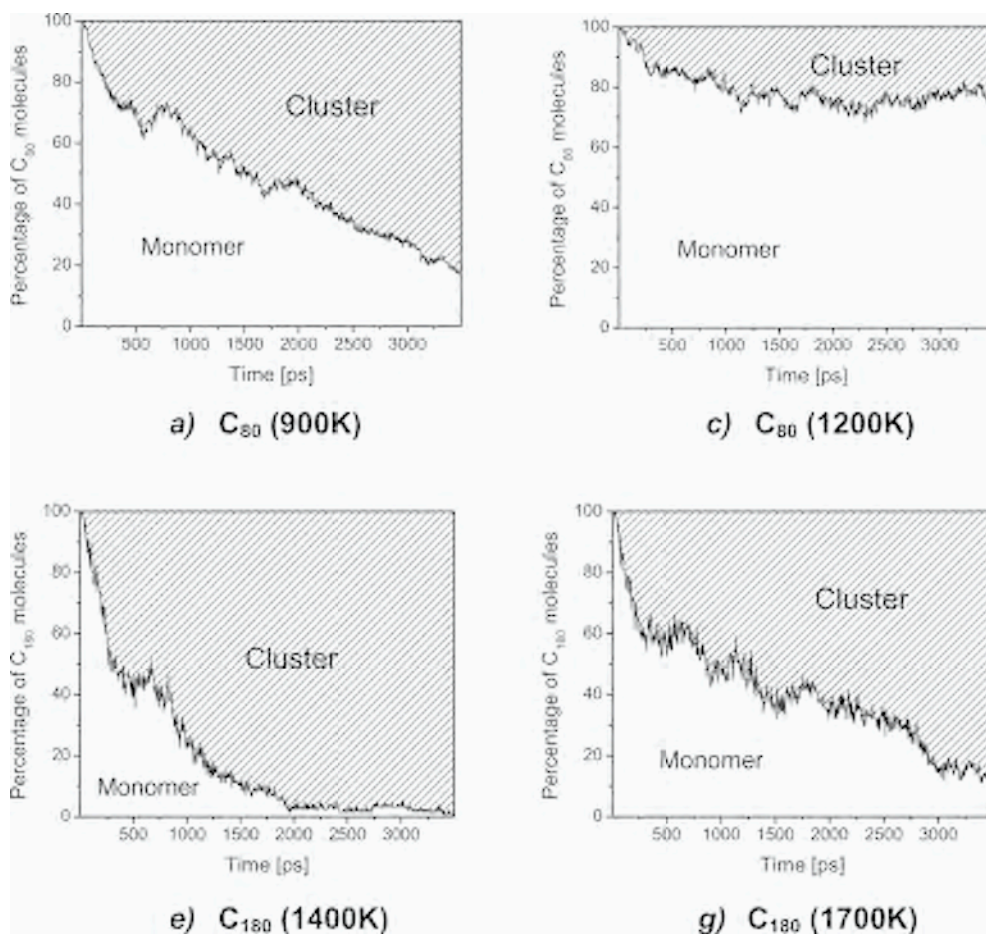


Figure 11. Computed percentage of C<sub>80</sub> and C<sub>120</sub> fullerene molecules in the form of monomers and clusters as function of time at different temperatures.

The AMPI code that describes the particle inception via chemical reactions is able to reproduce very well the experimental trends observed by Kang et al. for the SFO flame. We determined the particle formation zone computing the nanoparticle growth rates at eight locations in the flame. The growth rate was significant in the region where C<sub>2</sub>H<sub>2</sub> reached its peak and the main reaction sequence contributing to the growth was the HACA mechanism. For these flames, the inception region is characterized by high temperature (~2200K) and relatively high concentration of H and PAH. Particles, once generated are transported towards the higher temperature region and eventually they pass through an O and OH abundant zone to be oxidized. Oxidation regions were also well predicted by the AMPI code.

For the SF flame, we analyzed four points using the AMPI code. In this flame, the soot zone is on the oxidizer side of the stagnation plane and the flow field is directed

towards the fuel stream in the region between the flame and the particle stagnation plane. Particles, generated on the fuel side of the flame, are transported away from the flame. As a result, they cannot pass through the flame and they are not exposed to oxidizing species, such as OH and O<sub>2</sub>.

At the very beginning of the particle inception zone, the kinetic growth mechanism embedded in the AMPI code was able to describe particle formation due to the high concentration of C<sub>2</sub>H<sub>2</sub> and high temperature (~1900K). As soon as the temperature decreases (~1400K), the chemical growth is not enough to explain the inception rate experimentally identified in this region by Kang et al. A different process involving agglomeration of PAH or nanoparticles needs to be invoked to be responsible for the soot volume fractions in the low-temperature region of this flame.

To this end, we carried out Molecular Dynamics simulations of two systems of C<sub>80</sub> and C<sub>180</sub> fullerenes were analyzed at various temperatures to identify combustion regimes where the process of nanoparticle coagulation is important. The results show that at low temperatures, typical of the SF flame studied, coagulation can be important pathway once the particles reach a mass of ~2000amu (C<sub>180</sub> fullerenes). Future study will include the analysis of the coagulation processes between PAH-PAH, particle and PAH and particle-particle about how much they can contribute to the growth of particle.

## ACKNOWLEDGEMENTS

This research is funded by the National Science Foundation grant CTS 0553764. Figures 1, 3-6 and 8-10 have been reprinted with permission from CARBON.

## REFERENCES

1. A. Violi, *Combust. Flame* 139(4) (2004) 279-287.
2. A. Violi, A. F. Sarofim, G. A. Voth, *Combust. Sci. Technol.* 176(5) (2004) 991-1005.
3. A. Violi, G. A. Voth, A. F. Sarofim, *Proc. Combust. Inst.* 30 (2005) 1343-1351.
4. A. Violi, A. Venkatnathan, *J. Chem. Phys.* 125(5) (2006).
5. K. T. Kang, J. Y. Hwang, S. H. Chung, W. Lee, *Combust. Flame* 109(1-2) (1997) 266-281.
6. J. Du, R. L. Axelbaum, *Combust. Flame* 100(3) (1995) 367-375.
7. A. Violi, A. D'Anna, A. D'Alessio, A. F. Sarofim, *Chemosphere* 51(10) (2003) 1047-1054.
8. A. Violi, A. F. Sarofim, G. A. Voth, *Combust. Sci. Technol.* 176(5-6) (2004) 991-1005.
9. A. E. Lutz, R. J. Kee, J. F. Grcar, F. M. Rupley OPPDIF: A Fortran program for computing opposed-flow diffusion flames, 1996.
10. J. Y. Hwang, W. Lee, H. G. Kang, S. H. Chung, *Combust. Flame* 114(3-4) (1998) 370-380.
11. J. Y. Hwang, S. H. Chung, *Combust. Flame* 125(1-2) (2001) 752-762.
12. S. H. Chung, A. Violi, *Carbon* 45(12) (2007) 2400-2410.
13. A. Violi, *J. Phys. Chem. A* 109(34) (2005) 7781-7787.
14. L. A. Girifalco, M. Hodak, *Phys. Review B* 65(12) (2002) 125404.
15. L. A. Girifalco, *J. Phys. Chem.* 96(2) (1992) 858-861.

# Condensed phases in soot formation process

A. Ciajolo

*Istituto Ricerche sulla Combustione, CNR*

*Abstract: The complex condensed phases generated in the transition from gas to solid phase in a premixed fuel-rich laminar ethylene flame were sampled and analyzed by extraction, chromatography, mass spectrometry and absorption and emission spectroscopy.*

*The condensed phases were extracted with Dichloromethane (DCM) and subsequently with N-methylpyrrolidinone (NMP) in order to detach the organic species more strongly adsorbed on sampled soot particles. Size Exclusion Chromatography (SEC) was used to fractionate the DCM-extract and NMP-extract into molecular weight-selected classes in the 100-10<sup>5</sup> u molecular weight (MW) range to be further analysed.*

*Overall, the SEC analysis coupled with the UV-visible absorption and fluorescence spectroscopy and mass spectrometry put in evidence the presence in the condensed phases of two different classes of large MW polycyclic aromatic hydrocarbons (PAH's), namely pericondensed PAH's in the 100-1000 u MW range derived by chemical growth by acetylene and PAH's oligomers, from about 400 u to one or even more thousands of mass units, derived from chemical growth by aromatics. These aromatic classes could be formed to an extent that depends on the combustion conditions and fuel characteristics, mainly aromaticity, and can participate to soot inception and growth.*

## 1. INTRODUCTION

Gas-phase chemistry involved in hydrocarbon combustion has been successfully studied by means of on-line gas-phase diagnostics able to analyze the main combustion products as well as the complex gas hydrocarbon mixtures typical of fuel-rich combustion [1]. In the transition from gas to solid phase typical of fuel-rich combustion, the complexity of condensed phases generated from combustion reflects by the complexity of the chemical and physical routes through which particles suddenly arise from the homogeneous gas-phase to become a carbonaceous aerosol with a wide size distribution. The detailed analysis of the condensed phases is thus important to get knowledge about the mechanism of soot inception and maturation and it is also necessary for predicting their health effects and for interpreting the optical signals used for real time analysis of carbonaceous pollutants.

The main difficulty to be faced in resolving condensed phases in single components, or at least in classes of species, is the necessity of applying an array of many diagnostic tools, each of them able to give at most one of the many structurally-relevant parameters of condensed phases. The sampling of condensed phases more suitable for collecting enough material for the analytical assault is mainly based on the condensation of combustion products; hence a distinction between condensed phases really existing in flame and those produced during the sampling/quenching should be done. To this regard there is still debate about the existence of soot precursors in form of

liquid droplets early suggested in the pioneering work of Graham [2] and in form of droplets/particles containing low-boiling polycyclic aromatic hydrocarbons (PAH's) [3,4]. A tarry aromatic material including PAH's and unidentified aromatic species [5-8] has been found with a relatively high H/C [5, 9-10] suggesting a mixed aromatic/aliphatic nature of high molecular mass intermediates that could be present in flames in form of viscous tarry phase. However, the observation of liquid droplets and tarry material can merely derive from sampling-induced condensation of high molecular mass species present in flames as vapour-phase. Regardless their physical state, the analysis of the condensed phases deserves deeper analytical detail for understanding their role in soot inception. Since many years this has been the research topic on which the group in Naples involved in the chemical analysis of combustion processes and soot formation has devoted much experimental and analytical work.

This paper focuses on some recent experimental detail on the condensed phases sampled in a fuel-rich premixed ethylene flame. The approach used relatively to the different phases and to the different classes of aromatics, discriminated on the basis of solvent solubility and molecular weight (MW) is sketched below in Figure 1. On the basis of the different chemical characteristics, different aromatic classes can be grouped for each phase and molecular weight range. The chemical character of these compounds can be inferred by means of the analytical techniques also specified in the scheme.

Condensed phases have been subjected to extraction with dichloromethane (DCM) separating the DCM-extract, richer of PAH's, from DCM-insoluble species. The Size

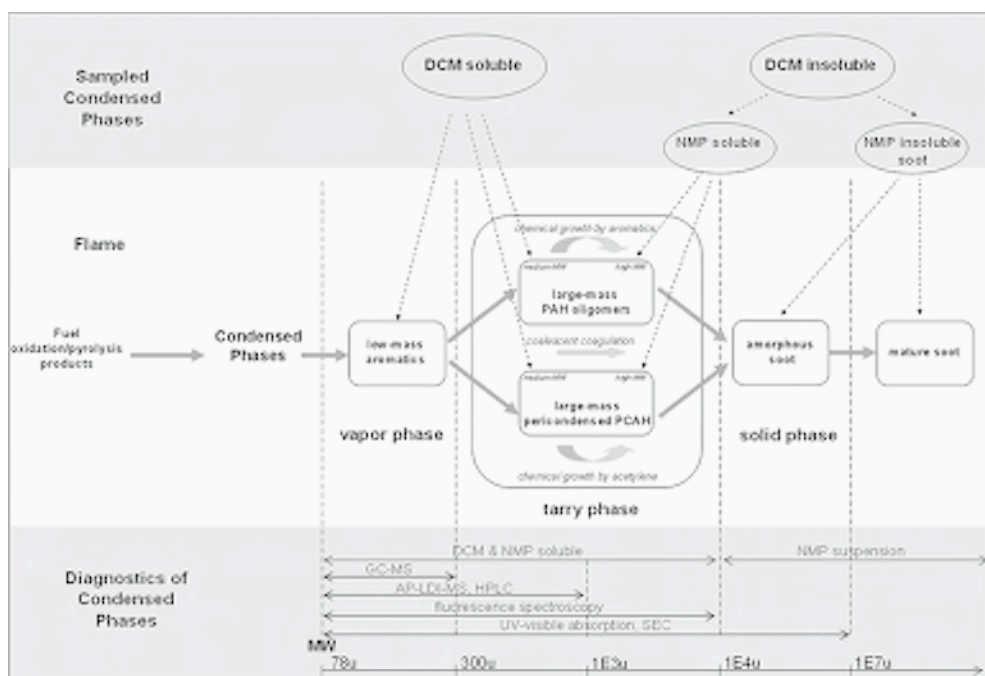


Figure 1. Classification of condensed phases formed in fuel-rich conditions and specific diagnostics.

Exclusion Chromatography (SEC) of the DCM-insoluble species carried out on a wide MW range column reveals a significant presence of relatively low molecular weight species up to  $10^5$  u, as reported in Figure 2. These species showed to be completely soluble in N-methylpyrrolidinone (NMP) so that the elution of NMP-extract filtered from soot particles on 20 nm porosity filters could be performed on a SEC column with high resolution in the  $10^2$ - $10^5$  u giving out the MW distribution reported in the inset of Figure 2.

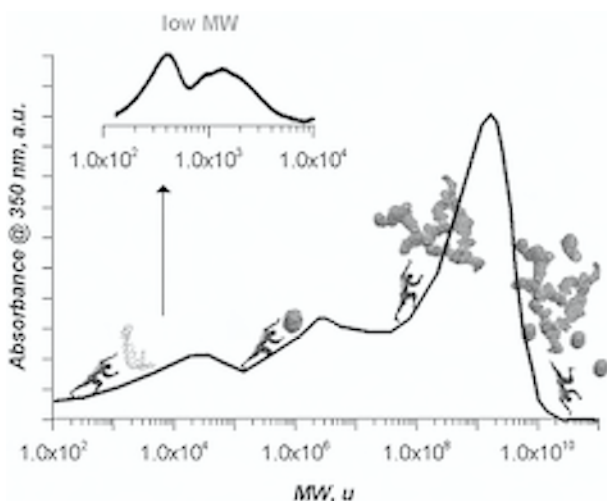


Figure 2. SEC chromatogram of DCM-insoluble fraction of condensed phases in a wide MW range  $100$ - $10^{10}$  u. The MW distribution of the low MW fraction performed on a  $100$ - $10^5$  u MW range column.

The MW distribution range of both DCM- and NMP-extract of condensed phases ( $100$  to  $10^4$  u) corresponds to the nanometric size range by considering a spherical shape and a density of  $1.2$ - $1.8$  g/cm<sup>3</sup>. The detection of species in this size/MW range is relevant for following soot inception, hence, the analytical work described in this paper has been devoted to the analysis of composition and MW distribution of DCM-solubles, NMP-solubles by means of i) Size Exclusion Chromatography coupled with UV-visible absorption and emission spectroscopy and ii) Atmospheric-Pressure Laser-Desorption Ionization Mass-Spectrometry (AP-LDI-MS).

## 2. BACKGROUND

The analysis of condensed phases has necessarily to start from the PAH's that are the first species recognized in fuel-rich combustion systems as flames that could be susceptible to in-flame condensation reactions. Indeed, the vast majority of PAH's identified in gas phase by means of chromatographic techniques are pericondensed PAH relatively small (from two to seven aromatic rings, carbon atom number < 24). The chemi-

cal, spectroscopic and biological properties of these PAH's having a carbon atom number below 24 are well known [11]. The critical temperatures of PAH's in high temperature and diluted flame environments are well below the soot formation temperature window (about 1300-1800 K). It is therefore logically concluded that these components cannot physically condense at atmospheric pressure at those temperatures and consequently, they should not properly belong to the condensed phases in flame. To this regard it is worth to mention that the existence in high-temperature environment of PAH-containing particles of polymeric nature, not originating from gas phase, is supported by real-time mass spectrometric analysis [12] and an intriguing hydrogen transfer and exchange mechanism involving PAH's in high temperature conditions has been suggested by the same authors. On the basis of the low H/C (about 0.6) and structural affinity of gas-phase PAH's with soot graphitic structure, it has been widely considered that gas-phase PAH (typically two- to four-ring species) are soot precursors [13, 14]. Most of the early modelling work considers soot inception deriving from aromatic growth in size due to chemical reactions and "as size increases PAH precursors acquire the properties of condensed phases through coagulation of PAH" [15]. The coagulation/growth process of PAH could not be followed by early mass spectroscopic work exhibiting a large mass gap between the last detectable gas-phase PAH and the first soot particles [13]. This has been attributed to the limit of the mass spectrometric analysis and/or to the too low temporal resolution of the sampling/mass spectrometric analysis compared to the high reactivity rate of high molecular mass aromatic intermediates.

In recent work the advancement of mass spectrometric diagnostics has shown the presence of so-called "aromers" composed of PAH parts [16] and of large PAH (L-PAH's) from C<sub>30</sub> to C<sub>70</sub> [17]. The recent availability of chemical and spectroscopic characteristics of some of these L-PAH's having a carbon number with 24 or more aromatic ring carbon, should render easier their identification [18]. On the basis of this experimental evidence it remains matter of debate how these L-PAH's are partitioned in gas or condensed phases (droplets and/or adsorbed on soot particles) since the partitioning depends in a complex way on their physical/chemical properties such as molecular weight (MW), vaporization temperature, chemical structure, etc. as well as on the reaction environment and sampling condition parameters like temperature and concentration.

Parallel to the progress in the analytical work developed for the analysis of condensed phases it can not avoid to mention the huge work developed by means of in-situ optical diagnostics as scattering, and broadband UV-visible absorption and laser induced fluorescence spectroscopy in the UV reported in many papers and collected in reviews, books and reports of round tables [13, 19-25] and in other parts of this book. The optical diagnostics have early shown the presence of absorbers other than soot, probably in form of condensed phase [2, 8] and recently the formation of nanoparticles has been also found by optical techniques and confirmed by aerosol size analyzers and microscopy diagnostic [26-29].

An intriguing hypothesis about the chemical/physical state and the evolution of PAH's rises from the work of Miller suggesting that the most critical step in soot inception is the transition from 2-dimensional to 3-dimensional structures. For soot formation, this transition is supposed to be the agglomeration of PAH's through intermolecular interactions of homo-molecular and hetero-molecular clusters of many percondensed PAH's spanning monomer masses up to about 2000u [30-32].

### 3. METHODS

#### 3.1. Sampling and separation procedure of condensed phases

The experimental combustion system has been described in detail elsewhere [10, 33]. Briefly, a stainless steel water-cooled probe was used to sample combustion products along the flame axis of premixed laminar flames. The chemical data of condensed phases reported in this paper refers to a sooting ethylene/air flame with C/O=1.0 stabilized on a commercial McKenna burner.

In order to obtain a high amount of condensed phases, the combustion products were collected at 14 mm height above the burner, corresponding to the end of soot formation region where the condensed species reach their maximum concentration [33].

Condensed phases from the probe walls, deposited on a teflon filter and trapped in an ice-cooled trap placed in the sampling line were extracted with DCM until there was no detectable UV-fluorescence signal in the DCM washings. PAH's up to 300 u were detected in the DCM-extract by gaschromatography-mass spectrometry (GC-MS) on an HP5890 gas chromatograph coupled with an HP5970 mass spectrometer.

After DCM extraction, soot was extracted again with the minimum volume of NMP in order to detach strongly-adsorbed species on soot. Both DCM- and NMP-extracts were analyzed by SEC and separated into MW classes for further examination by spectroscopic and mass spectrometric techniques.

#### 3.2. SEC

The SEC analysis of DCM-soluble and NMP-extracts dissolved in NMP was carried out on a PL-gel styrene-divinylbenzene individual pore column (Polymer Laboratories, Ltd, UK) with a column particle size of 5  $\mu\text{m}$  diameter and a pore dimension of 50 nm. This column is able to separate polystyrene standards in the molecular mass range 100-100,000 u. The relation between molecular mass of polystyrenes and PAH's, has been shown to hold for PAH standards [34] and is used for the MW evaluation of soot extracts. The on-line detection of species eluted from the SEC column was by an HP1050 UV-visible diode array detector measuring the absorbance signal at 350 nm wavelength.

#### 3.3. AP-LDI-MS

In the AP-LDI-MS configuration used for the mass spectrometric analysis of condensed phases the ions are produced in the source at normal atmospheric pressure in contrast to the conventional mass spectrometric ion source where ions are formed inside the vacuum system of the mass spectrometer. Operation at atmospheric pressure immediately eliminates the complicated procedure of introducing the sample probe into the high vacuum of the mass spectrometer. The AP-LDI-MS demonstrated large tolerance to the laser fluence variations (beneficial for automated MS analysis), and minimal fragmentation of molecular ions due to fast thermalization of the ion internal energy at atmospheric conditions.

The AP-LDI source interface flange, housing the laser focusing elements and imaging system, was attached directly to the Agilent 1100 series LC/MSD ion trap SL (Agilent Technologies, Palo Alto, CA, USA) ion source flange. A nitrogen laser (337 nm, mounted inside a laser and stage control box) produced a 10-Hz pulsed beam of UV light. Photons were conveyed to the interface flange via an optical fiber and focused by a quartz lens onto a mirror, which reflected the photons onto the target surface, upon which the sample and matrix was spotted. The AP-LDI source and control box combination was connected to the serial port of a Windows<sup>TM</sup>-based PC, which directed the target plate motion and laser firing via Target software (MassTech, Inc., Burtonsville, MD, USA).

### 3.4. UV-visible absorption spectroscopy

UV-visible spectra of the samples dissolved and/or dispersed in NMP were measured on an HP 84523 Diode Array spectrophotometer connected to a personal computer using 1-cm quartz cuvettes. The interference of the solvent (NMP) on the UV absorption limits the visualisation of the spectra to the range 260-800 nm.

### 3.5. Fluorescence spectroscopy

Fluorescence emission spectra of the samples were measured on a Perkin-Elmer LS-50 spectrofluorimeter connected to a personal computer. A xenon discharge lamp equivalent to 20 kW for 8  $\mu$ s duration was used as the excitation light source. The detection device was a gated photomultiplier with modified S5 response for operation to about 650nm. Monochromators were of the Monk-Gillieson type, which cover the following ranges: excitation 200-800 nm, emission 200-900 nm. The wavelength accuracy was  $\pm 1.0$  nm and the wavelength reproducibility was  $\pm 0.5$  nm. Instrumental parameters were controlled by the Fluorescence Data Manager Perkin Elmer software.

## 4. RESULTS AND DISCUSSION

The MW distribution of the aromatic species detected by SEC of the DCM-extract, reported in Figure 3, shows a first peak in the 100-400 u MW, named peak "a", and a second smaller and broader peak in the 400-2000 u MW range, named peak "b".

Aromatic species of the NMP-extract are distributed in similar MW ranges: 200-600 u (peak A) and 600-5000 u (peak B) (Figure 4) [34,35].

UV-visible and fluorescence emission spectra for each peak separated from both DCM- and NMP-extracts and dissolved in NMP are also reported in Figures 3 and 4.

The UV-visible spectrum of peak "a" of DCM-extract exhibits a fine structure mainly due to pericondensed PAH's with C<24 [11]. By contrast a broadband shape can be observed in the UV-visible spectrum of peak "b" (Figure 3).

Peak "A" of the NMP -extract exhibits a strong absorption in the 300-400 nm region of the UV-visible spectrum, with a shoulder at about 400 nm more typical of

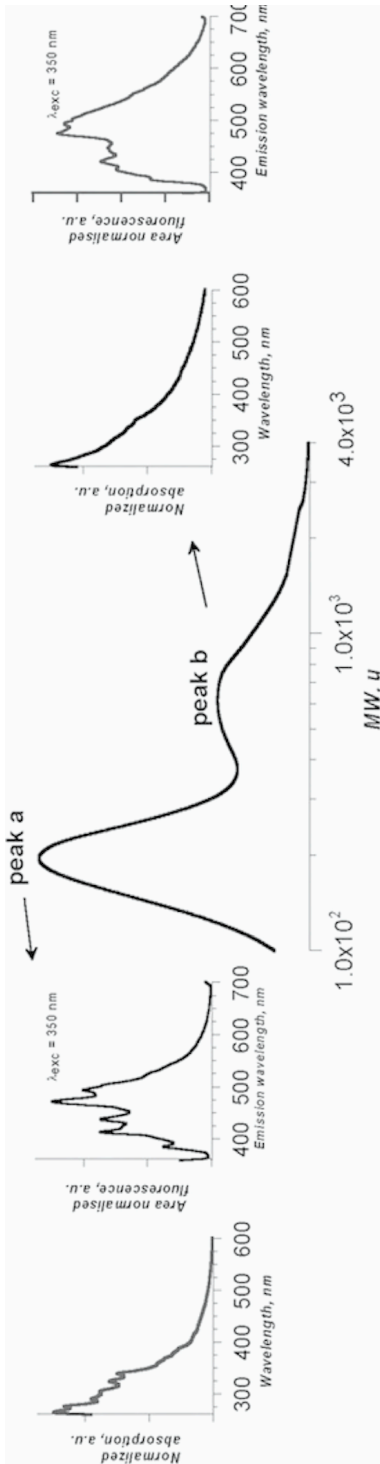


Figure 3. SEC chromatograms of DCM-extract of condensed phases at  $\lambda_{abs} = 350$  nm. UV-visible and fluorescence emission ( $\lambda_{exc}=350$  nm) spectra of peak “a” and peak “b”.

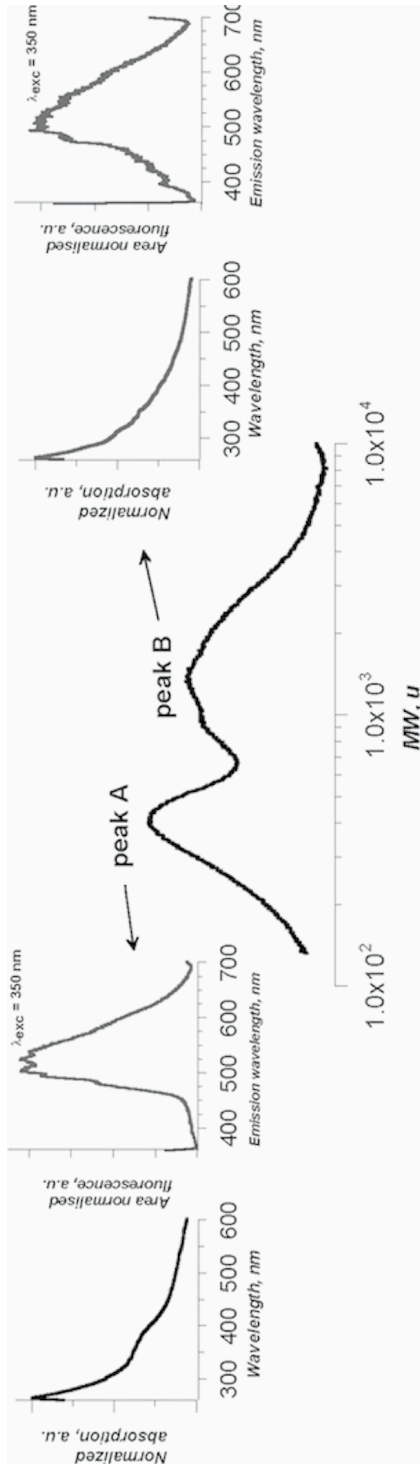


Figure 4. SEC chromatograms of NMP-extract of condensed phases at  $\lambda_{abs} = 350$  nm and UV-visible and fluorescence emission ( $\lambda_{exc}=350$  nm) spectra of peak “A” and peak “B”.

large PAH's ( $C \geq 24$ ) [18] whereas the peak B of NMP soot extract presents a uv-visible spectrum with a broadband shape (Figure 3).

Both peaks "a" and "b" of the DCM extract show fluorescence emission spectra in the 400-600 nm wavelength range (Figure 3) typical of relatively small aromatic functionalities whereas fluorescence emissions of peaks "A" and "B" of NMP-extract are shifted in the 450-650 nm spectral region (Figure 4), typical of highly condensed aromatic functionalities [36,37].

It is worth to note that the fluorescence emission spectrum of peak "a" of the DCM-extract exhibits the structured shape of planar PAH's [36]. The fluorescence spectra of the other peaks are quite similar and only a broadened spectral shape is shown indicating molecular flexibility leading to a wider distribution of energies for each ground or excited state configuration. A larger molecular flexibility causes the excess energy in the excited state might be dissipated by rotational movements. In this regard it is worth noting that the quantum efficiency of peak "a" in DCM-extract and peak "A" in the NMP-extract are one order of magnitude higher than the corresponding peaks "b" and "B" ( $10^{-2}$  vs  $10^{-3}$ ) This indicates that the dissipation of excess energy via radiative phenomena is more efficient for peak "a" and "A" and, by consequence, attributable to relatively rigid molecules as pericondensed PAH's [36]. By contrast the lower quantum efficiency of peaks "b" and "B" indicates that the aromatic moieties are linked together by aliphatic bonds, as occurs in aromatic-aliphatic linked hydrocarbons, and/or by non-covalent bonds, as in polymers of small size (oligomers), that allow the movement of the molecule and loss of internal energy by other routes than the radiative emission.

AP-LDI-MS of the SEC fractions of both DCM- and NMP-extract has been carried out. The analyses were performed in the same mass spectrometric conditions on the same sample holder allowing the detection of a wide range of masses (up to 2000 u in the present configuration).

The major limitation of this approach is due to the spotting technique on the target plate. SEC fractions are collected in NMP so, in order to achieve fast and complete evaporation of such a high boiling solvent, the plate is oven warmed at 60°C causing the evaporation and loss of the detection of light PAH's (up to 202 u) detectable by GC-MS.

Each AP-LDI mass spectrum is the result of the acquisition of a number of separate spectra which are summed to obtain the final analysis. A typical analysis consists of 100-150 co-added spectra collected on the whole spot surface (1-2 mm in diameter) in order to overcome the non-homogeneity of the sample on the target plate.

The AP-LDI mass spectra of peaks a and A, reported in Figure 5 extend from  $m/z$  200-500 and  $m/z$  300-700, respectively. Both the mass spectra consist of a sequence of major ions with a spacing of 24-26 u superimposed on a sequence of minor ions which present the same spacing of 24-26 u. The sequence of minor peaks is displaced at by 12 u relative to the sequence of the most abundant ions. It is reasonable to infer that both peaks "a" and "A" constitute a unique class of low to high-MW pericondensed PAH's, the latter strongly adsorbed on soot particles.

In the range  $m/z$  200-400, GC-MS analysis attributed the sequence of major peaks, spaced 24-26 u, to even-carbon-numbered (even-C-numbered PAH) and the sequence of minor peaks to odd-C-numbered PAH's. It is speculated that the trend observed in the PAH distribution up to  $m/z$  400 can be extended to the higher MW range of LDI-

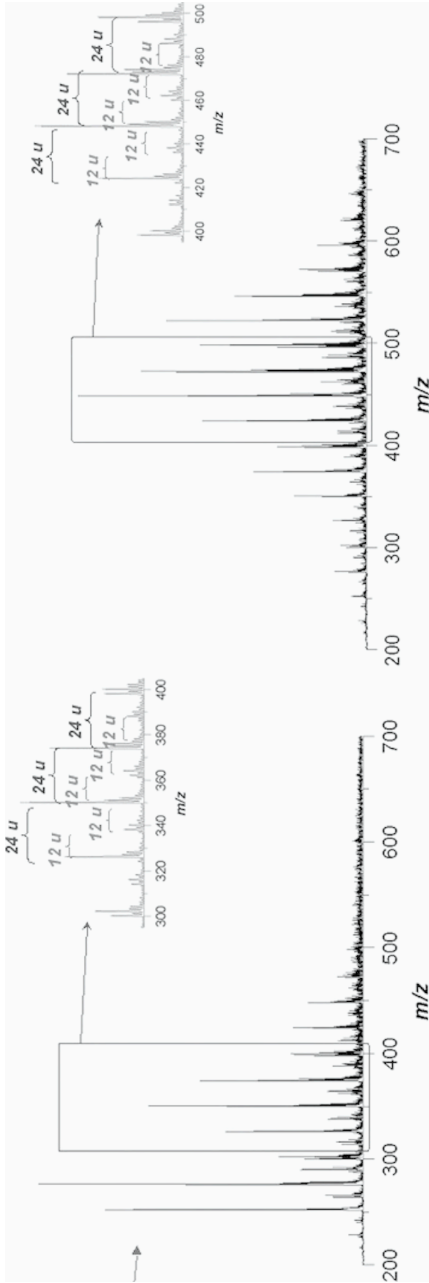


Figure 5. AP-LDI-MS spectra of peak "a" (DCM-extract) (left part of the figure) and peak "A" (NMP-extract) (right part of the figure).

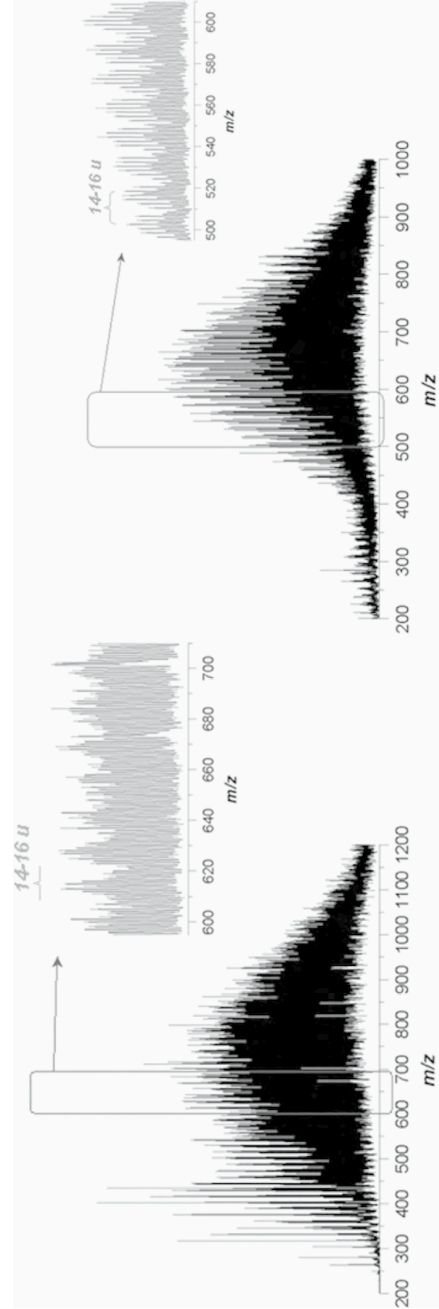


Figure 6. AP-LDI-MS spectra of peak "b" of DCM-extract (left part of figure) and peak "B" of NMP-extract (right part of figure) of condensed phases.

MS spectra by attributing the major ions to even-C-numbered PAH and the smaller ones to odd-C-numbered PAHs.

The AP-LDI mass spectra of peak "b" and "B" of DCM- and NMP-extract are reported in Figure 6. The mass spectrum of the 300-700 u DCM-extract (peak "b", left part of Figure 6) exhibits a continuous sequence of masses typical of polymeric structures [12]. However, regular mass peaks in the sequence separated by 14-16 u are observed. The same continuous mass sequence can be also observed in the 600-2000 u fraction of NMP-soluble soot fraction (peak "B", right part of Figure 6). Broad groups spaced at 14-16 u are visible also in this spectrum, probably due to species with the same number of C atoms, but different numbers of H atoms.

It can be speculated that peaks "b" and "B" are constituted of a very complex mixture of species derived from the combination of PAH's and L-PAH's which create non-planar products with aromatic moieties linked by aliphatic bond and/or non covalent bond as also suggested by the fluorescence spectroscopy above described. Similar classes of species with a nature intermediate between aromatic and oligomers have been found in previous work [12, 38-39]. These species may play a relevant role in the nucleation processes of soot inception mechanisms.

It is worth noting that the MW of peak "B" evaluated by SEC appear larger (Figure 4), than those obtained by the AP-LDI mass spectrometry. This can be due to the increased curved and three-dimensional shape of these polymeric species that causes the delay in the elution of large masses by SEC analysis and by consequence, the overvaluation of MW [40]. However, it can not be excluded that these polymeric species can also be thermally labile and prone to fragmentation when subjected to the mass spectral analysis causing the undervaluation of MW by AP-LDI-MS analysis.

Overall, the SEC analysis coupled with the spectroscopic and mass spectrometric put in evidence the presence in the DCM- and NMP-extracts of condensed phases of two different classes of large MW aromatics, namely PAH's oligomers and pericondensed PAH, the first one deriving from chemical growth by aromatics and the second one by chemical growth by acetylene (Figure 1). They could be formed to an extent that depends on the combustion conditions and fuel characteristics, mainly aromaticity, and can participate to soot inception.

The pericondensed PAH's are in the 100-1000 u MW range with the lower MW pericondensed PAH's presumably existing in gas phase and the higher MW pericondensed PAH's present in a tarry phase.

The PAH's oligomers are constituted of species from about 400 u to one or even more thousands of mass units. This class of aromatic species could be trivially due to sampling-induced condensation effects that beside to transform their physical state from vapour- to tarry-phase could change their chemical composition. For instance, in-flame PAH radicals can react each other and/or with other hydrocarbon fragments during the sampling forming these polymeric aggregates. However, real-time mass spectrometric analysis of in-flame condensed phases appear to support the existence in flame of PAH polymers (12, 39,41-43) probably in a tarry phase (12, 39).

The MW distribution analysis of the total condensed phases in a MW range enough wide to enclose the low to high MW aromatic molecules/particles and soot particles/aggregates (Figure 2), is object of further work.

## 5. FINAL REMARKS

The condensed phases sampled in a premixed laminar flame burning ethylene in fuel-rich conditions have been separated by extraction and characterized by SEC, mass spectrometry and spectroscopic analysis. The condensed phases were extracted by DCM (DCM-extract) and subsequently by NMP (NMP-extract) in order to detach all the low MW species adsorbed on sampled soot particles. SEC chromatography was used to fractionate the DCM-extract and NMP-extract into well-defined MW classes to be further analysed by using uv-visible absorption and fluorescence spectroscopy and by AP-LDI mass spectrometry. The mass spectra of both peak "a" and peak "A" of DCM- and NMP-extract, respectively, exhibited the mass spectra typical of pericondensed PAH's. They consisted of a sequence of major ions with a spacing of 24-26 u due to even-C-numbered PAH and L-PAH, superimposed on a sequence of minor ions presenting the same spacing of 24-26 u and ascribed to odd-C-numbered PAH and L-PAH. The mass spectra of both peak "b" and peak "B" of DCM-extract and NMP-extract, respectively, showed to be completely different with continuous sequence of masses, typical of polymeric structures. UV-Visible absorption and emission fluorescence spectroscopy of the SEC separated fractions furnished additional insights about the aromatic nature of pericondensed L-PAH's and polymeric aromatic species. Overall two classes of aromatic species could be discriminated in the medium-high-MW range. The first class is composed of pericondensed PAH's in the 100-1000 u MW range with the lower MW pericondensed PAH's presumably existing in gas phase and the higher MW pericondensed PAH's present in a tarry phase. The second class appears to be constituted of large mass polymeric aromatic species from about 400 u to one or even more thousands of mass units where the monomers are constituted of aromatic moieties connected by alkyl bonds and/or by non covalent bonds. Both aromatic classes could be formed to an extent that depends on the combustion conditions and fuel characteristics, mainly aromaticity, and can participate to soot inception.

## ACKNOWLEDGEMENTS

The paper is based on the collaboration with Rosalba Barbella, Antonio Tregrossi, Barbara Apicella and Michela Alfè. The author gratefully acknowledges the contribution of Andrea D'Anna with helpful discussion for the data interpretation.

## REFERENCES

1. J. F. Griffiths, J.A. Barnard, *Flame and Combustion*, Chapman & Hall, Oxford, 1995, 3rd ed.
2. S.C.Graham, J.B. Homer, J.L.J. Rosenfeld, *Proc. R. Soc. Lond. A* 344 (1975) 259-285.
3. R.A. Dobbins, R.A. Fletcher, W. Lu, *Combust. Flame* 100 (1995) 301-309.
4. R.A. Dobbins, R.A. Fletcher, H.-C. Chang, *Combust. Flame* 115 (1998) 285.
5. E. E. Tompkins, R. Long, *Proc. Comb. Inst.* 12 (1970) 625.
6. A. Ciajolo, A. D'Anna, R. Barbella, C. Bertoli, M.V. Prati, *International Symposium COMODIA 90:639-644*, Kyoto, Japan (1990).
7. R. Barbella, C. Bertoli, A. Ciajolo, A. D'Anna, A., *Proc. Combust. Inst.* 23 (1990) 1079.

8. A. D'Alessio, A. D'Anna, A. D'Orsi, P. Minutolo, R. Barbella, A. Ciajolo, *Proc. Combust. Inst.* 24 (1992) 973.
9. A. Ciajolo, R. Barbella, A. Tregrossi, L. Bonfanti, *Proc. Combust. Inst.* 27 (1998) 1481.
10. A. Ciajolo, A. D'Anna, R. Barbella, *Combust. Sci. Technol.* 100 (1994) 271.
11. E. Clar, *Polycyclic Hydrocarbons*, Academic Press, London 1964.
12. R. P. Rodgers, P. T.A. Reilly, W. B. Whitten, *J. M. Ramsey Chemical Physics Letters* 397 (2004) 324-328.
13. B.S. Haynes, H.Gg. Wagner, *Prog. Energy Combust. Sci.* 7 (1981) 229.
14. J.B. Howard, *Proc. Combust. Inst.* 23 (1990) 1107.
15. C. A. Schuetz, M. Frenklach, *Proc. Combust. Inst.* 29 (2002) 2307-2314.
16. M. Bachmann, W. Wiese, K.-H. Homann, *Proc. Combust. Inst.* 26 (1996) 2259.
17. A.Keller, R. Kovacs, K.H. Homann, *Phys. Chem. Chem. Phys.* 2 (2000) 1667.
18. J.C. Fetzer, *Large (C>= 24) polycyclic aromatic hydrocarbons*, Wiley & Sons, 2000, vol. 158.
19. B. S., Haynes, in *Fossil Fuel Combustion*, W. Bartok, A. F. Sarofim (Eds.) John Wiley & Sons, 1991, p. 261.
20. K. Kohse-Höinghaus, J.B. Jeffries (Eds.) *Applied Combustion Diagnostics*, Taylor and Francis, 2002.
21. K. Kohse-Höinghaus, *Prog. Energy Combust. Sci.* 20 (1994) 203.
22. D.C. Siegla, G.W. Smith (Eds.) *Particulate Carbon: Formation during Combustion*, Plenum, New York, 1981.
23. J. Lahaye, G. Prado (Eds.) *Soot in Combustion Systems and Its Toxic Properties*, Plenum, New York, 1983.
24. H. Jander, H.Gg. Wagner (Eds.) *Soot Formation in Combustion. An International Round Table Discussion*, Vandenhoeck & Ruprecht, Gottingen, 1990.
25. H. Bockhorn (Ed.) *Soot Formation in Combustion*, Springer, Berlin-Heidelberg-New York, 1994.
26. L.A. Sgro, A. De Filippo, G. Lanzaolo, A. D'Alessio, *Proc. Comb. Inst.* 31 (2007) 631.
27. B. Zhao, Z. Yang, J. Wang, M.V. Johnston, H. Wang, *Aerosol Sci. Technol.* 37 (2003) 611.
28. A.C. Barone, A. D'Alessio, A. D'Anna, *Combust. Flame* 132 (2003) 181.
29. M. Alfè, B. Apicella, R. Barbella, J.-N. Rouzaud, A. Tregrossi, A. Ciajolo, *Proc. Combust. Inst.* 32 (2009) doi:10.1016/j.proci.2008.06.193.
30. J. H. Miller, K. C. Smyth, W. G. Mallard, *Proc. Combust. Inst.* 20 (1985) 1139.
31. J. H. Miller, *Proc. Combust. Inst.* 23 (1991) 91-98.
32. J. H. Miller, *Proc. Combust. Inst.* 30 (2005) 1381-1388.
33. B. Apicella, R. Barbella, A. Ciajolo, A. Tregrossi, *Combust. Sci. Technol.* 174 (11-12) (2002) 309-324.
34. B. Apicella, A. Ciajolo, R. Barbella, A. Tregrossi, T. J. Morgan, A. A. Herod, R. Kandiyoti, *Energy & Fuels* 17 (2003) 565-570.
35. M. Alfè, B. Apicella, R., Barbella, A., Tregrossi, A., Ciajolo, *Energy & Fuels* 21(1) (2007) 136-140.
36. I.B. Beriman, *Handbook of Fluorescence Spectra of Aromatic Molecules*, Academic Press, New York 1971.
37. B. Apicella, A. Ciajolo, A. Tregrossi, *Anal. Chem.* 76(7) (2004) 2138.
38. M. Bachmann, W. Wiese, K.-H. Homann, *Proc. Combust. Inst.* 26 (1996) 2259-2267.
39. R.H. Hurt, Z-Y. Chen, *Physics Today* 53 (2000) 39.
40. F. Karaca, C.A. Islas, M. Millan, M. Behrouzi, T. Morgan, A.A. Herod, R. Kandiyoti, *Energy & Fuels* 18 (2004) 778-788.
41. P.T.A. Reilly, R.A. Gieray, W.B. Whitten, J.M. Ramsey, *Combust. Flame* 122 (2000) 90.
42. H.-H. Grotheer, H. Pokorny, K.-L. Barth, M. Thierley, M. Aigner, *Chemosphere* 57 (2004) 1335.
43. J. Happold, H.-H. Grotheer, M. Aigner, *Rapid Commun. Mass Spectrom.* 21 (2007) 1247.

**Part III**  
**Dynamic of mass and number growth**



# Electrical mobility based characterization of bimodal soot size distributions in rich premixed flames

M.M. Maricq

Research & Advanced Engineering

Ford Motor Company

Dearborn, Michigan 48121, USA

*Abstract: Differential mobility analysis (DMA) provides a powerful means to study soot. It not only has the capability to measure in detail the soot size distribution, but also the possibility to select particles of specific size for further study. Previous applications to rich premixed flames clearly demonstrated the generally bimodal nature of soot, and tandem DMA measurements revealed the accumulation mode particles to have a symmetric electrical charge described by the Boltzmann distribution at the flame temperature. The present work reviews these measurements and extends them to examine the transmission electron microscope (TEM) images and the thermal desorption / restructuring of size selected soot particles. The aim is to help build more complete physical descriptions of the nucleation versus accumulation mode soot particles. The results show a strong association of the accumulation mode measured by DMA to conventional soot particles that are solid, fractal-like in shape, evolve towards a graphitic structure, and are electrically charged. In contrast, the nucleation particles yield low contrast TEM images, are spherical, exhibit relatively larger thermal desorption / restructuring, and are electrically neutral. This mode is insensitive to height in the flame, but very sensitive to flame temperature and fuel composition. Their physical characteristics as well as their dependences on flame conditions suggest associating nucleation mode with soot precursor particles.*

## 1. INTRODUCTION

Soot formation by flames has held a fascination from both fundamental and practical perspectives. The ability of complex carbonaceous aggregates to form during the combustion of simple hydrocarbon fuels proceeds via a complex mechanism that remains under active study. Yet there is considerable practical motivation for soot study that originates from the combined desires to improve energy efficiency and reduce potential health risks associated with exposure to particulate matter (PM). Understanding how soot is formed offers the possibility to design engines that minimize these emissions [1]. And if this is not sufficient, knowledge of soot properties can help devise strategies to capture and eliminate these particles via aftertreatment devices [2].

The question of soot precursor particles has received considerable interest recently. They are observed in a variety of flames, including premixed, diffusion, and turbulent, via transmission electron microscopy (TEM) images as small nearly spher-

ical particles, a few to perhaps ten nanometers in diameter [3, 4 and references therein]. The particles appear semi-transparent in the images and, as they do not exhibit aggregate structures, are presumed to coalesce upon collision. Such particles have been inferred also from UV absorption studies in the form of an excess absorption that remains after accounting for gaseous species in the flame [5, 6]. This interpretation is corroborated by atomic force microscopy [7] and the UV spectroscopy of water soluble soot components [8]. The low contrast TEM images and relatively weak visible absorption observed in these studies suggest that precursor particles have lower C/H ratios than conventional soot particles, perhaps  $C/H \approx 2$  as compared to 5-10. Analysis of the spectroscopic data further suggest that, presumably because of their very small size, coagulation rates of the precursor particles may be significantly below the kinetic limit [6, 7].

Electrical mobility measurements have provided direct observations of two characteristic size classes of particles present in flames, one at 2-4 nm and the other 10-50 nm [9, 10, 11]. Not only their size, but the behavior of these modes as a function of flame conditions suggests identifying them with precursor and soot particles, respectively. Particles in the "accumulation" mode, the 10-50 nm particles, behave as expected of soot particles. With increasing height in a premixed flame their average size increases due to surface addition and coagulation, and their number density decreases owing to coagulation. The class of 2-4 nm particles, the "nucleation" mode, exhibits quite distinct behavior. The mean size and number density of this mode remains nearly independent of height in the flame, suggesting that new particle formation continues past the soot inception point, an interpretation consistent with the notion of precursor particles.

In recent work, Sgro et al. [12] have extended DMA size measurements down to nearly 1 nm, with indications of additional structure in the size distribution of these precursor particles. The application of X-ray scattering techniques by Hessler et al. [13], and the use of synchrotron small angle X-ray scattering by di Stasio et al. [14], have provided a sensitive in-situ means to study these particles that explore soot structures over multiple size scales. And, advances in mass spectrometry have enabled direct mass measurement of these particles that are small by particle, but large by molecular standards [15].

The aim of the present paper is to describe electrical mobility based characterization of soot particles. It begins by reviewing the sampling and measurement issues involved, including the loss of particles during sampling and analysis. Following this, results are presented from TEM, thermal, and electrical analysis of size selected soot particles. While these address primarily soot physical properties, it is likewise possible to combine chemical analysis with DMA size selection [16, 17, 18].

## 2. SOOT SAMPLING AND MOBILITY BASED CHARACTERIZATION

Exploring soot particle properties by their electrical mobility classification requires sampling soot from a flame in a representative and reproducible manner. The experimental methods used to accomplish this are reviewed here, since they differ from other techniques to examine soot, such as light scattering and thermophoretic sampling.

## 2.1. Sampling from the flame

A schematic diagram of the experimental apparatus is presented in Figure 1. Rich, pre-mixed flames are generated in a standard manner with a 6 cm diameter, water cooled, sintered bronze plate, McKenna burner. A nitrogen shroud of 30-50 L/min isolates the flame from the surrounding atmosphere. Air and fuel flow rates are set using Tylan flow controllers. These range from 4.3 to 11.8 L/min total flow. The corresponding flame velocities range from 15 to 43 cm/s. Data are recorded primarily at two air/fuel ratios: C/O = 0.67 (lightly sooting) and C/O = 0.81 (heavily sooting).

Representative sampling of soot from a flame environment is difficult because thermally driven soot growth processes can continue while extracting the sample, and because diffusion, thermophoresis, and coagulation lead to particle losses within the sampling system. Rapid dilution minimizes these issues by quenching flame chemistry, cooling the sample to reduce diffusion and thermophoresis rates, and diluting the sample to slow coagulation rates. The preferred method extracts soot through a pinhole ( $\sim 0.3$  mm) immediately into a flow of nitrogen diluent [19, 20, 21].

This is implemented in the present work via a coaxial probe (Figure 1). Dilution nitrogen ( $\sim 1$  L/min) enters via the outer annulus (4.5 mm o.d.), flows past the pinhole at the probe tip, where it mixes with the flame sample (at  $\sim 1:30$  dilution) and is drawn through the central sample tube ( $\sim 2$  mm i.d.) by an ejector pump. Nitrogen serves as the operating fluid for the pump and introduces a second stage of dilution ( $\sim 1:15$ ) as it mixes with the sample. A second ejector pump provides a third stage of dilution to bring the particle concentration into the range of  $\sim 10^6$  cm $^{-3}$ , sufficiently low to allow transport to the particle sizing instrumentation with minimal coagulation. The overall dilution factor derived by bubble flow meter measurements at room temperature is approximately 7000. The dilution factor when sampling from the flame is based on the CO $_2$  concentration measured in the diluted sample (at exit of first ejection

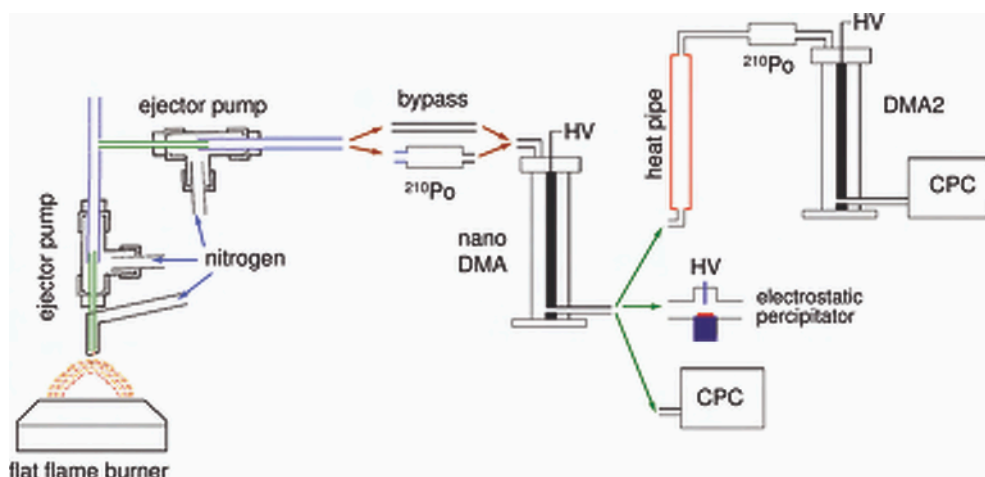


Figure 1. Experimental apparatus for sampling, dilution, and differential mobility size selection of flame generated soot particles.

tor pump) by non-dispersive infrared detection. This yields a dilution rate 2 times higher than recorded when sampling room air, indicating that the flame affects ejector pump operation, but not to a great extent. The soot data are corrected back to flame concentration based on the  $\text{CO}_2$  derived dilution factor. As discussed in the results section, the corrected data are consistent with the number densities required to explain observed soot coagulation rates.

Alternatively, one can sample the flame directly through a short tube (25 mm long, 2 mm i.d.) into a series of ejector pumps, foregoing the immediate dilution. Figure 2 contrasts these two sampling approaches. Both methods reveal bimodal size distributions. In each case the upper size mode (termed here the accumulation mode) includes electrically charged combustion particles. Allowing that these probes may influence the flame differently, they render similar views of the accumulation mode. However, their portrayal of the small particle mode (referred to as the nucleation mode) is quite different. The mode remains electrically neutral, but with immediate dilution at the pinhole this mode lies below 4 nm in diameter, whereas sampled through the short tube the mode shifts to 10 nm. This is likely dominated by surface growth within the probe, since the roughly 16 fold decrease in concentration expected from coagulation is not observed. The widths of the modes are also affected. Relative to the pinhole sampler, direct withdrawal of soot leads to a decrease in the accumulation mode width from a geometric standard deviation of  $\sigma_g = 1.61$  to 1.44, whereas the nucleation mode width increases from  $\sigma_g = 1.30$  to 1.45.

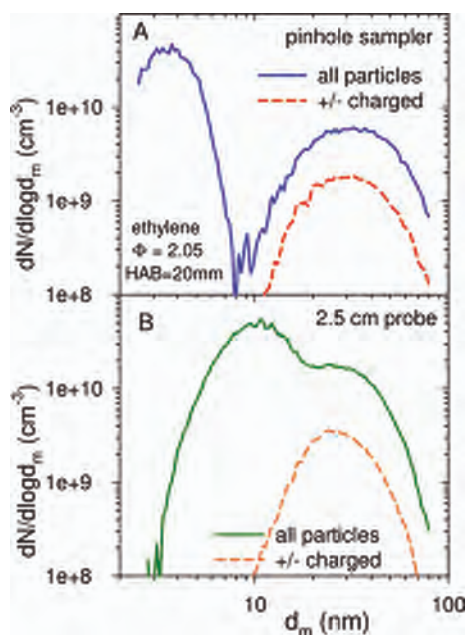


Figure 2. Influence of sample probe design on soot size distribution. A. Pinhole sampler with dilution immediately at sampling point. B. 25 mm long by 2 mm i.d. tube.

## 2.2. Characterization of size selected soot particles

Soot particle sizing is accomplished using a nano differential mobility analyzer (nDMA). Four types of measurements are described in this work. The first addresses the size distributions of flame generated soot particles. Following Figure 1, the diluted sample is ordinarily first passed through a  $^{210}\text{Po}$  neutralizer to bring the aerosol to a Boltzmann distribution of electrical charge [22]. In the 2–200 nm diameter range the exiting particles are predominantly uncharged. Approximately 1%–20%, increasing with particle size, carry a single positive charge, and a slightly higher fraction have unit negative charge. Multiply charged particles also exist, but at substantially reduced levels. As indicated in Figure 1, the neutralizer can be bypassed to investigate the distribution of soot particles already charged by the flame.

Next, particles are segregated according to mobility diameter within the cylindrical electric field of the DMA. A positive high voltage selects negatively charged particles and vice versa. Particles within a narrow range of electrical mobility exit the DMA and are counted by a condensation particle counter (CPC). Size distributions are recorded by sweeping the high voltage following the method of Wang and Flagan [23], and normalizing for the neutralizer charging efficiency. A nDMA (TSI Inc.) optimized for particles in the 2–100 nm range, and operated at 1 L/min aerosol and 15 L/min sheath flow rates, is used for these measurements [24]. In practice the dilute soot sample is transported from the ejector right to the entrance of the DMA column at 5 L/min, at which point 4 L/min is discarded. This bypass feature reduces diffusion losses in the transfer lines and  $^{210}\text{Po}$  neutralizer by allowing a higher transport rate than dictated by the DMA inlet flow setting.

The second type of measurement records transmission electron microscope (TEM) images of mobility selected soot particles. The nDMA is set to transmit the desired diameter soot particles, which then pass through an electrostatic precipitator, as illustrated in Figure 1. This consists of a pair of electrodes separated by  $\sim 5$  mm and placed transverse to the monodisperse aerosol flow. A TEM grid is mounted to one of the electrodes and 100–3000 volts is placed across them of the appropriate polarity to attract the selected particles, charged by virtue of the neutralizer that precedes the DMA. The voltage is increased to the point at which a substantial, circa 50%, reduction in the particle count is registered by the CPC. The third stage of dilution, normally used to record size distributions, is omitted to increase particle collection rates. Approximately 10 minutes suffices to collect an adequate TEM sample, but the pinhole must be cleaned at roughly 2 minute intervals to avoid clogging from thermophoretic soot deposition. Images of the soot particles are acquired with a JEOL FasTEM 2010 TEM.

The third type of soot measurement involves thermal desorption / restructuring of the soot particles. This is accomplished via the tandem DMA approach illustrated in Figure 1, which has also been used to study the volatility of diesel PM [25, 26, 27]. Again, the first DMA is set to transmit particles of the desired size (in this case a TSI long DMA operated at 1 L/min aerosol and 15 L/min sheath flow rates). Upon exiting DMA1, the particles proceed through a heat pipe and directly into DMA2 (TSI nDMA). As these particles are already 100% charged, the second  $^{210}\text{Po}$  neutralizer is bypassed to avoid reducing the fraction of charged particles. Scanning

DMA2 reveals how the heat pipe alters their size. The advantage of the tandem approach is that it separates true changes in size from apparent shifts that result from size dependent variations in particle concentration. If instead the heat pipe is simply placed in front of DMA1, a preferential loss of small particles in the heat pipe would appear as a shift of the distribution to larger size even if no particles actually change size.

The fourth type of measurement also takes the tandem DMA approach, in this case to record soot electric charge distributions [21]. The first  $^{210}\text{Po}$  neutralizer in Figure 1 is bypassed to select particles that are naturally charged by the flame (here DMA1 is the nDMA). Instead of the heat pipe, the mobility selected particles (all electrically charged) are re-neutralized to a room temperature Boltzmann charge distribution and then pass through DMA2 (long DMA). This process separates into individual peaks various particles sampled from the flame at the same “size to charge ratio”, but with different numbers of charges, all of which are transmitted through DMA1 at the selected mobility. Corrections are made to these data to account for small fractions of multiply charged particles produced by the neutralizer at the entrance of DMA2. By stepping DMA1 across the range of soot particle size, soot size distributions are measured for a specific state of charge ( $\pm 1$ ,  $\pm 2$ ,  $\pm 3$ , ...). These are augmented by the distribution of neutral particles, which is determined by subtraction of the charge specific distributions from the overall size distribution. Together, these data allow calculation of soot particle electrical charge distributions. A more complete description of the method is presented in reference [21], including an accounting of particle losses in the tandem DMAs and associated plumbing.

### 2.3. Particle losses during sampling and measurement

During sampling, transport, and measurement particles are lost via thermophoresis, diffusion, and coagulation. Thermophoretic losses play an important role only at the pinhole (and heat pipe when used), since thermal gradients become minor after dilution. This deposition mechanism is relatively independent of particle size. Particle concentration, measured as a function of sampling time with the DMA set to a fixed size, declines slowly over several minutes of sampling from a C/O = 0.67 flame, suggesting that losses at the pinhole are minor over the 30-60 seconds used to scan size distributions. The decline becomes much steeper for the heavily sooting C/O = 0.81 flame, with significant clogging already after 30 s.

Immediate dilution at the sampling point renders coagulation negligible. Thus, diffusion is the major loss mechanism in the remainder of the measurement process. Losses in the ejector pumps and transport lines are calculated using standard expressions based on flow through tubes [28]. These are size dependent, with the overall particle penetration from the pinhole to the scanning mobility particle sizer (SMPS) increasing from 60% at 2 nm to 99% at 65 nm.

Losses within the SMPS, which include an inlet impactor, neutralizer, nDMA, and ultrafine CPC (TSI 3025), increase significantly below  $\sim 10$  nm. Recently, TSI Inc. updated its SMPS software to incorporate loss correction. Particle penetration is plotted in Figure 3 for nDMA operation at a 1 L/min inlet flow rate and 15 L/min sheath

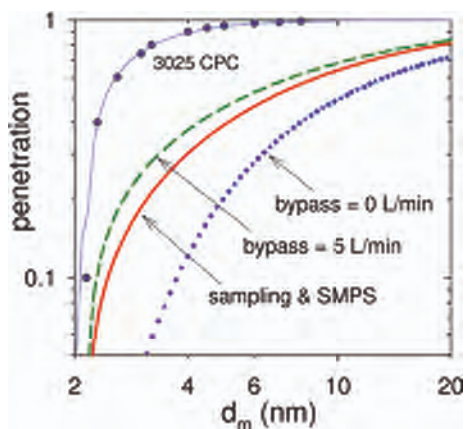


Figure 3. Particle penetration through sampling system and nano-SMPS.

flow rate. In standard operation it falls below 10% for particles smaller than 4 nm (blue dots). In this work the loss is recalculated for operation of the nanoDMA with the bypass feature. As illustrated in Figure 3, the ability to transport the sample at 5 L/min markedly improves the penetration (green dashed line) and permits measurements down to nearly 2 nm. Below this size, the CPC's ability to detect particles becomes the limiting factor. The solid red line depicts particle penetration for the combined sampling and measurement system.

### 3. MOBILITY BASED SOOT SIZE DISTRIBUTIONS

#### 3.1. Evolution of bimodal distributions

Electrical mobility measurements clearly show that many flames produce bimodal size distributions of soot particles. How these evolve as a function of height above the burner (HAB) is illustrated in Figure 4 for a  $\Phi = 2.05$  ethylene flame. Soot inception occurs at  $\sim 6$  mm and particle number density increases up to about 10 mm. At this height, two modes begin to separate. With subsequent increase in HAB, the nucleation mode remains fixed with respect to soot number density and mean diameter ( $\sim 3.5$  nm). While it has been argued that coagulation rates of very small ( $< \sim 3$  nm) particles are low because their sticking coefficients fall well below unity [6, 7], one would nonetheless expect them to coagulate with the much larger accumulation mode particles. Its persistence suggests that the nucleation mode represents a steady state, which requires the continual formation of new particles in the flame. Although there are indications, it is difficult to conclude from the present data the existence of a yet smaller particle mode because of the substantial particle losses at 2 nm. Recent measurements by Sgro et al. [12] with a TapCon 3/150 DMA system, however, do show high particle number densities extending down to  $\sim 1.5$  nm, below which it becomes difficult to distinguish flame generated particles from ion induced clusters.

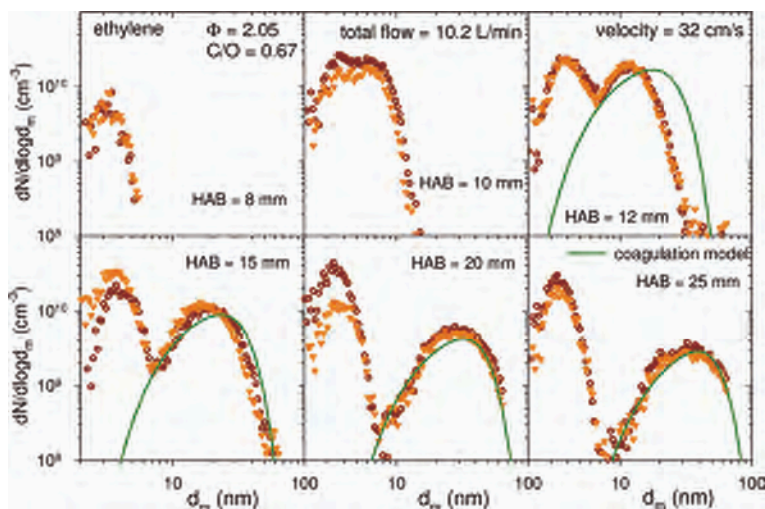


Figure 4. Evolution of a bimodal soot size distribution with increasing height above the burner for a  $\Phi = 2.05$  premixed ethylene flame. Two sets of data in each panel illustrate measurement variability. Evolution of the accumulation mode, assuming it to be entirely due to coagulation, is illustrated by the solid lines.

The accumulation mode that emerges above about 10 mm HAB appears to grow initially by surface addition. One indication of this is that the accumulation mode number density remains nearly constant between 10 and 12 mm. Model predictions of how the size distribution would evolve under coagulation alone are illustrated in the panels marked 12 mm–25 mm in Figure 4. A detailed description of the model is given in Ref. [29], including the incorporation of fractal-like morphology into the collision kernels and treatment of the transition regime between diffusion and free molecule dynamics. The initial primary particle concentration needed to match the eventual accumulation mode concentrations high in the flame exceeds the observed levels at 8 & 10 mm. Consequently low in the flame the predicted coagulative growth is too rapid and the model distribution is grossly wider than measured (as apparent at 12 mm HAB).

From 15 mm on, however, coagulation begins to dominate, with very good agreement between coagulation model and observation regarding the shape of the accumulation mode and its decreasing number density with increasing HAB. It is interesting to note that the predictions depicted in Figure 4 are predicated on choosing a fractal dimension of  $D_f = 2.5$ , a value larger than usually accepted for soot particles [30, 31]. There are two potential reasons for this. One is that the higher than expected fractal dimension arises from our use of mobility diameter in lieu of radius of gyration. Another possibility is that the displayed size distributions are recorded from a more lightly sooting flame than examined in the majority of previous studies. The TEM images presented below (Figures 7b and 7c), as well as the coagulation behavior and effective density measurements reported previously [29], corroborate that such higher fractal dimensions are plausible under lightly sooting conditions.

### 3.2. Fuel & flow rate impacts on size distributions

Bimodal soot size distributions are not universal. Figure 5 exhibits how the distribution shape varies with fuel/air flow rate and choice of fuel. In the case of ethylene, acetylene, and benzene/ethylene (0.27 / 1), soot is generated by fuel/air flames with  $C/O = 0.67$  and total flow rates of 5.9 to 11.8 L/min (cold). The propene flames are based on 1.0 L/min  $C_3H_6$  and 2.3 L/min  $O_2$ , with 1.0, 2.0, and 3.0 L/min  $N_2$  added to vary the total flow. Changing the fuel/air flow rate, equivalently the gas velocity above the burner, elicits relatively subdued changes in the accumulation mode. The mean diameter shifts to larger size, accompanied with a commensurate decrease in number density, as the flow rate is reduced. This is a consequence of the longer time available for coagulation and surface growth, as observed at a fixed height above the burner. The trend is most noticeable in the case of propene, for which fuel and oxygen flow rates remain constant, and the gas velocity increases only because of the added nitrogen.

The response of the nucleation mode to fuel/air flow rate changes is rather more dramatic. In the case of acetylene, for example, an increase of the fuel/air flow rate from 5.9-9.8 L/min completely eliminates the nucleation mode that at the lower flow dominates the size distribution (Figure 5). In the case of ethylene and acetylene, the nucleation mode persists over a wide range of conditions. But when benzene is added, and with propene, the nucleation mode appears only at very low flows, in the latter case

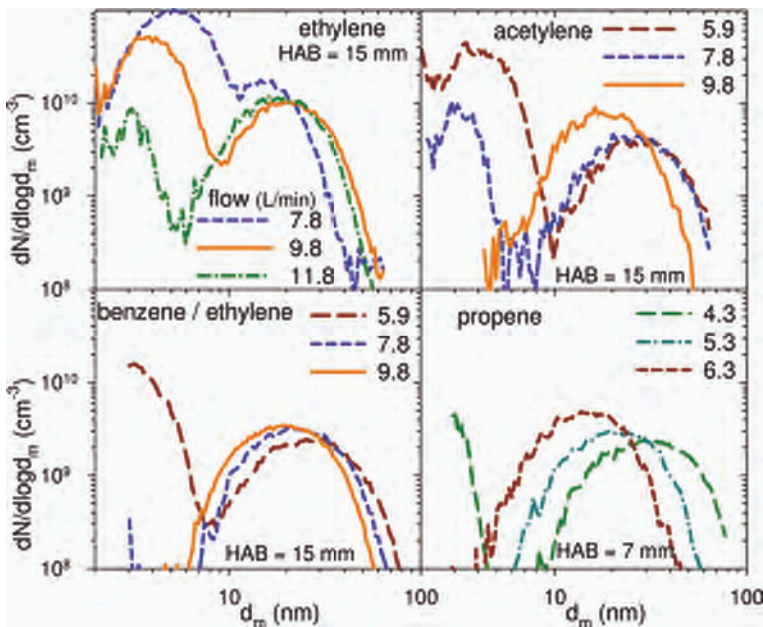


Figure 5. Influence of air/fuel flow rate on the bimodal nature of the soot size distribution for premixed flames using ethylene, acetylene, benzene/ethylene, and propene fuels at  $C/O = 0.67$ .

close to the lower limit needed to maintain a stable flame. As the number density of nucleation mode particles increases, the mean diameter shifts to larger values, from 3–5 nm in the case of the ethylene data. It is unclear whether this is a real phenomenon, or a result of coagulation that occurs in spite of immediate dilution at the pinhole when sampling particle concentrations that in the flame approach  $10^{11} \text{ cm}^{-3}$ .

While the mechanism leading to a bimodal distribution of soot particles remains unclear, it is interesting to note the dependence of the nucleation mode on flame temperature. Figure 6 plots the calculated flame temperature of the acetylene, ethylene, and benzene/ethylene flames as a function of fuel/air flow rate. The temperatures are based on the kinetic mechanism of Appel, Bockhorn, and Frenklach [32, 33], and are calculated using the Cantera combustion code [34]. Conditions leading to bimodal soot distributions are denoted by solid symbols, whereas unimodal distributions are indicated with open symbols. These trends suggest that a transition takes place at a flame temperature of about 1650 K, below which new particle nucleation continues to heights well above soot inception.

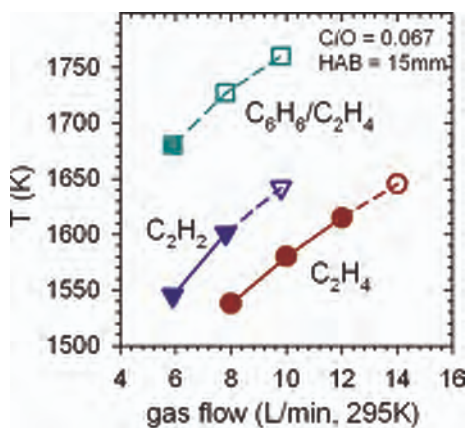


Figure 6. Calculated flame temperature versus air/fuel flow rate. Solid symbols indicate that the size distributions are bimodal. Open symbols denote a single mode.

#### 4. TEM IMAGES OF MOBILITY SELECTED SOOT

Owing to their fractal-like morphology, the size of soot particles is perforce described in terms of some equivalent diameter. In the case of DMA measurements, this is defined with respect to the particle's electrical mobility, which in turn is proportional to its diffusion constant. TEM images of soot particles collected with a well specified mobility diameter enable a visual comparison between this equivalent diameter and the particle's physical dimensions. Figure 7 illustrates soot images collected at various mobility diameters and flame conditions.

Panel A shows  $d_m = 15$  nm particles sampled from the nucleation mode of a  $\Phi = 2.05$  ethylene flame at 15 mm HAB (fuel/air flow = 10.2 L/min). The nucleation particles are ordinarily much smaller, 3-4 nm, but these were collected directly from the flame via the short tube sampling probe. Without immediate dilution, the nucleation particles grow to a size more amenable to TEM imaging of carbonaceous material. However, as demonstrated by the absence of charged particles Figure 2, this mode remains distinct from the accumulation mode. The particles are spherical, with very low contrast, and no discernable order. As expected, their physical and mobility diameters coincide.

The particles in Panel B are obtained from the same flame and at the same height. But they are selected from the accumulation mode at 20 nm diameter, the peak of this mode (Figure 4). Here the pinhole probe is employed to keep the nucleation mode particles at 3-4 nm diameter so that they do not interfere. These images, too, reveal amorphous particles with low contrast. Their shapes are irregular, but remain compact and lack a discernable structure of primary particles. The average projected area diameter of these particles is 19.4 nm with a standard deviation of 1.6 nm, in excellent agreement with their mobility diameter.

Higher in the  $\Phi = 2.05$  flame soot morphology changes. The particles displayed in Figure 7c are sampled from 30 mm HAB and at  $d_m = 60$  nm, a size larger than the

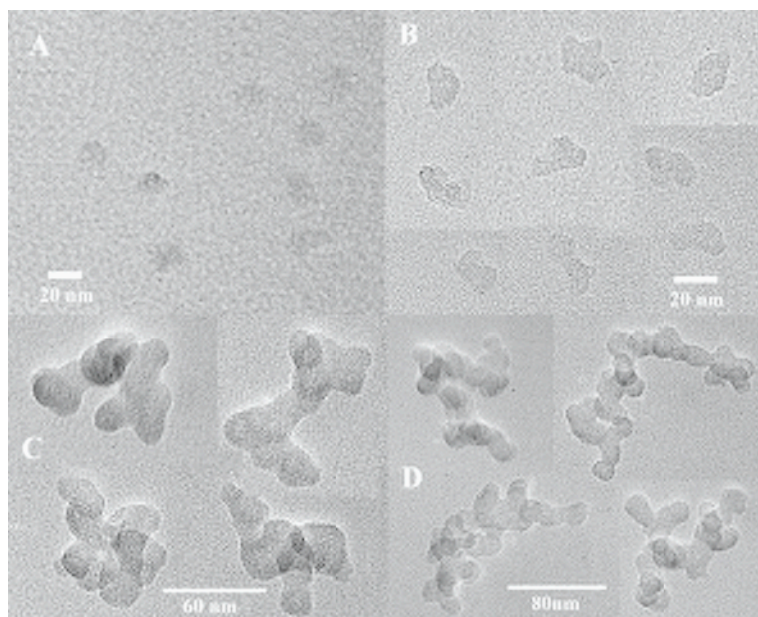


Figure 7. TEM images of mobility size selected soot particles from rich ethylene flames. Panel A: 15 nm particles sampled from nucleation mode, 15 mm HAB,  $\Phi = 2.05$ . Panel B: 20 nm particles sampled from accumulation mode, 15 mm HAB,  $\Phi = 2.05$ . Panel C: 60 nm particles sampled from accumulation mode, 30 mm HAB,  $\Phi = 2.05$ . Panel D: 80 nm particles sampled from accumulation mode, 25 mm HAB,  $\Phi = 2.45$ .

mean accumulation mode diameter of 40 nm at this height. These particles clearly exhibit a substructure of primary particles, which have diameters of  $d_0 = \sim 18$  nm. But there is considerable “necking”, and a lack of a distinct boundary between primary particles, which could arise from surface addition or from coagulation with nucleation mode particles. These aggregates have an average projected area equivalent diameter of 64.0 nm and a standard deviation of 3.6 nm (taken over 9 particles), agreeing well with the selected mobility diameter. As shown at higher magnification in Figure 8a, many of the primary particles are now beginning to exhibit signs of a layered graphene structure typical of a wide range of soots [35].

The 60 nm particles in Panel C comprise relatively few primary particles ( $\sim 12$  in 2-D projection) and retain a somewhat compact shape. In comparison, Figure 7d displays particles collected from the “heavily sooting”  $\Phi = 2.45$  ethylene flame at a height of 25 mm HAB, and a diameter of  $d_m = 80$  nm. These particles reveal a more open fractal-like morphology expected of soot. Modeling their coagulation requires a frac-

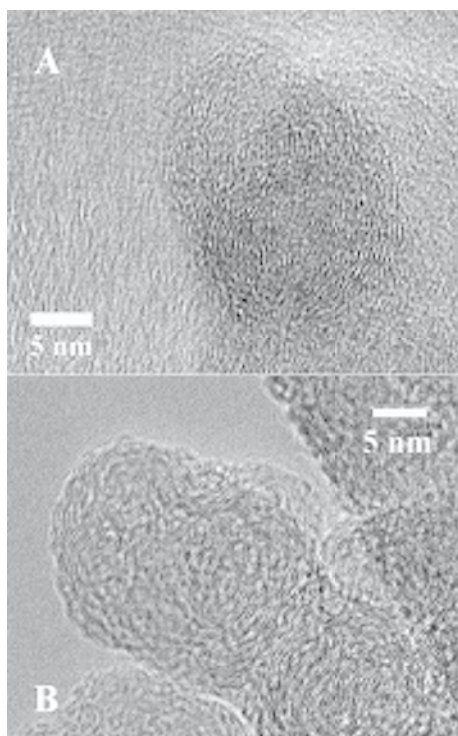


Figure 8. High resolution TEM images of primary particles in mobility selected soot aggregates. Panel A: In a 60 nm aggregate sampled at 30 mm HAB,  $\Phi = 2.05$ . Panel B: In an 80 nm aggregate sampled at 25 mm HAB,  $\Phi = 2.45$ .

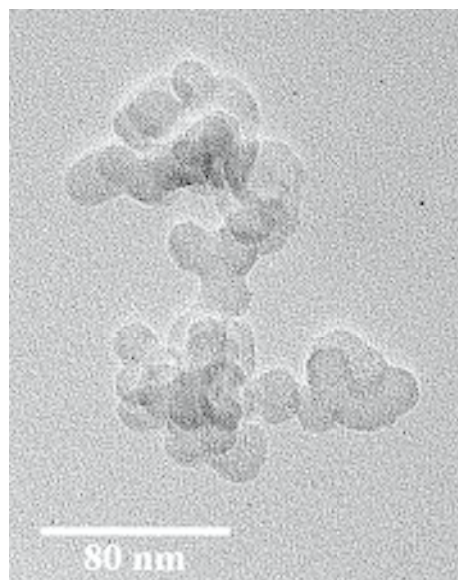


Figure 9. TEM image of a doubly charged 119 nm particle. Its electrical mobility equals that of a singly charged 80 nm particle.

tal dimension of  $D_f = 1.9\text{--}2.0$ , more typical of soot [29]. The primary particles,  $d_0 = 17$  nm, are more distinct and numerous than their counterparts in Figure 7c. These, too, show a substructure within the primary particles (Figure 8b). The aggregates continue to demonstrate a narrow range of projected area diameter, 82 nm on average with a 3 nm standard deviation, essentially equal to the mobility diameter set by the DMA. One of the selected particles (see Figure 9) exhibits a markedly larger size than the others. Its projected area diameter of 121 nm coincides nicely with a mobility diameter of 119 nm, the diameter of doubly charge particles also transmitted when the DMA is set at 80 nm. The +2 charging efficiency of the neutralizer is 0.042 at 120 nm relative to a +1 charging efficiency of 0.18. Combined with a  $\sim 1:4$  relative population of these sizes in the  $\Phi = 2.45$  flame, the expected collection efficiency of doubly charged particles is 6%, consistent with observing one such image in ten.

## 5. THERMAL DESORPTION / RESTRUCTURING

While TEM images typically depict soot as fractal-like aggregates of graphitic primary particles, soot emissions from many practical combustion systems, for example diesel engines, include sizeable fractions of condensed hydrocarbon and sulfate material. One way to examine this is via thermal desorption [36] or tandem DMA volatility analysis [25, 27]. In its simplest form, this consists of comparing the size distribution of particles measured before versus after passing the diluted soot sample through a thermodenuder (heat pipe followed by active carbon adsorbant). But, the tandem DMA method is better suited in the present case since it permits separate analysis of nucleation versus accumulation mode soot particles.

In this approach monodisperse soot particles are passed through a heat pipe, and any thermally induced size change is examined with a second DMA (Figure 1). The pinhole probe is used to sample soot particles, so that immediate dilution at the sampling point minimizes any changes to the particles as they are removed from the flame. Figure 10 presents the results recorded over a temperature range of 25–600 C for soot particles selected under a variety of flame conditions and initial diameters.

In all cases particle diameter shrinks with increasing temperature. The trend is essentially linear in temperature. For accumulation mode particles there is a net decrease of 1.3–2.0 nm in diameter by 600 C, a value that is relatively insensitive to initial size. This translates to a loss of 3–10% in diameter, or 6–20% by volume (calculated assuming  $D_f = 2.0$ ), where these fractional changes increase with decreasing initial size. All particles at a selected size shrink by about the same amount; that is, the monodisperse width (geometric st. dev.) of  $\sigma_g = 1.03$  dictated by the DMA1 transfer function increases only slightly to about 1.05 after passage through the heat pipe.

The thermally induced diameter decrease is larger for nucleation than accumulation mode particles both in relative and absolute terms. These decrease from 6 nm to about 3.5 nm by 600 C, a 40% diameter and 80% volume change. In this case the size selected nucleation particles do not remain monodisperse through the heat pipe, rather the distribution steadily broadens to a width of  $\sigma_g = \sim 1.15$ . There is also a large loss of particles through the heat pipe, reaching >60% at 600 C. Possibly this implies that a subset of particles is semivolatile, and thus completely evaporated. But more likely, this

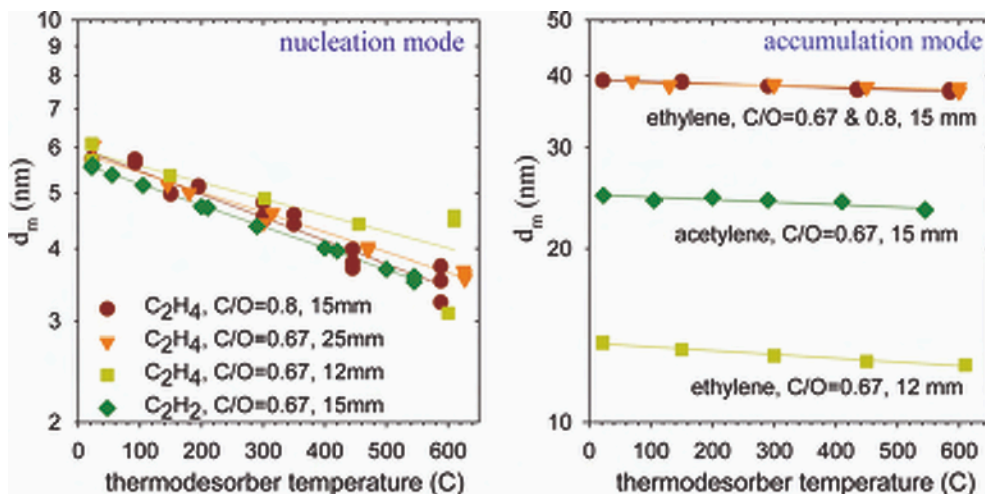


Figure 10. Thermal desorption / restructuring of size selected soot particles from a  $\Phi = 2.05$  ethylene flame. Left panel: nucleation mode particles. Right panel: accumulation mode particles.

is the result of the thermophoretic and diffusion losses of these very small particles exacerbated with increasing temperature of the heat pipe.

That the accumulation mode particles suffer only slight thermally induced diameter changes is not surprising and is consistent with a graphitic structure suggested by the TEM images. The small shrinkage that is observed is perhaps explained by residual condensation not completely avoided during sampling. This latter explanation could hold true as well for the relatively larger effect on nucleation mode particles. In this case, though, one might expect to observe a rapid initial decrease to a size that remains constant above a few hundred degrees C, as opposed to the observed linear decrease. Another possibility is that the nucleation mode particles have a more organic like structure with a relatively low C/H ratio that the increasing temperature pyrolyzes to a progressively more graphitic carbon, causing a restructuring of the particles to smaller size.

## 6. SOOT ELECTRICAL CHARGE

Electrical charge represents another property of interest with respect to soot particles. It was studied in low pressure flames by Wersborg et al. [37] and Howard et al. [38] partly to investigate higher than expected coagulation rates. Subsequently Wegert et al. [39] used a Wien filter approach to examine mass based soot charge distributions. In atmospheric pressure premixed flames, as shown in Figure 2, the nucleation and accumulation mode particles exhibit very different behavior in this respect. The nucleation mode particles are electrically neutral, even under non-ideal sampling conditions (Figure 2b). In contrast, a substantial fraction of accumulation mode particles carry

some non-zero charge, nearly equally balanced between positive and negative. These single DMA measurements are obtained by bypassing the neutralizer, but they do not readily yield information about the number of charges per particle. The tandem DMA approach provides a means to map out the size distributions of particles carrying a specified number of charges.

Figure 11 illustrates such charge specific size distributions recorded between 15 and 30 mm HAB from a  $\Phi = 2.06$  premixed ethylene flame. The same pattern is observed at each height. Uncharged particles exhibit a bimodal distribution. As the accumulation mode particles become progressively charged, their geometric mean diameter increases, but the number density decreases. Positive and negative charging efficiencies are indistinguishable within the data scatter. With increasing height in the flame the overall size distribution shifts to larger size, but the same pattern is repeated.

As noted above, even though nucleation and surface addition are important growth processes, the shape of the soot size distribution above  $\sim 15$  mm HAB appears to be progressively dictated by coagulation (Figure 4). This holds true as well for charged particles. The lines in Figure 5 represent predictions from a coagulation model that describes the kinetics of particle collisions including the attractive and repulsive forces that exist between charged particles. This model is described in detail in Ref. [21] for the case of free molecule collision dynamics, but here it has been revised to include the transition regime as well. Basically, attraction between unlike charged particles increases their collision cross section by drawing their trajectories toward each other. But collision probabilities between like charged particles decrease because the particles must overcome their Coulomb repulsion. Since the latter becomes progressively harder for small particles; thus, multiply charged particles tend to be on average larger. As evident from Figure 11, the model reproduces the observed trends in particle mean diameter and number density versus number of charges at heights above 15 mm. At lower heights the discrepancies already visible at 15 mm increase due to the omission of surface growth from the model. Consequently the purely coagulation model over predicts the fractions of multiply charged particles at low heights in the flame, as well as the width of the accumulation mode.

The data in Figure 11 can be recast to give electrical charge distributions as a function of particle diameter. These are illustrated in Figure 12 for the examples of  $d_m = 20$  nm and 60 nm. Within the data scatter, the observed charge distributions are symmetric and independent of the height in the flame at which the soot is sampled. The charge distribution width increases with particle diameter, showing an increased propensity for multiple charging that is reproduced by the coagulation model. However, the observed charge data agree also very closely with the Boltzmann charge distribution [28] (solid lines)

$$f_n(d_m) = \left( \frac{K_E e^2}{\pi d_m kT} \right)^{1/2} \exp\left( \frac{-K_E n^2 e^2}{d_m kT} \right) \quad (1)$$

when evaluated at 1650 K. Here  $K_E = 9.0 \times 10^9$  Nm<sup>2</sup>/C<sup>2</sup> in SI units,  $n$  is the number of charges,  $e$  is the electron charge,  $k$  is Boltzmann's constant, and  $T$  is the temperature.

Potential mechanisms leading to electrically charged soot particles in flames include the nucleation of ions [40], thermal ionization, and the attachment of molecular

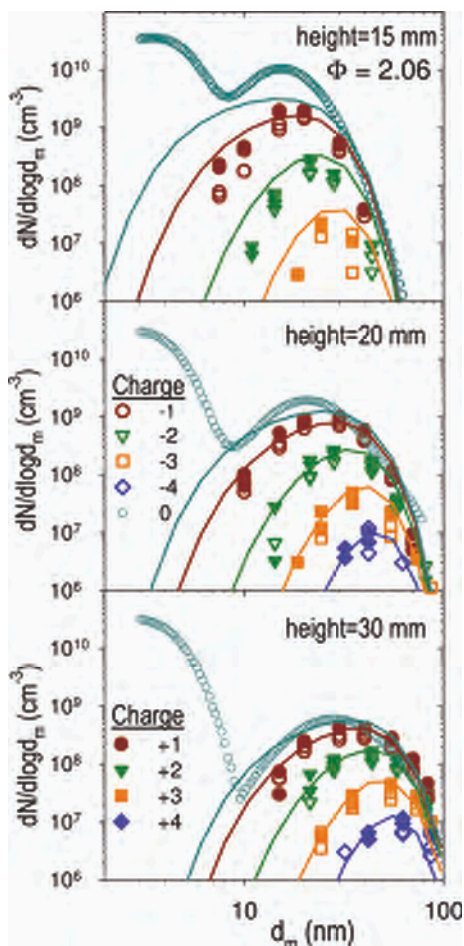


Figure 11. Charge specific soot size distributions. Top panel: 15 mm HAB. Middle panel: 20 mm HAB. Bottom panel: 30 mm HAB. Symbols represent experimental data and lines depict coagulation model predictions.

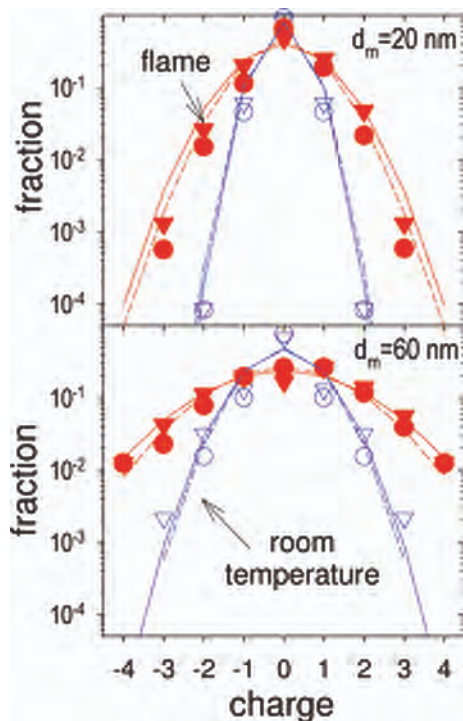


Figure 12. Soot electrical charge distributions. Top panel: 20 nm soot particles. Bottom panel: 60 nm soot particles. Filled symbols represent charge distributions in the flame at 15 mm HAB (circles) and 30 mm HAB (triangles). Open symbols show charge distribution after sampling from 10 mm HAB (circles) and 20 mm HAB (triangles), and cooling by dilution to room temperature. Solid lines represent the Boltzmann charge distribution. Dashed lines show coagulation model predictions.

ions. Neither of the first two adequately explains the nucleation mode. If produced by ion induced nucleation, the nucleation mode should be charged. Under thermal ionization one expects, according to the Boltzmann distribution, that approximately 1.2%

at 2 nm, increasing to 14% at 4 nm, of the nucleation particles carry a single positive or negative charge in the flame, yet experimentally less than 0.1% are charged.

Thus the proposed mechanism is that shortly after soot inception, soot particles attach molecular ions and electrons produced in the flame via chemiionization reactions. The kinetic model then suggests that coagulation between like charged particles leads to multiply charged particles in proportion to the Boltzmann distribution, as observed experimentally. The ability of coagulation to equilibrate (more properly coagulation is a steady state process) soot charge with the surrounding gas temperature is further demonstrated in Figure 12 by the “cooling” of the charge distribution that is observed after soot particles are removed from the flame and allowed to coagulate at room temperature. The lack of electrical charge in the nucleation mode can then be explained by the assumption that this mode is formed at heights in the flame where chemiionization reactions have ceased and, therefore, there are no ions left to attach.

## 7. SUMMARY AND CONCLUSIONS

Electrical mobility methods offer a valuable means to investigate soot particles. The combination of DMA and CPC provides a very sensitive and high resolution method to record particle size distributions. Advances in DMA design have enabled the investigation of particles down to about 2 nm, or about 1 nm if electrical detection is used instead of particle counting [12]. This provides the opportunity to examine soot near its inception, particles that are difficult to detect via light scattering or TEM. The technique clearly demonstrates the presence in many premixed flames of a second mode of particles, a few nanometers in diameter, which can coexist with conventional soot particles, and corroborates observations of soot precursor particles via UV absorption and TEM [4, 5, 6]. However, the method is intrusive, requiring soot to be sampled from the flame and transported to the measurement apparatus. Immediate dilution at the source point minimizes chemical and physical changes during sampling. This approach appears to be robust with respect to the accumulation mode, where its evolution in the flame as recorded by nDMA is consistent with light scattering measurements [9]. But the very small size of nucleation mode particles make them more susceptible to sampling effects and this deserves more study.

A strong dependence is observed between the fuel/air flow rate and the existence of the nucleation mode. But temperature, which increases with increasing flow rate, likely plays the fundamental role behind this correlation. While its effect on the soot mode is modest, in contrast the nucleation mode grows from non-existent to dominant in particle number within a  $\sim 100$  C drop in temperature. This suggests that a change occurs in the soot formation mechanism, perhaps with two pathways operative at lower temperatures. But nucleation is a nonlinear process. So it is also possible that this is predominantly a threshold effect, with soot precursor production sufficiently rapid below  $\sim 1650$  K to trigger new particle nucleation, whereas at higher temperatures the necessary concentrations are not reached.

The TEM images of mobility selected soot particles provide two important pieces of information. First, there is a well defined correspondence (COV of 4-8%) between

the projected area diameter of the soot particle image and the electrical mobility set by the DMA, at least for the soot examined here. Second, there is a variation in premixed flame soot morphology, whereby its fractal dimension decreases with increasing equivalence ratio and increasing height above the burner. Although not typical of the larger more developed soot particles that dominate the literature on this subject [31, 30, 41], this is consistent with the evolution of the accumulation mode exhibited in Figure 4, as well as with previous studies of soot particle effective density and its coagulation kinetics [29].

The terms nucleation mode and accumulation mode adopted here are descriptive of the respective particle behavior. Thus, the persistence in the size and number density of nucleation particles with height above the burner suggests these to be newly formed particles, while TEM images clearly show accumulation particles to be aggregates. While the same terminology is used in other applications, such as diesel particulate matter and atmospheric aerosols, this does not necessarily imply that the particles so described are identical.

The comparison of flame soot to diesel PM is interesting and relevant because of environmental concerns. Accumulation mode particles from flames and diesel exhaust are quite similar. Both are aggregates of primary particles dominated by graphene structures, with perhaps a more complex chemistry and the possibility of ash distinguishing the diesel case. In contrast, the nucleation modes differ. Besides being much smaller than their diesel counterparts ( $\sim 2\text{-}4$  nm versus  $15\text{-}30$  nm), flame generated nucleation particles exhibit different thermal properties. Thus, they undergo a linear decrease in size of up to  $\sim 40\%$  when subject to temperatures ranging from  $25\text{-}600$  C, while diesel nucleation mode particles, in contrast, are completely vaporized by  $< 250$ C under most engine operating conditions [25, 42]. Chemical analysis by thermal desorption particle mass spectrometry further indicates these particles are primarily composed of lube oil-like hydrocarbons with varying amounts of sulfate [16, 17]. Recently, engine formed nonvolatile nuclei particles, suggestive of the incipient soot particles in flames, have been observed in special circumstances, e.g., at idle; but they do not survive through a diesel particulate filter [43, 44].

Numerous other questions remain regarding soot formation and the appearance of two modes. Are these the result of separate mechanisms, or different manifestations of the same underlying pathways? What are the chemical characteristics of these particles? The small, elusive, nature of the nucleation mode particles poses challenges to answering these and other questions. In turn, continued advances in analytical methods, such as those discussed here, aerosol mass spectrometry, and others, will help overcome these hurdles to allow deeper insight to the both fundamentally and practically important problem of soot formation.

## ACKNOWLEDGMENTS

The author would like to thank Lee Ann Sgro and Andrea De Filippo (University Federico II of Naples) for their suggestion to extend the nanoDMA measurements down to 2 nm, Yi Lu (Wayne State University) for producing the TEM images, and Rick Soltis (Ford) for help with the CO<sub>2</sub> analyzer.

## REFERENCES

1. P. Zelenka, M. Egert, W. Cartellieri, SAE (2000) Technical Paper 2000-01-0181.
2. M. V. Twigg, *Appl. Catalysis B*, 70 (2007) 2-15.
3. R. A. Dobbins, R. A. Fletcher, H.-C. Chang, *Combust. Flame* 115 (1998) 285-298.
4. R. A. Dobbins, *Aerosol Sci. Technol.* 41 (2007) 485-496.
5. A. D'Alessio, A. D'Anna, G. Gambi, P. Minutolo, *J. Aerosol Sci.* 29 (1998) 397-409.
6. P. Minutolo, G. Gambi, A. D'Alessio, S. Carlucci, *Atmos. Environ.* 33 (1999) 2725-2732.
7. L. A. Sgro, G. Basile, A. C. Barone, A. D'Anna, P. Minutolo, A. Borghese, A. D'Alessio, *Chemosphere*, 51 (2003) 1079-1090.
8. L.A. Sgro, P. Minutolo, G. Basile, A. D'Alessio, *Chemosphere* 42 (2001) 671-680.
9. M. M. Maricq, S. J. Harris, J. J. Szente, *Combust. Flame* 132 (2003) 328-342.
10. B. Zhao, Z. Yang, M. V. Johnston, H. Wang, A. S. Wexler, M. Balthasar, M. Kraft, *Combust. Flame* 133 (2003) 173-188.
11. M. M. Maricq, *Combust. Flame* 144 (2006) 730-743.
12. L.A. Sgro, A. De Filippo, G. Lanzaolo, A. D'Alessio, *Proc. Combust. Inst.* 31 (2007) 631-638.
13. J. P. Hessler, R. S. Tranter, S. Vajda, N. VanWermeskerken, *Proc. of the 4th Joint Meeting of the U.S. Sections of the Combustion Institute*, 2005.
14. S. di Stasio, J. B. A. Mitchell, J. L. LeGarrec, L. Biennier, M. Wulff, *Carbon*, 44 (2006) 1267-1279.
15. H.-M. Grotheer, H. Polorny, K.-L. Barth, M. Thierley, M. Aigner, *Chemosphere* 57 (2004) 1335-1342.
16. H. J. Tobias, D. E. Beving, P. J. Ziemann, H. Sakurai, M. Zuk, P. H. McMurry, D. Zarling, R. Waytulonis, D. B. Kittelson, *Environ. Sci. Technol.* 35 (2001) 2233-2243.
17. J. Schneider, N. Hock, S. Weimer, S. Borrmann, U. Kirchner, R. Vogt, V. Scheer, *Environ. Sci. Technol.* 39 (2005) 6153-6161.
18. J. T. Jayne, D. C. Leard, X. Zhang, P. Davidovits, K. A. Smith, C. E. Kolb, D. R. Worsnop, *Aerosol Sci. Technol.* 33 (2000) 49-70.
19. M. Kasper, K. Siegmann, K.J. Sattler, *J. Aerosol Sci.* 28 (1997) 1569-1578.
20. B. Zhao, Z. Yang, J. Wang, M.V. Johnston, H. Wang, *Aerosol Sci. Technol.* 37 (2003) 611-620
21. M. M. Maricq, *Combust. Flame* 141 (2005) 406-416.
22. A. Wiedensohler, H. J. Fissan, *J. Aerosol Sci.* 19 (1988) 867-870.
23. S. C. Wang, R. C. Flagan, *Aerosol Sci. Technol.* 13 (1990) 230-240.
24. D. -R. Chen, D. Y. H. Pui, D. Hummes, H. Fissan, F. R. Quant, G. J. Sem, *J. Aerosol Sci.* 29:497 (1998).
25. H. Sakurai, K. Park, P. H. McMurry, D. D. Zarling, D. B. Kittelson, P. J. Ziemann, *Environ. Sci. Technol.* 37 (2003) 5487-5495.
26. S.-B. Kwon, K. W. Lee, K. Saito, O. Shinozaki, T. Seto, *Environ. Sci. Technol.* 37 (2003) 1794-1802.
27. B. Wehner, S. Philippin, A. Wiedensohler, V. Scheer, R. Vogt, *Atmos. Environ.* 38 (2004) 6081-6090.
28. W. C. Hinds, *Aerosol Technology* Wiley, New York, 1999.
29. M. M. Maricq, *J. Aerosol Sci.* 38 (2007) 141- 156.
30. C. Oh, C. M. Sorensen, *J. Aerosol Sci.* 28 (1997) 937-957.
31. Ü. Ö. Köylü, Y. Xing, D. E. Rosner, *Langmuir* 11 (1995) 4848-4854.
32. J. Appel, H. Bockhorn, M. Frenklach, *Combust. Flame*, 121 (2000) 122-136.
33. M. Frenklach, Soot modeling, <http://www.me.berkeley.edu/soot/mechanisms/abf.html>.

34. D. G. Goodwin, Cantera 1.5 Chemically Reacting Flow Software, <http://rayleigh.cds.caltech.edu/~goodwin/cantera/index.html> (2004).
35. A. Braun, F. E. Huggins, S. Seifert, J. Ilavsky, N. Shah, K. E. Kelly, A. Sarofim, G. P. Huffman, *Combust. Flame*, 137 (2004) 63-72.
36. H. Burtscher, U. Baltensperger, N. Bukowiecki, P. Cohn, C. Hüglin, M. Mohr, U. Matter, S. Nyeki, V. Schmatloch, N. Streit, E. Weingartner, *J. Aerosol Sci.* 32 (2001) 427-442.
37. B. L. Wersborg, J. B. Howard, G. C. Williams, *Proc. Combust. Inst.* 14 (1973) 929-940.
38. J. B. Howard, B. L. Wersborg, G. C. Williams, *Faraday Symp. of the Chemical Society* 7 (1973) 109-119.
39. R. Wegert, W. Wiese, K.-H. Homann, *Combust. Flame* 95 (1993) 61.
40. H. F. Calcutte, *Combust. Flame* 42 (1981) 215-242.
41. Ü. Ö.Köylü, G. M. Faeth, T. L. Farias, M. G. Carvalho, *Combust. Flame*, 100 (1995) 621-633.
42. M. M. Maricq, R. E. Chase, N. Xu, P. M. Laing, *Environ. Sci. Technol.* 36 (2002) 283-289.
43. T. Rönkkö, A. Virtanen, J. Kannosto, J. Keskinen, M. Lappi, L. Pirjola, *Environ. Sci. Technol.* 41, (2007) 6384-6389.
44. A. De Filippo, M. M. Maricq, *Environ. Sci. Technol.* (2008) 10.1021/es8010332.

# Size distribution and chemical composition of nascent soot formed in premixed ethylene flames

H. Wang, A. Abid

University of Southern California, Los Angeles, CA 90089, USA

*Abstract: The paper provides a brief review of the theories, applications and key results of an array of experimental techniques, including probe sampling/scanning mobility particle sizing, photoionization particle mass spectrometry, and atomic force microscopy, to probe nascent soot in atmospheric pressure, burner-stabilized ethylene flames. Important findings are: (a) the size distribution of nascent soot is ubiquitously bimodal; (b) nascent soot particles spreads into spherical tops on a surface upon impact, show little evidence of carbonization, and can have H/C ratios close to unity; and (c) the basic building blocks of nascent soot particles are polycyclic aromatic hydrocarbons (from  $C_{16}H_{10}$  to  $C_{32}H_{14}$ ), with  $C_{22}H_{12}$  and  $C_{24}H_{12}$  being the most abundant specie, but a substantial amount of aliphatics can exist, probably in the form of side chains on the aromatic building blocks.*

## 1. INTRODUCTION

A great deal of detailed problems of soot formation remains fundamentally unsolved. Although we are now able to predict the formation rate of soot and its precursors to some degree of accuracy [1-19], our understanding of particle nucleation and mass growth remains semi-empirical and phenomenological. For example, in most soot models particle nucleation is assumed to begin with the coalescence of polycyclic aromatic hydrocarbons (PAHs). Yet, according to thermodynamic considerations, the condensed-phase PAHs in flames should preferentially evaporate rather than condense. Recent Kinetic Monte Carlo (KMC) and Molecular Dynamics (MD) studies have shed new light on the nucleation and early mass growth processes [20-22]. However, the validity of these theoretical predictions is yet to be tested when pertinent experimental data are made available.

Meanwhile, growing evidence suggests that the environmental and human health effects of soot are directly related to the particle size distribution and chemical composition [23-28]. Ultra small particles do not contribute much in particulate mass. In engines, they form often as a result of soot oxidation. These particles tend to be more hydrophilic due to the presence of oxygenated surface functional groups. They can penetrate deeper into human airways and be absorbed and transported more effectively into the blood stream. The ability of soot to act as Cloud Condensation Nuclei (CCN) and to perturb the regional and global climate [26-28] is again related to its surface chemical composition. In addition, the light absorbing and scattering properties of soot critical to the global, atmospheric energy balances are also dependent on particle size distribution and chemical compositions.

Given these considerations, it is not difficult to foresee that future regulatory developments will have to take into consideration the size distribution of particles and their chemical composition. If this regulatory development does occur, the existing soot models will have to be drastically improved. Future models of soot formation should have the ability to predict the particle size distribution function (PSDF) and its evolution. They should also be able to describe and follow the kinetic evolution of surface and interior chemical composition. Both elements are critical to achieving the next level of understanding of the various processes in soot formation, including nucleation, mass growth, aggregation, carbonization, and oxidation. On the other hand, theoretical advances cannot be made unless we can observe the particle size distribution and chemical composition of soot in flames experimentally.

It was realized several years ago that advances of soot modeling would eventually be limited by a lack of suitable experimental techniques that can provide information necessary for model development and validation. For this reason new experimental approaches had emerged over the past few years. Small Angle X-ray Scattering (SAXS) and Small Angle Neutron Scattering (SANS) have been developed for probing soot volume fraction and to an extent, the particle size distribution function [29-32]. The probe sampling/Scanning Mobility Particle Sizing (SMPS) technique [33-44] offers the possibility that the detailed soot PSDFs may be followed. A variety of advanced aerosol techniques have been utilized to probe soot surface properties, oxidation and reaction [45-52]. Particle Photo Ionization Mass Spectrometry (PIAMS) [10,11] was shown to provide the resolution necessary for probing the bulk chemical composition of incipient soot [39,49]. Coupled with the traditional light extinction and scattering method, these new experimental techniques raise prospects for unambiguous and quantitative determination of size distribution, chemical composition, and morphology of nascent soot, from nucleation, aggregation, carbonization to oxidation. This paper will review the applications of probe sampling/SMPS, SANS, Atomic Force Microscopy (AFM), and Photo/Thermal Ionization Mass Spectrometry (PIAMS) in probing the reaction mechanism and kinetics of incipient soot formation. Emphasis will be placed on the general feature of particle size distributions in atmospheric-pressure, premixed ethylene flames and its implication in the nature and mechanism of particle nucleation and growth. Additionally the chemical composition of nascent soot and its corresponding morphology will be discussed on the basis of experimental observations.

## **2. RECENTLY DEVELOPED TECHNIQUES FOR NASCENT SOOT MEASUREMENTS – THEORIES AND APPLICATION**

### **2.1. Electric mobility**

Electric mobility measures the velocity of a charged particle in a dilute gas exposed to an electric field. In an externally imposed electric field, charged particles move in a carrier gas preferentially to the electrode of opposite charge at a settling velocity known as the electric mobility  $Z$ . Since the electrostatic force depends on the number of charge on the particle, and the drag resulting from the particle-fluid relative motion is

highly dependent on the particle size, a measure of the electric mobility yields the particle size. Historically the drag on a spherical particle in the free molecule and transition regimes has been described by the Cunningham-Slip correction [50,51] on Stokes' formula [52]. The correction accounts for the transition from the Stokes continuum regime where the viscous dissipation of the fluid dominates the particle-fluid momentum transfer, to the free molecule regime where the direct collision between the gas and particle is the dominant mechanism of momentum transfer. In commercial differential mobility analyzers (DMA), the relation between the mobility and particle size is given by the Stokes-Cunningham equation,

$$Z = N_c q \left\{ 1 + \text{Kn} \left[ A + B \exp(-E/\text{Kn}) \right] \right\} / (6\pi\mu\tilde{R}_p), \quad (1)$$

where  $N_c$  is the number of charge on a particle,  $q$  is the elementary charge,  $\text{Kn}$  is the Knudsen number,  $\tilde{R}_p$  is called the mobility diameter, and  $A$ ,  $B$ , and  $E$  are parameters fitted into the experiments of Millikan [53-55]. Here, the Knudsen number is defined as the ratio of gas mean free path  $\lambda$  to the particle radius, i.e.,  $\text{Kn} = \lambda/\tilde{R}_p$ , where

$\lambda = \left( \sqrt{2\pi}\sigma_g^2 N_g \right)^{-1}$ ,  $\sigma_g$  is the collision diameter of the fluid molecule, and  $N_g$  is the gas number density.

Equation (1) has several drawbacks. The slip correction is empirical in nature. Considering that the smallest oil droplets in Millikan's experiments are of the size of  $\sim 0.3 \mu\text{m}$ , there is little reason to believe that the empirical correction is valid for particles smaller than that size. Indeed, when the Stokes-Cunningham drag force is extrapolated to the molecular size, the resulting diffusivity via the Stokes-Einstein relation does not agree with the Chapman-Enskog theory of molecular diffusion [56]. The second drawback is that the Cunningham slip correction does not consider the van der Waals force which would become important as the particle approaches the molecular size. It is for these and other reasons (e.g., non-spherical particle shapes) that the particle size in eq. (1) is termed the mobility size, rather than the actual size.

This difficulty is now removed as the result of a transport theory of small, spherical particles developed recently from a rigorous gas-kinetic theory analysis [56,57]. In this theory, the electric mobility in the limit of zero field strength and free molecule regime is expressed by

$$Z = N_c q / \left( \frac{8}{3} \sqrt{2\pi m_r kT} N_g R_p^2 \Omega_{\infty}^{(1,1)*} \right), \quad (2)$$

where  $m_r$  is the reduced mass of the carrier gas molecule and the particle,  $k$  is the Boltzmann constant,  $T$  is the temperature,  $R_p$  is the particle radius. Mathematical expressions for the transition and continuum regimes are also available, through a similar analysis [57]. In Eq. (2),  $\Omega_{\infty}^{(1,1)*}$  is the average, reduced collision integral, which unfortunately remain empirical. It is known that this integral is dependent on the particle size and material, temperature, and the nature of the carrier gas [57]. More importantly, there is a marked transition of the momentum transfer mechanism, from specular scattering at molecular/cluster sizes to diffuse scattering for particles a few nanometers in diameter [57-59]. A theory that can capture all of effects are being developed. Mean-

while, the collision integral is expressed empirically by considering two limiting scattering cases for which rigorous mathematical expressions have been developed:

$$\Omega_{sc}^{(1,1)*} = (1 - \varphi)\Omega_s^{(1,1)*} + \varphi\Omega_d^{(1,1)*} \quad (3)$$

where  $\Omega_s^{(1,1)*}$  and  $\Omega_d^{(1,1)*}$  are the reduced collision integrals in the limiting cases of specular and diffuse scattering. The values of these limiting integrals have been tabulated and parameterized [57]. In eq. (3),  $\varphi$  is the momentum accommodation function. At present, this function may be obtained only empirically by fitting the TEM radius or mass of particles against electric mobility. Direct measurement for soot particles over the specular-to-diffuse transition is unavailable. For carbon-like materials, a tentative assignment of  $\varphi$  was made [59,60] on the basis of the polyethylene glycol data of Fernández de la Mora and coworkers [61,62]. The difference between eqs. (2) and (1) and thus the corrections needed to be made on the mobility diameter of a typical DMA may be parameterized by [60]

$$R_p/\tilde{R}_p = \left( 1.0676 - \frac{0.2232}{\tilde{R}_p} \right) \tanh\left( 1.4334 + 0.02496\tilde{R}_p \right) \quad (4)$$

for  $1 \leq \tilde{R}_p \leq 100$  nm. For mobility radius  $\tilde{R}_p \geq 6$  nm,  $0.95 \leq R_p/\tilde{R}_p \leq 1.06$ . For smaller particles, the mobility size is larger than the true particle size. For example,  $R_p/\tilde{R}_p$  is equal to 0.74 at  $\tilde{R}_p = 1$  nm.

A popular method of particle sampling uses a thin-wall, straight-through tube [33,34] in which the particle sample transverses a small orifice and is diluted by a large flow of cold nitrogen subsequently. This technique has the advantage that it can be easily adapted for particle collections and chemical analysis [39]. A key challenge of this technique is that particle losses due to particle-particle coagulation and particle diffusion to the wall must be carefully controlled. Methods to reduce particle losses have been discussed in detail [33,34]. In general, mobility measurements using commercial SMPS are capable of probing particles as small as  $\sim 3$  nm. It is possible to extend the lower-size limit to about 1.5 nm using an aerosol electrometer instead of a condensation nuclei counter [41, 63]. However, diffusive losses and size broadening become important factors that limit the experimental accuracy for particles just a few nanometers in size.

**2.2. Small angle neutron scattering**

Irradiating a particle laden flame with cold neutrons scatters coherently a small fraction of the incident neutrons [64]. For a dilute, spherical particle sample the coherent component of the scattering intensity is

$$I(q) = \int N_p(R_p) P(q, R_p) dR_p \quad (5)$$

where  $N_p$  is the particle size distribution function (PSDF),  $P(q, R_p)$  is the form factor, and  $q = (4\pi/\lambda)\sin(\theta/2)$  is the magnitude of the momentum transfer vector for neu-

tron wavelength  $\lambda$  and scattering angle  $\theta$ . Particle material properties enter into the form factor as

$$P(q, R_p) = \left[ 4\pi\rho_b (\sin qR_p - qR_p \cos qR_p) \right]^2 / q^6, \quad (6)$$

where  $\rho_b$  is the coherent scattering length density. It may be assumed that soot contain only carbon and hydrogen [31] and that

$$\rho_b = \rho_s (b_C + b_H/\gamma) / (m_C + m_H/\gamma), \quad (7)$$

where  $b_C$  and  $b_H$  are the scattering lengths of carbon and hydrogen, respectively,  $\rho_s$  is the mass density of soot material, and  $\gamma$  is the atomic C/H ratio.

In theory, a measurement of the scattering intensity  $I$  as a function of  $q$  yields the particle size distribution  $N_p(R_p)$ , but the inverse problem requires the use of a distribution function assumed for  $N_p(R_p)$ . In addition, the mass density and the particle composition are uncertain especially for nascent particles. Hence while the non-intrusive nature of the technique is attractive, an interpretation of the SANS data would have to be aided by data taken from independent techniques [42]. Because of the dependency of the scattering cross section on soot material properties, including the C/H ratio and mass density, the method also presents some opportunities to probe these properties, as will be discussed later.

### 2.3. Particle mass spectrometry

In the PIAMS technique, an aerosol lens system focuses the particles into a tight beam [39,49]. The aerosol passes through differential pumping stages and deposits on an aluminum probe. An infrared laser pulse desorbs semivolatile material from the probe, followed by an ultraviolet laser pulse that gently ionizes the plume. Because typical ionization potentials for PAH are on the order of 8 eV, fragmentation of PAH is minimal. The ions are analyzed using a reflectron time-of-flight mass spectrometer. To increase the chemical resolution of the instrument, a new generation of aerosol mass spectrometry [65] may be used in future studies. This aerosol mass spectrometry utilizes temperature programmed thermal desorption rather than photodesorption. In addition, the ion mobility of desorbed species and its mass may be closely examined.

## 3. RESULTS AND DISCUSSION

### 3.1. Particle size distribution functions in lightly sooting flames

It has become increasingly evident that nascent soot formed in premixed ethylene flames takes mostly a bimodal size distribution. Earlier studies [37] using the probe sample/SMPS technique show that for flame temperatures lower than 1800 K the soot PSDFs are decidedly bimodal, but for flame temperature higher than 1800 K the PSDFs are apparently unimodal. Subsequent sensitivity analyses using a detailed gas-

phase and gas-surface model with stochastic solution of aerosol dynamics [60] suggested that the apparent unimodality is a consequence of the lower-size cutoff limit of the SMPS ( $\sim 3$  nm). A recent experimental study showed that this is indeed the case [63]. Figure 1 shows the evolution of the soot PSDFs in an atmospheric-pressure, lightly sooting, burner-stabilized ethylene flame (16.3% $\text{C}_2\text{H}_4$ -23.7% $\text{O}_2$ -Ar flame, equivalence ratio  $\phi = 2.07$ , unburned gas velocity = 13 cm/s). With the use of an aerosol electrometer, the lower diameter limit of detection was extended to 1.6 nm. As seen, even at the maximum flame temperature of 1898 K ( $\pm 50\text{K}$ ), the distribution remains bimodal. Figure 2 shows similar plots of PSDFs in a flame with an identical unburned gas composition but a lower flame temperature ( $T_f = 1736 \pm 50\text{K}$ ). Qualitatively the size distributions beyond nucleation are identical between Figures 1 and 2. Quantitatively, they differ notably, as will be discussed later.

In general, the observed bimodality can be described by a bi-lognormal distribution function,

$$\frac{dN}{d \log D_p} = \sum_{k=1}^2 \frac{N_k}{\sqrt{2\pi} \log(\sigma_k)} \exp \left\{ -\frac{[\log(D_p / \langle D_p \rangle_k)]^2}{2[\log(\sigma_k)]^2} \right\}, \quad (8)$$

where  $D_p$  is the particle diameter,  $N$  is the number density, and  $N_k$ ,  $\sigma_k$ , and  $\langle D_p \rangle_k$  are parameters of the size distribution function, i.e., the number density, geometric standard deviation, and median diameter of the  $k^{\text{th}}$  mode, respectively. Selected parameter values are shown in Figures 1 and 2. The fits to the small-size mode are less certain because of truncation of the particle diameter below 1.6 nm. In general, a logarithmic function fits the data equally well. In comparison, the fits to the large-size mode are more reliable. As seen, the median diameter increases with an increase in the distance above the burner surface  $H$ . The distribution broadens accordingly, with the  $\sigma_2$  value increases from 1.35 at  $H = 0.35$  cm to 1.46 at  $H = 0.65$  cm, as expected from coagulation-dominated size growth. Meanwhile, the total number density remains relatively constant, which is indicative of the competition between persistent particle nucleation and particle-particle coagulation.

As was discussed in an early study [33], the bimodality is the result of competition between particle nucleation that persists into the post flame and particle-particle coagulation. Simple aerosol dynamics calculations show that as long as the nucleation kinetics is second-order in the monomer concentration and the monomer concentration does not drop to zero, the resulting size distribution is bimodal [33]. In addition, the persistence of the small particles is a steady-state kinetic phenomenon, though at the first glance the PSDF data may suggest that the smallest particles are resistant to mass and size growth. In fact, the disparity in the coagulation kernels causes the small, newly nucleated particles to preferentially coagulate with large particles. Meanwhile, the nuclei are continuously replenished through particle nucleation which persists well into the region of primary particle mass and size growth.

There are several key features observed for the distribution functions of nascent soot particles. We present these features in Figure 3. Because of instrument limitations, the current DMA can only probe particles down to  $\sim 1.6$  nm. This instrument cutoff is sufficiently close to the molecular size. For comparison, a pyrene molecule has a van

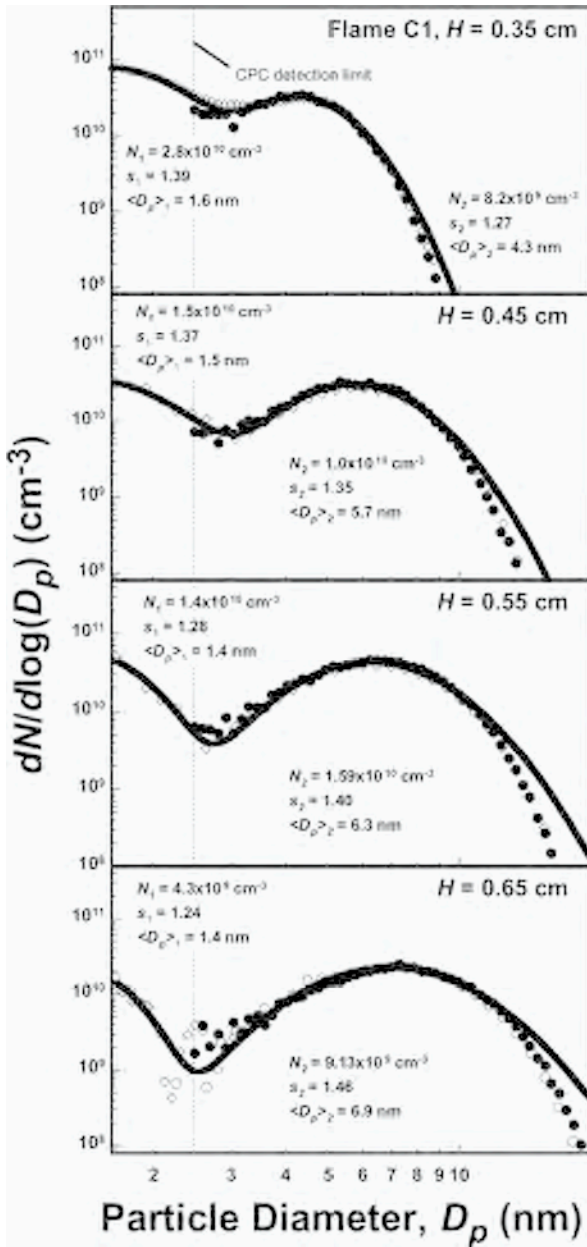


Figure 1. Evolution of particle size distribution functions of nascent soot in a 16.3% $\text{C}_2\text{H}_4$ -23.7% $\text{O}_2$ -Ar flame ( $\phi = 2.07$ ,  $p = 1$  atm, maximum flame temperature  $T_f = 1898 \pm 50\text{K}$ , cold gas velocity  $v = 13$  cm/s). Symbols are data taken from ref. 63 (filled symbols: condensation nuclei counter; open symbols: aerosol electrometer). Lines are fits to data using a bi-lognormal distribution function. Because of data truncation at 1.6 nm, the fits to the small size mode is less certain than those of the large size mode. The position  $H$  was shifted by 0.35 cm upstream due to flame perturbation by the probe [66].

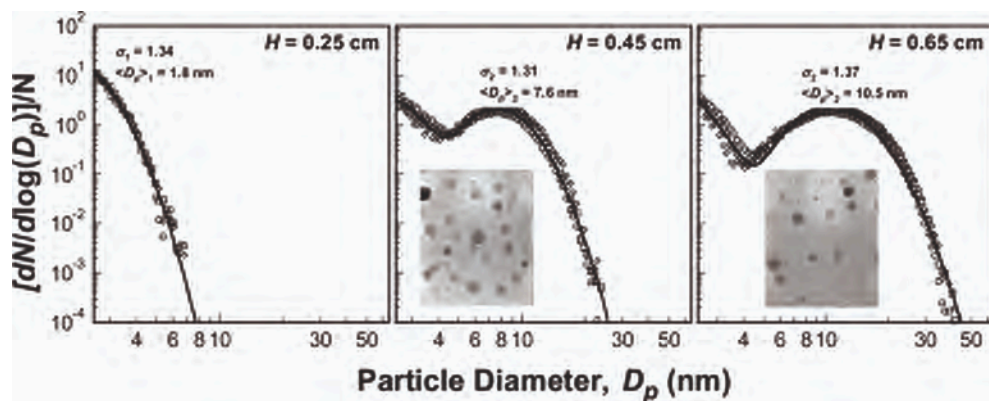


Figure 2. Evolution of particle size distribution functions of nascent soot in a 16.3% $C_2H_4$ -23.7% $O_2$ -Ar flame ( $\phi = 2.07$ ,  $p = 1$  atm,  $T_f = 1736 \pm 50$  K, cold-gas velocity  $v = 8$  cm/s) [63]. The spatial positions are shifted by 0.35 cm upstream to account for the probe cooling effect, as discussed in [63]. Lines are fits to data by a sum of two log-normal distribution functions. Inset: TEM images of particle samples collected by the rapid insertion technique.

der Waals collision diameter around 0.7 nm. Hence, below this cutoff we probably enter into the characteristic size of soot precursors or a small clusters of the precursors (i.e., the shaded area of Figure 3 where two distributions are postulated). Based on the discussion earlier, the bimodality consists of two modes: *persistent nuclei* and *primary soot particles*. They are separated by a trough.

The position of the trough may be characterized by the diameter  $D_{p,t}$ . Figure 4 presents the  $D_{p,t}$  values sampled in a series of flames of identical unburned reactant composition, but with varying flame temperatures. It is seen that  $D_{p,t}$  is relatively invariant in each flame, but the trough moves to larger particle sizes as the flame temperature is reduced. In general, a reduced flame temperature causes a smaller extent of precursor fragmentation, and hence a greater extent of persistent nucleation in the region of primary soot mass and size growth [37]. Indeed, as the flame temperature is reduced the persistent nuclei become more dominant in number in comparison to the primary soot particles, and consequently, the trough becomes shallower. In a numerical sensitivity analysis, Singh et al. [60] concluded that an increased  $D_{p,t}$  may be accomplished by increases in nucleation monomer size, nucleation rate, or surface growth rate. However, a simultaneous increase in  $D_{p,t}$  and a decrease in the trough depth, as observed with a decreased flame temperature, can be achieved only through an increased monomer size. This is in contrast to a large number of soot models in which the monomer size is assumed to be constant. Although an increased monomer size may be explained thermodynamically (due to the reduced rate of PAH fragmentation at reduced flame temperature), kinetically a drastically increased monomer size towards lower flame temperature infers a significantly faster PAH growth rates, which remains puzzling.

The persistent nuclei discussed above are basically the ubiquitous Nano Organic Carbon (NOC), a term championed by D'Alessio, D'Anna and coworkers over a long

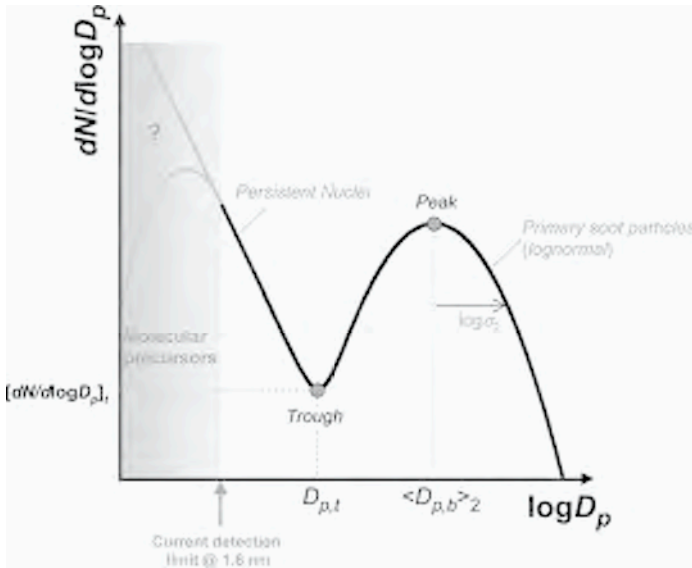


Figure 3. Characteristic nascent soot particle diameters and their corresponding number distribution in premixed, lightly sooting flames of ethylene-oxygen-argon.

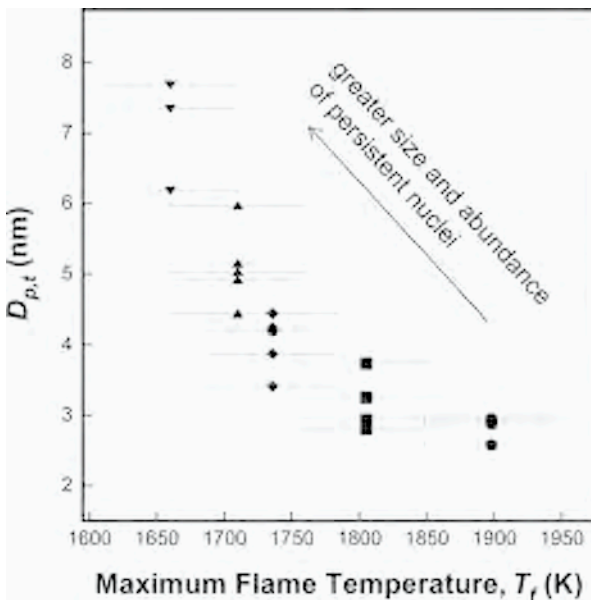


Figure 4. Variation of particle diameter at the trough sampled from  $H = 0.35$  to  $0.85$  cm, as a function of the maximum flame temperature ( $16.3\%C_2H_4-23.7\%O_2-Ar$ ,  $\phi = 2.07$ ,  $p = 1$  atm, cold gas velocity varied from  $5.5$  to  $13$  cm/s).

period of time [67-71]. What remains to be a point of debate is whether persistent nuclei (or NOCs) present different chemistry and physics, in a way that would influence the mass and size growth of the primary particles in a manner not currently understood. It is quite possible that this material has chemical and optical properties different from the grown, primary soot particles. However, growing experimental and computational evidence [33, 37, 60] suggests that to the first order these nuclei are the result of particle nucleation kinetics and aerosol dynamics, and more specifically, it is related to the second-order nucleation kinetics [33]. The lack of apparent size growth of these persistent nuclei is not because of their small coagulation efficiencies, but it is the result of steady-state competition of particle nucleation as the source and the coagulation of these nuclei with larger, primary soot particles as the sink.

The size distribution of the primary particle mode is ubiquitously lognormal. Figure 5 shows the variation of median particle diameter of this mode for a series of flames of different maximum flame temperatures and as a function of time beyond the point of the maximum flame temperature. As expected, the size growth of primary particles occurs earlier in higher temperature flames ( $> 1800$  K), but they do not grow to sizes as large as those in flames with somewhat lower flame temperature (1700 to 1800 K). The time-shift of particle size growth is indicative of the finite rate gas-surface reaction kinetics, yet the lack of apparently higher size growth rate at high flame temperatures is probably thermodynamic in nature. Namely, fragmentation or reversible condensation and coagulation play an increasingly important role above 1800 K.

### 3.2. Particle size distribution functions in a heavily sooting flame

In heavily sooting flames the particle size distribution remains bimodal. Figure 6 shows the evolution of the PSDFs for a premixed, burner stabilized ethylene flame (14.1% $C_2H_4$ -17.0% $O_2$ -Ar,  $\phi = 2.5$ ,  $p = 1$  atm,  $T_f = 1590 \pm 50$  K) [39]. At a first glance, the PSDFs appear to be an extension of those of Figures 1 and 2, but the cause for bimodality is fundamentally different. First, the small-size mode is not persistent nuclei seen in the lightly sooting flames. Particles in that mode are in fact primary soot, as evidenced by the TEM images accompanying the PSDF profiles. Before the separation of the two size modes (the middle panel of Figure 6), the particles sampled are nearly spherical, primary particles. After separation (the right panel), the particles are either aggregates, which correspond to those in the large-size mode, or single, spherical particles, which correspond to the small-size mode. In contrast, for the lightly sooting flames the large-size mode of PSDFs contains primary particles only, as seen in the inset of Figure 2. Unlike the lightly sooting flame, there is no evidence of persistent nuclei in this heavily sooting flame. The cause is likely to be PAH depletion resulting from a drastically increased rate of PAH scavenging by soot particles [7].

We label the bimodality that occurs in the lightly sooting, low C/O ratio flames as type I and that of heavily sooting, high C/O ratio flames as type II. Figure 7 summarizes the results obtained for premixed ethylene flames at the atmospheric pressure in the C/O ratio-versus-maximum flame temperature parameter space. As seen, type I bimodality has been studied quite extensively above the critical sooting threshold and towards the high-temperature side of the inverted bell curve of critical C/O ratio. In

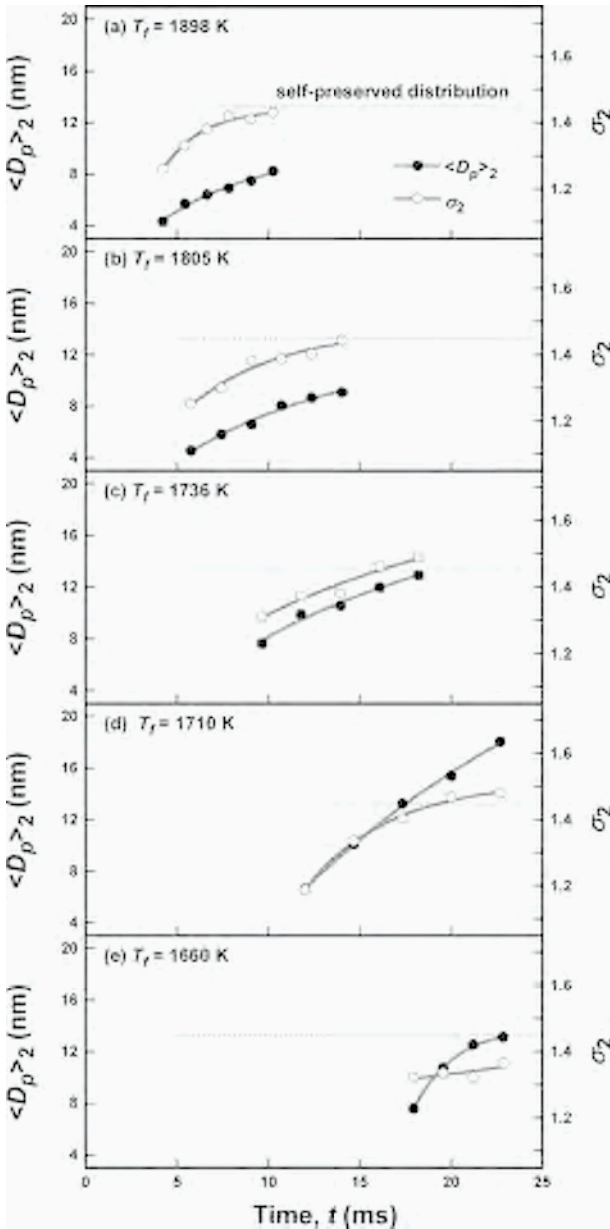


Figure 5. Variations of median diameter  $\langle D_p \rangle_2$  and geometric standard deviation  $\sigma_2$  of primary soot as a function of convective time beyond the maximum flame temperature.

contrast, studies on type II bimodality have been limited. It remains unclear whether the same bimodalities are present towards the low-temperature side of the inverted bell curve.

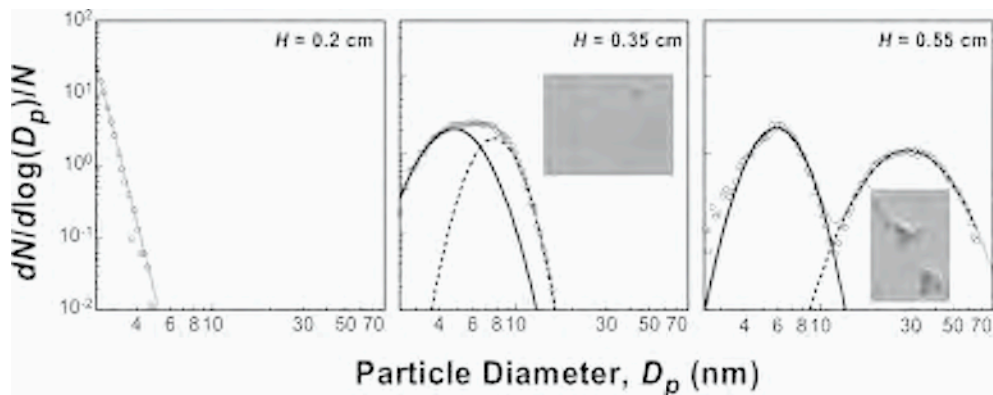


Figure 6. Evolution of particle size distribution functions of nascent soot in a 14.1% $C_2H_4$ -17.0% $O_2$ -Ar flame ( $\phi = 2.5$ ,  $p = 1$  atm,  $T_f = 1590 \pm 50$  K) [39]. The spatial positions are shifted by 0.35 cm to account for the probe cooling effect, as discussed in [63]. Lines are fits to data by a sum of two log-normal distribution functions. TEM studies show that for small  $H$  values particles are spherical and at large  $H$  values particles are of both single primary particles and aggregates (see, the insets in the middle and right panels).

### 3.3. Chemical composition and appearance of substrate deposited particles

Nascent soot particles spread on the substrate surface upon deposition by thermophoretic sampling. Barone et al. [73] used the AFM technique to probe particles deposited on mica and showed that soot particles are flattened. This result is independently reproduced by Abid et al. [63, 66]. In general, the particles imaged can be approximated as a spherical top (see, the inset of Figure 8), which may be characterized by two geometric parameters: height  $b$  and diameter  $a$ . Figure 8 shows the variation of the  $b/a$  ratio as a function of the spherical volume equivalent diameter

$$D_{s,VM} = \left[ b \left( \frac{3}{4} a^2 + b^2 \right) \right]^{1/3} \quad (9)$$

in two flames, i.e., those of Figures 1 and 3, and at two different flame positions. The  $b/a$  ratio does not appear to be dependent on the flame temperature or spatial position. The extent of flattening or spreading is clearly evidenced by the fact that in most cases the observed  $b/a$  ratio is substantially smaller than unity. Combined with the observation that the  $b/a$  ratio generally increases with an increase in the particle size, the results may be interpreted as the particles being flattened upon impact, eventually quenching into hills as they lose heat to the surface and solidify. In other words, nascent particles are liquid-like, far from being carbonized.

TEM studies show corroborating evidence of particle spreading upon impact with a surface. Examples are presented in the middle panels of Figures 2 and 6. These micrographs show that the apparent particle diameter is substantially larger than the diameter observed by mobility measurements, in agreement with the AFM results. The spreading of nascent soot on a surface is in direct contrast to similar studies on nano-

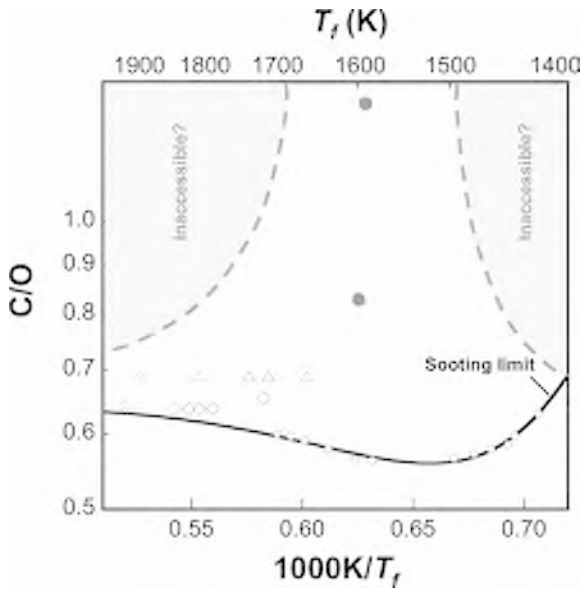


Figure 7. Variations of PSDF types observed for atmospheric-pressure, premixed ethylene flames. Open circles: sooting limit [72]; open triangles [66] and open diamonds [34]: bimodality of type I; filled symbols: bimodality of type II [39]. The inaccessible regions are speculative and for the purpose of illustration only.

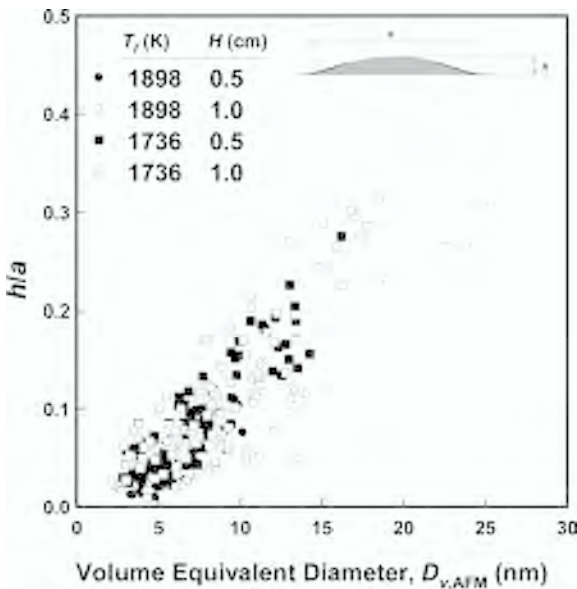


Figure 8. Apparent height( $h$ )-to-diameter( $a$ ) ratio of soot sampled by AFM as a function of the spherical volume-equivalent diameter. Soot samples were collected from flames with conditions of Figures 1 and 2.

sized single-crystal anatase  $\text{TiO}_2$  particles. It was shown that the particle diameter measured by electric mobility agrees very well with the size of substrate deposited sample probed by TEM and with the crystalline size of bulk  $\text{TiO}_2$  particle samples probed by X-ray diffraction [42]. Hence, the lack of spreading of the single-crystal  $\text{TiO}_2$  particles and the significant spreading observed for nascent soot is a direct indication that primary soot particles in the ethylene flame studied are tar-like without any evidence of carbonization.

The lack of carbonization is in fact supported by observations made with an array of other techniques, including PIAMS and SANS. Using PIAMS, we detected a substantial amount of aliphatic side chains in soot sampled in the heavily sooting flame ( $\phi = 2.5$ , see, Figure 6) [39]. This finding appears to be consistent with the notion of “precursor” soot in coflow diffusion flames discussed by Dobbins and coworkers [74]. As shown in Figure 9, the main chemical constituents of nascent soot are polycyclic aromatic hydrocarbons (PAHs). The PAHs observed ranged from  $\text{C}_{16}\text{H}_{10}$  (pyrene) to  $\text{C}_{32}\text{H}_{14}$ , with the most abundant being  $\text{C}_{22}\text{H}_{12}$  and  $\text{C}_{24}\text{H}_{12}$  (coronene). The distribution of the PAHs does not vary as a function of position above the burner surface or particle age, indicating that there is little carbonization. Meanwhile, the amount of aliphatic side chains in the soot and the H/C ratio increases with the distance from the burner surface. Because the temperature of the flame studied is rather low ( $\sim 1400$  K in the post flame where the increase in the H/C ratio was observed), the results should not be generalized to other flames. Nonetheless, the distribution of the constituent molecular units allowed us to determine the atomic H/C ratio to be about unity, which is substantially larger than the traditional value ranging from 1/8 to 1/6. Similar expe-

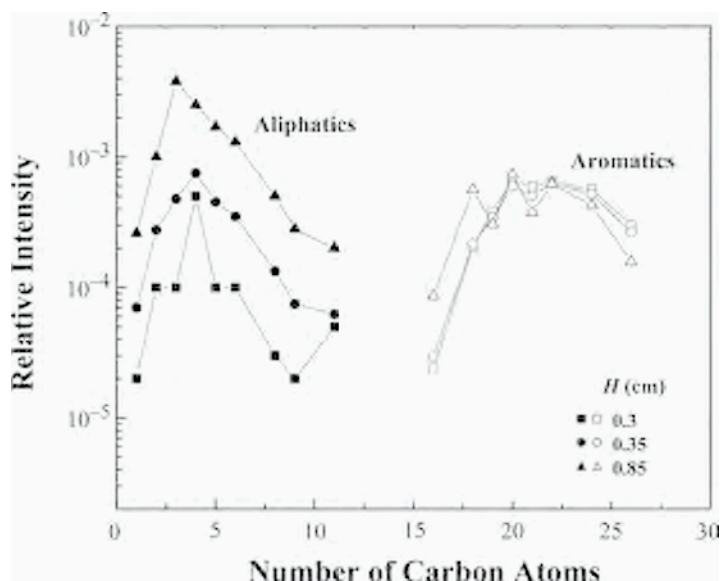


Figure 9. Relative abundance of chemical substructures of nascent soot sampled in a heavily sooting flame (see, the caption of Figure 6) as determined by the PIAMS [39].

periments were conducted for an ethylene flame with  $\phi = 4.0$ . The aromatics and aliphatics distributions were found to be similar to the flame at  $\phi = 2.5$ .

Other evidence for the high H/C ratio (and the corresponding low particle mass density) comes from a re-interpretation of data collected in an earlier SANS study [31]. It was shown [42] that in order to reconcile the soot volume fractions measured by Thermocouple Particle Densitometry, a technique developed by McEnally, Rosner and coworkers [75], and by inverting the data of neutron scattering cross section  $I$  using eq. (5), the atomic C/H ratio  $\gamma$  in eq. (7) must be as small as unity and the mass density  $\rho_s$  in the same equation must be as small as 1.5 g/cm<sup>3</sup>.

#### 4. SUMMARY

Three important conclusions may be drawn from observations made with a suite of experimental tools:

- (1) Size distribution functions of nascent soot in premixed ethylene flames are bimodal. In type I bimodality, the distribution consists of persistent nuclei and primary soot particles. In type II bimodality the distribution consists of two lognormal modes with the small-size mode being the primary particles and the large-size mode being the aggregates. The various features of the bimodality, including the particle size at the trough separating the two modes and the lognormal size distribution of the primary particles, offer useful test cases for model development and validation and for advancing a more basic understanding of the reaction kinetics and particle dynamics for nascent soot particles.
- (2) Evidence collected from TEM, AFM, SANS, SMPS, and PIAMS conclusively show that nascent particles exhibit behaviors that are liquid-like, and that because of the presence of aliphatic compounds and a lack of size growth of the PAH molecular units, the H/C ratio may be as large as unity, which is substantially larger than the values previously thought. Likewise, nascent soot should have mass densities close to 1.5 g/cm<sup>3</sup>, smaller than the 1.8 g/cm<sup>3</sup> assumed in a large number of soot models.
- (3) The basic building blocks of nascent soot particles are polycyclic aromatic hydrocarbons (from C<sub>16</sub>H<sub>10</sub> to C<sub>32</sub>H<sub>14</sub>), with C<sub>22</sub>H<sub>12</sub> and C<sub>24</sub>H<sub>12</sub> being the most abundant species.

#### ACKNOWLEDGEMENTS

This work was supported by the Strategic Environmental Research and Developmental Program and by the National Science Foundation (CBET 0651990). The authors wish to thank Dr. Markus Kraft and Professor Angela Violi for helpful discussion.

#### REFERENCES

1. M. Frenklach, H. Wang, Proc. Combust. Inst. 23 (1991) 1559-1566.

2. M. Frenklach, H. Wang, in *Soot Formation in Combustion: Mechanisms and Models of Soot Formation*, H. Bockhorn (Ed.) Springer Series in Chemical Physics, vol. 59, Springer-Verlag, Berlin, 1994, pp. 162-190.
3. P. Markatou, Wang, H., Frenklach, M., *Combust. Flame* 93 (1993) 467-482.
4. M. B. Colket, R. J. Hall, in *Soot Formation in Combustion: Mechanisms and Models of Soot Formation*, H. Bockhorn (Ed.) Springer Series in Chemical Physics, vol. 59, Springer-Verlag, Berlin, 1994, pp. 442-468.
5. F. Mauss, T. Schafer, H. Bockhorn, *Combust. Flame* 99 (1994) 697-705.
6. H. Wang, D. X. Du, C. J. Sung, C. K. Law, *Proc. Combust. Inst.* 26 (1996) 2359-2368.
7. A. Kazakov, H. Wang, M. Frenklach, *Combust. Flame* 100 (1995) 111-120.
8. N. M. Marinov, W. J. Pitz, C. K. Westbrook, M. J. Castaldi, S. M. Senkan, *Combust. Sci. Technol.* 116, 211-287 (1996).
9. H. Wang, M. Frenklach, *Combust. Flame* 110 (1997) 173-221.
10. I. M. Kennedy, *Prog. Energy Combust. Sci.* 23 (1997) 95-132.
11. M. D. Smooke, C. S. McNally, L. D. Pfefferle, R. J. Hall, M. B. Colket, *Combust. Flame* 117 (1999) 117-139.
12. J. Appel, H. Bockhorn, M. Frenklach, *Combust. Flame* 121 (2000) 122-136.
13. H. Richter, J. B. Howard, *Prog. Energy Combust. Sci.* 26 (2000) 565-608.
14. C. S. McEnally, L. D. Pfefferle, A. M. Schaffer, M. B. Long, R. K. Mohammed, M. D. Smooke, M. B. Colket, *Proc. Combust. Inst.* 28 (2000) 2063-2070.
15. M. Frenklach, *Phys. Chem. Chem. Phys.* 4 (2002) 2028-2037.
16. A. Violi, A. D'Anna, A. D'Alessio, A. F. Sarofim, *Chemosphere* 51 (2003) 1047-1054.
17. A. D'Anna, A. Violi, *Energy Fuel.* 19 (2005) 79-86.
18. H. Richter, S. Granata, W. H. Green, J. B. Howard, *Proc. Combust. Inst.* 30 (2005) 1397-1405.
19. J. Singh, M. Balthasar, M. Kraft, W. Wagner, *Proc. Combust. Inst.* 30 (2005) 1457-1465.
20. C. A. Schuetz, M. Frenklach, *Proc. Combust. Inst.* 29 (2002) 2307-2314.
21. A. Violi, A. F. Sarofim, G. A. Voth, *Combust. Sci. Technol.* 176 (2004) 991-1005.
22. A. Violi, A. Kubota, T. N. Truong, W. J. Pitz, C. K. Westbrook, A. F. Sarofim, *Proc. Combust. Inst.* 29 (2002) 2343-2349.
23. H. A. Gray, G. R. Cass, *Atmos. Environ.* 32 (1998) 3805-3825.
24. D. W. Dockery, C. A. Pope, S. Xu, J. D. Spengler, *New England J. Med.* 329 (1993) 1753-1759.
25. J. Haywood, V. Ramaswamy, *J. Geophys. Res.* 103 (1998) 6043-6058.
26. J. E. Penner, C. C. Chuang, K. Grant, "Climate change and radiative forcing by anthropogenic aerosols: A review of research during the last five years" in *La Jolla International School of Science*. La Jolla, CA, The Institute for Advanced Physics Studies, 1999.
27. J. T. Houghton, Y. Ding, D. J. Griggs, M. Noguera, P. J. van der Linden, X. Dai, in *Climate change 2001: the Scientific Basis*, K. Maskell, C. A. Johnson (Eds). Cambridge University Press, Cambridge, UK, 2001, chapt. 6.
28. S. Menon, J. Hansen, L. Nazarenko, Y. Luo, *Science* 297 (2002) 2250-2253.
29. J. P. Hessler, S. Seifert, R. E. Winans, T. H. Fletcher, *Faraday Discuss.* 119 (2002) 395-407.
30. J. P. Hessler, S. Seifert, R. E. Winans, *Proc. Combust. Inst.* 29 (2002) 2743-2748.
31. H. Wang, B. Zhao, B. Wyslouzil, K. Streletzky, *Proc. Combust. Inst.* 29 (2002) 2749-2757.
32. H. Wang, B. Wyslouzil, "Spatially-resolved measurement of soot dynamics in heavily sooting flames," NIST Neutron Research Facility Report, 2003.

33. B. Zhao, Z. Yang, M. V. Johnston, H. Wang, A. S. Wexler, M. Balthasar, M. Kraft, *Combust. Flame* 133, (2003) 173-188.
34. B. Zhao, Z. Yang, J. Wang, M. V. Johnston, H. Wang, *Aerosol Sci. Technol.* 37 (2003) 611-620.
35. M. M. Maricq, S. J. Harris, J. J. Szente, *Combust. Flame* 132 (2003) 328-342.
36. M. M. Maricq, *Combust. Flame* 137 (2004) 340-350.
37. B. Zhao, Z. Yang, Z. Li, M. V. Johnston, H. Wang, *Proc. Combust. Inst.* 30 (2005) 1441-1448.
38. M. M. Maricq, *Combust. Flame* 141 (2005) 406-416.
39. B. Öktem, M. P. Tolocka, B. Zhao, H. Wang, M. V. Johnston, *Combust. Flame* 142 (2005) 364-373.
40. M. M. Maricq, *Combust. Flame* 144 (2006) 730-743.
41. L. A. Sgro, A. De Filippo, G. Lanzaolo, A. D'Alessio, *Proc. Combust. Inst.* 31 (2007) 631-638.
42. B. Zhao, K. Uchikawa, H. Wang, *Proc. Combust. Inst.* 31 (2007) 851-860.
43. M. Thierley, H.-H. Grotheer, M. Aigner, Z. Yang, A. Abid, B. Zhao, H. Wang, *Proc. Combust. Inst.* 31 (2007) 639-647.
44. S. L. Manzello, D. B. Lenhert, A. Yozgatligil, M. T. Donovan, G. W. Mulholland, M. R. Zachariah, W. Tsang, *Proc. Combust. Inst.* 31 (2007) 675-683.
45. A. M. Nienow, J. T. Roberts, M. R. Zachariah, *J. Phys. Chem. B.* 109 (2005) 5561-5568.
46. H. J. Jung, D. B. Kittleson, M. R. Zachariah, *Combust. Flame* 136 (2004) 445-456.
47. K. J. Higgins, H. J. Jung, D. B. Kittleson, J. T. Roberts, M. R. Zachariah, *J. Phys. Chem. A* 106 (2002) 96-103.
48. S. H. Kim, R. A. Fletcher, M. R. Zachariah, *Environ. Sci. Technol.* 39 (2005) 4021-4026.
49. B. Öktem, M. P. Tolocka, M. V. Johnston, *Anal. Chem.* 76(2004) 253-261.
50. E. Cunningham, *Proc. R. Soc. London* 83 (1910) 357-365.
51. M. Knudsen, S. Weber, *Ann. Phys.* 36 (1911) 981-994.
52. G. G. Stokes, *Mathematical and Physical Papers*, Vol. III, No. 33, Johnson Reprint Corp, 1966.
53. R. A. Millikan, *Science* 32 (1911) 349-397.
54. R. A. Millikan, *Phil. Mag.* 34 (1917) 1-30.
55. R. A. Millikan, *Phys. Rev.* 21 (1923) 217-238.
56. Z. Li, H. Wang, *Phys. Rev. E.* 68 (2003) article 061206.
57. Z. Li, H. Wang, *Phys. Rev. E.* 68 (2003) article 061207.
58. Z. Li, H. Wang, *Phys. Rev. Lett.* 95 (2005) article 014502.
59. H. Wang, "Transport properties of small spherical particles," *Annals of the New York Academy of Science (Interdisciplinary Transport Phenomena V: Fluid, Thermal, Biological, Materials & Space Sciences, S. S. Sadhal Ed.)*, in press, 2008.
60. J. Singh, R. I. A. Patterson, M. Kraft, H. Wang, *Combust. Flame* 145 (2006) 117-127.
61. A. G. Nasibulin, E. I. Kauppinen, B. A. Thompson, J. Fernández de la Mora, *J. Nanoparticle Res.* 4 (2002) 449-453.
62. S. Ude, J. Fernández de la Mora, *J. Aerosol. Sci.* 34 (2003) 1245-1266.
63. A. D. Abid, E. D. Tolmachoff, D. J. Phares, H. Wang, Y. Liu, Y., A. Laskin, *Proc. Combust. Inst.* (2008) doi:10.1016/j.proci.2008.07.023.
64. G. Wilemski, *Phys. Rev. E* 61 (2000) 557-564.
65. D. J. Phares, personal communication, 2007.
66. A. D. Abid, N. A. Heinz, E. D. Tolmachoff, D. J. Phares, H. Wang, "On evolution of particle size distribution functions of soot in premixed ethylene-oxygen-argon flames," *Combust. Flame*, in press, 2008.

67. A. D'Alessio, A. D'Anna, A. D'Orsi, P. Minutolo, R. Barbella, A. Ciajolo, *Proc. Combust. Inst.* 24 (1992) 973-980.
68. A. D'Anna, D'Alessio, P. Minutolo, in *Soot Formation in Combustion: Mechanisms and Models of Soot Formation*, H. Bockhorn (Ed.) Springer Series in Chemical Physics, vol. 59, Springer-Verlag, Berlin, 1994, pp. 83-103.
69. P. Minutolo, G. Gambi, A. D'Alessio, *Proc. Combust. Inst.* 27 (1998) 1461-1469.
70. A. D'Alessio, A. D'Anna, G. Gambi, P., Minutolo, *J. Aerosol Sci.* 29 (1998) 397-409.
71. P. Minutolo, G. Gambi, A. D'Alessio, S. Carlucci, *Atmos. Environ.* 33 (1999) 2725-2732.
72. T. Hirasawa, C.-J. Sung, Z. Yang, A. V. Joshi, H. Wang, *Combust. Flame* 139 (2004) 288-299.
73. A. C. Barone, A. D'Alessio, A. D'Anna, *Combust. Flame* 132 (2003) 181-187.
74. R. A. Dobbins, R. A. Fletcher, H. C. Chang, *Combust. Flame* 115 (1998) 285-298.
75. C. S. McEnally, U. O. Koylu, L. D. Pfefferle, D. E. Rosner, *Combust. Flame* 109 (1997) 701-720.

# An experimental and modeling study of soot formation during shock-tube pyrolysis of toluene

G.L. Agafonov<sup>1</sup>, I. Naydenova<sup>2</sup>, V.N. Smirnov<sup>1</sup>, P.A. Vlasov<sup>1</sup>, J. Warnatz<sup>2</sup>

<sup>a</sup> *Semenov Institute of Chemical Physics, Russian Academy of Sciences,*

*Kosygin str. 4, 119991 Moscow, Russia. E-mail: iz@center.chph.ras.ru*

<sup>b</sup> *Interdisziplinäres Zentrum für Wissenschaftliches Rechnen, Universität Heidelberg,*

*Im Neuenheimer Feld 368, D-69120 Heidelberg. E-mail: warnatz@ivr.uni-heidelberg.de*

*Abstract: The experiments on the pyrolysis of toluene behind reflected shock waves under oxygen-free conditions were performed. The results obtained are in a good agreement with the experimental measurements performed in [7, 8]. The kinetic model of soot formation was developed. It consists of the gas phase reaction mechanism, which describes the pyrolysis and oxidation of the parent hydrocarbons, in particular toluene, and the formation and growth of PAHs through different reaction pathways up to coronene. The results of calculations are in satisfactory agreement with the experimental measurements of the main gas phase species during shock tube pyrolysis of a toluene/neon mixture [28]. The kinetic model considered was also tested to simulate the H concentration and CH<sub>3</sub> and OH mole fraction profiles measured in shock tube in [29-32]. Two mechanisms of surface growth were tested: the surface HACA mechanism [34, 35] and Harris model of surface growth [36]. Studying the combustion and pyrolysis of toluene is of considerable interest, since it is an important component of practical fuels and a promising model object for elucidating the basic aspects of oxidation and soot formation in hydrocarbon systems. In particular, toluene is notable for its high energetic characteristics and anti-knocking effect [1, 2]. The main goal of the present paper is the experimental and modeling study of soot formation in shock tube pyrolysis of toluene.*

## 1. EXPERIMENTAL SETUP

To provide information for modeling the sooting behavior of toluene, we performed experiments on the pyrolysis of toluene behind reflected shock waves under oxygen-free conditions over wide temperature and concentration ranges.

The experiments were conducted using a shock tube equipped with spectroscopic means of registration. The lengths of the driven and driver sections were 3.2 and 1.5 m, respectively; the inner diameter, 75 mm. The shock wave was initiated by spontaneous rupture of an aluminum-foil diaphragm of required thickness under the action of helium introduced into the driver section. The driven section was evacuated to  $10^{-3}$  Torr by a combination of a forepump and an oil diffusion pump, after which it was twice filled/evacuated (to  $10^{-1}$  Torr) with pure argon used for preparing the working mixtures (99.9994 % pure). The leakage plus degassing rate was measured to be  $\sim 2 \cdot 10^{-3}$  Torr/min.

The measurements were performed behind reflected shock waves. The parameters of the gas behind the reflected shock wave were calculated from the velocity of the incident shock wave and the composition of the test mixture within the framework of the ideal-flow shock-tube theory [3]. The incident wave velocity was measured with a set of three piezoelectric gauges spaced 528 and 280 mm apart, with the last one being located 40 mm from the observation section. The distance from the endplate to the observation section was 15 mm.

To determine the soot yield and the temperature of the soot particles, we used the double-beam absorption-emission arrangement shown in Figure 1. The horizontal optical channel served to measure the absorption by soot particles. The light source was a DKSSh-150 xenon arc lamp fed with a stabilized dc current supply. The required spectral range ( $\lambda = 632.8 \pm 3.5$  nm) was selected with the help of an MDR-4 two-prism monochromator. The light signal was transformed into an electric one with a FEU-39A photomultiplier tube, which, in turn, was fed into the first channel of a S9-8 two-channel digital oscilloscope connected to a PC. Since the effective temperature of the arc lamp is about 5000 K, the contribution from the emission of soot particles, the temperature of which did not exceed 2200 K, can be safely disregarded; i.e., the attenuation of the signal can be considered proportional to optical density of the soot-containing gas in the shock tube.

The vertical channel registered emission from the soot-containing gas. The channel was calibrated with the help of a SI-10-300 tungsten band lamp, which was fed with a homemade current source comprised of a transformer, diode bridge, a series of chokes and capacitors, and an ammeter. The current flowing through the lamp was 22 A, a value

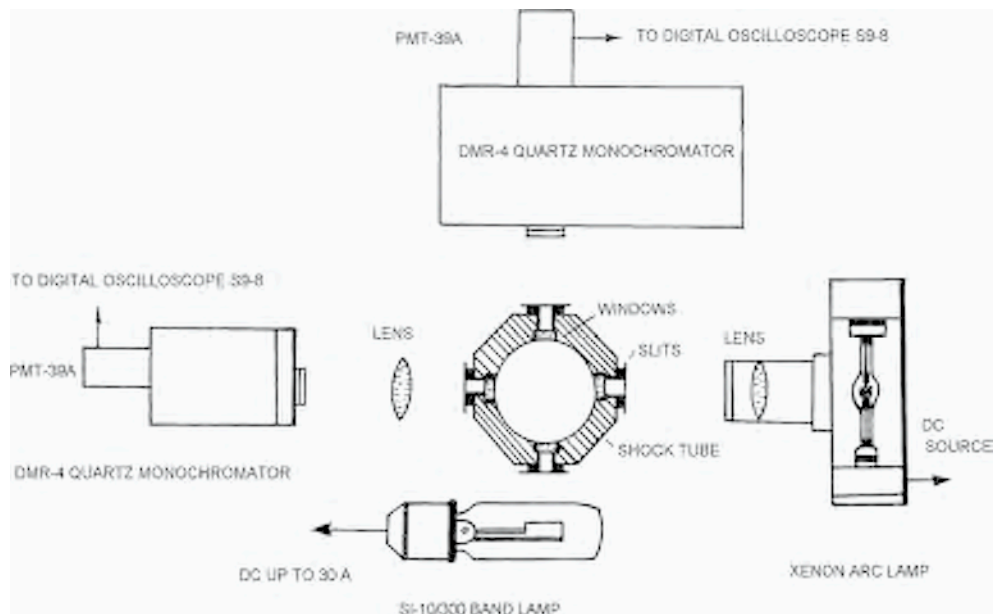


Figure 1. Schematic of the experimental setup used for studying soot formation.

corresponding to a brightness temperature of 2196 K (at  $\lambda = 632.8$  nm). The spectral range of the emission channel, identical to that of the absorption channel ( $\lambda = 632.8 \pm 3.5$  nm), was selected using a MDR-4 two-prism monochromator. The signal from the photomultiplier tube was fed into the second channel of the S9-8 oscilloscope.

An important aspect of the present study was that the concentration of toluene was measured immediately in the shock tube before each series of experiments at a wavelength of 204.2 nm, a feature that made it possible to substantially improve the accuracy of measurements. The absorption coefficient of gaseous toluene was borrowed from [4].

Figure 2 shows typical absorption (frame 1) and emission (frame 2) signals. The emission signal is presented in relative units, in percent with respect to the signal from the calibration band lamp. The time evolution of the soot yield and temperature were calculated under the standard assumptions: the soot particles are spherical and their optical properties are described by the Rayleigh limit (the particle size is much smaller than the wavelength of probing light). The squares in frame 4 demonstrate the calculated gas temperature.

## 2. SOOT YIELD DETERMINATION PROCEDURE

In our case, the absorbance, the logarithm of the ratio of the intensity of incident light to the intensity of light passed through an absorbing layer of length  $l$  containing  $n_i$  particles of radius  $r_i$  ( $i$  is the number of carbon atoms in the particle) in unit volume is given by

$$\ln\left(\frac{I_0}{I}\right) = \sum \sigma_i n_i l \quad (1)$$

where the absorption cross section of a particle of size  $i$  reads as [5]:

$$\sigma_i(\lambda) = \pi r_i^2 \frac{8\pi r_i}{\lambda} E(m) \quad (2)$$

Here,

$$E(m) = -4 \operatorname{Im}\left(\frac{m^2 - 1}{m^2 + 2}\right), \quad (3)$$

where  $m$  is the complex refractive index of soot.

Expressing the particle volume in Eq. (2) through the number of carbon atoms in the particle,

$$\frac{4}{3} \pi r_i^3 = \frac{\mu_c j}{\rho_c N_A},$$

( $\mu_c$  is the molar mass of carbon, 12 g/mol;  $\rho_c$  is the mass density of soot, 1.86 g/cm<sup>3</sup>;  $N_A$  is the Avogadro number,  $6.023 \cdot 10^{23}$ ), it can be recast as

$$\sigma_i(\lambda) = \frac{6\pi\mu_c j}{\lambda\rho_c N_A} E(m) \quad (4)$$

Substituting (4) into Eq. (1) gives

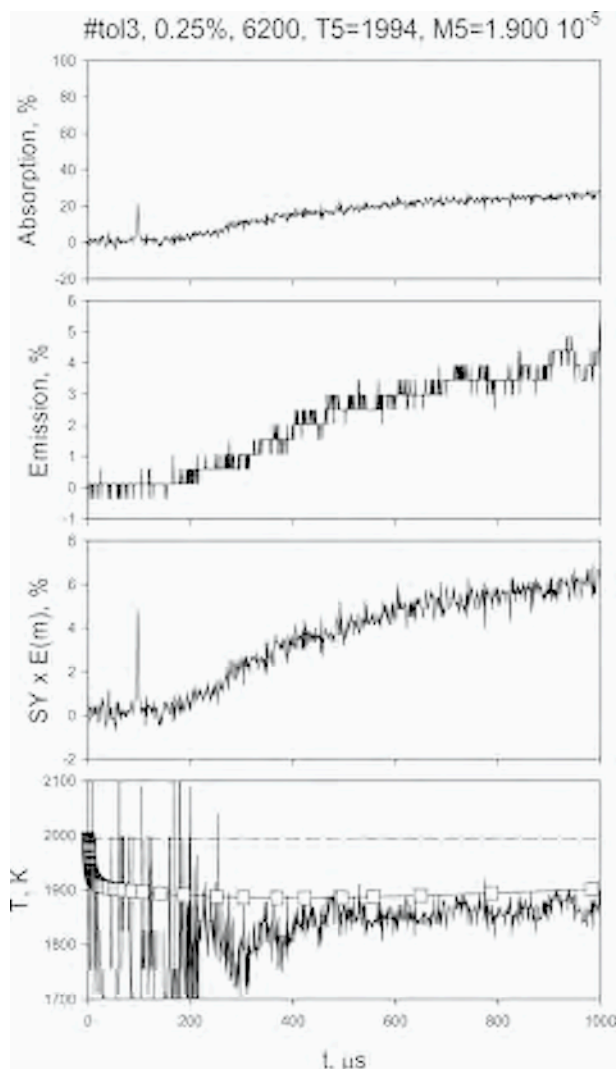


Figure 2. Typical absorption and emission signals and the time dependences of the soot yield and temperature obtained from them for a 0.25% toluene-argon mixture; initial temperature,  $T_5 = 1994$  K; total concentration  $[M]_5 = 1.9 \cdot 10^{-5}$  mol/cm<sup>3</sup>; wavelength,  $\lambda = 632.8$  nm. The emission signal is given in percent with respect to the signal from the calibration band lamp. The time evolution of the soot yield and temperature were calculated under the standard assumptions: the soot particles are spherical and their optical properties are described by the Rayleigh formula (the particle size is much smaller than the wavelength of probing light). The squares in frame 4 represent the calculated gas temperature.

$$\ln\left(\frac{I_0}{I}\right) = \frac{6\pi\mu_c E(m)l}{\rho_c \lambda} \sum \frac{n_l}{N_A} = \alpha E(m)l[C_{\text{soot}}] \quad (5)$$

where  $[C_{\text{soot}}]$  is the molar concentration of carbon atoms comprising the soot particles, mol/cm<sup>3</sup>. For  $\lambda = 632.8 \text{ nm}$ ,  $a = 1.92 \cdot 10^6 \text{ cm}^2/\text{mol}$ .

The soot yield, the ratio of the concentration of carbon atoms bound in soot particles to the total concentration of carbon atoms (in particles and in gaseous species), reads as

$$SY = \frac{[C_{\text{soot}}]}{[C_{\text{total}}]} = \frac{I}{\alpha I [C_{\text{total}}] E(m)} \ln\left(\frac{I_0}{I}\right) \tag{6}$$

Since there is a considerable scatter in values of  $E(m)$ , we plotted the quantity  $SY \times E(m)$  as a function of time. Studying the formation of soot during the pyrolysis of toluene behind reflected shock waves, we estimated  $E(m)$  as 0.37, in close agreement with the most recent data [6]. This value has the advantage that it was determined under conditions similar to those used in the present experiments. The time evolution of the soot yield is displayed in Figure 2 (frame 3). The temperature dependences of the experimentally measured soot yield for various toluene/Ar mixtures are presented in Figure 3. Comparisons of the experimentally measured soot yield and induction

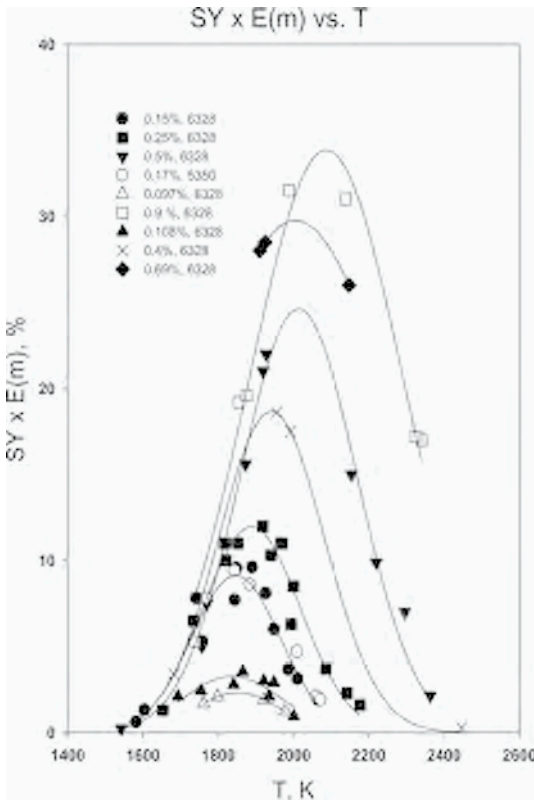


Figure 3. Temperature dependences of the experimentally measured soot yield for various toluene-argon mixtures.

time during toluene pyrolysis and oxidation [5, 6] (closed symbols) with our measurements (open symbols) are shown in Figures 4-6.

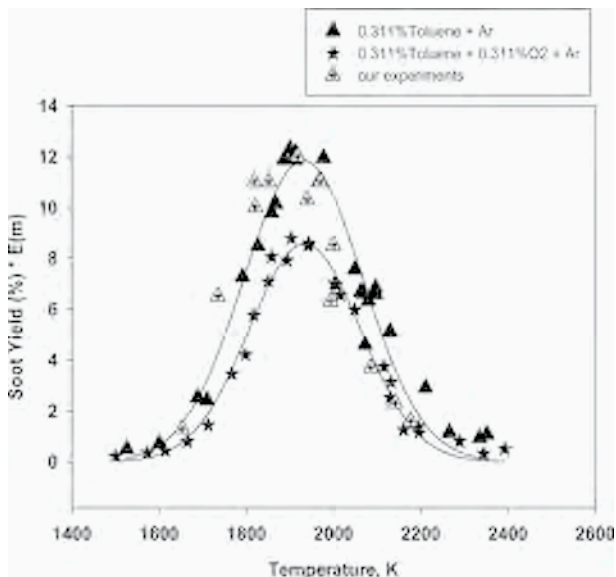


Figure 4. Comparison of the experimentally measured soot yield for pyrolysis and oxidation of toluene [7] (closed symbols) with our data (open symbols).

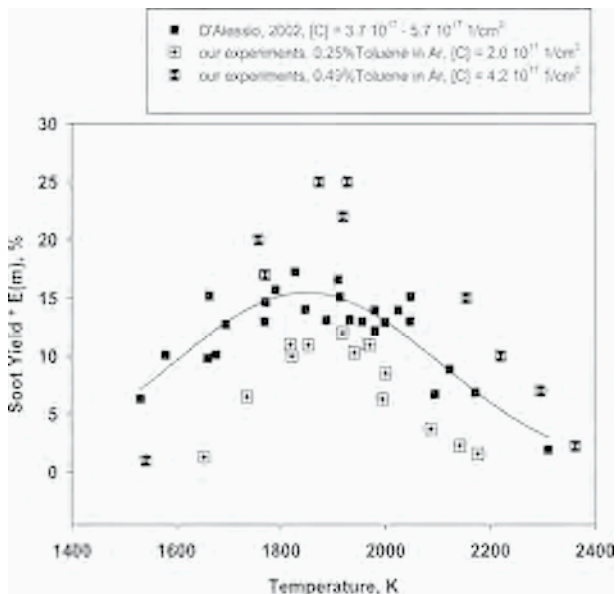


Figure 5. Comparison of the measured temperature dependences of the soot yield for toluene pyrolysis obtained in [8] (closed symbols) and the present work (open symbols).

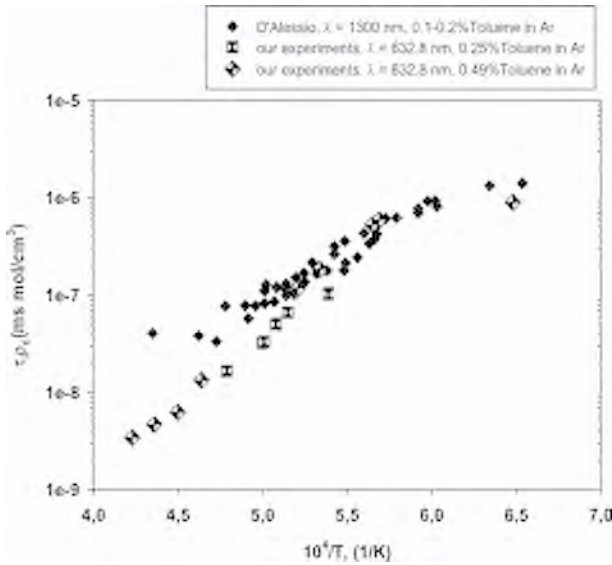


Figure 6. Comparison of the temperature dependence of the induction time for toluene pyrolysis measured in [8]] (closed symbols) and the present work (open symbols).

### 3. TEMPERATURE DETERMINATION PROCEDURE

The effective temperature of the soot particles was determined as follows. Treating the shock-wave-heated soot-gas mixture as a grey body, one can present the emission signal from it as

$$S_{\text{soot,em}} = A_{\text{instr}} \cdot \varepsilon \cdot J_{\text{bb}}$$

where  $A_{\text{instr}}$  is the instrument function,  $\varepsilon$  is the emissivity coefficient, and  $J_{\text{bb}}$  is the black-body radiance. The value of  $A_{\text{instr}}$  is determined by the geometry of the optical arrangement and the characteristics of the data acquisition system. By analogy, the signal from the calibration band lamp can be written as

$$S_{\text{bl}} = A_{\text{instr}} \cdot J_{\text{bl}}$$

Since the characteristic temperature of 632.8-nm radiation,  $h\nu/k = 22746$  K, is much higher than the temperature attained in the experiments and the temperature of the calibration band lamp, the black-body radiance and the radiance of the band lamp can be described by the Wien formula.

The emissivity coefficient is equal to the ratio of the intensity of absorbed light to the intensity of incident light,  $(I_0 - I)/I_0$  (see formula (1)). Thus, the temperature of soot particles was calculated from the absorption and emission signals by the formula

$$T_s = T_{bl} \left\{ 1 + \frac{kT_{bl}\lambda}{hc} \ln \left[ \frac{1}{S_{rel}} \left( 1 - \frac{I}{I_0} \right) \right] \right\}^{-1} \quad (7)$$

where  $T_{bl}$  is the brightness temperature of the band lamp,  $k$  is the Boltzmann constant,  $h$  is the Planck constant,  $\lambda$  is the radiation wavelength,  $c$  is the speed of light,  $S_{rel} = S_{soot\ em}/S_{bl}$  is the relative intensity of emission from soot particles, and  $I_0$  and  $I$  the intensities of incident light and light passed through the sooting medium. The squares in frame 4 of Figure 2 demonstrate the calculated gas temperature.

#### 4. DESCRIPTION OF THE KINETIC MODEL

The kinetic model of soot formation developed consists of the gas phase reaction mechanism, which describes the pyrolysis and oxidation of the parent hydrocarbons, in particular toluene, and the formation and growth of PAHs through different reaction pathways up to coronene.

The gas-phase reaction mechanism is based on the reaction sequence of PAH formation in laminar premixed acetylene and ethylene flames (HACA) [9], with all modifications presented in the work [10]. Several additional channels of PAH formation and growth (up to coronene) [11] and a comprehensive set of reactions of  $C_3$ -,  $C_5$ -, and  $C_7$ -hydrocarbons [12, 13] was also added in the kinetic mechanism. Thus, several pathways of PAH formation and growth are incorporated in the reaction mechanism: (1) the alternating H-abstraction/ $C_2H_2$ -addition (HACA) route, resulting in a successive growth of PAHs, (2) the combination reactions of phenyl with  $C_6H_6$ , (3) the cyclopentadienyl recombination, and (4) the ring closure reactions of aliphatic hydrocarbons. N-heptane oxidation was described within the kinetic scheme presented in [14]. Thus, the modified gas-phase reaction mechanism of the model consists of 2424 direct and reverse reactions between 230 different species, where the rate coefficients of some important reactions have pressure dependence. The main difference of the gas phase mechanism developed in the present work in comparison with the mechanism proposed in our previous works [15, 16] is the set of reactions of polyene hydration followed by subsequent decomposition of the products to smaller hydrocarbons [17, 18]. This provides the different behavior of polyynes, which concentration decreases by approximately one order of magnitude with increasing the number of carbon atoms in the polyene molecules. The higher polyynes ( $C_{10}H_2$  and  $C_{12}H_2$ ) were excluded from the kinetic scheme because of the absence of thermodynamic data.

Soot precursors are formed by radical-molecule reactions of different PAHs starting from ace- and ethynyl-naphthalene up to coronene and radical-radical reactions (from cyclopentaphenanthrene up to coronene radicals). These reactions result in the formation of polyaromatic molecules containing from 24 to 48 carbon atoms, which are stabilized by the formation of new chemical bonds. It should be noted that the C/H ratios of the soot precursors formed in these reactions are close to the upper boundary of the C-H diagram presented in [19]. Soot precursors are activated in reactions with H and OH radicals. They are deactivated in reactions with H,  $H_2$  and  $H_2O$ . Soot precursors grow in reactions with  $C_2H_2$ ,  $C_4H_2$ , and  $C_6H_2$ , whose concentrations are rather high in pyrolysis and oxidation of aliphatic and aromatic hydrocarbons, and

in reactions with polyaromatic molecules and radicals, and in coagulation. Soot precursors are oxidized by O and OH radicals. They are transformed into soot particles in the reactions of internal conversion, in which the number of active sites in the reacting system is preserved. Soot particles with active sites grow in the reactions with  $C_2H_2$ ,  $C_4H_2$ ,  $C_6H_2$  and PAH molecules and radicals. All types of soot particles participate in coagulation. Oxidation of soot particles is described by reactions with O and OH radicals. Taking into account the experimental observations presented in [19-22], the polyne sub-mechanism of soot formation, introduced in the kinetic model formulated in [15] and further developed in [16], was excluded from the soot formation model under consideration.

The formation, growth, and coagulation of soot precursors and soot particles are described within the framework of a discrete Galerkin technique suggested by Deuflhard and Wulkow [23]. The method is based on an error-controlled expansion of the size distribution function of heterogeneous particles into the orthogonal polynomials of a discrete variable, in particular, the chain length or number of monomers in the polymer particle. On the basis of the weight function, which is connected with the type of chemical process to be modeled, the orthogonal polynomials of a discrete variable are constructed. Thus, in the case of free radical polymerization, this function is just a so-called Schulz-Flory distribution [23]. This type of weight functions is connected with the associated orthogonal discrete Laguerre-type polynomials. As the weight function is known, the first statistical moments can be calculated making it possible to derive the mean size of the size distribution of particles. The time variation of the size distribution function (no assumptions concerning its shape are required), which depends on the chemical kinetics of the respective species, results in a complete set of ordinary differential equations for each expansion coefficient [23]. This approach makes it possible to preserve a discrete character of any elementary transformations of heterogeneous particles and to describe them as elementary chemical reactions for the heterogeneous particles of all sizes. The heterogeneous particles can also react with the gas-phase species, and thus, a connection with the gas-phase chemistry of soot particles is provided during the whole calculation. The first software implementing the analytical and numerical prerequisite of this method, in combination with the solution of a set of equation for the elementary gas-phase reactions, was the software package MACRON [24]. A considerably modified and extended version of this software was applied successfully to model the kinetics of condensation of pure carbon clusters [25-27] and soot formation during pyrolysis of various hydrocarbons [15].

## 5. RESULTS AND DISCUSSION

The results of calculations were compared with the experimental measurements of the main gas phase species during shock tube pyrolysis of a toluene/neon mixture [28]. As can be seen from Figure 7, the kinetic model developed provides a rather good prediction of toluene consumption. A satisfactory description of the  $C_2H_2$ ,  $C_4H_2$  and  $C_6H_2$  concentration profiles are observed. The total balance of C atoms in the reacting mixture is predicted quite well. The reaction flow analysis shows that the major reactions of toluene consumption are  $A1CH_2 + H = A1CH_3$  (43%),  $A1CH_3 + H =$

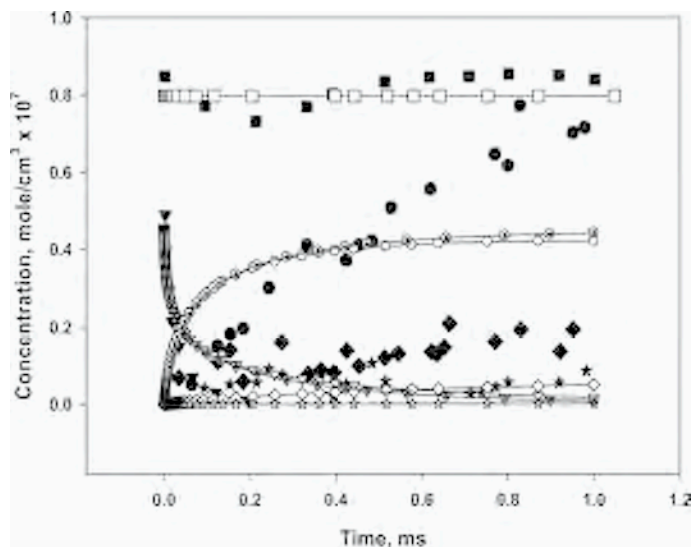


Figure 7. Concentrations of the most abundant gaseous species formed during the pyrolysis of a 1.8% toluene mixture in neon at  $T_5 = 1900$  K and  $p_5 = 0.4$  bar behind reflected shock wave: (triangles down) toluene, (circles)  $C_2H_2$ , (diamonds)  $C_4H_2$ , (stars)  $C_6H_2$ , and (squares)  $C_{total}/4$  ( $C_{total}$  is the total carbon atom concentration in the mixture). Open symbols and lines designate the results of our calculations, closed symbols the experimental measurements [28].

$A1CH_2 + H_2$  (41%),  $A1CH_3 + H = A1 + CH_3$  (10%). The main channel of acetylene production is the decomposition of toluene radical (45%). The nomenclature used in the present work was the same as in [10, 17, 18].

The kinetic model considered was also tested to simulate the H concentration and  $CH_3$  and OH mole fraction profiles recently measured in shock tube in [29-32]. Figures 8-10 demonstrate that the kinetic model predicts the H concentration and  $CH_3$  and OH mole fraction profiles rather good at the relatively high temperatures and predicts the shorter ignition delay times at the lower temperatures. The reaction flow analysis demonstrates that during toluene oxidation OH radicals are formed mainly in the reactions  $O + H_2 = H + OH$  (11%),  $HO_2 + H = OH + OH$  (21%),  $H + O_2 = O + OH$  (51%) and are consumed in the reactions  $OH + H_2 = H + H_2O$  (19%),  $CO + OH = CO_2 + H$  (44%).

It is pertinent to note that the model predicts properly the different behavior of the OH mole fraction in n-heptane and toluene oxidation (Figure 11). In n-heptane oxidation a quasistationary level of the OH concentration is attained at approximately 300  $\mu s$  and in toluene oxidation at 800  $\mu s$  under conditions presented in Figure 11. This difference is caused by the different times, when the maximal concentration of CO is attained, which consumes OH radicals: 232.8  $\mu s$  for n-heptane and 678.5  $\mu s$  for toluene.

The actual temperature behind reflected shock wave is one of the most important parameter, which governs the kinetic behavior of a reactive mixture. The kinetic model developed was tested against the experimentally measured temperatures in the

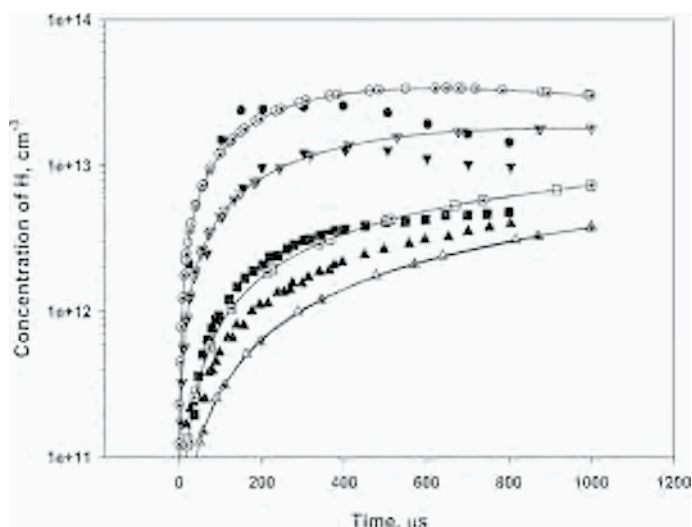


Figure 8. Comparison of the experimentally measured (closed symbols) and calculated (open symbols) time dependences of H atom concentration during shock tube pyrolysis of benzene [29] and phenol [30]: (circles)  $[C_6H_5OH]_0 = 20.5$  ppm in Ar,  $T_5 = 1536$  K,  $p_5 = 2.38$  bar, (triangles down)  $[C_6H_5OH]_0 = 24.0$  ppm in Ar,  $T_5 = 1477$  K,  $p_5 = 2.06$  bar, (squares)  $[C_6H_6]_0 = 1.8$  ppm in Ar,  $T_5 = 1840$  K,  $p_5 = 1.10$  bar, (triangles)  $[C_6H_6]_0 = 3.2$  ppm in Ar,  $T_5 = 1715$  K,  $p_5 = 1.74$  bar.

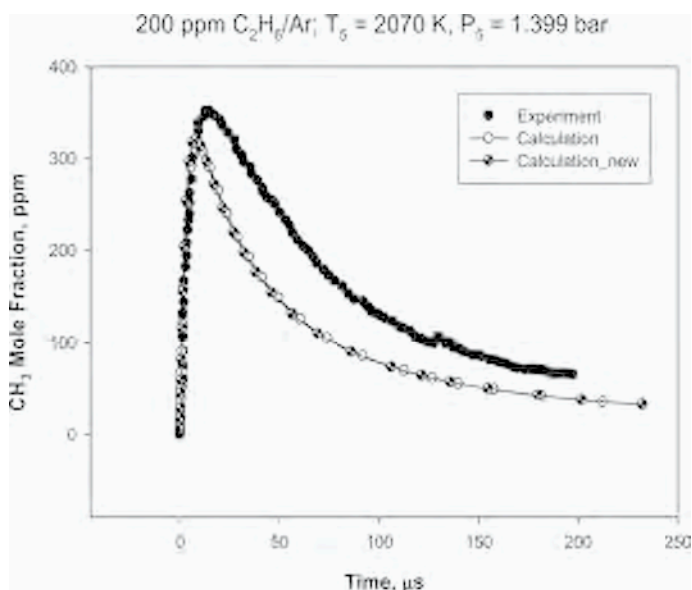


Figure 9. Example of modeling of an ethane decomposition kinetic curve. Reflected shock conditions: 2070 K, 1.399 atm, 200 ppm ethane/Ar; laser wavelength = 216.62 nm,  $k_{\lambda} = 19.1$   $\text{cm}^{-1} \text{atm}^{-1}$ , [31].

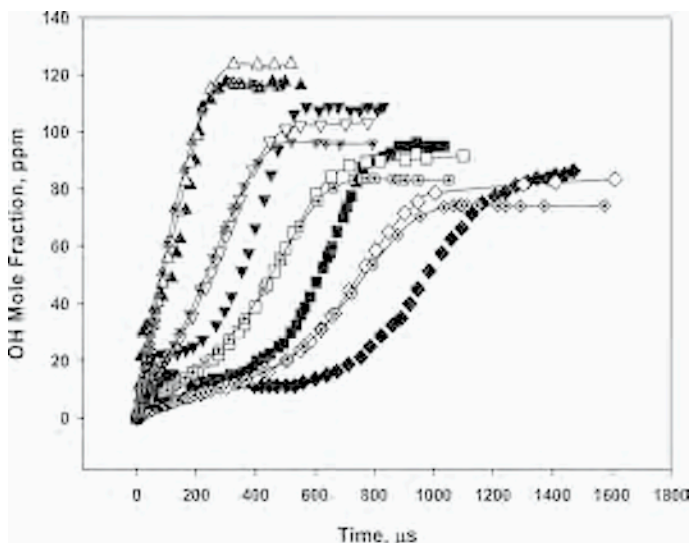


Figure 10. Time history of the OH mole fraction obtained behind reflected shock waves:  $\phi = 1$ , 0.025% toluene + 0.225%  $O_2$ , (triangles up)  $T = 1783$  K,  $p = 1.84$  bar, (triangles down)  $T = 1700$  K,  $p = 1.89$  bar, (squares)  $T = 1648$  K,  $p = 2.03$  bar, (diamonds)  $T = 1607$  K,  $p = 2.03$  bar. Open symbols and lines designate the results of our calculations, closed symbols the experimental measurements [32].

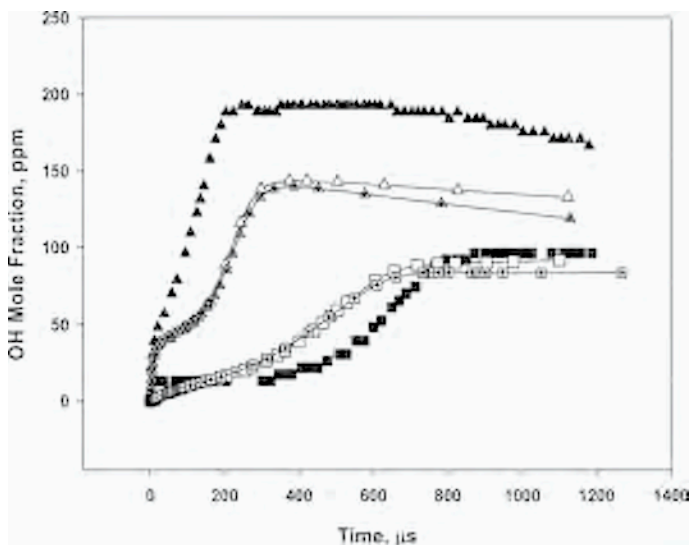


Figure 11. Time histories of the OH mole fraction for the oxidation of n-heptane and toluene behind reflected shock waves: (triangles up)  $\phi = 1$ , 300 ppm n-heptane,  $T = 1640$  K,  $p = 2$  bar, (squares)  $\phi = 1$ , 250 ppm toluene,  $T = 1648$  K,  $p = 2$  bar. Open symbols and lines designate the results of our calculations, closed symbols represent the experimental measurements [32].

CH<sub>4</sub>/O<sub>2</sub>/CO<sub>2</sub>/Ar mixtures behind reflected shock waves [33]. The time dependences of the temperature behind reflected shock wave for different CH<sub>4</sub>/O<sub>2</sub>/CO<sub>2</sub>/Ar mixtures and the initial reflected shock conditions are presented in Figure 12. Open symbols and lines designate the results of our constant density calculations, closed symbols the experimental measurements [33].

In our soot formation model we tested two different approaches for description of the surface growth of soot particles: the surface HACA (H-abstraction/C<sub>2</sub>H<sub>2</sub>-addition) model [34, 35] and the surface growth model proposed by Harris [36].

### 5.1. Surface HACA mechanism

The surface HACA mechanism is adopted based on the postulate that the H-abstraction/C<sub>2</sub>H<sub>2</sub>-addition (HACA) reaction sequence is responsible for high-temperature growth of all forms of carbonaceous materials.

Estimation of the rate coefficients of the heterogeneous reactions was based on analogous gas-phase reactions of one-ring aromatics: benzene and phenyl. In doing so, it was assumed that collision efficiencies on a per-site basis are the same for both gas-phase and gas-solid reactions. Thus, the rate expression for the *i*th particle was assumed to take the form  $(k_{g,s} C_g \alpha \chi_S S_i N_i)$  where  $k_{g,s}$  is the per-site rate coefficient,  $C_g$  is the concentration of the colliding gaseous species *g*, such as H or C<sub>2</sub>H<sub>2</sub>,  $\alpha$  is the fraction of surface sites available for a given reaction,  $\chi_S$  is the number density of surface sites (i.e., number of sites *S* per unit area),  $S_i$  is the surface area of the *i*th particle, and  $N_i$  is the number density of the *i*th particle,  $\alpha$  takes into account the probability for a gaseous species to collide with the prismatic (edge) planes instead of unreactive basal planes of a particle and that not all of the edge carbons are available for a given reaction. It is rather difficult to estimate  $\alpha$  from first principles, and therefore it was left as a free parameter.

$\chi_{C_{\text{soot}}\cdot\text{H}}$ , the number density of C<sub>soot-H</sub> sites, was estimated to be  $2.3 \cdot 10^{15}$  sites/cm<sup>2</sup>, i.e., one site per  $1.23 \cdot 3.51 \text{ \AA}^2$ , where 1.23 Å is the half-width of the benzene ring and 3.51 Å is the distance between PAH layers in soot. The number density of radical C<sub>soot</sub>· sites were determined assuming steady state for  $\chi_{C_{\text{soot}}\cdot}$ , implying that once a site on the particle surface was activated, it is more likely for this site to react with a major gaseous species (H, H<sub>2</sub>, C<sub>2</sub>H<sub>2</sub>, or O<sub>2</sub> in the present model) before it encounters another particle. The steady state assumption leads to the following equation:

$$\chi_{C_{\text{soot}}\cdot} = \chi_{C_{\text{soot}}\cdot\text{H}} \cdot (k_{C_{\text{soot}}\cdot\text{H}+\text{H}}[\text{H}] / (k_{C_{\text{soot}}\cdot\text{H}_2}[\text{H}_2] + k_{C_{\text{soot}}\cdot\text{H}}[\text{H}] + k_{C_{\text{soot}}\cdot\text{C}_2\text{H}_2}[\text{C}_2\text{H}_2]))$$

where, for clarity, the *k*'s subscripts refer to per-site rate coefficients  $k_{g,s}$  of the corresponding reactions. This equation implies that the number density of radical sites is independent of particle size and determined by the "state" of the gas phase.

Substituting this equation into the rate expression for reaction of C<sub>2</sub>H<sub>2</sub> addition, we obtain the rate of surface growth for the *i*th particles due to the acetylene addition, expressed in mass units of carbon atoms (the factor of 2 accounts for the addition of two carbon atoms to the soot particle mass per reactive collision) [34]:

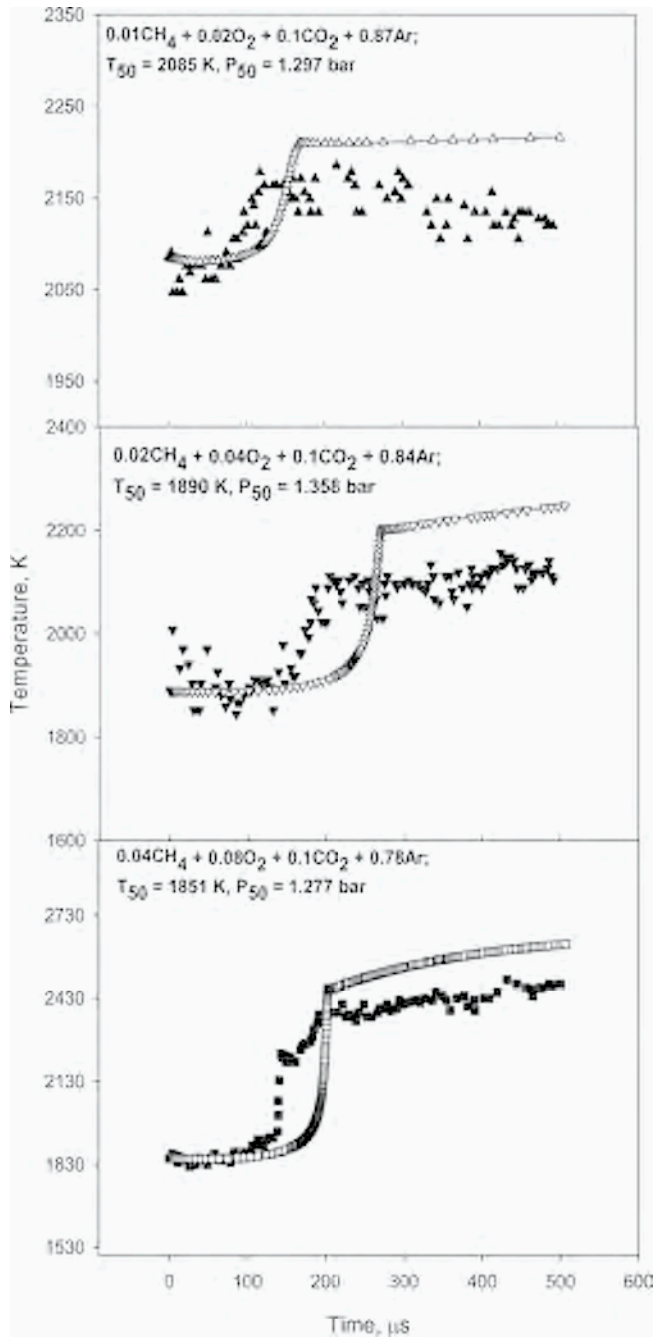


Figure 12. Time evolution of the temperature behind reflected shock wave for different  $\text{CH}_4/\text{O}_2/\text{CO}_2/\text{Ar}$  mixtures and the initial reflected shock conditions. Open symbols and lines designate the results of our constant-density calculations, while closed symbols are the experimental measurements [33].

$$r_{soot} = 2 \frac{\alpha \cdot Z_{C_{max-H}} \cdot k_{C_{max-H}+C_2H_2} [C_2H_2] \cdot k_{C_{max-H}+H} [H]}{k_{C_{max-H}+H_2} [H_2] + k_{C_{max-H}+H} [H] + k_{C_{max-H}+C_2H_2} [C_2H_2]} \cdot S_c \cdot N_s$$

The parameter  $\alpha$  represents a steric phenomenon. At high temperatures, soot particle crystallites are more mobile and align themselves in a more orderly fashion, such that the edge planes of neighboring crystallites face each other, thus limiting the access of gaseous species to the reactive carbon sites, and the unreactive basal planes constitute then most of the particle surface. For the fraction of reactive surface, the parameter  $\alpha$ , the following mathematical form was adopted [10]:

$$\alpha = \tanh(a/\log\mu_1 + b),$$

$$\alpha = \tanh(a/\log\mu_1 + b),$$

$$a = 12.65 - 0.00563 \cdot T,$$

$$b = -1.38 + 0.00068 \cdot T,$$

where  $\mu_1$  is the first size moment of the soot particle distribution, and  $a$  and  $b$  are fitted parameters,  $T$  is the local temperature in K. This formula expresses the desired physical trends of  $\alpha$  being a decreasing function of the particle size, properly bounded at the limits.

The implementation of this approach in MACRON gave the results shown in Figure 13. To improve the fitting with the experimentally measured curve of the soot yield, the temperature and particle size dependences of  $\alpha$ , which were obtained pre-

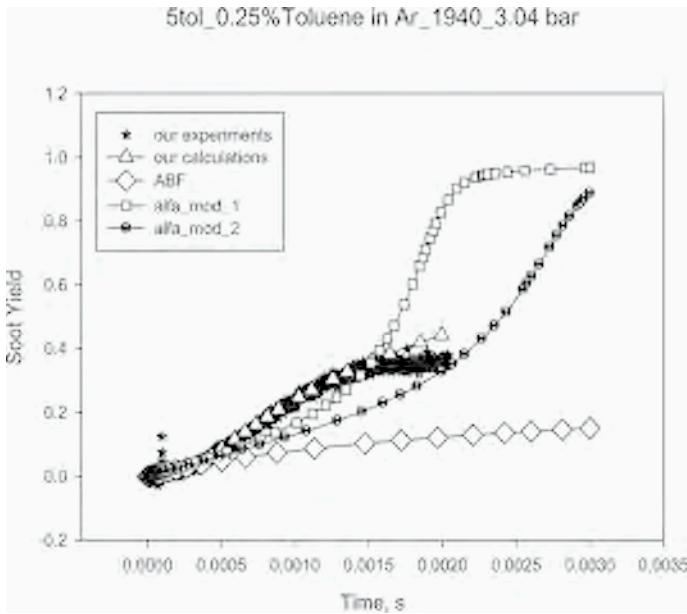


Figure 13. Time dependences of the experimentally measured (closed symbols) and calculated (open symbols) soot yield for toluene pyrolysis behind reflected shock waves.

viously in [10] for flame conditions, should be modified for shock tube conditions. This is the subject matter of separate study.

## 5.2. The Harris model of surface growth

The Harris model of surface growth is based on the following assumptions [36]. (i) The controlling experimentally measured variable determining the rate of surface growth is the amount of soot generated in the inception stage and delivered to the growth stage. (ii) Growth stops at long times because of changes in the reactivity of the soot particles, not because of depletion of gas phase growth species. (iii) Acetylene and to a lesser extent diacetylene are the principal growth species in all premixed flames, although PAH may dominate during particle inception, and other species may dominate in diffusion flames. (iv) Surface growth occurs on reactive sites such as defects or edges, which are lost by a temperature-dependent annealing process. The number of active sites is not directly affected by coagulation, surface growth, or gas phase chemistry.

The essence of the Harris model of surface growth lies in the following hypothesis. (1) Surface growth occurs primarily on active sites such as defects or edges. (2) The number of active sites is not directly affected by coagulation, surface growth, or gas phase chemistry. (This is the crucial proposal for the Harris model.) (3) The surface growth rate declines because active sites are lost by a temperature-dependent annealing process.

This surface growth model implemented in our kinetic model even without the annealing process gives rather promising results (Figure 14). The temperature dependences of the experimentally measured (closed symbols) and calculated (open symbols) soot yields for various toluene-argon mixtures for  $E(m) = 0.37$  are presented in Figure 15.

## 6. CONCLUSIONS

The experiments on the pyrolysis of toluene behind reflected shock waves under oxygen-free conditions were performed. To determine the soot yield and the temperature of the soot particles, the double-beam absorption-emission technique was utilized. The results obtained are in a good agreement with the experimental measurements performed in [7, 8].

The kinetic model of soot formation developed consists of the gas phase reaction mechanism, which describes the pyrolysis and oxidation of the parent hydrocarbons, in particular toluene, and the formation and growth of PAHs through different reaction pathways up to coronene. The results of calculations are in satisfactory agreement with the experimental measurements of the main gas phase species during shock tube pyrolysis of a toluene/neon mixture [28]. The kinetic model considered was also tested to simulate the H concentration and  $\text{CH}_3$  and OH mole fraction profiles measured in shock tube in [29-32].

Two mechanisms of surface growth were tested: the surface HACA mechanism [34, 35] and the Harris model of surface growth [36]. Implementation of the surface HACA mechanism in MACRON for shock tube conditions requires a modification of

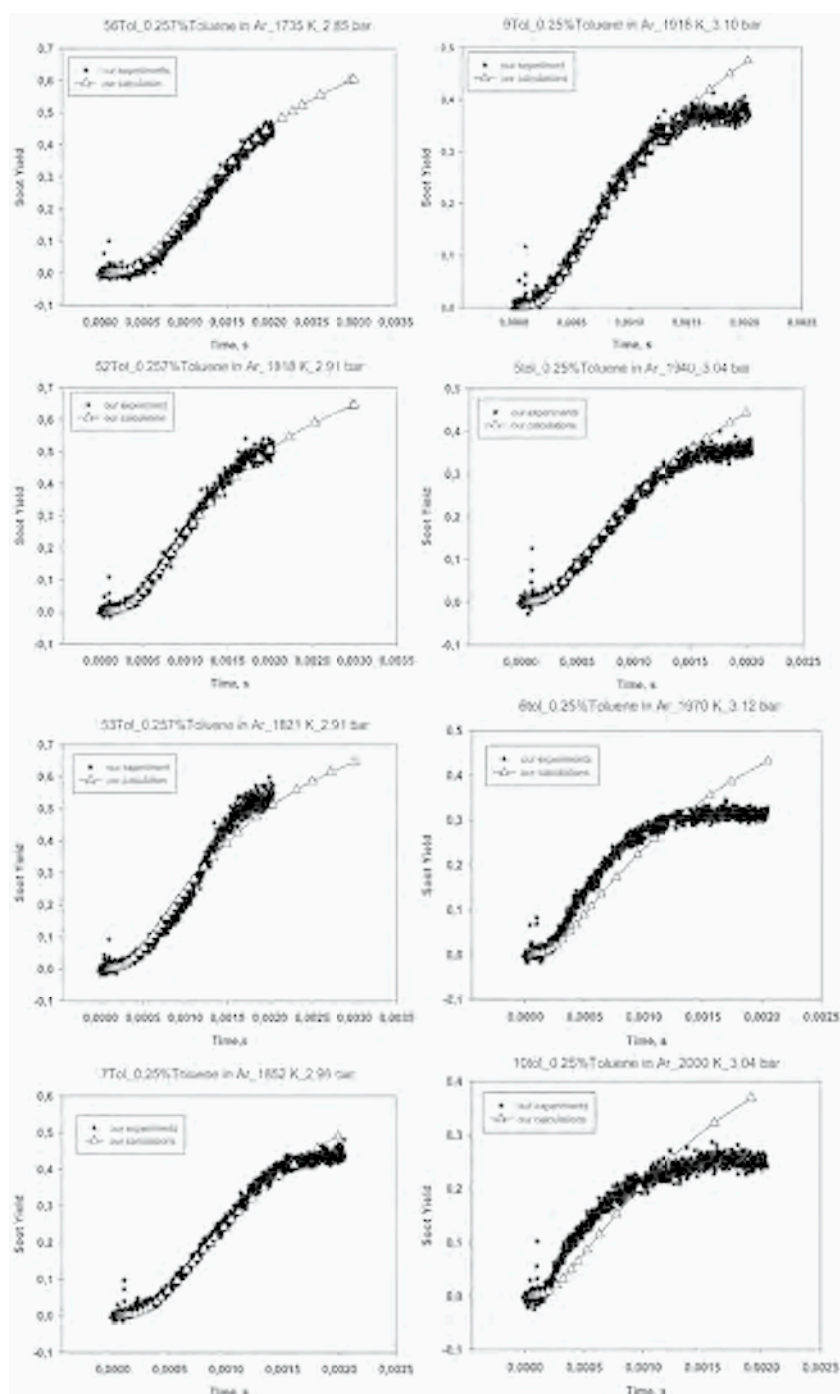


Figure 14. Experimentally measured (closed symbols) and calculated (open symbols) soot yield for toluene pyrolysis behind reflected shock wave as a function of time.

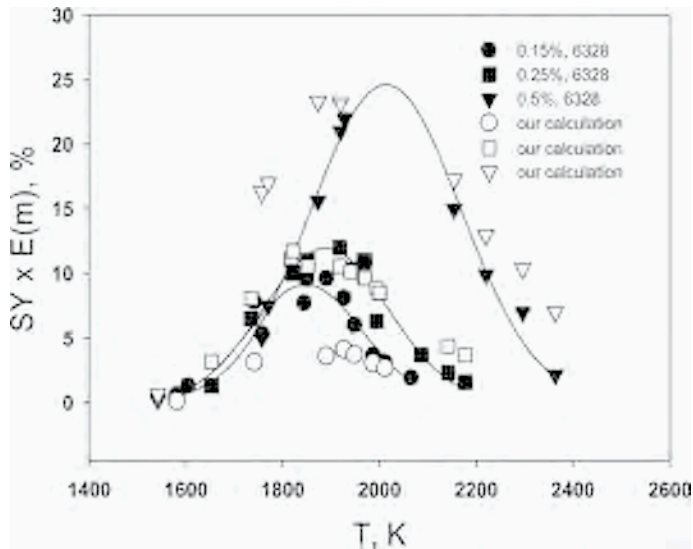


Figure 15. Temperature dependences of the experimentally measured (closed symbols) and calculated (open symbols) soot yields for various toluene-argon mixtures for  $E(m) = 0.37$ .

the temperature and size dependences of  $\alpha$ , which were obtained previously in [10] for flame conditions. The application of the Harris model of surface growth makes it possible to describe adequately the experimentally measured time dependences of the soot yield during toluene pyrolysis behind reflected shock waves.

Further studies are required to clear up the details of the actual surface growth mechanism of soot particles.

## ACKNOWLEDGMENTS

This work was supported by the Deutsche Forschungsgemeinschaft and by the Russian Foundation for Basic Research, project no. 08-08-00722.

## REFERENCES

1. R. Sivaramakrishnan, Robert S. Tranter, K. Brezinsky, *J. Phys. Chem. A* 110 (2006) 9388-9399.
2. A. Hamins, D. T. Anderson, J. H. Miller, *Combust. Sci. Technol.* 71 (1990) 175-195.
3. Ye. V. Stupochenko, S.A. Losev, A.I. Osipov, *Relaxation in shock waves*. New York, Springer-Verlag, 1967.
4. H. Hippler, J. Troe, J. Wendelken, *J. Chem. Phys.* 78(9) (1983).
5. H. C. Van de Hulst, *Light Scattering by Small Particles*, New York, Dover, 1981.
6. Schulz, B. F. Kock, M. Hofmann, H. A. Michelsen, S. Will, B. Bougie, R. Suntz, G. J. Smallwood, *Appl. Phys. B* 83 (2006) 333-354.

7. M. Frenklach, M.K. Ramachandra, R.A. Matula, *Proc. Combust. Inst.* 20 (1984) 871-878.
8. J. D'Alessio, M. Lazzaro, P. Massoli, V. Moccia, *Opt. Lasers Eng.* 37 (2002) 495-508.
9. H. Wang, M. Frenklach, *Combust. Flame* 110(1-2) (1997) 173-221.
10. J. Appel, H. Bockhorn, M. Frenklach, *Combust. Flame* 121(1-2) (2000) 122-136.
11. H. Richter, S. Granata, W.H. Green, J.B. Howard, *Proc. Combust. Inst.* 30 (2005) 1397-1405.
12. H. Richter, J.B. Howard, *Phys. Chem. Chem. Phys.* 4 (2002) 2038-2055.
13. M.S. Skjøth-Rasmussen, P. Glarborg, M. Østberg, J.T. Johannessen, H. Livbjerg, A.D. Jensen, T.S. Christensen, *Combust. Flame* 136 (2004) 91-128.
14. C. Correa, H. Niemann, B. Schramm, J. Warnatz, *Proc. Combust. Inst.* 28 (2000) 1607-1614.
15. P.A. Vlasov, J. Warnatz, *Proc. Combust. Inst.* 29 (2002) 2335-2341.
16. I. Naydenova, M. Nullmeier, J. Warnatz, P.A. Vlasov, *Combust. Sci. Technol.* 176 (2004) 1667-1703.
17. M. Frenklach, D.W. Clary, T. Yuan, W.C. Gardiner Jr., S.E. Stein, *Combust. Sci. Technol.* 50 (1986) 79-115.
18. M. Frenklach, J. Warnatz, *Combust. Sci. Technol.* 51 (1987) 265-283.
19. A. Keller, R. Kovacs, K.-H. Homann, *Phys. Chem. Chem. Phys.* 2 (2000) 1667-1675.
20. P. Weilmünster, A. Keller, K.-H. Homann, *Combust. Flame* 116 (1999) 62-83.
21. Berk Öktem, M.P. Tolocka, B. Zhao, H. Wang, M.V. Johnston, *Combust. Flame* 142 (2005) 364-373.
22. H. Böhm, H. Jander, *Phys. Chem. Chem. Phys.* 1 (1999) 3775-3781.
23. P. Deuflhard, M. Wulkow, *Impact of Computing in Science and Engineering* 1 (1989) 269-301.
24. J. Ackermann, M. Wulkow, MACRON-A Program Package for Macromolecular Kinetics, Preprint SC 90-14, Konrad-Zuse-Zentrum, Berlin (1990).
25. J. Sojka, J. Warnatz, P.A. Vlasov, I.S. Zaslanko, *Combust. Sci. Technol.* 158 (2000) 439-460.
26. H.Gg. Wagner, P.A. Vlasov, K.J. Dörge, A.V. Eremin, I.S. Zaslanko, D. Tanke, *Kinet. Catal.* 42(5) (2001) 645-656.
27. G.L. Agafonov, M. Nullmeier, P.A. Vlasov, J. Warnatz, I.S. Zaslanko, *Combust. Sci. Technol.* 174 (2002) 1-29.
28. R.D. Kern, H.J. Singh, M.A. Esslinger, P.W. Winkeler, *Product Profiles Observed during the Pyrolysis of Toluene, Benzene, Butadiene, and Acetylene*, *Proc. Combust. Inst.* 19 (1982) 1351-1358.
29. S. Scherer, *Untersuchung pyrolytischer Reaktionen des Ru vorläufermoleküls Propargyl im Sto wellenrohr*, Dissertation, Universität Stuttgart, Institut für Physikalische Chemie der Verbrennung des DLR in Stuttgart, 2001.
30. C. Horn, P. Frank, *High Temperature Pyrolysis of Phenol*, *Proc. 4th Int. Conf. on Chemical Kinetics*, NIST, July 14-18, 1997, Gaithersburg, USA.
31. M.A. Oehlschlaeger, D.F. Davidson, R.K. Hanson, *J. Quant. Spectrosc. Radiat. Transfer* 92(2005) 393-402.
32. V. Vasudevan, D.F. Davidson, R.K. Hanson, *Proc. Combust. Inst.* 30 (2005) 1155-1163.
33. M.A. Oehlschlaeger, *Shock Tube Studies of Thermal Decomposition Reactions Using Ultraviolet Absorption Spectroscopy*, Report No. TSD-160, 2005.
34. M. Frenklach, H. Wang, *Proc. Combust. Inst.* 23 (1991) 1559-1566.
35. M. Frenklach, H. Wang, in H. Bockhorn (Ed.) *Soot Formation in Combustion*, 1994, Springer-Verlag, Berlin, pp. 162-192.
36. S.J. Harris, A.M. Weiner, *Combust. Sci. Technol.* 31 (1983), 155-167.



# Soot formation simulation of shock tube experiments with the use of an empirical model

I. Naydenova, J. Marquetand, J. Warnatz

*Interdisciplinary Center for Scientific Computing (IWR), University Heidelberg, Germany*

*Abstract: The detailed description of the soot formation in three-dimensional simulations of technical combustors leads to an enormous computational effort. Therefore a simplification of the soot model is needed. In the current work an empirical two-equation soot model was optimised and implemented in a software package for the simulation of homogeneous reaction systems. The empirical model was tested with data from shock tube experiments of *n*-heptane. The obtained simulation results show good agreement with the experiment.*

## 1. INTRODUCTION

A direct simulation of the soot formation in a three-dimensional technical system is too expensive because of the resulting computation time. Therefore, a reduction of the soot reaction mechanism is needed.

In the present work this simplification was carried out with a semi-empirical model of soot formation [1,2] that was implemented into the program package HOMREA for homogeneous reaction system simulations [3]. The complex process of soot formation is described in terms of several global steps - nucleation, soot particle growth, coagulation, and particle oxidation.

For that purpose two differential equations are solved: for the temporal change of soot particle number density and for the soot volume fraction. The rate equations of the soot model are solved in a system of differential equations together with the gas-phase chemistry published in [4].

## 2. MODEL DESCRIPTION

The empirical model describes the soot formation in terms of two variables: the concentration of the soot particles  $C_S$  and volume fraction  $f_V$ , which gives the volume occupied by the soot particles normalised by the total volume.

### 2.1. Soot concentration

The soot concentration is influenced by the process of nucleation, the formation of the first aromatic ring, and coagulation, the process of sticking of two particles by which larger particles are formed.

Nucleation increases the number of soot particles, and so the soot concentration. The key step for the particle inception was considered to be the propargyl radical recombination  $C_3H_3 + C_3H_3 = C_6H_6$ , which delivers the first aromatic ring (benzene of phenyl) in the system. Reaction flow analysis confirmed that in many aliphatic fuels, this is the reaction producing the highest amount of benzene.

Coagulation decreases the soot concentration. In the current model, the formulation of the coagulation is derived from the chemical equation  $C_{\text{soot}}(N) + C_{\text{soot}}(M) = C_{\text{soot}}(N + M)$ . The resulting term for coagulation is described by means of the soot particle concentration and a collision number  $\beta$  [5, 6]. The overall source term for the soot concentration is given in Equation 1:

$$\frac{dC_S}{dt} = \underbrace{\alpha \cdot C_{C_3H_3}^2}_{\text{nucleation}} - \underbrace{\beta \cdot C_S^2}_{\text{coagulation}} \quad (1)$$

The rate coefficients used in this equation,  $\alpha$  for the nucleation and  $\beta$  for the coagulation, are given in Table 1. The rate coefficient  $\alpha$  for the nucleation process is chosen according to the rate coefficient of the gas-phase reaction between two propargyl radicals [4]. The value for the gas-phase chemistry was reduced by the factor of ten. This is a simplified representation for the assumption that ten benzene molecules are needed to build up a soot particle.

Table 1. Rate coefficients used for the soot concentration rate.

rate coefficients		
$\alpha$	$5.0 \cdot 10^5$	$\frac{m^3}{mol \cdot s}$
$\beta$	$1.0 \cdot 10^{10} \cdot T^{-1/2}$	$\frac{m^3}{mol \cdot s \cdot K^{1/2}}$

Surface growth influences the particle size, but does not change the number of soot particles. For the oxidation it is assumed that a soot particle is not completely destroyed, and the number of soot particles remains unchanged. Therefore, these two processes were not included in the term for the temporal change of soot concentration.

## 2.2. Volume fraction

The volume fraction depends on nucleation, surface growth and oxidation. Nucleation is formulated depending on the concentration of propargyl as in the equation for the soot concentration and the parameter  $\delta$  which is the unit transformed value of the gas phase reaction rate:

$$\delta = \alpha \cdot V_S \quad (2)$$

Here,  $V_S = M_S/\rho_S$  is the volume occupied by a soot particle, that is formed in the nucleation process.  $M_S$  is the molar mass of a soot particle (taken to be that of  $C_{60}H_{60}$ ) and  $\rho_S$  is the density of soot  $1800 \text{ kg/m}^3$  [7, 8].

The rate for the surface growth depends on the concentration of the available carbon-bearing species in the particle neighbourhood, on the temperature and on the reactivity of the particle surface. Therefore, an empirical correlation between the specific surface growth rates and the concentration of the growth species is needed.

The specific surface growth rate is the volume of the soot, added to a particle per unit aerosol surface area [9]. Previous investigations [10, 11, 12] and reaction flow analysis confirmed that the process of acetylene addition to the soot particle surface dominates the particle surface growth. According to that, the surface growth term takes into account the attachment of  $C_2H_2$  molecules onto the soot particle surface [11]. The source term is derived from the gas kinetics theory and gives first-order growth law, suggested in the literature [2, 5, 6, 13],

$$\dot{\gamma} = \sigma_G \cdot V_G \cdot \vartheta_e \cdot \frac{f_{V,\infty} - f_V}{f_{V,\infty}} \quad (3)$$

Here acetylene is considered as growth species, so the sticking coefficient  $\sigma_{C_2H_2} = 1.4 \cdot 10^{-3}$  published in [2] can be used. The volume  $V_{C_2H_2}$  of the absorbed growth species used in Equation 3 is calculated by  $V_{C_2H_2} = m_{C_2H_2} / \rho_S$ , with the mass  $m_{C_2H_2}$  of the growth species and the density of the soot particles  $\rho_S$ .

The effusion velocity  $\vartheta_e$  in Equation 3 is calculated from

$$\vartheta_e = \sqrt{\frac{k_B T}{2\pi m_{C_2H_2}}} \cdot N_A \cdot C_{C_2H_2} \cdot A_S \quad (4)$$

depending on the concentration  $C_{C_2H_2}$  and mass  $m_{C_2H_2}$  of acetylene, the temperature  $T$ , and the soot surface density  $A_S$ . Boltzmann's and Avogadro's constant are needed for unit transformation. The surface density  $A_S$  is calculated from Equation 5, depending on the diameter of a soot particle  $D_S$  and the number density  $N_S$ ,

$$A_S = \pi \cdot D_S^2 \cdot N_S \quad (5)$$

$$D_S = \sqrt[3]{\frac{6 \cdot f_V}{\pi \cdot C_S \cdot N_A}} \quad (6)$$

Formulating the soot diameter  $D_S$  in dependence of the volume fraction  $f_V$  and the soot concentration  $C_S$  (see Equation 6) the soot surface density can be written as

$$A_S = (36\pi \cdot C_S \cdot N_A)^{1/3} \cdot f_V^{2/3} \quad (7)$$

Combining the transformations given in Equation 4-7, the rate for the surface growth results in Equation 8, the formulation which is used in the source term of the soot volume fraction  $f_V$ ,

$$\dot{\gamma} = \gamma \cdot C_{C_2H_2} \cdot C_S^{1/3} \cdot f_V^{2/3} \cdot \frac{f_{V,\infty} - f_V}{f_{V,\infty}} \quad (8)$$

The rate coefficient  $\gamma$  resulting from this transformations is:

$$\gamma = \frac{\sigma_{C_2H_2}}{\rho_S} \sqrt{\frac{N_A R m_{C_2H_2}}{2\pi}} \cdot (36\pi \cdot N_A)^{1/3} \cdot T^{1/2}. \quad (9)$$

The factor  $(f_{V,\infty} - f_V) / f_{V,\infty}$  appearing in Equations 3 and 8 is an empirically obtained term that is used to preserve unrealistically high values for the volume fraction  $f_V$  [2]. In this work the maximum volume fraction  $f_{V,\infty} = 1.143 \cdot 10^{-5}$  was used for the simulations. This value is obtained from the experimental results of n-heptane rich-oxidation behind shockwave [14]. Therefore equation 6 is rearranged and the values of the soot number density and the particle diameter at the end of the reaction time are used.

The oxidation source term is calculated similarly to the surface growth, but in this case the sticking of OH on the soot particle surface was taken into account instead of  $C_2H_2$ . The source term then is given by

$$\dot{\varepsilon} = \varepsilon \cdot C_{OH} \cdot C_S^{1/3} \cdot f_V^{2/3}, \quad (10)$$

with the related rate constant

$$\varepsilon = \frac{\sigma_{OX}}{\rho_{soot}} \sqrt{\frac{N_A R m_{OH}}{2\pi}} (36\pi \cdot N_A)^{1/3} \cdot T^{1/2}. \quad (11)$$

In this term  $m_{OH}$  is the mass and  $C_{OH}$  is the molar concentration of the OH radicals in [kg] and [mol/m<sup>3</sup>] respectively. The sticking coefficient of OH is  $\sigma_{OX} = 0.1$  [6, 15].

Combining the rate definitions for the nucleation, surface growth, and oxidation the source term for the soot volume fraction results in Equation 12.

$$\begin{aligned} \frac{df_V}{dt} = & \underbrace{\delta \cdot C_{C_2H_2}^2}_{\text{nucleation}} \\ & + \underbrace{\gamma \cdot C_{C_2H_2} \cdot C_S^{1/3} \cdot f_V^{2/3} \cdot \frac{f_{V,\infty} - f_V}{f_{V,\infty}}}_{\text{surface growth}} \\ & - \underbrace{\varepsilon \cdot C_{OH} \cdot C_S^{1/3} \cdot f_V^{2/3}}_{\text{oxidation}} \end{aligned} \quad (12)$$

Inserting the given characteristics in the equations of the rate constants for nucleation, surface growth and oxidation, these terms can be simplified to just one parameter each. The resulting value for the rate coefficients are given in Table 2.

Table 2. Rate coefficients used for the volume fraction rate.

rate coefficients		
$\gamma$	$176.4 \cdot T^{1/2}$	$\frac{m^2}{\text{mol} \cdot s \cdot K^{1/2}}$
$\delta$	217	$\frac{m^3}{\text{mol} \cdot s}$
$\varepsilon$	$3.4 \cdot 10^3 \cdot T^{1/2}$	$\frac{m^2}{\text{mol} \cdot s \cdot K^{1/2}}$

Coagulation does not change the total volume of the soot particles and is therefore not represented in the source term of the volume fraction.

### 2.3. Gas phase

The rate laws of the gas-phase species, included in the different terms, are influenced by the soot formation. Therefore, additional terms for the temporal change of the concentration of  $C_3H_3$ ,  $C_2H_2$ , and OH were introduced in the model (Eq. 13-15):

$$\frac{dC_{C_3H_3}}{dt} = \frac{dC_{C_3H_3}}{dt} - 2 \cdot \bar{\alpha} \quad , \quad (13)$$

$$\frac{dC_{C_2H_2}}{dt} = \frac{dC_{C_2H_2}}{dt} - \bar{\gamma} \frac{\rho_{soot}}{m_{C_2H_2} \cdot N_A} \quad (14)$$

$$\frac{dC_{OH}}{dt} = \frac{dC_{OH}}{dt} - \bar{\varepsilon} \frac{\rho_{soot}}{m_{OH} N_A} \quad (15)$$

In this way, an interaction between the gas-phase and the particulate phase chemistry is taken into account during the entire simulation.

### 2.4. Particle diameter/Soot yield

The soot concentration and the volume fraction computed from the source terms 1 and 12 are used for the calculation of the particle diameter  $D_S$  (see Equation 6). These three values are used for the validation of the soot model as they are usually measured in experiments. Another important characteristic used to compare the simulation with the experiments is the soot yield  $Y_S$ . It expresses the fraction of carbon appearing as soot, which usually is calculated by

$$Y_S = \frac{C_S}{C_{C, total}} \quad (16)$$

where,  $C_S$  is the soot concentration and  $C_{C, total}$  is the total carbon atom concentration in the system (see Equation 17),

$$C_{C, total} = C_{C, fuel}^0 \cdot n_{C, fuel} \quad . \quad (17)$$

Here,  $C_{C, fuel}^0$  is the initial fuel concentration in  $\text{mol}/\text{m}^3$  and  $n_{C, fuel}$  is the number of C atoms in a fuel molecule.

## 3. RESULTS AND DISCUSSION

The simplified soot model was applied to predict soot formation during n-heptane rich-oxidation behind a shock wave [14]. The gas-phase chemistry is modeled with the use of

the detailed kinetic schemes described in [4]. The soot model was validated against the experimentally measured values of the soot concentration, the mean particle diameter, and the soot yield. The concentration of the gas-phase species ( $C_2H_2$ ,  $C_3H_3$ , OH) included into the simplified soot model described above, is simulated simultaneously with the soot characteristics during the whole reaction time. The results for the model predictions and the experimentally measured values [14], are shown in Figures 1-3.

The simulated soot yield (Figure 1) is in good agreement with the experiment. The model slightly underestimates the experimentally obtained soot yield at the longer reaction time ( $t_r = 1-2.5$  ms).

The mean particle diameter (see Figure 2) is overestimated at the beginning and underestimated at the end of the reaction time. One of the reasons for underestimating the particle diameter is the assumption of spherical particles with the density of graphite. This leads to more compact particles than in the experiments and therefore results in smaller particle diameters.

The prediction of a too big particle diameter at the beginning results from the too low soot concentration for reaction times up to 1 ms (Figure 3).

The soot model gives a rapid increase of the particle concentration right at the beginning of the simulation time and underestimates the maximum number density of the soot particles by a factor of hundred. But at the end of the reaction time, when the particle number density of the experiments reaches a plateau, the simulated particle concentration only differs by factor less than two.

The reason for the rapid increase of the soot concentration is the direct influence of the  $C_3H_3$  concentration on the nucleation. This correlation can be seen when comparing the time evolution of the soot concentration (see Figure 3) with Figure 4, where the time-dependent concentration profile of the nucleation species ( $C_3H_3$ ) is presented. The nucleation term may be improved if the formulation of the nucleation processes is described by means of the formation rate of benzene calculated in the gas-phase chemistry. In such way, all reactions responsible for the formation of the first aromatic ring will be taken into account.

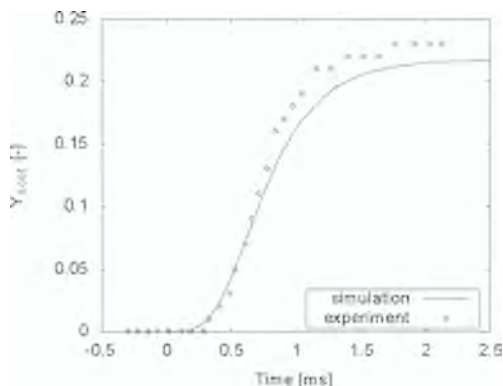


Figure 1. Time-resolved soot yield, measured [14] and calculated, during  $n-C_7H_{16}$  rich-oxidation,  $[C] = 7.89 \text{ mol/m}^3$ ,  $\Phi = 5$ ,  $T = 1750 \text{ K}$ ,  $p = 25 \text{ bar}$  and  $t_r = 2.5 \text{ ms}$ .

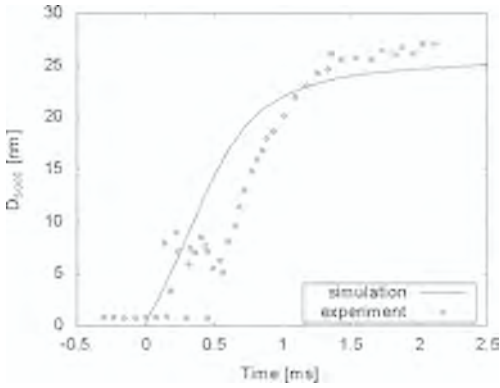


Figure 2. Time-resolved mean particle diameter, measured [14] and calculated, in  $n\text{-C}_7\text{H}_{16}$  rich-oxidation (conditions see Figure 1).

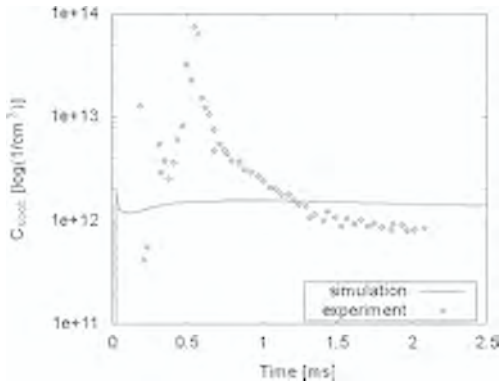


Figure 3. Time-resolved soot particle number density, measured [14] and calculated, during  $n\text{-C}_7\text{H}_{16}$  rich-oxidation (conditions as in Figure 1).

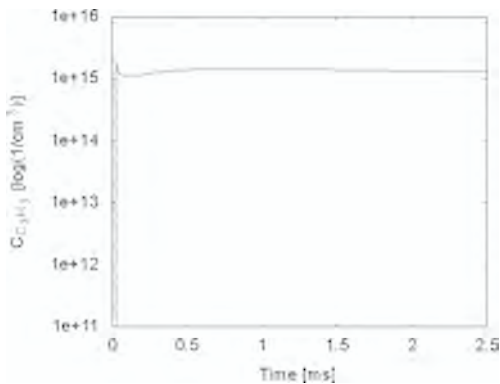


Figure 4. Time-resolved profile of the  $\text{C}_3\text{H}_3$  concentration, calculated at the conditions as in Figure 1.

#### 4. CONCLUSIONS

An empirical (two-equation) model was applied for soot formation simulation during shock tube oxidation of n-heptane. For the simulation of the gas-phase chemistry a reaction scheme published in [4] was used. The concentration profiles of the gas-phase species, introduced in the different terms, were simultaneously calculated together with the soot properties. The numerical results confirmed that the empirical model satisfactorily represents the experimentally-measured soot characteristics. The choice of the gas-phase species included in the model played a crucial role for the quality of the model predictions.

A good coincidence between the experimentally measured and calculated results can be achieved with relatively small computational effort. Therefore, the simplified soot model is suitable to be implemented and applied for soot formation simulation in more complex models like flame or CFD codes.

#### ACKNOWLEDGEMENTS

The financial support of the “Deutsche Forschungsgemeinschaft” (German Research Foundation) within the Collaborative Research Centre 568 is gratefully acknowledged.

#### REFERENCES

1. J. B. Moss, C. D. Stewart, K. J. Young, *Combust. Flame* 101 (1995) 491-500.
2. Jürgen Sojka. Simulation der Rußbildung unter homogenen Verbrennungsbedingungen. PhD thesis, Ruprecht-Karls-Universität Heidelberg, 2001.
3. U. Maas, J. Warnatz. *Proc. Combust. Inst.* 22 (1988) 1695-1704.
4. G. L. Agafonov, I. Naydenova, P. A. Vlasov, J. Warnatz, *Proc. Combust. Inst.* 31 (2007) 575-583.
5. B. S. Haynes H. Gg. Wagner, *Prog. Energy Combust. Sci.* 7 (1981) 229-273.
7. M. Frenklach, M. K. Ramachandra, R. Matula, *Proc. Combust. Inst.* 20 (1984) 871-878.
8. F. Douce, N. Djebaili-Chaumeix, C.-E. Paillard, C. Clinard, J.-N. Rouzard, *Proc. Combust. Inst.* 28 (2000) 2523- 2529.
9. W. Kollmann, I. M. Kennedy, M. Metternich, J.-J. Chen, in *Soot Formation in Combustion*, Springer-Verlag, Berlin, Heidelberg, 1994, pp. 503-526.
10. H. Gg. Wagner, in *Particle carbon formation during combustion*, Plenum Press, New York, 1981.
11. M. Frenklach, H. Wang, in *Soot Formation in Combustion*, Springer-Verlag, Berlin, Heidelberg, 1994, pp. 162-190.
12. H. Richter, S. Granata, W. H. Green, J. B. Howard, *Proc. Combust. Inst.* 30 (2005) 1397-1405.
13. P.W. Atkins, *Physical chemistry*. Oxford University Press, New York, 7th ed., 2002.
14. H. Kellerer, A. Müller, H.-J. Bauer, S. Wittig, *Combust. Sci. Technol.* 113-114 (1996) 67-80.
15. J. Warnatz, U. Maas, R.W. Dibble. *Physical and chemical fundamentals, modeling and simulation, experiments, pollutant formation*, 4th ed., Springer-Verlag, Berlin, Heidelberg, 2006.

# Multivariate soot particle models

M.S. Celnik, A. Raj, S. Mosbach, R.H. West, M. Kraft  
*Department of Chemical Engineering, Cambridge University, New Museums Site,  
Pembroke Street, Cambridge CB2 3RA, UK*

*Abstract: This paper presents a detailed model for soot which takes the chemical and structural properties of an individual particle into account. The model is applied to laboratory flames as well as to an internal combustion engine. An aromatic site model for soot particles is presented which incorporates detailed chemical information about a soot particle's reactive sites into the computationally efficient sitecounting model. A primary-particle aggregate model is presented which accounts for the fractal structure of soot particles. By approximating the collision steps of aggregate formation, 3D structural representation of soot particles can be generated for different pressure regimes, although only the free-molecular regime is considered here. An algorithm for such 3D particle structure generation is presented for the specific application of generating TEM-style images as a diagnostic tool. The Aromatic Site Counting -Primary Particle (ARS-SC-PP) model is used to simulate soot formation in a laminar premixed flame and in an internal combustion engine. The latter being achieved by incorporating the detailed soot model into the stochastic reactor model, previously used for engine simulations.*

## 1. INTRODUCTION

Soot particle growth models in the past have been very simple. This was in part due to the limitations of the numerical methods used, such as moment methods [1], sectional methods [2,3] and Galerkin methods [4]. These are efficient algorithms, but their complexity and computational expense scale approximately exponentially with the size of the particle type space. Monte Carlo methods [5], however, can be easily scaled to model very complex particles [6,7,8]. This paper shall focus on the implementation of complex multivariate particle models using Monte Carlo techniques.

In order to fully characterise soot particles a description of both the particle structure and the particle chemistry must be developed. Many current soot models are based on the work of Frenklach & Wang [9]. In that model soot growth occurs through the addition of acetylene ( $C_2H_2$ ) by processes analogous to those for small PAHs. Only one acetylene addition process was defined by Appel et al. [10], though a more complete set of processes has been presented since [11,8].

A large amount of work has been conducted into the shape and structure of soot particles. There is experimental evidence that soot particles consist of fractal-like structures [12], hence structure models of increasing complexity have been developed using this assumption. Surface-volume and fractal particle descriptions [13,14] have been used which describe particles by two coordinates, typically a volume and a shape parameter or surface area. Full 3D aggregate particle representations have also been used [15,7]. A lot of work has been completed to study the chemical nature of single particles

[16,11,17,18]. Frenklach [16] developed a detailed mechanistic model of PAH surface growth, which has been used to simulate the growth of PAH surfaces [19,11]. Violi [17] used kinetic Monte Carlo – molecular dynamics (KMC-MD) to simulate the growth of 3D PAH structures. Violi & Izvekov [18] also attempted to model the aggregate structure of soot particles using these PAH structures by considering their interaction.

In this paper a combined soot surface chemistry and primary particle model is presented which builds on the soot model of Frenklach & Wang [9] by describing soot particles by their aromatic structure. This model combines models presented elsewhere by Celnik et al. [8] and West et al. [20]. The model is then used to simulate a premixed flame and an internal combustion engine.

## 2. AROMATIC-SITE MODEL

The model reviewed in this section has previously been published by Celnik et al. [8]. A description of PAH surface sites was developed in order to identify a suitable data structure for the population balance model. This description was based on the following observable rules:

- (1) PAHs can be described by the number of surface “sites”. For filled PAHs these sites will form a closed loop around the PAH edge.
- (2) Each surface carbon belongs to two “sites”.
- (3) Each site consists of two surface carbon atoms (those available for reaction).
- (4) The previous points require that each site has two neighbouring sites.
- (5) A site can be distinguished by the total number of carbon atoms it contains. Acceptable counts are 2, 3, 4 and 5 carbon atoms.
- (6) Surface processes affect the reacting site and at least its two neighbouring sites.

In this nomenclature a surface carbon is one available for reaction which has a bonded H atom. Bulk carbon shall describe carbons in the graphene lattice. Figure 1 gives the nomenclature for different site types. A site with two carbon atoms is called a “free-edge” (ED), a site with three carbon atoms is called a “zig-zag” (ZZ) [16], a site with four carbon atoms is called an “armchair” (AC) [11] (also called elsewhere a “boat” site [16]) and a site with five carbon atoms shall be called a “bay” (BY). In general the addi-

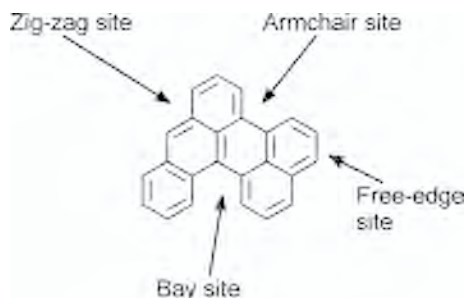


Figure 1. An example PAH structure showing all the different principal site types.

tion of a ring beside any site increases its carbon count by one, thereby converting it into a different site. Similarly the removal of a ring will decrease the carbon count of a site by one. The exception to these rules is the addition of a ring beside a bay. Clearly adding an additional carbon to a bay generates a new ring, which in turns affects the next neighbouring site of the bay. A model for 5-member ring addition and conversion to 6-member rings is included in this study similar to that presented by Frenklach et al. [11], however, 5-member rings are not modelled as part of the PAH graphitic lattice. In this nomenclature R5 denotes a 5-member ring on a zig-zag site. A zig-zag site cannot react further once occupied by a 5-member ring.

### 3. SURFACE PROCESSES

Only hydrogen-abstraction carbon-addition (HACA) processes, analogous to those for small PAHs, are considered here. These processes essentially proceed via the creation of surface radical sites by hydrogen abstraction, followed by the addition of acetylene to those sites. This mechanism for soot formation has been studied extensively since the early 1990s [9], and many variations on the theme have been discussed. The processes are discussed and listed by Celnik et al. [8]. The rate expressions for these jump processes have been obtained by assuming intermediate species to be in steady-state [8] and that the ring addition and desorption steps are irreversible. The jump processes are summarised in Table 1.

It is important to note that some of the processes listed in Table 1 are dependent on two sites occurring consecutively in the PAH edge. These are termed combined-sites here.

### 4. SITE-COUNTING MODEL

It is the goal of this work to develop a detailed chemical and physical model of soot particles which can be solved in acceptable computation times for whole ensembles of particles. This requires the aromatic structure of PAHs and soot particles to be formally defined in a computational context. Here the fundamental state space is described, which is the minimum sufficient to fully describe a planar PAH molecule. From this state space progressively simpler data structures can be defined to enable efficient computation, while retaining most of the fundamental information. The site-counting model is formulated under the assumption that soot particles are formed primarily of stacked planar PAHs. It is anticipated that 3D structures do exist and that the addition of aliphatic chemical species may also play an important role in soot formation, however, these have been neglected for the present model. In principal the concepts of the site-counting model should allow these assumptions to be relaxed in future.

#### 4.1. Fundamental particle state space

The structure of a PAH is defined by the position of the C atoms and the bonds between them. The similarity between the structures of PAHs and graphite ensures that

a C atom can form bonds with a maximum of three other C or H atoms. It is possible to determine the structure of a PAH molecule if the information about the position of a carbon atom and the relative positions of the surrounding C atoms bonded to it are known. Therefore, the simplest state space  $E$  required to track the structure of a planar PAH molecule can be given by:

$$E = (i, j, i_1, j_1, i_2, j_2, i_3, j_3) \in \mathbb{Z}^8 \quad (1)$$

where  $(i, j)$  are the coordinates of a C atom, and  $(i_n, j_n)_{n=1, 2, 3}$  are the coordinates of the C atoms bonded to the C atom at  $(i, j)$ . The further generalisation of this state space to 3D is possible by including an additional coordinate and defining them in the set of real numbers.

While this state space is sufficient to fully define a PAH structure, definition of the Monte-Carlo jump processes on it is very difficult. Higher order data structures are required.

## 4.2. Kinetic-Monte Carlo data structure

A 2D kinetic-Monte Carlo data structure can be defined for planar PAH molecules by placing the molecule on a 2D grid, such as that in Figure 2. This grid neglects the true bond lengths, which is acceptable as the bonds are implicitly represented in the rate expressions by the surface sites.

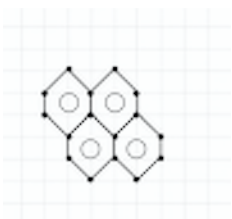


Figure 2. An example grid showing a pyrene molecule.

In order to make the definition of jump processes easier using the above defined state space, two vectors are defined: a carbon atom vector  $c$ , and a site vector  $s$ . The vector  $c$  stores the following information: the two site types of which the C atom is a part,  $S_1$  and  $S_2$ , the site indices (each site of a particular type is differentiated from others based on its index),  $S_{in1}$  and  $S_{in2}$ , the carbon atom type (bulk or surface),  $C_{type}$ , and its spatial coordinates,  $i$  and  $j$ . Thus,  $c$  can be represented as:

$$c = (S_1, S_2, S_{in1}, S_{in2}, C_{type}, i, j) \in \mathbb{Z}^7$$

A site vector  $s$  stores the following information: site type,  $S_{type}$ , site index (explained above),  $S_{in}$ , and the coordinates of the two surface C atoms,  $(i_1, j_1)$  and  $(i_2, j_2)$ . Therefore,  $s$  can be represented as:

$$s = (S_{type}, S_{in}, i_1, j_1, i_2, j_2) \in \mathbb{Z}^6$$

#### 4.2.1. Typical KMC-ARS result

A typical PAH structure generated using the KMC-ARS model is shown in Figure 3. This molecule was generated after 3 ms in a  $C_2H_2$  flame at 2.67 kPa, and with a C/O ratio of 0.8.

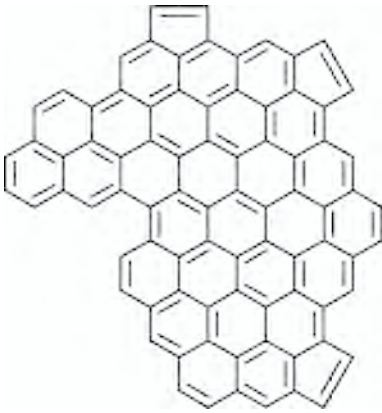


Figure 3. A typical PAH molecule generated using the KMC-ARS model.  $C_2H_2$  flame conditions were 2.67 kPa pressure a C/O ratio of 0.8. This molecule was generated after 3 ms of flow time.

#### 4.3. Site-counting data structure

The above KMC data structure is still too complex to be applied to an ensemble of particles, given that each particle would consist of many PAH molecules.

The site-counting model has been developed to describe the aromatic structure of soot particles by nine variables only. Hence particles are described by a 9-dimensional type  $X_{sc}$ :

$$X_{sc} = (C, H, N_{ed}, N_{zz}, N_{av}, N_{bay}, N_{R5}, S_a, N_{PAH})$$

where  $N_x$  is the number of site type  $x$ ,  $C$  and  $H$  are the number of carbon and hydrogen atoms respectively,  $S_a$  is the surface area of the particle and  $N_{PAH}$  is the number of PAHs

Table 1. Jump processes. The reaction steps and the rate constants have been obtained from Frenklach et al. and Celnik et al. [11,8]. The activation energies are in units of kcal/mol.

Reaction	Site	Jump process	Rate constant, k
(1) Free-edge growth	FE		$1.1 \times 10^7 T^{1.71} e^{-\frac{33.9}{RT}}$
(2) R6 desorption	R6		$1.3 \times 10^{11} T^{1.08} e^{-\frac{70.42}{RT}}$
(3) R5 addition	ZZ		$6.8 \times 10^{11} e^{-\frac{32}{RT}}$
(4) R5 desorption	R5		$1.6 \times 10^{14} e^{-\frac{42.42}{RT}}$
(5) Armchair growth	AC		$8 \times 10^7 T^{1.56} e^{-\frac{8.8}{RT}}$
(6) 5- to 6-member ring conversion at free-edge	R5FE		$1.1 \times 10^7 T^{1.71} e^{-\frac{33.9}{RT}}$
(7) 6- to 5-member ring conversion	R6AC		$1.3 \times 10^{11} T^{1.08} e^{-\frac{70.42}{RT}}$
(8) 5- to 6-member ring conversion at armchair	R5AC		$1.34 \times 10^{12}$
(9) R6 oxidation by O <sub>2</sub>	R6		$9.7 \times 10^3 T^{2.42} e^{-\frac{38.28}{RT}}$
(10) R6 oxidation by OH	R6		$2.2 \times 10^{12} e^{-\frac{31.4}{RT}}$
(11) AC oxidation by O <sub>2</sub>	FE		$9.7 \times 10^3 T^{2.42} e^{-\frac{38.28}{RT}}$
(12) AC oxidation by OH	FE		$2.2 \times 10^{12} e^{-\frac{31.4}{RT}}$
(13) R5 shift	R5ZZ		$1.34 \times 10^{12}$

which make up the particle. By tracking the number of sites, but neglecting their relative positions this data structure allows complete particle systems to be simulated quickly.

Each process listed in Table 1 must change the particle state space in a clearly defined way. The state space changes were formulated by consideration of the underlying physical processes and consideration of PAH sites discussed earlier. The particle state changes are given in Table 2. Note that the R5 shift process has no effect in the site-counting model, therefore it is neglected from this table.

When a ring is added or desorbed from a PAH site it necessarily changes the structure of the PAH surface. Each site has two neighbouring sites, which must both be updated. In general, ring addition increases the number of carbon atoms in the neighbouring sites by one each (incrementing), and ring desorption decreases the number of carbon atoms by one each (decrementing). This change to the neighbouring site types occurs according to the rules in Table 3.

#### 4.4. Equation closure

For particles of type  $x$ , the site counting model can be expressed as an ODE of the form:

$$\frac{dx}{dt} = F(x, N_{R6\_AC}, N_{R5FE}, N_{R5AC}, N_{R5ZZ}, N_{R6}, b_{ij}) \quad (2)$$

where  $N_j$  is the number of combined-site type  $y$  in the particle,  $b_{ij}$  is the number of site type  $j$  next to site type  $i$  and  $i, j \in (ED, ZZ, AC, BY, R5)$ . The form of the right-hand side function  $F$  is defined by the jump processes, the inception processes and the coagulation process. It is clear that the above equation is not closed, as expressions for  $N_{R6\_AC}$ ,  $N_{R5FE}$ ,  $N_{R5AC}$ ,  $N_{R5ZZ}$ ,  $N_{R6}$  and the  $b_{ij}$  values are required. In the previous work [8,21] estimates of the combined-site concentrations were found using linear correlations, obtained from the KMC-ARs model, with a single known quantity. These correlations are discussed in a subsequent section.

The linear correlations were developed by simulating the 2D structural evolution of a few PAH molecules in a fixed chemical environment at different temperatures in the range 1500 K to 2000 K using a KMC code. While such correlations may not be ideal, statistical studies of PAH structures are essentially non-existent, so they should give a reasonable first approximation. It is intended to perform an in-depth study on this topic at a future point.

Not all site configurations are equally likely, hence not all sites are equally probable to be neighbours of a reacting site. In order to correctly select neighbouring sites a further study was conducted using the KMC code [21]. For each process the current state of the PAH molecule, as it applies in the site counting model, was stored. The neighbours of the site selected for reaction were noted. The code was run several times at different temperature and for different molecules, to provide a large data set of reaction events and the corresponding neighbouring sites. This allowed the probability distribution of the neighbouring sites to be found. The neighbour weight distributions for each process are listed in Table 4. Generation of these weights is discussed in a subsequent section.

Table 2. Changes to particle state due to jump processes in Table 1<sup>a</sup>.

Process	C	H	N <sub>c,d</sub>	N <sub>z,z</sub>	N <sub>a,c</sub>	N <sub>b,a,y</sub>	N <sub>R5</sub>	N <sub>p,PAH</sub>	Inc. <sup>b</sup>	Dec. <sup>c</sup>
<b>Inception Processes</b>										
Pyrene inception	32	20	12	8	0	0	0	2	.	.
<b>Surface Processes</b>										
S1 Free-edge ring growth	+4	+2	+2	.	.	.	.	.	2	.
S2 Free-edge ring desorption	-4	-2	-2	.	.	.	.	.	.	2
S3 R5 addition	+2	.	.	-1	.	.	+1	.	.	.
S4 R5 desorption	-2	.	.	+1	.	.	-1	.	.	.
S5 Armchair ring growth	+2	.	+1	.	-1	.	.	.	2	.
S6 R5-R6 conversion at free-edge	+2	+2	+2	.	+1	.	-1	.	1	.
S7 R6-R5 conversion at free-edge	-2	-2	-2	.	-1	.	+1	.	.	1
S8 R5-R6 conversion at armchair	.	.	+1	.	.	.	-1	.	1	.
<b>PAH Condensation Processes</b>										
Pyrene condensation	+16	+10	+6	+4	.	.	.	+1	.	.
<b>Oxidation Processes</b>										
S9 Free-edge O <sub>2</sub> oxidation	-4	-2	-2	.	.	.	.	.	.	2
S10 Free-edge OH oxidation	-4	-2	-2	.	.	.	.	.	.	2
S11 Armchair O <sub>2</sub> oxidation	-2	.	-1	.	+1	.	.	.	.	2
S12 Armchair OH oxidation	-2	.	-1	.	+1	.	.	.	.	2

<sup>a</sup> Surface area is updated according to the surface-volume model of Patterson & Kraft [13].

<sup>b</sup> Increment number of uniformly chosen sites according to Table 3(a).

<sup>c</sup> Decrement number of uniformly chosen sites according to Table 3(b).

Table 3. Particle state changes when incrementing sites. Reverse signs for decrementing changes.

(a) Site Incrementing

Original Site	$N_{ed}$	$N_{zz}$	$N_{ac}$	$N_{bay}$	$N_{R5}$
Free-edge	-1	+1	.	.	.
Zig-zag	.	-1	+1	.	.
Armchair	.	.	-1	+1	.
Hole	.	.	.	-1	.

(b) Site Decrementing

Original Site	$N_{ed}$	$N_{zz}$	$N_{ac}$	$N_{bay}$	$N_{R5}$
Zig-zag	+1	-1	.	.	.
Armchair	.	+1	-1	.	.
Hole	.	.	+1	-1	.

## 5. MODEL VALIDATION

Development of the correlations for combined sites and the probabilities of sites acting as neighbours, which are required by the site-counting model, is detailed here. Additionally, the effect of steric hinderance in larger PAH structures is investigated.

### 5.1. Combined-site correlations

As explained above, the site-counting model requires information about the PAH structures in the form of correlations and statistics. Figure 4 shows two combined sites



Figure 4. A computed PAH molecule after a simulation time of 0.1 ms. The combined sites involving three adjacent free-edges (R6 ring) are shown inside circles. The combined sites involving an R6 ring next to an armchair (R6 AC) are shown inside ellipses.

on a PAH structure computed using the KMC-ARS model. The correlations for the combined sites were based on the variation in their counts with the count of one of their constituent elementary sites. To obtain the correlations, the simulation of the growth of PAH molecules was carried out 50 times and the combined site counts were stored along with the elementary site counts. Figure 5 shows an average variation in the number of two combined sites with the number of elementary sites. A nearly linear relationship was observed in all cases. A least-squares algorithm was used to fit a linear function to the data, averaged over all simulations, to obtain the correlations.

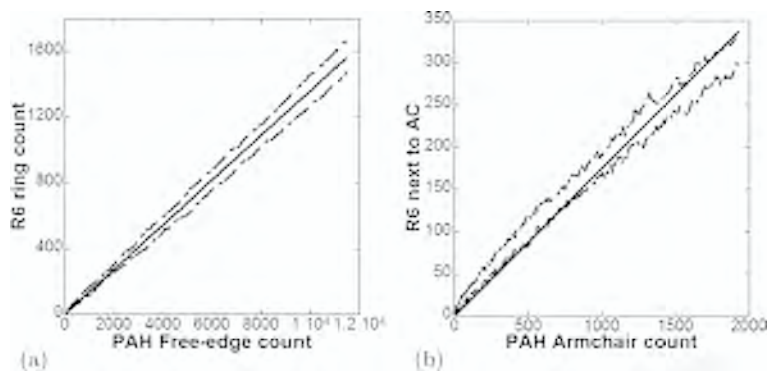


Figure 5. Correlations for combined sites. Solid lines show linear approximations, dashed lines show confidence intervals. Confidence interval is an estimate of the statistical fluctuation of a variable [21]. (a) R6 ring count as a function of free-edge count. (b) AC R6 site count (R6 ring next to an armchair) as a function of armchair count.

The correlations for all the combined sites required by the site-counting model are given below:

$$N_{R6} = \begin{cases} 0.136 \times (N_{FE} - 2) & \text{if } N_{FE} > 2 \\ 0 & \text{if } N_{FE} \leq 2 \end{cases} \quad (3)$$

$$N_{AC,R6} = \begin{cases} 0.174 \times N_{AC} & \text{if } N_{FE} > 2, N_{AC} > 0 \\ 0 & \text{if } N_{FE} \leq 2, N_{AC} \leq 0 \end{cases} \quad (4)$$

$$N_{R5,R6} = \begin{cases} 1.33 \times N_{R5} & \text{if } N_{FE} > 0, N_{R5} > 0 \\ 0 & \text{if } N_{FE} \leq 0, N_{R5} \leq 0 \end{cases} \quad (5)$$

$$N_{R5,AC} = \begin{cases} 0.1 \times N_{R5} & \text{if } N_{AC} > 0, N_{R5} > 0 \\ 0 & \text{if } N_{AC} \leq 0, N_{R5} \leq 0 \end{cases} \quad (6)$$

## 5.2. Neighbour statistics

A PAH process on a site affects at least two other neighbouring sites. Therefore, after every reaction, it is necessary to update the neighbouring sites. In the site-counting model, the neighbouring sites for each reaction are determined using the probability of occurrence of a site as a neighbour in a reaction. Only processes 1,2,5,7 and 9-12 in Table 1 are considered here, as those involving only 5-member rings do not change neighbouring sites, and processes 7 and 8 were observed to occur so infrequently that meaningful statistics could not be obtained. It was initially assumed that neighbouring sites of type  $S \in \{ED, ZZ, AC, BY\}$  are selected for process  $m$  with the probability  $P_{S,k}(m) = N_{S,k}/N_{tot,k}$ , where  $N_{S,k}$  is the number of sites of type  $S$  at time  $k$ ,  $N_{tot,k}$  is the total number of sites (ignoring 5-member rings), and  $m \in \{1, 2, 5, 7, 9, \dots, 12\}$  is the process index (see Table 1). However, it was found that when using these probabilities the site-counting model did not agree with the KMC-ARS model, which suggests that some sites are more likely than others to be neighbours for certain processes. Therefore, site count weights were introduced for each process such that the weighted counts are given by:  $N'_{S,k}(m) = W_{S,k}(m) \times N_{S,k}$ , hence the probability of a site of type  $S$  being selected at time  $k$  for process  $m$  becomes:

$$P_{S,k}(m) = \frac{N'_{S,k}(m)}{N'_{tot,k}(m)} \quad (7)$$

where  $N'_{tot,k}(m)$  is the sum of the weighted site counts and depends on the process  $m$ . It is assumed that the site weights do not depend strongly on PAH size, therefore they are considered to be constant for each process. This assumption is supported by the KMC-ARS simulations conducted for this study.

In order to calculate the site weights, several KMC-ARS simulations were performed. For each simulation there are  $K$  events, and  $K_m$  denotes the number of times event  $m$  occurred. On selection of the  $k^{\text{th}}$  jump process, where  $k = 1, 2, \dots, K$ , the following information was stored: the time point  $k$ , the jump process index,  $m_k$ , the types of both neighbour sites,  $T_{1,k}$  and  $T_{2,k}$  and the counts of all site types;  $N_{ED,k}$ ,  $N_{ZZ,k}$ ,  $N_{AC,k}$ ,  $N_{bay,k}$ .  $L_{S,m}$  shall denote the number of times a site of type  $S$  acted as a neighbour for process  $m$ . In the limit of large  $K_m$ , the probability of a site acting as a neighbour is assumed to approach  $P_{S(m)} = L_{S,m,k}/K_{m,k}$ , therefore, by summing over each jump process and solving the following equation, the site weights can be obtained:

$$\sum_{k=1}^{K_m} \frac{W_S N_{S,k}}{W_{FE} N_{FE,k} + W_{ZZ} N_{ZZ,k} + W_{AC} N_{AC,k} + W_{bay} N_{bay,k}} = L_{S,m} \quad (8)$$

where  $S \in \{ED, ZZ, AC, BY\}$  and  $m \in \{1, 2, 5, 7, 9, \dots, 12\}$ . As there are four possible site types which may act as neighbours; free-edges (FE), zigzags (ZZ), armchairs (AC) and bays, equation 8 gives a system of eight linear equations, which can be solved using a standard numerical technique such as a Newton method. Equation 8 was solved for the four elementary sites, with the additional constraints of  $W_S \geq 0$  and  $\sum_S W_S = 1$ . Table 4 shows the site-probabilities for the principal reactions.

Table 4. Neighbouring site probability weight distributions for each stochastic process.

Process	Site	$P_{ed}$	$P_{zz}$	$P_{ac}$	$P_{bay}$
S1 Free-edge growth	Free-edge	0.10	0.27	0.40	0.23
S2 Free-edge desorption	R6	0.00	0.05	0.61	0.34
S3 R5 addition	Zig-zag		N/A		
S4 R5 desorption	R5		N/A		
S5 Armchair growth	Armchair	0.68	0.20	0.04	0.08
S6 R5 free-edge conversion	ED-R5	0.25	0.25	0.25	0.25
S7 R5 free-edge desorption	AC-R6	0.00	0.06	0.57	0.37
S8 R5 armchair conversion	AC-R5	0.25	0.25	0.25	0.25
S9 O <sub>2</sub> free-edge oxidation	R6	0.00	0.32	0.39	0.29
S10 OH free-edge oxidation	R6	0.00	0.36	0.41	0.23
S11 O <sub>2</sub> armchair oxidation	Armchair	0.00	0.08	0.53	0.39
S12 OH armchair oxidation	Armchair	0.00	0.08	0.38	0.54

### 5.3. Unavailable sites

As a PAH molecule grows, some of the reactive sites become hindered due to the presence of neighbouring sites. Figure 6 shows the presence of unavailable free-edges and armchairs on a computed PAH molecule. Further growth on those reactive sites is possible only if the PAH molecule is allowed to adopt a 3D structure due to the interaction between nearby H atoms. However, in a stack, due to the presence of nearby PAHs, 3D geometry of a PAH may not be possible. It is most likely that the H atoms are abstracted and a six-member ring is formed through cyclo-dehydrogenation processes. These processes have been ignored in this study, and their influence is highlighted as work requiring further study.

It is possible to determine the number of unavailable sites using the KMC-ARS model. Figures 7a and 7b show the fraction of unavailable free-edges and armchairs respectively as functions of the free-edge and armchair counts. These fractions firstly increase with the site counts and then attains an asymptotic limit of about 0.9 at larger site counts. A function of the form  $Y = \tanh(a \times \log(bX + 1))$  was found to describe this asymptotic behaviour well. The curves in Figure 7 were fitted by trial and error, and the equations are given below:

$$N_{unavailFE} = \tanh(0.593 \times \log(0.054 \times N_{FE} + 1)) \quad (9)$$

$$N_{unavailAC} = \tanh(0.571 \times \log(0.23 \times N_{AC} + 1)) \quad (10)$$

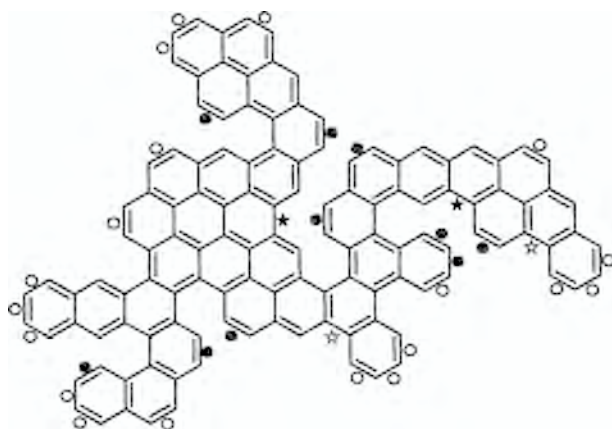


Figure 6. A computed PAH molecule formed after 0.1 ms. Filled circles and stars denote unavailable free-edges and armchairs respectively. Hollow symbols denote available sites. 2 out of 4 armchairs and 10 out of 29 free-edges are unavailable.

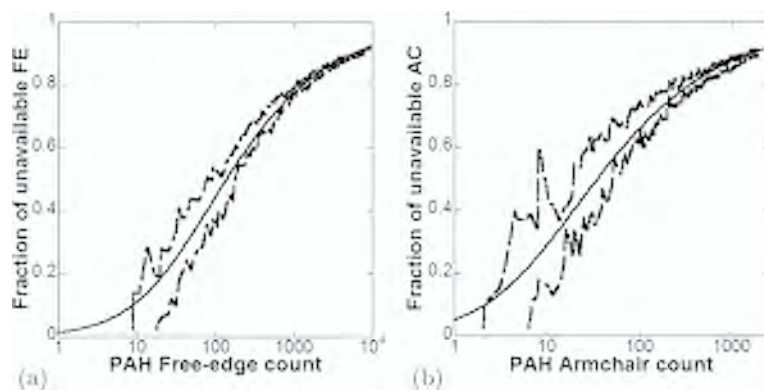


Figure 7. Unavailable sites. Solid lines show a tanh fit. Dashed lines show the confidence intervals. (a) Fraction of unavailable free-edges. (b) Fraction of unavailable armchairs.

#### 5.4. validation

To validate the site-counting model, the correlations and statistics described above were implemented in the site-counting model, and identical simulations were performed using the two models. The simulation parameters are given in Table 5.

Figure 8 shows the comparison of the PAH characteristics: carbon atom count and number of elementary sites on the PAH. Figure 8a shows that the sitecounting model and the KMC-ARS model predict similar carbon atom counts at all observed flow times. Figure 8b shows that the agreement for the number of free-edges, zig-zags and

Table 5. Simulation parameters for PAH growth validation simulations.

Parameters	Initial value
Temperature	1650 K
Pressure	1 atm
$X_{C_2H_2}$	$10^{-1}$
$X_{H_2}$	$10^{-1}$
$X_H$	$10^{-2}$
$X_{OH}$	$10^{-4}$
$X_{O_2}$	$10^{-2}$
Starting structure	Pyrene ( $C_{16}H_{10}$ )
Free edges	6
Zigzags	4
Residence time, $t_{stop}$	2.4 ms

armchairs is reasonable also. The close agreement of the number of elementary sites is important because the site counts are used to calculate the process rates. The extent of agreement of the computed PAH characteristics by the two models is very encouraging. These comparisons provide an adequate ground for the implementation of the site-counting model into a soot particle population balance.

As the PAH molecules present in flames are very small in size (PAHs with less than 100 C atoms are observed in flames [22,23]), a comparison between the two models was carried out over this range with and without the correlation for unavailable sites, to test its importance in the experimental size range. Figure 9 shows the variation in the number of PAH sites with the number of C atoms for this case. It can be concluded from this figure that the correlations for unavailable sites are not very significant for small PAH molecules.

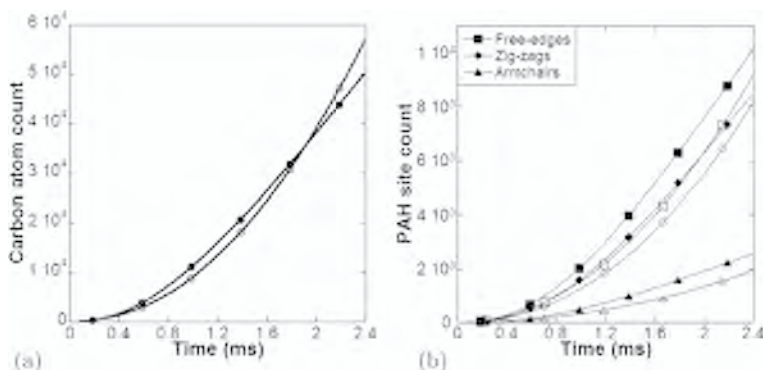


Figure 8. Comparison of the results from the KMC-ARS model and the site-counting model. Filled symbols show the results from the site-counting model and hollow symbols show the result from the KMC-ARS model. (a) C atom count as a function of time. (b) Site count as a function of time.

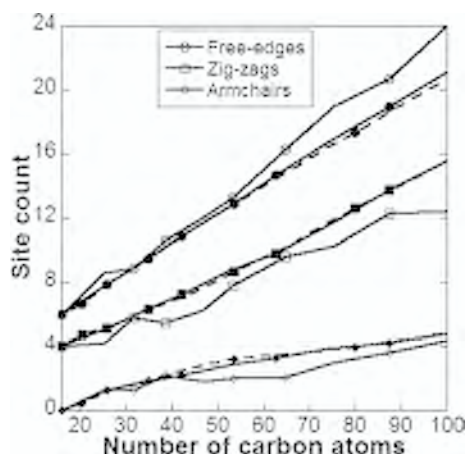


Figure 9. Comparison of the results: Filled symbols show the results from the site-counting model and hollow symbols from the KMC-ARS model. Dashed lines show the results from site-counting model without correlations for unavailable sites.

## 6. PARTICLE STRUCTURE MODEL

While 2D surface-volume models, such as that described by Patterson & Kraft [13], can provide an estimation of the aggregation structure of soot particles, they are limited by the restrictive assumptions made. An estimate average primary particle size can be calculated, although in reality there will be a distribution of primary-particle sizes within an aggregate. High-precision 3D models [15,7] are able to describe the aggregation structure of soot particles completely, but are very computationally expensive. Recently a simple primary-particle model has been developed [20], originally for titania nanoparticles, though the model also applies to sooting systems. The model is essentially an extension of the surface-volume model, in that it uses the volume and surface area prediction of that model to inform a list of spherical primary particles. This list is stored independently of the surface-volume parameters for each particle. In this extension to the model, the sizes of the primary particles within each agglomerate particle are also tracked, hence the minimum particle state space becomes  $E_{pp} = (C, S, p)$ , where  $p = (p_1, p_2, p_3, \dots)$  is the vector of primary particle masses. For a simulation in which the highest number of primaries in a single agglomerate reaches  $N$ , the population balance effectively has  $(N + 2 - 1)$  dimensions. When combined with the site-counting model, the complete state space of the computation particles is

$$E_{scpp} = (C, H, N_{ed}, N_{zz}, N_{ac}, N_{bay}, N_{R3}, S_a, NP_{AH}, p)$$

which has  $(N + 8)$  dimensions. This is the particle description used for subsequent simulations.

On inception a computation particle is assigned a single primary, with the same mass as the particle. On coagulation the primary particle lists of the two aggregates are

combined. The lists are stored in order of primary size for computational efficiency, and this order is maintained when the lists are combined. Surface growth processes are modelled as follows. According to the surface-volume model [13] all surface processes (growth and oxidation) cause particles to become rounder. This assumption is based on the TEM observation of soot particles. The sintering process, by its nature, also causes an increase of sphericity. The first step of surface growth/oxidation is to add or remove the required mass from the primary particles. As the mass is discretised as the number of carbon atoms, this simply involves adding/removing a set number of C atoms from the list. Atoms are added/removed randomly from primaries weighted by their surface area using a binomial process. A similar algorithm is used to describe particle rounding by any process. Rounding in general reduces the number of primary particles in the aggregate, and the primaries get larger. This is modelled by removing primaries, starting with the smallest, and distributing that mass over the remaining primaries in an identical manner as surface growth. This procedure is repeated until the surface area of the primary particles is less than or equal to the predicted by the surface-volume model. This is shown schematically in Figure 10.

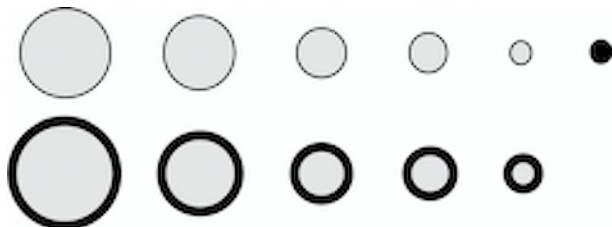


Figure 10. Primary particles before (top) and after (bottom) surface growth rounding

The combined soot particle model incorporating the ARS site-counting model and the primary-particle description has been integrated into the in-house stochastic particle solver SWEEP. This code is available upon request.

### 6.1. TEM-style image generation

In the models described so far no structural information about an aggregate, such as the position of the primary particles with respect to each other, is taken into account and hence is not available in an implementation. Nonetheless there exist several ways of deducing at least approximations to probable shapes of aggregates, for example diffusion limited cluster-cluster aggregation (DLCA) [24,25], valid in the continuum regime, and ballistic cluster-cluster aggregation (BCA) [26], valid in the free-molecular regime. Since these models are generally applied to systems in the free molecular regime, only BCA is considered here. However, for large aggregates formed in Diesel engines for example, BCA is not applicable since aggregation is diffusion limited in this case.

One of the simplest ways of generating an aggregate geometry is by imitating the physical history the aggregate goes through. In algorithmic language:

- (1) Create a list of aggregates where each aggregate is initialized as containing only a single primary particle of the original aggregate. In other words the list corresponds to the list of primary particles of the original aggregate.
- (2) Pick two distinct aggregates from the list randomly with uniform distribution.
- (3) Collide the two aggregates as described below, delete one of the picked aggregates and replace the other one with the collided one.
- (4) If there is more than one aggregate left in the list, go to step 2.

The collision of two aggregates is carried out as follows:

- (1) Place the first aggregate such that its center of mass is at the origin, and rotate it to a uniformly random orientation.
- (2) Place the second aggregate such that its center of mass lies on the positive  $z$ -axis sufficiently distant from the origin so that it does not touch or intersect the first aggregate, and rotate it to a uniformly random orientation.
- (3) Translate the second aggregate within the  $x$ - $y$ -plane by not more than the sum of the radii of the two aggregates.
- (4) Test collision if the second aggregate were moved along the  $z$ -axis towards the origin.
- (5) If there is no contact at all, go to step 2.

This algorithm is illustrated in Figure 11.

For small aggregates, testing the collision between every sphere (primary particle) in aggregate 1 with every sphere in aggregate 2 is computationally feasible. However, there exist much more efficient algorithms for collision testing of complex objects, developed by the video game programming community. Colliding two spheres is a simple exercise in elementary geometry.

Step 4 assumes free motion along a linear trajectory, which is valid in the free molecular regime.

A typical example for a structure resulting from the above algorithm, rendered with the POV-Ray ray tracing software, is given in Figure 15a.

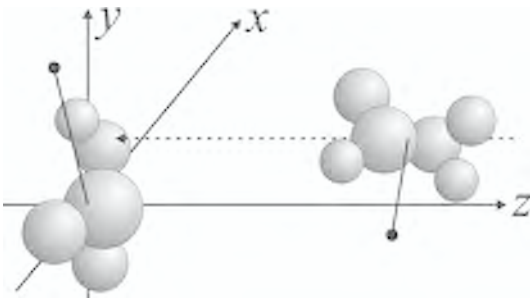


Figure 11. Schematic of ballistic aggregation of two clusters of primary particles.

## 7. PREMIXED FLAME SIMULATION

The premixed flame C4 of Abid et al. [27] have been simulated using the model detailed here, as experimentally obtained data were available for many properties of interest. The premixed flame chemistry was solved using the PREMIX code [28], including a method-of-moments approximation for soot formation [1]. The Monte-Carlo particle solver (SWEEP) was then run as a post-processing step [5] using the ARS-SC-PP model. An improved  $O_2$  oxidation rate, detailed by Celnik et al. [29], has been incorporated into the ARS chemistry and used for these simulations.

Figure 12 shows the comparison of the ARS-SC-PP model to the experimentally observed soot volume fraction ( $F_v$ ). There is a broad agreement between the simulations and the experiments, in particular when considering the confidence intervals due to the uncertainty in the measured temperature profiles. There is a difference between the soot density of  $1.5 \text{ g/cm}^3$  assumed by Abid et al. and the value of  $1.8 \text{ g/cm}^3$  used here, which might account for the small discrepancy between the simulations and the experiments.

Figure 13 shows the comparison of the ARS-SC-PP model to the experimentally obtained particle size distribution (PSD) at a height above burner of 1.0 cm. The PSDs were calculated using the kernel density estimation (density) function of the statistical package R [30] with a bandwidth of  $0.03 \times d$ , where  $d$  is the aggregate collision diameter [13]. The simulation demonstrates a reasonable fit to the experimental data. At the first HAB = 0.5 cm the simulation already predicts bimodality, which is not observed in the experimental data, however, there is a severe underprediction of the largest particles' concentrations, although the trough at around 4-4.5 nm almost match the expe-

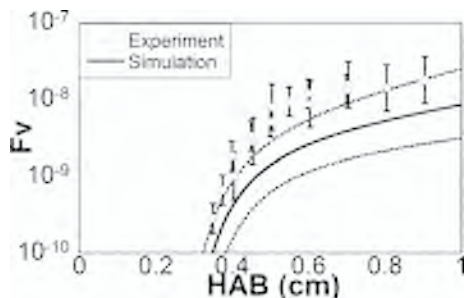


Figure 12. Soot volume fraction as a function of height above burner. Short-dashed lines indicate confidence intervals due to the 50 K uncertainty in the experimentally measured flame temperature. HAB shifted by +0.15 cm.

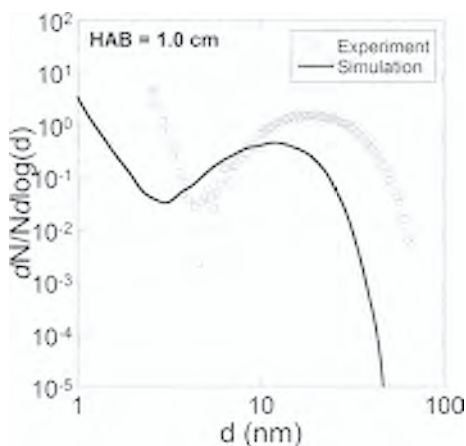


Figure 13. Particle size distribution at different a height above burner of 1.0 cm (shifted by +0.15 cm).

perimental data. The bimodal nature of the experimental data is well predicted. The disagreement at larger particle sizes is possibly indicative of a coagulation effect.

Figure 14 shows the particle C/H ratio distribution against particle diameter at HAB = 1.0 cm. The 2D kernel density estimation (kde2d) function of R was used to calculate the distribution, using 100 points in each direction. The bimodality of the particle distribution can be clearly seen. The left-most density maximum occurs around C/H = 1.6, which is equivalent to pyrene (C<sub>16</sub>H<sub>10</sub>). This is an artefact of the soot inception model used, which assumes that the dimerisation of pyrene is the only route of particle formation, so in this respect the result is uninteresting. The second peak occurs at C/H values around 2, which is consistent with reported values for young soot

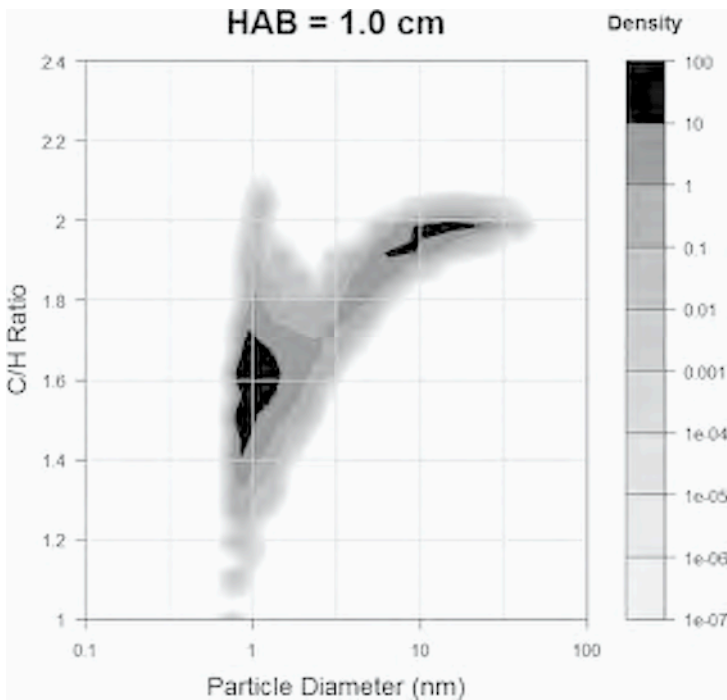


Figure 14. Particle C/H Ratio density plot against particle diameter at HAB = 1.0 cm.

particles [17]. It is interesting that there is little variation of the C/H ratio for particles between 10-40 nm, in fact the C/H ratio appears to converge on a value just below 2. Far higher ratios are presented in the literature, for example Harris & Weiner [31] report about 7 and Homann [32] reports about 10. It has been suggested [8] that a process such as graphitisation could be responsible for such an increase in C/H ratio, but this has not been considered here.

## 8. ENGINE SOOT MODELLING

The detailed soot models outlined in the previous sections have also been applied to soot formation in internal combustion engines. To this end, the SWEEP library has been implemented into the in-house engine model, called the Stochastic Reactor Model (SRM). The SRM is inspired by Probability Density Function (PDF) transport methods [33] and has been successfully employed in a number of earlier engine studies without taking soot into account, for example [34,35]. The main features of this model include detailed chemical kinetics, and a statistical representation of inhomogeneities in the in-cylinder gases, that is of stratification in composition as well as tem-

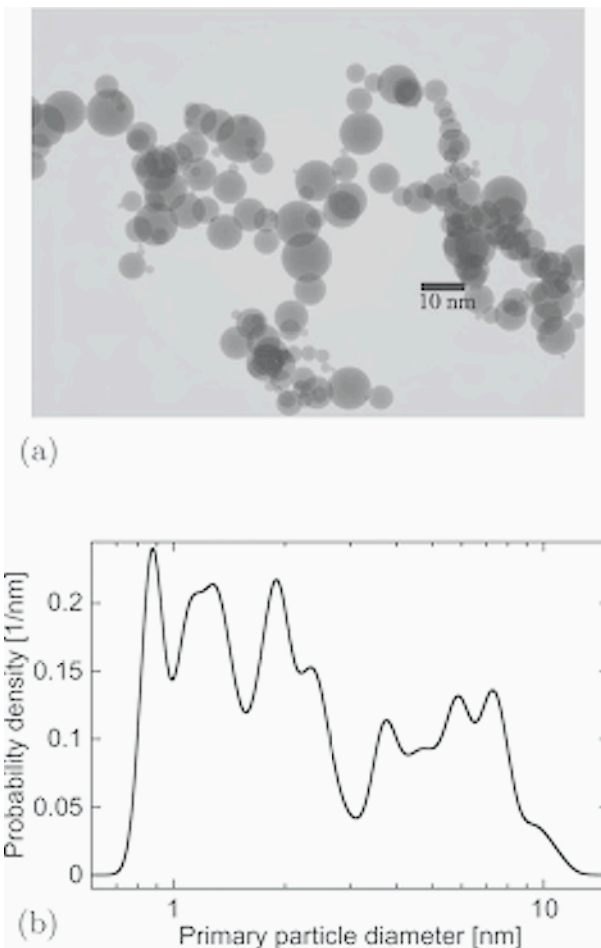


Figure 15. Typical simulated aggregate sampled at 48.2 CAD ATDC, with size distribution of primary particles. (a) TEM-style image of aggregate (223 primaries, collision diameter 77.8 nm). (b) Primary particle size distribution of aggregate 15(a).

perature. A key advantage compared to other approaches is that this model is computationally cheap with about one to two hours of CPU-time per engine cycle, enabling convenient multi-cycle and sensitivity studies.

As a fuel model a detailed chemical mechanism for Primary Reference Fuels (PRFs, n-heptane/iso-octane mixtures) containing 208 species and 1002 reactions is used, which has been extended [36] to include small PAHs such as pyrene which function as inception species as described in previous sections.

In a first attempt to model soot formation in detail in an engine, a Homogeneous Charge Compression Ignition (HCCI) engine is chosen, that is an engine in which fuel (here pure n-heptane) and air are fully premixed, and (auto-)ignition is triggered simply through compression. Since the aim is to study soot formation, an equivalence ratio of 1.93 was chosen. In order to operate an engine so rich, high levels of Exhaust Gas Recirculation (EGR) are required, that is significant amounts of burnt gases – including particulate matter such as soot if present – are fed back into the next engine cycle.

Figure 15 shows a typical simulated aggregate rendered in TEM-style (Figure 15a) together with its size distribution of primary particles (Figure 15b). It was sampled from the engine cylinder at 48.2 crank angle degrees (CAD) after top dead centre (ATDC) and possesses a collision diameter of about 77.8 nm.

In Figure 16, simulated in-cylinder aggregate size distributions at 11 CAD ATDC are shown for eight consecutive cycles. It is observed that the distributions converge

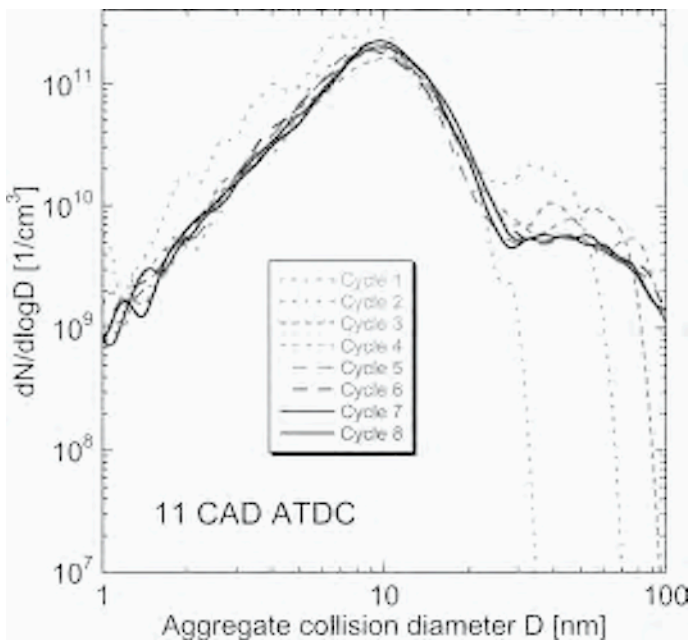


Figure 16. Simulated in-cylinder aggregate size distribution functions at 11 CAD ATDC for eight consecutive cycles. The distributions stabilize across the whole size range after the first few cycles, whilst revealing the role of the recirculated aggregates with sizes above about 30 nm.

quickly across the entire size range as the cycle number increases, and also that aggregates larger than in this case about 30 nm stem almost exclusively from previous cycles. From this it is concluded that, with high likelihood, parts of the aggregate in Figure 15a have been recirculated at least once.

## 9. CONCLUSIONS

In this article an overview of the multivariate soot particle model ARS-SC-PP has been presented. A discussion of a method of incorporating soot chemical structure into the particle model has been discussed in the context of the sitecounting model. The sitecounting model has been presented as an efficient method of tracking detailed soot chemical structure, but still allowing particle ensembles to be simulated in reasonable computation times. Validation and term closure of the site-counting model has been performed by using a 2D kinetic-Monte Carlo technique. A discussion of a primary-particle structure model, which has a complexity and speed advantage in between those of the surface-volume models and the full 3D aggregate models has been reviewed. The generation of an approximate 3D particle structure from this model has been presented, which allows representative TEM-style images to be generated for sooting systems. This is a very useful diagnostic tool. The soot model has been used to simulate a pre-mixed flame, and the predictions were compared to the experimental results. Finally an application of this advanced soot model has been presented, by incorporating the model into a stochastic reactor model for internal combustion engines. The computational efficiency and detailed chemical and structural information available from these models make them very useful for the characterisation of such complex systems.

## REFERENCES

1. M. Frenklach, *Chem. Eng. Sci* 57 (2002) 2229-2239.
2. H. Richter, S. Granata, W. H. Green, J. B. Howard, *Proc. Combust. Inst.* 30 (2005) 1397-1405.
3. J. Z. Wen, M. J. Thomson, S. H. Park, S. N. Rogak, M. F. Lightstone, *Proc. Combust. Inst.* 30 (1) (2005) 1477-1484.
4. J. Appel, H. Bockhorn, M. Wulkow, *Chemosphere* 42 (2001) 635-645.
5. M. Balthasar, M. Kraft, *Combust. Flame* 133 (2003) 289-298.
6. M. Balthasar, M. Frenklach, *Proc. Combust. Inst.* 30 (2005) 1467-1475.
7. N. Morgan, M. Kraft, M. Balthasar, D. Wong, M. Frenklach, P. Mitchell, *Proc. Combust. Inst.* 31 (2007) 693-700.
8. M. S. Celnik, A. Raj, R. H. West, R. I. A. Patterson, M. Kraft, *Combust. Flame* (2008) in press.
9. M. Frenklach, H. Wang, *Proc. Combust. Inst.* 23 (1990) 1559-1566.
10. J. Appel, H. Bockhorn, M. Frenklach, *Combust. Flame* 121 (2000) 122-136.
11. M. Frenklach, C. A. Schuetz, J. Ping, *Proc. Combust. Inst.* 30 (2005) 1389-1396.
12. U. O. Köylü, *Combust. Flame*. 109 (1996) 488-500.
13. R. I. A. Patterson, M. Kraft, *Combust. Flame* 151 (2007) 160-172.
14. A. Kazakov, M. Frenklach, *Combust. Flame* 114 (1998) 484-501.

15. M. Balthasar, M. Frenklach, *Combust. Flame* 140 (2005) 130-145.
16. M. Frenklach, *Proc. Combust. Inst.* 26 (1996) 2285-2293.
17. A. Violi, *Combust. Flame* 139 (2004) 279-287.
18. A. Violi, S. Izvekov, *Proc. Combust. Inst.* 31 (2007) 529-537.
19. M. Frenklach, J. Ping, *Carbon* 42 (2004) 1209-1212.
20. R. H. West, M. S. Celnik, O. R. Inderwildi, M. Kraft, G. J. O. Beran, W. H. Green, *Ind. Eng. Chem. Res.* 46 (19) (2007) 6147-6156.
21. M. S. Celnik, M. Sander, A. Raj, R. H. West, M. Kraft, *Tech. Rep. 52, c4e Preprint-Series, Cambridge* (2007), <http://como.cheng.cam.ac.uk>.
22. R. L. Vander Wal, *Combust. Sci. Tech.* 132 (1998) 315-323.
23. H.X. Chen, R. A. Dobbins, *Combust. Sci. Technol.* 159 (2000) 109-128.
24. P. Meakin, *Phys. Rev. Letters* 51 (13) (1983) 1119-1122.
25. R. Jullien, R. Botet, P. M. Mors, *Faraday Discuss. Chemical Society* 83 (1987) 125-137.
26. R. Jullien, *J. Phys. A: Math. Gen.* 17 (1984) L771-L776.
27. A. D. Abid, N. Heinz, E. D. Tolmachoff, D. J. Phares, C. S. Campbell, H. Wang, On the evolution of particle size distribution functions of soot in premixed ethylene-oxygen-argon flames, *Combust. Flame* (2008) in press.
28. J. Kee, K. Grcar, M. D. Smooke, J. A. Miller, *Premix: A fortran program for modelling steady laminar one-dimensional premixed flames*, Technical report, SANDIA National Laboratories (1985).
29. M. S. Celnik, A. Raj, R. I. A. Patterson, R. H. West, M. Kraft, A statistical approach to develop a detailed soot growth model using PAH characteristics, *Tech. Rep. 53, c4e Preprint-Series, Cambridge* (2007). URL <http://como.cheng.cam.ac.uk>.
30. R. Gentleman, R. Ihaka, *R statistical software, version 2.4.0* (2005), [www.r-project.org](http://www.r-project.org).
31. S. J. Harris, A. M. Weiner, *Ann. Rev. Phys. Chem.* 36 (1985) 31-52.
32. K. H. Homann, *Combust. Flame* 11 (4) (1967) 265-287.
33. S. B. Pope, *Prog. Energy Combust. Sci.* 11 (1985) 119-192.
34. S. Mosbach, H. Su, M. Kraft, A. Bhave, F. Mauss, Z. Wang, J.-X. Wang, *Int. J. Engine Res.* 8(1) (2007) 41-50.
35. S. Mosbach, A. M. Aldawood, M. Kraft, *Combust. Sci. Technol.* 180(7) (2008) 1263-1277.
36. S. Mosbach, M. S. Celnik, A. Raj, M. Kraft, H. R. Zhang, S. Kubo, K.-O. Kim, Towards a detailed soot model for internal combustion engines, in preparation (2008).



# A joint volume-surface-hydrogen multi-variate model for soot formation

G. Blanquart, H. Pitsch

*Department of Mechanical Engineering Stanford University, Stanford, USA*

*Abstract: In this article, we present a joint multi-variate model for soot formation. In this new formulation, each soot particle is represented as a fractal aggregate that is described by three independent parameters: its total volume ( $V$ ), total surface area ( $S$ ), and number of hydrogenated (or active) sites on its surface ( $H$ ). The moments of the Number Density Function (NDF) of soot particles are solved using the Direct Quadrature Method of Moments (DQMOM). This method allows for an accurate prediction of the moments without the cost of more expensive methods like Monte-Carlo (MC). The source terms for the transport equations include nucleation, coagulation, surface growth, and oxidation. The model relies on a coherent coagulation formulation which treats both the coalescence and the aggregation limits. This model, referred to as Volume-Surface-Hydrogen (VSH), is applied to a series of laminar premixed and diffusion flames. The soot volume fraction and primary particle diameter are predicted with good accuracy when compared to the experimental measurements. Furthermore, by directly solving for the number of active sites on the surface, the model also gives insight into the surface reactivity of soot particles at high temperatures.*

## 1. INTRODUCTION

Soot is formed in many industrial devices, such as furnaces, but also in automotive and aircraft engines and in fires. It is commonly assumed that the inception of soot particles occurs by the collision of heavy Polycyclic Aromatic Hydrocarbon (PAH) molecules [1,2]. The particles further grow by collision with other particles or by addition of mass on the surface through chemical reactions [3]. These reactions are assumed to follow the HACA mechanism (H-abstraction,  $C_2H_2$ -addition) and take place on active sites found on the surface of soot particles. The surface of a soot particle is very complex as the particle is not spherical. Indeed, experimental observations [4,5] suggest that soot particles are aggregates and are composed of a certain number of small spherical particles, called primary particles. These primary particles are arranged in ways to produce fractal shaped soot aggregates. Typical flames exhibit a vast diversity of particle sizes and shapes. An accurate prediction of those properties requires a correct description of the Particle Size Distribution Function (PSDF) of the particles which include both small spherical particles and large aggregates.

The fractal dimension of soot aggregates has been studied in detail both experimentally and numerically. This fractal dimension describes how fast the size of an aggregate increases with increasing number of primary particles. Mitchell and Frenklach [6,7] studied the coagulation of spherical particles onto a so called collector

particle. The work was performed in the free molecular regime with the incoming candidate particles having random ballistic trajectories characteristic of small particles (or large Knudsen number  $\text{Kn} \gg 1$ ). The results showed that in the limit of no surface reaction, the aggregates have a very compact structure with a rather high fractal dimension  $D_f \approx 2.97$ , close to the results of the early work of Meakin et al. [8] ( $D_f \approx 3.09$ ). However, the fractal dimension determined by these simulations is much higher than any of the experimental values, which range from 1.6 to 1.9 [4,5]. In fact, the assumption that every collision leads to an aggregate might not be valid. The colliding particles used in those simulations were very small, with diameters of only a few nanometers and below. Recent experimental studies of soot morphology and composition [9] suggest that such small soot particles have a liquid-like character. This would imply that the collision of two small soot particles will lead to the formation of a larger spherical particle, rather than an aggregate consisting of two spheres.

More recently, high fidelity simulations of cluster-cluster aggregation were performed [10,11]. Schmid et al. [11] considered coagulation and sintering in the so-called Diffusion Limited Cluster Aggregation (DLCA) regime, which is equivalent to the continuum regime characterized by Brownian random diffusion (small Knudsen number  $\text{Kn} \ll 1$ ). They found that in the limit of no sintering, the fractal dimension reaches a value close to  $D_f \approx 1.86$ . Köylü et al. [4] studied the fractal dimension of soot aggregates from turbulent non-premixed flames of acetylene, propylene, ethylene, and propane. Their measurements for the fractal properties of soot yield  $D_f = 1.82$ . A more recent analysis of soot fractal properties in JP-8 pool fires [5] revealed slightly lower values for the fractal dimension  $1.68 < D_f < 1.72$ . Most of the experimental measurements were performed on relatively large soot aggregates with primary particle diameters ranging from 20 to 70 nm, and number of primary particles reaching hundreds or thousands.

Over the years, several attempts have been made to model soot aggregates. The transition from small spherical particles to larger aggregates with more complex structure is typically described in an empirical way by specifying the diameter where this transition occurs [12,13]. Below that presumed threshold diameter, soot particles are assumed to be spherical, while beyond this diameter, they are assumed to be aggregates. This approach of aggregation is limited as it cannot accurately describe a typical population of soot particles, where small spherical particles and large aggregates coexist [9]. Recently, Balthasar and Frenklach [14] and Patterson and Kraft [15] introduced a model representing soot aggregates by their surface and volume. The aggregate morphology is typically described with a shape descriptor variable. This model has been formulated in the framework of Monte-Carlo (MC) simulations in order to simulate with great accuracy the entire population of soot particles. While this model allows for a better description of soot particles, a coherent coagulation model which spans the full spectrum from coalescence to aggregation is difficult to formulate. This approach remains promising and great emphasis should be placed upon comparing the diameters of the primary particles with experiments.

During its formation, the aggregate shape of a soot particle is affected by the addition of mass onto the surface through chemical reactions. The concept of active surfa-

ce sites has been applied by Frenklach and Wang [3] to describe the reactivity of the surface in the HACA mechanism. It has since been used in different soot models in the description of soot mass growth by heterogeneous surface reactions. Most soot models assume a given density of sites per unit soot surface (about  $\chi \approx 2.3 \times 10^{19} \text{ m}^{-2}$ ), and introduce a parameter  $\alpha$ , which describes the fraction of active sites. Appel et al. [12] expressed the parameter  $\alpha$  as a decreasing function of the local temperature and the first size moment of the soot particle distribution. The fit was empirically determined from a least square approach. More recently, Singh et al. [16] introduced an equation for the number of active sites per surface area. This relaxation equation assumes that the surface reactivity starts at  $\chi_0 = 2.3 \times 10^{19} \text{ m}^{-2}$  in the inception zone and decreases with residence time in the flame towards a limiting value of  $\chi_\infty = 4.6 \times 10^{18} \text{ m}^{-2}$ . The surface reactivity of the first soot particles appear to be overpredicted by this model, as a rough estimation for a pyrene dimer gives  $\chi_{\text{dimer}} = 8 \times 10^{18} \text{ m}^{-2}$ . A more detailed description of the reactivity of the surface of soot particles is needed to predict with good accuracy soot concentrations and properties in a large diversity of flames. Furthermore, small spherical and large soot aggregates might not exhibit the same reactivity towards chemical reactions.

A consistent representation of the Number Density Function (NDF) of soot is necessary for an accurate prediction of the soot volume fraction or aggregate properties. Monte-Carlo (MC) simulations has been shown to predict with good accuracy the full NDF of soot [16,17]. Results from MC also compared favorably with experimental measurements of the NDF from laminar ethylene flames [18,19]. However, the inherent cost of using MC for such simulations renders impossible its use for 3D or even 1D simulations. Recently, Marchisio and Fox [20] applied the Direct Quadrature Method of Moments to soot formation. Rather than assuming the full form of the NDF or simulating it completely, this method approximates the NDF by a series of delta functions. This method proved to be effective in predicting the main moments of the NDF, such as the volume, the surface area, and the number density. Furthermore, this method was found to be inexpensive in comparison to MC.

In this work, a new soot model is presented that introduces a more general description of the NDF, and which therefore allows for addressing several of the issues mentioned above. The model describes a soot particle with three independent parameters, the particle volume, the particle surface, and the number of hydrogenated surface sites. This model provides

- a coherent aggregation model with a particular treatment of sphere-sphere and sphere-cluster collisions,
- a more detailed description of the surface reactivity of soot particles,
- and a statistical representation of soot particles, which allows for bimodal particle size distributions.

The paper is organized as follows. First, the multi-variate model for soot formation is presented and formulated in the context of Direct Quadrature Method of Moments (DQMOM). Then, the source terms for the moments of the Number Density Function (NDF) are modeled. Finally, comparisons with experimental measurements for a series of laminar premixed and diffusion flames are provided.

## 2. SOOT REPRESENTATION

### 2.1. Multi-Variate Formulation

In the present formulation, a soot particle is represented as an aggregate composed of a certain number of small spherical particles called primary particles [21]. In a flame, it is likely that the primary particles within a given aggregate have been formed at the same time and hence have similar diameters, referred to as  $d_p$ . However, different aggregates can be composed of primary particle with different diameters. Given the number of primary particles per aggregate ( $n_p$ ), the total volume ( $V$ ) and total surface ( $S$ ) of a soot aggregate can be expressed as

$$V = \frac{\pi}{6} n_p d_p^3, \quad (1)$$

$$S = \pi n_p d_p^2. \quad (2)$$

Inversely, given the total volume and total surface area of one soot aggregate, one can reconstruct the primary particle diameter and the number of primary particles per aggregate as

$$d_p = \sqrt[3]{\frac{6V}{S}}, \quad (3)$$

$$n_p = \frac{1}{36\pi} S^3 V^{-2}. \quad (4)$$

The density of soot particles is considered to be constant and independent of the size and shape of the aggregate. The value used in the present work is  $\rho_s = 1800 \text{ kg/m}^3$ . Finally, it is assumed that only carbon atoms contribute to the mass of soot particles, as experimental measurements have reported that the C/H molar ratio is much greater than unity [22,5]. The following development can be equivalently written in terms of the mass of the soot particle. In the present work, the volume was preferred as experimental measurements usually report the soot volume fraction.

To better predict the soot volume fraction over a wide range of temperatures and pressures, a third parameter is introduced. This third quantity is the number of hydrogenated carbon sites or active sites on the surface of the soot aggregate, denoted in the following as  $H$ . The surface reactivity of a soot particle, defined as the density of active sites per unit surface area, is then written as

$$\chi = \frac{H}{S}. \quad (5)$$

In summary, in the present model, a soot particle is here described by three independent parameters: the total volume ( $V$ ), the total surface area ( $S$ ), and the total hydrogen content on the surface ( $H$ ). We will refer to this model subsequently as Volume-Surface-Hydrogen VSH-model. Similarly, a soot model which depends upon

the volume and surface only will be referred to as a VS-model, while a model which depends only upon the volume is called a V-model.

## 2.2. Direct Quadrature Method of Moments

To accurately describe the Number Density Function (NDF) of soot, the Direct Quadrature Method of Moments (DQMOM) is used [20]. The method has already been described for a bivariate VS-soot formulation [23,24], and is here extended to a trivariate formulation. Full details of the method can be found in [20,23]. Therefore, only a brief description of the method will be presented. Let us consider the Population Balance Equation (PBE):

$$\frac{\partial n}{\partial t} + \frac{\partial (u_j n)}{\partial x_j} - \frac{\partial}{\partial x_j} \left( \rho D \frac{\partial (n/\rho)}{\partial x_j} \right) + \frac{\partial}{\partial x_j} \left( 0.55 \frac{\nu}{T} \frac{\partial T}{\partial x_j} n \right) = \dot{S} \quad , \quad (6)$$

where  $n = n(V, S, H; \mathbf{x}, t)$  is the number density of soot particles that have a given volume  $V$ , a given surface  $S$ , and a given number of hydrogenated sites  $H$ .  $\rho$ ,  $T$ , and  $\nu$  are the density, temperature, and kinematic viscosity of the surrounding gas, and  $D$  is the diffusivity of soot particles. In the free molecular regime, the diffusion coefficient of soot particles is known to depend on the particle diameter as  $D \propto d^{-2}$  [25,26]. This implies that the effective particle Lewis numbers are large, even for very small particles [27]. Therefore, in the present work, the diffusion term in Eq. 6 is neglected. To simplify the notation, the thermophoretic term is combined with the convective term and will not appear later.

The source term  $\dot{S}$  that appears in the PBE is a function of this number density function. One is generally not interested in the full form of the number density function but only in some of its moments defined as

$$M_{k_1, k_2, k_3}(\mathbf{x}, t) = \iiint V^{k_1} S^{k_2} H^{k_3} n(V, S, H; \mathbf{x}, t) dH dS dV \quad . \quad (7)$$

For instance, predicting accurately the total volume ( $M_{1,0,0}$ ), the total surface area ( $M_{0,1,0}$ ), and the total number density ( $M_{0,0,0}$ ) is of primary importance. Transport equations for these moments can be formulated after integration of Eq. 6. The source terms in these equations appear in the form

$$\dot{S}_{k_1, k_2, k_3}(\mathbf{x}, t) = \iiint V^{k_1} S^{k_2} H^{k_3} \dot{S}(V, S, H; \mathbf{x}, t) dH dS dV \quad (8)$$

and are unclosed, since the NDF is unknown. Closure of the source terms is accomplished by a higher order quadrature approximation, which is equivalent to approximating the NDF by a set of delta functions as

$$n(V, S, H; \mathbf{x}, t) \approx \sum_{\alpha=1}^{n_d} w_{\alpha}(\mathbf{x}, t) \delta(V - V_{\alpha}(\mathbf{x}, t)) \times \delta(S - S_{\alpha}(\mathbf{x}, t)) \delta(H - H_{\alpha}(\mathbf{x}, t)) \quad , \quad (9)$$

where  $n_d$  is the number of delta functions used for the quadrature. The weights,  $w_{\alpha}(\mathbf{x}, t)$ , and the location of the delta-functions in the VSH-space, called abscissas  $V_{\alpha}(\mathbf{x}, t)$ ,

$S_\alpha(x,t)$ , and  $H_\alpha(x,t)$  of the delta functions, also vary with space and time. Using this expression, the source terms for the moments are approximated by

$$\dot{S}_{k_1, k_2, k_3} \approx \sum_{\alpha=1}^{n_d} V_\alpha^{k_1} S_\alpha^{k_2} H_\alpha^{k_3} \dot{S}(V_\alpha, S_\alpha, H_\alpha) w_\alpha \quad (10)$$

With the quadrature approximation, the evolution equations for the moments are closed, leading to the so called Quadrature Method of Moments (QMOM). The weights and abscissas appearing in Eq. 10 remain to be expressed in terms of the moments from Eqs. 7 and 9. This requires 4nd moments and can be quite complex. The product-difference algorithm [28] can be used for this in the case of a monovariate number density function. Unfortunately, for multi-variate number density functions, no such algorithm exists.

To avoid this problem, the Direct Quadrature Method of Moments (DQMOM) solves for the weights and abscissas directly rather than for the moments. By replacing the number density appearing in the PBE (Eq. 6) with its approximated form given by Eq. 9, transport equations for the weights and abscissas are obtained:

$$\frac{\partial w_\alpha}{\partial t} + \frac{\partial}{\partial x_j} (u_j w_\alpha) = \dot{a}_\alpha \quad (11)$$

$$\frac{\partial w_\alpha \xi_\alpha}{\partial t} + \frac{\partial}{\partial x_j} (u_j w_\alpha \xi_\alpha) = \dot{b}_\alpha \quad (12)$$

where  $\xi_\alpha$  can be any one of the three abscissas  $V_\alpha$ ,  $S_\alpha$  or  $H_\alpha$ . It can be shown that the source terms  $\dot{a}_\alpha$  and  $\dot{b}_\alpha$  are solutions of a linear system, whose right-hand side is exactly given by the source terms for the set of 4nd moments [20]. The matrix involved in the linear system only depends upon the abscissas of the  $n_d$  delta functions.

In summary, the source terms are first computed for a given set of moments of the number density function ( $\dot{S}_{k_1, k_2, k_3}$ ). Then, a linear system is solved to obtain the source terms for the weights and abscissas ( $\dot{a}_\alpha$  and  $\dot{b}_\alpha$ ). The transport equations for the weights and abscissas can then be solved. Finally, the moments of the NDF are reconstructed using Eqs. 7 and 9.

### 3. SOOT FORMATION

The source terms which appear in Eqs. 10, 11, and 12 account for different physical and chemical processes: particle inception by PAH dimerization, particle coagulation, growth through surface reaction, and loss of mass by surface oxidation.

#### 3.1. Nucleation & Condensation

In the present model, a newly formed soot particle is assumed to be a dimer of PAH molecules. Given the large concentration of these dimers, we can assume that they either collide with one another or with larger soot particles. The first case will be referred to as nucleation, while the second case will be referred to as condensation (Figure

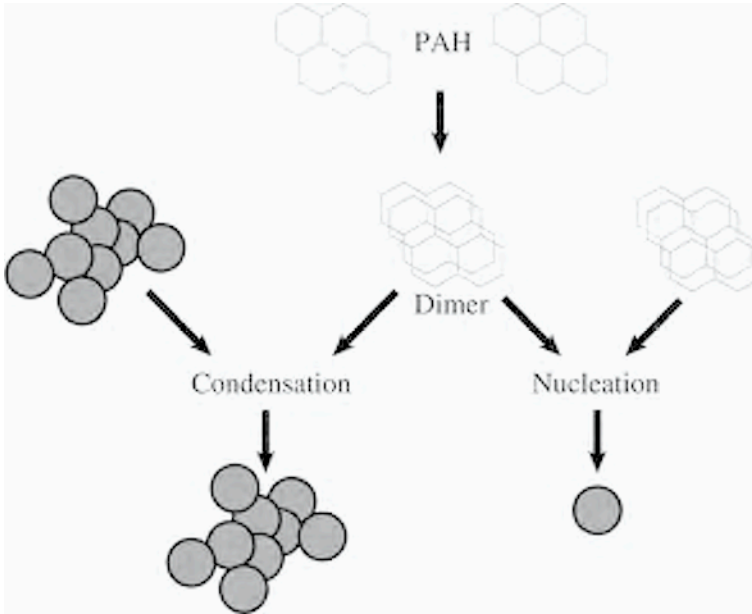


Figure 1. Nucleation & condensation of dimers.

1). The distinction between PAH dimers and other soot particles is introduced because of the weak binding energy and the small life time of the dimers. Here, we will first describe the formation of the dimers.

### 3.1.1. Dimerization of PAH molecules

Nucleation of soot particles is usually modeled as the collision and subsequent coalescence of two heavy PAH molecules [1-2]. For a given type of PAH molecule, the rate of self collisions is given by the kinetic gas theory as

$$\dot{\omega} = \sqrt{\frac{4\pi kT}{m}} d^2 [\text{PAH}]^2 \quad (13)$$

where  $d$  and  $m$  are the molecule diameter and mass, and  $k$  is the Boltzmann constant. The binding energy of such newly formed PAH dimers is very small. For instance, it is 19.6 kJ/mol [1] for a pyrene dimer. Also, because of the shallow potential well, the dimer lifetime is very small, from about 2 ps for naphthalene dimers to 20 ps for coronene dimers [2]. As a consequence, the effective rate of dimer formation is much smaller than that predicted by kinetic gas theory, and a sticking coefficient  $\gamma$  has to be introduced. Both experimental measurements and numerical modeling [29] have shown that the sticking efficiency increases with the size of the collider and can be very small for nanometer sized spheres ( $\gamma \approx 0.001$ ).

In the present model, nucleation is expressed as the self collision of a series of PAH molecules. No direct condensation of PAH species onto soot particles were included in

the present model, as the PAH-PAH collision rates are usually much larger than any PAH-soot particle collision rates. The species used for nucleation are listed in Table 1 together with their mass and sticking coefficient. The diameters of the PAHs were estimated by assuming that PAH molecules are hard spheres with the density of soot. This assumption is rather crude, as most PAH molecules are planar. However, corrections such as steric factors would appear in the sticking coefficient. D'Alessio et al. [29] showed that for small particles, the sticking coefficient scales with the square of the binding energy, which is estimated to depend upon the square of the mass. As a consequence, the sticking coefficients were assumed to scale with the mass of the PAH molecules to the fourth power

$$\gamma_i = C_N \cdot m_i^4 \quad , \quad (14)$$

where  $C_N$  is a constant that is adjusted to better match experimental concentrations of PAH molecules (cf. Section 4.2). The sticking coefficients for naphthalene ( $A_2$ ) and acenaphthylene ( $A_2R5$ ) were found too large and were further reduced by a factor of three. The effective rate of dimerization of PAH molecules is then given by

$$\dot{\omega}_{\text{dimer}} = \sum_i \gamma_i \left( \frac{4\pi kT}{m_i} \right)^{1/2} \left( \frac{6m_i}{\pi\beta_s} \right)^{2/3} [\text{PAH}_i]^2 \quad . \quad (15)$$

Rather than computing all possible PAH dimers, only the total rate of formation of dimers ( $\dot{\omega}_{\text{dimer}}$ ) and the average carbon ( $C_{\text{dimer}}$ ) and hydrogen ( $H_{\text{dimer}}$ ) content per dimer are evaluated.

Removal of dimers occurs by nucleation and condensation, which will be discussed next. Both the source terms for nucleation and condensation depend on the concentration of PAH dimers. Because of the high collision frequency with other dimers or larger soot particles, the dimers are assumed to be in quasi steady state. The dimer concentration can then be calculated as the solution of a quadratic equation given by

$$\dot{\omega}_{\text{dimer}} = \beta_N [\text{DIMER}]^2 + \left( \sum_{i=1}^{n_d} \beta_{C_i} w_i \right) [\text{DIMER}] \quad . \quad (16)$$

Table 1. List of species used for dimerization with their mass (in amu) and sticking coefficient.

Species name	Formula	$m_i$	$\gamma_i$
naphthalene	C10H8	128	0.0010
acenaphthylene	C12H8	152	0.0030
biphenyl	C12H10	154	0.0085
phenathrene	C14H10	178	0.0150
acephenanthrylene	C16H10	202	0.0250
pyrene	C16H10	202	0.0250
fluoranthene	C16H10	202	0.0250
cyclo[cd]pyrene	C18H10	226	0.0390

3.1.2. Nucleation

Although in the present model, the nucleation step involves two dimers composed of planar PAH molecules, this can be seen as a crude model for the actual nucleation step, which might involve both planar PAH and more complex aliphatically linked aromatic components [30,31]. Because of the small size of the PAH molecules and the aliphatic bonds, newly formed particles can undergo internal rearrangements, which leads to the experimentally observed liquid-like character and spherical shape of small particles. For instance, the binding energy of the pyrene-dimer, as the largest species participating in the nucleation process, is only 19.6 kJ/mol. At a temperature of  $T = 1600$  K, this is comparable to its kinetic energy of  $3/2RT = 20.0$  kJ/mol, where  $R$  is the universal gas constant, which again suggest that internal rearrangements might take place. We will therefore assume that particle nucleation always leads to a spherical particle.

Furthermore, because of the small size of the particle, it is assumed that all hydrogen atoms are located on the surface, and are therefore available for surface reactions. The source term for the moments of the NDF is then given by

$$\dot{S}_{k_1, k_2, k_3}^{nucl} = \frac{1}{2} \beta_N [\text{DIMER}]^2 V^{k_1} S^{k_2} H^{k_3}, \tag{17}$$

where  $\beta_N$  is the collision rate between two dimers, and  $[\text{DIMER}]$  represents their concentration. The volume, surface, and hydrogen variables of the newly formed soot particle are given by

$$\begin{cases} V = 2 W_C C_{dimer} \rho_s^{-1}, \\ S = \pi^{1/3} (6V)^{2/3}, \\ H = 2 H_{dimer}, \end{cases} \tag{18}$$

where  $W_C$  is the weight of a carbon atom.

3.1.3. Condensation

When a PAH dimer collides with a large soot particle, the weakly linked dimer will most likely break apart, and the two PAH molecules will deposit on the surface. The volume of the large soot particle participating in the collision will increase, and this aggregate will be rendered more spherical by the condensation of mass onto its surface. The hydrogen atoms from the two PAH molecules will be added to the number of active sites found on the surface of the large soot particle. During the surface absorption, some of the previously active sites might be rendered inactive as they are hidden by the two absorbed PAH molecules. However, this effect was not included in the present model. The source term for the moments of the NDF is then given by

$$\dot{S}_{k_1, k_2, k_3}^{cond} = [\text{DIMER}] \times \sum_{i=1}^{n_{st}} \beta_{C_i} \left( k_1 \frac{\delta V_i}{V_i} + k_2 \frac{\delta S_i}{S_i} + k_3 \frac{\delta H_i}{H_i} \right) V_i^{k_1} S_i^{k_2} H_i^{k_3} w_i. \tag{19}$$

The small changes in volume and hydrogen of the large soot particle are given by

$$\begin{cases} \delta V_i = 2 W_C C_{dimer} \rho_s^{-1}, \\ \delta H_i = 2 H_{dimer}. \end{cases} \quad (20)$$

The expression for the change in surface area ( $\delta S$ ) will be given later in Section 3.4.

### 3.2. Coagulation

The coagulation process represents the collision of two soot particles. When the particle resulting from the collision of two small particles is a sphere, coagulation is usually referred to as coalescence (Figure 2a). When the resulting particle retains the essential structure of the colliding particles, an aggregate is formed, and coagulation is referred to as aggregation (Figure 2b).

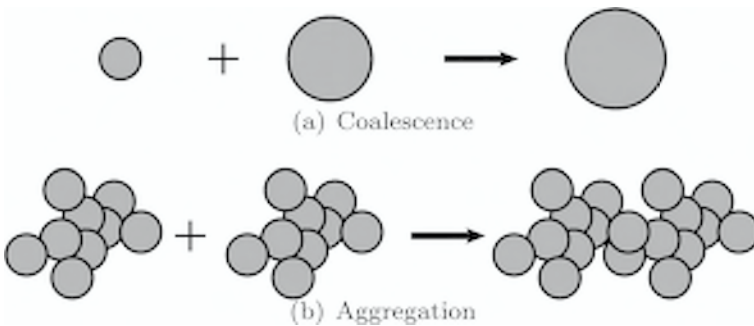


Figure 2. Results of two extreme coagulation cases.

The rate of coagulation is a function of the size and shape of the colliding particles. Small primary particles, characterized by a large Knudsen number ( $Kn \gg 1$ ), evolve in the free molecular regime, while large aggregates, characterized by a small Knudsen number, evolve in the continuum regime ( $Kn < 1$ ). Kazakov & Frenklach [13] developed expressions for the collision rates for the free molecular ( $\beta_{ij}^{f,m}$ ) and for the continuum regimes ( $\beta_{ij}^{cont}$ )

$$\beta_{i,j}^{f,m} = 2.2 \sqrt{\frac{\pi kT}{2m_{ij}}} (d_{c_i} + d_{c_j})^2, \quad (21)$$

$$\beta_{i,j}^{cont} = \frac{2kT}{3\mu} \left( \frac{C_i}{d_{m_i}} + \frac{C_j}{d_{m_j}} \right) (d_{c_i} + d_{c_j}), \quad (22)$$

where  $m_{ij} = \frac{m_i m_j}{m_i + m_j}$  is the reduced mass,  $\mu$  the dynamic viscosity of the surrounding

gas, and  $d_{ci}$  and  $d_{mi}$  are the collision and mobility diameters, respectively. The Cunningham slip correction factor takes the form  $C_i = 1 + 1.257 Kn_i$  with the Knudsen number expressed as  $Kn_i = \lambda/d_{ci}$ . The collision rate in the transition regime is approximated by the harmonic mean of the asymptotic values [32]

$$\beta_{i,j} = \frac{\beta_{i,j}^{f.m.} \beta_{i,j}^{cont.}}{\beta_{i,j}^{f.m.} + \beta_{i,j}^{cont.}} \quad (23)$$

Following the work of Kruis et al. [33], the collision and mobility diameters are assumed to be proportional to the radius of gyration, which is defined as

$$R_g = k_f d_p n_p^{1/D_f} \quad (24)$$

where  $D_f$  is the fractal dimension of the soot aggregates. The constant  $k_f$  is evaluated by considering the limit of a single sphere, where both the collision and the mobility diameters are equal to the diameter of the sphere

$$d_c \equiv d_m \equiv d_p n_p^{1/D_f} \quad (25)$$

In the present work, the fractal dimension is taken to be  $D_f = 1.8$ . This value corresponds to typical soot aggregates formed in premixed and diffusion flames [4,5]. The collision and mobility diameters can then be determined from the surface and volume of the particle using Eqs. 3, 4 and 25.

The source terms for the moments of the NDF are given by

$$\dot{S}_{k_1, k_2, k_3}^{coag} = \frac{1}{2} \sum_{i,j=1}^{n_d} \beta_{i,j} w_i w_j \times \left( V_{i+j}^{k_1} S_{i+j}^{k_2} H_{i+j}^{k_3} - V_i^{k_1} S_i^{k_2} H_i^{k_3} - V_j^{k_1} S_j^{k_2} H_j^{k_3} \right) \quad (26)$$

where the volume of the newly formed soot particle is given by

$$V_{i+j} = V_i + V_j \quad (27)$$

The reactivity of the newly formed soot particle is assumed to be the same as the weighted averaged reactivity of the two colliding particles [16]

$$H_{i+j} = \frac{H_i + H_j}{S_i + S_j} \times S_{i+j} \quad (28)$$

The surface area of the new particle ( $S_{i+j}$ ) will be expressed later in Section 3.4.

### 3.3. Growth by surface reactions

Several chemical reactions could take place on the surface of a soot particle. In the present model, we use the Habstraction  $C_2H_2$ -addition (HACA) mechanism [3]. In this mechanism, the addition of mass on the surface of a soot particle proceeds in several steps. Each of these steps is assigned a rate constant in the Arrhenius form as shown

in Table 2. The rate constants were taken from similar reactions on benzene and phenyl molecules, which were then rescaled to account for the number of active sites [34-37]. When available, the high pressure limit of the rate constant was considered. The addition of acetylene on a radical site is assumed to be irreversible, and the rate has been multiplied by two to better match experimental measurements.

After the acetylene addition, several stabilization reactions can occur (Figure 3). These reactions can lead to cyclopentafused aromatics (path 1), ethynyl substituted aromatics (path 2), or ring closure (path 3 and 4). Furthermore, previously stable portions of the surface can be subject to rearrangements to form new 5-membered or 6-membered rings (path 5 and 6) [38].

Table 2. Rate coefficients for the surface reactions in Arrhenius form ( $k = AT^n \exp(-E/RT)$ ). Units are  $\text{cm}^3$ , K, mol, s, and kJ.

Reactions	A	n	E	ref.
1: Soot - H + H $\rightleftharpoons$ Soot* + H <sub>2</sub>	$1.00 \times 10^8$	1.80	68.42	[34]
	$8.68 \times 10^4$	2.36	25.46	
2: Soot - H + OH $\rightleftharpoons$ Soot* + H <sub>2</sub> O	$6.72 \times 10^1$	3.33	6.09	[35]
	$6.44 \times 10^{-1}$	3.79	27.96	
3: Soot - H $\rightleftharpoons$ Soot* + H	$1.13 \times 10^{16}$	-0.06	476.05	[36]
	$4.17 \times 10^{13}$	0.15	0.00	
4: Soot* + C <sub>2</sub> H <sub>2</sub> $\Rightarrow$ Soot - H	$2.52 \times 10^9$	1.77	13.54	2×[37]

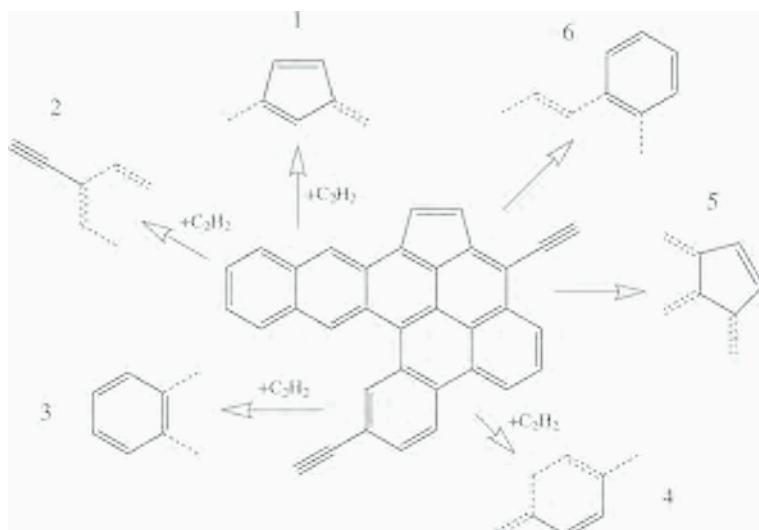


Figure 3. Possible stabilization processes resulting from the addition of acetylene C<sub>2</sub>H<sub>2</sub> on a radical site.

In the present model, we do not directly distinguish between these reaction pathways, since we cannot keep track of all possible outcomes. Tracking the different types of active sites requires information about their relative locations to one another and would lead to an excessive model. Instead, we just consider the resulting increase or decrease in the number of hydrogenated sites or active sites on the soot surface.

Because of the possible rearrangements between types of active sites (path 5 and 6), all hydrogenated sites on the surface of a soot particle are considered to be active. Most of the possible stabilization reactions will keep the number of hydrogenated sites constant ( $\delta H = 0$  for path 1, 2, and 4). Only the ring closure with an ethynyl substituted aromatic site could lead to an increase in the hydrogen content ( $\delta H = 2$ ). Therefore, it is a reasonable assumption to consider that surface reactions do not change the number of active sites on the particle surface, i.e.

$$\delta H_i = 0 \quad . \quad (29)$$

The change in the volume corresponds to the addition of two carbon atoms, hence

$$\delta V_i = 2W_r \rho_s^{-1} \quad . \quad (30)$$

To reduce the cost of the simulation, the radical sites on the soot surface are assumed to be in quasi steady-state and their concentration is expressed as

$$[\text{Soot} - C^*] = \frac{r}{1+r} M_{0,0,1} \quad , \quad (31)$$

$$r = \frac{k_{1f} [H] + k_{2f} [OH] + k_{3f}}{k_{1b} [H_2] + k_{2b} [H_2O] + k_{3b} [H] + k_4 [C_2H_2]} \quad , \quad (32)$$

where  $M_{0,0,1}$  corresponds to the total concentration of hydrogenated carbon sites per unit volume. The source term for the moments of the NDF is given by

$$\begin{aligned} \dot{S}_{k_1, k_2, k_3}^{surf} = & k_4 [C_2H_2] \frac{r}{1+r} \times \\ & \sum_{i=1}^{n_d} \left( k_1 \frac{\delta V_i}{V_i} + k_2 \frac{\delta S_i}{S_i} \right) V_i^{k_1} S_i^{k_2} H_i^{k_3+1} w_i \quad . \end{aligned} \quad (33)$$

The expression for the change in total surface area ( $\delta S$ ) requires further analysis and will be discussed in the following section.

### 3.4. Surface area change by addition of mass

Several processes will contribute to an increase in the mass of a soot particle. The addition of mass can be very small, as in the case of dimer absorption (a few carbon atoms) and surface reactions (two carbon atoms), or it can be significantly larger as in the case of coagulation.

3.4.1. *Small mass addition*

A small addition of mass on the surface of an aggregate will slowly transform this aggregate into a more spherical particle. The number of primary particles per aggregate will decrease ( $\delta(n_p) < 0$ ), while their diameter will increase ( $\delta(d_p) > 0$ ). The rates of change of those two quantities are linked.

The collision diameter is given by the smallest sphere that encloses the aggregate particle. Mass addition which takes place on the entire surface of the aggregate will increase the collision diameter by the same amount that the diameter of the primary particles touching the enclosing sphere is increased. From this follows that

$$\delta(d_p) = \delta(d_c) \quad (34)$$

Then, using Eq. 25, the change in the total surface area can be expressed as a function of the volume increase and is given by

$$\frac{\delta S}{S} = \frac{\delta V}{V} \left[ \frac{1 - n_p^{-1/D_j} - \frac{2}{D_j}}{1 - n_p^{-1/D_j} - \frac{3}{D_j}} \right] \quad (35)$$

The surface area of the new particle is simply  $S + \delta S$ . In the limit of a pure spherical particle ( $n_p = 1$ ), the expression for a sphere is recovered

$$\frac{\delta S}{S} = \frac{2}{3} \frac{\delta V}{V} \quad (36)$$

3.4.2. *Larger mass addition*

The mass to be added on an aggregate can be of the same order as the mass of the aggregate itself, as it is the case for the collision between two large aggregates. In this limiting case, the two particles are assumed to be linked by point contact. For two particles  $i$  and  $j$ , the surface area of the new aggregate is

$$S_{i+j} = S_i + S_j \quad (37)$$

For an addition of mass of intermediate size, a geometrically weighted average of the two limiting cases is used. This blending function is based on the ratio of the volume of the smaller particle ( $V_j$ ) to the volume of the larger particle ( $V_i$ )

$$\bar{\alpha} = V_j/V_i < 1 \quad (38)$$

and reads

$$S_{i+j} = (S_i + S_j)^\alpha \times \left( S_i + \int_0^{V_j} \delta S_i(\delta V) \right)^{(1-\alpha)} \quad (39)$$

where the expression for  $\delta S_j$  is given by Eq. 35. The integration is introduced to account for cases where the volume increase is not infinitesimal ( $V_j \approx V_j$ ).

### 3.5. Oxidation

In addition to the reactions previously mentioned in the context of the surface growth mechanism, other heterogeneous reactions can occur on the particle surface. Reactions describing the oxidation of soot by  $O_2$  or OH are very important since they account for most of the mass loss of soot in flames. The main product formed by oxidation of soot is carbon monoxide CO. The rate of oxidation by  $O_2$  is taken from Kazakov et al. [39], where it is proportional to the number of radical sites on the soot surface. The rate of oxidation by OH, which is proportional to the soot surface, is taken from Neoh et al. [40]. Those reactions are summarized in Table 3. This simple oxidation mechanism was used for the simulations as the oxidation process was found to show small impact on the soot predictions for the current set of premixed and diffusion flames.

When these reactions occur, the volume of a soot particle decreases by loss of one (oxidation by OH) or two (oxidation by  $O_2$ ) carbon atoms. As in the case of surface growth by acetylene addition, the total surface area is changed. In the case of oxidation, it is assumed that the number of primary particles per aggregate remains constant throughout the oxidation process

$$d(n_p) = 0. \tag{40}$$

Following this assumption, the rate of change of the total surface can be expressed with the rate of change of the total volume. Furthermore, the number of active sites on the surface decreases similarly to the decrease of the total surface area. It is simply assumed that the number of hydrogenated sites per unit surface is kept constant, in other words

$$d(\chi) = 0. \tag{41}$$

As a consequence, the rate of change of the surface area and the number of hydrogenated sites take the form

$$\frac{\delta H}{H} = \frac{\delta S}{S} = \frac{2}{3} \frac{\delta V}{V}. \tag{42}$$

Table 3. Rate coefficients for the surface oxidation in Arrhenius form ( $k = AT^n \exp(-E/RT)$ ). Units are  $cm^3$ , K, mol, s, and kJ.

Reactions	A	n	E	ref.
1: Soot* + $O_2 \Rightarrow$ Soot - H + 2 CO	$2.20 \times 10^{12}$	0.0	31.38	[39]
2: Soot - H + OH $\Rightarrow$ Soot - H + CO	Reaction probability		0.13	[40]

The source term for the moments of the NDF is given by

$$\begin{aligned} \dot{S}_{k_1, k_2, k_3}^{soot} = & \frac{1}{3} \delta V (3k_1 + 2k_2 + 2k_3) \times \\ & \left( 2\dot{\omega}_{O_2} \frac{M_{k_1-1, k_2, k_3+1}}{M_{0,0,1}} + \dot{\omega}_{OH} \frac{M_{k_1-1, k_2+1, k_3}}{M_{0,1,0}} \right), \end{aligned} \quad (43)$$

where

$$\delta V = -W_c \rho_s^{-1}. \quad (44)$$

## 4. RESULTS

### 4.1. Flame configurations

The present soot model is applied to four atmospheric rich premixed flames [42,41] and one diffusion flame [43]. The parameters for the premixed flames are given in Table 4 while Table 5 lists the parameters for the diffusion flame. These simulations are performed with the FlameMaster code [44] using a detailed chemical mechanism [45]. This chemical mechanism is composed of 151 species and 1658 reactions and accounts for all major pathways of PAH formation up to cyclopenta[cd]pyrene ( $C_{18}H_{10}$ ). This mechanism has been validated for a large set of fuels ranging from methane to iso-octane and one-ring aromatics using different configurations including homogeneous auto-ignition, laminar premixed flames, and diffusion flames.

Large uncertainties in the temperature measurements are reported for the sooting premixed flames (about 100 K for the benzene flame [42]). Because of these uncertainties and unknown heat losses at the wall due to conduction, the experimental temperature profiles were imposed after some corrections. Two of the ethylene flames ( $C/O = 0.98$  and  $C/O = 0.78$ ) exhibit atypical temperature profiles with a large maximum in the temperature, followed by a sudden drop and then a linear decay. This linear decay is mainly due to radiation heat losses by the gas phase. However, the large measured maximum temperature results from catalytic effect of non-ceramic-coated thermocouples [46]. As a consequence, the maximum temperatures of these two ethylene flames were reduced, and the new values are listed in Table 4 together with the corresponding temperature reduction ( $\Delta T_{max}$ ). The downstream decay of the temperature was not affected and a piecewise cubic Hermite interpolation was used between the experimental points. The experimental temperature of the benzene flame was imposed without any changes.

For the diffusion flame, the temperature profile was not imposed, and an enthalpy equation was solved. However, due to uncertainties in the exact composition of the oxidizer stream, the dilution by nitrogen was reduced to better match the experimental profiles of CO and CO<sub>2</sub>. The mass fractions of oxygen and ethylene were increased by about 20% while keeping the same equivalence ratio of  $\phi = 0.62$ . The composition of the two streams used in the simulations are listed in Table 5.

DQMOM is implemented as part of the FlameMaster code and is coupled with the gas phase chemistry. During these simulations, the total mass of carbon atoms is con-

Table 4. Parameters for the considered premixed flames.  $T_\theta$  is the temperature at the burner surface,  $T_{10}$  the temperature at 10 mm above the burner, and  $T_{\max}$  the maximum temperature (in K).  $v_0$  is the cold gas velocity (in cm/s).

Fuel	$\phi$	C/O	$v_0$	T0	T10	Tmax	$\Delta T_{\max}$	Ref.
C2H4	2.93	0.98	6.93	400	1746	1878	-30	[41]
C2H4	2.64	0.88	6.93	400	1832	1929	0	[41]
C2H4	2.33	0.78	6.93	400	1871	1986	-120	[41]
C6H6	1.80	0.72	4.0	333	1614	1850	0	[42]

Table 5. Mass fractions, temperatures (in K), and cold gas velocities (in cm/s) for the diffusion flame [43].

Stream	T	$v_0$	$Y_{\text{N}_2}$	$Y_{\text{O}_2}$	$Y_{\text{C}_2\text{H}_2}$
Fuel	400	4.176	0.5096	0	0.4904
Oxidizer	400	8.403	0.7794	0.1836	0.0370

served, since the mass transferred to the soot particles due to PAH dimerization or surface growth is removed from the gas phase. The simulations have been performed with a quadrature approximation of order two by representing the number density function with two delta functions ( $n_d = 2$ ). Therefore, eight moments of the number density function are required (c.f. Section 2.2). This set of moments should include the quantities of primary importance such as  $M_{0,0,0}$  (number density),  $M_{1,0,0}$  (total volume),  $M_{0,1,0}$  (total surface), and  $M_{0,0,1}$  (total hydrogen content on the surface). The four other moments were chosen based on dimensional analysis, and are  $M_{1/3,0,0}$ ,  $M_{2/3,0,0}$ ,  $M_{0,1/2,0}$ , and  $M_{0,0,1/2}$ . In the pure coalescence limit,  $M_{1/3,0,0}$  and  $M_{0,1/2,0}$  represent the diameter, and  $M_{2/3,0,0}$  is equivalent to  $M_{0,1,0}$ . In the case of a constant surface reactivity ( $\chi = \text{const}$ ), the last moment  $M_{0,0,1/2}$  is proportional to  $M_{0,1/2,0}$ . This set of eight moments was found to produce accurate results with a good matrix condition number [24] for the inversion of the source terms (Eqs. 11 and 12).

## 4.2. Premixed benzene flame

Figure 4 gives a comparison of the predicted mole fractions of the main species as well as some of the PAH molecules for the premixed benzene flame. The agreement for CO, CO<sub>2</sub>, CH<sub>4</sub>, and C<sub>2</sub>H<sub>2</sub> is very good given the level of uncertainty of the temperature profile (about 100 K [42]).

This flame was used as a target for obtaining the sticking coefficient for the PAH dimerization model. The constant in the sticking coefficient model was chosen to reproduce correctly the concentration of the C<sub>16</sub>H<sub>10</sub> species like pyrene (A<sub>4</sub>), acenaphthylene (A<sub>3</sub>R5) and fluoranthene (FLTN). However, by following this procedure,

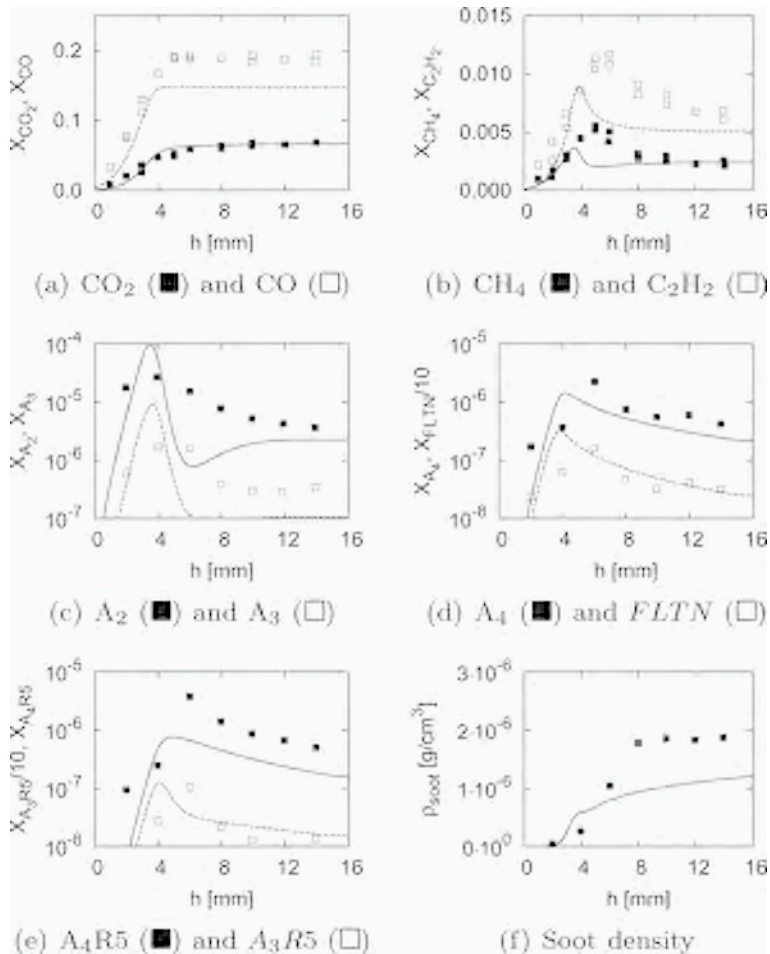


Figure 4. Mole fractions of some species and soot density (in soot mass per unit volume of gas phase) for the benzene flame [42]. First line refers to the first shown species, dashed line to the second.

the sticking coefficients for naphthalene ( $A_2$ ) and acenaphthylene ( $A_2R5$ ) were found too large and were further reduced by a factor of three. As expected, the mole fractions of the target PAH molecules (Figure 4d) are reproduced very accurately, while the mole fractions of the other PAH molecules are predicted with reasonable accuracy (Figures 4c and 4e).

Finally, the soot density profile is compared with the experimental measurements in Figure 4f. Both the shape and the maximum of the profile are predicted with reasonable accuracy.

### 4.3. Acetylene diffusion flame

#### 4.3.1. Base case

Figure 5 presents the comparison of the simulation of the diffusion flame of acetylene with experimental results. As was already mentioned, the temperature profile was not imposed in this simulation. As a result, a small deviation of approximately 0.5 mm in the location of the maximum occurs, mainly due to buoyancy effects, which were neglected [48]. The profiles of CO and CO<sub>2</sub> (Figure 5b) are also correctly predicted, since the composition of the lean premixed flame at  $h = 16$  mm has been adjusted. Soot precursors like allene (CH<sub>2</sub>CCH<sub>2</sub>), propyne (CH<sub>3</sub>CCH), and benzene (A<sub>1</sub>) are also well predicted by the current chemical mechanism (Figures 5c and 5d).

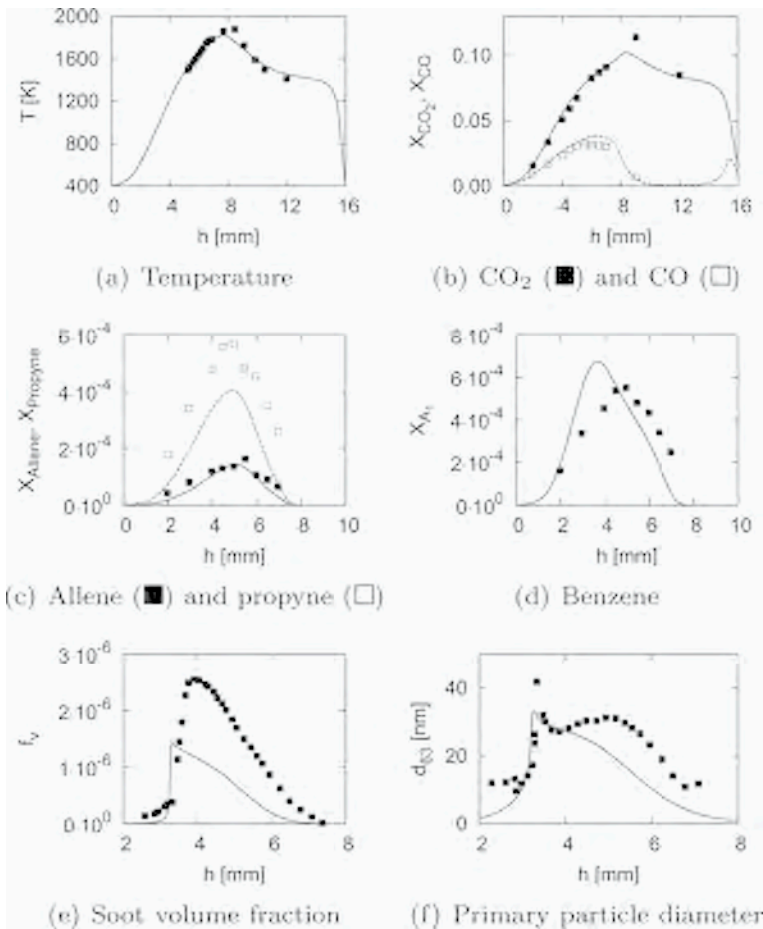


Figure 5. Mole fractions of some species, soot volume fraction, and primary particle diameter ( $d_{63}$  from Eq. 45) for the acetylene flame [43,47].

The soot volume fraction predicted by the current model compares favorably with the experimental measurements (Figure 5e). Soot starts to form at a height above the lower burner of  $h = 7$  mm, and increases monotonically past the stagnation plane at  $h = 3.7$  mm because of thermophoretic effects. The entire profile appears to be shifted towards the fuel nozzle, similar to the temperature profile because of buoyancy effects.

Finally, Figure 5f shows a comparison of the diameter of the primary particles. This diameter has been evaluated experimentally by comparing the scattering coefficient (proportional to  $d_p^6$ ) to the extinction coefficient (proportional to  $d_p^3$ ). With the current representation of a soot particle (Eqs. 1, 2, 3, and 4), the experimental value corresponds to

$$d_{63} = 6 \left( \frac{M_{1,-3,0}}{M_{1,0,0}} \right)^{1/3} . \quad (45)$$

Figure 5f shows the evaluation of the primary particle diameter from Eq. 45. Both the scattering and the extinction coefficients depend strongly on the particle diameter. As a consequence, for a bimodal distribution, the  $d_{63}$  diameter mainly represents the diameter of the large spherical particles. In the present numerical simulations, two delta functions were used to represent the soot NDF. Throughout this flame, the first delta function remains mostly at the inception zone with a diameter of about  $d_{p1} \approx 1$  nm. On the other hand, the second mode ( $d_{p2} \approx d_{63}$ ) slowly increases and then reaches a plateau, as measured experimentally. Furthermore, close to the stagnation plane, because of the long residence time, the soot particles suddenly grow by addition of mass on the surface through coalescence of smaller particles and adsorption of PAH dimers.

This flame has been used as a test case for the coagulation model. Because of the low temperature in the sooting region (below 1600 K), the pool of gas phase radicals is not sufficient to enhance the soot growth by surface reaction through the HACA mechanism. As a consequence, most of the mass in soot comes from the nucleation and adsorption of PAH dimers. This flame exhibits a typical bimodal NDF, where the first mode corresponds to small spherical particles and the second mode to large aggregates. These bimodal NDFs have also been found in the experimental work of Wang et al. [19] in low temperature flames. To validate the formulation of the coagulation model presented in Sections 3.2 and 3.4, two additional simulations have been carried out for the case of pure coalescence (all particles are spheres) and pure aggregation (no merging after collision). As for the VSH model, these simulations were performed with two delta functions, thus ensuring that a bimodal distribution can be represented.

#### 4.3.2. Coalescence limit

The first simulation corresponds to the case when coagulation of two soot particles always leads to coalescence (Eq. 39 with  $\alpha = 0$ ). This simulation is equivalent to the commonly used model where soot particles are treated as spheres. In this model, a soot particle is described simply by its volume (V-model).

Figures 6a and 6b show the soot volume fraction and particle diameter for this simulation. As expected, the volume fraction does not differ significantly from the case

with the full VSH model as surface reactions play only a minor role. On the other hand, the particle diameter is largely overpredicted. In the V-model, the mean particle diameter keeps increasing because of coalescence. Therefore, the diameter predicted with the V-model is much larger than the primary particle diameter predicted with any aggregation model. In other words, for this particular case, a soot particle cannot be adequately represented by only its volume. The structure of the soot particles has to be considered.

4.3.3. Aggregation limit

The second simulation corresponds to the case when coagulation of soot particles always leads to aggregation (Eq. 39 with  $\alpha = 1$ ). This model corresponds to the Monte-Carlo simulations performed by Mitchell & Frenklach [6] or the DQMOM simulations of Fox [24] in the absence of sintering.

The predicted volume fraction is slightly greater than for the full coagulation model (Figure 7a). However, the particle diameter is underestimated by about a factor of two (Figure 7b). In the case of pure aggregation, the diameter of primary soot particles can only increase through surface reactions or adsorption of PAH dimers on the surface.

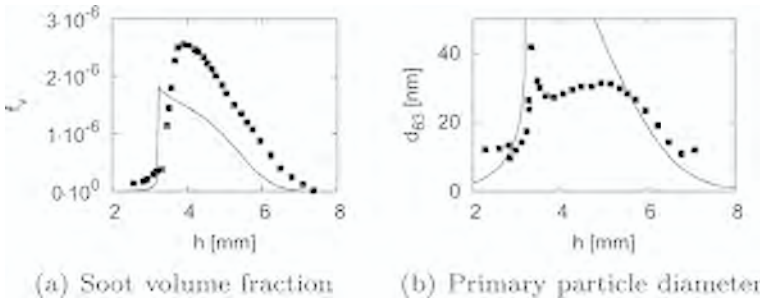


Figure 6. Soot volume fraction and primary particle diameter ( $d_{63}$  from Eq. 45) for the acetylene flame [43,47] in the pure coalescence case.

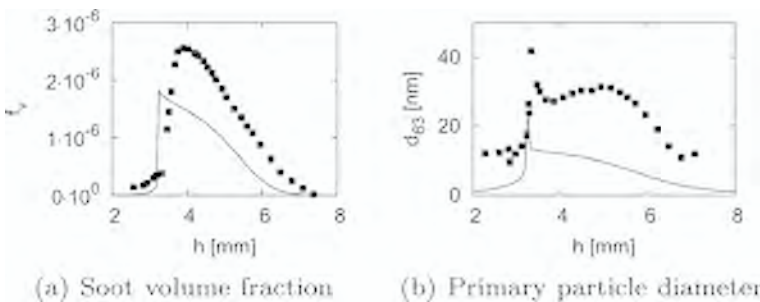


Figure 7. Soot volume fraction and primary particle diameter ( $d_{63}$  from Eq. 45) for the acetylene flame [43,47] in the pure aggregation case.

For this flame, the increase of the diameter is mainly due to surface adsorption as growth by surface reaction is limited. The simulation shows that a large number of the soot particles are very small (around  $d_p = 1$  nm). One would expect that their collision with larger particles would lead to mostly spherical particles and not aggregates. Thus proving the necessity of considering both limits, coalescence and aggregation, as given by Eq. 39.

#### 4.4. Premixed ethylene flames

Figure 8 gives a comparison of the predicted mole fractions of the main gas phase species with the experimental measurements. As for the other flames, the main combu-

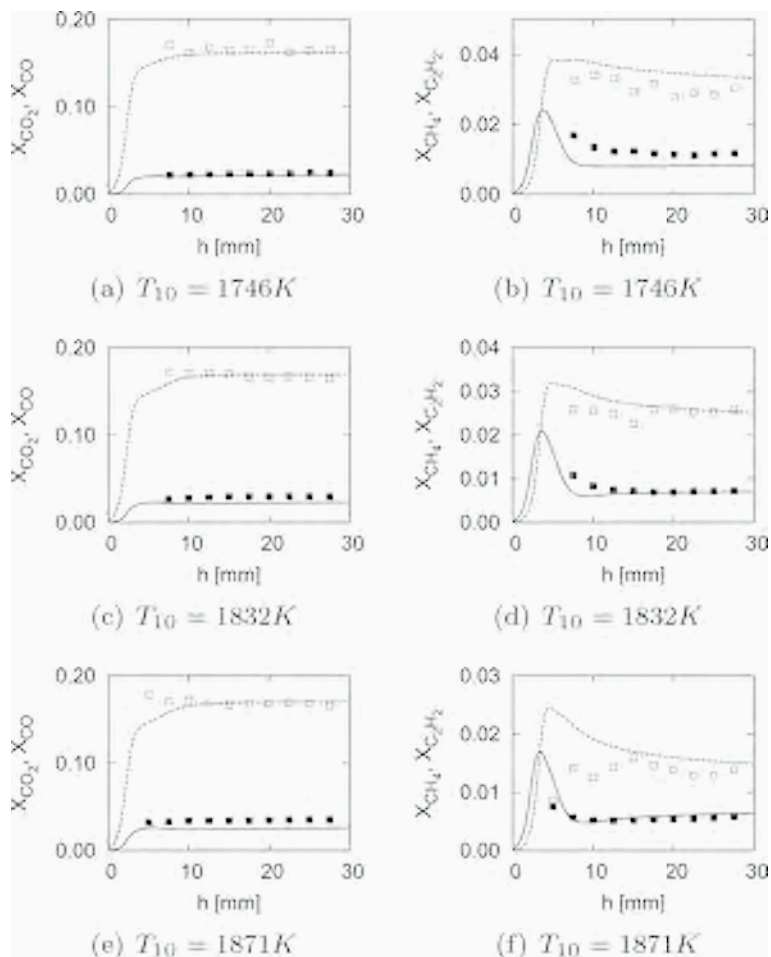


Figure 8. Mole fractions of  $\text{CO}_2$  (■) and  $\text{CO}$  (□) (left graphs), and  $\text{CH}_4$  (■) and  $\text{C}_2\text{H}_2$  (□) (right graphs).

stion products (CO and CO<sub>2</sub>), as well as intermediate species relevant for soot formation (CH<sub>4</sub> and C<sub>2</sub>H<sub>2</sub>), are correctly predicted by the chemical mechanism.

4.4.1. Soot volume fraction

Figure 9 provides a comparison between predicted and measured soot volume fraction. The present soot model is able to predict the soot volume fraction for the three flames with good accuracy. Interestingly, the soot volume fraction decreases with increasing temperature. This is an experimentally well known and characterized phenomenon [49]. At low temperatures, the soot volume fraction increases with increasing temperature. Then, beyond a threshold temperature, the soot volume fraction decreases if the

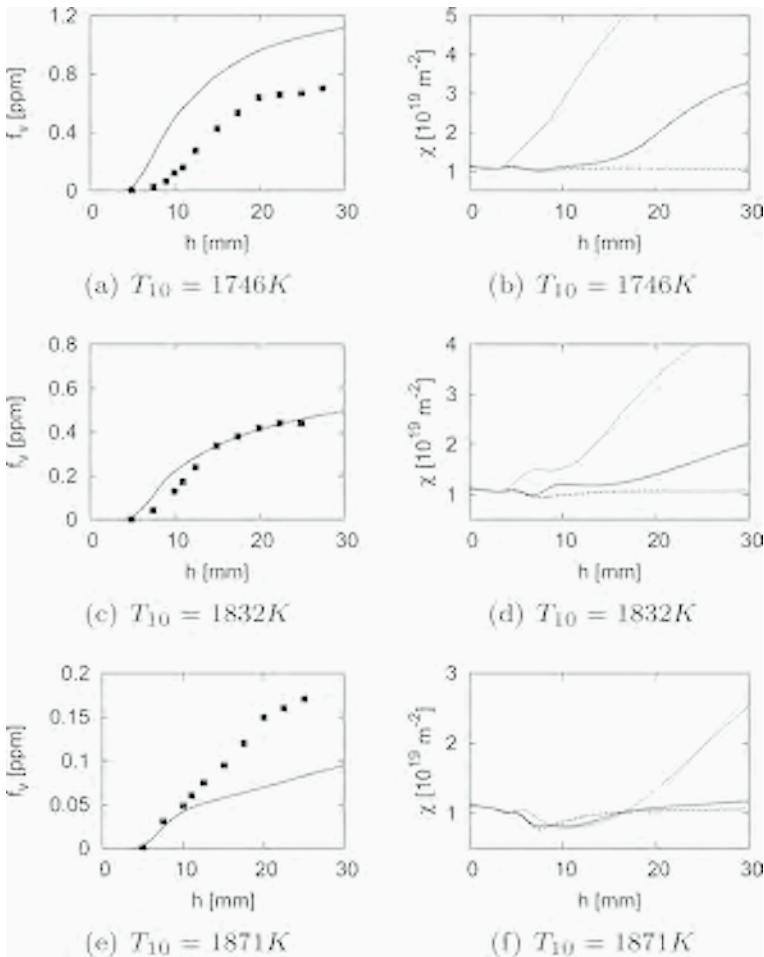


Figure 9. Soot volume fraction (left graphs) and surface reactivity (right graphs). Solid line: mean, dashed line: first mode, dotted line: second mode.

temperature is further increased. This bell-shaped curve has been measured experimentally for several premixed flames by Böhm et al. [49]. The value of the threshold temperature was found to be a function of the fuel and other flame parameters. The flames considered here and measured by Xu et al. [41] are all in the high temperature region.

#### 4.4.2. Aggregate properties

The primary particle diameters were measured experimentally using Transmission Electron Microscopy (TEM) [41]. Large aggregates composed of a widely varying number of primary particles were visual observed on the TEM grids, and their diameter was estimated. For proper comparison, the experimental values should be compared to the diameter of the particles from the second mode of the NDF.

Figure 10 shows a comparison of the predicted diameter of the primary particles with experimental values. For most of the time, the first delta function remains at a small diameter around  $d_p \approx 1$  nm corresponding to the size of the first soot particles formed by nucleation. The second mode reaches rapidly a steady state value between 10 nm and 20 nm. This second mode compares qualitatively well with the experimental values for the three flames studied. While the experimental measurements were characterized by low uncertainties (less than 10%), the technique used has been shown to disagree with other techniques such as Scanning Mobility Particle Sizer (SMPS) [9]. The soot particles are liquid-like and will spread upon collision on a TEM grid. Therefore, the diameter measured by analysing TEM pictures might be overestimated.

Finally, Figure 10 shows the number of primary particles per aggregate ( $n_p$ ). While there are no experimental values for this quantity, one can estimate from the TEM pictures provided in [41] that this number lies somewhere between 10 to 100. In the current simulations, the number of primary particles per aggregate starts at one, since the first soot particles are assumed to be spherical. Later during the simulation, larger aggregates will form from the collision with smaller soot particles. The computed number of primary particles is for all flames in the expected range.

#### 4.4.3. Discussion

As shown in Figure 9, the decay of the soot volume fraction with increasing temperature is reasonably predicted by the present model. The analysis of the results shows that this is because of the decrease in PAH concentration for higher temperatures. This causes, first of all, a lower rate of nucleation and condensation, which decreases the soot volume fraction. Because of this, the surface reactivity, shown in Figure 9, also goes down, which leads to a further decrease in the soot volume fraction.

Figures 9b, 9d, and 9f show the density of active sites per unit soot surface area for the three flames. The mean value varies from about  $\chi \approx 1 \times 10^{19} \text{ m}^{-2}$  to around  $\chi \approx 3 \times 10^{19} \text{ m}^{-2}$ . As initially assumed by Kazakov and Frenklach [39], the surface reactivity appears to depend on the temperature. Both the averaged surface reactivity and the surface reactivity corresponding to the second mode are smaller at higher temperature.

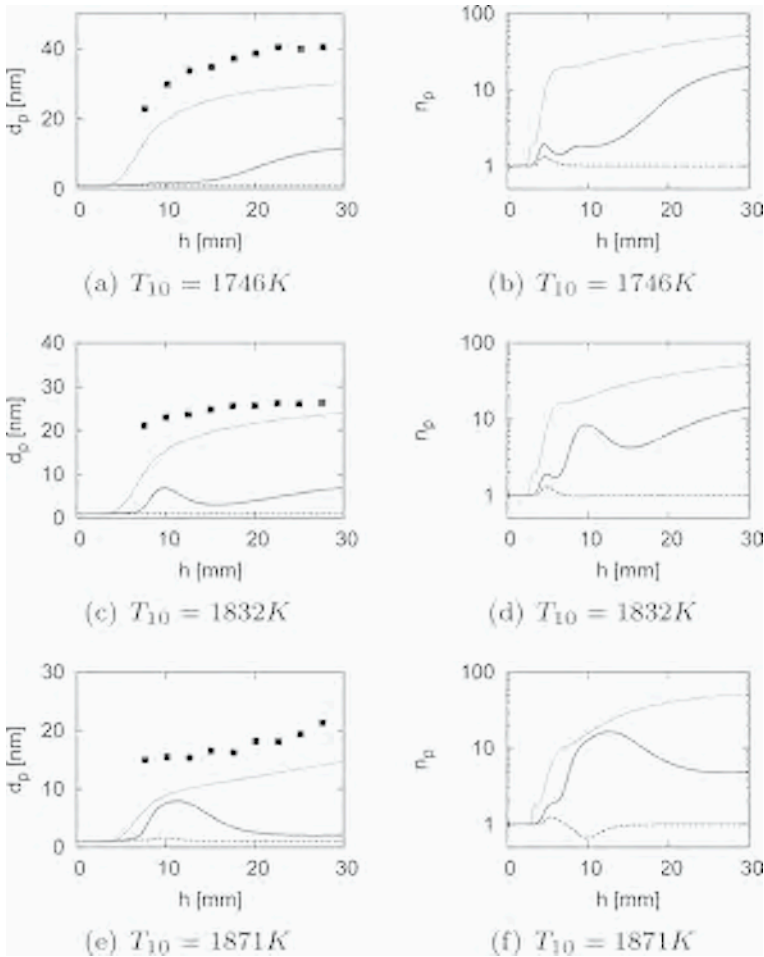


Figure 10. Primary particle diameter (left graphs) and number of primary particles per aggregate (right graphs). Solid line: mean, dashed line: first mode, dotted line: second mode.

For the flames considered here, the small particles are less reactive than the large particles. However, it is important to note that this is not an assumption in the model. In the present formulation, it is not the size that determines the reactivity, but the history of the soot particles, and the growth mechanisms that have contributed to the particle mass.

## 5. CONCLUSION

In this work, a new model describing soot particle dynamics has been formulated. A soot particle is represented as a fractal-shaped aggregate composed of many spherical primary particles. Three independent parameters are used to characterize a soot parti-

cle; the total volume ( $V$ ), the total surface area ( $S$ ), and the total number of hydrogenated (or active) sites on the surface ( $H$ ). This multivariate model (VSH) is formulated in the framework of Direct Quadrature Method of Moments (DQMOM). This allows for an adequate description of typical bimodal number density function of soot particles. The VSH model has been applied to a series of laminar premixed and diffusion flames. For all flames, the soot volume fraction was predicted with good accuracy. Aggregate properties, such as primary particle diameter and size of the aggregates, were also analyzed. The results were in reasonable agreement with experiments. Because of its inherent description of coagulation with volume and surface area as independent parameters, the VSH model can describe the two limiting cases of pure coalescence and aggregation, as well as intermediate cases.

The reactivity of the surface, expressed by the density of active sites per unit surface area, is also computed as part of the model because of the joint description of particle surface area and active surface sites. For high temperatures, the reactivity is shown to decrease when the temperature of the flame increases. The combined effect of depletion of PAH molecules in the gas phase and stronger rate of surface reactions could partially explain the reduced soot surface reactivity at high temperature. Furthermore, the current model predicts an increasing surface reactivity with particle size and residence time for the three ethylene flames.

These results contradict some common assumptions about soot surface reactivity. Further analysis and modeling of the surface should be performed to resolve this contradiction.

## ACKNOWLEDGMENTS

The authors gratefully acknowledge funding by the US Department of Energy within the ASC program and the US Department of Defense within SERDP.

## REFERENCES

1. M. Schuetz, C. A. Frenklach, *Proc. Combust. Inst.* 29 (2002) 2307-2314.
2. D. Wong, R. Whitesides, C.A. Schuetz, M. Frenklach, in *Combustion Generated Fine Carbonaceous Particles*, H. Bockhorn, A. D'Anna, A.F. Sarofim, H. Wang (Eds.) Karlsruhe University Press, 2009, pp. 247-258.
3. M. Frenklach, H. Wang, *Proc. Combust. Inst.* 23 (1991) 1559-1566.
4. U. O. Köylü, G. M. Faeth, T. L. Farias, M. G. Carvalho, *Combust. Flame* 100 (1995) 621-633.
5. K. A. Jensen, J. M. Suo-Antilla, L. G. Blevins, *Characterization of soot properties in two-meter JP-8 pool fires*, technical report SAND2005-0337, Sandia National Laboratories (2005).
6. P. Mitchell, M. Frenklach, *Proc. Combust. Inst.* 27 (1998) 1507-1514.
7. P. Mitchell, M. Frenklach, *Phys. Rev. E* 67 (2003) 061407.1-061407.11.
8. P. Meakin, *J. Colloid Interface Sci.* 96 (1983) 415-424.
9. B. Zhao, K. Uchikawa, H. Wang, *Proc. Combust. Inst.* 31 (2007) 851-860.
10. M. Lattuada, H. Wu, M. Morbidelli, *J. Colloid Interf. Sci.* 268 (2003) 106-120.

11. H. Schmid, S. Tejwani, C. Artelt, W. Peukert, J. Nanopart. Res. 6 (2004) 613-626.
12. J. Appel, H. Bockhorn, M. Frenklach, Combust. Flame. 121 (2000) 122-136.
13. A. Kazakov, M. Frenklach, Combust. Flame 114 (1998) 484-501.
14. M. Balthasar, M. Frenklach, Combust. Flame 140 (2005) 130-145.
15. R. I. A. Patterson, K. M., Combust. Flame 151 (2007) 160-172.
16. J. Singh, R. I. A. Patterson, M. Kraft, H. Wang, Combust. Flame 145 (2006) 117-127.
17. J. Singh, M. Balthasar, M. Kraft, W. Wagner, Proc. Combust. Inst. 30 (2005) 1457-1465.
18. B. Zhao, Z. Yang, M. V. Johnston, H. Wang, A. S. Wexler, M. Balthasar, M. Kraft, Combust. Flame 133 (2003) 173-188.
19. B. Zhao, Z. Yang, Z. Li, M. V. Johnston, H. Wang, Proc. Combust. Inst. 30 (2005) 1441-1448.
20. D. L. Marchisio, R. O. Fox, J. Aerosol Sci. 36 (2005) 43-73.
21. A. H. Park, S. N. Rogak, Aerosol Sci. Technol. 37 (2003) 947-960.
22. S. J. Harris, A. M. Weiner, Combust. Sci. Technol. 31 (1983) 155-167.
23. A. Zucca, D. L. Marchisio, A. A. Barressi, R. O. Fox, Chem. Eng. Sci. 61 (2006) 87-95.
24. R. O. Fox, J. Aerosol Sci. 37 (2006) 1562-1580.
25. S. K. Friedlander, Wiley & Sons, 1986.
26. J. H. Seinfeld, Wiley & Sons, 2006.
27. H. Pitsch, E. Riesmeir, N. Peters, Combust. Sci. Technol. 158 (2000) 389-406.
28. R. Gordon, J. Math. Phys. 9 (1968) 655.
29. A. D'Alessio, A. C. Barone, R. Cau, A. D'Anna, P. Minutolo, Proc. Combust. Inst. 30 (2005) 2595-2603.
30. A. Violi, A. F. Sarofim, G. A. Voth, Combust. Sci. Technol. 176 (2004) 991-1005.
31. A. Violi, Combust. Flame 139 (2004) 279-287.
32. S.E. Pratsinis, J. Colloid Interface Sci. 124 (1988) 416-428.
33. F. E. Kruijs, K. A. Kusters, S. E. Pratsinis, B. Scarlett, Aerosol Sci. Technol. 19 (1993) 514-526.
34. A. M. Mebel, M. C. Lin, T. Yu, K. Morokuma, J. Phys. Chem. A 101 (1997) 3189-3196.
35. I.V. Tokmakov, M. C. Lin, J. Phys. Chem. A 106 (2002) 11309-11326.
36. L. B. Harding, Y. Georgievskii, S. J. Klippenstein, J. Phys. Chem. A 109 (2005) 4646-4656.
37. I. V. Tokmakov, M. C. Lin, J. Phys. Chem. A 108 (2004) 9697-9714.
38. M. Frenklach, C. A. Schuetz, J. Ping, Proc. Combust. Inst. 30 (2005) 1389- 1396.
39. A. Kazakov, H. Wang, M. Frenklach, Combust. Flame 100 (1995) 111-120.
40. K. G. Neoh, J. B. Howard, A. F. Sarofim, Soot Oxidation in Flames, Plenum Press, New York, 1981.
41. F. Xu, P. B. Sunderland, G. M. Faeth, Combust. Flame 108 (1997) 471-493.
42. A. Tregrossi, A. Ciajolo, R. Barbella, Combust. Flame 117 (1999) 553-561.
43. C. Pels Leusden, N. Peters, Proc. Combust. Inst. 28 (2000) 2619-2625.
44. H. Pitsch, FlameMaster, a C++ computer program for 0D combustion and 1D laminar flame calculations.
45. G. Blanquart, P. Pepiot-Desjardins, H. Pitsch, Chemical mechanism for high temperature combustion of engine relevant fuels with emphasis on soot precursors, Combust. Flame (2008) submitted.
46. R. A. Shandross, J. P. Longwell, J. B. Howard, Combust. Flame 85 (1991) 282-284.
47. C. Pels Leusden, Experimentelle und theoretische untersuchung der rusbildung in laminaren gegenstromdiffusionsflammen, Ph.D. thesis, RWTH Aachen (2001).
48. R. Seiser, L. Truett, D. Trees, K. Seshadri, Proc. Combust. Inst. 27 (1998) 649-657.
49. H. Bohm, D. Hesse, H. Jander, B. Luers, J. Pietscher, H. G. Wagner, M. Weiss, Proc. Combust. Inst. 22 (1988) 403-411.



# Modelling the soot particle size distribution functions using a detailed kinetic soot model and a sectional method

F. Mauss<sup>1</sup>, K. Netzell<sup>1</sup>, C. Marchal<sup>2</sup>, G. Moréac<sup>2</sup>

<sup>1</sup> Division of Thermodynamics and Thermal Process Engineering, BTU Cottbus,  
Sielower Strasse 12, 03044 Cottbus, Germany

<sup>2</sup> Renault, Direction des Techniques Avancées de l'Automobile  
1, Avenue du Golf, 78288 Guyancourt, France

*Abstract: In the present work, we describe a newly developed sectional method that optimizes high accuracy in the calculated PSDF and the need in CPU time to calculate the PSDF. We apply a detailed kinetic soot model to model fuel rich laminar premixed ethylene air flames. An offset in height above burner is introduced to correct for the intrusion of the measuring device. This offset is set such that the PSDF in the coagulation mode is in optimum agreement between experiment and calculation. We discuss in the paper that rate kinetic data can be deduced from the concentration of the smallest soot particles and from the gradient of soot particle number density in particle size. For this accurate measurements of the temperature and the PSDF are needed, and thereby a better understanding of the probe effects in the flame.*

## 1. INTRODUCTION

The formation of soot in flames results from a number of complex physical and chemical processes. Several of these processes are still not fully understood and modeling soot formation relies on empirical assumptions. In addition to the complexity of the problem the modeler was in the past confronted to the fact that the experimental data were limited to measurements of global quantities; i.e. number density and soot volume fraction, namely the first and second moment of the particle size distribution function (PSDF) [1,2]. Information about the PSDF or the shape and consistency of soot particles have been very rare [3]. For the latter, probes from particulates through thermophoretic sampling in flames were taken. Today, measurements of particle size distribution functions are available for simple flame configurations [4, 5].

Until the late nineties modeling soot formation was directed towards understanding the most sensitive processes only. Model validation was performed by comparing calculated profiles of soot volume fraction against experimental data. This caused, that most mathematical methods describing the soot PSDF included the first and second moment of the PSDF only [6,7]. These developments have been consolidated through the formulation of the method of moments with interpolative closure (MoM) for soot particles and the soot precursors, rigorously deriving the governing equations for any moment of the PSDF. At the same time the hydrogen abstraction carbon addition

mechanism was introduced as the major chemical growth mechanism for soot particles [8, 9, 10]. In [11] it was shown that the HACA mechanism can explain the sensitivity of soot formation on varying H and H<sub>2</sub> concentrations in the flame. In [11, 12] the method of moments was formulated including convection, size dependent diffusion and thermophoreses.

The absolute amount for the soot volume fraction was often adjusted by optimizing the active site coefficient, as in ref. [13], where it was made temperature dependent to cover a full regime of experimental data. This limited the validation of the models to validating the general trends, i.e. pressure dependence, fuel dependence etc.. Comparison of calculated and measured soot number densities suffered often from the fact, that the numerical models include particles down to sizes of 1 nm, while the experimental data were limited to certain sizes. Measurements of particle size distribution functions as presented in [6, 7] offer additional information on the processes of soot formation in flames; i.e. the rate of particle inception, surface reactions and coagulation decide on the modality of the PSDF, the gradient of particle concentration with size in the nucleation mode, the valley between nucleation mode and the coagulation mode, and the width of the distribution in the coagulation mode.

Beside the aspects in chemistry and physics, research in soot formation is often motivated by soot emissions from technical devices such as Diesel engines, diffusion gas turbines, or furnaces. In these devices combustion occurs in turbulent diffusion flames. Hence, one technical aspect of the mathematical formulation of the soot PSDF is its applicability in turbulent diffusion flame models. Since the formation of soot cannot be avoided in diffusion flames of the most hydrocarbon fuels, research concentrates on the transport of soot from fuel rich conditions through the main reaction layer to fuel lean conditions. Most of the soot formed under fuel rich conditions is oxidized in the main reaction layer, and one demand to the turbulent diffusion flame model is its ability to predict the break through of the soot particles. The laminar flamelet model has been shown to be the most accurate model for this process [14].

The method of moments with interpolative closure has been successfully applied together with laminar flamelet models. This was done by calculating the soot transport equations in the mixture fraction coordinate in transient flamelets interactively with the CFD calculation [15-18]. In an alternative approach the chemical source terms for PAH formation and heterogeneous surface growth and oxidation have been calculated and stored in a flamelet library. The surface dependent terms have been normalized by the particle surface. The transport equations for the moments of the PSDF have then been calculated by the CFD program, using the flamelet library of sources, the local particle surface, and local coagulation source terms [19-21].

In this study a sectional method [22] is chosen to model the PSDF in laminar premixed flames [5]. The sectional method has the advantage, that similar transport equations can be formulated as for the method of moments without any further approximations [23]. This allows transferring the model from simple reactor to complex CFD models. However for CFD software the CPU time demanded by the model can be decisive for the applicability of the development in practice. The model formulated in the following [24] formulates most source terms with second order accuracy, and limits thereby the number of sections. It also limits the necessary number of integrations that during run time of the model.

In the following we first discuss some physical aspects of the applied soot model. Thereafter we present some detail of the mathematical description of the particle size distribution function. Finally we present comparisons of predicted and experimental particle size distribution functions.

## 2. SOOT MODEL

In this work we apply a detailed kinetic soot model [25] which consists of 5 parts: (1) Poly Aromatic Hydrocarbon (PAH) formation, which includes a detailed chemical kinetic description of fuel pyrolysis and oxidation, formation of the first aromatic ring and its subsequent growth up to a prescribed size, (2) nucleation or particle inception for the formation of the primary soot particles, (3) condensation of PAHs on the surface of soot particles, (4) coagulation between particles and (5) heterogeneous surface reactions accounting for surface growth, and oxidation by  $O_2$  and  $OH$ .

Models for soot formation include physics, chemistry and a mathematical description of the particle size distribution function (PSDF). Physical models describe particle dynamics i.e.: inception, condensation and coagulation processes, whereas the chemical models describe the gas phase chemistry including soot precursor formation and the surface reactions, i.e. including surface growth and oxidation. For the mathematical description we apply a sectional method to discretize the PSDF.

The physical model is based on collision phenomena due to the size dependant motion [26, 27] of the particles leading to coalescence or agglomeration. For the flames investigated in this paper no agglomerates have been reported [5] experimentally. Hence, we limit the description to coalescence.

Defining  $n(v,t)dv$  as the number density of the particles in a volume range between  $v$  and  $v+dv$  at time  $t$ , the collision of particles is described by the Smoluchowski's master equation [28]:

$$\frac{\partial n(v)}{\partial t} = \frac{1}{2} \int_0^{v-\infty} \beta(u, v-u) n(u) n(v-u) du - \int_0^{\infty} \beta(u, v) n(u) n(v) du \quad (1)$$

where  $u$  is defined in analogy to  $v$ . Equation (1) gives the change in time of the number of particles of volume  $v$ . The first integral on the Right Hand Side (RHS) of the equation refers to the collisions between small particles leading to the formation of particles of volume  $v$ . The second integral describes the collision of particles of volume  $v$  with particles of any other size, leading to larger particles.

The collision factor  $\beta$  is a function of the Knudsen number  $Kn$  which is defined by the ratio of the mean free path between two collisions of a gas molecule  $\lambda$ , and the particle radius  $d/2$ :

$$Kn = 2\lambda / d,$$

with

$$\lambda = \frac{k_b T}{\sqrt{2} \pi \sigma^2 p},$$

being a function of the temperature  $T$ , the pressure  $p$  and the gas molecule diameter  $\sigma$ .  $k_b$  is the Boltzmann constant.

For  $Kn \gg 1$  the particles move independent on the gas conditions in the free molecular regime. Free Brownian motion (index  $fm$ ) is established. For  $Kn \ll 1$ , the particles recognize the gas as a continuum (index  $c$ ). The particles are in the continuum regime. The collision frequencies are described for each regime as functions of the particle volumes.

$$\beta_{fm}(u, v) \propto \left(\frac{1}{u} + \frac{1}{v}\right)^{1/2} (u^{1/3} + v^{1/3})^2,$$

and

$$\beta_c(u, v) \propto (u^{1/3} + v^{1/3}) \left(\frac{1}{u^{1/3}} + \frac{1}{v^{1/3}}\right) = 2 + \frac{u^{1/3}}{v^{1/3}} + \frac{v^{1/3}}{u^{1/3}}.$$

In the continuum regime – other than in the free molecular regime – the dependence of the collision frequency on the particle volume is weak. For the spherical particle model the collision diameter of the particles is the ordinary diameter of the spheres, and the collision frequency functions are given by [29, 30]:

$$\beta_{fm}(u, v) = \varepsilon(u, v) \left(\frac{3}{4\pi}\right)^{1/6} \left(\sqrt{\frac{6k_b T}{\rho_g}}\right) \left(\frac{1}{u} + \frac{1}{v}\right)^{1/2} (u^{1/3} + v^{1/3})^2,$$

and

$$\beta_c(u, v) = \frac{2k_b T}{3\eta} (u^{1/3} + v^{1/3}) \left(\frac{C(u)}{u^{1/3}} + \frac{C(v)}{v^{1/3}}\right),$$

with  $\eta$  the gas dynamic viscosity. The Cunningham slip factor  $C$ , correcting the expression for the non-continuum gas behavior of the motion of small particles [31, 32] is given by:

$$C(v) = 1 + 1.257 Kn(v).$$

The gas dynamic viscosity  $\eta$  can be calculated from Sutherland’s law:

$$\eta = \frac{C_1 T^{3/2}}{T + C_2},$$

where  $C_1 = 1,4558 \cdot 10^{-6} \text{ kg}\cdot\text{m}^{-1}\cdot\text{s}^{-1}\cdot\text{K}^{-1/2}$  and  $C_2 = 110,4 \text{ K}$  are the Sutherland coefficients.

In the transition regime (index  $tr$ ), we use the harmonic mean of the free molecular and continuum collision frequencies as proposed by Pratsinis [33] instead of the more complex semi-empirical formula of Fuchs [34]. The resulting collision frequency can then be used in the entire range of Knudsen number.

$$\beta_{tr}(u, v) = \frac{\beta_{fm}(u, v)\beta_c(u, v)}{\beta_{fm}(u, v) + \beta_c(u, v)} \tag{2}$$

The collisions were treated as irreversible having a sticking coefficient of 1. Van der Waals forces enhance the collision frequency by  $\varepsilon(u, v) = 2.2$  for particle inception as

was calculated for pyrene in [35, 36]. For particle inception the free molecular regime is considered only.

In this paper we discuss differences between the predicted and the experimental PSDF. Since the physics of particle collisions in the free molecular regime is well understood, there are not many unknown parameter that can influence the resulting PSDF. One parameter is the size dependence of the enhancement factor for collisions of PAH's with particles, and of small with large particles. The enhancement factor for the coagulation and the condensation process was calculated as function of the particle volume in free molecular regime as:

$$\varepsilon^{fm} = \frac{1}{2} \int_0^1 \frac{1}{x^2} \frac{d}{dx} \left( x \frac{d\hat{\Phi}(x)}{dx} \right) \exp \left[ \frac{x}{2} \frac{d\hat{\Phi}(x)}{dx} - \hat{\Phi}(x) \right] dx + \exp \left[ \frac{1}{2} \frac{d\hat{\Phi}(x)}{dx} \Big|_{x=1} - \hat{\Phi}(1) \right], \quad (3)$$

where  $\hat{\Phi}(x)$  corresponds to the van der Waals potential, calculated following the approach of Pailthorpe and Russel [37]. This technique has been applied before by Kennedy [38, 39] and Balthasar et al. [36]. It is based on the Hamaker theory [40] including retarded van der Waals interaction [41] and a geometrical factor to account for the sphericity of the particles. The van der Waals potential can be written as:

$$\hat{\Phi}^{adv}(x) = -\frac{A}{6k_B T} \left[ \frac{2s(1-s)x^2}{1-x^2} + \frac{2s(1-s)x^2}{1-(2s-1)^2x^2} + \ln \left( \frac{1-x^2}{1-(2s-1)^2x^2} \right) \right],$$

where  $A$  is the retarded Hamaker constant and  $s=d_1/(d_1+d_2)$ , with  $d$  corresponding to the diameters of the particles.

The solution of Equation (3) is visualized in Figure 1. A value of 2.2 is a good approximation [38, 39] for the collision of particles with approximately equal sizes

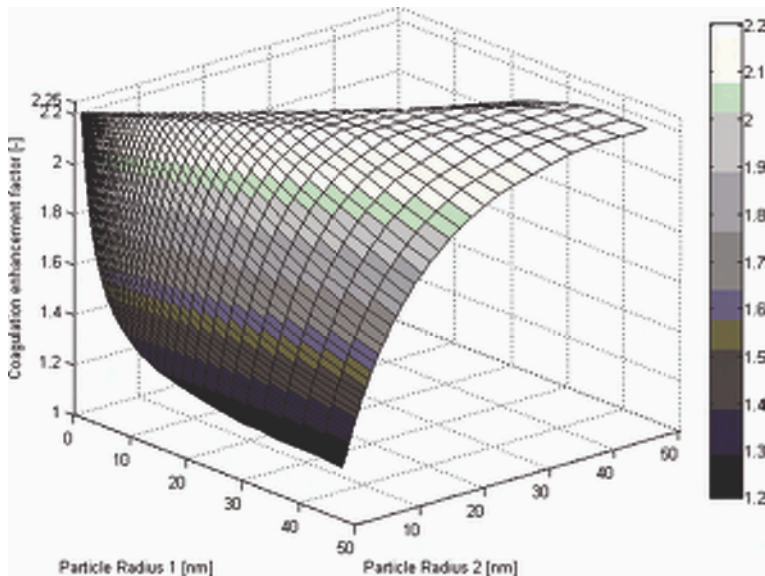


Figure 1. The size dependent enhancement factor for coagulation processes.

and for all particles with sizes greater than 15 nm and was used before (see for example Ref. [8]). A value of 1.3 is a good approximation of the average condensation enhancement factor for pyrene as the condensating PAH and was used in previous work [18].

In this paper we apply the kinetic model for fuel oxidation, PAH formation and growth, and particle formation, growth and oxidation (HACA with ring closure) from Reference [12, 25]. In the following section we discuss the basics of the sectional method that is used to discretize the PSDF.

### 3. SECTIONAL METHOD

Details on the sectional method applied in this publication are given in ref. [24]. The mathematical formulation follows the formulation in ref. [22]. Transport equations are derived for the integrals of the PSDF over each section. A density weighted soot volume fraction for all particles within a section represents the transport property.

The particle volumes  $v_{i,min}$  and  $v_{i,max}$  are defined at the left and right boundary of section  $i$ , and  $q_i(v)$  is the distribution within this section and is in this paper approximated by a first order polynomial:

$$Q_i = \int_{v_{i,min}}^{v_{i,max}} q_i(v) dv \quad , \quad (4)$$

with:

$$q_i(v) = q_i^* v + q_i^{\#} \quad , \quad (5)$$

and

$$q_i^* = \frac{k_i^+ + k_i^-}{2} \quad .$$

The  $k_i^+$  and  $k_i^-$  are introduced as the slopes of  $q_i(v)$  at the left and right boundary of the section. They are calculated such, that both the fluxes of particle number density and soot volume fraction over the section boundaries are conserved. By integrating equation (4), using the definition (5)  $q_i^{\#}$  can be calculated as:

$$q_i^{\#} = \frac{Q_i}{v_{i,max} - v_{i,min}} - q_i^* v_{i,max} \quad , \quad (6)$$

with

$$v_{i,max} = \frac{v_{i,max} + v_{i,min}}{2} \quad ,$$

The size dependent volume weighted number density is given by.

$$n_i(v) = \frac{q_i(v)}{v} \quad (7)$$

As mentioned before, the advantage of the approach is, that both soot volume fraction and number density of particles can be conserved when formulating the source terms for each section.

The size of each section is chosen adaptively. However the section size increases with particle size such that the inequality  $(v_{i+1,max} - v_{i+1,min}) > x(v_{i,max} - v_{i,min})$ ,  $x > 1$  is always true. Through this function a fine size resolution for small particle classes is reached, while the resolution for large particles is coarse. In the literature  $x > 2$  is frequently applied to limit the number of integrations necessary to calculate the coagulation source terms for each section. This limits the number of sections, and thereby the accuracy of the discretisation of the PSDF. In our approach we allow any number of  $x > 1$ , but limit the number of integration, through simplifying the treatment of the coagulation process, as discussed below.

For particle inception, using the Smoluchowski equation and limiting the PAH size to pyrene we obtain the source  $\Omega$ :

$$\begin{aligned} \Omega_{i,py} &= 2v_{PAH} \beta_{inc,py}(v_{PAH}, v_{PAH}) N_{PAH}^2; \quad i = 1 \\ \Omega_{i,py} &= 0; \quad i > 1 \end{aligned} \quad (8)$$

For condensation three terms are considered in equation (9). The first term accounts for particles entering section  $i$  through condensation of PAH on particles in section  $i-1$  with volumes larger than  $v_{i,min} - v_{PAH}$ . For the first section this term is equal to zero. The second term accounts for particle growth through condensation resulting in particle with volumes smaller than  $v_{i,max}$ . These particles will remain in section  $i$ . The third term considers particles that grow beyond the volume  $v_{i,max}$  and leave section  $i$ . This term is not considered in the last section. This implies that the last section includes all particles with  $v_{n,min}$  where  $n$  is the number of sections.

$$\begin{aligned} \Omega_{i,cond} &= (v_{PAH} + v_{i,min}) N_{PAH} \int_{v_{i,min} - v_{PAH}}^{v_{i,max}} \beta_{inc,cond}(v_{PAH}, v) n(v) dv \\ &+ v_{PAH} N_{PAH} \int_{v_{i,min}}^{v_{i,max} - v_{PAH}} \beta_{inc,cond}(v_{PAH}, v) n(v) dv \\ &- v_{i,max} N_{PAH} \int_{v_{i,min} - v_{PAH}}^{v_{i,max}} \beta_{inc,cond}(v_{PAH}, v) n(v) dv \end{aligned} \quad (9)$$

For coagulation we proceed similarly. However, coagulation is calculated from the mean particle sizes in each section, and CPU expensive integration is avoided. We increased the accuracy of this method, by defining "coagulation subsections" within each section. However, we find that the introduction of subsections did not change our predicted particle size distribution functions, and concluded that it was accurate enough to calculate kinetic growth and oxidation processes at the highest possible accuracy [24]. Calculations shown in this paper have been calculated by defining only one subsection.

The section in which a particle  $k$  will fall after collision with particle  $j$  is calculated directly after the discretisation process of the particle size distribution function, and is not repeated throughout the calculation. The coagulation source term is given by:

$$\begin{aligned}
 \Omega_{i, \text{coag}} = & \sum_{v_{j, \text{min}} < v_k + v_j < v_{i, \text{max}}} (v_k + v_j) n(k) n(j) \beta_{\text{coag}}(v_k, v_j) \\
 & + n(i) \sum_{v_k + v_j < v_{i, \text{min}}} v_k n(k) \beta_{\text{coag}}(v_k, v_j) \\
 & - v_i n(i) \sum_{v_i = v_k > v_{i, \text{max}}} n(k) \beta_{\text{coag}}(v_i, v_k) \\
 & - 2v_i n(i) n(i) \beta_{\text{coag}}(v_i, v_i)
 \end{aligned}
 \tag{10}$$

The first term on the RHS of Equation (10) refers to the particles moved into section  $i$ , the second term describes the growth process of particles within section  $i$  through coagulation with small particles. The third and fourth term on the RHS correspond to the particles leaving section  $i$  since their size after collision is larger than the upper boundary of the section.

For surface growth the chemical model leads to the following equations:

$$\Delta Q_{i, \text{sg}} = \alpha V_{C_2} (k_d - k_{\text{rev}}) \int_{v_{i, \text{min}}}^{v_{i, \text{max}}} \left( \frac{v}{V_{C_2}} \right)^{\theta/3} n(v) dv
 \tag{11}$$

where  $\theta$  denotes geometry of soot particles which is equal to 2 in this work since the observed particles were spherical [5].  $V_{C_2}$  is the volume added to the soot particle through the addition of two carbon atoms.  $k_d$  is the rate coefficient of ring closure and  $k_{\text{rev}}$  is the rate coefficient of the ring opening reaction.  $\alpha$  is the active site parameter.

Equation (11) can then be integrated:

$$\begin{aligned}
 \Delta Q_{i, \text{sg}} = & \alpha (V_{C_2})^{\frac{3-\theta}{3}} (k_d - k_{\text{rev}}) \\
 & \left( \frac{3}{3+\theta} q_i (v_{i, \text{max}}^{\frac{3+\theta}{3}} - v_{i, \text{min}}^{\frac{3+\theta}{3}}) + \frac{3}{\theta} q_i'' (v_{i, \text{max}}^{\frac{\theta}{3}} - v_{i, \text{min}}^{\frac{\theta}{3}}) \right)
 \end{aligned}
 \tag{12}$$

Number density conservation puts constraints on the distribution of  $\Delta Q_{i, \text{sg}}$  among the sections. If  $\Delta q_{i, \text{sg}}^{\rightarrow}$  is the soot volume entering and  $\Delta q_{i, \text{sg}}^{\uparrow}$  is the soot volume leaving section  $i$  and:

$$\Delta Q_{i, \text{sg}} = \Delta q_{i, \text{sg}}^{\rightarrow} - \Delta q_{i, \text{sg}}^{\uparrow}
 \tag{13}$$

The conservation of number density gives:

$$\Delta \eta_i = \Delta \eta_{i+1}
 \tag{14}$$

Assuming  $\Delta q_{\text{sg}}$  is evenly spread over the sections, the previous equation can be transformed using equation (7):

$$\frac{\Delta q_{i,sg}^{\uparrow}}{v_{i,max} - v_{i,min}} \int_{v_{i,min}}^{v_{i,max}} \frac{1}{v} dv = \frac{\Delta q_{i,sg}^{\rightarrow}}{v_{i+1,max} - v_{i+1,min}} \int_{v_{i+1,min}}^{v_{i+1,max}} \frac{1}{v} dv \quad (15)$$

Finally we combine the equations (13) and (15) and find:

$$\Delta q_{i,sg}^{\uparrow} = \frac{1}{\frac{(v_{i+1,max} - v_{i+1,min}) \ln(v_{i,max} / v_{i,min})}{(v_{i,max} - v_{i,min}) \ln(v_{i+1,max} / v_{i+1,min})} - 1} \Delta Q_{i,sg} \quad (16)$$

$$\Delta q_{i,sg}^{\rightarrow} = \frac{1}{1 - \frac{(v_{i,max} - v_{i,min}) \ln(v_{i+1,max} / v_{i+1,min})}{(v_{i+1,max} - v_{i+1,min}) \ln(v_{i,max} / v_{i,min})}} \Delta Q_{i,sg} \quad (17)$$

And source terms for surface growth can be written:

$$\begin{aligned} \Omega_{1,sg} &= -\Delta q_{1,sg}^{\uparrow} \\ \Omega_{i,sg} &= \Delta q_{i-1,sg}^{\rightarrow} - \Delta q_{i,sg}^{\uparrow} \quad i = 2, 3, \dots, i_{max} - 1 \\ \Omega_{i_{max},sg} &= \Delta q_{i_{max}-1,sg}^{\rightarrow} \end{aligned} \quad (18)$$

We proceed the same way for oxidation:

$$\begin{aligned} \Delta Q_{i,ox} &= \alpha (k_{O_2} + k_{OH}) (V_{C_2})^{\frac{1-\theta}{3}} \\ &\left( \frac{3}{3+\theta} q_i (v_{i,max}^{\frac{3+\theta}{3}} - v_{i,min}^{\frac{3+\theta}{3}}) + \frac{3}{\theta} q_i^{\theta} (v_{i,max}^{\frac{\theta}{3}} - v_{i,min}^{\frac{\theta}{3}}) \right) \end{aligned} \quad (19)$$

In equation 19 we introduce the rates of soot oxidation with O<sub>2</sub> and OH,  $k_{O_2}$  and  $k_{OH}$ .

The set of transport equations for  $Q_i$  (20) in one-dimensional laminar flames, are comparable to the transport equation that have been derived before of the moments  $\mu_r$  (21) of the PSDF [12], which are presented below.

$$\rho \frac{\partial Q_i / \rho}{\partial t} + \rho v \frac{\partial Q_i / \rho}{\partial x} = \frac{\partial}{\partial x} \left( \rho D_{p, v_{i,max}} \frac{\partial Q_i / \rho}{\partial x} \right) + \frac{\partial}{\partial x} \left( 0.55 \eta \frac{1}{T} \frac{\partial T}{\partial x} Q_i \right) + \Omega_i \quad (20)$$

$$\rho \frac{\partial \mu_r / \rho}{\partial t} + \rho v \frac{\partial \mu_r / \rho}{\partial x} = \frac{\partial}{\partial x} \left( \rho D_{p, v_{i,max}} \frac{\partial \mu_{r-2/3} / \rho}{\partial x} \right) + \frac{\partial}{\partial x} \left( 0.55 \eta \frac{1}{T} \frac{\partial T}{\partial x} \mu_r \right) + \Omega_r \quad (21)$$

The only difference is that the size dependent diffusion coefficient that causes the broken moment  $\mu_{r-2/3}$  (see ref. [12] for details) has been replaced by the mean diffusion coefficient  $D_{p, v_{i,max}}$  within each section. In equations (20) and (21) the density  $\rho$ , the viscosity  $\eta$ , the temperature  $T$ , the time  $t$ , the spatial coordinate  $x$  and the source terms for the moments  $\Omega_r$  or sections  $\Omega_i$  are used.

$$\Omega_i = \Omega_{i,ni} + \Omega_{i,oxid} + \Omega_{i,coag} + \Omega_{i,sg} + \Omega_{i,ox} \quad (22)$$

For the calculations shown in the next chapter we used 50 sections which give a very good accuracy. Comparisons of results obtained with 20 and 100 sections do not show significant differences in the calculated PSDF [24].

#### 4. RESULTS AND DISCUSSION

The collision regime of particles in flames discussed in this paper [4,5] is limited to the free molecular regime. Further, the particles are found to be spherical, and agglomeration effects do not need to be discussed. The physics of the PSDF in the coagulation regime is therefore well known. Independent on the collision kernel the size distribution function is known to develop a self preserving size distribution function in the coagulation regime. Surface growth processes are expected to move this distribution to slightly larger particles.

In the nucleation regime the dependence of number density on size is logarithmic, which can be explained through the growth of the particles through surface growth and oxidation, and through the collision of the particles with particles in the coagulation regime. In [12, 25] an analysis of the growth of PAH was performed. PAH growth was calculated using a HACA mechanism, and condensation of PAH on soot particle surfaces have been considered. For this situation a logarithmic growth law could be analytically derived for the size  $i$  dependent concentrations  $[PAH_i]$ :

$$\begin{aligned} [PAH_i] &= \gamma^i [PAH_1]; \quad \gamma < 1 \\ \log[PAH_i] &= i \log(\gamma) + \log([PAH_1]) \end{aligned} \quad (23)$$

where the growth factor  $\gamma$  is dependent on the surface growth rate coefficients, and the collision frequencies. The concentration of the particle in the smallest size class ( $[PAH_1]$  in equation 23) is in addition dependent on the rate of nucleation. This logarithmic growth law is experimentally found for the particles in the nucleation regime [4]. The analysis from ref. [12, 25] could be repeated by replacing the PAH condensation on soot particles, by collisions of particles in the nucleation regime with particles in the coagulation regime. To really collect the data of particle inception and surface growth from the number density of the smallest particles, and from the gradient of the number density in particle size accurate measurements of the temperature, and the local PSDF in nucleation and coagulation mode are needed.

The discussion above shows that the development of the PSDF is physically well understood. There are only a limited number of unknown parameters in this system. Therefore the knowledge of the PSDF in the nucleation regime can help to refine the kinetic and physical models for particle inception and surface growth. In reference [5] the particle size distribution functions have been measured for different flame temperatures as given in Table 1. The form of the PSDF in the coagulation regime is just dependent on the coagulation kernel and thereby on the total soot volume, and on the time. Following this statement we argue, that we can correct the experimental data for

Table 1. Summary of flame studied ( $C_2H_4$ : 16.3%,  $O_2$ : 23.7%, Ar: 60%).

Flame No.	Cold gas velocity $v_0$ (cm/s) <sup>a</sup>	Maximum Flame Temperature $T_f$ (K)
C1	13	$1898 \pm 50$
C2	10	$1805 \pm 50$
C3	8	$1736 \pm 50$
C4	6,53	$1710 \pm 50$
C5	5,5	$1660 \pm 50$

a Standard Temperature and Pressure condition.

probe effects, by searching the height above burner that gives the same PSDF in the coagulation regime as the calculated PSDF, if the calculated number density and soot volume fraction agree well enough with the experimental data. This statement is controversial, but we did not find any parameter in the calculation of the coagulation kernel, that is sensitive enough to explain the difference between experiment and calculation.

In the following we discuss this approach for flame C1 from Reference 5. For all our calculations we did not solve the energy conservation equation, and applied experimental temperature data instead. In Figure 2 we show the comparison of experimental and calculated soot volume fraction. The height above burner on the coordinate is the one presented in Reference 5 after correction by the experimentalist. The correction applied by the experimentalist is almost a constant shift of 3 mm [5]. Two calculated profiles of the soot volume fraction are presented in the Figure 2: 1) the

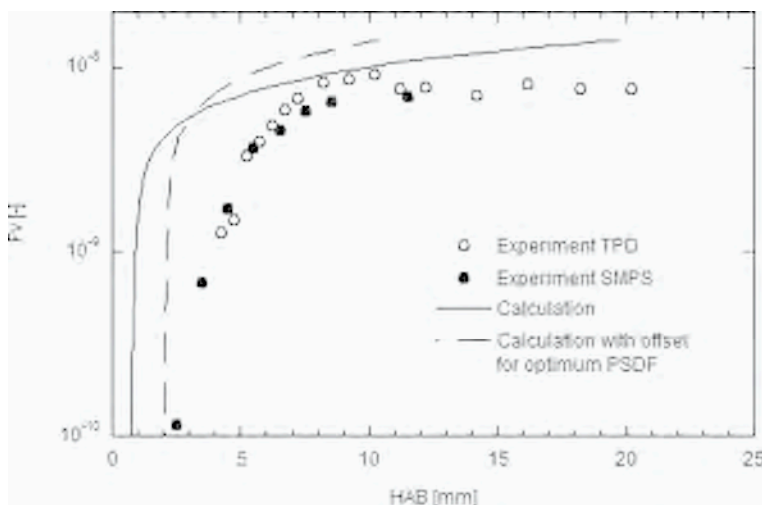


Figure 2. Experimental and calculated profiles of the soot volume fraction for flame C1.

profile with uncorrected height above burner, and 2) the profile corrected by optimizing the PSDF in the coagulation regime.

In Figure 3 we show the corresponding profiles for the soot particle number density. In general it is seen that the calculated number density is at its maximum one order of magnitude higher than the experimental data. The profile that resulted from an optimum shift (optimizing the PSDF as discussed above) is best explained, when comparing Figures 2-4. In Figure 4 it is seen that the optimum shift results in a perfect

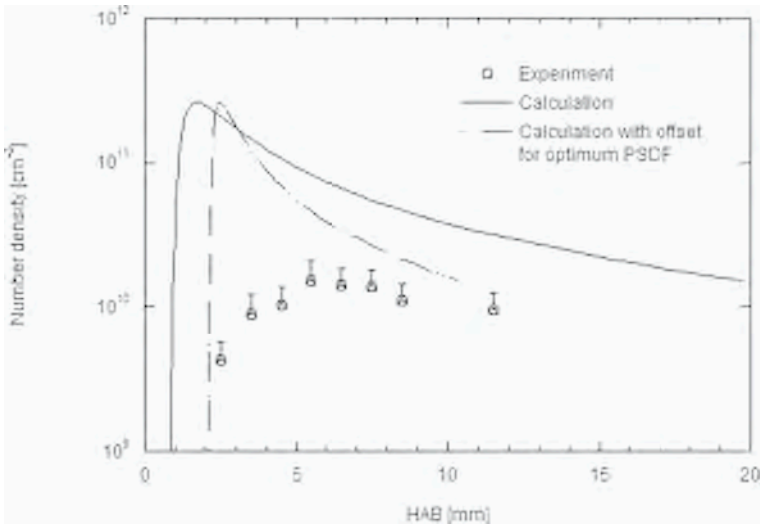


Figure 3. Experimental and calculated profiles of the soot number density for flame C1.

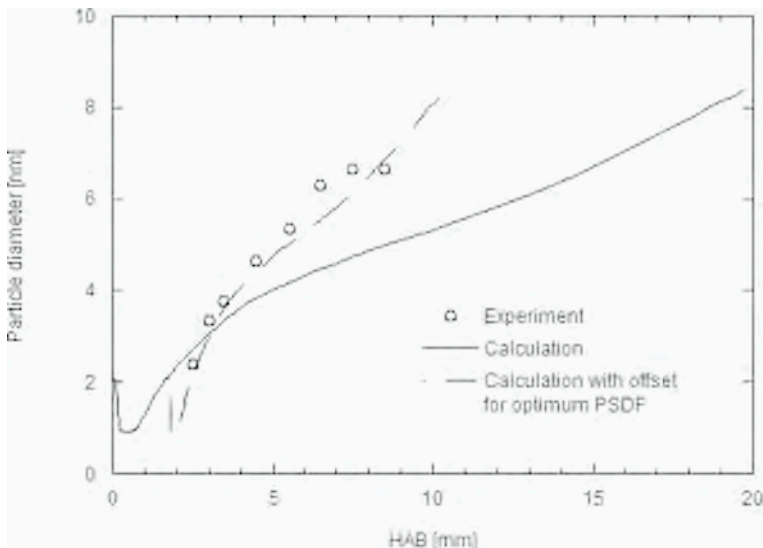


Figure 4. Experimental and calculated profiles of the soot diameter for flame C1.

agreement between the experimental and calculated mean particle diameter. This is a result from the correction in height above burner that optimizes the agreement between experimental and calculated PSDF. At all heights above burner both – number density and soot volume fraction – are calculated to be higher compared to the experimental data. This should result in a faster development of the PSDF, since the collision frequency will be increased. However, it is found that the calculated PSDF develops slower than the experimental PSDF.

In Figures 5a-5f we compare experimental and calculated PSDF at different height above burner. All PSDF are in very good agreement, and we may assume that the distribution function is very close to the self preserving size distribution function. The difference between experiment and calculation is the height above burner, at which the respective profile is collected. This is best seen from Figure 6, where the corrections in the experiment and calculation are shown.

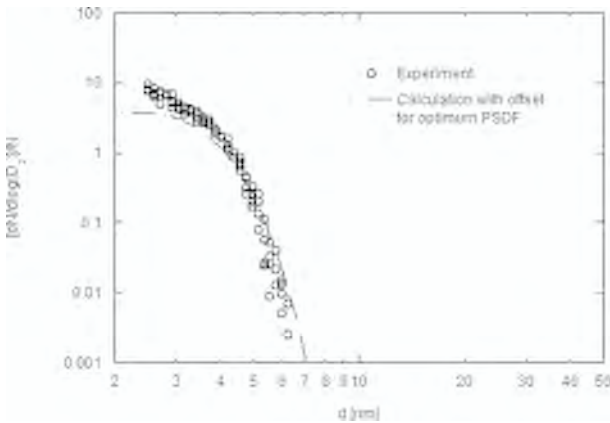


Figure 5a. Experimental and calculated PSDF at 2.5 mm height above burner for flame C1.

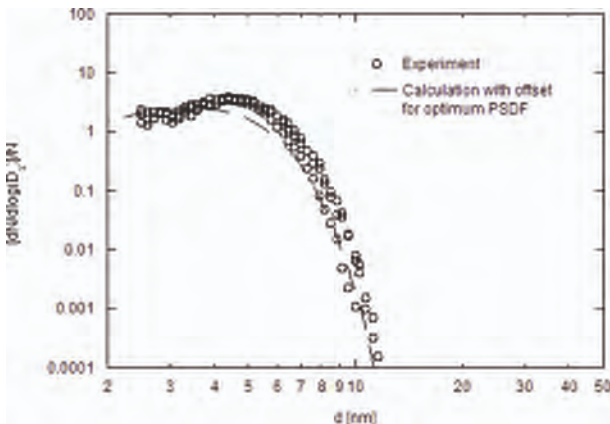


Figure 5b. Experimental and calculated PSDF at 3.5 mm height above burner for flame C1.

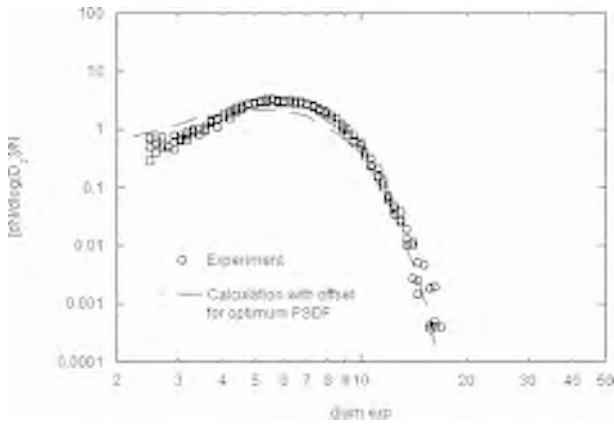


Figure 5c. Experimental and calculated PSDF at 4.5 mm height above burner for flame C1.

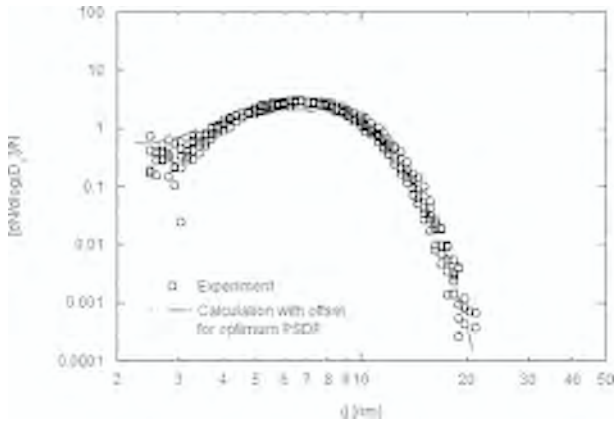


Figure 5d. Experimental and calculated PSDF at 5.5 mm height above burner for flame C1.

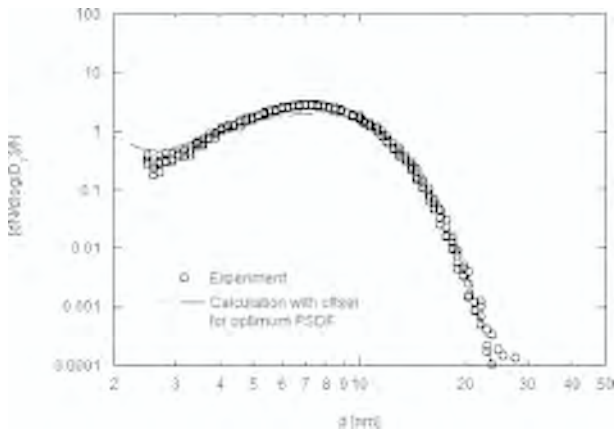


Figure 5e. Experimental and calculated PSDF at 6.5 mm height above burner for flame C1.

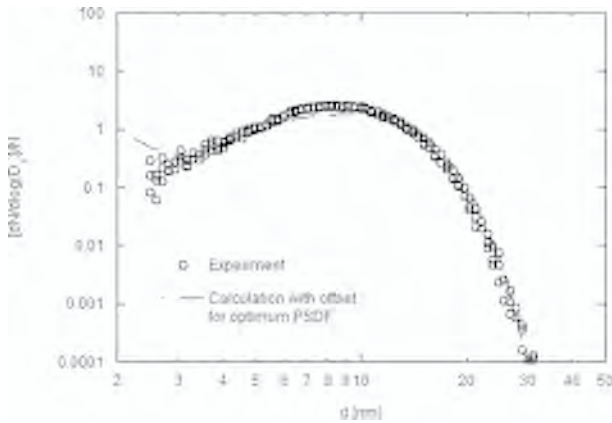


Figure 5f. Experimental and calculated PSDF at 8.5 mm height above burner for flame C1.

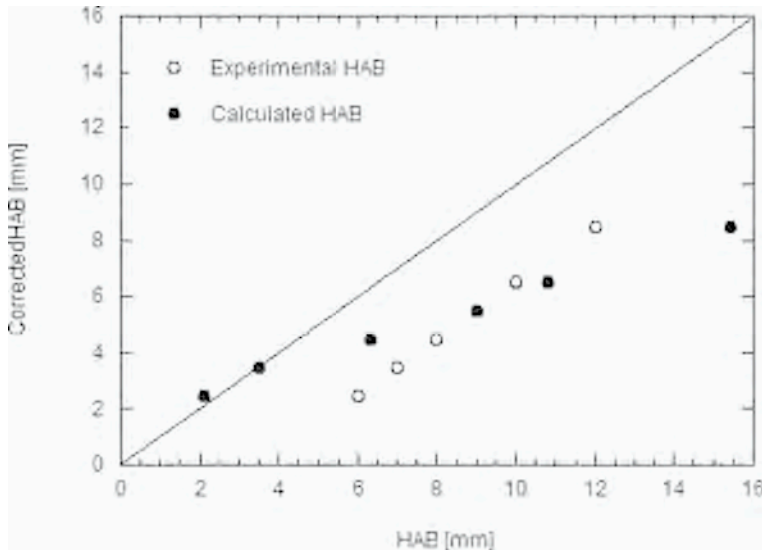


Figure 6. Corrected experimental and calculated height above burner.

At 2.5 mm and 3.5 mm the calculated data have been taken from almost the same height as suggested by the experimentalists after correction. At these heights the probe has a strong influence on the flame chemistry in the inner layer of the flame. At lower heights, the flame will most probably extinguish in front of the probe. At 4.5 mm the calculated profile was taken from 6.3 mm in the original calculation, at 5.5 mm from 9 mm (this is the experimental height before correction), at 6.5 mm from 10.8 mm, and at 8.5 mm from 15.4 mm. This suggests that the experimental data should be corrected downstream at heights greater than 5.5 mm. We find that the PSDF develops slower in the calculation than in the experiment.

The calculated number densities and soot volume fractions are higher than the experimental data. This should result in a faster development of the PSDF and can not explain the difference in the development of the PSDF. The only explanation we have for this phenomenon is a stagnation point in front of the probe, which gives the PSDF more time to develop.

To support our argument we investigate the parameter needed to calculate the collision frequency in Equation (2). Since particle sizes are small, and pressure is low all particles are found in the free molecular regime. The temperature profile needed for the calculation of  $\beta_{fm}$  is taken from the experiment, and the reported error of 50 K cannot explain the difference between experiment and calculation. Also the density of soot ( $1700 \text{ kg/m}^3$ ) is accurate for particles with mean sizes greater than 5 nm. Even the size dependent collision enhancement factor cannot explain the difference in the development in the PSDF. To support this statement we compared calculations with constant and variable collision enhancement factor (see Figure 1). This is shown in Figure 7 for the particle distribution at 6.5 mm height above burner. The size dependent collision factor has an influence on the gradient in the nucleation mode and on the concentration of the smallest particle. Please note that particle inception occurs in the calculation at 1 nm particle size. We notice that the gradient is decreased, as the enhancement factor for collisions of small and large particles is significantly smaller than the overall constant enhancement factor of 2.2. We further find from the comparison in Figure 7, that particle inception and collisions of small and large particles have a minor effect on the self preserving size distribution in the coagulation mode. We conclude, that the discussion of the enhancement factors is important to deduce rate kinetic data from particle size distribution functions. However it does not influence the dynamics of the PSDF for larger particle sizes. Future work will need to include a discussion on the influence of particle ionization of the PSDF in the nucleation mode. Particle ionization will increase the enhancement factor of small and large particles [36].

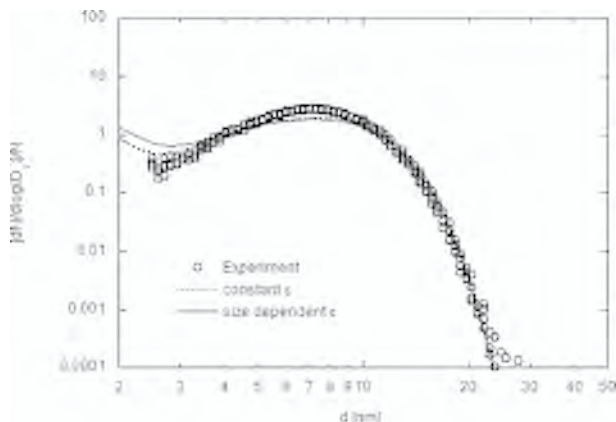


Figure 7. Experimental and calculated PSDF at 6.5 mm height above burner for flame C1. Comparison of calculations with size dependent and constant collision factor.

## 5. CONCLUSION

In this paper we calculated particle size distribution functions in laminar premixed flames, and compared them with experimental data. For this we developed a sectional method that uses first order polynomials within each section of the discretized PSDF. The formulation allows deriving transport equations for the soot volume fraction within each section of the PSDF. This allows using the method for calculating PSDFs in laminar and turbulent flames, as was demonstrated in Reference [23].

When comparing experimental and calculated PSDFs we find that both develop self preserving size distribution functions. However, the development of the function appears apparently faster in the experiment. The accuracy of the parameters needed to calculate the PSDF can not explain the difference between experiment and calculation. We conclude, that a stagnation point in front of the probe increases the residence time of the particles significantly, which would explain the difference between experiment and calculation.

We demonstrated in this paper that the data in the nucleation mode of the PSDF can be used to calculate particle inception rates from the number density of the smallest particles, and surface growth rates from the gradient of the number densities in particle size. However accurate temperature data, and measured PSDF are needed to deduce these kinetic data. Since the probe effects on the flame are very strong, we conclude that a better understanding of the probe effects is needed before these data are collected.

## REFERENCES

1. A. D'Alessio, A. Di Lorenzo, A.F. Sarofim, F. Beretta, S. Masi, C. Venitozzi, *Proc. Combust. Inst.* 15 (1974) 1427-1438.
2. M. Bönig, Chr. Feldermann, H. Jander, B. Lüers, G. Rudolph, H.Gg. Wagner, *Proc. Combust. Inst.* 23 (1990) 1581-1587.
3. R.A. Dobbins, H. Subramaniasivam, *Soot Formation in Combustion, Mechanisms and Models*, Chemical Physics 59, H. Bockhorn (Ed.) Springer Verlag, Heidelberg, 1994, p. 290-301.
4. B. Zhao, Z. Yang, J. Wang, M.V. Johnston, H. Wang, *Aerosol. Sci. Technol.* 37 (2003) 611-620.
5. A.D. Abid, N. Heinz, E.D. Tolmachoff, D.J. Phares, C.S. Campbell, H. Wang, *Combust. Flame* 154 (2008) 775-788.
6. P.A. Tesner, T.D. Snegiriova, V.G. Knorre, *Combust. Flame* 17 (1971) 253-271.
7. K.M. Leung, R.P. Lindstedt, W.P. Jones, *Combust. Flame* 87 (1991) 289.
8. M. Frenklach, *Chem. Eng. Sci.* 40(10) (1985) 1843-1849.
9. M. Frenklach, S.J. Harris, *J. Colloid Interface Sci.* 118(1) (1987) 252-261.
10. M. Frenklach, *Chem. Eng. Sci.* 57 (2002) 2229-2239.
11. F. Mauss, T. Schäfer, H. Bockhorn, *Combust. Flame* 99 (1994) 697-705.
12. F. Mauss, B. Trilken, H. Breitbach, N. Peters, *Soot Formation in Combustion, Mechanisms and Models*, Chemical Physics 59, H. Bockhorn (Ed.) Springer Verlag, Heidelberg, 1994, p. 325-349.
13. P. Markatou, H. Wang, M. Frenklach, *Combust. Flame* 93 (1993) 467-482.
14. N. Peters, *Turbulent Combustion*, Cambridge University Press, Cambridge, UK, 2000.

15. H. Pitsch, M. Chen, N. Peters, *Proc. Combust. Inst.* 27 (1998) 1057-1064.
16. H. Barths, N. Peters, N. Brehm, A. Mack, M. Pfitzner, V. Smiljanowski, *Proc. Combust. Inst.* (1998) 1841-1847.
17. H. Pitsch, E. Riesmeier, N. Peters, *Combust. Sci. Technol.* 158 (2000) 389-406.
18. F. Mauss, K. Netzell, H. Lehtiniemi, *Combust. Sci. Technol.* 178 (2006) 667-674.
19. X.S. Bai, L. Fuchs, M. Balthasar, F. Mauss, *Proc. Combust. Inst.* 27 (1998) 1623-1630.
20. M. Balthasar, F. Mauss, M. Pfitzner, A. Mack, *J. Eng. Gas Turbine Power* 124 (2002) 66-74.
21. P. Wenzel, A. Gezgin, R. Steiner, C. Krueger, K. Netzell, H. Lehtiniemi, F. Mauss, *Modelling Soot Size Distribution in Diesel Engines*, THIESEL 2006 Conference on Thermo- and Fluid Dynamic Processes in Diesel Engines, Valencia Spain, September 13-15 2006.
22. F. Gelbard, Y. Tambour, J.H. Seinfeld, *J. Coll. Interface. Sci.* 76(2) (1980) 541-556.
23. K. Netzell, H. Lehtiniemi, F. Mauss, *Proc. Combust. Inst.* 31 (2006) 667-674.
24. K. Netzell, *Development and Application of Detailed Kinetic Models for the Soot Particle Size Distribution Function*, PhD Thesis, Lund Institute of Technology, 2006.
25. F. Mauss, *Entwicklung eines kinetischen Modells der Russbildung mit schneller Polymerisation*, PhD Thesis, RWTH Aachen, 1997.
26. R. Brown, *Phil. Mag.* 4 (1828) 161-173.
27. P. Langevin, *C. R. Acad. Sci. (Paris)* 146 (1908) 530-533.
28. M.V. Smoluchowski, *Z. Phys. Chem.* 92 (1917) 129-168.
29. S.K. Friedlander, *Smoke, Dust and Haze*, Wiley, New-York, 1982.
30. A. Kazakov, M. Frenklach, *Combust. Flame* 114 (1998) 484-501.
31. W. Hinds, *Aerosol Technology*, Wiley, New-York, 1982.
32. J.H. Seinfeld, S.N. Pandis, *Atmospheric chemistry and physics: from air pollution to climate change*, Wiley-Interscience, 1998.
33. S.E. Pratsinis, *J. Colloid Interface Sci.* 124 (1988) 416-428.
34. N.A. Fuchs., *Mechanics of Aerosols*, Pergamon, New York, 1964.
35. M. Balthasar, *Detailed Soot Modelling in Laminar and Turbulent Reacting Flows*, PhD Thesis, Lund University, 2000.
36. M. Balthasar, F. Mauss, H. Wang, *Combust. Flame* 129 (2002) 204-216.
37. B. A. Pailthorpe, W. B. Russel, *J. Colloid Interface Sci.* 89 (1982) 563-566.
38. S.J. Harris, I.M. Kennedy, *Combust. Sci. Technol.* 59 (1988) 443-454.
39. I.M. Kennedy, *Combust. Flame* 68 (1987) 1-16.
40. H.C Hamaker, *Physica* 4 (1937) 1058-1072.
41. E.M. Lifshitz, *J. Exper. Theoret. Phys. USSR* 29 (1955) 94-110.
42. B.B. Mandelbrot, *The Fractal Geometry of Nature*, W.H. Freeman and Company, New York, 1983.
43. R. Schlögl, in F. Schüth, K. Sing, J. Weitkamp (Eds.) *Handbook of Porous Solids*, Wiley-VCH, Weinheim, 2002, p. 1863-1900.
44. H. Bockhorn, F. Fetting, H.W. Wenz, *Ber. Bunsenges. Phys. Chem.* 87 (1981) 1067-1073.
45. F. Mauss, N. Peters, H. Bockhorn, *A Detailed Chemical Model for Soot Formation in Premixed Acetylene- and Propane-Oxygen Flames*, Joint Meeting of the British and German Section, Cambridge, 1993.

# Modeling particle formation and growth in a stirred reactor and its exhaust

M.B. Colket

United Technologies Research Center  
East Hartford, CT 06108  
colketmb@utrc.utc.com

*Abstract: The formation of carbonaceous particulate matter has recently been studied in a toroidal well-stirred reactor using ethylene as the fuel. In the present study, a modified version of the CHEMKIN-based code for 'perfectly stirred reactors' has been used to model soot particle formation, including computations of particle size distribution. Experimental trends are modeled by the code. The model indicates that a portion of the soot mass is formed in the exhaust stream following the reactor, where gas temperatures are increasing and  $O_2$  and OH levels rapidly decay. Furthermore, the particle size distribution continues to evolve from the exit of the stirred reactor. The importance of accurate knowledge and control of reactor temperature is discussed.*

## 1. INTRODUCTION

Combustion-generated soot particles from both land-based and airborne sources pose a significant health risk and are the subject of stringent new EPA regulations (PM<sub>2.5</sub>) in the United States. These particles may also play a role in the radiation budget that impacts global warming. In addition, soot contributes to thermal radiation loads on combustor hardware. A quantitative understanding of soot growth and oxidation mechanisms and the ability to model these processes during system design are critical to the development of strategies to control emissions.

Stirred reactors provide a useful representation of processes occurring in a well-mixed, highly turbulent, fuel-rich front end of an advanced Rich-Quench-Lean (RQL) combustor. In recent studies, Stouffer et al. [1] and Reich et al. [2] studied soot formation in a well-stirred reactor. Key results from those works, relative to the total mass production of soot particulates and the importance of temperature effects, have been modeled and analyzed by Colket et al. [3]. Manzello, et al. [4] recently extended the experimental studies to include use of a high dilution probe [5] to freeze particle size distributions, which have resulted in peak particle sizes much lower than those reported in the earlier work, despite dilution ratios on the order of ten in the early studies.

It is the objective of this study to perform some modeling of soot formation in a stirred reactor to determine whether models quantitatively accurate and to help guide ongoing studies on soot growth in the downstream plug flow reactor regime.

## 2. MODEL

A toroidal-shaped, well-stirred reactor (WSR) research combustor with a volume of 250 mL was modeled in this study, including treatment of the downstream exhaust flow. Experimental results analyzed in this study have previously been presented in detail by Manzello et al. [4]. Airflow rates were 175 slpm and ethylene was added to provide reactor equivalence ratios of 1.8 to 2.1. Resulting WSR residence times are on the order of 10-12 milliseconds, at atmospheric pressure.

A high dilution sampling probe penetrated the exhaust stack, entering the plug flow region above the reactor. Particulates (size distribution and number densities) were measured using a nano-DMA (differential mobility analyzer), the results of which are considered in this work.

A series of perfectly stirred reactors (PSR) was assumed to simulate the behavior of this system, where the first reactor simulated the well-stirred reactor and series of many small (short residence times) reactors was used to simulate the (plug flow) exhaust stream. The modeling was performed utilizing a modified version of the CHEMKIN II-based code for stirred reactors into which soot aerosol equations have been coupled [3]. For a perfectly stirred reactor (PSR), sufficiently intense mixing is assumed such the concentrations of all species and temperature are uniform throughout the reactor and that these values are identical to the exit conditions.

The growth of soot spheroids in the reactor is modeled as a classical aerosol dynamics problem, involving the division of the size range of interest into discrete intervals or size classes with a logarithmic transformation of the size range, and then deriving a source for the size class mass densities with terms representing inception, surface growth (or oxidation) and coalescence. The sectional analysis utilized selected algorithms of the well-known MAEROS program [6]. The method is described in detail by Hall et al. [7]. The extension to stirred reactors is made through the use of the modified governing equations:

$$\dot{m}(Y_k - Y_k^*) - (\dot{\omega}_k^g + \dot{\omega}_k^t) W_k V = 0, \quad k = 1, 2, \dots, K$$

$$\dot{m}(Y_k - Y_k^*) - \dot{Q}_k V = 0, \quad k = K + 1, K + 2, \dots, K + M$$

$$\dot{m} \sum_{k=1}^K (Y_k h_k - Y_k^* h_k^*) + Q = 0$$

where  $Y_k$  is the mass fraction of the  $k$ th species (a total of  $K$  species);  $\dot{m}$  is the mass flow rate through the reactor volume,  $V$ ;  $W_k$ , the molecular weight of the  $k$ th species;  $\dot{\omega}_k^g$ , the molar rate of production by chemical reaction of the  $k$ th (gaseous) species per unit volume;  $h_k$ , the specific enthalpy per unit mass of the  $k$ th species; and  $Q$ , the reactor loss. The superscript (\*) indicates the inlet conditions. The 2nd equation represents the conservation equations for the sectional (particulate) species.  $Y_k$  ( $k = K+1$  to  $M$ ) represent the mass fractions of the  $M$  sectional 'species' or particulates;  $\dot{\omega}_k^g$  is the molar rate of production of the  $k$ th gaseous species per unit volume due to reactions involving soot particulates (i.e., scrubbing/replenishment of gaseous species from surface reactions during soot growth/oxidation processes); and  $\dot{Q}_k$  is the net mass rate of

change of particulates in section  $k$  per unit volume due to aerosol processes (including soot inception, surface growth and oxidation, as well as collisional dynamics). The enthalpy of all the sectional species were assumed equivalent to a large polycyclic aromatic hydrocarbon (PAH), that is, slightly larger, but nearly identical to that for condensed carbon (0.0 kcal/gm). A total of 25 soot sections were assumed for this study, ranging from an equivalent midpoint particle diameter of about 1 nm to 267 nm (assuming a soot density of 1.8 gm/cc). This model does not account for potential particle density changes during the early phase of soot formation and growth (e.g., carbonization) such as observed by Dobbins et al. [8] and others.

The kinetics model used in this work is that by Babushok and Tsang [9], selected for its more complete compilation of reactions associated with the growth of polycyclic aromatic hydrocarbons. Reactions/species associated with aromatics above 202 amu were excluded. The soot dynamics model [7] treats coupled gas-phase kinetics, soot inception/nucleation, surface growth and oxidation. Implicitly, the model assumes collisional coalescence (to form spherical particles), while particulate ageing/carbonization and coagulation effects are not included. Nucleation is computed based on irreversible dimerization of pyrene and similarly sized molecules [10]. Surface growth is based upon the 'MODFW' model developed by Colket and Hall [11], which has been shown to compare well with data in premixed flames [12], although it is been multiplied by a factor of three here to provide better agreement with the experimental data. This MODFW model was derived from an earlier work by Frenklach and Wang [13]. In addition, PAH species larger than mass of 130 amu are allowed to condense onto the soot particle surface. Oxidation by OH and O<sub>2</sub> were also included [7]. Adiabatic conditions were assumed for the results presented here, although it is recognized the temperature changes (and related energy losses) will have a significant impact on these results.

### 3. RESULTS

Consistent with the character of a (short residence time) stirred reactor, its exhaust has incompletely consumed reactants. Temperature and concentrations of key species are plotted in Figure 1 as a function of initial time for the simulation of the  $\phi=2$  experiments. Following the initial 11 milliseconds in the stirred reactor, the exhaust flows into a plugged flow regime where reactants complete combustion, temperature rises and oxidizing species rapidly decay. Even H-atom concentrations decay from what are likely super-equilibrium conditions in the reactor. Because of the very high O<sub>2</sub> level in the exhaust, soot oxidation by O<sub>2</sub> dominates over oxidation by OH, although surface growth processes still dominate by more than an order of magnitude. Nevertheless, as O<sub>2</sub> rapidly decays over several orders of magnitude, OH becomes the dominant oxidizer within 5 milliseconds.

The evolution of particles also continues beyond the reactor exit. Computed particle size distributions for several elapsed times are shown in Figure 2. Clearly, the smallest particles exiting the reactor decay due to coalescence and growth within a few milliseconds, although some evidence for continued nucleation continues (according to this model). Hence average particle size increases slightly with time.

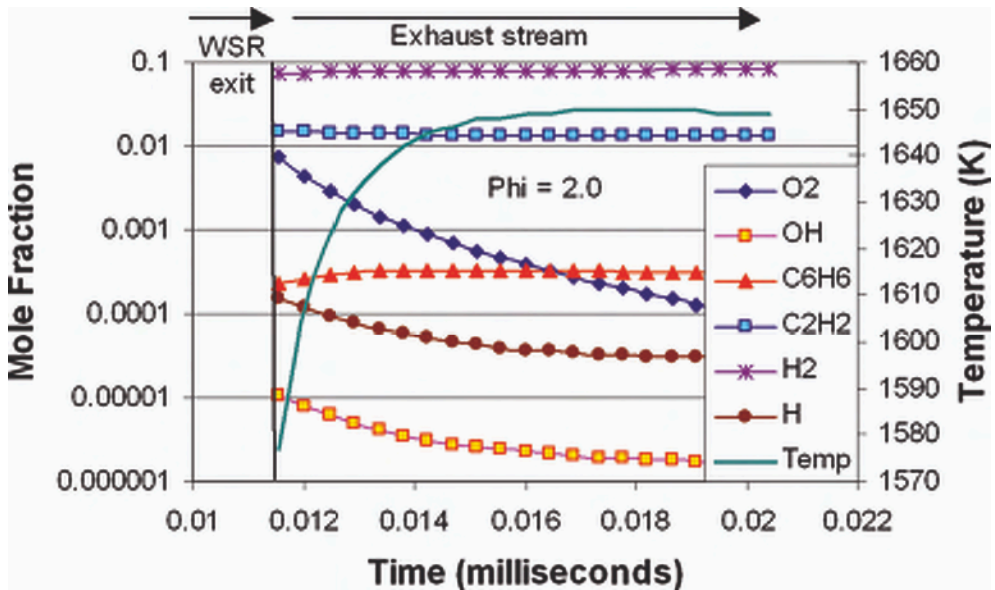


Figure 1. Temperature and concentration of key species in reactor exhaust for  $\phi=2$ .

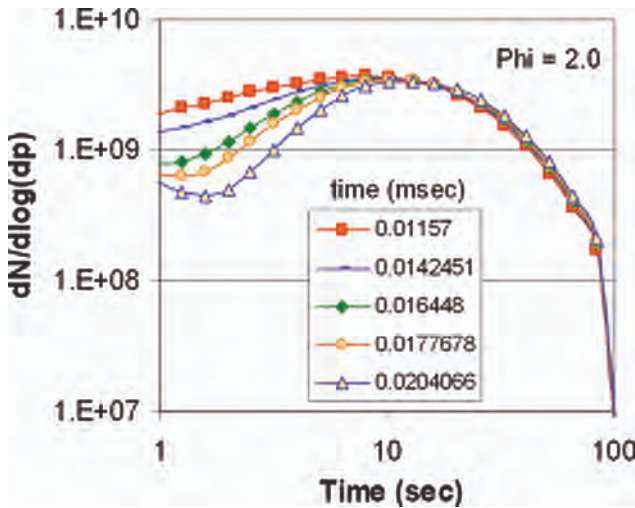


Figure 2. Evolving particle size distribution in reactor exhaust for  $\phi=2$ .

A comparison of size distributions for the different equivalence ratios at approximately 5 milliseconds in the exhaust is shown Figure 3. It is acknowledged that in comparison to the experimental data, these predictions do not exhibit as much difference in peak number density, nor do they predict the measured width of the distribu-

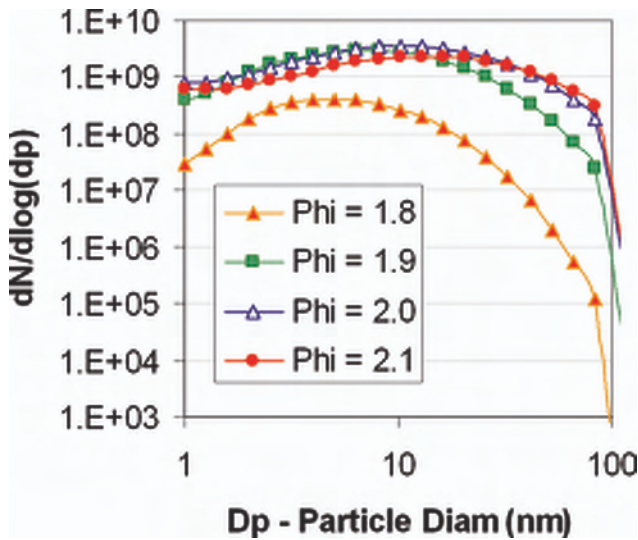


Figure 3. Particle size distribution in reactor exhaust for various equivalence ratio.

tion correctly, as the experiments indicate a much narrower distribution. The predictions do quantitatively predict the trend in increasing particle size as well as absolute peak number densities. Part of the differences may be due to the very significant impact of temperature as indicated by Manzello et al. [4] and by Colket et al. [3] and the use of an adiabatic assumption in this modeling work.

#### 4. CONCLUSIONS

The gas-phase kinetics, soot aerosol model as coupled into a stirred reactor model do a reasonable job of predicting qualitative trends in particle size number density, distributions, and average sizes. The simulations indicate that significant chemistry is occurring in the immediate exhaust of the reactor and that future studies need to consider such effects.

#### REFERENCES

1. S. D. Stouffer, R. C. Streibich, C. W. Frayne, J. Zelina, 38th Joint Propulsion Conference, AIAA 2002-3723, 2002.
2. R. F. Reich, S. D. Stouffer, V. R., Katta, H. T., Mayfield, C. W., Frayne, J. Zelina, 41st AIAA Aerospace Sciences Meeting, AIAA 2003-0664, Jan. 6-9, 2003.
3. M.B. Colket, R.J. Hall S.D. Stouffer, Proc. of ASME Turbo Expo 2004, GT2004-54001, Vienna, Austria, June 14-17, 2004.
4. S.L. Manzello, D.B. Lenhert, A. Yozgatligil, M.T. Donovan, G.W. Mulholland, M.Z. Zachariah, W. Tsang, Proc. Combust. Inst. 31, 675-683, 2007.

5. B. Zhao, Z. Yang, J. Wang, M.V. Johnston, H. Wang, *Aerosol. Sci. Technol.* 37 (2003) 611-620.
6. F. Gelbard, MAEROS User Manual, NUREG/CR-1391, SAND80-0822, 1982.
7. R. J. Hall, M. D. Smooke, M. B. Colket, in *Physical and Chemical Aspects of Combustion: A Tribute to Irvin Glassman*, R. F. Sawyer, F. L. Dryer (Eds.) Combustion Science and Technology Book Series, Gordon and Breach, PA, 1997, pp. 189-230.
8. R.A. Dobbins, G.J. Govaatzidakis, W. Lu, A.F. Schwartzman, R.A. Fletcher, *Combust. Sci. Technol.* 121 (1996) 103.
9. V.I. Babushok, W. Tsang, *J. Prop. Power* 20(3) (2004) 403-414.
10. J. Appel, H. Bockhorn, M. Frenklach, *Combust. Flame*, 121 (2000) 122.
11. M. B. Colket, R. J. Hall, in *Soot Formation in Combustion*, H. Bockhorn (Ed.) Springer Verlag, Berlin, 1994, pp. 417-470.
12. F. Xu, P.B. Sunderland, G.M. Faeth, *Combust. Flame* 108 (1997) 471-493.
13. M. Frenklach, H. Wang, *Proc. Combust. Inst.* 23 (1991) 1559-1566.

# Laminar smoke points of condensed fuels

P.B. Sunderland<sup>1</sup>, J.L. de Ris<sup>2</sup>

<sup>1</sup> Department of Fire Protection Engineering, Univ. of Maryland, College Park, MD 20742, USA

<sup>2</sup> FM Global Research, 1151 Boston-Providence Hwy., Norwood, MA 02062, USA

*Abstract: An investigation of laminar smoke points of condensed fuels is presented. Fuels considered emphasize waxes burning in candles, but also include selected liquid fuels and polymers. For the candles, adjustable wicks with diameters of 1.7-7.3 mm were used to measure smoke points of 14 different waxes. Candle smoke points increased with wick diameter and with heat loss to the liquid pool. When interpolated to a wick diameter of 4.5 mm, the candle smoke points were between 41-80 mm and increased from commercial waxes (candelilla, carnauba, beeswax, paraffin) to normal alkanes (hexatriacontane, octacosane, tetracosane) to primary alcohols (octadecanol, docosanol, hexadecanol) to carboxylic acids (stearic, palmitic, lauric, myristic). Smoke points of various fuel types were correlated with carbon number and generally decreased with increasing carbon number. Alkane and alcohol wax smoke points decreased with increasing fuel C/H ratio and were correlated with past measurements of liquid fuels and polymers.*

## 1. INTRODUCTION

Several flame tests are used to determine the relative sooting propensities of different fuels. In premixed flames a sooting limit is typically measured [1]. In diffusion flames the most commonly used test is the laminar smoke point test, although measurements of peak soot volume fraction are increasingly used [2]. Differences in the tests are significant enough that rankings of fuel sooting propensity can be test dependent [2-4].

A laminar smoke point is defined as the length of a diffusion flame at the point of incipient soot emission. Smoke points occur in buoyant flames because an increase in fuel supply rate increases soot formation time but has a smaller effect on soot oxidation time [4].

Laminar smoke point measurements have several important applications. They correlate with gas turbine soot emissions [5]. For this reason, the sale of most aviation jet fuel is required to have a laminar smoke point in a standard wick lamp of at least 25 mm [6,7]. It is important to match smoke points in the selection of surrogate fuels [8,9]. Laminar smoke points correlate with soot concentrations [10] and radiative emissions [11] of turbulent diffusion flames. They have been used in computational combustion simulations [12] because the most detailed models of soot kinetics and transport, e.g., [13,14], are still too computationally intensive for use in most turbulent flames.

The first published laminar smoke points used a wick lamp [15]. Several subsequent studies also used wick lamps [8,9,16-19]. Among these, Olson et al [18] considered 42 liquid fuels, the largest number of any study to date. Laminar smoke points for gaseous fuels have also been widely reported [4,20-24]. These measurements involve a round

fuel port. Laminar smoke points of gaseous fuels in normal gravity are generally independent of burner diameter.

Prior to recent work in this laboratory [25], laminar smoke points of fuels that are solid at standard temperature and pressure had been the subject of only two studies. Tewarson [26] reported smoke points of five polymers, which were vaporized and supplied to gas-jet flames via a burner tube with an inside diameter of 9 mm. de Ris and Cheng [27] measured smoke points of polymethylmethacrylate and particle board by heating 12.5 mm diameter samples with a CO<sub>2</sub> laser.

A promising alternative test of sooting tendency in diffusion flames was developed by McEnally and Pfefferle [2]. In their work, diluted methane laminar diffusion flames were doped with 400 ppm of a liquid test fuel, supplied by a syringe pump. Peak soot volume fraction was measured using laser-induced incandescence. Fuels with carbon numbers up to 30 have been tested. This method is especially attractive for highly sooting fuels and fuels with limited availability. However its highly diluted fuel concentrations may not accurately represent the burning of pure fuels such as candle wax or aviation fuel.

In the U.S., 70% of residences burn candles, accounting for \$2 billion in annual sales [28]. Soot emissions from candles can present health and property hazards [29-31].

Despite their interest to the public, wax candles have rarely appeared in combustion research. Candles were among the first flame experiments observed in earth orbit [32]. This work motivated a detailed computational model of candle flames [33]. Candle fire hazards were considered by Hamins et al. [34]. Takahashi [35] considered similarities between candle flames and gas fuel flames. Candle soot nanoparticles were characterized by Lui et al. [36]. Finally, candle smoke points were reported by [25], and are revisited here.

The objectives of this study are to:

- 1) summarize past measurements of smoke points of condensed fuels, including candles [25], liquid fuels [18] and polymers [26];
- 2) correlate the measurements, considering the effects of wick diameter, wick length, and heat loss to the liquid pool; and
- 3) rank the fuels according to their sooting propensities.

## 2. EXPERIMENTAL

Laminar smoke points of 14 waxes were reported by Allan et al. [25]. The testing methods are summarized here, but additional details are available in [25]. The waxes considered are summarized in Table 1. The monomer waxes had purities of 98% or higher. Where available, Table 1 includes chemical formula, molecular weight (MW), melting point (MP), and boiling point (BP).

Wax granules were melted in 50 mL glass beakers. The samples were then cooled, removed, and drilled on axis. Wicks were braided round cotton (Atkins and Pearce) and had diameters of 1-7.3 mm. The wicks were stiffened using melted wax and inserted in the candles.

The candles were mounted in a testing table. A 300 mm clear acrylic cube with one open face was installed over the flames to eliminate drafts. Air vitiation was avoided by using test times of 30 s or less. Wicks protruded from beneath the candles, allowing

Table 1. Summary of waxes tested by Allan et al. [25]. Reproduced from [25].

Family	Wax <sup>a</sup>	Formula	MW, g/mol	MP <sup>b</sup> , °C	BP <sup>c</sup> , °C
commercial	beeswax			63	
	candelilla			72	
	carnauba			83	
	paraffin			66	350-430
normal alkane	<i>n</i> -tetracosane	C <sub>24</sub> H <sub>50</sub>	339	50.4	391.3
	<i>n</i> -octacosane	C <sub>28</sub> H <sub>58</sub>	395	61.1	431.6
	<i>n</i> -hexatriacontane	C <sub>36</sub> H <sub>74</sub>	507	75.8	298.4 <sup>3</sup>
primary alcohol	1-hexadecanol	C <sub>16</sub> H <sub>34</sub> O	242	49.2	312
	1-octadecanol	C <sub>18</sub> H <sub>38</sub> O	270	57.9	335
	1-docosanol	C <sub>22</sub> H <sub>46</sub> O	327	72.5	180 <sup>0.22</sup>
carboxylic acid	lauric acid	C <sub>12</sub> H <sub>24</sub> O <sub>2</sub>	200	43.8	299.2
	myristic acid	C <sub>14</sub> H <sub>28</sub> O <sub>2</sub>	228	54.2	318
	palmitic acid	C <sub>16</sub> H <sub>32</sub> O <sub>2</sub>	256	62.5	353.8
	stearic acid	C <sub>18</sub> H <sub>36</sub> O <sub>2</sub>	284	69.3	370

<sup>a</sup> Additional details are: beeswax, refined, yellow; candelilla, natural; carnauba number 1, yellow, refined.

<sup>b</sup> Melting points sources are: commercial waxes [37], all others [38].

<sup>c</sup> Boiling points are at 760 mm Hg except where a different pressure is shown in superscript. Sources are: paraffin [39], alkanes and aliphatic alcohols [38], carboxylic acids [40].

adjustment by hand. A quasi-steady smoke point was visually identified, at which time the flame was photographed.

The observer viewed the flames in front of a white background to facilitate the visual detection of emitted soot. Dark-field photography was used for image clarity. A color digital single-lens reflex camera was used, providing spatial resolution of 0.04 mm.

Measurements were obtained from the digital images. These included laminar smoke point flame height ( $L_v$ ), wick height ( $L_w$ ), wick diameter ( $d_w$ ), maximum flame width ( $w$ ), and flame attachment height above the liquid pool ( $H$ ). All heights ( $L_v$ ,  $L_w$ , and  $H$ ) were measured relative to the liquid wax pool.

There were two main sources of uncertainty in the wax measurements. First, it was difficult to see the small quantities of soot coming from flames slightly above their smoke points. Second, there was a delayed response of flame length to changes in wick length. The reported measurements were repeatable within  $\pm 5\%$ , and had an estimated uncertainty of  $\pm 10\%$ .

### 3. RESULTS AND DISCUSSION

A representative color image of a candle flame at its smoke point is shown in Figure 1. This is for candelilla wax with a wick diameter of 1.7 mm. Visible in the image is the liquid wax melt pool and its meniscus at the wick base. Flame luminosity does not



Figure 1. Color image of a candelilla candle flame at its smoke point. This smoke point is 37.0 mm, the wick diameter is 1.7 mm, and the wick length is 9.3 mm. These dimensions are slightly different from the mean values reported elsewhere in this manuscript.

obscure the wick. The lowest regions of the flame are blue, and the widest part of the flame is coincident with the wick tip. Soot first appears on the fuel side of the blue flame sheet. Studies of laminar gas jet diffusion flames have found that at the smoke point the stoichiometric (blue) flame is about 50% as long as the luminous (yellow) height [41]. The yellow luminous regions of the present flames generally taper inward with increased height. The above descriptions of flame appearance are pertinent to all the candle flames of [25] at their smoke points.

Schug et al. [20] defined the smoke points of laminar gas-jet flames as the flame height when soot wings are equally high as the flame centerline. In contrast, Markstein [21] defined the smoke point at incipiently sooting conditions. For many flames the equal wings condition occurs when flames are slightly shorter than incipiently sooting conditions, see de Ris and Cheng [27] for details. For other flames, such as those in vitiated atmospheres, less soot is formed, particularly in the wings, and soot is released before the occurrence of equal wings. Flames with equal-wings smoke points first emit soot from an annulus, while other flames first emit soot from the centerline [21]. Two types of smoke point behavior have also been observed in microgravity flames [23]: closed tip and open tip, where open-tipped flames were partially extinguished. The hypothesis that normal-gravity smoke points also can be associated with local flame extinction is worthy of additional study.

In Allan et al. [25], candle smoke points were defined as conditions associated with incipient soot emission. Soot wings were visible in most of the candle smoke-point

flames of [25]. Soot wings diminished or disappeared altogether with increasing smoke-point length. In general, smoke-point flames shorter than 50 mm were at equal-wing conditions, while those longer than 65 mm did not have soot wings. Soot wings are clearly visible in the candle smoke-point flame Figure 1, where they are equally long as the flame centerline.

Figure 2a shows the laminar smoke points of waxes [25], plotted versus wick diameter. Each symbol represents a mean of 4-7 tests. The dominant trend here is that smoke points increase with wick diameter. Smoke point variation with wick diameter had been reported once before, by Rakowsky and Hunt [17] for liquids, but only a small number of measurements were presented.

Allan et al. [25] found candle smoke points to generally increase from commercial waxes to alkanes to alcohols to acids, see Figure 2a. Within measurement uncertainties, the ranking of wax smoke points is independent of wick diameter. Wicks smaller than 1.7 mm could not support steady soot emission for any wick length for any wax. For carboxylic acids this limit was 2.9 mm.

Figure 2b is a plot of wick length versus wick diameter for the measurements of Figure 2a. For smoke point flames, a decreased wick diameter requires a longer wick for sufficient fuel vaporization. Sooting conditions could not be obtained when wicks were shorter than 5.9 mm for any wax. For carboxylic acids this limit was 7.7 mm.

The increase in smoke point with increasing wick diameter (Figure 2a) is attributed to increased heat losses from the flame base to wax pool, both directly and via the wick. Such heat losses decrease temperatures and soot formation rates in the soot

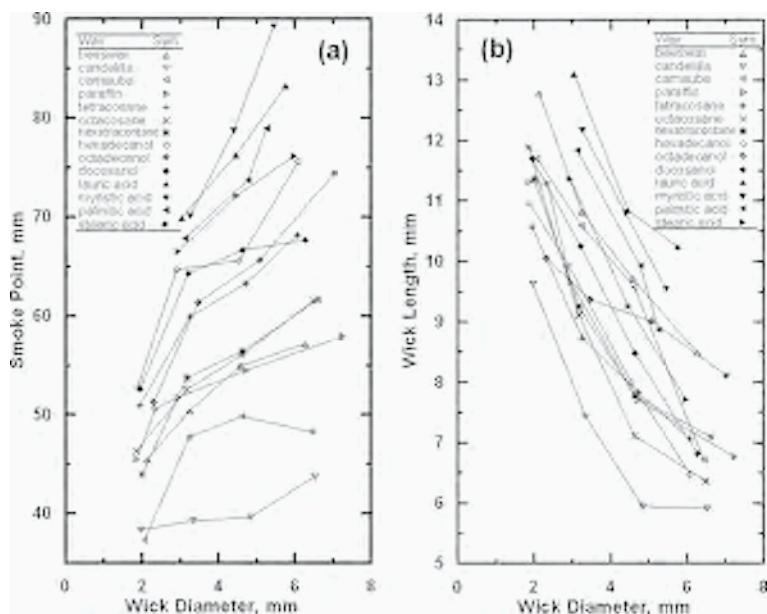


Figure 2. (a) Measured laminar smoke points versus wick diameter. (b) Measured wick lengths at the laminar smoke points versus wick diameter. Reproduced from [25].

forming regions. In gas-jet flames Markstein [21] also found smoke points to increase with increased flame base heat loss. An increase in wick length can also reduce temperatures in the soot formation region; when wick length exceeds 50% of the luminous flame length this results in local flame quenching on the centerline. It is important to report and consider wick diameter and wick length in studies of wick-fed flames.

Further insight into heat loss effects can be gained from simple scaling analyses of heat loss rate from the flame base. Assuming constant flame thickness and constant standoff distance at the attachment point, the rate of heat lost to the pool via the wick scales with wick diameter. Extrapolating to a wick diameter of zero in Figure 2 should yield smoke points that are free of heat loss effects, i.e., smoke points that are intrinsic fuel properties. Unfortunately, measurement uncertainties complicate the extrapolation here.

The heat loss rate directly to the wax pool,  $Q_p$ , can be approximated as:

$$Q_p \sim A_p \approx 0.25 \pi (w^2 - d_w^2), \tag{1}$$

where  $A_p$  is the area of the annulus on the pool surface bounded by the flame base and the wick,  $w$  is the width of the flame annulus at its widest point,  $d_w$  is wick diameter, and  $\sim$  denotes proportionality. In agreement with observations, it is assumed that the flames have similar attachment heights and have annulus diameters near the pool surface that are similar to  $w$ . The laminar smoke points of Figure 2 are plotted in Figure 3 as functions of  $A_p$ . For each wax, Figure 3 reveals that laminar smoke points increase with increased heat loss rate to the pool. This is expected because an increase

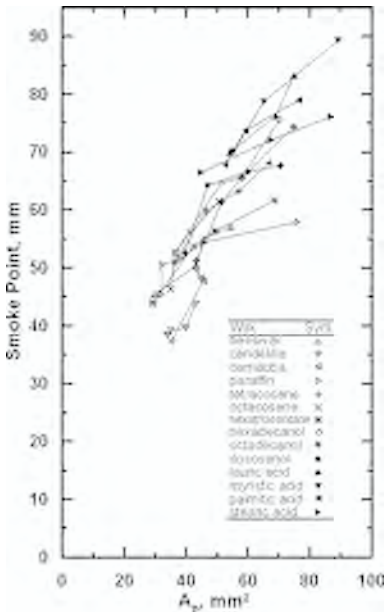


Figure 3. Measured laminar smoke points versus area of the flame annulus in contact with the wax pool surface,  $A_p$ .

in  $Q_p$  decreases temperatures in the soot formation regions of these flames and thus retards soot formation. As above, extrapolation to zero heat loss is possible, but is not presented here owing to measurement uncertainties.

A quantitative ranking of sooting propensities of waxes is complicated by the variation of smoke point with wick diameter. Allan et al. [25] overcame this by interpolating the measurements to a fixed wick diameter of 4.5 mm using a least-squares linear fit for each wax. This diameter is close to the mean wick diameter in Figure 2 and is comparable to the  $5.0 \times 6.1$  mm rectangular wicks used in the ASTM [6] tests.

The interpolated smoke points are plotted in Figure 4. The waxes are ordered according to increasing interpolated smoke points. The smoke points of Figure 4 increase from commercial waxes to alkanes to alcohols to acids. Note that paraffin and beeswax, widely used in commercial candles [28], have very short smoke points. Stearic acid, which is also widely used in candles, has one of the lowest sooting propensities of the waxes tested.

Fuel properties are such that it would be impossible to match both wick diameter and wick length in smoke point tests of different fuels. As Figure 4 shows, wick diameters of 4.5 mm required interpolated wick lengths of 7.0–11.3 mm at smoke points. Owing to heat losses associated with long wicks, discussed above, some of the increase in smoke points from left to right in Figure 4 may result from longer wicks.

Several past studies have correlated sooting propensity with carbon number [2,3,16,18]. Such a correlation is shown in Figure 5 for wax smoke points. Commercial waxes cannot be included here because their representative carbon numbers are unknown. A reasonable correlation is obtained for waxes, with smoke points that generally decrease with increasing carbon number. The carboxylic acids are above the correlation owing to increased fuel oxygen content.

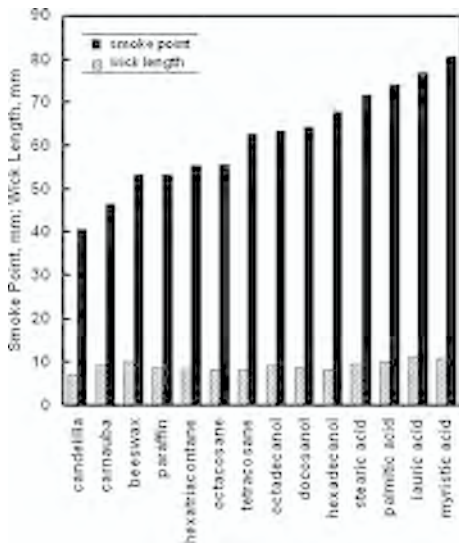


Figure 4. Measured laminar smoke points and wick lengths at smoke points, both interpolated to a 4.5 mm diameter wick. Reproduced from [25].

Also shown in Figure 5 are the smoke points of liquid alkanes and alkenes, measured in a wick lamp with a wick diameter of 5.5 mm and a forced co-flow [18]. These liquid alkane smoke points decrease more quickly with carbon number than the wax alkanes do. This is attributed to the approach to infinity of smoke points as carbon number approaches zero. Smoke points of the liquid alkenes increase with carbon number owing to the decreasing ratio of C=C double bonds to C-C single bonds.

Another fuel chemical property used in past correlations of sooting propensity is C/H ratio [3,20]. Figure 6 is a plot of smoke point versus C/H ratio for the waxes and liquids of Figure 5 and the two alkane polymers of Tewarson [26]. Sooting propensity generally increases with increasing C/H ratio, as expected. This plot collapses the alkanes, alkenes, alcohols, and polymers into a single correlation such as the power law shown. This power law correctly predicts infinite smoke points as carbon number approaches zero. The acids are not correlated by this fit because the presence of a C=O double bond increases C/H ratio and moves acids well to the right of the fit in Figure 6. The C/H ratios of the wax alkanes, liquid alkanes and alcohols are  $n / (2n + 2)$ , where  $n$  is carbon number. For a given carbon number, these fuels have identical C/H ratios and similar smoke points, and thus are correlated by the same fit.

Candle flames are probably the most widely used laminar diffusion flames where soot is a concern. Thus the availability of new measurements of laminar smoke points of candles should have an immediate application.

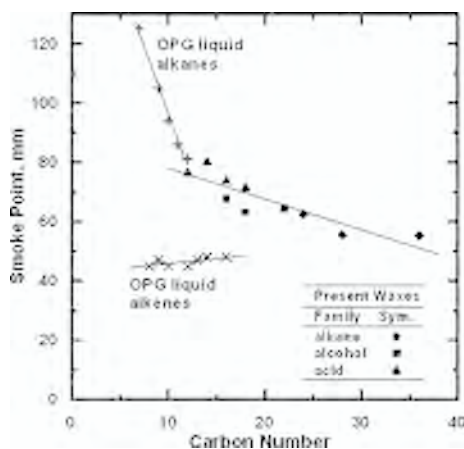


Figure 5. Measured laminar smoke points versus fuel carbon number. Values for waxes are interpolated to a wick diameter of 4.5 mm. Values for liquids come from OPG [18]. The least-squares linear fits have these equations:  $y = -1.03x + 88.3$  (present waxes);  $y = -9.04x + 187$  (OPG liquid alkanes);  $y = 0.341x + 42.4$  (OPG liquid alkenes). Reproduced from [25].

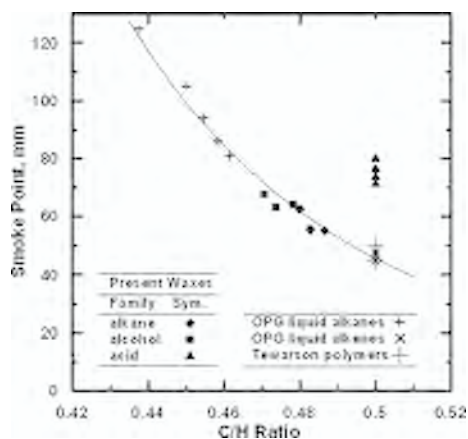


Figure 6. Measured laminar smoke points versus fuel C/H ratio. Values for waxes are interpolated to a wick diameter of 4.5 mm. Values for liquids come from OPG [18] and values for polymers are from [26]. The least-squares fit is for all measurements except the acids and has the equation  $y = 0.279x^{-7.36}$ . Reproduced from [25].

## 4. CONCLUSIONS

Laminar smoke points of condensed fuels were examined, emphasizing the tests of 14 waxes in candles [25]. This study has led to the following conclusions:

- 1) Candle smoke points increase with wick diameter owing to effects of heat loss at the flame base. Wick diameters and lengths should be considered in studies of smoke points of wick-fed flames.
- 2) Candle smoke points could not be obtained for any wax when wick diameter or length was below 1.7 mm or 5.9 mm, respectively.
- 3) When interpolated to 4.5 mm diameter wicks, wax smoke points increased from commercial waxes to alkanes to alcohols to acids and varied from 41-80 mm. It is significant to candle manufacture that paraffin and beeswax had high sooting propensities, while stearic acid had a low sooting propensity.
- 4) Smoke points of waxes, and liquids from the same chemical family, correlate with carbon number and generally decreased with increasing carbon number.
- 5) C/H ratio correlates the smoke points of liquid alkanes and alkenes, wax alkanes and alcohols, and alkane polymers. For these fuels smoke points decrease with increasing C/H ratio. Smoke points of carboxylic acids are not correlated by C/H ratio.

These findings could aid the manufacture of cleaner burning candles and they reveal the importance of considering wick effects in testing of smoke points of liquid fuels such as aviation fuel.

## ACKNOWLEDGMENTS

This research was supported by a Minta-Martin award and a General Research Board award from the University of Maryland. The candle measurements were performed by K.M. Allan and J.R. Kaminski. Helpful discussions with J.C. Bertrand and J. Head are acknowledged.

## REFERENCES

1. F. Takahashi, I. Glassman, *Combust. Sci. Technol.* 37 (1984) 1-19.
2. C.S. McEnally, L.D. Pfefferle, *Combust. Flame* 148 (2007) 210-222.
3. H.F. Calcote, D.M. Manos, *Combust. Flame* 49 (1983) 289-304.
4. I. Glassman, *Proc. Combust. Inst.* 22 (1988) 295-311.
5. Y. Yang, A.L. Boehman, R.J. Santoro, *Combust. Flame* 149 (2007) 191-205.
6. Standard Test Method for Smoke Point of Kerosine and Aviation Turbine Fuel, ASTM International, Standard D1322, West Conshohocken PA, 2002, pp. 527-533.
7. Standard Specification for Aviation Turbine Fuels, ASTM International, Standard D1655, West Conshohocken PA, 2003, pp. 614-619.
8. S. Yan, E.G. Eddings, A.B. Palotas, R.J. Pugmire, A.F. Sarofim, *Energy & Fuels* 19 (2005) 2408-2415.
9. I.M. Aksit, J.B. Moss, *Fuel* 84 (2005) 239-245.

10. J.H. Kent, *Combust. Flame* 67 (1987) 223-233.
11. G.H. Markstein, *Proc. Combust. Inst.* 20 (1984) 1055-1061.
12. C.W. Lautenberger, J.L. de Ris, N.A. Dembsey, J.R. Barnett, H.R. Baum, *Fire Safety J.* 40 (2005) 141-176.
13. M.D. Smooke, M.B. Long, B.C. Connelly, M.B. Colket, R.J. Hall, *Combust. Flame* 143 (2005) 613-628.
14. J. Singh, R.I.A. Patterson, M. Kraft, H. Wang, *Combust. Flame* 145 (2006) 117-127.
15. J. Kewley, J.S. Jackson, *J. Instit. Petrol. Technol.* 13 (1927) 364-397.
16. R.L. Schalla, G.E. McDonald, *Proc. Combust. Inst.* 5 (1955) 316-324.
17. F.W. Rakowsky, R.A. Hunt, Jr., *Anal. Chem.* 28 (1956) 1583-1586.
18. D.B. Olson, J.C. Pickens, R.J. Gill, *Combust. Flame* 62 (1985) 43-60.
19. Ö.L. Gülder, *Combust. Flame* 78 (1989) 179-194.
20. K.P. Schug, Y. Manheimer-Timat, P. Yaccarino, I. Glassman, *Combust. Sci. Technol.* 22 (1980) 235-250.
21. G.H. Markstein, *Proc. Combust. Inst.* 21 (1986) 1107-1114.
22. P.B. Sunderland, S. Mortazavi, G.M. Faeth, D.L. Urban, *Combust. Flame* 96 (1994) 97-103.
23. D.L. Urban, Z.-G. Yuan, P.B. Sunderland, K.-C. Lin, Z. Dai, G.M. Faeth, *Proc. Combust. Inst.* 28 (2000) 1965-1972.
24. T.L. Berry, W.L. Roberts, *Combust. Flame* 145 (2006) 571-578.
25. K.M. Allan, J.R. Kaminski, J.C. Bertrand, J. Head, P.B. Sunderland, *Laminar smoke points of wax candles*, *Combust. Sci. Technol.*, accepted.
26. A. Tewarson, *Prediction of Fire Properties of Materials. Part 1. Aliphatic and Aromatic Hydrocarbons and Related Polymers*, Report No. GCR-86-521, National Institute of Standards and Technology, 1986.
27. J. de Ris, X.-F. Cheng, *Fire Safety Science, Proc. of the Fourth International Symposium*, 1994, 301-312.
28. National Candle Association, [www.candles.org](http://www.candles.org), 2007.
29. C.K. Huynh, H. Savolainen, T. Vu-Duc, M. Guillemin, F. Iselin, *Sci. Tot. Environ.* 102 (1991) 241-251.
30. P.M. Fine, G.R. Cass, B.R.T. Simoneit, *Environ. Sci. Technol.* 33 (1999) 2352-2362.
31. C. Tejada, *Wall Street J.*, March 31, 1999, p. 1.
32. D.L. Dietrich, H.D. Ross, Y. Shu, P. Chang, J.S. T'ien, *Combust. Sci. Technol.* 156 (2000) 1-24.
33. A. Alsairafi, S.-T. Lee, J.S. T'ien, *Combust. Sci. Technol.* 176 (2004) 2165-2191.
34. A. Hamins, M. Bundy, S.E. Dillon, *J. Fire Prot. Eng.* 15 (2005) 265-285.
35. F. Takahashi, in *Combustion Phenomena: Selected Mechanisms of Flame Formation, Propagation and Extinction*, J. Jarosinski, B. Veyssiere (Eds.) Taylor and Francis, Boca Raton, 2007, submitted.
36. H. Lui, T. Ye, C. Mao, *Angewandte Chemie* 46 (2007) 6473-6475.
37. Sigma-Aldrich, [www.sigmaaldrich.com](http://www.sigmaaldrich.com), 2007.
38. D.R. Lide (Ed.) *CRC Handbook of Chemistry and Physics*, CRC Press, New York, 2007, pp. 3.224-3.472.
39. R.J. Reed (Ed.) *North American Combustion Handbook*, North American Mfg. Co., Cleveland, 1997, p. 285.
40. J.G. Speight (Ed.) *Lange's Handbook of Chemistry*, McGraw-Hill, New York, 2005 pp. 2.162-2.233.
41. K.-C. Lin, G.M. Faeth, P.B. Sunderland, D.L. Urban, Z.-G. Yuan, *Combust. Flame* 116 (1999) 415-431.

# Oxidation of two-ringed aromatic species as models for soot surface reactions

R.P. Lindstedt, V. Markaki, R.K. Robinson

*Department of Mechanical Engineering, Imperial College London, South Kensington Campus,  
London SW7 2BX, United Kingdom*

*Abstract: The study by Bhatt and Lindstedt on the impact of agglomeration and surface chemistry models on soot formation and oxidation identified the onset of soot inception and the associated poly-aromatic hydrocarbon (PAH) chemistry as particularly challenging. A strong sensitivity to temperature close to the soot inception limit was also identified. Past studies have predominantly considered PAH formation paths and comparatively little attention given to the oxidation processes. The current study (i) considers oxidation paths for two-ringed aromatics and (ii) provides a further evaluation of the ability of a sectional method to reproduce the temporal evolution of the soot particle size distribution in the temperature range of 1520-1620 K. The sensitivity to the van der Waals enhancement factor was also assessed. The applied gas phase reaction mechanism was initially created from reaction classes derived from toluene, benzene and cyclo-pentadiene oxidation, augmented by the naphthalene to pyrene steps of Wang and Frenklach, and features 285 chemical species and 1520 reactions. Critical oxidation steps were identified and the subject of detailed investigations via quantum mechanical methods using Gaussian 03. Rate constants for the  $C_9H_7 + O_2/HO_2$  channels were derived from the potential energy surfaces using the Rice-Ramsperger-Kassel-Marcus/master equation approach and variable transition state theory. Improved thermodynamic data for a wide range of intermediate species was also determined at the G3MP2B3 level in combination with density functional theory analysis for internal rotations.*

## 1. OUTLINE

The formation pathways of higher aromatics have been the subject of a number of past studies with the need to understand soot nucleation a dominant driving force. Possible naphthalene formation paths considered have included initiation via *HACA* type sequences and  $C_5H_5 + C_5H_5$ ,  $C_6H_5 + C_4H_4$  and  $C_7H_7 + C_3H_3$  reactions [1, 2, 3, 4, 5]. It has been shown that a number of formation channels are plausible and that their relative importance is strongly dependent upon oxidation/pyrolysis conditions. Indene type structures have received significantly less attention despite measured concentrations similar to those of naphthalene. Furthermore, indene also plays a key part in the oxidation of naphthalene. Past work [3, 5, 6] suggests that reactions of the type  $C_9H_7 + CH_3$  may provide a mass growth source that link five and six member ring structures and that sequences initiated by  $C_6H_5 + C_3H_3$  and leading to indene, through repeated isomerisations, are likely formation paths [3]. The ability to predict the inter-conversion of PAHs is also of increasing relevance given differences in their harmful effects. A further issue is related to the complexity of practical fuels, such as Jet-A and

Diesel, where model fuel blends have to be used in numerical simulations of practical combustion devices. The need to understand the oxidation behaviour of PAHs again comes to the fore as conventional fuels typically contain around 20% of aromatics. Furthermore, the burnout of soot particles presents a challenging issue as the final level of emissions may be a small fraction of the initial soot formed and a better understanding of the soot surface chemistry is desirable. Past work on the oxidation of single-ring aromatics include the studies by Emdee et al. [7], Klotz et al. [8], Lindstedt & Maurice [9] and Richter & Howard [4]. Studies of two-ringed structures are less prevalent. However, Shaddix [10] investigated the oxidation of naphthalene and 1-methylnaphthalene under turbulent PFR conditions and Pitsch [11] proposed a detailed kinetic mechanism for the latter species. Lindstedt et al. [3] considered a wide range of PAH formation paths and Dagaut & co-workers [12, 13] have recently considered the oxidation of *m*-xylene and 1-methyl naphthalene under JSR conditions.

The current study extends past work on the oxidation of two-ringed aromatics and also provides a further evaluation of the ability of a sectional method to reproduce the temporal evolution of the soot Particle Size Distribution (PSD). The sensitivity to the van der Waals enhancement factor was also assessed. Rate constants for the  $C_9H_7 + O_2/HO_2$  channels were derived from Potential Energy Surfaces (PES) using the Rice-Ramsperger-Kassel-Marcus/Master Equation (RRKM/ME) approach and Variable Transition State Theory (VTST) and the resulting reaction mechanism evaluated through comparisons with experimental data obtained in a PFR configuration [10]. Accurate thermodynamic data is particularly important given the large number of isomerisation reactions present in detailed reaction sequences for PAH formation/oxidation. As part of the present work, earlier estimates, often derived on the basis of variants of Benson's additivity method, are replaced by data derived from quantum mechanical methods using Gaussian 03 (at the G3MP2B3 level) in combination with Density Functional Theory (DFT) analysis for internal rotations.

## 2. COMPUTATIONAL METHODS

In the current work, DFT and composite energy calculations were performed using Gaussian 03 [14]. Prior to the main quantum mechanical computations, molecules were subjected to a molecular mechanics minimisation to determine their basic configurations. If a molecule was found to have many torsion angles, or if the structure appeared to be strained, a conformational analysis was performed. Subsequently, DFT calculations, with the B3LYP [15, 16] functional and 6-31g(d) basis set were used to locate stationary points along the potential energy surface. Vibrational frequency calculations were performed at the same level of theory to identify the latter as either transition states, having one imaginary frequency, or minima with no imaginary frequencies. The calculations also provided the zero point energy (ZPE) for each species.

Intrinsic reaction coordinate (IRC) calculations were carried out starting from each transition state in order to link reactants and products. The calculations were allowed to follow the energy profile in both directions from the maxima, the number/size of steps were optimized for each calculation to allow enough movement to identify the reactants and products and to confirm that the correct transition state had been loca-

ted. The resulting structures were then used as the basis for high accuracy composite calculations using the G3MP2B3 method of Baboul et al. [17]. The latter provides precise energy data while requiring less computation than a single calculation at a higher level of theory. Furthermore, other related methods often failed to deal with the transition states and intermediates encountered in the current study. The G3MP2B3 method consists of a geometry optimisation carried out at HF/6-31(d) level, the resulting structure was then used to calculate vibrational frequencies at the B3LYP/6-31G(d) level of theory. Frequencies were scaled by a correction factor of 0.96 and then used to calculate the ZPE. The geometry was further refined at the B3LYP/6-31G(d) level to provide the final structure, which was then used for a series of single point energy calculations at higher levels of theory: B3LYP/6-31G(d), QCISD(T,FC)/6-31G(d) and, finally, MP2(FU)/G3Large. The resulting energies were then combined and a higher-level correction obtained by taking into account remaining deficiencies in the energy calculation. Finally, the total energy was calculated by adding the ZPE from the previously calculated vibrational frequencies.

The G3MP2B3 method has the advantage that the B3LYP method is used to calculate the molecular frequencies. Durant [18, 19] reported that B3LYP density functional methods provides improved geometries and vibrational frequencies in comparison to MP2 and Hartree-Fock ab-initio methods. As mentioned above, a correction factor of 0.96 [20] was applied to B3LYP calculated frequencies to provide the best fit to experimental IR and Raman measurements. Internal rotations can significantly influence thermochemical properties, therefore rotors were investigated for the relevant species. Each molecule underwent a series of scans, whereby each internal rotation was rotated though  $360^\circ$  in  $15^\circ$  steps. At each step the molecular structure was optimised and the energy of the molecule was calculated at the B3LYP/6-31g(d) level. An in-house code (SCANCALC) fitted the calculated energy profile to the following series,  $V = \frac{1}{2} \sum V_n (1 - \cos(n\Theta))$  with  $n$  ranging from 1 to 6. SCANCALC also produced internal rotational constants and the symmetry number for the respective rotations. The energy profiles calculated for both internal rotations present in  $C_9H_7OOH$  are shown as an example in Figure 1.

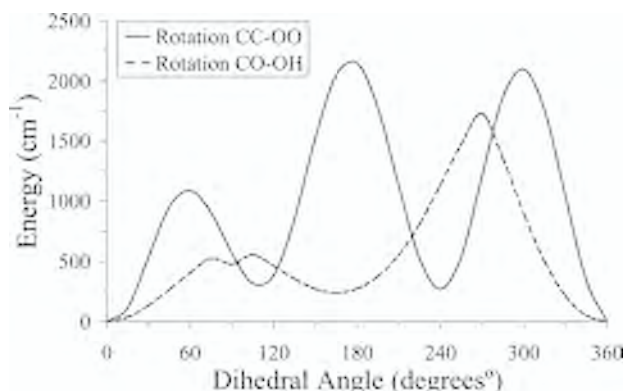
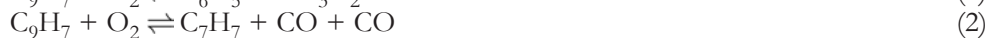


Figure 1. Potential barriers to internal rotation in  $C_9H_7OOH$ .

Vibrational frequencies, enthalpies of formation, moments of inertia and molecular symmetry numbers were extracted via a script from the G3MP2B3 log file and, if required, data for low frequency vibrations were omitted and modelled as hindered internal rotors. The NASA statistical mechanics Properties and Coefficients 99 (PAC99) program [21] was then used with the rigid rotor harmonic oscillator (RRHO) approximation to calculate thermodynamic data from the molecular properties. The enthalpy at 298 K was anchored to the G3MP2B3 calculated value. The procedure provided thermochemical data for enthalpy, heat capacity, entropy and Gibbs free energy in the range 200 K to 6000 K which was fitted to standard 7 term JANAF polynomials.

### 3. APPLICATION TO SELECTED OXIDATION CHANNELS

The studies by Lindstedt et al. [3] and Potter [22] identified the importance of the linkages between aromatic  $C_5$  and  $C_6$  structures and the key role of the indene/indenyl system. In particular, the oxidation of indenyl was found to exert a strong influence on the overall oxidation kinetics of larger aromatic species (e.g. naphthalene and 1-methyl naphthalene) and on the subsequent product distribution of single ringed aromatics. The studies identified possible reactions channels featuring molecular oxygen (1,2,3) though accurate estimates of the rates of reaction proved problematic [22]. In the current work, the following channels were considered,



Along with reactions (4) and (5), featuring the  $HO_2$  radical. For both sets of reactions, DFT and composite quantum mechanical methods were used to calculate the PES for the oxidation channels. Both RRKM/ME theory and VTST were used to derive estimates of the rate constants.



More accurate thermochemical data for key intermediates such as  $C_9H_8$ ,  $C_9H_7$ ,  $C_9H_7O$ ,  $C_9H_7OOH$  and  $C_9H_6O$  was also obtained. Additional oxidation paths were estimated on the basis on similarities with the cyclo-pentadiene system [5] as outlined below.

#### 3.1. Potential energy surfaces

The oxidation of  $C_9H_7$  is accompanied by the breakup of the five membered ring [3]. Bozzelli & Zhong [23] investigated the related oxidation of the cyclo-pentadienyl radical and found two channels through which the reaction could proceed. Thus, after the initial molecular oxygen attack, the second oxygen atom could bond to either of the

adjacent carbons (prior to the ring opening) or, in the alternative channel, to the carbon opposite leading to a bridge structure as shown in Figure 2. Initial DFT calculations covering (1,2,3) showed that the most favourable site of attack for the oxygen molecule was on either of the carbons adjacent to the six membered ring. The second oxygen can then bond to one of three carbons, either those directly adjacent or the carbon opposite. Bonding to an adjacent carbon allows breakup of the five membered ring, similar to first channel described by Bozzelli & Zhong [23], whereas bonding to the opposite carbon would form a bridge structure.

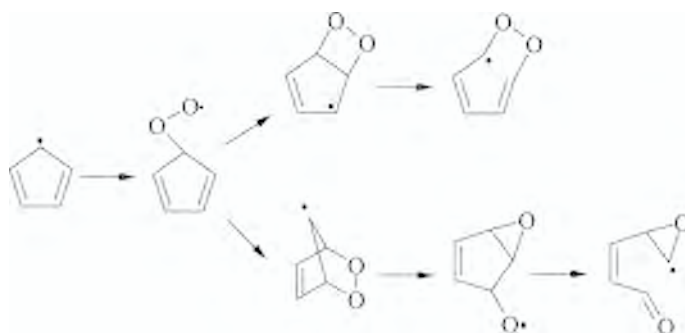


Figure 2. Initial section of the Zhong and Bozzelli [23] reaction mechanism for the oxidation of the cyclopentadienyl radical with 2 channels for the breakdown of the five membered ring.

By exploring the potential energy surface at the B3LYP/6-31g(d) level, the second channel proved to be energetically unfavourable for the current larger molecule. The structure would have to pass through a particularly large energy barrier of  $155 \text{ kJ mol}^{-1}$  in order to allow the oxygen molecule to bridge across the ring. Accordingly, it was assumed that the second oxygen would bond to one of two adjacent carbons. Attachment to the six membered ring would allow the reaction to follow through to the products shown in reaction (1), whereas bonding to the adjacent carbon on the five membered ring allows the reaction to follow through to the products from reactions (2) and (3). All three reaction paths follow a similar pattern: The potential energy rises until the five membered ring is broken when large amounts of energy are released. Some smaller energy barriers then need to be traversed to rearrange the structure in order to form the final products. Heats of formation for all steps were calculated at the G3MP2B3 level and the identified potential energy surfaces for the reaction pathways are shown in Figures 3-5. Tables 1-3 show total energies, including the ZPE, as well as relative energies calculated using DFT, and enthalpies of formation at 298 K.

For the cases considered here, it was assumed that once the reaction had advanced past the highest energy point, sufficient energy was present in the system to allow rearrangement to the products without stabilization of intermediates. Therefore all three channels were modelled as one step processes, with the slowest step prior to the breakup of the five-membered ring controlling the reaction rate for each channel. From the

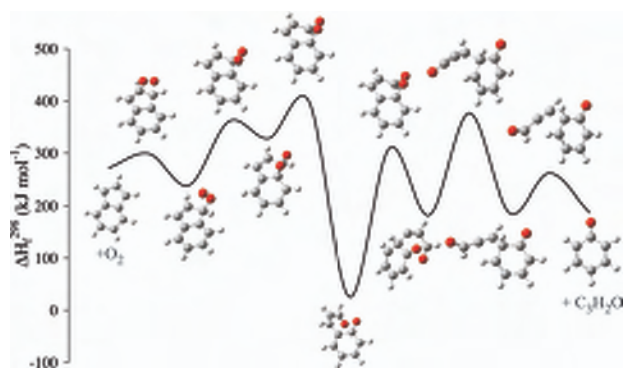


Figure 3. Potential energy surface for reaction (1) showing enthalpies of formation 298 K at the G3MP2B3 level of theory, B3LYP/6-31g(d) optimised geometries shown.

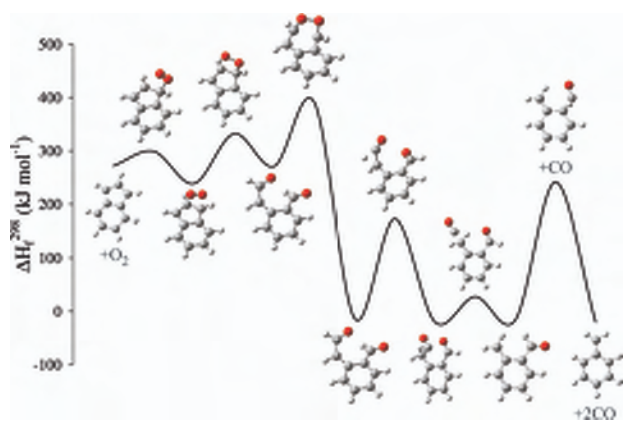


Figure 4. Potential energy surface for reaction (2) showing enthalpies of formation 298 K at the G3MP2B3 level of theory, B3LYP/6-31g(d) optimised geometries shown.

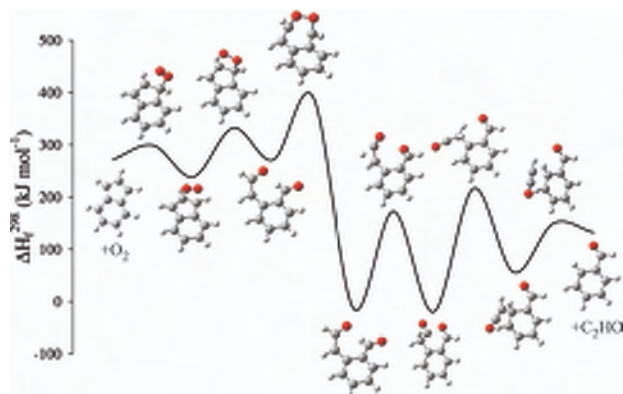


Figure 5. Potential energy surface for reaction (3) showing enthalpies of formation 298 K at the G3MP2B3 level of theory, B3LYP/6-31g(d) optimised geometries shown.

Table 1. Energies of species for reaction (1) including ZPE.

Species	B3LYP/6-31(d)	$E_{\text{Relative}}$	G3MP2B3 $\Delta_f H^{298\text{K}}$	$E_{\text{Relative}}$
	Hartrees	$\text{kJ mol}^{-1}$	$\text{kJ mol}^{-1}$	$\text{kJ mol}^{-1}$
$\text{C}_9\text{H}_7+\text{O}_2$	-497.32	0.00	271.89	0.00
TS1	-497.31	19.75	298.93	27.04
1a	-497.33	-19.02	238.50	-33.39
TS2	-497.28	104.55	360.85	88.96
1b	-497.28	87.47	328.49	56.60
TS3	-497.26	140.15	398.50	126.61
1c	-497.41	-236.78	25.71	-246.18
TS4	-497.30	53.15	308.99	37.10
1d	-497.34	-51.67	182.24	-89.65
TS5	-497.27	134.27	376.73	104.84
1e	-497.34	-67.95	186.70	-85.19
TS6	-497.32	0.04	261.70	-10.19
$\text{C}_6\text{H}_5\text{O} + \text{C}_3\text{H}_2\text{O}$	-497.34	-68.89	187.36	-84.53

Table 2. Energies of species for reaction (2) including ZPE.

Species	B3LYP/6-31(d)	$E_{\text{Relative}}$	G3MP2B3 $\Delta_f H^{298\text{K}}$	$E_{\text{Relative}}$
	Hartrees	$\text{kJ mol}^{-1}$	$\text{kJ mol}^{-1}$	$\text{kJ mol}^{-1}$
$\text{C}_9\text{H}_7+\text{O}_2$	-497.32	0.00	271.89	0.00
TS1	-497.31	19.75	298.93	27.04
2a	-497.33	-19.02	238.50	-33.39
TS2	-497.29	74.47	331.99	60.10
2b	-497.31	20.43	271.06	-0.83
TS3	-497.27	126.37	390.74	118.85
2c	-497.42	-277.45	-13.08	-284.97
TS4	-497.35	-79.30	172.61	-99.28
2d	-497.42	-258.64	-19.96	-291.85
TS6	-497.41	-229.20	27.36	-244.53
2e+CO	-497.42	-259.03	-16.17	-288.06
TS7+CO	-497.31	26.71	241.33	-30.56
$\text{C}_7\text{H}_7+2\text{CO}$	-497.41	-239.22	-20.33	-292.22

PES for reaction (1), it is evident that the largest energy barrier of  $122.35 \text{ kJ mol}^{-1}$  occurs for the second step. Therefore the rearrangement from species 1a to 1b, through transition state 2, is rate controlling. Reactions (2) and (3) proceed identically until the break up of the five-membered ring, followed by rearrangement to different products. The third step, from species 2b to 2c, has a large energy barrier of  $119.68 \text{ kJ mol}^{-1}$  and Figure 6 shows the potential energy from the IRC calculation for this rate controlling step.

Table 3. Energies of species for reaction (3) including ZPE.

Species	B3LYP/6-31(d)	$E_{\text{Relative}}$	G3MP2B3 $\Delta_f H^{298\text{K}}$	$E_{\text{Relative}}$
	Hartrees	$\text{kJ mol}^{-1}$	$\text{kJ mol}^{-1}$	$\text{kJ mol}^{-1}$
$\text{C}_9\text{H}_7+\text{O}_2$	-497.32	0.00	271.89	0.00
TS1	-497.31	19.75	298.93	27.04
2a	-497.33	-19.02	238.5	-33.39
TS2	-497.29	74.47	331.99	60.10
2b	-497.31	20.43	271.06	-0.83
TS3	-497.27	126.37	390.74	118.85
2c	-497.42	-277.45	-13.08	-284.97
TS4	-497.35	-79.30	172.61	-99.28
2d	-497.42	-258.64	-19.96	-291.85
TS5	-497.34	-50.80	216.23	-55.66
3e	-497.39	-186.22	56.02	-215.87
TS6	-497.36	-109.16	149.76	-122.13
$\text{C}_7\text{H}_6\text{O}+\text{C}_2\text{HO}$	-497.37	-125.82	132.00	-139.90

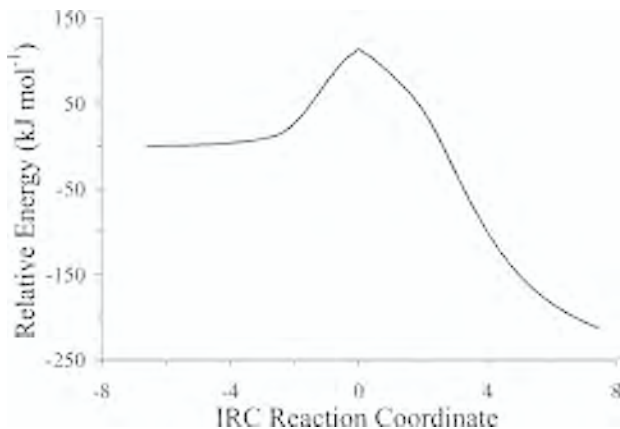


Figure 6. Potential energy from the IRC calculation for the rate determining step for reactions (2,3) starting from TS3.

### 3.2. Rate constant calculations

Rate constants were calculated using two different methods, microcanonical RRKM/ME theory through ChemRate [24] and VTST through POLYRATE [25]. The RRKM/ME approach was used to compute rates for all reactions in the temperature range 500 to 2500 K at 1 atmosphere and at the high pressure limit with the rate constants ( $k(E)$ ) determined from Eq. (1).

$$k(E) = I^+ \left( \frac{G^+(E)}{hN(E + E_0)} \right) \quad (1)$$

In the above equation,  $G^+(E)$  is the total number of states of the transition structure and  $I^+$  is the reaction path degeneracy,  $N$  is the density of states of the reactant at energy  $E + E_0$  and  $h$  is Plank's constant. The master equation was used to model pressure fall-off. Lennard-Jones parameters  $\sigma$  (Å) and  $\epsilon$  (K), used to estimate the frequency of collisions, were obtained from databases or calculated from a method based on molar volumes and compressibility [26]. The calculation requires critical temperatures, critical volumes and acentric factors for each species and data for related molecules was used for cases where literature values could not be found. For  $C_9H_7$  and its intermediates, values of  $\sigma = 6.17$  Å and  $\epsilon = 580.92$  K were used along with  $\sigma = 3.44$  Å and  $\epsilon = 119.44$  K for Argon. The value of  $\langle \Delta E \rangle_{down}$  was taken to be  $800 \text{ cm}^{-1}$  using the standard form of the exponential down model [27]. A maximum energy limit ( $E_{max}$ ) of  $1000.0 \text{ kJ mol}^{-1}$  was used for the energy integration in the master equation computation to ensure convergence at high temperatures. To provide a complementary evaluation of the determined rates for all three reactions, VTST [25] was used to determine the high pressure limit rates in the temperature range 500 to 2500 K. Canonical variation transition state theory (CVT) [28] with small curvature tunnelling (SCT) [29, 30] corrections were applied to calculate the rate constants. The CVT rate for temperature  $T$  is expressed as,

$$k^{CVT}(T, s) = \min k^{GT}(T, s) \quad (2)$$

where  $k^{GT}(T, s)$  is the rate constant in generalised transition state theory at the dividing surface  $s$ . Data from the PES for each step of the process was required and the GAUSSRATE interface [31] was used to provide direct dynamics calculations of energies, gradients and Hessians on the reaction path.

A comparatively good fit between the high pressure rates for both methods was obtained for reaction (1). Table 4 shows calculated rate constants obtained with both methods at the high pressure limit and Figure 7 shows the same information graphically. Both selected rate controlling steps showed little or no pressure dependency up to 1200 K though at higher temperatures there is fall-off at lower pressures. The initial steps of the reaction channels are somewhat pressure dependent, including the initial collision with oxygen. However, these steps are significantly faster and do not affect the overall rate of reaction. Therefore the high pressure rates were chosen to model these reactions as it appeared pressure did not play a large role in the rate determining isomerisation steps. As shown below, the current choice is consistent with the oxidation of naphthalene under atmospheric pressure conditions.

Rate constants ( $k(T)$ ) were fitted to the modified three-parameter form of the Arrhenius equation (see Eq. (3)) and Tables 5 and 6 show the values of the rate parameters  $A$ ,  $n$  and  $Ea$  obtained from the RRKM/ME and VTST calculations. As part of the validation computations discussed below, it was found that the high pressure RRKM based rates provided a better fit to experimental data and were hence used in the subsequent kinetic modelling of the oxidation of naphthalene.

Table 4. Estimated rate constants as a function of temperature for reactions (1,2,3) at the high pressure limit.

Temp K	Reaction (1)		Reaction (2,3)	
	RRKM/ME $\text{m}^3 \text{ kmol}^{-1} \text{ s}^{-1}$	VTST $\text{m}^3 \text{ kmol}^{-1} \text{ s}^{-1}$	RRKM/ME $\text{m}^3 \text{ kmol}^{-1} \text{ s}^{-1}$	VTST $\text{m}^3 \text{ kmol}^{-1} \text{ s}^{-1}$
500	1.32E - 03	2.21E - 01	1.60E - 03	4.39E - 01
600	1.94E - 01	8.47E + 00	2.35E - 01	2.44E + 01
700	6.85E + 00	1.17E + 02	8.37E + 00	4.41E + 02
800	9.92E + 01	8.47E + 02	1.23E + 02	3.91E + 03
900	7.92E + 02	3.96E + 03	9.94E + 02	2.15E + 04
1000	4.17E + 03	1.37E + 04	5.32E + 03	8.40E + 04
1200	5.03E + 04	8.81E + 04	6.64E + 04	6.54E + 05
1400	2.98E + 05	3.35E + 05	4.05E + 05	2.84E + 06
1600	1.13E + 06	9.14E + 05	1.58E + 06	8.58E + 06
1800	3.18E + 06	2.00E + 06	4.59E + 06	2.02E + 07
2000	7.29E + 06	3.75E + 06	1.08E + 07	4.02E + 07
2250	1.67E + 07	7.03E + 06	2.55E + 07	7.99E + 07
2500	3.23E + 07	1.16E + 07	5.08E + 07	1.38E + 08

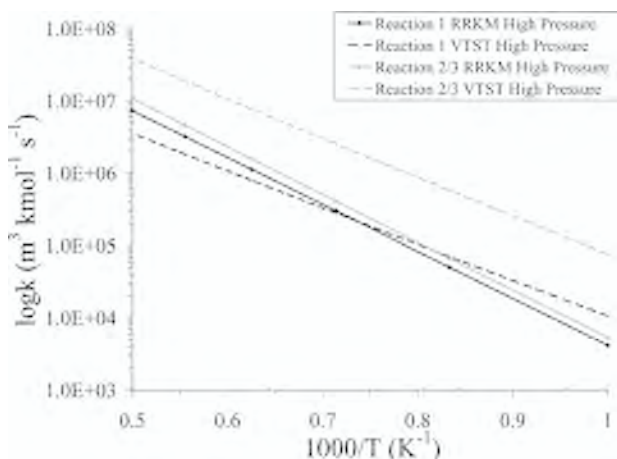


Figure 7. Estimated rates of reaction at the high pressure limit for reactions (1,2,3) using RRKM/ME theory and VTST.

$$k(T) = AT^n \exp\left(\frac{-E_a}{RT}\right) \quad (3)$$

The reaction of indenyl with the hydroperoxyl radical was also explored and the resulting potential energy diagram, see Figure 8, shows that for reactions (4) and (5), the intermediate species have a lower energy than the starting products and are unli-

Table 5.  $C_9H_7+O_2$  reaction coefficients in the form  $k = AT^n \exp(-E/RT)$  at the high pressure limit. Estimated using RRKM/ME theory, units are kmol,  $m^3$ , s, K and  $kJ mol^{-1}$ .

Reaction Number	Reaction	A $m^3 kmol s^{-1} / s^{-1}$	n	E a kJ
1	$C_9H_7 + O_2 \rightleftharpoons C_6H_5O + C_3H_2O$	1.876E+10	-0.047	124.689
2	$C_9H_7 + O_2 \rightleftharpoons C_7H_7 + CO + CO$	1.742E+09	0.305	123.108
3	$C_9H_7 + O_2 \rightleftharpoons C_7H_6O + C_2HO$	1.742E+09	0.305	123.108

Table 6.  $C_9H_7+O_2$  reaction coefficients in the form  $k = AT^n \exp(-E/RT)$  at the high pressure limit. Estimated using VTST, units are kmol,  $m^3$ , s, K and  $kJ mol^{-1}$ .

Reaction Number	Reaction	A $m^3 kmol s^{-1} / s^{-1}$	n	E a kJ
1	$C_9H_7 + O_2 \rightleftharpoons C_6H_5O + C_3H_2O$	7.239E+05	0.893	86.370
2	$C_9H_7 + O_2 \rightleftharpoons C_7H_7 + CO + CO$	1.364E+07	0.877	93.592
3	$C_9H_7 + O_2 \rightleftharpoons C_7H_6O + C_2HO$	1.364E+07	0.877	93.592

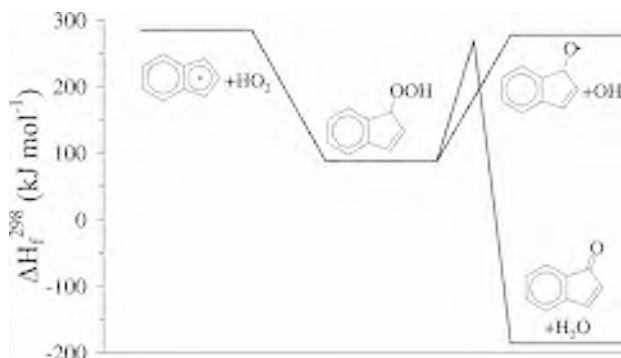


Figure 8. Potential energy diagram for reaction of the indenyl radical with the hydroperoxyl radical.

kely to stabilize. Therefore the rate determining step is likely to be analogous to the corresponding cyclo-pentadienyl reaction, with the addition of the hydroperoxyl radical controlling the overall reaction rates. Reaction rates were calculated using RRKM/ME theory as it was thought that these reactions would be particularly sensitive to pressure fall-off and that collisional effects would be important in the initial addition reactions. Hence, rates were calculated at 1 atmosphere and the high pressure limit by using the same collisional properties and energies as previously outlined. It was found that

pressure effects become significant around 700 K and therefore rates calculated at 1 atmosphere were selected for use in the current kinetic modelling described below. The rates were fitted to the modified Arrhenius equation and values for  $A$ ,  $n$  and  $E_a$  are shown in Table 7. Thermochemical data extracted from the polynomials for all species involved in the kinetic modelling are shown in Table 8.

Table 7.  $C_9H_7+HO_2$  reaction coefficients in the form  $k = AT^n \exp(-E/RT)$  at 1 atmosphere. Estimated using RRKM/ME theory, units are kmol,  $m^3$ , s, K and  $kJ\ mol^{-1}$ .

Reaction Number	Reaction	A $m^3\ kmol\ s^{-1} / s^{-1}$	n	E a kJ
4	$C_9H_7 + HO_2 \rightleftharpoons C_9H_7O + OH$	8.577E+65	-16.689	101.786
5	$C_9H_7 + HO_2 \rightleftharpoons C_9H_6O + H_2O$	8.577E+65	-16.689	101.786

Table 8. Thermochemical data for species involved in kinetic modelling.

Species	$\Delta_f H^{298K}$ kJ $mol^{-1}$	$S^{298K}$ J $K^{-1}\ mol^{-1}$	$S_p^{298K}$ J $K^{-1}\ mol^{-1}$	$\Delta_f H^{1000K}$ kJ $mol^{-1}$
$O_2$	0.00	205.14	29.38	22.71
$H_2O$	-241.81	188.82	33.59	-215.81
$HO_2$	12.55	229.09	34.89	42.10
CO	-110.52	197.65	29.14	-88.83
$C_2HO$	178.26	249.24	50.60	221.72
$C_3H_2O$	128.67	277.37	69.36	193.50
$C_7H_7$	215.28	318.42	109.94	354.16
$C_7H_6O$	-39.04	342.33	112.69	100.81
$C_9H_7$	281.38	339.17	123.67	442.95
$C_9H_8$	160.97	336.40	125.24	328.41
$C_9H_6O$	54.97	352.13	132.10	220.64
$C_9H_7O$	243.619 <sup>a</sup>	365.04	137.87	418.63
$C_9H_7OOH$	79.98	404.44	168.49	278.81

<sup>a</sup> Ascertained from B3LYP/6-311++g(3d,3p) energy difference.

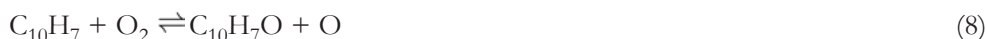
#### 4. OXIDATION OF NAPHTHALENE

The derived reaction mechanism for the oxidation of naphthalene was based on the above reaction steps and reaction classes derived from the oxidation of benzene and cyclo-pentadiene with parameters adjusted according to molecular size and reactive site differences. Computations performed here show that under the PFR conditions of Shaddix [10] ( $\phi = 1.1$ ,  $T = 1197\ K$  and  $P = 1\ atm$ ), the major naphthalene oxidation

pathways are via *H* abstraction featuring *OH* and via *O* atom addition to the ring leading to the naphthoxy radical as shown in Figure 9.



The rate assigned to reaction (6) was based on the relative reaction rate of the hydrogen atom abstraction from the benzene ring as discussed by Leung and Lindstedt [32]. Similarly, reaction rate adjustments based on the oxygen addition to the benzene ring were applied to reaction (7) with the reference rate proposed by DiNaro et al. [33]. Reaction (6) is the major pathway leading to the naphthyl radical, which then decomposes to the naphthoxy radical (8). The carbon monoxide expulsion from the latter species via (9) constitutes the major (65%) formation channel for the indenyl radical ( $\text{C}_9\text{H}_7$ ).



The  $\text{C}_9\text{H}_7$  radical recombines with the *H* atom leading to the formation of indene (10) (32%) and also undergoes oxygen atom addition via  $\text{HO}_2$  attack (14%) (4), as discussed above, or *C*–*C* breakage leading to  $\text{C}_8\text{H}_7$  and *CO* (19%) (11).



Past studies of the indenyl reaction channels have highlighted thermal decomposition or *H*, *O* and  $\text{HO}_2$  addition (e.g. Shaddix et al. [34], Laskin & Lifshitz [6], Lindstedt et al. [3]) and the current results are in agreement with these studies. Reaction (11) was included with a rate as suggested by Lindstedt et al. [3] and was found to be of key importance to the evolution of species such as  $\text{C}_2\text{H}_2$ ,  $\text{C}_2\text{H}_4$ ,  $\text{C}_4\text{H}_4$  and  $\text{C}_5\text{H}_6$ . More specifically, the channel increased acetylene concentrations by 31%, ethylene by 68%,  $\text{C}_4\text{H}_4$  by 70% and  $\text{C}_5\text{H}_6$  by 44%. The concentration levels of  $\text{C}_8\text{H}_6$  are sensitive to reaction (12), which contributes around 10% of the  $\text{C}_8\text{H}_6$  consumption using the rate proposed by Wang & Frenklach [2].

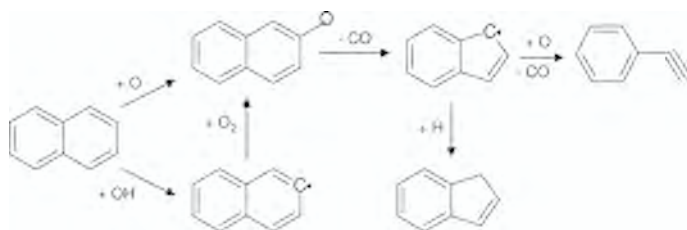


Figure 9. Naphthalene and indene oxidation pathways.

Table 9. Selected rate constants. Naphthalene reaction mechanism with rate coefficients in the form  $k = AT^n \exp(-E/RT)$ . Units are kmol, m<sup>3</sup>, s, K and kJ mol<sup>-1</sup>.

No.	Reaction	A	n	E	Ref.
1	$C_9H_7 + O_2 \rightleftharpoons C_7H_7 + CO + CO$	1.74E+09	0.305	123.108	pw
2	$C_9H_7 + O_2 \rightleftharpoons C_6H_5O + C_3H_2O$	1.87E+10	-0.047	124.689	pw
3	$C_9H_7 + O_2 \rightleftharpoons C_7H_6O + C_2HO$	1.74E+09	0.305	123.108	pw
4	$C_9H_7 + HO_2 \rightleftharpoons C_9H_7O + OH$	8.57E+65	-16.69	101.786	pw
6	$C_{10}H_8 + OH \rightleftharpoons C_{10}H_7 + H_2O$	1.70E+05	1.42	6.070	adj.[32]
7	$C_{10}H_8 + O \rightleftharpoons C_{10}H_7O + H$	2.50E+10	0	19.54	adj.[33]
8	$C_{10}H_7 + O_2 \rightleftharpoons C_{10}H_7O + O$	2.15E+10	0	25.61	adj.[49]
9	$C_{10}H_7O \rightleftharpoons C_9H_7 + CO$	1.80E+12	0	183.68	adj.[32]
10	$C_9H_7 + H \rightleftharpoons C_9H_8$	2.00E+11	0	0.0	pw
11	$C_9H_7 + O \rightleftharpoons C_8H_7 + CO$	1.00E+11	0	0.0	[3]
12	$C_8H_6 + O \rightleftharpoons C_6H_5O + C_2H$	2.20E+10	0	18.95	[2]
13	$C_9H_8 + H \rightleftharpoons C_9H_7 + H_2$	2.11E+10	0	9.453	adj.[5]
14	$C_9H_8 + O \rightleftharpoons C_9H_7 + OH$	1.365E+10	0	12.87	adj.[32]
15	$C_9H_8 + OH \rightleftharpoons C_9H_7 + H_2O$	8.62E+05	1.18	-1.87	adj.[50]
16	$C_8H_7 \rightleftharpoons C_8H_6 + H$	1.30E+41	-8.65	46.10	[2]
17	$C_8H_6 + O \rightleftharpoons C_6H_5 + C_2HO$	6.51E+03	2.09	6.54	[3]
18	$C_8H_6 + OH \rightleftharpoons C_8H_5 + H_2O$	2.10E+10	0	19.1	[1]
19	$C_6H_6(F) + H \rightleftharpoons C_6H_6 + H$	3.00E+09	0.5	8.372	[51]
20	$C_7H_6O + O \rightleftharpoons C_6H_6 + CO_2$	2.00E+10	0	0.0	pw
21	$C_7H_8 \rightleftharpoons C_7H_7 + H$	2.09E+15	0	366.141	[38]
22	$C_6H_5 + O_2 \rightleftharpoons C_6H_5O + O$	2.60E+10	0	25.61	[49]
23	$C_5H_6 \rightleftharpoons C_5H_5 + H^a$	$k_0$ 1.58E+59	-12.6	332.628	[39]
		$k_\infty$ 1.00E+19	-0.655	368.192	[39]
24	$C_5H_4O \rightleftharpoons C_4H_4 + CO$	2.50E+11	0	221.90	adj.[40]

<sup>a</sup> Troe parameter is  $F_c=0.8$ .

<sup>pw</sup> is present work.

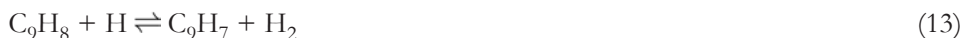
The oxidation of indenyl via molecular oxygen addition makes a contribution with steps (1,2,3) each contributing 3-4% under the current comparatively low temperature conditions. The impact on the product distribution of single-ringed aromatics is significant as discussed below.

## 5. COMPUTATIONAL RESULTS

The first part of the current section describes the results obtained for the oxidation of naphthalene under the conditions studied by Shaddix [10]. The second part outlines the application of the complete chemistry coupled with the sectional model developed by Bhatt & Lindstedt [35] to the computation of the soot PSD under the conditions studied experimentally by Marr et al. [36] and Kronholm & Howard [37].

## 5.1. Gas phase chemistry

The experimental data set used to validate and verify the naphthalene chemistry under turbulent flow reactor conditions was obtained by Shaddix [10] for a stoichiometry of  $\Phi = 1.1$ , an initial temperature of  $T = 1197$  K and an initial fuel concentration of  $\sim 1200$  ppm. Predictions of reactants and intermediate species are shown in Figures 10-12. Measured naphthalene concentrations show considerable scatter with the trend in reasonable agreement with computations. Indene is well reproduced as shown in Figure 11 and the major formation channel is via hydrogen radical recombination with the indenyl radical (10). The consumption of indene leads to a re-cycling to the indenyl radical and proceeds through hydrogen abstraction with  $H$ ,  $O$  and  $OH$  via reactions (13,14,15).



The oxidation of the indenyl radical has been discussed above and proceeds partly via the  $C_9H_7 \rightarrow C_9H_7O \rightarrow C_9H_6O \rightarrow C_8H_6$  chain, which is responsible for 46% of  $C_8H_6$  formation. An additional phenylacetylene pathway passes via the  $C_8H_7$  (11) radical and contributes (20%) via the subsequent decomposition (16).



The oxidation of phenylacetylene proceeds through reactions with  $O$  and  $OH$  that either remove the side chain via  $C-C$  cleavage or abstract a  $H$  atom. Reaction (17) is responsible for 30% of the  $C_8H_6$  consumption with a rate suggested by Lindstedt et al. [3]. Moreover, reaction (12) consumes 10% of the phenylacetylene leading to the formation of the phenoxy radical. The hydrogen abstraction via  $OH$  leads to  $C_8H_5$  (18) and consumes  $C_8H_6$  (18%) with the rate recommended by Frenklach & Wang [1].



Benzene is formed (35%) through hydrogen assisted isomerization (19) and (30%) from benzaldehyde (20). Benzaldehyde comes predominantly (45%) from indenyl consumption via reaction with molecular oxygen which proceeds with the rate determined in the current study. Benzene is subsequently consumed to the phenyl and phenoxy radicals.



The molecular oxygen addition to the indenyl radical is also responsible for the formation of the benzyl radical (42%), which subsequently forms toluene (100%). Reaction (21) also constitutes the major benzyl radical consumption channel (58%) with the rate adopted from the study by Oehlschlaeger et al. [38].

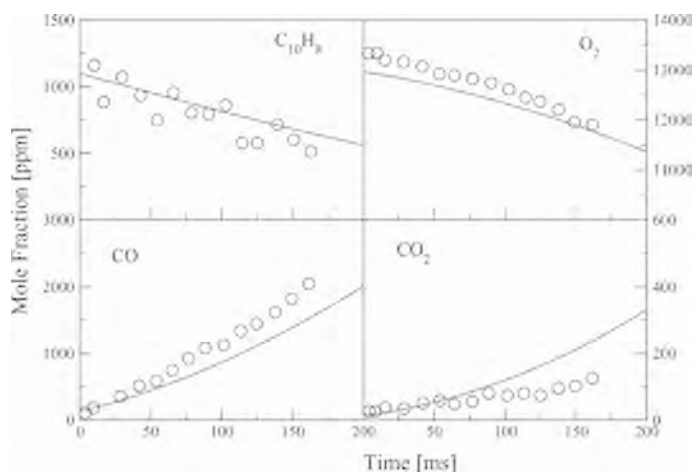


Figure 10. Concentration profiles of major species during naphthalene oxidation in a plug flow reactor [10] for a stoichiometry of  $\phi = 1.1$ . Solid lines are the computations using the detailed chemical mechanism.

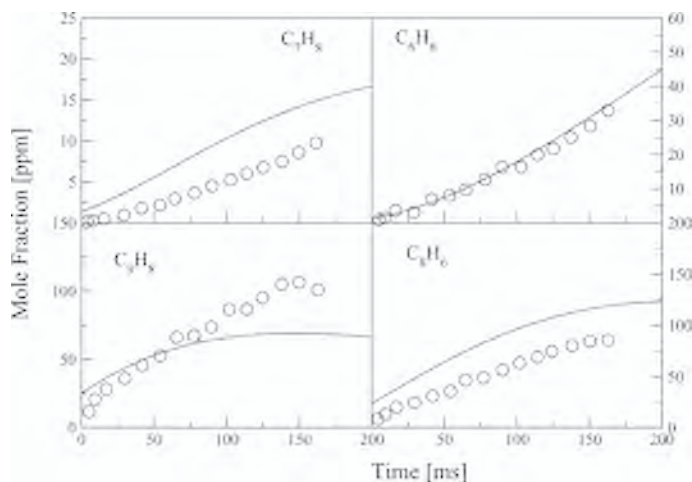


Figure 11. Concentration profiles of major species during naphthalene oxidation in a plug flow reactor [10] for a stoichiometry of  $\phi = 1.1$ . Solid lines are the computations using the detailed chemical mechanism.



The oxidation of phenylacetylene leads to the phenyl (17) and phenoxy (22) radicals with the latter leading to carbon monoxide and cyclo-pentadienyl (98%) with the rate proposed by Leung & Lindstedt [32]. Around 33% of  $C_5H_5$  forms  $C_5H_6$  via  $H$

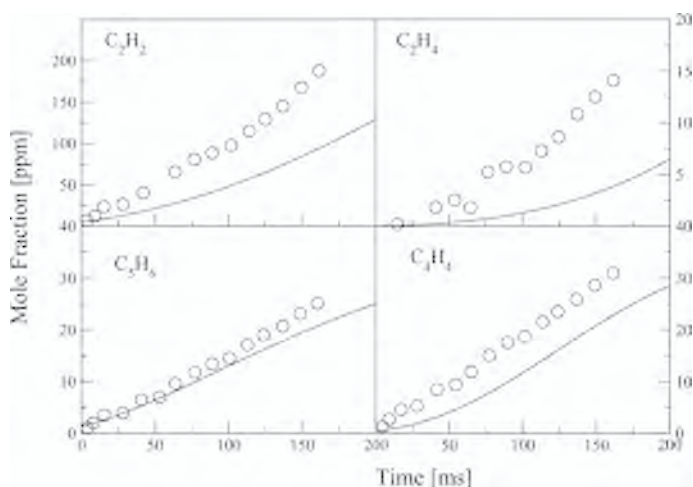


Figure 12. Concentration profiles of major species during naphthalene oxidation in a plug flow reactor [10] for a stoichiometry of  $\phi = 1.1$ . Solid lines are the computations using the detailed chemical mechanism.

atom recombination (23) with the rate proposed by Kern et al. [39]. Cyclopentadiene predominantly (53%) recycles back to  $C_5H_5$  via hydrogen abstraction.



The formation of acetylene (43%) is controlled by the thermal decomposition of  $C_5H_5$  which has been allocated the rate suggested by Kern et al. [39]. Moreover, the evolution of  $C_2H_4$  is also affected by  $C_5H_5$  via reactions channels that include  $C_2H_2$  and  $C_2H_2O$ .

Vinyl acetylene production is controlled initially by phenylacetylene consumption via  $C_8H_5O$ , which thermally decomposes to  $C_7H_5$  leading to  $C_4H_4$  via  $C_5H_4O$ . A rate by Ristori et al. [40] was assigned to reaction (24), which is responsible for 94% of the  $C_4H_4$  production.



The above analysis has shown that the the molecular oxygen reactions with indenyl have a key role in determining the distribution of single ring aromatics and the key importance of the cyclo-pentadienyl radical has also been further emphasized.

## 5.2. Soot particle dynamics

The fixed sectional approach developed by Bhatt and Lindstedt [35] for soot particle dynamics is based on the approach of Kumar and Ramkrishna [41]. The correspon-

ding Population Balance Equations (PBEs) were designed to conserve two moments simultaneously and a newly aggregated particle is ‘split’ and assigned to two adjacent bins such that any two general properties are conserved should the particle size not match any of the representative sizes on the grid. The strategy gives the method the potential to reproduce the PSD more accurately and the splitting coefficients need to be calculated only once. The PBEs for aggregation are given by

$$\frac{dn_i}{dt} = \sum_{\substack{k \leq j \leq i \\ j, k \\ m_{i-1} \leq (m_j + m_k) \leq m_{i+1}}} \left(1 - \frac{\delta_{j,k}}{2}\right) \eta_{i,j,k} \beta_{j,k} n_j n_k - n_i \sum_{k=1}^{N_{\text{bins}}} \beta_{i,k} n_k, \quad (4)$$

where  $n_i$  is the number concentration of size class  $i$  at time  $t$ ,  $\beta_{j,k}$  is the rate (in  $\text{m}^3/\text{s}$ ) at which particles of size class  $j$  attach with class  $k$  and  $\delta_{j,k}$  is the Kronecker delta. For a particle size class  $i$ , the first and second terms on the right hand side correspond to birth and death due to aggregation. The parameter  $\eta_{i,j,k}$  is the fraction of a newly created particle that the size class  $i$  will receive when two particles of sizes  $j$  and  $k$  are combined. Hence,  $\eta_{i,j,k}$  effectively assigns the new particle to two adjacent bins and is given by

$$\eta_{i,j,k} = \begin{cases} \frac{m_{i+1} - (m_j + m_k)}{m_{i+1} - m_i}, & m_i \leq m_j + m_k \leq m_{i+1} \\ \frac{m_{i-1} - (m_j + m_k)}{m_{i-1} - m_i}, & m_{i-1} \leq m_j + m_k \leq m_i. \end{cases} \quad (5)$$

The rate constants  $\beta_{i,j}$  appearing in Eq. (4) take different forms depending on the Knudsen number as outlined elsewhere [35] and in the current work the density of soot ( $\rho_s$ ) is  $1800 \text{ kg/m}^3$  and the sensitivity to the van der Waals enhancement factor ( $C_a$ ) has been evaluated using values in the range 1-9 [35, 42]. Soot particles are here assumed to be spherical up to a diameter of 25 nm, after which they start aggregating into linear chain-like structures with a fractal dimension assigned the value  $D_f = 1.8$  [43, 44].

The fixed sectional method of Park and Rogak [45] was used to incorporate surface growth and oxidation effects. The corresponding set of PBEs for the ‘three-point’ method, which tends to reduce diffusion at the expense of stability, are written in the form

$$\frac{dn_i}{dt} = \frac{A_{i-1} I_{i-1} n_{i-1}}{m_{i-1}} + \frac{B_i I_i n_i}{m_i} + \frac{C_{i+1} I_{i+1} n_{i+1}}{m_{i+1}}. \quad (6)$$

In the above equations,  $I_i = dm_i/dt$  is the surface mass addition (or subtraction) rate for the  $i$ -th section and  $A_i$ ,  $B_i$  and  $C_i$  are size dependent parameters. If a purely geometric grid is used, as in present case, then the spacing factor ( $f_s$ ) is constant for all values of  $i$ :

$$f_s = m_{i+1}/m_i = m_i/m_{i-1}. \quad (7)$$

By setting conservation equations for three moments, Park and Rogak [45] obtained expressions for the parameters  $A_i$ ,  $B_i$  and  $C_i$  for a purely geometric grid. For boundary bins, namely  $i = 1$  and  $i = N_{\text{Bin}}$ ,

$$\begin{aligned} C_1 &= 0, & A_{N_{\text{Bin}}} &= 0, \\ A_1 &= 1/(f_s - 1), & B_1 &= -1/(f_s - 1), \\ B_{N_{\text{Bin}}} &= f_s/(f_s - 1), & C_{N_{\text{Bin}}} &= -f_s/(f_s - 1) \end{aligned} \quad (8)$$

and for  $2 \leq i \leq N_{\text{Bin}} - 1$ ,

$$\begin{aligned} B_i &= \begin{cases} -\frac{f_s}{f_s - 1} \operatorname{erf} \left( \frac{1}{4} \frac{d \ln n_i}{d \ln m_i} \right), & \frac{d \ln n_i}{d \ln m_i} \leq 0 \\ -\frac{1}{f_s - 1} \operatorname{erf} \left( \frac{1}{4} \frac{d \ln n_i}{d \ln m_i} \right), & \frac{d \ln n_i}{d \ln m_i} > 0 \end{cases} \\ A_i &= \frac{f_s - B_i(f_s - 1)}{f_s^2 - 1} \\ C_i &= -(A_i + B_i). \end{aligned} \quad (9)$$

Hence, particle splitting depends on the instantaneous slope of the population distribution at a given  $i$  which reduces the numerical diffusion. Bhatt and Lindstedt [35] noted that the above formulation may become unstable under strongly oxidative conditions. However, for the current, comparatively fuel rich case ( $\phi = 2.2$ ) of Kronholm and Howard [37] and Marr et al. [36, 46], no such difficulties were encountered. In agreement with earlier studies, the active site density was taken to be  $2.32 \times 10^{19}$  sites/m<sup>2</sup> [1] and the value for the proportionality constant indicating the fraction of surface sites available for chemical reaction, follows the functional form proposed by Kazakov et al. [47]

$$\alpha_s = \frac{1}{2} \left[ \tanh \left( \frac{8168}{T_{\text{max}}} - 5.74 \right) + 1 \right] \quad (10)$$

with the constant factor changed from 4.57 to 5.74 to account for experimental differences such as residence time [35]. The value for  $\alpha_s$  was evaluated at a temperature of 1550 K. The latter value was selected as an intermediate value between the WSR temperature of 1630 K and the PFR value of 1520 K. The PFR was also subject to radial stratification as shown by Marr [46] and uncertainties prevail regarding the choice of the appropriate temperature.

The level of agreement obtained with the experimental data obtained by Marr et al. [46] at a PFR temperature of 1520 K is shown in Figure 13. The computations have not been time shifted and the experimental data represents the sum of both soot and tar contents. The current computations consider soot particles from a size corresponding to pyrene upwards and no attempt was made to characterize the size classes in terms of soot or tar. For all computations, the residence time in the WSR was assumed to be 7.6 ms and the temperature 1630 K [46]. The corresponding results obtained at the higher PFR temperature of 1620 K are shown in Figure 14. The total mass of soot and tar is also shown in the lower right hand panel. An estimate of the total soot mass in the system suggest that an optimal value of the van der Waals enhancement factor

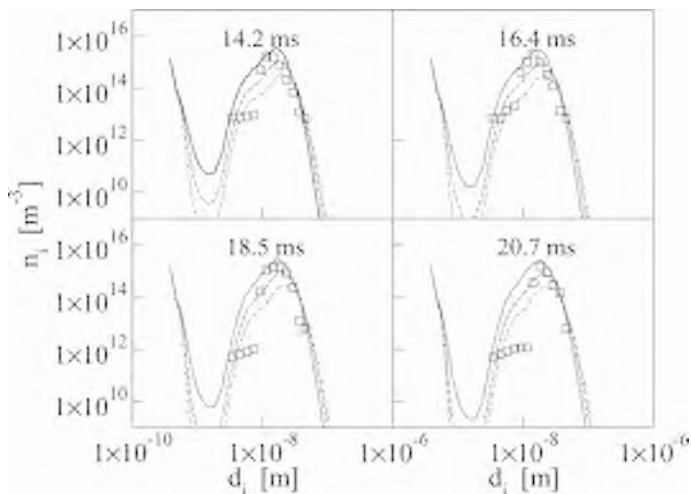


Figure 13. Soot number densities computed for the WSR/PFR configuration of Kronholm and Howard [37] at  $\phi = 2.2$  and a temperature of 1520 K. The times correspond to the time in the PFR section with a residence time in the WSR of 7.6 ms. The solid line corresponds to a unity van der Waals enhancement factor ( $C_d$ ), the dashed line a value of 3 and the dot-dashed line to a value of 9.

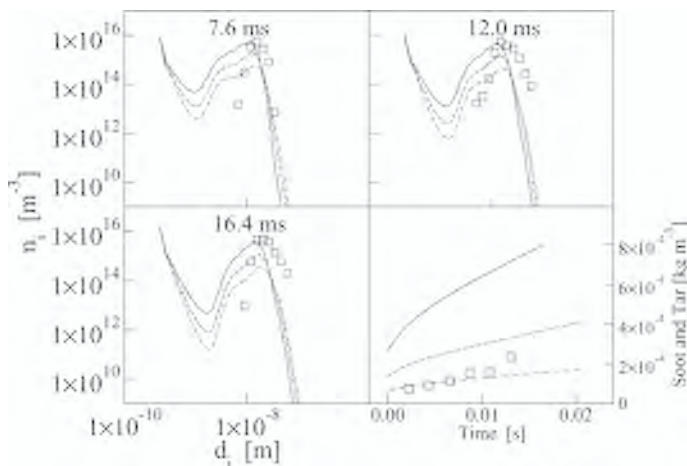


Figure 14. Soot number densities computed for the WSR/PFR configuration of Kronholm and Howard [37] at  $\phi = 2.2$  and a temperature of 1620 K. The times correspond to the time in the PFR section with a residence time in the WSR of 7.6 ms. The lines correspond to those given in Figure 13. The bottom right hand panel shows the corresponding evolution of the total soot mass for the different values of  $C_d$  compared to measurements by Marr [46].

is in the range 3 to 9 and it is evident that coagulation has a strong impact on the available surface area for mass growth. However, the computed number densities do suggest a lower value and, accordingly, uncertainties regarding the appropriate value of  $C_a$  prevail. Also, as mentioned above, the PFR data [46] suggests some radial stratification of the temperature and, rather than fine-tuning parameter values, the same value for  $\alpha_s$  was used for both sets of computations.

The above findings are not inconsistent with the study of Bhatt & Lindstedt [35] who compared the current approach against the WSR/PFR data obtained by Manzello et al. [48]. The computed PSD were in good agreement with experimental data away from sooting limits. However, the prediction of the impact of temperature suggested that the sooting limit for the case  $\phi = 2.0$  was lower than the experimental value of 1558 K. The current related experimental study suggests that for similar residence times in the WSR ( $\approx 10$  ms [48] and  $\approx 7.6$  ms [37]) the PSD is reasonably well reproduced at the lower temperature of 1520 K and uncertainties in the the temperature measurements [35, 48], which impact the value of  $\alpha_s$ , can not be ruled out as a contributing factor.

## 6. CONCLUSIONS

The current work has derived improved rate constant data for key reaction channels involved in the oxidation of two-ringed aromatic species. The work suggests that the current approach based on quantum mechanically determined PES of key channels can be used to estimate rate constants for the current rather complex systems. The derived rate constants were combined with a reaction class based approach for additional reactions and evaluated against data obtained for naphthalene oxidation in a PFR. The full closure was subsequently combined with a fixed sectional method and applied to compute the evolution of the PSD of soot obtained in a WSR/PFR device. The work shows that the main oxidation channels are well represented and that the  $C_9H_7 + O_2$  reactions have an important role in determining the product distribution of single ringed aromatics. The computed soot PSDs suggest that reasonable agreement may be obtained under the current conditions. However, the work also suggests that further experimental data sets are essential in order to refine current predictive methods.

## ACKNOWLEDGEMENT

The authors are grateful for the financial support of the CEC under the FlameSOFC project, the EOARD, under award FA8655-06-1-3052, and BP Global Fuels Ltd. The preliminary computations performed by Mark Potter and Jayesh Bhatt are also gratefully acknowledged.

## REFERENCES

1. M. Frenklach, H. Wang, Detailed Mechanism and Modelling of Soot Particle Formation in Combustion: Mechanisms and Models, 1st ed., Springer-Verlag, 1994.

2. H. Wang, M. Frenklach, *Combust. Flame* 110 (1997) 173-188.
3. R. P. Lindstedt, L. Q. Maurice, M. P. Meyer, *Faraday Discuss.* 119 (2001) 409-432.
4. H. Richter, J. B. Howard, *Phys. Chem. Chem. Phys.* 4 (2002) 2038-2055.
5. R. P. Lindstedt, K. A. Rizos, *Proc. Combust. Inst.* 29 (2003) 2291-2298.
6. A. Laskin, A. Lifshitz, *Proc. Combust. Inst.* (1998) 313-320.
7. J. L. Emdee, K. Brezinsky, I. Glassman, *J. Phys. Chem.* 96 (1992) 2151-2161.
8. S. D. Klotz, K. Brezinsky, I. Glassman, *Proc. Combust. Inst.* 27 (1998) 337-344.
9. R. P. Lindstedt, L. Q. Maurice, *Combust. Sci. Technol.* 120 (1996) 119-167.
10. C. R. Shaddix, *An Experimental Study of the High Temperature Oxidation of 1-Methylnaphthalene*, Ph.D. thesis, Princeton University, Princeton NJ (1993).
11. H. Pitsch, *Proc. Combust. Inst.* 26 (1996) 721-728.
12. S. Gail, P. Dagaut, *Combust. Sci. Technol.* 5 (2007) 813-844.
13. K. Mati, A. Ristori, G. Pengloan, P. Dagaut, *Combust. Sci. Technol.* 179 (2007) 1261.
14. M. J. Frisch, G. W. Trucks, H. B. Schlegel, G. E. Scuseria, M. A. Robb, J. R. Cheeseman, J. A. Montgomery, T. Vreven, K. N. Kudin, J. C. Burant, J. M. Millam, S. S. Iyengar, J. Tomasi, V. Barone, B. Mennucci, M. Cossi, G. Scalmani, N. Rega, G. A. Petersson, H. Nakatsuji, M. Hada, M. Ehara, K. Toyota, R. Fukuda, J. Hasegawa, M. Ishida, T. Nakajima, Y. Honda, O. Kitao, H. Nakai, M. Klene, X. Li, J. E. Knox, H. P. Hratchian, J. B. Cross, V. Bakken, C. Adamo, J. Jaramillo, R. Gomperts, R. E. Stratmann, O. Yazyev, A. J. Austin, R. Cammi, C. Pomelli, J. W. Ochterski, P. Y. Ayala, K. Morokuma, G. A. Voth, P. Salvador, J. J. Dannenberg, V. G. Zakrzewski, S. Dapprich, A. D. Daniels, M. C. Strain, O. Farkas, D. K. Malick, A. D. Rabuck, K. Raghavachari, J. B. Foresman, J. V. Ortiz, Q. Cui, A. G. Baboul, S. Clifford, J. Cioslowski, B. B. Stefanov, G. Liu, A. Liashenko, P. Piskorz, I. Komaromi, R. L. Martin, D. J. Fox, T. Keith, M. A. Al-Laham, C. Y. Peng, A. Nanayakkara, M. Challacombe, P. M. W. Gill, B. Johnson, W. Chen, M. W. Wong, C. Gonzalez, J. A. Pople, *Gaussian 03, Revision D.02*, Gaussian, Inc., Wallingford, CT, 2004.
15. A. D. Becke, *J. Chem. Phys.* 98 (1993) 5648-5652.
16. C. Lee, W. Yang, R. G. Parr, *J. Phys. Rev.* B41 (1988) 785-789.
17. A. G. Baboul, L. A. Curtiss, P. C. Redfern, K. Raghavachari, *J. Chem. Phys.* 110 (1999) 7650-7657.
18. J. L. Durant, *Chem. Phys. Lett.* 256 (1996) 595-602.
19. J. L. Durant, C. M. Rohlfing, *J. Chem. Phys.* 98 (1993) 8031-8036.
20. NIST Computational Chemistry Comparison and Benchmark Database, NIST Standard Reference Database Number 101 (2006). Available from <http://srdata.nist.gov/cccbdb>.
21. B. J. McBride, S. Gordon, *Computer Program for Calculating and Fitting Thermodynamic Functions*, NASA RP 1271, (1998).
22. M. L. Potter, *Detailed Chemical Kinetic Modelling of Propulsion Fuels*, Ph.D. thesis, Imperial College, London (2003).
23. X. Zhong, J. W. Bozzelli, *J. Phys. Chem. A* 102 (1998) 3537-3555.
24. V. Mokrushin, V. Bedanov, W. Tsang, M. Zachariah, V. Knyazev, *CHEMRATE* version 1.5.2, National Institute of Standards and Technology, Gaithersburg, MD (2006).
25. J. C. Corchado, Y. Y. Chuang, P. L. Fast, W. P. Hu, Y. P. Liu, G. C. Lynch, K. A. Nguyen, C. F. Jackels, A. F. Ramos, B. A. Ellingson, B. J. Lynch, V. S. Melissas, J. Villa, I. Rossi, E. L. Coitino, J. Pu, T. V. Albu, R. Steckler, B. C. Garrett, A. D. Isaacson, D. G. Truhlar, *POLYRATE* version 9.5, Department of Chemistry and Supercomputer Institute, University of Minnesota (2007).
26. D. Ben-Amotz, D. Herschbach, *J. Phys. Chem.* 94 (1990) 1038-1047.
27. B. S. Rabinovitch, D. C. Tardy, *J. Chem. Phys.* 45 (1966) 3720-3730.

28. B. C. Garrett, D. G. Truhlar, *J. Chem. Phys.* 70 (1979) 1593-1598.
29. D. H. Lu, T. N. Truong, V. S. Melissas, C. G. Lynch, Y. P. Liu, B. C. Garrett, R. Steckler, A. D. Issacson, S. N. Rai, G. C. Hancock, J. G. Lauderdale, T. Joseph, D. G. Truhlar, *Comput. Phys. Commun.* 71 (1992) 235-262.
30. Y. P. Liu, C. G. Lynch, T. N. Truong, D. Lu, D. G. Truhlar, B. C. Garrett, *J. Am. Chem. Soc.* 115 (1993) 2408-2415.
31. J. C. Corchado, Y. Y. Chuang, E. L. Coitino, B. A. Ellingson, D. G. Truhlar, GAUSSRATE version 9.5, Department of Chemistry and Supercomputer Institute, University of Minnesota (2007).
32. K. M. Leung, R. P. Lindstedt, *Combust. Flame* 102 (1995) 129-160.
33. J. L. DiNaro, J. B. Howard, W. H. Green, J. W. Tester, J. W. Bozzelli, *J. Phys. Chem.* 104 (2000) 10576-10586.
34. C. R. Shaddix, K. Brezinsky, I. Glassman, *Proc. Combust. Inst.* 24 (1992) 683-690.
35. J. S. Bhatt, R. P. Lindstedt, *Proc. Combust. Inst.* (2009) 10.1016/j.prcoi.2008.06.201.
36. J. A. Marr, L. M. Giovane, J. P. Longwell, J. B. Howard, A. L. Lafleur, *Combust. Sci. Technol.* 101 (1999) 301-309.
37. D. Kronholm, J. Howard, *Proc. Combust. Inst.* 28 (2000) 2555-2561.
38. M. A. Oehlschlaeger, D. F. Davidson, R. K. Hanson, *Proc. Combust. Inst.* 31 (2007) 211-219.
39. R. D. Kern, Q. Zhang, J. Yao, B. S. Jursic, R. S. Tranter, M. A. Greybill, H. Kiefer, *Proc. Combust. Inst.* (1998) 143-150.
40. A. Ristori, P. Dagaut, A. E. Bakali, G. Pengloan, M. Cathonnet, *Combust. Sci. Technol.* (2001) 223-256.
41. S. Kumar, D. Ramkrishna, *Chem. Eng. Sci.* 51 (1996) 1311-1332.
42. A. Kazakov, M. Frenklach, *Combust. Flame* 114 (1998) 484-501.
43. R. Jullien, R. Botet, *Aggregation and fractal aggregates*, World Scientific, Singapore, 1987.
44. U. O. Kooylu, G. M. Faeth, T. L. Farias, M. G. Carvalho, *Combust. Flame* 100 (1995) 621-633.
45. S. H. Park, S. N. Rogak, *J. Aerosol Sci.* 35 (2004) 1385-1404.
46. J. A. Marr, PAH Chemistry in a Jet Stirred/Plug Flow Reactor System, Ph.D. thesis, MIT, Cambridge MA (1993).
47. A. Kazakov, H. Wang, M. Frenklach, *Combust. Flame* 100 (1995) 111-120.
48. S. L. Manzello, D. Lenhart, A. Yozgatligl et al., *Proc. Combust. Inst.* 31 (2007) 675-683.
49. P. Frank, J. Herzler, T. Just, C. Wahl, *Proc. Combust. Inst.* (1994) 833-840.
50. K. A. Rizos, Detailed Chemical Kinetic Modelling of Homogeneous Systems, Ph.D. thesis, Imperial College, London (2003).
51. N. M. Marinov, M. J. Castaldi, C. F. Melius, W. Tsang, *Combust. Sci. Technol.* 128 (1997) 295-342.



# Soot oxidation

J.S. Lighty, V. Romano, A.F. Sarofim

Department of Chemical Engineering  
University of Utah

*Abstract: The focus of this paper is on soot oxidation. Much of the research on reducing soot emissions has focused on soot formation since it is more important to eliminate the formation of soot than to oxidize it once it is formed. However, soot oxidation is important for the control of soot emissions from both diesel engines and gas turbine combustors for which the extent of soot burnout for the soot formed often exceeds 90 percent. The oxidation of soot under higher O<sub>2</sub> conditions is especially important in these systems. A review of the literature discussing the oxidation of soot and the implications of soot structure is given. A few studies have indicated the role of fragmentation in soot oxidation under fuel lean conditions. Scanning mobility particle size results suggest that there is a regime of temperature and O<sub>2</sub> in which significant particle fragmentation occurs; the fragmentation needs to be quantified inasmuch as the resulting increase in surface area needs to be taken into account in modeling soot oxidation.*

## 1. INTRODUCTION

The reduction of particulate matter (PM), especially PM with an aerodynamic diameter of 2.5  $\mu\text{m}$  or less (PM<sub>2.5</sub>) is important for a variety of reasons. First, PM<sub>2.5</sub> can deposit more efficiently in the lungs as compared to larger particles and is potentially more damaging [1]. Studies have linked PM<sub>2.5</sub> to adverse health effects [2-4] and, specifically, the soot content of PM has been linked to dysrhythmia [4]. In addition to health effects, soot emissions are a concern for climate forcing and cloud formation [5, 6].

The formation of soot and its subsequent oxidation involves a series of complicated steps, including: gas-phase precursor formation; particle inception; particle aggregation; and aggregate oxidation. While fundamental understanding of each step is important, jet and diesel engine manufacturers are primarily concerned with the oxidation of soot since, under normal circumstances, approximately 90% or more of the soot formed is ultimately destroyed [7]. Soot oxidizes by reactions with molecular oxygen (O<sub>2</sub>), oxygen radical (O), and hydroxyl radical (OH).

Numerous studies have investigated the oxidation of soot and various models have been proposed [7, 8]. This paper will discuss the literature regarding soot oxidation with an emphasis on O<sub>2</sub> oxidation and fragmentation. For such studies, a two-stage burner is especially effective at investigating these mechanisms as it separates soot formation and oxidation mechanisms [9, 10]. Results from this system, illustrating evidence of fragmentation of particles under fuel lean conditions will be presented.

## 2. BACKGROUND

### 2.1. OH oxidation kinetics

Fenimore and Jones [11] investigated the rate of oxidation of soot for low oxygen gas partial pressures and temperatures from 1530 to 1890K and were the first to report the importance of OH as a major oxidation reactant. They attributed their faster rates, as compared to those predicted by Lee, et al.[12], to OH oxidation. Their observations suggested that about 10% of the collisions of OH with the soot resulted in carbon removal. Neoh [10] also demonstrated that OH was the dominant oxidant in near stoichiometric and rich conditions. The rate of OH oxidation can be described by a collision efficiency  $\Gamma_{OH}$ , representing the fraction of collisions of OH with soot particles that resulted in the removal of a carbon atom, times the collision frequency, i.e.,

$$w = 1.29 \times 10^3 \Gamma_{OH} P_{O_2} \sqrt{T} \quad (1)$$

where  $w$  is the rate in  $\text{kg}/\text{m}^2\text{s}$  and  $P$  is partial pressure in atmospheres. Neoh found the collision efficiency,  $\Gamma_{OH}$ , to be 0.13 and relatively independent of equivalence ratio and height within the flame. Other researchers have investigated the role of OH oxidation and have found similar collision efficiencies, as shown in Table 1. This literature suggests that OH oxidation is the predominant reaction mechanism, particularly under fuel-rich conditions. In addition, some oxidation occurs via collisions with O. Table 1 also shows collision efficiencies for O oxidation. For example, for temperatures greater than 1900K, Vierbaum and co-workers found a collision efficiency of 10% for O [13]. Given that OH oxidation is usually the predominant mechanism, and the fact that considering only  $\text{O}_2$  oxidation will yield lower rates, other investigators have

Table 1. Collision efficiencies for OH and O radical soot oxidation

Investigator(s)	Experimental conditions	OH collision efficiency	O collision efficiency
Fenimore and Jones [11]	Two-stage type burner	0.10	
Page and Ates [42]	Two-stage burner	0.25	
Roth [43]	Diaphragm-type shock tube	0.13-0.31	
Bradley and Dixon-Lewis [44]	Premixed flat-flame burner, graphite carbon	0.28	0.50
Puri and Santoro [45]	Methane/butane flame	0.14	
Xu and Faeth [46]	Diffusion flame with acetylene	0.06-0.32; avg. 0.14	
Neoh [10]	Two-stage burner	0.13	
Vierbaum [13]	Shock tube		0.10
Garo et al. [47]	Methane laminar diffusion flame	0.10	

used a purposely high power-law  $O_2$  rate equation to make average allowance for the contribution of OH [14].

Work using a Scanning Mobility Particle Sizer (SMPS) and a two-stage burner also showed a collision efficiency of 0.13 [8]. Under a fuel-rich condition of 1.2 equivalence ratio, it was found that OH accounted for over 80% of the oxidation with the remainder accounted by O. The concentration of the radicals was determined by ChemKin modeling.

## 2.2. $O_2$ oxidation

The reaction rate of pyrolytic graphite with  $O_2$  developed by Nagle-Strickland-Constable (NSC) [15], with parameters fitted to data obtained over a temperature range of 1273 to 2273K, and updated to temperatures up to 2673K [16] is a widely used expression for  $O_2$  oxidation. The rate equation, in g-atoms of carbon  $cm^{-2} sec^{-1}$ , is based on the assumption that reaction occurs on sites with two widely different reactivities and is given by:

$$w = \left[ \left( \frac{k_A P_{O_2}}{1 + k_Z P_{O_2}} \right) x + k_B P_{O_2} (1-x) \right] \quad (2)$$

where P is the partial pressure, k are the reaction constants, and x is the fraction of sites A, the more reactive sites. The fraction of x is given by:

$$x = \left[ 1 + \frac{k_T}{k_B P_{O_2}} \right]^{-1} \quad (3)$$

The coefficients for the equation are given in Table 2. Park and Appleton [17] found that the NSC expression fit their shock tube data for reactions of carbon black with  $O_2$  over a temperature range of 1700 to 4000K, but the expression underestimated the rates at high temperatures. Graphitic materials have two types of sites, the reactive edge carbons and the less reactive basal planes. Although NSC is an empirical equation, it is consistent with such a physical model with sites 'A' corresponding to the edge sites and sites 'B' to the basal plane. It is also known that graphites can be ordered by thermal annealing, which would correspond to the transformation of A to B sites. This interpretation of sites A and B in the NSC correlation is supported by the experimental data of Acharya and Olander [18] on the rates of oxidation of the edge (prism) sites and basal plane of graphite. However, they found that as a result of pit-

Table 2. Empirical parameters for Nagle and Strickland-Constable Model [16],  $k = A e^{-E/RT}$ .

Rate constant	E, kcal/mole	A	Units for A
$k_A$	30	20	$g\text{-atom cm}^{-2}\text{sec}^{-1}\text{atm}^{-1}$
$k_B$	15.2	$4.46 \times 10^{-3}$	$g\text{-atom cm}^{-2}\text{sec}^{-1}\text{atm}^{-1}$
$k_T$	97	$1.51 \times 10^5$	$g\text{-atom cm}^{-2}\text{sec}^{-1}$
$k_Z$	4.1	21.3	$\text{atm}^{-1}$

ting as the reaction proceeded, the rate constants, at low temperatures ( $< 1700\text{K}$ ), for the basal plane could be measured only at very low partial pressures or short times. As the edge (prism) planes became exposed through pitting, the rate constants quickly approached that of the edge plane. For practical purposes, the lower reactivity corresponding to the basal plane became important only at higher temperatures ( $> 2500\text{K}$ ), where thermal annealing was important, consistent with the NSC correlation. This dominance of the edge sites at normal combustion conditions accounts for the relatively small reactivities of soots. Regions of amorphous carbon will affect the reactivity, a factor that is yet to be studied.

Additional data on oxidation of soot include those by Higgins et al. [19] who used a tandem differential mobility analyzer to determine the reactivity of soot from an ethylene flame reacted in a quartz flow reactor over the temperature range of 1073 to 1393 K and found oxidation rates comparable to NSC. Lee et al. [12] introduced a power-law form to investigate  $\text{O}_2$  oxidation, where,

$$w = A e^{-\frac{E_a}{RT}} T^{0.5} p^{0.1} \quad (4)$$

with  $n=1$ . Other researchers [20] also found that the rate was first order with respect to oxygen and a function of conversion, taking into account the surface area and conversion. Yezerets, et al. [21] found a reaction order between 0.6 and 0.7 depending upon the soot sample. Recent studies have shown that carbon reactivity can be modeled by sites with a distribution of adsorption and desorption energies [22]. This approach leads to a rate expression with a fractional order for gaseous oxygen [23], rationalizing the power-law correlations which have been used for decades.

A summary of some of the rate constants is provided in Figure 1 which provides an update to Figure 4 in Stanmore, et al. [7]. As seen in this figure, for many cases, rates are comparable for a given surface area and oxygen partial pressure. Since the oxygen dependence of the rate postulated by different researchers varied, the comparison in Figure 1 was carried out for a particle pressure of oxygen of 0.1 atm. However, as discussed in [7] and above, the role of structure is not clear and further work is warranted.

### 2.3. Structural effects

The structure of soot has been shown to change as a function of conditions of formation and fuel; in addition, oxidation kinetics have been shown to vary greatly as a result of these changes. For example, investigators have shown that fuel type also has an effect on ordering [24] of microstructures of grapheme within soot particles as determined by high resolution transmission electron microscopy (HRTEM). This is shown in Figure 2, for work at the University of Utah in a premixed, flat flame burner using ethylene and benzene. The data were taken at equivalent heights above burner, 10 mm, and C/O ratios, 0.89. For the ethylene flame, the soot nanostructure was complex, with a low degree of order corresponding to more complex aliphatic/aromatic structure with a large variety of aromatics. Soot derived from benzene fuel revealed a fairly well developed "onion-ring" structure which was much more ordered with a nar-

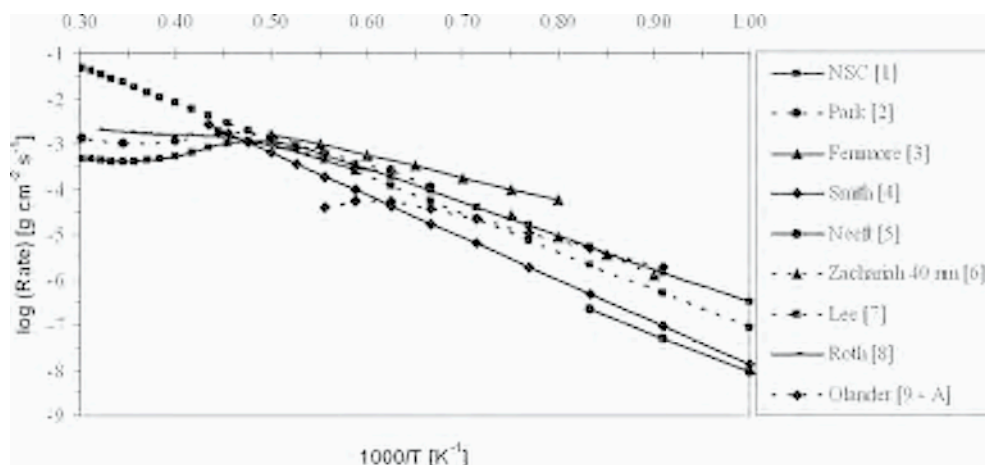


Figure 1. Analysis of data from others and compared to NSC. Conditions are for a constant oxygen partial pressure of 0.1 atm and 120 m<sup>2</sup>/g. Table 3 lists the references for the figure and conditions.

Table 3. References for the work shown in Figure 1 and experimental conditions.

1. Nagle and Strickland-Constable [15]	Carbon rods electrically heated with an oxygen jet on the surface over temperature range of 1170-2270K
2. Park & Appleton [17]	Channel black and furnace combustion black, in a shock tube over 1700-3000K and 0.05-0.13 atm of oxygen
3. Fenimore & Jones [11]	Ethylene-flame-produced soot, in a two-stage burner over 1530-1800 k and 0.0001-0.3 atm of oxygen
4. Smith [48]	Porous and non-porous carbons over 580-2200K
5. Neeft [20]	Flame soot and diesel soot
6. Zachariah [19]	Ethylene diffusion Flame soot generated in a Santoro-type burner
7. Lee [12]	Hydrocarbon laminar diffusion flame
8. Roth [43]	Shock wave
9. Olander [18]	Basal (A) and prism (B) faces of pyrolytic graphite with a rotating disk contactor

rower aromatic system. These conclusions are consistent with the observations by Vander Wal and co-workers [25, 26] who also saw a higher reactivity for benzene soot which was attributed to the smaller size of the graphene layers and higher degree of

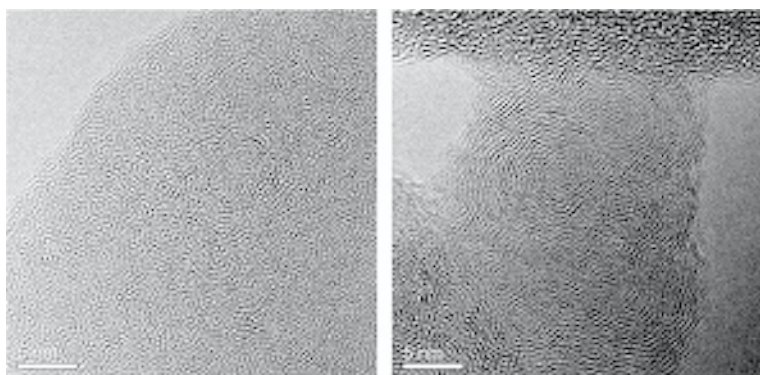


Figure 2. HRTEM from ethylene (left) and benzene flames (right) in a premixed burner.

curvature, since edge size carbon is more reactive than carbon in the basal plane. Their work extended toward investigating atmospheric aerosols and potentially using HRTEM as a means for source apportionment [27].

As shown in Figure 3, the ordering of carbon increased with heat treatment and also with extent of reaction [25, [28]. As determined by the use of HRTEM and image analysis [29], the ordering of a synthetic char (Spherocarb) increased with extent of burnout. Hurt and co-workers [30] found that such increased ordering was potentially responsible for particle shrinkage. Soot collected in a large JP-8 pool fire by Shaddix et al. [31] exhibited a larger interplanar spacing indicative of possible lower temperatures within the soot formation region. Zhu, et al. [32] showed a difference in soot morphology for diesel engine particulates under different load conditions. In comparing diesel soot samples and carbon black, Vander Wal et al. [33] found that samples that were obtained from a urban bus running a real route and an engine under high load both exhibited particles with partial voids and hollow interiors. In comparison, a low-load engine yielded soot exhibiting shorter lamella with tortuosity, possibly promoting higher

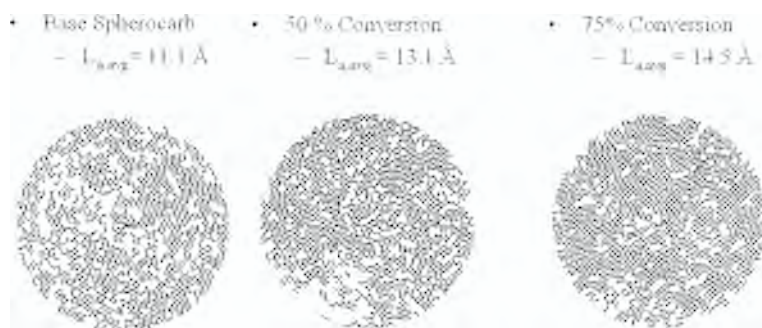


Figure 3. Illustration of how the ordering of carbons varies with combustion conditions, in this case increasing with carbon conversion [49].

porosity. Upon partial oxidation, this sample began to exhibit the development of hollow interiors. Other researchers [34, 35] have shown selective internal hollowing by oxidation consistent with a concept that the external layers of the primary particles in carbon black had more ordered graphene layers parallel to the surface while the center of the particles are disordered and more reactive. Such behavior is also expected with soots that also show preferential ordering of the surface layers with graphene layers.

Du [36] also showed that soots have surface area, perhaps explaining further the different in reactivities. Surface areas initially corresponding to the superficial area of about  $60 \text{ m}^2/\text{g}$  increased with increasing conversion, up to  $700\text{--}800 \text{ m}^2/\text{g}$  (Figure 4). Clearly internal surface area needs to be factored into the calculation of particle reactivity.

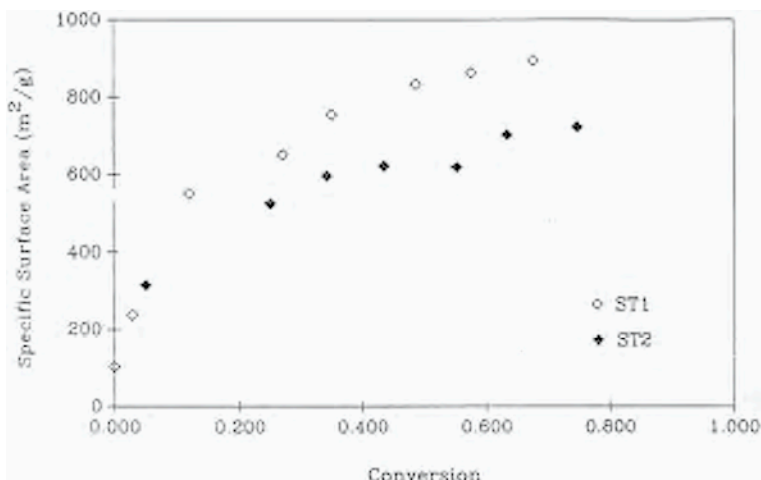


Figure 4. Increased surface area with increased conversion [36].

## 2.4. Fragmentation

Neoh [10, 37] reported fragmentation, as evidenced by an increase in particle number under equivalence ratios of 0.85 and 0.95, from her two-burner system using optical methods, electrical mobility, and electron microscopy. The increase was not seen for fuel-rich conditions. The increase in particle number was attributed to oxygen penetrating the pores of soot particles, causing internal burning, which, in turn, caused the soot aggregates to break apart. The fragmentation occurred at approximately 80% soot burnout. Garo and Prado [38] also saw evidence of soot fragmentation, occurring at approximately 75% burnout. Furthermore, Harris and Maricq [39] included fragmentation in their simulation of diesel engine particle size distributions. They found that allowing fragmentation improved the predictions and especially noteworthy was that no parameters were adjusted.

### 3. EXPERIMENTAL SYSTEM AND RESULTS

As previously discussed, the oxidation of soot independent of soot formation can be studied using a two-stage burner. A schematic of the two-stage burner is shown in Figure 5 with further details provided in [9]. In the two-stage burner, soot is formed in the first burner, passes through a mixing zone where additional air is added depending upon the equivalence ratio to a second burner. The second burner is then used to oxidize the soot under both fuel rich and fuel lean conditions. Data were taken using a SMPS with a size range down to 3 nm and a dilution probe was used to collect the samples and minimize coagulation within the probe.

Using this system, we have also showed fragmentation [9] for ethylene premixed flames. Figure 6 shows results for both fuel rich (left, equivalence ratio 1.2) and fuel lean (right, equivalence ratio 0.8) conditions. Samples were taken at the end of the flame. As seen in the fuel rich case, the initial mean particle size from the first burner

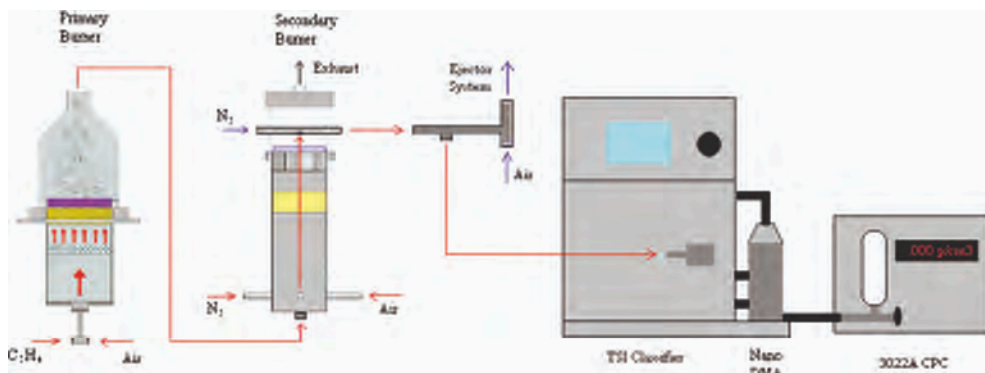


Figure 5. Two-stage burner set up.

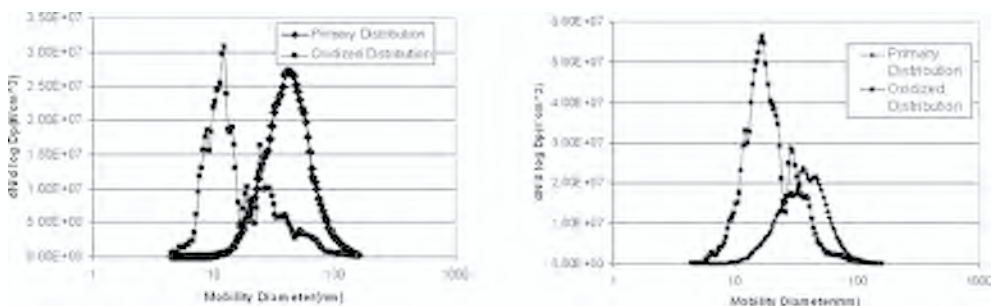


Figure 6. Results for fuel rich (left) and fuel lean (right) experiments. Diamonds data are initial particle size distributions (prior to the second burner) and squares show PSDs after the second burner.

was larger as compared with that obtained after the second burner. Furthermore, the number of particles declined. As previously discussed data from this system at different temperatures suggested that OH, and to a lesser extent O, oxidation was occurring with a collision efficiency representative of previous studies, 0.13-0.15. However, for the fuel lean case, the initial mean particle size distribution was larger than the oxidized but the number of particles increased. This suggests that the aggregates fragmented creating more particles of smaller mean diameter. In addition, TEM measurements showed single particles versus aggregates for the fuel lean conditions.

Additional experiments were performed using two differential mobility analyzers (DMA) systems, to define the size distribution of the particles being studied and to characterize the size distribution after oxidation. In this system, the first DMA separated a specific size range of particles from the first premixed, ethylene burner which were then passed to the second burner. These size-segregated particles were then burned under fuel lean conditions (equivalence ratio was 0.80). A second DMA was then used to size the particles and the condensation particle counter (CDC) was used to count the number. These data are shown in Figure 7. As seen in this plot, the initial particle size distribution was rather narrow and around the set point of 60 nm. However, the post oxidation particle size distribution is much broader and in a smaller size range, suggesting that the mobility diameter was simply not getting smaller, but particles of different sizes were formed. Clearly, the number of particles increased dramatically, even though the burnout was approximately 39% (the scales are such that the areas are proportional to total particle number). The increase in the particle number was a factor of almost 30.

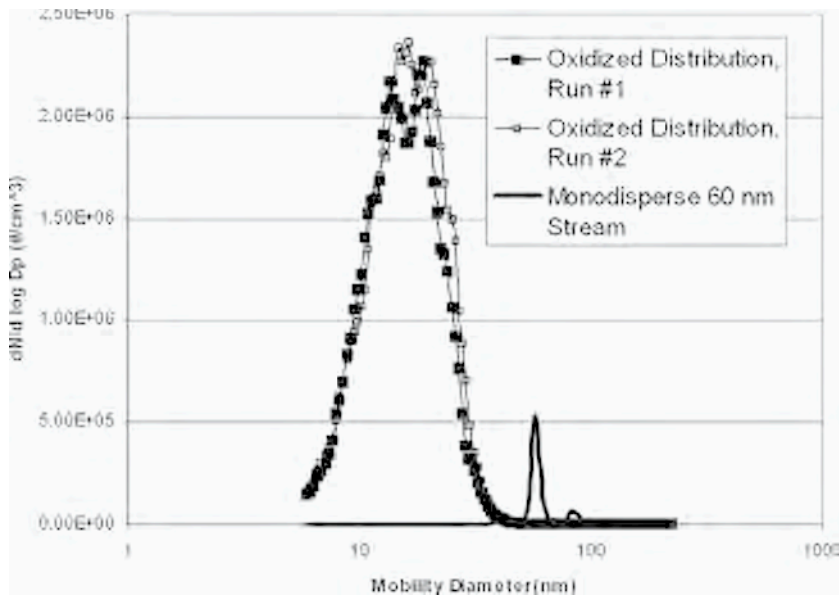


Figure 7. Initial particle size approximately 60 nm, shown as black line. Two runs are shown after oxidation under fuel-lean conditions.

Additional data were obtained as a function of height above burner. These data were obtained at equivalence ratios from 0.9 to 0.7. The flame with ethylene as a fuel had with a peak temperature of 1580K. As seen in Figure 8 at an equivalence ratio of 0.80, at HAB from 1.5-2.5 mm, the diameter of the particles decreased while the number increased, indicating fragmentation or a change in structure resulting in a change in mobility diameter. At higher heights above burner, 2.75 mm, the particle size distributions shifted toward larger sizes with a reduction in number, consistent with the preferential oxidation of the smaller particles. Figure 9 shows the total number concentration of all particle diameters as a function of HAB for the different fuel lean con-

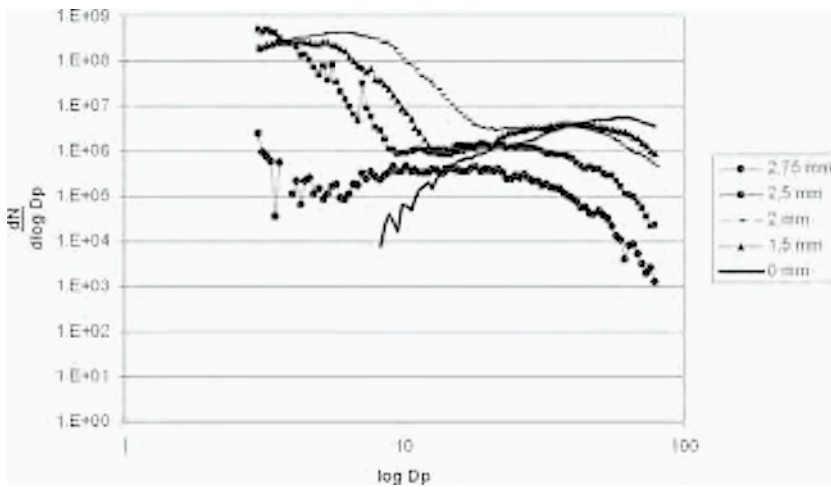


Figure 8. Particles size distributions as a function of height above burner for ethylene soot oxidation at an equivalence ratio of 0.80.

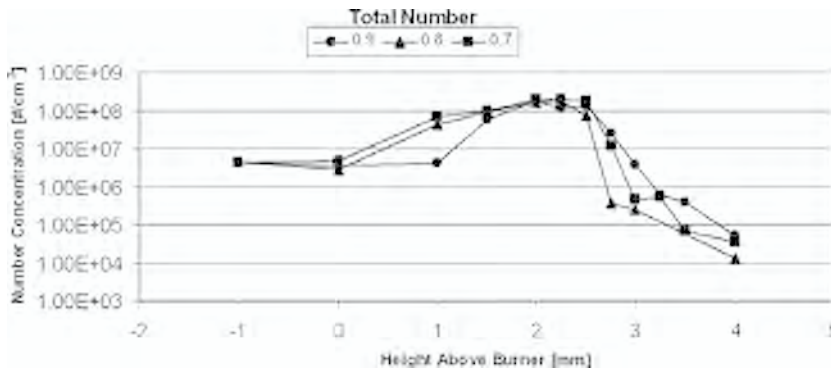


Figure 9. Total number concentration as a function of height above burner for different equivalence ratios.

ditions. As seen in this figure, the total number of particles almost immediately increased by an order of magnitude, followed by a decrease in number. The analysis shown in Figure 10 illustrates the mass of soot as a function of height above burner. The analysis includes figures less than 80 nm in mobility diameter, the higher diameter limit of the nano-SMPS. Current work is investigating the role of larger mobility diameter particles. As seen in this figure, the change in mass is relatively constant throughout the time that the particle number increases, accompanied by a decrease in mean particle size (Figure 11). At approximately 2 mm HAB, the rate of oxidation increases significantly, probably as a result of increased surface area with the smaller particles or

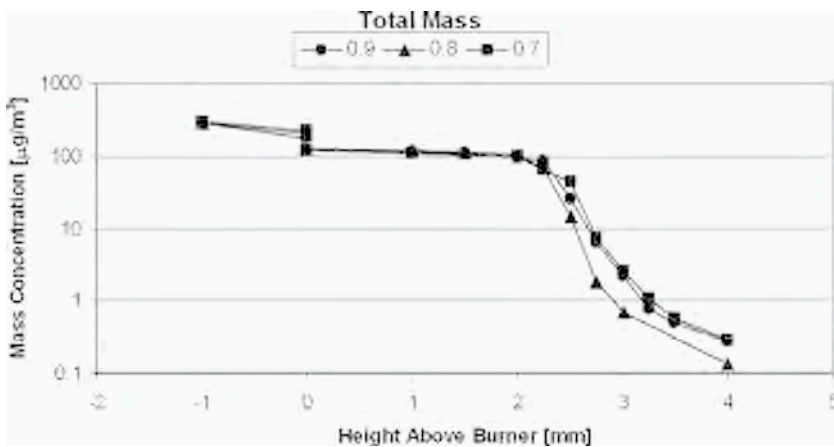


Figure 10. Mass concentration as a function of height above burner for different equivalence ratios.

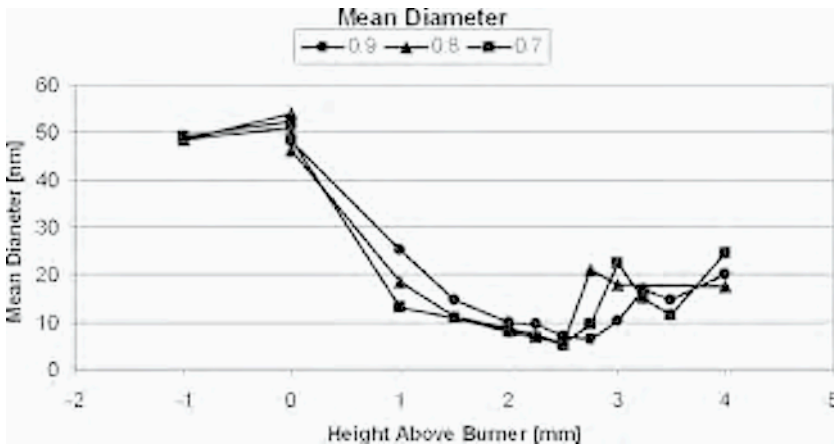


Figure 11. Mass mean diameter as a function of height above burner for different equivalence ratios.

other resulting structural changes. This is evident from the change in mass mean diameter with height, shown in Figure 11, which passes through a minimum at a height at which the rate of decay of mass is at a maximum.

#### 4. DISCUSSION

There remain several questions regarding the changes in structure of the soot under fuel lean conditions. Namely, are there inherent structural changes which perhaps could cause particles to fragment, as discussed in Vander Wal [33] or is the oxidation of bridges between particles the cause of increased particle numbers? An alternative to the oxidation of bridges between particles in an aggregate as the mechanism for fragmentation is the internal oxidation of the particles, opening up the pores, and leading to particle fragmentation. Evidence for internal oxidation of soot and carbon black is provided, for example by the data of Du [36] that shows the increase in total surface area as a function of soot burnout. This increase in internal area contributes to both increases in rate of reaction and also, possibly, to percolative fragmentation. Kerstein and Niksa [40] used percolation theory to define the fragmentation of porous solids. Their results suggested that a critical porosity exists for fragmentation as shown in Table 4. Based on the observations of change in porosity with oxidation, their predictions suggest that at porosities of about 0.70, fragmentation of char will occur.

Further work is needed to discern the actual mechanism; however, there are many ways to describe the potential fragmentation of soot particles. Harris and Maricq [39] and Jiang [41] used a fragmentation rate,

$$S_i = Ai^x \quad (5)$$

where  $i$  is the number of primary particles in an agglomerate and  $x$  is roughly the inverse of the fractional dimension,  $D_f$ . The factor  $A$  was determined from data on fragmentation as a function of equivalence ratio. The fact that fragmentation occurred at some step-change in oxidation was accounted for. The simulation results suggest that particle size does decrease while particle number increased.

Table 4. Prediction of critical porosity for fragmentation based on pore structure [40].

Pore Network Structure	Cylinder	Sphere	Complement of a sphere
Square/cubic	0.785	0.965	0.476
Close packed	0.907	0.960	0.260
Random network	0.675	0.968	0.705
Random network & pore size	0.682	—	0.697

## 5. CONCLUSIONS

Current research on soot oxidation suggests that the role of OH oxidation is well-defined and represented by a surface reaction with OH. In addition, OH oxidation is faster as compared with O<sub>2</sub>. Oxygen gas oxidation has been well-represented by power-law kinetics; however, research has indicated that importance of structure in oxidation, both initial structure of soot and changes in structure during oxidation. These changes might account for higher oxidation rates due to increased surface area and should be further examined in order to determine the proper reaction rates. Significant fragmentation of soot occurs with increased burnout, probably as the result of the increased porosity resulting from internal burning.

## ACKNOWLEDGMENTS

This research is supported by the University of Utah Center for the Simulation of Accidental Fires and Explosions (C-SAFE), funded by the Department of Energy, Lawrence Livermore National Laboratory, under subcontracts B341493 and B524196. Additional support from the National Science Foundation (Grant No. 0304433) and the Strategic Environmental Research and Development Program (SERDP) are appreciated. The HR-TEM in Figure 2 is the result of work done by Mr. Carlos Andres Echavarria.

## REFERENCES

1. J. S. Lighty, A. F. Sarofim, J. M. Veranth, *J. Air Waste Manage. Assoc.* 50 (2000) 1565-1618.
2. D. W. Dockery, e. al., *New Engl. J. Med.* 329 (1993) 1753-1758.
3. A. Peters, D. W. Dockery, J. E. Muller, M. A. Mittleman, *Circulation* 2001, 2810-2815.
4. P. E. Tolbert et al., *J. Exposure Anal. Environ. Epidemiol.* 10 (2000) 446-460.
5. J. E. Penner, D. H. Lister, D. J. Griggs, D. J. Dokken, M. McFarland, *Aviation and the Global Atmosphere: A Special Report of the Intergovernmental Panel on Climate Change, Working Groups I and II*, 1999.
6. F. M. Luther et al., in UCRL-52861, Lawrence Livermore National Laboratory: Livermore, CA, 1979.
7. B. R. Stanmore, J. F. Brillhac, P. Gilot, *Carbon* 39 (2001) 2247-2268.
8. B. S. Haynes, in *Fossil Fuel Combustion: A Source Book*, W. Bartok, A. F. Sarofim, (Eds.) Wiley, New York, 1991, pp. 261-326.
9. C. J. Merrill. The oxidation and fragmentation of soot in a two-stage burner. University of Utah, Salt Lake City, 2005.
10. K. G. Neoh, J. B. Howard, A. F. Sarofim, in *Particulate Carbon: Formation during Combustion*, G. W. S. D. C. Siegl, (Ed.) Plenum, New York, 1981, pp. 261-277.
11. C. P. Fenimore, G. W. Jones, *J. Phys. Chem.* 71 (1967) 593-597.
12. K. B. Lee, M. W. Thring, J. M. Beer, *Combust. Flame* 6 (1962) 137-145.
13. R. Vierbaum, P. Roth, *Proc. Combust. Inst.* 29 (2002) 2423-2429.
14. K. M. Leung, R. T. Lindsedt, W. P. Jones, *Combust. Flame* 87 (1991) 289-305.

15. J. Nagle, R. F. Strickland-Constable, in Proc. of the Fifth Carbon Conference, Pergamon Press, 1962, pp. 154-164.
16. J. R. Walls, R. F. Strickland-Constable, Carbon 1 (1964) 333-338.
17. C. Park, J. P. Appleton, Combust. Flame 20 (1973) 369-379.
18. T. R. Acharya, D. R. Olander, Carbon 11 (1973) 7-18.
19. K. J. Higgins, K. Jung, D. B. Kittelson, J. T. Roberts, M. R. Zachariah, J. Phys. Chem. 106 (2002) 96-103.
20. J. P. A. Neeft, Nijhuis, T. Xander, Smakman, Erik, Makkee, Michiel, Moulijn, Jacob A., Fuel 76 (1997).
21. A. Yezerets, N. W. Currier, D. H. Kim, H. A. Eadler, W. S. Epling, C. H. F. Peden, Appl. Catal., B 61 (2005) 120-129.
22. B. S. Haynes, T. G. Newbury, Proc. Combust. Inst. 28 (2000) 2197-2204.
23. R. H. Hurt, B. S. Haynes, Proc. Combust. Inst. 30 (2004) 2157-2164.
24. M. Alfè, B. Apicella, R. Barbella, A. Tregrossi, A. Ciajolo, Proc. Combust. Inst. 31 (2007) 585-591.
25. R. L. V. Wal, A. J. Tomasek, Combust. Flame 136 (2004) 129-140.
26. R. L. V. Wal, A. J. Tomasek, Combust. Flame 134 (2003) 1-9.
27. M. D. Hays, R. L. V. Wal, Energy & Fuels 21 (2007) 801-811.
28. A. P. Palotàs, L. C. Rainey, A. F. Sarofim, J. B. V. Sande, P. Ciambelli, Energy & Fuels 10 (1996) 254-259.
29. A. P. Palotàs, L. C. Rainey, C. J. Feldermann, A. F. Sarofim, J. B. V. Sande, Microsc. Res. Tech. 33 (1996) 266-278.
30. R. H. Hurt, A. F. Sarofim, J. P. Longwell, Combust. Flame 95 (1993) 430-432.
31. C. R. Shaddix, A. B. Palotas, C. M. Megaridis, M. Y. Choi, N. Y. C. Yang, Int. J. Heat Mass Transfer 48 (2005) 3604-3614.
32. J. Zhu, K. O. Lee, A. Yozgatligil, M. Y. Choi, Proc. Combust. Inst. 30 (2005) 2781-2789.
33. R. L. V. Wal, A. Yezerets, N. W. Currier, D. H. Kim, C. M. Wang, Carbon 45 (2007) 70-77.
34. J. B. Donnet, J. C. Bouland, Rev. Gen. Caoutch. 1964, 41.
35. F. A. Heckman, D. E. Harling, Rubber Chem. Technol. 39(1) (1966).
36. Z. Du. Kinetic modeling of carbon oxidation, MIT, 1990.
37. K. G. Neoh, J. B. Howard, A. F. Sarofim, Proc. Combust. Inst. 20 (1984) 951-957.
38. A. Garo, Lahaye, J., Prado, G., Proc. Combust. Inst. 21 (1986) 1023.
39. S. J. Harris, M. M. Maricq, J. Aerosol Sci. 33 (2002) 935-942.
40. A. R. Kerstein, S. Niksa, G., Proc. Combust. Inst. 20 (1984) 941-949.
41. P. Jiang, Modeling of Aerosol Dynamics in Flames and Exhaust Plumes. University of Utah, Salt Lake City, 2003.
42. F. M. Page, F. Ates, Adv. Chem. Ser. 166 (1978) 190-197.
43. P. Roth, O. Brandt, S. V. Gersum, Proc. Combust. Inst. 21 (1990) 1485-1491.
44. D. Bradley, G. Dixon-Lewis, S. El-Din Habik, E. M. J. Mushi, Proc. Combust. Inst. 20 (1984) 931-940.
45. R. P. R. J. Santoro, K. C. Smyth, Combust. Flame 97 (1994) 125-144.
46. F. Xu, A. M. El-Leathy, C. H. Kim, G. M. Faeth, Combust. Flame 132 (2003) 43-57.
47. A. Garo, G. Prado, J. Lahaye, Combust. Flame 79 (1990) 226-233.
48. I. W. Smith, Fuel 7 (1978) 409-414.
49. A. W. Kandas, Structural evolution of carbon during oxidation, MIT, Cambridge, 1997.

# Size resolved soot surface oxidation kinetics

A.A. Lall, M.R. Zachariah

*Departments of Mechanical Engineering and Chemistry and Biochemistry*

*University of Maryland, College Park, MD 20742*

*Ph: 301-405-4311, Fax: 301-314-9477*

*Email: mrx@umd.edu*

*Abstract: In this paper we summarize a number of our soot surface-oxidation kinetics measurements. The measurement methods include: (a) direct visualization using electron microscopy and (d) tandem differential mobility analysis (TDMA). Arrhenius kinetic analysis allows us to extract the oxidation rate, and activation energies for flame, diesel and bio-diesel soot as well as the role of metals in soot oxidation.*

*For flame soot oxidation, a activation energy of 148 kJ/mol was found at low temperatures (< 800K). Using the TDMA method, the activation energy of soot oxidation in air was equal to 163 kJ·mol<sup>-1</sup> over the temperature range 800°-1120° C. The reasons for the difference in activation energies at low and high temperatures are discussed. The activation energies were 114, 109, and 108 kJ mol<sup>-1</sup> for the 10, 50, and 75% load diesel nanoparticles sampled directly from a medium duty diesel engine exhaust over the temperature range of 800 1140 °C. The reason for the low activation energies of diesel soot compared to that of flame soot is attributed to the presence of metals in the diesel fuel, possibly coming from lubricating oils. To test the influence of metals in soot oxidation, cerium was added to diesel fuel and iron was added to flame soot in two separate studies. It was found that the addition of iron to a flame reduced the activation energy significantly from ~162±3 kJ/mol to ~116±3 kJ/mol, comparable with diesel engine generated soot with an activation energy ~ 110 kJ/mol.*

*The oxidation kinetics for bio-diesel was found to be ~6 times higher than that of regular diesel fuel in the temperature range of 700 to 825 °C.*

## 1. INTRODUCTION

Soot is produced by incomplete combustion or pyrolysis of hydrocarbon fuels and is a useful material termed “carbon black” which is widely used in printing inks, and in rubber and plastic products. The global market demands carbon black in millions of tons every year. On the other hand, soot is released into the atmosphere as an undesirable product by several natural and man-made combustion processes such as wood burning, diesel engine exhaust emissions [1], power plants, air craft emissions[2]. Soot is known to be harmful to the respiratory tract if inhaled, especially when the particles are less than 5 μm in diameter. Recently it has been revealed that carbon soot emission from combustion is an important factor leading to climate change [3, 4]. A typical transmission electron microscope (TEM) image of a soot aggregate is shown in Figure 1. The aggregate is composed of individual particles termed primary particles of about 30 nm in diameter.

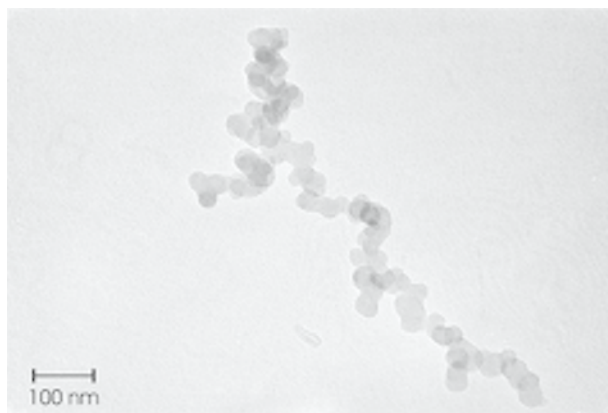


Figure 1. A typical transmission electron microscope (TEM) image of an atmospheric aggregate is shown in Figure 1. The aggregate is composed of individual particles called primary particles of about 30 nm in diameter (reproduced from [54]).

Ultimately it is the surface of the soot that communicates to the surrounding environment, either for future growth, oxidation, or as a substrate for heterogeneous nucleation. These surface processes and the reaction kinetics determine soot size, composition, mass and the surface area. This implies that we need both the tools, and methodology to characterize surface processes on soot. In what follows, we describe size resolved soot surface oxidation kinetics in a systematic manner. The soot surface oxidation kinetics in the presence of metals is also discussed. Studies are shown for three types of soot: diesel soot, bio-diesel soot and flame soot (carbon black).

### 1.1. Soot formation and growth

Soot formation is a multi-stage process which includes nucleation, coagulation, surface growth, aggregation, agglomeration and oxidation. At the initial nucleation stage the first condensed phase materials form from the gas species originating from the pyrolysis or oxidation products of the fuel molecules such as acetylene and PAH. This process leads to very small particles with diameters up to 2 nm which have only a small fraction of the total particulate mass ultimately formed.

Once soot nucleation has occurred, the amount of soot generated is determined by the competing processes of growth through the addition of gas-phase species, and destruction through oxidation by  $O_2$ , OH, and other gas-phase oxidants. In order to understand and model soot production, it is necessary to obtain a molecular level understanding of these processes. This includes, as a start, measuring oxidation and growth rates as functions of temperature and chemical composition. It is the purpose of the current study to present a new method for obtaining information on fundamental surface processes on nanoparticles, starting with the oxidation of soot in air.

### 1.1.1. Flame soot

The description of flame soot used in this study is as follows. The flame soot was generated in a Santoro type diffusion burner [5]. It consists of two concentric tubes: a 4 inch outer brass cylinder for air flow, and a 0.5 inch inner brass tube for fuel flow. Between the concentric tubes there is a honeycomb and a stack of beads and mesh to provide a uniform exit flow profile for the air. A 10 inch high glass cylindrical shroud is placed on the outer tube to prevent the flame from being disturbed by outside air currents. For the experiments presented in this paper, ethylene was used at a flow rate of  $85 \text{ cc min}^{-1}$  to produce a flame 50 mm high.

### 1.1.3. Diesel and bio-diesel soot

Biodiesel is a generic term that refers to various fatty-acid mono-esters that can be used as diesel fuel. It is made from the conversion of triglyceride (vegetable oil and animal fats) to esters (primarily methyl esters) via various esterification processes [6]. Biodiesel has very similar physical properties to conventional diesel fuel [7]; but is renewable, non-toxic, and biodegradable [8]. Biodiesel is the only alternative fuel to have fully completed the health effects testing requirements of the Clean Air Act. It may be made from a variety of different vegetable oils or animal fats. For example, in Germany rapeseed oil based biodiesel, RME, is the most abundant [9], whereas soy based biodiesel, SME, the fuel used in this study is the most widely used in the United States [10].

In general it is reported that biodiesel has a less adverse effect on human health than petroleum based diesel fuel. Schröder et al. [9] and Krahl et al. [11] reported that mutagenicity of biodiesel particulate emissions is much lower than that of petroleum based fuel. Finch et al. [12], in their study of rats exposed to biodiesel emissions, showed only modest health effects at the highest exposure level. Even these effects were described as “no-observed-adverse-effect” within the uncertainties of their study.

Europe is the most significant biodiesel producer in the world [13, 14]. Germany and France lead the production having tax benefit for producing biodiesel. In South America, Brazil launched national program for biodiesel in 2002 [15], leads the production and considers export of biodiesel to other countries [16].

## 1.2. Size measurement and resolution

Soot aerosol consists of a wide size distribution of nanoparticles and nanoparticle aggregates. The soot surface reaction kinetics is a strong function of the size and the surface area. Thus to study the size dependent reaction kinetics, a method is needed to separate soot nanoparticles with respect to the size.

Aerosol size distributions are commonly measured using differential mobility analyzer (DMA) that measures the electrical mobility of the particles. The electrical mobility is translated into mobility diameter for spherical particles by equating the drag on spheres to the electric force inside the DMA. For non-spherical particles such as soot nanoparticle aggregates (with low fractal dimension  $< 2$ ), it is generally accepted that

the surface area calculated using the mobility diameter is close to the actual surface area of the particles[17].

### 1.2.1. Differential mobility analyzer

A differential mobility analyzer (DMA), illustrated schematically in Figure 2, is a class of ion-mobility spectrometer, which sizes or selects particles based on electrical mobility. The DMA consists of a center rod upon which a voltage is placed and an outer cylinder held at ground. The sheath flow is introduced at one end and flows coaxially between the outer cylinder and the inner rod. Aerosol particles enter the DMA in a thin ring adjacent to the outer cylinder, and the charged particles are attracted or repelled by the potential on the center rod. Near the end of the center rod is a slit through which particles of the desired electric mobility pass, while particles of higher electric mobility (particles that are smaller and/or more highly charged) hit the center rod upstream of the sample slit and particles of lower electric mobility (larger and/or

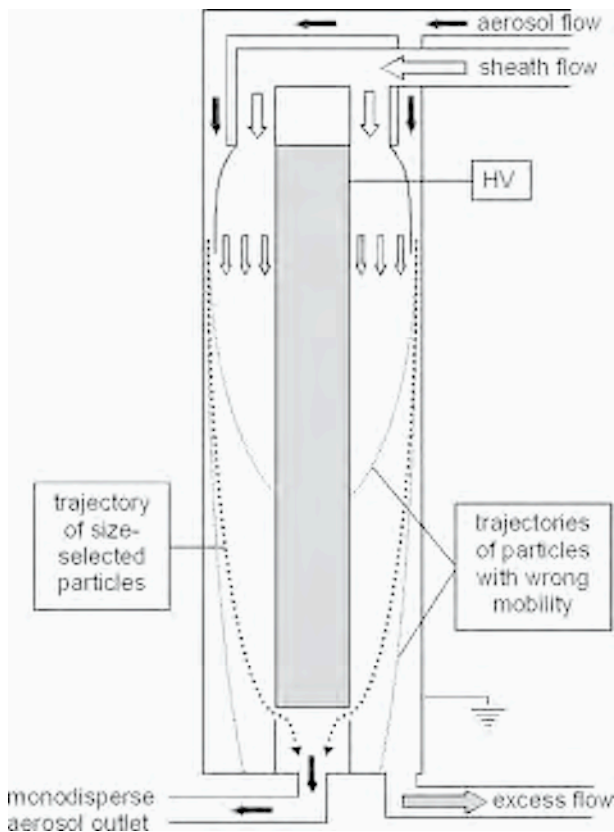


Figure 2. Schematic of differential mobility analyzer.

uncharged) pass out of the DMA through the excess output flow. If the DMA is used to select a particular particle size, the center rod is held fixed at a voltage and the sample output flow will contain only particles of a single electric mobility. In this mode the DMA acts like a high resolution band-pass filter. For the particle sizes used in the current experiments the vast majority of charged particles in a steady state charge distribution will carry a single charge, so the output aerosol will be essentially monodisperse. If the DMA is used to measure the size distribution of a particle stream, the voltage on the center rod is stepped and the sample output flow is monitored for particle concentration as a function of applied voltage.

As shown in Figure 1, soot particles are geometrically complicated agglomerates of smaller particles, therefore the meaning of size used here is not straightforward. In the free-molecular and transition regimes, where the particle size is smaller than or comparable to the mean free path of the gas molecules ( $\sim 65$  nm for air at room temperature and one atmosphere pressure), it has been shown that the particle mobility is inversely proportional to the mass transfer rate to the particle, which in turn is proportional to the gas-accessible surface area of the particle [18-20]. Therefore, for the particle sizes under consideration in this work, the DMA will select particles based on their accessible surface area. The particle size is still described by a mobility diameter,  $D_p$ , which is the diameter of a spherical particle of equivalent mobility, and therefore of the same surface area.

### 1.2.2. Tandem differential mobility analyzer

The term “tandem” is used for a DMA (usually identical) which is placed downstream of another DMA. The tandem DMA (TDMA) system can be used for online monitoring of size changes occurring by some process condition imposed between the two DMA's. In this manner the TDMA system operates much like a MS-MS system. For example, a DMA classified aerosol stream can be passed through a tubular furnace at an elevated known temperature whereby the aerosol undergoes a change in mobility due to processes like oxidation, sintering, or change in charge state [21]. The resulting mobility change can be measured by a second DMA, which can be related to a change in size or charge. If the process time and chemistry is known then the size change can be used to measure the process kinetics.

Figure 3 shows the TDMA system [22] for measuring oxidation kinetics of freshly generated and size-selected soot nanoparticles. The TDMA method as described in section 2.2, was advantageous because for freshly generated soot, effects of aging and transport/diffusion of the reactant can be minimized.

### 1.3. Soot oxidation and kinetics

We define the mass based oxidation rate as:

$$\frac{dm_s}{dt} = -\dot{w}A_s \quad (1)$$

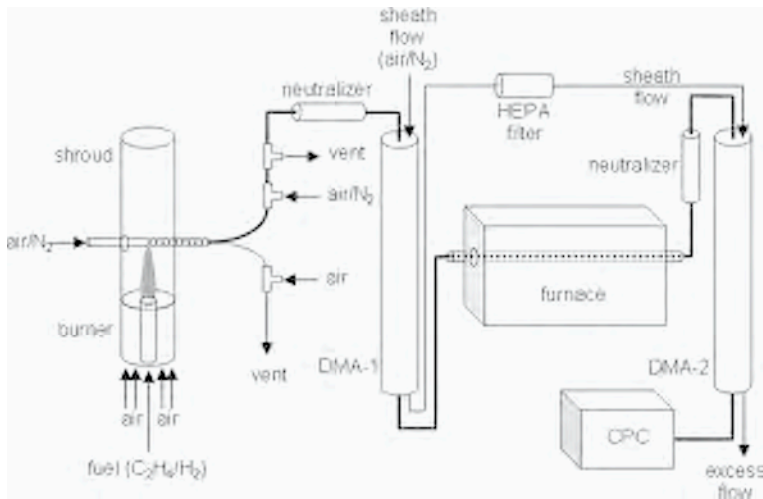


Figure 3. Soot oxidation kinetics measurements using TDMA system. The bold line indicates the path taken by the soot aerosol particles.

with  $A_s$  the soot surface area and  $\dot{w}$  is the mass-based surface specific rate, often modeled using a modified Arrhenius expression,

$$\dot{w} = AT^{1/2} \exp\left(\frac{-E_a}{RT}\right) \quad (2)$$

where  $A$  is size independent preexponential factor,  $E_a$  is an activation energy,  $R$  is gas constant, and  $T$  is temperature in Kelvin.

For a non-uniform axial-temperature profile in a flow reactor the diameter change can be integrated as a particle travels the length of the reactor:

$$\Delta D_p = 2 \int_0^X \frac{\dot{w}(x)\tau(x)}{\rho_s} dx \quad (3)$$

where  $x$  is the axial distance in the reactor tube and  $X$  is the length of the reactor tube. The dependence of the rate and residence time on horizontal position is a result of their dependence on temperature,

$$\frac{\dot{w}}{\rho_s} = A_{nm} \cdot [T(x)]^{1/2} \cdot \exp\left[-\frac{E_a}{RT(x)}\right] \quad (4)$$

$$\tau = \tau_0 \frac{T_0}{T(x)} \quad (5)$$

where  $A_{nm}$  is a different frequency factor for each initial soot particle size,  $E_a$  is the activation energy, and  $\tau_0$  is a characteristic residence time at temperature  $T_0$ . The residence time is calculated assuming laminar flow and a flow velocity equal to the peak volumetric flow velocity of  $4/3 u_m$ , where  $u_m$  is the mean flow velocity calculated from

the volume flow rate and the cross-sectional area of the flow tube. The flow velocity as a function of axial position can be written as

$$u(x) = \frac{4}{3} u_m \frac{T(x)}{T_w} \quad (6)$$

## 2. SOOT OXIDATION KINETICS MEASUREMENTS

Soot oxidation kinetics is measured by both offline and online methods: (a) the offline method employs direct visualization using TEM analysis, (b) the online method uses TDMA system.

### 2.1. Offline method: TEM observations

The soot oxidation was qualitatively visualized by Tanaka [23] using TEM analysis of diesel soot collected on a thin  $\text{Al}_2\text{O}_3$  plate. Tanaka [23] observed the size change of an agglomerate and found that each of the primary particles gets smaller as it is oxidized. In this section we extend Tanaka's [23] method and describe a method to quantify soot oxidation: An experimental protocol is described to measure the oxidation rate of soot particles at low temperatures ( $< 800$  K) using TEM image analysis.

#### 2.1.1. Method

The size-selected soot particles were deposited on TEM grids. A section of TEM grid containing a number of particles sufficient to provide statistically meaningful data was selected. A series of TEM images taken using a digital CCD camera from low to high magnification are shown in Figure 4. A map of the grid was made. The grid is then removed from the TEM and inserted into a furnace for a specified time and temperature. The soot particles on the TEM grid were oxidized in heated air for the given time and temperature. Analysis of the oxidation exposed grid used the same field of view as was used prior to oxidation using the procedure illustrated in Figure 4. The projected area change is related to the surface specific reaction rate for soot oxidation. The projected area determined using a public domain image program (NIH *Image*).

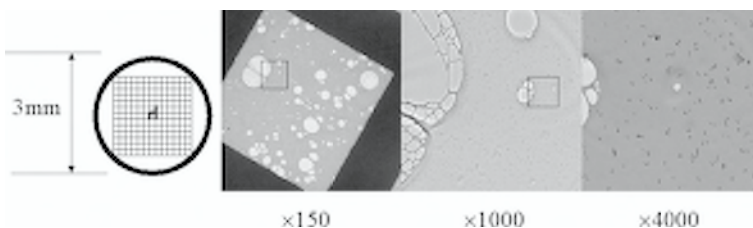


Figure 4. Maps of TEM images to track a field of view.

### 2.1.2. Visualization of soot oxidation- Tracking individual particles

Figure 5 shows examples of individual particles during oxidation at different cumulative oxidation time at 450 °C. Initial images of particles (a) and (e) were taken and those particles were tracked separately. The soot aggregates are composed of primary particles in 20-30nm size range. Clearly the primary particles are shown shrinking during this process, but we also observe that some changes in the aggregate morphology. The latter observation presumably has to do with how the particles find themselves anchored to the grid, and one might expect differences from what might occur in the gas phase. Most of the primary particles were observed to shrink evenly during oxidation. For these particular images an arm of the aggregate seemed to move during oxidation (Figures 5a-d) whereas the particle in Figures 5e-h shrank in size without significant changes in shape.

The individual particles can undergo different projected area reduction rates due to the following reasons:

- A. A portion of a particle can disappear during oxidation.
- B. The oxidation rate can be different due to differences in chemical composition for individual particles).

Thus, in the following sections, we track a group of particles rather than individual particles to quantify the oxidation rate.

### 2.1.3. Comment on hollow particles

Our more gradual evolving particle shape and size is in contrast to Heckman's [24] observation. He employed high temperature heat treatment (partial graphitization in an inert atmosphere) before carrying out an oxidation experiment. His work found very

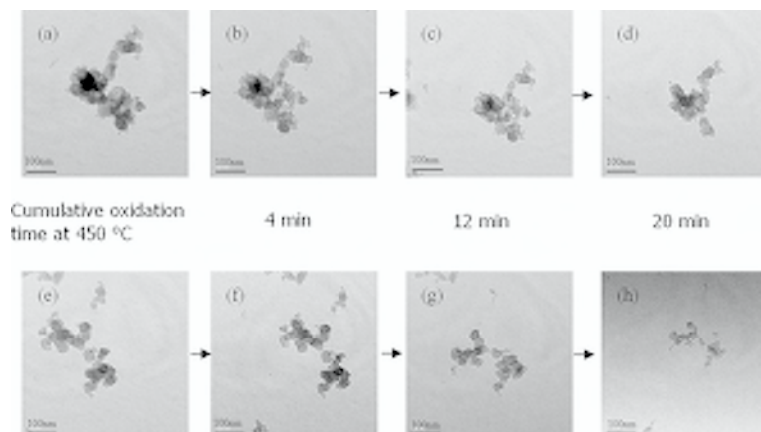


Figure 5. TEM images of individual particles during oxidation at different cumulative oxidation time at 450 °C.

little shrinking, but rather an internal hollowing out of the particles. He speculated that a more ordered graphitic layer structure, at the surface of the particles was stable against oxidation, and Gilot et al. [25] also reported internal oxidation of carbon black spherules after 60% burn-off at low temperature. We observed no selective hollowing of soot particles in this study, which we believe is related to the absence of a pre-graphitization process [26].

#### 2.1.4. Visualization of soot oxidation- Tracking a group of particles

A field of view containing about 100 particles was chosen for tracking during oxidation. In order to observe such a large number of particles in a single image the magnification used ( $\times 4000 \sim \times 5000$ ) is about 6 times lower than that used for tracking individual particles and is shown in Figure 6a. Figure 6b shows the image after oxidation in a furnace for 4 minutes at a furnace set temperature of  $450^\circ\text{C}$ . Qualitatively we see that particles are clearly shrinking, but some particles are oxidizing faster, and in some

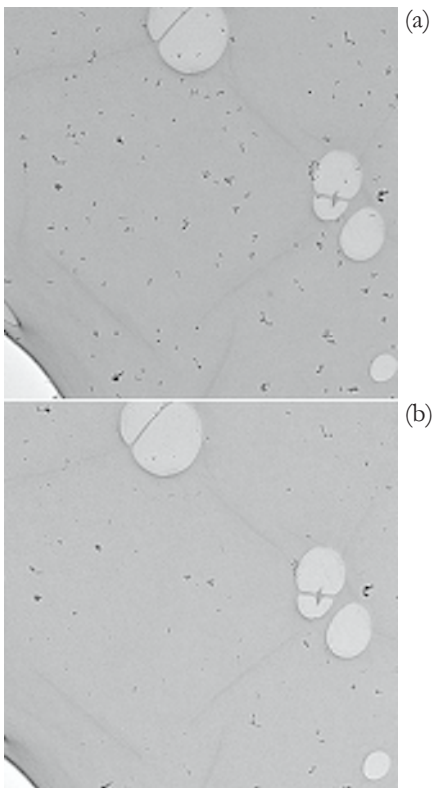


Figure 6. TEM images before and after oxidation for a group of particles. (a) Size classified soot particles before oxidation ( $d_m = 50\text{nm}$ ). (b) After oxidation (4min at  $450^\circ\text{C}$  of furnace set temperature).

cases particles disappeared entirely. These differences in oxidation rate would seem to indicate that even though all particles were sampled from a single location and size segregated with a DMA, they may not be chemically the same. Particles that disappeared were excluded manually during image analysis so that the exactly same group of particles could be tracked.

Figure 7 shows the resulting size distributions for particles in Figure 6 using the data analysis procedure described. Both the size distributions were broadened and shifted towards lower sizes. In the following section, the change in size is quantified by relating the projecting area equivalent diameter to the mobility equivalent diameter.

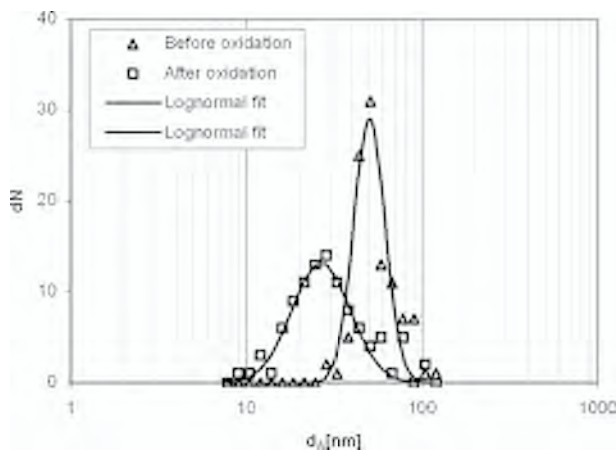


Figure 7. Size distributions based on projected area equivalent diameter for particles shown in Figure 6.

### 2.1.5. Projected area equivalent diameter vs. mobility equivalent diameter

The mobility equivalent diameter ( $d_m$ ) is based on the DMA measurements and the projected area equivalent diameter ( $d_A$ ) is based on the TEM measurements. In order to quantify these size changes, it is necessary to establish a relationship between the two diameters. The DMA was used to classify particles with mobility diameters: 50nm, 100nm, 130nm, and 150nm. The TEM samples for each selected size were taken. It is assumed that both  $d_A$  and  $d_m$  are orientation-averaged properties, since the agglomerates are expected to rotate randomly in a DMA column, and in an impactor. Figure 8a, shows size distributions of the TEM samples for a given mobility diameter as a function of  $d_A$ . Figure 8a shows that the selected mobility size from the DMA (50nm) coincides with the peak of the projected area equivalent diameter obtained by analyzing the particles on the TEM grid. The second peak (at 75nm) corresponds to particles of the same electrical mobility but with two charges. Figure 8b shows a mobility size distribution measured using the TDMA method with the furnace turned off. The peak, which is around 75nm in  $d_m$  as shown in Figure 8b, represents particles, which

were doubly charged when they passed through the DMA-1 but singly charged when they passed through the DMA-2.

The excellent agreement between Figure 8a,b confirm that  $d_m$  is effectively equivalent to  $d_A$  in the size ranges of interest to this study. The TEM data is noisier because we limited the analysis to only 100 particles, while the DMA effectively is sampling several orders of magnitude of particles. Similar results were obtained for mobility diameter 100, 130 and 150 nm. For these measurements, the relationship between  $d_m$  and  $d_A$  is shown in Figure 9. It is found that the mobility diameter scales linearly with the projected area equivalent diameter with a slope of unity.

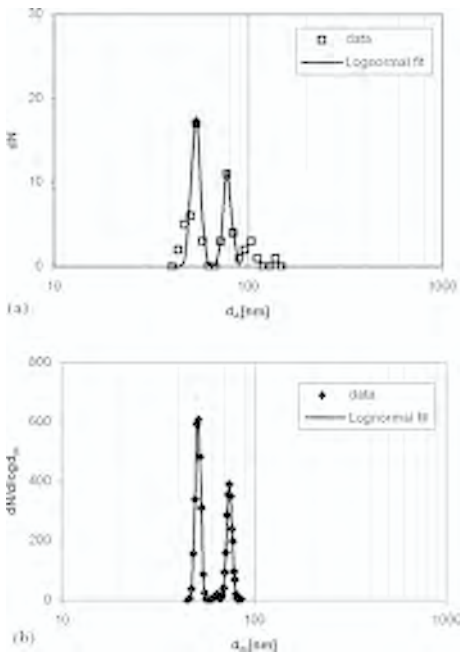


Figure 8. Comparison between size distributions measured as a function of projected area equivalent diameter ( $d_A$ ) and as a function of mobility equivalent diameter ( $d_m$ ) for a given mobility diameter selection ( $d_m=50\text{nm}$ ) by a DMA. (a) TEM measurement. (b) TDMA measurement.

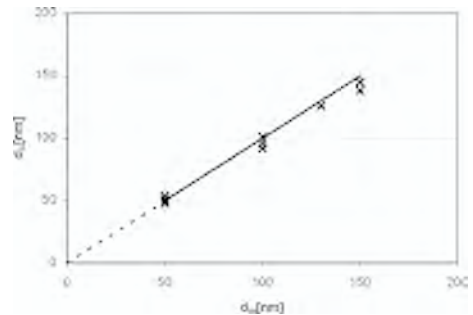


Figure 9. The relationship between projected area equivalent diameter ( $d_A$ ) and mobility equivalent diameter ( $d_m$ ) for soot agglomerates.  $d_m/2\lambda$  is the normalized particle diameter by  $2\lambda$ , where  $\lambda$  is the mean free path of the carrier gas.

### 2.1.6. Determination of the soot oxidation rate

As we see in the previous section,  $d_m$  and  $d_A$  are equal for the set of experiments discussed in this study. Thus  $d_A$  can be replaced by  $d_m$  for calculating the rate of oxidation.

The surface area for mass transfer of the soot particles in the free molecular regime is  $\pi d_m^2$ . By definition the effective density is

$$m_s = \rho_{\text{effective}} \frac{\pi d_m^3}{6} \quad (7)$$

After mass and area are expressed in terms of the mobility equivalent diameter, Eq. (1) becomes

$$\frac{dd_m}{dt} = -\frac{2\dot{w}}{\rho_{\text{effective}}} \quad (8)$$

The effective density is assumed constant and equal to 1800 kg/m<sup>3</sup> (Kennedy [27]). Eq. (8) can be integrated over time as follows:

$$\Delta d_m = \Delta d_A = \int_0^t -\frac{2\dot{w}(t)}{\rho} dt \quad (9)$$

Using experimental data on the change in  $d_A$  at different furnace set of temperatures, a least-square fit was carried out to determine  $A$  and  $E_a$  for  $\dot{w}$ .

For the low temperatures (< 800K) discussed in this study, the soot oxidation activation energy was found to be ~148 kJ/mol. The surface area specific oxidation rate of soot particles at temperatures below 800 K is higher than found in prior studies: A comparison is discussed in the next section. Further work is necessary to identify what caused the difference between low and high temperature oxidation rates.

## 2.2. Online method

### 2.2.1. Size selected TDMA measurements

Soot particles were generated in an ethylene diffusion flame. Samples for TEM analysis were collected directly in the flame or in the sampling stream. The TEM images shows that the soot particles were agglomerates of spherical particles, with primary particle diameter of about 20-30 nm.

The size distributions were measured using a DMA. The DMA was also used as an electrostatic classifier to separate particles in a given mobility diameter range. The mono-disperse soot particles were oxidized in the presence of air at a high temperature inside a tube furnace. The resulting changes in mobility diameter were measured using a second DMA. The experimental system is shown in Figure 3.

In order to check for size reduction due to thermal effects such as particle collapse, rearrangement, or evaporation, experiments were run with the furnace set at 1100° C using nitrogen as the soot sampling carrier gas, the dilution gas, and as the sheath gas for the two DMAs. All other conditions were kept the same as for the oxidation experiments.

The TDMA scans for the oxidation in air of the three initial soot particle sizes are presented in Figure 10. The initial ~1% decrease in  $D_p$  at 500° C for all three particle sizes was most likely due to volatile or semi-volatile material evaporating off of the particles, and the size decrease due to oxidation is calculated relative to the particle sizes at 500° C. An increase in the width, or spreading, of the size distributions as oxi-

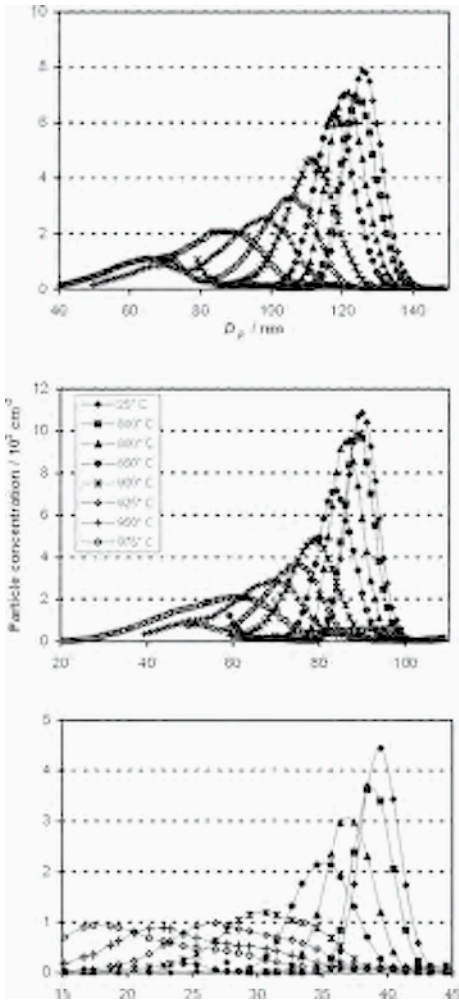


Figure 10. TDMA soot oxidation results in air for furnace settings of 25° to 975° C (see legend). Results from higher furnace settings are omitted for clarity. (a) 40 nm initial particle size, (b) 90 nm initial particle size, and (c) 126 nm initial particle size.

dation occurs can be seen in Figure 10, along with the appearance of a bimodal distribution at higher temperatures for the 40 nm particles. What appears to be a bimodal distribution for the larger particles is actually a blending of the peak due to singly-charged particles with the peak due to doubly-charged particles.

The decrease in particle size assuming spherical particles and no density change during oxidation is

$$\Delta m_s = \frac{\pi \rho_s}{6} (D_{p,i}^3 - D_{p,f}^3) \tag{9}$$

where  $m_s$  is the soot particle mass,  $\rho_s$  is the mass density of a soot particle, and  $D_p$  is the mobility diameter of a soot particle. Assuming spherical soot particles and integrating Eq. 1 over the residence time  $\tau$ , we get

$$\dot{W} = \frac{\rho_s (D_{p,i} - D_{p,f})}{2\tau} \quad (10)$$

Eq. 10 suggests that the surface specific rate is linearly proportional to the change in diameter. Thus given experiments at a series of constant temperatures and a known residence time in the reaction region, one can calculate the activation energy and pre-exponential factor using the standard Arrhenius equation (Eq. 2).

A non-linear least-squares fit to the experimental data was performed by numerically integrating Eq. 10 for each furnace setting and initial particle size combination. Temperature profiles for furnace settings other than 800° or 1000° C were estimated using a linear interpolation or extrapolation of the points measured using the shielded thermocouple at 800° and 1000° C, while interpolation for a specific furnace setting was performed by fitting the points measured at specific distances in the flow tube to a sixth-order polynomial. Figure 11 presents the observed and calculated size decreases of the soot particles.

The activation energy was found to be 162 kJ/mol. An attempt was made to fit the exponent of the temperature in Eq. (4), but this was highly correlated with the  $A_{nm}$  parameters and therefore not determinable from our data. Also, fitting with a single size-dependent  $A$  parameter was attempted, but no adequate functional dependence on particle size could be found to fit the data for all three initial particle sizes. This indicates that the differences in oxidation rate observed for the three initial particle sizes is most likely more a function of the initial particle structure rather than the particle mobility size measured by the DMA.

The largest uncertainty in the present experiments comes from the assumption of laminar flow. This may not be too inaccurate, because the laminar flow assumption results in a spread in particle residence times. Experimentally, the observed spread in

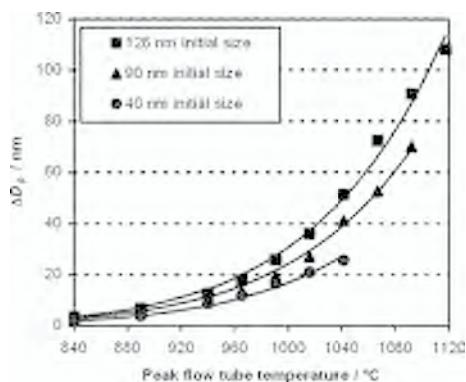


Figure 11. Particle size change as a function of peak flow tube temperature for the three initial particle sizes. Solid lines show size change calculated from the fitted model.

the size distributions is in line with the later residence time assumption. In such cases, if we assume that the uncertainty in residence time is linearly proportional to the residence time, then it translates linearly into an uncertainty in the  $A_{nm}$  parameters without affecting the activation energy.

There is a factor of 1.7 difference between the measured oxidation rates of the 40 and 126 nm particles. This may be due to a difference in the effective densities of the soot particles, or in the chemical composition of the particles. Because of the agglomerate structure of the soot particles, the effective density of the larger particles is lower than that of the smaller particles. This could lead to a higher rate of observed size reduction for the larger particles. Preliminary experiments in altering the soot composition indicate that increasing the amount of hydrogen in the soot leads to a higher oxidation rate. It can be conjectured that the different size particles have had different histories within the flame, and thus different elemental composition can be expected.

### 2.3. Comparison of oxidation rates based on TEM observations and TDMA measurements

In this section, we verify, both online and offline kinetics measurements against each other. The comparison between the two methods is made. A comparison of size distributions at 25 C (room temperature) and a furnace temperature of 1000°C is presented in Figure 12. The two experimental methods show excellent agreement in the most probable particle diameter before and after oxidation. Furthermore it provides another validation for the equivalence of  $d_A$ , and  $d_m$ .

Figure 13 shows Arrhenius plots of the surface specific oxidation rate for our measurements and prior studies. The activation energy of low temperature flame soot oxidation, was determined to be 148 kJ/mol by TEM method and is consistent with the 143 kJ/mol used in the Nagle and Strickland-Constable (NSC) [28] oxidation model (curve “d” in Figure 13) as extracted by Stanmore et al. [29]. However, our oxidation rate is an order of magnitude higher, than the extrapolated NSC model and even more than that for the other studies presented in this temperature range. To assess the possibility that this experimental approach somehow results in a higher observed reaction rate, we conducted an experiment under the same conditions (i.e. higher temperature) as our TDMA oxidation measurement. The results are shown in Figure 13 as the open circle, and overlaps with excellent agreement with our TDMA measurements [30], rate curve “c”. The agreement suggests that the TEM sizing approach should be yielding accurate results at the lower temperature conditions.

To assess other possibilities for our higher rate, the soot sampled on the TEM grid was pretreated under a  $N_2$  environment at 550 C for 5 min from which no noticeable size change was observed.

Another possibility considered was that the soot which was in contact with the  $SiO_2$  TEM grid might somehow accelerate oxidation, however van Doorn et al. [31] have shown that  $SiO_2$  has no catalytic effect on diesel soot particles. One may expect a lower activation energy along with an increased rate if catalytic effects are important as

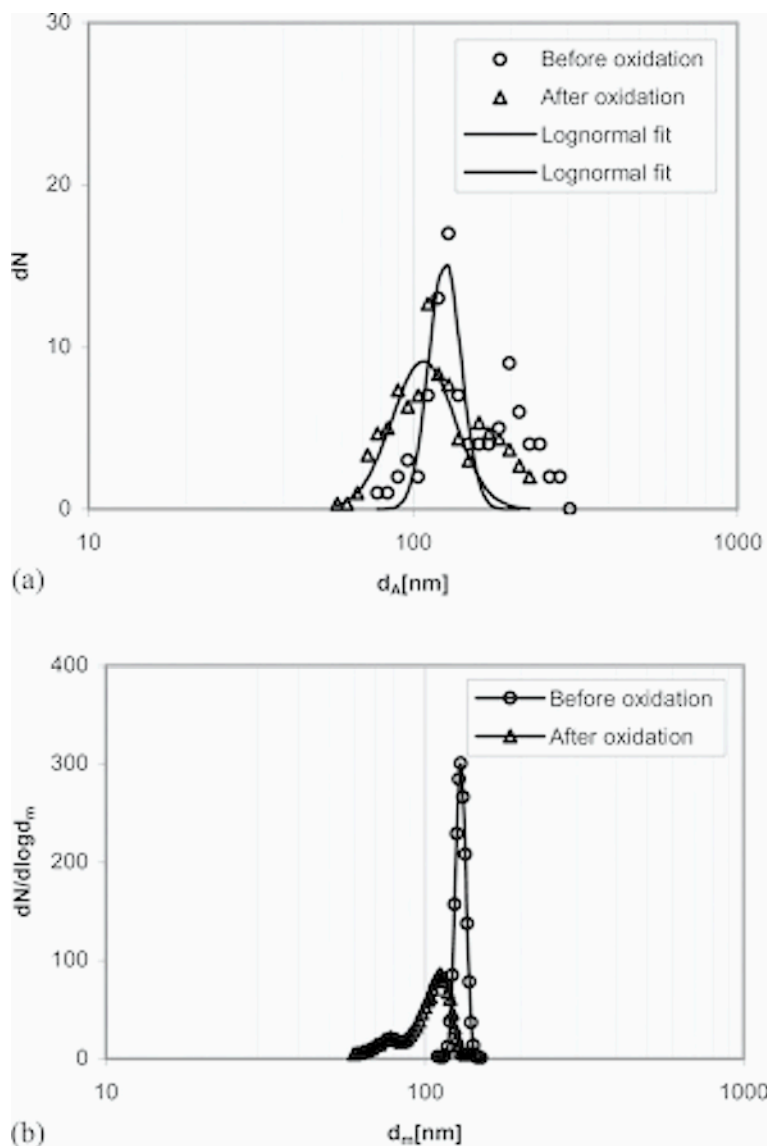


Figure 12. Comparison of (a) TEM and (b) TDMA measurements: The number distributions are shown before and after soot oxidation at 1000 °C.

observed by Miyamoto et al. [32]. In their work they saw enhanced rates for calcium laden diesel soot of up to 2 orders of magnitude higher (curve “e” in Figure 13) as compared with undoped soot (curve “f” in Figure 13).

Temperature is one of the most sensitive variables in determining reaction rate. Our uncertainty analysis indicates an uncertainty of  $< \pm 2$  K. If one were to assume a

worst case scenario and assume an uncertainty ten times larger, the resulting effect on the rate is shown in Figure 13, as the thin lines above and below rate curve “a”. Obviously uncertainty in temperature cannot explain our observed higher rate.

The uncertainty related to the image analysis in the measurement of a 20 nm diameter is expected to be less than  $\pm 2\text{nm}$ . However, for particle below 20 nm, the uncertainty increases due to a decrease in the number of pixels which constitute a given particle. The dotted lines seen in Figure 13 “a” show  $\pm 1\sigma$  confidence lines. The propagation of the uncertainty in determination of  $d_A$  to the final rate is negligible, since it lies within the confidence lines limits above.

Stanmore et al. [29] in their recent review has discussed the variation in the measured oxidation rates, some of which are presented in Figure 13. They suggested the possibility that some of the measured rates might be corrupted by mass transfer effects which would tend to make the observed rate lower. We should also note that

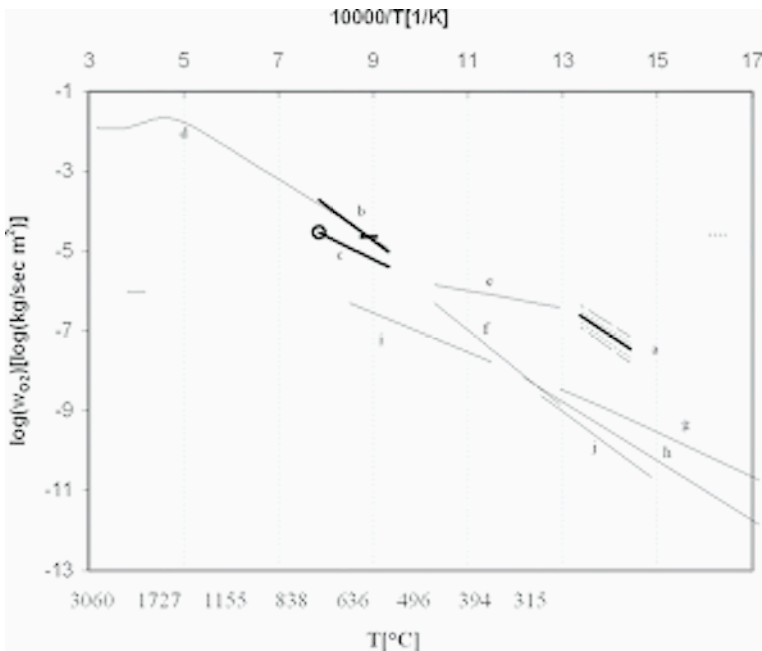


Figure 13. Arrhenius plot of the surface specific rates of soot oxidation for the current study and for other relevant prior studies. Previous studies produced a variety of activation energies, as can be seen by the varying slope of the lines. Results are presented for 21%  $\text{O}_2$ . (a) Flame soot by TEM method (—), rates for  $\pm 1\sigma$  confidence lines (.....), rates for  $\pm 20\text{K}$  variation (—). (b) Flame soot by TDMA method (c) Diesel soot (d) Nagle and Strickland-Constable using a pyrographite rod (e) Miyamoto et al. TGA of catalyzed (Ca added to fuel) Diesel soot. (f) Miyamoto et al. TGA of uncatalyzed Diesel soot. (g) Ahlström and Odenbrand flow reactor study of Diesel soot. (h) Otto et al. TGA of Diesel soot. (i) Gilot et al. thermogravimetric analysis (TGA) of carbon black. (j) Neeft et al. flow reactor study of Printex-U flame soot from Degussa AG.

in the low temperature range, curve “j” reflects results for black carbon, while curves “h and g” are Diesel soot results from Otto et al. [33], and Ahlström and Odenbrand [34], respectively. This difference in source may also create differences in measured rates.

Ishiguro et al. [35] studied the microstructure evolution for Diesel soot oxidation at about 800 K using an analytical electron microscope. During oxidation they observed flaking of crystallites from the outer most shell of the particles. This would certainly make the apparent rate higher than NSC prediction, however that does not explain the discrepancy between our results and the other low temperature data. Furthermore, given the resolution of our instruments we were not able to assess if this flaking phenomena was taking place for our particles.

We conclude that the measured higher rate by TEM method is attributed to a measurement protocol that more effectively assesses the intrinsic chemical reactivity, without the corruption of heat and mass transfer effects associated with bulk methods. These results are consistent with our single particle mass-spectrometry studies on condensed phase chemical kinetics, much higher reaction rates were observed for small particles over bulk samples [36].

## 2.4. Bio-diesel soot kinetics

In this study the kinetics of particle oxidation are measured for particles emitted by a diesel engine operating on a 100% soy methyl ester (SME) biodiesel fuel (B100). The TDMA method described in section 2.2 is employed to measure surface-specific oxidation rates from size-selected diesel exhaust particles over the temperature range of 700 to 825 °C. The change in particle diameter after oxidation took place was measured and converted into the surface specific oxidation rate using method described in section 1.3.

Figure 14 shows representative TDMA data for 89 nm particles generated using biodiesel at 1400 RPM, 75% load. Results for the other initial particle sizes tested (40 and 128 nm) are not presented here but are similar. Figure 14 illustrates that the particles shrink as the furnace temperature increases, and that the mobility diameter decreases by 2 nm at 500 °C and 9 nm at 800 °C.

The initial shrinkage in size below 500 °C is likely due to desorption or evaporation of volatile materials. We previously [37] found that the total particle size decrease, due to non-oxidative effects at 500 °C, measured using nitrogen as the carrier gas, amounted to ~1 nm at 75% load using regular diesel fuel. The larger 2 nm shrinkage we observed at 500 °C using biodiesel can be attributed to the presence of more volatile PM with biodiesel. Above 500 °C, most of the change in diameter is a result of particle oxidation. In addition to a decrease in particle size with increasing oven temperature, we also observed a decrease in the number of particles. This decrease is not associated with chemical reactivity, but rather, it is associated with thermophoretic transport losses, which become more important at higher temperatures [38].

Figure 15a shows experimentally determined size reductions at various oxidation temperatures for 40, 89 and 128 nm. For comparison purposes, Figure 15b shows results from our prior oxidation work using regular diesel fuel [37]. In both cases, we

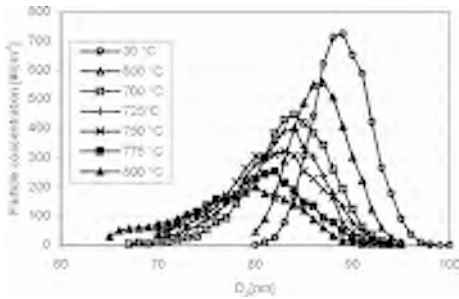


Figure 14. TDMA diesel particle oxidation results in air for furnace settings of 30–800 °C. 89 nm initial particle size with B100 biodiesel at 1400 RPM, 75% load.

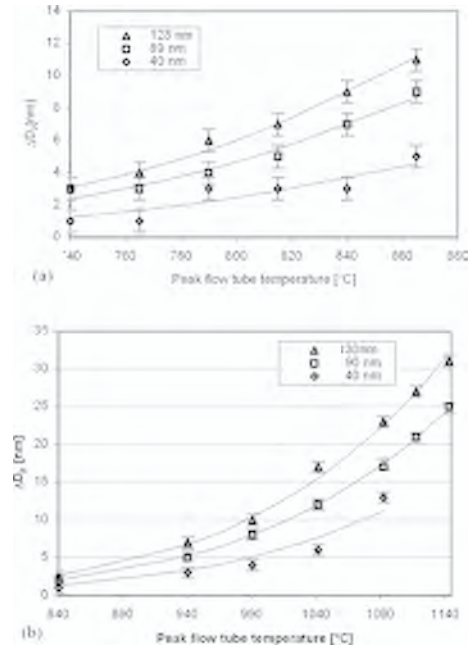


Figure 15. Particle size change as a function of peak flow tube temperature for the three initial particle sizes. (a) B100 biodiesel. (b) D2 fuel [37].

observed an increase in the apparent oxidation rate with increasing initial particle size. That result was investigated in our previous study [37]. It is necessary to correct the rates for the effective density of soot, which was measured [39] using an Aerosol Particle Mass analyzer. We [39] observed that the effective density increases as the particle size decreases. Normalization to the effective density using their data resulted in an oxidation rate that was essentially particle size independent [37].

For practical convenience, we define the light-off temperature of oxidation as the peak-flow tube temperature, where the particle shrinks  $\sim 1$  nm (beyond that due to thermal evaporation). This is not the same as the light-off or balance point temperatures used in describing DPF performance which are generally much lower than those observed here. The difference is due to the much shorter reaction times, about 1 s, used in our experiments compared to DPF regeneration times. Our light-off temperatures are a fundamental measurement of particle reactivity in a system not constrained by heat and mass transfer effects. The light-off temperature was determined to be  $\sim 840$  °C for the regular diesel (D2) particles as shown in Figure 15b, but decreased significantly to 740 °C for biodiesel, as shown in Figure 15a. The data in Figure 15a were fitted to an Arrhenius expression (Eq. 1). The activation energy was  $88.5 \text{ kJ mol}^{-1}$ . The  $A_{nm}$  factors were 0.77, 1.5 and  $1.9 (\times 10^4) \text{ nm K}^{-1/2} \text{ s}^{-1}$  for 40, 89 and 128 nm mobility diameter aggregates.

## 2.5. Role of metals

In this section, the role of metals in soot oxidation is examined. Diesel soot and flame soot are discussed. As shown in previous sections, the oxidation kinetics of these two types of soot differs. It is hypothesized that the presence of metals in diesel possibly coming from the lubricating oil leads to a higher oxidation rate. Furthermore, recent studies show that metal based fuel additives can lower the particulate emissions and enhance oxidation rates. In these works, a variety of metal additives have been tested. Miyamoto et al. [32, 40] investigated the effect of Ca, Ba, Fe, and Ni naphthenates. They found Ca and Ba most efficiently reduced the soot, by both suppressing soot formation and enhancing soot oxidation. Valentine et al. [41] studied the catalytic effect of bimetallic Pt/Ce additives in an attempt to lower the dosing level of the metal additive down to 4 ppm to reduce ash loading on the diesel particulate filter (DPF) and the emission of metallic ultrafine particles. Skillas et al. [42] studied the effect of Ce and Fe on the size distribution and composition of Diesel PM; they observed a reduction in the accumulation mode, but an increase in ultrafines. Lahaye et al. [43] studied the catalytic effect of Ce on simulated Diesel PM oxidation and observed that the cerium was both on and within the soot as cerium oxides. Kasper et al. [44] added ferrocene to the fuel and speculated that the enhancement of oxidation was more effective in reducing soot than a suppression effect.

Many studies [45, 46] have focused on the change in ignition temperature of the Diesel PM bed with different metal additives. While these results are of obvious practical benefit, it has been difficult to decouple the role of the catalyst on the increase in the oxidation rate from other effects that may also promote an increase in oxidation rate and a decrease in ignition temperature (i.g, the heat and mass transfer effect, particle size, etc.).

In view of the complex interrelationships discussed above, we have attempted to extract intrinsic oxidation kinetics in the following sections, in order to assess the role of the catalyst in the enhancement of the oxidation rate. First, the role of cerium additive on the diesel soot oxidation is discussed. Then, the role of metals in diesel soot oxidation is examined against iron-doped flame soot oxidation.

### 2.5.1. Influence of cerium additive on the size distribution

Figure 16 shows the effect of the cerium additive on the particle size distribution for various dosing levels at fixed engine condition (75 % engine load (300 N m) at 1400 RPM). The addition of the cerium additive clearly had a significant effect on reducing the number concentration of particles in the accumulation mode. A 50 % reduction in peak concentration was observed at the 25 ppm dosing level, which was further reduced to 65 % with 100 ppm of additive. The relative insensitivity of the results to dosing level was qualitatively consistent with work from Skillas et al. [42]; they found significant reduction of particles in accumulation mode at 20 ppm of cerium, but did not see any noticeable effect of further increases in cerium additives. While the accumulation mode clearly decreased, a dramatic increase in the nuclei mode was observed with the addition of cerium, which has also been confirmed by Skillas et al. [42]. This behavior

is consistent with particle physics. A decrease in the accumulation mode, and therefore available surface area, as shown in Figure 16b, reduces scavenging of particle precursors, thus promoting homogeneous nucleation, while at the same time decreasing coagulation of nuclei mode particles with accumulation mode particles.

### 2.5.1.1. TDMA results

The experimental system is described by Jung et al. [47]. Figure 17 shows representative TDMA data for 90 nm particles generated under 25 ppm cerium added fuel, at a fixed engine condition (75 % engine load (300 N m), 1400 RPM). Results for other initial particle sizes at 25 ppm and 100 ppm cerium doping were similar to those presented in Figure 17. The particles shrink as the furnace temperature increases and the mobility diameter decreased by 1 nm at 300 °C and 7 nm at 650 °C. The total particle size decrease, due to non-oxidative effects at 500 °C, measured using nitrogen as the carrier gas, amounted to ~1 nm at 75 % load using regular diesel [37]; this is consistent with the shrinkage we observed at 300 °C for cerium loading. The initial shrinkage in size below 300 °C is inconsistent with the kinetic results observed at higher temperatures and is likely due to the evaporation of semi-volatile materials condensed on the diesel particles. Sakurai et al. [48] have also reported such shrinkage. Above 300 °C,

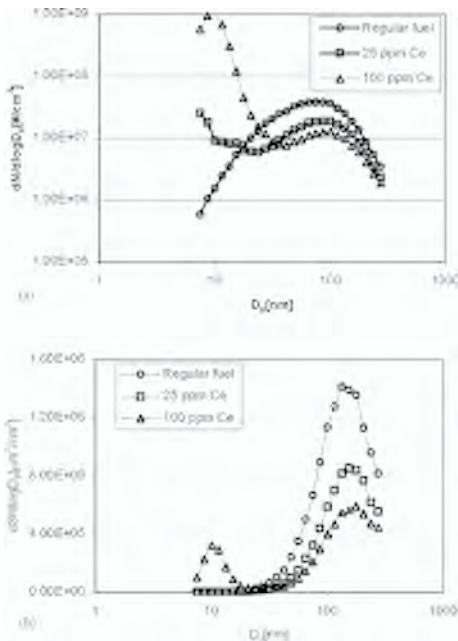


Figure 16. Size distributions of diesel particles with cerium dosed fuel for various dosing levels at 1400 RPM, 75 % load. (a) Number distributions. (b) Geometric surface area distributions.

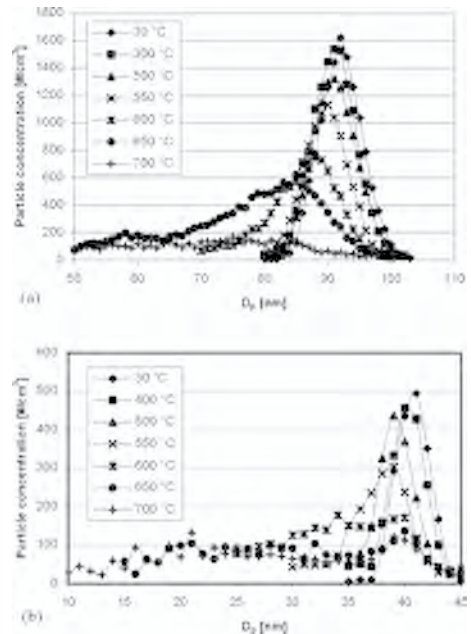


Figure 17. TDMA Diesel particle oxidation results in air for furnace settings of 30-700 °C. (a) 92nm initial particle size with 25 ppm cerium dosed fuel. (b) 41nm initial particle size with 100 ppm cerium dosed fuel.

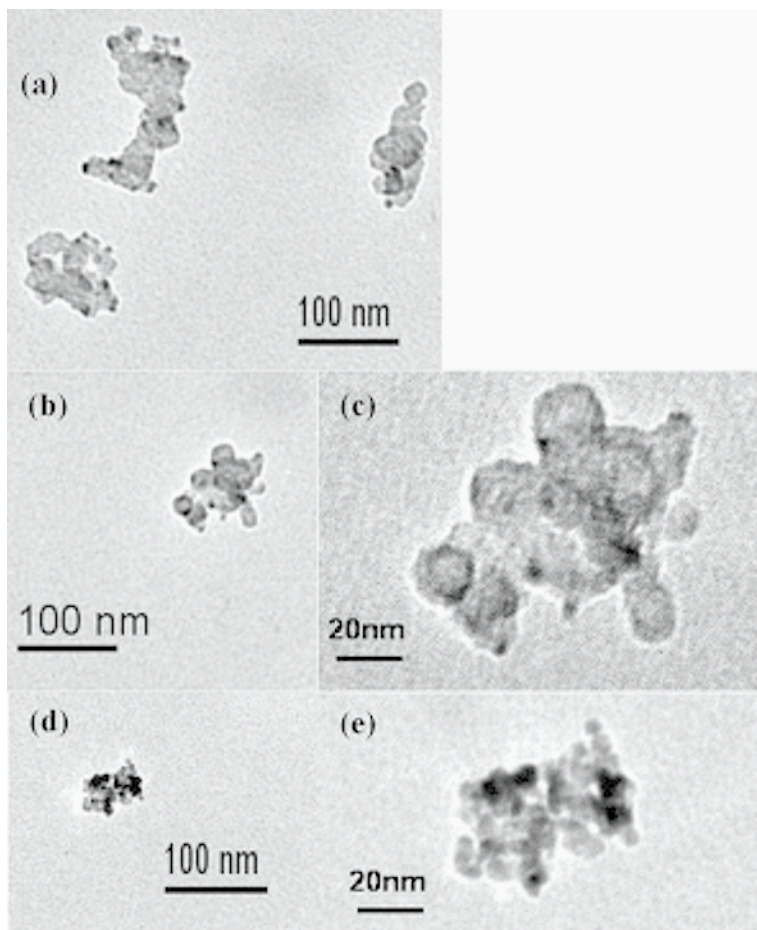


Figure 18. TEM images of 50 nm mobility diameter selected cerium-laden diesel particles. Samples are taken under the condition of 75 % load at 1400 RPM using 100 ppm cerium doping level. (c) and (e) are at higher magnification.

most of the diameter change results from particle oxidation. In addition to a decrease in particle size with increasing oven temperature, we also observed a decrease or loss of particles. This decrease in number concentration was not associated with chemical reactivity, but rather, thermophoretic transport losses, which become most important at higher temperatures [49]. In Figure 19b, we see results for 40 nm particles at 100 ppm cerium doping. At higher oven temperatures, two modes were observed. In this case, rather than a steady decrease to smaller sizes by the primary peak, as observed in all our previous studies, here we saw a mode (e.g., at 600 and 650 °C) near 40 nm, and another peak at about 34 and 32 nm, respectively. This behavior may be attributed to some particles being primarily composed of cerium compounds that homogeneously condensed from the vapor and have an associated carbon coating. The mixture of 40

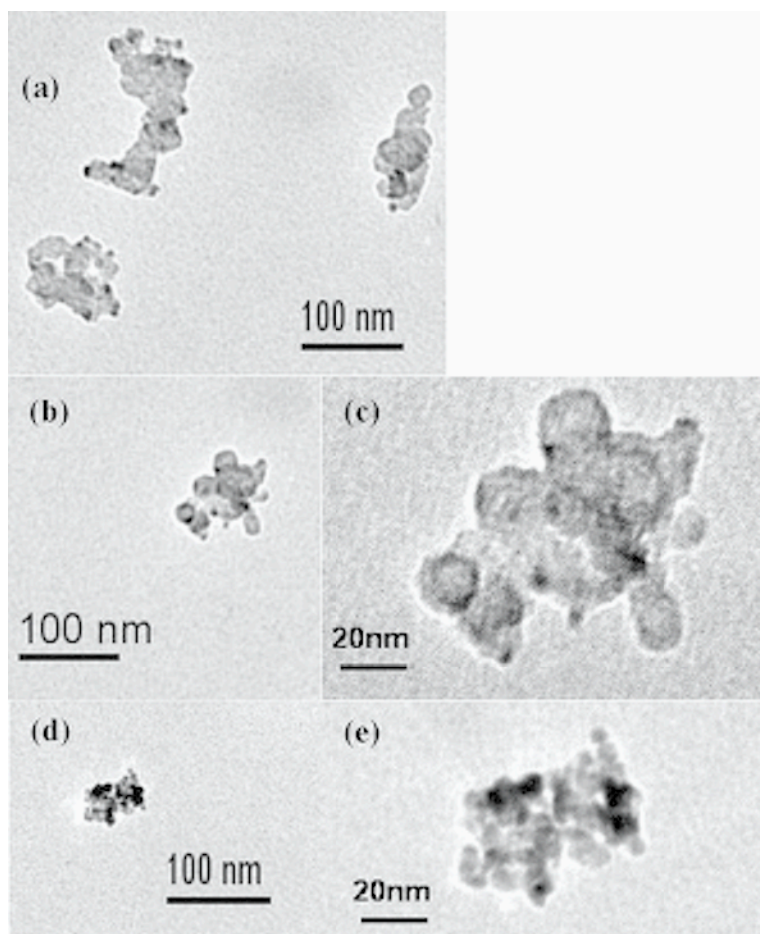


Figure 19. TEM images of 130 nm mobility diameter selected of cerium-laden diesel particles. Samples were taken under the condition of 75% load at 1400 RPM using 100 ppm cerium doping level. (b) and (c) at higher magnification compared to (a).

nm, predominately either cerium or carbon, resulted in a bimodal size distribution after oxidation. This is consistent with the TEM observations discussed below.

Figures 18 and 19 show TEM images of cerium-laden-diesel particles under 75%, 1400 RPM at 100 ppm cerium doping level. Sampling particles on  $\text{SiO}_2$  coated nickel TEM grids follows the procedure detailed in our previous study [50]. In brief, the aerosol flow after the 1st stage of the dilution tunnel was sent to a DMA and the resulting monodisperse output was sent to a Low Pressure Impactor (LPI)[51]. Particles were collected on the TEM grid at the bottom stage of the LPI.

Referring to Figure 17b, we observed a bimodal distribution after oxidation at 700 °C. The first mode consists of pre-selected 40 nm particles that remained after oxidation, while the other mode reflects shrinkage to  $\sim 20$  nm. This is consistent with

some particles exiting the engine being primarily composed of metal, as seen in Figure 18d.

Size decreases due to oxidation were determined relative to the size of the particles at 300 °C. This is lower than the temperature of 500 °C which we used in our previous studies [37, 49]. Lowering the base temperature was necessary because of the increased reactivity of the diesel particles by the addition of metal additives.

#### 2.5.1.2. Kinetic rates

Figure 20 shows experimentally determined size reductions at various oxidation temperatures for 41, 92 and 132 nm particles at 25 ppm (Figure 20a) and 100ppm (Figure 20b) cerium doping levels. Figures 20a,b can be compared with Figure 15b for undosed Diesel oxidation in Section 2.4. One of the obvious differences seen between this work and the undosed results is that we did not see any size dependant oxidation. In the undosed case, we observed an increase in the apparent oxidation rate with increasing initial particle size. That result was investigated in our previous study [37] to correct the rates for the effective density of soot, which was measured by [39] using an Aerosol Particle Mass analyzer. Park et al. [39] observed that the effective density increases as the particle size decreases and that normalization to the effective density resulted in an effective oxidation rate that was essentially particle size independent [37]. At this point, we do not have a definitive explanation of the differences observed between the dosed and undosed cases; however, it is possible that the nature of the soot structure in the dosed case is different and it is also possible that the mass fraction of cerium in the soot particles is size dependent. All that can be concluded without further investigation is that the apparent oxidation rate for dosed Diesel is size invariant.

The light-off temperature was determined to be ~ 840 °C for the undosed Diesel particles as shown in Figure 15b, but decreased significantly to 540 and 590 °C respectively, for the 25 ppm and 100 ppm dosing level, as shown in Figures. 20a,b. The results suggest that the catalyst fulfilled a major, practical objective of decreasing the thermal budget of a DPF and that, after a threshold concentration, there is little benefit to operating at higher doping levels. The data in Figures 20a,b were fitted to an Arrhenius expression (Eq. 1). Table 1 lists the Arrhenius parameters (frequency factors,  $A_{nm}$ 's, and activation energy,  $E_a$ ) obtained.

The activation energies of Diesel particle oxidation for 25 and 100 ppm cerium-dosing rate were essentially equivalent, within experimental error, and equaled 107 and 102 kJ mol<sup>-1</sup>, respectively. More interesting, perhaps, is that the activation energy of the dosed fuel was not any different from that of the undosed case (108 kJ mol<sup>-1</sup>), even though the absolute oxidation rate in the range of temperature studies was some ~ 20 times faster. These results are qualitatively consistent with the study by Stanmore et al. [29]. Using the thermogravimetric method, they compared oxidation rates of cerium dosed Diesel particles with that of undosed Diesel particles at various engine conditions (idle, medium speed, and high speed). They found that the presence of the catalyst did not change the activation energy, consistent with our observation; however, their measured activation energy (210 kJ mol<sup>-1</sup>) was a factor of two higher than our observation. Miyamoto et al. [32] also found an increase in the oxidation rate (Figure 13 'g') for Ca-catalyzed DPM. However, they observed a two stage oxidation process. In their TGA study, they observed an initial stage of rapid oxidation with very

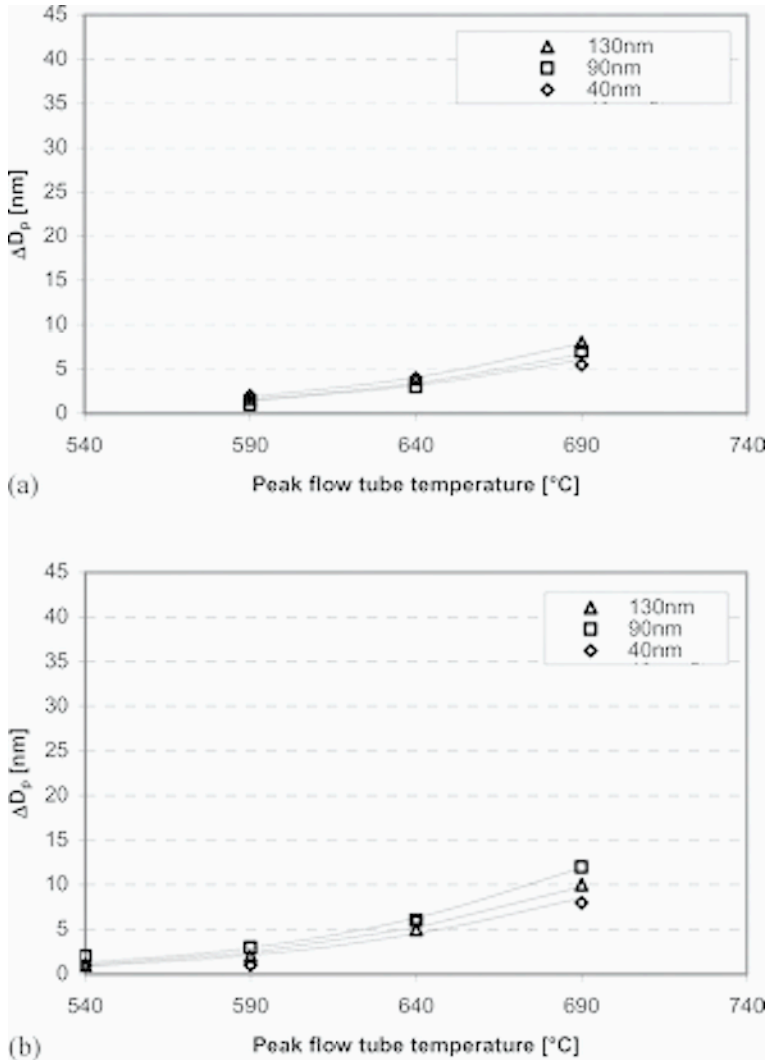


Figure 20. Particle size change as a function of peak flow tube temperature for the three initial particle sizes. (a) 25 ppm cerium dosed fuel. (b) 100 ppm cerium dosed fuel. Compare with Figure 15b for regular base fuel [37].

low activation energy (Figure 13 'h') followed by slower and higher activation energy kinetics (Figure 13 'g') of a similar magnitude to other studies. This rapid early stage is similar to an observation referred to as auto-acceleration by Lahaye et al. [43]. While our experiments are unable to resolve transients such as described above, we do note that, the general addition of metals does not seem to change the activation energy, but does increase the oxidation rate significantly.

Table 1. The preexponential factors and the activation energies of diesel soot oxidation under different loads and cerium doping for mobility diameters of 40 and 93 and 130 nm. The bio-diesel soot data is presented for 40, 89, 128 nm mobility diameter. The oxidation kinetic parameters of flame soot with and without iron doping is also shown.

	Diesel particles [37]			Bio-diesel particles [55]	Cerium-doped flame diesel particles [47]		Diffusion soot particles [56]	
	10% load	50% load	75% load		25 ppm	100 ppm	Non-iron doping	Iron doping
$E_a$ [kJ mol <sup>-1</sup> ]	114	109	108	88.5	107	102	162±3	116±3
$A_{40}$ [10 <sup>4</sup> nm K <sup>-1/2</sup> s <sup>-1</sup> ]	8.8	3.1	2.6	0.77	66	50	1200	800
$A_{89}$ [10 <sup>4</sup> nm K <sup>-1/2</sup> s <sup>-1</sup> ]				1.5				
$A_{93}$ [10 <sup>4</sup> nm K <sup>-1/2</sup> s <sup>-1</sup> ]	7.7	4.5	3.8		73	70	2200	1100
$A_{128}$ [10 <sup>4</sup> nm K <sup>-1/2</sup> s <sup>-1</sup> ]				1.9				
$A_{130}$ [10 <sup>4</sup> nm K <sup>-1/2</sup> s <sup>-1</sup> ]	11.2	5.4	4.8		86	58	3200	1800

This corroborated observation that the use of a catalyst did not reduce the activation energy. We have previously observed that Diesel soot oxidation has a lower activation energy than flame generated soot; it has been speculated that small quantities of metals from lube oil may serve as an inadvertent catalyst [37, 49]. This provides a consistent picture for the observed results, although further work is still needed to establish if, indeed, sufficient metals from lube oil are incorporated into soot. Stanmore et al. [29] observed the fall-off of the reactivity above 600 °C for cerium dosed particles, which was not seen in our work. It is possible that the, so called, auto-acceleration may be an artifact of the TGA measurements, which are notorious for being corrupted by mass and heat transfer effects as demonstrated by Mahadevan et al. [36]. From a practical point, the similarity of Ca vs. Ce might suggest the opportunity that other metals may serve the function of oxidant accelerator and that one is left with the opportunity to choose the dopant based on cost, ease of use, and environment/health concerns, as well as oxidation rate.

Literature on the health effects of a cerium additive is limited. A report [52] from the Health Effect Institute was the only extensive study, we could find on the health effect of cerium additive. The report concluded that the risk of inhaling cerium at the estimated worst-case ambient level (1.2 µg/m<sup>3</sup>) arising from heavy Diesel traffic, using a cerium additive with a particulate trap, appears to be small. However the absence of more complete information precluded their fully assessing the possible health effects of using cerium as a fuel additive. They mentioned that risk of chronic exposure was more difficult to estimate due to the lack of adequate studies, and the possible increase in cerium emissions during the regeneration process of the particulate trap. It should be further noted that no one is proposing to use Ce or any metal as a soot suppression additive on its own. It would only be used in combination with a particle filter. Used in this manner Ce has a double benefit, it reduces the amount of soot collected in the filter, and thus the frequency of regeneration, and facilitates regeneration when it occurs.

### 2.5.2. Difference between flame and diesel soot

The flame soot and diesel soot show significantly different temperature sensitivity to oxidation (i.e. activation energy). In the previous section we saw that adding cerium oxide a known catalyst, to diesel fuel increased the oxidation rate, but did not affect the activation energy. Similarly, the addition of lubrication oil, which contains significant quantities of metal, increased the oxidation rate but did not affect the activation energy [53]. All these results point to an indirect conclusion that Diesel soots already contain metals that catalyze the oxidation of soot. The addition of metal additives to diesel may result in a decrease in soot emissions, which can be attributed to either suppressing soot inception and growth, or promoting oxidation in the combustion chamber.

The flame soot has significantly higher activation energy for oxidation than the diesel soot. It is hypothesized that metals, possibly coming from lubricating oils, within the diesel soot may be responsible for lowering the activation energy. In order to test the hypothesis metals are added to the soot in a systematic manner as described below. The TDMA method described above is used to find out the size dependent oxidation kinetics for flame soot and flame soot doped with iron.

The representative TDMA measurement for the 130 nm initial particle size with and without iron-doped soot is presented in Figure 21. For pure soot particles as shown in Figure 21a, the particle size changed by less than 1% for temperatures up to 500°C and is likely due to evaporation of volatile materials condensed on the soot particles. This fact is verified by employing nitrogen carrier gas instead of air. Above 500°C, the soot particles undergo significant oxidation and higher extents of oxidation with increasing temperature for fixed residence time. Careful observation of the profiles in Figure 21a also shows small satellite peaks. These correspond to the small fraction of particles that have two charges and are larger particles with the equivalent mobility diameter. The decrease in number density with increasing temperature can be attributed to thermophoretic deposition of soot particles to the reactor wall. The thermophoretic loss of soot particles is promoted with increasing temperature due to the higher temperature gradient. With increasing reactor temperature a greater fraction of the aerosol is lost to the walls at the exit of the reactor. However, since thermophoretic velocity is particle size independent we expect no changes to the resulting size distribution. Since our analysis relies on size change, and does not depend on number concentration, these losses have no impact on our data analysis. Figure 21b shows the evolution of size distribution of iron-doped soot nanoparticles at various oxidation temperatures. Unlike the pure soot particles, the mean size of the iron-doped soot particles decreased significantly even at 500°C. At the higher temperature range (700°C-900°C), particle shrinkage ceases as shown in the inserted graph. Here we believe we have completely burned out the soot leaving behind iron which also has presumably been oxidized. If we assume that the iron nanoparticles are oxidized to  $\text{Fe}_2\text{O}_3$ , and using the bulk densities of iron and iron oxide with 7.86 and 5.18 g/cc, respectively, we can work backwards to determine the effective size of the original iron constituent. In this way the 60 nm peak corresponds to a volume equivalent diameter of 41 nm for pure iron. Working back further we can determine that the relative volume loading from the original 131 nm soot particle we started at, gives a  $\sim 3\%$  iron volume loading relative to soot mass.

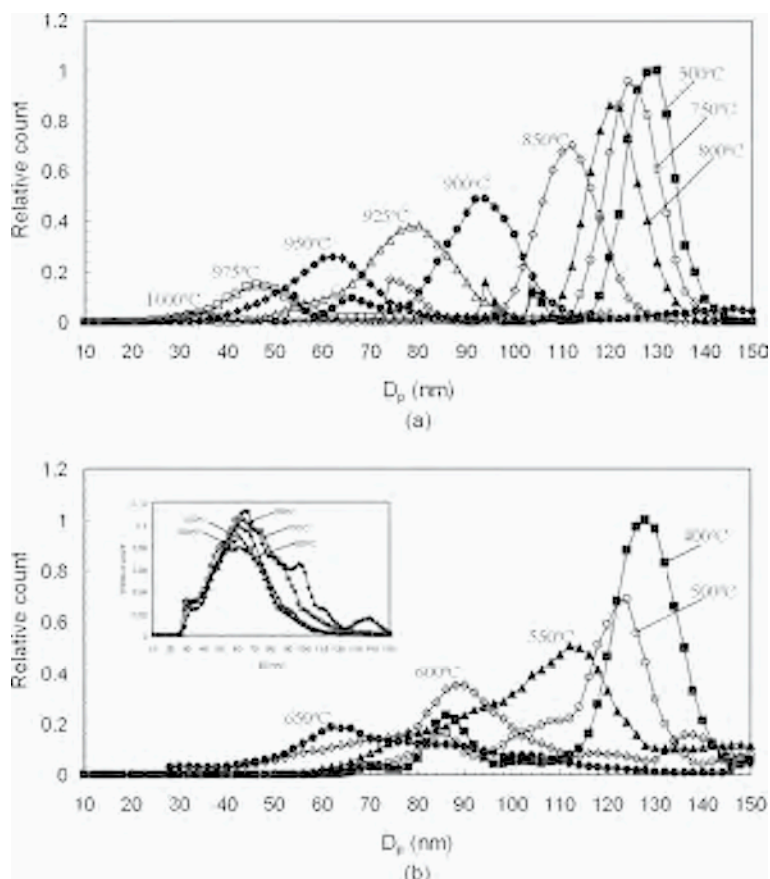


Figure 21. TDMA results for soot oxidation in air for various temperatures from 400 to 1000°C: (a) non iron-doped soot nanoparticles and (b) iron-doped soot nanoparticles. Initial mobility diameter = 130 nm.

Figure 22 presents the size decrease measured by TDMA system (symbols) and the fitted into Eqs. 1-6. The open circle data represent the iron-doped case clearly show a much reduced on-set temperature relative to the undoped case (solid symbols). Table 1 summarizes the kinetic parameters, ( $A_{40}$ ,  $A_{93}$ ,  $A_{130}$ , and  $E_a$ ) found by a best fit to the experimental data, which are also plotted in Figure 22 as the solid lines. We first note a significant decrease in the activation energy from  $162 \pm 3$  kJ/mol for the pure soot, to  $116 \pm 3$  kJ/mol for the iron-doped case. The pre-exponential factors for the iron-doped soot particles are slightly smaller (factor of 2) as compared to the undoped case. However, due to the sensitivity of the fit to the activation energy it is difficult to assess if this is a real effect or simply an artifact of the fit. The absolute values of the A factor are consistent with the data shown in earlier sections. The slight size dependent rates observed, whereby the larger particles have an increased apparent oxidation rate

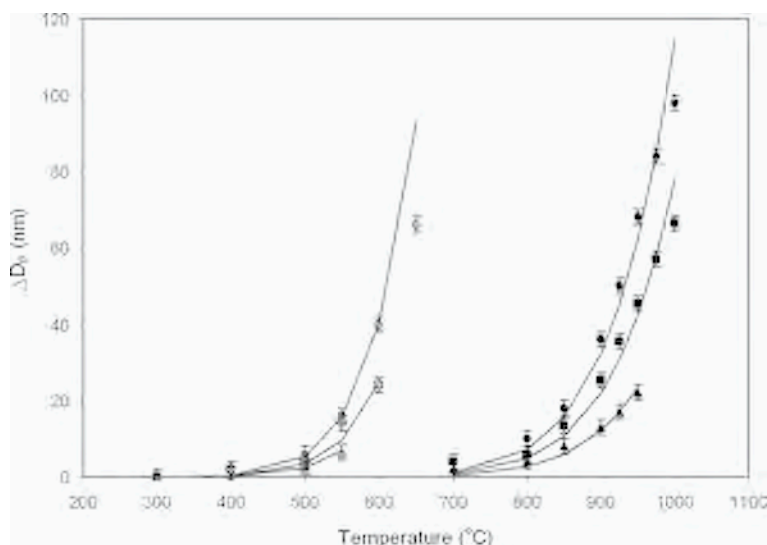


Figure 22. Comparison of particle size change as a function of temperature for the 40 nm (triangles), 93 nm (squares) and 130 nm (circles) initial sizes of non iron-doped (solid symbols) and iron-doped (open symbols) soot nanoparticles. Solid lines are the fitted models based upon the kinetic parameters of Arrhenius equation as shown in Table 1.

has been discussed in our prior work and have been attributed to an assumption made of constant effective density. One also notes that there is a large difference in pre-exponential factors between diesel and flame soot particles. This observation, as seen above, is presumably related to some inherent chemical difference between flame and diesel generated soot which has not yet to be addressed adequately. For example hydrogen content is generally higher and diesel soot also generally contains a significant amount of sulfur and nitrogen [34].

Since the volume fraction of metal content in the current flame soot matrix ( $\sim 3\%$  volume fraction) is larger than that of diesel soot ( $\sim 1\%$  volume fraction), we reduced the iron addition down by a factor of 5 ( $\sim 0.02$  mol % of the fuel) to observe the effect of the amount of iron loading on the activation energy and A factor. For comparison, 93 nm initial iron-doped flame soot particles were selected for TDMA measurement. The kinetic parameters found were  $161 \pm 3$  kJ mol $^{-1}$  [ $2.2 \cdot 10^7$  nm K $^{-1/2}$  s $^{-1}$ ],  $133 \pm 3$  kJ mol $^{-1}$  [ $1.2 \cdot 10^7$  nm K $^{-1/2}$  s $^{-1}$ ], and  $116 \pm 3$  kJ mol $^{-1}$  [ $1.1 \cdot 10^7$  nm K $^{-1/2}$  s $^{-1}$ ] for non-iron loading, 0.02 mol % iron loading, and 0.1 mol % iron loading cases, respectively. These results are consistent with the hypothesis that small quantities of metal seeding in soot matrix increases the reactivity of the resulting soot nanoparticles by significantly decreasing their activation energy. These results are consistent with the idea that small quantities of metals during diesel combustion may play an important role in soot abatement.

## 2.6. Conclusions

In this paper we summarize our studies on the oxidation kinetics of size selected soot particles. The size dependent Arrhenius kinetic parameters are measured using two methods: (a) direct observation by TEM and (b) TDMA method. We found that the oxidation rate of flame soot measured by the TEM method at low temperatures ( $< 800$  K) was higher than that measured by TDMA method over the temperature range  $800^{\circ}$ - $1120^{\circ}$  C. Using the TDMA method, the activation energy of soot oxidation in air was equal to  $163 \text{ kJ mol}^{-1}$ .

The TDMA method is also used to measure oxidation kinetics for diesel and bio-diesel soot. The activation energy of diesel soot ( $114 \text{ kJ/mol}$ ) is found to be higher than the bio-diesel soot ( $88.5 \text{ kJ/mol}$ ). The faster oxidation kinetics of bio-diesel fuel should facilitate regeneration when used with a diesel particulate filter.

A comparison of the behavior of flame vs. Diesel soot suggest that Diesel soot behaves as though it has small amounts of catalytically active metals, which we confirm by adding metal to flame soot. These results are consistent with idea that metals in lubrication oils are incorporated into soot formed during combustion. More importantly perhaps is that combustion modeling of soot formation in Diesel should incorporate the understanding that metals will play a role not only in soot oxidation but soot production as well, and that nascent flame soot studies may not capture this effect.

### Nomenclature

$A$	Pre-exponential factor
$A_{nm}$	Frequency factor for each initial soot particle size
$d_a$	Projected area equivalent diameter
$d_m$	Mobility diameter
$E_a$	Activation energy
$m_s$	Mass of soot particle
$R$	Universal gas constant
$T$	Temperature
$t$	Time
$u_m$	Mean flow velocity
$\dot{w}$	Mass based surface specific rate
$X$	Horizontal position in the tube
$X$	Length of the tube
$\rho_{effective}$	Effective density of soot particle
$\rho_s$	Mass density of soot particle
$\tau_0$	Characteristic residence time

## REFERENCES

1. A. Chung, A. A. Lall, S. E. Paulson, *Atmos. Environ.* (2007) in review.
2. T. L. Barone, A. A. Lall, Y. F. Zhu, R. C. Yu, S. K. Friedlander, *J. Nanopart. Res.* 8(5) (2006) 669-680.
3. C. Venkataraman, G. Habib, A. Eiguren-Fernandez, A. H. Miguel, S. K. Friedlander, *Science* 307(5714) (2005) 1454-1456.
4. T. C. Bond, *Geophys. Res. Lett.* 28(21) (2001) 4075-4078.
5. R. J. Santoro, H. G. Semerjian, R. A. Dobbins, *Combust. Flame* 51(2) (1983) 203-218.
6. M. S. Graboski, R. L. McCormick, *Prog. Energy Combust. Sci.* 24(2) (1998) 125-164.
7. A. K. Babu, G. Devaradjane, SAE Technical Paper Series (2003) 2003-2001-0767.
8. P. H. Abelson, *Science* 195(268) (1995) 955.
9. O. Schröder, J. Krahl, A. Munack, J. Bünger, SAE Technical Paper Series (1999) 1999-1901-3561.
10. A. Monyem, J. H. Van Gerpen, *Biomass Bioenergy* 20(2001) 317-325.
11. J. Krahl, A. Munack, O. Schröder, H. Stein, J. Bünger, SAE Technical Paper Series (2003) 2003-2001-3199.
12. G. L. Finch, C. H. Hobbs, L. F. Blair, E. B. Barr, F. F. Hahn, R. J. Jaramillo, J. E. Kubatko, T. H. March, R. K. White, J. R. Krone, M. G. Ménache, K. J. Nikula, J. L. Mauderly, J. Van Gerpen, M. D. Merceica, B. Zielinska, L. Stankowski, K. Burling, S. Howell, *Inhalation Toxicology* 14 (2002) 1017-1048.
13. J. B. Williams, *Eur. J. Lipid Sci. Technol.* 104(6) (2002) 361-362.
14. W. Korbitz, *Renewable Energy* 16(1-4) (1999) 1078-1083.
15. R. L. Pereira, W. H. Maria, *Appl. Biochem. Biotechnol.* 121 (2005) 807.
16. <http://www.soyatech.com/bluebook/news/viewarticle.ldml?pa=20041214-20041216>.
17. H. J. Jung, D. B. Kittelson, M. R. Zachariah, *Combust. Flame* 136(4) (2004) 445-456.
18. P. Meakin, B. Donn, G. W. Mulholland, *Langmuir* 5 (1989) 510.
19. S. N. Rogak, U. Baltensperger, R. C. Flagan, *Aerosol Sci. Technol.* 14 (1991) 447.
20. A. Schmidt-Ott, U. Baltensperger, H. W. Gäggeler, D. T. Jost, *J. Aerosol Sci.* 21 (1990) 711.
21. S. H. Kim, K. S. Woo, B. Y. H. Liu, M. R. Zachariah, *J. Colloid Interface Sci.* 282(1) (2005) 46-57.
22. K. J. Higgins, H. J. Jung, D. B. Kittelson, J. T. Roberts, M. R. Zachariah, *J. Phys. Chem. A* 106(1) (2002) 96-103.
23. T. Tanaka, in 22nd International Vienna Engine Symposium, Vol. 2, OVK and Technical University of Vienna, 2001.
24. F. A. Heckman, *Rubber Chem. Technol.* 37 (1964) 1245.
25. P. Gilot, F. Marcuccilli, G. Prado, *Corrosion of Advanced Ceramics* (1963) 329-339.
26. W. Hess, M. C. R. Herd, in *Carbon Black*, J.-B. Donnet, R. C. Bansal, M.-J. Wang (Eds.) Marcel Dekker, NY, 1993, 2nd ed.
27. I. M. Kennedy, *Prog. Energy Combust. Sci.* 23 (1997) 95.
28. J. Nagle, R. F. Strickland-Constable, in *Fifth Carbon Conference*, Vol. 1, Pergamon, Oxford, 1962, pp. 154-164.
29. B. Stanmore, B. J.-F., P. Gilot, SAE Technical Paper Series (1999) 1999-1901-0115.
30. K. J. Higgins, H. J. Jung, D. B. Kittelson, J. T. Roberts, M. R. Zachariah, *Environ. Sci. Technol.* 37(9) (2003) 1949-1954.
31. J. v. Doorn, J. Varloud, P. Mériaudeau, V. Perrichoni, *Appl. Catal., B* 1 (1992) 117.
32. N. Miyamoto, H. Zhixin, O. Hideyuki, SAE Technical Paper Series (1988) 881224.
33. K. Otto, M. H. Sieg, M. Zinbo, L. Bartosiewicz, SAE Technical Paper Series (1980) 800336.
34. A. F. Ahlström, C. U. I. Odenbrand, *Carbon* 3 (1989) 475.

35. T. Ishiguro, N. Suzuki, Y. Fujitani, H. Morimoto, *Combust. Flame* 85 (1991) 1.
36. R. Mahadevan, D. Lee, H. Sakurai, M. R. Zachariah, *J. Phys. Chem. A* 106(46) (2002) 11083-11092.
37. K. J. Higgins, H. Jung, D. B. Kittelson, J. T. Roberts, M. R. Zachariah, *Environ. Sci. Technol.* 37 (2003) 1949-1954.
38. K. J. Higgins, H. Jung, D. B. Kittelson, J. T. Roberts, M. R. Zachariah, *J. Phys. Chem. A* 106 (2002) 96-103.
39. K. Park, C. Feng, D. B. Kittelson, P. H. McMurry, *Environ. Sci. Technol.* 37 (2003) 577-583.
40. N. Miyamoto, H. Zhixin, A. Harada, H. Ogawa, T. Murayama, SAE Technical Paper Series (1987) 871612.
41. J. M. Valentine, J. D. Peter-Hoblyn, G. K. Acres, SAE Technical Paper Series (2000) 2000-2001-1934.
42. G. Skillas, Z. Qian, U. Baltensperger, U. Matter, H. Burtscher, *Combust. Sci. Technol.* 154 (2000) 259-273.
43. J. Lahaye, S. Boehm, P. H. Chambrion, P. Ehrburger, *Combust. Flame* 104 (1996) 199-207.
44. M. Kasper, K. Sattler, K. Siegmann, U. Matter, H. C. Siegmann, *J. Aerosol Sci.* 30 (1999) 217.
45. N. Kyriakis, Z. Samaras, E. Vouitsis, T. Manikas, T. Seguelong, G. Blanchard, SAE Technical Paper Series (2002) 2002-2001-0429.
46. K. Pattas, N. Kyriakis, Z. Samaras, T. Manikas, A. Mihailidis, W. Mustel, P. Rouveirrolles, SAE Technical Paper Series (1998) 980543.
47. H. J. Jung, D. B. Kittelson, M. R. Zachariah, *Combust. Flame* 142(3) (2005) 276-288.
48. H. Sakurai, H. J. Tobias, K. Park, D. Zarling, S. Docherty, D. B. Kittelson, P. H. McMurry, P. J. Ziemann, *Atmos. Environ.* 37(9-10) (2003) 1199-1210.
49. K. J. Higgins, H. Jung, D. B. Kittelson, J. T. Roberts, M. R. Zachariah, *J. Phys. Chem.* 106 (2002) 96-103.
50. H. Jung, D. B. Kittelson, M. R. Zachariah, *Combust. Flame* (2003) submitted.
51. S. V. Hering, S. K. Friedlander, J. J. Collins, L. W. Richards, *Environ. Sci. Technol.* 13 (1979) 184-188.
52. M. G. Costantini, R. Henderson, D. S. Greenbaum, H. Greim, E. D. Pellizzari, R. Sawyer, J. Warren, J. Ball, S. Cadle, J. M. Davis, N. Englert, D. B. Kittelson, A. Mayer, J. McAughy, R. McClellan, R. F. Phalen, G. Simon, M. Waalkes, Health Effects Institute (2001) Communication 9.
53. H. Jung, D. B. Kittelson, M. R. Zachariah, SAE Paper 2003-01-3179 (2003).
54. A. A. Lall, S. K. Friedlander, *J. Aerosol Sci.* 37(3) (2006) 260-271.
55. H. J. Jung, D. B. Kittelson, M. R. Zachariah, *Environ. Sci. Technol.* 40(16) (2006) 4949-4955.
56. S. H. Kim, R. A. Fletcher, M. R. Zachariah, *Environ. Sci. Technol.* 39(11) (2005) 4021-4026.

**Part IV**  
**Turbulent flames and practical applications**



# On the transport of soot relative to a flame: modeling differential diffusion for soot evolution in fire

J.C. Hewson<sup>1</sup>, A.J. Ricks<sup>1</sup>, S.R. Tieszen<sup>1</sup>, A.R. Kerstein<sup>2</sup>, R.O. Fox<sup>3</sup>

<sup>1</sup>Fire and Aerosol Science, Sandia National Laboratories, Albuquerque, NM 87185-1135, USA

<sup>2</sup>Combustion Research Facility, Sandia National Laboratories, Livermore, CA, 94551-0969, USA

<sup>3</sup>Department of Chemical and Biological Engineering, Iowa State University, Ames, IA 50011-2230, USA

*Abstract: The conditional-moment-closure (CMC) equation for the evolution of a large-Lewis-number scalar, soot, is derived starting from the joint-pdf equation for the gas-phase mixture fraction,  $\xi_g$ , and the soot mass fraction,  $Y_s$ . Unlike previous approaches starting with the joint pdf, the present derivation allows different diffusivities among the different species. In addition, the residual terms that result from the typical closure models were considered. A new formulation of the one-dimensional turbulence (ODT) model suitable for spatially evolving flows with buoyant acceleration and radiative transport in participating media was employed to carry out simulations of a prototypical ethene fire. The resulting ODT evolution of  $\xi_g$  and  $Y_s$  was used to assess the significance of various terms in the CMC equation including the residual correlations. The terms involving differential diffusion are found to be important along with the soot source terms and the large-scale evolution of both  $\xi_g$  and  $Y_s$ . Of particular importance in the regions in mixture fraction space around the soot production and consumption is a residual term, not previously identified, related to the correlation between the differential diffusion and  $Y_s$ . This term results in a diffusion-like behavior of  $Y_s$  in the mixture-fraction coordinate that has an apparent Lewis number near unity. In scenarios where the large-Lewis number component is a non-negligible component of the mixture fraction (i.e. large soot loading), it is found easier to employ a mixture fraction neglecting this component. Such a mixture-fraction variable has a chemical source term, but this appears easier to model than the differential diffusion and dissipation terms that result when the large-Lewis-number component is retained in the mixture-fraction definition.*

## 1. INTRODUCTION

Soot plays a dominant role in the hazard posed by hydrocarbon fires. In fires, heat transfer by radiation is the dominant means by which fires spread and cause damage. The primary source of radiant heat flux is thermal emissions from soot. Furthermore, the primary in-fire sink for radiant flux is also soot. All soot is capable of emitting and absorbing radiative flux and the relative degree to which any soot does emit or absorb is a function of the soot temperature distribution. Therefore, the net radiative flux in fires depends on the quantity of soot present and its joint probability density function (pdf) with temperature.

In turbulent fires, knowledge of the joint soot-temperature pdf is not readily obtained. One class of approaches that can be used to approximate this quantity is the con-

served-scalar modeling approach. This approach is based on the idea that the thermochemical state can be referenced to a reduced set of variables for which the pdf is easier to predict. In nonpremixed combustion, this reduced variable is the mixture fraction, the fraction of the local mixture that originated from the fuel source. If the mixture-fraction pdf can be obtained and if the temperature and soot can be obtained as a function of the mixture fraction, then the joint soot-temperature pdf is obtained.

There are two general frameworks for deriving conserved-scalar modeling approaches: conditional moment closure (CMC) [1] and unsteady-laminar flamelet models (ULFM) [2]. In the limit where all of the transport coefficients are equal, both approaches are relatively straightforward and have been employed successfully in many studies. When species diffusivities differ, additional complications arise in the formulation. A model for flamelets with full differential diffusion has been derived in Ref. [3], but in the application to jet flames the best agreement with scalar fields was obtained by switching from full differential diffusion to unity Lewis numbers at the end of the jet potential core [2]. For CMC, Kronenburg and Bilger

[4] developed a model to account for the effects of differential diffusion based on the analysis of direct numerical simulations. This model retains the different diffusivities of the species, but provides a restorative term that tends to move species profiles closer to that which would be obtained with equal diffusivities; evaluation of this term requires the solution of additional transport equations for each differentially diffusing scalar. For flames with soot where differential diffusion is important, results have been reported in Refs. [5, 6]. Here, we take another look at the modeling of differential diffusion and identify an alternate model for addressing the effects of differential diffusion. This model does not require the solution of an additional transport equation and further explains the transition to unity Lewis numbers observed by [2].

To evaluate conserved-scalar modeling approaches and to develop new closure models, we employ a new spatially-evolving formulation of the one-dimensional turbulence (ODT) model [7]. Within the ODT model the reaction and diffusion processes relevant to the mixture fraction, enthalpy and soot evolution are fully resolved while the nonlinear turbulent advection is modeled as a stochastic process as described by [8]. The ODT model provides a data set for *a priori* evaluation of the terms in the CMC equations as they are derived here. Unique to ODT is the ability to span the range of length scales (sub-millimeter to meters) and the range of time scales (sub-millisecond to seconds) relevant to fire problems. This large range of scales arises because of the need to resolve the flame-scale chemical source terms for soot while simultaneously allowing the buoyant acceleration to drive the mixing process to fully turbulent flow and capturing the observed large-scale evolution of soot and enthalpy in fires.

## 2. CONDITIONAL-MOMENT EQUATIONS WITH DIFFERENTIAL DIFFUSION

In this section the basic conservation equations for the soot evolution and the mixture fraction evolution are provided in the form in which they are used in the ODT simulations. Based on these equations, CMC equations are then derived.

## 2.1. Soot and mixture fraction evolution

Soot evolution is modeled using a simplified two-equation treatment that retains sufficient physics for the present purposes. Equations for the soot mass fraction,  $Y_s$ ,

$$\frac{\partial \rho Y_s}{\partial t} + \nabla \cdot (\rho \vec{v} Y_s) = \nabla \cdot (\rho D_s \nabla Y_s) + \nabla \cdot (\rho D_T Y_s \nabla \ln T) + \rho w_s \quad (1)$$

and the soot number density, which evolves similarly,

$$\frac{\partial \rho N_s}{\partial t} + \nabla \cdot (\rho \vec{v} N_s) = \nabla \cdot (\rho D_s \nabla N_s) + \nabla \cdot (\rho D_T N_s \nabla \ln T) + \rho w_N \quad (2)$$

are evolved. Here,  $\rho$  is the density,  $\vec{v}$  is the velocity vector,  $D_s$  is the soot diffusivity,  $T$  is the temperature,  $D_T = 0.75 \mu / [\rho(1 + \pi \alpha_T / 8)]$  is the thermophoretic diffusion coefficient,  $\mu$  is the viscosity,  $\alpha_T$  is the thermal accommodation coefficient and  $w_s$  is the source term for soot mass fraction taken from the empirical model of Fairweather et al. [9]. The source terms are evaluated using a steady-flamelet approximation based on the mixture fraction and enthalpy [7].

## 2.2. The mixture fraction

The mixture fraction can be expressed in terms of the element mass fractions that originated in the fuel stream. The element mass fraction is expressed in terms of the species mass fractions,  $Y_i$  as  $\beta_k = \sum_{i=1}^n \psi_{i,k} Y_i$  where  $k$  is an element and  $\psi_{i,k}$  is the mass fraction of element  $k$  in species  $i$ . For the present purposes we employ elemental carbon and hydrogen to define the mixture fraction, so that the mixture fraction is defined as  $\xi = (\beta_C + \beta_H) / \beta_f$  where the normalization by the fuel-stream composition is provided by  $\beta_f$ .

A common diffusion coefficient,  $D_\xi$ , is selected for the mixture fraction, but not all of the species share this diffusion coefficient. Accounting for the differing diffusivities of the various species leads to a source term in the mixture-fraction conservation equation (c.f. Eq. 3). Generally, the differential-diffusion source term on the right-hand side is negligible in hydrocarbon combustion. However, in fires and in other scenarios the mass fraction associated with the particle phase is a substantial fraction of the mixture fraction, so it is necessary to include this term. For the special case where  $\xi = \xi_g + Y_s / \beta_f$  and where  $\xi_g$  is the mixture fraction contribution from the gaseous species that are all assumed to have diffusion coefficients  $D_\xi$ , the conservation equation for  $\xi$  is

$$\frac{\partial \rho \xi}{\partial t} + \nabla \cdot (\rho \vec{v} \xi) - \nabla \cdot (\rho D_\xi \nabla \xi) = \nabla \cdot [\rho (D_s - D_\xi) \nabla Y_s + \rho D_T Y_s \nabla \ln T] / \beta_f. \quad (3)$$

It turns out that the CMC equations derived using this mixture-fraction conservation equation are more challenging to model as will be discussed in Section 4. Because of these difficulties, an alternative formulation based only on the gas-phase mixture fraction is considered. The evolution equation for  $\xi_g$  is

$$\frac{\partial \rho \xi_g}{\partial t} + \nabla \cdot (\rho \vec{v} \xi_g) - \nabla \cdot (\rho D_\xi \nabla \xi_g) = -\rho w_s. \quad (4)$$

The soot source term appears in this equation, but it is found here that the modeling of this term is more straightforward and accurate than the modeling of the differential diffusion terms.

### 2.3. The joint-pdf equation for soot and mixture fraction

There are two approaches to deriving the CMC equations. The method proposed originally by Bilger [10], decomposing the variables into conditional means and fluctuations, was employed by Kronenburg [4] to analyze differential diffusion and then to study soot evolution in jet flames ([6]). In the present work, we derive the CMC equation following the alternate method of Klimenko [11] that is based on the joint-pdf evolution equation. The derivation from the joint-pdf equation yields the unclosed terms in different forms that provide additional insight into the issues that arise in differential diffusion.

The joint-pdf equation is obtained in a standard manner using the conservation equations for the soot and the mixture fraction; an exposition for the equal diffusivity, variable density and inhomogeneous flow case from which the mechanistic details can be obtained is available in [1]. Only the soot mass fraction joint with the mixture fraction,  $f_{Y_s \xi_g}$  will be considered since the soot number density joint with the mixture fraction takes the same form. The evolution of  $f_{Y_s \xi_g}$  is according to

$$\frac{\partial f_{Y_s \xi_g}}{\partial t} = -\frac{\partial}{\partial y} \left( \left\langle \frac{\partial Y_s}{\partial t} \middle| y, \eta \right\rangle f_{Y_s \xi_g} \right) - \frac{\partial}{\partial \eta} \left( \left\langle \frac{\partial \xi_g}{\partial t} \middle| y, \eta \right\rangle f_{Y_s \xi_g} \right) \quad (5)$$

where the notation  $\langle \cdot | y, \eta \rangle$  indicates conditional averaging with the sample-space variables  $y$  and  $\eta$  (i.e.  $f_{Y_s \xi_g}(y, \eta)$ ). Equations 1 and 4 are used to replace the time derivatives of  $Y_s$  and  $\xi_g$  and continuity is used to bring the pdf equation into conservative form. Mathematical manipulations replace the diffusive terms with scalar dissipation rates and several terms that describe the diffusive transport of the joint-pdf.

The evolution of the joint-pdf  $f_{Y_s \xi_g}$  is according to

$$\begin{aligned} \frac{\partial \langle \rho | y, \eta \rangle f_{Y_s \xi_g}}{\partial t} + \nabla \cdot (\langle \rho \bar{v} | y, \eta \rangle f_{Y_s \xi_g}) = & -\frac{\partial}{\partial y} (\langle \rho w_s | y, \eta \rangle f_{Y_s \xi_g}) \\ & -\frac{\partial^2}{\partial \eta^2} [\langle \rho D_s (\nabla \xi_g)^2 | y, \eta \rangle f_{Y_s \xi_g}] \\ & -\frac{\partial^2}{\partial y \partial \eta} [(2\rho D_s (\nabla Y_s \nabla \xi_g) | y, \eta) f_{Y_s \xi_g}] \\ & -\frac{\partial^2}{\partial y^2} [\langle \rho D_s (\nabla Y_s)^2 | y, \eta \rangle f_{Y_s \xi_g}] \\ & -\frac{\partial}{\partial \eta} (\langle \nabla \cdot [\rho (D_\xi - D_s) \nabla \xi_g] | y, \eta \rangle f_{Y_s \xi_g}) \\ & -\frac{\partial}{\partial y} [\langle \nabla \cdot (\rho D_T Y_s \nabla \ln T) | y, \eta \rangle f_{Y_s \xi_g}] \\ & +\frac{\partial}{\partial \eta} (\langle \rho w_s | y, \eta \rangle f_{Y_s \xi_g}) / \beta_f \\ & +\nabla^2 (\langle \rho D_s | y, \eta \rangle f_{Y_s \xi_g}) \\ & -\nabla \cdot (\langle \nabla (\rho D_s) | y, \eta \rangle f_{Y_s \xi_g}). \end{aligned} \quad (6)$$

### 2.4. Conditional-moment-closure equations for soot

The CMC equation for  $Y_s$  is obtained from the joint pdf by multiplying by  $Y_s$  and integrating across all variables of the joint pdf except for the mixture fraction to obtain an equation for the marginal pdf of just the mixture fraction,  $f_{\xi_g}$ , and the conditional soot mass fraction

$$\begin{aligned}
 \frac{\partial \langle \rho Y_s | \eta \rangle f_{\xi_g}}{\partial t} + \nabla \cdot (\langle \rho \vec{v} Y_s | \eta \rangle f_{\xi_g}) = & \langle \rho w_s | \eta \rangle f_{\xi_g} \\
 & - \frac{\partial^2}{\partial \eta^2} [\langle \rho D_s (\nabla \xi_g)^2 Y_s | \eta \rangle f_{\xi_g}] \\
 & + \frac{\partial}{\partial \eta} [\langle 2 \rho D_s (\nabla Y_s \nabla \xi_g) | \eta \rangle f_{\xi_g}] \\
 & - \frac{\partial}{\partial \eta} (\langle (\nabla \cdot [\rho (D_\xi - D_s) \nabla \xi_g] Y_s | \eta) \rangle f_{\xi_g}) \quad (7) \\
 & + \frac{\partial}{\partial \eta} (\langle \rho w_s Y_s | \eta \rangle f_{\xi_g}) / \beta_f \\
 & + \langle \nabla \cdot (\rho D_T Y_s \nabla \ln T) | \eta \rangle f_{\xi_g} \\
 & + \nabla^2 (\langle \rho D_s Y_s | \eta \rangle f_{\xi_g}) \\
 & - \nabla \cdot (\langle \nabla (\rho D_s) Y_s | \eta \rangle f_{\xi_g}).
 \end{aligned}$$

where the notation  $\langle \cdot | \eta \rangle$  indicates conditional averaging with the sample-space variable  $\eta$  (i.e.  $f_{\xi_g}(\eta)$ ). The terms on the right-hand side (r.h.s.) represent the conditional averages of contributions from the soot source term, the product of the dissipation and  $Y_s$ , the  $\xi_g$ - $Y_s$  cross dissipation, the differential diffusion, the source of mixture fraction from Eq. 3, thermophoresis and the diffusion of the pdf (two terms). Up to this point, Eq. 7 is an exact equation. Since the majority of the terms involve unknown correlations between various variables, a useful form of the equation requires some modeling assumptions. The conditional averages of density,  $Y_s$ , the scalar dissipation rate and the diffusion velocity are defined for convenience

$$\rho_\eta = \langle \rho | \eta \rangle \quad Q_s = \frac{\langle \rho Y_s | \eta \rangle}{\rho_\eta}, \quad \chi_\eta = \frac{\langle 2 \rho D_\xi (\nabla \xi)^2 | \eta \rangle}{\rho_\eta}, \quad M_\eta = \frac{\langle \nabla \cdot (\rho D_\xi \nabla \xi) | \eta \rangle}{\rho_\eta} \quad (8)$$

It will also be useful to define conditional fluctuations associated with the soot mass fraction and with the mixture fraction diffusion

$$y'_s = \frac{\rho Y_s - \rho_\eta Q_s}{\rho_\eta}, \quad M' = \frac{\nabla \cdot (\rho D_\xi \nabla \xi) - \rho_\eta M_\eta}{\rho_\eta} \quad (9)$$

For the second and third terms on the r.h.s., the closures

$$\langle \nabla \cdot [\rho (D_\xi - D_s) \nabla \xi_g] Y_s | \eta \rangle f_{\xi_g} \approx \left( 1 - \frac{1}{Le_s} \right) \rho_\eta M_\eta Q_s f_{\xi_g} \quad (10)$$

are suggested [1]. The first of these is exact if there is no correlation between the dissipation and the scalar while the second is exact if the scalar gradient is perfectly correlated with the mixture fraction gradient by  $\nabla \xi_g = \nabla Y_s \partial Q_s / \partial \eta$ . The analogous approximation for the fourth term is

$$\langle \nabla \cdot [\rho(D_\xi - D_s)\nabla \xi_g] Y_s | \eta \rangle f_{\xi_g} \approx \left(1 - \frac{1}{Le_s}\right) \rho_\eta M_\eta Q_s f_{\xi_g} \quad (11)$$

The Lewis number for the soot has been introduced and it is defined,  $Le_s = D_\xi/D_s$ ; here the mixture-fraction diffusivity is taken to be equivalent to the temperature diffusivity. For the fifth term, the approximation

$$\langle \rho w_s Y_s | \eta \rangle \approx \langle \rho w_s | \eta \rangle Q_s \quad (12)$$

will be employed. It is also common to separate the mean and fluctuating components of the scalar flux

$$\nabla \cdot (\langle \rho \vec{v} Y_s | \eta \rangle f_{\xi_g}) = \nabla \cdot (\langle \rho \vec{v} | \eta \rangle Q_s f_{\xi_g}) + \nabla \cdot (\langle \rho \vec{v}' y'_s | \eta \rangle f_{\xi_g}) \quad (13)$$

While the approximations in Eqs. 10, 11 and 12 are suitable for many cases, we investigate here the degree to which relaxing these assumptions will lead to improved predictions in the present case where the scalar evolution is strongly affected by differential diffusion. In doing so we introduce the residual correlation term

$$\begin{aligned} R_{DD} &= \frac{\partial}{\partial \eta} \left[ \langle \nabla \cdot [\rho(D_\xi - D_s)\nabla \xi_g] Y_s | \eta \rangle f_{\xi_g} - \left(1 - \frac{1}{Le_s}\right) \frac{\rho_\eta M_\eta Q_s}{2} f_{\xi_g} \right] \\ &\approx \frac{\partial}{\partial \eta} \left[ \left(1 - \frac{1}{Le_s}\right) \rho_\eta \langle M' y'_s | \eta \rangle f_{\xi_g} \right] \end{aligned} \quad (14)$$

Using Eqs. 8 through 14 in Eq. 7 along with the mathematical identity

$$\frac{\partial}{\partial \eta} (\rho_\eta M_\eta f_{\xi_g}) = \frac{\partial^2}{\partial \eta^2} \left( \frac{\rho_\eta \chi_\eta f_{\xi_g}}{2} \right) - \langle \nabla \cdot (\rho D_\xi \nabla f_{\xi_g}) | \eta \rangle \quad (15)$$

the CMC equation for soot mass fraction is

$$\begin{aligned} \frac{\partial \langle \rho Y_s | \eta \rangle f_{\xi_g}}{\partial t} + \nabla \cdot (\langle \rho \vec{v} | \eta \rangle Q_s f_{\xi_g}) &= \langle \rho w_s | \eta \rangle f_{\xi_g} \\ &+ \frac{\rho_\eta \chi_\eta f_{\xi_g}}{2 Le_s} \frac{\partial^2 Q_s}{\partial \eta^2} \\ &- \frac{\partial^2}{\partial \eta^2} \left( \frac{\rho_\eta \chi_\eta f_{\xi_g}}{2} \right) Q_s \\ &- \left(1 - \frac{1}{Le_s}\right) \frac{\partial}{\partial \eta} \left( \frac{\rho_\eta \chi_\eta f_{\xi_g}}{2} \right) \frac{\partial Q_s}{\partial \eta} \\ &+ \frac{\partial}{\partial \eta} (\langle \rho w_s | \eta \rangle Q_s f_{\xi_g}) / \beta_f \\ &- R_{DD} \\ &- \nabla \cdot (\langle \rho \vec{v}' y'_s | \eta \rangle f_{\xi_g}) \\ &+ (\nabla \cdot (\rho D_T Y_s \nabla \ln T) | \eta \rangle f_{\xi_g} \\ &+ \nabla^2 (\langle \rho D_\xi Y_s | \eta \rangle f_{\xi_g}) \\ &- \nabla \cdot (\langle \nabla (\rho D_\xi) Y_s | \eta \rangle f_{\xi_g}). \end{aligned} \quad (16)$$

The terms on the last three lines of Eq. 7 and 16 are found to be small at reasonably large Reynolds numbers and are not discussed from this point forward.

### 3. THE ONE-DIMENSIONAL-TURBULENCE MODEL

The ODT model of [8] is employed to evolve the mixture fraction (Eq. 4), enthalpy, soot mass fraction (Eq. 1) and number density conservation equations over larger length and time scales than accessible with direct numerical simulations while simultaneously resolving the reaction and diffusion processes. This is done to create a flow field relevant to buoyant fires as a means of estimating the relative contributions of the terms in Eq. 16 in fire environments [7].

Within ODT a reaction-diffusion equation is solved along a one-dimensional computational domain that may be thought of as a material line through a flow field. The reduction of the computational domain to a single spatial dimension enables the resolution (along that domain) of the full range of length scales from the largest scales of the fire to the Kolmogorov and Corrsin scales. A model is employed to mimic the nonlinear effects of three-dimensional turbulent mixing. Despite of the reduction to 1-D of the computational domain, ODT has been shown to reproduce many characteristics of three-dimensional turbulent flows [8].

Turbulent mixing is mimicked in ODT by stochastic stirring events called triplet maps, first introduced in the Linear Eddy Model of turbulence, on a 1-D domain [12]. A triplet map increases gradients and transfers fluctuations to higher wave numbers without changing the domain integrals of conserved scalars or introducing discontinuities in the solution. Triplet maps are the ODT analog of eddies in a turbulent flow field. To reproduce turbulent scalings in ODT, the triplet map is coupled with a mixing-rate model. Mixing rates are calculated based on the energy available to drive the mixing process in solved velocity and density fields [8]. ODT has been applied to reacting flow problems [13, 14].

To evolve the one-dimensional domain forward, a parabolic marching solution method is employed. This provides a second dimension of evolution that can be time or a second spatial dimension; here spatial evolution is employed as in [15]. The spatially-developing formulation is preferable for the present work because the longer time scales in the low velocity regions are reproduced along with the entrainment of air at the edges of the fire. This results in a field, depicted in Figure 1, representing a planar-symmetric fire. While the resulting field is twodimensional, the ODT model represents the nonlinear three-dimensional effects through the action of the triplet maps.

A number of simplifying assumptions were employed for the present work. The flow was assumed to be steady and gradients in the vertical direction were assumed to be small compared to gradients in the lateral direction. The pressure field was assumed to be constant everywhere with a Boussinesq acceleration model. These assumptions are similar to boundary-layer assumptions and reduce the elliptic flow problem to a parabolic one. For the present work the gas-phase composition was assumed to be a function of the mixture fraction and enthalpy, providing the inputs to the soot source terms from [9]. The soot diffusivity is set relative to the temperature-dependent visco-

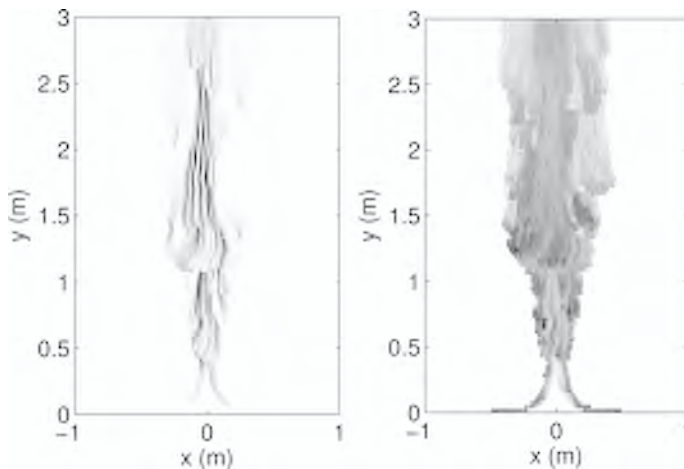


Figure 1. The evolution of the ODT domain (horizontal direction) in the vertical direction results in the depicted soot volume fraction (left) and temperature (right) fields for a single typical realization. Fields are filtered over the grid used for radiation transport solution.

sity by fixing a soot Schmidt number at  $Sc_s = 30$ . Such a Schmidt number is probably small for soot in fires but is large enough that other transport processes will dominate over actual soot diffusion. In addition, a large but finite Schmidt number allows for actual resolution of the soot field through the use of adaptive gridding. The mixture fraction Schmidt number is unity so that  $Le_s = 30$ . Additional details of the simulation are available in [7, 16]

In addition to the evolution of the enthalpy equation in the ODT model, the radiative transport equation is also modeled using the discrete ordinates method to account for the redistribution of energy through radiative transport. Both emission and absorption of soot are considered while gas-phase contributions are neglected. Because of the nature of the simulation with only one line of the domain available at an instant, an averaged radiation field was computed based on the soot and temperature fields of previous realizations of the simulation. This averaged radiation field couples to the ODT evolution through radiative absorption and emission source terms in the instantaneous enthalpy equation. Coupling the radiation solution in this manner enables the ODT evolution to proceed as a parabolic marching problem.

In the ODT simulations reported here, a fire nominally 1 m in width at its base is simulated on a computational domain 4 m in width to a height of 6 m. The fuel is ethene supplied at a constant mass flux rate of  $60 \text{ g/m}^2/\text{s}$  to match typical fire heat release rates. An adaptive gridding technique, based on gradients of mixture fraction and soot, was employed for efficiency. The smallest length scales resolved were  $\approx 100 \text{ }\mu\text{m}$  in width, which is approximately the smallest estimate for the soot dissipative (Corrsin) scale, and the average vertical step size was less than  $10 \text{ }\mu\text{m}$ . Statistics were sampled over 2000 realizations. Statistics were further combined to reduce statistical noise in averaging regions of height 0.1 m that were extended across the domain.

#### 4. RESULTS AND DISCUSSION

In this section, the general characteristics of the simulation describing the soot evolution in fires are presented followed by an analysis of the terms in Eq. 16. The results of the ODT simulations are employed to conduct an *a priori* analysis to assess the significance of these terms and the quality of the proposed closures. Results are presented here by averaging across the domain at heights one to two pool widths above the pool. Earlier in the evolution the turbulence is still developing and later in the evolution the majority of the rich regions have been mixed out so that the results are less interesting. In Figure 2 the mixture-fraction pdf and the soot mass fraction are shown for three heights above the pool. As the flow evolves (moving up from the pool), the mixture is observed to become leaner as rich pockets are mixed out. (Because the flow is averaged across the entire domain, there is always a preponderance of ambient air leading to the peak in the air stream around  $Z=0$ .) Simultaneously, the soot mass fraction just to the rich side of the flame ( $\eta \approx 0.1$  to 0.15 compared to a stoichiometric value of 0.06) increases. The evolution of the soot is in qualitative agreement with the observed evolution of soot over the scale of the fire (not shown) except that in the ODT simulation the results are resolved in the mixture-fraction coordinate; resolution of scalars with respect to the mixture fraction is beyond current experimental capabilities in sooting environments. The observed evolution is a consequence of the relatively slow soot chemistry, radiative heat losses and the various means of soot transport in mixture-fraction space. The focus here is on modeling the latter. There is one additional item of note in the mixture-fraction pdf evolution shown in Figure 2a: in fires and other environments where the soot mass fraction is large, the soot source term appearing on the r.h.s. of Eq. 4 represents a significant contribution to the mixture-fraction pdf and this is evident as a local maxima in Figure 2a where soot is oxidized (around  $\eta \approx 0.06$ ).

Before discussing the different means of soot transport in detail, the diffusion coefficients appearing in Eq. 7 provide some immediate guidance as to the importance of

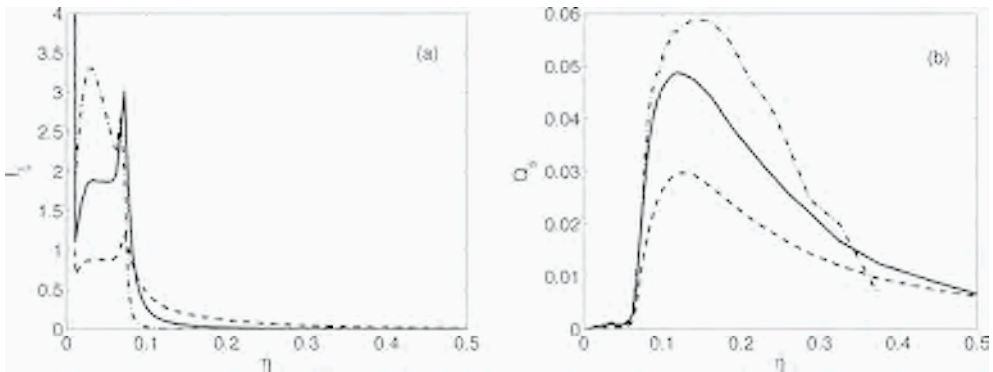


Figure 2. The (a) mixture-fraction pdf,  $f_{\xi}$ , is shown with (b) the conditionally averaged soot mass fraction,  $Q_s$ . Heights above the pool are 0.95 (dashes) 1.45 (solid) and 1.95 (dash-dot) source widths.

certain terms. In the second and third terms of Eq. 7 the soot diffusivity appears implying that these terms are reduced by a factor of  $1/Le_s$  relative to the fourth term in which the mixture fraction diffusivity also appears. These terms are transformed by Eq. 10 into the second term on the r.h.s. of Eq. 16. For near-unity Lewis-number species, this term is often of primary importance for transport relative to the mixture fraction, but the opposite is true here because of the large magnitude of  $Le_s$ . There are residuals associated with the approximations of these same terms in Eq. 7 using Eq. 10. These residuals have generally been neglected in first-order CMC, but in fact, these terms are the same magnitude as the second term on the r.h.s. of Eq. 16. Because all of these terms are inversely proportional to  $Le_s$ , all of these contributions are relatively small in the present case. Similarly small are the thermophoretic contributions and the diffusion of the pdf, the last three terms in Eqs. 7 and 16. The terms describing the diffusion of the pdf are small because they involve gradients of averaged quantities that are typically small at large Reynolds numbers [1]. The thermophoretic term is small because the thermophoretic velocity is small relative to the flame (mixture-fraction) diffusion velocity. The flame diffusion velocity is related to  $\nabla \cdot [\rho D_\xi \nabla \xi]$  appearing in the fourth term on the r.h.s. of Eq. 7 to be discussed next.

The major contributions to the evolution of  $Y_s$  in Eq. 7 come from the differential diffusion of soot and the mixture fraction (fourth term on r.h.s.) and the soot source terms (first and fifth terms on r.h.s.) as well as the vertical advective flux (left-hand side). Through Eqs. 11 and 14 and the application of the chain rule, the differential-diffusion term is split into the third and fourth terms on the r.h.s. of Eq. 16 as well as  $R_{DD}$ . Each of these terms is plotted in Figure 3 for three averaging regions (0.95, 1.45 and 1.95 source widths above the pool) and discussed in the following. The significance of these locations is that they represent a transition in the mixture-fraction pdf from one having substantial rich regions to one where the rich regions are being mixed into the soot-oxidation regions.

The differential-diffusion term in Eq. 7 is important because the mixture fraction, and thus the flame, diffuses more rapidly than the soot itself. This diffusive motion of the flame past soot leads to the most substantial diffusion-driven transport in mixture-fraction space. This is split into three terms on the r.h.s. of Eq. 16. The first involves  $\partial(\rho_\eta \chi_\eta f_\xi)/\partial \eta^2$  that is understood from the equation for  $f_{\xi_\eta}$  to be related to the evolution of  $f_{\xi_\eta}$  through terms like  $\nabla \cdot \langle \rho \vec{v} | \eta \rangle f_\xi$  that also appear on the left-hand side if the chain rule is applied to the advective scalar flux term. This partially offsets the advective scalar flux since a large part of the flux is associated with the evolution of  $f_\xi$ . This term does not appear if Eq. 16 is written in non-conservative form.

The second term involves  $\partial(\rho_\eta \chi_\eta f_\xi)/\partial \eta$  and  $\partial Q_s/\partial \eta$ . The first of these is a velocity in the mixture-fraction coordinate so that the combined term is a flux in the mixture-fraction coordinate due to the contraction of  $f_{\xi_\eta}$ , referred to as the differential diffusion due to the evolution of  $f_{\xi_\eta}$  in Figure 3. This has previously been recognized as being significant in transporting soot towards lean regions [17]. At the heights of 1.45 and 1.95 m where the remaining rich mixtures are being mixed toward stoichiometric, this term increases in importance and is among the most significant in bringing the soot into the highest temperature regions.

The residual associated with the approximation for the differential-diffusion terms in Eq. 11,  $R_{DD}$ , is of the same order of magnitude as the original term, and it is seen

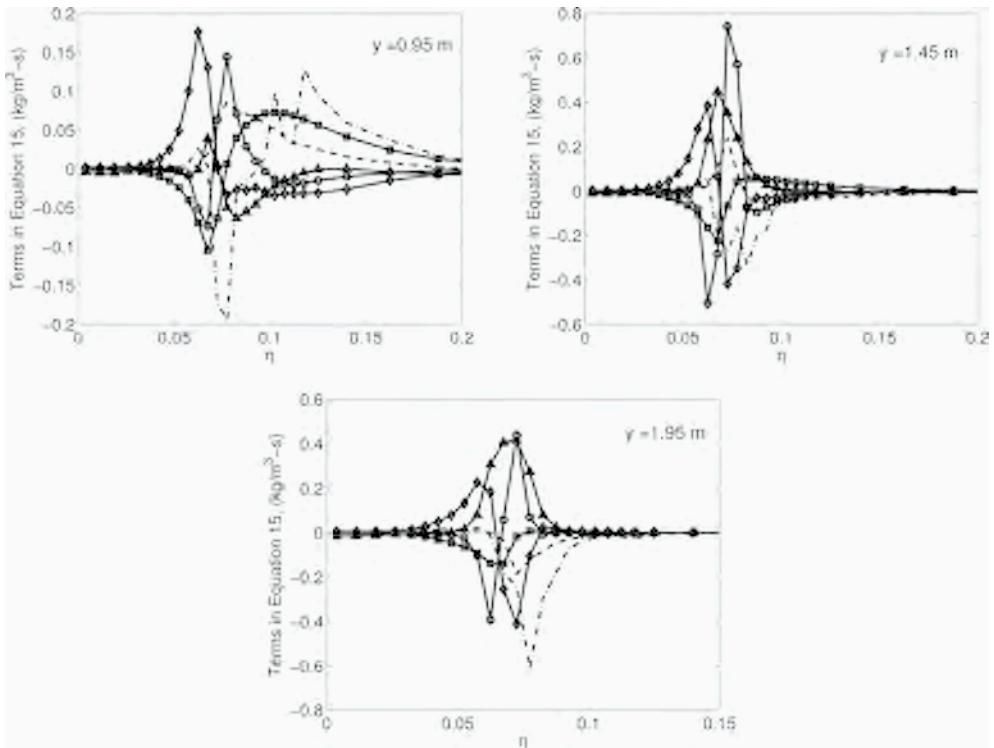


Figure 3. The significant terms in Eq. 16 are shown for heights of 0.95, 1.45 and 1.95 source widths. The dashed line is the vertical advective flux; the dash-dot line is the flux of  $f_{\xi}$  (r.h.s. term 3); the solid line with squares is the soot source term (r.h.s. term 1); the solid line with circles is the soot source term contribution to the mixture fraction evolution (r.h.s. term 5); the solid line with triangles is the differential diffusion due to the evolution of  $f_{\xi}$  (r.h.s. term 4); the solid line with diamonds is the differential diffusion due to fluctuations ( $R_{DD}$ ).

in Figure 3 to be an important contribution to soot transport. This term has previously not been considered, but is discussed here. In Figure 4 the two sides of Eq. 11 are plotted along with their difference (related to  $\langle M' y'_s | \eta \rangle$ ), which each appear differentiated in Eq. 14. It is clear that the approximation using  $M_{\eta} Q_s$  provided in Eq. 11 is poor, especially in the important region where soot is produced and oxidized and where the radiative source term is significant. In Figure 3 it is seen that this poor approximation results in  $R_{DD}$  that is of such a magnitude as to be one of the most significant sources in the CMC equation there. The approximation in Eq. 11 is equivalent to a presumption that  $\nabla \cdot [(D_{\xi} - D_{\eta}) \nabla \xi_{\eta}]$  and  $Y'_s$  (or  $M'$  and  $y'_s$ ) are independent, but Figure 4 suggests that they are fairly well correlated. This correlation is explained by understanding that a negative value for  $\nabla \cdot [(D_{\xi} - D_{\eta}) \nabla \xi_{\eta}]$  implies that the mixture fraction of a fluid element is getting leaner. It is reasonable to presume that a fluid element that was rich and is getting leaner will be associated with larger soot concentration (and vice-versa), at least in the near stoichiometric regions shown in Figure 4.

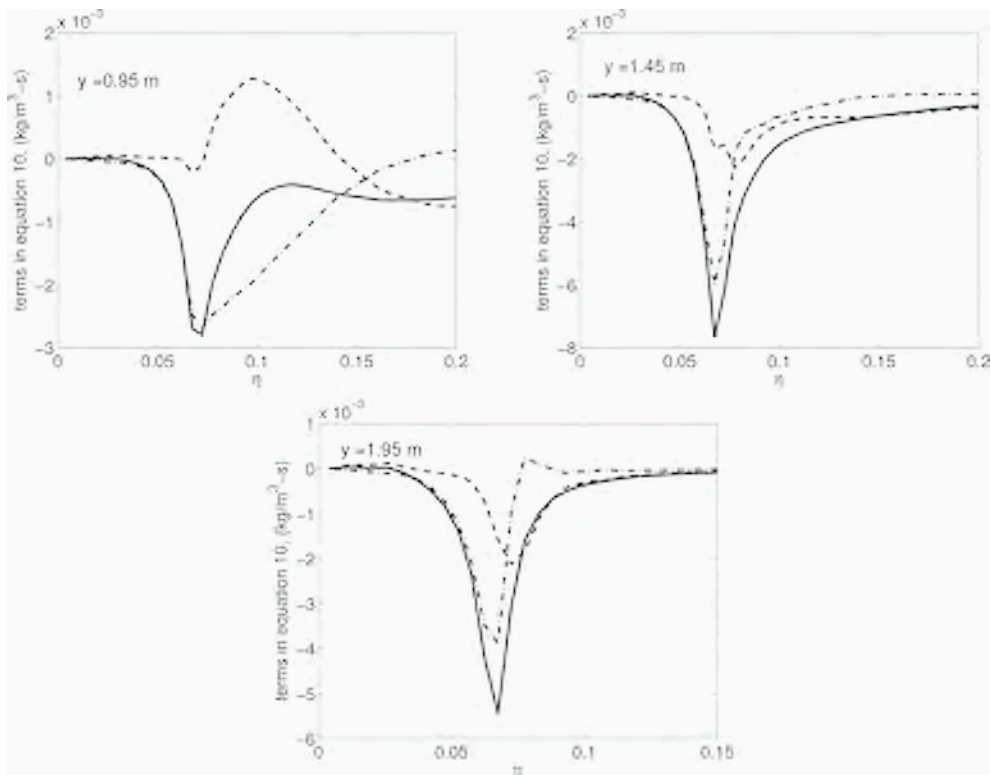


Figure 4. Terms involved in transport due to differential diffusion. The left-hand side of Eq. 11 is shown in solid, the right-hand side is the dashed line and the difference between the two is the dash-dot line. Heights above the pool are 0.95, 1.45 and 1.95 source widths as indicated within the panels.

To better understand the contributions to  $R_{DD}$ , the root-mean-square conditional fluctuations of the soot mass fraction,  $y'_{s,rms} = [\langle (y'_s)^2 | \eta \rangle]^{1/2}$ , are shown in Figure 5 for the various heights considered. It is observed that the conditional fluctuations are of the same order of magnitude as the conditional means (c.f. Figure 2). This is atypical of conditional moment methods. The sources of this behavior will require further investigation (i.e. second order CMC [18]), but it is expected that this is attributable to the relatively slow chemical evolution of soot [19] and perhaps to the strong differential diffusion associated with soot. The fact that conditional fluctuations are substantial is directly responsible for the need to retain the residual term  $R_{DD}$  in Eq. 14 to be discussed in the subsequent paragraphs. Also shown in Figure 5 are the root-mean-square conditional fluctuations of the mixture fraction diffusion,  $M'_{rms} = [\langle (M')^2 | \eta \rangle]^{1/2}$  and the correlation coefficient between  $M'$  and  $y'_s$ ,  $\langle M' y'_s | \eta \rangle / (M'_{rms} y'_{s,rms})$ . The mixture fluctuations are seen to increase in the stoichiometric regions, although this evolution will depend on the nature of the mixing process because this term is directly related to the mixture-fraction pdf evolution. The correlation coefficient is observed

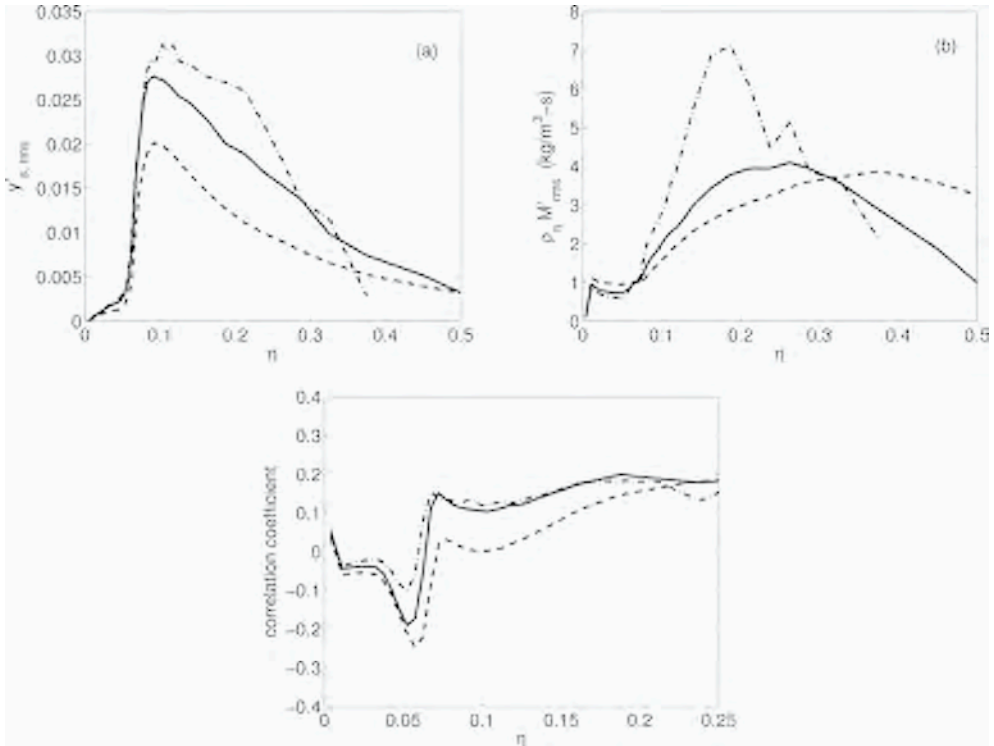


Figure 5. Root-mean-square fluctuations of the (a) soot mass fraction, (b) mixture-fraction diffusion and (c) the correlation coefficient between  $y'_s$  and  $M'$ . Heights above the pool are 0.95 (dashes) 1.45 (solid) and 1.95 (dashdot) source widths.

to be of the opposite sign as the slope of  $\partial Q_s / \partial \eta$  as would be expected based on the reasoning above. That is, the correlation coefficient is clearly negative between the flame and the peak of  $Q_s$ , and it is clearly positive from the peak towards the rich side (as far as statistically significant). These together contribute to the residual (dashed line) in Figure 4 that leads to the significance of  $R_{DD}$ .

Because  $R_{DD}$  is indicated to be a significant term in the transport of soot in mixture-fraction space, it is desirable to identify a suitable model. A model is suggested by the nature of  $\nabla \cdot [(D_\xi - D_\eta) \nabla \xi_\eta]$ . This source of differential diffusion is strongest at the highest wave numbers and can be expected to be short lived and of random sign. In mixture fraction space, this causes fluid elements to experience short-lived motions of random direction in  $\eta$ , suggesting a turbulent diffusion process. This could be modeled using the form of the second term on the r.h.s. of Eq. 16 so that we propose

$$R_{DD} \approx \frac{\rho_\eta \chi_\eta f_{\xi_0}}{2Le_{DD}} \frac{\partial^2 Q_s}{\partial \eta^2} \tag{17}$$

Here the scalar dissipation rate acts as a turbulent diffusivity with an empirical correction provided by an effective turbulent Lewis number associated with turbulent diffusion due to differential diffusion,  $L_{\ell DD}$ . Setting  $L_{\ell DD} = 3$  the left and right side of Eq. 17 are plotted in Figure 6. There is substantial noise in the evaluation of the second derivative,  $\partial^2 Q_s / \partial \eta^2$ , but the results indicate that the model for  $R_{DD}$  proposed in Eq. 17 has the correct form. Further, the results indicate that  $L_{\ell DD}$  is close to unity. This is particularly significant since it suggests that the model is consistent with the observations that a unity Lewis number works well for species subject to differential diffusion. The results shown in Figure 6 further suggest a trend in  $L_{\ell DD}$ : As the flame evolves (upward) it appears that the best fit to the Lewis number would be trending towards unity. For example, while  $L_{\ell DD} = 3$  is used in figure in agreement with the value found in applying this same model to another configuration [20], a better fit at 0.95 widths might be obtained with  $L_{\ell DD} = 6$  and at 1.95 widths with  $L_{\ell DD} = 1.5$ . Since the Reynolds number increases as the flow evolves upward, this suggests that  $L_{\ell DD}$  may trend towards unity at larger Reynolds numbers in agreement with scaling arguments [21]. Such a trend would also agree with the model proposed in Ref. [4] where

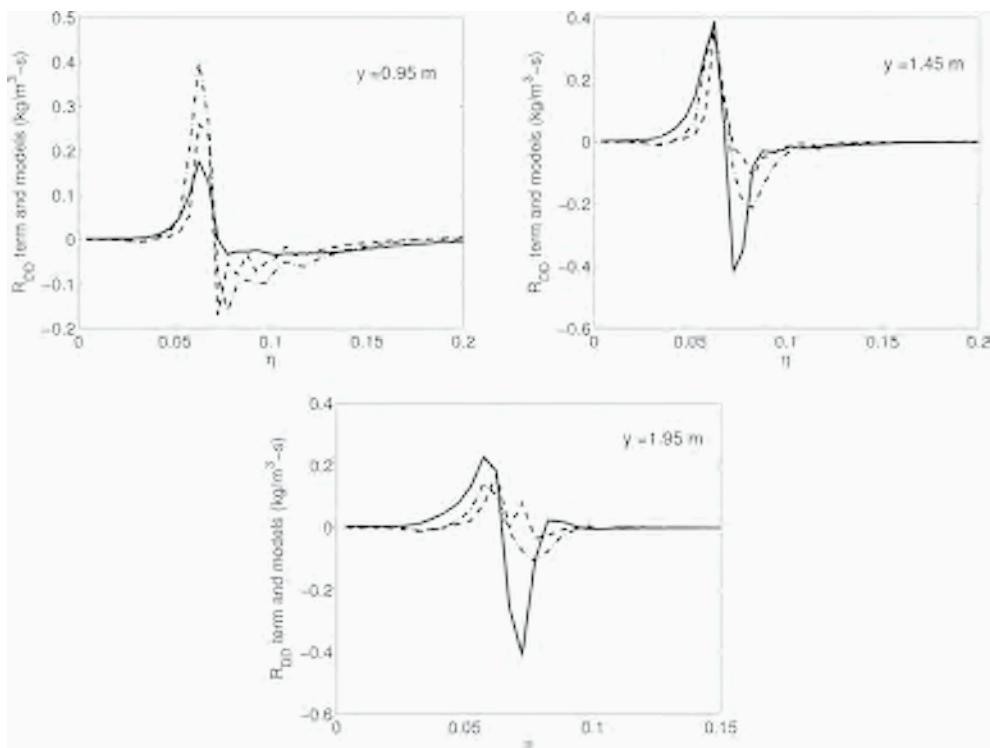


Figure 6. Proposed model for  $R_{DD}$ . The left-hand side of Eq. 17 is shown in solid, the right-hand side is the dashed line. Also shown with the dash-dot line is the alternate model from Eq. 18. Heights above the pool are 0.95, 1.45 and 1.95 source widths as indicated within the panels.

a Kolmogorov time scale was employed to introduce a Reynolds number dependence to the differential-diffusion mixing process.

In addition, this model does not require the solution of an additional transport equation for every species subject to differential diffusion as proposed by [4].

We note that the turbulent diffusion process is often written as

$$R_{DD} \approx \frac{\partial}{\partial \eta} \left( \frac{\rho \chi \eta f_{\xi_s}}{2Le_{DD}} \frac{\partial Q_s}{\partial \eta} \right). \quad (18)$$

where the variation of the turbulent diffusion coefficient in  $\eta$ -space is included. This is also shown in Figure 6. Given the present results, it is not possible to differentiate between the two approximations to  $R_{DD}$ . Because the expression provided in Eq. 17 is of a form familiar in CMC modeling, this term can be tentatively recommended.

Also important in Figure 3 are the two contributions of the soot source terms. These act together to produce the soot and to move it to leaner regions because the gas phase becomes leaner where carbon is transformed to soot (and vice-versa). The modeling of the coupled source with the scalar proposed in Eq. 12 is found to be accurate to within a few percent.

Finally, the vertical flux of the soot is significant, showing the strong effect of the evolution over the entire fire on the soot profiles in the  $\eta$  coordinate. The scalar flux fluctuations,  $\nabla \cdot \langle \rho \vec{v}'_s | \eta \rangle f_{\xi_s}$ , are small, at least in the region where the results are presented here. This is surprising since both Refs. [4] and [22] found that this term was important for moving the differentially diffusing scalars back towards the equal mixing line. Because of the different derivation of the CMC equation employed here, it is possible that this effect is retained in a different term. Specifically, the residual correlation term  $R_{DD}$  does not appear in their derivations. Also, as noted in [4], the evaluation of the scalar flux fluctuations is challenging, and within the context of ODT it is even more so; this term requires additional analysis.

In Sec. 2.2 it was suggested that employing a mixture-fraction equation with a soot source term was preferable in the present scenario. This deserves comment. If Eq. 3 were retained to define the evolution of  $\xi$ , the differential-diffusion term on the r.h.s. of Eq. 3 would result in a term in the CMC equation of similar form to the fourth term on the r.h.s. of Eq. 7 except that the gradients would involve the soot mass fraction and the term would be of the opposite sign,  $-\nabla \cdot [\rho(D_\xi - D_s)\nabla Y_s]$ . This term is found to be almost as large as, and of opposite sign to, the fourth term on the r.h.s. of Eq. 7; this indicates that the differential diffusion is not determined by  $\nabla \cdot [\rho(D_\xi - D_s)\nabla \xi]$  but by the difference between  $\nabla \cdot [\rho(D_\xi - D_s)\nabla \xi]$  and  $\nabla \cdot [\rho(D_\xi - D_s)\nabla Y_s]$ , which just happens to be  $\nabla \cdot [\rho(D_\xi - D_s)\nabla \xi_s]$  as appears in Eq. 7. Further, in every term where  $\nabla \xi$  appears in any form (i.e. the scalar-dissipation rate as well as the differential-diffusion terms) the gradient would be composed of the combined gradients of  $\xi_g$  and  $Y_s$ . With  $Le_s$  being large, the maximum values for  $\nabla Y_s$  can be greater than those for  $\nabla \xi_g$ , and the contribution of  $\nabla Y_s$  to all of these terms is significant. The result is that scalar-dissipation rates need to be known for the total mixture fraction, including the contribution from the soot, and also for just  $\xi_g$  to estimate the differential-diffusion terms from Eq. 15. Because the simple model suggested in Eq. 12 for the contribution of  $m_s$  the evolution of  $\xi_g$  works well, it is found that the use of the gas-phase mixture fraction results in an easier closure problem than the use of the total mixture fraction.

## 5. CONCLUSIONS

The CMC equation for the evolution of soot was derived starting from the joint-pdf equation for  $\xi_g$  and  $Y_s$  and retaining residual terms associated with errors in the typical closure models. The resulting CMC equation is compared with the results of ODT simulations based on a new spatially evolving formulation. The terms involving differential diffusion are found to be important along with the soot source terms and the large-scale evolution of both the mixture fraction and the soot. Of particular importance in the regions in mixture fraction space around the soot production and consumption is a residual term not previously identified that comprises the correlation between the differential diffusion and the soot mass fraction. This term results in a diffusion-like behavior in the mixture fraction coordinate that has an apparent Lewis number near unity.

The results here also suggest that when a large-Lewis number component is a non-negligible component of the mixture fraction, it may be easier to employ a mixture fraction, like  $\xi_g$ , neglecting this component. Such a mixture fraction variable has a source term that can be closed with the simplest of models.

## ACKNOWLEDGMENTS

This work was carried out in part while several of the authors (J. C. H., S. R. T. and R. O. F.) were attending the Center for Turbulence Research 2006 Summer Program at Stanford University. We are indebted to fellow summer program participants for their helpful suggestions, in particular to Luc Vervisch and Heinz Pitsch. Valuable discussions with Jay Gore throughout the development of the ODT models are appreciated. This work was conducted through support from Sandia National Laboratories, a multiprogram laboratory operated by Sandia Corporation, a Lockheed Martin Company, for the United States Department of Energy's National Nuclear Security Administration under Contract DE-AC04-94AL85000.

## REFERENCES

1. A. Y. Klimenko, R. W. Bilger, *Prog. Energy Combust. Sci.* 25 (1999) 595-687.
2. H. Pitsch, M. Chen, N. Peters, *Proc. Combust. Inst.* 27 (1998) 1057-1064.
3. H. Pitsch, N. Peters, *Combust. Flame* 114 (1998) 26-40.
4. A. Kronenburg, R. W. Bilger, *Phys. Fluids* 9(5) (1997) 1435-1447.
5. H. Pitsch, E. Riesmeier, N. Peters, *Combust. Sci. Technol.* 158 (2000) 389-406.
6. A. Kronenburg, R. W. Bilger, J. H. Kent, *Combust. Flame* 121 (2000) 24-40.
7. A. J. Ricks, J. C. Hewson, A. R. Kerstein, J. P. Gore, S. R. Tieszen, W. T. Ashurst, *Combust. Sci. Technol.* 2008 submitted.
8. A. R. Kerstein, *J. Fluid Mech.* 392 (1999) 277-334.
9. M. Fairweather, W. P. Jones, R. P. Lindstedt, *Combust. Flame* 89 (45-63) 1992.
10. R. W. Bilger, *Phys. Fluids A* 5 (1993) 436.
11. A. Y. Klimenko, *Fluid Dynamics* 25 (1990) 327-333.
12. A. R. Kerstein, *J. Fluid Mech.* 231 (1991) 361-394.

13. T. Echehki, A. R. Kerstein, J.-Y. Chen, T. D. Dreeben, *Combust. Flame* 125 (2001) 1083-1105.
14. J. C. Hewson, A. R. Kerstein, *Combust. Theory Modeling* 5 (2001) 669-697.
15. W. T. Ashurst, A. R. Kerstein, L. M. Pickett, J. B. Ghandhi, *Phys. Fluids* 15 (2003) 579-582.
16. A. J. Ricks, ODT-Soot, Preliminary, Purdue University (2007).
17. H. Pitsch, Modellierung der Zündung und Schadstoffbildung bei der dieselmotorischen Verbrennung mit Hilfe interaktiven Flamelet-Modells, Ph.D. thesis, RWTH-Aachen (1998).
18. S. H. Kim, *Phys. Fluids* 16 (6) (2002) 2011-2014.
19. J. H. Kent, D. Honnery, *Combust. Sci. Technol.* 54 (1987), 383-397.
20. D. O. Lignell, J. C. Hewson, J. H. Chen, *Proc. Combust. Inst.* 32 (2008) doi:10.1016/j.proci.2008.07.007.
21. A. R. Kerstein, M. A. Cremer, P. A. McMurtry, *Phys. Fluids* 7 (8) (1995) 1999-2007.
22. V. Nilsen, G. Kosály, *Phys. Fluids* 9(11) (1997) 3386-3397.



# Characterisation of the flame properties of moderately oscillating sooting methane-air diffusion flames

M. Charwath, J. Hentschel, R. Suntz, H. Bockhorn

Universität Karlsruhe (TH)

Institut für Technische Chemie und Polymerchemie

Kaiserstraße 12, 76128 Karlsruhe, Germany

*Abstract: Soot particle properties of stationary and moderately oscillating methane-air diffusion flames have been experimentally and numerically investigated. Experimentally, laser based optical diagnostic techniques have been applied to determine soot volume fractions, particle number densities, particle size distributions, and particle temperatures in the investigated flames. The focus of the investigations is on the flame oscillated at 10 Hz, which is close to the frequency of self induced flickering. Additionally, further measurements at varying frequencies have been performed to determine the transition from linear to non-linear coupling of excitation and soot formation. Numerically, a modified flamelet approach has been applied to predict soot particle quantities in the investigated flames. The applied detailed kinetic model of soot formation is based on gaseous species mole fractions (>100 different chemical species) that interact through a complex mechanism (532 reactions).*

## 1. INTRODUCTION

The knowledge about stationary laminar diffusion flames exhibits rapid progress during the last few years. This allows also a proper modelling of different aspects like pollutant emission or soot formation. However, practical combustion devices frequently operate under non-stationary conditions. Laminar oscillating flames provide an opportunity to investigate phenomena of non-stationary combustion and simultaneously take advantage of the reproducibility of the system from cycle to cycle. Moreover, these flames keep their rotational symmetry which simplifies experimental data evaluation as well as the numerical effort. In this study both stationary and oscillating laminar methane-air diffusion flames under elevated pressure have been investigated. The oscillation is induced by a periodical modulation of the fuel flow. The investigated frequencies are in the magnitude of the typical self induced flickering frequency [1,2], whereas the amplitudes are relatively low compared to other experiments found in the literature [3-8].

The experimental results from this work represent a dataset of soot and flame properties which give on the one hand detailed insight into soot formation kinetics, and on the other hand allow the rigorous testing of computational methods. Moreover, they provide quantitative information about the influence of a time-varying flow field on flame and soot properties, and thus, they help to enhance the understanding of the

transient combustion process. Numerically, a method is introduced which is shown to be applicable to calculate soot particle quantities in the investigated flames properly. Thus, this approach covers the prediction of the most relevant experimental findings.

## 2. EXPERIMENTAL

The burner system used in the experiments consists of a co-annular laminar diffusion burner placed in a pressure chamber, and the fuel flow modulation system. The burner is made from two concentric plates of sintered metal. The inner plate has an open diameter of 10mm. The outer plate has an inner diameter of 22mm and an outer diameter of 50mm. By means of a water cooling system the pressure chamber's wall temperature is controlled to be 80°C. In order to induce the oscillations the methane air flow is periodically modulated by a magnetic valve just outside the pressure chamber. The frequency of modulation was varied between 2 and 20Hz. The effective oscillation of the gas flow is probed by a constant temperature anemometry system 2mm above the burner. The oscillation of the gas flow can be described by a sinusoidal variation and small amounts of its higher harmonics. The amplitude of the oscillations is 30% of the average flow rate.

The applied RAYLIX measurement technique is based on the simultaneous detection of Rayleigh-scattering, LII, and extinction, yielding in 2-dimensional (2-D) spatial information about soot volume fractions, particle number densities and mean particle radii of a log-normal size distribution with an a priori assumed constant width of  $\sigma=0.34$  [9,10]. Additionally, measurements of soot luminosity at different wavelengths and OH\*-chemiluminescence at 309 nm were performed. By applying Planck's law the different spectral luminosity intensities are converted into particle temperatures. All RAYLIX measured 2-D images of soot and OH\*-luminosity consist of several superposed images of different heights above the burner if the flame height exceeds the detectable area of the CCD camera. The single images are Abel deconvoluted by using an onion peeling algorithm as described by Dasch [11].

Moreover, the 2-colour TIRE-LII technique has been applied to characterise size distributions of soot particle ensembles. This technique's principal is based on the detection of time-resolved LII signals. These signals occur due to the absorption of a high intensive laser pulse of short duration. Thus, the particle ensemble is heated up far above the ambient gas temperature. After the laser pulse the particles cool down due to heat transfer to the surrounding gas, evaporation, and radiation. Because small particles are cooling down faster compared to larger ones the multi-exponential temperature decay of the LII signal is characteristic for the particle size distributions. The latter ones are obtained by fitting the simulated particle temperature decays onto measured ones. Assuming a priori a log-normal shape of the size distribution two fit parameters, the medium size  $r_m$  and the width  $\sigma$  are sufficient to describe the distribution. These two parameters are obtained using multi-dimensional non-linear regression [12,13]. Thus, in contrast to RAYLIX, this technique enables the determination of log-normal size distributions with variable distribution widths. Moreover, the 2-colour TIRE-LII technique also allows the determination of soot volume fractions. Because the maximum LII signal intensity is proportional to the soot volume fraction, it can be

regarded as an advantage that the determination of soot volume fractions is done from the same LII signals which are used to determine the particle size distributions. However, those soot volume fractions have to be appropriately normalized because the LII signals are not calibrated to absolute intensities.

### 3. NUMERICAL

When performing numerical simulations of soot formation with CFD codes, the large number of chemical species and chemical reactions involved in soot formation and oxidation is prohibitive for solving the species and energy equations simultaneously to the equations which describe the flow field (Navier-Stokes-equations). Under the assumption of sufficiently separated time scales for chemical reactions and transport processes, the combustion chemistry adjusts with short relaxation times to local flow conditions. By this, the chemical kinetics can be decoupled from the mixing process. This idea is realised in the flamelet concept [14].

Supposing a one-dimensional behaviour of the flame properties in the normal direction to the flame front, from energy and species transport equations and applying a coordinate transformation, “flamelet equations” can be derived. In these equations, temperature and species mass fractions are functions of the conserved scalar  $Z$  (mixture fraction), see equations (1) to (3). In addition, the scalar dissipation rate  $\chi$  totally represents the influence of the flow field on the flamelet structure.

$$\rho \cdot \frac{\partial Y_i}{\partial t} - \rho \cdot \frac{\chi_{st}}{2} \cdot \frac{\partial^2 Y_i}{\partial Z^2} = \omega_i \cdot M_i \quad \left[ \frac{kg_i}{m^3 \cdot s} \right] \quad (1)$$

$$\rho \cdot c_p \cdot \frac{\partial T}{\partial t} - \rho \cdot c_p \cdot \frac{\chi_{st}}{2} \cdot \frac{\partial^2 T}{\partial Z^2} = - \sum_{i=1}^m h_i \cdot \omega_i + q_r + \frac{\partial p}{\partial t} \quad \left[ \frac{kJ}{m^3 \cdot s} \right] \quad (2)$$

$$\chi_{st} = 2\alpha \cdot \left( \left( \frac{\partial Z}{\partial x_1} \right)^2 + \left( \frac{\partial Z}{\partial x_2} \right)^2 + \left( \frac{\partial Z}{\partial x_3} \right)^2 \right) \quad \left[ \frac{1}{s} \right] \quad (3)$$

The solution of the flamelet equations for different scalar dissipation rates can be performed in a pre-processing step. Pursuing the flamelet concept rigorously, the species mass fractions and temperatures are tabulated in dependence on the mixture fraction and the scalar dissipation rate. Subsequently, in multidimensional CFD simulations of laminar flames, local values of species and temperature can be extracted from these tables. For this, only a transport equation for the mixture fraction needs to be solved in the CFD code, whereas the scalar dissipation rate  $\chi$  is evaluated from the mixture fraction distribution. In this concept, the number of equations to be solved is dramatically reduced [14]. Equations (1) and (2) have to be corrected for non-unity Lewis numbers [15].

To build the flamelet tables we used the FORTRAN program code SOFOKLES [15]. The program calculates the gas phase composition in flamelet coordinates accor-

ding to a detailed kinetic mechanism. This mechanism includes also the reactions which describe the formation of species considered to be the precursors of soot (HACA-mechanism). Therefore, the calculated flamelet tables include besides the detailed gas phase composition also soot volume fractions. Moreover, in this work the tabulated flamelets have been calculated with and without considering radiative heat transfer of soot to estimate the respective effects of radiation on the computed soot volume fraction field and flame structure. Depending on the solution strategy for the numerical simulation of soot formation in laminar diffusion flames the flamelet tables can be utilized in different ways. The first way is the rigorous flamelet approach as described above assuming that the time scale for soot formation is also much shorter than that of convection and diffusion. In this case the flamelet tables contain soot volume fractions and particle number densities in terms of  $Z$  and  $\chi$ . By this, local values of the soot volume fractions can directly be extracted from the flamelet libraries.

For fuels with high global soot formation rates (e.g. acetylene) the classical flamelet approach yields reasonable results which are in good agreement with measurements [16]. Global time scales for soot formation for different fuels are given e.g. in [17]. For fuels with smaller global soot formation rates (e.g. methane) the time scales of soot formation and chemical conversion of the fuel differ, the latter being closer to the flamelet assumptions than the former. Thus, in this study we modified the rigorous flamelet approach by following the idea to decouple these time scales by solving also a transport equation for the soot mass fraction in the CFD code in addition to the transport equation of  $Z$ .

$$\rho \cdot u_i \cdot \frac{\partial(y_i)}{\partial x_i} = \frac{\partial}{\partial x_i} \left( 0,55 \cdot \mu \cdot \frac{1}{T} \cdot \frac{\partial T}{\partial x_i} \cdot y_i \right) + source \left[ \frac{kg_{Soot}}{m^3 \cdot s} \right] \quad (4)$$

The transport equation for the soot mass fraction, Eq. (4), includes besides the convective and thermo-diffusive terms also the rates of the single steps of soot formation. These formation rates clearly depend on the local values of the mixture fraction  $Z$  and the scalar dissipation rate  $\chi$ . In the CFD simulations the soot transport equation is simultaneously solved with the mixture fraction transport equation by extracting the tabulated formation rates according to the local values of the mixture fraction  $Z$  and the scalar dissipation rate  $\chi$ . It has to be pointed out that tabulating the soot formation rates instead of absolute soot volume fractions is not affecting the gas phase composition in any way. Thus, species concentrations and gas temperatures are similar for the two different approaches. The CFD code used is the commercial code CFX. All necessary model specific options have been implemented as user defined subroutines.

## 4. EXPERIMENTAL RESULTS

### 4.1 RAYLIX Measurements

The results presented in section 4.1 are centred about a laminar diffusion flame with a cold gas flow rate of 0.2 l<sub>N</sub>/min for methane and 12 l<sub>N</sub>/min for air operating at a pressure of 250 kPa. This flame was operated either under stationary conditions or with sinusoidal excited fuel flow variations, whereas the amplitude variation amounted to 30%.

4.1.1 Stationary flame

Figure 1 shows soot particle properties, particle temperatures and OH\*-chemiluminescence as 2-D images. From the figure the following can be observed: (a) Soot particle inception within short residence times is the dominating process in the lower parts of the flame. The soot concentration increases with longer residence times and the soot

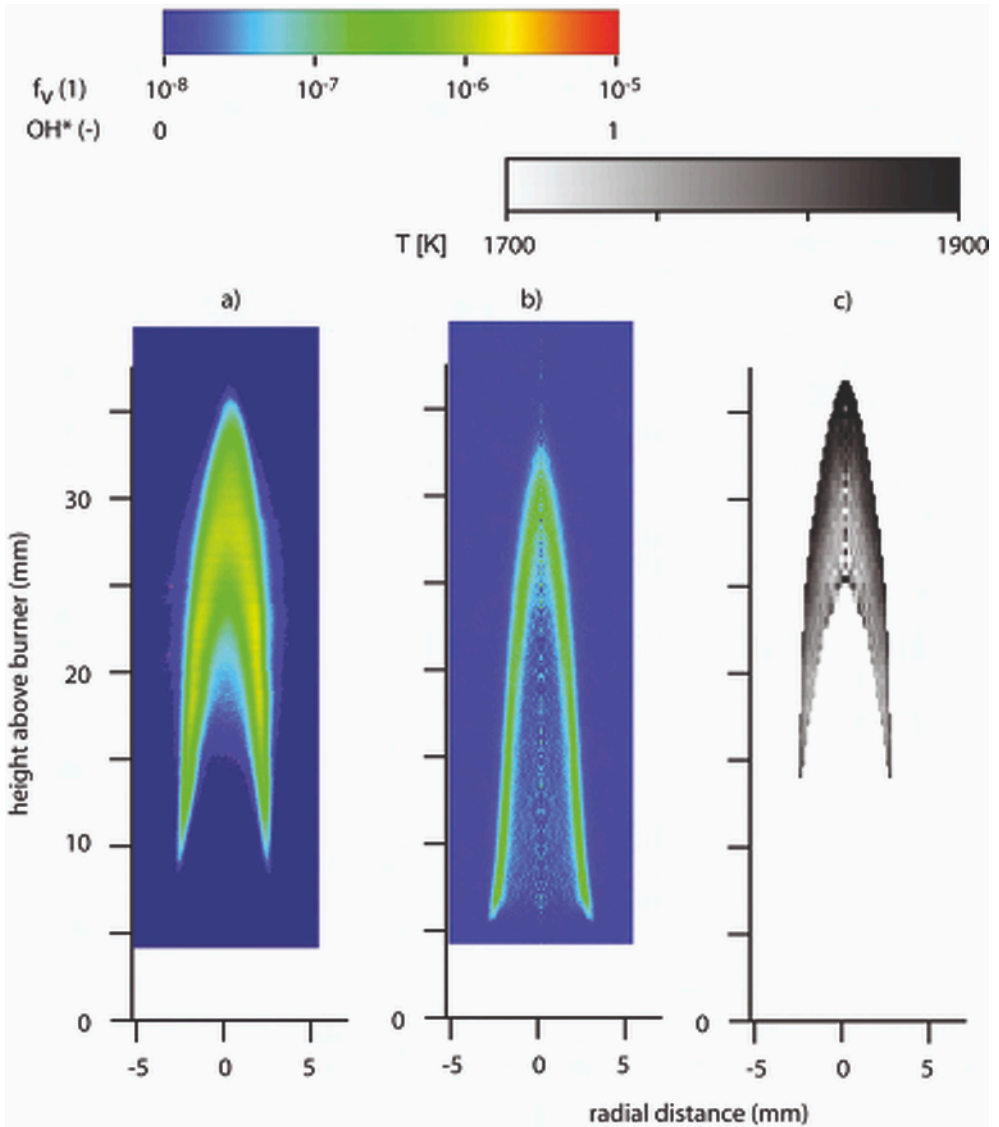


Figure 1. Experimental results of the stationary flame measured with the RAYLIX technique: soot volume fraction (a), OH\*-emission, Abel inverted (b), particle temperature (c).

concentration field moves towards the centre until the soot is oxidized in the flame tip. (b) The soot particle temperatures are in the 1700-1900 K range, close to the stoichiometric line the temperature is highest and decreases towards the flame centre. (c) Figure 1b shows that at very low heights above the burner exit the OH\*-chemiluminescence signal is detectable. Over the complete flame height both the thickness of the OH\*-chemiluminescence layer as well as the detected intensities are almost constant. (d) The comparison of the 2D field of soot volume fraction (Figure 1a) with the 2D field of the OH\*-chemiluminescence (Figure 1b) shows, that the soot is surrounded by the OH\* layer until in the tip of the flame the OH\* layer closes in and overlaps with the soot layer. The overlapping of OH\* and soot luminosity is an indicator of the zone of soot oxidation.

#### 4.1.2 Oscillating flame

In Figure 2 the phase resolved soot luminosity signals of the flame forced with 10Hz excitation frequency is shown. This figure illustrates that for some points in time the contour of the soot luminosity of the oscillating flame is qualitatively not comparable to the contour of the stationary flame. Additionally, at  $t=20\text{ms}$  a detachment of the flame tip can be observed. These observations already indicate a non-linear correlation in the temporal evolution of soot formation and the fuel flow variation for the given boundary conditions. A quantitative analysis of these non-linear correlations is shown in Figure 3. This figure displays the temporal evolution of RAYLIX measured volume-integrated soot volume fractions of an oscillating flame at 10Hz. The values of the oscillating flame are normalised by the volume-integrated soot volume fraction of a stationary flame with a mean fuel flow rate of  $0.2 \text{ l}_N/\text{min}$ . Also, the figure illustrates the sinusoidal temporal evolution of the fuel flow. One observes that at  $t = 20\text{-}30 \text{ ms}$  the soot volume fraction is almost reduced to zero. At later times the soot volume fraction is increased, reaching a maximum value at  $t = 5 \text{ ms}$ , to decrease again to the ini-

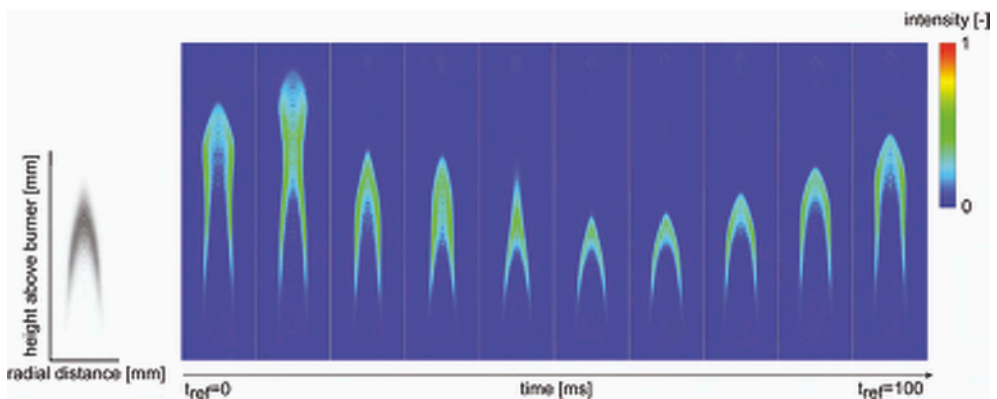


Figure 2. Soot luminosity intensities in the stationary flame (left-most) and oscillating flame (10Hz) at ten different phase angles; delay times  $t_{\text{ref}}$  relative to valve trigger.

tial value within 15 ms. It is evident that the temporal course of the oscillating soot volume fraction shows a strong asymmetric behaviour and differs significantly from the sinusoidal fuel flow variation. Moreover, the maximum value is increased by a factor of almost 7 compared to the soot volume fraction of the stationary flame. Thus, the response function of the oscillating flame exhibits not only an asymmetric behaviour in time but also a non-linear amplification of soot concentration variations. This non-linear amplitude coupling results in increased time-averaged volume-integrated soot concentrations (factor of approximately 2) in the oscillating flame compared to the stationary flame with an equivalent mean fuel flow.

#### 4.2 Two-colour TIRE-LII

As it could be shown in section 4.1, the RAYLIX technique is an appropriate diagnostic tool for the quantitative determination of soot volume fractions, particle number densities, mean particle radii, and particle temperatures in the flames under investigation. By this, the effects of the time-varying flow field on soot particle quantities can be discussed in comparison to the stationary case. More detailed information about the evolution of particle size distributions in stationary and time-varying flow fields can be obtained by applying the 2-colour TIRE-LII technique. In the following measured particle size distributions of a laminar diffusion flame with a cold gas flow rate of 0.2

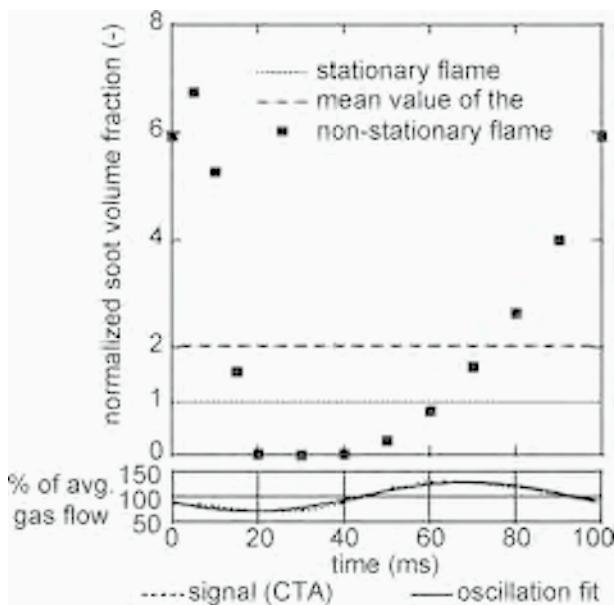


Figure 3: Time evolution of the normalized volume-integrated soot volume fraction in the RAYLIX-light sheet. The sinusoidal fuel flow variation is measured with a constant temperature anemometry (CTA).

$l_N/\text{min}$  for methane and  $12 l_N/\text{min}$  for air operating at a pressure of 200 kPa are presented. This flame either was operated under stationary conditions or with sinusoidal excited fuel flow variations. The frequency of the presented flame accounted to 10 Hz, the amplitude amounted to 30%.

#### 4.2.1 Stationary Flame

Figure 4 exhibits mean particle radii  $r_m$ , distribution widths  $\sigma$ , as well as soot volume fractions  $f_v$  as radial profiles for 20mm height above the burner exit. The results show that the maximum soot volume fraction corresponds on the one hand with the minimum mean particle radius and on the other hand with the maximum distribution width. Towards the symmetry axis the soot volume fraction is significantly decreased while the mean particle radius is increasing. Decreasing temperatures in the vicinity of the symmetry axis prevent noteworthy soot particle inception which would cause the formation of new soot particles and, therefore, the formation of noteworthy soot mass. By this, smaller soot volume fractions are observed. The larger particles and the smaller distribution widths can be explained by coagulation processes which do not affect the total mass of the particulate matter. In the vicinity of lean fuel mixture fraction regions ( $r_{fl} > 2 \text{ mm}$  at 20 mm) soot oxidation due to higher oxygen concentration is the dominating process. Because the smallest soot particles are completely oxidised, smaller distribution widths and increased apparent mean particle radii can be observed. At 30 mm height above the burner (see Figure 5) the maximum soot volume fraction is shifted towards the symmetry axis. Again, the maximum soot volume fraction corresponds with the minimum mean particle radius and the maximum distribution width. In reference to the location of the maximum soot volume fraction the latter one and the distribution width are decreasing while the mean particle radius is increasing

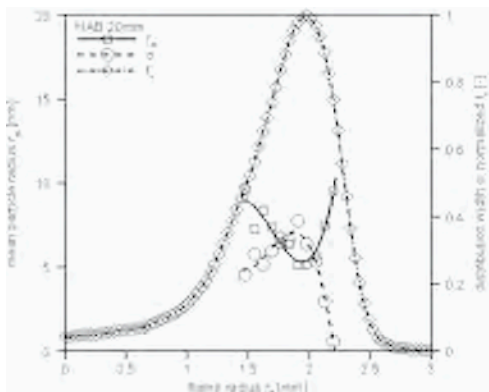


Figure 4. Experimentally determined soot volume fractions  $f_v$ , mean particle radii  $r_m$ , and distribution widths  $\sigma$  of a stationary flame (200 kPa) at 20mm above the burner exit.

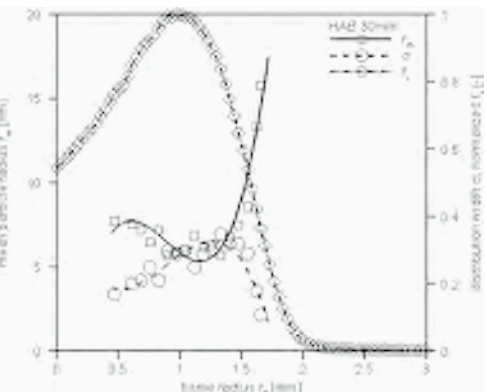


Figure 5. Experimentally determined soot volume fractions  $f_v$ , mean particle radii  $r_m$ , and distribution widths  $\sigma$  of a stationary flame (200 kPa) at 30mm above the burner exit.

towards the symmetry axis, however, less distinct compared to 20 mm height above the burner. This less distinct increase or decrease, respectively, in the profiles of the single soot particle properties can be explained by still sufficiently high temperatures which induce particle inception. The occurrence of particle inception takes account for a) an increased formation of the total soot mass, and thus, increased soot volume fractions, b) the formation of numerous small, new soot particles, and thus, smaller mean particle radii and c) wider distributions. Again, in the vicinity of lean fuel mixture fractions ( $r_{fl} > 1$  mm at 30 mm above the burner) the predominating oxidation process results in smaller distribution widths and increased apparent mean particle radii.

#### 4.2.2 Oscillating flame

In Figure 6, left part, radial profiles of mean particle radii of the oscillating flame are compared with those of a stationary flame. The oscillating flame refers to  $t = 40$  ms of the cycle and the fuel flow rate of the stationary flame refers to the same point in time, too. The right part of the figure contains radial profiles of soot particle mean radii from the oscillating flame at  $t = 20$  ms at different distances from the exit nozzle compared with that of a stationary flame. Again, the fuel flow rate of the stationary flame corresponds to that of the oscillating flame at  $t=20$ ms. At  $t = 20$  ms the mean particle radii  $r_m$  are increasing with increasing height above the burner to maximum values at 35 mm. At higher distances smaller mean particle radii can be observed. The corresponding distribution widths  $\sigma$  (not displayed) show the contrary behaviour: decreasing distributions widths with increasing distances and wider distributions at larger heights. It is evident, that the profiles of the oscillating flame are clearly different from those of a stationary flame (see Figure 4 and Figure 5). The major discrepancies are: a) At lower heights the course of the profiles of the oscillating flame exhibit no local minimum like

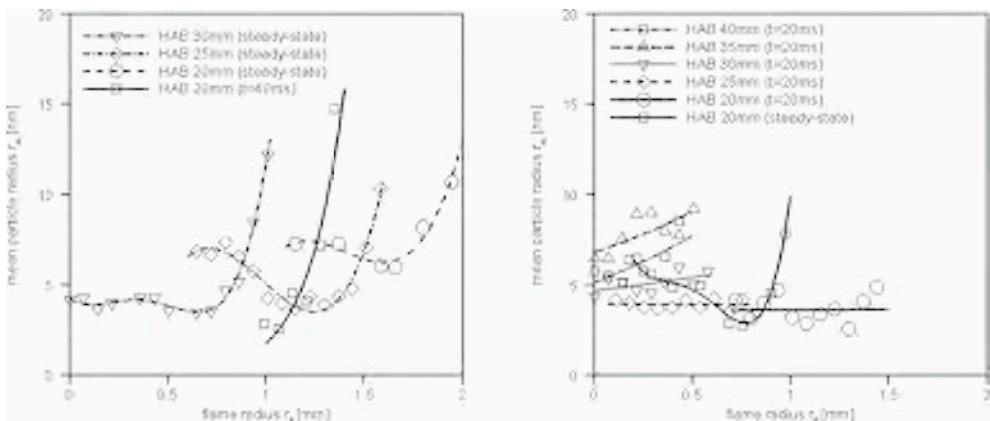


Figure 6. Comparison of radial profiles of the mean particle radii  $r_m$  of the oscillating flame (10Hz) with the ones of fuel flow equivalent stationary flames at two different phases (left figure:  $t=40$ ms; right figure:  $t=20$ ms) of the oscillation cycle.

it is observed in the stationary flame. The oscillating flame profiles are rather flat. b) At higher distances the oscillating flame profiles tend to increase continuously with increasing flame radius. However, the plateau region typical for the stationary flame in the vicinity of the symmetry axis cannot be identified. The maximum height above the burner at which time resolved LII signals could be detected in the oscillating flame and the fuel flow equivalent stationary flame are significantly different.

### 4.3 Flame at varying frequencies

The non-linear coupling of soot formation and fuel flow variation has been shown by analyzing the temporal evolution of the volume-integrated soot volume fraction of the oscillating flame at 10 Hz (see paragraph 4.1, Oscillating flame, Figure 3). At this frequency the variations of integral soot volume fractions are not symmetrical in contrast to the fuel flow variations. At lower frequencies a transition towards symmetric variations of the soot volume fractions should be detected. Thus, in order to determine the degree of asymmetry by means of an experimentally accessible parameter, the temporal evolution of soot luminosity signals in oscillating flames forced with different excitation frequencies (from 2 to 20 Hz) have been recorded. These signals are then analysed by Fourier transformation in order to determine the fundamental mode and the higher harmonics. The phase angles of the single oscillations are shifted in such a way that the fundamental mode is a pure cosine function. The higher harmonics are considered to be a linear combination of a sine and cosine function. The amplitudes of the single sine functions represent the asymmetric components of the detected signal, whereas the amplitudes of the single cosine functions represent the symmetric components. The absolute values of the single amplitudes are summed up and the asymmetric components are divided by the symmetric components. This ratio, noted in this study as the asymmetry ratio, reflects the degree of asymmetry of the response function and indicates either a linear or non-linear, respectively, coupling of the soot luminosity intensity and the fuel flow variation. Low values of the asymmetry ratio indicate a symmetric response function; increasing values denote an increasing asymmetric and therewith non-stationary behaviour of the flame.

In Figure 7 asymmetry ratios at two different heights above the burner are displayed. The results show that the flames at 6 Hz and below are less asymmetric than those at 7 Hz and above. This indicates a strong non-linear correlation between the fuel flow variation and the temporal evolution of the soot luminosity signal for frequencies  $\geq 7$  Hz. In consequence an oscillating flame excited with frequencies higher than 7 Hz cannot be represented by a continuous sequence of fuel flow equivalent stationary flames. Below 7 Hz excitation frequency the symmetry analysis indicates that the oscillating flame can be regarded as a continuous sequence of stationary flames.

## 5. COMPUTATIONAL RESULTS

In the following a comparison between experimental and predicted soot volume fractions is discussed, see Figure 8 and following. The 2-D images of measured soot volu-

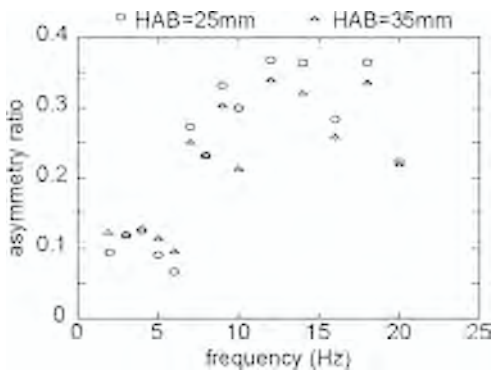


Figure 7. Asymmetry ratio of the soot luminosity signal in the oscillating flame (250 kPa) at different modulation frequencies.

me fractions consist of superposed 1-D profiles from different heights above the burner. Because these profiles are derived from 2-colour TIRE-LII measurements the soot volume fractions are normalized to the global maximum. The results of the calculations shown were obtained applying the modified flamelet approach (see above). Again, the results are normalized to the global maximum (normalization factor:  $3 \cdot 10^{-9}$  [-]). In order to demonstrate the influence of soot radiation on particle and flame properties, the calculations have been carried with and without radiative heat loss. The excitation frequency is 10 Hz, the amplitude variation amounts to 30%, and the ambient pressure is 200kPa.

### 5.1 Stationary flame

Figure 8 displays a comparison of experimental and simulated soot volume fractions. In the experiments (left part) it can be seen that soot was detected up to 42 mm above the burner exit. At heights lower than 16 mm the emitted intensities were too small to derive sufficiently accurate values for the soot volume fractions. The figure shows that at lower heights above the burner the maximum soot volume fraction is located at the edges of the flame. With increasing height the maximum shifts towards the symmetry axis forming a centred zone at distances higher than 35 mm. Due to oxidation the soot volume fraction is decreasing in the very tip of the flame. Figure 8, right part, shows the predicted field of soot volume fractions. The calculations are done including radiative heat loss of soot particles. The major discrepancies between the prediction and the measurement are: a) At the tip of flame the predicted soot concentration in the centreline region is lower than in the experiment. The shoulders do not merge as completely in the tip of the flame as in the experiment. b) The predicted visible flame height is marginal lower which is supposed to be the consequence of a). Nevertheless, despite the observed discrepancies the measurements and the simulations agree quite well. Thus, the presented modified flamelet approach is applicable to predict soot particle quantities in the stationary case.

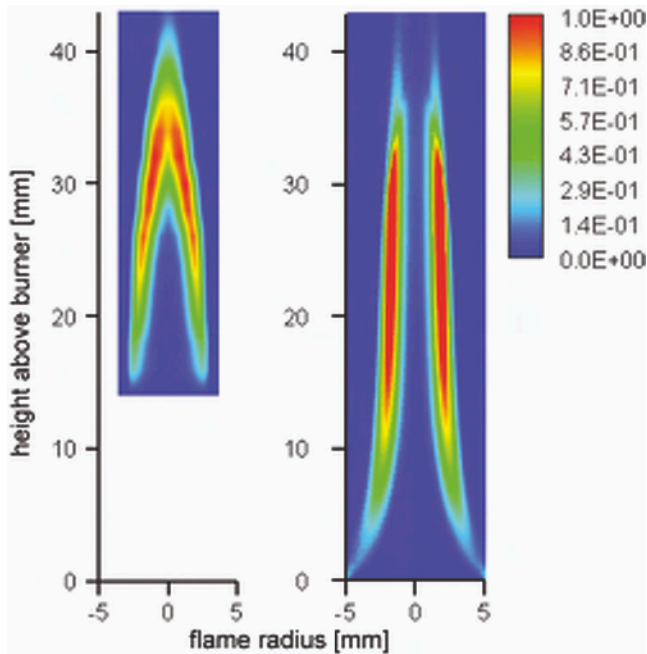


Figure 8. Comparison of experimental and simulated soot volume fractions considering soot radiation in a stationary diffusion flame (normalization factor:  $3 \cdot 10^{-9}$ ).

## 5.2 Oscillating flame

Figure 9 shows the temperature field computed excluding radiative heat transfer of soot particles. The temperature for the stationary case shows a global maximum of 2232 K, which is the adiabatic temperature for a stoichiometric methane-air mixture. The flame length, referring by definition to the tip of the stoichiometric contour, is at about 48 mm distance from the exit nozzle. The structure of the single isotherms of the oscillating flame in parts of rising fuel flow rates and in parts of decreasing fuel flow rates, respectively, are qualitatively different. This observation can be explained by strong buoyancy effects caused by high temperatures and low densities. Furthermore, these effects lead to a longer flame including a characteristic contraction followed by a displacement of hot gas at the flame tip. The flame length of the oscillating flame varies about 20% which is less than the amplitude variation of the fuel flow rate. Moreover, the structures of the flame completely deviate from the structure seen in the stationary case for each time interval.

In Figure 10 the appropriate isoplots of soot volume fractions are depicted. It is evident that no soot can be found beyond the stoichiometric contour towards lean mixtures. Highest soot volume fractions are located in the vicinity of mixture fractions from 0.07 to 0.2. The behaviour of the oscillating flame is different from what one expects in the case of fuel flow equivalent stationary flames. In the stationary case the

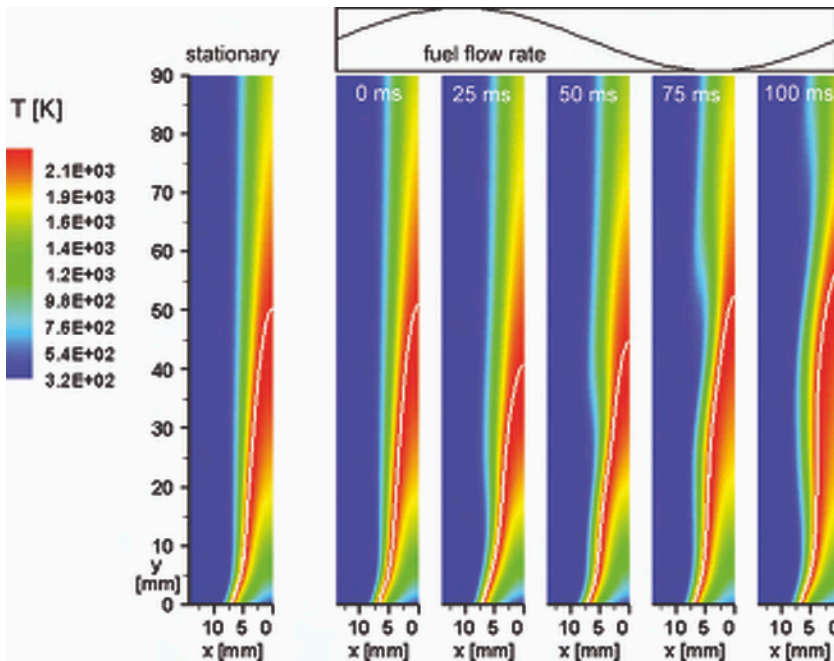


Figure 9. Calculation without soot radiation (10Hz, 200kPa): temperature field and contour of the stoichiometric mixture fraction (white line).

maximum distance for the stoichiometric mixture fraction contour on the centreline increases or decreases, when the fuel flow rate is increased or decreased, respectively. However, in Figure 10 at  $0 \text{ ms} < t < 25 \text{ ms}$  a decreasing maximum distance for the stoichiometric mixture fraction contour with increasing fuel flow rate can be observed. At  $25 \text{ ms} < t < 75 \text{ ms}$  the maximum distance is increasing with decreasing fuel flow rates. An increase of the stoichiometric mixture fraction contour with increasing fuel flow occurs only at  $75 \text{ ms} < t < 100 \text{ ms}$ . The resulting phase shift of the soot volume fraction oscillations compared to the fuel flow rate variation is about 230 degree. In Figure 11 the computed isoplots of soot volume fractions including soot radiation are shown. Compared to the calculations excluding soot radiation the results of the stationary and oscillating flame qualitatively show similar behaviour. However, the phase shift between excitation and flame length (about 180 degree) seems to be smaller as in the case without soot radiation.

A time resolved illustration of the evolution of the integral soot mass in the predicted oscillating flame is given in Figure 12. The course of the total soot mass differs in either considering or not considering radiative heat transfer from soot. The computed results including soot radiation  $\bar{f}_{v, \text{simu, radiation}}$  show indeed a phase shift of about 180 degrees between fuel flow rate and overall soot mass and exhibit a symmetric temporal evolution. Moreover, the soot mass varies symmetrically about a time-mean average. Compared with the experimental findings the computations predict the phase

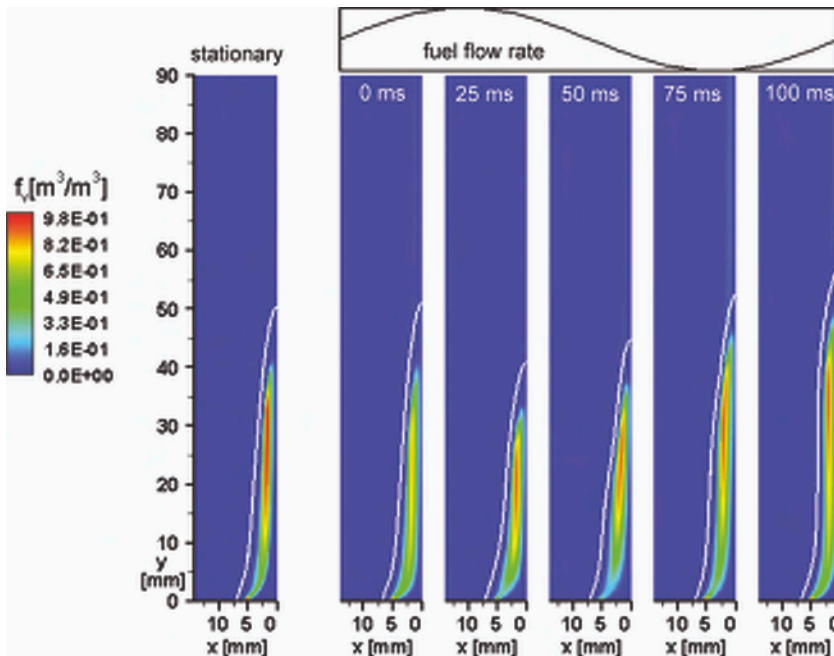


Figure 10. Calculation without soot radiation (10Hz, 200kPa): soot volume fraction and contour of the stoichiometric mixture fraction, white line (normalization factor:  $3 \cdot 10^{-9}$ ).

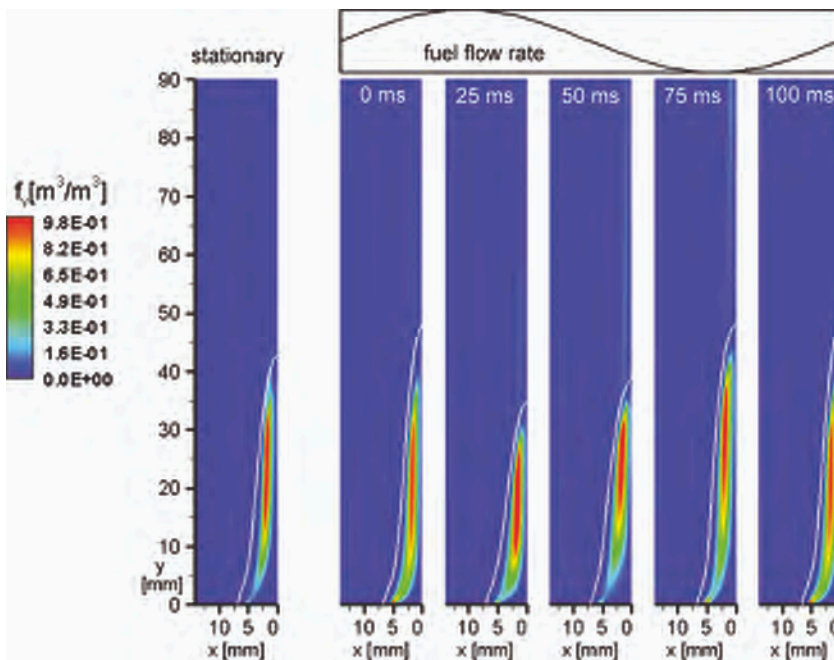


Figure 11. Calculation with soot radiation (10Hz, 200kPa): soot volume fraction and contour of the stoichiometric mixture fraction, white line; (normalization factor:  $3 \cdot 10^{-9}$ ).

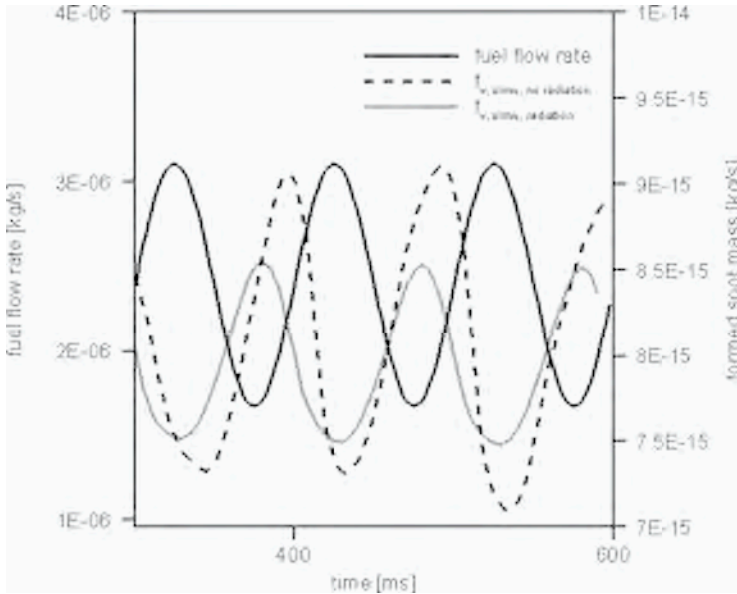


Figure 12. Computed soot mass as function of time in the oscillating flame at 10Hz either considering soot radiation or not considering; sinusoidal fuel flow variation at 10Hz and with an amplitude of 30%.

shift, however, the experimentally observed increased time-averaged soot quantities of the oscillating flame and the asymmetric temporal evolution could not be predicted. In contrast, the course of the integral soot mass of the oscillating flame without soot radiation  $f_{v, \text{simu, no radiation}}$  shows different characteristics. The general course does not follow a pure sinusoidal function and shows a slightly asymmetric behaviour. The amplitude of the soot mass variation is twice as much as in the case including soot radiation (12% versus 6%). The phase shift between fuel flow rate and overall soot mass is about 230 degrees. Again, an increased time-averaged soot mass of the oscillating flame cannot be predicted by the computations.

While the differences between including and excluding radiation may be explained by effects of buoyancy and the influence of temperature on soot formation and oxidation, the failure in predicting the asymmetry of the time variations, see Figure 7, of the soot volume fractions and the increased time average, see Figure 3, seems to necessitate the extension of the flamelet approach to non stationary flamelets.

## 6. CONCLUSIONS

Experiments with moderately oscillating laminar diffusion flames at an excitation frequency of 10 Hz show a strong non-linear correlation between the excitation and the response of soot particle quantities. The volume-integrated soot volume fraction in the oscillating flame varies asymmetrically with time and is not in phase with the fuel flow

modulation. Thus, the time-averaged soot concentrations in the oscillating flame are increased. The single phases of the flame cannot be represented by stationary flames of equivalent fuel flow rates. Moreover, a detachment of the flame tip takes place. At 7Hz a transition towards a series of stationary flames can be observed.

It could be shown by numerical simulation that the presented modified flamelet approach is applicable to model soot and particle properties in the investigated stationary and oscillating laminar diffusion flames reasonably well. Excluding soot radiation yields results which predict the experimental observed phase shift, and, moreover, the asymmetric time evolution of the overall soot mass. However, increased time-averaged soot concentrations of the oscillating flame compared with the equivalent fuel flow rate stationary flame could not be predicted. Therefore, the extension of the flamelet approach to non stationary flamelets seems to be necessary.

## ACKNOWLEDGEMENT

This work was performed within the scope of the Sonderforschungsbereich 606 on non-stationary combustion. The authors gratefully acknowledge the financial support of the Deutsche Forschungsgemeinschaft.

## REFERENCES

1. A. Hamins, J.C. Yang, T. Kashiwagi, *Proc. Combust. Inst.* 24 (1993) 1695-1702.
2. B.M. Cetegen, T.A. Ahmed, *Combust. Flame*, 93 (1993) 157-184.
3. C.R. Shaddix, J.E. Harrington, K.C. Smyth, *Combust. Flame*, 99 (1994) 723-732.
4. O.A. Ezekoye, K.M. Martin, F. Bisetti, *Proc. Combust. Inst.* 30 (2005) 1485-1492.
5. B.A. Strayer, D. Dunn-Rankin, F. Jabbari, *Proc. Combust. Inst.* 27 (1999) 1247-1254.
6. T.K. Kim, J. Park, H.D. Shin, *Combust. Sci. Technol.* 89 (1-4) (1993) 83-100.
7. M. Saito, M. Sato, A. Nishimura, *Fuel* 77 (9/19) (1998) 973-978.
8. G. Papadopoulos, R.A. Bryant, W.M. Pitts, *Ex. Fluids* 33 (2002) 472-481.
9. H. Geitlinger, T. Streibel, R. Suntz, H. Bockhorn, *Proc. Combust. Inst.* 27 (1999) 1613-1621.
10. H. Bockhorn, H. Geitlinger, B. Jungfleisch, T. Lehre, A. Schön, T. Streibel, R. Suntz, *Phys. Chem. Chem. Phys.* 4 (15) (2002) 3780-3793.
11. C.J. Dasch, *Appl. Opt.* 31 (8) (1992) 1146-1152.
12. Lehre, H. Bockhorn, B. Jungfleisch, R. Suntz, *Chemosphere* 51, pp. 1055-1061 (2003)
13. T. Lehre, PhD Thesis, University of Karlsruhe (2004)
14. N. Peters, *Prog. in Energy and Combust. Sci.* 10, 319-339 (1984)
15. J. Appel, H. Bockhorn and M. Frenklach, *Combust. Flame* 121, 122 (2000).
16. A. Schön, Th. Streibel, R. Suntz and H. Bockhorn, *Proc. Combust. Inst.* 29 (2002) 2399.
17. H. Bockhorn, Soot Formation and Oxidation, in: *Pollutants Formation from Combustion*, (C. Vovelle ed.) p. 205, Kluwer Academic Publishers, Dordrecht (2000).

# Prediction of particulates in turbulent diffusion flames by conditional moment closure

J.H. Kent

*School of Aerospace, Mechanical and Mechatronic Engineering  
University of Sydney*

*Abstract: A full chemical kinetic and particle dynamics scheme used in laminar non-premixed flames is applied to the prediction of particulate loading in turbulent non-premixed flames. The gas-phase scheme models the growth of aromatic compounds and acetylene for particle formation and growth. A sectional approach for particle dynamics allows size effects to be modelled. Previous predictions of particulates in laminar ethylene and methane flames by this scheme have been reasonably successful. Here the model is applied to turbulent flames of these fuels using conditional moment closure. The predictions show that fuel effects and residence time trends are well represented by the model, but the particulate concentrations are lower than the data.*

## 1. INTRODUCTION

The accurate prediction of particulate concentration and size distribution in hydrocarbon combustion remains a long-standing problem. Even in relatively simple configurations such as laboratory premixed and non-premixed laminar flames there is plenty of scope for improving the predictive capability of models applied generally to differing fuels. After decades of research the conclusion must be that particulate formation and growth is complex and it is unlikely to be predicted by a simple scheme. In turbulent flames, which are more interesting from the practical viewpoint adds another level of complexity another level of complexity is added. Nevertheless this research needs to proceed simultaneously to determine how particulate dynamics in turbulent combustion differ from laminar flames. In the present work a particulate model which has shown some success in non-premixed, laminar flames is applied to non-premixed, turbulent flames. Axisymmetric, ethylene and methane fuelled flames are tested.

Soot concentrations in turbulent flames are not predicted well by steady-state flamelet modelling because formation rates are relatively slow compared with major species fast reactions [1] and so explicit models for formation and oxidation rates are needed. Relatively simple particulate inception and growth expressions have been used for turbulent combustion[2-8], because of the computational expense associated with increasing numbers of species when using PDF methods [2]. The present approach differs from these because a full chemical kinetic scheme for gas and particle phases is used. Turbulent reaction is modelled by Conditional Moment Closure (CMC) [9] which is much less intensive computationally and therefore allows solution of a large number of species within reasonable time, at least for two-dimensional flows. The chemical kinetic scheme has been tested in laminar non-premixed flames with several fuels to predict gas-phase species and particulate concentrations with some degree of success

[10, 11]. The aim of the present investigation is to apply the same scheme in turbulent non-premixed flames to determine whether similar accuracy is achievable.

## 2. SCHEME

The scheme of D'Anna, as detailed in previous papers [10,11], is used and it includes growth of species by fuel pyrolysis, particulate formation, growth, aggregation and oxidation. PAH formation includes reaction pathways leading to the formation of nanometric-sized particles and their coagulation to larger soot particles. A discrete-sectional approach [12] is used for the gas-to-particle process; the ensemble of compounds with molecular mass higher than the largest aromatic compound in the gas-phase is divided into classes of different molecular mass and all reactions are treated in the manner of gas phase chemistry using compound properties such as mass and the numbers of carbon and hydrogen atoms averaged within each section. Particle size distributions are obtained by solution of the transport equation for each section. A brief summary of the scheme is given here.

### 2.1. Gas phase

The gas-phase formation and growth of aromatic compounds bridges the main oxidation chemistry and particulate formation. The gas-phase kinetic mechanism to model hydrocarbon oxidation and pyrolysis is built onto the GRI mechanism for C1 and C2 species [13] and Miller and Melius suggestions for benzene formation [14]. The formation of naphthalene, the first compound in the PAH series, is modeled through two routes: the first, usually known as the HACA mechanism [15] is also used here to model the formation of multi-ring structures such as phenanthrene, pyrene and higher order PAHs up to coronene. The second is the combination of resonantly stabilized cyclopentadienyl radicals; two different reaction sequences are included for the formation of naphthalene: the combination of two cyclopentadienyl radicals and the combination of benzyl and propargyl. The cyclopentadienyl and indenyl radical combination is also used for the modeling of phenanthrene.

Details of the reaction pathways and the choice of the reaction constant used are reported in a previous paper [10] where the complete kinetic scheme for the gas-phase is listed. However the rate for the reaction  $C_2H_4 + M = C_2H_2 + H_2 + M$  was changed in the subsequent paper [11] to  $A = 15 \times 10^{14}$  (mol,cm,s) in accordance with literature data[16]. There are some 70 species in the gas phase and about 380 gas-phase reactions.

### 2.2. Growth of aromatics and particle inception

Acetylene and aromatics, from benzene to coronene, are the building blocks for the growth process which lead to the formation of high-molecular-mass, molecular particles. The mechanism consists of the sequential addition of either acetylene or aroma-

tic molecules to aromatic radicals. Classes of compounds termed sections, each covering a mass range are utilised. Sections are characterized by their average molecular mass and by their number of carbon and hydrogen atoms. The chemical reactions are treated in the same way as for gas phase chemistry and Table 1 reproduces the detailed sectional particle phase kinetic scheme [11]. Here  $A_i$  is an aromatic compound having a molecular mass corresponding to the  $i^{\text{th}}$  class of compounds and  $R_j$  is its radical. Also shown are the gas-phase reactions leading to the first sections. The rate constants are determined by using the Arrhenius formulation multiplied by a size dependent factor and a collision efficiency  $\gamma$  set to unity, except for the coagulation reactions marked by #.

### 2.3. Coagulation

The aromatics growth process can occur by formation of molecular clusters from collision of molecular compounds. The interaction energy is due to van der Waals forces. Small molecular mass aromatics may exhibit low interaction energy and as molecular mass increases interaction energy increases and the coagulation efficiency becomes more effective. The model of D'Alessio et al. [17], for premixed flame coagulation, is applied to the non-premixed flames. For particles around 1nm diameter the coagulation efficiency is about  $10^{-4}$  increasing to unity for particles around 10nm diameter.

In summary the complete scheme is made up of the gas-phase and particle phase schemes detailed previously [10,11] and added to the GRI mechanism [13].

There are 26 sections each containing the compound and its radical, starting with  $C_{12}$  and increasing by a constant factor of two. The C/H ratio is kept at 0.5 and the diameter range is 1nm-200nm. The largest sizes are to ensure that the series does not artificially truncate the solution. Reactions are balanced on carbon number; a sectional reaction generally results in two product classes proportioned to satisfy carbon element balance, but hydrogen element is not strictly balanced. The particle phase sectional combinations generate about 1850 reactions.

## 3. COMPUTATIONAL MODEL

The governing equations for unconditional and conditional-average quantities are steady-state, axisymmetric and the treatment follows Cleary and Kent [18]. Transport of momentum in axial and radial directions, mixture fraction and its variance, standardised enthalpy, together with turbulent kinetic energy and dissipation are solved as unconditional quantities. Turbulence is closed by the  $k$ - $\epsilon$  model using typical coefficients for axisymmetric flow [19]. All unconditional quantities are put in the following common form to facilitate numerical modelling where the terms in  $S_\phi$  are conventional.

$$\rho \mathbf{U} \cdot \nabla \phi = \nabla \cdot \left( \frac{\mu_t}{\sigma_\phi} \nabla \phi \right) + S_\phi \quad (1)$$

Heat loss by radiation is modelled broadband by the discrete transfer method [20]. The absorption coefficients are dominated by soot where present and they are adju-

Table 1. Sectional particle-phase reaction scheme. Rate constant  $k = \gamma (mC_n)^p AT^m \exp(-E/RT)$  · [cal,mole,cm<sup>3</sup>,s]. For particle-particle reactions  $C_n$  is average carbon number; for gas-particle reactions  $C_n$  refers to the particle. Collision efficiency  $\gamma$  for reactions marked # is modelled [11];  $\gamma = 1$  for other reactions. Sectional reactants are summed over all classes  $i, j$  and  $k$  represents the product sections.

	<b>A</b>	<b>n</b>	<b>E</b>	<b>p</b>	<b>m</b>	
R x 1	$A_i \Rightarrow R_i + H$	6.00E+14	0	113100	0.89	1
R x 2	$A_i + H \Rightarrow R_i + H_2$	5.20E+13	0	16000	0.8	1
R x 3	$A_i + OH \Rightarrow R_i + H_2O$	5.20E+13	0	4560	0.8	1
R x 4	$R_i + H_2 \Rightarrow A_i + H$	2.00E+16	0	0	-1.0	1
R x 5	$R_i + H_2O \Rightarrow A_i + OH$	2.00E+16	0	0	-1.0	1
R x 6	$R_i + C_2H_2 \Rightarrow A_k + H$	3.00E+06	1.787	3262	0.616	1
R x 7	$A1 + R_i \Rightarrow A_k + H$ $A2 + R_i \Rightarrow A_k + H$ $A2R5 + A2R5- \Rightarrow A_k + H$ $A2R5 + R_i \Rightarrow A_k + H$ $A3 + A2- \Rightarrow A_k + H$ $A3 + A2R5- \Rightarrow A_k + H$ $A3 + R_i \Rightarrow A_k + H$ $Ai + A1- \Rightarrow A_k + H$ $Ai + A2- \Rightarrow A_k + H$ $Ai + A2R5- \Rightarrow A_k + H$ $Ai + R_i \Rightarrow A_k + H$	8.00E+12	0.5	15000	1/6	12
R x 8	$A1- + R_i \Rightarrow A_k$ $A2- + R_i \Rightarrow A_k$ $A2R5- + A2R5- \Rightarrow A_k$ $A2R5- + R_i \Rightarrow A_k$ $R_i + R_i \Rightarrow A_k$	8.00E+12	0.5	0	1/6	12
R x 9	$R_i + H \Rightarrow A_i$	7.83E+13	0	0	0	0
R x 10	$A_i + OH \Rightarrow A_k + HCO$	3.00E+12	0.5	10600	2/3	1
R x 11	$R_i + O2 \Rightarrow A_k + 2CO$	4.30E+11	0	8000	2/3	1
R x 12	# $A1 + A_i \Rightarrow A_k$ # $A2 + A3 \Rightarrow A_k$ # $A2 + A_i \Rightarrow A_k$ # $A2R5 + A2R5 \Rightarrow A_k$ # $A2R5 + A3 \Rightarrow A_k$ # $A2R5 + A_i \Rightarrow A_k$ # $A3 + A3 \Rightarrow A_k$ # $A3 + A_i \Rightarrow A_k$ # $A_i + A_j \Rightarrow A_k$	8.00E+12	0.5	0	1/6	12
	<b>Gas-phase to particle-phase</b>					
	$A2- + A2- \Rightarrow A_k + 2H2$	1.78E+13	0.5	0	0	1
	$A2- + A2R5- \Rightarrow A_k + H2$	1.81E+13	0.5	0	0	1
	$A2 + A2 \Rightarrow A_k + 3H2$	5.45E+06	0.5	0	0	1
	$A2 + A2R5 \Rightarrow A_k + 2H2$	6.43E+06	0.5	0	0	1
	$A2 + A1- \Rightarrow A_k + 2H2$	1.71E+13	0.5	15000	0	1
	$A2 + A2- \Rightarrow A_k + 2H2$	1.78E+13	0.5	15000	0	1
	$A2 + A2R5- \Rightarrow A_k + 2H2$	1.81E+13	0.5	15000	0	1
	$A2R5 + A1- \Rightarrow A_k + 2H2$	1.75E+13	0.5	15000	0	1
	$A2R5 + A2- \Rightarrow A_k + 2H2$	1.81E+13	0.5	15000	0	1

sted so that predicted temperatures match measurements. Elsewhere absorption coefficients of the gas are temperature-dependent, weighted-sum, Planck mean absorption coefficients for carbon dioxide and water vapour [21].

Mean species and density of the mixture are obtained by Conditional Moment Closure (CMC) [9]. Fluctuating reaction rates in a turbulent, reacting flow are modelled by considering species conditioned upon the mixture fraction,  $\xi$ , defined as the mass fraction of the mixture having its origin in the fuel stream.

The instantaneous mass fraction of species  $i$  is

$$Y_i(\mathbf{x}, t) = Q_i(\xi(\mathbf{x}, t), \mathbf{x}, t) + Y_i'(\mathbf{x}, t) \tag{2}$$

where  $Y_i' = (x, t)$  is the fluctuation about the conditional mean  $Q_i(\eta(x, t), (x, t))$ , conditioned upon the mixture fraction,  $\xi$ , having a particular value  $\eta$ .

Unconditional average species mass fractions are determined from the conditional averages with an assumed PDF,  $P(\eta)$  [22].

$$\bar{Y}_i = \int_0^1 Q_i(\eta) P(\eta) d\eta \tag{3}$$

Clipped Gaussian PDF's are used here although  $\beta$ -function PDFs have also been tested elsewhere[23].

The transport equation for  $Q_i$  [9] in steady-state axisymmetric coordinates is

$$\begin{aligned} & \frac{\partial}{\partial x} \left( \rho_\eta u_\eta P(\eta) Q_i - \rho_\eta D_\eta P(\eta) \frac{\partial Q_i}{\partial x} \right) + \frac{1}{r} \frac{\partial}{\partial r} r \left( \rho_\eta v_\eta P(\eta) Q_i - \rho_\eta D_\eta P(\eta) \frac{\partial Q_i}{\partial r} \right) \\ & = \rho_\eta w_\eta P(\eta) - Q_i \frac{\partial^2 (\rho_\eta N_\eta P(\eta))}{\partial \eta^2} + \rho_\eta N_\eta P(\eta) \frac{\partial^2 Q_i}{\partial \eta^2} \end{aligned} \tag{4}$$

where gradient diffusion modelling  $\langle U' Y_i' | \eta \rangle = -D_\eta \nabla Q_i$  is used.

The PDF transport equation for  $P(\eta)$  is an adjoint equation to the conditional species transport equation and both must be satisfied for the model to be valid.

$$\frac{\partial}{\partial x} (\rho_\eta u_\eta P(\eta)) + \frac{1}{r} \frac{\partial}{\partial r} (r \rho_\eta v_\eta P(\eta)) = - \frac{\partial^2 (\rho_\eta N_\eta P(\eta))}{\partial \eta^2} \tag{5}$$

Favre PDFs are modelled; Reynolds and Favre forms of the PDF are related by[24]

$$\rho_\eta P(\eta) = \bar{\rho} \tilde{P}(\eta) \tag{6}$$

Putting  $\gamma = \bar{\rho} \tilde{P}(\eta)$ , Eq. 4 and 5 can be rewritten as

$$\frac{\partial}{\partial x} \left( \gamma u_\eta Q_i - \gamma D_\eta \frac{\partial Q_i}{\partial x} \right) + \frac{1}{r} \frac{\partial}{\partial r} r \left( \gamma v_\eta Q_i - \gamma D_\eta \frac{\partial Q_i}{\partial r} \right) = \gamma w_\eta - Q_i \frac{\partial^2 (\gamma N_\eta)}{\partial \eta^2} + \gamma N_\eta \frac{\partial^2 Q_i}{\partial \eta^2} \tag{7}$$

and

$$\frac{\partial}{\partial x} (\gamma u_\eta) + \frac{1}{r} \frac{\partial}{\partial r} (r \gamma v_\eta) = - \frac{\partial^2 (\gamma N_\eta)}{\partial \eta^2} \tag{8}$$

The transport terms now appear the same as for unconditional quantities where  $\gamma$  takes the place of density. Equation 8 is multiplied by  $Q$  and substituted into Eq. 7 which results in a conservative form of the equation suitable for finite volume discretisation.

$$\frac{\partial}{\partial x} \left( \gamma u_x Q_i - \gamma D_i \frac{\partial Q_i}{\partial x} \right) + \frac{1}{r} \frac{\partial}{\partial r} r \left( \gamma v_x Q_i - \gamma D_i \frac{\partial Q_i}{\partial r} \right) = \gamma w_{s,i} + \gamma N_{\eta} \frac{\partial^2 Q_i}{\partial \eta^2} + Q_i \left( \frac{\partial}{\partial x} (\gamma u_x) + \frac{1}{r} \frac{\partial}{\partial r} r (\gamma v_x) \right) \tag{9}$$

Without the spatial transport terms above we are left with the conditional average form of the Stationary Laminar Flamelet Model (SLFM).

$$w_{s,i} + N_{\eta} \frac{\partial^2 Q_i}{\partial \eta^2} = 0 \tag{10}$$

For first-order closure in CMC

$$w_{s,i} = w_i(\mathbf{Q}, T_{\eta}) \tag{11}$$

where the conditional temperature  $T_{\eta}$  is required.

Conditional temperature can strongly influence conditional reaction rates. The complexity of a conditional enthalpy with transparent medium radiation is not considered here. Instead the conditional temperature profile in a field with significant radiation losses is scaled from a corresponding adiabatic profile. The scaling is pivoted at  $\eta = 0$  and  $\eta = 1$ , the air and fuel temperatures as shown in Figure 1.

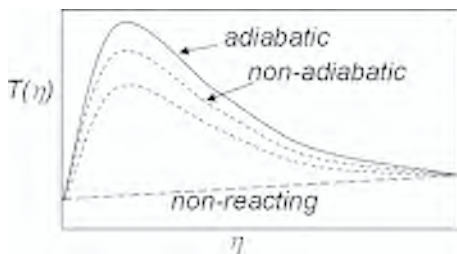


Figure 1. Schematic of conditional temperature modelling.

At each point in the field mean (unconditional) temperature  $\tilde{T}$  is obtained from the unconditional enthalpy and species concentration fields in conventional manner. The mean adiabatic temperature  $\tilde{T}_{ad}$  is also obtained for the same species concentrations. The scaling for the conditional temperature distribution is then obtained by satisfying

$$\tilde{T} - \tilde{T}_{\infty} = \int_0^1 [T(\eta) - T_{\infty}(\eta)] P(\eta) \kappa \eta \tag{12}$$

Thus the temperature distribution satisfies the unconditional enthalpy; the principal modelling assumption is that the shape of the adiabatic conditional temperature distribution is used as a template for the non-adiabatic distribution.

A gradient model for conditional velocity [25] is used.

$$\mathbf{U}_\eta = \hat{\mathbf{U}} - \frac{D_t}{\bar{P}(\eta)} \nabla \hat{P}(\eta) \quad (13)$$

The conditional scalar dissipation is obtained from the unconditional mean scalar dissipation for all  $\eta$ .

$$N_\eta = D \nabla \xi_{\eta_1} \cdot \nabla \xi_{\eta_1} = \frac{\tilde{\epsilon}}{k} \bar{g} \quad (14)$$

The finite-volume discretised equation for conditional quantities is obtained in similar fashion to unconditional quantities by integrating Eq.9 over a grid cell volume and dividing by  $\gamma V$ .

$$\begin{aligned} \frac{\gamma_c A_c}{\gamma V} \left( u_\eta Q_i - D_t \frac{\partial Q_i}{\partial x} \right)_c - \frac{\gamma_w A_w}{\gamma V} \left( u_\eta Q_i - D_t \frac{\partial Q_i}{\partial x} \right)_w + \frac{\gamma_r A_r}{\gamma V} \left( v_\eta Q_i - D_t \frac{\partial Q_i}{\partial r} \right)_r \\ - \frac{\gamma_b A_b}{\gamma V} \left( v_\eta Q_i - D_t \frac{\partial Q_i}{\partial r} \right)_b = w_{\eta,c} + N_\eta \frac{\partial^2 Q_i}{\partial \eta^2} + \frac{Q_i}{\gamma V} \left[ (\gamma u_\eta A)_c - (\gamma u_\eta A)_w + (\gamma v_\eta A)_r - (\gamma v_\eta A)_b \right] \end{aligned} \quad (15)$$

This expression has the same form as for unconditional variables, but for terms in the extra dimension  $\eta$ . The PDF ratios contained in terms  $\gamma_c/\gamma_w$ ,  $\gamma_r/\gamma_b$  etc. determine the magnitude of conditional variable spatial fluxes relative to the chemical reaction rate and relative to flux in mixture fraction space. If all the PDF ratios are small the conditioned variable approaches the SLFM solution of Eq. 10.

The PDF ratio at the cell boundary is evaluated from the cell boundary values of mean mixture fraction and variance assumed to be linearly distributed between cells. At pure air and pure fuel boundaries mixture fraction variance is zero and the PDF ratio approaches zero. Consequently the conditional boundary conditions at fuel and air inlets have zero conditional flux.

Central differencing is used for diffusive terms and first-order hybrid upwind differencing for the advection terms in Eq.15. A set of linearised equations is obtained where  $Q_i$  is given in terms of spatial and  $\eta$  neighbours by

$$Q_i = \frac{w_{\eta,c} + \sum a_i Q_{i,k}}{\sum a_i} \quad (16)$$

At each spatial location in turn Eq.16 is solved simultaneously for all species and all  $\eta$  using a modified Newton-Raphson scheme. The Jacobian includes all conditional species at the spatial location. An initial solution is obtained from an SLFM library. The criterion for convergence is that the mean absolute residual for all conditional species, normalised by the maximum value of the species, is about  $101^{-6} \cdot 10^{-5}$ .

The spatial grid expands in direction of increasing axial and radial distance from the nozzle and has a finest resolution of about 0.7mm in the radial direction and about 5mm in the axial direction. There are 40 points in  $\eta$  with closer increments around

stoichiometry. The unconditional grid covers 1m axially  $\times$  0.3m radially. The CMC grid only covers about 0.85m  $\times$  0.05m radially this being the region of significant interest defined by the mixture fraction field.

### 4. LAMINAR FLAME PREDICTIONS

An indication of the particulate modelling capability in laminar flames, presented previously [11], is shown in Figures 2 and 3 for ethylene and methane fuels. These fuels have markedly differing sooting propensity as shown and the model gives reasonable representation of particulate volume fractions in both cases over the length of the flames. For methane smaller particulates predominate and the modelled size distribution is split at 10nm into precursor (density 1g/cm<sup>3</sup>) and soot (density 1.8g/cm<sup>3</sup>) classes. These show good correspondence with the volume fraction of precursors measured

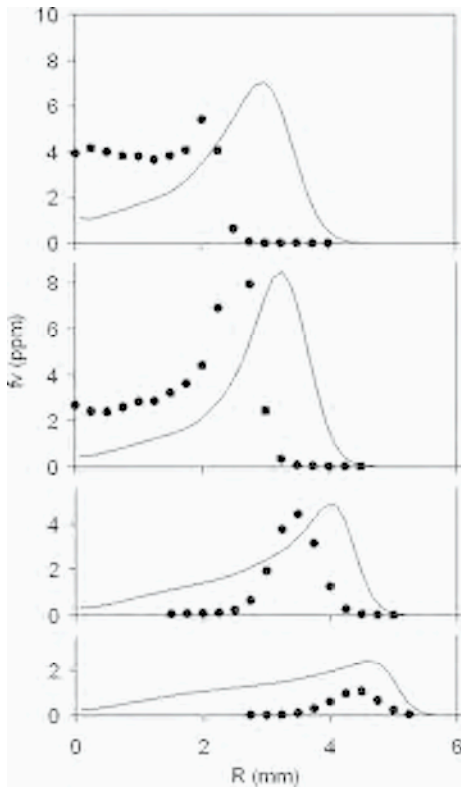


Figure 2. Predicted and measured [26] soot volume fraction in a laminar, non-premixed, ethylene flame at heights from bottom to top: 10mm, 20mm, 40mm, 60mm.

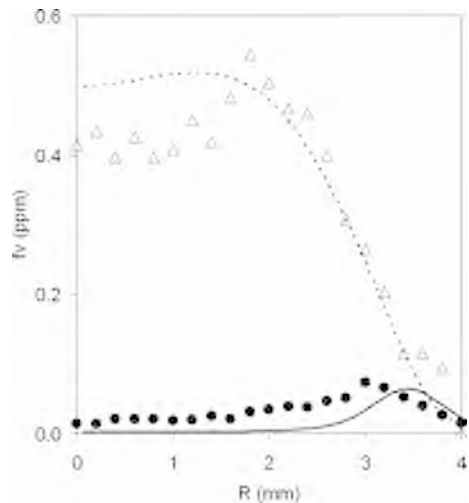


Figure 3. Predicted and measured [11,28] soot volume fraction and nanometric-sized organic carbon (NOC) in a laminar, non-premixed, methane flame at 25mm height. — ● soot; ····· Δ NOC.

by laser induced fluorescence and the soot measured by laser-induced incandescence and thermophoretic deposition [27,28]. Generally the model shows quite good predictions compared with data of important gas-phase species such as acetylene and benzene and these details are contained elsewhere [11].

## 5. TURBULENT FLAME PREDICTIONS

The model with the same scheme is applied to turbulent non-premixed ethylene and methane flames. The ethylene flame data [1] is for a vertical jet nozzle 3mm diameter issuing into still air. Flame A has a jet velocity of 52m/s and a characteristic residence time (axial distance at soot maximum / nozzle velocity)  $\tau = 7$ ms; flame B is at 22m/s with  $\tau = 13$ ms. The normalised height to stoichiometry on the axis  $X_{st}/D$  is about 150 for flame A and 130 for flame B. The methane turbulent flame [29] issues from a 2.5mm diameter nozzle at 22m/s ( $\tau \approx 10$ ms) and it has a disc around the nozzle to assist in stabilising the flame. The flame normalised stoichiometric length  $X_{st}/D$  is about 90.

All the flames have high scalar dissipation rates near the nozzle which rapidly decay and in the main body of the flame to  $N < 1s^{-1}$ . To prevent extinguishment in the model near the nozzle and consequent extinguishment of the whole modelled flame the scalar dissipation rate is limited; for ethylene to  $50s^{-1}$  and for methane to  $10s^{-1}$ . The limit only exerts its influence near the nozzle for  $X/D < 10$ .

Figure 4 shows temperature predictions for the ethylene Flame B. These are generally quite good because the radiation absorption coefficient is adjusted to get a good fit; a necessary prerequisite for species predictions. Soot volume fraction predictions are shown in Figure 5 for Flame B. Two conditional temperature models to account for radiation losses are used. The first scales the adiabatic conditional temperature profile based on the local conditional species concentrations (model T1). The second scales a representative adiabatic flamelet profile, at a scalar dissipation  $N = 50/s$  (model T2). Generally T1 predicts soot volume fraction lower than the measurements and T2 shows better agreement.

The difference between the two conditional temperature models is shown in Figure 6 at a location in the flame where soot formation is occurring. Both models give the same mean temperature when integrated with respect to the pdf. However, model T2 shows that conditional temperature is relatively higher in the rich region (stoichiometric  $\eta = 0.063$ ) where soot is forming and this affects the soot formation rate.

The predictions for ethylene Flame A, with the shorter time constant, are shown in Figures 7 and 8. Temperatures are well represented by the model as shown. The predicted soot volume fraction by model T1 is however quite low relative to measurements and it is apparent that the modelled rates are not keeping pace with measured formation rates. Again the use of model T2 shows better agreement.

The methane flame particulate volume fraction predictions and data are shown in Figure 9. This is a low-sooting fuel where data is obtained by laser-induced emission to detect nanometric particles of organic carbon (NOC) characterized by a size range of 1-10 nm and soot particles with sizes in the range 10-100 nm by fluorescence and incandescence [29]. Also shown are one set of measurements of total carbon as soot volume fraction obtained by sampling in a very similar turbulent methane flame [30].

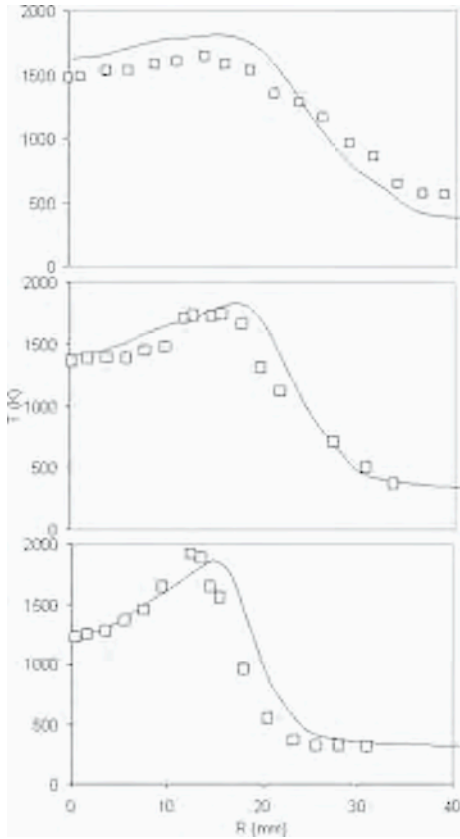


Figure 4. Predicted (T1) and measured mean temperature in turbulent ethylene Flame B,  $\tau = 13$ ms. From bottom to top:  $X/D = 40, 60, 80$ .

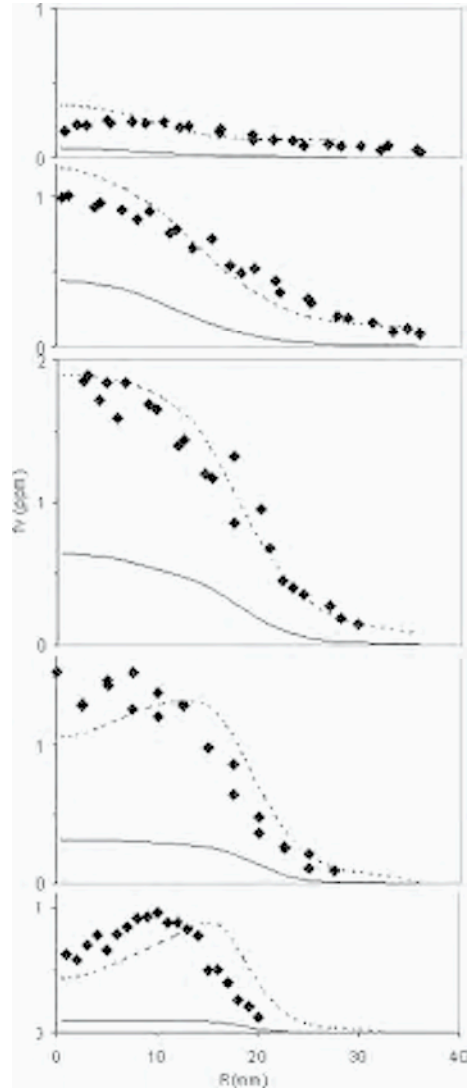


Figure 5. Soot volume fraction in turbulent ethylene Flame B [1]. — model T1; ..... model T2. Bottom to top:  $X/D = 60, 80, 97, 140, 170$ .

The predictions again show similar trends to the ethylene flames. Generally the T1 model is somewhat low in particulate concentration and T2 gives closer agreement. However, in this flame there is very little radiation loss and so the T1 model, which in this case is almost adiabatic, is the appropriate conditional temperature profile. A comparison of predicted mean temperature with measured temperature available in the

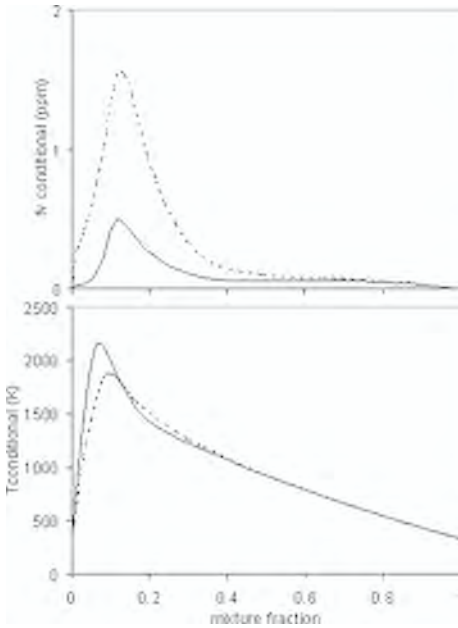


Figure 6. Modelled conditional temperature and soot volume fraction. Flame B at  $X/D = 87$ . — model T1; ..... model T2.

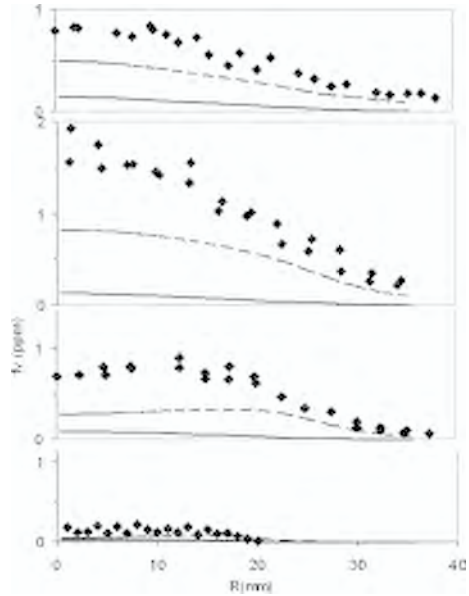


Figure 8. Soot volume fraction in turbulent ethylene Flame A,  $\tau = 7\text{ms}$  [1]. — model T1; ..... model T2. Bottom to top:  $X/D = 46, 80, 115, 163$ .

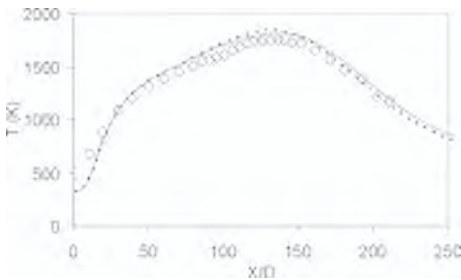


Figure 7. Predicted and measured mean temperature on axis of Flame A. — model T1; ..... model T2.

Brookes and Moss flame [30], not presented here, gives good agreement. Figure 10 shows  $D_{63}$  particle diameter predictions and here T1 reveals better agreement than T2 against data. The measurements [29] showed that there is negligible loading as soot in the larger size range for the methane flame and the predictions by T1 are also strongly biased to the small size particulates.

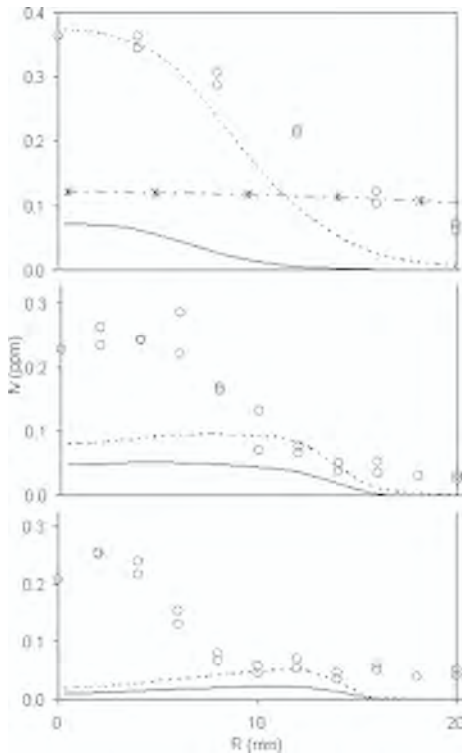


Figure 9. Particulate volume fraction in turbulent methane flame [29]. Bottom to top:  $X/D = 28, 40, 80$ .  $\circ$  measured NOC [29];  $\cdot\cdot$  \*  $\cdot\cdot$  measured total carbon [30] at  $x/D = 86$ ; — model T1;  $\cdots\cdots$  model T2.

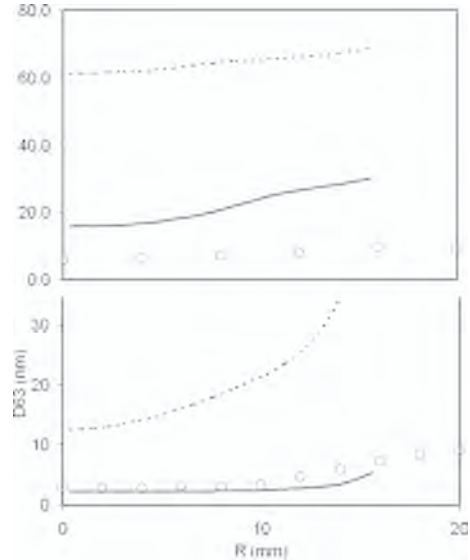


Figure 10. Particulate  $D_{63}$  diameter in turbulent methane flame [29]. Bottom to top:  $X/D = 40, 80$ . — model T1;  $\cdots\cdots$  model T2.

## 6. CONCLUSION

The objective of the present work is to evaluate the accuracy of a full chemical kinetic scheme in predicting particulate characteristics in turbulent non-premixed flames. The scheme is the same as used with reasonable accuracy in laminar, non-premixed flames of ethylene and methane. In the turbulent flames of the same fuels the use of a conditional temperature model based on a scaled adiabatic from the local species concentrations (T1) gives predicted particulate concentrations which are about a fifth to a half of the measured values. The use of an alternative flamelet template for the conditional temperature gives better results, but it is at present an arbitrary model and serves to show the sensitivity of the model to this parameter.

Overall it is demonstrated that a complex chemical kinetic and particle dynamics scheme can be applied to modelling turbulent non-premixed combustion generated particulates. The scheme shows general trends which are in line with data for two dif-

ferent fuels and for different residence times. There is great potential for further development by this approach.

<b>Notation</b>	
$A$	face area of finite volume cell
$a$	flux coefficients in the finite volume scheme
$D$	nozzle diameter
$F$	specific mass flow in the finite volume scheme
$f$	advection scheme weighting factor
$f_v$	particulate volume fraction
$k$	turbulent kinetic energy
$N$	scalar dissipation
$P(\eta)$	mixture fraction probability density function (PDF)
$Q$	conditional average mass fraction
$R, r$	radial coordinate
$S_\phi$	source/sink term for variable $\phi$
$T$	temperature
$t$	time
$U$	velocity vector
$u, v$	velocity components in the $x$ and $r$ directions
$w$	chemical source term
$V$	volume of finite volume cell
$X, x$	axial coordinate
$Y$	species mass fraction
$\varepsilon$	turbulent dissipation of energy
$\phi$	any variable
$\gamma$	$\equiv \bar{\rho} \tilde{P}(\eta)$
$\eta$	sample space variable for $\xi$
$\rho$	density
$\sigma_\phi$	turbulent Prandtl-Schmidt number
$\xi$	mixture fraction
$\xi'^2 \equiv g$	mixture fraction variance
<b>Subscripts</b>	
$i$	species $i$
$\eta$	conditional averaged
$w, e, s, n$	at axial and radial cell boundaries
$W, E, S, N$	at axial and radial neighbouring cell centres
$k, K$	at cell boundary, in neighbouring cell centre, spatial and $\eta$
<b>Superscripts</b>	
/	fluctuation about the unconditional mean
/ /	fluctuation about the conditional mean
—	Reynolds average
~	Favre average

## REFERENCES

1. J.H. Kent, D. Honnery, *Combust. Sci. Technol.* 54 (1987) 33-397
2. R.P. Lindstedt, S.A. Louloudi, *Proc. Combust. Inst.* 30 (2005) 775-783.
3. A. Kronenburg, R.W. Bilger, J.H. Kent, *Combust. Flame* 121 (2000) 24-40.
4. B. Zamuner, F. Dupoirieux, *Combust. Sci. Technol.* 158 (2000) 407-438.
5. S.J. Brookes, J.B. Moss, *Combust. Flame* 116 (1999) 486-503
6. R.P. Lindstedt, in *Soot Formation in Combustion: Mechanisms and Models*, H. Bockhorn (Ed.) Springer-Verlag, Berlin, 1994, pp. 417-441.
7. W. Kollmann, I.M. Kennedy, M. Metternich, J.-Y. Chen, in *Soot Formation in Combustion: Mechanisms and Models*, H. Bockhorn (Ed.) Springer-Verlag, Berlin, 1994, pp. 503-526.
8. I.M. Kennedy, W. Kollmann, J.-Y. Chen, *Combust. Flame* 81 (1990) 73-85.
9. A.Y. Klimenko, R.W. Bilger, *Prog. Energy Combust. Sci.* 25 (1999) 595-687.
10. D'Anna, A. and Kent, J.H., *Combust. Flame* 144(1-2) (2006) 249-260.
11. D'Anna, A. and Kent, J.H., *Combust. Flame* 152 (2008) 573-587.
12. C.J. Pope, J.B. Howard, *Aerosol Sci. Technol.* 27 (1997) 73-94.
13. G.P. Smith, D.M. Golden, M. Frenklach, N.W. Moriarty, B. Eiteneer, M. Goldenberg, C.T. Bowman, R.K. Hanson, S. Song, W.C. Gardiner Jr., V.V. Lissianski, Z. Qin. [http://www.me.berkeley.edu/gri\\_mech/index.html](http://www.me.berkeley.edu/gri_mech/index.html).
14. J.A. Miller, C.F. Melius, *Combust. Flame* 91 (1992) 21-39.
15. M. Frenklach, *Phys. Chem. Chem. Phys.* 4 (2002) 2028-2037.
16. M. Musick, P. J. Van Tiggelen, J. Vandooren, *Bull. Soc. Chim. Belg.* 105(9) (1996) 555-574.
17. A. D'Alessio, A.C. Barone, R. Cau, A. D'Anna, P. Minutolo, *Proc. Combust Inst.* 30(2) (2005) 2595-2603.
18. M.J. Cleary, J.H. Kent, *Combust. Flame* 143 (2005) 357-368.
19. G.M. Faeth, *Prog. Energy Comb. Sci.* 13(4) (1987) 293-345
20. F.C. Lockwood, N.G. Shah, *Proc. Combust. Inst.* 18 (1980) 1405-1414.
21. R.S. Barlow, International workshop on measurement and computation of turbulent non-premixed flames, <http://www.ca.sandia.gov/TNF>.
22. R.W. Bilger, *Prog. Energy Combust. Sci.* 1 (1976) 87-109.
23. M.J. Cleary, Ph.D thesis, University of Sydney, 2004.
24. R.W. Bilger, *Combust. Sci. Technol.* 11 (1975) 215-217.
25. P.J. Colucci, F.A. Jaber, P. Givi, S.B. Pope, *Phys. Fluids* 10 (1998) 499-515.
26. R.J. Santoro, H.G. Semerjian, R.A. Dobbins, *Combust. Flame* 51 (1983) 203-218.
27. M.D. Smooke, C.S. McEnally, L.D. Pfefferle, *Combust. Flame* 117 (1999) 117-139.
28. M. Commodo, S. Violi, A. D'Anna, C. Allouis, P. Minutolo, 29th Meeting of the Italian Section of the Combustion Institute, Pisa, June 14-17, 2006.
29. M. Commodo, E. Bichi, A. D'Anna, P. Minutolo, R. Pagliara, C. Allouis, 3rd European Combustion Meeting ECM (2007).
30. S.J. Brookes, J.B. Moss, *Combust. Flame* 116 (1999) 49-61.

# Experimental comparison of soot formation in turbulent flames of kerosene and surrogate model fuels

R. Lemaire, E. Therssen, J.F. Pauwels, P. Desgroux

*Laboratoire de Physico-Chimie des Processus de Combustion et de l'Atmosphère (PC2A)*

UMR CNRS 8522

*Centre d'Etudes et de Recherches Lasers et Applications (CERLA)*

*Fédération de Recherche CNRS 2416*

*Université des Sciences et Technologies de Lille*

*59655 Villeneuve d'Ascq cedex, France*

*Abstract: This paper reports on the comparison of soot formation in turbulent diffusion flames of kerosene and surrogate model fuels. To this end, a laboratory burner has been specially designed to burn a high speed spray of small liquid fuel droplets. Thanks to the atomisation system used here, hydrodynamic characteristics of the spray are shown to be relatively independent of the physical-chemical properties of the tested liquid fuel, thus leading to comparable flame structure and soot distribution among a variety of fuels. The comparison of soot formation is based on 2D measurements of Laser Induced Fluorescence (LIF) at 532 nm assigned to fluorescent soot precursors (among which large polycyclic aromatic hydrocarbons) and of soot volume fraction obtained by Laser Induced Incandescence (LII) at 1064 nm. In addition, information on optical and morphological properties of soot particles are derived from the analysis of the LII signals. The selected six-component surrogate fuels were initially formulated by Eddings et al. (Combust. Sci. Technol. 177 (2005) 715) for pool fires applications. It is shown that the soot formation process in the surrogate flames is similar to that for the kerosene flame. Hex-12 surrogate appears to be the best one, while a modified Hex-12 surrogate containing 4 components is also proposed. N-decane clearly fails to reproduce the sooting tendency of kerosene.*

## 1. INTRODUCTION

An important factor controlling soot formation in flames and gas turbines is the fuel hydrocarbon composition. While an extensive literature has been devoted to the understanding and simulation of soot formation from individual hydrocarbons, the complexity of jet fuels containing hundreds of compounds with composition varying from batch to batch, make impractical the simulation of soot exhausts. Typically kerosene Jet A-1 is a mixture of alkanes (50-65 % vol), polyaromatics (10-20 % vol) and cyclo alkanes or naphthenes [1,2]. In order to study the combustion of jet fuels, surrogate blends composed of a relatively small number of pure hydrocarbons have been formulated. Surrogates allow well controlled and reproducible experiments and help the development of computational codes for combustor design and fire simulation of more complex commercial fuels.

A recent review from Dagaut and Cathonnet [1] describes the ignition, oxidation and combustion of kerosene. An extensive list of experiments performed on kerosene or surrogates is synthesised with a literature survey focused on the chemical kinetic modelling of Jet A-1/JP-8 combustion. Briefly, main results rely on measurements of ignition delays taken in flow tubes and shock tubes, detailed mole fraction profiles in jet stirred reactor (JSR) or flat flame burners and flame speeds [see details in ref 1]. It has been found that most of the concentration profiles from the oxidation of n-decane or kerosene in a JSR were very similar [3], as was the structure of n-decane and kerosene flat flames [4, 5]. However, benzene concentration was found to be one order of magnitude larger during the oxidation of jet A-1 than in decane one. The oxidation of jet A-1 and surrogates containing a mixture of n-decane and n-propyl-benzene or n-decane and 1,2,4-trimethyl-benzene has been analysed in a JSR and confirmed the previous results indicating that n-decane represents well the n-alkane fraction of jet A-1 while the non-alkane fraction cannot be represented by a single component such as n-propyl-benzene or 1,2,4-trimethyl-benzene [1]. As mentioned in [1] the oxidation of the alkane portion of kerosene produces the necessary active species for the oxidation of the fuel mixture but the aromatic and naphthenic fraction of kerosene leading to specific oxidation products such as trimethylbenzenes, toluene and xylenes requires the formulation of more complex surrogates. Therefore large efforts have been undertaken recently by several groups [1 and references therein, 2,6-7] to refine the model fuel composition and particularly to provide a better prediction of benzene concentration. Indeed this species should be involved in larger aromatics formation and consequently in soot formation. Unfortunately only a few experiments on soot formation during jet fuel combustion have been performed despite the crucial need of extensive databases. Most of the simulations have been tested on the basis of kerosene and n-decane detailed flame structures issued from Vovelle's group [4,5]. Young et al. [8] also provided soot measurements in high pressure turbulent jet flames burning prevaporized kerosene.

Studies regarding the ability of surrogate mixtures to reproduce the sooting tendency of kerosene in flames or in pool fires are almost non-existent. Recently Eddings et al. [9] formulated several JP-8 surrogates to simulate pool fires combustion. The mixtures of components were selected to match the volatility, flash point, sooting tendency and heat of combustion of JP-8. These surrogates have been improved from a previous work [2]. The soot tendency of individual hydrocarbon is often expressed using the threshold sooting index (TSI) which simply correlates with the smoke point (SP) according to  $TSI = a MW/SP + b$  where MW is the molecular weight of the fuel, SP is the greatest flame height without smoke emission under laminar diffusion combustion and a and b are constants dependent on the apparatus used for the SP measurement that scale the TSI from 0 to 100 [10, 13]. The TSI of a large number of compounds can be found in [10, 11]. Furthermore the TSI of a mixture can be estimated from a simple additivity rule:  $TSI_{mix} = \sum_i X_i TSI_i$ , where  $TSI_i$  and  $X_i$  are the soot index and the mole fraction of the  $i^{th}$  component [11, 12]. Based on this simple rule and the above criteria, Eddings et al. [9] proposed two six-component surrogates named Hex-11 and Hex-12 whose characteristics are summarized in Table 1. The combustion behaviour of JP-8 and its surrogates were tested in a 30-cm diameter pool fire by measuring the burning rate, the radiant heat flux and the SP. Both surrogates were shown to satisfactorily reproduce the jet-fuel characteristics under steady-state pool fire con-

Table 1. Composition of the tested fuels (in mol % except for kerosene in wt %) and fuel threshold soot index (TSI). The mixture of xylene isomers proposed by Eddings et al. [9] has been replaced here by pure m-xylene which had only limited effect on the overall boiling range according to Violi et al. [2].

<b>n-decane</b>		<b>Kerosene</b>		<b>Hex-11</b>		<b>Hex-12</b>		<b>Modified Hex-12</b>	
n-decane	100.0	n-paraffin	18.0	n-octane	3.5	n-octane	3.0	n-decane	45.0
		Branched paraffin	37.6	n-dodecane	40.0	n-dodecane	30.0	m-xylene	15.0
		Mono-aromatics	17.9	n-hexadecane	5.0	n-hexadecane	12.0	Tetralin	13.0
		Diaromatics	1.2	m-xylene	8.5	m-xylene	15.0	Decalin	27.0
		Cycloparaffin	15.8	Tetralin	8.0	Tetralin	13.0		
		Decalin and Tetralin	5.1	Decalin	35.0	Decalin	27.0		
		Others (alkene, cyclo-alkene, alcohol...)	4.4						
Sum	100.0		100.0		100.0		100.0		100.0
TSI	4.3		26.7		17.6		22.1		20.8

ditions. It must be noted that the TSI correlation has recently been revisited [13] with a particular emphasis for gas turbine combustion. A new correlation approach based on the use of the peak soot volume fraction has also been proposed [14].

In this work, the soot formation issued from the combustion of jet A-1 and of the two mentioned six-component surrogates Hex-11 and Hex-12 has been investigated and compared in atmospheric turbulent diffusion flames. To this end, a laboratory hybrid burner allowing the combustion of a liquid fuel spray in order to resemble practical combustors has been specially designed. It consists of a modified McKenna burner where a nebulizer has been inserted through a hole in the central of the porous plug. A high speed spray of small liquid fuel droplets is formed at the nebulizer tip and is ignited by the methane flat flame stabilized on the porous burner. A turbulent diffusion flame of around 18-cm height and 2-cm width is then obtained. The use of highly atomized and hence rapidly vaporizing sprays generates quite comparable hydrodynamic conditions for each fuel without fractional distillation and leads to very similar sooting flame patterns. This feature facilitates the analysis of the impact of fuel composition on soot formation. Furthermore the flames were found to be very reproducible leading to an accurate comparison of the measured characteristics of the various fuels. It must be emphasized that this work considers weakly sooting flames. Thus, it contrasts with the initial tests performed in pool fires. We report here 2D-quantitative measurements of soot volume fraction obtained by Laser Induced Incandescence (LII) at 1064 nm. The calibration has been achieved using a laminar methane diffusion flame in which the absolute soot volume fraction was determined by Cavity Ring-Down Spectroscopy (CRDS) in a previous work [15]. Using laser excitations at 532 nm and 1064 nm, the Laser Induced Fluorescence (LIF) signal from fluorescent species could also be extracted from the total collected signal, using a two-

colour LII/LIF method described previously [16, 17]. Fluorescent species are soot precursors [18] including large Polycyclic Aromatic Hydrocarbons (PAH), known to fluoresce upon visible laser radiation [19-21]. The comparison of the Jet A-1 with the surrogate blends mainly relies on the soot and LIF mappings, the hydrodynamic behaviour of the different sprays being quite similar. In addition comparative information on the soot optical properties and the primary particle diameter could be derived from the LII signals analysis. Finally, the alkane contribution to soot formation has been studied by producing sprays of pure n-decane and of a modified four-component Hex-12 blend in which the three initial alkanes have been replaced by n-decane.

## 2. EXPERIMENTAL SET-UP

### 2.1. Description of the burner and of the liquid fuel injection system

#### 2.1.1. *The burner*

The burner is an atmospheric hybrid Holthuis (previously McKenna) burner composed of a 60-mm diameter bronze porous with a central 6.35-mm diameter tube allowing the introduction of an injector. A premixed methane-air flat flame (equivalence ratio = 0.8, cold gas velocity = 12 cm.s<sup>-1</sup>) stabilised on the porous allows the ignition of the fuel jet exiting the injector. Perturbations from ambient atmosphere are minimised by an air shroud (cold gas velocity = 28 cm.s<sup>-1</sup>). A quartz collector located at 200 mm above the flat flame burner improves the stability of the jet flames. In a first version of the burner [15, 17], laminar jet flames of gaseous hydrocarbons anchored on a 4 mm inner diameter central injector tube were stabilised on the same hybrid Holthuis burner. This setup was used here for a methane laminar diffusion flame used for LII calibration. In the present work, turbulent jet flames of liquid fuels have been stabilised by developing an original set-up based on the use of a Direct Injection High Efficiency Nebulizer (DIHEN). A high speed spray of small liquid fuel droplets is formed at the exit of the nebulizer and is ignited by the methane flat flame, resulting in turbulent diffusion flames of around 18-cm height and 2-cm width. The performance of the injection system and its adequacy to be combined with the hybrid burner are described hereafter.

#### 2.1.2. *The fuels*

Experiments have been performed using five fuels whose composition has been specified in Table 1. The kerosene fuel is Jet A-1 provided by TOTAL. The gas-chromatography (GC) spectrum was found to contain more than 900 peaks. Only the main composition has been determined and is displayed in Table 1. The two kerosene surrogates Hex-11 and Hex-12 are issued from Eddings work [9]. The three-alkanes of Hex-12 have been replaced (at equal mol %) by n-decane to develop a new surrogate tested in this work and named modified Hex-12. In order to simplify the comparison of the studied flames, fuel mass rates were maintained constant to achieve a nearly constant hydrodynamic behaviour for each fuel. The TSI of each blend has been estimated using the TSI

of the individual compounds issued from Calcotte [10] and Olson et al. [11]. For n-hexadecane a TSI value of 5.5 was deduced from [9]. TSI values are reported in Table 1 and fall between 17 and 27 for the jet-fuels while n-decane is characterised by a low TSI (4.3).

### 2.1.3. Characteristics of the liquid fuel injection system

In two-phase flow combustion, the atomisation system plays a major part especially in the characteristics of the obtained flames. Indeed the smaller the droplets will be, the faster the vaporisation of the liquid will occur and then, the more effective the combustion will be. To fulfil this condition, we used a DIHEN nebulizer (Model DIHEN 170-AA) originally designed for Inductively Coupled Plasma (ICP) applications. The operating principle of this coaxial atomizer is based on assisted atomisation that is to say that the high velocity gas flow circulating in the annulus area (of 0.0094 mm<sup>2</sup>) tears off the low velocity liquid flow circulating in the central 104- $\mu$ m diameter capillary. Different studies have been undertaken to characterise the spatial droplet size distributions or the structure of sprays obtained with this material but with a particular interest for ICP applications [22–24].

This nebulizer was found very well suited for combustion applications because it can deliver a spray of very small droplets. In our study, the nebulization gas is nitrogen. The gas flow rate was fixed at 0.32 L/min and controlled using an external mass flow controller (Tylan FC-260). The various liquid hydrocarbons were introduced in the nebulizer capillary with a mass flow rate of 46 g/h controlled with a liquid mass flow controller (Bronkhorst High-Tech L2C2I). Following Lasheras et al. [25] the most important parameters for the development of a spray can be determined according to the value of several non-dimensional numbers. Thus an effective Reynolds number is defined to characterize the total flow (gas plus liquid) in the jet:

$$\text{Re}_{\text{eff}} = \left( \frac{U_g D_g}{\nu_g} \right) \left[ \left( 1 - \frac{D_l^2}{D_g^2} \right) + \frac{D_l^2}{M D_g^2} \right] \quad (1)$$

where the momentum flux ratio per unit volume M is:  $M = \frac{\rho_g U_g^2}{\rho_l U_l^2}$  (2)

$D_l$  is the solution capillary internal diameter,  $D_g$  is the gas orifice internal diameter,  $\rho$  is the specific density and U the velocity of the gas. Subscripts (g) and (l) refer to gas and liquid respectively.  $\text{Re}_{\text{eff}}$  is an important parameter which has to be large to have a good atomization. Other relevant parameters in the atomization process are the mass

flux ratio  $m = \frac{\rho_l U_l A_l}{\rho_g U_g A_g}$  where  $A_l$  and  $A_g$  are the capillary annulus area and the gas

annulus area respectively and the non-dimensional initial Weber number ( $We_0$ ) which is the ratio between the inertial force and the surface tension  $\sigma$  of the liquid:

$$We_0 = \frac{\rho_g D_l (U_g - U_l)^2}{\sigma}. \text{ Lasheras et al. [25] determined that high momentum flux ratio}$$

and high Weber number are required to strongly and quickly destabilize the liquid in order to form a small droplets spray. Furthermore, a small mass flux ratio is recommended to have only droplets and no liquid fibre-type ligaments outside the atomiser. As shown in Table 2, which summarizes the main relevant quantities of each liquid spray, those conditions are fulfilled for all the liquid fuels atomized in this work. Furthermore, according to the previous equations, we can notice that only the specific density and the surface tension of the liquid hydrocarbons will really influence the characteristics of the spray for given liquid and gas flows. Since these properties are quite similar for all the tested fuels in this work (see Table 2), it is expected that the sprays will be identical too. To check this point, Mie-scattering measurements at 532 nm have been carried out in the cold sprays of the different fuels in order to determine the global spray structure. As shown in Figure 1, the shape of the cold sprays is the same for

Table 2. Some properties of the liquid fuels and characteristics of their cold sprays.

Fuel	n-decane	Kerosene	Hex-11	Hex-12	Modified Hex-12
Density ( $\text{kg}/\text{m}^3$ )	730.0	794.0	819.2	825.5	822.5
Surface tension ( $\text{N}/\text{m}$ )	0.024	0.028	0.028	0.028	0.028
$\text{Re}_{\text{eff}}$	4450	4450	4450	4450	4450
$M$	130	139	143	143	143
$m$	1.92	1.93	1.93	1.94	1.94
$\text{We}_0$	1700	1460	1450	1440	1470

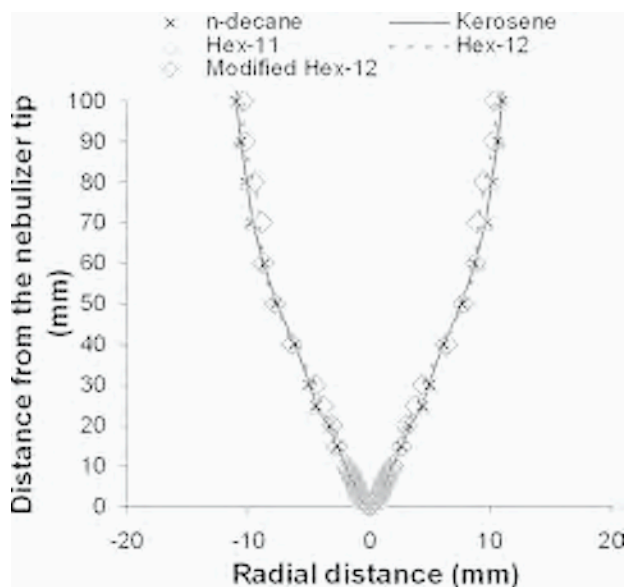


Figure 1. Cold spray contours obtained by Mie scattering at 532 nm for the five investigated fuels.

all the tested hydrocarbons. After ignition by the pilot flame, the liquid phase of the spray could also be easily imaged by Mie scattering at 1064 nm without perturbation from the fluorescence of PAHs contained in the fuel. Images of the ignited spray are shown in the bottom of Figure 5 (described later) for each flame. It is found that all the liquid sprays are completely vaporised without fractional distillation above 15 mm HAB, the volatility of the tested fuels being very similar. After this height, flames behave similarly as a turbulent diffusion gas flame.

#### *2.1.4. Performance of the spray burner*

As detailed before, the nebulization process allows the generation of very small droplets sprays with nearly identical characteristics between fuels. Since the vaporization occurs very quickly, the hydrodynamic behaviours of the produced sooting flames are very similar and thus it is reasonable to neglect the hydrodynamic influence when comparing the sooting propensity of the investigated fuels. The absence of fractional distillation is an important advantage for the results interpretation while this distillation appears inevitable in pool fires experiments [9]. Despite the turbulent feature of the flames intentionally generated to be representative of jet fuel injectors, measurements of the peak LII intensity on the flame axis were found to be highly reproducible. Indeed, a statistical study made up over 500 individual LII images has shown that the precision of the average peak LII signal was similar to that obtained in a laminar methane flame ( $\pm 1\%$ ). By contrast it reaches  $\pm 7\%$  in the edges of the turbulent jet fuel flames.

## **2.2. The LII set-up**

The LII experimental set-up is shown in Figure 2 and slightly differs from [17]. The laser is a 6 ns Nd:YAG laser (Quantel Brilliant) operating at 1064 nm and 532 nm. The two laser beams are aligned with dichroic plates and prisms so that their positions in the flame are perfectly coincident. A movable beam dump allows the selection of the wavelength. A half-wave plate is used to turn the polarisation plane of the 532 nm beam in the horizontal position, so that background signals (Mie and Rayleigh scattering, Raman scattering from  $O_2$  and  $N_2$ ) are minimized or suppressed. Using a 1-mm diaphragm, the central part of the unfocussed near-Gaussian laser beams has been selected and the beam propagated through the flame in the horizontal direction. The position of the diaphragm was adapted so that the diameter of the laser beam in the flame was the same when the laser wavelength was changed from 532 nm to 1064 nm. In order to ensure that radial profiles of the laser irradiance were identical for the two selected wavelengths, the spatial characteristics of the laser beam irradiance were experimentally monitored using a CCD beam profiler (Photon 2340-2321). The choice of the diaphragm/flame distance  $D$  was made so that the concentric rings are negligible in the Airy diffraction pattern. Adequate positions were found to be  $D = 69$  cm and  $D = 34.5$  cm at 532 nm and 1064 nm respectively and led to the profiles of the laser irradiance shown in Figure 3. The energy after the diaphragm was fixed to 0.22 and

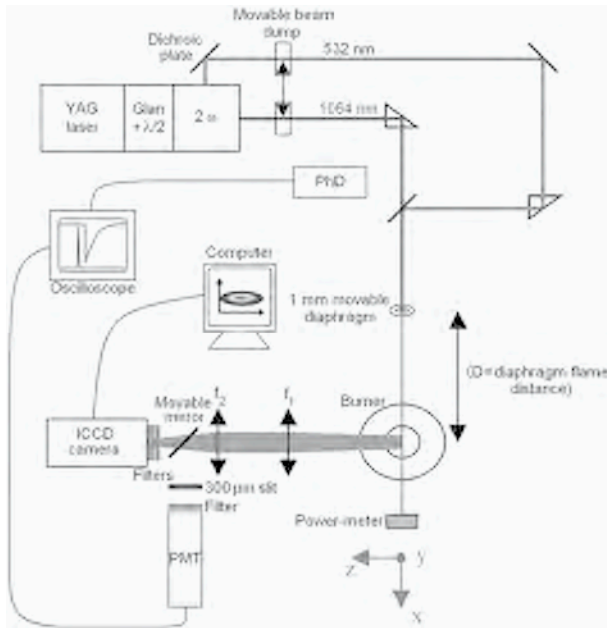


Figure 2. Experimental LII/LIF set-up.

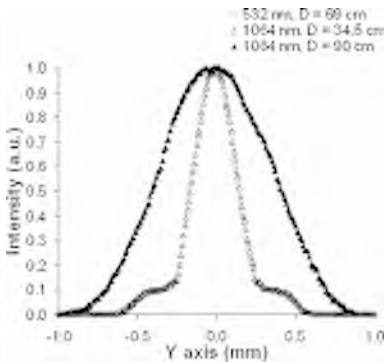


Figure 3. Radial profiles of normalized laser irradiance.

0.44 mJ/pulse at 532 nm and 1064 nm respectively (i.e. just below the LII plateau region) using the combination of a half-wave plate and a Glan prism. The choice of these energies and of the diaphragm positions is explained in the next section.

The sooting region of interest was imaged perpendicularly to the laser propagation direction ( $x$  axis) to give the LII signal distribution along the beam. The broadband LII and LIF signals were collected at right angle using a set of two achromatic doublets ( $f_1$

= 400 mm and  $f_2 = 200$  mm) and imaged onto a 512 x 512 ICCD Princeton camera (pixel size = 19  $\mu\text{m}$ , 1 pixel image = 38  $\mu\text{m}$  in the flame). 500 laser shots were accumulated. The gate width of the ICCD camera was 20 ns. It was timed to start at the peak laser pulse (prompt LII). Radiation (532 nm) was rejected with two 532 nm dielectric mirrors (total transmission at 532 nm =  $10^{-4}$ ). The process of the images is detailed in [17, 26] and leads to 1D images of the soot distribution along the flame diameter ( $x$  axis).

Time resolved LII measurements were also performed at 1064 nm by imaging a thin volume of the flame on a 300  $\mu\text{m}$  horizontal slit placed in front of a head-on photomultiplier tube PMT, Photonis XP2237. The LII signal was spectrally filtered using a Schott OG 550 filter in order to reduce the measurement noise caused by the flame emission. The PMT signal was digitized and stored by an oscilloscope (LeCroy 9350 AM). This set-up was also used to record the variation of the LII signal with the laser fluence (fluence curves). For those applications the diaphragm/flame distance  $D$  was adjusted to 90 cm in order to obtain a gaussian laser profile displayed in Figure 3.

Since the soot concentrations in the studied flames were very low, the attenuation of the laser through the flame is negligible and the laser energy was continuously measured with a power-meter located behind the flame.

### 3. LII PROCEDURE AND CALIBRATION

The two-colour LII/LIF method has been used in our laboratory in several laminar flames [15-17]. It is based on the fact that the measured radiation emission ( $S_{1064\text{nm}}$ ) from 1064 nm heated soot is only assignable to soot (LII signal) while the emission from 532 nm irradiation ( $S_{532\text{nm}}$ ) originates from the LII signal and the LIF from fluorescent species. While the fluorescence was assigned to large PAHs in the former papers, the contribution of fluorescent nanoparticles has also to be considered [18]. The term "fluorescent soot precursors" is used here to design the species responsible of the fluorescence upon 532 nm laser excitation.

By comparing the signals at both laser wavelengths under appropriate conditions, it is possible to extract the LIF signal according to these relations:

$$S_{1064\text{nm}} = LII_{1064\text{nm}} = K_{1064\text{nm}} \cdot f_v$$

$$S_{532\text{nm}} = LII_{532\text{nm}} + LIF_{532\text{nm}} = K_{532\text{nm}} \cdot f_v + LIF_{532\text{nm}}$$

$$LIF_{532\text{nm}} = S_{532\text{nm}} - S_{1064\text{nm}} \cdot \frac{K_{532\text{nm}}}{K_{1064\text{nm}}}$$

In these equations the prompt LII signal has been set proportional to the soot volume fraction  $f_v$  [27-28] using a constant  $K_\lambda$ , which depends on the temperature reached by the particle and on the soot refractive index function  $E(m)$  at the emission wavelength. The determination of the ( $K_{532\text{nm}}/K_{1064\text{nm}}$ ) ratio requires the application of an experimental procedure detailed in [17]. Applicability of the method in turbulent flames is demonstrated in this work. By using the same spatial distribution of the laser irradiance (see Figure 3) and by adjusting the laser energies to 0.44 mJ/pulse at 1064nm

and 0.22 mJ/pulse and 532 nm, a perfect coincidence of the temporal and spatial LII averaged-signals could be achieved for the two excitation wavelengths in a region exempt of soot precursors, thus allowing a measure of the ( $K_{532\text{nm}}/K_{1064\text{nm}}$ ) ratio which was determined to be one [16]. Thus the LIF radial profile is simply deduced from the difference between the radial profiles obtained at 532 and 1064 nm while the soot profile is that obtained at 1064 nm. An illustration of the method is given in the next section. Finally the calibration of the LII measurements was carried out by comparing the peak LII signal obtained in our turbulent flames with the peak value recorded in a known laminar diffusion flame in which  $f_v$  had previously been determined by Cavity Ring Down Spectroscopy (CRDS) [15]. In this procedure we considered a constant soot refractive index function  $E(m)$  between methane and jet fuels flames. It must be noticed that the knowledge of the absolute soot volume fraction is not crucial in this work. By contrast the relative variation of the peak LII signals between jet flames is very accurate (+/- 1 %). It has been implicitly interpreted as being representative of the variation of soot volume fractions as in [14]. The analysis of the fluence curves recorded in the jet flames tends to support this assumption as shown in next section.

#### 4. COMPARISON OF SOOT FORMATION IN THE TURBULENT JET FLAMES

In this work, the flames burning the five fuels listed in Table 1 have been investigated using the two-colour LII/LIF technique described above. The fuel mass flow rates are identical for each flame. Figure 4a illustrates the different steps allowing soot and soot precursors LIF radial profiles to be obtained. It shows especially the radial profiles of the raw signals obtained at 532 nm and 1064 nm. Those signals are recorded in zones of the kerosene flame exhibiting different proportions of the LIF signal relatively to the soot one. The intensity units at 1064 nm and 532 nm correspond to the number of counts collected by the camera pixels. The selected zones are (1) the soot precursors zone at 30 mm HAB, (2) a zone where soot precursors and soot coexist at 72 mm HAB and (3) the soot oxidation zone at 110 mm HAB. From the raw signal profiles obtained upon 532 and 1064 nm excitation, the LIF profile is extracted using the two-colour method. The behaviour is quite similar to that obtained in laminar diffusion sooting flames [15, 16, 20]. At low height above the burner, soot precursors LIF is observed while soot particles are not yet formed. Soot precursors fluorescence is present in the centre core of the flame and peaks at 60 mm HAB. At this height soot particles are present and the LII signal has almost the same magnitude than the LIF signal. Then the LIF contribution is decreasing while soot formation is progressing. LIF completely disappears in the soot oxidation zone (above 100-mm HAB). Soot particles are formed at low heights in the outer edges of the soot precursor's core and join the flame axis at higher height. Similar features were found in most of our turbulent jet flames but differ in the decane flame (Figure 4b, commented in the next section). From the initial 1D-radial profiles recorded each 2-millimetre and averaged on 500 laser shots, 2D images maps of the averaged LII and LIF signals could be reconstituted using a procedure developed in Matlab<sup>®</sup>. 2D-images of the studied flames are presented in Figure 5. The LII signal was converted into absolute soot volume fraction  $f_v$

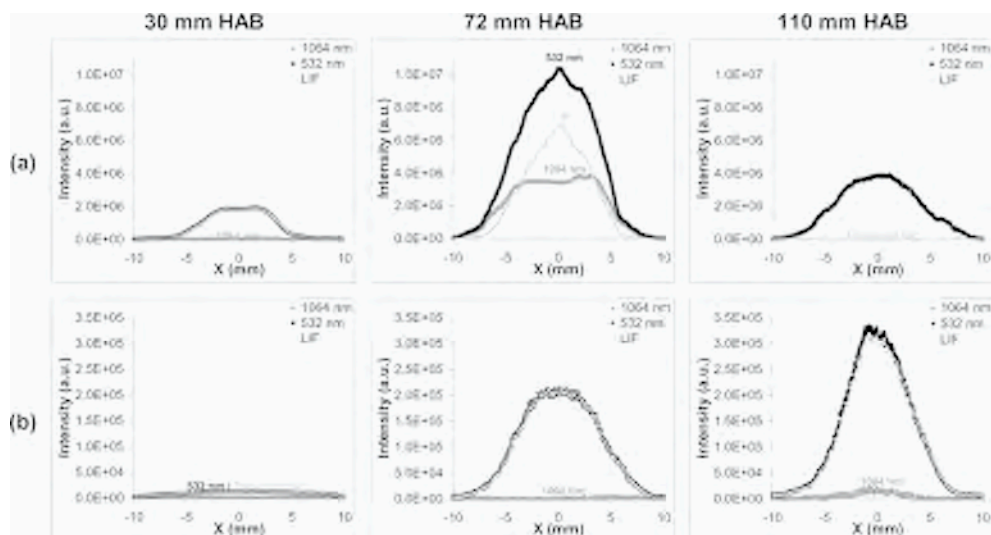


Figure 4. Radial profiles of LIF and LII obtained at different heights above the burner in kerosene flame (a) and n-decane flame (b). The soot precursors LIF profile is deduced from the two-colour LII/LIF procedure.

as indicated on the right colour bar (Figure 5b). The LIF intensity is reported on the left colour bar in arbitrary units but are directly comparable between flames. The emission patterns of each flame taken with a digital camera without any spectral filtering are also shown in Figure 5a. In this case the gain of the camera was automatically set to the peak luminosity of the flame. Therefore while the flame shapes look quite identical the decane flame is indeed much less luminous.

The presentation of the results is divided into two parts. First a comparison of the kerosene and n-decane flame is made. Then the ability of the Hex-11, Hex-12 surrogates to reproduce the sooting behaviour of the parent jet A-1 flame is discussed and a new simplified surrogate is finally proposed.

#### 4.1. Comparison of the kerosene and n-decane flames

As indicated in the introduction heavy alkanes have been shown to satisfactorily describe the oxidation of multicomponent jet-fuels in JSR or flow tubes. However data concerning the combustion behaviour of alkanes or jet fuels under rich or sooting conditions are very scarce. In premixed flat flames, it has been shown that the structures of n-decane and kerosene low-pressure sooting flames [4] and atmospheric rich flames [5] are very similar except that benzene is formed in much higher concentration in the kerosene flame. Since the concentrations of the intermediates involved in the formation of benzene were within the same range of magnitude in the both flames, the higher production of benzene in the kerosene flame was assigned to a direct formation from the aromatic part of the jet fuel.

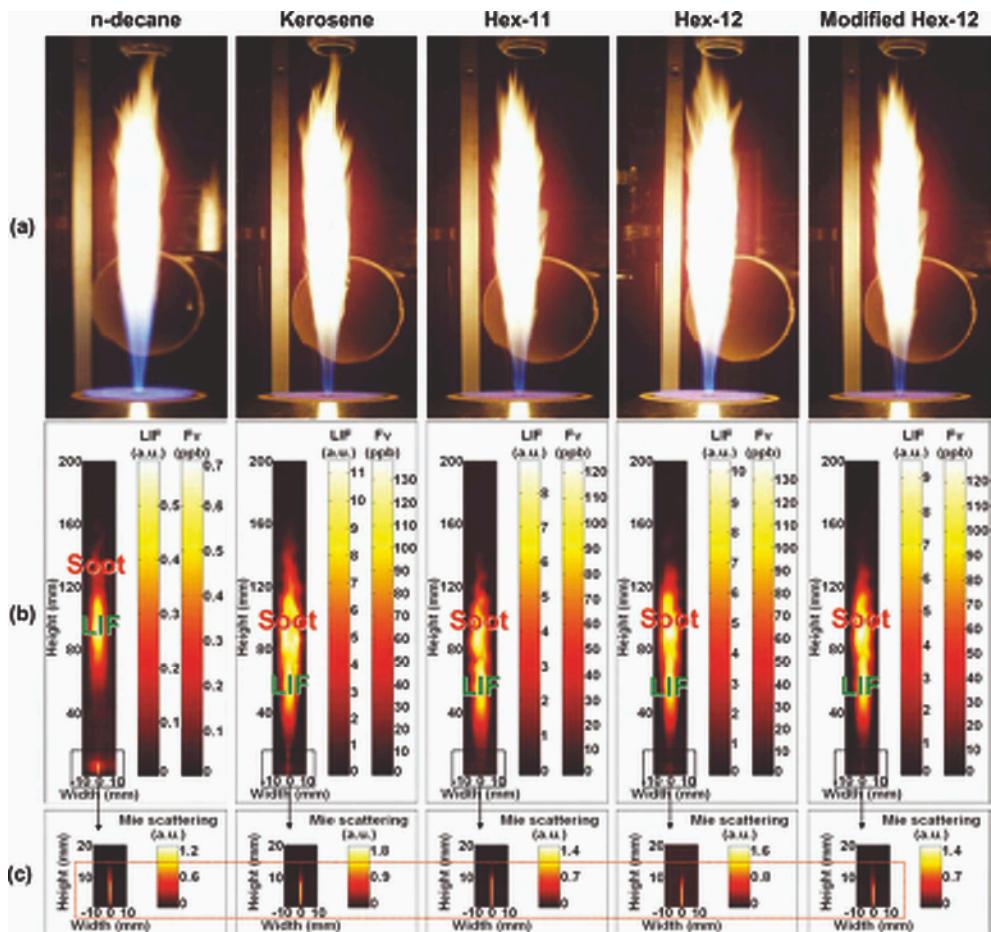


Figure 5. 2D images of (a) flame emission (b) LII and soot precursors LIF (reconstituted images) and (c) hot spray (liquid phase) using 1064 nm Mie scattering. LII scale in (b) has been converted in absolute soot volume fraction after calibration in a known methane diffusion flame. The arbitrary unit in (b) and (c) represents respectively the LIF intensity and the Mie intensity. The scale is identical for each flame.

In this work the comparison between the turbulent diffusion sooting flames is based on the comparison between 2D images of soot precursors LIF and LII. Figures 4 and 5 clearly exhibit the structure differences of the flames. Indeed the soot precursors, including large PAHs and identified by LIF, are formed much later in the decane flame than in the kerosene one. The LIF intensity peaks at 100 mm HAB and is more than ten-fold lower than in Jet A-1 flame. Consequently the soot particles are in very low concentration with a measurable peak at around 0.7 ppb. This is more than two orders of magnitude lower than in the kerosene flame (138 ppb). This indicates that the combustion of kerosene and n-decane drastically differs in sooting diffusion flames. So, the modelling of jet-fuel combustion under rich conditions cannot be done using an alkane-model fuel.

## 4.2. Comparison of kerosene and surrogates flames

In this section the kerosene flame is compared with those issued from the combustion of Hex-11 and Hex-12 surrogates. In addition we tested a simplified surrogate named modified Hex-12 in which the three initial alkanes of Hex-12 have been replaced by n-decane (conserving the same mol %). N-decane was selected because of its relatively low cost and because many experiments have shown that it satisfactorily mimics the jet-fuel consumption.

From Figure 5 it can be seen that the three surrogate flames reproduce satisfactorily the LIF and soot patterns of the kerosene flame both in shape and intensity. Figure 6 displays the profiles of the peak LIF signal (Figure 6a) and of the peak LII signal (Figure 6b) as a function of the height above the burner. It must be noticed that the profiles of the signals integrated along the flame diameter gave quite identical results. The signal near the burner (HAB < 10 mm) is present in each flame and comes from the droplets scattering which is captured by the camera at the both wavelengths (532 and 1064 nm) even in presence of rejecting filters. By contrast the presence of a 532-nm signal between 10 and 20 mm HAB is observed in the kerosene flame only and has been assigned to the LIF from heavy PAHs or other components contained in the fuel. This signal is absent in the surrogate fuels which do not contain high-number rings PAHs. Figure 6 shows that a very good agreement is found between the kerosene flame and the surrogate flames particularly with Hex-12 surrogate, which appears to be the best one. This conclusion is confirmed in Figure 7, which exhibits the radial profiles of soot precursors LIF (Figure 7a) and soot (Figure 7b) at medium height (72 mm HAB). The good concordance of LIF profiles and their location relatively to the soot ones suggest that species responsible of the fluorescence are actively involved in the soot formation process. Therefore an identification of these reactive species would be particularly helpful for soot modelling.

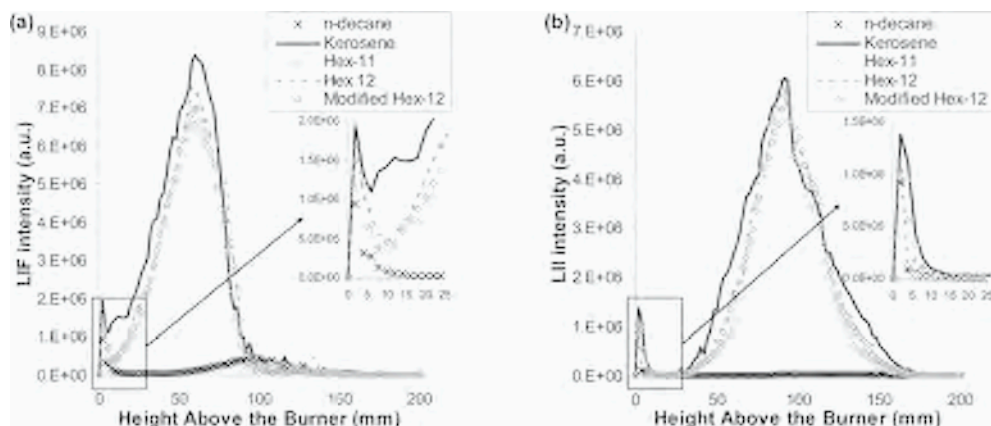


Figure 6. Profiles of the peak intensity of soot precursors LIF (a) and LII (b) as a function of the height above the burner obtained in the 5 flames.

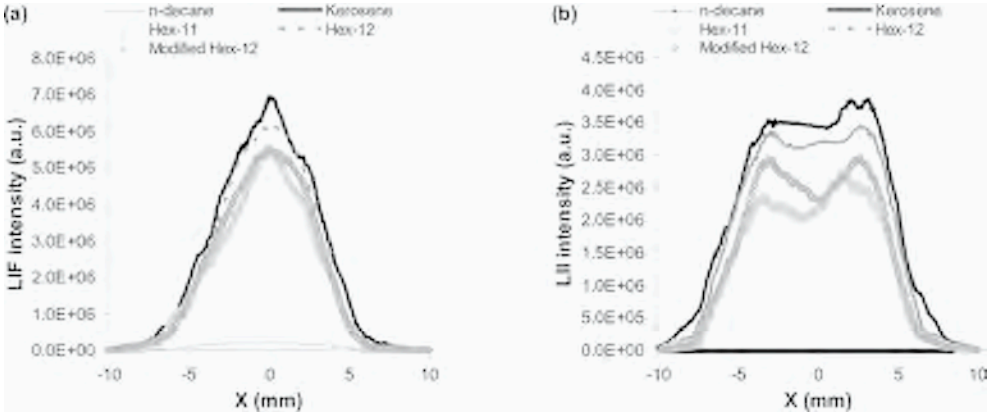


Figure 7. Radial profiles of soot precursors LIF (a) and LII (b) at 72 mm HAB obtained in the 5 flames.

Following McEnally and Pfefferle [14], the correlation between the peak soot volume fraction and the TSI of the fuel has also been evaluated in Figure 8. A relatively good tendency between  $f_v$  and the TSI is observed at high TSI value. A linear correlation would have led to an overestimation of  $f_v$  in the decane flame.

In addition to the soot load of each flame, information concerning the optical and morphological characteristics of the soot could be obtained. Indeed the behaviour of the LII signal with laser energy (excitation or fluence curve) is an intrinsic characteristic of the LII process. It especially reflects the impact of several factors such as the absorption soot function  $E(m)$ , the spatial distribution of laser energy in the collection volume, the temperature of soot particles, the primary particle size and other physical

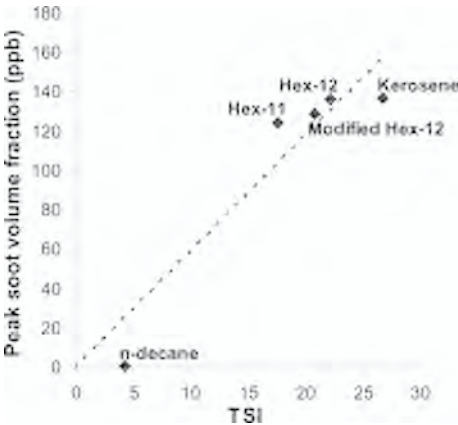


Figure 8. Peak soot volume fraction obtained in each flame as a function of the fuel threshold soot index (TSI).

properties such as the heat capacity and the density of the particles [29-31]. For example the excitation curves obtained with a gaussian laser irradiance follow a monotonically increase of the signal above a given threshold (expressed in fluence unit:  $\text{J}/\text{cm}^2$ ), known to be strongly dependent on  $E(m)/\lambda_{\text{laser}}$  and then reach a plateau region in which the signal is weakly dependent on the fluctuations of laser energy. In this work, the LII signal variation with laser energy was recorded at the peak soot location ( $\text{HAB} = 92 \text{ mm}$ ) in each flame and is plotted in Figure 9. The measurements have been performed at  $1064 \text{ nm}$  with a laser irradiance profile shaped to a gaussian one to make easier comparison with the literature. The laser section at  $1/e^2$  was determined to be  $0.015 \text{ cm}^2$  from the laser profile shown in Figure 3. As expected, the recorded fluence curves exhibit a plateau at high fluence and a sharp increase after  $0.03 \text{ J}/\text{cm}^2$  which is conform to the literature. It is noteworthy that fluence curves obtained in each flame are perfectly coincident indicating that the physical properties of soot particles should be the same at the peak soot location. At each flame location the fluence curves obtained in each jet fuel flame were found perfectly coincident. This is an important finding also justifying that the LII signals measured in the flames are well directly comparable in terms of soot volume fraction. Furthermore we examined the LII temporal decays which are known to be strongly correlated to the soot particle diameter at a given laser fluence. The time decays, recorded at the peak soot location of each flame with  $0.17 \text{ J}/\text{cm}^2$ , are plotted in Figure 10. They exhibit a perfect coincidence. Although quantitative determination of the primary particle diameter from LII temporal decays was not done in this work, this comparison indicates that the soot particle diameter has grown to the same size at the peak soot location and also at the same rate, since this time-decay coincidence was observed along the entire soot history for each fuel.

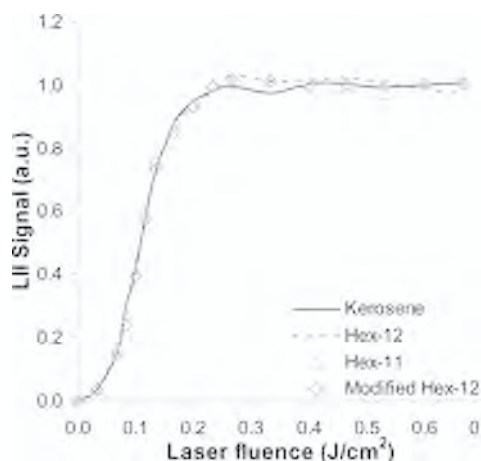


Figure 9. LII signal as a function of laser fluence ( $\text{J}/\text{cm}^2$ ). The fluence curves have been recorded at  $92 \text{ mm}$  HAB (height of the LII peak in Figure 6b) in the 4 jet fuel flames.

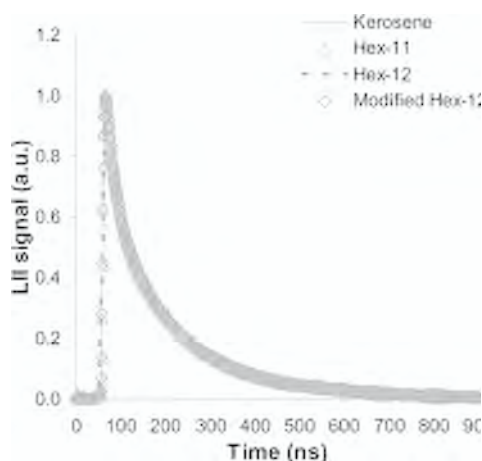


Figure 10. Time-resolved LII measurements obtained at  $92 \text{ mm}$  HAB in each flame with a laser fluence of  $0.16 \text{ J}/\text{cm}^2$ .

This last characterisation of soot particles, in terms of optical property and particle sizing history, completes the analysis of the 2D-images of fluorescent soot precursors and LII signals. These results lead to the conclusion that the soot process is the same in the surrogate flames and in the kerosene flame. However the soot mapping indicates a slightly better performance of Hex-12 surrogate. This study confirms the very good ability of Hex-12 surrogate initially (and successfully) formulated to mimic jet fuel behaviour over the lifetime of a batch pool fire [2, 9]. This surrogate fuel was also found very satisfying to describe the low temperature reactivity of JP8 in a pressurized reactor [32]. Another 6-component surrogate (named Sur1 from ref. 2), having a composition close to that of Hex-12, was compared to JP-8 in a non-sooting counterflow diffusion flame [33]. A good agreement between the temperature profiles and the extinction limits was also found.

Finally the modified-Hex-12 appears to be also an interesting surrogate because it only contains four components. The substitution of the n-C8, n-C12, n-C16 blend by n-C10 does not really affect the soot formation in our turbulent diffusion flames. Additional tests in pool fire would be very interesting. The modified-Hex-12 allows a simplification of the blend preparation. In addition the selected alkane (n-decane) has been more studied both experimentally and by modelling than heavier alkanes and thus can lead to more reliable modelling results.

## 5. CONCLUSION

In this work, the soot volume fraction has been spatially and quantitatively compared in turbulent diffusion flames of liquid fuels representative of jet-fuels: n-decane, kerosene and surrogate model fuels.

A laboratory burner has been specially designed and developed to this end. This burner allows the ignition of small droplets liquid sprays thanks to a pilot methane flat flame stabilized on a hybrid McKenna burner. The high speed sprays are generated by a DIHEN nebulizer inserted in the central of the porous plug. Hydrodynamic characteristics of the cold sprays are shown to be independent of the physical-chemical properties of the selected fuels. Under combustion conditions, a complete vaporisation of the fuels without fractional distillation occurred above 15 mm HAB. The obtained flames of around 18-cm height and 2-cm width have very similar structure and soot distribution leading to an easy comparison between the fuels in terms of PAH and soot formation.

Five different fuels have been tested and compared. In a first part, kerosene jet A-1 and two six-component surrogates (Hex-11 and Hex-12) previously tested in pool fire [9] have been studied. Then, the impact of alkane content on soot formation has been studied by testing pure n-decane and a simplified four-components blend in which the three initial alkanes of Hex12 have been replaced by n-decane in equal mol percentage.

The different flames are analyzed using reconstituted-2D LIF and LII images. The LIF signal was obtained from the comparison of the signals collected successively upon 532 nm and 1064 nm laser excitation using the two-colour LII method developed previously [15-17]. LIF at 532 nm allows the detection of large PAHs and other

fluorescent soot precursors and LII at 1064 nm is used for the soot volume fraction measurement. The calibration of the LII measurements has been carried out by comparing the peak LII signal obtained in our turbulent flames with the peak value recorded in a known laminar diffusion flame in which  $f_v$  had been determined previously by Cavity Ring Down Spectroscopy [15]. It must be noticed that these flames exhibit a very weak soot volume fraction (<150 ppb) in contrast with the initial tests on surrogates performed in pool fires. In addition, information on optical and morphological properties of soot particles have been derived from the analysis of the LII signals.

The comparison of Jet A-1 with the surrogate blends mainly relies on soot and fluorescent soot precursors mappings. We found that the soot formation process is similar in the surrogates and in the kerosene flames. Nevertheless, Hex-12 surrogate appears to be the best one.

A modified Hex-12 surrogate containing 4 components has been proposed. This simplified surrogate is found to better mimic the kerosene jet-A1 behavior than the Hex-11 surrogate. Modelling and experiments using such a simplified surrogate will be easier to perform. The combustion of n-decane produces 200-fold less soot than kerosene under our spray conditions.

Finally, information on optical and morphological properties of soot particles have been derived from the analysis of the LII signals. At a given combustion stage, the LII decay-times are found identical for each flame suggesting the absence of particle diameter variation between flames. Moreover the perfect concordance between the fluence curves obtained in each flame (at a given height) also suggests that the optical properties of the soot particles should not differ.

In this work, we have shown that the developed experimental strategy is well suited to compare the sooting tendency of different liquid fuels. It has recently been applied in diesel and diesel surrogates flames [34]

## ACKNOWLEDGEMENTS

The authors thank the Nord – Pas de Calais Region and the European Funds for Regional Economic Development and The Agence Nationale pour la Recherche through contract ANR-06-BLAN-0349-01 for their financial support. Fabrice Cazier from the Center of measurement (MREID) of ULCO University is warmly thanked for providing the GC composition of kerosene. The authors also thank Kevin Thomson from NRC Ottawa for fruitful discussions.

## REFERENCES

1. P. Dagaut, M. Cathonnet, *Prog. Energy Combust. Sci.* 32 (2006) 48-92.
2. A. Violi, S. Yan, E.G. Eddings, A.F. Saforim, *Combust. Sci. Technol.* 174 (2002) 399-417.
3. P. Dagaut, A. El Bakali, A. Ristori, *Fuel* 85 (2006) 944-956.
4. C. Vovelle, J-L. Delfau, M. Reuillon, in *Soot Formation in Combustion : Mechanisms and Models*, H. Bockhorn (Ed.) Springer-Verlag, Berlin (1994) pp. 50-65.

5. C. Douté, J.-L. Delfau, R. Akrich, C. Vovelle, *Combust. Sci. Technol.* 106 (1995) 327-344.
6. C. Douté, J.L. Delfau, C. Vovelle, *Combust. Sci. Technol.* 130 (1997) 269-313.
7. P. Lindstedt, L.Q. Maurice, *J. Propul. Power* 16 (2000) 187-195.
8. K.J. Young, C.D. Stewart, J.B. Moss, *Proc. Combust. Inst.* 25 (1994) 609-617.
9. E.G. Eddings, S. Yan, W. Ciro, A.F. Sarofim, *Combust. Sci. Technol.* 177 (2005) 715-739.
10. H.F. Calcote, D.M. Manos, *Combust. Flame* 49 (1983) 289-304.
11. D.B. Olson, J.C. Pickens, R.J. Gill, *Combust. Flame* 62 (1985) 43-60.
12. R.J. Gill, D.B. Olson, *Combust. Sci. Technol.* 40 (1984) 307-315.
13. Y. Yang, A.L. Boehman, R.J. Santoro, *Combust. Flame* 149 (2007) 191-205.
14. C.S. McEnally, L.D. Pfefferle, *Combust. Flame* 148 (2007) 210-222.
15. Y. Bouvier, C. Mihean, M. Ziskind, E. Therssen, C. Focsa, J.F. Pauwels, P. Desgroux, *Proc. Combust. Inst.* 31 (2007) 841-849.
16. C. Schoemaeker-Moreau, E. Therssen, X. Mercier, J.F. Pauwels, P. Desgroux, *Appl. Phys. B* 78 (2004) 485.
17. E. Therssen, Y. Bouvier, C. Schoemaeker-Moreau, X. Mercier, P. Desgroux, M. Ziskind, C. Focsa, *Appl. Phys. B* 89 (2007) 417-427.
18. A. Bruno, C. de Lisio, P. Minutolo, A. D'Alessio, *Combust. Flame* 151 (2007) 472-481.
19. G. Zizak, F. Cignoli, G. Montas, S. Benecchi, R. Dondé, *Recent Res. Dev. App. Spectrosc.* Vol. 1 (1996) 17-24.
20. K.C. Smyth, J. H. Miller, R.C. Dorfman, W.G. Mallard, R.J. Santoro, *Combust. Flame* 62 (1985) 157-181.
21. E. Heinecke, D. Hartmann, R. Müller, A. Hese, *J. Chem. Phys.* 109 (1998) 906-911.
22. B.W. Acon, J.A. McLean and A. Montaser, *Anal. Chem.* 72 (2000) 1885-1893.
23. J.A. McLean, M.G. Minnich, L.A. Lacone, H. Liu and A. Montaser, *J. Anal. At. Spectrom.* 13 (1998) 829-842.
24. M.G. Minnich, J.A. McLean, A. Montaser, *Spectrochim. Acta, Part B* 56 (2001) 113-1126.
25. J.C. Lasheras, E. Villermaux, E.J. Hopfinger, *J. Fluid Mech.* 357 (1998) 351-379.
26. H. Bladh, P.E. Bengtsson, J. Delhay, Y. Bouvier, E. Therssen, P. Desgroux, *Appl. Phys. B* 83 (2006) 423-433.
27. L.Y. Melton, *Appl. Opt.* 23 (1984) 2201.
28. B. Axelsson, R. Collin, P. E. Bengtsson, *Appl. Phys. B* 72 (2001) 367.
29. H. Michelsen, *J. Chem. Phys.* 18 (2003) 7012-7045.
30. C. Schulz, B.F. Kock, M. Hofmann, H. Michelsen, S. Will, B. Bougie, R. Suntz, G. Smallwood, *Appl. Phys. B* 83 (2006) 333-354.
31. H. Bladh, P.E. Bengtsson, *Appl. Phys. B* 78 (2004) 214-248.
32. D.B. Lenhert, D.L. Miller, N.P. Cernansky, *Combust. Sci. Technol.* 179 (2007) 845-861.
33. J.A. Cooke, M. Belluci, M.D. Smooke, A. Gomez, A. Violi, T. Faravelli, E. Ranzi, *Proc. Combust. Inst.* 30 (2005) 439-446.
34. R. Lemaire, A. Faccinetto, E. Therssen, M. Ziskind, C. Focsa, P. Desgroux, *Proc. Combust. Inst.* 32 (2008) doi:10.1016/j.proci.2008.05.019.

# Computational and experimental investigation of soot and NO in coflow diffusion flames

B.C. Connelly<sup>1</sup>, M.B. Long<sup>1</sup>, M.D. Smooke<sup>1</sup>, R.J. Hall<sup>2</sup>, M.B. Colket<sup>3</sup>

<sup>1</sup> Department of Mechanical Engineering, Yale University, New Haven, Connecticut, 06520-8284, USA

<sup>2</sup> Consultant, United Technologies Research Center, East Hartford, Connecticut, 06108, USA

<sup>3</sup> United Technologies Research Center, East Hartford, Connecticut, 06108, USA

*Abstract: A combined computational and experimental investigation that examines the relationship of soot formation and NO in coflow ethylene air diffusion flames is presented. The results of a computational model that includes a sectional representation for soot formation with a radiation model are compared against laser-induced fluorescence measurements of NO. Experimentally, a laser near 225.8 nm is used to excite the  $\gamma(0,0)$  band in NO. Spectrally resolved fluorescence emission is imaged radially, for the (0,0), (0,1), (0,2), (0,3), and (0,4) vibrational bands, at varying axial heights to create a two-dimensional image of NO fluorescence. A reverse quenching correction is applied to the computational results to determine an expected fluorescence signal for comparison with experimental results. Modeling results confirm that Fenimore NO is the dominant mechanism for NO production and suggest that for lightly sooting flames (peak soot volume fraction < 0.5 ppm), soot reduces only the Zeldovich NO formation (by a factor of two). For flames with increased soot levels (peak soot volume fraction ~ 3 ppm), the model indicates not only that Zeldovich NO decreases by a factor of 2.5 through radiation loss, but that non-Zeldovich NO is reduced in the top center of the flame by about 30% through the oxidation of soot.*

## 1. INTRODUCTION

As emissions legislation becomes more restrictive, a detailed understanding of pollutant formation in flames will become even more critical for the design of pollutant abatement strategies and for the preservation of the competitiveness of combustion related industries. In particular, it is clear that there will be continuing pressure to lower both NO<sub>x</sub> emission indices and soot volume fractions in practical combustion devices. This is in response to the toxicological effects that small particles can have on the body's cardio-pulmonary system [1, 2] and to the impact, for example, that soot can have on thermal radiation loads in combustors and on turbine blades. Moreover, soot emissions can enhance contrail formation [3] and such "man made" clouds may have an impact ultimately on the Earth's climate [4, 5]. Hence, the study of sooting flames remains important from practical, economic, environmental and safety standpoints, as well as for purely scientific interests in the fundamental processes.

The temperature decrease due to radiative losses in systems in which significant soot is produced can affect flame length and other temperature-dependent processes such as the formation of NO. While both NO and soot formation are often studied independently, there is a desire to understand their coupled relationship as a function

of system parameters such as fuel type, temperature and pressure. We combine a computational and experimental investigation to examine the interrelationship of soot formation and NO in coflow ethylene air diffusion flames. The results of a computational model that includes detailed chemistry for gas-phase processes and a sectional representation for soot formation, along with optically thin radiation, are compared against laser-induced fluorescence (LIF) measurements of NO. The detailed information on the temperature and species concentrations in the computed flame are combined with an NO quenching model to predict the laser-induced fluorescence signal from NO that is measured experimentally. Once the modeling technique is qualitatively validated against the data sets, computations are performed to assess the impact of soot (and related radiation) on the NO field.

## 2. SOOT FORMATION MODEL

The soot formation model is described in detail in [6]. For completeness, we outline only the essential features:

### 2.1. Inception

The model is based on the sequence of growing naphthalenyl to pyrenyl through sequential acetylene addition, H-atom elimination, H-atom abstraction, and acetylene addition followed by ring closure. Overall, the reaction can be written  $C_{10}H_7 + 3C_2H_2 \rightleftharpoons C_{16}H_9 + 2H + H_2$ . This sequence is assumed to continue to form yet larger PAH structures with the overall balance of  $C_{10}H_7 + 3nC_2H_2 \rightleftharpoons C_{10+6n}H_{7+2n} + 2nH + nH_2$ . Quasi steady-state concentrations of intermediate polycyclic aromatic hydrocarbons are assumed, leading to steady-state expressions for the formation rates of these high molecular weight condensed polycyclic aromatic hydrocarbons (PAH). The computed soot results are relatively independent of the number,  $n$ , assigned to the inception species and equal to 21 in this work. Limitations and major assumptions of the model are discussed in more detail in [7,8] scrubbing of gas phase species by soot growth processes, generally accounted for, was neglected for inception because the kinetic models utilized in this study already under predict benzene mole fractions by approximately a factor of two (see also, [7]). The inception rate was not augmented by the factor of two included in [6].

### 2.2. Surface growth and oxidation

The surface growth model used in the numerical simulations was based on the premixed flame data of Harris-Weiner [9] where we assumed an activation energy of  $E_s = 31.8$  kcal/mole [10] and where we multiplied the nominal Arrhenius factor by two (see also [6-8]). Surface growth is first order in acetylene concentration in this model. (Also available is the 'MODFW' surface growth mechanism [11], as corrected by [12] and referred to as the 'CH' model. This 'CH' model was shown to be successful in mode-

ling soot growth in high temperature flames [13] and is similar to the HACA model [14]). Oxidation of soot by  $O_2$  and OH is treated as described in [7,8]. In the assumed free-molecule regime, surface growth and oxidation rates are proportional to particle surface area.

### 2.3. Particle dynamics

The growth of soot particles is modeled as a free-molecule aerosol dynamics problem, using the well-known sectional particle size representation for spheres [15]. The application of this approach to soot modeling is described in [6-8,16]. The contributions from the inception processes are incorporated as a source term in the dynamical equation for the first sectional bin, whose lower mass boundary is set equal to the mass of the assumed inception species. Calculated results were not significantly sensitive to the number of sections assumed, with 20 sections used in all the calculations reported here.

The spherical particle sectional model nominally imposes no constraint on the final particle size, and does not account for aggregate formation. Coalescence destroys particle surface area, whereas aggregation, to the first order, does not. This is an important consideration because of the dependence of surface growth and oxidation on particle surface area. Adding equations for the number of primary spheroids within a section would make it possible to model accurately the formation of soot aggregates [17-19], but this is beyond the scope of the present paper. Instead, an approximate treatment of aggregate formation effects on surface area has been employed, as will be discussed.

### 2.4. Radiative power loss

For flames with sub-ppm soot volume fractions, the power radiated from soot and gas bands ( $CO_2$ ,  $H_2O$ , and CO, using the exponential wideband model) is computed in the optically thin limit using the expressions in [20].

### 2.5. Soot ageing

Two principal deficiencies of the soot model used in [7,8] were that (i) centerline soot was always substantially under predicted and (ii) the computed wings of the flame were extended much beyond those determined by experiment. The original model allowed the formation of primary particles that were much larger than typical maximum experimental values ( $\sim 25\text{nm}$ ). These large particles slowed the oxidation process and caused the extended sooting region. In practice, soot primary particles reach a maximum size due to active surface site deactivation (ageing). Dobbins [21] has given a measured deactivation rate for the process, and some modeling of the effect has been carried out in premixed flames [19,22]. Hall and Colket [19] used a decay rate similar to that of Dobbins in a study of aggregate formation using sectional analysis, and

Singh, et. al. [22] tested different functional dependences of surface reactivity on age in their study of high pressure coagulation using Monte Carlo techniques. Frenklach and co-workers [23,24] have fitted to various premixed flame data an empirical expression for the fraction of active sites that is a function of the average particle size and gas temperature, but not explicitly to individual particle age. Much remains uncertain about how to model this effect, particularly in a diffusion flame, however. Given this uncertainty, in this work a simple step function dependence of surface reactivity on particle size was assumed in which growth is shut off above a cut-off particle size (25 nm in these simulations).

Further, to simulate approximately the preservation of particle surface area in aggregate-aggregate collisions, coalescence was disallowed above a certain particle size, denoting a boundary between “liquid” particles and larger aggregates. Particles of this size (again 25 nm was chosen) and larger will not coalesce with each other. Coalescence is still allowed for all collisions involving “liquid” particles, and hence particles larger than 25 nm can still be formed in the simulations by small particle scrubbing. Particles with sizes larger than 25 nm can be crudely viewed as aggregated particles with multiple individual spheroids. This is an approximate treatment of particle morphology that we plan ultimately to improve by adding equations for the number of primary spheroids within each aggregate size class. The primary particle size at which coalescence ceases and particles start to fuse together to form aggregates might ultimately be more accurately determined from a multi-component sectional analysis in which the dehydrogenation of the particles is calculated. Such a multi-component analysis might also be a route to calculating ageing effects more accurately. Even with the heuristic modifications to surface growth and coalescence, as adopted here, primary particle size was limited and the extended soot wings were eliminated, consistent with the experimental data.

### 3. EXPERIMENTAL PROCEDURE

Atmospheric pressure, axisymmetric, coflowing, nonpremixed laminar diffusion flames are generated with a burner (see Figure 1) in which the fuel flows from an uncooled 4.0 mm inner diameter vertical steel tube (wall thickness 0.38 mm, parabolic flow) into a concentric, 74 mm diameter air coflow (plug flow). The details of the burner used are kept consistent with previous studies [6, 25]. The flame is lifted above the burner surface, preventing heat transfer from the flame to the burner. The fuel (ethylene) is diluted with varying levels of inert (nitrogen) to control the soot loading within the flame. Two flames with different fuel dilutions are examined: a 40% ethylene/60% nitrogen flame and an 80% ethylene/20% nitrogen flame.

The third harmonic of a Nd:YAG laser pumps a dye laser containing coumarin 450 dye. The 452 nm dye laser output is doubled using a BBO crystal, producing an ultraviolet (UV) beam near 225.8 nm, which is used to excite transitions in the  $\Lambda^2\Sigma^+ - X^2\Pi$  (0,0) band of NO. An excitation scan over a spectral range from 225.5-226.5 nm was matched with the various spectral features of NO [26]. The  $Q_1(18)$  transition ( $44275.684\text{ cm}^{-1}$ ) was selected for this work. This transition is reasonably well separated from neighboring transitions and has significant population from room tempera-

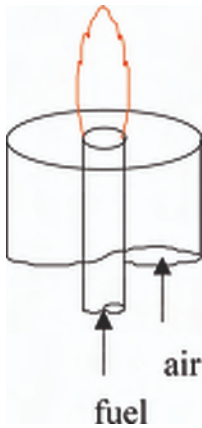


Figure 1. Schematic of the coflow burner.

ture to the flame temperatures investigated. Aside from soot interferences, which poses a broadband spectrum, no significant spectral interferences were encountered in the laminar flames investigated [27].

There are two burners in the optical path. A dichroic mirror steers the UV beam down the measurement path, and to remove the majority of the laser energy at 452 nm. A beamsplitter steers  $\sim 30\%$  of the energy in the UV beam 4 cm above a premixed reference burner. NO fluorescence from the center of a lean propane flame is imaged with a quartz lens onto a 1 mm slit, through an interference filter at 260 nm (12.5 nm bandwidth) centered on the (0,3) vibrational band. The signal is detected with a PMT (Hamamatsu R166UH) connected to a digital oscilloscope. This signal is used to provide a fluorescence normalization that accounts for variations in laser energy and ensures that the laser wavelength does not shift off of the peak of the NO transition being pumped. The UV beam remaining after the beamsplitter ( $\sim 60 \mu\text{J}$  per pulse) is directed across the target diffusion flame burner. Because the remaining energy from the 452 nm beam ( $\sim 100 \mu\text{J}$ ) causes interference in sooty regions of the flame, the two wavelengths are separated using a quartz prism. The remaining UV beam still produces unavoidable soot interferences. A 25 cm focal length quartz lens focuses the UV beam across the diffusion flame. To ensure that the fluorescence is in the linear regime, the measurements are made 10 cm before the focus of the UV beam, resulting in a beam diameter of 0.5 mm in the measurement region. While this beam diameter sacrifices some spatial resolution in the axial direction, features of the NO LIF in the axial direction are observed (both experimentally and computationally) to be larger than the beam diameter. Finer structures in the NO LIF occur in the radial direction, where the spatial resolution is superior (0.13 mm, using Nyquist sampling criteria). The laser energies at 225.8 nm and at 452 nm are monitored using two pyroelectric energy meters (LaserProbe RjP-734) connected to a second oscilloscope.

NO fluorescence in the diffusion flame is imaged onto a  $500\text{-}\mu\text{m}$  entrance slit of a spectrograph (SPEX 270M) using a UV camera lens (UV-Nikkor 105 mm, f/4.5) and a 10 cm focal length quartz lens. When taking data in sooty regions within the flame,

a colored glass filter (Corning 7-54) is placed between the two collection lenses to suppress the Rayleigh scattering by the soot, which would otherwise saturate the detector. Spectral resolution is sacrificed by using a relatively wide entrance slit to compensate better for wandering of the beam through the measurement volume. The fluorescence is dispersed with a 300 groove/mm grating (250 nm blaze angle) and imaged with an intensified CCD detector (a gated Gen II intensifier optically coupled to a Princeton Instruments TE/CCD-512 CCD). The CCD image contains information in one spatial and one spectral dimension. Spatially, a line extending from the centerline to 10 mm in the radial direction is imaged, and spectrally the region from 220-300 nm is recorded. The spectral region includes Rayleigh scattering (overlapped with the (0,0) fluorescence) as well as the (0,1), (0,2), (0,3) and (0,4) vibrational fluorescence bands. The fluorescence signal is integrated on the detector for 12.8 seconds (128 laser pulses), chosen to correspond to event sampling on the oscilloscopes. The experiment is controlled through a computer, which records synchronized data from the CCD camera and the digital oscilloscopes. Data are acquired both with the laser tuned to the  $Q_1(18)$  peak, and with the laser tuned off-resonance (near 225.65 nm), to provide a correction for soot interferences.

The final fluorescence image is obtained by summing the fluorescence intensity over a 7.5 nm spectral region centered on the (0,2) transition [28]. No significant difference is noted when the detection band is centered on the (0,1) or on the (0,3) transition. A two-dimensional image of the NO fluorescence distribution is created by tiling together a series of spatial/spectral images recorded at 0.5-mm intervals from 2-100 mm above the burner. Each image is corrected for detector and soot incandescence backgrounds, normalized by the reference fluorescence signal recorded by the PMT, and corrected for nonuniform detector gain and optical throughput. This latter "response" correction is obtained by imaging the fluorescence from a calibration gas (45.2 ppm NO in  $N_2$  mixed with 3%  $O_2$ , by volume), which results in a uniform NO concentration field in the imaged region that also provides a room temperature signal calibration. The final corrected fluorescence image has a signal-to-noise ratio of  $\sim 50$  in the downstream region, where the NO signal was highest, and a pixel volume of  $0.1 \times 0.5 \times 0.5 \text{ mm}^3$ .

For fluorescence in the linear regime, the scattered intensity is dependent on a number of variables, including the total number density, the Boltzmann population fraction, and the total collisional quenching rate. For NO, the quenching term is particularly important, and varies significantly with temperature and with quenching partners. Fortunately, a good deal of information is available on NO quenching, both in the form of experimental measurements and models [28-30]. Due to the soot within the target flames, it is difficult to characterize the flame temperature and major species. Consequently, we cannot apply the quenching and Boltzmann corrections to the measured fluorescence signal. Instead, we have applied a reverse quenching correction [31,32] to the calculated flame to determine an expected fluorescence signal for comparison with the experimental results. The model of Settersten et al. [30] is used to account for the temperature-dependent quenching by  $CO_2$ ,  $H_2O$ ,  $O_2$ ,  $N_2$ , and CO. Both the measured fluorescence and the calculated fluorescence are normalized using the calibration gas to provide a quantitative comparison of fluorescence signals.

#### 4. COMPUTATIONAL APPROACH

The axisymmetric computational model [7,8] employs the gas-phase diffusion flame equations in the velocity-vorticity formulation with buoyancy and the particle sectional approach presented in [16]. The result is a strongly coupled set of elliptic partial differential equations. The gas and soot equations are additionally coupled through non-adiabatic radiative loss. Radial and axial velocities, the vorticity, the temperature, the gas-phase species and the particle sectional mass fractions are computed. Twenty soot sections are included in the formulation. The system is closed with the ideal gas law and appropriate boundary conditions are applied on each side of the computational domain. Local properties are evaluated via transport and chemistry libraries. The sectional thermophoretic velocities in the free molecule regime are given in [16] as are the sectional diffusion velocities written with a mass-weighted mean diffusion coefficient for each size class. The governing conservation equations are solved on a two-dimensional mesh by combining a Newton-based steady-state and a time-dependent solution method [6]. A time-dependent solution is first obtained on a coarse grid and then grid points are inserted adaptively to increase the resolution in regions of high spatial activity. Computations were performed on an AMD Dual Opteron 240 system running at 1.4 GHz.

#### 5. RESULTS

In this section we present the results of a series of computations and LIF experiments in which NO formation is examined in sooting, ethylene-air, coflow diffusion flames where the radiation field is computed with an optically thin model. We consider flames with 40% and 80% (mole fraction) ethylene diluted with nitrogen. The computations employ the ethylene mechanism in [33] coupled with the nitrogen chemistry submechanism in GRI 2.11 [34]. We decided on the GRI 2.11 submechanism as opposed to the newer one in GRI 3.0 [35] as the latter significantly over-predicts (by a factor of 2.5) NO downstream in our coflow flames [36]. The result is a reaction network containing 84 chemical species with 578 reactions. The velocity profile of the ethylene fuel tube was parabolic with an average velocity of 35 cm/sec. The air coflow was a plug flow profile with a velocity of 35 cm/sec. The gases emerged from the burner at 298 K. All computations were performed on a 1.4 GHz AMD Dual Opteron processor.

NO can be formed in hydrocarbon flames by several different mechanisms (see e.g., [37-39]). The Zeldovich or thermal NO mechanism [40] as extended by Bowman and Seery [41] is initiated by the reaction of  $N_2$  with O. This well known 3-step reaction sequence is the dominant NO forming route at temperatures above 1850 K. A second path consists of reactions involving  $N_2O$ , which form NO. NO formed via this mechanism increases at higher pressures. A third mechanism responsible for NO formation is (prompt) "Fenimore NO." The main steps influencing this reaction sequence are  $N_2+CH=HCN+N$ ,  $N_2+CH_2=HCN+NH$  and other reactions involving  $N_2$  and hydrocarbon radicals. Lastly, NO can be formed via the  $H+N_2=NNH$ , followed by  $O+NNH=NO+NH$  sequence. GRI

2.11 includes these latter reactions but not with the higher rates suggested by Bozzelli and Dean [37]. The NO formation rates of each of these reaction sequences can be enhanced through super-equilibrium levels of O-atoms and other radical species in the flame front.

To assess the Zeldovich/non-Zeldovich NO distribution, additional computations were carried out with only the extended Zeldovich submechanism appended to the hydrocarbon mechanism. We note that in prior work in which we examined the origins of NO in atmospheric pressure coflow methane-air diffusion flames [32], we found that the  $N_2O$  and NNH submechanisms contributed minimally to overall NO levels. As a result, we will not examine the impact of these two submechanisms specifically on the overall NO levels but will assign all NO above the Zeldovich mole fraction levels as non-Zeldovich NO (in practice, this is almost totally Fenimore NO).

In Figure 2 we illustrate NO mole fractions for the 40% ethylene/60% nitrogen flame computed with the extended Zeldovich submechanism. When soot is included in the model (Figure 2a), we obtain a maximum soot volume fraction of 1.3 ppm with a peak NO of 22 ppm. The peak temperature is 2006 K. When the computation was performed without the inclusion of soot (Figure 2b), the peak temperature increased to 2055 K and the NO increased to 40 ppm. From the isopleths in the figure, we note that the region of NO above 20 ppm is larger in extent in the nonsooting flame compared to that of the sooting flame.

The NO mole fractions for the 40% flame computed with the complete NO mechanism are also illustrated in Figure 2. When soot is included in the computation (Figure 2c), the peak NO increases to 140 ppm. Most of the 118 ppm increase compared to the Zeldovich computation is due to Fenimore NO. If soot is removed from the computation (Figure 2d), the NO increases to 160 ppm and again the 120 ppm increase over the Zeldovich computation is due mostly to Fenimore NO. The spatial distribu-

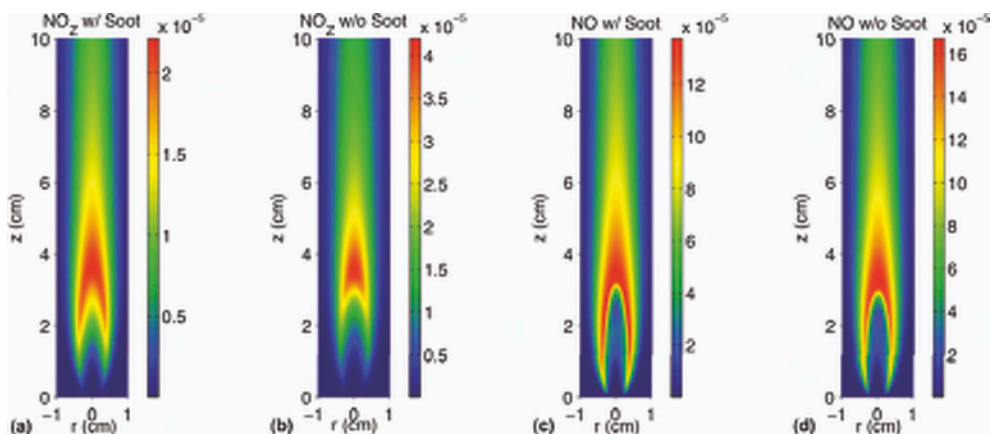


Figure 2. Computational NO mole fractions for the 40% ethylene/60% nitrogen flame generated with: (a) the extended Zeldovich submechanism, including soot; (b) the extended Zeldovich submechanism, neglecting soot; (c) the complete  $NO_x$  submechanism, including soot; (d) the complete  $NO_x$  submechanism, neglecting soot.

tion of the NO is generally quite similar for these two computations. For reference purposes, we point out that the sooting 40% flame had an overall powerloss of 16.1 W of the total 102 W generated.

As mentioned earlier, due to soot formation within the flame, we cannot easily characterize the flame temperature and major species. Hence, the quenching and Boltzmann corrections cannot be applied to the measured fluorescence signal. Instead, we have applied a reverse quenching and Boltzmann correction to the computed flame profiles to determine an expected fluorescence signal. This simulated signal is calibrated by an expected fluorescence signal from a gas of the same composition as in the experiment, to provide a quantitative comparison. In Figure 3 we plot the computed and measured NO fluorescence signals as a function of the spatial variables for the 40% flame. Also plotted is the soot volume fraction measured using laser-induced incandescence (LII). For details on the LII experiment for both the 40% and 80% flames, as well as comparison to numerically computed soot volume fractions, see [25]. The results show good qualitative agreement overall; for example, the fairly constant signal level in the regions above the flames, as well as the lower signal inside the flame/sooty areas, are captured. We note that the computed fluorescence signal underpredicts the measured fluorescence signal by approximately 30%.

We next performed computations for the 80% ethylene/20% nitrogen flame. In Figure 4 NO mole fractions are plotted for the computations with only the Zeldovich sub-mechanism. When soot is included (Figure 4a), we obtain a maximum soot volume fraction of 4.4 ppm and a total of 40 ppm of NO. The peak temperature of 2083 K occurred in the wings of the flame while the peak centerline temperature was 1736 K. When the computation is performed without soot (Figure 4b), the NO increases to 110 ppm and the peak temperature of 2107 K occurs on the centerline. Once again

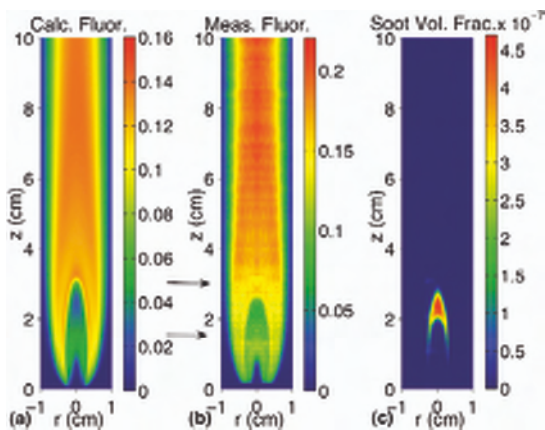


Figure 3. Comparison of the computed (a) and measured (b) fluorescence signal from NO for the 40% ethylene/60% nitrogen coflow flame. The fluorescence signal has been normalized with respect to a calibration gas for both the computed and measured plots. Experimentally, a colored glass filter was added to the input optics in the region between the arrows to minimize soot interferences. The soot volume fraction (c) is measured using LII.

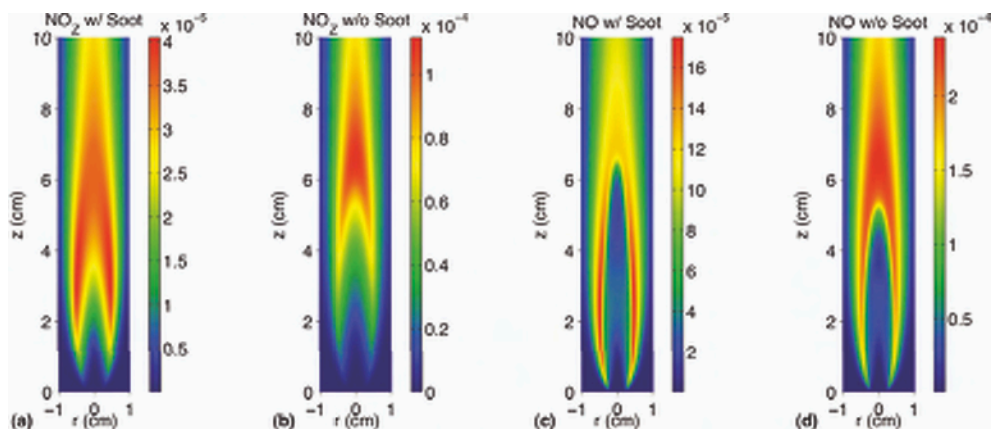


Figure 4. Computational  $\text{NO}_2$  mole fractions for the 80% ethylene/20% nitrogen flame generated with: (a) the extended Zeldovich submechanism, including soot; (b) the extended Zeldovich submechanism, neglecting soot; (c) the complete  $\text{NO}_x$  submechanism, including soot; (d) the complete  $\text{NO}_x$  submechanism, neglecting soot.

the spatial extent of the high NO levels is significantly larger for the computation in which soot is not included though the higher region of NO in the sooting flame extends further down the wings of the flame.

The 80% flame was then rerun with the complete NO mechanism. In the sooting case (Figure 4c), the peak NO increased to 170 ppm. Most of the 130 ppm increase was due to Fenimore NO. If soot was removed from this computation (Figure 4d), the NO increased to 240 ppm and again the 130 ppm increase over the Zeldovich submechanism computation was due mostly to Fenimore NO. What is striking in these two results is the change in the spatial orientation of the NO with or without soot. For the sooting flame, the highest NO extends in a narrow region in the wings of the flame. For the case when soot was neglected, the NO extends much further downstream with somewhat smaller extent in the wings. The 80% sooting flame had an overall power-loss of 53.3 W of the total 203 W generated.

In Figure 5 we plot the computed and measured NO fluorescence signals and the measured soot volume fraction as a function of the spatial variables for the 80% flame. As with the 40% flame, there is qualitative agreement between the computed and measured fluorescence signals, with the computed signal approximately 30% lower overall than the measured signal.

A clear contrast exists in the NO and temperature levels between the two 80% flames with the full NO mechanism. In the solution with soot, the NO levels and temperature are noticeably depressed along the centerline relative to the off-centerline conditions in the “wings” of the flame. Such results not only contrast with the 40% flame solutions, but also for the 80% flame solutions without any soot or its radiation. In the latter case, elimination of soot removes an important loss of energy from the flame and centerline temperatures nearly recover and peak NO levels occur on the centerline.

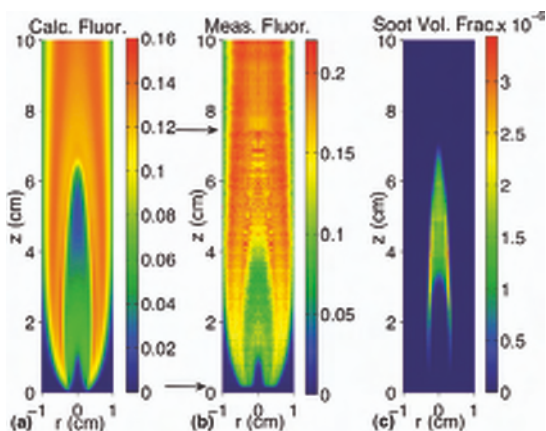


Figure 5. Comparison of the computed (a) and measured (b) fluorescence signal from NO for the 80% ethylene/20% nitrogen coflow flame. The fluorescence signal has been normalized with respect to a calibration gas for both the computed and measured plots. Experimentally, a colored glass filter was added to the input optics in the region between the arrows to minimize soot interferences. The soot volume fraction (c) is measured using LII.

Perhaps the most unusual feature of Figure 4c is the depression of NO concentration in the upper centerline region. (A similar depression did not exist for the 40% flame depicted in Figure 2c.) The NO concentration in this upper centerline region is  $\sim 120$  ppm vs. the 170 ppm in the side wings of the flame. Given that the Zeldovich mechanism gives a large broad contour in this region, it can be deduced that the Fenimore mechanism is suppressed in this region. To examine whether this is soot-related, we have plotted the difference between panels in Figures 4c and 4a, as well as the difference between panels 4d and 4b. These differences are shown in Figures 6a and 6b, respectively. These figures provide a qualitative assessment on the change in Fenimore NO with and without soot.

The depression in the upper centerline region for the flame with soot is quite significant. Similar plots for the 40% flame do not exhibit this strong effect.

As Fenimore NO is weakly dependent on temperature, the results in Figure 6 are clearly due to the presence of soot in the flame. To help appreciate the effect that soot has on NO formation, it is worthwhile to recognize that in premixed flames with soot levels of  $f_v = 4$  ppm and  $\phi = 2$ , about  $1/4$  of the total fuel carbon is converted to soot. We propose that some of the difference in the upper centerline regions between Figures 6a and 6b may be due simply to fewer hydrocarbon fuel fragments available to form CH or  $\text{CH}_2$  as the soot oxidizes directly to CO and H after attack by OH. In addition, soot oxidation along the centerline slightly delays the completion of combustion (relative to that by gas phase species). The slower oxidation rate reduces local super-equilibrium radical levels that promote NO formation and reduce the driving force for diffusion of molecular oxygen to the centerline of the flame, reducing NO production rates and lengthening the flame in the process. The relative importance of each of these phenomena will take additional computation and analysis.

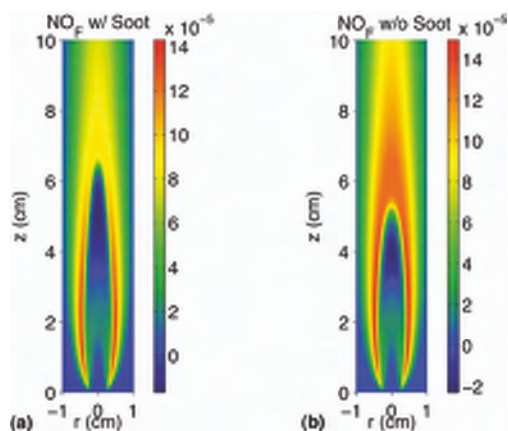


Figure 6. Computational NO mole fractions for the 80% ethylene/20% nitrogen flame, plotted as differences between the complete  $\text{NO}_x$  submechanism and the extended Zeldovich submechanism to approximate Fenimore NO: (a) the difference between panels in Figures 4c and 4a, including soot; (b) the difference between panels in Figures 4d and 4b, neglecting soot.

It is well established that, as we have found, many practical systems exhibit a reverse trend in NO and sooting levels. Typically, it is assumed that this is at least partially a result of local conditions, with more soot formed in a local fuel-rich environment and more NO formed in the near stoichiometric regions. The present results from both the 40% and the 80% flames imply a complication of this interdependency, with mitigation of NO production rates directly due to the formation of soot and local radiation losses. For the 80% flames the affects are so significant that they alter the NO profile shape in the flame, shifting the peak NO from the centerline to the wings of the flame.

## 6. CONCLUSIONS

We have combined LIF measurements and computations using a detailed chemistry coflow diffusion flame model with a sectional aerosol model to examine the effects of soot formation on NO levels in ethylene-air diffusion flames. Results indicate that while the dominant route to NO in these flames is due to non-Zeldovich NO (primarily prompt), Zeldovich NO is more pronounced in the 80% ethylene flame compared to the 40% ethylene flame. Moreover, when the soot field is removed from the model and the solution recomputed with a new radiation field, Zeldovich NO accounts for nearly 46% of total NO in the 80% flame and 25% of total NO for the 40% flame which are significantly larger than 24% and 16%, respectively, for the sooting flames. Furthermore, the results indicate that not only does soot and accompanying radiation loss (virtually all from Zeldovich NO) reduce the levels of NO throughout the flame, but for heavier sooting flames, the shape of the NO profile shifts, with NO levels in the wings noticeably higher than centerline levels. These results imply a coupled rela-

tionship between soot levels and NO that require a careful application of diagnostics and computation to help elucidate our understanding of these flames.

## ACKNOWLEDGMENTS

The authors would like to acknowledge support for this work from the DOE Office of Basic Energy Sciences (Dr. Larry Rahn, contract monitor), the National Science Foundation (Dr. Phil Westmoreland, contract monitor), and NASA (Dr. Dennis Stocker, contract monitor) under contracts DE-FG02-88ER13966, CTS-0328296, and NNC04AA03A, respectively. In addition, we gratefully acknowledge the Strategic Environmental Research and Development Program (SERDP) under a contract coordinated by Dr. Mel Roquemore of the Air Force Research Laboratories (Wright Patterson AFB).

## REFERENCES

1. J. Schwartz, *Environ. Res.* 62 (1993) 7-13.
2. D.W. Dockery, J.H. Ware, B.G. Ferris, F.E. Speizer, N.R. Cook, S.M. Herman, *J. Air Pollution Control Association* 32 (1982) 937-942.
3. U. Schumann, J. Strom, R. Busen, R. Baumann, K. Gierens, M. Krautstrunk, F.P. Schroder, J. Stingl, *J. Geophys. Res. [Atmos.]* 101 (1996) 6853-6869.
4. S. Menon, J. Hansen, L. Nazarenko, Y.F. Luo, *Science* 297 (2002) 2250-2253.
5. J.E. Penner, D.H. Lister, D.J. Griggs, D.J. Dokken, M. McFarland, *Aviation and the Global Atmosphere, A Special Report of IPCC Working Groups I and III.* 1999: Cambridge University Press.
6. M. D. Smooke, R. J. Hall, M. B. Colket, J. Fielding, M. B. Long, C. S. McEnally, L. D. Pfefferle, *Combust. Theor. Model.* 8 (2004) 593-606.
7. C. McEnally, A. Shaffer, M. B. Long, L. Pfefferle, M. D. Smooke, M. B. Colket, R. J. Hall, *Proc. Combust. Inst.* 27 (1998) 1497-1505.
8. M. D. Smooke, C. S. McEnally, L. D. Pfefferle, R. J. Hall, M. B. Colket, *Combust. Flame* 117 (1999) 117-139.
9. S. J. Harris, A. M. Weiner, *Combust. Sci. Technol.* 31 (1983) 155-167.
10. H. S. Hura, I. Glassman, *Proc. Combust. Inst.* 22 (1988) 371-378.
11. M. B. Colket, R. J. Hall, in *Soot Formation in Combustion, Mechanisms and Models*, H. Bockhorn (Ed.) Springer Series in Chemical Physics, 59, Springer-Verlag, 1994, p. 442.
12. F. Xu, P. B. Sunderland, G. M. Faeth, *Combust. Flame* 108 (1997) 471-493.
13. M. D. Smooke, R. A. Yetter, T. P. Parr, D. M. Hanson-Parr, M. A. Tanoff, M. B. Colket, R. J. Hall, *Proc. Combust. Inst.* 28 (2000) 2013-2020.
14. M. Frenklach, H. Wang, *Proc. Combust. Inst.* 23 (1990) 1559-1566.
15. F. Gelbard, J. H. Seinfeld, *J. Coll. Int. Sci.* 78 (1980) 485-501.
16. R. J. Hall, M. D. Smooke, M. B. Colket, in *Physical and Chemical Aspects of Combustion: A Tribute to Irvin Glassman, R.F. Sawyer, F.L. Dryer (Eds.)* Combustion Science and Technology Book Series, Gordon and Breach, 1997.
17. S. N. Rogak, PhD dissertation, Cal. Tech. 1991.
18. S. N. Rogak, *Aerosol Sci. Technol.* 26 (1997) 127-140.

19. R. J. Hall, M. B. Colket, Fall Technical Meeting of the Eastern States Section of the Combustion Institute, Raleigh, North Carolina, pp. 348-350, October 13-15, 1999.
20. R. J. Hall, *J. Quant. Spectrosc. Radiat. Transfer* 51 (1994) 635-644.
21. R. A. Dobbins, *Combust. Sci. Technol.* 121 (1996) 103.
22. J. Singh, M. Balthasar, M. Kraft, W. Wagner, *Proc. Combust. Inst.* 30 (2005) 1457-1466.
23. A. Kazakov, H. Wang, M. Frenklach, *Combust. Flame* 100 (1995) 111-120.
24. J. Appel, H. Bockhorn, M. Frenklach, *Combust. Flame* 121 (2000) 122-136.
25. M.D. Smooke, M.B. Long, B.C. Connelly, M.B. Colket, R.J. Hall, *Combust. Flame* 143 (2005) 613-628.
26. R. Engleman Jr., P.E. Rouse, H.M. Peek, V.D. Baiamonte, *Beta and Gamma Systems of Nitric Oxide*, Los Alamos Scientific Laboratory, Los Alamos, 1970.
27. C.D. Carter, R.S. Barlow, *Opt. Lett.* 19 (1994) 299-301.
28. M.C. Drake, J.W. Ratcliffe, *J. Chem. Phys.* 98 (1993) 3850-3865.
29. P.H. Paul, J.A. Gray, J.L. Durant, J.W. Thoman, *Appl. Phys. B* 57 (1993) 249-259.
30. T.B. Settersten, B.D. Patterson, J.A. Gray, *J. Chem. Phys.* 124 (2006) 234308.
31. V. Sick, F. Hildenbrand, P. Lindstedt, *Proc. Combust. Inst.* 27 (1998) 1401-1409.
32. M.D. Smooke, A. Ern, M.A. Tanoff, B.A. Valdati, R.K. Mohammed, D.F. Marran, M.B. Long, *Proc. Combust. Inst.* 26 (1996) 2161.
33. C.J. Sun, C.J. Sung, H. Wang, C.K. Law, *Combust. Flame* 107 (1996) 321-335.
34. C.T. Bowman, R.K. Hanson, D.F. Davidson, W.C. Gardiner Jr., V. Lissianski, G.P. Smith, D.M. Golden, M. Frenklach, H. Wang, M. Goldenberg, GRI-Mech version 2.11. 1995: available at [http://www.me.berkeley.edu/gri\\_mech](http://www.me.berkeley.edu/gri_mech).
35. G.P. Smith, D.M. Golden, M. Frenklach, N.W. Moriarty, B. Eiteneer, M. Goldenberg, C.T. Bowman, R.K. Hanson, S. Song, W.C. Gardiner Jr., V.V. Lissianski, Z. Qin, GRI-Mech version 3.0: available at [http://www.me.berkeley.edu/gri\\_mech](http://www.me.berkeley.edu/gri_mech).
36. B.A.V. Bennett, M.D. Smooke, R.J. Osborne, R.W. Pitz, *Combust. Theor. Model.* (2008) in press.
37. J.W. Bozzelli, A.M. Dean, *Int. J. Chem. Kinet.* 27 (1995) 1097-1109.
38. M.C. Drake, R.J. Blint, *Combust. Sci. Technol.* 75 (1991) 261-285.
39. J.A. Miller, C.T. Bowman, *Prog. Energy Combust. Sci.* 15 (1989) 287-338.
40. Y.B. Zeldovich, *Acta Physicochem USSR* 21 (1946) 557.
41. C.T. Bowman, D.V. Seery, *Emissions from Continuous Combustion Systems*, New York, Plenum Press, 1972, p. 123.

# In-cylinder soot nanoparticle formation mechanism

S. Kubo

Frontier Research Center, Toyota Central R & D Labs., Inc.

*Abstract: Theoretical analysis and experimental analysis have been conducted to clarify a formation process of soot nanoparticles under engine combustion conditions. Kinetic energy calculation and molecular dynamics calculation were performed to estimate the stability of polycyclic aromatic hydrocarbon (PAH) dimer which would be the first step in the formation process of soot nanoparticles. A single cylinder engine for observing in-cylinder soot formation process was operated under the condition of homogeneous charged-compression ignition (HCCI) combustion with n-heptane as fuel. Particles collected from an engine combustion chamber were analyzed using a scanning mobility particle sizer (SMPS), a time-of-flight secondary ion mass spectrometry (TOF-SIMS), an atomic force microscope (AFM) and a high-resolution transmission electron microscope (HRTEM).*

*The calculation results show that giant PAHs beyond C<sub>100</sub> can form a stable dimer at 1,500K and 5.0MPa. The giant PAH containing 100 carbon atoms is comparable to about 2nm in diameter if that have condensed six-ring structure. In the earlier stage of the engine combustion, number weighted particle distributions are mono-modal and the number density of nanoparticles less than 3nm in diameter starts to increase steeply over the temperature of 1,400K. The number weighted particle size distributions change from mono-modal into bi-modal with the progress of the engine combustion. TOF-SIMS analysis and AFM analysis show that molecules having molecular weights over 1,000 increase with the progress of nanoparticle formation and the changes of particle thickness distributions correspond to monomer, dimer and trimer of planar-structured molecules having molecular weights over 1,000. Soot nanoparticles observed with the HRTEM consist of random agglomerate of the dimers and trimers of planar-structured molecules beyond 2nm in diameter. It is concluded that soot nanoparticles are formed by random agglomerate of the dimers and trimers of the giant PAHs beyond C<sub>100</sub> in the engine combustion process.*

## 1. INTRODUCTION

Nanometer size soot particles emitted from internal combustion engines have the potential to influence atmospheric environment and human health. The influences depend strongly on chemical and physical properties of soot particles. We should understand the formation mechanism of soot particles under engine combustion conditions to clarify the chemical and physical properties of soot particles. The formation process of soot nanoparticle is not completely understood although many researches have been performed to clarify the transition from gas-phase compounds to soot nanoparticles [1-6].

Soot particles generated in a combustion process have the morphology of the agglomerate of carbonaceous nanoparticles with around 20nm in diameter. It has

been also found by a high-resolution transmission electron microscopy (HR-TEM) analysis that the carbonaceous nanoparticles have layered structures or shell-core-like structures [7-10]. The structures will consist of regular agglomerate of graphenes, describing its nature by analogy to a polycyclic aromatic hydrocarbon (PAH) of quasi infinite size. PAHs thought to be key intermediates in the formation of soot nanoparticles. Soot nanoparticle formation from PAHs larger than pyren is supported by the measurement of PAH species which contain tens to hundreds of carbon atoms [11,12]. Zhao et al. [13] used a scanning mobility particle sizer (SMPS) to study the evolution of particle size distribution functions for incipient soot nanoparticles as small as 3 nm in diameter in premixed ethylene flames and concluded from a theoretical modeling study that the incipient soot nanoparticles could be formed through dimerization of PAHs of sizes somewhat larger than pyren. In recent years, a number of research focusing on PAHs larger than pyren and the incipient soot nanoparticles has been increasing [14-20]. Any researchers, however, have not reached the clarification of the transition from gas-phase PAH compounds to the incipient soot nanoparticles in detail yet.

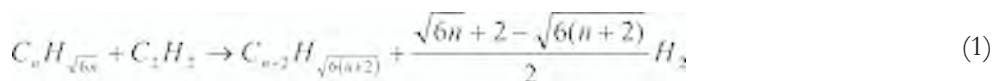
The purpose of this study was to clarify the formation process of soot nanoparticles by way of the dimerization of PAHs larger than pyren in the engine combustion on the basis of theoretical analysis and experimental analysis of soot nanoparticles sampled under the engine combustion process.

## 2. EXPERIMENTAL

### 2.1. Numerical analysis

Numerical analysis was conducted to estimate a critical PAH size for the dimerization from the view points both of the PAH growth by the reaction of  $C_2H_2$  addition and stability of a PAH dimer.

In order to estimate the critical PAH size, the reaction energy of  $C_2H_2$  addition to a certain PAH and an interplanar binding energy of the dimer of the PAHs were compared assuming the regular hexagonal circumcoronene-type structures which have the relationship of  $m = (6n)^{1/2}$  for  $C_nH_m$ . Overall PAH growth reaction by  $C_2H_2$  addition to  $C_nH_m$  PAH can be expressed by the following scheme;



By applying the group additivity rule [21] to the formation energy of the PAHs, the reaction energy is expressed as follows;

$$\Delta E = \left\{ 0.49 \left( \sqrt{6(n+2)} - \sqrt{6n} \right) - 2.35 \right\} / n \quad (\text{eV/C-atom}) \quad (2)$$

The other hand, the interplanar binding energy of the PAH dimer was calculated applying the Lennard-Jones potentials for the interaction between atoms in two PAHs constituting the dimer. The potential parameters for graphene and poly-methylene were applied for C-C [22] and H-H [23], respectively, and Lorentz-Berthelot mixing

rule was applied for unlike atoms. Brenner potentials [24] were applied for the inter-atomic interactions in one PAH.

The stability of various kinds of PAH dimers under high temperature conditions was simulated using molecular dynamics calculations assuming argon (Ar) as other gas molecules. The same interaction potentials (Brenner and Lennard-Jones) were applied in these calculations.

## 2.2. Experimental analysis

The engine experiment was carried out to observe the formation process of soot nanoparticles in the engine combustion. The experimental set-up is shown in Figure 1 and the experimental conditions were listed in Table 1. A single cylinder engine equipped with a fuel-air premixing chamber was operated under the condition of homogeneous charged compression ignition (HCCI) combustion with n-heptane as fuel at the equivalence ratio of 1.93. The HCCI combustion has a characteristic of uniform reaction progress in a whole combustion chamber. This characteristic has the advantage that the changes of molecular species by chemical reactions are only the function of time and not dependent on space. The equivalence ratio of 1.93 was decided in consideration of a growth rate and number concentration of soot nanoparticles because the equivalence ratio where soot particles start to form is 1.8 when n-heptane is used as a fuel.

Chemical compounds in the progress of the engine combustion were sampled using an in-house developed fast in-cylinder gas sampling system which had a piezo-driven valve. The piezo-driven valve was installed in the head of the single cylinder engine. The gas sampling duration of the piezo-driven valve is 0.2ms which corresponds to 1/50 at combustion duration (10ms). This high resolution time of the in-cylinder gas sampling system makes it possible to observe the transition from gas-phase PAH compounds to the incipient soot nanoparticles in the engine combustion.

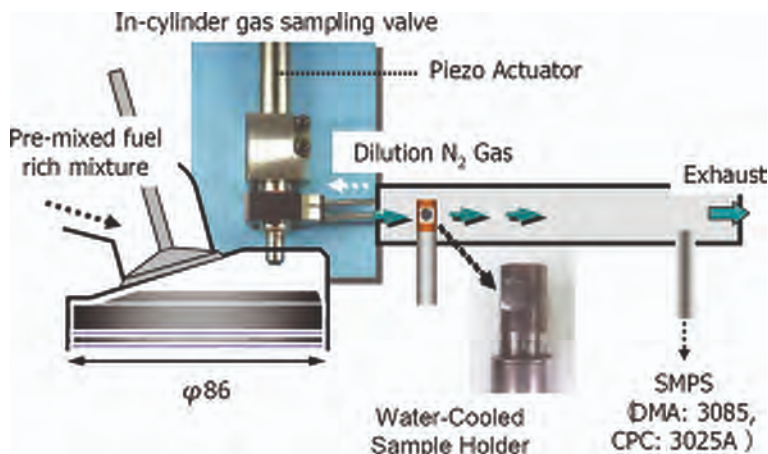


Figure 1. Experimental set-up.

Table 1. Engine experimental conditions.

Engine displacement	499cm <sup>3</sup>
Compression ratio	12
Speed	600rpm
Fuel	n-heptane (C <sub>7</sub> H <sub>16</sub> )
Equivalence ratio	1.93

In-cylinder gas including the incipient soot nanoparticles was diluted with nitrogen gas close after the in-cylinder gas passed through the piezo-driven valve. The dilution ratio was kept more than 1,000 times to suppress agglomeration of the incipient soot nanoparticles. The schematic of the piezo-driven valve is shown in Figure 2. In-cylinder gas sampling points during one cycle of the engine combustion are shown in Figure 3. (In this figure, changes both of heat release rate and in-cylinder gas temperature are also shown.) The sampling points were plotted on an in-cylinder gas temperature line. The sampling points were set on the basis of a critical time (0ms in Figure 3) when in-cylinder pressure during the engine combustion reached any set value. The gas sampling at any point was repeated several hundred times to decrease dispersion of data.

A part of diluted sample gas was led to a scanning mobility particle sizer (DMA: model 3085, CPC: model 3025A, TSI Inc.) to measure number weighted particle size distribution. On the other hand, low volatile compounds including the incipient soot

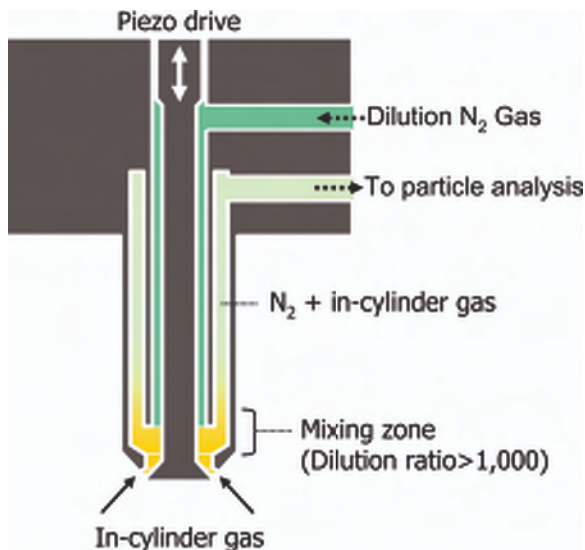


Figure 2. Schematic of in-cylinder particle sampling valve.

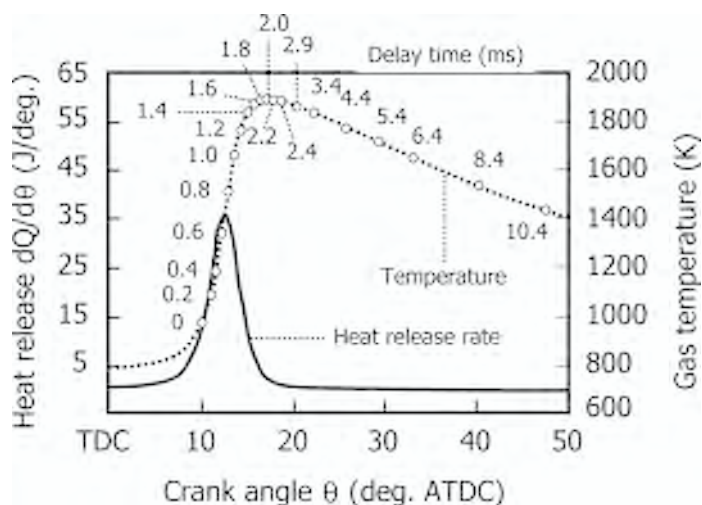


Figure 3. In-cylinder particle sampling points during one cycle of engine combustion compared to changes both of heat release rate and in-cylinder gas temperature.

nanoparticles in the diluted sample gas were gathered on a substrate by using the effect of thermal phoresis. Three kinds of the substrates were used according to analytical techniques; a silicon wafer tip for the measurement of a time-of-flight secondary ion mass spectrometry (TOF-SIMS), a mica cleaved film for the analysis of an atomic force microscope (AFM) and ultra-thin amorphous carbon film on copper grid for the observation of a high-resolution transmission electron microscope (HRTEM).

TOF-SIMS measurements [25] were performed using a Physical Electronics TFS-2100 (TRIEF II) instrument to measure mass spectra of the low volatile compounds. Mass spectra were acquired using bunched  $^{69}\text{Ga}^+$  ion pulses at an impact energy of 15 keV, an ion current of 600 pA (dc), and a pulse width of 13 ns. Total ion doses in the measurements were approximately  $5 \times 10^{11}$  ions/cm<sup>2</sup> under a static limit. The thickness changes of nanoparticles in the progress of the engine combustion were measured with AFM (D3100 AFM, Nanoscope IIIa, Veeco) to investigate the agglomeration process of the low volatile compounds. This instrument was run in a tapping-mode because the absence of strong tip-sample interactions was avoided. Furthermore, a silicon super sharp tip characterized by a very low apical curvature radius (ca 5 nm), was used to minimize tip-sample convolution effects [26]. HRTEM measurements using a JEOL JEM-2000EX instrument (Accelerating voltage was set for 200 kV) were performed to study the microstructure of soot nanoparticle compared with the AFM measurement result.

### 3. RESULTS AND DISCUSSION

Figure 4 shows changes in the reaction energy of  $\text{C}_2\text{H}_2$  addition to certain PAH and an interplanar binding energy of the dimer of the PAHs as a function of the number of

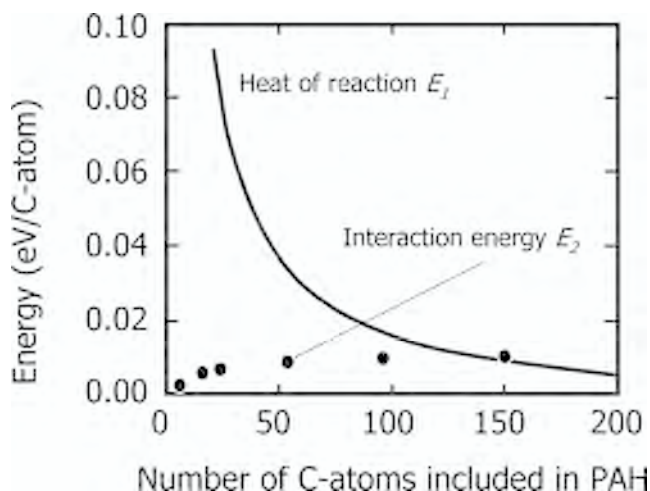


Figure 4. Changes both in reaction energy of  $C_2H_2$  addition to certain PAH and inter-planar binding energy of dimer of the PAHs as a function of the number of carbon atoms included in the PAH.

carbon atoms included in PAH. Change curve of the interplanar binding energies ( $\sim 0.02\text{eV/atom}$ ) crosses with that of PAH growth energies at the point where the carbon number of PAH is larger than 100. This means that PAH molecules start to dimerize when the carbon number composing the PAH is larger than 100. The PAH containing 100 carbon atoms is comparable to about 2 nm in diameter if that have condensed six-ring structure. This result perfectly denies the current views of condensation processes of 3 to 4 aromatic rings [3] or unsaturated, radicalic hydrocarbons which have chainlike and aliphatic structure [5] to form the incipient soot nanoparticles.

The molecular dynamics calculation results for the stability of two PAH dimers under the combustion condition at 1,500 K and 5.0 MPa are shown in Figure 5 for 5 different initial conditions for configurations and velocities. Figure 6 shows snapshots of planar  $C_{96}H_{24}$  dimer structure expressed by the molecular dynamics calculation. Figures 5 and 6 show that the dimer of the planar  $C_{96}H_{24}$  PAHs is stable during much longer time than the typical vibration period of inter-molecular distance except one case which two molecules start to separate at 65 picoseconds. We have confirmed by the additional calculations that the dimer of non-planar similar size molecules is less stable than that of planer molecules. The other hand, the dimer of planer  $C_{54}H_{18}$  is easily separated by the thermal vibration of two PAH molecules. This critical carbon numbers constituting the PAH molecules is almost same under different pressures between 0 to 5MPa.

From the numerical analysis, we get following clear conclusions for the formation mechanism of the PAH dimers under the engine combustion conditions;

- 1) PAH molecules grow up to giant PAHs containing about 100 carbon atoms under gas phase reactions. The PAH containing 100 carbon atoms is comparable to about 2 nm in diameter.

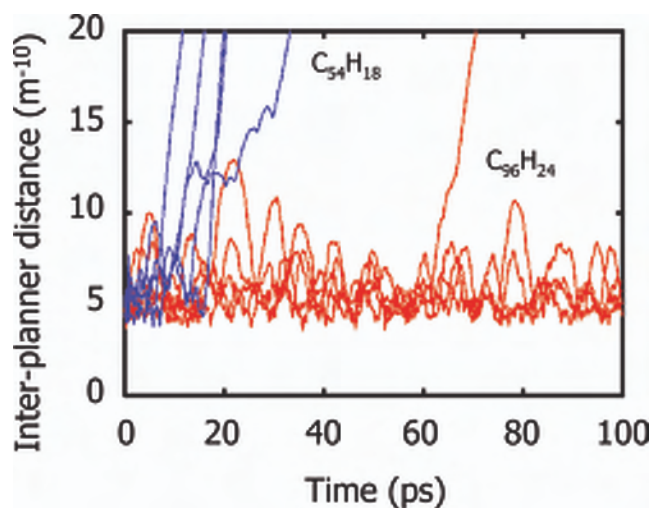


Figure 5. Molecular dynamics calculation results for stability of two PAH dimers under the combustion condition at 1,500K and 5.0MPa.

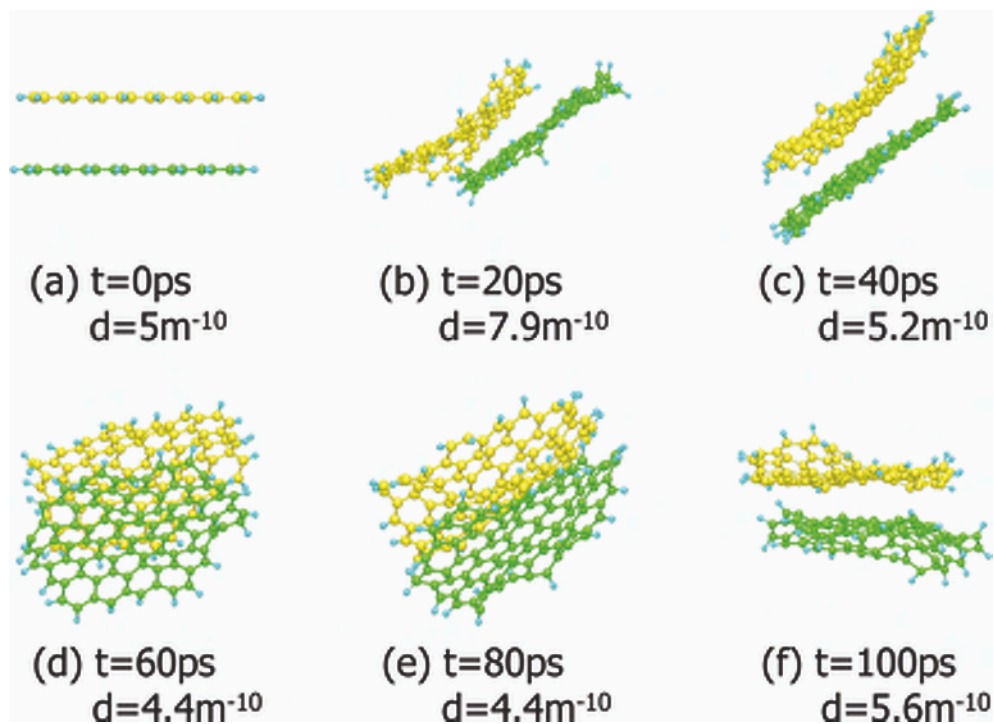


Figure 6. Snapshots from MD simulation of planar  $\text{C}_{96}\text{H}_{24}$  dimer structure.

- 2) The PAHs containing about 100 carbon atoms dimerize more stably than those react with  $C_2H_2$ . The dimer is stable even under the temperature near 1500K as it has the strong molecular interaction potential between the PAH molecules. The dimer will be the smallest unit in the incipient soot nanoparticles.

The experimental analysis of the incipient soot nanoparticles in the engine combustion process was conducted to verify the numerical analysis results.

The changes of number weighted particle size distribution measured using SMPS are shown in Figures 7a and 7b. Figures 7a and 7b show those before and after com-

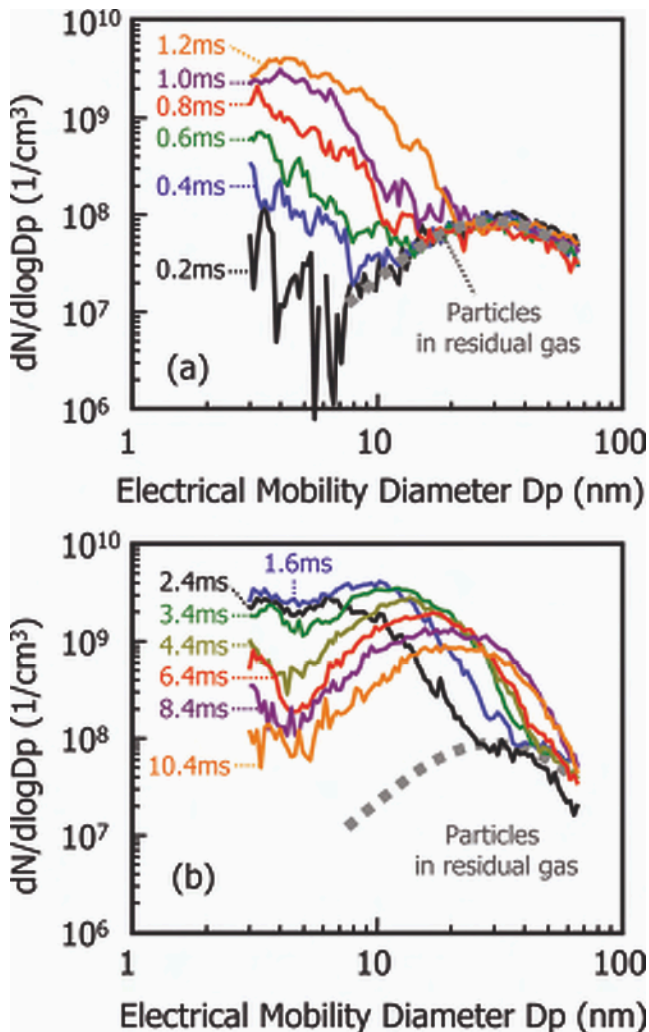


Figure 7. Changes of number weighted particle size distributions during engine combustion. (a) and (b) show those before and after combustion temperature reaches maximum value, respectively.

bustion temperature reaches maximum value, respectively. Because particle size distribution with the peak size of 30 nm was caused by remaining particles in residual gas of the previous engine cycle, the remaining particles were removed from an analytical object. (Dotted lines in Figure 7 show estimated profile of the remaining particle distribution in the residual gas of the previous engine cycle.)

In the earlier stage of the combustion, the particle size distributions appear to be monomodal above the smallest size measurable with the SMPS. The peak position of the size distribution moves from around 3 nm to 7 nm by the progress of the combustion. Number density of nanoparticles less than 3 nm in diameter starts to steeply increase over the temperature at 1,400 K. (The relationship between the sampling points and the in-cylinder gas temperature is shown in Figure 3.) Although the SMPS with 3 nm cutoff does not indicate the size distribution at smaller sizes, it is nevertheless indicative of strong particle inception at that stage. In contrast to the earlier stage, at 1.6 ms in the latter half of the engine combustion, the second mode appears and becomes distinct with the characteristic dip between the first and second modes and while the maximum number density of the first mode decreases, the peak position of the second mode shifts to larger one in the range of 2.4 ms to 10.5 ms. The results of the SMPS measurement mean that the first mode is formed by crystallites as a smallest unit constituting the soot nanoparticles and the second mode results from the coagulation of the crystallites. Our engine experimental results are in good agreement with the results of recent flame studies [13-15, 17, 20].

Figure 8 shows TOF-SIMS mass spectra of samples taken at sampling points of 0.6 ms, 1.0 ms and 1.2 ms in the formation process of the crystallites in comparison to that of a silicon wafer substrate as background data. The mass spectra were measured in the mass range  $m/z$  0-3,000. The ion counts of molecules beyond  $m/z$  1,000 increase with the progress in the formation process of the crystallites. It is thought that particles with diameters of a few nanometers composing the first mode as shown in Figure 7a are corresponding to the molecules beyond  $m/z$  1,000.

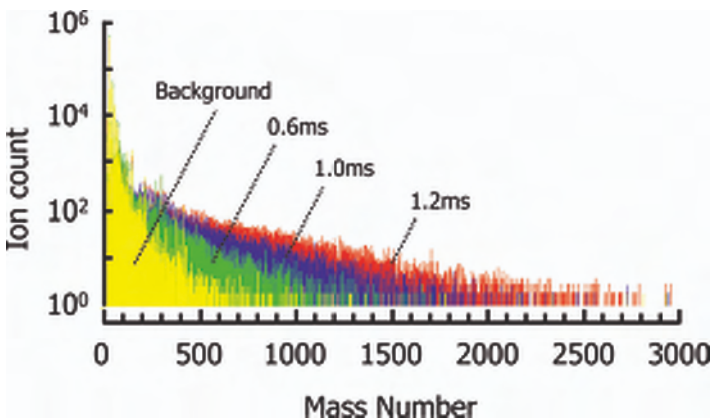


Figure 8. TOF-SIMS mass spectra of particles taken in the formation process of soot nanoparticles at sampling points of 0.6ms, 1.0ms and 1.2ms.

Particle thickness in the samples taken at sampling points of 0.6 ms, 1.0 ms and 1.2 ms was measured using the AFM to clarify the structure of the molecules beyond  $m/z$  1,000. Figure 9 shows AFM 3D images of particles in the formation process of the crystallites. The changes of the particle thickness calculated from the AFM 3D images are shown in Figure 10. Particle thickness distribution of the sample taken at the sampling point of 1.0 ms shows the peak position at 0.35 nm in thickness. This peak position shifts to around 0.7 nm at the sampling point of 1.2 ms. The difference of these two values is consistent with the interplanar distance of graphite structure, 0.35 nm.

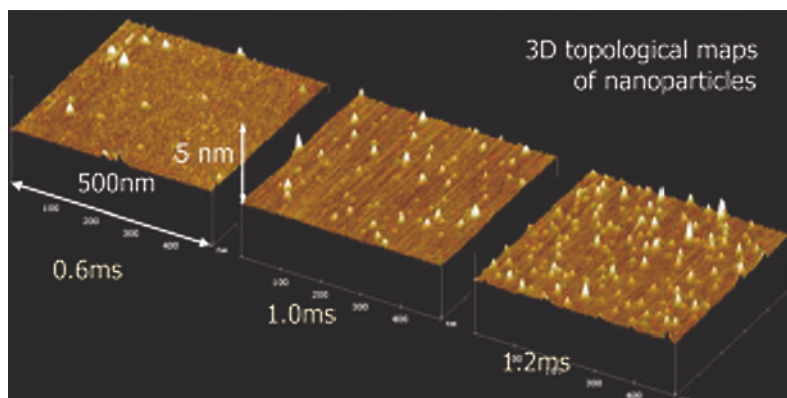


Figure 9. AFM 3D images of particles in the formation process of soot nanoparticles at sampling points of 0.6ms, 1.0ms and 1.2ms.

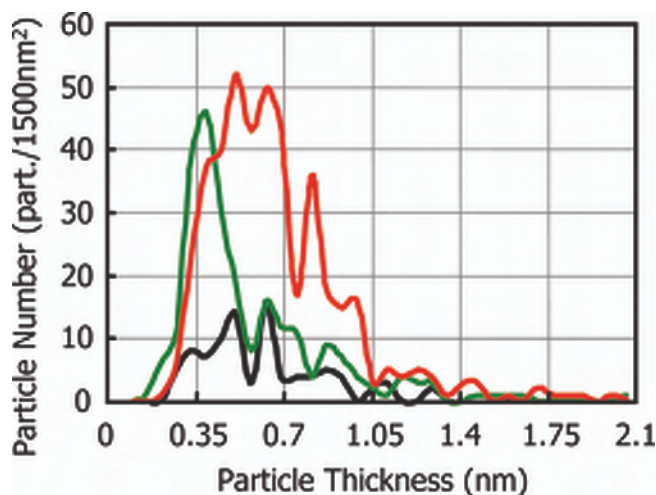


Figure 10. Changes of the particle thickness calculated from the AFM 3D images shown in Figure 9.

It can be concluded from the TOF-SIMS and AFM measurements that nearly planar-structured PAHs that grow up to around 100 carbon atoms dimerize in the formation process of the crystallites.

Precise examinations of particulate nanostructures were conducted at high TEM magnifications to reveal internal structures of the incipient soot nanoparticles. TEM images of the sample taken at the sampling period of 1.4 ms are shown in Figure 11. Soot nanoparticles do not have shell-core-like graphitic structures known well and consist of agglomerate of the dimers and trimers of the planar structured molecules with a few nanometers in diameter. Engine-out soot particles, however, have layered structures like cross-sectional structure of onion. This means that the particulate nanostructures change greatly in the engine combustion process. The TEM images appear to be consistent with the TOF-SIMS and AFM conclusion that the dimer and trimer of the planar structured giant PAHs play an important role in the incipient soot nanoparticles.

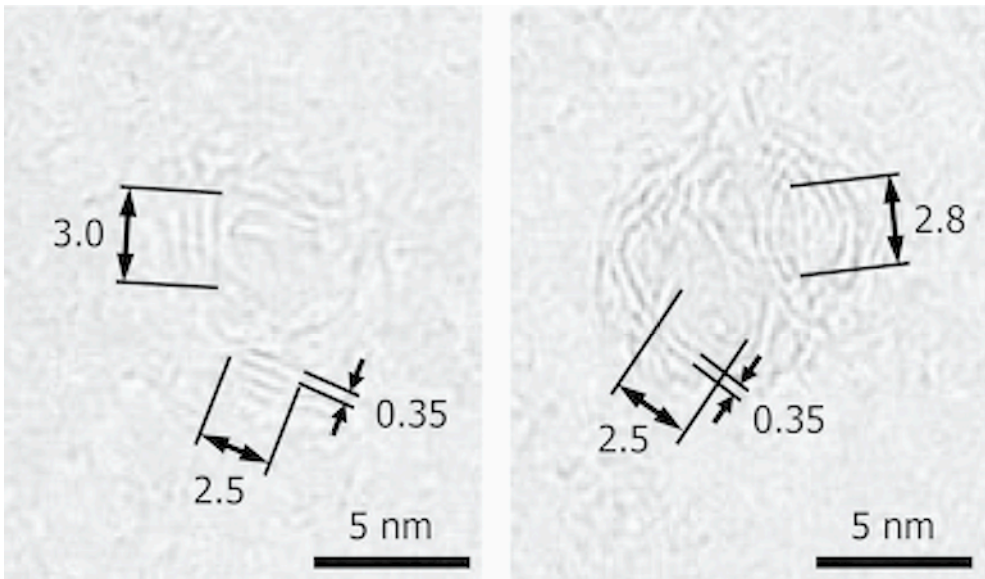


Figure 11. TEM images of the soot nanoparticles taken at the sampling period of 1.4ms.

#### 4. CONCLUSIONS

From the experimental and theoretical analysis, we get following clear conclusions for the formation mechanism of soot nanoparticles in the engine combustion;

1. PAH molecules grow up to near 100 carbon atoms under gas phase reactions.
2. The PAHs grow up to near 100 carbon atoms dimerize. The dimer is stable even under the temperature near 1500 K by the strong molecular interaction potential

between the PAH molecules. The dimer is the smallest unit to consist of soot nanoparticles.

3. The incipient soot nanoparticles consist of the agglomerate of the dimers and trimers of the planar structured PAHs with a few nanometers in diameter.
4. The dimer and trimer of the planar structured giant PAHs play an important role in the incipient soot nanoparticles in the engine combustion.

## REFERENCES

1. J. Appel, H. Bockhorn, M. Wulkow, *Chemosphere* 42 (2001) 635-645.
2. M. Frenklach, H. Wang, *Proc. Combust. Inst.* 23 (1991) 1559-1566.
3. C. A. Schuetz, M. Frenklach, *Proc. Combust. Inst.* 29 (2002) 2307-2314.
4. A. D'Alessio, A. D'Anna, G. Gambi, P. Minutolo, *J. Aerosol Sci.* 29 (1998) 397-409.
5. A. Violi, A. D'Anna, A. D'Alessio, A. F. Sarofim, *Chemosphere* 51(10) (2003) 1047-1054.
6. K. Siegmann, *J. Aerosol Sci.* 31 Suppl. (2000) S217-S218.
7. T. Ishiguro, Y. Takatori, K. Akihama, *Combust. Flame* 108 (1997) 231-234.
8. R. Dobbins, *Physical and Chemical Aspects of Combustion: A Tribute to Irwin Glassman, Gordon and Breach, Amsterdam, 1997*, p. 107.
9. G. Faeth, *Proc. of the 2002 Technical Meeting of the Central States Section of the Combustion Institute, 2002*, p. 2.
10. W. Merchan-Merchan, A. Saveliev, L. Kennedy, *Combust. Sci. Technol.* 175 (2003) 2217-2236.
11. A. L. Lafleur, K. Taghizadeh, J. B. Howard, J. F. Anacleto, M. A. Quilliam, *J. Am. Soc. Mass Spectrom.* 7 (1996) 276-286.
12. A. Keller, R. Kovacs, K.-H. Homann, *Phys. Chem. Chem. Phys.* 2 (2000) 1667-1675.
13. B. Zhao, Z. Yang, M. V. Johnston, H. Wang, A. S. Wexler, M. Balthasar, M. Kraft, *Combust. Flame* 133 (2003) 173-188.
14. M. M. Maricq, S. J. Harris, J. J. Szente, *Combust. Flame* 132 (2003) 328-342.
15. M. M. Maricq, *Combust. Flame* 137 (2004) 340-350.
16. A. Violi, *Combust. Flame* 139 (2004) 279-287.
17. B. Oktem, M. P. Tolocka, B. Zhao, H. Wang, M. V. Johnston, *Combust. Flame* 142 (2005) 364-373.
18. M. M. Maricq, *Combust. Flame* 114 (2006) 730-743.
19. B. Apicella, A. Carpentieri, M. Alfe, R. Barbella, A. Tregrossi, P. Pucci, A. Ciajolo, *Proc. Combust. Inst.* 31 (2007) 547-553.
20. L. A. Sgro, A. De Filippo, G. Lanzuolo, A. D'Alessio, *Proc. Combust. Inst.* 31 (2007) 631-638.
21. W. C. Herndon, P. C. Nowak, D. A. Connor, P. Lin, *J. Am. Chem. Soc.* 114 (1992) 41-47.
22. L. A. Girifalco, M. Hodak, R. S. Lee, *Phys. Rev. B* 62 (2000) 13104-13110.
23. A. H. Widmann, M. Laso, U. Suter, *J. Chem. Phys.* 102 (1995) 5761-5769.
24. D. W. Brenner, *Phys. Rev. B* 42 (1990) 9458-9471.
25. M. Inoue, A. Murase, M. Yamamoto, S. Kubo, *Appl. Surf. Sci.* 252 (2006) 7014-7017.
26. A.C. Barone, A. D'Alessio, A. D'Anna, *Combust. Flame*, 132 (2003) 181-187.

# Soot modelling in heavy-duty diesel engines

M. Balthasar, J. Eismark, I. Magnusson

*Department of Energy Conversion and Physics  
Volvo Technology Corporation, Göteborg, Sweden*

*Abstract: The development of Diesel engines has extensively been driven by emission legislation of particulate matter and NO<sub>x</sub> during the last decades. Much effort has thus been put into the development of predictive soot models and the modelling of other processes playing an important role during Diesel combustion by both academia and industry. The purpose of this paper is to demonstrate the use and quality of results obtained with detailed soot models in the development of heavy-duty Diesel engines at Volvo. The capability of a detailed soot model combined with the RIF combustion model has been evaluated for a large set of diesel engine experimental data and for a constant volume diesel combustion case.*

*Results for the constant volume diesel combustion case indicate that an accurate description of the soot formation rate can be obtained by the model used but only under conditions for which the flame lift-off is modelled. A lifted flame is obtained with a sufficiently large number of RIFs needed to keep at least one of the RIFs un-ignited during the entire fuel injection period. Calculated soot concentrations agree satisfactorily with measured local concentrations for a wide range of operating conditions.*

*In engine calculations, it is not always possible to model the lifted flame. However, for cases where mixing and oxidation is the dominant effect on engine out soot, the soot model is capable to predict the relative influence by different measures well, although the absolute amount of soot is mostly under-predicted. The model performs particularly well for engine cases with EGR. For very high EGR levels, leading to partially pre-mixed combustion, the model can also explain the early soot formation process in the engine case.*

*The RIF combustion combined with a detailed soot model performs sufficiently well for many engine applications, even better than expected given the assumptions that have to be made when formally deriving the underlying flamelet concept. Nevertheless, a model with full predictive capability would need major improvements.*

## 1. INTRODUCTION

Particulate emission resulting from soot formation is a remaining problem for modern diesel engines. Turbo charging together with sophisticated fuel injection equipment, allowing high injection pressures and different means for rate shaping, provide the possibility to operate diesel engines with virtually zero soot in the exhaust. Measures to decrease NO<sub>x</sub> emissions as EGR, however, typically increase soot emissions. The introduction of particulate filters provides new opportunities to combine low NO<sub>x</sub> emissions with very low particulate emissions but to the expense of fuel efficiency, particularly if frequent regeneration of the filter is required. Low engine

out soot emissions are therefore a necessity to keep the fuel efficiency advantage of the diesel engine.

Modelling of soot formation in diesel engines is still a challenging task although many results showing good agreement with measurements have been reported. Predictive modelling of soot formation requires a number of accurate sub-models including the spray model, the turbulence model, the combustion chemistry, the turbulence-chemistry interaction model and evidently the soot model itself. Models of different complexity have been used to model soot formation in laminar and turbulent flames [1]. Models for diesel engines calculations are, however, restricted in complexity due to restrictions in CPU time. Two types of combustion-turbulence interaction models are often used in engine simulations: the first type is based on characteristic time scales [2] while the second is based on the flamelet approach [3]. The chemistry within these models varies from simple mechanisms to detailed reaction schemes. Soot models typically used range from semi-empirical [4] to detailed models [5].

At some companies, including Volvo, combustion calculations of diesel engines have become accepted tools for combustion system optimisation. The available models have predictive capability for heat release and NO<sub>x</sub> emissions generating absolute numbers in good agreement with engine measurements over a large range of conditions. Perhaps most importantly, however, the available soot model is sufficiently accurate to predict major trends for engine out soot emissions. In fact, the accuracy of the model is surprisingly high taking into account well known limitations in both soot and combustions models. For the model validation a large set of in-house experimental data has been available in form of engine out emissions. In many cases the results originate from ongoing development projects. For that reason, a detailed explanation of the engine set-up and running conditions had to be omitted. The main intention of the work presented here is to give an impression of the capability of present models in industrial engine applications. However also weak links will be identified and some important issues concerning the further development of models are discussed. Besides the engine simulations some complementary results, including a more systematic variation of important parameters affecting soot formation, were obtained from calculations for constant volume diesel combustion cases from the literature.

## 2. MODEL DESCRIPTION

### 2.1. Basic soot model

The soot model that is used in the present study is based on the work by Frenklach, Wang and Mauss (FWM) [5, 6, 7, 8]. A detailed chemical scheme for n-decane/ $\alpha$ -methylnaphthalene is employed including a pathway to the formation of PAHs. Nucleation is described by the collisions of two PAHs, surface growth by the well-known HACA mechanism [5]. Condensation is modelled as collisions of PAHs and soot particles and the oxidation by both O<sub>2</sub> and OH is included in the model. The soot equations are formulated based on the method of moment approach [7].

## 2.2. The RIF model

A variant of the FWM soot model has been implemented into the Representative Interactive Flamelet (RIF) combustion model [3, 8, 9, 10, 11] (this implementation will be referred to as RIF soot in the following) in which also the fuel oxidation chemistry is solved in so-called representative interactive flamelets as a function of mixture fraction and the scalar dissipation rate. The model incorporates detailed chemistry and an elaborated treatment of the interaction with the turbulent flow field including a direct influence on chemistry through the scalar dissipation rate. The model also includes a statistical treatment of turbulent fluctuations with small-scale specie-specie-temperature correlations that are needed for a proper treatment of the involved non-linear chemical reaction processes. The pressure and boundary conditions for the air side (mixture fraction  $Z=0$ ) are taken from the CFD simulation at each time step. The model is solved interactively with the CFD simulations. The basic assumption of the flamelet model is that for locations in the flame having the same mixture fraction and the same scalar dissipation rate the mean species concentrations, enthalpy and soot mass are equal. This means that only transport equations of the mean and variance of mixture have to be solved instead of all species mass fractions. This assumption has in fact been shown to be rather accurate for species concentration. If this assumption also applies for soot is, however, more uncertain. If the single RIF model is used only one scalar dissipation rate is used for the whole spatial domain. The spatial resolution of the scalar dissipation rate is increased using the multi-RIF model, typically with eight RIFs.

In the CFD code additional equations for the mean and variance of mixture fraction are solved determining the pdf of mixture fraction for which a beta-function is used. The mean number density and soot mass is then obtained at every grid point by integrating  $M_0$  and  $M_1$  with the pdf:

$$\tilde{M}_i = \int_0^{Z_{max}} pdf(Z) M_i(Z) dZ$$

The advantages of the RIF soot model are thus that the soot equations are solved in an instationary manner. However, the underlying assumption that soot is directly coupled to mixture fraction is questionable.

## 2.3. Other models

A basic requisite in order to evaluate soot models is that spray and fuel/air mixing is modelled accurately. The spray model used in this work is a well-tested in-house model of the traditional Lagrangian type but with modified stripping break-up and evaporation mechanisms. The spray model has earlier been validated [12] using experimental data from the high pressure vessel at Sandia [13, 14] and for the purpose of the present investigation the spray, evaporation and mixing processes are assumed to be modelled with sufficient precision. The flow field was solved using the CFD code STAR-CD in which the spray and the RIF models were implemented. Turbulence was modelled using the k- $\epsilon$  model.

### 3. ENGINE CASES

The engine cases used for the model assessment were in most cases taken from ongoing development projects. The advantage using such cases is that the models are tested for conditions that are most relevant for the development engineers. The disadvantage is that the data does not always include the full range of conditions for which the models should be valid. The experimental data was generated in a one-cylinder research engine that allows good control of boundary conditions and high flexibility.

#### 3.1. Piston geometry

Modern diesel combustion systems make use of heavy EGR. Increased EGR decreases flame temperature and thus NO<sub>x</sub>. However for conventional diffusion controlled combustion an increase in EGR will increase soot mainly since the air/fuel ratio,  $\lambda$ , is decreased. It is thus of particular importance to optimize the combustion system in order to minimize the amount of engine-out soot.

An important parameter when optimizing the combustion system is the geometry of the piston bowl. We will therefore start by showing results from a study where a larger number of piston geometries were evaluated by means of simulations for a case where the engine was operated with EGR. Results obtained by using the RIF soot and combustion model for 10 of the tested piston geometries are compared with results from engine-tests in Figure 1. Values are normalized with the measured engine-out result to the left in the figure, i.e. with the piston 1. The RIF soot model is capable of predicting trends reasonably well although the relative increase in soot for pistons 4, 7 and 10 is under-predicted. However, already this kind of accuracy is valuable in the

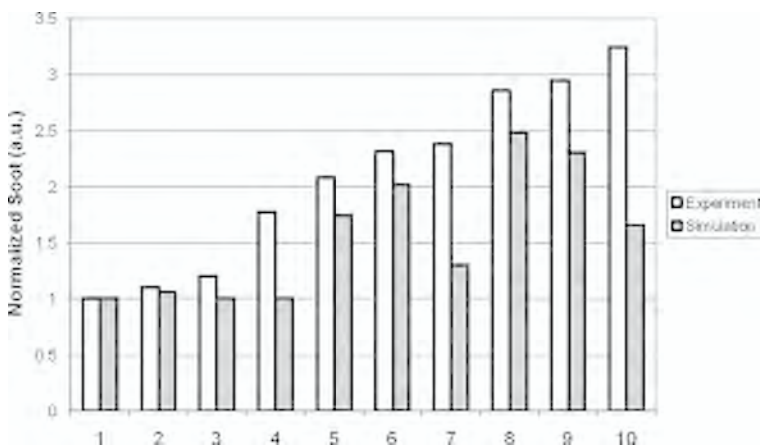


Figure 1. Comparison of simulated and measured engine-out soot for different piston geometries. Simulated and measured values are normalized with their respective values for piston geometry 1.

pre-selection of piston bowl geometries in an early stage of development prior to engine testing. The results shown in Figure 1 reflect the experience obtained from numerous engine simulations within internal development projects.

Figure 2 shows a similar comparison as Figure 1 but for an engine operated without EGR at full load and medium speed conditions. A comparison of measured and calculated soot emissions for different piston bowl geometries is shown. Again, the RIF model is able to predict trends and rank the pistons in the right order. The relative changes in soot emissions are in fair agreement with measurements. Similar agreement was observed with the engine operated at other loads and speeds.

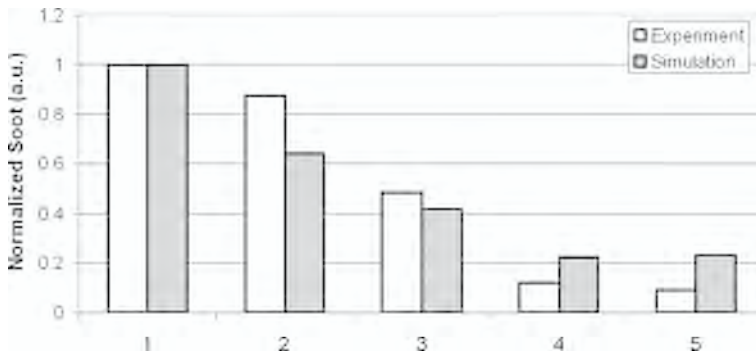


Figure 2. Soot emissions for five different piston geometries and for engine operated at full load and medium speed with no EGR, measurements (1-cylinder) and calculations using the RIF model. Results were normalised with measurements for piston 1.

### 3.2. Timing and number of nozzle holes

In another study the effect of timing and the number of nozzle holes was investigated for six different cases. The same piston geometry was used for all cases and the operating point corresponds to full load and high speed. Three different nozzles were used, a 5-, 6- and a 7-hole nozzle. Two different timings were chosen for each nozzle. The engine-out soot was very similar for all three nozzles at a timing of 3° BTDC. Changing the timing to 1° ATDC soot increased slightly for the 6-hole nozzle while it increased by a factor of 2.5 for the 7-hole nozzle as illustrated in Figure 3. For the 5-hole nozzle the later timing resulted in a decrease of soot by a factor of 2. From the left panel of Figure 3 we can see that the RIF soot model predicts these trends very well.

The rich mixture fraction is a quantity defined as the local mixture fraction subtracted by the stoichiometric mixture fraction and is useful in describing the degree of fuel air mixing. For the same engine cases, the right panel of Figure 3 shows the normalised total rich mixture fraction. It can be observed that the rich mixture fraction correlates well with the soot emissions shown in the left panel and could in fact be used to rank the different cases. For the early timing there is a clear difference in the values of the rich mixture fraction, it is much larger for the 5-hole nozzle and lower for the

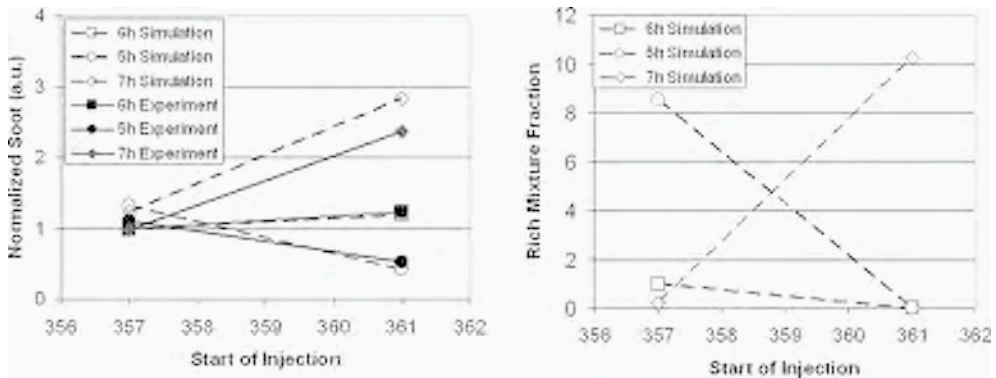


Figure 3. Left panel: Normalized values for engine-out soot compared to experimental data (full symbols) for different start of injections and number of nozzle holes. Right panel: Normalized values for the total mixture compared to the same measured soot results.

7-hole nozzle. The RIF soot model predicts the engine-out soot to be more or less similar for the three cases, which is in better agreement with measurements. Going to the later timing, the trends observed experimentally are clearly visible in the rich mixture fraction. A decrease in the rich mixture fraction is observed for the 5-hole nozzle while a dramatic increase is seen for the 7-hole nozzle (note that the value in Figure 3 is divided by 10). It is clear that part of the changes in soot emissions observed experimentally are due to the degree of mixing, however, the rich mixture fraction can not be used alone as a measure of the relative variations.

In the figures above only normalized values of calculated engine-out soot are shown. While the correct prediction of trends in engine-out soot is more important, a quantitative prediction of the engine-out soot values would be desirable. The ratio of the engine-out soot values from the RIF model and the experimental values is therefore shown in Figure 4. The calculated results are for these cases around a factor of 10 lower than measurements. Part of the difference is due to the fact that pure n-decane was used as a model fuel rather than the IDEA fuel (consisting of a mixture of 70% n-decane and 30% of  $\alpha$ -methyl-naphthalene). From measurements we also know that this will reduce the amount of soot by typically a factor of two. When accounting for this factor of two the predicted engine-out soot values are five times lower than the measured ones. Since the ratio is however rather constant an adjustment of the model to predict the correct absolute numbers would be possible.

### 3.3. Post injection

Post injection is a possible means to lower the soot emissions from diesel engines. The probable explanation for the decrease of soot is the improved mixing during the expansion stroke caused by the post injection. As in all cases, a prerequisite for accurate soot modelling is an accurate mixing model. The heat release can be considered as

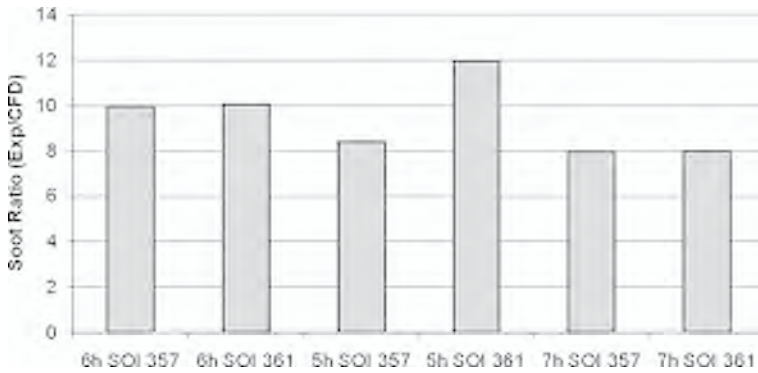


Figure 4. Comparison of absolute engine-out soot values between CFD simulations and engine tests. The simulated engine-out soot follows the right trends but is lower than the experimental values.

a global measure of the mixing and Figure 5 shows the rate of heat release for an example of a case with post injection. The agreement between the calculated and measured rate is a good indication that the mixing model provides satisfactory conditions as an input to the subsequent soot model.

Figure 6 provides results in form of soot for the same engine operated with three different strategies for post. The baseline corresponds to a case with just a single injection while a main and a post injection is used for the two remaining cases. The two cases

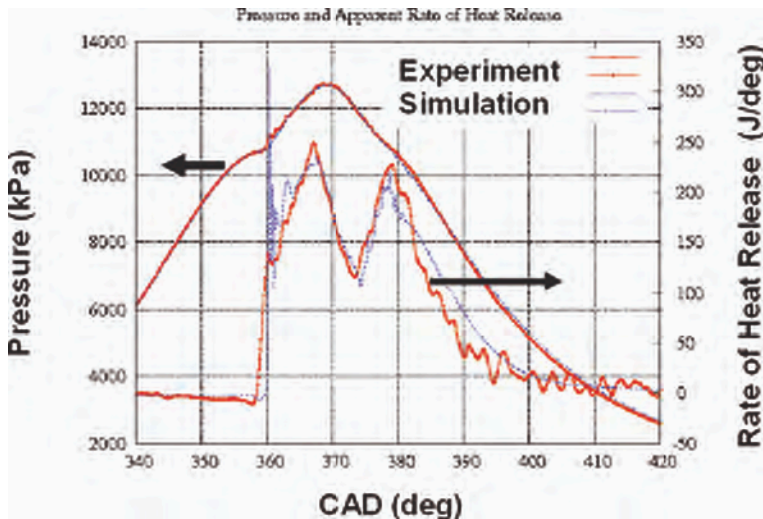


Figure 5. Rate of heat release (right axis) and pressure (left axis) for a HD engine case with post injection. Red and blue dotted lines correspond to measurements and calculations respectively.

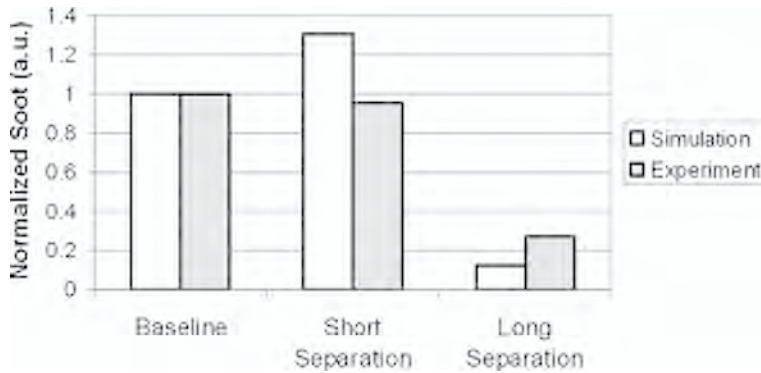


Figure 6. Calculated and measured engine out emissions of soot for three cases with post injection.

with a post injection differ in the temporal separation between main and post. It can be seen that under the present conditions a long separation results in a considerable decrease in engine-out soot. As for the cases above the RIF soot model is capable of predicting the right trends in terms of normalized engine-out soot. The model can thus be used to optimize injection strategies besides the geometry optimization shown above.

### 3.4. EGR variation

Engine tests were performed with EGR levels ranging from 0 to 47% for 25% load cases. A typical soot/NOx trade-off curve is shown in the right panel of Figure 7. As the amount of EGR is increased, NOx is decreasing while soot is increasing. At a certain level of EGR the trend in soot is reversed and NOx and soot are decreasing with increasing EGR. Three cases were selected: a) a case to the right of the soot maximum, i.e. low EGR, b) on the soot maximum and c) to the left of the soot maximum, i.e. high EGR. The case with the highest EGR can be characterised by partially premixed conditions with long ignition delay and ignition after end of injection. CFD simula-

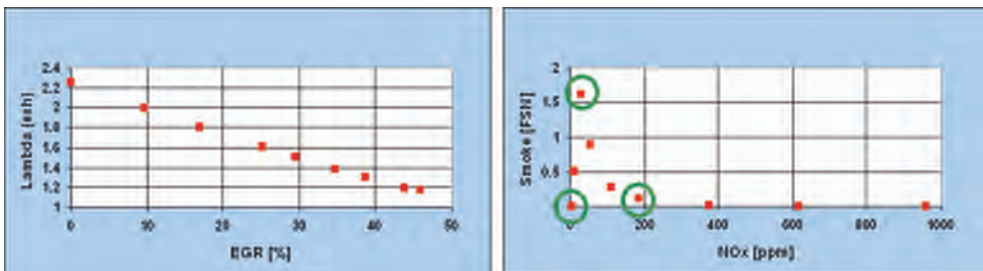


Figure 7. Engine data available for the EGR swing at 25% load. The green circles indicate the cases selected for CFD analysis.

tions for these three cases were performed to investigate if the models were capable of predicting these trends.

Figure 8 displays the resulting soot emissions as a function of NOx. From the figure, it is evident that the changes in NOx are predicted very well by the RIF model. Soot is predicted with the correct trends but the sensitivity to variations is too low.

Since trends are predicted correctly, the results can be used to investigate the causes for the trends in soot. For this purpose, the temporal evolution of the total in-cylinder soot mass as predicted by the RIF soot model is shown in Figure 9. It can

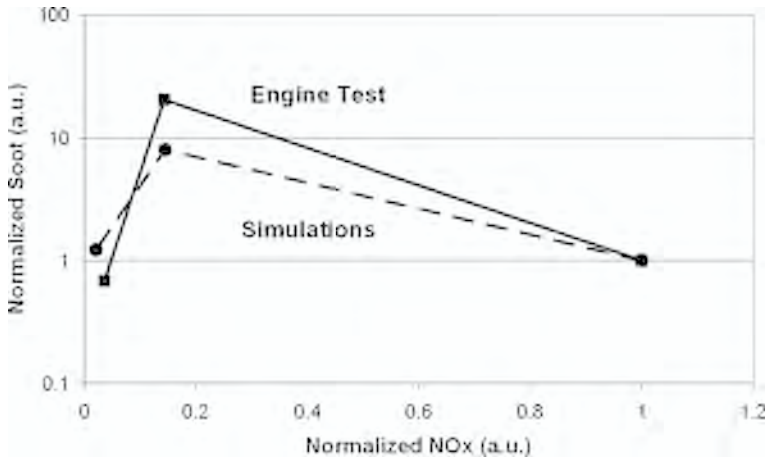


Figure 8. Soot emission as a function of NOx for three different EGR levels.

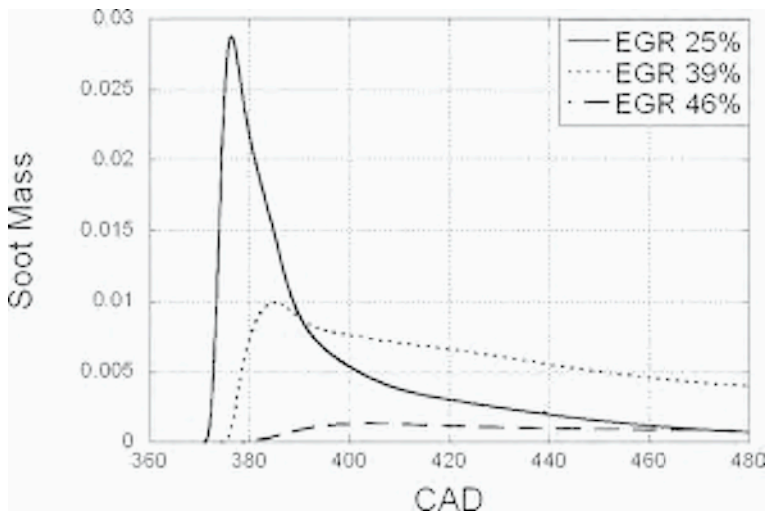


Figure 9. Temporal evolution of the soot mass in the cylinder as predicted by the RIF soot model.

be seen that both soot formation and oxidation are decreased when increasing EGR from 25 to 39%. Although the soot maximum is lower for the 39% the engine-out soot is higher than for the 25% EGR case due to a decrease in oxidation. The decreased oxidation rate thus dominates. Increasing the EGR level to 46% leads to a further decrease of both the formation and oxidation rate. Here the decrease in the formation rate is dominating, however, leading to a reduction in the engine-out soot value.

#### 4. CONSTANT VOLUME CASE

In this study, the RIF model was evaluated against results from detailed soot measurements in diesel sprays in a constant volume. A possible problem with the RIF model is that the spatial resolution for the chemistry calculation is limited using a single flamelet approach. The aim of the work was to investigate if this problem might be circumvented using a multiple RIF approach.

##### 4.1. Operating conditions

The investigated operating conditions correspond to experimental data for diesel like constant volume conditions generated by researchers at Sandia National Laboratories [15, 16, 17]. The operating conditions are summarised in Table 1.

The numerical model was set up to match the experimental conditions as close as possible and a reference condition was selected defined by nozzle diameter 100  $\mu\text{m}$ , orifice pressure drop 138 MPa, ambient gas temperature 1000 K, ambient density 14.8  $\text{kg}/\text{m}^3$  (pressure 42 bar) and oxygen concentration 21%. The measured nozzle coefficients  $C_d$  and  $C_a$  were both necessary inputs to the spray model that also used liquid and evaporation properties given by a reference diesel fuel with similar properties as the fuel used in the measurement. The chemical properties of the fuel was modelled by the IDEA fuel matching the relative concentrations of the two components. Specific modelling assumptions are summarised in Table 2.

##### 4.2. Calculation of KL

In the experiments, an absorption technique was used to measure the optical thickness, KL, a number that represents the soot concentration averaged across the spray. In order to make a direct absolute comparison the calculated results were post processed to obtain a corresponding optical thickness. Obtaining soot concentrations from KL values requires several assumptions as described in detail by Pickett and Siebers [16]. Using similar assumptions the KL values can be calculated from the CFD results as:

$$KL = 2 \cdot 7.74 \cdot 10^8 \sum_{i=1, \dots, N} F_{\nu}(i) \Delta r(i) \quad (1)$$

Table 1. Experimental operating conditions [16].

Ambient temperature	850-1300 K
Ambient density	7.3-30.0 kg/m <sup>3</sup>
Oxygen concentration	21 and 15%
Orifice pressure drop	43-184 MPa
Injection system	Common-rail
Injection rate profile	Top-hat
Fuel type	Phillips #2 diesel
Fuel cetane number	46
Fuel composition by volume	33.8, 65, 1.2% (aromatics, paraffins, olefins)
Fuel temperature	436 K
Fuel density	712 kg/m <sup>3</sup>
Orifice diameter	45-180 $\mu\text{m}$
Discharge coefficient, $C_d$	0.8
Area contraction coefficient, $C_a$ , as a function of orifice pressure drop $\Delta P$ [MPa]	44: 0.91 89: 0.89 138, 184: 0.86

Table 2. Model specifications.

Combustion model	mRIF (single, 8, 16 and 40)
Fuel in RIF	IDEA (n-decane/ $\alpha$ -methyl-naphthalene)
Fuel composition by volume	34%, 66% (aromatics, paraffins)
Injection duration	4.5 ms
Mesh	2-D axisymmetric
Number of cells	4000
Typical cell size close to injector	0.4 mm
Time step	1.0 $\mu\text{s}$

where  $F_p(i)$  is the soot volume fraction in a cell  $i$ ,  $\Delta r(i)$  is the length of the cell and where the sum is made, at a certain down stream position, over cells in the radial direction. The factor of 2 is needed to obtain the value corresponding to a 3D spray.

### 4.3. Time dependence of the soot concentration

The temporal evolution of the soot concentration at a position 50 mm downstream of the injector for the reference condition with nozzle diameter 100  $\mu\text{m}$ , injection pressure 138 MPa, with temperature 1000 K, ambient density 14.8 kg/m<sup>3</sup> and oxygen concentration 21% is displayed in Figure 10. Measurements were carried out with injection duration of 4.5 ms and it was found that the distribution of the soot concentration reaches quasi-steady state after approximately 1.5 ms. In the calculations a quasi steady-state is reached at a slightly later time of approximately 2 ms.

Simulated results using a single RIF and a 16 RIF model are displayed in Figure 10. Comparing the absolute numbers it can be concluded that, for the particular operating condition and downstream location, the single RIF model gives an absolute soot concentration close to the measured one whereas the 16 mRIF model under predicts the absolute value by a factor of approximately 6.

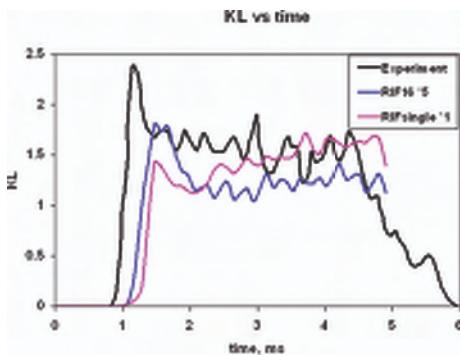


Figure 10. Calculated absorption coefficient,  $K_L$ , 50 mm downstream of the injector as a function of time using the single RIF and the 16 RIF model together with experimental data [16]. The result from the 16 RIF calculation is multiplied with a factor of 5.

### 4.4. Spatial soot distribution

Images of calculated relative soot mass concentration for the reference operating condition at 4.0 ms after start of injection for different numbers of RIFs are shown on the left side of Figure 11 together with a corresponding experimental image of the soot distribution [17]. It is evident that the calculated results depend on the number of RIFs used. Calculated temperature distributions displayed on the right side of Figure 11 show that the temperature is very similar using a single and an 8 RIF model with high temperatures reaching regions close to the nozzle. Increasing the number of RIFs to 16 and 40 a lifted flame is predicted whereas the maximum temperatures further downstream are similar to those using a lower number of RIFs. The effect of the number of RIFs on the lift-off behaviour can be explained by investigating the

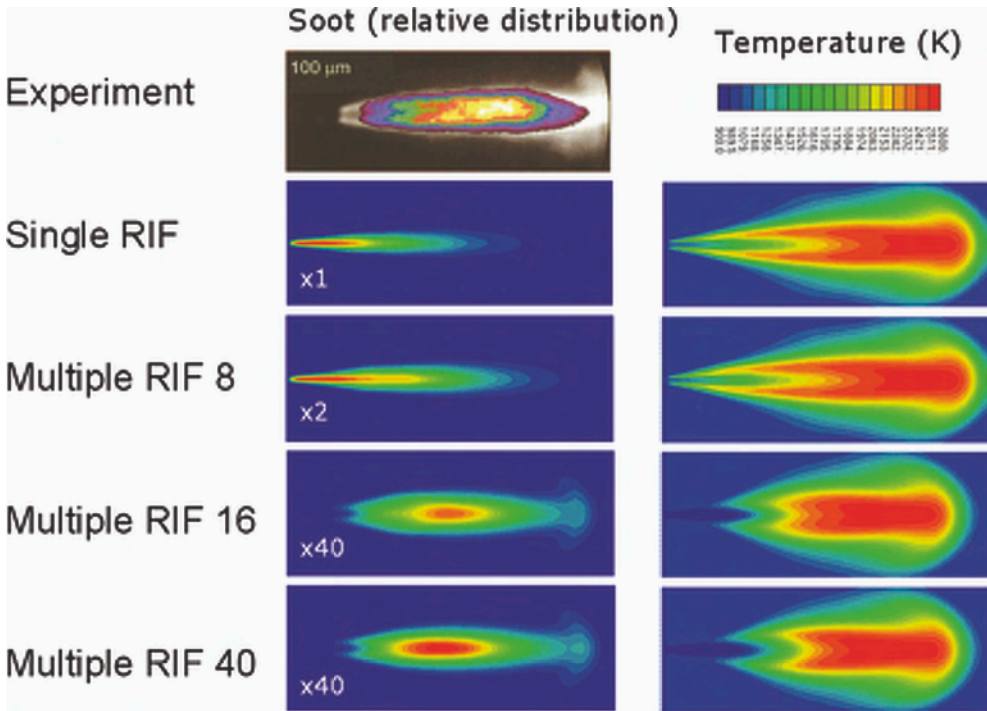


Figure 11. Figure illustrating soot and temperature distributions for the reference case. The top left image shows the result from a qualitative measurement of the soot distribution in colour scale [17], the same image also shows the measured OH distribution in gray scale. Calculated soot mass concentrations using different number of RIFs are presented on the left side of the figure using a relative colour scale. Corresponding calculated temperature distributions are displayed on the right side using an absolute temperature scale from 900 to 2600 K. Calculated images represent snapshots at 4.0 ms after start of injection whereas the experimental image is averaged over 3.0 ms.

state of the individual RIFs. Using a sufficient number of RIFs one or several of the “youngest” RIFs close to the nozzle remain un-ignited and a lifted flame is predicted with a lift-off length similar to that observed experimentally. With flame lift-off also the calculated relative soot distributions show better qualitative agreement with measurements.

A quantitative comparison of soot concentrations in terms of KL values for different position downstream the nozzle is illustrated in Figure 12. The high concentration of soot close the nozzle obtained with the single and the 8 RIF model is not observed in the experiment. However, at axial positions of 50 mm and further downstream, the agreement with measured KL values is reasonable also in absolute terms (it should be observed the scale for the calculated KL values is divided by 2). KL values calculated with 16 and 40 RIFs are similar to each other and show a better agreement with measurements in relative terms but absolute values are lower by a factor of approximately

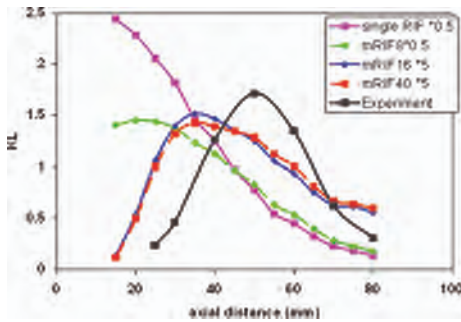


Figure 12. Calculated and measured [15] KL values at different axial positions for the reference operating condition.

5. A major difference compared to measurements is that, for the present operating condition, the calculated curves are shifted upstream towards the injector by approximately 15 mm. A similar shift is observed also for other operating conditions as will be illustrated later.

The spatial distributions of the soot mass concentration obtained with the 16 RIF model for three different nozzle orifice diameters and for the same ambient condi-

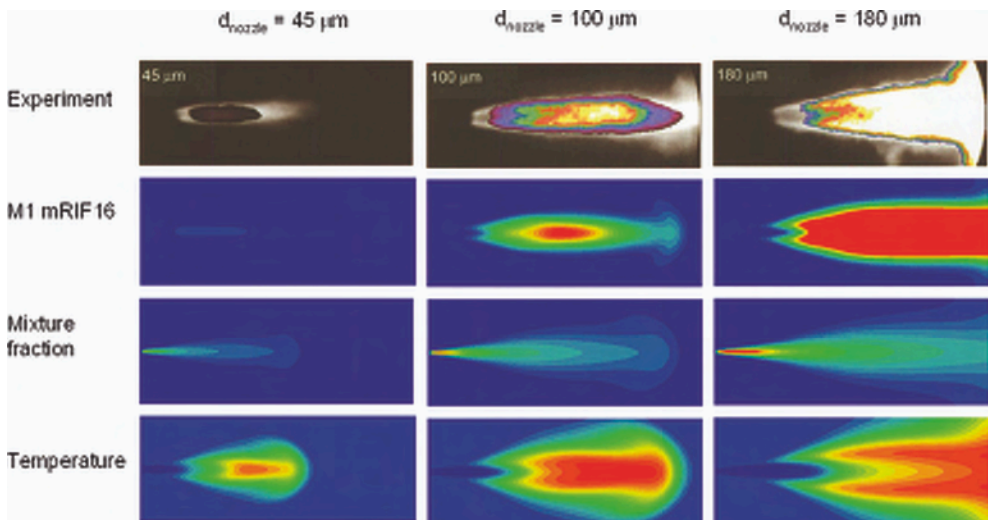


Figure 13. The top row shows images of measured soot distribution [15]: for the reference condition in the centre, for the same ambient conditions but using a nozzle orifice diameter of 45  $\mu\text{m}$  to the left and using an orifice diameter of 180  $\mu\text{m}$  to the right. The second row shows calculated soot mass concentrations. The third and fourth rows illustrate calculated mixture fractions and temperatures respectively. The colour scales are for all images normalised to give the full range of values for the 100  $\mu\text{m}$  orifice diameter case displayed in the centre.

tions as for the reference case are illustrated in the second row of Figure 13. The colour scale is set to display the full range of values for the middle column, the reference case, and the same scale is kept for the left and right column. The qualitative agreement with measured soot images displayed in the top row is good. Increased orifice diameter extends the regions with high soot concentrations and leads to higher maximum concentrations. The corresponding calculated mixture fractions, in the third row of Figure 13, illustrate that the extension of regions with high soot concentration is due to a larger extension of the region with high fuel concentrations. High soot concentrations are found only in regions with rich mixture fraction. The calculated temperature, in the fourth row of Figure 13, illustrates lifted flames with lift-off lengths that increase with increasing orifice diameter and that follow the lift-off lengths illustrated by the images of OH included in a gray scale in the experimental images.

#### 4.5. Quantitative soot concentrations

The experimental data includes results from quantitative measurements of soot concentrations for a wide range of different parameter combinations. Measurements were performed at different positions along the spray axis and results are available either in form of absorption coefficients,  $KL$ , or as soot volume fractions,  $F_v$ , averaged across the spray. Calculations were performed with the same parameter combinations as in the measurements and results were post processed to provide either  $KL$  values or averaged soot volume fractions. The experimental data were typically obtained by time averaging over 3 ms [16]. Since also the calculations displayed some fluctuations, see Figure 10, the results were time average, typically between 3.0-4.5 ms.

##### 4.5.1. Variation of nozzle orifice diameter and oxygen concentration

Calculations using 16 RIFs were carried out for reference ambient conditions for three different orifice diameters. The right side of Figure 14 shows results in terms of  $KL$  values for different positions in the spray. Although some differences can be observed a comparison with the experimental data, left side of the figure, shows that calculated results follow the experimental trends well. An increase in orifice diameter leads to higher soot concentrations and a shift of the maximum concentration further downstream. However, absolute values from the calculations are lower by approximately a factor of five (note that the calculated results in Figure 14 are multiplied by 4). It can also be observed that the calculated curves are slightly shifted in the upstream direction. Experimental data were limited to values of  $KL$  below 4.

Results for the same conditions as in Figure 14 but with the oxygen concentration decreased to 15% are presented in Figure 15. The experimental results indicate that a decrease of the oxygen concentration from 21 to 15% leads to a shift of regions with high soot in the downstream direction whereas the shape of the curves and the maximum concentrations of soot are only marginally affected. The calculated results show the same trends.

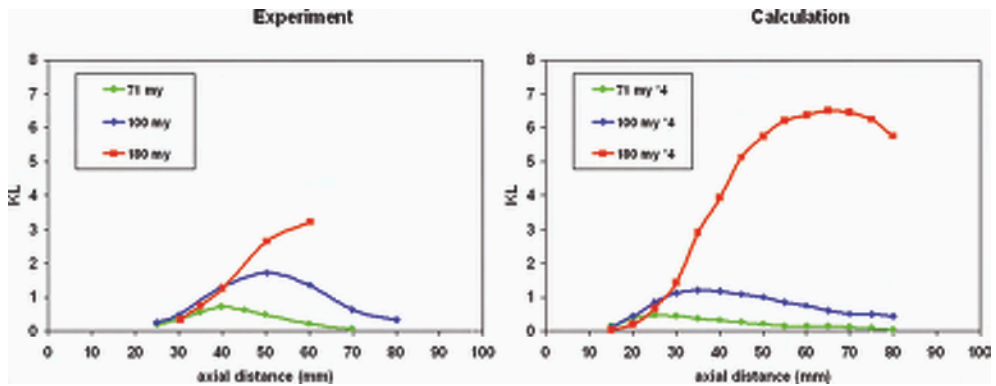


Figure 14. Optical thickness,  $KL$ , as a function of axial distance from the nozzle for three different orifice diameters and for reference ambient conditions, experimental results to the left [15] and calculated results to the right.

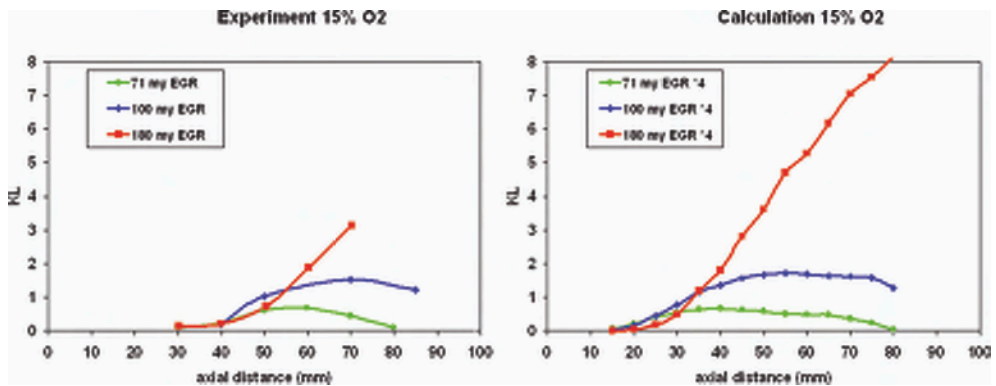


Figure 15. Optical thickness,  $KL$ , as a function of axial distance from the nozzle for the same conditions as in Figure 14 but with an oxygen concentration of 15%, experimental results to the left [15] and calculated results to the right.

#### 4.5.2. Variation of ambient gas temperature

The effect of the ambient gas temperature on soot concentrations was investigated using a nozzle orifice diameter of  $100\ \mu\text{m}$ , orifice pressure drop  $138\ \text{MPa}$ , ambient density  $14.8\ \text{kg/m}^3$  and oxygen concentration 21%. For these conditions a model with 40 RIFs was used since 16 RIFs were not enough to obtain a lifted flame (to keep an un-ignited RIF) for the 1100 K condition. For the higher temperature conditions, 1200 and 1300 K, not even 40 RIFs were enough to get lift-off and unrealistic results were obtained as indicated on the right side of Figure 16. It was not possible to further increase the number of RIFs due to limitations set by the CFD code for the

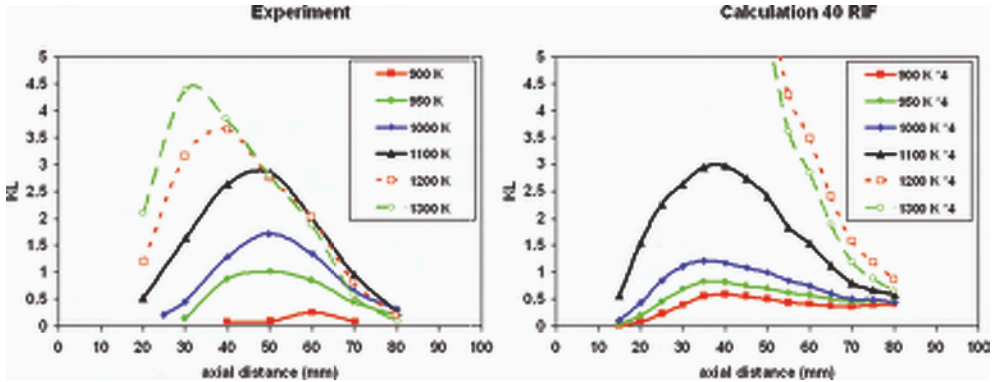


Figure 16. Optical thickness,  $KL$ , as a function of axial distance from the nozzle for different temperatures with a nozzle orifice diameter of  $100\ \mu\text{m}$ , orifice pressure drop  $138\ \text{MPa}$ , ambient density  $14.8\ \text{kg/m}^3$  and oxygen concentration  $21\%$ , experimental results to the left [15] and calculated results to the right.

maximum number of scalars. For the conditions with lower temperatures, however, the agreement with measurements is satisfactory. The trend of increasing soot concentrations with increasing temperatures is captured although the relative increases are not fully in accordance with those observed in the experiment. Especially for the condition with the lowest temperature of  $800\ \text{K}$  the relative concentrations are too large and the extension of the soot region too long. For the cases with temperatures below  $1100\ \text{K}$  the calculated results using 16 RIFs were almost identical to those using 40 RIFs.

#### 4.5.3. Variation of orifice pressure drop

The orifice pressure drop was varied using a nozzle orifice diameter of  $100\ \mu\text{m}$ , ambient temperature  $1000\ \text{K}$ , ambient density  $14.8\ \text{kg/m}^3$  and oxygen concentration  $21\%$ . Calculations for these cases were performed using 16 RIFs and results displayed on the right side of Figure 17 again show good correlation with measurements. However, the case with the lowest orifice pressure drop of  $48\ \text{MPa}$  gives a too high relative increase in soot concentrations. Another difference is that the distance between the nozzle and the locations where soot appears is fairly constant in the calculations. Experimental results indicate that the position of soot appearance is shifted downstream as the orifice pressure drop increases.

#### 4.5.4. Variation of ambient density

In a final investigation the ambient density was varied using a nozzle orifice diameter of  $100\ \mu\text{m}$ , orifice pressure drop  $138\ \text{MPa}$ , ambient temperature  $1000\ \text{K}$  and oxygen

concentration 21%. Calculations were made using 40 RIFs to obtain a lifted flame for the case with the highest density of 30 kg/m<sup>3</sup> and results are given in Figure 18.

The trend observed in the experiment, that increased densities lead to increased soot concentrations, is also observed in the calculated results. However, the calculated relative variations are too large, especially for the case with the lowest density of 7.3 kg/m<sup>3</sup> for which the calculated values given in Figure 18 have been multiplied by a factor of 40.

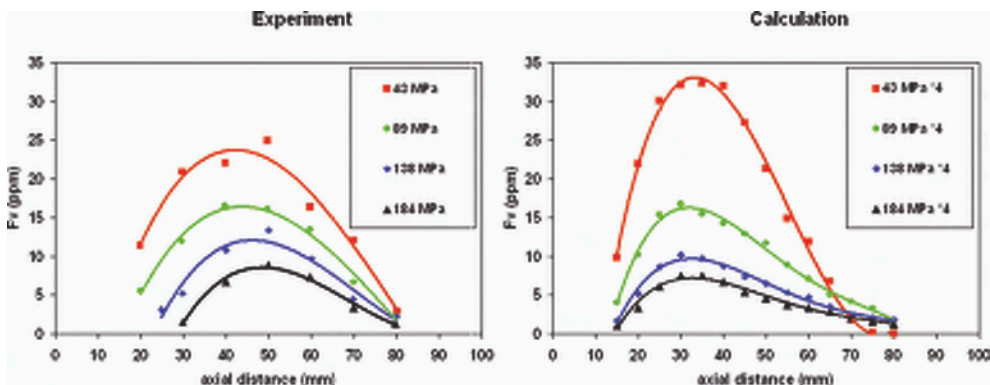


Figure 17. Averaged soot volume fraction,  $F_v$ , as a function of axial distance from the nozzle for different orifice pressure drop with a nozzle orifice diameter of 100  $\mu\text{m}$ , ambient temperature 1000 K, ambient density 14.8 kg/m<sup>3</sup> and oxygen concentration 21%, experimental results to the left [15] and calculated results to the right.

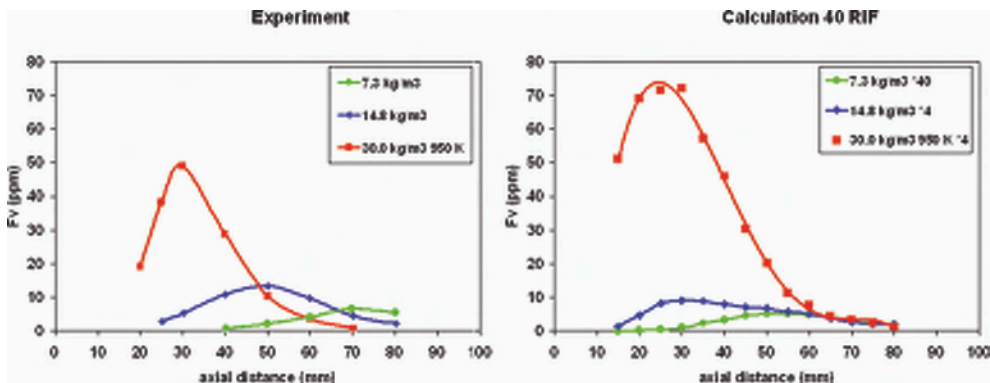


Figure 18. Averaged soot volume fraction,  $F_v$ , as a function of axial distance from the nozzle for different ambient gas densities with a nozzle orifice diameter of 100  $\mu\text{m}$ , ambient temperature 1000 K, orifice pressure drop 138 MPa and oxygen concentration 21%, experimental results to the left [15] and calculated results to the right.

## 5. EFFECT OF NUMBER OF FLAMELETS FOR ENGINE CALCULATIONS

Following the results for the constant volume cases the effect of the number of flamelets was evaluated for engine cases using the same set of models. For the engine cases, the experimental database was more limited and only a few engine parameters were varied. The nozzle diameter was typical for production engines, 0.2 mm, and much larger than the 0.1 mm reference nozzle studied in the constant volume case. In addition, a fuel with lower aromatic content and thus having a smaller sooting tendency was used. The investigated engines base cases were characterised by:

1. High load – high speed,
2. Part load – medium speed.

The effects of decreased inlet temperature, decreased EGR and decreased injection pressure were examined for both engine base cases using the RIF model with a single flamelet and with 40 flamelets.

Results for the second engine case, with part load and medium speed, are presented in Figure 19. The upper row of the figure displays results for the different variations using a single flamelet approach. The soot concentrations are captured 10 CA after TDC at a time when the flame is fully developed during ongoing fuel injection. For the cases with a single RIF there is no visible flame lift-off. Using a 40 flamelets approach the results differ as displayed in the lower row of the figure. A lifted flame is obtained for all variations. Soot starts to form at a certain distance from the injector indicating a more realistic modelling of the underlying combustion processes. The results using 40 flamelets also indicate a larger sensitivity to the different variations. This is most prominent for the case with low EGR where the soot concentration in the centre of the jet is substantially larger than for the baseline case.

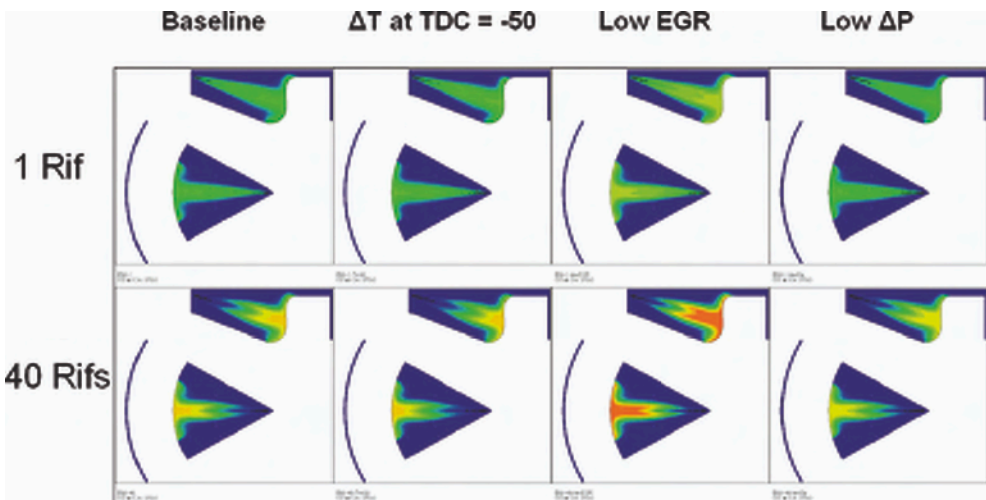


Figure 19. Calculated soot concentrations for the part load – medium speed case.

The next figure, Figure 20, displays the time evolution of the calculated total mass of soot in the cylinder half-load high-speed baseline engine case using a single and a 40 RIF approach. The main difference seems to be the amplitude of the curves; the results are almost identical except for a factor of approximately two. For the constant volume case, the typical difference in total soot mass was a factor of eight comparing a single and a 40 RIF calculation. The ability to predict a lifted flame seems to affect soot formation less for the engine calculations. A possible explanation is the very high local soot concentrations obtained using single RIF with small diameter nozzles and high ambient temperatures. For these conditions droplet evaporations is almost immediate and fuel rich gas appear just at the exit of the nozzle. With larger nozzle diameters and lower temperatures, evaporation occurs more gradually resulting in lower soot concentrations close to the nozzle.

The corresponding results for the high-load medium-speed baseline engine case differ only marginally because not even 40 RIFs were sufficient to establish a lifted flame for this case.

Figure 21 presents the calculated engine out soot for the different variations of the half load – high-speed engine case using single and forty RIFs. Soot values are for all variations a factor of approximately two lower using forty RIFs.

The effect on engine out NOx was marginal for the half load cases but for higher load cases NOx predictions are typically more accurate using a multiple RIF approach.

## 6. RATES OF SOOT FORMATION

When analysing CFD results usually only the distribution of soot mass in the cylinder is shown, see Figure 22.

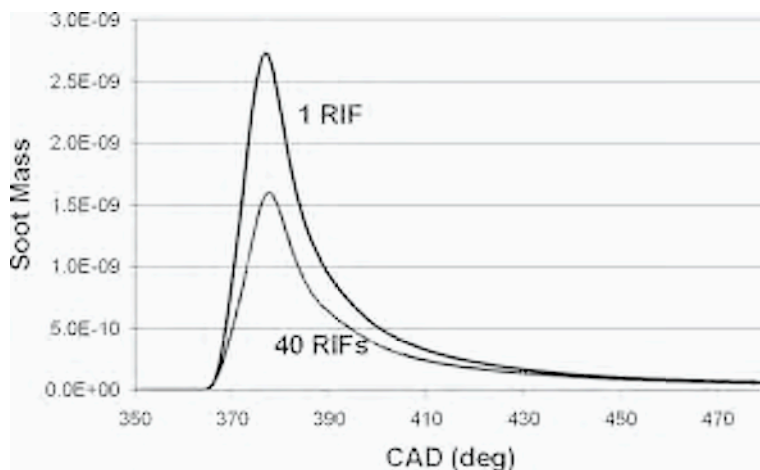


Figure 20. Calculated in-cylinder total soot for the half load – high-speed baseline engine case using a single and a 40 RIF approach.

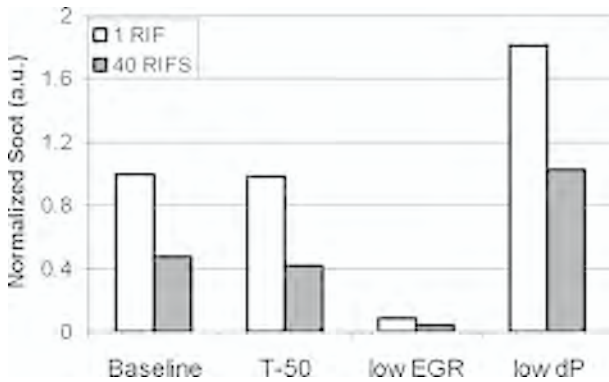


Figure 21. Calculated engine out soot for the half load – high-speed engine cases using single and forty RIFs.

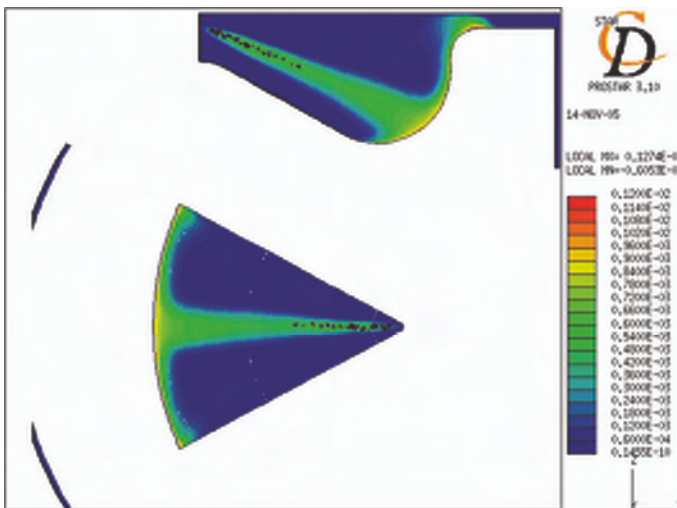


Figure 22. Distribution of the soot mass in the cylinder.

Much more information about the soot formation and oxidation processes is available when using detailed soot models including following formation processes:

- a) particle inception;
- b) condensation;
- c) surface growth;
- d) oxidation.

An example of the total in-cylinder rates is shown in Figure 23. In this plot the rates of particle inception, condensation and surface growth are added to provide a total

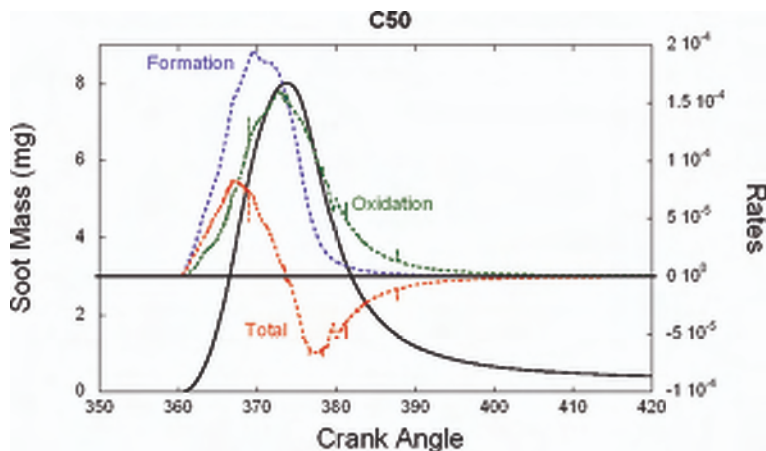


Figure 23. Global rates of soot formation and oxidation for a half-load engine case. Also shown is the total mass of soot in the cylinder.

soot formation rate. Also shown are the oxidation rate and the net rate (formation – oxidation rate).

During injection soot formation is larger than oxidation, which however is not negligible during injection. The maximum net rate is reached about half-way between start and end of injection. The soot mass typically has its maximum close to end of injection. At this point the global net rate is zero and soot oxidation starts to dominate. After end of injection, oxidation is efficient and the soot mass decreases by more than an order of magnitude for the case studied. The rate of oxidation depends, however, strongly on the level of EGR (compare with Figure 9).

Figure 24 shows the spatial distribution of soot formation and oxidation rates, i.e. particle inception, condensation, surface growth and oxidation during injection. Particle inception and condensation are very similar while a minor variation can be observed for surface growth. This indicates that soot particle formation and growth occurs mainly in the rich core of the jet at some distance to the nozzle. Soot formation close to the piston bowl seems to be intense as well. In contrary, oxidation occurs on the edges of the flame at stoichiometric conditions, where soot-oxidising agents such as OH-radicals are present and the temperature is high.

## 7. CONCLUSIONS

The capability of a detailed soot model implemented in the RIF combustion model to predict soot formation and oxidation in heavy-duty truck engines and in diesel sprays in a constant volume chamber has been assessed. The main objective has been to study relative changes. The capability to predict soot in absolute numbers would be desirable but is, in many cases, not essential.

The results of this study show that a correct prediction of flame lift-off is necessary to model soot formation in a diesel spray. In engine calculations, it is not always possible to model the lifted flame with the models used in this study. However, in many applications, as for example piston geometry studies, it is the oxidation efficiency and not the formation rate that determines the performance of a particular piston geometry. For cases where mixing and oxidation is the dominant effect on engine-out soot, the RIF soot model is capable to predict the relative influence of different parameters well, although the absolute amount of soot is mostly under-predicted. On the other hand, for cases where the initial formation process has a dominating influence, as for variations in the intake air temperature, the results from the model might be unreliable.

The majority of results have been obtained for engines operated with EGR that usually run with a low air/fuel ratio  $\lambda$ . Due to the low  $\lambda$ , fuel rich pockets containing most of the soot are present until the opening of the exhaust valve. The RIF soot model seems to handle such situations particularly well. A few non-EGR cases were presented for which the model also performed well. For non-EGR cases, effects not presently included in the model, such as local heat transfer to walls, might increase in relative importance and improved model capability can be of crucial to capture the right trends.

For the constant volume cases, it was shown that the RIF soot model is able to capture all major trends for the soot concentrations in a diesel spray when different parameters are varied over a large range. Absolute numbers are, however, typically under-predicted by a factor of four. Some other discrepancies were observed, for example, the model did not capture the downstream shift of the position for soot appearance with increasing injection pressure. A reason might be inaccurate modelling of the scalar dissipation rate close to the nozzle. The scalar dissipation rate varies strongly with injection pressure. This effect should be investigated in future work.

Engine cases where both the early formation and the mixing and oxidation process were varied, such as injection timing and amount of EGR, also gave encouraging results. Trends were predicted well and simulation results were very useful in explaining the effects on engine-out soot. The EGR variations included the transition from mixing limited combustion to partially premixed combustion. For these cases, the model predicted correct trends and was able to provide a basic understanding, also of early soot formation processes.

Results from diesel combustion modelling rely heavily on a proper modelling of fuel spray and mixing. It should be noted that present state of art spray and mixing models still contain oversimplifications and lack important features as coupling to the injector fuel flow and size distribution of primary droplets. The accuracy of results depends on user experience and sometimes a certain amount of tuning of model parameters. In the present work, the only tuning concerned an unknown parameter coupling the spray model to the fuel injector flow.

The RIF combustion and soot model performs sufficiently well for many engine applications, in fact, better than expected given the assumptions that have to be made when formally deriving the underlying flamelet concept. Nevertheless, a model with full predictive capability would need major improvements.

A major weakness of the RIF model is the limited resolution for local conditions when chemistry is calculated. Especially, local effects close to the nozzle leading to a lifted flame are important to incorporate. The problem for engine calculations, in many

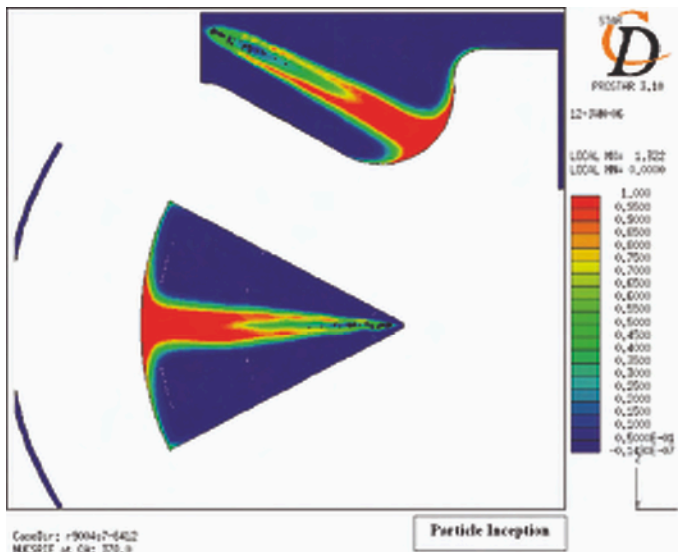


Figure 24. Rates of soot formation: particle inception.

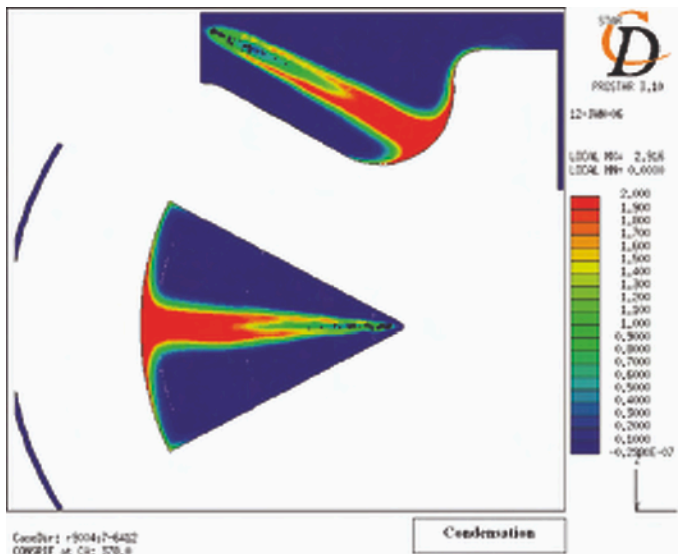


Figure 24. Rates of soot formation: condensation.

cases, is that introducing the required number of flamelets makes the calculations too time consuming. Several procedures to avoid long computational are possible and should be investigated.

A more realistic modelling of multiple injections would need a model to mix flamelets with each other, to exchange species and heat. Several strategies to achieve this have already been investigated [18, 19].

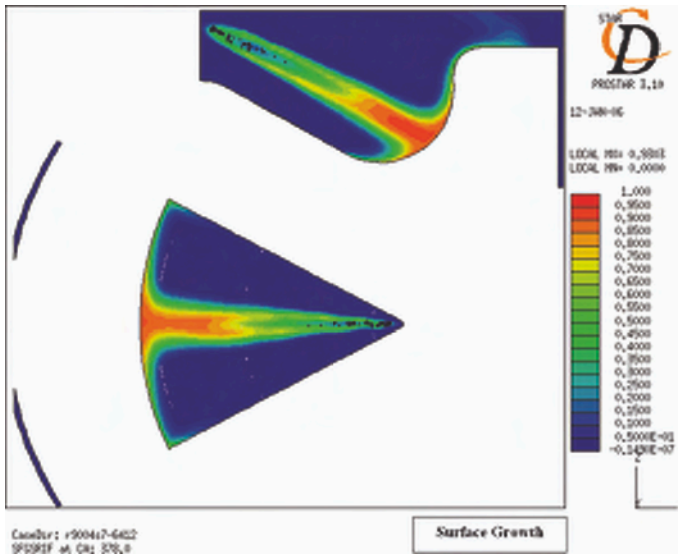


Figure 24. Rates of soot formation: surface growth.

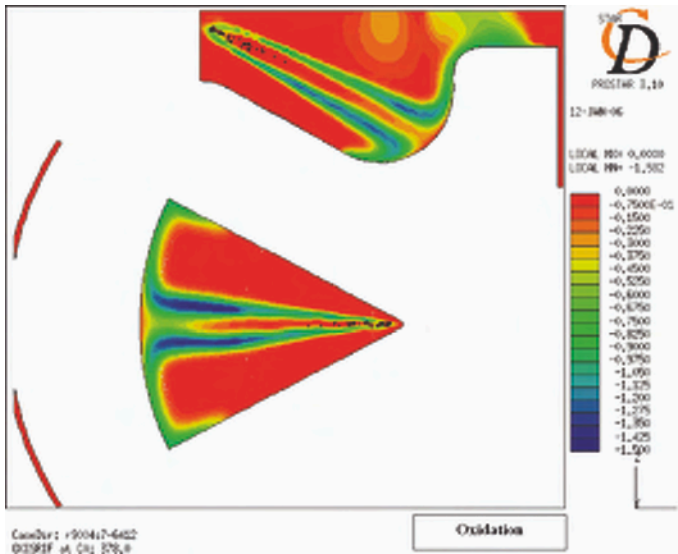


Figure 24. Rates of soot formation: oxidation.

Modern heavy duty diesel engines operate with in-cylinder pressures up to 200 bar. The development and validation of fuel oxidation chemistry at this elevated pressure, including species important for soot formation and oxidation, is another challenge.

The present set of chemistry models does only provide very limited options to study fuel effects on soot emissions. The ability to study different fuels will become

increasingly important and the development of new chemical mechanisms representing important properties of different fuels should be encouraged.

Future legislation will most probably include limitations on the number of emitted particles. The soot model incorporates, in principle, a model for both size and number of particles. Experience using the model for this purpose is, however, very limited and probably model improvements are needed to obtain accurate results from engine calculations. The modelling of aggregation of particles might also be of importance to accurately model the total particle number.

## ACKNOWLEDGEMENT

Dr. Magnus Christensen at Volvo Technology is acknowledged for generating the high quality experimental engine data.

## REFERENCES

1. I. Kennedy, *Prog. Energy Combust. Sci.* 23 (1997) 95-132.
2. Liu, Tao, Foster, Reitz, Application of a Multi-Step Phenomenological Soot Model to HSDI Diesel Multiple Injection, SAE 2005-01-0924 (2005).
3. N. Peters, *Turbulent Combustion*, Cambridge University Press, Cambridge, UK (2000).
4. Kazakov, Foster, Modeling of Soot Formation During DI Diesel Combustion Using a Multi-Step Phenomenological Soot Model, SAE 982463 (1998).
5. M. Frenklach, H. Wang, in *Soot Formation in Combustion: Mechanisms and Models*, H. Bockhorn (Ed.) Springer Series in Chemical Physics, Vol. 59, Springer-Verlag, Berlin, 1994, pp. 162-190.
6. M. Frenklach, *Phys. Chem. Chem. Phys.* 4 (2002) 2028-2037.
7. M. Frenklach, *Chem. Eng. Sci.* 57 (2002) 2229-2239.
8. F. Mauss, B. Trilken, H. Breitbach, N. Peters, in *Soot Formation in Combustion: Mechanisms and Models*, H. Bockhorn (Ed.) Springer Verlag, Berlin-Heidelberg, 1994, p. 325.
9. H. Pitsch, H. Barths, N. Peters, SAE 962057 (1996).
10. H. Pitsch, N. Peters, *Proc. Combust. Inst.* 26 (1996) 721-728.
11. H. Pitsch, N. Peters, Reduced kinetics of multi-component fuels to describe the auto-ignition, flame propagation and post-flame oxidation of gasoline and Diesel fuels, IDEA EFFECT Technical report (1996).
12. A. Karlsson (2006) personal communication.
13. D. Siebers, *Trans. SAE* 107-980809 (1998) 1205-1227.
14. J. Naber, D. Siebers, SAE 960034 (1996).
15. C. Idicheria, L. Pickett, SAE 2005-01-3834 (2005).
16. L. Pickett, D. Siebers, *Combust. Flame* 138 (2004) 114-135.
17. L. Pickett, D. Siebers, *J. Eng. Gas Turbines Power* 127 (2005) 187-196.
18. H. Barths, C. Hasse, G. Bikas, N. Peters, *Proc. Combust. Inst.* 28 (2000) 1161-1168.
19. H. Bensler, T. Bo, A. de Risi, F. Mauss, E. Montefrancesco, K. Netzell, J. Willand, Prediction of Non-premixed Combustion and Soot Formation using an Interactive Flamelet Approach, Conference on Thermo- and Fluid Dynamic Processes in Diesel Engines, THIESEL 2006, Valencia, 2006.

# Challenges of soot modelling in gas turbine combustors

H. Brocklehurst  
*Rolls Royce, UK*

## 1. INTRODUCTION

In the development of gas turbine, environmental aspects become more and more important. Many conventional combustion chambers use the rich-quench lean concept to reduce NOx formation through minimising the residence time in high temperature regions and hence NOx formation.

However, the rich primary zone leads to large amounts of soot, which has to be oxidised before the exit of the combustor. Any soot model must therefore be capable of capturing the difference between two large numbers.

## 2. CURRENT ROLLS-ROYCE SOOT MODELLING

The current soot model uses a flamelet approach and solves for two additional equations, the Favre mean number density ( $\tilde{N}$ ) and soot mass fraction ( $\tilde{C}_m$ ). A single particle size is assumed at each node and the oxidation is dependent on soot surface area.

$$\begin{aligned} \bar{\rho} \frac{d(\tilde{N})}{dt} &= \bar{\rho} (\tilde{R}_{\text{nucl}} - \tilde{R}_{\text{coag}} \tilde{N}^2) \\ \bar{\rho} \frac{d(\tilde{C}_m)}{dt} &= \bar{\rho} (\tilde{R}_{\text{sg}} \tilde{N} + C_p \tilde{R}_{\text{nucl}} - \tilde{R}_{\text{oxid}} (\text{mean surface area})) \end{aligned}$$

where  $R_{\text{nucl}}$  = nucleation rate  
 $R_{\text{coag}}$  = coagulation rate  
 $R_{\text{sg}}$  = surface growth rate  
 $R_{\text{oxid}}$  = oxidation rate

This model is capable of capturing trends with operating condition and changes in geometry in many cases, although absolute values are significantly over-predicted.

Figure 1 reports normalized exit soot as a function of pressure in the gas turbine combustor. Combustion chambers can operate at up to 50bar with inlet temperatures in excess of 900K. In this case, combustor exit peak soot occurs at climb conditions. The CFD analysis shows that though more soot is produced at in the primary zone at take-off, it is accompanied by more net oxidation in the quench and dilution zones leading to lower exit values.

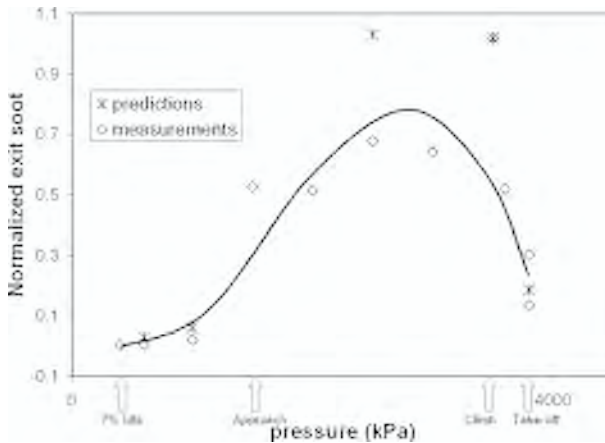


Figure 1.

### 3. MODEL DEFICIENCIES

Predicted final soot levels are sensitive to small changes in the model, particularly ones that lead to the reduction in soot formation. Oxidation has no effect on number density and as the soot mass fraction decreases this can lead to a rapid increase in mean particle surface area and hence a sharp increase in the oxidation of the soot mass fraction. This can lead to negligible exit soot being predicted, in contrast with measurements, in conjunction with non-negligible number densities. A better resolution of soot particle size distribution should help this.

### 4. METHOD OF MOMENTS IMPLEMENTATION

As a part of the EU project SiA-TEAM, the method of moments has been implemented within the laminar flamelet framework. This will give a better resolution of the soot size distribution.

- 6 transport equation for the soot moments are solved in the CFD solver with source terms from the Enhanced Soot Model developed by DLR [4], based on the original work by Frenklach and Wang [1,2].
- Species from laminar flamelet model; no feedback
- The PAH used to initiate soot formation is pyrene; no detailed model of the formation of higher mass PAH's is included.

The model has been applied to a double annular combustor run at circa 7 bar [3]. Figure 2 reports the 3D view of the double annular combustor.

Soot is formed mainly in the rich region of the combustor with negligible exit soot. Figure 3 reports soot mass distribution inside double annular combustor.

The main results of the Method of moments implementations are (Figures 4 and 5):

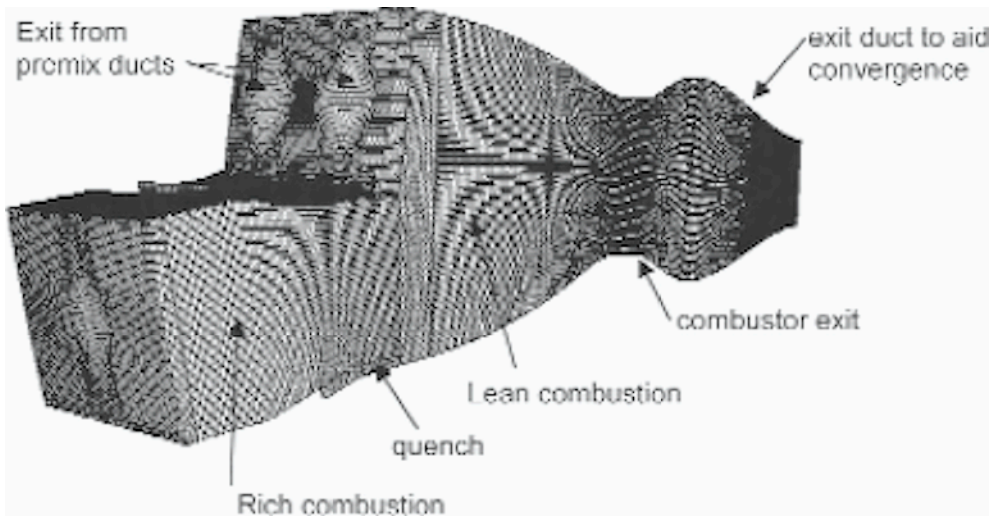


Figure 2. 3D computational grid of the double annular combustor.

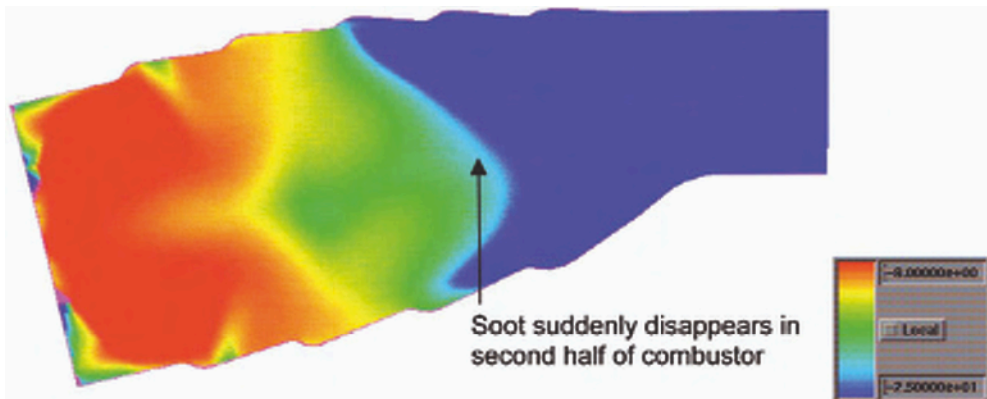


Figure 3. Soot mass distribution inside double annular combustor (logarithm scale).

- Soot mass fractions of comparable order to the existing model, but the number density is significantly higher.
- The soot is formed earlier in the combustor, probably due to using pyrene as PAH.
- It also has a finite exit number density, with negligible exit soot mass fraction. The number density includes only nucleation and coagulation, so there is no direct effect of oxidation.
- There are numerical problems in the lean regions of the combustor, where oxidation can reduce the higher moments to values lower than the first moment, which is unphysical.

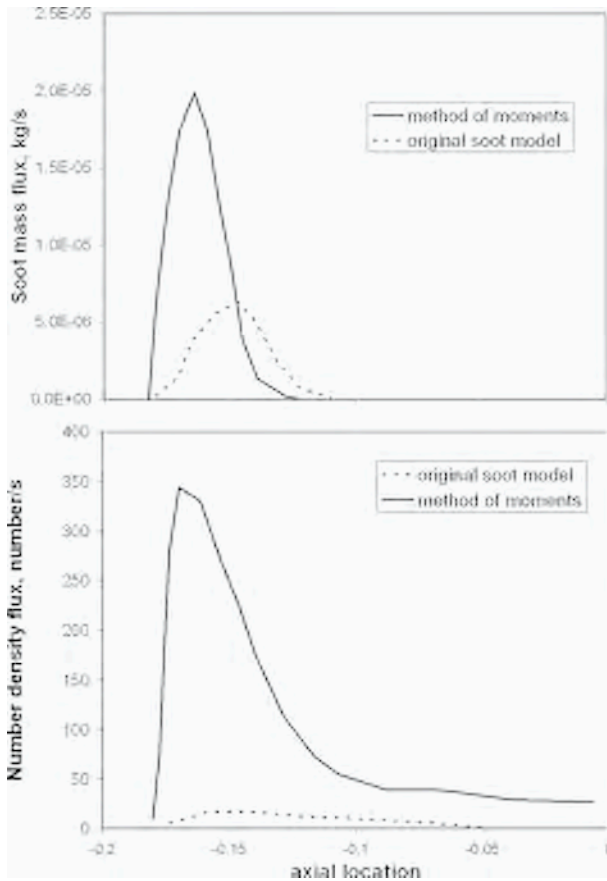


Figure 4. Predicted sum of soot mass fraction and number density fluxes crossing axial planes along the combustor with the original soot model and the enhanced soot model.

## 5. FUTURE WORK

- Links to more appropriate combustion models required
- Inclusion of the PAH formation step is necessary
- Further work on validation / verification of method of moments model is required in industrially relevant geometries.

## 6. SOOT MODELLING ISSUES

- The issues with the number density need resolving; is this a fundamental model issue?
- Has this behaviour been found in other simulations?

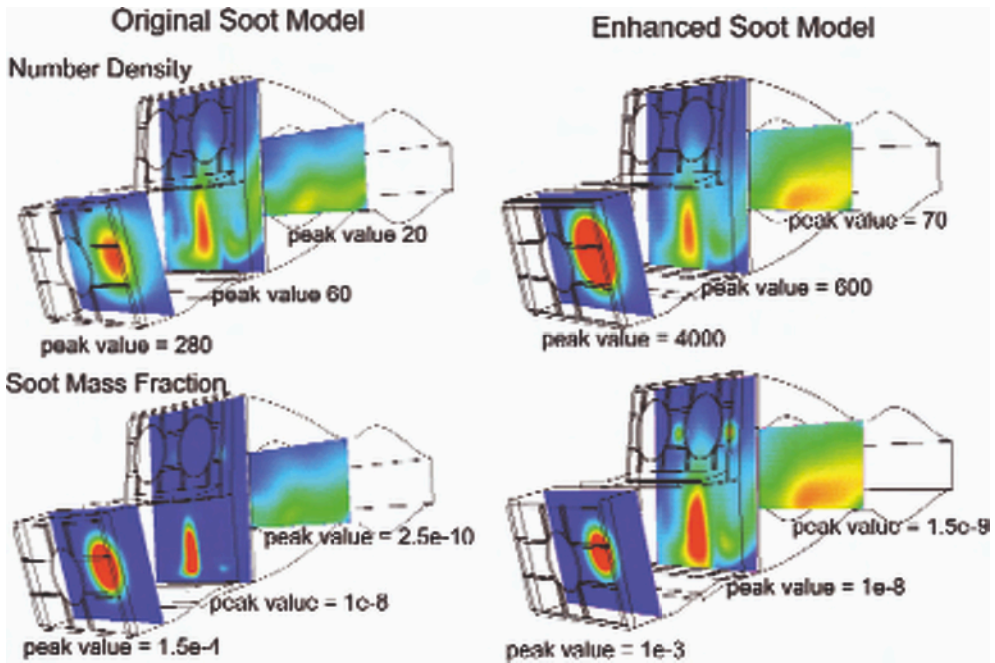


Figure 5. Comparison of soot mass fraction and number density predictions with the original soot model and the enhanced soot model.

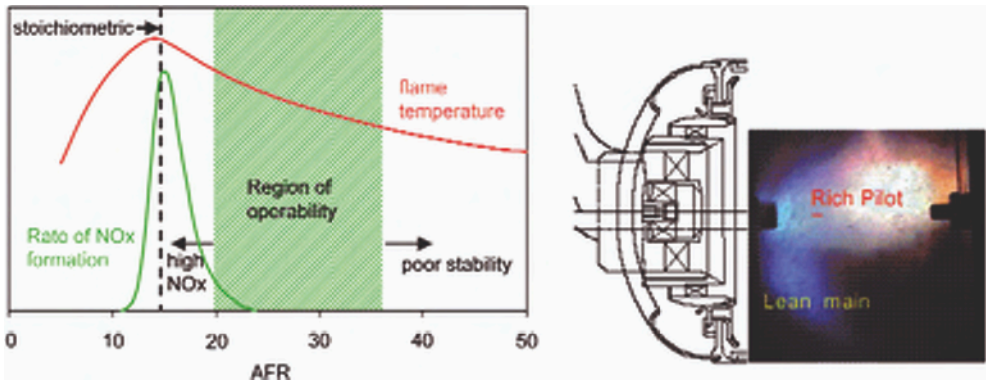


Figure 6.

- Does this demonstrate that laboratory flames / shock tube data used for model development and validation do not capture all the physics present in industrial geometries?
- Is more focus on research into soot oxidation required?
- More validation data at industrial relevant conditions is required.

## 7. FUTURE PERSPECTIVES

- Future combustor designs will be the lean direct injection concept; NO<sub>x</sub> production is avoided by running the fuel injector weak. Soot production in this regime should be minimal
- However, a rich pilot is required to ensure stability at low power conditions, and this can result in soot formation at idle to approach conditions.
- This could exacerbate the modelling problems with both models, as more of the combustor volume will be running lean.

## ACKNOWLEDGEMENTS

This work has been completed with financial support of the European Union through the Brite-Euram programme, ‘Soot in Aeronautics - Towards Enhanced Aeroengine Combustor Simulation’ (SiA-TEAM), GRD1-2001-41804.

There has also been significant support from Deutsches Zentrum fuer Luft- und Raumfahrt e.V. (DLR) in the implementation of the model. SNECMA supplied the geometry and boundary conditions for the double annular combustor calculation.

## REFERENCES

1. K.L. Revzan, N.J. Brown, M. Frenklach, <http://www.me.berkeley.edu/soot>.
2. M. Frenklach, H. Wang, in *Soot Formation in Combustion: Mechanisms and Models*, H. Bockhorn (Ed.) Springer-Verlag, Heidelberg, 1994, pp. 165.
3. A. Platz, SiA-TEAM report, 2005.
4. E. Goos, SiA-TEAM report, 2005.

**Part V**  
**Establishment**  
**of an international soot collaborative**



# A study on the effect of experimental setup configuration on soot formation in a laminar premixed ethylene-air flame

G. Gothaniya, S.-Y. Lee, A.V. Menon, S. Iyer, M.J. Linevsky,  
R.J. Santoro, T.A. Litzinger

*Department of Mechanical and Nuclear Engineering,  
The Pennsylvania State University, University Park, PA 16802 United States*

*Abstract: An experimental investigation was conducted to study the effect of various experimental configurations and burner operating conditions on the measured soot volume fraction in laminar premixed ethylene-air flames at equivalence ratios of 2.34 and 2.64. Soot volume fractions were measured using light extinction for all the experimental conditions. The experimental configurations studied included variation of the height above the burner of the stabilization plate, the diameter of the hole in the center of the stabilization plate, use of a solid stabilization plate and a screen with a 30 mm hole in the center, variation in the cooling water flow to the burner, and variation in the nitrogen shroud flow rate. The observed soot volume fractions show that changes in the height above the burner of the stabilization plate having either the 30 mm or 40 mm diameter center hole as well as changes in the cooling water flow rate do not significantly affect the measured soot volume fraction. The change in the shroud nitrogen flow rates influence the observed soot volume fraction at high nitrogen flow rates. Use of a stabilization plate with a 20 mm diameter center hole or a solid stabilization plate also affected the measured soot volume fraction.*

## 1. INTRODUCTION

Soot formation has been extensively studied in premixed [1-5] and diffusion flames [6-9]. In diffusion flames, there is general agreement between measurements of soot volume fractions obtained by different researchers on similar flames. On the contrary, several researchers have measured significantly different soot volume fractions in premixed flames with similar equivalence ratios even when using similar measurement techniques. Figure 1 shows the soot volume fractions measured by Harris et al. [2, 10], Feitelberg et al. [11] and Ritrievi et al. [12]. The soot volume fraction profiles labeled 2, 3 [2] and 4 [10] are all for flames with  $C/O = 0.76$ , but show a variation of more than 70% in the measured soot volume fraction. Soot profiles 5 ( $C/O = 0.77$ ) and 6 ( $C/O = 0.78$ ) also show a variation of more than 100% and the soot profiles 7 [2] and 8 ( $C/O = 0.80$ ) show a variation of 20-30%.

Xu et al. [3, 13] also observed differences in soot volume fraction and soot growth rates for comparable flame conditions. They state in their paper that reasons for observed differences are either unknown [3] or argued to be due to the non-uniform distribution of soot volume fraction over the flame cross-section [13].

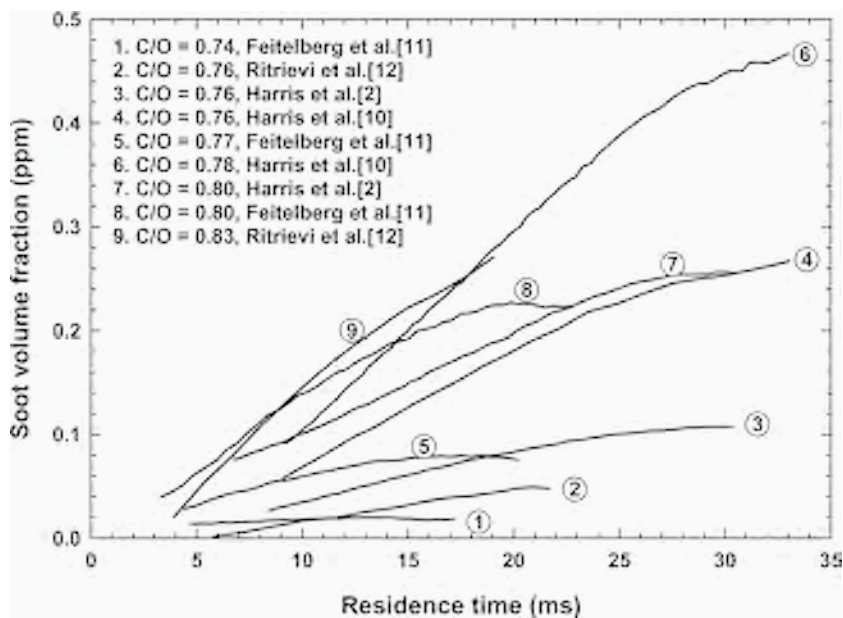


Figure 1. Soot volume fractions measured by Harris et al. [2, 10], Feitelberg et al. [11] and Ritrievi et al. [12].

For these experiments as well as for the experiments conducted by others [14-23], the experimental conditions such as the equivalence ratio, fuel and oxidizer flow rate, mixture inlet temperature and pressure used were well documented. These premixed flame studies were targeted towards understanding the soot formation in flames. The studies investigated surface growth [2, 10], the effect of pressure [14], the effect of additives [1, 15, 16], soot particle size [17, 18], soot inception kinetics or precursor formation [15, 19, 21], optical and radiative properties of soot [5, 20] and the effect of equivalence ratio [22]. These results have been used for flame modeling studies, developing computational models for various combustion systems and the design of combustion devices.

For premixed flame studies, though the experimental conditions are specified, the burner and configuration of the experiment varies considerably from investigator to investigator. Different types of stabilization plates have been used, for example, a solid plate [5, 15], a solid plate with a center hole in the center [3, 13], water cooled solid plate [20], water cooled perforated plate [11], a stainless steel mesh [16, 23], and a mesh with a hole in the center [1, 2, 10]. These plates have different hole diameters, for example, 30 mm [2, 3, 13, 23] and 45 mm [1]. The height above the burner (HAB) surface at which these plates are located also varies, for example, 20-30 mm [2, 10], 30-40 mm [1], 30 mm [3, 5] and 32 mm [13]. To shield the flame from the surroundings, different shroud flows using argon [16], nitrogen [3, 13, 15], and shroud flames surrounding the main flame [1, 14], with different flow rates have been used. Quartz shrouds have been used to further stabilize some flames [15].

The above discussion shows that a wide variety of experimental configurations have been employed in experiments to study soot formation in premixed flames. This indicates the need for quantifying the effects of the various experimental configurations on the process of soot formation. The objective of the present work, therefore, is to provide sets of experimental data under different experimental configurations, and suggest configurations which can be used to produce reproducible results. The current work is focused on studying the effect of experimental parameters including HAB of the stabilization plate, type of stabilization plate and nitrogen shroud flow rate. These are the main parameters defining the differences in experimental configurations used by different researchers. We have also included cooling water flow rate to the burner as a parameter in our study as it may affect the burner surface temperature and thus have an effect on the soot formation.

## 2. EXPERIMENTAL SETUP

### 2.1. Burner

A commercially available McKenna burner was used to produce laminar premixed flat flames at atmospheric pressure. The burner consisted of 60 mm diameter water cooled burner plug made of a sintered stainless steel matrix surrounded by 6 mm annulus made of a sintered bronze matrix. Nitrogen is passed through the surrounding annulus to shield the flame from disturbances and prevent formation of peripheral diffusion flames. The burner assembly was mounted on a linear translation stage controlled by stepper motors and could be traversed in the horizontal and vertical direction with positioning accuracies of 12.7 and 25.4  $\mu\text{m}$ , respectively.

The flame was stabilized using various stabilization plates including a solid plate, a plate with a hole in the center and a wire mesh with a hole in the center. The stabilization plate was a 10 mm thick circular stainless steel plate with outer diameter of 130 mm and a 40 mm hole at the center. Rings of different inner diameter were used to change the effective center hole size for the stabilization plate. The wire mesh used was a 152 mm by 152 mm stainless steel mesh with a spacing size of 2 mm, similar to the wire mesh used by Haynes et al [1]. (A solid wire mesh without a center hole was not used because excess soot deposition led to flow blockage and changed the flame properties.)

### 2.2. Optical setup

Soot volume fraction measurements were obtained for all flames using a laser extinction technique. The experimental layout for the extinction measurements is shown in Figure 2. It consists of a 4W Argon Ion laser operated at 514.5 nm line and incident power of approximately 500 mW. A half-wave plate is used to ensure that the laser beam is vertically polarized. The laser beam is modulated using a mechanical chopper operating at 1000 Hz and is focused into the flame region using 1m focal length lens. A photodiode receiving a fraction of the incident laser through a beam splitter is used to monitor the incident laser power. Another photo diode, placed after the burner, is

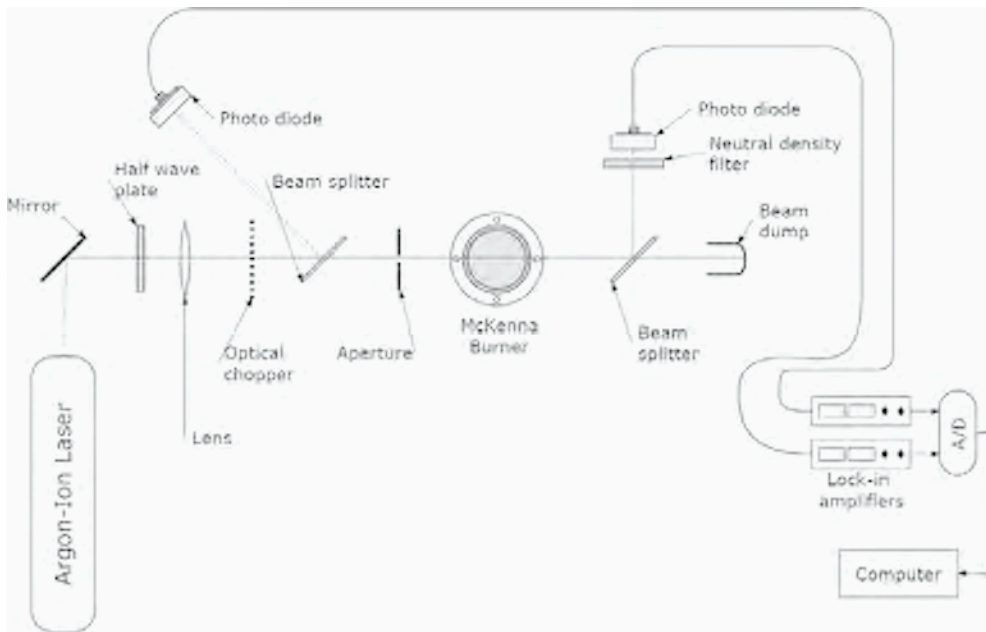


Figure 2. Layout of optical diagnostics.

used to measure the intensity of the attenuated beam. The output from each photo diode is fed to a lock-in amplifier to minimize interference from extraneous light, including flame radiation, on the extinction measurement.

### 2.3. Soot volume fraction measurement

Extinction measurements were carried out on each flame at 21 heights above the burner surface along the centerline of the flame. The heights were 1.016 mm apart. At each height above the burner 45 readings were obtained over a period of 15 seconds. These readings were subsequently averaged and stored on a computer. To determine soot volume fraction from the light extinction measurements a value of  $1.57-0.56i$  was assumed for the refractive index of the soot particles [24]. The particles were assumed to be in the Rayleigh size limit. (i.e.  $\pi D/\lambda$  is less than 0.3, where  $D$  is the primary particle diameter of soot aggregate and  $\lambda$  is wavelength of laser used.)

### 2.4. Test matrix

Flames of ethylene and air at two equivalence ratios and with different plate configurations, different shroud flows and different cooling water flows were studied. For each equivalence ratio the different configurations used are listed in Table 1. Corres-

Table 1. Test configurations.

Equivalence Ratio	2.34			2.64			
C/O Ratio	0.78			0.88			
Air Flow Rate (mg/s)	194.3			190.9			
Fuel Flow Rate (mg/s)	30.8			34.1			
Shroud Nitrogen Flow Rate(s) (mg/s)	550		550, 650, 750 and 850	550		550, 650, 750 and 850	
Cooling Water Flow Rate(s) (g/s)	9	5, 9 and 21	9	9	5, 9 and 21	9	
Stabilization Plate Hole Diameter(s) (mm)	30	20 <sup>C</sup> , 30, 40, Solid plate <sup>C</sup> and Mesh <sup>B</sup> w/ Hole	30	30	30 Mesh <sup>B</sup>	30, 40, Solid plate <sup>C</sup> and w/ Hole	30
Stabilization Plate HAB(s) (mm)	25, 30, 32, 35 <sup>A</sup> , 38 <sup>A</sup>	32	32	32	25, 30, 32, 35 <sup>A</sup> , 38 <sup>A</sup>	32	32

Shroud nitrogen flow rate changed to stabilize the flame: <sup>A</sup>605 mg/s; <sup>B</sup>650 mg/s; <sup>C</sup>850 mg/s.

pondingly soot volume fraction measurements were obtained in these flames. The experimental configurations studied included variation of: HAB of the stabilization plate from 25 mm to 38 mm,

- Configuration of the stabilization plate: solid plate, plates with center hole diameters of 20 mm, 30 mm and 40 mm, and a wire mesh screen with a 30 mm center hole,
- Cooling water flow to the burner from 5 g/s to 15 g/s
- Nitrogen shroud flow rate from 550 mg/s to 850 mg/s.

These parameter variations include most of the flames used by various researchers. In addition to these configurations, soot volume fraction was measured for flames at both equivalence ratios without a stabilization plate. A nitrogen shroud flow rate of 1250 mg/s was required to stabilize the flame without a plate. This configuration was tested

by Harris et al. [23] and they stated that they did not use screens for most of their experiments since the extra stability provided by the screen was found to be unnecessary. However, the exact nitrogen shroud flow rate was not specified in their paper. Thus, the nitrogen shroud flow rate used is the value required for our flame.

A stabilization plate with a 30 mm diameter center hole at 32 mm HAB with a nitrogen shroud flow rate of 550 mg/s and cooling water flow rate of 9g/s was used as the reference configuration, as this configuration has been used the most in this laboratory for studying laminar premixed flames.

The fuel and oxidizer used in all the flames were ethylene (CP – 99.5% purity) and air (Breathing quality Grade D – 99.5% purity). The nitrogen used for the shroud flow was of 99.995 % purity. The fuel flow was controlled using Teledyne Hastings model 202D ( $\pm 1\%$ ) mass flow meter and the air flow was controlled using Porter Instruments Model 111 ( $\pm 1\%$ ) mass flow meter. The shroud nitrogen flow rate was measured using a Matheson model FM 1050 ( $\pm 1\%$ ) rotameter.

To determine soot volume fraction using light extinction measurements requires knowing the optical path lengths. For measurements along the center line, the optical path length is the same as the flame diameter. The variation of flame diameter with HAB is measured using images of the flames recorded by an intensified charge coupled device (ICCD) camera. An image of a standard ruler is used to convert the size in pixels to mm.

### 3. RESULTS AND DISCUSSION

For the light extinction technique, the soot volume fraction is determined using the ratio of transmitted intensity to the initial intensity ( $I_t/I_0$ ) and the flame width at a particular height determined from the flame images. Thus, the uncertainty of the soot volume fraction measurements for a fixed index of refraction is determined by the accuracy of these two measured quantities. The uncertainty for the soot volume fraction is calculated using the procedure given by Iyer [25], which is taken from the work of Moffat [26]. The uncertainty in the measurement of  $I_t/I_0$  is estimated to be less than 1% [25]. The uncertainty calculated from the above procedure yields an uncertainty of about 10% for the measured soot volume fraction for index of refraction used in this study [24]. As the procedure and assumptions described above are the same for all the measurements, the uncertainty bar for the stabilization plate with a 30 mm hole at the center (shown in Figure 5) is representative for all the soot volume fractions measured.

#### 3.1. Effect of stabilization plate height

Figure 3 shows the axial profile of soot volume fraction,  $f_{vs}$ , for flames at equivalence ratios of 2.34 and 2.64 for five different HAB for the stabilization plate of 25 mm, 30 mm, 32 mm, 35 mm and 38 mm. For this set of experiments, the diameter of the hole at the center of the stabilization plate is 30 mm and cooling water flow rate is 9 g/s. As shown in Table 1, different shroud flow rates were used if the flame was not

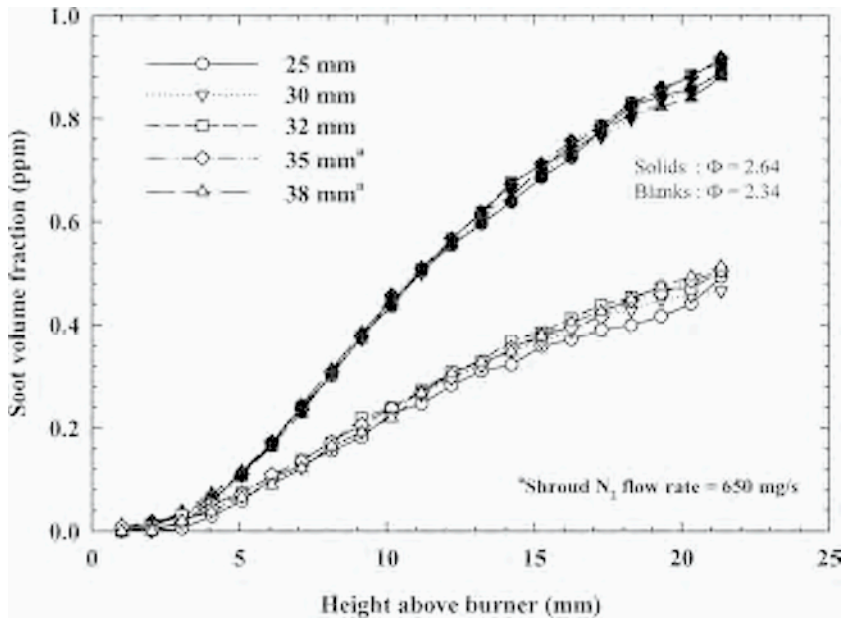


Figure 3. The axial profile for soot volume fraction for different HAB for the stabilization plate.

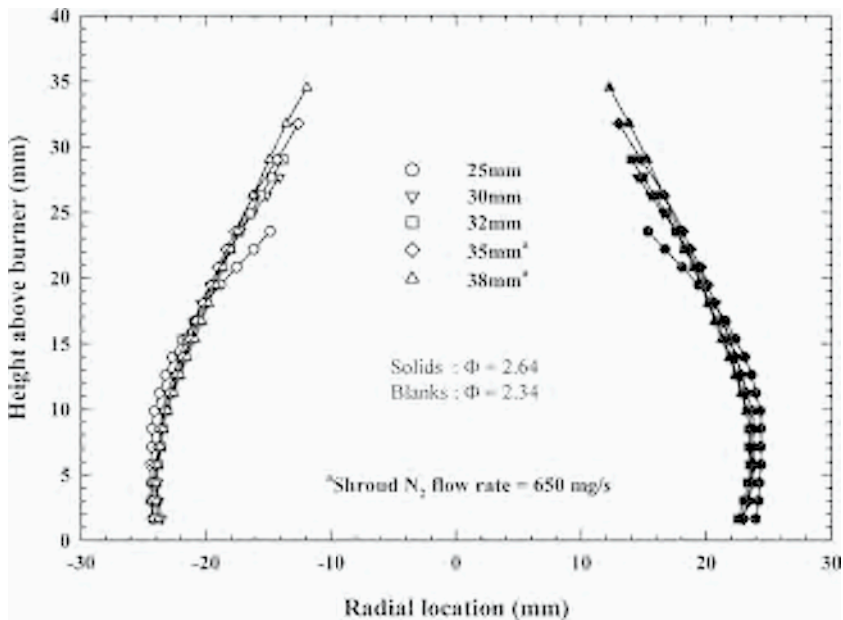


Figure 4. Flame shape for different stabilization plate HAB.

stable with a reference shroud flow rate of 550 mg/s. In particular, for the 35 mm and 38 mm HAB, a higher nitrogen flow rate of 605 mg/s was required to stabilize the flame.

It is observed from Figure 3 that the soot volume fraction is not significantly affected by the change in the stabilization plate height. Soot volume fraction profile has similar trends for equivalence ratios of 2.34 and 2.64. As observed from Figure 4, the flame shapes are also not significantly affected by the change in height of the stabilization plate. The maximum variation in the diameter is only 5 %. Also, it is observed that with a decrease in the plate height the flames appear to swell slightly outwards.

### 3.2. Effect of stabilization plate type

The axial variation of the soot volume fraction ( $f_v$ ) and the integrated soot volume fraction are as shown in Figures 5a and 5b, respectively. The integrated soot volume fraction is simply the product of the soot volume fraction and the flame cross sectional area at the same HAB [7]. Flames with an equivalence ratio of 2.64 exhibit similar trends as the flames with an equivalence ratio of 2.34, hence for greater clarity, results only for an equivalence ratio of 2.34 are shown on each figure. For these set of experiments, the plate height is 32 mm, nitrogen shroud flow rate used is 550 mg/s except where otherwise noted and cooling water flow rate used is 9 g/s. The types of stabilization plates used include a solid plate, plates with a hole in the center, and a wire mesh with a 30 mm diameter hole in the center. For the stabilization plate with a hole at the center, the diameters of the holes used were 20 mm, 30 mm and 40 mm.

The nitrogen shroud flow rates needed to stabilize the flame with a wire mesh, solid stabilization plate and one with a 20 mm diameter hole at the center were higher than the reference shroud flow rate of 550 mg/s. The different nitrogen shroud flow rates used are listed in Table 1. Figure 5a also shows the uncertainty in the measurement of the soot volume fraction for the flame with the reference configuration.

The soot volume fraction decreases by about 7% for the flame using a stabilization plate with a 40 mm hole at the center in comparison to the soot volume fraction for the reference flame. The soot volume fraction profile for the flame stabilized using a wire mesh with a 30 mm hole at the center, increases by about 7% in comparison to the soot volume fraction profile for the reference flame. These variations are within the measurement uncertainty.

As shown in Figure 6, the soot volume fractions for the flame at  $\Phi = 2.34$ , using wire mesh with a 30 mm hole at the center as the stabilization plate agrees well with the soot volume fractions measured by Harris et al. [10] for C/O ratio of 0.78 ( $\Phi = 2.34$ ). Harris et al. [2, 10] used stainless steel wire mesh screens with a 30 mm opening held about 20-30 mm above the burner to stabilize the flame. The soot volume fraction profile for the flame at  $\Phi = 2.64$  (C/O = 0.88) stabilized with a wire mesh with 30 mm hole at the center again shows similar trends as measured by Harris et al. [2] for C/O = 0.90. Figure 6 also shows the soot volume fractions for the flames ( $\Phi = 2.34$  and  $\Phi = 2.64$ ) without a stabilization plate in comparison to the soot volume fractions measured by Harris et al. [2, 10]

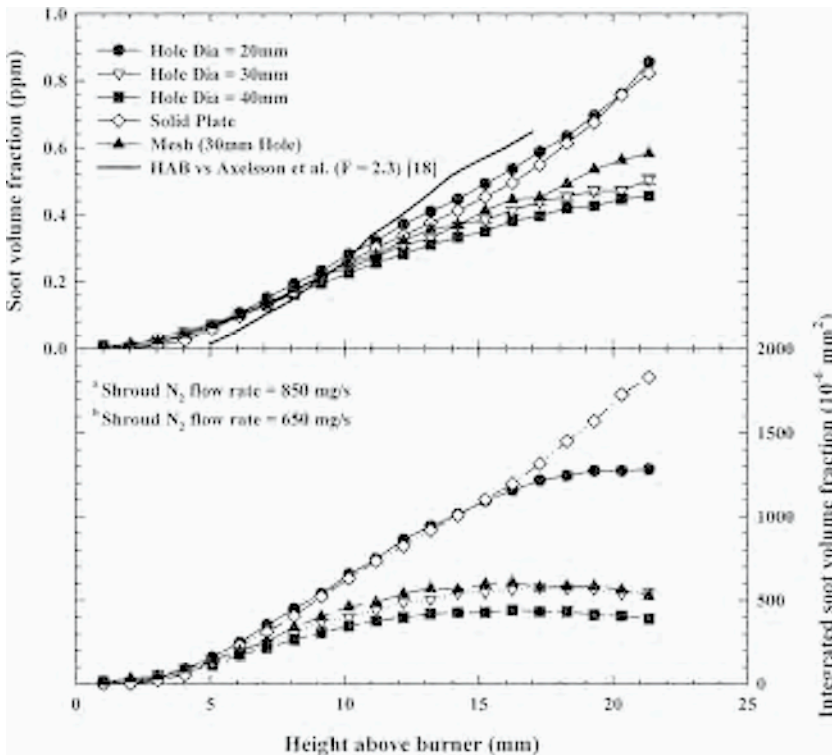


Figure 5. Axial profiles of a) Soot volume fraction with uncertainty shown in the measurement for the reference configuration and b) Integrated volume fraction of soot for flame with  $\Phi = 2.34$  and different tubes of stabilization plates. Soot volume fraction measured by Axelsson et al. [18] is plotted for comparison.

For the flame with the solid stabilization plate, the soot volume fraction profile is higher by about 22% in comparison to the soot volume fraction profiles for the flame with the reference configuration. This increase in the soot volume fraction profile for a flame stabilized using a stabilization plate with 20 mm diameter center hole is about 27%. As seen in Figure 5a, the soot volume fraction measured for the solid stabilization plate at  $\Phi = 2.34$  is very similar to the soot volume fraction reported by Axelsson et al. [18] for  $\Phi = 2.30$ .

The shape of the flame with different stabilization plates is as shown in Figure 7. For the stabilization plate with a 40 mm hole at the center, the flame diameter decreases only by about 8% for  $\Phi = 2.34$  and 7% for  $\Phi = 2.64$  from the diameter of the reference flame. The shape for the flame with the wire mesh as the stabilization plate also does not vary significantly from the reference flame. There is an increase of about 4 % for  $\Phi = 2.34$  and 3 % for  $\Phi = 2.64$ . The shape of the flame for  $\Phi = 2.34$ , using a solid plate or a stabilization plate with 20 mm diameter center hole is about 30% larger compared to shape of the reference flame. The flames with a solid stabi-

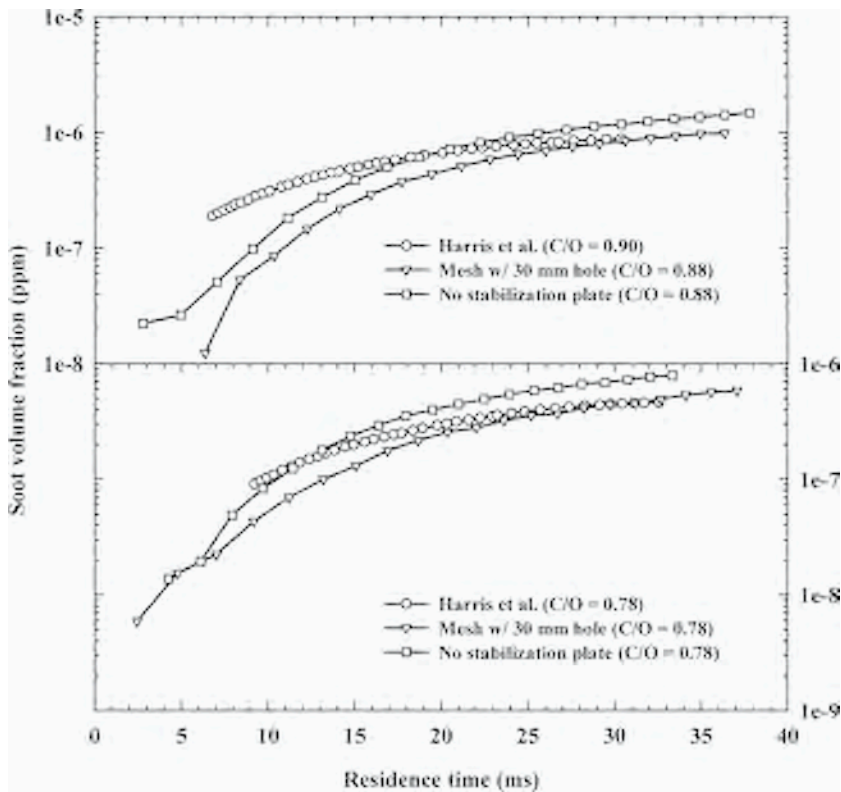


Figure 6. Comparison of soot volume fractions measured in the present study to soot volume fractions measured by Harris et al. for (a)  $C/O = 0.90$  [2] and (b)  $C/O = 0.78$  [10].

lization plate and a stabilization plate with a 20 mm diameter center hole both required using a higher nitrogen shroud flow rate of 850 mg/s, as compared to 550 mg/s shroud flow rate.

The integrated soot volume fraction at a particular height indicates the combined effect of the change in shape and the soot volume fraction. As seen from Figure 5b, the integrated soot volume fraction increases by 60-70% for the flame with a solid stabilization plate, in comparison to the reference flame. It is observed from Figure 7 that a solid stabilization plate or one with a 20 mm diameter center hole obstructs the flow profile of the flame. It is possible that soot impinges on to these stabilization plates and is re-circulated around the flame thereby contributing to an error in the extinction measurement. This is particularly true of extinction measurements that are made close to the stabilization plate. As a higher nitrogen shroud flow rate of 850 mg/s is necessary to stabilize these flames, this increased nitrogen shroud flow rate could affect the temperature distribution inside the flame. It also may have an effect on the residence time of soot in the flame, which can have an important effect on the soot volume fraction [27, 28].

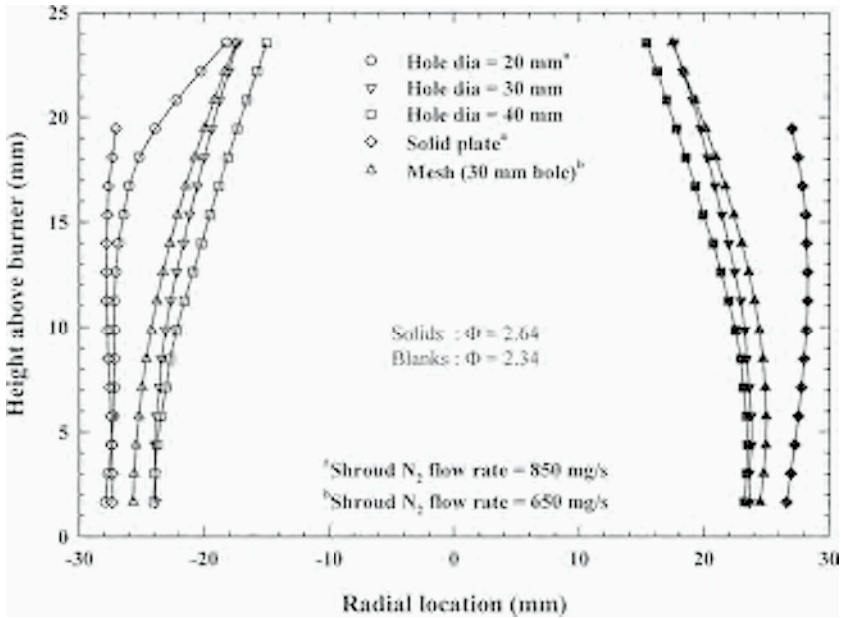


Figure 7. Flame shapes for different types of stabilization plates.

### 3.3. Effect of nitrogen shroud flow rate

Figures 8a and 8b show the axial variation of the soot volume fraction profile and the integrated soot volume fraction respectively, for flames with an equivalence ratio of 2.34 and different nitrogen shroud flow rates. The flame with an equivalence ratio of 2.64 exhibits similar trends as flame with equivalence ratio of 2.34, hence results only for equivalence ratio of 2.34 are shown. For this set of experiments the stabilization plate HAB is 32 mm, the

diameter of the center hole is 30 mm and the cooling water flow rate used is 9 g/s. The different nitrogen shroud flow rates used were 550 mg/s, 650 mg/s, 750 mg/s and 850 mg/s.

As shown in Figure 8a the soot volume fraction profiles for the flame with a nitrogen shroud flow rate of 650 mg/s is higher by about 15% from the soot fraction profile for the flame with the reference configuration. For the flame with a shroud flow rate of 750 mg/s, the increase in the soot volume fraction profile compared to the soot volume fraction profile for flame with reference configuration is about 25%. In comparison to the soot volume fraction profile for flame with the reference configuration, there is a significant increase of about 40% in the soot volume fraction profile for flame with a nitrogen shroud flow rate of 850 mg/s.

Figure 8b shows the axial profile of the integrated soot volume fraction; which depicts the combined effect of the change in soot volume fraction and the change in flame shape. There is approximately an increase of 25-30% in the integrated soot volu-

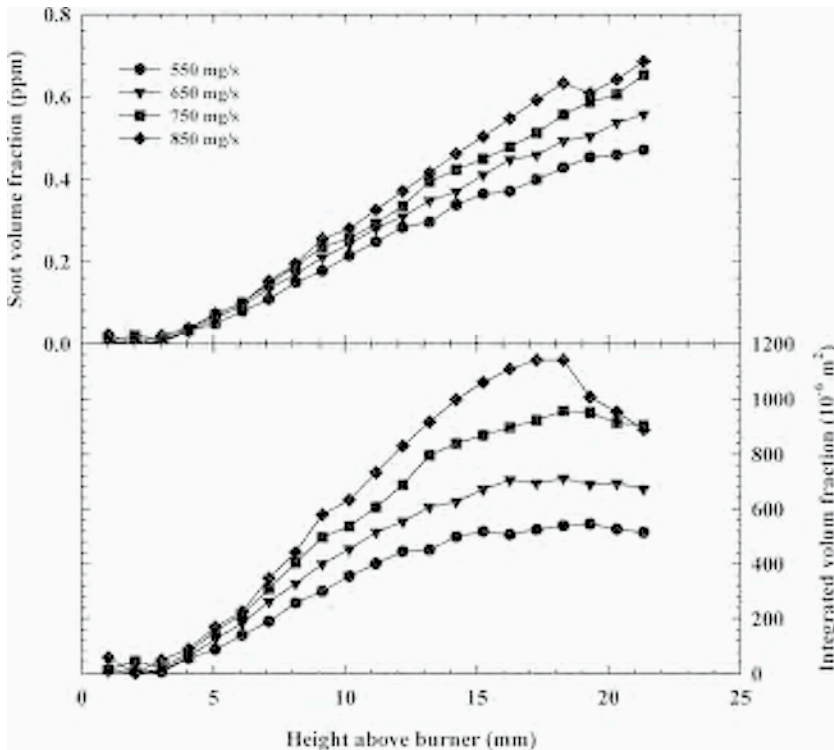


Figure 8. Axial profiles of (a) Soot volume fraction and (b) Integrated soot volume fraction for flame at  $\Phi = 2.34$  and various nitrogen shroud flow rates.

me fraction for each 100 mg/s increase in the shroud nitrogen flow rate. As described earlier, the presence of a re-circulation zone around the flame containing soot can lead to higher soot measurements using a light extinction technique due to its line of sight nature.

The shape of the flames for different nitrogen shroud flow rates is as shown in Figure 9. As seen from Figure 9, the flame shape broadens at the base and narrows at the top with an increase in the nitrogen shroud flow rate. The expansion in flame shape, for a flame with equivalence ratio of 2.34 and shroud flow rates of 650 mg/s, 750 mg/s and 850 mg/s is 7%, 13% and 16%, respectively, compared to the flame shape with the reference configuration. The flame with an equivalence ratio of 2.64 has similar deviations from the reference configuration.

### 3.4. Effect of cooling water flow rate

For this set of experiments, the stabilization plate HAB was 32 mm, diameter of the center hole was 30 mm and nitrogen shroud flow rate used was 550 mg/s. The cooling

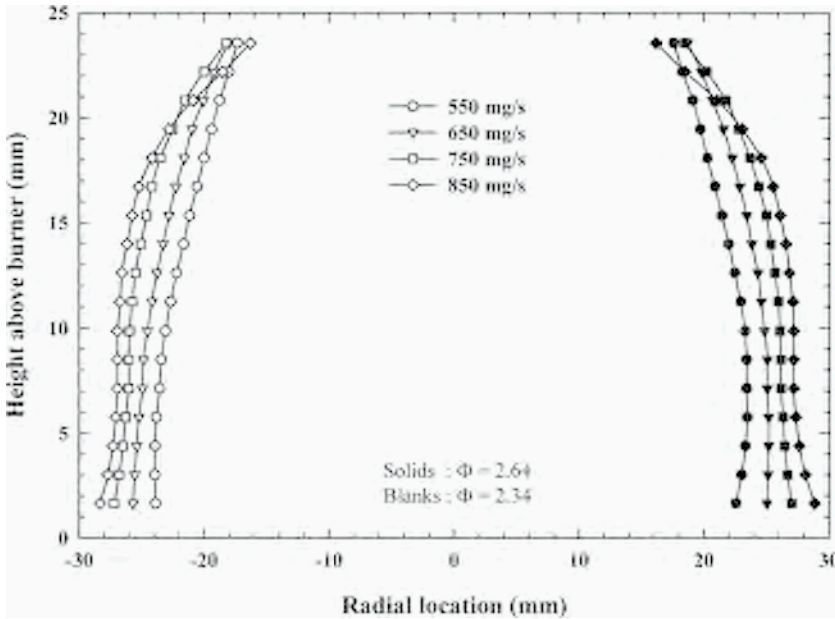


Figure 9. Flame shapes for different nitrogen shroud flow rates.

water flow rates used are 5 g/s, 9 g/s and 15 g/s. The soot volume fraction profiles for the flames at an equivalence ratio of 2.34 and cooling water flow rates of 15 g/s and 5 g/s have less than a 5% deviation from the soot volume fraction profile for the reference flame  $\Phi = 2.34$  (see Figure 3). For the flame with an equivalence ratio of 2.64 and cooling water flow rates of 15 g/s and 5 g/s, the deviation in the soot volume fraction profiles is less than 8%, when compared to the soot volume fraction profile for the reference flame at  $\Phi = 2.64$  (Figure 3). These variations are within the uncertainty of the measurements. The shape of the flame is not affected by the change in the cooling water flow rate. The variations in the shape of the flame with  $\Phi = 2.34$  and  $\Phi = 2.64$  is less than 1%, when compared to the shape of the flame with the reference configuration at  $\Phi = 2.34$  and  $\Phi = 2.64$ .

#### 4. SUMMARY AND CONCLUSIONS

Flame shape and soot volume fractions were studied in laminar premixed ethylene-air flames for different experimental configurations, including those considered by Harris et al. [2, 10, 23], Xu et al. [3, 13] and Axelsson et al. [18]. The main conclusions of the present study are as follows:

1. For the baseline stabilization plate with a center hole diameter of 30 mm changing the HAB of the stabilization plate did not significantly affect the soot volume fraction or the shape of the flame. Neither increasing the diameter of the center hole

- to 40 mm nor changing to a stainless steel wire mesh with a center hole had a significant effect on the soot volume fraction or the flame shape.
2. Using a stabilization plate with a 20 mm diameter hole at the center or a solid stabilization plate affected the stability of the flame. Higher shroud flow rates were required to stabilize the flame in these configurations. These flames as well as the flames with higher shroud flow rates used in conjunction with the stabilization plate with 30 mm diameter center hole showed an increased amount of soot and a significant variation in the flame shape.
  3. It is suggested to use experimental configurations with stabilization plates (plate or screen) with a center hole diameter between 30 and 40 mm, so that the flame can be stabilized with a nitrogen flow rate of less than 650 mg/s. Shroud flow rates above 650 mg/s resulted in large differences in the soot volume fraction as compared to the reference configuration. The results from this study indicate that using the above configuration reduces the variations observed in the measured soot volume fraction due to variations in the HAB location of the stabilization plate or wire mesh for this center hole diameter range.
  4. The possibility of a recirculation zone containing soot near the stabilization plate could introduce errors in the soot volume fractions measured using a light extinction technique. It is therefore suggested that Laser-Induced Incandescence (LII) be used to study the soot field and also investigate where a soot recirculation zone exists.
  5. The shroud flow rate was found to have an effect on the measured soot volume fraction. To better understand this effect, gas temperatures and velocities inside the flame should be measured. These data would determine whether residence time is affected.
  6. The flames that are stabilized without a stabilization plate have the advantage that they have only one control parameter, i.e. the shroud flow. Therefore, these flames may represent the 'simplest' configuration possible and warrant more detailed study.

## ACKNOWLEDGMENTS

The authors acknowledge the financial support for this work provided by the Strategic Environmental Research and Development Program (SERDP), Project PP-1179, under the direction of Dr. Charles Pellerin.

## REFERENCES

1. B. S. Haynes, H. Jander, H. G. Wagner, *Proc. Combust. Inst.* 17 (1979) 1365-1374.
2. S. J. Harris, A. M. Weiner, *Combust. Sci. Technol.* 32 (1983) 267-275.
3. F. Xu, K.-C. Lin, G. M. Faeth, *Combust. Flame* 115 (1998) 195-209.
4. H. Böhm, H. Hesse, B. Jander, J. Lüers, H. Pietscher, G. Wagner, M. Weiss, *Proc. Combust. Inst.* 22 (1988) 403-411.
5. A. D'Alessio, A. Di Lorenzo, F. Beretta, C. Venitozzi, *Proc. Combust. Inst.* 14 (1972) 941-953.

6. R. J. Santoro, T.-W. Lee, B. Quay, T. Ni, *Combust. Flame* 97 (1994) 384-392.
7. R. J. Santoro, R. A. Dobbins, H. G. Semerjian, *Combust. Flame* 51 (1983) 203-218.
8. B. Mewes, J. M. Seitzman, *Appl. Opt.* 36 (1997) 709-717.
9. J. H. Kent, H. Jander, H. G. Wagner, *Proc. Combust. Inst.* 18 (1981) 1117-1126.
10. S. J. Harris, A. M. Weiner, *Combust. Sci. Technol.* 31 (1983) 155-167.
11. A. S. Feitelberg, J. P. Longwell, A. F. Sarofim, *Combust. Flame* 92 (1993) 241-253.
12. K. E. Ritrievi, J. P. Longwell, A. F. Sarofim, *Combust. Flame* 70 (1987) 17-31.
13. F. Xu, P. B. Sunderland, G. M. Faeth, *Combust. Flame* 108 (1997) 471-493.
14. M. S. Tsurikov, K. P. Geigle, V. Kruger, Y. Schneider-Kuhnle, W. Stricker, R. Luckerath, R. Hadeff, M. Aigner, *Combust. Sci. Technol.* 177 (2005) 1835-1862.
15. P. A. Bonczyk, *Fuel* 70 (1991) 1403-1411.
16. T. Hirasawa, C.-J. Sung, Z. Yang, A. Joshi, H. Wang, *Combust. Flame* 139 (2004) 288-299.
17. M. M. Maricq, S. J. Harris, J. J. Szente, *Combust. Flame* 132 (2003) 328-342.
18. B. Axelsson, R. Collin, P.-E. Bengtsson, *Appl. Opt.* 39 (2000), 3683-3690.
19. A. D'Alessio, A. D'Anna, A. D'Orsi, P. Minutolo, R. Barbella, A. Ciajolo, *Proc. Combust. Inst.* 24 (1992) 973-980.
20. M. B. Hamadi, P. Vervisch, A. Coppalle, *Combust. Flame* 68 (1987) 57-67.
21. S. J. Harris, A. M. Weiner, C. C. Ashcraft, *Combust. Flame* 64 (1986) 65-81.
22. T. R. Melton, F. Inal, S. M. Senkan, *Combust. Flame* 121 (2000) 671-678.
23. S. J. Harris, A. M. Weiner, *Combust. Sci. Technol.* 38 (1984) 75-87.
24. K. C. Smyth, C. R. Shaddix, *Combust. Flame* 107 (1996) 314-320.
25. S. S. Iyer, Ph.D. dissertation, The Pennsylvania State University, 2005, pp. 247-251.
26. R. J. Moffat, *Exp. Therm. Fluid Sci.* 1 (1988) 3-17.
27. T. F. Richardson, Ph.D. dissertation, The Pennsylvania State University, 1993, p. 95.
28. R. J. Santoro, T. T. Yeh, J. J. Horvath, H. G. Semerjian, *Combust. Sci. Technol.* 53 (1987) 89-15.



# Epilogue

The Anacapri meeting highlighted current research in fine carbonaceous particles in combustion. The meeting saw the notable progress made towards the mechanism and models of soot formation – a central focus of the 1991 Heidelberg meeting. Attended by a significant number of participants of that earlier meeting, the Anacapri meeting also saw a younger generation of researchers and newcomers. Likewise, new theoretical, modeling, and experimental tools were brought into the discussion. This epilogue highlights the discussions recorded at the meeting, with an emphasis on the challenges facing this community and research opportunities arising from a range of unresolved fundamental questions.

There is a general consensus on the mechanisms and kinetics of the first aromatic ring formation in the combustion of neat fuels. The progress highlights the usefulness of *ab initio* theoretical approaches, including quantum mechanical evaluation of thermodynamic parameters and potential energy of interactions, and solution of the master equation of collision energy transfer for rate parameters. The theoretical advancements are accompanied by progress made in measurements of short-lived chemical intermediates in flow reactors, flames and shock tubes. Molecular beam mass spectrometry (MBMS) again proves to be instrumental to this development. Coupled with multitudes of ionization techniques, notably tunable synchrotron radiation, MBMS is expected to continue to play a critical role in research into the reaction kinetics and mechanisms of multi-ring aromatic hydrocarbons, which remain under constrained. This includes the formation of the second aromatic ring, *i.e.*, naphthalene and its derivatives from resonantly stabilized free radical species, *e.g.*, benzyl. Although the hydrogen-abstraction-carbon-addition (HACA) mechanism has been broadly used in numerical models of soot formation, the role of resonantly stabilized species in the formation of polycyclic aromatic hydrocarbons requires further study.

Kinetics of diesel and jet fuel surrogates presents a significant challenge as well as opportunity. Current research efforts in real fuel chemistry will potentially bring the kinetics and mechanisms of PAH formation to a degree of closure over the next decade. A fundamental approach, paired with some empiricism, will prove to be useful in this endeavor. While it is prohibitive to probe all possible reaction pathways to soot precursors in a real fuel, a well-formulated surrogate strategy can. Measurements of global sooting indices can be useful in this strategy.

Since the Heidelberg meeting, we saw a great deal of attention placed on the mechanism of soot inception. An issue closely related to this problem is the nature and chemical composition of particles just a few nanometers in diameter. Consensus shows that these incipient particles are quite different from mature soot. Incipient particles have been described as liquid-like, having high H/C ratios, low contrasts under electron microscopes and small mass densities. They can have interesting coagulation behaviors, and dehydrogenate as they mature. While many of the key characteristics of particles in that size range have been identified and characterized, a quantitative, kinetic description of the underlying surface and condensed-phase reaction mechanism

and kinetics remains missing. To address this and related questions, physical characterization of young soot particles is only the first step towards a molecular understanding of their properties. At the cluster level it is important to make observations about the chemical nature and composition of these particles. Recent progress in chemical analysis of incipient soot constitutes a major step in this direction.

Considering the different possible routes to particle inception, including PAH stacking/clustering or sequential size growth of PAHs by addition of acetylene and other small species, it is possible that incipient particles can have measurable composition variations from flame to flame. These variations, in turn, can offer valuable insights into the mechanism of particle nucleation. Ultimately, simultaneous measurements of particle size and composition and their time evolution will be instrumental towards a quantitative kinetic knowledge of particle nucleation as well as other particle processes. Current experimental capabilities indeed offer this possibility. These include non-intrusive methods, e.g.,

- UV/Visible extinction and fluorescence,
- small angle X-ray scattering,
- small angle neutron scattering,
- fluorescent polarization anisotropy,
- fluorescent correlation spectroscopy,

intrusive, but online methods, e.g.,

- nano-scanning mobility particle sizing,
- photo/thermo-ionization particle mass spectrometry,

and intrusive, offline techniques, e.g.,

- atomic force microscopy, scanning tunneling microscopy and electron microscopy,
- size exclusion chromatography;
- laser desorption mass spectrometry;
- Fourier transform infrared spectroscopy,
- surface enhanced Raman spectroscopy.

Meaningful progress, leading to a quantitative description of particle nucleation, can be made most effectively through a comprehensive experimental approach. In this approach, the size and composition measurements are accompanied by a careful characterization of the detailed flame properties, including the flame boundary conditions, species and particle time and temperature histories. Recognizing that growing soot may be very reactive and its properties may be governed by a range of flame processes, soot extracted from the flame may undergo chemical and physical transformation in ambient air before offline characterization. To this end, a systematic examination of this transformation would be very useful to transform the various offline techniques into the realm of quantitative characterization.

Nano-Organic Carbons (NOCs) are ubiquitously found in flames. UV absorption suggested that NOCs may exist below the sooting threshold. What remain inconclusive are the fundamental cause for their occurrence and their relation to primary soot. While NOCs can provide an alternative pathway to larger structures or primary soot, they also can be the consequences of persistent particle nucleation and aerosol dyna-

mics, which invariably produce bimodal size distributions. Suggestions were made that NOCs have small sticking probabilities, and hence, long lifetimes in flames. Theoretical evidence seems to support this notion. Nanoparticles often bounce upon collision, especially when their surfaces are saturated with hydrogen. Sticking probability can be a strong function of the particle/cluster structure. A less considered factor is that steady-state kinetics, in which NOCs are continuously nucleated out of the gas phase, but they are quickly destroyed by coagulating with existing soot particles, can also account for the lack of size variations observed for these particles. These different perspectives are reflected by the use of different terminologies for the ultrafine particles. Nucleation-mode particles, persistent nuclei, and bimodal-tail particles have been used to describe particles similar to NOCs.

There are significant opportunities that exist to address the question of soot carbonization. From the relatively hydrogen-rich PAHs to hydrogen-poor mature soot, dehydrogenation must occur, but the exact kinetic process and the chemical transformation in the particles that accompanies dehydrogenation have eluded us for quite a long time. The observation that incipient soot is more hydrogen-rich than previously thought shows this process to be gradual. It takes place during particle mass and size growth. Dehydrogenation may compete with hydrogenation that can occur during mass growth, depending on the conditions of the flame. Hence the C/H ratio of soot can vary widely in different flame environments and for different particle time-temperature histories. For this reason, it is important to keep in mind that the observations about the C/H ratio and other properties of young, primary soot may not be generalized from one flame to another.

The kinetics of particle carbonization is related, at least in part, to the primary particle size typically found in soot aggregates – the particles must solidify to an extent that they will not coalesce into each other before aggregates can form. An alternative and perhaps parallel explanation exists in the framework of the HACA mechanism. It views the characteristic size of primary particles (e.g., 20-50 nm) as a consequence of the surface reaction and aerosol dynamics coupled with the need for hydrogen atoms to initiate surface hydrogen abstraction for subsequent carbon addition. The latter is indeed supported by experimental observations of diffusion flames in which the soot surface-reaction activity may be re-initiated when hydrogen atom is “injected.”

Soot oxidation remains to be an important problem, especially for practical combustors. In comparison to the formation of soot, surprisingly less work is done on its oxidation. In terms of mass reduction, the kinetic parameters of soot oxidation by  $O_2$ , OH and O are quite well established, but depending on the conditions of the flame and initial soot material and size, the oxidation can lead to a reduction of particle number density or a number increase, depending on whether the particle fragments. A complete kinetic description of the competition between the two cases presents a notable opportunity that can enhance the predictive accuracy of soot emission from diesel engines and gas turbines.

Since the Heidelberg meeting, significant progresses have been made towards quantitative prediction of soot mass. Solution methods of aerosol dynamics are robust, to an extent that the evolution of particle size distribution function, including the production of aggregates may be calculated. These solution methods and the underlying

models have found their way into the engine design community – indeed an illustration of triumph of a fundamental science-based approach to an exceedingly complex engineering problem. Existing kinetic models of soot formation generally consider soot nucleation to start from the interactions of two PAH molecules, but the underlying mechanism may be separated into two limiting cases – one that involves PAH stacking and the other through sequential reactions of PAHs with small hydrocarbon species. Particle mass and size growth follows, involving coagulation, PAH surface condensation, surface reactions and oxidation in much the same way as those discussed at the Heidelberg meeting. The surface reaction model remains to be based on the HACA mechanism. More recent advances include the simulation of aggregate formation, detailed particle size distribution, and the evolution of the C/H ratio in soot.

Questions have been raised regarding the sensitivity of soot mass to the nucleation rate. The consensus is, as long as a critical number of nuclei are produced, soot mass is insensitive to the exact rate of nucleation and perhaps the nucleation mechanism even. However, if the underlying question is about the toxicity, environmental impact and combustor performance, as discussed in the Overview section of this book, we will need to have the ability to predict the particle size distribution and chemical composition. Given the experimental evidence that NOCs and young soot particles can have chemical compositions quite different from those of mature soot, surface reaction mechanism and the kinetic parameters may be affected also by the chemical composition and its evolution. Hence, future modeling efforts may have to consider this effect in particle nucleation, growth and oxidation.

Experimental knowledge about particle size evolution and chemical composition is central to the aforementioned modeling effort. On-the-fly chemical composition determination will be critical to its progress. Ideally, measurements should be made in such a way that one can formulate a map of structure, composition and reactivity relations for a wide range of kinetic processes, including nucleation, coagulation, surface reactions, oxidation, carbonization and aggregation. Towards this goal, challenges in flame experiments include data accuracy, reproducibility, and comparison of results obtained from different techniques. Uncertainty quantification is critical to quantitative understanding of kinetic processes of soot formation. It is known and reinforced through the discussion at the meeting that flat flame data could vary widely even if the burner is operated under marginally different setups. Hence, standardizing burners and operating conditions should be pursued in future research. Reproducibility of flame experiments from one laboratory to another is an important element to achieve progress. In this way, a wide range of diagnostic tools may be applied to the same flames. Measurements could be compared with each other and common questions could be answered for a common set of flames.

The modeling community is facing the challenge equally in model intercomparisons. The vast number of kinetic parameters and model assumptions makes model evaluation a difficult task. The wealth of information already available or to be generated poses a significant challenge about optimal utilization of the information and the community resources. In this regard, PrImE ([www.PrImeKinetics.org](http://www.PrImeKinetics.org)) is an exceedingly welcome development. The concept and application of PrImE not only offers a venue for coordinating experimental, theoretical and modeling efforts, it can reduce the occurrence of duplicating and unnecessarily competing efforts – a notable advan-

tage for this research community given the magnitude of the problems it needs to solve and the limited resources available to it.

It is perceivable that in the next decade the kinetic models of soot formation and oxidation will be able to provide predictions for particle size distribution, surface area, chemical composition, C/H and C/O ratios, and active surface sites in addition to soot mass and volume fraction. Ultimately these models will evolve into tools that can predict toxicity, optical properties, and environmental impacts of combustion-generated fine carbonaceous particles directly.



## Author index

Abid, A.	367	Hansen, N.	79
Agafonov, G.L.	385	Happold, J.	277
Aigner, M.	277	Harding, L.B.	49
Awan, I.A.	55	Hentschel, J.	589
Balthasar, M.	663	Herdman, J.D.	259
Blanquart, G.	437	Hewson, J.C.	571
Bockhorn, H.	589	Iyer, S.	697
Brezinsky, K.	75	Kahandawala, M.	173
Brocklehurst, H.	689	Kasper, T.	79
Bruno, A.	231	Kennedy, I.	1
Celnik, M.S.	413	Kent, J.H.	605
Charwath, M.	589	Kerstein, A.R.	571
Chaumeix, N.	163	Klippenstein, S.J.	49
Chung, S.H.	321	Kohse-Höinghaus, K.	79
Ciajolo, A.	333	Kraft, M.	413
Colket, M.B.	483, 637	Kubo, S.	651
Connelly, B.C.	637	Kumfer, B.	1
Cool, T.A.	79	Lall, A.A.	537
Corporan, E.	173	Lee, S.-Y.	697
D'Alessio, A.	205, 231	Lemaire, R.	619
D'Anna, A.	205, 231, 289	Lighty, J.S.	523
Darius, D.	163	Lindstedt, R.P.	499
de Ris, J.L.	489	Linevsky, M.J.	697
Desgroux, P.	619	Litzinger, T.A.	697
DeWitt, M.	173	Long, M.B.	637
Dobbins, R.A.	189	Magnusson, I.	663
Eddings, E.G.	137	Manion, J.A.	55
Eismark, J.	663	Marchal, C.	465
Fox, R.O.	571	Maricq, M.M.	347
Frenklach, M.	247	Markaki, V.	499
Georgievskii, Y.	49	Marquetand, J.	405
Gothaniya, G.	697	Mauss, F.	465
Grotheer, H.-H.	277	Mayne, C.L.	137
Hall, R.J.	637	McEnally, C.S.	125
		McGivern, W.S.	55
		Menon, A.V.	697
		Miller, J.A.	49

Miller, J.H.	259	Shaddix, C.R.	17
Minutolo, P.	205, 231	Sidhu, S.	173
Moréac, G.	465	Sivaramakrishnan, R.	75
Mosbach, S.	413	Smirnov, V.N.	385
		Smooke, M.D.	637
Naydenova, I.	385, 405	Struckmeier, U.	79
Netzell, K.	465	Sunderland, P.B.	489
		Suntz, R.	589
Oßwald, P.	79		
		Therssen, E.	619
Paillard, C.	163	Tieszen, S.R.	571
Pauwels, J.F.	619	Tsang, W.	55
Pfefferle, L.D.	125		
Pitsch, H.	437	Violi, A.	321
Pugmire, R.J.	137	Vlasov, P.A.	385
Qi, F.	79	Wang, H.	367
		Wang, J.	79
Raj, A.	413	Warnatz, J.	385, 405
Raman, A.	75	West, R.H.	413
Ranzi, E.	99	Westmoreland, P.R.	37, 79
Ricks, A.J.	571	Whitesides, R.	247
Robinson, R.K.	499	Williams, T.C.	17
Romano, V.	523	Wong, D.	247
Santoro, R.J.	697	Yang, Z.	137
Sarofim, A.F.	137, 523		
Schuetz, C.A.	247	Zachariah, M.R.	537
Sgro, L.A.	205, 231	Zhang, H.R.	137

# Sponsors

National Science Foundation, USA  
Air Force Research Laboratory, USA  
Air Force Office of Scientific Research, USA  
CNR Dipartimento Energia e Trasporti, Italy  
United Technologies Research Center, USA  
AMRA Analysis and Monitoring of Environmental Risk, Italy  
ENI, Italy  
Riello Burners, Italy  
Volvo, Sweden  
ENEA, Italy  
Rolls-Royce, UK

ISBN: 978-3-86644-441-6

[www.uvka.de](http://www.uvka.de)

